

GUSTAVO ROQUE DA SILVA ASSI

PRINCÍPIOS FÍSICOS DA SUPRESSÃO DE  
VIBRAÇÕES INDUZIDAS PELO ESCOAMENTO  
EM CORPOS ROMBUDOS

São Paulo  
2021

GUSTAVO ROQUE DA SILVA ASSI

**PRINCÍPIOS FÍSICOS DA SUPRESSÃO DE  
VIBRAÇÕES INDUZIDAS PELO ESCOAMENTO  
EM CORPOS ROMBUDOS**

Resenha Crítica da Obra apresentada à  
Escola Politécnica da Universidade de São  
Paulo como requisito para obtenção do  
Título de Professor Livre Docente junto  
ao Departamento de Engenharia Naval e  
Oceânica.



GUSTAVO ROQUE DA SILVA ASSI

**PRINCÍPIOS FÍSICOS DA SUPRESSÃO DE  
VIBRAÇÕES INDUZIDAS PELO ESCOAMENTO  
EM CORPOS ROMBUDOS**

Resenha Crítica da Obra apresentada à  
Escola Politécnica da Universidade de São  
Paulo como requisito para obtenção do  
Título de Professor Livre Docente junto  
ao Departamento de Engenharia Naval e  
Oceânica.

Área de Concentração:

Hidrodinâmica de Sistemas Oceânicos

Aos meus filhos,  
Cecília e Daniel

# AGRADECIMENTOS

Sou grato a muitos colegas, alunos e amigos que participaram, direta ou indiretamente, do meu esforço de pesquisa na última década. Certamente não conseguirei incluir todos nominalmente neste agradecimento, mas escolho o Prof. Bruno Carmo e o Prof. André Mendes, mais que amigos e colegas, para representar a todos. Ao longo da minha carreira acadêmica tive excelentes orientadores que, além de instrução, me ofereceram inspiração. Sou grato à mentoria dos professores Peter Bearman, Celso Pesce, J. Aranha, Kazuo Nishimoto e Oscar Augusto. Em especial, agradeço a confiança, amizade e companheirismo do Prof. Julio Meneghini desde nosso inesquecível primeiro contato em 2001.

Agradeço também o apoio dos meus colegas docentes do Departamento de Engenharia Naval e Oceânica da EPUSP, representado pelo Prof. Bernardo Andrade, incentivador e bom amigo. Sem o apoio das equipes técnicas e administrativas do PNV, Núcleo de Dinâmica e Fluidos e do Research Centre for Gas Innovation da USP o trabalho teria sido muito mais difícil, senão impossível. Agradeço aos amigos Lucia Messa, Lânia Camillo e Douglas Silva por representarem a todos.

Sou grato ao CNPq, CAPES, FAPESP, ANP e Marinha do Brasil pelas bolsas de pesquisa no Brasil e no exterior que financiaram projetos meus e dos meus alunos. Lembro-me do Prof. Richard Willden e do Prof. Mory Gharib, que me receberam para visitas acadêmicas na University of Oxford e no California Institute of Technology, respectivamente.

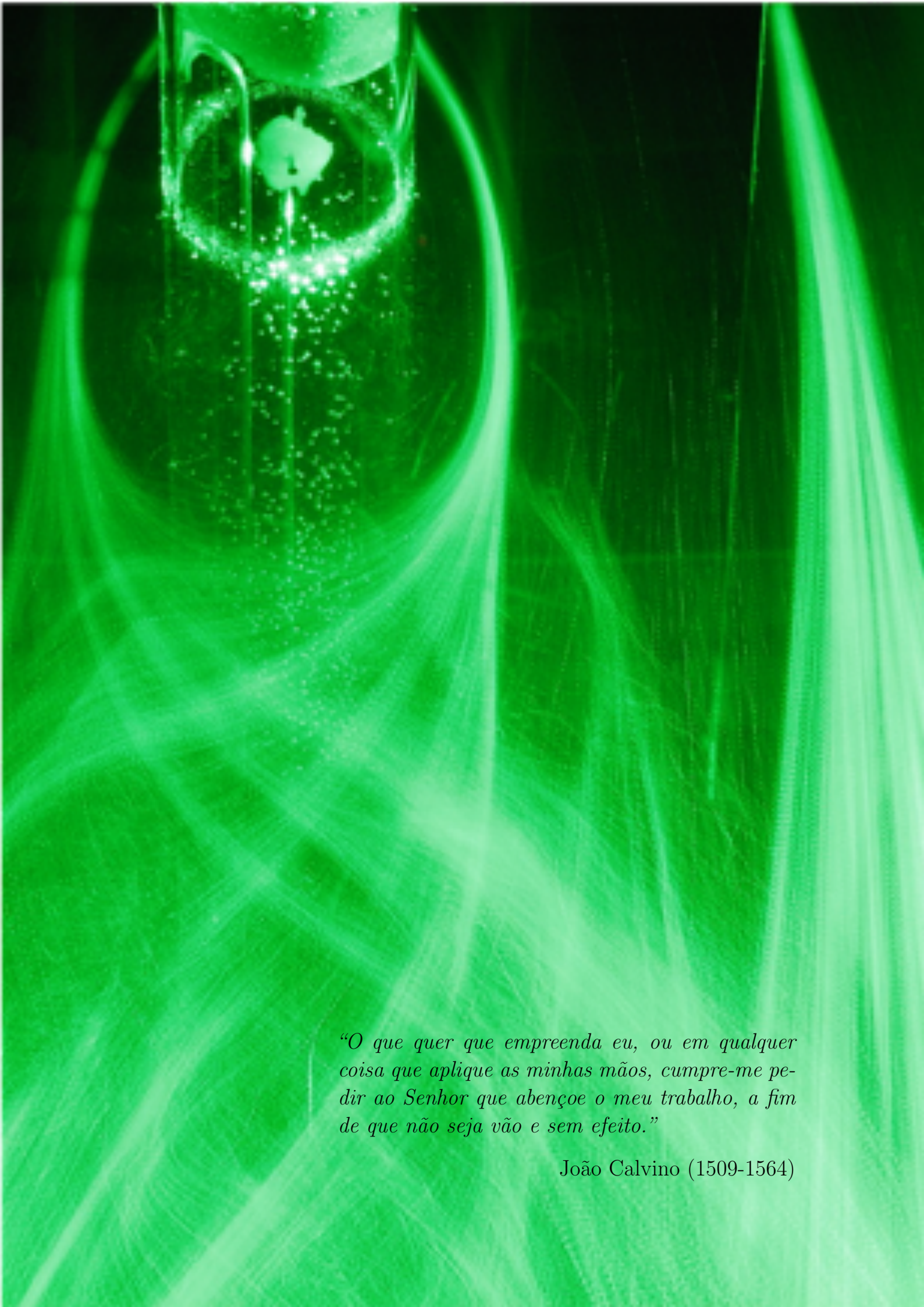
O trabalho de desenvolvimento tecnológico não teria frutos se não fosse pelo interesse das empresas que atuam no setor. Por isso, sou grato ao apoio da Petrobras, Shell, Repsol, BP, BG, Lankhorst, Voith, Oxiten e outras empresas com que trabalhamos no período.

Este texto resume um genuíno esforço coletivo de pesquisa desenvolvido pelos muitos alunos orientados de trabalho de formatura, iniciação científica, mestrado e doutorado. Em especial, sou profundamente grato aos alunos de pós-graduação que depositaram sua confiança em minha supervisão: Angelo A. N. Silva, Daniel Kantorowitz, Emerson B. Santana, Felipe S. Castro, Fernando M. Almeida, Filipe F. Buscariolo, Gabriel B. Martins, Guilherme F. Giachero, Gustavo Bochio, Gustavo G. Gomes, Hélio C. Silva Jr, Icaro A. Carvalho, José Rodolfo Chreim, Lucas M. Padial, Mariana Silva-Ortega, Murilo M. Cicolin, Paulo H. N. Silva, Rafael Salles, Raiza O. P. Silva, Ricardo Sampaio, Robin L. G. Basso, e Rubens C. Silva.

Sou grato aos irmãos da Associação Brasileira de Cristãos na Ciência, que têm me ajudado a enxergar com outro brilho a interação sadia entre os campos da Ciência, Tecnologia e Fé Cristã. Tornaram-se uma nova família com quem encontro grande prazer no serviço.

Agradeço à minha esposa Lilian e aos meus filhos, Cecília e Daniel, pela compreensão e apoio permanentes nesta carreira. Seu amor é fonte de grande motivação e alegria. Sou também grato aos meus pais, irmãos e cunhados pelo incentivo constante.

Finalmente, sou grato a Deus por nos encher de alegria e satisfação quando nos dedicamos à investigação da sua Criação. A Ele toda a glória.



*“O que quer que empreenda eu, ou em qualquer coisa que aplique as minhas mãos, cumpre-me pedir ao Senhor que abençoe o meu trabalho, a fim de que não seja vão e sem efeito.”*

João Calvino (1509-1564)

# SUMÁRIO

|   |           |
|---|-----------|
| <b>Apresentação</b>   | <b>8</b>  |
| <b>Parte I: RESENHA CRÍTICA DA OBRA</b>                         | <b>10</b> |
| <b>1 Introdução</b>   | <b>11</b> |
| 1.1 Desenvolvimento científico e tecnológico . . . . .          | 13        |
| 1.2 Objetivos desta linha de pesquisa . . . . .                 | 15        |
| <b>2 Fenômenos de interação fluido-estrutura</b>                | <b>17</b> |
| 2.1 Geração e desprendimento de vórtices . . . . .              | 17        |
| 2.2 Vibração induzida por vórtices (VIV) . . . . .              | 18        |
| 2.3 Vibração induzida pela esteira (WIV) . . . . .              | 20        |
| 2.4 Galloping . . . . .   | 23        |
| <b>3 Supressores bidimensionais</b>                             | <b>25</b> |
| 3.1 Supressores de VIV de placas pivotantes . . . . .           | 25        |
| 3.1.1 Placa plana . . . . .                                     | 26        |
| 3.1.2 Fairings . . . . .  | 27        |
| 3.1.3 Placas inclinadas . . . . .                               | 29        |
| 3.1.4 Placas paralelas . . . . .                                | 30        |
| 3.1.5 Placas oblíquas . . . . .                                 | 31        |
| 3.2 Supressores de WIV de placas pivotantes . . . . .           | 33        |
| 3.3 Galloping de placas planas . . . . .                        | 35        |
| 3.4 Supressores de cilindrinhos de controle rotativos . . . . . | 38        |
| <b>4 Supressores tridimensionais</b>                            | <b>43</b> |

|          |  |           |
|----------|--|-----------|
| 4.1      | Strakes helicoidais . . . . .                                    | 45        |
| 4.1.1    | Strakes convencionais . . . . .                                  | 45        |
| 4.1.2    | Strakes não convencionais . . . . .                              | 47        |
| 4.2      | Malhas permeáveis . . . . .                                      | 50        |
| 4.2.1    | Ventilated Trousers . . . . .                                    | 50        |
| 4.2.2    | Outras malhas . . . . .  | 52        |
| 4.3      | Cilindro ondulado e elíptico . . . . .                           | 53        |
| <b>5</b> | <b>Conclusão</b>   | <b>56</b> |
|          | <b>Parte II: ATIVIDADES CORRELATAS</b>                           | <b>58</b> |
| <b>6</b> | <b>Equipamentos e métodos experimentais</b>                      | <b>59</b> |
| 6.1      | Canal de Água Recirculante . . . . .                             | 59        |
| 6.2      | Canal Recirculante de Baixo Número de Reynolds . . . . .         | 61        |
| 6.3      | Bases elásticas . . . . .  | 62        |
| <b>7</b> | <b>Além da técnica</b>   | <b>68</b> |
| 7.1      | Difusão do conhecimento . . . . .                                | 68        |
| 7.2      | Ensino de engenharia . . . . .                                   | 69        |
| 7.3      | Filosofia da tecnologia . . . . .                                | 71        |
|          | <b>Referências Bibliográficas</b>                                | <b>73</b> |
|          | <b>Parte III: ANEXOS – ARTIGOS PUBLICADOS EM PERIÓDICOS</b>      | <b>77</b> |
| A.1      | Assi, Meneghini, Aranha, Bearman, and Casaprima (2006) . . . . . | 78        |
| A.2      | Assi, Bearman, and Kitney (2009) . . . . .                       | 87        |
| A.3      | Assi, Bearman, and Meneghini (2010b) . . . . .                   | 97        |
| A.4      | Assi, Bearman, Kitney, and Tognarelli (2010a) . . . . .          | 134       |
| A.5      | Carmo, Assi, and Meneghini (2013) . . . . .                      | 147       |

|      |  |     |
|------|--|-----|
| A.6  | Assi, Bearman, Carmo, Meneghini, Sherwin, and Willden (2013) | 157 |
| A.7  | Assi (2014a)   | 193 |
| A.8  | Assi (2014b)   | 204 |
| A.9  | Assi, Srinil, Freire, and Korkischko (2014a)                 | 222 |
| A.10 | Assi, Franco, and Vestri (2014c)                             | 237 |
| A.11 | Assi, Bearman, and Tognarelli (2014b)                        | 246 |
| A.12 | Assi and Bearman (2015)                                      | 257 |
| A.13 | Cicolin and Assi (2017a)                                     | 275 |
| A.14 | Silva-Ortega and Assi (2017a)                                | 287 |
| A.15 | Silva-Ortega and Assi (2017b)                                | 296 |
| A.16 | Cicolin and Assi (2017b)                                     | 308 |
| A.17 | Silva-Ortega and Assi (2018)                                 | 316 |
| A.18 | Assi and Bearman (2018)                                      | 324 |
| A.19 | Assi, Orselli, and Silva-Ortega (2019)                       | 345 |
| A.20 | Buscariolo, Assi, and Sherwin (2021)                         | 357 |
| A.21 | Assi, Crespi, and Gharib (2021)                              | 378 |
| A.22 | Cicolin, Buxton, Assi, and Bearman (2021)                    | 403 |

## APRESENTAÇÃO

Este texto apresenta uma resenha autocrítica sobre a obra de pesquisa do Prof. Dr. Gustavo Roque da Silva Assi, docente do Departamento de Engenharia Naval e Oceânica da Escola Politécnica da Universidade de São Paulo (EPUSP), desenvolvida principalmente nos últimos 10 anos, no tema de supressão das vibrações induzidas pelo escoamento (VIE) em corpos rombudos.

O material aqui reunido é fruto de um esforço coletivo de muitos alunos de graduação, pós-graduação e pesquisadores que trabalharam sob nossa orientação no grupo de pesquisa na USP. O texto está dividido em três partes:

(Parte I) Inicialmente, apresentamos rapidamente a motivação tecnológica que nos aproximou deste tópico de estudos, a saber, a tecnologia de exploração *offshore* em águas profundas e ultraprofundas. Em seguida, oferecemos uma breve explicação de quatro fenômenos que governam a física dos problemas deste assunto: geração e desprendimento de vórtices, vibração induzida por vórtices (VIV), vibração induzida pela esteira (WIV) e *galloping*.

Os dois capítulos seguintes resumem os principais resultados obtidos no desenvolvimento de supressores de VIE de corpos rombudos. A maioria deles foi fruto de investigação experimental em escala reduzida, sendo esta uma temática que permeia todo o texto. Os supressores discutidos são agrupados quanto à natureza do princípio físico de supressão em supressores bidimensionais e tridimensionais. Nossa intenção não foi sermos exaustivos na descrição ou comparação dos resultados, mas mostrar ao leitor como esta linha de pesquisa se desenvolveu naturalmente ao longo da última década, de modo que a compreensão dos fenômenos levou ao desenvolvimento de outros supressores, a assim sucessivamente.

(Parte II) Tão importante quanto os resultados do desenvolvimento de supressores foram os equipamentos, técnicas e métodos experimentais desenvolvidos ao longo destes anos. Este patrimônio permitiu e permitirá o desenvolvimento de muitas outras áreas de pesquisa experimental que não estão relatadas aqui. Em um primeiro capítulo destacamos os canais recirculantes como as principais ferramentas utilizadas nos experimentos, além do desenvolvimento de bases elásticas. Aproveitamos a oportunidade para registrar nesta



resenha a nossa opinião sobre três aspectos muito importantes que foram elaborados pela experiência paralelamente ao avanço técnico do pesquisador, a saber: difusão do conhecimento, ensino de engenharia e filosofia da tecnologia.

(Parte III) Na terceira e última parte, que reúne a obra literária propriamente dita, anexamos os 22 artigos completos publicados pelo autor em periódicos internacionais relacionados com o tema desta resenha. Não anexamos artigos publicados em anais de conferência por brevidade e por entender que o conteúdo deles está mais bem consolidado nas publicações de periódicos especializados. Esta coletânea representa a síntese do esforço de pesquisa reconhecido pela comunidade científica.

# PARTE I

## RESENHA CRÍTICA DA OBRA

# 1 INTRODUÇÃO

*“Quando você transforma seu hobby em trabalho, tem tempo para um novo hobby.”*

-- Egbert Schuurman (1937-)

Vibração induzida pelo escoamento (VIE) é um dos problemas mais instigantes que une a dinâmica dos fluidos à dinâmica das estruturas no campo que chamamos de interação fluido-estrutura. É um problema tão rico em fenômenos fluídoelásticos que facilmente desperta o interesse e a curiosidade de pesquisadores atraídos apenas pelo prazer em estudá-lo (neste grupo nos incluímos). Porém, o desafio das VIE vai além da curiosidade científica e se apresenta em diversas aplicações na engenharia, da oscilação do tabuleiro de grandes pontes estaiadas às pequenas instabilidades na válvula tricúspide de corações artificiais.

Mas foi no contexto da exploração oceânica que as VIE se tornaram um tópico de pesquisa e desenvolvimento na indústria e na academia brasileiras. A descoberta de óleo e gás nas águas profundas da costa do Brasil (década de 1970), seguida pela descoberta dos reservatório do pré-sal em águas ultraprofundas (década de 2000) alavancou o campo de desenvolvimento científico e tecnológico de nosso país, desafiando a indústria brasileira ao patamar de líder mundial em exploração nestas condições.

Desde o início das explorações *offshore*, e muito mais agora com a maturidade dos campos do pré-sal, o problema das VIE sempre esteve presente. Seja nas linhas de ancoragem, nos cabos umbilicais, nas longas tubulações de produção ou nas colunas de perfuração, os sistemas submarinos são compostos por diversas estruturas esbeltas e de geometria rombuda sujeitas à correnteza e outras intempéries marinhas. A figura 1 ilustra a variedade de sistemas oceânicos flutuantes com seus inúmeros *risers*, linhas e tendões submersos.

Destaque deve ser dado aos *risers* de produção, longas tubulações de aço (ou mesmo tubos flexíveis com várias camadas poliméricas e malhas estruturais de reforço) instaladas para levar óleo, gás e água do poço de produção no leito marinho para a plataforma flutuante na superfície. Pois um campo de exploração *offshore* é repleto de dezenas de *risers* com diferentes funções e restrições. Estas estruturas esbeltas e muito longas se

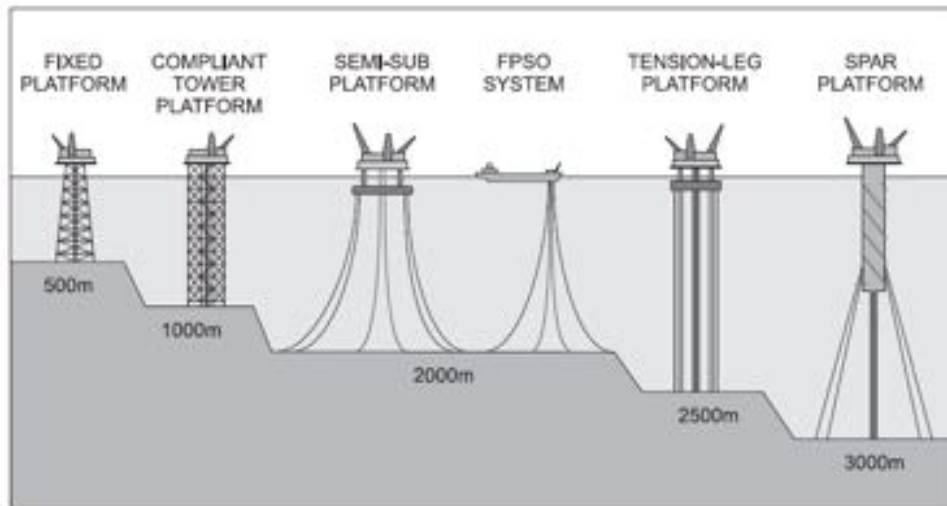


Figura 1: Tipos de plataformas de petróleo onde se verifica a presença de elementos cilíndricos, como cabos e dutos, sob a ação da corrente marítima (Assi, 2009).

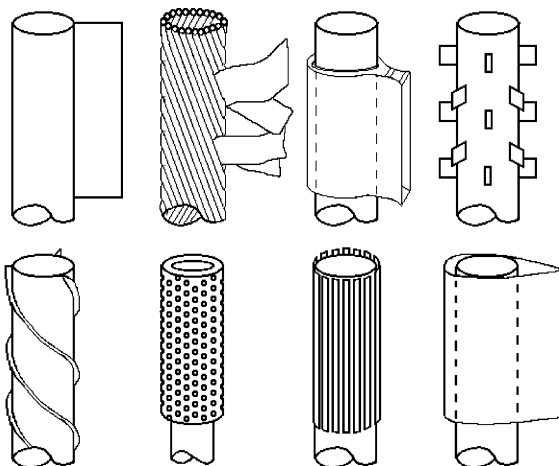


Figura 2: Exemplos de supressores de VIE. Reproduzido de Blevins (1990).

comportam como linhas flexíveis, desafiando pesquisadores que enxergam o problema do ponto de vista da integridade estrutural (Pesce, 1997; Martins, 2000). Como o próprio nome indica, as vibrações destas estruturas são induzidas pelo escoamento externo ao gerar carregamento cíclico ao redor destes corpos elásticos e de geometria rombuda. Assim, o problema requer ainda outro olhar nesta interface da interação fluido-estrutura, justamente sob a perspectiva do escoamento (Meneghini, 2002).

Esta linha de pesquisa enquadra-se neste contexto, alinhada à segunda perspectiva, a do escoamento. Por princípio, uma maneira de mitigar as vibrações é alterar o comportamento do escoamento de modo a reduzir (ou eliminar) a fonte da excitação. Dispositivos supressores de VIE podem ser instalados nestes corpos com esta finalidade, tomando di-

versas formas como os exemplos ilustrado na figura 2. Portanto, nosso objetivo é duplo: desenvolver supressores que tenham aplicação na indústria *offshore*; e, ao mesmo tempo, revelar a beleza e a complexidade dos mecanismos físicos por detrás destes fenômenos fluídoelásticos que tanto nos fascinam.

## 1.1 Desenvolvimento científico e tecnológico

O nosso envolvimento com o desenvolvimento de supressores de VIE começou através de um projeto tecnológico solicitado pela BP (British Petroleum – operadora britânica do setor de energia) enquanto estávamos no programa de doutorado em Engenharia Aero-náutica no Imperial College London. A empresa manifestou o interesse de investigar o comportamento dinâmico de *fairings* e outros supressores desta família de sistemas pivotantes (ou *free-to-rotate*), já que pouco se conhecia do comportamento dinâmico destes sistemas.

Nossos estudos com modelos em escala reduzida em condições controladas de laboratório permitiram a identificação dos principais parâmetros que governam a dinâmica de sistemas desta natureza, abrindo caminho para uma longa jornada de investigação e desenvolvimento de novas geometrias de supressores pivotantes. Este esforço de pesquisa resultou na publicação de uma série de artigos científicos, com forte aplicação tecnológica, explicando os fundamentos e os mecanismos físicos do comportamento destes sistemas. Tais artigos, que serão citados ao longo deste texto, atraíram a atenção tanto dos operadores quanto dos fabricantes de supressores da indústria *offshore*, além da comunidade científica que estuda o tema.

A pesquisa continuou e se expandiu com nosso retorno à Universidade de São Paulo em 2010, agora como docente do Departamento de Engenharia Naval e Oceânica da Escola Politécnica. No ano de 2011 fomos contemplados com um financiamento regular da FAPESP (2011/00205-6), permitindo a construção de uma bancada de testes, além de um novo canal recirculante para experimentos com escoamentos a baixo número de Reynolds (apresentado no capítulo 6).

Estudamos uma série de supressores dessa família de sistemas pivotantes (livres para rotacionar), com foco na otimização geométrica para mitigação de vibrações e redução de arrasto. Esta série de supressores envolvia sistemas com placas planas, posicionadas de diversas formas à jusante de um cilindro. As placas, solidárias umas às outras, podiam rotacionar livremente ao redor do cilindro, sem que houvesse rigidez torcional

restringindo seu movimento. O atrito rotacional – parâmetro cuja importância foi identificada nos primeiros estudos fundamentais ainda em Londres – sempre foi mantido o mais baixo possível. Os testes com supressores compostos por placas planas variaram entre configurações com placas paralelas, oblíquas e conjuntos com três ou mais placas associadas. Os resultados mostraram que algumas configurações apresentavam instabilidades fluídoelásticas, enquanto outras mitigavam as vibrações com eficiente redução de arrasto.

As técnicas de visualização do escoamento e medição de campos de velocidades foram extremamente úteis para a compreensão dos mecanismos envolvidos. Desde o início desta linha de pesquisa, percebemos que compreender a topologia do escoamento separado interagindo com o cilindro e o supressor na região da esteira próxima era fundamental para se entender o mecanismo físico em ação. Desenvolvemos técnicas de PIV (*particle-image velocimetry*) que nos permitiram obter informações detalhadas dos campos de velocidade e vorticidade ao redor das pequenas estruturas dos supressores, revelando a complexa interação do escoamento turbulento com a dinâmica dos supressores. Também desenvolvemos técnicas de visualização de escoamento com tintura fluorescente e, principalmente, com emissão de bolhas de hidrogênio por eletrólise da água, que permitiram a identificação das estruturas dominantes no escoamento separado, tanto no plano bidimensional quanto no espaço tridimensional ao longo do comprimento do cilindro.

Vale destacar que as técnicas citadas acima foram aprimoradas ao longo da última década e renderam imagens e vídeos de valor científico e pedagógico. Diversos alunos orientados foram instruídos nestas técnicas e muito do material produzido foi utilizado nas aulas do curso de pós-graduação de Interação Fluido-Estrutura, além de cursos de graduação. Animações e vídeos publicados e disponibilizados na internet tiveram excelente repercussão e são utilizados por diversos centros de pesquisa do mundo para instrução de seus pesquisadores. Com satisfação, continuamos recebendo mensagens de agradecimento pela disseminação desse material.

A investigação evoluiu naturalmente para outras famílias de supressores, algumas não convencionais, sempre mantendo nosso foco na busca pelos mecanismos físicos por detrás dos fenômenos. Realizamos experimentos com *strakes* helicoidais de geometrias variadas, malhas permeáveis e cilindros ondulados (além de outros que não entraram no recorte final deste texto). O principal método investigativo continuou sendo o experimento com modelos em escala reduzida montados em bases elásticas em um canal de água recirculante, apesar de que simulações numéricas do escoamento também tiveram papel significativo na elucidação dos fenômenos.

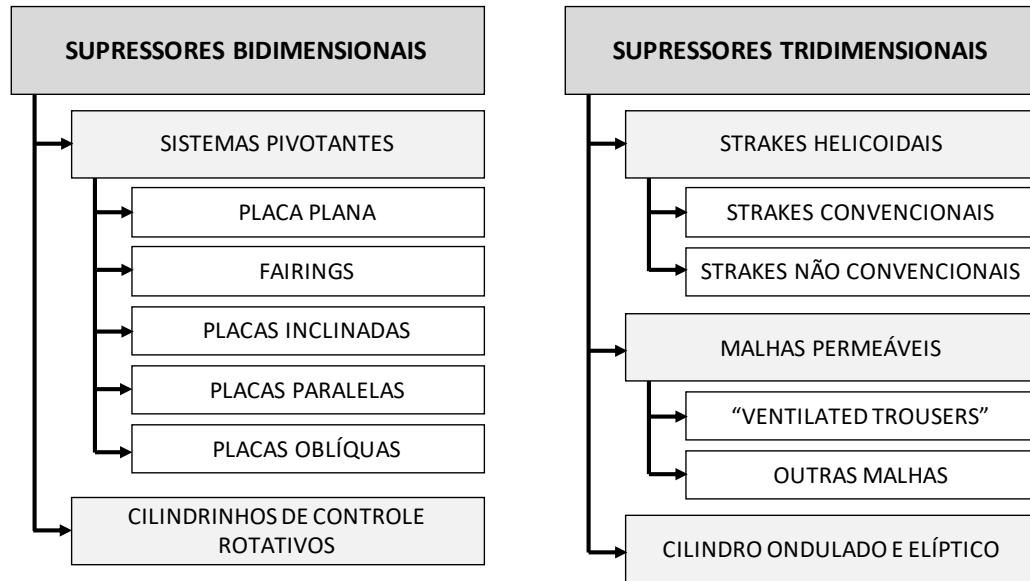


Figura 3: Classificação dos supressores de VIE apresentados neste texto quanto à natureza do mecanismo de supressão.

Podemos classificar os supressores de vibrações induzidas pelo escoamento (VIE) em corpos rombudos em duas categorias relacionadas à natureza do mecanismo de supressão: supressores bidimensionais (apresentados no capítulo 3), e supressores tridimensionais (no capítulo 4). A figura 3 apresenta um diagrama agrupando os supressores discutidos neste texto.

Para antecipar uma conclusão alcançada ao longo de muitos experimentos com supressores bidimensionais e tridimensionais, entendemos que a supressão de VIV com considerável redução de arrasto dificilmente será alcançada por supressores tridimensionais. Para manter as estruturas do escoamento úteis para a atenuação da emissão de vórtices e consequente redução de VIV, os supressores tridimensionais requerem aletas ou outros apêndices que elevam a carga de arrasto. Acreditamos que a melhor eficiência em supressão de VIV e redução de arrasto esteja na categoria dos supressores bidimensionais, aqueles que atuam na origem do mecanismo de formação dos vórtices, impedindo a interação das camadas cisalhantes. Os próximos capítulos apresentarão os resultados que dão suporte a esta conclusão geral.

## 1.2 Objetivos desta linha de pesquisa

Apesar de este texto apresentar os avanços de uma linha de pesquisa genuinamente tecnológica, com forte aplicação para problemas reais da engenharia oceânica, sempre foi do nosso interesse manter viva a investigação científica dos fenômenos. Em outras palavras,

mantivemos um interesse pessoal em estudar os fenômenos físicos por detrás das repostas dinâmicas dos sistemas investigados, sempre em busca de explicações que elucidassem a natureza e o comportamento dos mecanismos identificados.

É premissa deste estudo a ideia de que o conhecimento científico fundamental auxilia no desenvolvimento tecnológico. Portanto, este texto se dedica, especialmente, ao destaque dos mecanismos físicos investigados ao longo desta linha de pesquisa. Assim, seus objetivos gerais sobre os princípios físicos da supressão de vibrações induzidas pelo escoamento em corpos rombudos se resumem em:

1. Desenvolver metodologia experimental para a realização de experimentos com modelos em escala reduzida em condições controladas em laboratório.
2. Aplicar técnicas de medição para caracterizar os mecanismos físicos por detrás dos fenômenos fluidoelásticos.
3. Identificar os parâmetros que governam a dinâmica dos sistemas a fim de promover estudos de otimização.
4. Desenvolver estudos exploratórios com famílias de supressores não convencionais.
5. Aplicar métodos de simulação numérica do escoamento para elucidar os fenômenos hidrodinâmicos associados.
6. Sintetizar e sistematizar o conhecimento adquirido para subsidiar ferramentas de desenvolvimento tecnológico e projeto de sistemas reais.
7. Fornecer informação adequada para subsidiar o desenvolvimento de modelos analíticos e fenomenológicos.
8. Oferecer resultados que sirvam de paradigma para simulações numéricas do escoamento em interação fluido-estrutura.

Antes de destacarmos os principais resultados obtidos da investigação dos supressores, apresentaremos brevemente os principais conceitos dos fenômenos fluidoelásticos mais relevantes para este texto.



## 2 FENÔMENOS DE INTERAÇÃO FLUIDO-ESTRUTURA

*“Aprender é ensinar para alguém aquilo que  
você ainda não sabe.”*

-- Anatol Roshko (1923-2017)

### 2.1 Geração e desprendimento de vórtices

Quando um corpo rombudo (um cilindro, no nosso caso) está exposto a um escoamento transversal incidente, verificamos a formação de uma esteira de vórtices alternados que se desprendem do corpo e são convectados à jusante pelo escoamento. Há um misto de beleza e complexidade neste processo que nos fascina desde o primeiro contato com o fenômeno por volta de 2001.

As camadas limites que se desenvolvem à medida que o escoamento externo percorre o perímetro do cilindro são separadas pelo efeito do gradiente adverso de pressão. Neste momento, a partir dos pontos de separação localizados nos dois lados do cilindro, as camadas ricas de vorticidade se tornam camadas cisalhantes livres, concentrando circulação na região de base do corpo. É nesta região, próximo da face traseira do cilindro, que tem início a interação cíclica das camadas cisalhantes numa verdadeira “dança” governada pelo ritmo de emissão de vórtices.

Gerrard (1966) descreveu este mecanismo de emissão e desprendimento de vórtices, destacando o processo de comunicação entre as camadas cisalhantes que resulta na bela esteira de vórtices de von Kármán. A visualização do escoamento através de bolhas de hidrogênio iluminadas com laser ao redor de um cilindro estático sob o escoamento de água (figura 4) nos permite contemplar esta rica interação na região da esteira próxima.

Uma excelente revisão do mecanismo de formação e emissão de vórtices na esteira de cilindros oscilando foi compilada por Bearman (1984). Recomendamos este artigo ao leitor interessado. No momento, basta saber que qualquer corpo rombudo imerso em um escoamento desenvolverá uma esteira de vórtices com frequência característica em função do seu diâmetro e da velocidade do escoamento incidente.

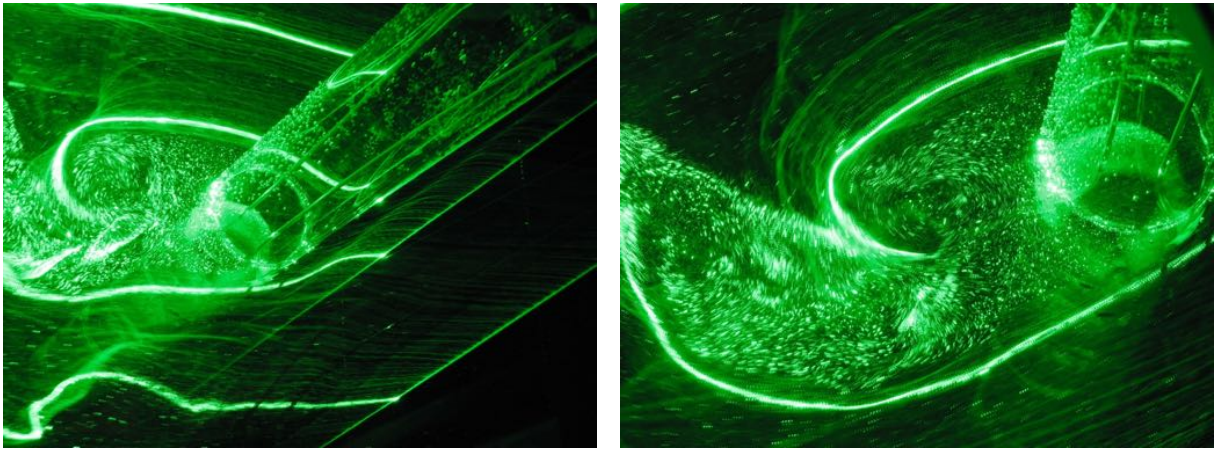


Figura 4: Visualização do escoamento na região da esteira próxima de um cilindro através da emissão de bolhas de hidrogênio iluminadas com laser.

## 2.2 Vibração induzida por vórtices (VIV)

Se o corpo cilíndrico em questão for elástico, poderá responder à excitação do escoamento cíclico desenvolvendo um fenômeno fluidoelástico chamado vibrações induzidas por vórtices (VIV). Tome por exemplo o cilindro ilustrado na figura 5, que pode se deslocar apenas em um grau de liberdade na direção transversal ao escoamento incidente. A característica da estrutura elástica pode ser representada nesta seção bidimensional através de parâmetros de massa ( $m$ ), rigidez ( $k$ ) e amortecimento ( $c$ ).

Sabemos que um vórtice coerente é uma região de baixa pressão no escoamento por conta da rotação do fluido. A emissão alternada de vórtices gera flutuações cíclicas no campo de pressão ao redor do cilindro, governadas pelo ritmo da esteira, excitando o cilindro com carregamentos flutuantes de arrasto e sustentação, representados pelos vetores ortogonais  $F_x$  e  $F_y$ , respectivamente, na figura 5.

Se a frequência de emissão de vórtices coincidir com a frequência natural da estrutura, o sistema dinâmico entra em ressonância e o cilindro desenvolve vibrações com amplitude considerável de deslocamento. A esteira de vórtices governa a excitação do cilindro, injetando energia no sistema, que será dissipada pelo amortecimento da estrutura. Entretanto, à medida que o corpo oscila, ele também controla a formação da sua própria esteira. Por isso dizemos que VIV é um fenômeno fluidoelástico autocontrolado, com amplitude de oscilação governada por um ciclo limite, atingindo deslocamento máximo da ordem de 1 diâmetro na direção transversal.

Esta é a gênese das vibrações induzidas por vórtices (*vortex-induced vibrations*, em inglês). Porém, a característica mais peculiar deste fenômeno está no fato da ressonância

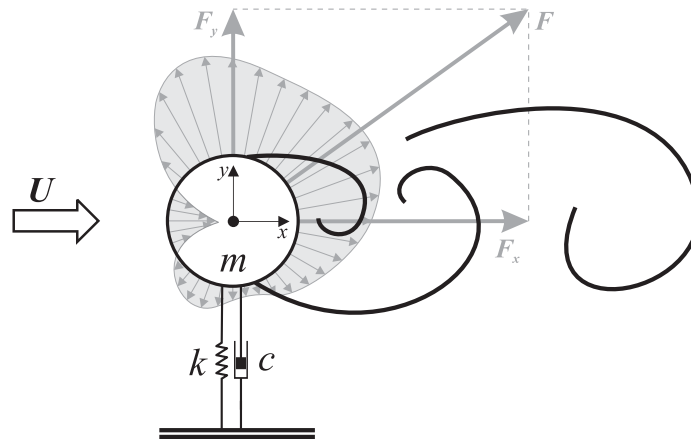


Figura 5: Esquema de um cilindro com um grau de liberdade sujeito a VIV. Reproduzido de Assi (2009).

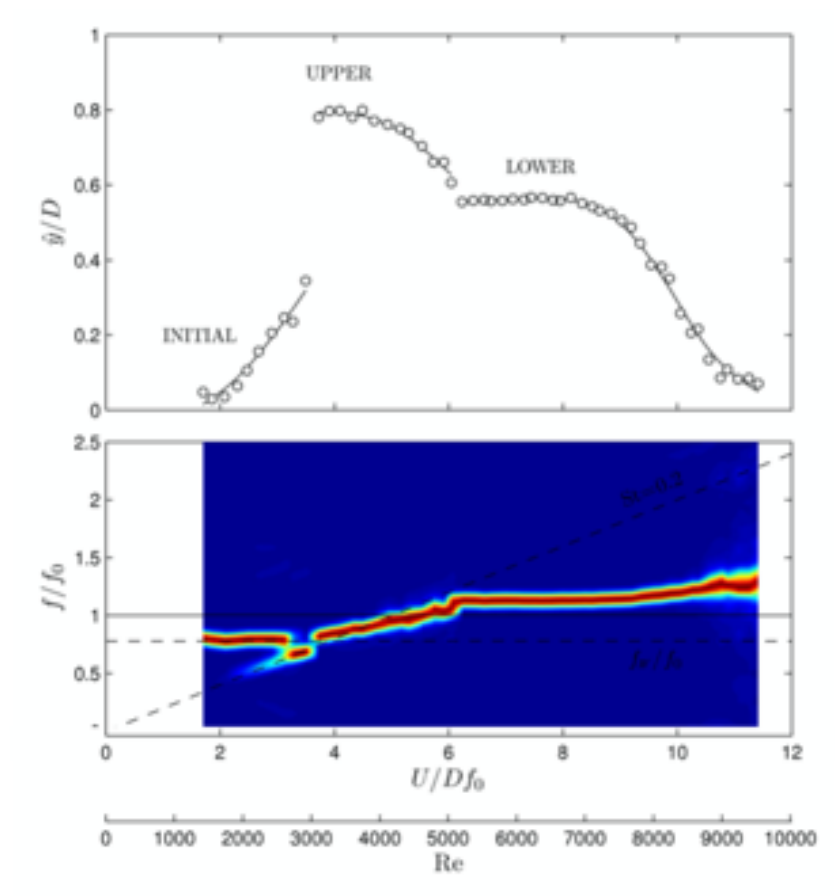


Figura 6: Resposta dinâmica típica de VIV para um cilindro com um grau de liberdade transversal. Reproduzido de Assi (2009).

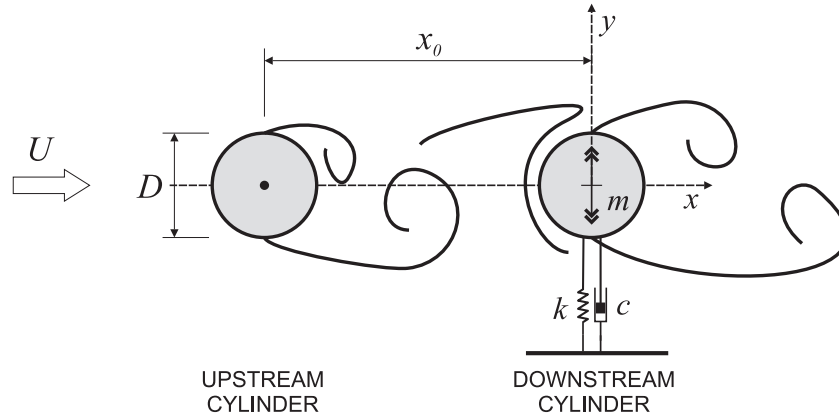


Figura 7: Arranjo de dois cilindros alinhados com o escoamento incidente. Reproduzido de Assi et al. (2010a).

entre os dois osciladores (esteira e cilindro elástico) deste sistema autocontrolado acontecer numa faixa de velocidades do escoamento e não apenas quando as duas frequências são idênticas. Esta é a “alma não linear” de VIV e acontece porque a esteira e o movimento do cilindro controlam um ao outro durante uma faixa de sincronização (chamada faixa de *lock-in*, em inglês).

A resposta típica de um cilindro sob VIV com um grau de liberdade transversal pode ser expressa em termos da amplitude de deslocamento ( $\hat{y}/D$ ) e frequência de vibração ( $f/f_0$ ) em função do parâmetro de velocidade reduzida ( $U/Df_0$ ), conforme ilustrado na figura 6. Williamson e Govardhan (2004) apresentaram uma excelente revisão do fenômeno de VIV que merece ser estudada pelo leitor interessado (leitura obrigatória para os pesquisadores que se iniciam neste tema).

## 2.3 Vibração induzida pela esteira (WIV)

Quando mais de um corpo rombudo está imerso no escoamento, a interferência hidrodinâmica entre suas esteiras produz fenômenos fluidoelásticos mais complexos que VIV. Tome, por exemplo, o arranjo simples de dois cilindros alinhados com a direção do escoamento incidente e separados entre si de alguns diâmetros, como ilustrado na figura 7. O segundo cilindro, elástico, pode se movimentar apenas na direção transversal, enquanto o primeiro cilindro está fixo. Porquanto a esteira de vórtices plenamente desenvolvida e proveniente do cilindro à montante interfere com a dinâmica do cilindro à jusante, fazendo com que este responda com vibrações induzidas pela esteira (WIV, do inglês *wake-induced vibration*).

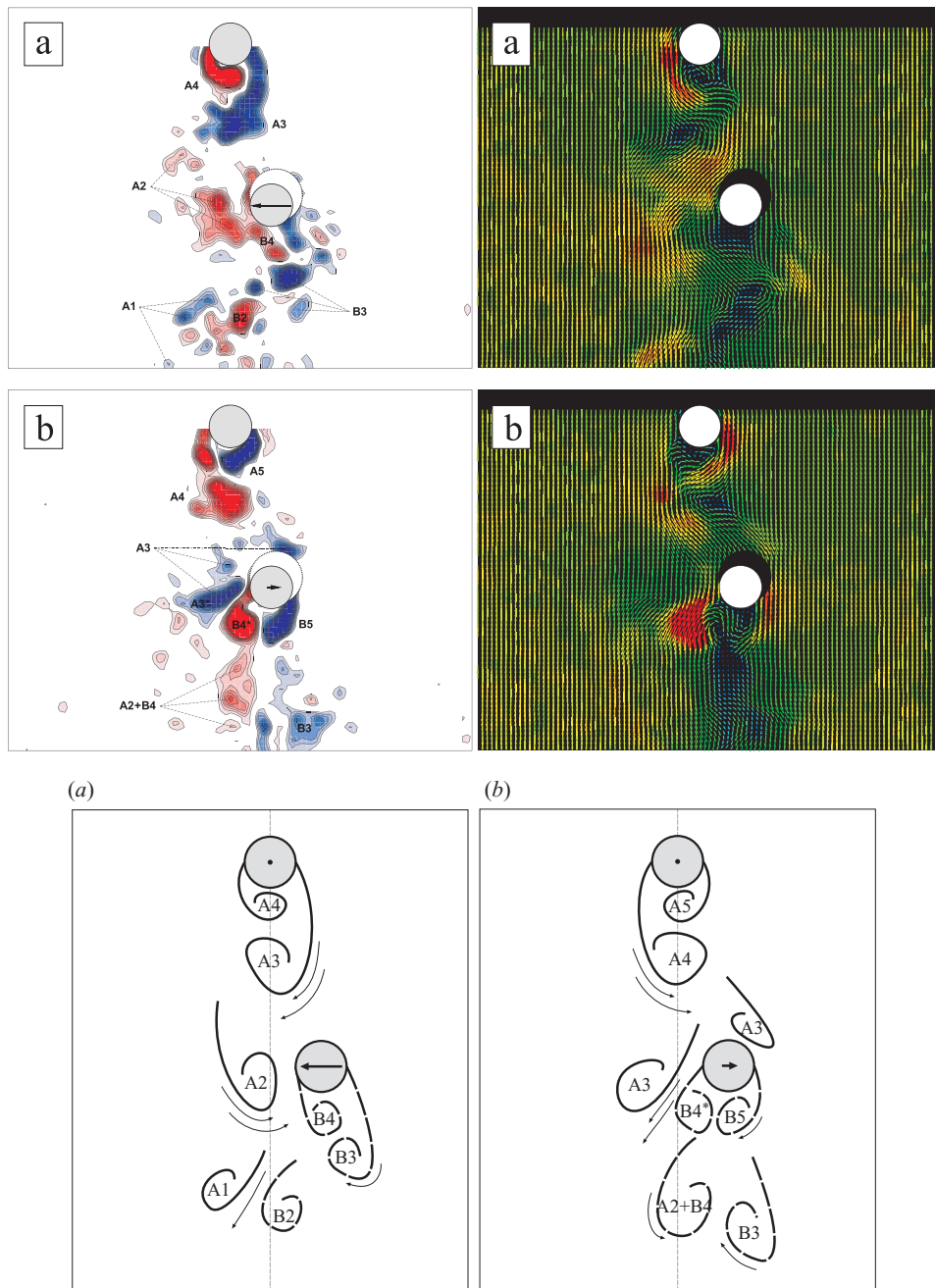


Figura 8: Mecanismo de excitação de WIV produzido pela da interação dos vórtices na esteira, explicado a apartir de campos de velocidade e vorticidade. Reproduzido de Assi et al. (2010b).

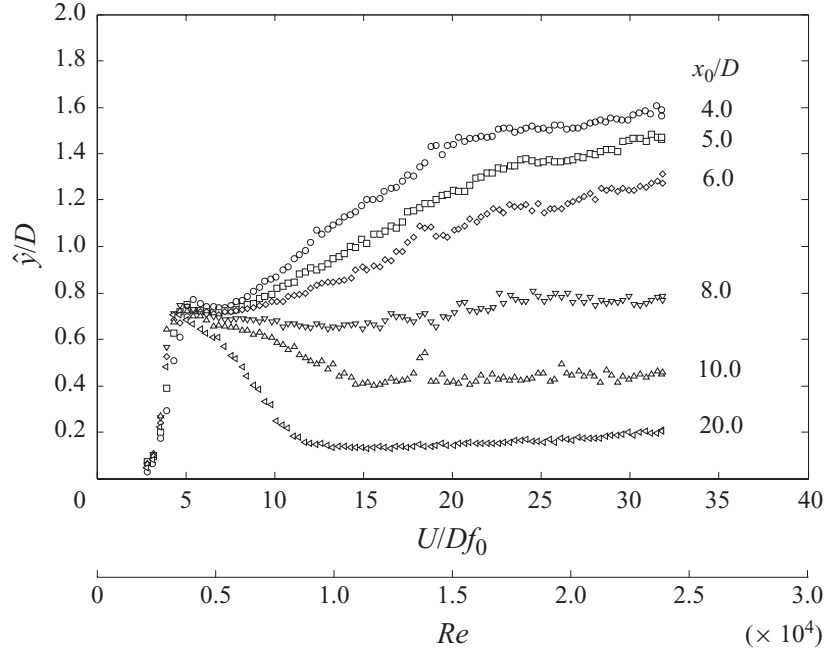


Figura 9: Resposta de WIV para o cilindro à jusante de um par alinhado em função da separação longitudinal de centro a centro ( $x_0/D$ ). Reproduzido de Assi et al. (2010b).

O mecanismo de excitação e transferência de energia do escoamento para a estrutura é mais complexo do que aquele explicado como a causa de VIV. Obviamente, o segundo cilindro produz sua própria esteira de vórtices, mas ele também sofrerá o efeito de uma esteira já desenvolvida que se origina do corpo à montante. Na verdade, o efeito da esteira à montante domina sobre a excitação causada pela própria esteira do corpo. Como exemplificado na figura 8, cujos campos de velocidade e vorticidade foram obtidos com PIV, a interação do segundo cilindro com os vórtices já existentes causa impulsos que transferem energia ao sistema à medida que este atravessa a região da esteira. Como resultado, o segundo cilindro não desenvolve uma resposta dinâmica com vibrações elevadas em uma faixa de ressonância, mas responde com vibrações não ressonantes de grande amplitude que perduram por uma ampla faixa de velocidades reduzidas, como pode ser visto na figura 9. Obviamente, a amplitude das oscilações transversais depende da separação longitudinal entre os corpos, relacionada com a intensidade dos vórtices que geram os impulsos de WIV.

Durante o projeto de pesquisa de doutorado, desenvolvido no Imperial College London sob a supervisão do Prof. Peter Bearman, nos dedicamos à compreensão e modelagem deste fenômeno de vibrações induzida pelo escoamento dominado pelo efeito de interferência da esteira. Na época, cunhamos o termo *wake-induced vibration* para diferenciá-lo dos outros mecanismos como VIV e *galloping*, o que foi bem aceito pela comunidade científica.

Talvez este estudo sistemático de WIV tenha sido a contribuição científica mais significativa da nossa carreira até agora, cristalizada em dois artigos publicados no *Journal of Fluid Mechanics* (Assi et al., 2010b, 2013). Neles descrevemos o mecanismo de excitação e propomos um modelo não estacionário para a reposta de WIV de dois cilindros alinhados com o escoamento.

Como se pode imaginar, as WIV impõem um desafio maior para o desenvolvimento de supressores de vibrações induzidas pelo escoamento em corpos rombudos. Ao invés de lidar apenas com a própria geração de vórtices, o sistema supressor também terá que mitigar a excitação proveniente da esteira à montante.

## 2.4 Galloping

O último fenômeno fluídoelástico relevante para a compreensão deste texto é o *galloping*. (Não nos agrada a tradução “galope” no português, por isso manteremos o termo em inglês.) Diferentemente de VIV e WIV, *galloping* se caracteriza por uma instabilidade hidrodinâmica relacionada à geometria do corpo e às condições dinâmicas do oscilador estrutural. Por exemplo, considere um corpo elástico qualquer imerso em um escoamento e livre para se movimentar em apenas um grau de liberdade na direção transversal ao escoamento incidente. Dependendo da geometria do corpo e da sua velocidade de oscilação, pode acontecer de o escoamento gerar força de sustentação em fase com a velocidade do corpo. Ocorrendo, o sistema dinâmico pode ser compreendido como tendo “amortecimento negativo”, tal que o escoamento transfere energia para o corpo durante o ciclo de vibração. Repare que este não é um fenômeno ressonante nem requer a formação de uma esteira de vórtices, mas se inicia e se sustenta exclusivamente a partir da instabilidade hidrodinâmica da estrutura.

Como resposta, *galloping* pode produzir oscilações cuja amplitude de deslocamento cresce indefinidamente com o aumento da velocidade do escoamento incidente. Isto pode ter efeitos muito prejudiciais à estrutura, com dano por fadiga estrutural. Por princípio, *galloping* não pode ocorrer em corpos axissimétricos, já que a geometria circular de um cilindro não produz força de sustentação em fase com a velocidade do corpo. Mas, como alguns dos supressores de VIV de cilindros que veremos adiante alteram a geometria externa do corpo rombudo, é necessário avaliar se, ao invés de suprimir vibrações, tais supressores podem excitar oscilações ainda mais danosas por *galloping*. Esta será uma preocupação especial com a família de supressores bidimensionais.

Por outro lado, se o objetivo não for mitigar vibrações, mas amplificar o movimento do corpo, o fenômeno de *galloping* (assim como WIV) pode se mostrar promissor, por exemplo, por sua aplicação em sistemas de geração de energia. Apesar de muito interessante, este aspecto não será abordado neste texto, que se restringirá ao estudo da supressão das vibrações. Ao leitor interessado, recomendamos o livro de Blevins (1990) para uma boa revisão sobre *galloping* e outros fenômenos de vibração induzida pelo escoamento.



### 3 SUPRESSORES BIDIMENSIONAIS

*“Scientists study the world as it is. Engineers create the world that has never been.”*

-- Theodore von Kármán (1881-1963)

A tentativa mais elementar de se suprimir VIV de um cilindro está na eliminação da interação entre as camadas cisalhantes que dão origem aos vórtices na esteira. Impedir que as camadas cisalhantes livres se desenvolvam em vórtices coerentes seria “cortar o mal pela raiz”. Supressores capazes deste feito atuariam eliminando o mecanismo bidimensional descrito por Gerrard (1966), portanto dizemos que supressores desta natureza atuariam na bidimensionalidade do escoamento. Apesar do termo “na bidimensionalidade” não ser correto ou elegante, ele resume bem o que queremos expressar para o leitor que tenha algum conhecimento sobre bi e tridimensionalidade de escoamentos.

Por bidimensionais qualificamos supressores que atuam no processo fundamental de interação entre as camadas cisalhantes livres na esteira próxima, atrasando a formação de vórtices. Podemos dizer que este processo de emissão e desprendimento de vórtices (Gerrard, 1966) é essencialmente um processo bidimensional em se tratando de um corpo cilíndrico de comprimento consideravelmente maior que seu diâmetro. As camadas cisalhantes emitidas dos lados opostos do cilindro interagem no plano, alimentando e fortalecendo fluxo de circulação injetada na esteira próxima e estabelecendo o ritmo de emissão de vórtices. A figura 4 ilustra bem este processo.

#### 3.1 Supressores de VIV de placas pivotantes

Como a direção do escoamento incidente pode variar em relação ao cilindro, os supressores que pretendem atuar na mitigação de VIV devem ser omnidirecionais, isto é, funcionar qualquer que seja a direção do escoamento. No nosso exemplo de motivação, a variação da direção do escoamento se dá pela alteração da corrente marinha em relação ao *riser*, podendo variar inclusive ao longo da profundidade. Se a ideia for instalar algum apêndice externo ao cilindro que impeça a interação das camadas cisalhantes, este dispositivo deve estar pronto para rotacionar ao redor do cilindro acompanhando a variação do escoamento

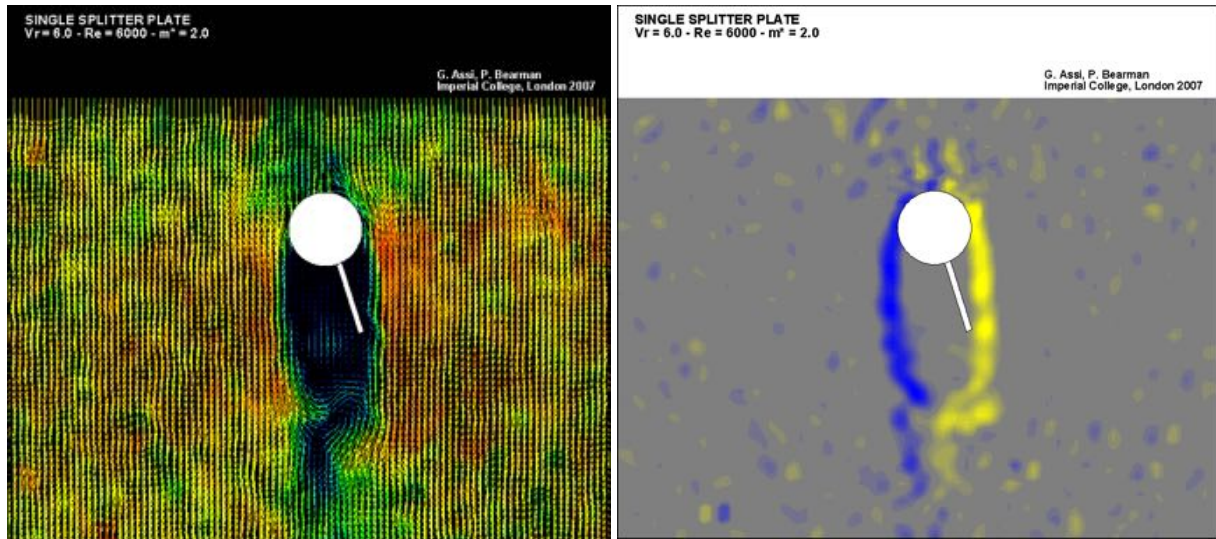


Figura 10: Campos de velocidade e vorticidade ao redor de um cilindro com placa plana pivotante. Reproduzido de Assi et al. (2009)

incidente. Daí surge a necessidade de se desenvolver supressores pivotantes. Alguns deles serão descritos nas seções que se seguem, iniciando com as geometrias mais elementares e aumentando em complexidade e eficiência.

### 3.1.1 Placa plana

A inserção de uma placa plana na linha central da esteira, conhecida na literatura como *splitter plate*, impede a comunicação destas camadas cisalhantes, atrasando a formação e o desprendimento dos vórtices à jusante. Os supressores desta família (placas com comprimentos distintos) atuam exatamente desta forma, interferindo com a comunicação das camadas cisalhantes e alterando a região de formação de vórtices próxima da região de base do cilindro. A figura 10 apresenta os campos de velocidade e vorticidade obtidos com PIV do escoamento ao redor de um cilindro com placa plana pivotante. Nas imagens, verifica-se que a placa impede que a camada cisalhante de um lado interaja com a camada do outro, eliminando a formação de vórtices próxima do cilindro.

Contudo, neste mecanismo, algumas geometrias são mais eficientes que outras em mitigar a formação de vórtices alternados e reduzir o arrasto no corpo. Placas de diferentes comprimentos também podem permitir que o conjunto formado pelo corpo e o supressor apresente instabilidades fluídoelásticas. A eficiência da supressão bem como a estabilidade do supressor estão diretamente associadas ao comprimento da placa e à sua liberdade para rotacionar livremente ao redor do cilindro.

Numa série de experimentos com modelos montados em base elástica com dois graus

de liberdade (Assi et al., 2009) verificamos que o atrito rotacional entre o supressor e o cilindro era um parâmetro fundamental para a dinâmica do sistema. Havendo pouco atrito rotacional, a placa plana não encontra uma posição de equilíbrio, mas oscila de um lado para o outro da esteira, amplificando a vibração do cilindro. Havendo muito atrito, a placa não consegue rotacionar livremente e trava numa posição ao redor do cilindro, induzindo instabilidades fluídoelásticas do tipo *galloping*. Este resultado foi surpreendente e deixou claro como o amortecimento rotacional, vindo do atrito entre o supressor e o cilindro, governa a estabilidade do sistema. A figura 10 também revela que a posição de equilíbrio da placa plana não é alinhada com o escoamento incidente, mas pende para um dos lados até que a camada cisalhante separada do cilindro se recale na extremidade da placa.

Analisando a reposta dinâmica de um cilindro equipado com supressor pivotante de placa plana, verificamos que supressores desta natureza têm grande eficácia na supressão de VIV com redução do arrasto médio. Percebemos que a compreensão destes mecanismos fundamentais, ainda que em condições idealizadas de laboratório, é fundamental para o desenvolvimento de supressores mais eficientes e não vulneráveis aos problemas de instabilidade fluídoelásticas. Contudo, como será discutido adiante, um supressor com uma única placa plana gera uma indesejável força de sustentação para o lado em que a placa se deflete. Este efeito ocorre para supressores longos e curtos, com variações dependendo do comprimento e arranjo geométrico do supressor.

### 3.1.2 Fairings

*Fairings* são supressores pivotantes projetados com a intenção de “afilar” a geometria do corpo rombudo numa tentativa de manter o escoamento aderido ao longo da sua superfície. No extremo, o *fairing* ideal transformaria a geometria de um cilindro em um fólio de corda longa. Contudo, restrições de fabricação e nas condições de operação não permitem que os *fairings* sejam demasiadamente longos. Assim surgiram os *fairings* curtos, com comprimento da ordem do diâmetro do cilindro, também instalados de maneira a se orientarem livremente com a direção do escoamento incidente (Allen e Henning, 1995). Porém, *fairings* curtos não cumprem seu papel de “afilar” o escoamento ao redor do corpo, mas convivem com grandes porções de bolhas de recirculação e escoamento separado. Não são, portanto, “*fairings*” no sentido estrito do termo, mas apenas dispositivos que de fato interferem na interação entre as camadas cisalhantes após o escoamento ter se separado.

Através de experimentos com modelos reduzidos (Assi et al., 2009), demonstramos que *fairings* curtos funcionam pelo mesmo mecanismo que as placas planas. Verificamos que

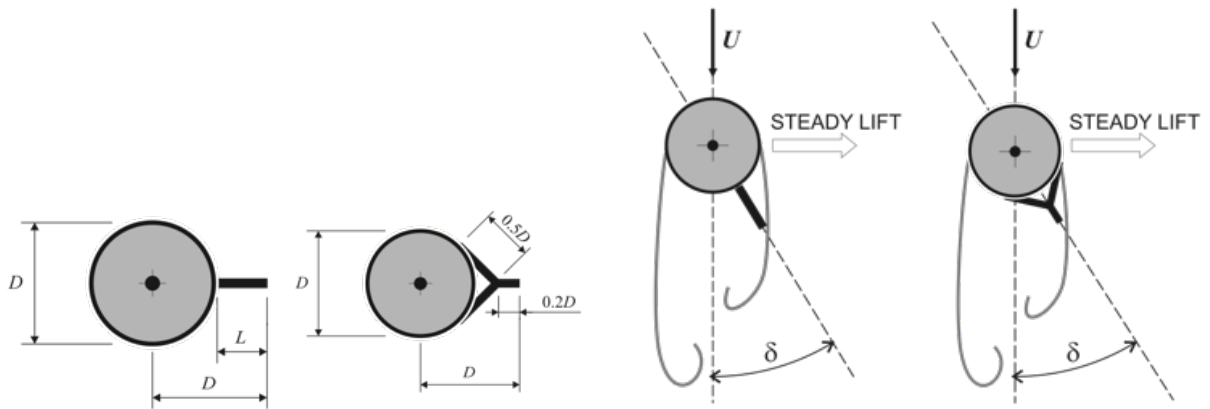


Figura 11: Supressores pivotantes curtos (placa plana e *fairing*) e sua interação com as camadas cisalhantes livres quando na posição de equilíbrio. Reproduzido de Assi et al. (2014b).

não há diferença qualitativa entre o comportamento de um *fairing* e uma placa plana de dimensões semelhantes e que, em alguns casos, as placas planas podem ser mais eficientes em relação ao arrasto gerado, além de serem de mais simples construção.

De modo semelhante, os *fairings* e as placas planas apresentaram a mesma tendência à instabilidade dependendo do atrito rotacional presente nos sistemas. Ou seja, os *fairings* também requerem um mínimo de atrito rotacional para se estabilizarem. De igual modo, se um *fairing* travar ao redor do cilindro, também induzirá *galloping* assim como a placa plana. A figura 11 ilustra a dinâmica da esteira ao redor de um *fairing* curto e de uma placa plana travados ao redor do cilindro durante uma resposta de *galloping*.

Por fim, um comportamento interessante e contraintuitivo descoberto durante esta campanha experimental está relacionado com a posição estável encontrada pelo supressor pivotante em relação ao escoamento incidente. Inicialmente imaginava-se que tanto uma placa plana quanto um *fairing* se alinhassem com a direção do escoamento incidente, ocupando a posição central na esteira e mantendo o escoamento simétrico. Contudo, verificamos que sistemas desta natureza se estabilizam numa posição de equilíbrio inclinada em relação ao escoamento, pendendo aleatoriamente para um dos lados do cilindro e buscando a região onde a camada cisalhante separada do cilindro se recole na extremidade da placa. A posição estável depende do comprimento da placa ou do *fairing*. Nesta posição há supressão de VIV. Mas, como consequência, o escoamento assimétrico produz uma força de sustentação que aponta para o lado do cilindro em que a placa se estabilizou.

Após a comprovação experimental deste comportamento, recebemos depoimentos de operadores de campo relatando observações de que seus *fairings* de fato não se alinhavam com o escoamento, mas pendiam para um dos lados do *riser*. Tal comportamento nos levou

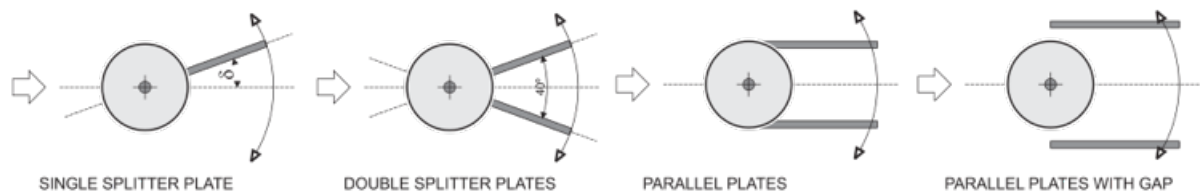


Figura 12: Família de supressores pivotantes: (a) placa plana, (b) placas inclinadas, (c) placas paralelas, (d) placas paralelas com espaçamento. Reproduzido de Assi et al. (2009).

a investigar arranjos de supressores que mantivessem a simetria do escoamento e ainda encontrassem posição estável para promover a supressão da vibração. Assim chegamos nos supressores pivotantes com duas placas inclinadas e paralelas, apresentados a seguir.

### 3.1.3 Placas inclinadas

Adicionamos uma segunda placa plana, oposta à primeira em relação à linha de centro da esteira, com a intenção de se eliminar a força de sustentação permanente que se origina quando uma única placa plana quebra a simetria do escoamento, pendendo e estabilizando-se em um dos lados do cilindro. Assim, conforme ilustrado na figura 12, passamos do modelo com uma *single splitter plate* para o modelo com *double splitter plates*. O ângulo entre as duas placas foi ajustado de modo que ambas estivessem próximas da posição estável identificada pelo sistema no experimento anterior. As duas placas eram solidárias, livres para se moverem em conjunto ao redor do cilindro mantendo o ângulo de 40 graus entre elas.

Como resultado, o sistema permaneceu estável e suprimiu completamente VIV. A simetria do escoamento foi recuperada e a força de sustentação média foi eliminada. Consequentemente, a força de arrasto média também foi reduzida em relação ao sistema com uma única placa plana. Este supressor com duas placas inclinadas também apresentou um comportamento dinâmico que dependia do atrito rotacional. Novamente, havendo pouco atrito, o conjunto de placas não encontrava posição estável capaz de suprimir VIV, mas induzia o conjunto a entrar em instabilidade fluídoelástica de grande amplitude.

Através de visualização do escoamento, verificamos que havia separação e recirculação do escoamento numa bolha entre o cilindro e o lado externo das placas inclinadas. Certamente esta recirculação resultava em perda de energia cinética, contribuindo para a força de arrasto no sistema.

### 3.1.4 Placas paralelas

Assim, demos mais um passo na evolução do arranjo alterando a inclinação das *double splitter plates* para criar duas placas paralelas (*parallel plates*) que se alinhavam com o escoamento incidente no diâmetro do cilindro (figura 12). De fato, verificamos uma redução considerável no arrasto médio sobre o sistema, uma vez que a bolha de recirculação foi eliminada e o escoamento fluía aderido ao cilindro e ao longo das placas paralelas. O conjunto mostrou-se estável e capaz de suprimir VIV com grande eficiência. Novamente, foi necessário fornecer atrito mínimo para que o sistema encontrasse posição estável, mas sem travar a rotação evitando o surgimento de *galloping*. Este foi o supressor de placas planas pivotante de maior eficiência tanto em mitigação de VIV quanto em redução de arrasto.

Mais uma vez as visualizações do escoamento e medições com PIV mostraram que a região de base do cilindro (região à jusante do cilindro localizada entre as placas paralelas) se caracterizava por uma região de escoamento estagnado. Este fenômeno contribui para o arrasto de pressão, oriundo da diferença de pressão entre a frente e a base de um corpo rombudo. Numa tentativa de reduzir este efeito, partimos para uma nova configuração de placas paralelas, agora com um espaçamento entre o bordo frontal das placas e a parede do cilindro, resultando nas *parallel plates with gap* da figura 12 e com variação de comprimento (figura 13).

A intenção desta modificação era que o escoamento incidente injetasse quantidade de movimento na região de base pelo espaço aberto na lateral do cilindro. Este fluxo entre as placas, ainda confinado e controlado pela presença delas, diminuiria a diferença de pressão, reduzindo o arrasto total. Contudo, o que se verificou foi a criação de um sistema mais instável, com grande dificuldade de se manter alinhado com o escoamento incidente e suprimir VIV. De fato, houve redução do arrasto, mas a perda de estabilidade foi um ponto negativo em se tratando de supressores pivotantes. Talvez esta modificação tenha valor para reduzir o arrasto de corpos rombudos fixos em que a direção do escoamento não varie (por exemplo, no suporte cilíndrico do trem de pouso de uma aeronave).

Para tentar estabilizar este último tipo de supressor pivotante, ainda em busca de um sistema com menor geração de arrasto, investigamos variações nos parâmetros geométricos das duas placas, produzindo placas oblíquas com espaçamento lateral da parede do cilindro.

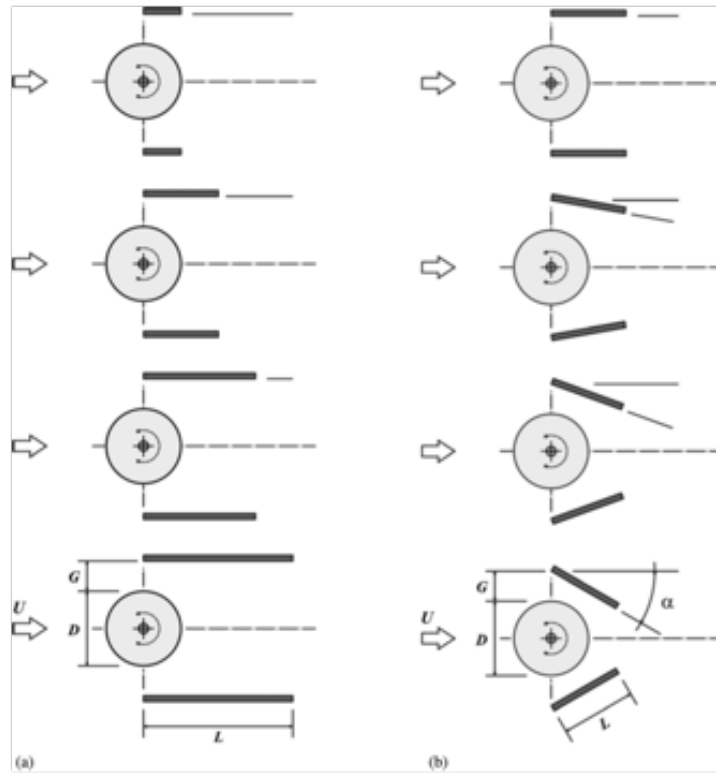


Figura 13: Variações geométricas de comprimento ( $L$ ), separação ( $G$ ) e ângulo ( $\alpha$ ) dos supressores de placas oblíquas. Reproduzido de Assi et al. (2014c).

### 3.1.5 Placas oblíquas

A figura 13 apresenta geometrias de supressores pivotantes formados por placas oblíquas empregados nos testes realizados por Assi et al. (2014c). Verificamos que o sistema pode apresentar instabilidades dependendo dos parâmetros geométricos de comprimento ( $L$ ), separação ( $G$ ) e ângulo de ataque das placas ( $\alpha$ ). Contudo, se estas relações geométricas forem ajustadas adequadamente, o sistema suprime VIV com excelente eficiência na redução de arrasto em relação a um cilindro liso.

Variações desta família de supressores de placas oblíquas podem envolver a adição de mais placas com a intenção de se controlar o escoamento separado e reduzir a intensidade dos vórtices gerados na esteira. Este efeito foi verificado nas simulações numéricas exemplificadas na figura 14, onde se verifica uma atenuação na esteira de vórtices à jusante dos corpos cilíndricos. De fato, a separação das placas da parede do cilindro permite que parte do escoamento incidente alimente a região de base do cilindro (entre as placas) com quantidade de movimento. Entretanto, outras regiões de escoamento separado aparecem ao redor das oblíquas, aumentando a largura da esteira e intensidade dos vórtices, especialmente para ângulos  $\alpha$  grandes.

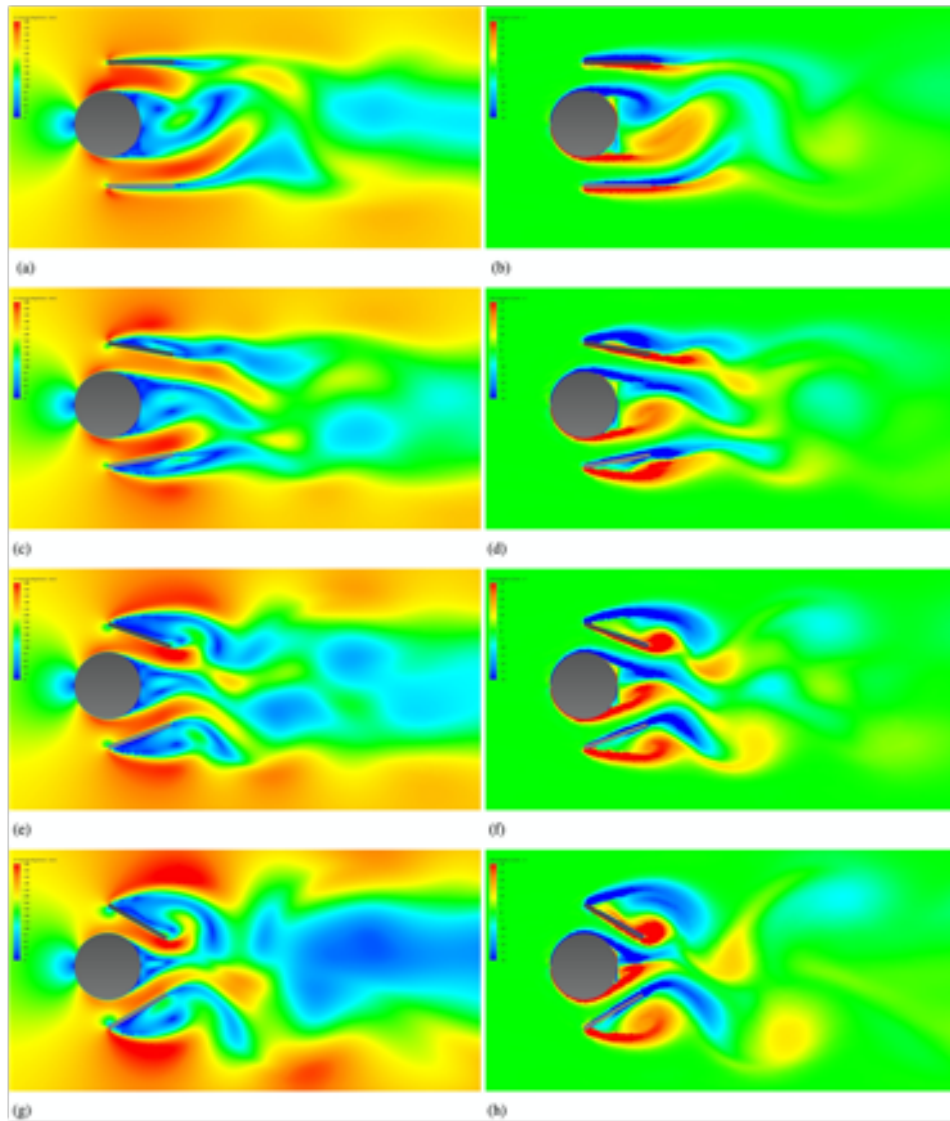


Figura 14: Campos de velocidade e vorticidade ao redor de supressores de placas oblíquas obtidos de simulações numéricas do escoamento. Reproduzido de Assi et al. (2014c).



O projeto conceitual de supressores desta natureza não é trivial. No limite, uma cascata de placas e aletas cada vez menores seria necessária para controlar todo o escoamento separado ao redor de cada elemento do conjunto. Como resultado, a geometria convergiria para aquela de um corpo afilado, próxima da geometria de um fólio.

## 3.2 Supressores de WIV de placas pivotantes

Como vimos anteriormente, variações geométricas de placas planas podem constituir supressores pivotantes com grande eficácia na mitigação de VIV (*vortex-induced vibration*) e boa eficiência na redução de arrasto. Contudo, muitos sistemas dinâmicos, como os *risers* de produção *offshore*, não operam isoladamente, mas são instalados em conjunto com outras estruturas adjacentes. Como destacado no capítulo 2, a interferência hidrodinâmica entre corpos rombudos imersos no mesmo escoamento pode causar vibrações induzidas pela esteira, denominadas WIV (*wake-induced vibration*).

A presença de uma esteira de vórtices desenvolvida de outro corpo rombudo à montante pode reduzir a eficiência dos supressores instalados num segundo corpo à jusante, especialmente quando os dois corpos estão alinhados com a direção do escoamento. Em se tratando de supressores pivotantes, que dependem de uma posição de equilíbrio estável para mitigar a formação dos vórtices, WIV se apresenta como um problema ainda maior: os vórtices vindos da esteira à montante podem facilmente desestabilizar o supressor, induzindo vibrações de grande amplitude no cilindro à jusante.

Os campos de velocidade e vorticidade obtidos por PIV e apresentados na figura 15 mostram que a placa plana pivotante está vulnerável às perturbações produzidas pelos vórtices vindos da esteira à montante. Por conta das flutuações de pressão na esteira, a placa não se estabiliza e não consegue suprimir a resposta de WIV do segundo cilindro. O supressor de placas paralelas tem melhor desempenho, já que não requer uma posição de equilíbrio deslocada para mitigar a formação dos vórtices, mas, mesmo assim pode apresentar instabilidades de acordo com as condições do escoamento.

Para verificar a eficácia de supressores pivotantes de placas planas em mitigar WIV, realizamos experimentos com modelos em escala reduzida com agrupamentos de cilindros equipados com supressores de placas planas e paralelas (o mais simples e o mais eficiente dos supressores mencionados anteriormente). A figura 16 apresenta as três configurações investigadas em que ora o cilindro à montante, ora o cilindro à jusante ou ambos estavam equipados com supressores de placas paralelas.

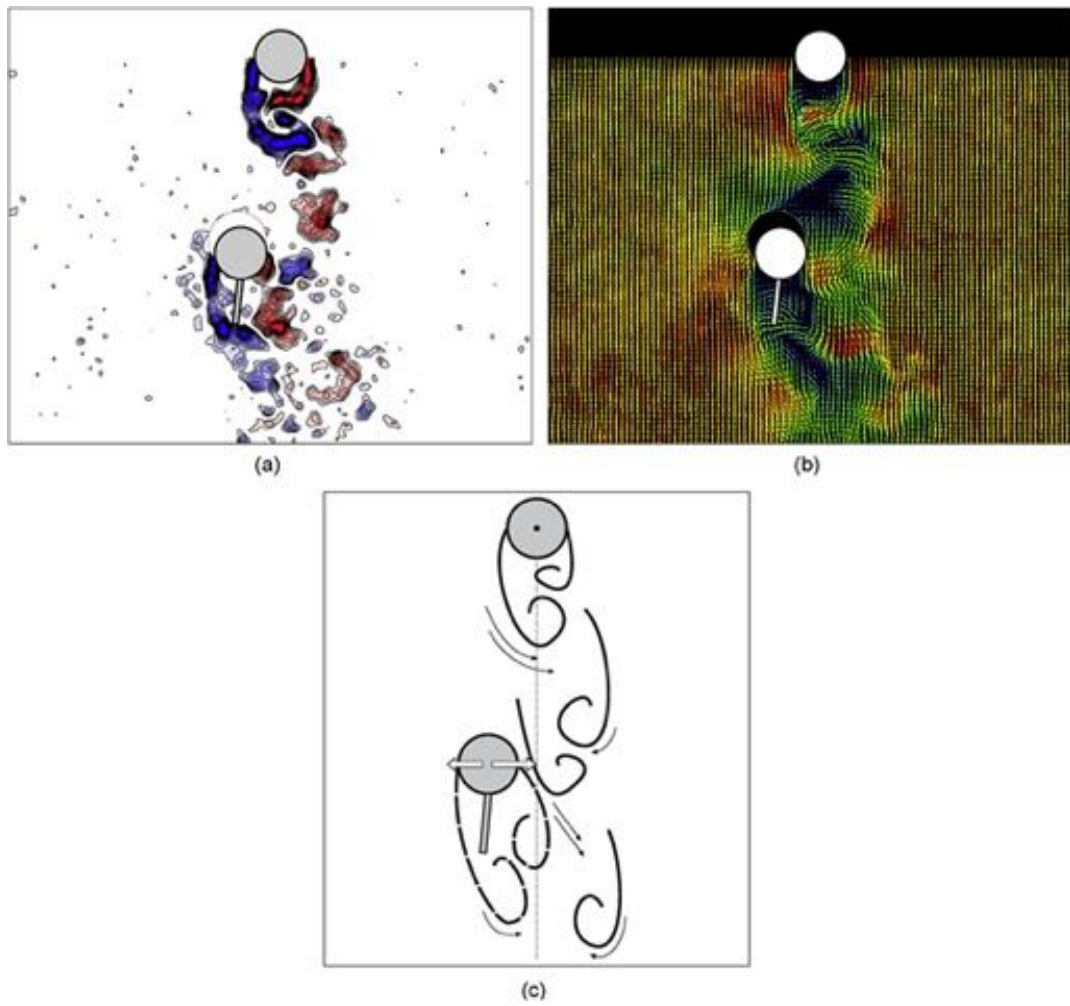


Figura 15: Instabilidade da placa plana pivotante instalada no cilindro à jusante de um par sob WIV. Campos de vorticidade e velocidade obtidos com PIV. Reproduzido de Assi et al. (2010a).

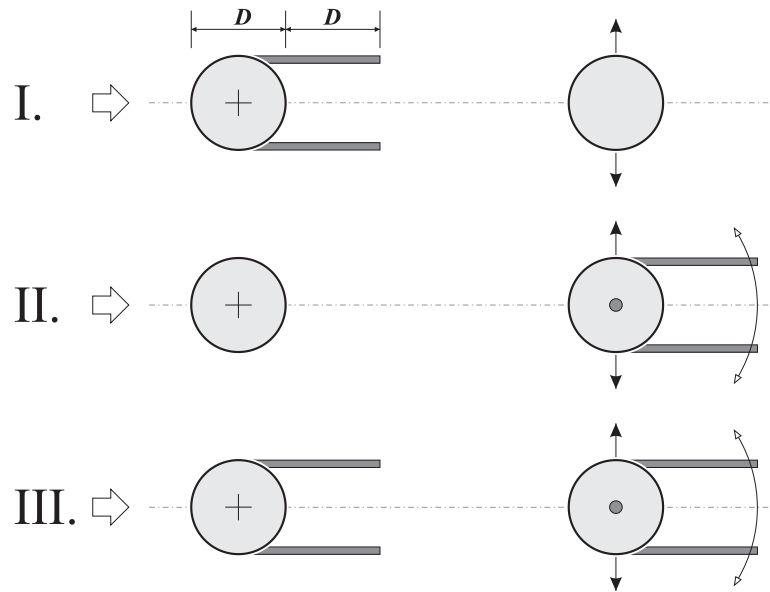


Figura 16: Agrupamentos de cilindros alinhados com o escoamento e equipados com placas paralelas pivotantes. Reproduzido de Assi et al. (2010a).

Concluimos que a esteira do cilindro à montante tem efeito de fato sobre a eficiência do supressor instalado no cilindro à jusante. As respostas dinâmicas indicaram ser fundamental que o cilindro à jusante, aquele imerso na esteira desenvolvida, esteja equipado com o supressor. Houve queda na eficiência de supressão, mas, oferecido atrito rotacional favorável à estabilização do supressor pivotante, o sistema foi capaz de suprimir WIV. Como esperado, verificou-se melhor desempenho do conjunto quando os dois cilindros estavam equipados com supressores de placas paralelas.

### 3.3 Galloping de placas planas

Outro fenômeno fluidoelástico interessante observado ao longo de vários experimentos com supressores pivotantes foi o desenvolvimento de instabilidades de *galloping* (Assi e Bearman, 2015). Como destacado no capítulo 2, *galloping* clássico pode acontecer com corpos rombudos não axissimétricos quando as condições dinâmicas do movimento e do escoamento produzem força de excitação com a característica de amortecimento negativo, em outras palavras, força em fase com a velocidade do corpo.

Quando um supressor pivotante, uma placa plana, por exemplo, tem atrito rotacional excessivo ou se trava ao redor do cilindro, sua posição em relação ao escoamento incidente pode produzir condições favoráveis ao *galloping*. Observamos este fenômeno acontecendo com diversos dos supressores pivotantes mencionados acima, mesmo nos mais simples for-

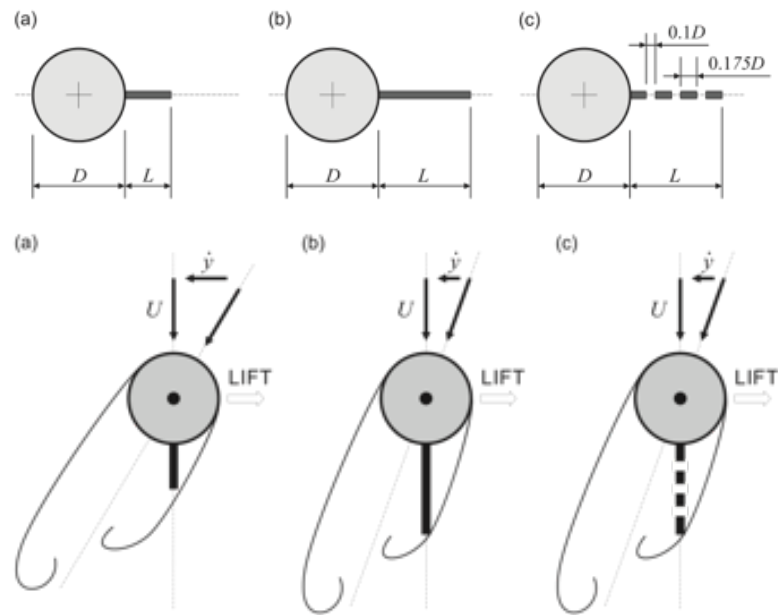
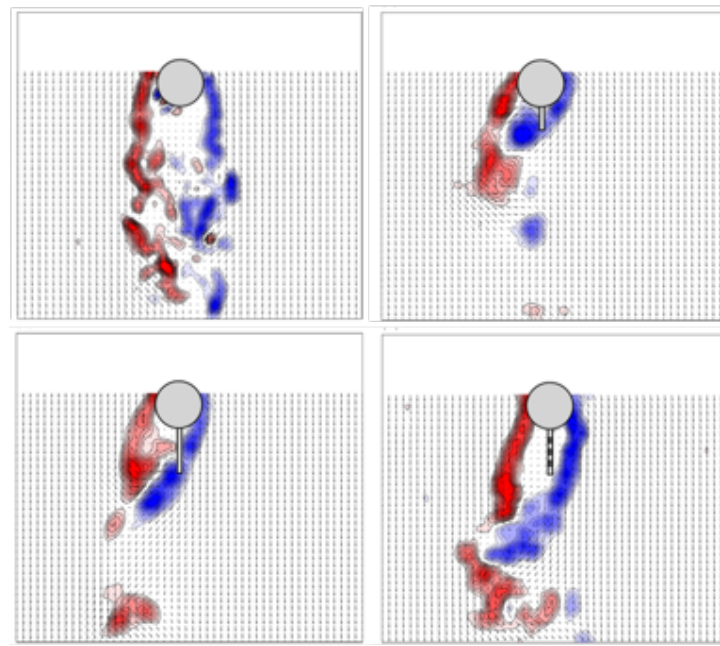


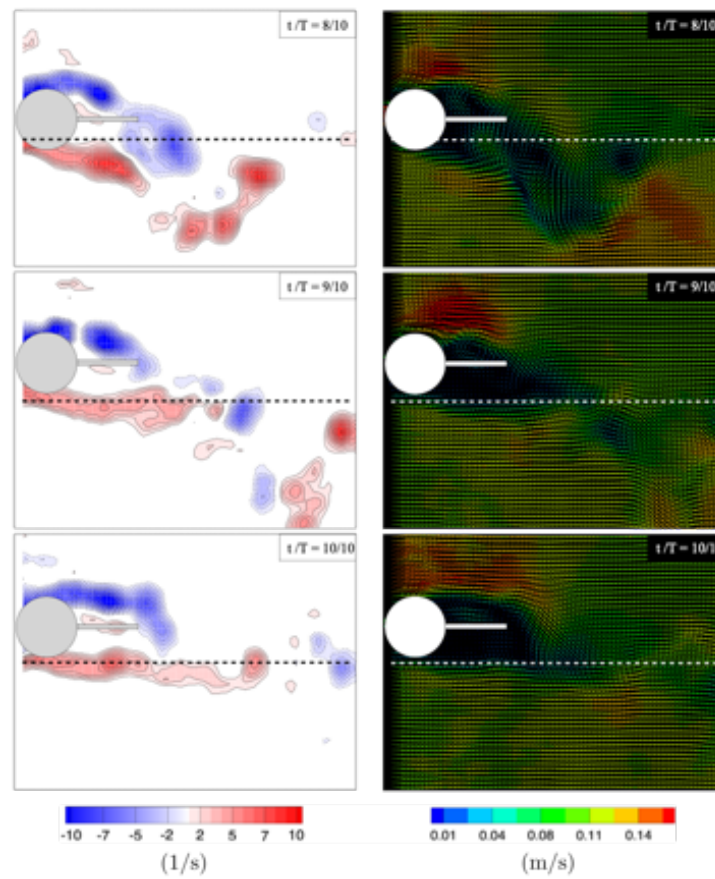
Figura 17: Variações de placas planas: (a) curta, (b) longa, (c) com rasgos; e sua interação com as camadas cisalhantes durante *galloping*. Reproduzido de Assi e Bearman (2015).

mados por placas planas (*splitter plates*). Realizamos, então, uma campanha de experimentos com cilindros equipados com placas planas não pivotantes (travadas) e alinhadas com a direção do escoamento incidente. Variamos o comprimento e a porosidade das placas com a finalidade de permitir alguma interação hidrodinâmica entre as camadas cisalhantes, como visto na figura 17. Também realizamos experimentos semelhantes com *fairings* curtos travados ao redor do cilindro. Como resultado, verificamos que todos os sistemas não pivotantes, tanto placas planas quanto *fairings*, desenvolveram instabilidade de *galloping* com grandes amplitudes de vibração.

A figura 18 (topo) apresenta os campos de velocidade e vorticidade característicos da resposta de *galloping* de um cilindro com as diversas placas planas travadas, evidenciando o recolamento do escoamento separado no supressor causando a força de sustentação em fase com a velocidade transversal do corpo. Detalhes do campo de vorticidade obtidos para um cilindro com *fairing* também indicam o mesmo comportamento para um supressor curto. Enquanto a resposta de *galloping* pode ser benéfica se a intenção for a concepção de um sistema para a extração de energia, ela certamente não é quando se pretende reduzir vibrações induzidas pelo escoamento em sistemas *offshore*.



(a)



(b)

Figura 18: (a) Campo de vorticidades para *galloping* de placas planas. (b) Evolução temporal da esteira durante *galloping* de placa plana. Reproduzido de Assi e Bearman (2015).

### 3.4 Supressores de cilindrinhos de controle rotativos

Outra família distinta de supressores que atuam na bidimensionalidade do mecanismo físico da formação e desprendimento de vórtices é formada por cilindrinhos rotativos que interferem com o escoamento nas regiões próximas à parede do cilindro principal. É sabido que a injeção de quantidade de movimento angular na camada limite atrasa a separação do escoamento por aumentar sua resistência ao gradiente adverso de pressão. Esta técnica, denominada *moving surface boundary layer control*, foi originalmente desenvolvida para aplicações em corpos afilados, instalando-se pequenos elementos rotativos embutidos na superfície de asas e perfis aerodinâmicos (ver referências em Modi, 1997; Korkischko e Meneghini, 2012).

O controle do escoamento separado em corpos rombudos é mais complexo que em corpos afilados devido ao efeito do elevado gradiente adverso de pressão sobre a camada limite e regiões de recirculação. Experimentos e simulações numéricas com cilindros demonstraram que a atuação de cilindrinhos rotativos em regiões específicas ao redor do corpo rombudo pode evitar a separação ou até mesmo favorecer o recolamento do escoamento já separado. Supressores deste tipo requerem energia para que os cilindrinhos rotativos operem. Consequentemente, são sistemas ativos que não encontram aplicação na supressão de vibrações induzidas pelo escoamento em pequenas estruturas ou em corpos flexíveis, com os *risers*. Por outro lado, sistemas desta natureza podem encontrar aplicação para a supressão de vibrações do tipo VIM (*vortex-induced motion*) em grandes sistemas flutuantes, como plataformas do tipo *spar* ou monocoluna (figura 1). Grandes sistemas *offshore* deste tipo têm energia a bordo para fornecer rotação aos cilindrinhos ativos.

Novamente, nossa investigação desta família de supressores se iniciou com estudos fundamentais com modelos em escala reduzida e simulações numéricas do escoamento com a finalidade de se compreender os mecanismos hidrodinâmicos e fluídoelásticos que governam o fenômeno. Iniciamos com um cilindro equipado com agrupamentos de cilindrinhos de controle igualmente distribuídos ao redor. Os parâmetros da investigação envolviam variações geométricas do sistema, considerando o número de cilindrinhos de controle, seu diâmetro, sua separação da parede do cilindro principal, além da velocidade de rotação destes atuadores. A figura 19 ilustra uma das configurações com 8 cilindrinhos de controle rotativos posicionados ao redor do cilindro maior.

Os experimentos foram realizados no canal de água recirculante com o conjunto montado em base elástica com um grau de liberdade. As configurações em que os cilindros de

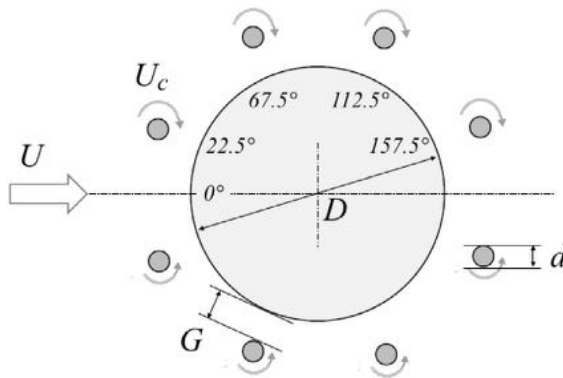


Figura 19: Cilindro equipado com supressor de 8 cilindrinhos rotativos ao redor. Reproduzido de Silva-Ortega e Assi (2017a).

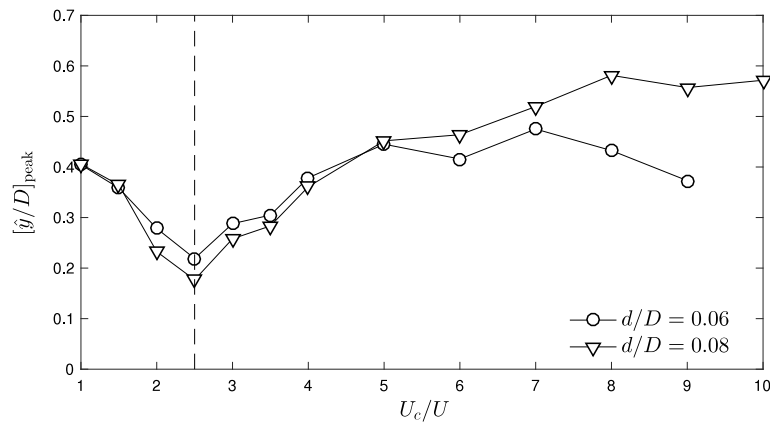


Figura 20: Resposta dinâmica de VIV suprimido com cilindrinhos rotativos. Reproduzido de Silva-Ortega e Assi (2017b).

controle não estavam rotacionando serviram de referência para a análise dos resultados. Destaca-se que apenas a presença dos cilindrinhos estáticos ao redor do cilindro principal foi suficiente para provocar alterações significativas no carregamento hidrodinâmico e na resposta dinâmica de VIV do sistema. Este efeito de interferência havia sido identificado por Zdravkovich (1981), quando instalou uma série de *interfering rods* ao redor de cilindros estáticos em túnel de vento. Na investigação de Silva-Ortega e Assi (2017b), o principal parâmetro de controle foi a rotação do conjunto de cilindrinhos, cuja velocidade tangencial era expressa em função da velocidade do escoamento incidente. Os melhores resultados foram obtidos com o arranjo de 8 cilindrinhos de controle. Dependendo da velocidade de rotação, o arrasto gerado no conjunto pôde ser reduzido para zero e, em alguns casos, atingiu valores negativos (na forma de propulsão). Este efeito levantou a hipótese de que a rotação dos cilindrinhos poderia ser utilizada para produzir força útil para movimentar o sistema como, por exemplo, numa operação de posicionamento dinâmico de uma plataforma oceânica.

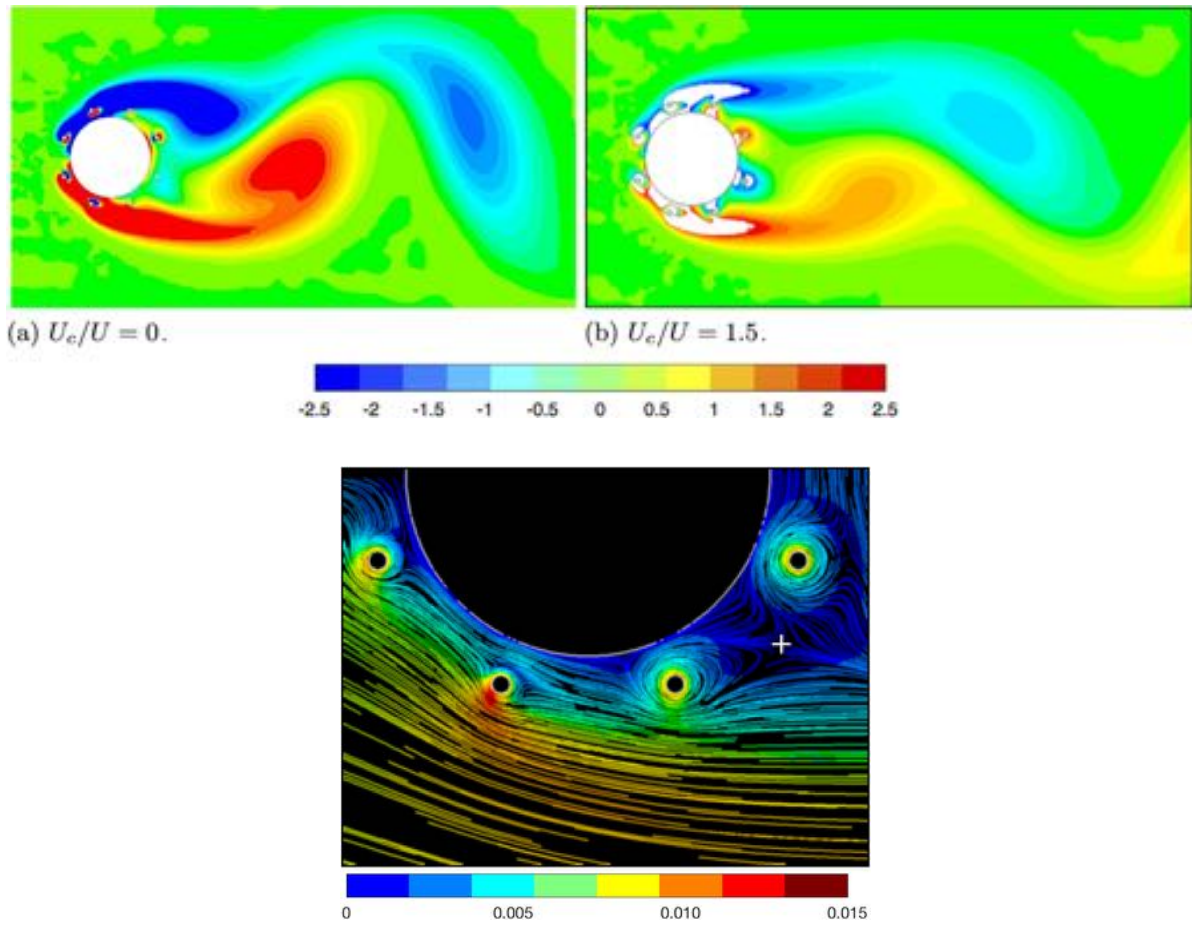


Figura 21: Campo de vorticidade para um sistema com 8 cilindrinhos de controle rotativos em função da velocidade de rotação. Reproduzido de Silva-Ortega e Assi (2017b).

Em se tratando da supressão de VIV, os cilindrinhos rotativos se mostraram uma solução interessante, capaz de reduzir a amplitude de vibração com significativa redução do arrasto no sistema, obviamente às custas do consumo de energia para sustentar os elementos ativos em rotação. A figura 20 apresenta a redução na amplitude máxima transversal ( $[\hat{y}/D]_{\text{peak}}$ ) de VIV do sistema em função da rotação dos cilindrinhos de controle ( $U_c/U$ ) para um arranjo com 8 atuadores rotativos ao redor. Uma vantagem deste sistema está na sua omnidirecionalidade, podendo atuar qualquer que seja a direção do escoamento incidente, bastando-se alterar a rotação dos cilindrinhos.

Simulações numéricas do escoamento foram fundamentais para elucidar os complexos mecanismos físicos presentes na escala da camada limite, na região da separação e na maior escala da esteira próxima. A figura 21 apresenta o campo de vorticidade do escoamento ao redor de um cilindro com 8 cilindrinhos de controle em duas condições de rotação: parados e girando com velocidade tangencial 1,5 vezes maior que a velocidade do escoamento incidente. No segundo caso, verifica-se uma atenuação da esteira de vórtices,



ainda remanescente, à jusante do cilindro. Um detalhe do campo de velocidades próximo dos cilindrinhos de controle ilustra a interação destes elementos com a camada limite do cilindro principal.

As ilustrações dos campos de velocidade e vorticidade apresentadas na figura 22 evidenciam o efeito do aumento da rotação dos cilindrinhos de controle esteira. À medida que a rotação aumenta, o supressor é capaz de eliminar a emissão de vórtices e estabilizar a esteira do cilindro principal, quase recuperando uma condição que remete ao escoamento potencial ao redor de um cilindro. Como consequência, há grande redução no arrasto.

Esta linha de pesquisa com cilindrinhos de controle rotativos está em pleno desenvolvimento tanto na abordagem numérica quanto na experimental. Trabalhos atuais, desenvolvidos por alunos orientados no grupo de pesquisa, se dedicam à otimização do sistema através da rotação independente de cada cilindrinho, a fim de reduzir o consumo de energia, mitigar VIV e gerar forças úteis para o controle do posicionamento dinâmico do sistema. Esperamos que esta tecnologia possa ser aplicada no controle de grandes sistemas oceânicos, cada vez mais demandados para a exploração *offshore*.

— — —

Outras famílias de supressores bidimensionais foram investigadas ao longo da última década de pesquisa. Porém, escolhemos destacar neste texto aquelas que produziram resultados mais interessantes do ponto de vista dos mecanismos físicos.

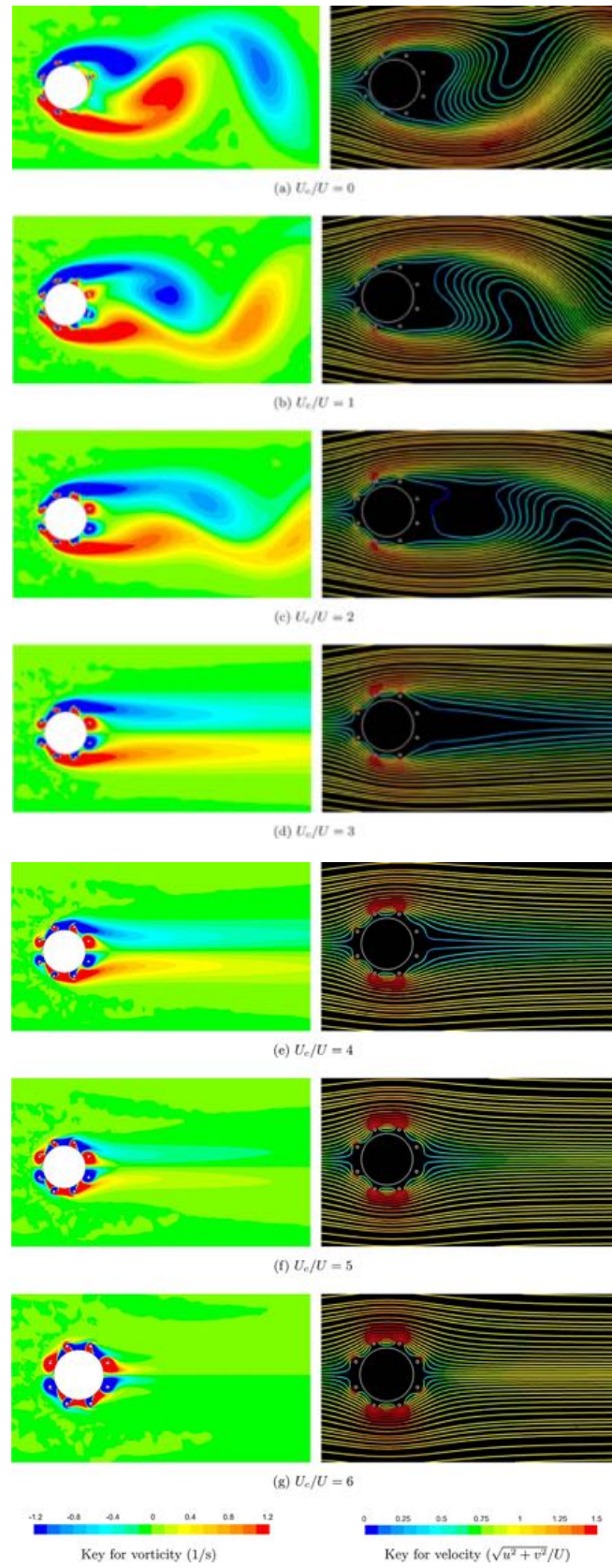


Figura 22: Evolução do controle da esteira com 8 cilindrinhos rotativos em função da velocidade de rotação. Reproduzido de Assi et al. (2019).

## 4 SUPRESSORES TRIDIMENSIONAIS

*“Life is tough... and then you graduate.”*

-- Mike Slackenerny (PhD comics by Jorge Cham)

O fenômeno de formação e desprendimento de vórtices é rico em estruturas tridimensionais no escoamento. Como detalhado na abrangente revisão de Williamson e Govardhan (2004), a esteira já apresenta estruturas tridimensionais complexas para número de Reynolds acima de 200 (baseado no diâmetro do cilindro). Todos os supressores apresentados no capítulo 3 foram projetados para atenuar ou impedir o processo de comunicação entre as camadas cisalhantes, que é predominantemente bidimensional (isto é, não depende da posição ao longo da terceira dimensão que é o comprimento do cilindro). Contudo, uma outra maneira de promover interferência na esteira de modo a mitigar a formação dos vórtices é atuar justamente nas estruturas tridimensionais do escoamento.

A simulação numérica de Carmo et al. (2013), apresentada na figura 23, destaca a rica interação entre tubos tridimensionais de vórtices ao redor de dois cilindros alinhados com o escoamento incidente para  $Re = 400$ . A esteira de um cilindro isolado na mesma faixa de número de Reynolds não é qualitativamente diferente. Portanto, projetar supressores para VIV e WIV que se beneficiem dos efeitos tridimensionais da esteira para enfraquecer a correlação das forças hidrodinâmicas durante a emissão de vórtices pode produzir resultados interessantes.

Com base neste princípio, investigamos três supressores que atuam na tridimensionalidade do escoamento: *strakes* helicoidais, malhas permeáveis, e cilindros ondulados. Recentemente iniciamos estudos com supressores biomiméticos, inspirados na geometria tridimensional de cactos. Contudo, ainda não dispomos de resultados conclusivos para acrescentá-los nesta resenha. A figura 24 ilustra alguns outros supressores tridimensionais, todos baseados na modificação da geometria do cilindro ao longo do seu comprimento. Dentre eles destacamos o *strake* helicoidal (a) e o cilindro ondulado (f). O grande desafio no desenvolvimento de supressores desta natureza é produzir uma geometria passiva que não perca sua eficiência quando o cilindro começa a oscilar. Normalmente, a oscilação transversal do corpo é capaz de aumentar a correlação do escoamento ao longo do comprimento do cilindro o que, de certo modo, torna o escoamento mais bidimensional.

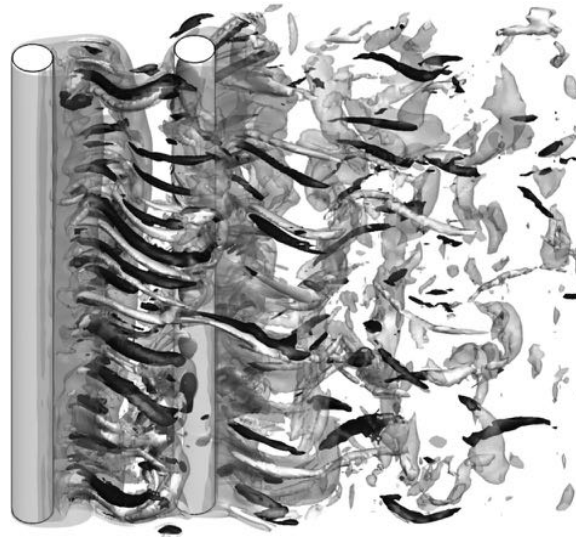


Figura 23: Estruturas tridimensionais no escoamento ao redor de dois cilindros alinhados. Reproduzido de Carmo et al. (2013).

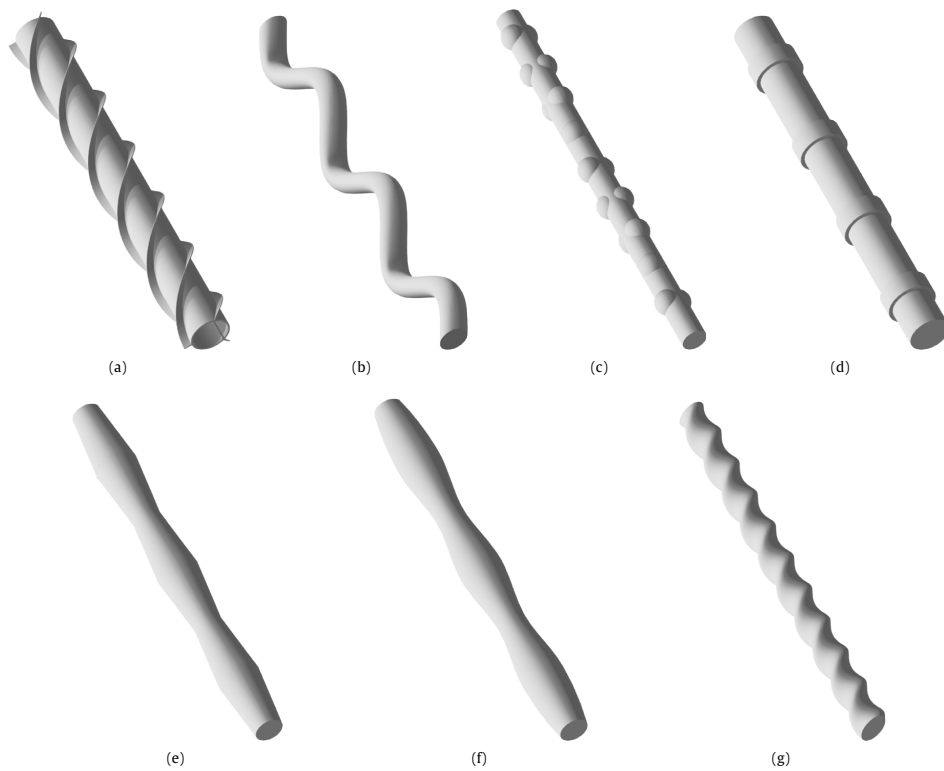


Figura 24: Ilustração de diversas modificações tridimensionais no cilindro como tentativa de suprimir VIE. Reproduzido de Assi e Bearman (2018).

## 4.1 Strakes helicoidais

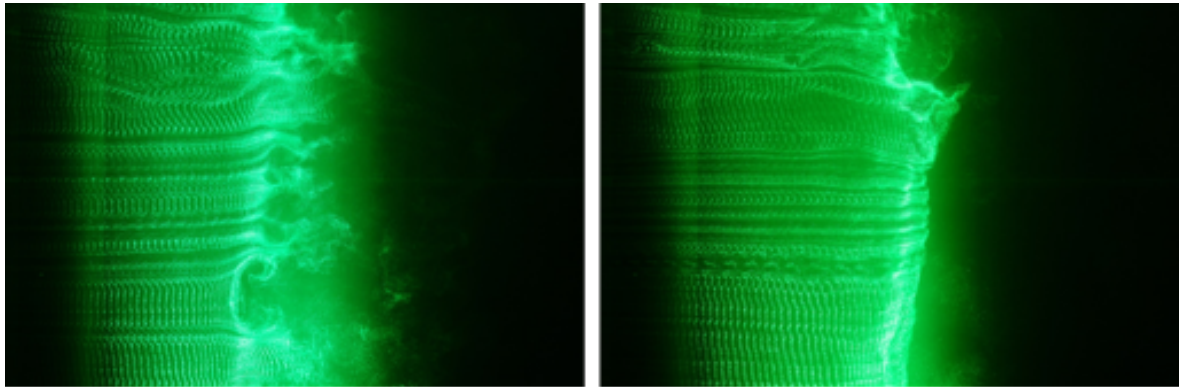
*Strakes* helicoidais são supressores antigos, com origem na indústria do vento, e amplamente utilizados em sistemas oceânicos, apesar de gerarem elevada carga de arrasto. A tecnologia ainda sofre com as dificuldades de fabricação, armazenamento e instalação. Por exemplo, *strakes* empregados em *risers* de produção são normalmente confeccionados como capas de polímero injetado que devem ser instaladas ao redor da tubulação durante o processo de lançamento do *riser* no mar, ocupando grande área do convés e atrasando a manobra de lançamento.

Apesar de serem utilizados há décadas, o desenvolvimento desta tecnologia foi bastante empírico e houve pouco interesse na compreensão da hidrodinâmica dos *strakes*. Apenas recentemente surgiram estudos detalhando as estruturas e mapeando a topologia do escoamento tridimensional ao redor destes supressores. Korkischko e Meneghini (2011), por exemplo, apresentaram medições do campo tridimensional de velocidades ao longo do comprimento de um cilindro com *strakes* helicoidais, evidenciando a riqueza e complexidade do escoamento presente na esteira próxima.

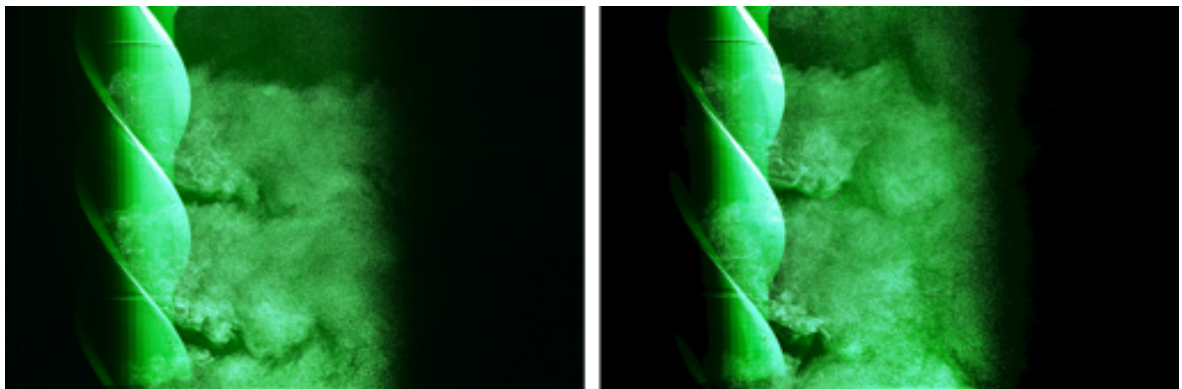
### 4.1.1 Strakes convencionais

*Strakes* de fato têm alguma atuação na interação bidimensional entre as camadas cisalhantes, mas seu efeito preponderante para a mitigação de VIV está na quebra da correlação das forças hidrodinâmicas ao longo do comprimento do corpo. A geometria helicoidal das aletas do *strake* fixam a separação do escoamento em linhas espirais que percorrem uma helicoidal ao longo do corpo. As aletas devem ter altura considerável para fixar a linha de separação em sua extremidade, consequentemente, gerando mais arrasto. Portanto, trata-se de um supressor essencialmente tridimensional, como mostrado nas visualizações do escoamento com bolhas de hidrogênio apresentadas na figura 25.

Quando o cilindro está fixo e não pode vibrar, os *strakes* fazem um bom papel e podem manter a separação do escoamento ao longo da linha helicoidal sem induzir arrasto desnecessário ao corpo. Chaminés rígidas e pesadas, por exemplo, pouco se deslocam em resposta à excitação de vórtices causada pelo vento. Neste caso, *strakes* com aletas baixas (da ordem de 1% do diâmetro) são suficientes para manter as linhas de separação e, consequentemente, geram pouco arrasto. Por outro lado, para sistemas relativamente leves e flexíveis, como *risers* imersos em água ou plataformas flutuantes do tipo *spar* (figura 1), *strakes* com aletas altas (com altura de 10% a 20% do diâmetro) são necessários para



(a) Bare cylinder.



(b) CS continuous helical strake.

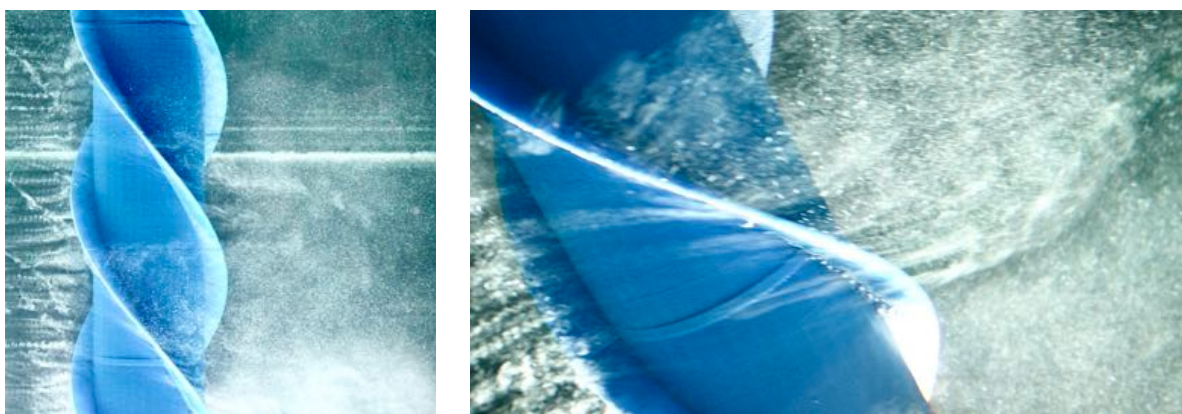


Figura 25: Visualização do escoamento ao redor de um cilindro liso e um cilindro equipado com *strakes* convencionais. Reproduzido de Assi et al. (2021).



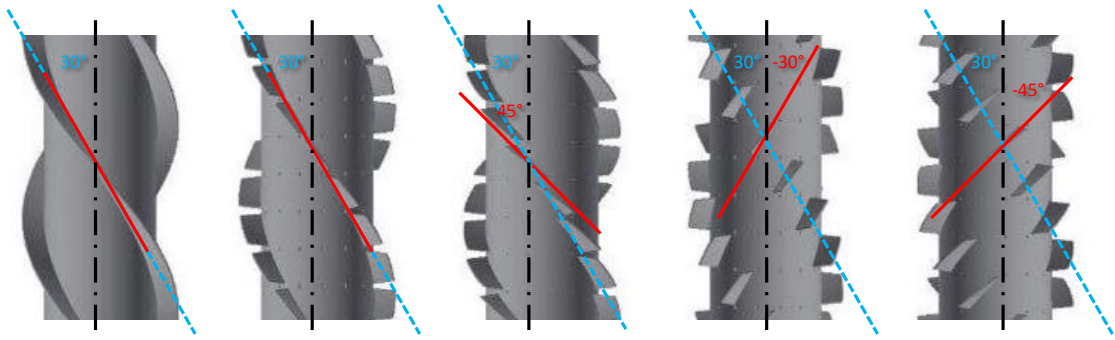


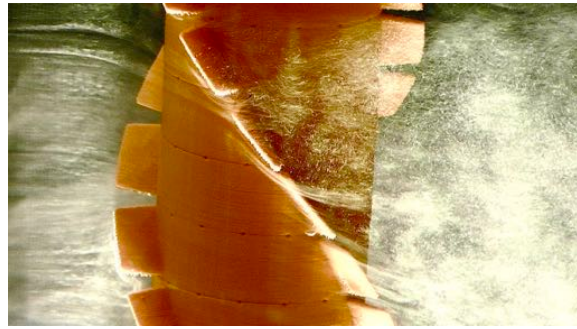
Figura 26: Variações geométricas nas aletas de *strakes* não convencionais. Reproduzido de Assi et al. (2021).

manter os pontos de separação em configuração helicoidal ao longo do comprimento. Por conta da altura excessiva, a interferência com o escoamento gera arrasto considerável na estrutura.

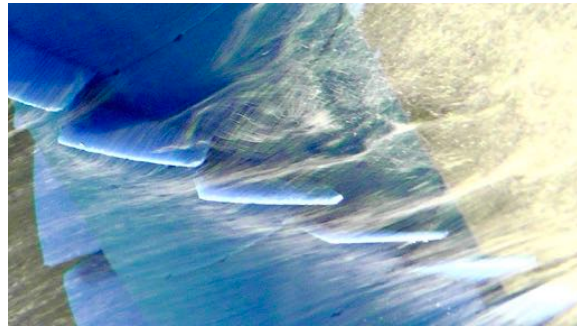
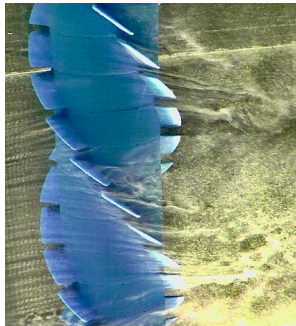
Esta perda de eficiência para corpos com baixa razão de massa (razão entre a massa da estrutura e a massa do volume de fluido deslocado) se dá por conta da recuperação da correlação do carregamento ao longo do comprimento. Estruturas relativamente leves respondem ao mínimo carregamento dos vórtices com oscilações transversais capazes de correlacionar o padrão da esteira ao longo do comprimento a partir do movimento do corpo. Em resumo, estruturas com baixa razão de massa requerem *strakes* com aletas mais altas e que produzem mais arrasto por consequência; estruturas com razão de massa elevada requerem *strakes* com aletas baixas, portanto mais eficientes quanto ao arrasto gerado.

#### 4.1.2 Strakes não convencionais

Como tem sido a tônica deste texto, defendemos que a compreensão dos mecanismos de interação fluido-estrutura propiciam o avanço tecnológico e permitem a identificação de parâmetros relevantes para a otimização destes sistemas. Recentemente, em um recente estudo experimental, rico em visualizações do escoamento (Assi et al., 2021), apresentamos resultados do desempenho de *strakes* não convencionais a partir de variações na geometria das aletas. A quebra das aletas helicoidais em segmentos curtos e a introdução de leves torções (variações do ângulo de ataque local) nestes segmentos (figura 26) modificam consideravelmente a eficiência destes supressores em relação aos *strakes* convencionais. As figuras 27 e 28 apresentam visualizações do escoamento com bolhas de hidrogênio para as variações geométricas apresentadas na figura 26.

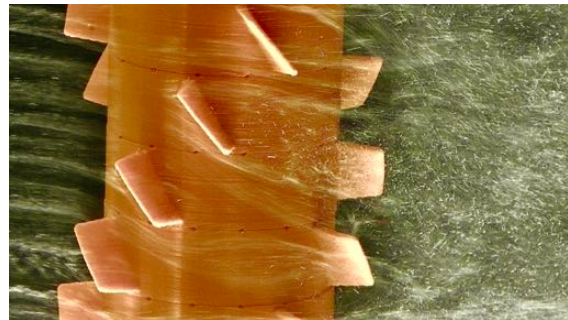
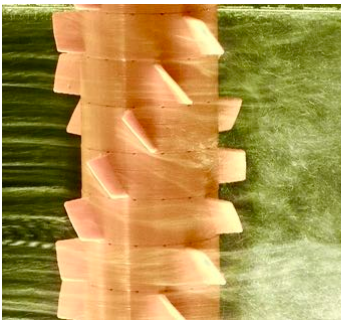


(a) S30 serrated 30-strake.

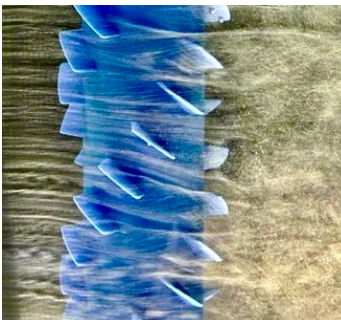


(b) S45 serrated 45-strake.

Figura 27: Visualização do escoamento ao redor de *strakes* não convencionais com aletas seccionadas e torcidas. Reproduzido de Assi et al. (2021).



(a) I30 inverted 30-strake.



(b) I45 inverted 45-strake.

Figura 28: Visualização do escoamento ao redor de *strakes* não convencionais com aletas seccionadas e invertidas. Reproduzido de Assi et al. (2021).



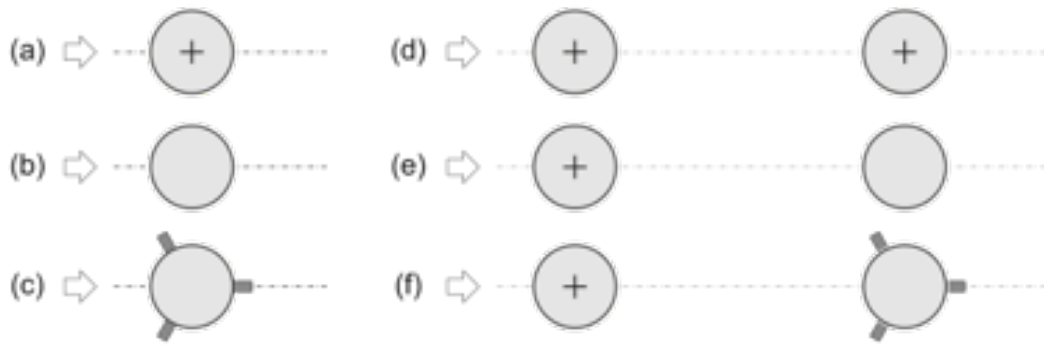


Figura 29: Agrupamentos de cilindros com *strakes*. Reproduzido de Assi et al. (2010a).

Contudo, nossa principal contribuição neste tema talvez esteja na comprovação de que o mecanismo de funcionamento dos *strakes* seja mais complexo do que imaginávamos. De fato, a quebra de correlação causada pela fixação das linhas de separação ao longo do comprimento foi verificada. Porém, verificou-se também fortes componentes de velocidades, transversal ao escoamento e na direção do eixo do cilindro, induzidas com direções contrárias em lados opostos do cilindro. A região da esteira próxima também se mostrou rica em escalas tridimensionais, mais complexas quanto mais segmentos apresentarem as aletas seccionadas. Obviamente, há uma relação ótima entre os comprimentos de onda dessas estruturas tridimensionais que favorecem a atenuação da esteira. Esta relação ainda precisa ser investigada. Estudos desta natureza com modelos em escala reduzida abrem caminho para o desenvolvimento de novas geometrias de *strakes* que podem ser mais eficientes para suprimir vibrações induzidas pelo escoamento e reduzir arrasto.

Em outro estudo (Assi et al., 2010a), também conduzido com modelos em escala reduzida, demonstramos como a eficiência de supressão de *strakes* convencionais se reduz quando o cilindro em questão sofre interferência hidrodinâmica da esteira de outro corpo rombudo posicionado à montante, como visto nos arranjos da figura 29. Como explicado anteriormente, durante o fenômeno de WIV (*wake-induced vibration*) um cilindro responde com vibrações não ressonantes à excitação proveniente da esteira de vórtices que se origina em outro corpo posicionado à montante. Como os *strakes* atuam para mitigar a emissão de vórtices do cilindro em que estão instalados, eles se tornam impotentes para suprimir vibrações quando a excitação vem da esteira coerente de outro corpo rombudo, conforme mostra o arranjo da figura 29f. Em outras palavras, *strakes* perdem drasticamente a eficiência quando imersos nas esteiras de outros corpos, o que não é incomum quando se tem agrupamentos de *risers* ou outros corpos rombudos alinhados com o escoamento incidente.

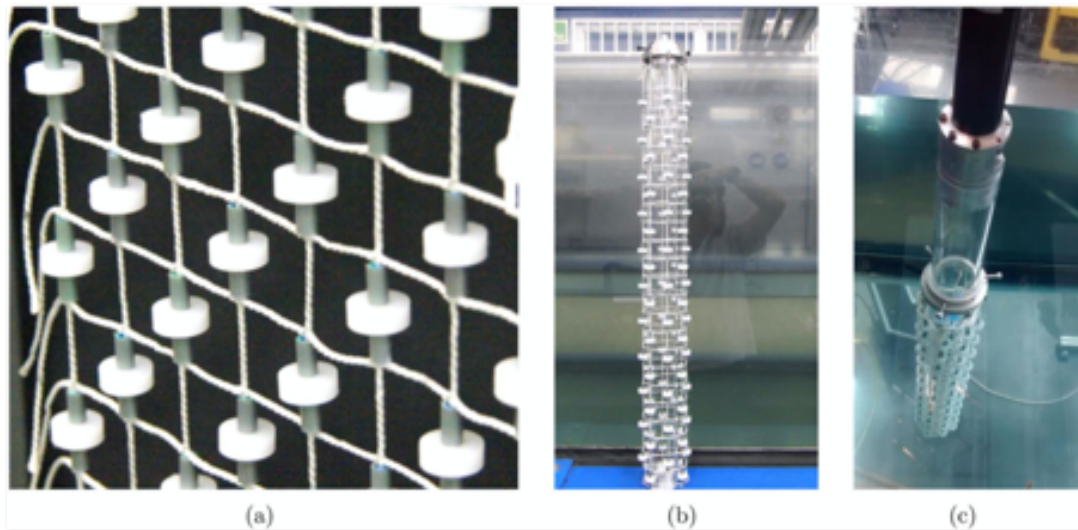


Figura 30: Detalhe de um modelo de cilindro equipado com *ventilated trousers* para testes no canal recirculante. Reproduzido de Cicolin e Assi (2017b).

## 4.2 Malhas permeáveis

Uma ideia interessante surgiu no final da década de 2000, quando inventores experimentaram envolver o cilindro com uma malha permeável repleta de corpos tridimensionais na forma de pequenos carreteis, chamados *bobbins*. A malha foi confeccionada com cabos de nylon e os *bobbins*, fabricados de PVC. Este supressor omnidirecional, patenteado por Brown (2010), foi chamado de *ventilated trousers*, aqui simplificado por VT, por aludir à imagem de um cilindro vestido com um tecido perfurado.

### 4.2.1 Ventilated Trousers

Supressores de malha permeável apresentam vantagens consideráveis em comparação com supressores de placas pivotantes ou *strakes*. Eles têm custo de fabricação mais baixo, podem ser armazenados sem ocupar tanto espaço no convés da embarcação de lançamento e são mais facilmente instalados e removidos durante a operação. Por não apresentarem peças móveis ou mancais de rotação e por utilizarem componentes disponíveis no mercado (como cabos de *nylon*, por exemplo), requerem baixa manutenção e têm vida útil estendida.

A figura 30 ilustra a geometria de um modelo de VT instalado em um cilindro em escala reduzida para testes no laboratório. De fato, a geometria de VT investigada apresentou considerável redução na resposta dinâmica de VIV para sistemas com baixa razão de massa e amortecimento, que caracteriza o cenário mais desafiador para a supressão.

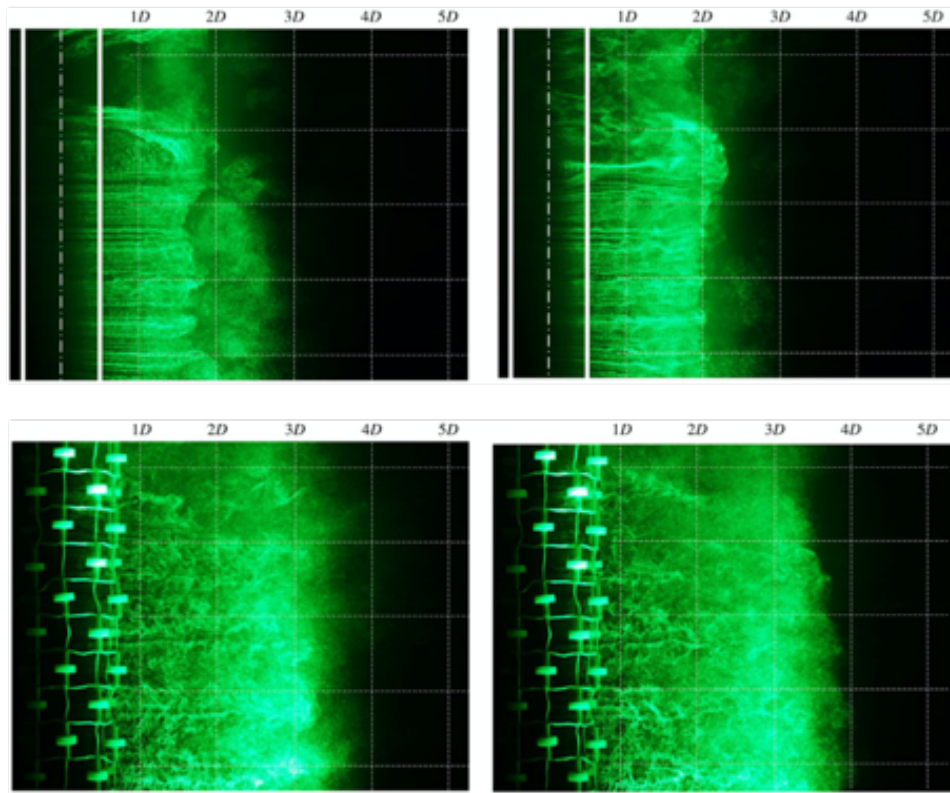


Figura 31: Visualização do escoamento ao redor de um cilindro liso (acima) e de um cilindro equipado com VT (abaixo). Reproduzido de Cicolin e Assi (2017b).

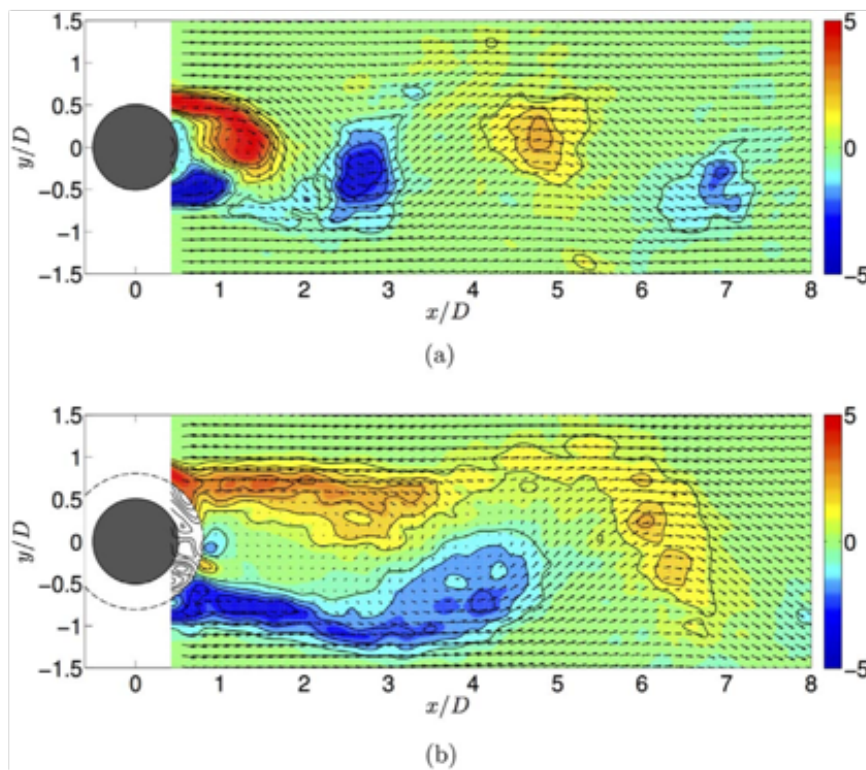


Figura 32: Campos de vorticidade obtidos com PIV para (a) cilindro liso e (b) cilindro com VT. Reproduzido de Cicolin e Assi (2017b).

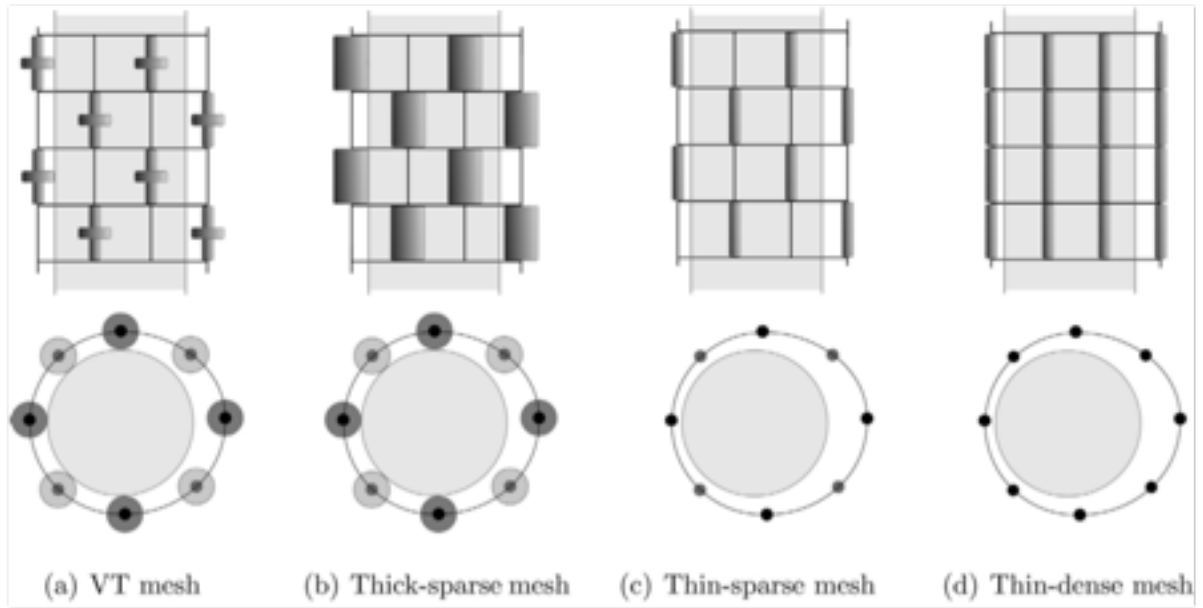


Figura 33: Outras configurações de malhas permeáveis. Reproduzido de Cicolin e Assi (2017a).

Como apresentado nas imagens da figura 31, obtidas através da visualização do escoamento com bolhas de hidrogênio iluminadas com laser, os *bobbins* presentes na malha são capazes de produzir estruturas tridimensionais na região da esteira próxima, dificultando a interação entre as camadas cisalhantes e atrasando a formação dos vórtices. Este efeito foi claramente capturado com medições do campo de vorticidade por PIV, apresentadas na figura 32, que indica um considerável aumento no comprimento de formação de vórtices para o cilindro equipado com VT em relação àquele do cilindro liso.

#### 4.2.2 Outras malhas

A fim de investigarmos o mecanismo físico através do qual o VT atua no escoamento, produzimos uma série de supressores do tipo malha permeável com diferentes corpos instalados na malha em substituição aos *bobbins*, conforme ilustrado na figura 33. Níveis de supressão semelhantes àqueles do VT original foram obtidos pelos demais supressores, indicando que, provavelmente, a perturbação tridimensional na esteira não era uma exclusividade daquela geometria de *bobbin* patenteada como VT.

Por outro lado, os demais supressores não foram tão eficientes na redução de arrasto quanto o VT original. De modo semelhante aos *strakes*, os supressores de malhas permeáveis tendem a aumentar o arrasto do sistema em relação ao arrasto de um cilindro liso e estático. Imagens obtidas com PIV (figura 34) indicam que os demais supressores

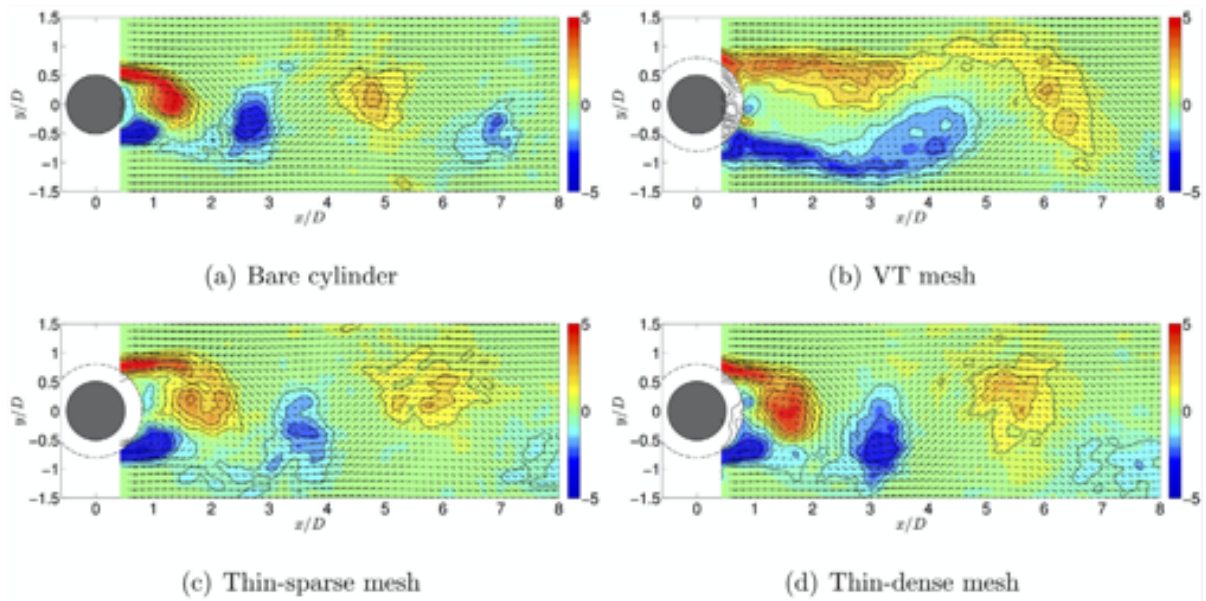


Figura 34: Campos de vorticidade obtidos com PIV para as malhas permeáveis apresentadas na figura 33. Reproduzido de Cicolin e Assi (2017a).

estenderam o comprimento de formação de vórtices, mas nenhum teve um desempenho tão eficiente quanto ao do VT.

Esta campanha experimental com modelos de supressores de malhas permeáveis abriu caminho para o desenvolvimento de novas geometrias desta natureza. Assim como o estudo com os *strakes* não convencionais, a perturbação tridimensional causada pelas malhas permeáveis pode ser otimizada para produzir escalas do escoamento que contribuam para a mitigação da formação de vórtices na esteira. A correta compreensão dos mecanismos hidrodinâmicos contribui nesta direção.

### 4.3 Cilindro ondulado e elíptico

A última tentativa avaliada no desenvolvimento de supressores tridimensionais apresentada nesta resenha está relacionada à alteração da geometria do próprio cilindro ao invés da instalação de apêndices externos. Vimos que os *strakes* helicoidais dependem da geometria protuberante das aletas para produzir os efeitos tridimensionais na esteira que reduzem a correlação das forças originárias dos vórtices. Contudo, as aletas geram grande força de arrasto, a principal deficiência dos *strakes*. Com o objetivo de reduzir a força de arrasto e ainda manter a quebra de correlação causada pelo efeito tridimensional, buscamos alterar a geometria externa do cilindro de maneira suave, produzindo um cilindro ondulado de seção transversal elíptica (*elliptical wavy cylinder*) apresentado em Assi e



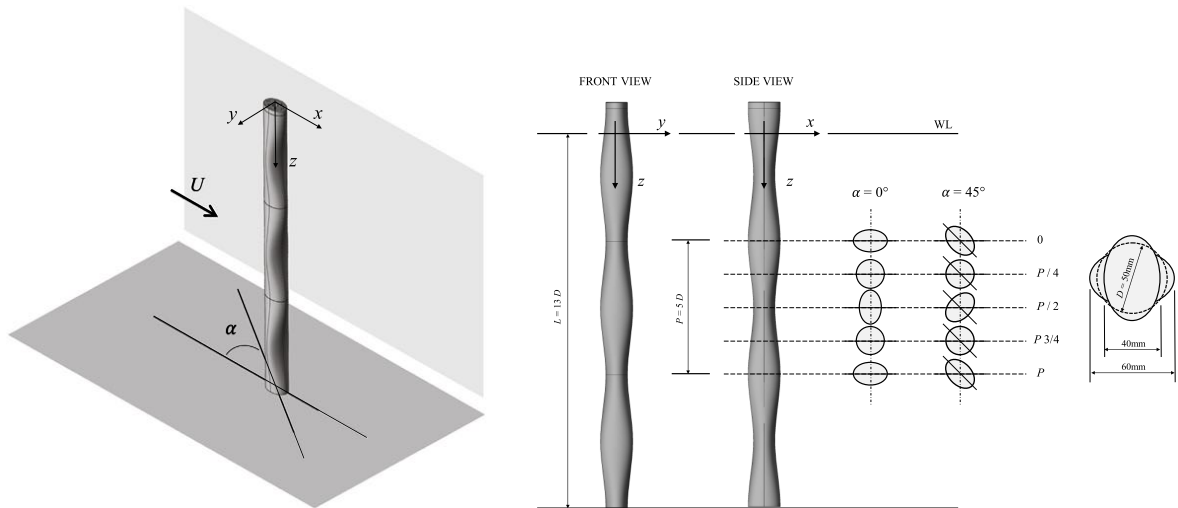


Figura 35: Geometria do cilindro ondulado de seção elíptica. Reproduzido de Assi e Bearman (2018).

Bearman (2018).

O cilindro circular foi envolto com uma capa formada por seções transversais elípticas, cujos eixos maiores e menores se alternavam repetidamente nas direções ortogonais ao longo do comprimento do cilindro. O resultado foi um cilindro ondulado nas duas direções ortogonais ao eixo do cilindro, conforme ilustrado na figura 35. Outras tentativas de cilindros ondulados encontradas na literatura são apresentadas na figura 24. O modelo foi então montado na base elástica e livre para responder à excitação de VIV na direção transversal. Enquanto estava fixo, verificamos que o cilindro ondulado apresentava considerável redução de arrasto e flutuação da força de sustentação. Mas, assim que o sistema foi permitido oscilar transversalmente, a resposta dinâmica de VIV foi muito similar àquela de um cilindro liso.

A partir de visualizações do escoamento com bolhas de hidrogênio e tintura fluorescente, foi possível constatar que as ondulações na geometria do cilindro de fato produziam o efeito de alterar a linha de separação ao longo do comprimento e afilar a esteira formada (ver figura 36a). Como resultado, o cilindro estático produzia menor carregamento de arrasto e sustentação. Mas, assim que as primeiras e pequenas oscilações se iniciavam, as suaves ondulações do cilindro não conseguiam fixar as linhas de separação, permitindo a retomada da correlação da esteira ao longo do comprimento (figura 36b e c) e recuperando VIV.

Mais tarde, alguns anos após a realização destes experimentos, tomamos conhecimento de estudos interessantes que investigaram a hidrodinâmica de bigodes de focas (Beem e

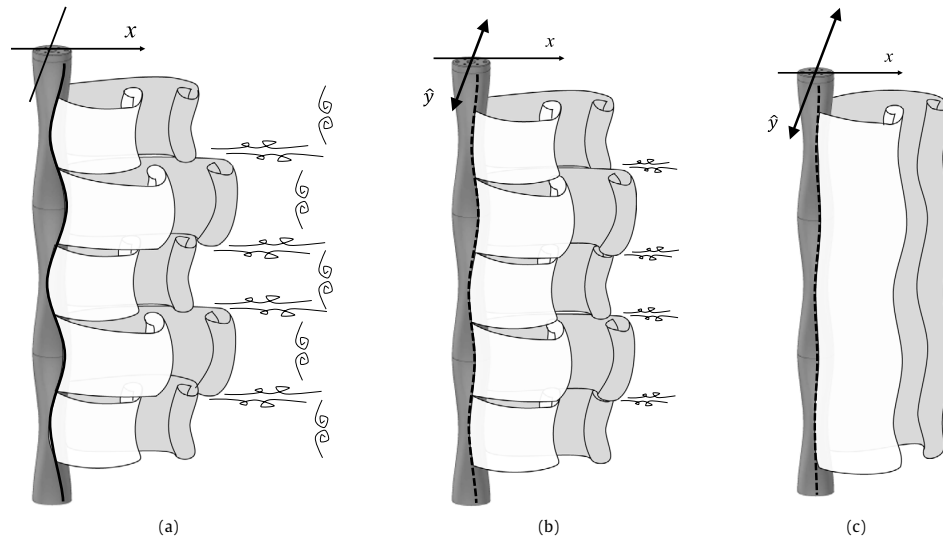


Figura 36: Interpretação do comportamento da esteira de um cilindro ondulado. Reproduzido de Assi e Bearman (2018).

Triantafyllou, 2015; Rinehart et al., 2017). Fomos surpreendidos com a similaridade entre a geometria externa do bigode da foca e o cilindro ondulado estudado. Para a foca, a geometria ondulada favorece a sensibilidade para capturar flutuações de pressão na água, favorecendo a caça submarina. O bigode produz menor arrasto quando estático e vibra amplamente quando excitado por pequenas flutuações no escoamento.

— — —

Outras inspirações da natureza podem ser investigadas para o desenvolvimento de supressores, atenuadores ou mesmo amplificadores de vibrações, dependendo da aplicação na engenharia. No momento, temos desenvolvido estudo com geometrias inspiradas em cactos e outras plantas esbeltas que evoluíram para resistir a condições extremas de vento. É certo que seres vivos, tanto animais quanto plantas, desenvolveram estratégias eficientes para suprimir ou utilizar as vibrações induzidas pelo escoamento. Parte da satisfação que temos em estudar estes fenômenos vem da contemplação das soluções apresentadas na natureza. Cabe a nós desvendá-las e transformá-las para o benefício da humanidade.

## 5 CONCLUSÃO

*“Si hortum in biblioteca habes, deerit nihil.”*

-- Cicero (106-43 a.C.)

Esta resenha autocrítica teve o objetivo de apresentar o desenvolvimento da pesquisa de supressores de vibrações induzidas pelo escoamento ao redor de corpos rombudos. Especial ênfase foi dada à explicação dos fenômenos fluidoelásticos e elucidação dos mecanismos físicos hidrodinâmicos por detrás destes fenômenos.

Concluimos que supressores bidimensionais, aqueles que atuam na raiz do mecanismo de geração de vórtices, têm grande potencial para mitigação de VIE com considerável redução do arrasto gerado na estrutura. Tomando-se o cuidado para que os supressores pivotantes atuem dentro dos limites críticos de atrito rotacional, é possível garantir que os sistemas sejam omnidirecionais e não causem instabilidades fluidodinâmicas mais danosas. Novas geometrias de supressores curtos podem ser desenvolvidas com base no conhecimento adquirido até aqui, agora com foco na otimização dos sistemas.

Sobre supressores tridimensionais, concluimos que dificilmente esta categoria atingirá a combinação de supressão eficaz de VIE com redução de arrasto. Mesmo assim, supressores tridimensionais continuam sendo uma solução interessante, especialmente quando o reduzido custo de fabricação, instalação e manutenção justifica sua aplicação. Desde *strakes* convencionais até novas geometrias tridimensionais inspiradas em soluções da natureza, cremos que haja grande campo para a otimização destes dispositivos para aplicações em problemas de engenharia.

Mais uma vez, além dos resultados de supressores específicos, entendemos que a principal contribuição técnica desta linha de pesquisa esteja no desenvolvimento e amadurecimento de uma metodologia de investigação experimental e numérica capaz de elucidar os mecanismos físicos que governam fenômenos fluidoelásticos. Este conhecimento alimentará a investigação científica e tecnológica de diversas linhas de pesquisa correlatas.

Todas as imagens, discussões e conclusões foram retiradas de artigos científicos publicados pelo autor e seus colaboradores em periódicos internacionais. Estes são anexados a seguir na Parte III deste texto. Porém, vale ainda destacar algumas atividades técni-



cas, científicas e acadêmicas pertinentes ao desenvolvimento deste tema de pesquisa e à experiência adquirida pelo autor na última década.

## PARTE II

### ATIVIDADES CORRELATAS

## 6 EQUIPAMENTOS E MÉTODOS EXPERIMENTAIS

*“Eu gosto da vida também da cidade  
E sei que existe a felicidade  
Mas deve ser filha do interior”*

-- Comp.: Goiá e Amir

### 6.1 Canal de Água Recirculante

Experimentos com modelos em escala reduzida capazes de reproduzir a riqueza dos fenômenos fluidoelásticos requerem equipamentos bem projetados e bem operados para reproduzir as condições ideais e controladas no laboratório. O principal equipamento utilizado na grande maioria dos experimentos discutidos nos capítulos anteriores é o Canal de água recirculante do Núcleo de Dinâmica e Fluidos da Escola Politécnica da Universidade de São Paulo (NDF/EPUSP). Muitos pesquisadores e alunos de graduação e pós-graduação passam pelo laboratório todos os anos, que atrai também o interesse de grupos internacionais que gostariam de desenvolver lá seus experimentos.

O canal, ilustrado na figura 37, foi desenvolvido pelo autor no contexto do projeto temático FAPESP (01/00054-6) Vibração Induzida por Emissão de Vórtices em Estruturas Oceânicas, sob a coordenação geral do Prof. José Augusto P. Aranha, com a coordenação temática do Prof. Clóvis A. Martins e do Prof. Julio R. Meneghini.

Vale registrar nossa profunda gratidão ao Prof. Meneghini, que não poupou esforços para nos envolver nas atividades do projeto quando ainda em um programa de Iniciação Científica. Foi o empenho e a confiança deste orientador que nos impulsionaram para a carreira científica quando nos confiou a tarefa de projetar e construir o canal recirculante, um dos principais equipamentos do projeto temático. Neste processo, participamos de um estágio de pesquisa nos laboratórios do *Department of Aeronautics* do Imperial College London que, além de consolidar nosso interesse pela carreira acadêmica, abriu as portas para o doutorado no exterior.

O canal, cujo projeto conceitual foi inspirado no equipamento que tivemos a oportunidade de utilizar por algumas semanas no Imperial College London, foi projetado e



Figura 37: Canal de Água Recirculante do NDF USP. Reproduzido de Assi (2005); Assi et al. (2005).

construído durante o nosso projeto de mestrado (Assi, 2005). O canal possui uma seção de testes paralela de vidro (permitindo acesso ótico dos modelos por todas as direções) com seção transversal de 700mm de largura por 700mm de profundidade e com 7,5m de comprimento. O escoamento com perfil de velocidades plano pode alcançar velocidades até 0,6m/s com intensidade de turbulência abaixo de 2%. Considerando experimentos de interação fluido-estrutura com corpos cilíndricos de diâmetro médio entre 20mm e 100mm, este canal recirculante permite experimentos tipicamente na faixa de número de Reynolds moderados entre  $10^3$  e  $10^4$ .

Este versátil equipamento foi inaugurado no final de 2004 e está em pleno funcionamento desde então, servindo para o desenvolvimento de diversos projetos de pesquisa da equipe experimental do NDF e formação de diversos alunos e pesquisadores. Por ter sido projetado para permitir a fácil utilização por parte dos usuários, o canal também é frequentemente utilizado para atividades didáticas de graduação, projetos de iniciação científica e projetos de conclusão de curso. Uma apresentação do projeto e construção do canal pode ser encontrada em Assi (2005) e Assi et al. (2005).

Avaliamos que a construção deste canal tenha sido uma das nossas principais contribuições para o avanço do conhecimento no tema, por criar um equipamento compartilhado



Figura 38: Canal recirculante de baixo número de Reynolds.

que reforça o trabalho em grupo e permite a realização de inúmeros outros estudos. Vale ressaltar que nossos projetos nele desenvolvidos também serviram como referência para comparação de muitas simulações numéricas do escoamento produzidas por outros autores ao redor do mundo. Como frequentemente empregamos PIV, pesquisadores utilizam os resultados das nossas medições de esteira para a validação de seus códigos numéricos, especialmente para escoamentos em números de Reynolds moderados.

## 6.2 Canal Recirculante de Baixo Número de Reynolds

O segundo canal recirculante, também instalado no NDF/EPUSP, foi projetado para preencher a lacuna do equipamento anterior, permitindo experimentos de interação fluido-estrutura para números de Reynolds abaixo de  $10^3$ . A figura 38 apresenta o canal construído em aço inoxidável. O equipamento foi financiado pelo projeto regular de pesquisa da FAPESP (11/00205-6), cujo objetivo foi o desenvolvimento de supressores de vibrações induzidas pelo escoamento.

O canal possui seção de testes aberta permitindo escoamento através de uma área com 500mm de largura por 500mm de altura e 1.500mm de comprimento. As paredes e

o fundo são de vidro, permitindo acesso óptico por todos os lados. O fluido de trabalho pode ser uma mistura em qualquer proporção de água e glicerina, elevando a viscosidade e diminuindo o número de Reynolds o quanto se queira. Impulsionado por uma bomba centrífuga, o escoamento plano atinge velocidades entre 0,001m/s e 0,1m/s com baixa intensidade de turbulência.

Este canal de baixo número de Reynolds é especialmente útil para investigações do início das instabilidades fluidodinâmicas, como geração de vórtices, modos tridimensionais na esteira e células de *stall* em perfis de asa. Os resultados nele produzidos também chamam a atenção da comunidade de simulações numéricas, sempre em busca de paradigmas experimentais para validação de seus códigos computacionais.

### 6.3 Bases elásticas

Se os canais recirculantes provêm o escoamento de qualidade, as bases elásticas são responsáveis por emular as condições dinâmicas da estrutura nas condições idealizadas do laboratório. Obviamente é impossível manter a semelhança hidrodinâmica e estrutural de um *riser* real quando o problema é reduzido à escala do laboratório. Assim, as bases elásticas foram projetadas para criar as condições de inércia, rigidez e amortecimento adequadas que representem o comportamento deste pequeno segmento da estrutura dentro do escoamento de água.

Três conceitos de bases elásticas foram desenvolvidos para a maior parte dos experimentos discutidos neste texto: duas bases elásticas que permitem o movimento da estrutura em apenas um grau de liberdade e uma terceira que permite movimentos em dois graus de liberdade. O mesmo princípio construtivo foi utilizado nas três bases. Foram projetadas e confeccionadas da maneira mais leve possível, sempre com a opção de se adicionar massa ao sistema para se aumentar o parâmetro de inércia do sistema. Também foram construídas com o menor amortecimento estrutural possível, permitindo que amortecimento extra fosse adicionado, se necessário. Por fim, a rigidez do sistema foi ajustada através de conjuntos de molas externas ou através de lâminas flexoras.

A primeira base elástica construída foi inspirada em um projeto do Prof. André Fajarra, hoje na Universidade Federal de Santa Catarina. É um projeto simples e elegante, formado por duas lâminas flexoras de aço-mola, paralelas, que suportam o modelo de cilindro. As lâminas permitem movimento na direção transversal e o deslocamento é medido a partir de extensômetros instalados nas lâminas. O sistema é leve e tem baixo

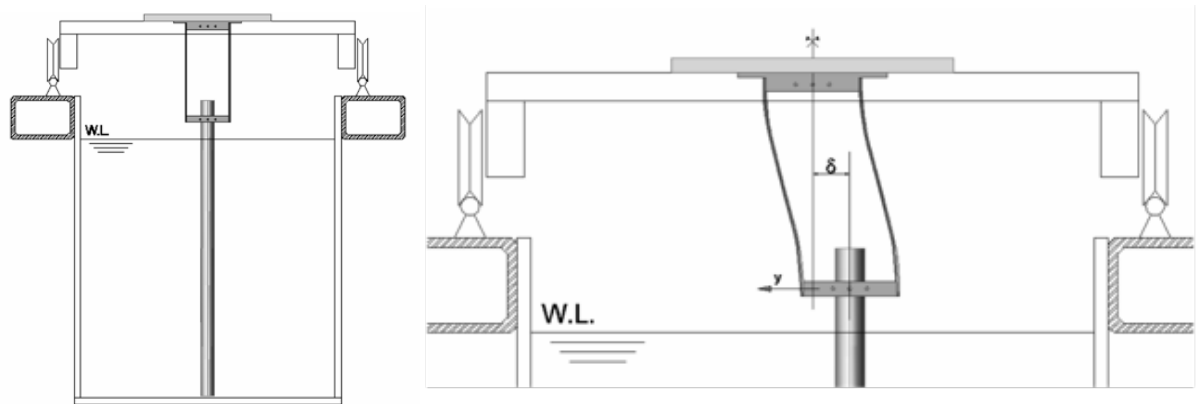


Figura 39: Conceito de base elástica flexora. Reproduzido de Assi et al. (2006).

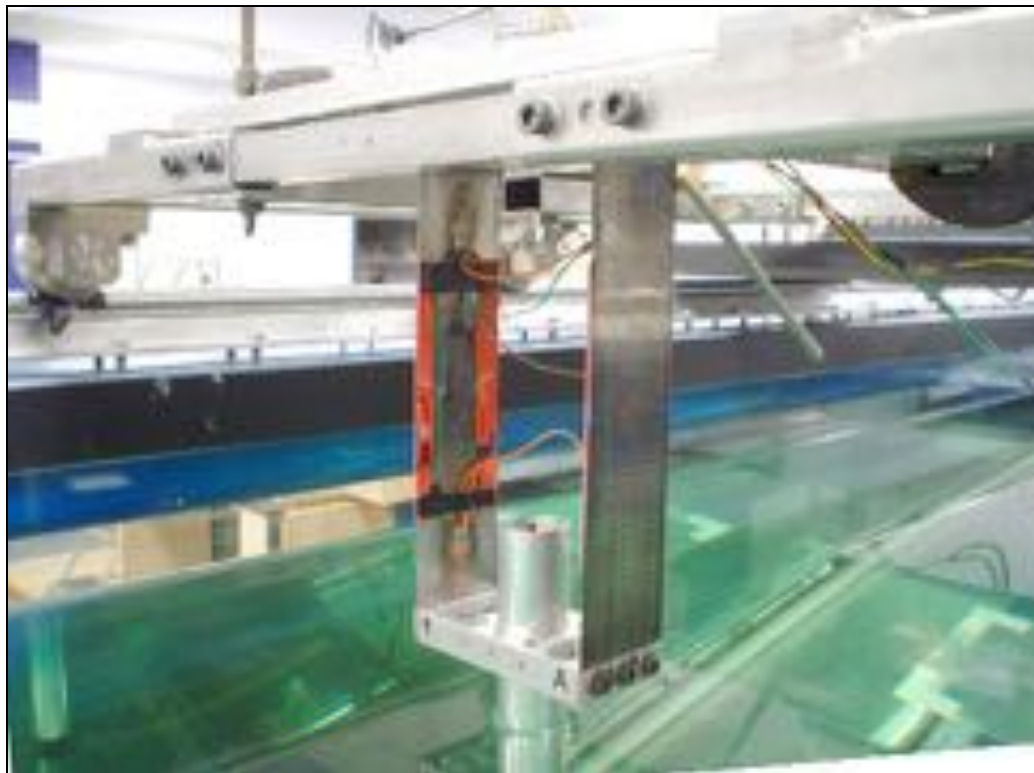


Figura 40: Base flexora (1 grau de liberdade) montada no canal do NDF/EPUSP. Reproduzido de Assi (2005)

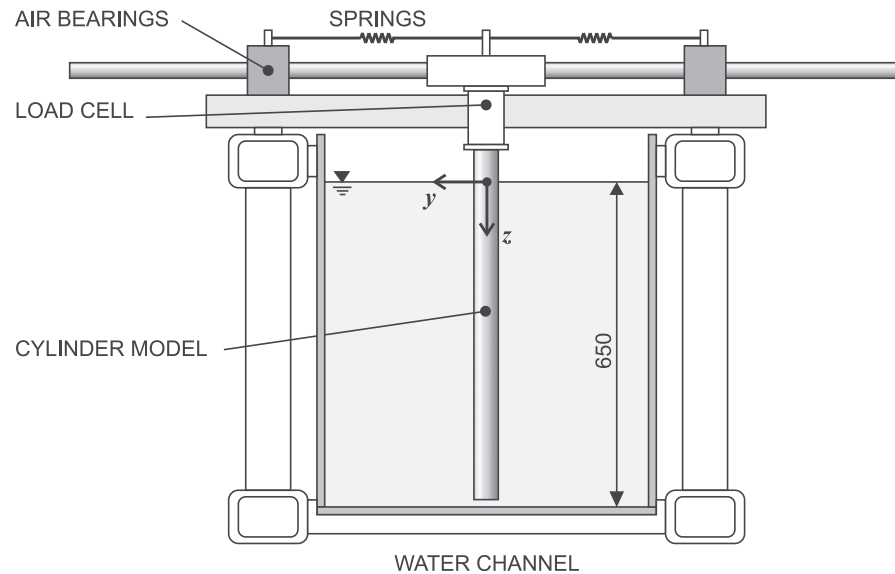


Figura 41: Conceito da base elástica de mancais a ar comprimido (1 grau de liberdade). Reproduzido de Assi (2009).

amortecimento, já que os únicos elementos móveis são as lâminas, que conferem também a rigidez estrutural. O conceito é apresentado na figura 39 e a base pode ser vista instalada no canal na figura 40.

Esta base foi utilizada nos experimentos de Assi (2005), também publicados em Assi et al. (2006). Diversos alunos deram continuidade a este projeto, aprimorando a célula para experimentos mais complexos. Contudo, uma limitação deste conceito está na possibilidade de movimento indesejado na direção do escoamento quando a força de arrasto no modelo é alta e as lâminas apresentam flambagem estrutural.

A segunda base elástica foi a mais utilizada nos experimentos relatados nestes texto e ainda é o equipamento mais demandado para experimentos de interação fluido-estrutural no canal do NDF/EPUSP. Alguns protótipos foram construídos até que chegamos no projeto de uma base elástica formada por quatro mancais de deslizamento pressurizados com ar comprimido. Dois longos tubos de fibra de carbono atravessam os mancais, flutuando entre o filme de ar, conferindo à base baixo amortecimento estrutural devido ao atrito quase nulo. Uma plataforma instalada entre os tubos suporta a célula de carga que, por sua vez, suporta o modelo de cilindro dentro da água. Os elementos móveis são muito leves e a rigidez do sistema é proveniente de duas molas helicoidais instaladas na plataforma central. O deslocamento do modelo é medido através de um sensor óptico para não introduzir nenhum amortecimento no sistema. As figuras 41 e 42 ilustram o conceito e a instalação da base no canal.



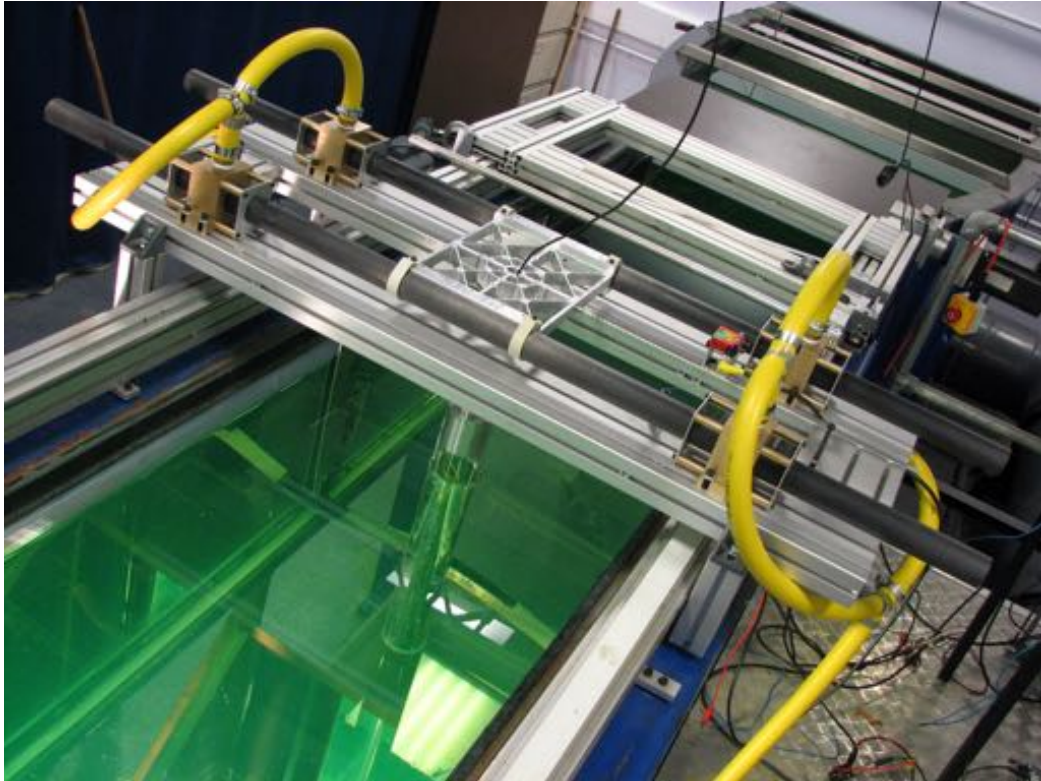


Figura 42: Base elástica de mancais a ar comprimido (1 grau de liberdade) montada no canal do Imperial College London. Reproduzido de Assi (2009).

Esta base resolveu o problema da anterior, apresentando alta rigidez na direção do escoamento e ainda mantendo baixo amortecimento mesmo para elevados carregamentos de arrasto. Ela foi construída pela excelente equipe técnica do *Department of Aeronautics* do Imperial College. Após o término do doutorado, a base foi trazida para o Brasil e hoje se encontra em operação no canal recirculante do NDF/EPUSP.

A terceira base permite movimentos dos cilindros em dois graus de liberdade, a saber, longitudinal e transversal à direção do escoamento incidente. Ela foi projetada a partir de um pêndulo longo, com uma haste de fibra de carbono presa ao teto do laboratório através de uma junta universal de baixo atrito. A célula de carga que suporta o modelo foi instalada na extremidade inferior da haste, onde também são presos dois pares de molas helicoidais para ajustar a rigidez. A base também foi projetada da maneira mais leve possível. Os deslocamentos nas duas direções são medidos com sensores ópticos para não introduzir amortecimento espúrio.

Obviamente, neste tipo de base pendular, o movimento do cilindro não é perfeitamente ortogonal à direção do escoamento, mas construindo-se uma haste de pêndulo suficientemente longa é possível minimizar o desvio do cilindro do prumo vertical. A figura 43 apresenta uma vista lateral do conceito, enquanto a figura 44 detalha sua instalação com

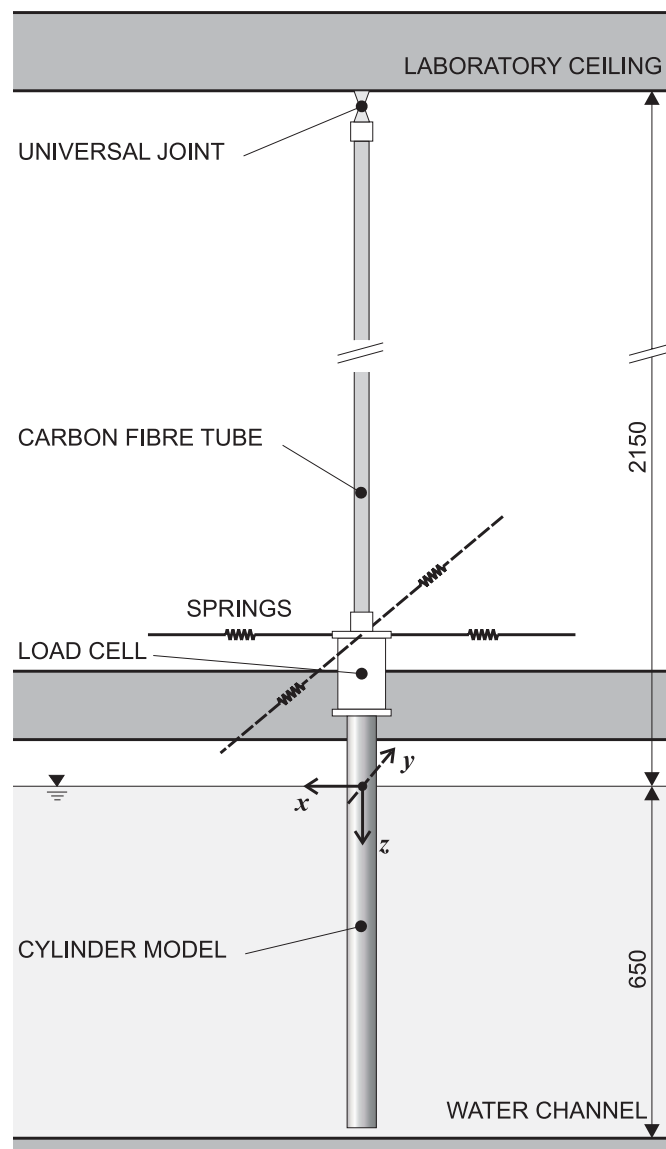


Figura 43: Conceito de base elástica pendular (2 graus de liberdade). Reproduzido de Assi (2009).

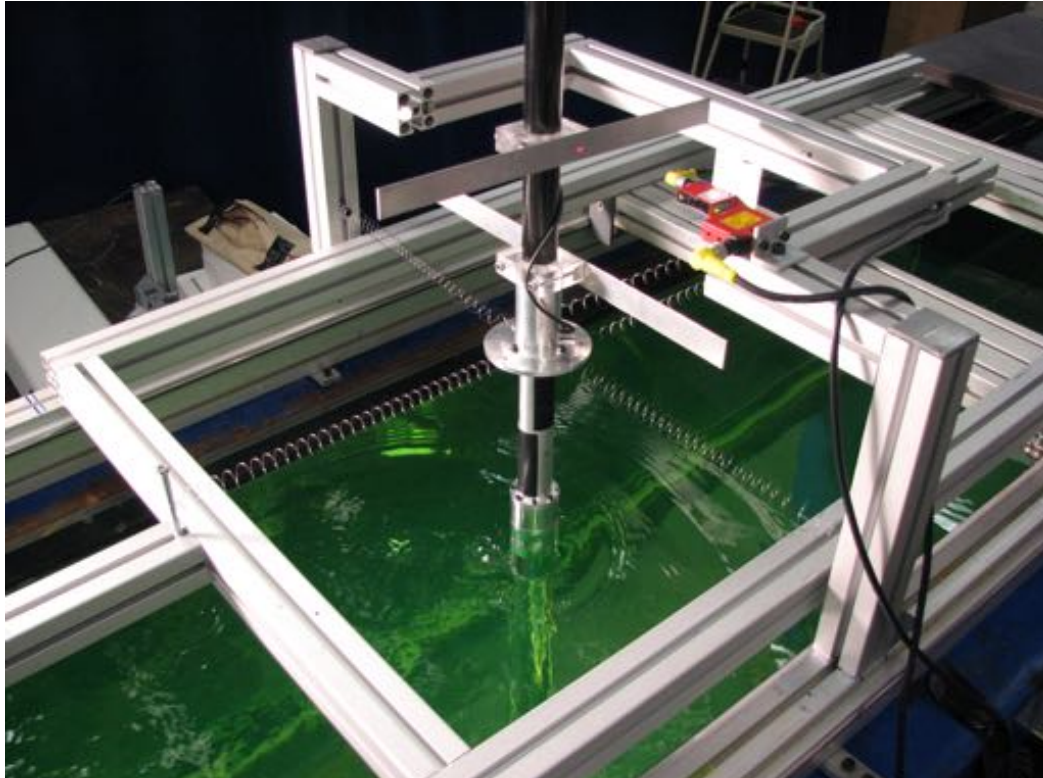


Figura 44: Base elástica pendular (2 graus de liberdade) montada no Imperial College London. Reproduzido de Assi (2009).

um cilindro imerso na água do canal do Imperial College.

— — —

Além dos equipamentos experimentais apresentados neste capítulo, desenvolvemos e adaptamos uma série de outras técnicas e dispositivos aos experimentos de interação fluido-estrutura ao longo dos anos. Muitas vezes a melhor solução não existe na prateleira nem é, necessariamente, a mais cara de um catálogo. A experiência de um grupo de pesquisa, passada de geração para geração de alunos orientados, é patrimônio importante para o grupo de experimentalistas e deve ser valorizada. Conseguir planejar e realizar um bom experimento traz tanta satisfação quanto analisar os dados coletados ou tirar uma boa conclusão.

## 7 ALÉM DA TÉCNICA

*“Eu fui aquele que andou  
Sessenta léguas num dia  
Para ver se breganhava  
Tristeza por alegria”*

-- Comp.: Renato Teixeira

Por fim, apesar deste texto ter como foco uma linha de pesquisa claramente definida (a supressão de vibrações induzidas pelo escoamento), entendemos que outras atividades de cunho acadêmico e científico, que foram desenvolvidas em paralelo ao esforço de pesquisa, também merecem destaque por terem apreço e papel central na experiência do autor. Talvez, com o passar dos anos, este trabalho “além da técnica” produzirá mais frutos que a própria “contribuição fluídoelástica” acima relatada.

### 7.1 Difusão do conhecimento

Um pesquisador pode ser um exímio técnico, excelente em seu trabalho de análise e síntese no laboratório. Todavia, seu trabalho só estará concluído quando for propriamente comunicado. Muitos menosprezam este aspecto de comunicação e difusão do conhecimento, enquanto outros o reduzem ao simples acúmulo de artigos publicados em periódicos científicos. Percebemos que há uma deficiência na habilidade de comunicação em boa parte dos cientistas e acadêmicos. Nossos alunos, por tabela, também não são incentivados ou treinados neste aspecto. Cada vez mais, num mundo de facilidades de comunicação, estamos produzindo uma multidão de solitários que não têm a capacidade de articular argumentos complexos, de ser assertiva sem ser inconveniente, de ouvir o contraponto com respeito ou, simplesmente, de comunicar seu trabalho.

A difusão do conhecimento gerado nas universidades deve ser tarefa obrigatória, deve ser considerada uma necessidade e não um apêndice, e tratada como parte fundamental de qualquer carreira de pesquisa. Consequentemente, deve ser fomentada e praticada. Desde o cultivo do hábito de seminários científicos, da participação em fóruns de áreas ortogonais do conhecimento, do simples interesse pelos avanços da ciência, do domínio da língua inglesa... tudo faz parte deste treinamento que alunos, professores e pesquisadores em

geral devem desenvolver. Todavia, difusão do conhecimento não se resume ao oferecimento das ferramentas, mas está relacionada à criação de uma cultura que, normalmente, leva gerações para se estabelecer.

As ferramentas e os canais de comunicação refletem o presente momento, mudando constantemente com o tempo. Há poucos anos nenhum cientista sonhava em ter seu próprio canal de divulgação científica gratuitamente disponível para todo o planeta. Hoje, qualquer garoto sabe “subir” um vídeo na internet e avaliar sua repercussão nas redes sociais. Mesmo pessoas que “não tem muito o que dizer” tornaram-se formadoras de opinião. Se quisermos que a ciência e a tecnologia brasileiras (que têm excelência em muitas áreas) tenham impacto mundial positivo, devemos investir também na difusão do conhecimento de maneira intencional e assertiva.

Finalmente, defendemos que o engajamento com a difusão do conhecimento seja um papel a ser desempenhado e, portanto, incentivado e treinado, por alunos, docentes e a própria universidade no campo institucional. A comunicação com a sociedade deve se dar em vários níveis e com vários públicos. Difundir conhecimento apenas à comunidade científica através de periódicos especializados é abordar apenas um deles. Precisamos ficar atentos e preparados para comunicar adequadamente o impacto dos avanços da ciência e da tecnologia para a sociedade na riqueza de sua variedade. Isto se faz necessário especialmente em tempos de alarmismo, negacionismo, cientificismo ou tecnicismo.

## 7.2 Ensino de engenharia

O ensino de engenharia segue uma curva característica de amadurecimento. E engenheiro é, por definição, um agente transformador do mundo natural. Seu objetivo é usar do conhecimento adquirido e da técnica bem aplicada para conduzir mudanças que beneficiem a humanidade nos seus mais diversos aspectos. Porém, isto não se aprende da noite para o dia, mas requer esforço e engajamento intelectual.

No momento em que escrevo este texto passamos por uma transformação no ensino de engenharia. Durante a pandemia de COVID-19 fomos forçados a nos adaptar e renovar as ferramentas e métodos de ensino, interagindo com multidões de alunos através de pequenas telas impessoais, porém invasivas. A concentração e a dedicação dos alunos dessa geração imediatista está cada vez menor, provocando em todos uma insatisfação com as antigas metodologias de ensino e aprendizagem. De fato, estamos vivenciando uma transição no ensino.

Temos nos preocupado com esse movimento. Muitas vezes, na estrutura universitária, os alunos são a parte mais frágil por passarem apenas um período de cinco anos no curso (docentes passam aqui a sua vida). Contudo, é na análise de gerações de alunos, que entram e saem da Escola Politécnica, que temos observado este comportamento e refletido sobre como estruturar cursos que despertem o interesse, evidenciem as potencialidades e desenvolvam as virtudes de um bom engenheiro nos nossos tutorados.

Na nossa humilde opinião, três aspectos no ensino de engenharia merecem destaque no momento em que vivemos: (i) tutoria próxima e relacional com alunos, (ii) aprendizado na fronteira do conhecimento e (iii) visão ampla além da técnica. Permitam-nos desenvolver rapidamente estas ideias.

(i) Temos o privilégio (e as dificuldades associadas, evidentemente) de sermos um grupo relativamente pequeno no curso de graduação em Engenharia Naval na Escola Politécnica da USP. Cerca de 12 docentes têm contato direto com 150 alunos em média (do terceiro ao quinto ano) num determinado momento. Isto permite uma relação muito próxima entre professores e alunos, fortalecida pela identidade que a Engenharia Naval oferece. Defendo que precisamos aproveitar melhor este aspecto relacional, promovendo trocas de experiências além da sala de aula e aproximando a experiência do aluno da experiência do professor. Por exemplo, através de projetos de iniciação científica, acompanhamento de grupos de extensão, tutoria individualizada, dentre outras atividades, é possível que alunos e professores se tornem co-participantes do processo de aprendizagem em um nível mais profundo que o da sala de aula. Novamente, num tempo de relacionamentos fragilizados, agravados pelo fenômeno das redes sociais, a relação de confiança e credibilidade entre tutores e tutorados é benéfica para todos. Em resumo, defendemos medidas que transformem docentes em mentores e alunos em aprendizes.

(ii) A Universidade de São Paulo é, reconhecidamente, a principal universidade de pesquisa do Brasil. Cerca de 25% de todos os artigos científicos internacionais publicados por brasileiros têm autores da USP. Fazer um curso nesta universidade e não ser beneficiado por esta característica é um desperdício. Muitos dos nossos grupos de pesquisa em engenharia são mundialmente reconhecidos por estarem atuando na fronteira do conhecimento. Nosso desafio como docentes e pesquisadores é fazer com que o impacto do laboratório e dos resultados de pesquisa cheguem na rotina de formação dos engenheiros. Estamos convencidos de que alunos em contato com o desenvolvimento da engenharia na fronteira do conhecimento mantêm o interesse e despertam mais cedo para o impacto que sua carreira profissional eventualmente terá para o desenvolvimento tecnológico na nossa sociedade. Precisamos garantir que o conhecimento de ponta produzido nos laboratórios

permeie para todos os alunos que passam por esta universidade.

(iii) Enquanto educadores, devemos nos esforçar para que os futuros engenheiros sejam instruídos levando em conta os mais diversos aspectos envolvidos no processo do desenvolvimento tecnológico. A engenharia (e antes a tecnologia) não é um ente monolítico. Ensinar alunos a verificarem a viabilidade técnica e econômica de um projeto não é o suficiente. Os alunos devem ser induzidos a refletir no impacto que a sua engenharia produzirá além do seu bolso, da sua pessoa, da sua família e da sua empresa. É necessário estimular uma visão transformadora e ao mesmo tempo altruísta, que considere os diferentes aspectos da realidade em que vivemos mesmo num projeto de engenharia. Em outras palavras, é preciso engajar-se intelectualmente com os alunos, provocando-os e conduzindo-os numa jornada além da técnica. (Este terceiro ponto está diretamente relacionado com o que discutiremos na próxima seção.)

— — —

Valores como transdisciplinaridade, internacionalização, customização do ensino, empreendedorismo, inovação, criatividade... são todos muito importantes e bem-vindos em qualquer processo de aprendizagem de engenharia. Contudo, cremos que estes três aspectos destacados anteriormente sejam prementes e estejam no cerne de uma boa atividade de aprendizagem, seja no nível de graduação ou de pós-graduação, na engenharia dos dias de hoje.

## 7.3 Filosofia da tecnologia

Nos últimos anos temos refletido mais proximamente sobre o papel da tecnologia no desenvolvimento humano e social. Podemos afirmar que encontramos ferramental teórico e inspiração prática acessível ao engenheiro que se disponha a este exercício. Permita-nos apresentar-lhe o Prof. Egbert Schuurman, engenheiro e filósofo holandês, professor emérito das universidades de Delft, Eindhoven e Wageningen. Em julho de 2016 tivemos o privilégio de sermos recebidos por ele em sua residência na vila de Breukelen. Na ocasião, aproveitamos para conduzir uma entrevista, que hoje está disponível em nosso canal na internet.

O Prof. Schuurman foi, até hoje, o mais longo senador da Holanda, servindo no parlamento por 28 anos (feito heróico para nossos padrões brasileiros, visto que senadores na Holanda são servidores públicos no sentido estrito do termo: não recebem salários, apartamentos ou benefícios extraordinários além de uma ajuda de custo). Schuurman,

enquanto senador, manteve suas atividades normais como docente nas universidades em que atuava e viajava de trem semanalmente para servir no parlamento em Haia.

Para Egbert Schuurman, “a causa-raiz dos principais problemas que ameaçam a cultura ocidental é o *tecnicismo*, que pode ser entendido como o depósito da esperança última na tecnologia. Como tal, o tecnicismo envolve a inclinação dos afetos para a técnica, entregando-lhe lágrimas de súplica e exclamações de louvor, temor e maravilhamento. Portanto, trata-se de uma atitude religiosa para com a tecnologia. A fonte última de significado, legisladora sobre todos os aspectos da vida, é atribuída à invenção e ao uso de ferramentas capazes de moldar a realidade. Entendemos que o desenvolvimento da boa tecnologia deva ser perseguido com responsabilidade moral e, portanto, o tecnicismo, tão permeado na sociedade ocidental, deve ser confrontado.” A Filosofia da Tecnologia da tradição reformacional holandesa, da qual Schuurman é um representante contemporâneo, contribui nesta direção.

De certo modo, o contato com este admirado mestre enriqueceu nosso interesse pelo campo da Filosofia da Tecnologia. Não é nosso objetivo aqui definir ou discorrer sobre o tema, mas basta dizer que se trata de um ramo da Filosofia que reflete criticamente sobre o papel da tecnologia, dos artefatos tecnológicos, dos usuários, do impacto na sociedade e, em última instância, do agente tecnológico que provoca a transformação (no nosso caso, o engenheiro). O trabalho do Prof Schuurman é inspirador. Sua abordagem sólida, profunda e, ao mesmo tempo, prática da tecnologia promove uma reflexão genuína do papel do engenheiro e, em especial, do professor de engenharia. Ao interessado no tema, recomendamos o livro “Filosofia da Tecnologia, uma Introdução” (Verkek et al., 2018), que traz muito do pensamento de Schuurman, e a sua obra prática “Fé, Esperança e Tecnologia” (Schuurman, 2016), ambas recém lançadas no Brasil.

— — —

Temos reconhecido como nossa função na carreira docente não apenas a transmissão de conhecimento técnico e teórico aos alunos de graduação e pós-graduação. Zelamos por incentivar em nossos tutorados o desenvolvimento de virtudes intelectuais e sociais, o compromisso com a excelência, e a reflexão crítica sobre nosso papel como agentes de transformação tecnológica. Sinceramente, esperamos que nosso impacto nas futuras gerações de engenheiros e pesquisadores não seja apenas no tema de supressão de vibrações induzidas pelo escoamento, mas, principalmente, que frutifiquem neste último aspecto, com o qual encerramos esta resenha.



## REFERÊNCIAS BIBLIOGRÁFICAS

- D. W. Allen and D. Henning. Small fixed teardrop fairings for vortex induced vibration suppression. United States Patent (number 5,410,979), May 1995.
- G. R. Assi. Wake-induced vibration of tandem cylinders of different diameters. *Journal of Fluids and Structures*, 50:329–339, 2014a.
- G. R. Assi, N. Srinil, C. M. Freire, and I. Korkischko. Experimental investigation of the flow-induced vibration of a curved cylinder in convex and concave configurations. *Journal of Fluids and Structures*, 44:52–66, 2014a.
- G. R. S. Assi. Estudo experimental do efeito de interferência no escoamento ao redor de cilindros alinhados. Master’s thesis, Universidade de São Paulo, São Paulo, Brazil, 2005. Disponível em [www.teses.usp.br](http://www.teses.usp.br).
- G. R. S. Assi. *Mechanisms for flow-induced vibration of interfering bluff bodies*. PhD thesis, Imperial College London, London, UK, 2009. Available from [www.ndf.poli.usp.br/~gassi](http://www.ndf.poli.usp.br/~gassi).
- G. R. S. Assi. Wake-induced vibration of tandem and staggered cylinders with two degrees of freedom. *J. Fluids Structures*, Submitted for publication, 2014b.
- G. R. S. Assi and P. W. Bearman. Transverse galloping of circular cylinders fitted with solid and slotted splitter plates. *Journal of Fluids and Structures*, 54:263–280, 2015.
- G. R. S. Assi and P. W. Bearman. Vortex-induced vibration of a wavy elliptic cylinder. *Journal of Fluids and Structures*, 80:1–21, 2018.
- G. R. S. Assi, J. R. Meneghini, J. A. P. Aranha, and W. G. P. Coletto. Design, assembling and verification of a circulating water channel facility for fluid dynamics experiments. *COBEM 2005: proceedings*, 2005.
- G. R. S. Assi, J. Meneghini, J. Aranha, P. W. Bearman, and E. Casaprima. Experimental investigation of flow-induced vibration interference between two circular cylinders. *J. Fluids Structures*, 22:819–827, 2006.

- G. R. S. Assi, P. W. Bearman, and N. Kitney. Low drag solutions for suppressing vortex-induced vibration of circular cylinders. *J. Fluids Structures*, 25:666–675, 2009.
- G. R. S. Assi, P. W. Bearman, N. Kitney, and M. Tognarelli. Suppression of wake-induced vibration of tandem cylinders with free-to-rotate control plates. *J. Fluids Structures*, 26:1045–1057, 2010a.
- G. R. S. Assi, P. W. Bearman, and J. Meneghini. On the wake-induced vibration of tandem circular cylinders: the vortex interaction excitation mechanism. *J. Fluid Mech.*, 661:365–401, 2010b.
- G. R. S. Assi, P. W. Bearman, B. Carmo, J. Meneghini, S. Sherwin, and R. Willden. The role of wake stiffness on the wake-induced vibration of the downstream cylinder of a tandem pair. *J. Fluid Mech.*, 718:210–245, 2013.
- G. R. S. Assi, P. W. Bearman, and M. A. Tognarelli. On the stability of a free-to-rotate short-tail fairing and a splitter plate as suppressors of vortex-induced vibration. *Ocean Engineering*, 92:234–244, 2014b.
- G. R. S. Assi, G. S. Franco, and M. S. Vestri. Investigation on the stability of parallel and oblique plates as suppressors of vortex-induced vibration of a circular cylinder. *Journal of Offshore Mechanics and Arctic Engineering*, 136(3):031802, 2014c.
- G. R. S. Assi, R. M. Orselli, and M. Silva-Ortega. Control of vortex shedding from a circular cylinder surrounded by eight rotating wake-control cylinders at  $Re = 100$ . *Journal of Fluids and Structures*, 2019.
- G. R. S. Assi, T. Crespi, and M. Gharib. Experiments with novel geometries of serrated helical strakes to suppress vortex-induced vibrations. *Submitted for publication in Ocean Engineering*, 2021.
- P. W. Bearman. Vortex shedding from oscillating bluff bodies. *Annu. Rev. Fluid Mech.*, 16:195–222, 1984.
- H. R. Beem and M. S. Triantafyllou. Wake-induced ‘slaloming’ response explains exquisite sensitivity of seal whisker-like sensors. *Journal of Fluid Mechanics*, 783:306–322, 11 2015.
- R. Blevins. *Flow-Induced Vibration*. Van Nostrand Reinhold, 2nd edition, 1990.
- A. Brown. Device and method for suppressing vortex-induced vibrations. Technical report, United States Patent Application Publication, 2010.

- F. F. Buscariolo, G. R. Assi, and S. J. Sherwin. Computational study on an ahmed body equipped with simplified underbody diffuser. *Journal of Wind Engineering and Industrial Aerodynamics*, 209:104411, 2021. ISSN 0167-6105.
- B. S. Carmo, G. R. S. Assi, and J. R. Meneghini. Computational simulation of the flow-induced vibration of a circular cylinder subjected to wake interference. *Journal of Fluids and Structures*, 41:99–108, 2013.
- M. M. Cicolin and G. R. S. Assi. Experiments with flexible shrouds to reduce the vortex-induced vibration of a cylinder with low mass and damping. *Applied Ocean Research*, 65:290–301, 2017a.
- M. M. Cicolin and G. R. S. Assi. Laboratory-scale investigation of the ventilated-trousers device acting as a suppressor of vortex-induced vibrations. *Ocean Engineering*, 142:411–418, 2017b.
- M. M. Cicolin, O. R. H. Buxton, G. R. S. Assi, and P. W. Bearman. The role of separation on the forces acting on a circular cylinder with a control rod. *Accepted for publication in the Journal of Fluid Mechanics*, 2021.
- J. Gerrard. The mechanics of the formation region of vortices behind bluff bodies. *J. Fluid Mech.*, 25:401–13, 1966.
- I. Korkischko and J. Meneghini. Suppression of vortex-induced vibration using moving surface boundary-layer control. *Journal of Fluids and Structures*, 34:259 – 270, 2012. ISSN 0889-9746.
- I. Korkischko and J. R. Meneghini. Volumetric reconstruction of the mean flow around circular cylinders fitted with strakes. *Experiments in fluids*, 51(4):1109, 2011.
- C. A. Martins. Uma ferramenta expedita para estudo de viabilidade de risers rígidos em catenária. Resenha de Livre Docência apresentada a Escola Politécnica da Universidade de São Paulo, 2000.
- J. R. Meneghini. Projetos de pesquisa em geração e desprendimento de vórtices no escoamento ao redor de cilindros. Resenha de Livre Docência apresentada a Escola Politécnica da Universidade de São Paulo, 2002.
- V. Modi. Moving surface boundary-layer control: a review. *Journal of Fluids and Structures*, 11(6):627 – 663, 1997. ISSN 0889-9746.

- C. P. Pesce. Mecânica de cabos e tubos submersos lançados em catenária: uma abordagem analítica e experimental. Resenha de Livre Docência apresentada a Escola Politécnica da Universidade de São Paulo, 1997.
- A. Rinehart, V. Shyam, and W. Zhang. Characterization of seal whisker morphology: implications for whisker-inspired flow control applications. *Bioinspiration & Biomimetics*, 12(6):066005, 2017.
- E. Schuurman. *Fé, Esperança e Tecnologia*. Ed. Ultimato, 2016.
- M. Silva-Ortega and G. R. S. Assi. Flow-induced vibration of a circular cylinder surrounded by two, four and eight wake-control cylinders. *Experimental Thermal and Fluid Science*, 85:354 – 362, 2017a. ISSN 0894-1777.
- M. Silva-Ortega and G. R. S. Assi. Suppression of the vortex-induced vibration of a circular cylinder surrounded by eight rotating wake-control cylinders. *Journal of Fluids and Structures*, 74:401 – 412, 2017b. ISSN 0889-9746.
- M. Silva-Ortega and G. R. S. Assi. Hydrodynamic loads on a circular cylinder surrounded by two, four and eight wake-control cylinders. *Ocean Engineering*, 153:345 – 352, 2018. ISSN 0029-8018.
- M. J. Verkek, J. Hoogland, J. van der Stoep, and M. J. de Vries. *Filosofia da Tecnologia, uma Introdução*. Ed. Ultimato, 2018.
- C. H. K. Williamson and R. Govardhan. Vortex-induced vibrations. *Annu. Rev. Fluid Mech.*, 36:413–55, 2004.
- M. M. Zdravkovich. Review and classification of various aerodynamic and hydrodynamic means for suppressing vortex shedding. *J. Wind Eng. Industrial Aerodynamics*, 7:145–189, 1981.

## PARTE III

### ANEXOS – ARTIGOS PUBLICADOS EM PERIÓDICOS



# Experimental investigation of flow-induced vibration interference between two circular cylinders

G.R.S. Assi<sup>a</sup>, J.R. Meneghini<sup>a,\*</sup>, J.A.P. Aranha<sup>a</sup>, P.W. Bearman<sup>b</sup>, E. Casaprima<sup>c</sup>

<sup>a</sup>NDF, “Escola Politécnica”, Department of Mechanical Engineering, University of São Paulo, CEP 05508-900 São Paulo, SP, Brazil

<sup>b</sup>Department of Aeronautics, Imperial College, London SW7 2BY, UK

<sup>c</sup>Petrobras, CENPES, Rio de Janeiro, Brazil

Received 1 October 2005; accepted 9 April 2006

Available online 24 July 2006

## Abstract

This paper presents experimental results concerning flow-induced oscillations of circular cylinders arranged in tandem. New measurements on the dynamic response oscillations of an isolated cylinder and flow interference of two cylinders are shown. Preliminary flow visualization employing a PIV system is also shown. The models are mounted on an elastic base fitted with flexor blades and instrumented with strain gauges. The base is fixed on the test-section of a water channel facility. The flexor blades possess a low-damping characteristic ( $\zeta \simeq 0.008\text{--}0.0109$ ) and they are free to oscillate only in the cross-flow direction. The Reynolds number of the experiments is from 3000 to 13 000, and reduced velocities, based on natural frequency in still water, vary up to 12. The interference phenomenon on VIV is investigated by conducting experiments in which the upstream cylinder is maintained fixed and the downstream one is mounted on the elastic base. The results for an isolated cylinder are in accordance with other measurements found in the literature for  $m^* \simeq 2$  and 8. For the tandem arrangement and  $m^* \simeq 2$ , the trailing cylinder oscillation presents what previous researchers have termed interference galloping behaviour for a centre-to-centre gap spacing ranging from  $2D$  to  $5.6D$ . These initial results validate the experimental set-up and lead the way for future work, including tandem, staggered and side-by-side arrangements with the two cylinders free to move.

© 2006 Elsevier Ltd. All rights reserved.

**Keywords:** Vortex-induced vibration; Flow interference; Vortex shedding

## 1. Introduction

Flow interference among groups of cylinders has been the subject of many studies in the past. The interference is responsible for several changes in the characteristics of fluid loads when more than one body is placed in a fluid stream. Investigations of the flow around pairs of cylinders can provide a better understanding of the vortex dynamics, pressure distribution and fluid forces, in cases involving more complex arrangements.

This paper presents an experimental study of the flow interference between a pair of rigid cylinders, in tandem configurations, with the rear cylinder elastically mounted and free to oscillate transversely to the flow. In addition, it presents new measurements for an isolated rigid cylinder. In all cases the cylinders are allowed to oscillate only in the

---

\*Corresponding author. Tel.: +55 11 3091 5641; fax: +55 11 3091 5642.

E-mail address: [julio.meneghini@poli.usp.br](mailto:julio.meneghini@poli.usp.br) (J.R. Meneghini).

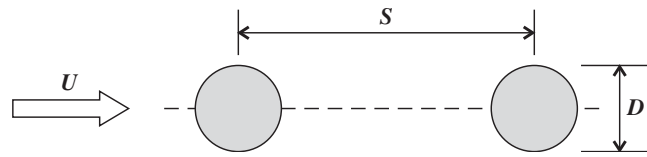


Fig. 1. Configuration for the tandem arrangement.

transverse direction. Dynamic response and forced oscillations of an isolated cylinder have been carefully studied through the past years. Detailed information and accurate data are found in many reviews and recent studies: Bearman (1984), Blevins (1990), Khalak and Williamson (1996, 1999), Krishnamoorthy et al. (2001), and Williamson and Govardhan (2004) among others. Recently, new studies have been published focusing on understanding vortex-suppressor devices, as presented by Bearman and Branković (2004) and Owen et al. (2001).

Many of the previous works regarding the flow around two circular cylinders identified various *interference regimes* and were based primarily on flow visualization in experiments. Investigations such as those by Igarashi (1981), Zdravkovich (1977, 1987) and Sumner et al. (2000) proposed classifications of these regimes. Quoting Zdravkovich, “when more than one bluff body is placed in a fluid flow, the resulting forces and vortex shedding pattern may be completely different from those found on a single body at the same Reynolds number.” A variety of flow patterns, characterized by the behaviour of the wake region, may be discerned as the centre-to-centre spacing between two circular cylinders (gap  $S$ ) is varied; see Fig. 1. The phenomenon has also been intensely analysed by numerical methods, as seen in Meneghini et al. (2001), for instance.

Some results about flow interference between a pair of cylinders in tandem can also be found in the investigations by King and Johns (1976), Bokaian and Geoola (1984), Brika and Laneville (1997, 1999), and Hover and Triantafyllou (2001). All these papers present experimental results of a trailing rigid cylinder oscillating in the wake of an upstream one. According to Bokaian and Geoola (1984), in the case of a fixed leading cylinder, both vortex-resonance and wake galloping instability phenomena are relevant and can occur separately or combined, depending on the separation distance. For  $7 \leq S/D \leq 8.5$ , Brika and Laneville (1999) observed that the downstream cylinder exhibited a combination of galloping and vortex-induced vibration.

This paper presents new measurements of vortex-induced vibration of a single cylinder. The experiments are carried out in order to validate the experimental set-up and data processing for future investigations. In addition, they introduce the base results for comparisons with induced oscillations of a trailing rigid cylinder in a tandem arrangement. A brief description of the apparatus and some remarks regarding future investigations complements the material. Some preliminary PIV flow visualization techniques are shown for two fixed cylinders arranged in tandem.

## 2. Experimental set-up

Tests were conducted at the Hydrodynamics Laboratory of Imperial College (IC), London, and at the Fluid-Dynamics Research Group Laboratory of the University of São Paulo (USP). The circulating water channel facility at IC had a  $0.60 \times 0.70 \times 8.00$  m test-section, and the facility at USP had a  $0.70 \times 0.80 \times 7.50$  m test-section. Both could operate at good quality and well-controlled flows up to 0.7 m/s. Rigid cylinder models were made of aluminium tubes with diameter  $D = 32$  mm and wet-length  $L = 560$  mm under the water level. Cylinders were vertically clamped by their upper end at the bottom block of elastic supports (firmly fixed on the channel structure) and terminated at their lower end with a 2.0 mm gap on to the test-section floor. The open section channel facilities at IC and USP were equipped with glass walls and a glass floor offering a complete view of the models. For tandem arrangements, the gap between the cylinder centres varied through four different discrete displacements:  $S/D = (2.0, 3.0, 4.0, 5.0, 5.6)$ . Fig. 2 presents a schematic cross-sectional view of the apparatus mounted on the channel structure.

Both cylinders were independently mounted under an individual elastic base free to oscillate transversely to the flow direction, i.e., only in the cross-flow direction. For each flexible base system, the transverse degree of freedom could be locked, so every model could or could not be free to move in cross-flow oscillations, resulting in different tandem oscillating configurations. Both elastic systems were built with two parallel rigid aluminium blocks, coupled by a pair of thin spring-steel blade flexors. These bases not only act as the cylinder support, but also provide the restoration system response. This flexion-based arrangement was confirmed as a low-damping elastic system. In order to measure cylinder displacements, four strain gauges were built in each pair of blades close to the highest bending region of the face. A complete bridge was built up enabling a linear cylinder displacement signal to be acquired. A set of three base systems was available for isolated cylinder experiments, while another two systems were prepared for tandem arrangement tests.

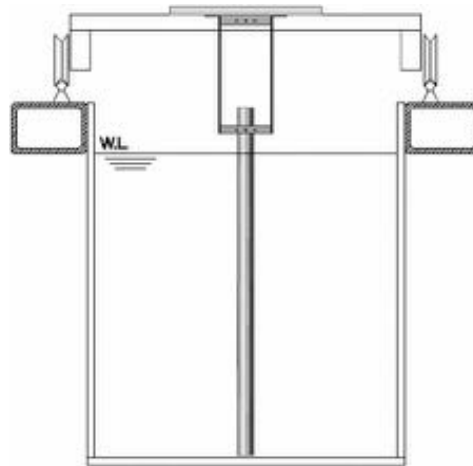


Fig. 2. Cylinder and elastic base mounted on the channel test-section structure.

Table 1  
Oscillation parameters for the bases tested

| Base identification              | $m^*$ | $f_N$ | $\zeta$ | $m^*\zeta$ |
|----------------------------------|-------|-------|---------|------------|
| Single cylinder (low mass IC)    | 0.96  | 1.56  | 0.008   | 0.008      |
| Single cylinder (low mass USP)   | 0.90  | 1.17  | 0.0109  | 0.010      |
| Single cylinder (median mass IC) | 1.92  | 0.98  | 0.007   | 0.013      |
| Single cylinder (high mass IC)   | 8.06  | 1.17  | 0.002   | 0.016      |
| Pair: downstream cylinder (IC)   | 1.92  | 0.98  | 0.007   | 0.013      |
| Pair: downstream cylinder (USP)  | 0.90  | 1.17  | 0.0109  | 0.010      |

The different bases providing different mass ratios. Mass ratio and spring stiffness were the structural parameters that were varied. Table 1 lists the oscillation parameters obtained for all those configurations. Models tested at Imperial College are indicated by IC, and those models tested at the University of São Paulo are indicated by USP.

Decay tests in water were employed to obtain the natural oscillation frequency ( $f_N$ ), while the structural damping parameter ( $\zeta$ ) was obtained from decay test performed in air. Mass ratio ( $m^*$ ) is defined as  $m^* = 4M/\rho\pi D^2 L$  (where  $M$  represents the total oscillating mass and  $\rho$  is the water density). The added mass has not been considered in this definition. Fig. 3 details the elastic base and its spring blades (cross-flow direction is identified by the  $y$ -axis) and Fig. 4 shows the experimental apparatus installed in the channel test-section.

### 3. Results and discussion

The dynamic responses of the models are described in terms of reduced amplitude  $A/D$  versus reduced velocity  $V_r$ . Some results found in the literature are shown for comparison. Amplitude peaks were calculated employing the Hilbert transform, as described in Khalak and Williamson (1999). Reynolds number (calculated for a single cylinder with diameter  $D$  and current velocity  $U$ ) ranges from  $Re = 3000$  and  $13\,000$  in all experiment cases. The reduced velocity  $V_r = f_N U/D$  range extended to a maximum value of 12, hence covering the occurrence of several possible phenomena.

#### 3.1. Single circular cylinder

The responses for an isolated cylinder, with three values of mass and damping parameters, are shown in Figs. 5, Fig. 6, and Fig. 7. These three figures compare the present data to results found in the literature for the three different conditions mentioned before: low mass, median mass, and high mass. They are employed as a baseline for comparisons with the tandem arrangement cases. The following series presents the dynamic response of a single cylinder, free to oscillate in the cross-flow direction, mounted on a low-damping elastic system. In Fig. 5, the nondimensional amplitude of oscillation is presented versus the reduced velocity for  $m^* \simeq 1$ . The current speed was increased in order to obtain this



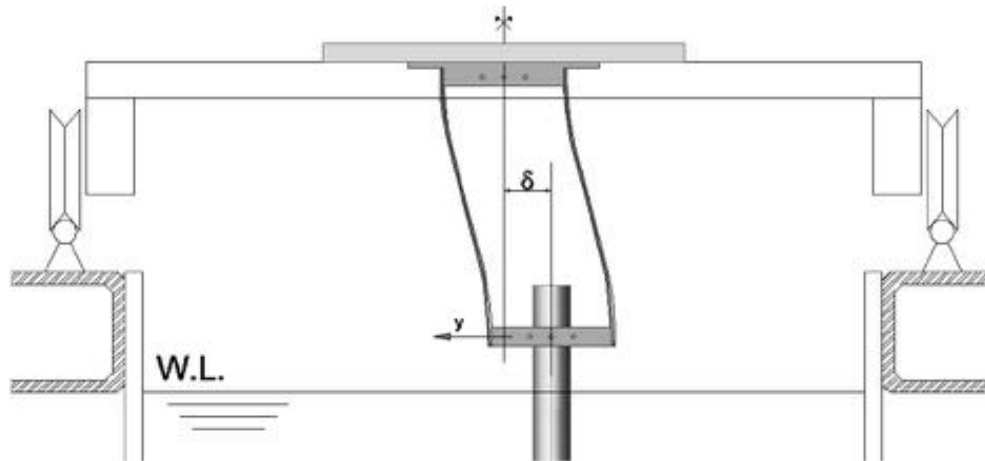


Fig. 3. Detail of the elastic base at a flexing instant. W.L. represents the water line level and  $\delta$  the horizontal displacement of the cylinder centre.



Fig. 4. Cylinder and elastic base mounted on the channel test-section structure.

curve. Our maximum amplitude for the IC model is slightly below  $1D$  and it occurs at a reduced velocity  $V_r \simeq 6$ . The maximum amplitude for the USP model is about  $1.2D$  and it takes place at about the same reduced velocity. Our results compare relatively well with those obtained by Branković (2004), in which the reduced velocity range was extended up to 14. For this low mass parameter case, one can notice that oscillation starts at about  $V_r \simeq 2.5$  and is sustained up to very high reduced velocity. Such behaviour is expected for very low mass parameter experiments and has already been observed in other investigations. For the low mass parameter model in the IC experiment, the maximum reduced velocity tested could not be increased beyond  $V_r = 7$  due to the low stiffness of the flexor blades. In order to increase the in-line stiffness of the base, a third flexor blade has been added to the models tested at USP, which allowed higher velocities to be tested. For this model, reduced velocities up to 12 have been tested.

Fig. 6 shows the response for  $m^* \simeq 2$ . In this case, we compare our results with those by Khalak and Williamson (1999), and Hover and Triantafyllou (2001). Although the experimental apparatuses used were based on different concepts, the mass and damping parameters are very similar and the observed responses are in close agreement. The oscillations start at about  $V_r \simeq 3.0$  and are sustained up to  $V_r = 12.0$ . The peak amplitude in the present investigation is around  $0.9D$ . Finally, in Fig. 7, the results for  $m^* \simeq 8$  are shown and compared to those by Khalak and Williamson (1999) and Fujarra (2002). The oscillation starts at about  $V_r \simeq 3.5$  and the peak amplitude observed in the present results is around  $1D$ .

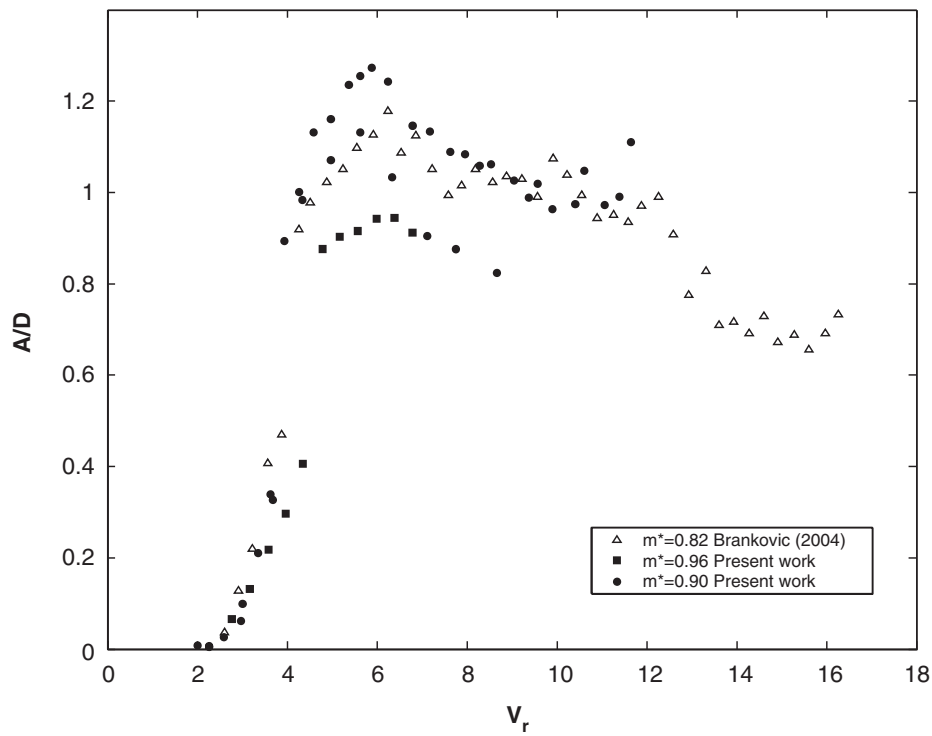


Fig. 5. Variation of the reduced amplitude  $A/D$  versus reduced velocity  $V_r$  for an isolated cylinder with low mass ratio parameter. Present work: ■, IC model,  $m^* = 0.96$ ,  $(m^*\zeta) \simeq 0.008$ ; ●, USP model,  $m^* = 0.90$ ,  $(m^*\zeta) \simeq 0.010$ ; △, Branković (2004),  $m^* = 0.82$ ,  $(m^*\zeta) \simeq 0.0001$ .

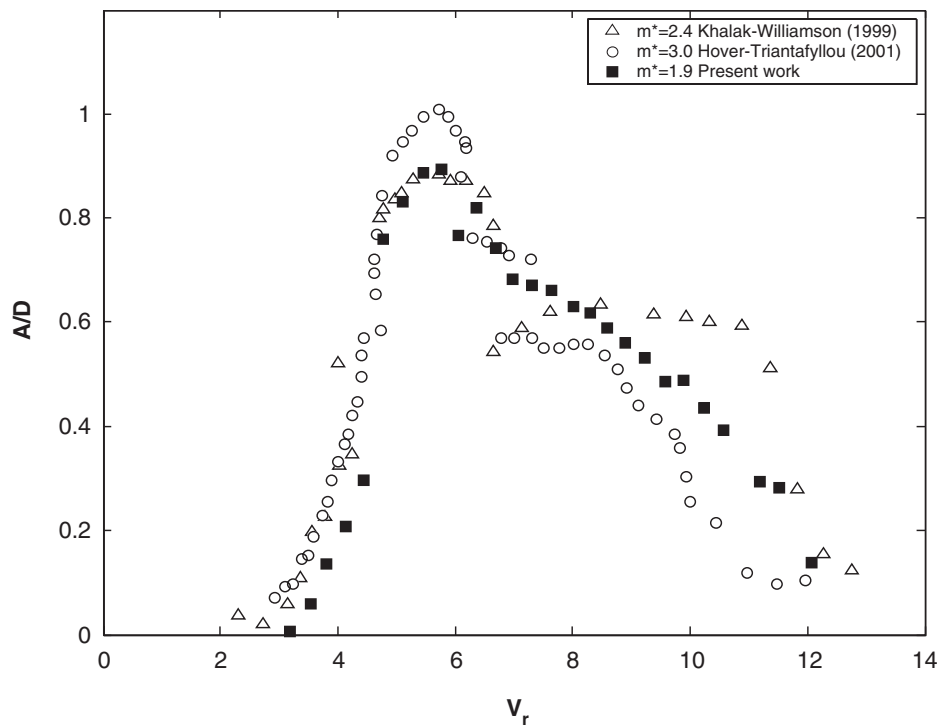


Fig. 6. Variation of the reduced amplitude  $A/D$  versus reduced velocity  $V_r$  for an isolated cylinder with the median mass ratio parameter. Present work: ■,  $m^* \simeq 2$ ,  $(m^*\zeta) \simeq 0.013$ ; △, Khalak and Williamson (1999),  $m^* \simeq 2$ ,  $(m^*\zeta) \simeq 0.014$ ; ○, Hover and Triantafyllou (2001),  $m^* \simeq 3$ .

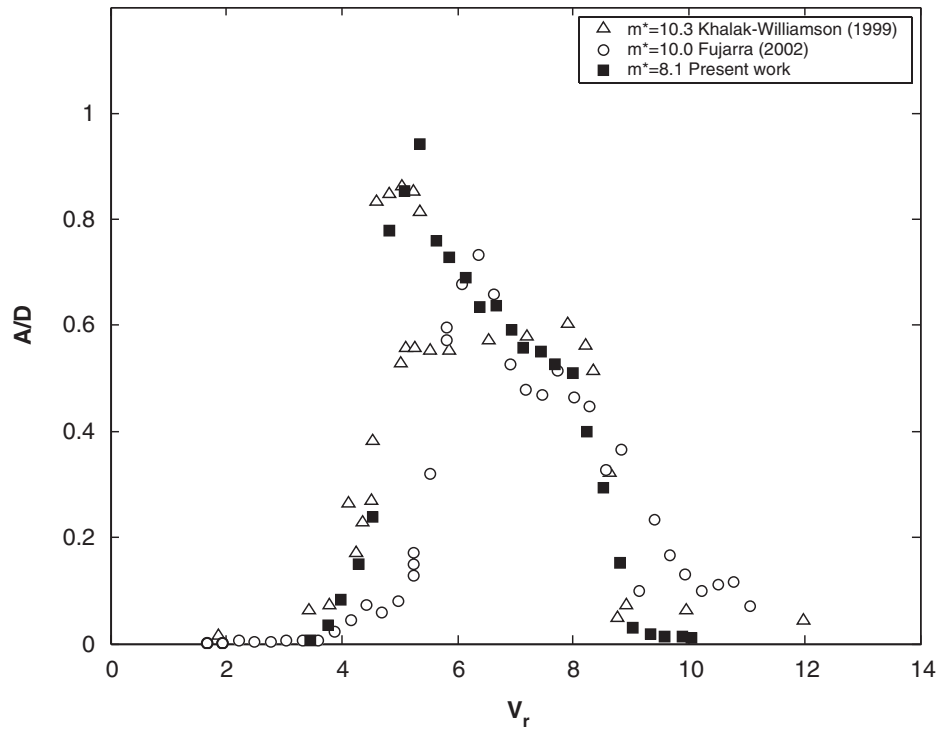


Fig. 7. Variation of the reduced amplitude  $A/D$  versus reduced velocity  $V_r$  for an isolated cylinder with the highest mass ratio parameter. Present work: ■,  $m^* \simeq 8$ ,  $(m^*\zeta) = 0.016$ ; △, Khalak and Williamson (1999),  $m^* \simeq 10$ ,  $(m^*\zeta) \simeq 0.017$ ; ○, Fujarra (2002),  $m^* \simeq 10$ ,  $(m^*\zeta) \simeq 0.03$ .

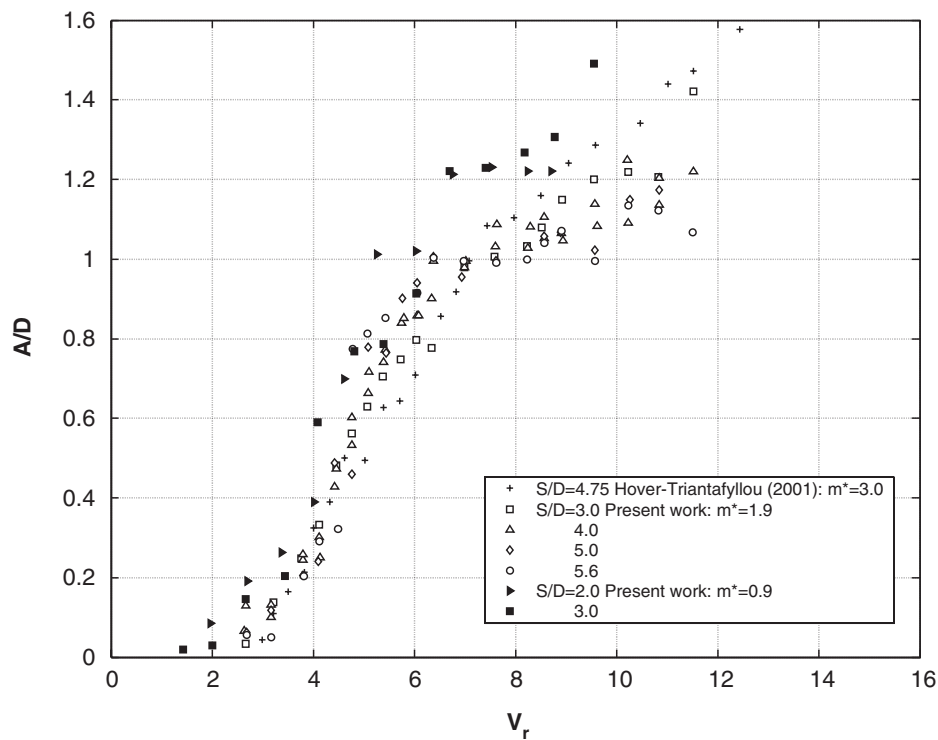


Fig. 8. Variation of the reduced amplitude versus  $A/D$  reduced velocity  $V_r$  for the trailing cylinder of a pair in tandem arrangement. Present work: □, △, ◇, ○, IC model,  $m^* \simeq 2$ ,  $(m^*\zeta) = 0.013$ ; ■, ▲, USP model,  $m^* = 0.9$ ,  $(m^*\zeta) = 0.010$ ; \*, Hover and Triantafyllou (2001),  $m^* \simeq 3$ .

### 3.2. Two circular cylinders in tandem

Fig. 8 presents the dynamic results for flow interaction of a trailing rigid cylinder oscillating in the wake of a fixed leading one. The downstream body is free to move only in the cross-flow direction. For this case,  $m^* \simeq 2$  and  $m^*\zeta \simeq 0.013$ . The results are compared with those obtained by Hover and Triantafyllou (2001) with a cylinder with a slightly higher mass parameter. The distance  $S/D$  is measured centre to centre. The results shown in Fig. 8 are for four gaps:  $S/D = 2.0, 3.0, 4.0, 5.0$ , and  $5.6$ . For each gap the response is found to be a monotonically increasing curve without an upper and lower branch typical of an oscillating single cylinder. This continuous increase in the response with increasing reduced velocity is usually found in galloping like- oscillations. To verify this galloping behaviour, higher reduced velocity tests are planned.

The oscillation starts at about  $V_r = 2.5$  and grows continuously. The peak amplitude in our experiment is about  $1.4D$ , which is 50% higher than the maximum amplitude observed for the isolated cylinder case. This peak occurred for the maximum reduced velocity that could be reached by the water channel, i.e.,  $V_r = 12$ . This peak amplitude of the downstream cylinder is observed for a gap  $S/D = 3$ . It is interesting to note that this increase in amplitude is not observed in interference experiments carried out in air at a higher mass ratio, as reported by Brika and Laneville (1999). Although they observed a continuous response curve, the amplitude reached a maximum similar to the case of an

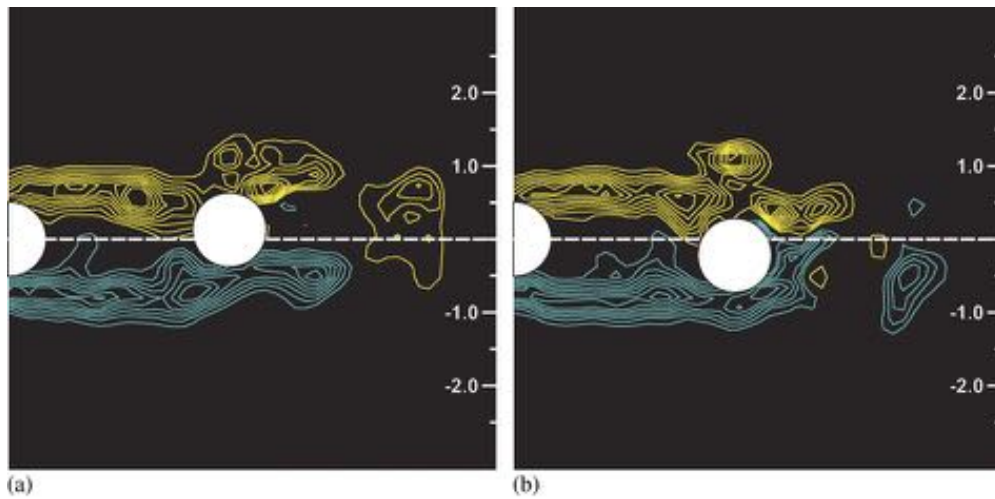


Fig. 9. Flow visualizations employing a PIV system, two cylinders in tandem,  $S/D = 3.0$ ,  $Re = 3200$ ,  $V_r = 2.6$ ,  $A/D \simeq 0.2$ ; downstream cylinder at (a) uppermost position and (b) lowermost position.

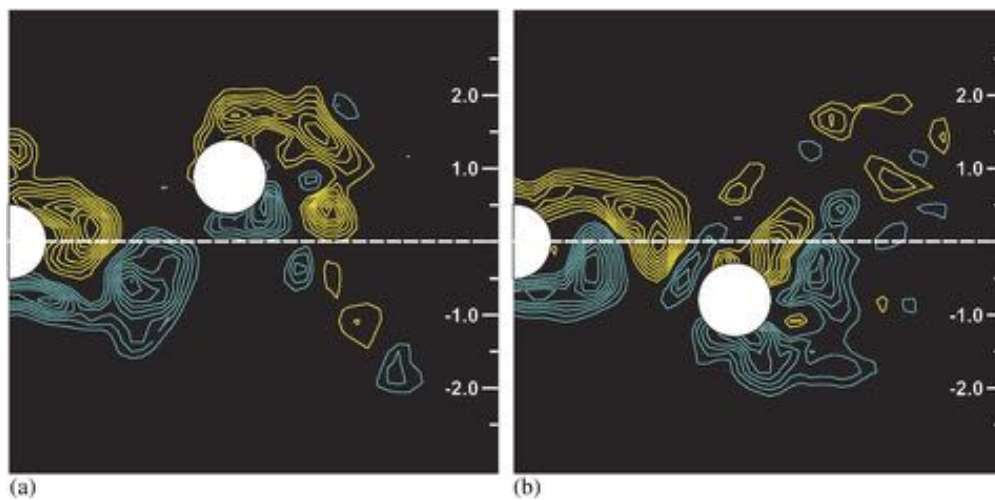


Fig. 10. Flow visualizations employing a PIV system, two cylinders in tandem,  $S/D = 3.0$ ,  $Re = 7300$ ,  $V_r = 6$ ,  $A/D \simeq 0.9$ ; downstream cylinder at (a) uppermost position and (b) lowermost position.

isolated cylinder. As one can see in Fig. 8, the response of the downstream cylinder at  $V_r = 12$  decreases slowly with increasing gap spacing. For  $S/D = 5.6$ , the largest gap spacing tested, the influence of the upstream cylinder is still pronounced.

Finally, flow visualizations of the USP model, employing a PIV system, are shown in Figs. 9 and 10. The case for a gap  $S/D = 3$  is considered, and the vorticity contours are shown when the oscillating downstream cylinder is at its uppermost and lowermost positions. Fig. 9 shows the results for  $V_r = 2.6$  and Fig. 10 the results for  $V_r = 6.0$ . In the first case, the maximum amplitude is slightly below  $0.2D$ , and the flow visualization shows that the shear layers roll up after the downstream body. Although the second body is oscillating with low amplitude, the cylinders almost behave as a single body, and vortex shedding does not occur in the gap region. In the case for  $V_r = 6.0$ , vortex shedding occurs in-between the cylinders and the shedding is synchronized with the oscillation. The amplitude of oscillation, for this reduced velocity, is about  $0.9D$ . Fig. 10 clearly shows that when the cylinder is at its uppermost position, a counterclockwise vortex shed from the upstream cylinder passes close to the lower half of the downstream cylinder. This will create a low-pressure region which acts to pull the cylinder downwards. Whether similar behaviour is observed for higher reduced velocities is still unknown. In the next phase of the current research, PIV images will be employed to investigate such cases.

Despite the fact that the amplitude response curve is similar to galloping, new measurements and CFD calculations suggest that the transverse forces on the downstream cylinder are due to vortex shedding and they are enhanced by vortices coming from the upstream cylinder. Therefore, a better term to illustrate the observed behaviour would be WIV, *wake-interference vibrations*, which describes the phenomenon responsible for these excitations and combines: lock-in of shedding frequency from VIV and interference from the vortices shed from the upstream body.

#### 4. Conclusions

The results for an isolated cylinder were found to be in accordance with other reported measurements for  $m^* \simeq 1, 2$ , and 8. Consequently, the results are satisfactory to validate the experimental set-up. The decay tests performed in air verified the low-damping behaviour of the base. For the tandem configuration ( $m^* \simeq 1$  and 2), one can notice a predominance of the galloping-like phenomenon for the gap range  $3.0 < S/D < 5.6$ , since the amplitude curve does not show a peak response, and increases continuously with increasing reduced velocity. Higher reduced velocity experiments are planned to be carried out to confirm such behaviour. The peak amplitude observed for the downstream cylinder was about 50% higher than the one observed for the isolated cylinder case. The experiments shown in this paper are still preliminary and are part of an ongoing research project. Future investigations will include tandem, staggered and side-by-side arrangements with the two cylinders free to move.

#### Acknowledgements

The authors gratefully acknowledge the support by FINEP/CTPetro, FAPESP, CNPq and Petrobras, for providing a research grant for this investigation. The first author is also grateful to FAPESP for his MSc research grant. Special thanks are due to Maša Branković, from Imperial College, London (where part of the experiments were conducted), for her valuable help. The comments and suggestions made by Profs André L.C. Fajarra, Fábio Saltara, Clóvis A. Martins, and Celso P. Pesce are greatly appreciated.

#### References

- Bearman, P.W., 1984. Vortex shedding from oscillating bluff bodies. *Annual Review of Fluid Mechanics* 16, 195–222.
- Bearman, P.W., Branković, M., 2004. Experimental studies of passive control of vortex-induced vibration. *European Journal of Mechanics B: Fluids* 23, 9–15.
- Blevins, R.D., 1990. *Flow-Induced Vibration*, second Edition. Van Nostrand Reinhold, New York.
- Bokaian, A., Geoola, F., 1984. Wake-induced galloping of two interfering circular cylinders. *Journal of Fluid Mechanics* 146, 383–415.
- Branković, M., 2004. Vortex-induced vibration attenuation of circular cylinders with low mass and damping. Imperial College, University of London, London, UK.
- Brika, D., Laneville, A., 1997. Wake interference between two circular cylinders. *Journal of Wind Engineering and Industrial Aerodynamics* 72, 61–70.

- Brika, D., Laneville, A., 1999. The flow interaction between a stationary cylinder and a downstream flexible cantilever. *Journal of Fluids and Structures* 13, 579–606.
- Fujarra, A.L.C., 2002. Estudos experimentais e analíticos das vibrações induzidas pela emissão de vórtices em cilindros flexíveis e rígidos. Ph.D. Thesis, Escola Politécnica da Universidade de São Paulo, São Paulo, Brazil.
- Hover, F.S., Triantafyllou, M.S., 2001. Galloping response of a cylinder with upstream wake interference. *Journal of Fluids and Structures* 15, 503–512.
- Igarashi, T., 1981. Characteristics of the flow around two circular cylinders arranged in tandem. *Bulletin of JSME* 24 (188), 323–331.
- Khalak, A., Williamson, C.H.K., 1996. Dynamics of a hydroelastic cylinder with very low mass and damping. *Journal of Fluids and Structures* 10, 455–472.
- Khalak, A., Williamson, C.H.K., 1999. Motions, forces and mode transitions in vortex-induced vibrations at low mass-damping. *Journal of Fluids and Structures* 13, 813–851.
- King, R., Johns, D.J., 1976. Wake interaction experiments with two flexible cylinders in flowing water. *Journal of Sound and Vibration* 45, 259–283.
- Krishnamoorthy, S., Price, S.J., Païdoussis, M.P., 2001. Cross-flow past an oscillating circular cylinder: Synchronization phenomena in the near wake. *Journal of Fluids and Structures* 15, 955–980.
- Meneghini, J.R., Saltara, F., Siqueira, C.L.R., Ferrari Jr., J.A., 2001. Numerical simulation of flow interference between two circular cylinders in tandem and side-by-side arrangements. *Journal of Fluids and Structures* 15, 327–350.
- Owen, J.C., Bearman, P.W., Szewczyk, A.A., 2001. Passive control of VIV with drag reduction. *Journal of Fluids and Structures* 15, 597–605.
- Sumner, D., Price, S.J., Païdoussis, M.P., 2000. Flow-pattern identification for two staggered circular cylinders in cross-flow. *Journal of Fluid Mechanics* 411, 263–303.
- Williamson, C.H.K., Govardhan, R., 2004. Vortex-induced vibrations. *Annual Review of Fluid Mechanics* 36, 413–455.
- Zdravkovich, M.M., 1977. Review of flow interference between two circular cylinders in various arrangements. *ASME Journal of Fluids Engineering* 99, 618–633.
- Zdravkovich, M.M., 1987. The effects of interference between circular cylinders in cross flow. *Journal of Fluids and Structures* 1, 239–261.



ELSEVIER

Journal of Fluids and Structures 25 (2009) 666–675

JOURNAL OF  
FLUIDS AND  
STRUCTURES

www.elsevier.com/locate/jfs

# Low drag solutions for suppressing vortex-induced vibration of circular cylinders

G.R.S. Assi<sup>a,\*</sup>, P.W. Bearman<sup>a</sup>, N. Kitney<sup>b</sup>

<sup>a</sup>*Department of Aeronautics, Imperial College, London SW7 2AZ, UK*

<sup>b</sup>*BP Exploration Operating Company Ltd., Sunbury-on-Thames TW16 7LN, UK*

Received 2 April 2008; accepted 7 November 2008

## Abstract

Measurements are presented of response and drag for a flexibly mounted circular cylinder with low mass and damping. In one set of experiments it is free to respond in only the cross-flow direction and in a second it is free to respond in two degrees of freedom. It is shown how vortex-induced vibration can be practically eliminated by using free-to-rotate, two-dimensional control plates. Further it is shown that these devices achieve VIV suppression with drag reduction. The device producing the largest drag reduction was found to have a drag coefficient equal to about 60% of that for a plain, fixed cylinder over the Reynolds number range of the experiments, up to 30 000. The importance of torsional resistance of the devices is discussed and it is shown that if it is too low large oscillations of the device and cylinder will develop and if it is too high galloping is initiated.

© 2009 Elsevier Ltd. All rights reserved.

**Keywords:** VIV Suppression; Drag reduction; Two-dimensional control plates; Circular cylinder

## 1. Introduction

Vortex-induced vibrations (VIV) are a continuing problem in many branches of engineering and can be particularly severe for the risers used in deepwater offshore oil operations. A widely used method for suppressing VIV of long slender bodies of circular cross section is the attachment of helical strakes. Developed originally in the wind engineering field, strakes suffer from two major problems: the first being that they increase drag and the second that, for a given strake height, their effectiveness reduces with decreases in the response parameter  $m^*\zeta$ , where  $m^*$  is the ratio of structural mass to the mass of displaced fluid and  $\zeta$  is the structural damping expressed as a fraction of critical damping. Whereas a strake height of 10% of cylinder diameter is usually sufficient to suppress VIV in air at least double this amount is often required in water, and this increase in height is accompanied by a corresponding further increase in drag. For a fixed cylinder it is known that if regular vortex shedding is eliminated, say by the use of a long splitter plate, then drag is reduced. Hence in theory an effective VIV suppression device should be able to reduce drag rather than increase it. This idea underlies the work presented in this paper.

According to Bearman (1984) a simple analysis for a linear oscillator model of VIV assuming harmonic forcing and harmonic response shows that response is inversely proportional to the product of  $m^*$  and  $\zeta$ . Hence the most rigorous

\*Corresponding author.

E-mail address: g.assi05@imperial.ac.uk (G.R.S. Assi).



way to test the effectiveness of a VIV suppression device is to work at low mass and damping. In the experiments to be described in this paper the parameter  $m^*\zeta$  was equal to or less than 0.014. Owen et al. (2001) describe a method for low drag VIV suppression that had shown itself to be effective down to values of  $m^*\zeta$  of about 0.5. This is the attachment of large scale bumps to induce three-dimensional separation and eliminate vortex shedding. However, later experiments at lower values of  $m^*\zeta$  have shown a return of VIV with amplitudes similar to those of a plain cylinder. This behaviour has been observed by the authors with even grosser forms of continuous surface, three dimensionality where regular vortex shedding has been eliminated from the body when it is fixed but it returns when the cylinder is free to respond under conditions of low mass and damping. From this experience it is concluded that sharp-edged separation from strakes, with its accompanying high drag, is required to maintain three-dimensional separation and suppress VIV. Hence at values of  $m^*\zeta$  typical for risers (less than 0.1) it seems that three-dimensional solutions are unlikely to provide the required combination of VIV suppression and low drag.

There are a number of two-dimensional control devices to weaken vortex shedding and reduce drag, with the most well known being the splitter plate. In this paper we describe the results of experiments to suppress VIV and reduce drag using various configurations of two-dimensional control devices.

## 2. Experimental arrangement

### 2.1. Flow facility

The investigation was carried out in a recirculating water channel with a free surface and a test section 0.6 m wide, 0.7 m deep and 8.4 m long. The flow speed,  $U$ , is continuously variable and flow with turbulence intensity less than 3% can be obtained up to at least 0.6 m/s. The circular cylinder model was constructed from 50 mm diameter perspex tube, giving a maximum Reynolds number of approximately 30 000, based on cylinder diameter  $D$ . With a wet-length of 650 mm (total length below water level) the resulting aspect ratio of the model was 13. Various VIV suppression devices were attached to the model and in the first set of experiments the cylinder was free to respond in only the transverse direction. In the second set it was free to respond in both the transverse and in-line directions. In order to have a reference to assess suppression effectiveness, experiments were also carried out on the cylinder without any devices, referred to here as the plain cylinder.

### 2.2. One-degree-of-freedom rig

Models were mounted on two different rigs: the first was a one-degree-of-freedom (1-dof) elastic system that allowed the cylinder to oscillate only in the transverse direction (Fig. 1(a)). Models were mounted on a very low damping, air bearing support system spanning the width of the test section. The cylinder was mounted such that there was a 2 mm gap between the lower end of the cylinder and the glass floor of the test section. A pair of springs connecting the moving base to the fixed supports provided the restoration force of the system, setting the natural frequency of oscillation in air ( $f_{y0}$ ). An optical positioning sensor was installed to measure the  $y$ -displacement of the cylinder without introducing extra friction to damp the oscillations. Thus, the cylinder is free to oscillate only in the  $y$ -direction with a very low structural damping  $\zeta = 0.7\%$ , calculated as the percentage of the critical damping obtained from free decay oscillations performed in air.

### 2.3. Two-degree-of-freedom rig

The second rig, a two-degree-of-freedom (2-dof) system, allowed the cylinder to freely respond in both transverse and in-line directions (Fig. 1(b)). The cylinder model was mounted at the lower end of a long carbon fibre tube which formed the arm of a rigid pendulum. The top end of the arm was connected to a universal joint fixed at the ceiling of the laboratory so that the cylinder model was free to oscillate in any direction in a pendulum motion. The distance between the bottom of the cylinder and the pivoting point of the universal joint was 2800 mm. Two independent optical sensors were employed to measure displacements in the  $x$ - and  $y$ -directions. All displacement amplitudes presented for 2-dof measurements are for a location at the mid-length of the model. It should be noted that for a displacement equal to 1 diameter the inclination angle of the cylinder was only just over  $1^\circ$  from the vertical axis.

Two pairs of springs were installed in the  $x$ - and  $y$ -axes to set the natural frequencies in both directions of motion allowing different natural frequencies to be set for each direction. Although the cylinder was initially aligned in the vertical position, in flowing water the mean drag displaces the cylinder from its original location. To counteract this



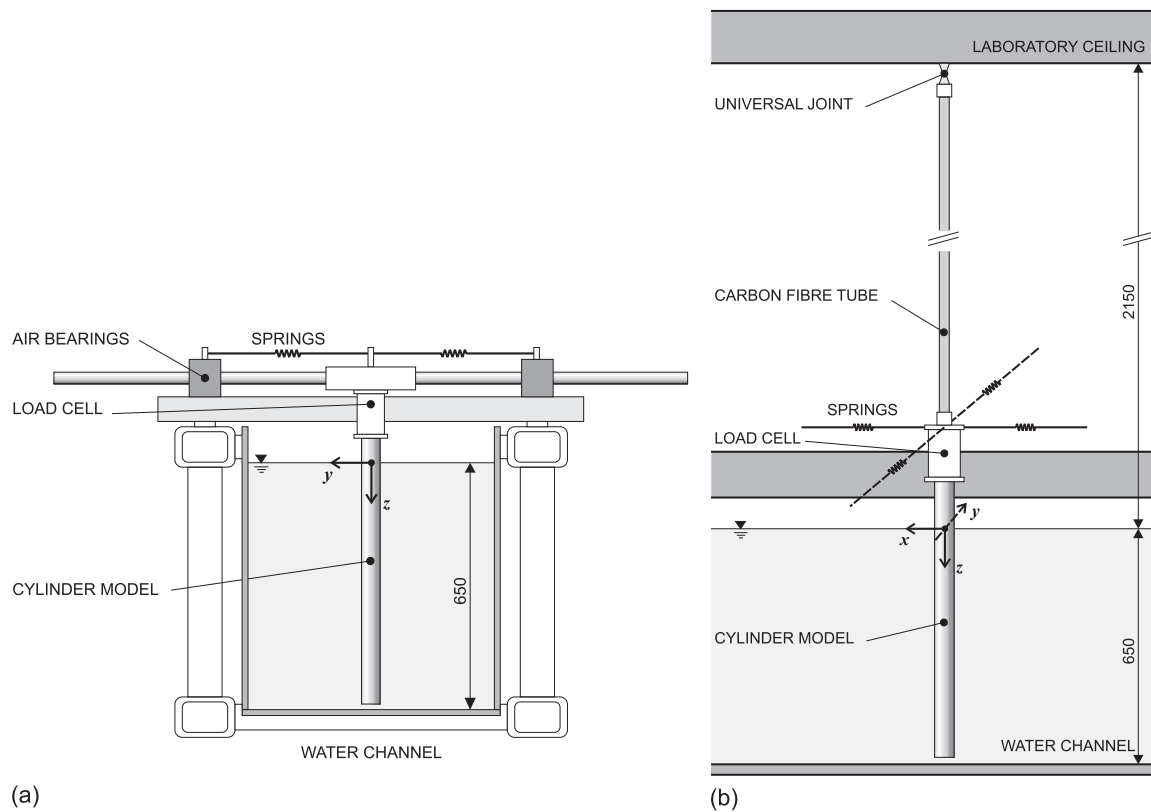


Fig. 1. Experimental apparatus: (a) 1-dof rig and (b) 2-dof rig. Water flow in  $x$ -axis.

effect, the in-line pair of springs was attached to a frame that could be moved back and forth in the direction of the flow. For each flow speed there was a position of the frame that maintained the mean position of the cylinder in the vertical direction. By using two pairs of springs perpendicular to each other, the assembly has nonlinear spring constants in the transverse and in-line directions. Movement in the transverse direction will cause a lateral spring deflection in the in-line direction and *vice versa*. This nonlinearity is minimised by making the springs as long as possible, hence the in-line springs were installed at the end of 4 m-long wires, fixed at the extremities of the frame.

It is known that during the cycle of vortex shedding from bluff bodies the fluctuation of drag has double the frequency of the fluctuation of lift. Hence a particularly severe vibration might be expected to occur if the hydrodynamic forces in both directions could be in resonance with both in-line and transverse natural frequencies at the same time. For this reason, we set the in-line natural frequency ( $f_{x0}$ ) to be close to twice the transverse ( $f_{y0}$ ) by adjusting the stiffness of both pairs of springs. The structural damping of the 2-dof rig was  $\zeta = 0.3\%$ , approximately the same for both principal directions of motion and lower than the one measured for the 1-dof rig.

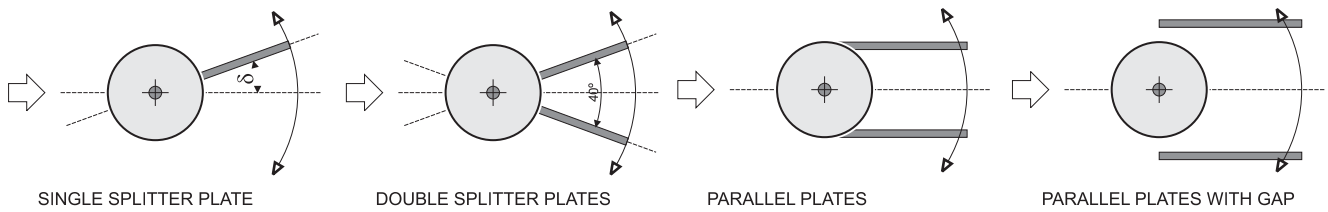
In both rigs a load cell was attached between the cylinder and the support system to deduce the instantaneous and time-averaged hydrodynamic forces on the cylinder model. In order to obtain the dynamic forces acting, the inertia force (cylinder structural mass times acceleration) was subtracted from the forces recorded by the load cell. For the 1-dof tests, the mass ratio ( $m^*$ , defined as vibrating mass divided by the displaced mass of water) was adjusted by adding extra mass to the cylinder so that all models fitted with the respective devices would present the same mass ratio of 2. On the other hand, all the devices tested on the 2-dof rig were kept to the lowest possible  $m^*$  and varied between 1.6 and 2. Table 1 presents the structural parameters for all the arrangements of cylinder and suppression device tested. A description of each device presented in Fig. 2 is given later.

For each rig, measurements were made using a fixed set of springs and the reduced velocity range covered was from 1.5 to 23 for 1-dof and 1.5 to 13 for 2-dof experiments, where reduced velocity ( $U/Df_{y0}$ ) is defined using the cylinder natural frequency of oscillation in the transverse direction measured in air ( $f_{y0}$ ). This frequency is very close to the true natural frequency that would be recorded in a vacuum. The only flow variable changed during the course of the experiments was the flow velocity  $U$ , which, as for full-scale risers, alters both the reduced velocity and the Reynolds number.

Table 1

Structural properties and average drag coefficients with corresponding drag reduction relative to a fixed cylinder..

| Model                      | 1-dof rig |            | 2-dof rig |            | $f_{x0}/f_{y0}$ | $\overline{C_D}$ | Drag reduction |
|----------------------------|-----------|------------|-----------|------------|-----------------|------------------|----------------|
|                            | $m^*$     | $m^*\zeta$ | $m^*$     | $m^*\zeta$ |                 |                  |                |
| ■ Fixed cylinder           | —         | —          | —         | —          | —               | 1.03             | Reference      |
| ● Plain cylinder           | 2.0       | 0.014      | 1.6       | 0.0047     | 1.93            | —                | —              |
| ◇ Single splitter plate    | 2.0       | 0.014      | 1.7       | 0.0051     | 1.89            | 0.88             | 14%            |
| ○ Double splitter plates   | 2.0       | 0.014      | 1.8       | 0.0055     | 1.88            | 0.70             | 32%            |
| △ Parallel plates          | 2.0       | 0.014      | 1.9       | 0.0056     | 1.86            | 0.63             | 38%            |
| ▷ Parallel plates with gap | 2.0       | 0.014      | 2.0       | 0.0060     | 1.88            | 0.69             | 33%            |

Fig. 2. Sketch of proposed control plates free to rotate about the centre of a circular cylinder: single splitter plate (length varying from  $0.25D$  to  $2D$ ), double splitter plates, parallel plates (after Grimminger, 1945), parallel plates with  $0.1D$  gap.

Throughout the study, cylinder displacement amplitudes in both directions ( $A_x$  and  $A_y$ ) were found by measuring the root mean square value of response and multiplying by  $\sqrt{2}$ . This is likely to give an underestimation of maximum response but was judged to be perfectly acceptable for assessing the effectiveness of VIV suppression devices. Displacements  $A_x$  and  $A_y$  are nondimensionalised by dividing by the plain cylinder diameter  $D$ .

In addition to response and force measurements, flow visualisation was carried out using laser-illuminated fluorescent dye and hydrogen bubbles. Flow field measurements to obtain instantaneous spatial distributions of velocity and vorticity were obtained using a digital PIV system.

### 3. Experimental results and discussion

#### 3.1. Plain cylinder results

Initially experiments were conducted on a plain cylinder to help validate the apparatus and the experimental method. Fig. 3(a) shows transverse amplitude versus reduced velocity for 1-dof and the form of the results is close to that found by other investigators. Measurements of the time mean drag coefficients versus reduced velocity for a plain responding cylinder and also a fixed cylinder are presented in Fig. 3(b).

In the same way, Figs. 7(a), (c) and (e) present transverse and in-line displacement amplitudes and drag coefficients for a plain cylinder responding in 2-dof, complemented by the trajectories of motion shown in Fig. 9. The results are repeated in other parts of Fig. 7 for comparison. These results were found to be in good agreement with those presented by other researchers.

#### 3.2. Response of suppressors in 1-dof

##### 3.2.1. Fixed splitter plate

Splitter plates could be rigidly attached to the rear of the cylinder and tests were carried out with plates of length ( $L_{SP}$ ) between  $0.25D$  and  $2D$ . The result in all cases was a very vigorous transverse galloping oscillation that, with increasing reduced velocity, would apparently increase without limit. In this first experiment the maximum amplitude of transverse oscillation was limited to  $2D$  and this was reached at a reduced velocity of about 13 for a  $1D$ -long splitter plate (Fig. 3(a)). A similar galloping response was also observed for a 2-dof experiment, but these results are not presented in this paper.

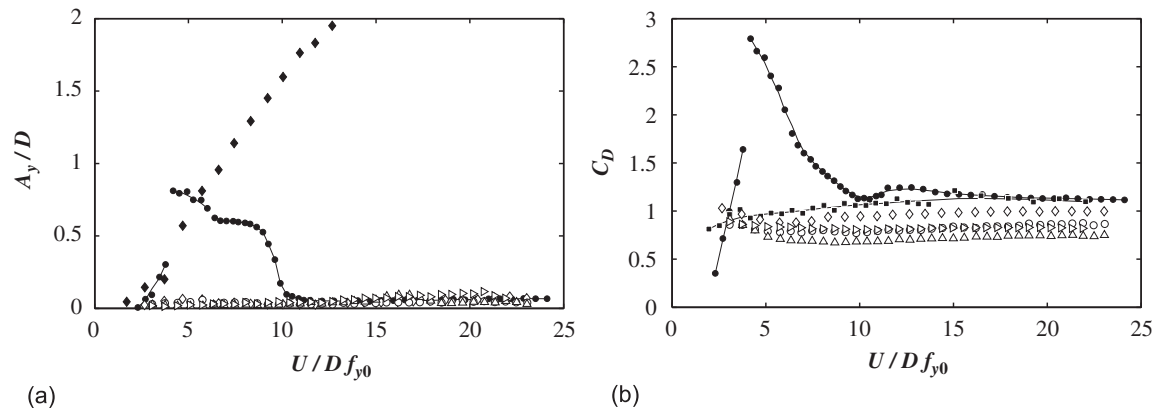


Fig. 3. Response of suppressors in 1-dof compared with a plain cylinder: (a) transverse amplitude versus reduced velocity and (b) drag coefficient versus reduced velocity. Key: ●, plain oscillating cylinder; ■, plain fixed cylinder; ◆, fixed splitter plate. Free to rotate devices: ◇, single splitter plate; ○, double splitter plate; △, parallel plates; ▽, parallel plates with 0.1D gap.

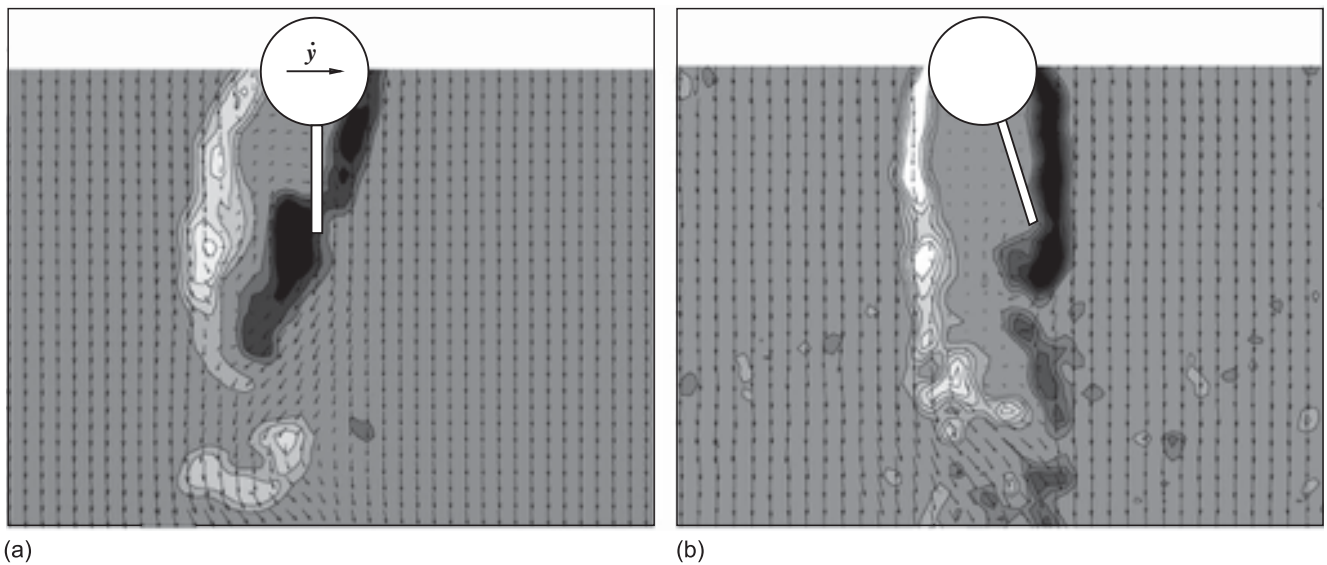


Fig. 4. Instantaneous velocity vectors and vorticity contours for fixed and f-t-r splitter plates at reduced velocity 6: (a) fixed splitter plate under galloping oscillations and (b) free-to-rotate splitter plate suppressing vibrations.

Flow visualisation and PIV measurements were carried out to investigate the interaction between the wake and the splitter plate. Fig. 4(a) presents the instantaneous velocity and vorticity fields for a reduced velocity of 6. The data was acquired when the cylinder is crossing the centreline from left to right, therefore presenting maximum transverse velocity  $\dot{y}$ . The vorticity contours show that the shear layer separated from the right-hand side of the cylinder apparently reattaches at the tip of the fixed splitter plate. This interaction with the tip and the proximity of the shear layer running along the splitter plate causes a region of lower pressure on the right-hand side of the plate and cylinder. A transverse force develops in the same direction as the cylinder motion, energy is extracted from the free stream and galloping oscillations are sustained in essentially the same way as for classical galloping of square section cylinders. We also note from Fig. 4(a) that the shear layers are free to interact after the splitter plate forming vortices further downstream. The behaviour described above is illustrated in Fig. 5(a) where the resultant velocity approaching the cylinder is the vectorial addition of the free stream velocity  $U$  and the cylinder's transverse velocity  $\dot{y}$ . Since a device to be used in the ocean must have omni-directional effectiveness the next stage was to pivot the splitter plate about the centre of the cylinder, leaving just a small gap between the plate and the cylinder surface. As with all the free-to-rotate (f-t-r) devices described, the splitter plate was mounted on bearings at each end of the cylinder.

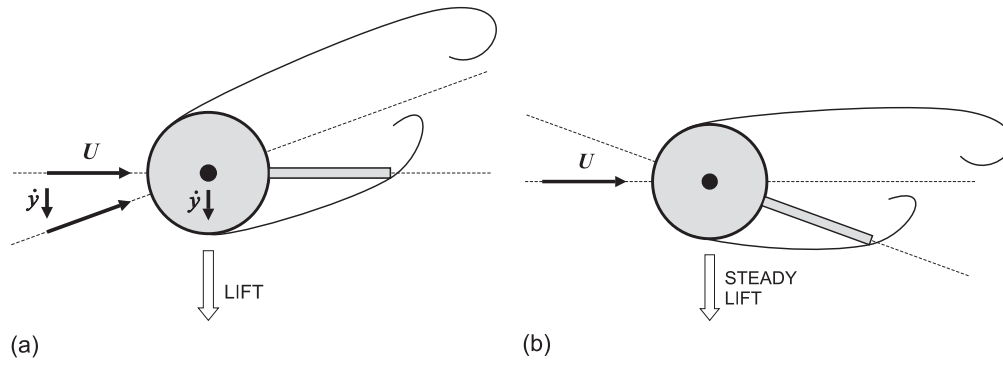


Fig. 5. Diagram showing offset position of plate and direction of steady lift force: (a) fixed splitter plate under galloping oscillations and (b) free-to-rotate splitter plate suppressing vibrations (therefore the cylinder is stationary at  $\dot{y} = 0$ ).

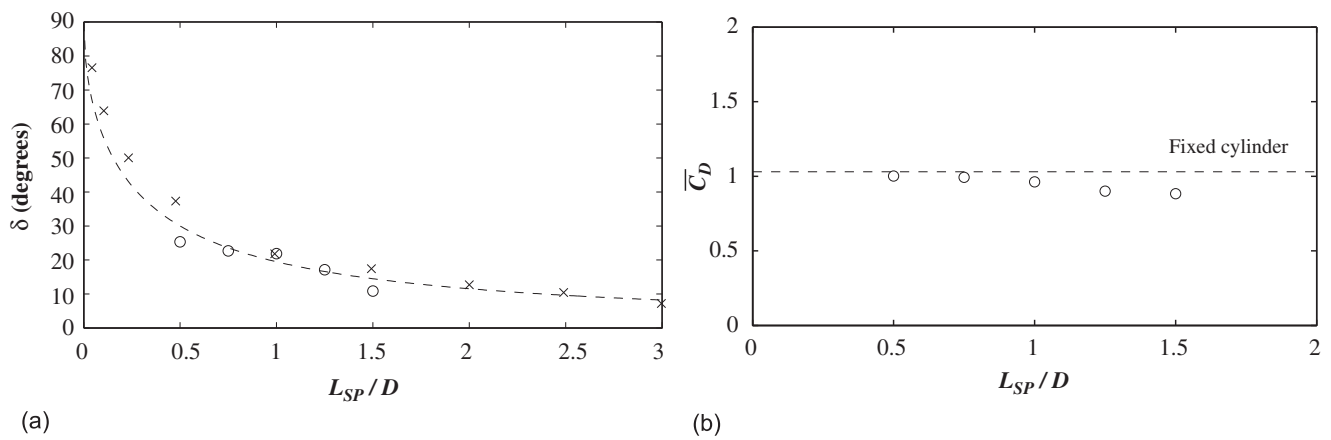


Fig. 6. Effect of splitter plate length on its offset position and cylinder drag: (a) stable offset angle versus plate length and (b) average drag coefficient versus plate length. Key:  $\circ$ , present work;  $\times$ , Cimbalá and Garg (1991),  $5 \times 10^3 < Re < 2 \times 10^4$ .

### 3.2.2. The free-to-rotate splitter plate

Following the disappointing results with a fixed plate, it was hoped that a plate free to rotate might provide sufficient hydrodynamic damping to suppress the galloping. However, when an f-t-r splitter plate was used there were found to be two stable positions for the plate at roughly  $\pm 20^\circ$  to the free stream direction and the plate rapidly adopted one or other of these positions when it was released. VIV was suppressed, throughout the range of reduced velocity investigated, and drag reduced below that of a plain cylinder. Cimbalá and Garg (1991) also observed this bi-stable behaviour for an f-t-r cylinder fitted with a splitter plate. In their experiments the cylinder and the splitter plate were manufactured into one solid body allowed to rotate around the axis of the cylinder. However, the pivoting axis of their system was rigidly mounted on a wind tunnel section not allowing any flow-induced vibration. Our measurements of transverse response for the 1D f-t-r splitter plate are shown in Fig. 3(a) and time mean drag coefficients are plotted in Fig. 3(b). Results for a plain cylinder, fixed and free, are shown for comparison. The results for other devices are also shown in these figures and they will be described later.

PIV measurements presented in Fig. 4(b) show that on the side to which the plate deflected the separating shear layer from the cylinder appeared to attach to the tip of the plate and this had the effect of stabilising the near wake flow. Vortex shedding was visible downstream but this did not feed back to cause vibrations.

An unwanted effect was that a steady transverse lift force developed on the cylinder. The splitter plate was free to rotate so the force, caused by differing flow on the two sides of the combination of cylinder and splitter plate, must be acting primarily on the cylinder rather than the plate. As shown in Fig. 5(b), the direction of the force was opposite to that which occurs on an aerofoil with a deflected flap, and caused the cylinder to adopt a steady offset position to the side to which the splitter plate deflected. It was this force which was responsible for the strong galloping response with the fixed splitter plate explained earlier. As a cylinder with a fixed splitter plate aligned with the free stream plunges downwards (Fig. 5(a)), say, the instantaneous flow direction is approximately the same as that shown in Fig. 5(b).

All the results presented so far have been for an f-t-r plate having a length equal to the cylinder diameter. Further tests were carried out with a series of f-t-r splitter plates with various lengths ( $L_{SP}$ ) in order to assess the effect of plate length on VIV suppression effectiveness. The results showed that f-t-r splitter plates with lengths between  $0.5D$  and  $1.5D$  of a cylinder diameter are all effective in suppressing VIV. Also they all had drag coefficients below the value for a plain fixed circular cylinder. When f-t-r plates outside the range  $0.5D$  to  $1.5D$  were attached to the cylinder a transverse flow-induced vibration returned. Cimbala and Garg (1991) found stable positions outside this range but this may have been because their system was not allowed to respond to flow-induced excitation. A secondary effect might have been the level of friction in their ball bearings (as discussed later in this paper).

The plates that successfully suppressed VIV adopted slightly different offset angles ( $\delta$ , defined in Fig. 2), depending on plate length. These steady angles are plotted in Fig. 6(a) along with results from Cimbala and Garg (1991). It can be seen that the longer the splitter plate the smaller the angle. The dashed line in the figure is the angle the plate would adopt if it is assumed that the tip of the plate just intercepts a line leaving the shoulder of the cylinder and trailing back in the flow direction. The data generally support the observation that the shear layer from the side of the cylinder to which the splitter plate deflects just reattaches at its tip. Also shown in Fig. 6(b) is the variation of drag coefficient with splitter plate length. These results suggest that a successful VIV suppression and drag reduction device using a f-t-r splitter plate can be shorter than one cylinder diameter.

### 3.2.3. Pairs of plates

In order to try to eliminate the steady transverse force found for an f-t-r splitter plate, a pair of plates was introduced. The plates were  $1D$  long and set at  $\pm 20^\circ$  to the free stream direction. The angle between the plates was fixed but the pair of plates was free to pivot about the centre of the cylinder. The configuration is shown as *double splitter plates* in Fig. 2.

As shown by the results plotted in Fig. 3, this configuration suppressed VIV and reduced drag below that of a plain cylinder. It also eliminated the steady side force found with the single plate. With this arrangement the shear layers from the cylinder stabilised and reattached to the tips of the plates. Downstream of the plates vortex shedding was observed but this did not generate an excitation sufficient to cause any serious VIV. Maximum amplitudes recorded were around 5% of the cylinder diameter.

Further variations on the concept of double plates, some inspired by the early work of Grimminger (1945) related to suppressing VIV of submarine periscopes, were also studied. These included plates parallel to the flow and trailing back from the  $\pm 90^\circ$  points on the cylinder. In one case there was a very small gap between the plates and the cylinder (*parallel plates* in Fig. 2) and in a second case the gap was set at 10% of the cylinder diameter (*parallel plates with gap* in Fig. 2). The plates trailed back  $1D$  from the back of the cylinder. In Grimminger's experiments the plates were fixed since the flow direction was known but in our work the plates were free to rotate. It was found that the plates with the very small gap give the better performance. As shown in the plots in Fig. 3 of amplitude and drag coefficient against reduced velocity, this configuration of plates provided excellent VIV suppression and a reduction in drag below the plain cylinder value.

### 3.3. Response of suppressors in 2-dofs

It has been shown here that various arrangements of two-dimensional control plates are effective in suppressing transverse VIV. However, is this achieved at the expense of larger in-line VIV amplitudes? To answer this question a set of experiments was conducted in the 2-dof rig. Experiments were repeated with the various arrangements of plates and the measured transverse ( $A_y$ ) and in-line ( $A_x$ ) amplitudes and drag coefficients ( $C_D$ ) are shown in Fig. 7 plotted against reduced velocity. Results for the plain cylinder are also shown as well as a sample of the trajectories of motion (Fig. 9) and these agree with those found by other investigators.

After confirming that all the devices would successfully suppress VIV in 1-dof oscillations, we mounted the same models in the 2-dof rig. This produced further unexpected findings. Starting with the single splitter plate, we found out that the plate was not able to stabilise in the expected  $\pm 20^\circ$  position, but oscillated severely from one side to the other and the cylinder developed high amplitudes, both in-line and transverse. We observed that the splitter plate oscillated so much that it almost reached the  $\pm 90^\circ$  positions. This behaviour was also observed for all the other devices. Figs. 7(a) and (c) present the transverse and in-line amplitudes versus reduced velocity and show that all devices led to considerable vibrations of the cylinder, in many cases greater than that for the plain cylinder. As one might expect, almost all drag coefficients presented in Fig. 7(e) were increased above the ones for a plain cylinder. Apart from moving from 1-dof to 2-dof, the only other change in the apparatus was to use lower friction bearings in the mounts for the suppression devices. This prompted us to consider additional parameters that might be important in stabilising the devices.

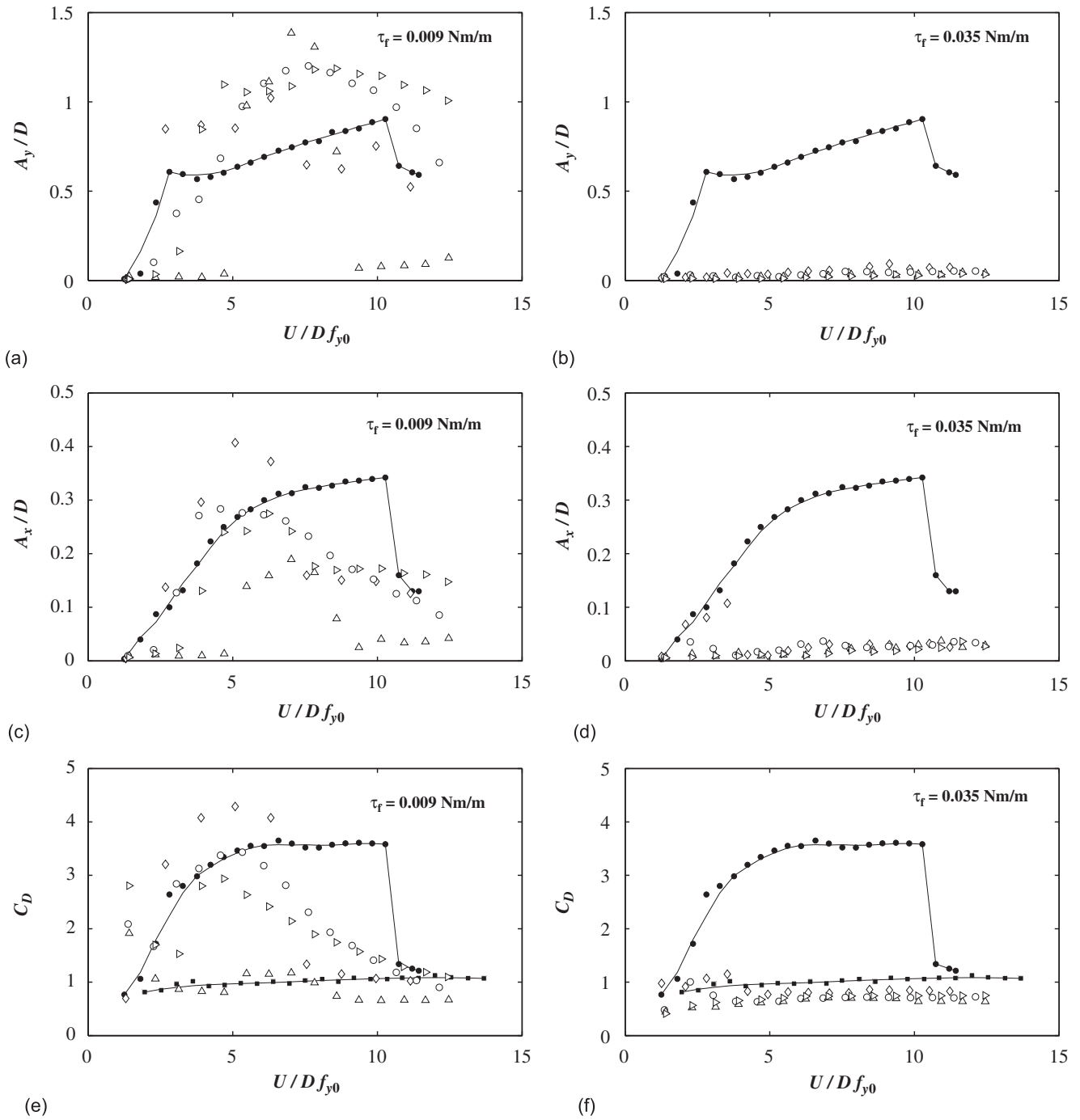


Fig. 7. Transverse displacement (top), in-line displacement (middle) and drag coefficient (bottom) versus reduced velocity for devices with 2-dof: (a), (c) and (e) torsional friction below critical value, and (b), (d) and (f) torsional friction above critical value. Key: ●, plain oscillating cylinder; ■, plain fixed cylinder. Free to rotate devices: ◇, single splitter plate; ○, double splitter plate; △, parallel plates; ▽, parallel plates with  $0.1D$  gap.

### 3.3.1. Effects of torsional resistance and rotational inertia

Two additional parameters that may influence the effectiveness of the suppression devices are: the rotational inertia of the plates and the torsional resistance resulting from friction in the bearings holding the plates. Experiments with mass added to the splitter plate to increase its rotational inertia produced no obvious change in behaviour. However, we noted that small increases in torsional friction were sufficient to suppress vibration. This finding prompted a study of



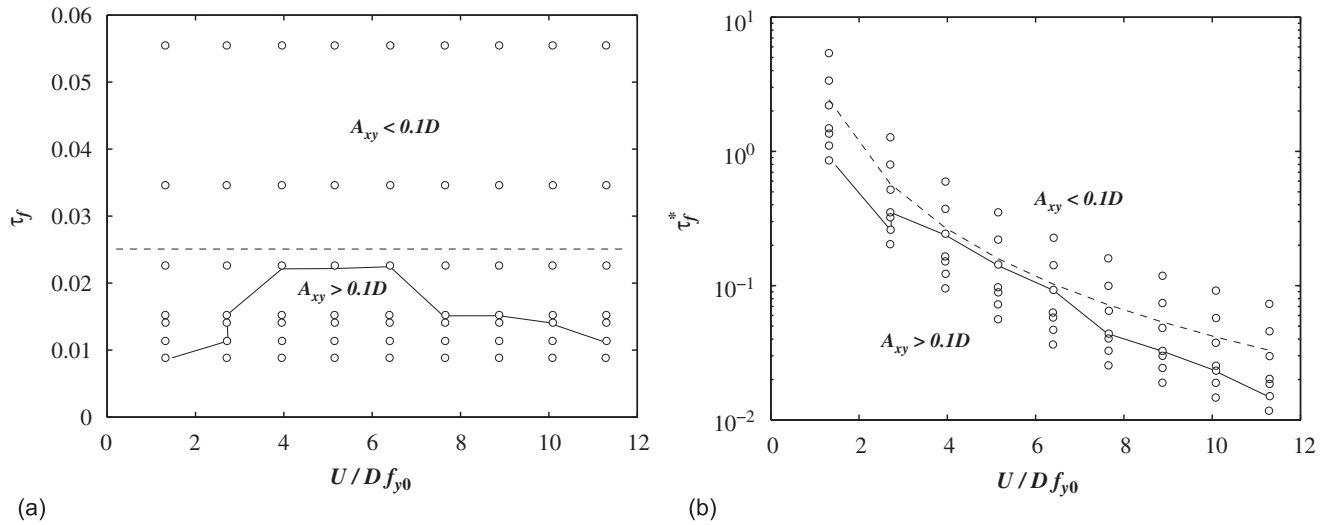


Fig. 8. VIV suppression map for an f-t-r splitter plate showing dependence on torsional friction. The solid line represents the contour where  $A_{xy} = 0.1D$ : (a) torsional friction versus reduced velocity and (b) nondimensionalised torsional friction parameter versus reduced velocity.

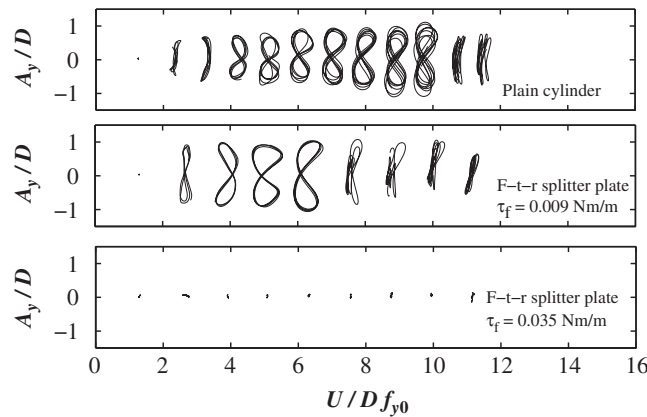


Fig. 9. A few cycles of 2-dof trajectories versus reduced velocity: plain cylinder (top), f-t-r splitter plate below critical  $\tau_f$  (middle) and f-t-r splitter plate above critical  $\tau_f$  (bottom).  $A_y/D$  and  $A_x/D$  are plotted to the same scale.

the effect of torsional friction which we now knew would lead to severe oscillations if it was below some critical value and presumably would result in galloping oscillations if it was too large.

A simple modification was made to the apparatus in order to control the torsional resistance ( $\tau_f$ ), which was varied in small increments between 0.009 and 0.055 N m per unit length of the cylinder with the lowest value being for just the bearings. With a value higher than 0.055 N m/m the splitter plate did not move over the range of reduced velocity tested and galloping returned. A nondimensional friction torque parameter is defined as  $\tau_f^* = \tau_f / \rho U^2 D^2$ , which represents the ratio of structural torsional resistance to a hydrodynamic torque. Use of this parameter provides a means of determining the required torsional resistance for full-scale risers.

A set of 56 runs varying the reduced velocity was completed for the single splitter plate model of length  $1D$  in order to map the amplitude response for different values of  $\tau_f$ . The displacement amplitude parameter  $A_{xy}$  (defined as  $A_{xy} = \sqrt{A_x^2 + A_y^2}$ ) was determined for each run and maps of the cases studied are shown in Fig. 8. The solid line gives an indication of the effectiveness of suppression. For all points above the solid line  $A_{xy}$  is less than  $0.1D$ . Fig. 8(b) presents the same stability map as shown in Fig. 8(a) but instead plots the nondimensional friction torque parameter  $\tau_f^*$  on the vertical axis. The dashed line is for  $\tau_f = 0.025$  N m/m, illustrating that any value of torsional friction between this line and the upper threshold would be sufficient to suppress VIV with a single splitter plate.

Fig. 9 shows examples of trajectories of motion for a single splitter plate with two different torsional friction levels, below and above the critical value, compared with the response of a plain cylinder. In the low-friction case ( $\tau_f = 0.009 \text{ N m/m}$ ) the splitter plate was unstable and the trajectories show amplitudes higher than those for a plain cylinder. However, when the friction level was set to  $0.035 \text{ N m/m}$  the trajectories are little more than small dots over the whole range of reduced velocity.

We next wanted to verify that the other suppressors would also work if the torsional friction was set to a suitable critical value. Because the critical value was unknown for each device, we arbitrarily chose the value  $\tau_f = 0.035 \text{ N m/m}$  from the single splitter plate map of Fig. 8(a), which is in a region where suppression is effective. All devices were set at this torsional friction level and runs over a range of reduced velocity were performed. Figs. 7(b) and (d) show results that should be compared with the low-friction case ( $\tau_f = 0.009 \text{ N m/m}$ ). Immediately we notice that the amplitude levels in both directions of motion are very much less than those for the low-friction case. In fact, at this torsional friction level all suppressors were effective in reducing VIV below 5% of cylinder diameter. Fig. 7(f) shows that all devices reduced drag below that of a fixed cylinder for most of the range of reduced velocity and Table 1 shows that parallel plates achieved the highest average drag reduction of 38% when compared with a plain fixed cylinder. The drag coefficient data given in Table 1 for the plain cylinder and the cylinder fitted with suppression devices is an average over the range of flow velocity used (that is one value of  $C_D$  averaged between  $3 \times 10^3 < Re < 3 \times 10^4$ ). Hence for each test case the Reynolds number range is the same and for the freely mounted models the reduced velocity ranges are also the same.

It seems likely that different suppressors might have different stability boundaries for torsional resistance, but there is clearly a range of  $\tau_f$  within which VIV suppression would be achieved for the devices we studied. A further observation is that the critical torsional friction required to stabilise the splitter plate in 2-dof motion is greater than that required for 1-dof, presumably because in-line vibrations play some role.

#### 4. Conclusions

Suppression of cross-flow and in-line VIV of a circular cylinder, with resulting drag coefficients less than that for a fixed plain cylinder, has been achieved using two-dimensional control plates. This has been accomplished at values of the combined mass and damping parameter up to 0.014. The maximum drag reduction occurs with parallel plates and is about 38%. A free-to-rotate splitter plate was also found to suppress VIV but this configuration develops a mean transverse force. This force can be eliminated by using a pair of splitter plates arranged so that the shear layers that spring from the cylinder attach to the tips of the plates.

The level of torsional friction plays a fundamentally important role, needing to be high enough to hold the devices in a stable position, while still allowing them to realign if the flow direction changes. Devices with torsional friction below a critical value oscillate themselves as the cylinder vibrates, sometimes increasing the amplitude of cylinder oscillation higher than that for a plain cylinder. All devices with torsional friction above the critical value appeared to suppress VIV and reduce drag for 1-dof and 2-dof motions. However, if the torsional resistance is above a limiting threshold the suppressors may not rotate and an undesired galloping response can be initiated.

With two-dimensional control plates proving to be effective VIV suppressors, future studies need to concentrate on optimising the devices in respect of overall length and geometry. Also, more detailed parametric studies on the effects of rotational inertia and torsional resistance should be carried out for each family of device.

#### Acknowledgements

The authors wish to thank BP Exploration for their support of this research. Gustavo R.S. Assi is in receipt of a Ph.D. scholarship from the Brazilian Ministry of Education (CAPES). Thanks are also due to the reviewers for pointing out the work of Cimbala and Garg (1991).

#### References

- Bearman, P.W., 1984. Vortex shedding from oscillating bluff bodies. *Annual Review of Fluid Mechanics* 16, 195–222.
- Cimbala, J.M., Garg, S., 1991. Flow in the wake of a freely rotatable cylinder with splitter plate. *AIAA Journal* 29, 1001–1003.
- Grimminger, G., 1945. The effect of rigid guide vanes on the vibration and drag of a towed circular cylinder. *David Taylor Model Basin Report* 504.
- Owen, J.C., Bearman, P.W., Szewczyk, A.A., 2001. Passive control of VIV with drag reduction. *Journal of Fluids and Structures* 15, 597–605.



# On the wake-induced vibration of tandem circular cylinders: the vortex interaction excitation mechanism

G. R. S. ASSI<sup>1</sup>†, P. W. BEARMAN<sup>1</sup> AND J. R. MENEZHINI<sup>2</sup>

<sup>1</sup>Department of Aeronautics, Imperial College, London SW7 2AZ, UK

<sup>2</sup>Department of Mechanical Engineering, NDF, POLI, University of São Paulo, São Paulo, 05508-900, Brazil

(Received 28 October 2009; revised 25 May 2010; accepted 1 June 2010;  
first published online 16 August 2010)

The mechanism of wake-induced vibrations (WIV) of a pair of cylinders in a tandem arrangement is investigated by experiments. A typical WIV response is characterized by a build-up of amplitude persisting to high reduced velocities; this is different from a typical vortex-induced vibration (VIV) response, which occurs in a limited resonance range. We suggest that WIV of the downstream cylinder is excited by the unsteady vortex–structure interactions between the body and the upstream wake. Coherent vortices interfering with the downstream cylinder induce fluctuations in the fluid force that are not synchronized with the motion. A favourable phase lag between the displacement and the fluid force guarantees that a positive energy transfer from the flow to the structure sustains the oscillations. If the unsteady vortices are removed from the wake of the upstream body then WIV will not be excited. An experiment performed in a steady shear flow turned out to be central to the understanding of the origin of the fluid forces acting on the downstream cylinder.

**Key words:** flow–structure interactions, vortex flows, wakes/jets

## 1. Introduction

Great strides have been made in understanding the mechanisms involved in vortex-induced vibration (VIV) of an isolated circular cylinder free to vibrate transverse and/or in-line to a fluid flow. Progress has been reviewed by Sarpkaya (1979, 2004), Bearman (1984), Parkinson (1989), Blevins (1990) and Williamson & Govardhan (2004). With the development of offshore oil fields and the deployment of riser pipes, much of the research related to cylinder response focused on conditions with low mass ratio  $m^*$  and damping  $\zeta$ . Here,  $m^*$  is the ratio of mass per unit length of the structure,  $m$ , to fluid displaced,  $\rho\pi D^2/4$ , where  $\rho$  is fluid density,  $D$  is cylinder diameter and  $\zeta$  is structural damping expressed as a fraction of critical damping. This research revealed a number of extremely interesting phenomena associated with VIV of isolated cylinders.

However, there are many flow-induced vibration (FIV) problems that involve two or more cylinders in configurations where the flow field of one cylinder influences

† Present address: Department of Naval Architecture and Ocean Engineering, NDF, POLI, University of São Paulo, Av. Prof Mello Moraes 2231, 05508-900, São Paulo SP, Brazil. Email address for correspondence: g.assi@usp.br

the flow on one or more other cylinders. One of the best-known examples of closely spaced cylinder arrays that are susceptible to FIV is the crossflow heat exchanger. Other examples include arrays of offshore riser pipes, closely spaced chimneys and overhead conductor cables. If we now consider a cylinder array where the cylinders have low mass and damping then, compared to an isolated cylinder, the possibilities for response are greatly increased. In such a complex flow environment, one of the greatest challenges is to understand the physical mechanisms responsible for FIV.

We have approached this problem from a fundamental perspective by just considering two cylinders. An important advantage is that now the possible parameter space is much reduced and hence it should be easier to focus on some of the basic mechanisms responsible for FIV of cylinders in arrays. However, limiting the problem to two cylinders can still involve a large number of variables, hence we have imposed some further restrictions. The cylinders are of equal diameter, and when at rest, are aligned one behind the other in a tandem arrangement. Only the rear cylinder is free to respond and response is restricted to the direction transverse to the approaching stream. Also, we consider the cylinder to be rigid but flexibly mounted. Applying dimensional analysis to the primary variables, the response  $\hat{y}$  is then given by the relation

$$\frac{\hat{y}}{D} = f\left(\frac{\rho U D}{\mu}, \frac{U}{D f_0}, \frac{x_0}{D}, m^*, \zeta\right), \quad (1.1)$$

where  $U$  is free-stream velocity,  $\mu$  is viscosity,  $f_0$  is the cylinder natural frequency and  $x_0$  is the centre-to-centre spacing between the cylinders. It should be noted that  $f_0$  is the natural frequency *in vacuo* and  $U/Df_0$  is the reduced velocity. In practice, the cylinder frequency is measured in air but this provides a very close approximation to the natural frequency  $f_0$ .

A considerable amount of work has been published relating to the flow about two fixed cylinders in a tandem arrangement but substantially less has appeared on the response of tandem cylinders. Bokaian & Geoola (1984) carried out experiments on tandem cylinders, to be described in more detail later, where the front one was fixed and the rear one was free to respond transverse to the flow. They observed that, depending on the value of  $U/Df_0$ , the response could be of the VIV type or it could be similar to galloping. They refer to the latter regime, which commences at values of reduced velocity beyond the peak response due to VIV, as wake-induced galloping.

Is this galloping similar to the classic kind described by den Hartog (1956) where a fluid-dynamic instability occurs, related to the cross-sectional shape of the body, such that motion of the body generates forces that increase the amplitude of vibration? It cannot be because when the rear cylinder is displaced in the transverse direction away from the line of centres, there is a hydrodynamic restoring force that is acting to return the cylinder to its original position. This suggests stability of the rear cylinder rather than instability. The restoring force was observed long before the work of Bokaian & Geoola (1984) and prompted a number of researchers to develop theories to seek its origin and to predict its magnitude. Price (1976) concluded that none of the explanations that had been proposed were completely satisfactory.

Paidoussis & Price (1988) developed mathematical models to describe the response of cylinders in closely spaced arrays and also simplified the problem by considering only two cylinders. They concluded that there needed to be a time delay between cylinder displacement and the transverse force to sustain wake-induced vibration (WIV). However, they did not provide a detailed explanation of the physical mechanism responsible for this delay beyond saying that there was likely to be a lag between the cylinder moving and the wake adjusting. Hence, two outstanding

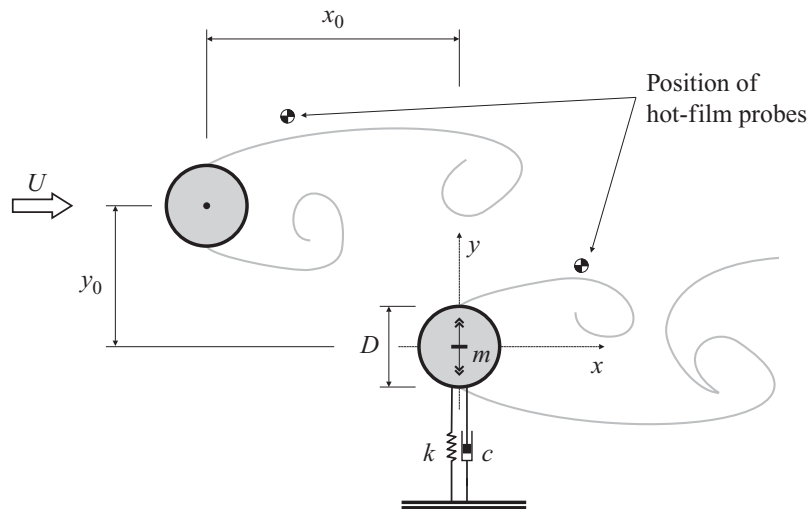


FIGURE 1. Arrangement of a pair of cylinders. The downstream cylinder is elastically mounted. The static upstream cylinder may be removed during experiments with a single cylinder.

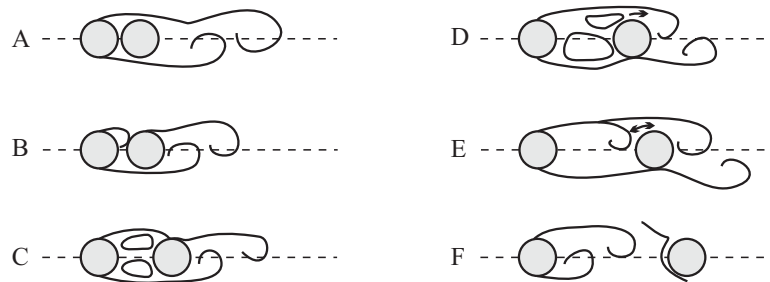


FIGURE 2. Regimes of flow interference for static cylinders for different tandem separations. Classification of interference regimes proposed by Igarashi (1981).

questions remain: what is the origin of the restoring force and what is the mechanism driving the transverse oscillation of the downstream cylinder in the regime described by Bokaian & Geoola (1984) as wake-induced galloping?

### 1.1. Flow interference around a pair of cylinders

An arrangement of a pair of cylinders is shown in figure 1, and our interest is in the particular case where the line of centres is parallel to the free stream, i.e.  $y_0 = 0$ . The upstream cylinder is exposed to a free stream with velocity  $U$ , but the downstream body is immersed in a disturbed-flow region created by the wake of the upstream cylinder. The Reynolds number in this study is always based on the velocity approaching the upstream body. Vortices shed from the first body will not only pass by or impinge on the downstream cylinder, but will also interfere with vortex shedding from the downstream cylinder. Hence, if the downstream cylinder is mounted on an elastic base, the response of the body will be influenced by the wake coming from the upstream body.

Early experiments with tandem static cylinders identified two main interference regimes associated with the type of flow that develops in the gap between the bodies. The gap flow is characterized by the presence of two unstable shear layers that, depending on  $x_0$  and  $Re$ , may reattach to the downstream cylinder, to form a region of recirculation, or roll up to initiate vortex shedding in the gap. Igarashi (1981) presented a more detailed classification dividing the gap-flow behaviour into six categories, as illustrated by 'A' to 'F' in figure 2. More recently, Sumner, Price &

Paidoussis (2000) produced a detailed classification of interference regimes for various configurations of staggered cylinders.

In this study, we are only concerned with the regime in which alternate vortex shedding is present in the gap. The transition from 'E' to 'F' in figure 2 marks the change to this type of flow. For a sufficiently large separation beyond a critical  $x_0$ , the shear layers start to roll up in the gap (pattern 'E'), and finally, a regime is reached in which a vortex street is formed behind the upstream cylinder (pattern 'F'). Zdravkovich (1977) comments that 'the commencement of vortex shedding behind the upstream cylinder strongly affects and synchronises the vortex shedding behind the downstream one. Hence, both cylinders should be equally prone to flow-induced vibrations due to vortex shedding.' Other excitation mechanisms may occur for  $x_0$  below the critical value, but the mechanism we are calling WIV only occurs when a developed wake is present in the gap.

The critical  $x_0$  appears to have some dependency on Reynolds number and free-stream turbulence intensity. Ljungkrona, Norberg & Sunden (1991) performed experiments around  $Re = 2.0 \times 10^4$  and observed that the critical separation is in the range  $x_0/D = 3.0$ – $3.5$  for a low turbulence intensity of 0.1 %, while it decreases to  $x_0/D = 2.0$ – $2.5$  for turbulence intensities of 1.4 and 3.2 %. Both Ljungkrona *et al.* (1991) and Zdravkovich (1986) suggested that this phenomenon may originate in instabilities in the separated shear layers from the upstream cylinder. Ljungkrona *et al.* (1991) also stated that the critical  $x_0$  'is high at very low  $Re$ , then decreases and passes through a minimum at moderate  $Re$ , followed by a maximum at higher  $Re$  and then it begins to decay with increasing  $Re$ '. They have found similarities between this behaviour and the  $Re$  dependency of the vortex-formation length of single cylinders reported by Norberg & Sunden (1987). Lin, Towfighi & Rockwell (1995) and Norberg (1998) showed that it decreases with increases in  $Re$  in the range  $Re = 10^3$ – $10^5$ , resulting in vortices forming closer to the base of the cylinder. Lin, Yang & Rockwell (2002) and Assi (2005) also showed evidence of this phenomenon occurring with a pair of tandem cylinders.

Another less-pronounced variation in the critical  $x_0$  may be due to hysteretic behaviour depending on whether cylinders are moved apart or brought closer together during the experiment. Liu & Chen (2002) showed that this phenomenon occurs for a pair of square cylinders in tandem and Zdravkovich (1977) suggested this possibility may occur for circular cylinders. Additionally, numerical studies performed by Jester & Kallinderis (2003) for  $Re = 10^3$ , Papaioannou *et al.* (2006) for  $Re = 10^2$ – $10^3$  and Carmo, Meneghini & Sherwin (2010*a,b*) for  $Re = 500$  also provide a clear demonstration of the hysteresis of both regimes in relation to  $Re$  and  $x_0$ . All these aforementioned factors may cause the critical separation to present considerable variation.

The classification of flow interference regimes presented so far is for a pair of tandem cylinders that are stationary. Chen (1986) observed that 'When either or both of the cylinders are elastic or vibrate, the flow field becomes significantly more complicated because of the interaction of the fluid flow and the cylinder motion'. Assi *et al.* (2006) showed that when the downstream cylinder is allowed to oscillate, the interference between both bodies changes drastically depending on the amplitude of oscillation and Reynolds number.

### 1.2. Wake-induced vibration of the downstream cylinder

King & Johns (1976) performed experiments in water ( $Re = 10^3$  to  $2 \times 10^4$ ) with two flexible cylinders for separations in the range  $x_0/D = 0.25$ – $6.0$ . They observed that for



$x_0/D = 5.5$ , the upstream cylinder response showed a typical VIV pattern reaching amplitudes around  $\hat{y}/D = 0.45$  at the resonance peak, comparable to their tests with a single cylinder at the same  $Re$ . On the other hand, the downstream cylinder also started to build up oscillations together with the upstream one, but instead of the oscillations disappearing after the synchronization range, they remained at roughly the same level up to the highest reduced velocity tested. They classified the response of the downstream cylinder as a type of buffeting, since it originated from the wake interference coming from the upstream cylinder.

Brika & Laneville (1999) performed tests with a pair of long cylinders in a wind tunnel in the range  $Re = 5000$ – $27\,000$  with a flexible cylinder positioned from 7 to 25 diameters downstream of a rigid cylinder. They presented amplitude data for different separations revealing that as  $x_0$  increases, the interference effect from the upstream wake is reduced until the response resembles that of a single cylinder without any (or with very little) interference. It is interesting to note that even between separations 16 and 25 they were still able to identify some change in the interference effect with the second cylinder positioned so far downstream. Because their experiments were performed in air, the mass ratio ( $m^* = 821$ ) was two orders of magnitude higher than other experiments in water. Yet their damping parameter was extremely low, resulting in a combined mass damping of only  $m^*\zeta = 0.068$ .

Moving from fully flexible to flexibly mounted rigid cylinders, we refer to experiments performed by Zdravkovich (1985) with two rigid cylinders free to respond in 2 degrees of freedom (d.o.f.) mounted in a wind tunnel ( $Re = 1.5 \times 10^4$ – $9.5 \times 10^4$ ,  $m^* = 725$  and  $\zeta = 0.07$ ). Due to a very high combined mass-damping parameter ( $m^*\zeta = 50$ ), Zdravkovich was only able to observe a build-up of oscillations for  $x_0/D = 4.0$  at reduced velocities beyond  $U/Df_0 = 50$ , asymptotically reaching a maximum of  $\hat{y}/D = 1.7$  at around a reduced velocity of 80. Zdravkovich & Medeiros (1991) performed similar 2-d.o.f. tests in a wind tunnel varying  $m^*\zeta$  between 6 and 200 ( $Re = 5 \times 10^3$ – $1.4 \times 10^5$ ). A similar asymptotic behaviour for crossflow vibrations was observed for high reduced velocities. Their results revealed a strong dependency of the response on  $m^*\zeta$  and showed that very high values of mass damping are required to inhibit WIV on the downstream cylinder. The maximum amplitude was obtained at their highest reduced velocity of 120.

Moving a step further in the simplification of the problem, we find a few studies for rigid cylinders responding only in 1-d.o.f. Bokaian & Geoola (1984) performed experiments with two cylinders in tandem in a water channel ( $Re = 700$ – $2000$ ). The upstream cylinder was fixed, while the downstream cylinder was elastically mounted on air bearings and free to respond only in the crossflow direction. They varied centre-to-centre separation in the range  $x_0/D = 1.09$ – $5.0$  covering the interference regimes with and without vortex shedding in the gap. Results for amplitude of response versus reduced velocity (with  $f_w$  being the natural frequency in still water) are presented in figure 3(a) for three values of  $x_0$ . A vigorous build-up of oscillations with increasing flow speed was observed for all flow speeds greater than a critical threshold velocity. Such a severe 1-d.o.f. vibration was observed to resemble the response due to classical galloping of non-circular bodies and they referred to the phenomenon as ‘wake-induced galloping’. Bokaian & Geoola (1984) concluded that depending on  $x_0$ ,  $m^*$  and  $\zeta$ , the downstream cylinder ‘exhibited vortex-resonance, or galloping, or a combined vortex-resonance and galloping, or a separated vortex-resonance and galloping’ response.

In figure 3(a), two examples of these different responses are found, with  $x_0/D = 1.5$  presenting a vortex resonance that is followed by (or combined with)

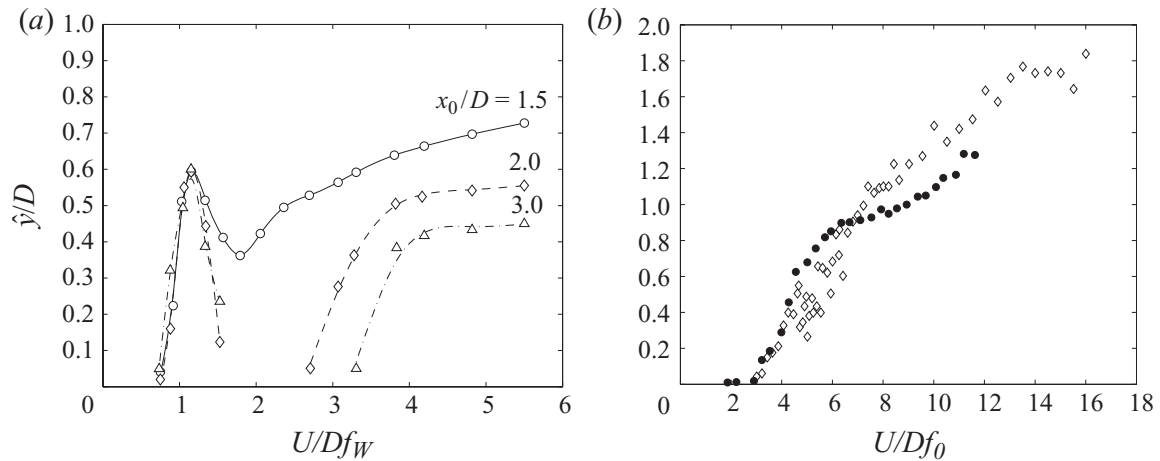


FIGURE 3. WIV response of the downstream cylinder. (a) Varying  $x_0$ ,  $m^* = 8.4$ ,  $\zeta = 0.013$  and  $Re = 700$ – $2000$  (Bokaian & Geoola 1984). (b)  $\diamond$ ,  $x_0/D = 4.75$ ,  $m^* = 3.0$ ,  $\zeta = 0.04$  and  $Re = 3 \times 10^4$  (Hover & Triantafyllou 2001);  $\bullet$ ,  $x_0/D = 4.0$ ,  $m^* = 1.9$ ,  $\zeta = 0.007$  and  $Re = 3000$ – $13\,000$  (Assi *et al.* 2006).

a ‘galloping response’, and  $x_0/D = 2.0$  and  $3.0$  presenting separated vortex-resonance and ‘galloping’ regimes. Unfortunately, the form of the flow in the gap is not known; however, from the classification of regimes proposed by Igarashi (1981) for static cylinders, and shown in figure 2, it seems likely that for the smallest gaps vortex shedding did not occur ahead of the downstream cylinder. Hence, it is not apparent if the ‘galloping-type’ response found by Bokaian & Geoola (1984), for all the separations shown in figure 3(a), is the WIV that we are studying. A mechanism of gap-flow switching sustains vibrations of cylinders in close proximity, as described by Zdravkovich (1974, 1988). It occurs for the first regime of flow interference when the upstream shear layers reattach to the downstream cylinder and no vortex wake is developed in the gap flow. Zdravkovich (1974) offers a convincing explanation for the excitation of tandem cylinders in close proximity, but leaves open the question of the mechanism when cylinders are farther apart.

A clearer example of WIV is shown in the work of Hover & Triantafyllou (2001) who measured displacements and forces for rigid cylinders in a water-towing tank at a constant  $Re = 3 \times 10^4$ . They used a closed-loop control system that forces the oscillation of a cylinder in response to the fluid force measured on the cylinder. Using this technique, they are able to control the key parameters:  $f_0$ ,  $m^*$  and  $\zeta$ . Their constant  $Re$  results presented in figure 3(b) were obtained by keeping  $U$  constant and varying  $f_0$ . For their experiments,  $m^*\zeta = 0.12$ , which is very close to the value of  $m^*\zeta = 0.11$  obtained by Bokaian & Geoola (1984). The differences in the levels of amplitude found in the two investigations is probably related to a difference of one order of magnitude in  $Re$ , as discussed in Assi (2009). For a separation of  $x_0/D = 4.75$ , Hover & Triantafyllou (2001) observed one single branch of response that builds up monotonically reaching amplitudes of  $[\hat{y}/D]_{\max} = 1.9$  for reduced velocities around 17.

More recently, Assi *et al.* (2006) performed 1-d.o.f. experiments with two rigid cylinders in a recirculating water channel ( $Re = 3 \times 10^3$ – $1.3 \times 10^4$ ). Their measurements of the transverse amplitude of the rear cylinder, also presented in figure 3(b), were obtained at  $Re$  values close to those tested in the experiments carried out by Hover & Triantafyllou (2001). However, Assi *et al.* (2006) employed a very low damping elastic system resulting in  $m^*\zeta = 0.013$ , which is one order of magnitude lower.

Nevertheless, both sets of results are in reasonably good agreement showing the expected WIV branch of high-amplitude oscillation building up as reduced velocity is increased. However, the results of Assi *et al.* (2006) also show a smooth hump around  $U/Df_0 = 6.0$ , indicating a VIV response.

### 1.3. The wake-induced vibration mechanism

A major difficulty in using quasi-steady arguments to explain the origin of WIV is that when the rear cylinder of a tandem pair is displaced sideways, a force develops that is acting to return the cylinder to its original position. The various theories about how this force is generated have been well explained by Price (1976) and he concludes that none can successfully predict the magnitude of the force.

Zdravkovich (1977) proposed that the displacement of the wake of the upstream cylinder by the downstream one towards the wake centreline would induce a lift force towards the centreline. Maekawa (1964) attributed the origin of the force to a buoyancy effect. The static pressure is a minimum at the centreline of the wake; hence, the pressure gradient across the wake generates a buoyancy force towards the centreline. However, Best & Cook (1967) and Wardlaw & Watts (1974) showed, by integrating the pressure field around the downstream cylinder, that only 30–50 % of the total lift could be attributed to a buoyancy effect. Maekawa (1964) also suggested that turbulence generated by the wake may affect the separation on the internal side of the cylinder, changing the symmetry of the pressure field around the downstream body. However, this phenomenon was not confirmed by experiments that examined transition on the downstream cylinder.

Mair & Maull (1971) proposed that the side force was caused by an entrainment of flow into the wake of the upstream cylinder generating an inclined free-stream velocity approaching the downstream body. The lift force towards the centreline would then be due to resolved drag, i.e. the component of inclined drag that contributes in the crossflow direction of displacement. Using estimated flow inclination angles, Price (1976) estimated that the lift force due to resolved drag is only 25 % of the total lift-force measure on the cylinder. Rawlins, referenced in Price (1976), stated that because of variations of velocity across the wake, the boundary layer on the downstream cylinder feeds different amounts of vorticity into the associated shear layers. He concluded that a circulation is built up around the cylinder until rates at which vorticity is discharged into the two separated shear layers are equal. This circulation would generate lift towards the centreline. Rawlins' lift curves have the same general shape as the lift profile measured experimentally, but do not obtain the required magnitude, generating only 75 % of the lift measured at the position of the maximum. Hence, following the detailed study by Price (1976) of the available theories, it appears that there is no fully satisfactory explanation for the origin of the transverse force acting on the rear cylinder of a cylinder pair.

It is clear that a simple quasi-steady theory will not be able to predict the fluid-elastic instability of the downstream cylinder if it is only free to oscillate in 1-d.o.f. Price (1984) improved a quasi-steady model by inserting a time delay between the cylinder displacement and the fluid force. This phase lag was intended to account for a possible flow retardation generated in the gap flow between the pair of cylinders; however, the physical origin of this effect is unclear. Granger & Paidoussis (1996) proposed yet another improvement of the quasi-steady theory employed by Price (1984) with the aim of modelling the most relevant unsteady effects neglected by the quasi-steady approach. In essence, their model, referred to as quasi-unsteady, incorporates a memory effect into the same time-delay idea, 'the physical origin

of which arises from the diffusion–convection process of the vorticity induced by successive changes in the velocity of the body’.

Paidoussis, Mavriplis & Price (1984) employed potential-flow theory to investigate fluid-elastic instability of an array of cylinders. Although they were not calculating any viscous forces in their model itself, they had to include a phase-lag effect in the fluid force in order to generate any oscillatory instability. Probably, the most intuitive explanation for the existence of a phase lag on the fluid force was offered by Paidoussis & Price (1988), who attributed this effect to a time delay associated with the reorganization of the viscous wake flow as the cylinder is displaced. Paidoussis *et al.* (1984) concluded that ‘if viscous effects are neglected altogether, then the only form of instability possible is divergence, which is a static, non-oscillatory instability’.

Each improved quasi-steady model gave better agreement with experimental data and they all include a phase lag between the cylinder displacement and the fluid force, yet a precise explanation for the origin of this time delay has not been produced. In this paper, we aim to study the mechanisms responsible for WIV of the downstream cylinder of a tandem pair.

## 2. Experimental set-up

Experiments were performed in the Department of Aeronautics at Imperial College London. Tests were carried out in a recirculating water channel with a free surface and a test section 0.6 m wide, 0.7 m deep and 8.0 m long. The side walls and bottom of the section were made of glass mounted on a steel frame, allowing a complete view of the models for flow-visualization purposes. Flow speed was continuously variable and an electromagnetic flow meter provided a reading of the instantaneous flow rate, which was divided by the area of the test section yielding the value of  $U$ . Free-stream turbulence intensity mapped across the section was  $(3.1 \pm 0.7)\%$  on average. Bokaian & Geoola (1984) performed experiments with a pair of cylinders in a water channel and found no significant difference in their WIV results for free-stream turbulence intensity of 6.5 and 11.9 %. The actual flow quality proved to be adequate to perform our FIV study. This was validated by good agreement between our preliminary VIV results for an isolated cylinder and other experiments presented in the literature (as will be shown later).

Two circular cylinders were made from a 50 mm diameter acrylic tube, giving a maximum  $Re = 30\,000$ , based on cylinder diameter  $D$ . With a wetted length of 650 mm (total length below water level), the resulting aspect ratio of the model was 13. The cylinders were hollow and contained air in order to keep the mass low. It was judged preferable not to install end plates on the cylinder in order not to increase the fluid damping in the system. Instead, it was chosen to have the models terminating as close as possible to the glass floor of the test section. One single cylinder occupies 8.3 % of the total area of the test section. If one cylinder is oscillating behind the other, the maximum projected area of both cylinders would result in a blockage ratio of 16.6 % if it is displaced by more than  $1D$ . Brankovic (2004) performed VIV tests on a single cylinder in the same water channel with three ratios of blockage: 11.3, 13.6 and 17 %. She concluded that although the maximum amplitude of oscillation decreased slightly for higher blockage ratios, the results remained qualitatively the same, meaning that the hydrodynamic mechanism did not change for the three cases studied.

The upstream cylinder was rigidly attached to the structure of the channel preventing displacements in any direction, while the downstream cylinder was fixed at its upper end to a 1-d.o.f. elastic mounting. The initial streamwise and crossflow



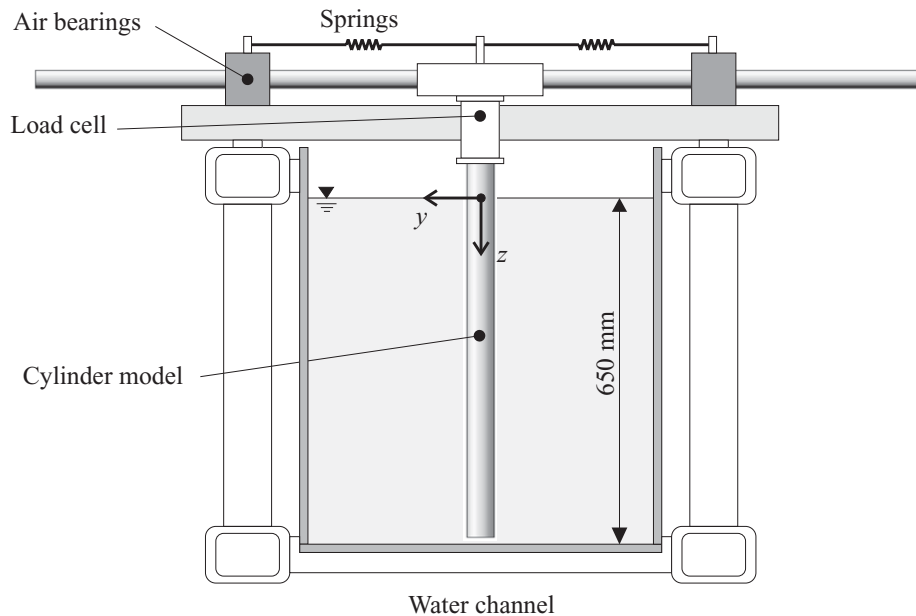


FIGURE 4. Schematic representation of the 1-d.o.f. rig holding the downstream cylinder. The free stream flows out of the page in the  $x$ -axis direction.

separations between cylinders ( $x_0$  and  $y_0$  in figure 1) could be varied by changing the position of the upstream model, so that the downstream cylinder always oscillated around the centreline of the test section. For most of the experiments performed in this study, both cylinders were initially aligned with the free-stream direction ( $y_0 = 0$ ), arranged in a tandem configuration. Figure 4 shows a schematic representation of the 1-d.o.f. rig on which the downstream cylinder was mounted. The models were aligned in the vertical direction passing through the free-water surface and the downstream cylinder was mounted such that there was a 2 mm gap between the lower end of the cylinder and the glass floor of the test section. The support system was firmly attached to the channel structure and sliding cylindrical guides were free to move in the transverse direction defined as the  $y$ -axis. A pair of coil springs connecting the moving base to the fixed supports provided the restoration force for the system. A pair of sliding guides made out of a carbon fibre tube with a smooth finish ran through air bearings at each side. The tubes were connected at mid-length by a light, stiff platform machined out of a block of aluminium, to which the cylinder was firmly attached.

It is known that the dynamic response of a cylinder is extremely sensitive to the structural characteristics of the system; therefore, extra care was taken to determine the precise value of natural frequency, mass and damping of the structure. The spring stiffness ( $k$ ) combined with the mass of all oscillating parts ( $m$ ) resulted in a natural frequency of oscillation of  $f_0 = 0.30$  Hz, determined by performing a series of free decay tests in air. It was possible to vary reduced velocity to a maximum of  $U/Df_0 = 40$  when  $U$  was increased up to  $0.6 \text{ m s}^{-1}$ . The minimum flow speed in the channel was  $U = 0.03 \text{ m s}^{-1}$ , resulting in the lower limit of  $U/Df_0 = 2.0$ . All moving parts of the elastic base contributed to the effective mass oscillating with the cylinder, resulting in a mass ratio of  $m^* = 2.6$  (calculated as the total mass divided by the mass of displaced water). The air bearings proved to be an effective way to reduce damping without compromising the stiffness of the structure, especially in resisting drag loads for higher flow speeds. By carrying out free decay tests in air, it was also possible to estimate the structural damping of the system resulting in  $\zeta = 0.7\%$ , calculated

as a percentage of the critical damping. Therefore, the product  $m^*\zeta = 0.018$  for the majority of the experiments.

A load cell was attached between the model and the platform to measure instantaneous and time-averaged hydrodynamic forces acting on the cylinder. It consisted of two independent load cells machined out of one block of a hard aluminium alloy. The cells were perpendicular to each other in order to measure components of the hydrodynamic force in the streamwise and crossflow directions lift and drag, respectively. Each cell was individually calibrated up to 50 N with an uncertainty of 1 % and no significant cross-talk between them was observed. Drag could be measured directly by the load cell, since the cylinder was not allowed to move in the  $x$ -axis. However, the crossflow component needed to be corrected in order to remove the inertia force due to the moving mass of the cylinder.

An optical positioning sensor was installed to measure the  $y$ -displacement of the cylinder without affecting the damping. Completing the instrumentation, a pair of hot-film probes was employed to measure velocity fluctuations in the gap between the cylinders and in the developed wake downstream of the second cylinder (see figure 1). A Dantec particle-image velocimetry (PIV) system was used to map velocity fields. A laser sheet entered the section through one of the side walls illuminating the flow at the mid-height of the section. A digital camera was positioned underneath the channel and the illuminated plane was visualized through the glass floor. Flow visualization was also carried out using the same laser to illuminate fluorescent dye or hydrogen bubbles. More details about the experimental set-up, flow quality, the design of the load cell and operation of the 1-d.o.f. rig can be found in Assi (2009).

### 3. Analytical modelling and preliminary results

A preliminary experiment was performed with a single cylinder free to oscillate in 1-d.o.f. in a uniform flow to serve as validation of the experimental methodology. The analytical modelling as well as the VIV results that follows will be useful when understanding the WIV excitation mechanism.

Allowing for displacements only in 1-d.o.f., the equation of motion for an elastically mounted body is expressed by

$$m\ddot{y} + c\dot{y} + ky = \frac{1}{2}\rho U^2 DL[\bar{C}_y + \hat{C}_y \sin(2\pi ft + \phi)], \quad (3.1)$$

where  $y$ ,  $\dot{y}$  and  $\ddot{y}$  are, respectively, the displacement, velocity and acceleration of the body and  $C_y(t)$  is the time-dependent fluid force coefficient in the crossflow direction (lift). Following an analysis presented by Parkinson (1971) and others, the displacement of a cylinder under VIV may be expressed by the harmonic response

$$y(t) = \hat{y} \sin(2\pi ft), \quad (3.2)$$

where  $\hat{y}$  and  $f$  represent the harmonic amplitude and frequency of oscillation, respectively. For large-amplitude oscillation under a steady-state regime of VIV, the fluid force and the body response oscillate at the same frequency  $f$ , which is usually close to the natural frequency of the system. According to this ‘harmonic forcing and harmonic motion’ assumption  $C_y$  can be expressed by a time-average term  $\bar{C}_y$  and a transient term modelled as a sine wave with amplitude  $\hat{C}_y$ , frequency  $f$  and phase delay between the transverse force and the motion of  $\phi$ . In our single-cylinder experiment, we expect  $\bar{C}_y$  to be 0.

Throughout this study, cylinder-displacement amplitude ( $\hat{y}/D$ ) was found by measuring the root-mean-square value of response and multiplying by  $\sqrt{2}$ . Such

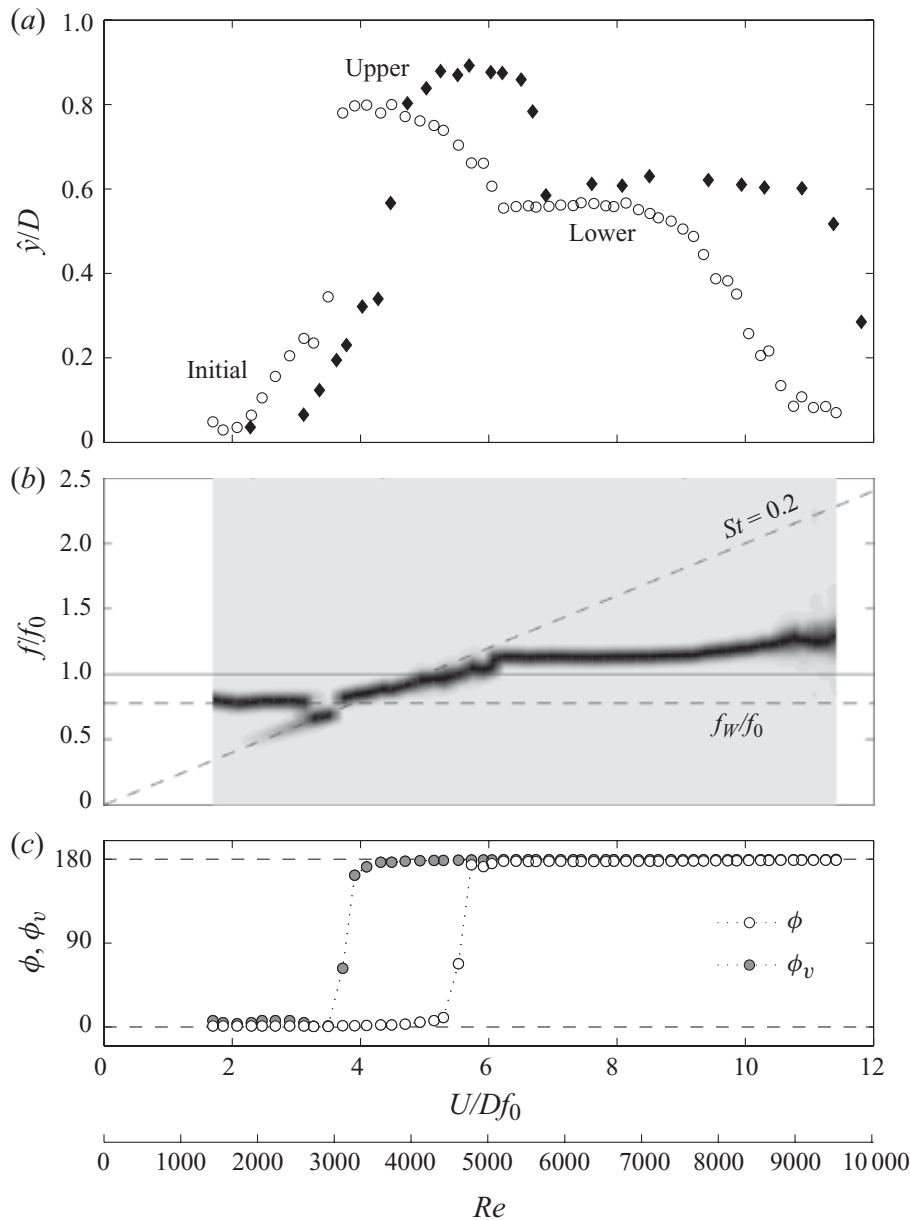


FIGURE 5. VIV response of a single cylinder free to oscillate in the crossflow direction. (a) Displacement ( $\circ$ , the present study;  $\blacklozenge$ , Khalak & Williamson (1997),  $m^* = 2.4$ ,  $\zeta = 0.0059$ ). (b) Normalized PSD of frequency of oscillation. (c) Phase angle between lift and displacement.

a harmonic amplitude assumption is likely to underestimate the maximum response but was judged to be acceptable for assessing the average amplitude of response for many cycles of steady-state oscillations. An alternative method was to measure the amplitude of individual peaks of displacement in order to estimate an average value, but this was found to give very similar results to the harmonic amplitude mentioned above, thus proving that a sinusoidal approximation for the response is indeed very reasonable. The same procedure was employed to determine the magnitude of all other fluctuating variables, such as  $\hat{C}_y$  and  $\hat{C}_x$ .

Figure 5 presents the response of the single cylinder under VIV. Since  $U$  is increased in order to vary the reduced velocity,  $Re$  also varies along the reduced-velocity axis and is plotted as a reference in a parallel axis. In the  $\hat{y}/D$  curve, it is possible to identify the typical three branches of response for low  $m^*\zeta$  systems discussed by Williamson & Govardhan (2004) – initial, upper and lower branches – clearly

defining a finite synchronization range. In the original curve presented by Khalak & Williamson (1997), the reduced velocity was calculated by employing the natural frequency measured in still water ( $U/Df_w$ , in our notation); hence, their curve plotted here has been offset in order to agree with our  $U/Df_0$  axis (considering an added mass coefficient of  $C_a = 1.0$ ). In the  $f/f_0$  graph, a variation from light to dark grey represents dominant peaks in the normalized power spectral density (PSD) of the frequency of oscillation (see Assi (2009) for more details).

As discussed by Williamson & Govardhan (2004), the total fluid force acting on the cylinder can be divided into two components: a potential-force component  $C_{yp}$ , given by the ideal flow inertia force, and a vortex-force component  $C_{yv}$ , due only to the dynamics of the vorticity field around the body. By definition,  $C_{yp}$  is always opposing the body's acceleration and its magnitude is proportional to the product of the displaced fluid mass and the acceleration of the body. On the other hand,  $C_{yv}$  essentially depends on the dynamic of vortices in the wake and may be expressed in terms of another  $\hat{C}_{yv}$  and phase angle  $\phi_v$  in relation to the displacement of the cylinder, resulting in

$$\hat{C}_y \sin(2\pi ft + \phi) = \hat{C}_{yp} \sin(2\pi ft + 180^\circ) + \hat{C}_{yv} \sin(2\pi ft + \phi_v). \quad (3.3)$$

This decomposition is useful when analysing the actual contribution the vortices in the wake are having on the total force acting on the cylinder. The almost  $180^\circ$  phase shift experienced by  $\phi$  and  $\phi_v$ , associated with the transition in the vortex-shedding mode, is also clearly identified in figure 5(c). Khalak & Williamson (1999) verified that changes in  $\phi$  and  $\phi_v$  are related to changes in the modes of vortex shedding.

A careful analysis of the time series will serve as reference for the discussion of WIV results to come later. Time series of  $\hat{y}/D$  are plotted for different reduced velocities in figure 6(a, c, e) (where  $T$  is the period of an average cycle). The first data set ( $U/Df_0 = 4.0$ ) is collected from a point in the upper branch of VIV; the second ( $U/Df_0 = 5.7$ ) is in the transition from the upper to the lower branch; and the third ( $U/Df_0 = 7.9$ ) is in the lower branch. In the first and third series, it is possible to note that the envelope of  $\hat{y}/D$  is more regular than during the transition between branches.

The plots in figure 6(b, d, f) compare several cycles of  $\hat{y}/D$  and  $C_y$  superimposed in one figure, each representing around 20 % of the total number of acquired cycles with displacement around the average  $\hat{y}/D$ . Again, it is evident that the deviation of  $\hat{y}/D$  from the mean curve (thick line in black) is accentuated during the transition between branches. Looking at  $C_y$  curves of figure 6, we observe that although the magnitude of lift shows considerable variations, the phase angle between cycles is reasonably constant in the upper and lower branches.  $C_y$  is clearly almost in phase with  $\hat{y}$  in the upper branch and out of phase in the lower. However, the behaviour of  $C_y$  for only a few cycles of oscillation is enough to show that a constant phase angle is not observed during the transition from the upper to the lower branch. This is the intermittence phenomenon described by Khalak & Williamson (1999), and it is clear from the graph that both magnitude and phase of the lift are changing during the transition between modes.

$\hat{C}_y$  was directly measured with the load cell, and  $\hat{C}_{yp}$  and  $\hat{C}_{yv}$  were calculated as suggested by Williamson & Govardhan (2004). Force measurements and decomposition were in good agreement with results presented by Khalak & Williamson (1999), but are not presented here for brevity. In addition, PIV measurements also found good agreement with their work in identifying the

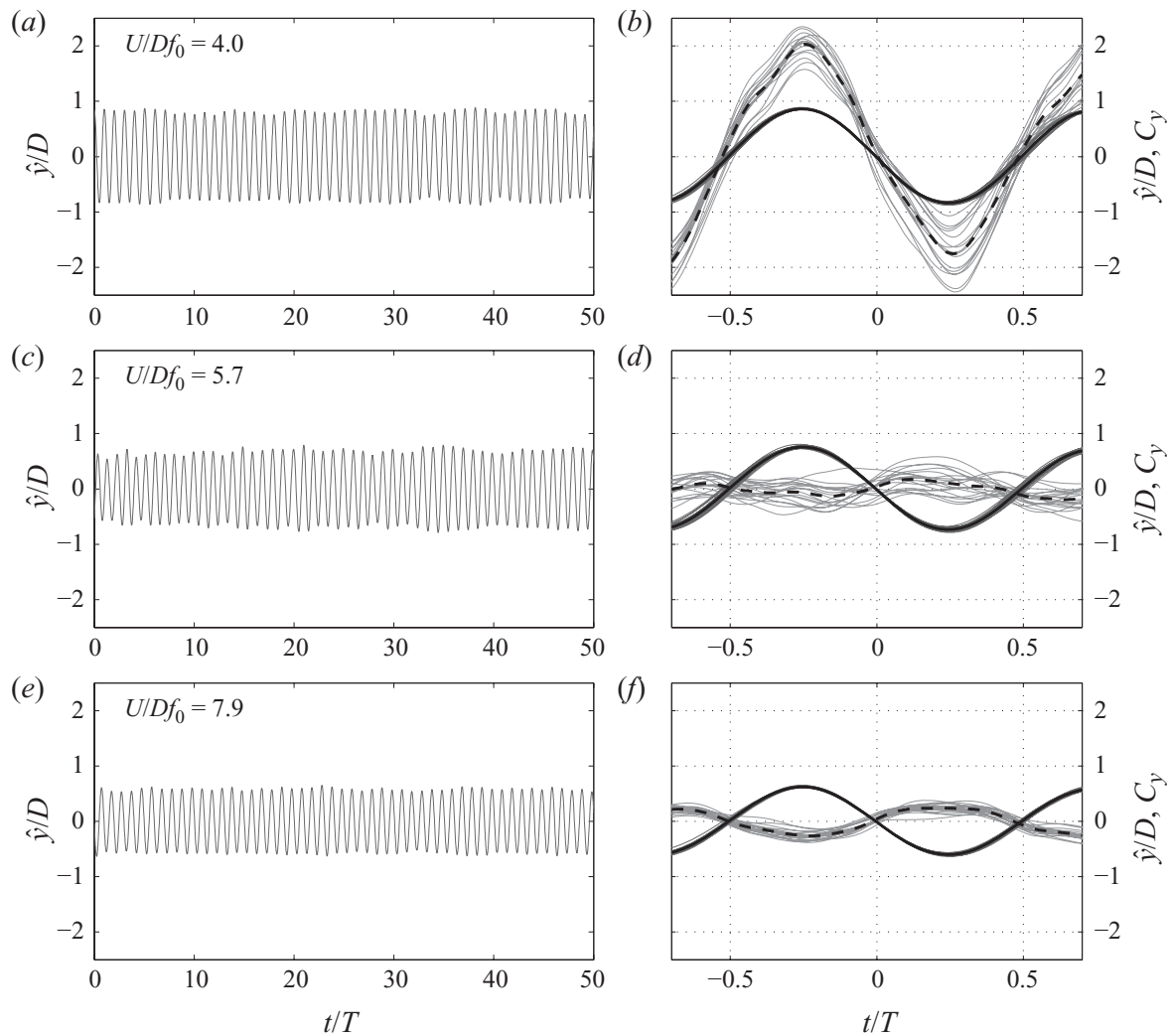


FIGURE 6. (a, c, e) Time series of displacement for around 50 cycles of oscillation. (b, d, f) Superimposed plots of similar cycles.  $\hat{y}/D$  in dark grey and  $C_y$  in light grey with average cycle in black.

appropriate vortex-shedding modes in the wake. These results can be found in Assi (2009).

#### 4. WIV of the downstream cylinder

We have investigated WIV responses for the downstream positioned at various locations beyond the critical separation of  $x_0/D = 2.5$  and the results are presented in figure 7. The upstream cylinder was stationary and only the downstream cylinder was free to respond in 1-d.o.f. in the crossflow direction ( $y$ -axis). Fully developed vortices were observed in the gap flow for all separations with  $x_0/D > 2.5$ .

The response curves demonstrate that the overall amplitude of vibration in the WIV regime decreases as the cylinders are moved farther apart. The smallest separation of  $x_0/D = 4.0$  presented the highest amplitudes of vibration with increasing amplitude for higher reduced velocities. In contrast, for  $x_0/D = 20.0$ , the response is drastically reduced and, overall, more closely resembles that of VIV of a single cylinder. As will be explained later, the WIV mechanism that excites high-amplitude vibrations grows weaker as the cylinders are separated, until the interference is irrelevant and the cylinder behaves like an isolated body.



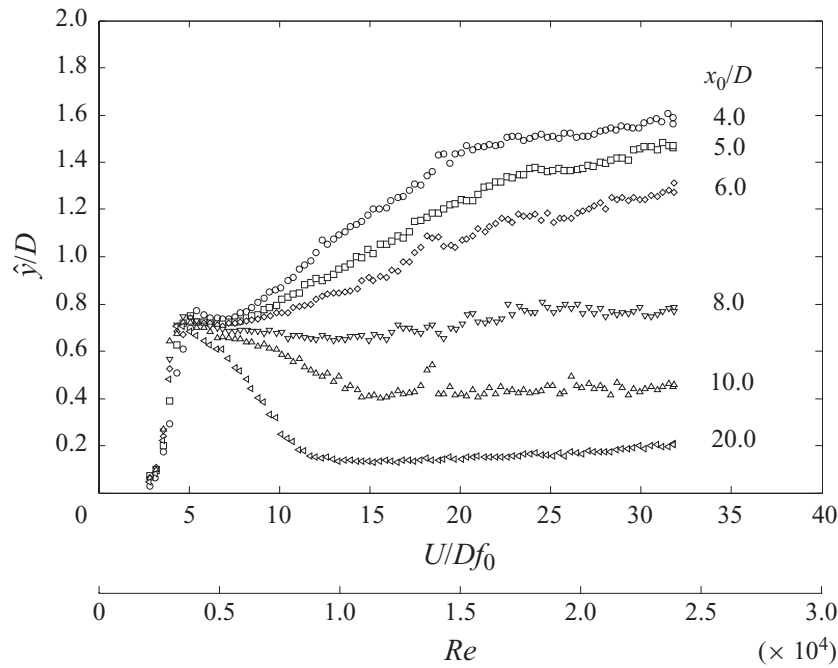


FIGURE 7. WIV response of the downstream cylinder at various  $x_0/D$  separations.

In order to develop a clearer understanding of the WIV excitation mechanism, we will focus our attention on a single separation of  $x_0/D = 4.0$ , as will be discussed in detail in the following sections.

#### 4.1. WIV of the downstream cylinder at $x_0/D = 4.0$

A separation of  $x_0/D = 4.0$  was chosen for various reasons: (i) it was beyond the critical separation where a bistable reattachment of the shear layers may occur and vortex shedding was observed to be present in the gap for all flow speeds; (ii) it gives a WIV response that is qualitatively consistent with that for larger separations; (iii) the displacements and magnitudes of fluid forces were comparatively large and can be measured to a good accuracy; (iv) it was sufficiently small to allow the wakes of both cylinders to be measured simultaneously using PIV.

Figure 8(a) plots the displacement versus reduced velocity.  $\hat{y}/D$  is the harmonic amplitude of displacement discussed above and gives a good measure of the average amplitude of vibration for many cycles of oscillation. However,  $\hat{y}/D$  does not provide a good estimate of the maximum amplitude that the cylinder might reach if displacement varies from cycle to cycle. By considering individual peaks of oscillation, it was possible to estimate a maximum and a minimum peak amplitude taking an average of the 10% highest and lowest peaks of the whole series, yielding  $[\hat{y}/D]_{\max}$  and  $[\hat{y}/D]_{\min}$ , respectively. Therefore, we can say that for a certain reduced velocity, the cylinder oscillates on average with  $\hat{y}/D$ , but reaches the maximum and minimum limits given by the other curves. This provides considerable new information about the response since it shows that  $\hat{y}/D$  is not only building up with reduced velocity, but also the deviation from the average amplitude, i.e. the irregularity of the envelope, is increasing.

Figure 8(b) shows that  $f$  increases above  $f_0$  but does not reach the line for  $St = 0.2$ . The PSD contours reveal that for any other frequencies present in the spectrum, the levels are much smaller than the dominant branch that is evident across the reduced-velocity range. That is to say, there is no significant trace of a frequency branch

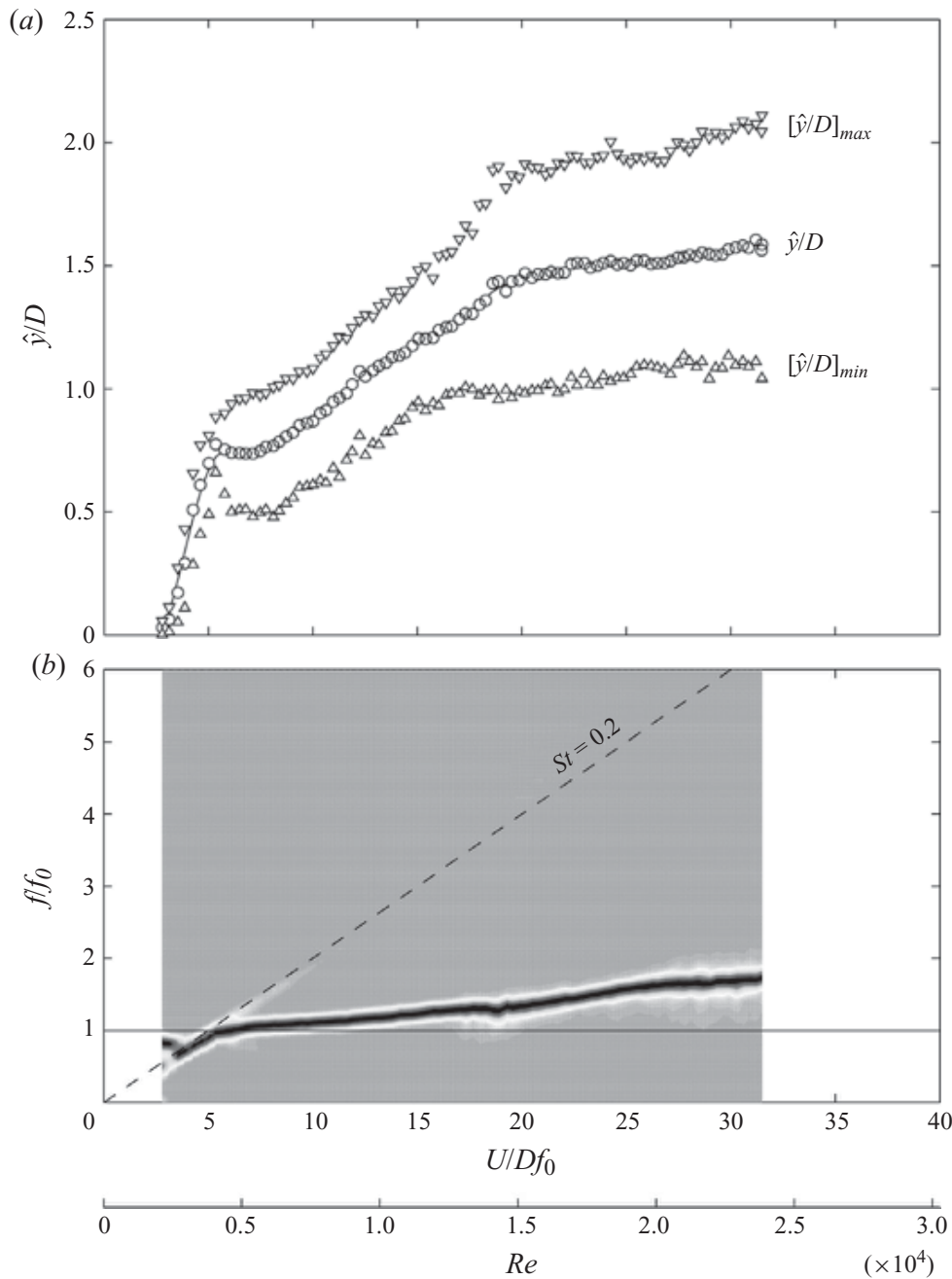


FIGURE 8. WIV response of the downstream cylinder at  $x_0/D = 4.0$ . (a) Displacement; (b) normalized PSD of frequency of oscillation.

associated with  $St = 0.2$  beyond reduced velocity of 10, with only a hint appearing between 5 and 10.

As shown in figure 6, the envelope of the single-cylinder VIV response is fairly regular except during the transition between branches. This is generally not the case for the WIV response, as illustrated in figure 9. We note that the envelope of response is already irregular at  $U/Df_0 = 4.6$  and becomes more irregular for higher reduced velocities. This is also revealed in the plots shown in figure 9(b, d, f), which show the cycles for the 20 % highest peaks.

By comparing the variation of  $C_y$  and  $\hat{y}/D$  in one cycle, it is possible to estimate the phase between them and also the overall frequency content of the signals. For  $U/Df_0 = 4.6$ , very close to the VIV resonance region, we note that lift and displacement

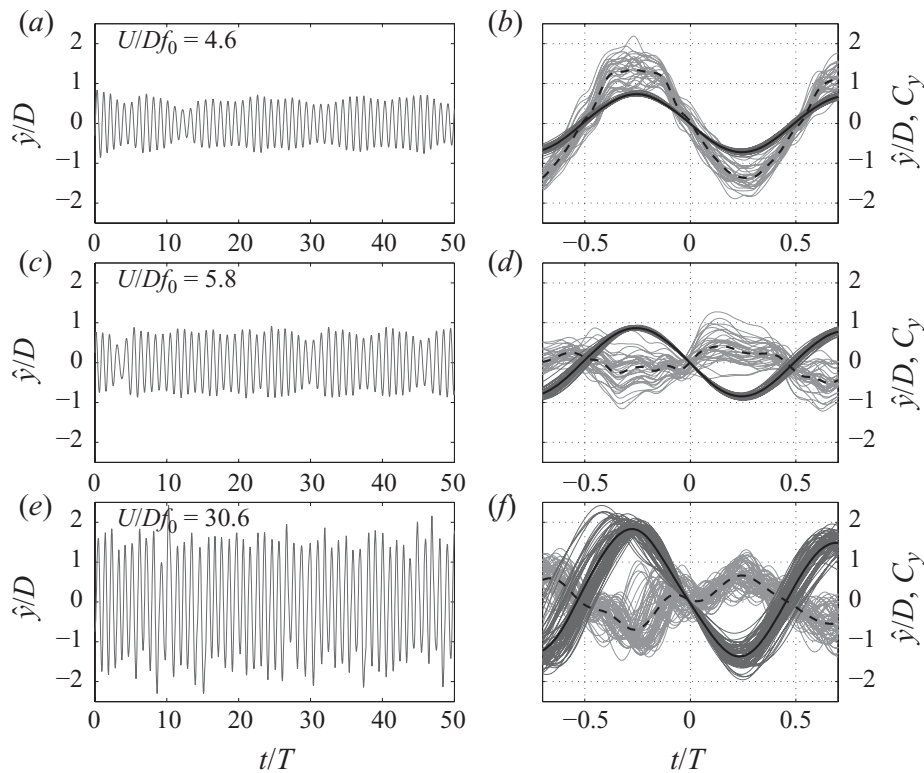


FIGURE 9. (a, c, e) Displacement signal for around 50 cycles of oscillation. (b, d, f) Superimposed plots of similar cycles;  $\hat{y}/D$  in dark grey and  $C_y$  in light grey with average cycle in black.

are almost in phase and there seems to be a single dominant frequency present in  $C_y$ . However, moving to a slightly higher reduced velocity of 5.8, the behaviour of lift changes considerably. Not only does a second frequency appear in the signal, but also the magnitude and phase of  $C_y$  are more variable. Moving away from the VIV influence towards the upper end of the reduced-velocity range, we note that a higher frequency has appeared in  $C_y$ , although it is not noticeable in the displacement curves.

The upstream cylinder was not only fixed at all times in these experiments, but it was also mounted on a load cell, allowing measurements of instantaneous lift. Analysing the normalized PSD of the lift force on both cylinders, it is possible to identify other branches of frequency in  $C_y$ . Figure 10(a, c) shows the normalized PSD of lift measured on both cylinders. From figure 10(a) it is evident that the lift force acting on the upstream cylinder is directly related to the vortex-shedding mechanism since there is only one distinct frequency branch that follows very closely the  $St = 0.2$  line. It can also be concluded that the lift force on the upstream cylinder sees little effect of the oscillation of the downstream one, since only a minor trace of the frequency data presented in figure 8 is identified. On the other hand, figure 10(c) shows that the lift force on the downstream cylinder has two clear branches bifurcating after the VIV resonance region. The lower branch corresponds to the frequency of oscillation captured in figure 8, but the higher branch is clearly associated with a vortex-shedding frequency that follows the  $St = 0.2$  line.

Now, this vortex-shedding branch is predominant at lower reduced velocities, probably related to the typical synchronization range of VIV, but diminishes beyond  $U/Df_0 = 15$ . The lower branch appears around a reduced velocity of 5 but only becomes dominant beyond a reduced velocity of 10. Within the range  $U/Df_0 = 10$ –20, both branches appear with equivalent energy content determining the region where both VIV and WIV are occurring together. In fact, looking again at the response



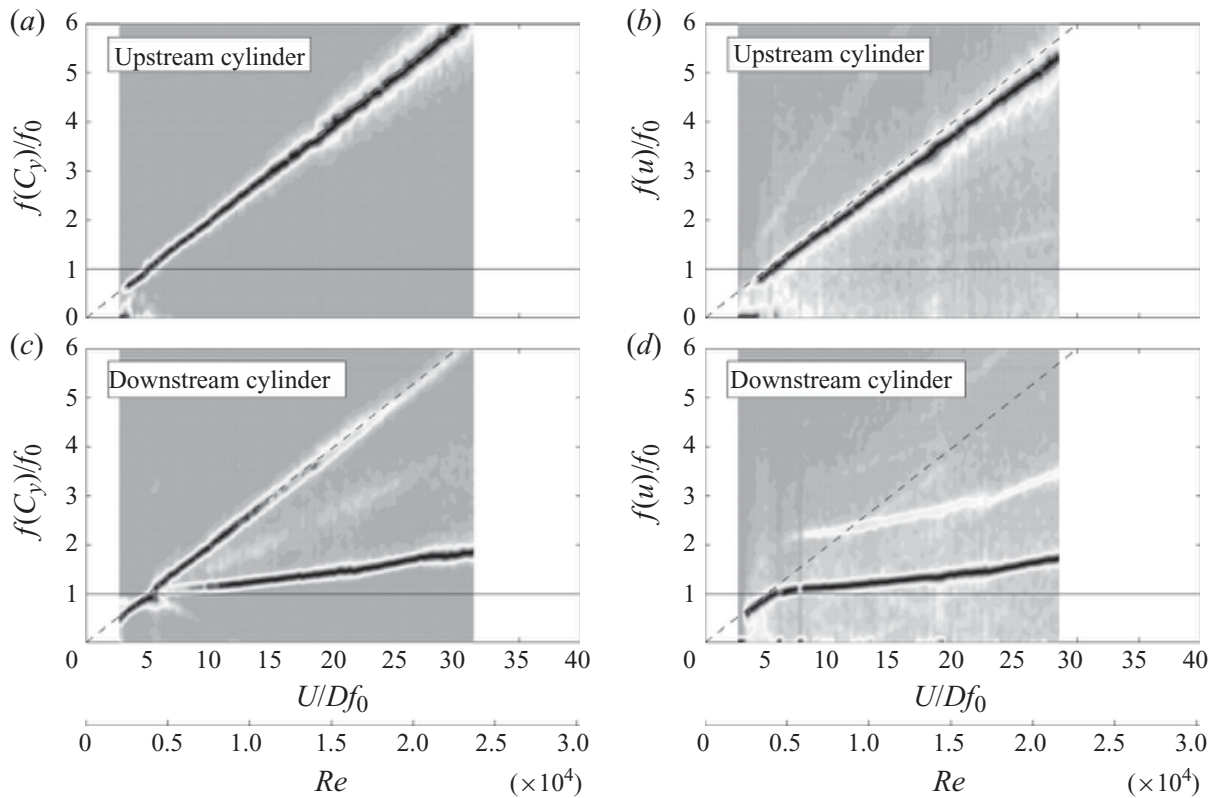


FIGURE 10. Normalized PSD of (a, c) lift force and (b, d) velocity fluctuation in the wake of a static upstream and an oscillating downstream cylinder. (The normalization applied to all PSD graphs does not allow comparison of energy magnitudes along the reduced-velocity axis, but only over vertical slices for a fixed reduced velocity.)

curve in figure 8, it is quite apparent that three different regimes can be identified by different slopes of the displacement curve: (i) a VIV resonance region around  $U/Df_0 = 5$  (equivalent to the VIV upper branch); (ii) combined VIV (reminiscent of a lower branch) and WIV regimes roughly in the range  $U/Df_0 = 5-17$ ; and (iii) a pure WIV regime for  $U/Df_0 > 17$ .

It is plausible to think that the VIV regime should involve synchronization of vortex shedding from both cylinders. In order to investigate this, we measured velocity fluctuations with hot-film probes, one downstream of each cylinder (see figure 1). Figure 10(b, d) presents the PSDs for both probes confirming that the upstream cylinder is shedding vortices as a fixed, isolated cylinder with minimal interference from the downstream one. On the other hand, no clear identification of vortex shedding close to  $St = 0.2$  was observed for the downstream cylinder that is oscillating. Of course, once the cylinder is vigorously moving ahead of a fixed probe, it is very difficult to measure any fluctuations other than the component of flow velocity that relates to the fluctuations associated with its movement. However, even when this low-frequency branch was filtered out, no clear trace of vortex shedding was identified. This does not mean that the downstream cylinder is not shedding vortices – on the contrary, fully developed vortices were observed in PIV measurements, as will be demonstrated later – it simply means that a hot-film probe positioned in the near wake was not suitable to capture this phenomenon. Placing the probe further downstream made it possible to observe combined velocity fluctuations from the vortex shedding of both cylinders, but still it was not possible to distinguish a shedding signal that could be directly associated with the downstream body.

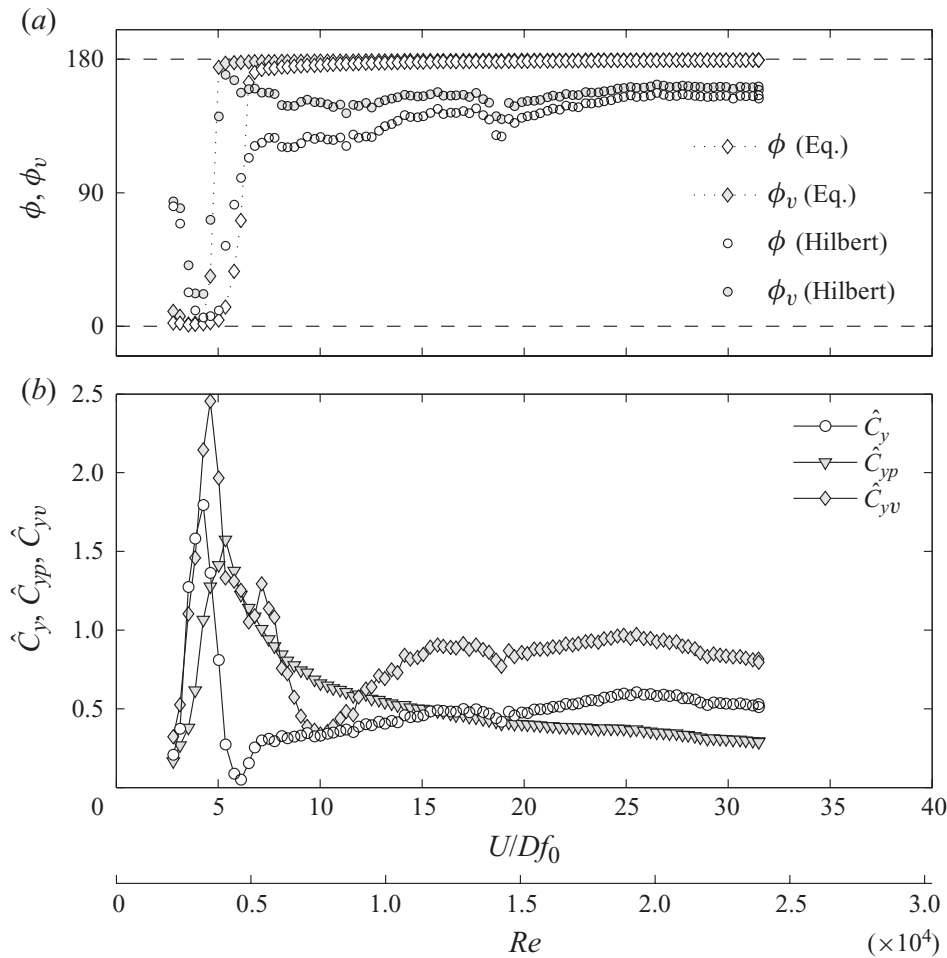


FIGURE 11. (a) WIV phase angles calculated according to Williamson & Govardhan (2004) and the Hilbert transform of the signals. (b) Decomposition of lift coefficient into potential and vortex components calculated according to Williamson & Govardhan (2004).

In figure 11 we show the fluid force components acting on the downstream cylinder. In order to estimate  $\phi$ ,  $\phi_v$ ,  $\hat{C}_{yv}$  and  $\hat{C}_{yp}$ , we have employed a ‘harmonic forcing and harmonic motion’ hypothesis identical to that presented earlier for VIV of an isolated cylinder, which means that the fluid force and the response have the same frequency but delayed by a phase angle  $\phi$ . In the pure VIV case, we know that fluctuations in the fluid force come directly from the vortex-shedding mechanism; therefore,  $f = f_s$  in the synchronization range. However, in the WIV case we have seen that  $f$  is not directly related to  $f_s$  as it does not follow the  $St = 0.2$  line closely. Nevertheless, even without knowing the origin of the fluid force, we can verify from figures 8 and 10 that the dominant component of  $C_y$  has the same frequency as the response. Hence, the harmonic assumption might still throw some light on the phenomenon.

Figure 11(a) displays  $\phi$  and  $\phi_v$  versus reduced velocity showing that a phase shift from almost 0° to 180° occurs at around the same reduced velocity as for typical VIV; beyond the resonance peak, both  $\phi$  and  $\phi_v$  remain close to 180° until the upper end of the reduced-velocity range. This plot also compares  $\phi$  and  $\phi_v$  calculated by two different methods: the first solves  $\phi$  and  $\phi_v$  from the equations derived in the harmonic analysis of Williamson & Govardhan (2004) (which also assumes lift and response with a single dominant frequency), and the second averages the phase angles from the instantaneous Hilbert transform for the whole series. If the force and the response indeed present a single harmonic frequency – as they do for single-cylinder VIV – both approaches are equivalent and the curves collapse. However,

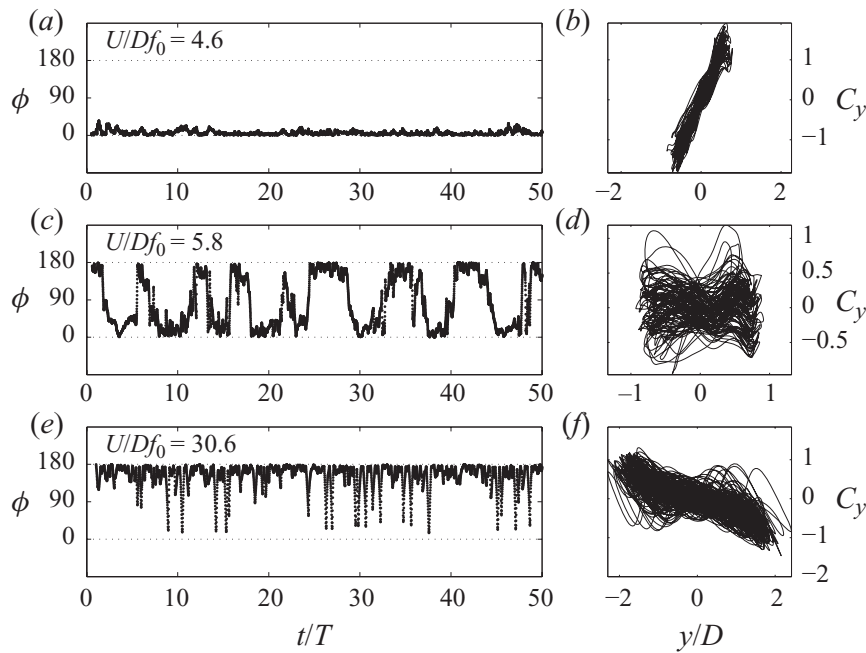


FIGURE 12. Three examples of WIV phase angles. (a, c, e) Instantaneous phase angle  $\phi$  for around 50 cycles of oscillation. (b, d, f) Lissajous figures of  $C_y$  versus  $\hat{y}/D$ .

figure 11(a) shows that the harmonic hypothesis must be an over-simplification of the WIV phenomenon. The actual phase angles calculated with the Hilbert transform of the displacement and lift signals are at a lower level for the whole range of the WIV excitation. This result reveals that the lag between displacement and lift is actually less than the one predicted by a harmonic assumption.

Figure 11(b) shows the decomposition of the lift coefficient. For reduced velocities up to the VIV resonance peak, the curves show behaviour very similar to that found for single-cylinder VIV. But instead of  $C_y$  and  $C_{y_v}$  reducing and tending to zero by the end of the synchronization range, both rise from around a reduced velocity of 7 up to 17, marking the second regime of combined VIV (a possible lower branch) and WIV. A clear WIV regime is identified in  $C_y$  and  $C_{y_v}$  curves for  $U/Df_0 > 17$ , as mentioned above, and their values remain roughly at the same level as reduced velocity is increased.

The instantaneous behaviour of  $\phi$  or  $\phi_v$  may be analysed by employing a Hilbert analytical transform to the signal, as described in Hahn (1996) and employed by Khalak & Williamson (1999) for VIV. Figure 12 presents the results for about 50 cycles of oscillation.  $\phi$  remains very close to  $0^\circ$  for the whole time series at  $U/Df_0 = 4.6$ , resulting in a clean Lissajous figure in figure 12(b, d, f). During the transition at  $U/Df_0 = 5.8$ , it appears that an intermittent phase shift is also present, consistent with the data plotted in figure 9. When the regime reaches our highest reduced velocity of  $U/Df_0 = 31.2$ , the phase is predominantly close to  $\phi = 180^\circ$ , but it still varies more than for VIV of a single cylinder. The corresponding Lissajous figure may suggest that a second dominant frequency may also be playing a role, in agreement with the third case analysed in figure 9.

## 5. The wake-induced vibration excitation mechanism

In order to understand the fluid mechanics behind the WIV mechanism, we investigated two aspects of the force acting on the downstream cylinder: firstly, the origin of the restoring lift force occurring on static cylinders in staggered

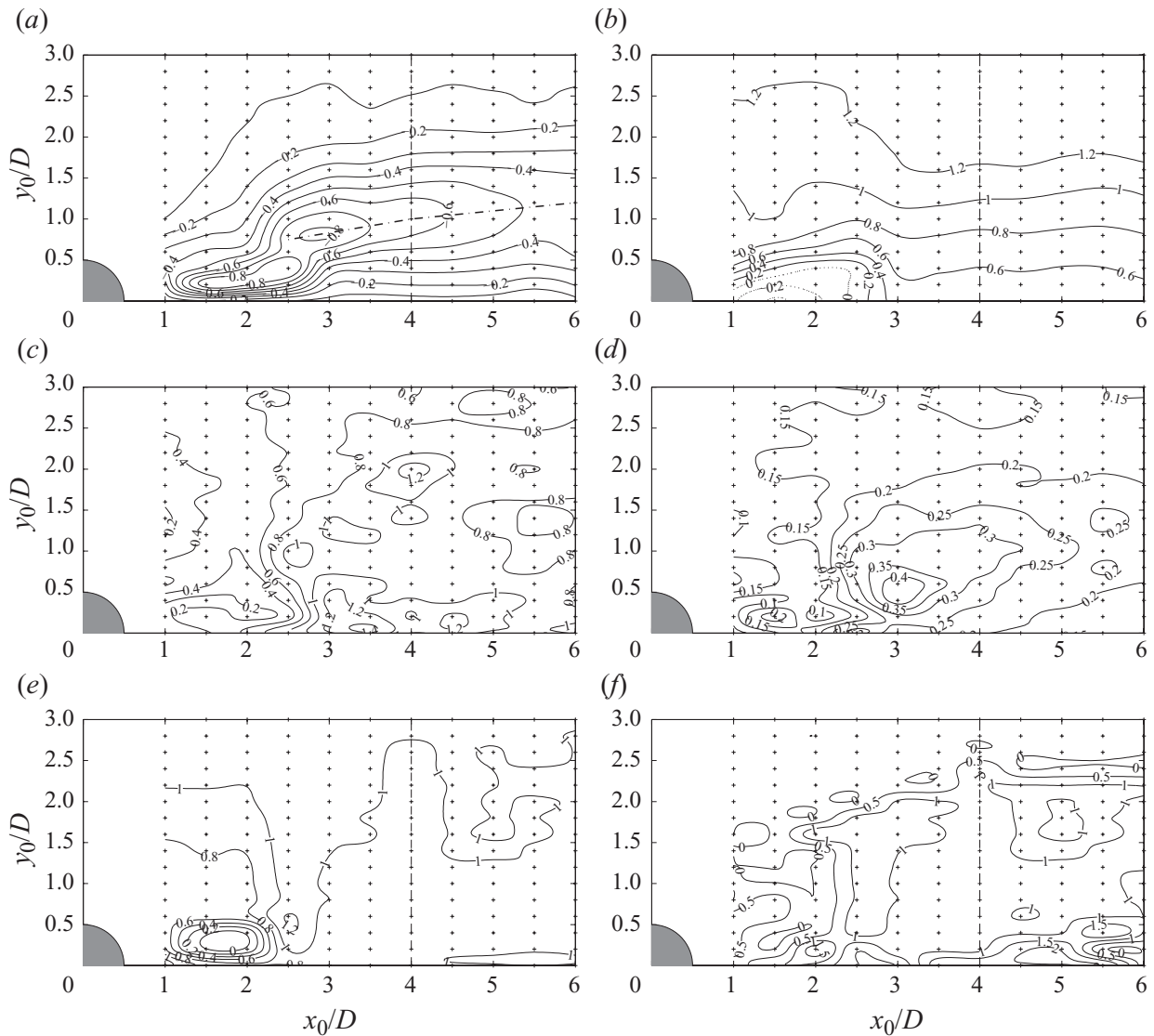


FIGURE 13. Contours for the downstream cylinder of a static pair at  $Re = 19\,200$ : (a) steady lift ( $\overline{C}_y$ ); (b) steady drag ( $\overline{C}_x$ ); (c) fluctuating lift ( $\hat{C}_y$ ); (d) fluctuating drag ( $\hat{C}_x$ ); (e) frequency of lift ( $f(C_y)/f_s$ ); (f) frequency of drag ( $f(C_x)/f_s$ ).

arrangements; secondly, the origin of the phase lag between  $C_y$  and  $y$  that, combined with the lift field, results in the WIV excitation.

### 5.1. Fluid force on static cylinders in staggered arrangement

Measurements were obtained by holding the upstream cylinder fixed and traversing the downstream cylinder across 160 stations (each marked by a small cross in figure 13) in and out of the wake-interference region. Results are presented in figure 13 in a series of maps that are symmetrical about the centreline of the wake.

Figure 13(a) presents the steady lift acting on the downstream cylinder for different regions of wake interference. A negative value of  $\overline{C}_y$  indicates lift acting towards the centreline. As expected, the first evident observation is that the steady-lift force points in the direction of the centreline for all configurations investigated, which is in agreement with Bokaian & Geoola (1984) and Zdravkovich (1977). The  $\overline{C}_y$  map reveals two regions of steady lift as large as  $-0.8$ . The first region, between  $x_0/D = 1.5$  and  $2.5$ , is associated with the gap-flow-switching mechanism described by Zdravkovich (1977) and occurs in the first wake-interference regime. The second



region occurs for larger lateral separations around  $y_0/D = 0.8$ ; it begins around  $x_0/D = 2.5$ – $3.0$  and develops a trend of maximum  $\overline{C}_y$  (indicated by the dot-dashed line) that will decrease in intensity as the second cylinder is moved farther downstream. This second region is associated with the second interference regime, in which vortex shedding takes place in the gap.

In the steady drag map presented in figure 13(b), positive contours of  $\overline{C}_x$  denote drag in the streamwise direction. Dotted lines represent contours of zero or negative drag that occur when the cylinders are close enough for the gap flow to be enclosed by the reattaching shear layers. For  $x_0/D > 2.5$ , the tandem downstream cylinder only experiences positive drag, indicating that a developed wake starts to be formed in the gap.

If a quasi-steady assumption is to be used to understand WIV, then these maps of time-average force coefficients should be adequate to provide the necessary gradients of  $C_y$  and  $C_x$  to satisfy a classical-galloping-like model. However, by also analysing the fluctuating components of the fluid force, it is possible to identify if and where the unsteadiness of the flow is playing a significant role.

Figures 13(c) and 13(d) present maps similar to those discussed above, but plot contours of the fluctuating-force coefficients  $\hat{C}_y$  and  $\hat{C}_x$  (3.3). Both graphs reveal regions of increased fluctuating lift and drag that only occur for  $x_0/D > 2.5$ . A contour of  $\hat{C}_y > 1.0$  appears for tandem arrangements but relatively high values of  $\hat{C}_y > 0.8$  also appear for staggered locations around the wake-interference region.  $\hat{C}_y$  is reduced to levels below 0.4 for separations below the critical value. Interestingly, the region of maximum  $\hat{C}_x$  does not occur for tandem arrangements but only when the downstream cylinder has an offset of about  $y_0/D = 0.5$ .  $\hat{C}_x = 0.4$  is observed for the second interference regime at  $x_0/D = 3.0$  and a trend of higher fluctuating drag is developed from this point, decreasing in intensity as  $x_0$  is increased.

The distribution of  $\hat{C}_y$  and  $\hat{C}_x$  across the wake gives support to the idea that coherent vortices from the upstream cylinder contribute to the fluctuating component of the fluid forces for separations of  $x_0/D > 3.0$ . The magnitude of  $\hat{C}_y$  is another important factor. Taking the example of  $x_0/D = 4.0$  and  $y_0/D = 1.0$ , we observe that the magnitude of the fluctuating lift is greater than that of the steady lift, i.e. the actual lift on the cylinder is  $C_y = -0.6 \pm 0.8$ , probably even reaching an instantaneous positive (outwards) value once in a few cycles.

We believe this to be strong evidence that the steady-lift force acting towards the centreline, as well as the fluctuating component, originate in some way from the unsteady interference of the vortex wake coming from the upstream cylinder with the wake being formed from the downstream cylinder. If this is true, we expect to find that the frequency of fluctuation of  $C_y$  and  $C_x$  is related to the frequency of vortex shedding from upstream. Now, we know that the upstream cylinder is shedding vortices at the same frequency as an isolated cylinder (see figure 10). Figures 13(e) and 13(f) show plots of the frequencies of  $C_y$  and  $C_x$ , respectively (normalized by the equivalent  $f_s$  for  $St = 0.2$ ). We observe that the dominant component of the fluctuating forces is close to 1 once the second regime of interference is established. For close separations, the frequency of  $C_y$  is distinctively lower than  $f_s$ , revealing that a developed wake is indeed not present in the gap. This result is in agreement with Alam *et al.* (2003), who measured lift coefficients for both cylinders in tandem arrangements.

Our experimental results for the steady components are in good agreement with other works found in the literature, including Zdravkovich (1977). We believe this is the first time the magnitude and frequency of the fluctuating components of the lift and drag forces have been presented for staggered arrangements of cylinders.

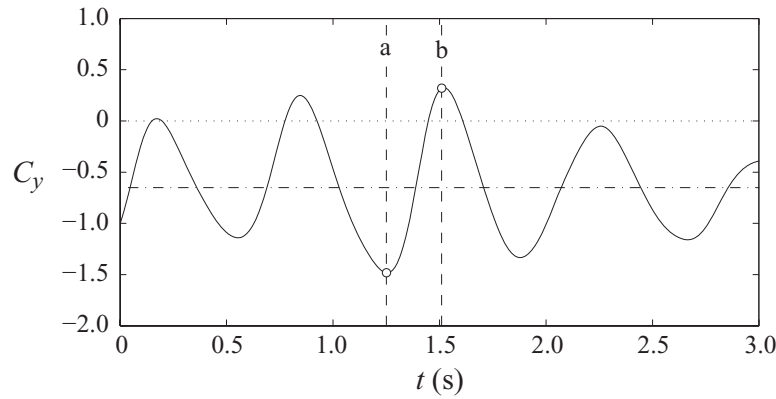


FIGURE 14. Time series of lift on the downstream cylinder of a static pair in staggered arrangement  $x_0/D = 4.0$  and  $y_0/D = 1.0$ .  $Re = 19\,200$ .

Now, a quasi-static analysis of WIV requires the downstream cylinder to extract energy from the flow as it moves across the steady-force fields discussed above. In other words, the excitation force acting on the body should not depend on its movement or any unsteady interaction with the upstream wake, but only on the relative position of the cylinder across the wake. This might be true for bodies with very small transverse velocities  $\dot{y}$ , but certainly this is not the case observed in the WIV response presented above. Even a quasi-steady hypothesis may be too much of an over-simplification in this case. Based on data from figure 8, we can estimate the maximum transverse speed the cylinder reaches as it crosses the centreline of the wake for the maximum reduced velocity point. On average,  $\dot{y}$  is around 55 % of the free-stream velocity  $U$ , but it can reach values up to 67 % for the most severe cycles. With such vigorous crossflow movement, it is difficult to accept that the downstream cylinder is not affecting or interacting with the wake coming from the upstream body, making implausible any quasi-static or quasi-steady assumptions. Therefore, we believe that a completely unsteady investigation of the force–displacement interaction is required to understand how the WIV mechanism works.

#### 5.1.1. Analysis of unsteady lift on fixed cylinders

Before investigating the instantaneous lift force acting on a moving downstream cylinder, we shall consider the unsteady flow field that generates the steady and fluctuating forces on a pair of static cylinders.

Figure 14 shows a short time series of  $C_y$  measured on a static downstream cylinder at  $x_0/D = 4.0$  and  $y_0/D = 1.0$ . The dot-dashed line represents a steady lift of  $\overline{C_y} = -0.65$  estimated from figure 13. There are two data points, marked with circles, representing the maximum and minimum  $C_y$  in this short time series for which we will investigate the corresponding flow fields using PIV. Figure 15 shows instantaneous vorticity contours and the corresponding velocity field for instant ‘a’ in the trough, i.e. when  $C_y = -1.4$ , and for instant ‘b’ at the crest, where  $C_y = 0.32$  and acts outwards. Vortices identified with the symbols A and B were, respectively, shed from the upstream and downstream cylinders; odd indices mean that vortices have positive vorticity and were shed from the right-hand sides of the bodies, and even indices mean the opposite. Vortices are identified at both instants; therefore, we can follow the development of the wake from ‘a’ to ‘b’. A simplified sketch is presented in figure 16.

The flow passing around the upstream cylinder generates and sheds vortices in the gap. In figure 15, we see the instant when vortex A4 is being formed very

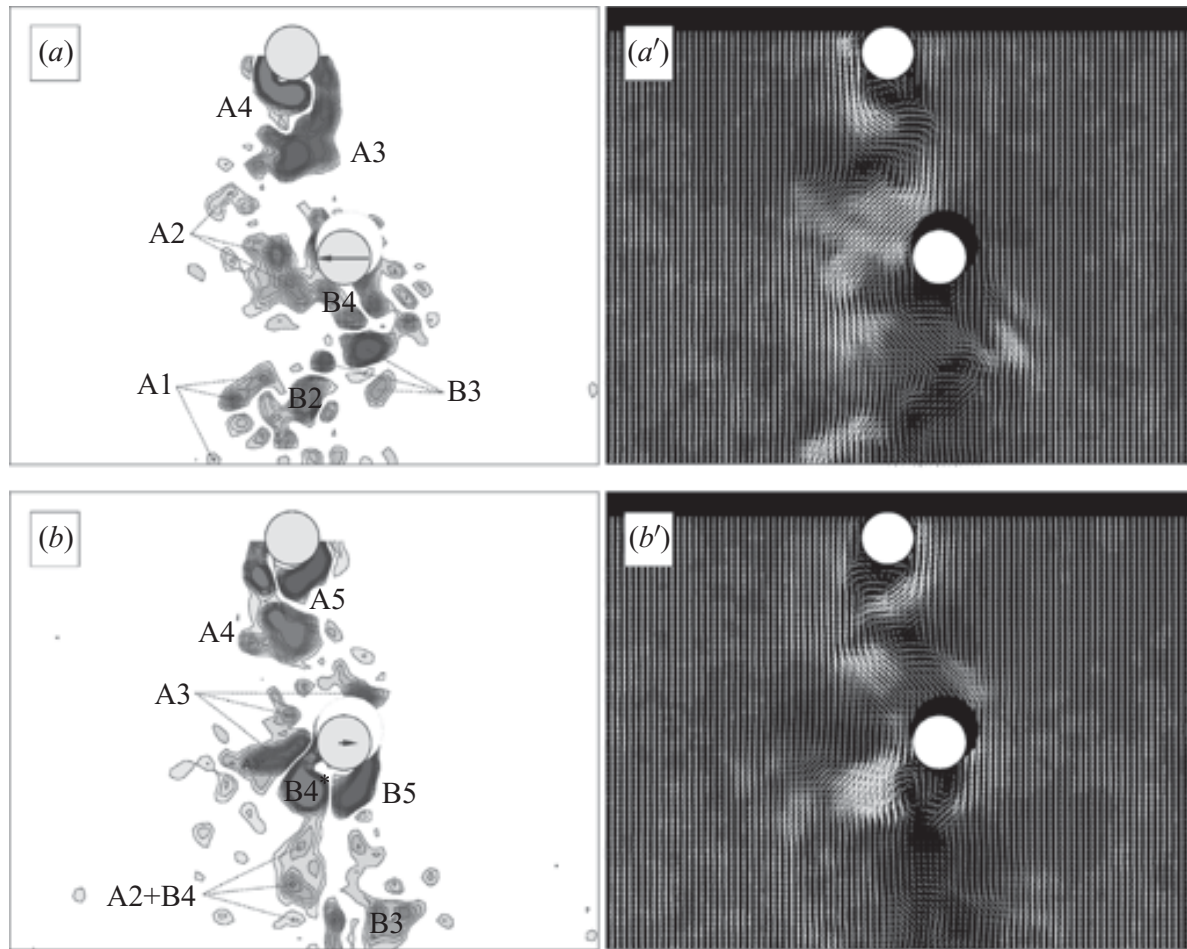


FIGURE 15. (a, b) Instantaneous vorticity contours and (a', b') velocity field (velocity magnitude increases from dark to light grey) obtained with PIV around a pair of static cylinder in staggered arrangement.  $x_0/D = 4.0$ ,  $y_0/D = 1.0$ ,  $Re = 19\,200$ . (See figure 14.)

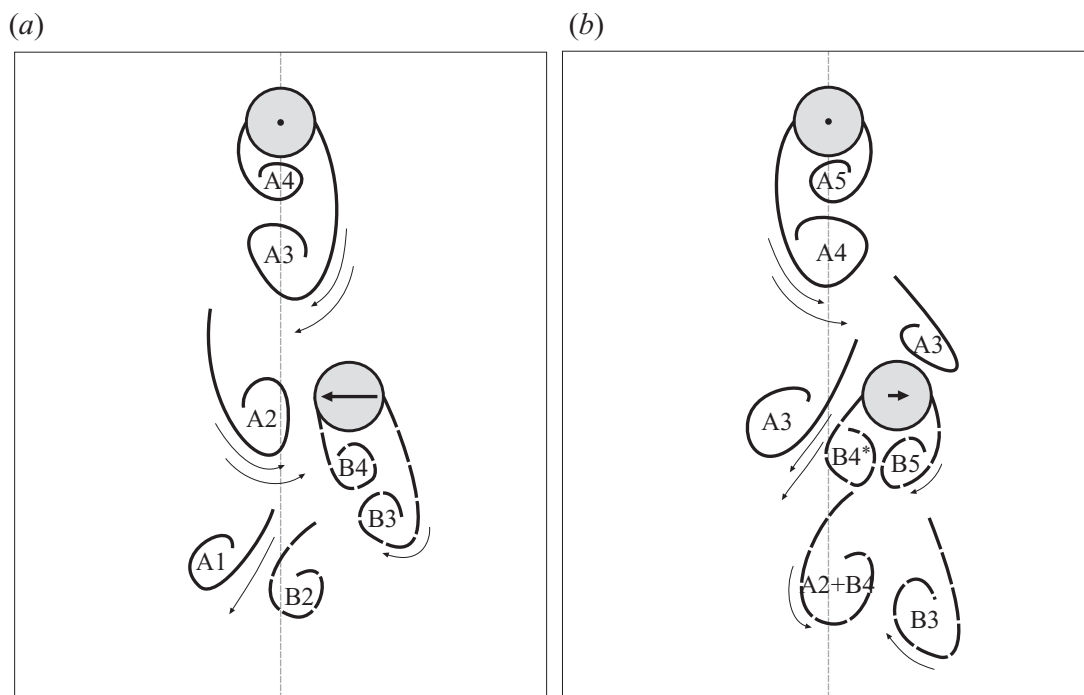


FIGURE 16. Sketch of vortex-structure interaction that (a) enhances or (b) diminishes  $C_y$  on the downstream cylinder at  $x_0/D = 4.0$  and  $y_0/D = 1.0$ . (See figures 14 and 15.)

close to the cylinder, inducing a high-speed flow that is shown with white vectors in the velocity field. A fully developed vortex A3, which was formed half a cycle before, is convected downstream and induces high-speed flow on the inner side of the downstream cylinder. This high-speed flow accelerates the boundary-layer flow running on that side, adding more circulation into the shear layer. Consequently, vortex B4 forming from the downstream cylinder will have a higher circulation than a typical vortex on a single-cylinder fully developed vortex A2, shed in the previous cycle, passes around the downstream cylinder and induces a flow field that will hold B4 closer to the downstream cylinder. We suggest that this combination of high-speed flow induced on the inner side, increasing the strength of the vortex being formed, and the flow holding this vortex closer to the downstream cylinder is responsible for generating the high lift of  $C_y = -1.4$  shown in figure 14. Of course, the interaction between vortices from previous cycles is occurring in the wake downstream of the second body – with vortices from both cylinders (A1 and B2) merging together and moving in pairs – but what is happening around the downstream cylinder has significantly more influence on the force being generated than the wake further downstream.

Now, moving to instant ‘b’ in figure 15, we observe that vortices have been convected further downstream and a new vortex A5 is being formed from the upstream cylinder. Downstream of the second cylinder, we observe that A2 has merged with B4, forcing B3 to be released and giving way to a new B4\* that starts to roll up. A fully developed A3 impinges and splits around the downstream cylinder with a portion A3\* passing by the inner side and the rest following around the outside of the cylinder. As A3\* and the new B4\* interact, they induce a very high-speed flow across the wake that forces the formation of B4\* further inwards. On the other side, B5 is also forced and rolls up closer to the downstream cylinder, contributing to generating a small lift  $C_y = 0.32$  acting outwards.

Figure 16 highlights the main vortex–structure interactions occurring in the wake. The effect of upstream vortices on the downstream cylinder is seen to be paramount in both cases: (a) when A3 induces high-speed flow on the inner side and A2 displaces the downstream wake outwards and (b) when A3 splits around the body and interacts with B4 to generate high-speed flow inwards.

We observe that identical wake patterns are not repeatable, as vortices from both cylinders may be forming at different rates and strengths. Nevertheless, we believe this flow-field investigation offers a good illustration of the complex vortex dynamics occurring in the wake associated with large lift fluctuations on the downstream cylinder. We should expect to find even more complex dynamics when the downstream cylinder is oscillating with high transverse velocities.

We saw that a strong and complex vortex–structure interaction is present, and hence, must be involved in the excitation mechanism. We cannot guarantee *a priori* that a quasi-steady assumption for the fluid forces (even if it accounts for hysteretic effects) will represent the phenomenon with all its unsteadiness. Instead, we suggest that a phase lag is generated as the unsteady wake is modified by the movement of the downstream cylinder. Hence, we propose that a simple steady wake without the unsteadiness of the vortices is not able to generate the necessary forces and phase lag to excite WIV. In order to evaluate this hypothesis, we will proceed in two steps. Firstly, we present an idealized experiment designed to reproduce a wake with a steady shear-flow profile but without the unsteadiness of vortices. Then we will investigate lift-force measurements paired with instantaneous flow fields to assess whether there



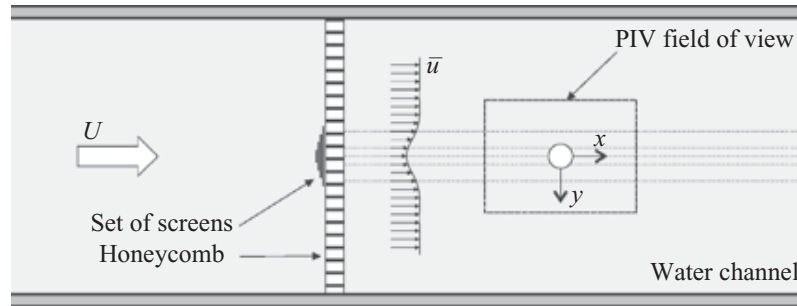


FIGURE 17. Set-up of set of screen and honeycomb for the shear-flow experiment.

is a phase lag related to the vortex–structure interaction as the downstream cylinder oscillates.

## 6. The effect of a steady shear flow

If a quasi-steady approach is to be used to predict WIV then the fluid forces on the downstream cylinder will not depend on the unsteadiness of the wake but only on the steady flow velocity profile. Therefore, if we could generate a wake with a similar steady profile but without the unsteadiness of the vortices and immerse an elastically mounted cylinder in this velocity field, we should expect to see a response similar (at least qualitatively) to WIV. According to the quasi-steady approach, the phase lag between lift and displacement would still have to be present in such a flow. A qualitatively similar WIV response would be sound evidence that unsteady vortices are not required to generate the phase lag and sustain vibrations.

### 6.1. Experimental set-up

A series of screens made of thin stainless-steel wire was cut in strips of different widths. Then a combination of superimposed screens was positioned vertically in the centre of the test section to produce a mean velocity profile. The set of screens was fixed on an aluminium honeycomb to remove any crossflow components. The set-up is illustrated in figure 17, where  $\bar{u}$  represents the resultant shear-flow profile. The flow field around a pair of cylinders under WIV was measured with PIV to serve as reference. The velocity profile of the wake was averaged from a number of snapshots (corresponding to more than 100 cycles of oscillation and many more cycles of vortex shedding), resulting in the flow fields presented in figures 18(a) and 18(b). The process was repeated for four  $Re$  within the range of the experiments, although only two are plotted here for brevity. Two dashed circles mark the average amplitude of oscillation of the cylinder.

When considering fluid forces acting on the downstream cylinder Price (1976) had already noticed that the lift profile on the body depends ‘on its own characteristics in the wake and not particularly on the wake characteristics’. He concluded that ‘the use of wake parameters, measured without the presence of the [downstream] body when attempting to assess the forces thereon, is an over-simplification of the situation as far as lift is concerned, while appearing to work quite well for drag’. For this reason, flow-field measurements were performed with the downstream cylinder in place and oscillating in order to account for the interaction between the body and the upstream wake.

With the cylinders removed, the set of screens was adjusted to generate the best possible match to the profiles of the reference cases. Figures 18(c) and 18(d) present the steady profiles obtained downstream of the screens for two of the  $Re$  investigated.

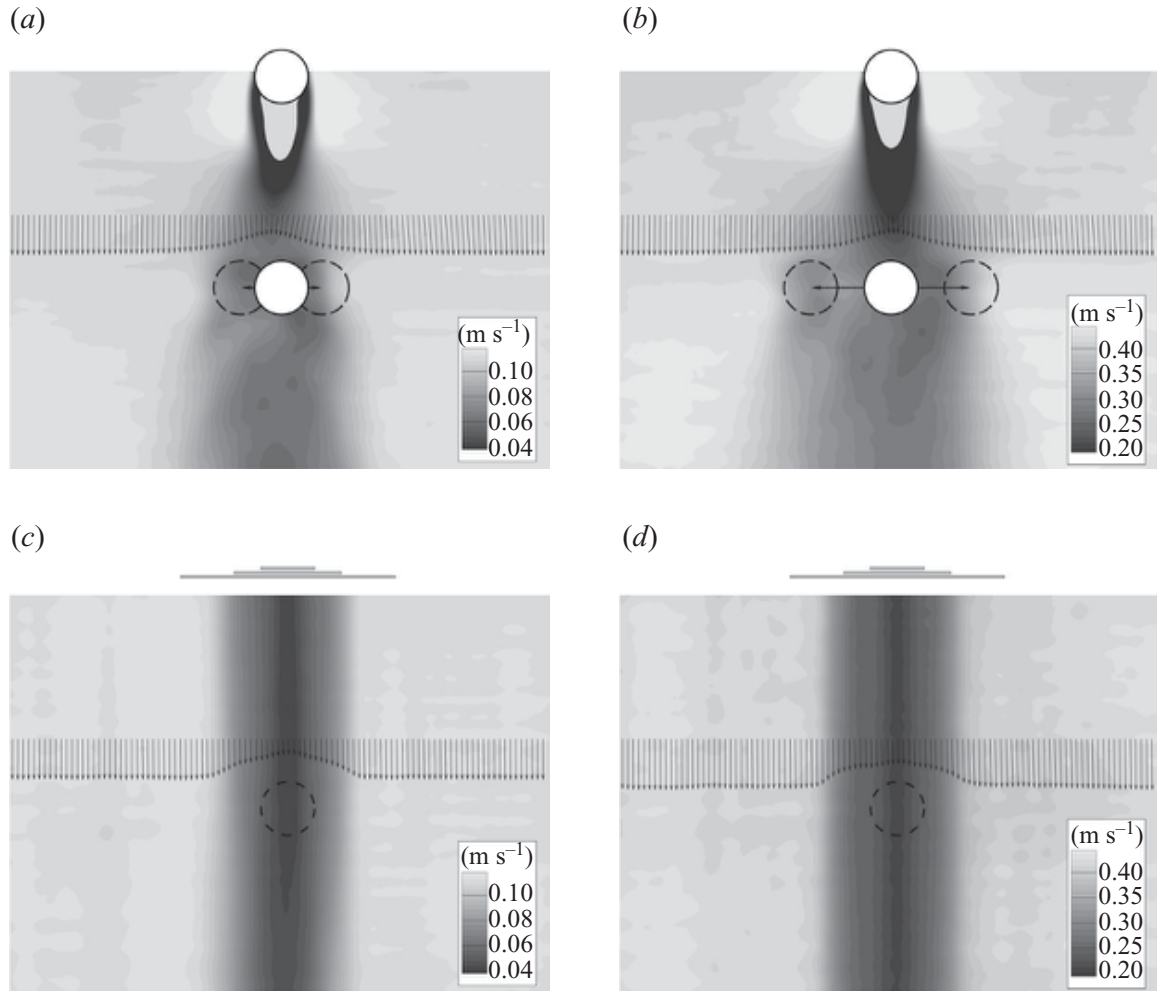


FIGURE 18. Steady flow velocity field (*a, b*) around a pair of cylinders while the downstream cylinder is oscillating under WIV, and (*c, d*) generated by a set of screens ( $Re$  based on the cylinder diameter). Contours of  $\bar{u}$  coloured by velocity magnitude. (*a, c*)  $Re = 4800$ ; (*b, d*)  $Re = 19\,200$ .

The dashed circle represents the position where the cylinder would be placed. The streamwise velocity profile across the wake at  $x_0/D = 3.0$ , represented by an array of vectors plotted across the wake in the gap, was extracted from the PIV flow fields and used to validate the comparison. The result is plotted in figure 19 for the four  $Re$  investigated. The average breadth of the wake and the minimum flow speed on the centreline were the main wake parameters employed to calibrate the screens. Nevertheless, the geometry was optimized to guarantee that the correlation coefficients between corresponding profiles were above  $R = 95\%$ ,

$$R = \frac{1}{n} \sum_{i=1}^n \left( \frac{u_{1i} - \bar{u}_1}{\sigma_{u_1}} \right) \left( \frac{u_{2i} - \bar{u}_2}{\sigma_{u_2}} \right), \quad (6.1)$$

where  $\bar{u}$  and  $\sigma_u$  represent the mean and standard deviation, respectively, of the  $n$  points defining each velocity profile  $u_1$  and  $u_2$ . Figure 19 reveals a reasonably good agreement between reference and generated profiles in spite of the complexity of the set-up designed to achieve these results.

An instantaneous snapshot of the vorticity field plotted in figure 20 reveals that the shear profile generated by the screens does not have the coherent vortices typical of bluff-body vortex shedding. This is even clearer when the instantaneous wake is

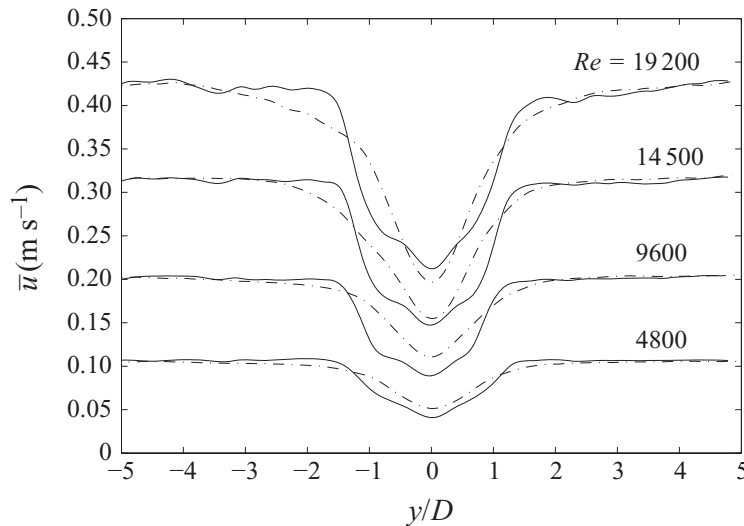


FIGURE 19. Comparison between steady velocity profiles for various flow speeds measured across the wake at  $x_0/D = 3.0$ : —, set of screens; - · -, pair of cylinders.  $R = 98, 97, 97$  and  $96\%$  from the lowest to the highest  $Re$ .

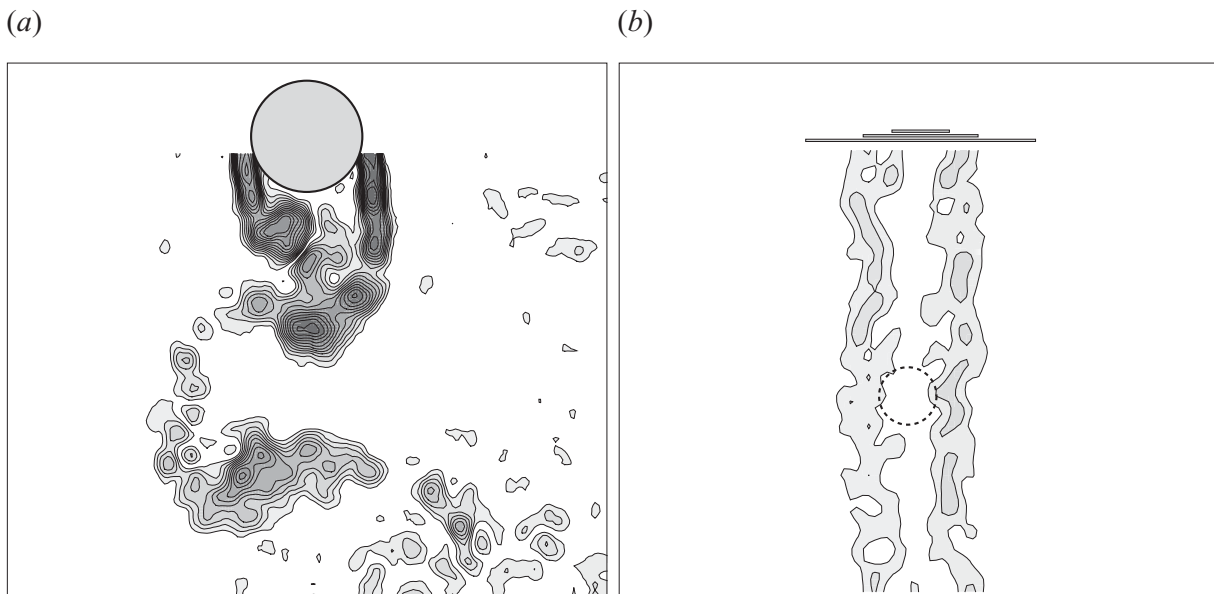


FIGURE 20. Instantaneous vorticity contours of the wake downstream of (a) a single cylinder and (b) a set of screens. Both images have the same contour-colour scale to allow direct comparison.  $Re = 9600$  based on cylinder diameter.

contrasted with the wake of a static-cylinder shedding vortices in the 2S mode. Both vorticity fields in figure 20 have the same contour-colour scale, with dark-grey colour meaning greater vorticity, allowing direct comparison between fully developed wakes. (The position of the screens in figures 18 and 20 is merely illustrative. In reality, the set of screen was positioned at around  $10D$  upstream of the cylinder, as shown in figure 17.)

## 6.2. Steady forces on a static cylinder

We begin by investigating the steady fluid forces acting on a static cylinder as it traverses across the shear flow for various Reynolds numbers. Figure 21(a, c) shows maps of lift and drag that can be compared to the steady-force maps of a pair of staggered cylinders (extracted from figure 13). We immediately see a considerable

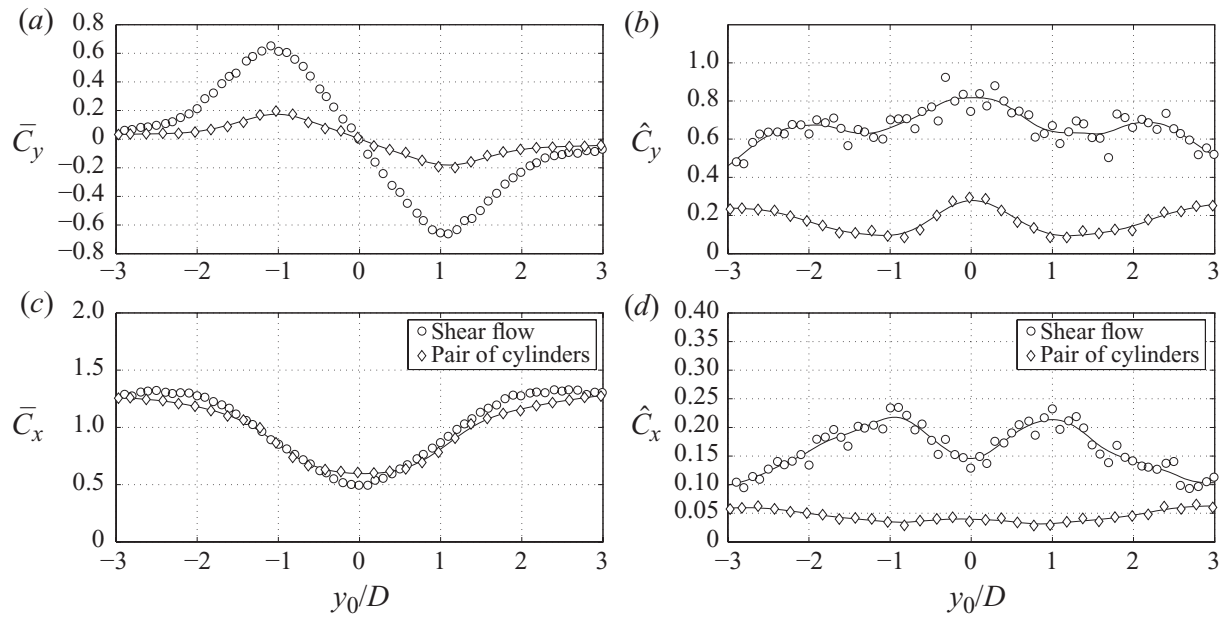


FIGURE 21. Steady (*a, c*) and fluctuating (*b, d*) fluid forces on a static cylinder in shear flow and on the downstream cylinder of a pair with  $x_0/D = 4.0$ .  $Re = 19\,200$ .

difference between the lift curves. While for a pair of cylinders the minimum lift towards the centreline reached  $\bar{C}_y = -0.65$  at around  $y_0/D = 1.0$ , the cylinder immersed in a shear flow only reaches a minimum of  $\bar{C}_y = -0.2$  for the same position. Nevertheless, the similarity in steady drag between the two cases is remarkable. Both reach a minimum around  $\bar{C}_x = 0.5$  on the centreline of the wake with a very similar behaviour as the cylinder is displaced outwards. This correspondence must be related to the fact that the streamwise component in both cases is very similar; therefore, the shielding effect observed in the steady flow field is well reproduced by the screens.

In addition, we also note a remarkable reduction in the fluctuating fluid forces if vortices are not present in the upstream wake. Figure 21(*b, d*) compares  $\hat{C}_y$  and  $\hat{C}_x$  on static cylinders for both experiments. While the fluctuating lift coefficient reaches values around  $\hat{C}_y = 0.8$  for the downstream cylinder of a tandem pair, the maximum fluctuation of lift in the shear flow is only around  $\hat{C}_y = 0.3$ , which is very close to the magnitude of  $\hat{C}_y = 0.35$  due to vortex shedding measured for a single static cylinder. The fluctuation in drag is also affected, with a 10-fold amplification at  $y_0/D = 1.0$  if vortices are present in the upstream wake. Note that for larger separations out of the wake-interference region, the curves for both cases seem to be converging to the value of an isolated cylinder.

This is strong evidence suggesting that vortex interactions from the upstream wake are responsible for the high steady and fluctuating lift on static cylinders in staggered arrangements. Remove the unsteadiness from the wake and the steady lift towards the centreline is considerably reduced, almost disappearing, with the fluctuating term tending towards values measured for a single cylinder.

Previous works tried to attribute the existence of a steady force towards the centreline to the other mechanisms, as summarized by Price (1976), but none of those mechanisms accounted for the total magnitude of  $\bar{C}_y$  on the downstream cylinder. In figure 21(*a, c*), we showed that a residual  $\bar{C}_y = -0.2$  at  $y_0/D = 1.0$  still remains even when vortices are removed from the upstream wake. Of course, not all the unsteady vorticity in the wake could be removed, as seen in the instantaneous flow contours

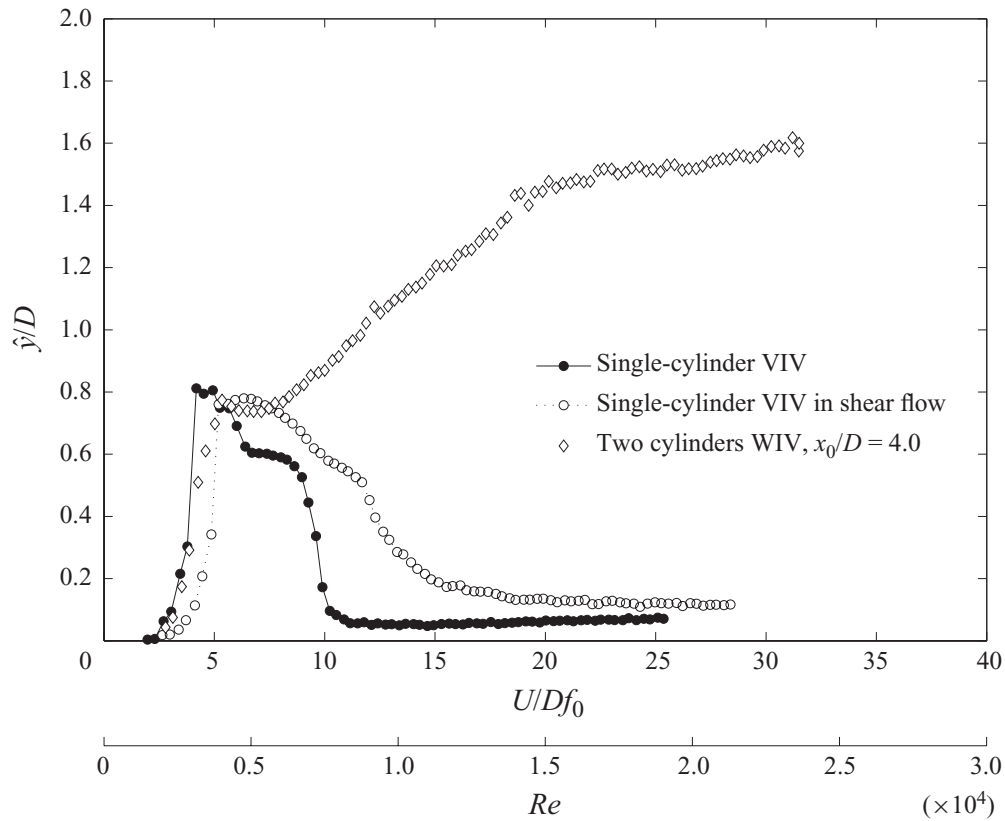


FIGURE 22. Response of the downstream cylinder in shear flow compared with typical VIV and WIV responses.

of figure 20, and the residual  $\overline{C}_y$  towards the centreline may as well be an effect of this weak unsteady vorticity field that still remains. Nonetheless, we were able to show that the presence of vortices is indeed responsible for the high  $\overline{C}_y$  measured for staggered cylinders. In summary, the presence of a steady shear flow contributes to a minimum  $\overline{C}_y = -0.2$ , but only with the presence of unsteady vortices will the total  $\overline{C}_y = -0.65$  be reached – not to mention the effect of unsteady vortices in enhancing the fluctuating term of the fluid force presented in figure 21(b, d). This result combined with the unsteady analysis presented in figure 15 offers a good explanation for the role of vortical structures in enhancing lift on the downstream body.

### 6.3. Response of an elastic cylinder in shear flow

We then placed an elastically mounted cylinder in the shear flow in order to investigate the FIV response. However, the response that built up was completely different from previous WIV results. Figure 22 shows the comparison.

Instead of developing a high-amplitude branch that increases with reduced velocity, the response resembled that of a single cylinder under VIV. A clear resonant peak is observed around  $U/Df_0 = 7$  (note that here  $U$  is the free-stream velocity outside the shear flow), but drops steeply towards a residual level below  $\hat{y}/D = 0.2$  for reduced velocities higher than 15. Even though upper and lower branches are not as clearly distinguishable as for a single-cylinder VIV, a synchronization range is still evident. The response is slightly different from the typical VIV curve, but it is strikingly similar to VIV rather than to the measured WIV curve also plotted in figure 22. In fact, the similarity is so strong that we cannot avoid concluding that the cylinder in shear flow is only responding with a type of VIV modified by the steady shear flow. The



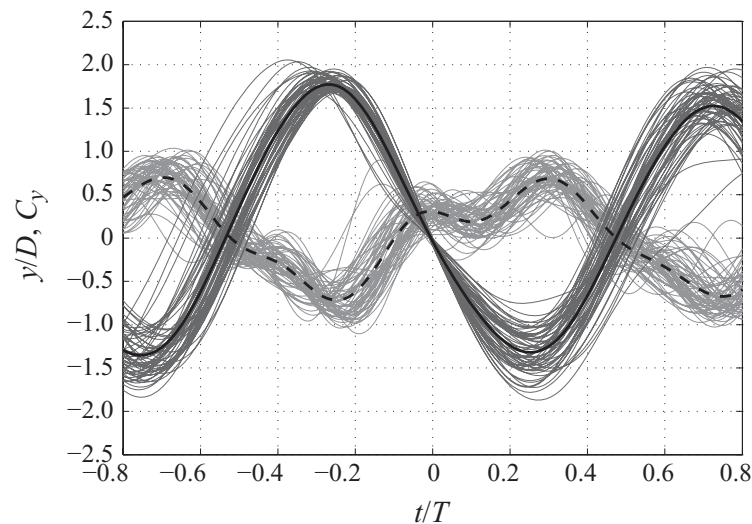


FIGURE 23. Superimposed plots of WIV cycles with similar amplitude;  $y/D$  in dark grey and  $C_y$  in light grey with average cycle in black.  $x_0/D = 4.0$ ,  $U/Df_0 = 25$  and  $Re = 19\,200$ .

fact that the resonance peak is slightly offset towards higher reduced velocities is in agreement with the shielding effect of the steady wake. From the velocity profiles presented before (see figure 19), we note that the deficit in streamwise velocity in the wake is on average around 45 %, resulting in precisely the observed offset from the WIV peak for an isolated cylinder.

Although we have the evidence to show that vortex–structure interaction is important and necessary for the mechanism to be sustained, so far it is still not clear how vortices from the upstream wake interact with the downstream cylinder during oscillation. Hence, we still need to investigate why vortices enhance the steady and fluctuating lift on the downstream cylinder and also how the phase lag is generated.

## 7. Analysis of unsteady lift on an oscillating cylinder

As discussed before, the WIV response is characterized by considerable variations between cycles as far as displacement is concerned (figure 9); an irregular envelope of displacement is more evident in WIV than in a typical VIV. Figure 23 shows another example of the time series of displacement and lift at  $U/Df_0 = 25$ , far from the influence of the VIV regime.

In order to investigate the relation between displacement and fluid force in more detail, we shall plot a collection of several superimposed cycles with similar displacement amplitudes. Figure 23 shows the displacement and lift for 20 % of the total number of cycles recorded at this reduced velocity; once more, the variation in both  $y$  and  $C_y$  is evident. It is also clear that the fluid force signal shows a component of higher frequency apart from the lower frequency that matches the cylinder oscillation frequency. Taken as a whole, it appears that the fluid force is indeed out of phase with the displacement; however, if we look carefully at the multitude of light-grey lines crossing  $C_y = 0$  in figure 23, we will note that the lift force anticipates the displacement practically in all cycles. In fact, if we estimate  $\phi$  based on the average cycles given by the black lines, we conclude that the displacement lags the lift by a phase angle which is rather close to the average value of  $\phi = 161^\circ$ , calculated as an average of all points represented in the curve ‘ $\phi$  (Hilbert)’ in figure 11.

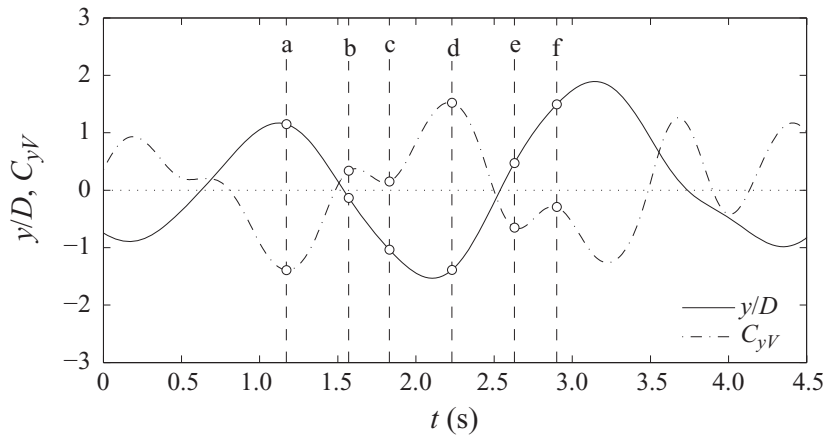


FIGURE 24. Time series of displacement and vortex-force component of lift on the downstream cylinder under WIV.  $x_0/D = 4.0$ ,  $U/Df_0 = 25$  and  $Re = 19\,200$ .

In fact, if we start from (3.1) and take all other variables from the results presented above, we conclude that for such very low values of mass and damping ( $m^*\zeta = 0.018$ ) a minute phase lag of  $\phi = 179.4$  would be enough to excite the system with  $\hat{y}/D = 1.5$  at  $U/Df_0 = 25$ . This is the curve ' $\phi$  (Eq.)' in figure 11. However, if we employ the same harmonic hypothesis for the actual  $\phi = 161^\circ$  averaged from the Hilbert transform (curve ' $\phi$  (Hilbert)' in figure 11), we conclude that the amplitude of oscillation would reach the unrealistic value of  $\hat{y}/D = 45$ . Hence, we conclude that a simple 'harmonic forcing and harmonic motion' hypothesis does not apply to the WIV mechanism. Rather, a more complex modelling that considers multiple frequencies present in the wake should be developed.

Turning again to figure 23, it appears that the phase lag is accentuated by the existence of the higher frequency present in the lift signal. Since  $f_s$  from the upstream cylinder is increasing with flow speed as  $St = 0.2$  and the oscillation frequency of the downstream cylinder is increasing at a different rate, the relationship between both frequencies is also changing. Essentially, this higher frequency must be associated with the vortex-shedding frequency of the upstream wake – at least this is observed for static cylinders – but one cannot tell how repeatable this forcing is as the downstream cylinder oscillates and interacts with upstream vortices.

The only conclusion we can draw is that with such an irregular forcing it is most likely that the fluid force will not be perfectly in phase (or out of phase) with the displacement, especially as the cylinder crosses the centreline of the wake where strong vortices are present. Therefore, the phase lag must be coming from the unsteadiness of the wake, i.e. from the vortex–structure interaction, as we have been arguing so far.

### 7.1. Unsteady vortex-structure interaction

As in the investigation presented for a static cylinder in a staggered arrangement of  $y_0/D = 1.0$ , we can analyse the wake configuration that generates the corresponding lift trace for a cylinder undergoing WIV. Figure 24 shows a short sample from the time series presented in figure 23 for which the flow fields were captured with PIV. Note that the  $C_{y_v}$  component of lift only accounts for the force generated by the vorticity in the wake. Vorticity contours and velocity fields for six instants 'a' to 'f' are shown in figures 25(a, a') to 25(f, f').

Frame 'a' was taken with the cylinder very close to maximum displacement when lift was the strongest towards the centreline. Like the wake configuration observed

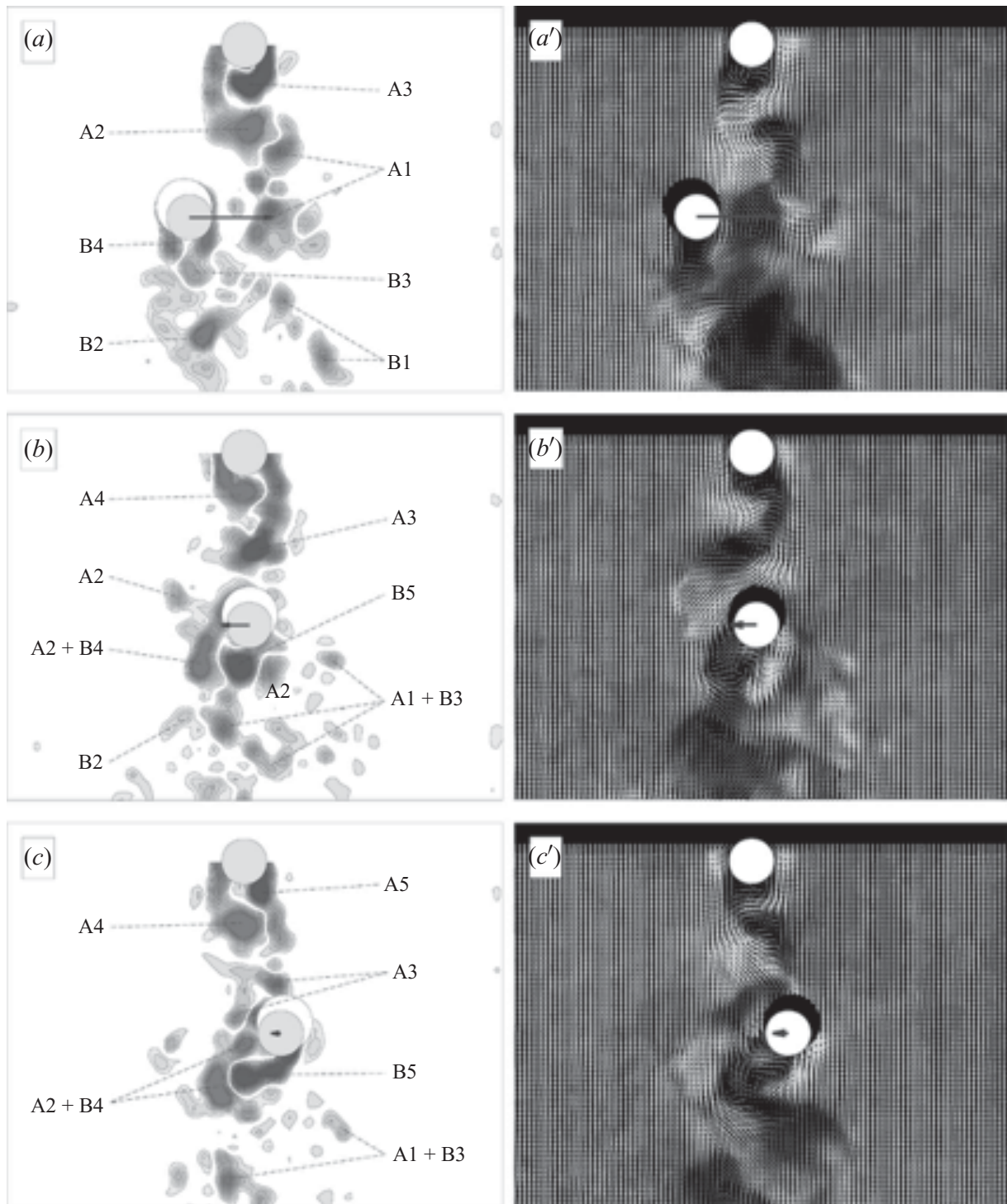


FIGURE 25(*a, a', b, b', c, c'*). For caption see facing page.

for static cylinders, we find vortex A2 inducing high-speed flow close to the inner side of the cylinder, while A1 induces vortex B3 to form closer to the cylinder surface. However, as the cylinder accelerates towards the centreline, B3 is suddenly released and a new vortex B5 forms in its place. In figure 24, we see that the lift force changes its direction slightly before the cylinder crosses the centreline. In frame 'b', we see that vortex A2 impinges on the downstream cylinder, splitting into two parts around the body as it crosses the centreline: one part will merge with B4 and the other part will join B5 in the downstream wake. At the same time, we see that A3 coming from the upstream cylinder induces a high-speed flow that is contrary to the motion of



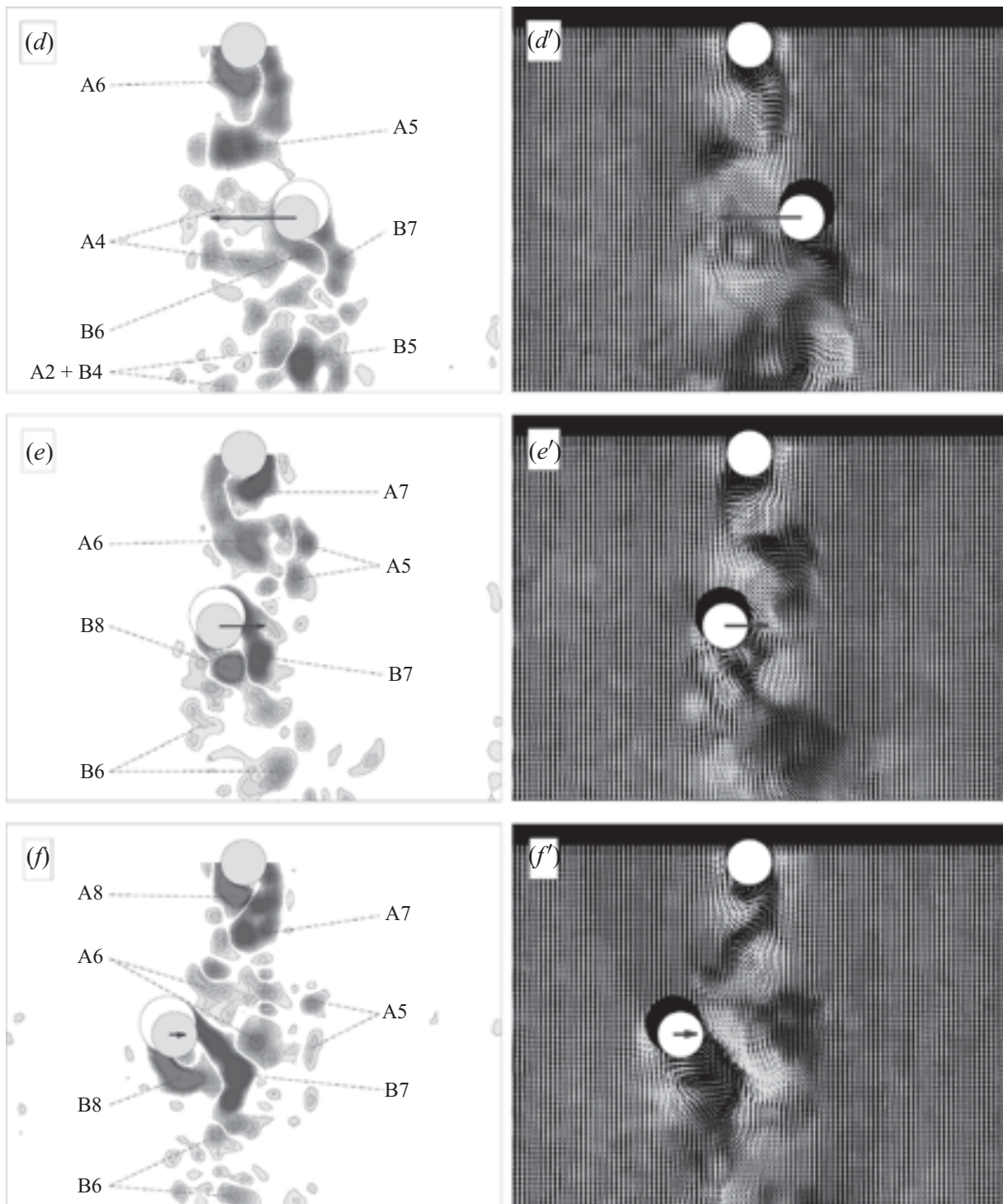


FIGURE 25(*d, d', e, e', f, f'*). (*a, b, c, d, e, f*) Instantaneous vorticity contours and (*a', b', c', d', e', f'*) velocity field (coloured by velocity magnitude) obtained with PIV around a pair of cylinder under WIV. Horizontal arrows represent the lift acting on the cylinder (see figure 24).  $x_0/D = 4.0$ ,  $U/Df_0 = 25$  and  $Re = 19\,200$ .

the downstream cylinder. This strong interaction is responsible for the local peak in the lift curve in figure 24. A moment later, in frame 'c', vortex A3 is splitting around the downstream cylinder and inducing A2+B4 away from the body, while a strong B5 rolls up on the other side resulting in an almost zero lift as the cylinder decelerates towards the minimum peak of response.

The process is repeated for the other half of the cycle as the cylinder crosses the wake in the opposite direction. Frame 'd' shows that maximum lift towards the centreline occurs when vortex A5 induces high-speed flow on the inner side of the body, while A4 induces B6 to form closer to the cylinder. Note that maximum lift was not registered for the lowermost displacement, but when the cylinder encountered that particular wake configuration on its way towards the centreline. Again, the lift reversal happened slightly before the cylinder crossed the centreline. Similarly, another local peak of lift shown in frame 'e' is caused by the impingement of vortex A5; it splits around the cylinder merging with B7 on the inner side and with B8 on the outer side. Almost zero lift is obtained in frame 'f' when the cylinder experiences the same wake interaction as in 'c', though in the opposite direction.

We chose to analyse this portion of the time series because the lift force in the first half of the cycle is mirrored in the second half, giving more of an opportunity to understand the wake–structure interaction taking place. However, we note that the peak of amplitude in frame 'a' is different from the peak that the cylinder will reach just after frame 'f'. This reveals that the response of the body is very dependent on the configuration of the wake it encounters for each cycle. With the crossing velocity  $\dot{y}$  changing for each cycle, the vortex–structure interaction will also be different, resulting in different responses. In fact, if we look again at the short time series presented in figure 24, we will note that the lift signal for the previous cycle between  $t = 0$  and 1.0 s is different from the cycle that we investigated between  $t = 1.1$  and 3.1 s, and also different from the next cycle after  $t = 3.1$  s. Even the phase lag varies from cycle to cycle. At  $t = 0.7$  s, the opposite is also observed and now it is the displacement that anticipates the fluid force. This variation between successive cycles imposes on the system the irregularity in response observed in the displacement and lift envelopes. But the fact that the phase lag will rarely be equal to zero also guarantees that energy will be transferred from the fluid to the structure sustaining WIV, albeit in irregular amounts from cycle to cycle.

## 8. Conclusion

Up to now, the wake-displacement mechanism proposed by Zdravkovich (1977) seemed to be the most plausible explanation for the WIV phenomenon, even though he could not conclude how the wake was being 'displaced' to generate the necessary phase lag to sustain the vibrations. In this paper, we have shown that WIV is indeed a wake-dependent type of FIV. Yet we found that it is the unsteadiness of the wake that plays the main role in the WIV process and not simply the displacement of a steady flow field.

We suggest that the WIV mechanism is sustained by unsteady vortex–structure interactions that input energy into the system as the downstream cylinder oscillates across the wake.

We have verified that WIV is not a resonant phenomenon. While VIV finds its maximum amplitude of vibration at  $f_s = f_0$ , WIV keeps increasing  $\hat{y}/D$  even when  $f_s$  is much higher than  $f_0$ . In the shear-flow experiment, we removed the upstream shedding frequency from the system, leaving only  $f_s$ , which is generated by the downstream cylinder. As a result, the oscillations returned to a typical VIV response, meaning that the upstream frequency – or the upstream vortex shedding – was somehow important to sustain the excitation. Hence, WIV is essentially a type of vortex-induced mechanism, in the sense that it requires the interaction of the structure with vortices, even though these vortices are coming from an upstream wake.

Energy input from the fluid to the structure will only occur when there is a phase lag greater than  $\phi = 0^\circ$  or less than  $180^\circ$  between the fluid force and displacement. Coherent vortices impinging on the downstream cylinder and merging with its own vortices induce fluctuations in lift that are not synchronized with the motion. Strong vortices from the upstream wake induce considerable changes in the lift force. The shear-flow experiment proved that a steady shear flow without vortices cannot excite a cylinder into WIV. Remove the unsteady vortices from the wake and WIV will not be excited.

The characteristic response of the downstream cylinder is consistent with the arguments presented above. Irregular envelopes of the displacement and lift indicate that the downstream cylinder encounters different wake configurations from cycle to cycle. As the second cylinder is moved farther downstream, vortices coming from the upstream wake have more time to diffuse and the resulting vortex–structure interaction is weakened. This is in agreement with the response curves presented for separations up to  $x_0/D = 20.0$  and also agrees with the fact that the lift force (both steady and fluctuating terms) also diminishes with increasing  $x_0$ . The flow's three-dimensionality is also likely to increase with  $x_0$  and contribute to reducing the response.

We have shown that WIV had been referred to as a type of galloping mostly because the typical response presents a build-up of amplitude for higher reduced velocities. We argue that quasi-steady assumptions, commonly employed in classical galloping theory, would not fit the WIV phenomenon, as we now understand it. For that reason, we have been insisting on a dissociation of WIV from the classical galloping idea. When Bokaian & Geoola (1984) call this mechanism 'wake-induced galloping' they are correct in the sense that it is a 1-d.o.f. fluid-elastic mechanism generated by the interference of the upstream wake. However, we do not agree that the excitation mechanism is similar to that of classical galloping of non-circular bluff bodies.

The authors are grateful for the interesting comments made by one of the referees. G.R.S.A. wishes to thank CAPES, Brazilian Ministry of Education, for his PhD scholarship. J.R.M. thankfully acknowledges Finep-CTPetro/Petrobras, CNPq and Fapesp for financial support. Support from EPSRC is also gratefully acknowledged.

## REFERENCES

- ALAM, M. M., MORIYA, M., TAKAI, K. & SAKAMOTO, H. 2003 Fluctuating fluid forces acting on two circular cylinders in tandem arrangement at a subcritical Reynolds number. *J. Wind Engng Ind. Aerodyn.* **91**, 139–154.
- ASSI, G. R. S. 2005 Experimental study of the flow interference effect around aligned cylinders. Master's thesis, University of São Paulo, São Paulo, Brazil (in Portuguese). Available at: [www.ndf.poli.usp.br/~gassi](http://www.ndf.poli.usp.br/~gassi).
- ASSI, G. R. S. 2009 Mechanisms for flow-induced vibration of interfering bluff bodies. PhD thesis, Imperial College London, London, UK. Available at: [www.ndf.poli.usp.br/~gassi](http://www.ndf.poli.usp.br/~gassi).
- ASSI, G. R. S., MENEGHINI, J. R., ARANHA, J. A. P., BEARMAN, P. W. & CASAPRIMA, E. 2006 Experimental investigation of flow-induced vibration interference between two circular cylinders. *J. Fluids Struct.* **22**, 819–827.
- BEARMAN, P. W. 1984 Vortex shedding from oscillating bluff bodies. *Annu. Rev. Fluid Mech.* **16**, 195–222.
- BEST, M. S. & COOK, N. J. 1967 The forces on a circular cylinder in a shear flow. *Tech. Rep.* 103. Aeronautical Engineering Department, University of Bristol.
- BLEVINS, R. D. 1990 *Flow-Induced Vibration*, 2nd edn. Van Nostrand Reinhold.



- BOKAIAN, A. & GEOOLA, F. 1984 Wake-induced galloping of two interfering circular cylinders. *J. Fluid Mech.* **146**, 383–415.
- BRANKOVIC, M. 2004 Vortex-induced vibration attenuation of circular cylinders with low mass and damping. PhD thesis, Imperial College, London, UK.
- BRIKA, D. & LANEVILLE, A. 1999 The flow interaction between a stationary cylinder and a downstream flexible cylinder. *J. Fluids Struct.* **13**, 579–606.
- CARMO, B. S., MENEGHINI, J. R. & SHERWIN, S. J. 2010a Possible states in the flow around two circular cylinders in tandem with separations in the vicinity of the drag inversion spacing. *Phys. Fluids* **22**, 054101.
- CARMO, B. S., MENEGHINI, J. R. & SHERWIN, S. J. 2010b Secondary instabilities in the flow around two circular cylinders in tandem. *J. Fluid Mech.* **644**, 395–431.
- CHEN, S. S. 1986 A review of flow-induced vibration of two circular cylinders in crossflow. *J. Pressure Vessel Tech.* **108**, 382–393.
- GRANGER, S. & PAIDOUSSIS, M. P. 1996 An improvement to the quasi-steady model with application to cross-flow-induced vibration of tube arrays. *J. Fluid Mech.* **320**, 163–184.
- HAHN, S. L. 1996 *Hilbert Transforms in Signal Processing*. Artech House.
- DEN HARTOG, J. P. 1956 *Mechanical Vibrations*, 4th edn. McGraw-Hill.
- HOVER, F. S. & TRIANTAFYLLOU, M. S. 2001 Galloping response of a cylinder with upstream wake interference. *J. Fluids Struct.* **15**, 503–512.
- IGARASHI, T. 1981 Characteristics of the flow around two circular cylinders arranged in tandem. *Bull. JSME – Japan Soc. Mech. Engng* **24**, 323–331.
- JESTER, W. & KALLINDERIS, Y. 2003 Numerical study of incompressible flow about fixed cylinder pairs. *J. Fluids Struct.* **17**, 561–577.
- KHALAK, A. & WILLIAMSON, C. H. K. 1997 Investigation of relative effects of mass and damping in vortex-induced vibration of a circular cylinder. *J. Wind Engng. Ind. Aerodyn.* **69–71**, 341–350.
- KHALAK, A. & WILLIAMSON, C. H. K. 1999 Motions, forces and mode transitions in vortex-induced vibrations at low mass-damping. *J. Fluids Struct.* **13**, 813–851.
- KING, R. & JOHNS, D. J. 1976 Wake interaction experiments with two flexible circular cylinders in flowing water. *J. Sound Vib.* **45**, 259–283.
- LIN, J. C., TOWFIGHI, J. & ROCKWELL, D. 1995 Instantaneous structure of the near-wake of a circular cylinder: on the effect of Reynolds number. *J. Fluids Struct.* **9**, 409–418.
- LIN, J. C., YANG, Y. & ROCKWELL, D. 2002 Flow past two cylinders in tandem: instantaneous and average flow structure. *J. Fluids Struct.* **16**, 1059–1071.
- LIU, C. H. & CHEN, J. M. 2002 Observations of hysteresis in flow around two square cylinders in a tandem arrangement. *J. Wind Engng Ind. Aerodyn.* **90**, 1019–1050.
- LJUNGKRONA, L., NORBERG, C. & SUNDEN, B. 1991 Free-stream turbulence and tube spacing effects on surface pressure fluctuations for two tubes in an in-line arrangement. *J. Fluids Struct.* **5**, 701–727.
- MAEKAWA, T. 1964 Study on wind pressure against ACSR double conductor. *Electr. Engng Japan* **84**, 21–28.
- MAIR, W. A. & MAULL, D. J. 1971 Aerodynamic behaviour of bodies in the wakes of other bodies. *Phil. Trans. R. Soc. A* **269**, 425–437.
- NORBERG, C. 1998 LDV-measurements in the near wake of a circular cylinder. In *Advances in Understanding of Bluff Body Wakes and Flow-Induced Vibration* (ed. C. H. K. Williamson & P. W. Bearman), pp. 1–12. ASME.
- NORBERG, C. & SUNDEN, B. 1987 Turbulence and Reynolds number effects on the flow and fluid forces on a single tube in cross-flow. *J. Fluids Struct.* **1**, 337–357.
- PAIDOUSSIS, M. P., MAVRIPLIS, D. & PRICE, S. J. 1984 A potential-flow theory for the dynamics of cylinder arrays in cross-flow. *J. Fluid Mech.* **146**, 227–252.
- PAIDOUSSIS, M. P. & PRICE, S. J. 1988 The mechanisms underlying flow-induced instabilities of cylinder arrays in crossflow. *J. Fluid Mech.* **187**, 45–59.
- PAPAIIOANNOU, G., YUE, D. K. P., TRIANTAFYLLOU, M. S. & KARNIADAKIS, G. E. 2006 Three-dimensionality effects in flow around two tandem cylinders. *J. Fluid Mech.* **558**, 387–413.
- PARKINSON, G. V. 1971 Wind-induced instability of structures. *Phil. Trans. R. Soc. Lond.* **269**, 395–413.
- PARKINSON, G. V. 1989 Phenomena and modelling of flow-induced vibrations of bluff bodies. *Prog. Aerosp. Sci.* **26**, 169–224.

- PRICE, S. J. 1976 The origin and nature of the lift force on the leeward of two bluff bodies. *Aeronaut. Q.* **26**, 1154–1168.
- PRICE, S. J. 1984 An improved mathematical model for the stability of cylinder rows subject to cross-flow. *J. Sound Vib.* **97**, 615–640.
- SARPKAYA, T. 1979 Vortex-induced oscillations: a selective review. *J. Appl. Mech.* **46**, 241–258.
- SARPKAYA, T. 2004 A critical review of the intrinsic nature of vortex-induced vibrations. *J. Fluids Struct.* **19**, 389–447.
- SUMNER, D., PRICE, S. J. & PAIDOUSSIS, M. P. 2000 Flow-pattern identification for two staggered circular cylinders in cross-flow. *J. Fluid Mech.* **411**, 263–303.
- WARDLAW, R. L. & WATTS, J. A. 1974 Wind-tunnel and analytical investigations into the aeroelastic behaviour of bundled conductors. In *IEEE Power Engineering Society Summer Meeting*, Anaheim, CA.
- WILLIAMSON, C. H. K. & GOVARDHAN, R. 2004 Vortex-induced vibrations. *Annu. Rev. Fluid Mech.* **36**, 413–455.
- ZDRAVKOVICH, M. M. 1974 Flow-induced vibrations of two cylinders in tandem and their suppression. In *International Symposium of Flow Induced Structural Vibrations* (ed. E. Naudascher), pp. 631–639. Springer, Berlin.
- ZDRAVKOVICH, M. M. 1977 Review of flow interference between two circular cylinders in various arrangements. *J. Fluids Engng* pp. 618–633.
- ZDRAVKOVICH, M. M. 1985 Flow induced oscillations of two interfering circular cylinders. *J. Sound Vib.* **101**, 511–521.
- ZDRAVKOVICH, M. M. 1986 Discussion: effect of vibrating upstream cylinder of two circular cylinders in tandem arrangement. *J. Fluids Engng* **108** (3), 383–384.
- ZDRAVKOVICH, M. M. 1988 Review of interference-induced oscillations in flow past two circular cylinders in various arrangements. *J. Wind Engng Ind. Aerodyn.* **28**, 183–200.
- ZDRAVKOVICH, M. M. & MEDEIROS, E. B. 1991 Effect of damping on interference-induced oscillations of two identical circular cylinders. *J. Wind Engng Ind. Aerodyn.* **38**, 197–211.

# Suppression of wake-induced vibration of tandem cylinders with free-to-rotate control plates

G.R.S. Assi<sup>a,\*</sup>, P.W. Bearman<sup>a</sup>, N. Kitney<sup>b</sup>, M.A. Tognarelli<sup>c</sup>

<sup>a</sup>*Department of Aeronautics, Imperial College, London, UK*

<sup>b</sup>*BP Exploration Operating Company Ltd., Sunbury-on-Thames, UK*

<sup>c</sup>*BP America Production Company, Houston, USA*

Received 14 December 2009; accepted 21 August 2010

Available online 20 October 2010

---

## Abstract

Experiments have been carried out on a pair of circular cylinders to investigate the effectiveness of pivoting parallel plates as wake-induced vibration suppressors. Measurements of amplitude of vibration and average drag are presented for a circular cylinder, free to respond in the cross-flow direction, with mass ratio 2 and a damping level of 0.7% of critical damping. Reduced velocities were up to nearly 30, with associated Reynolds numbers up to  $2.3 \times 10^4$  and the results presented are for a centre-to-centre separation of cylinders of 4 diameters. It is shown how vortex-induced vibration and wake-induced vibration of the downstream cylinder of a tandem pair can be practically eliminated by using free to rotate parallel plates. The device achieves vibration suppression with a substantial drag reduction when compared to a pair of fixed tandem cylinders at the same Reynolds number. Results for a single splitter plate and helical strakes are also presented for comparison and were found not to be effective in suppressing wake-induced vibration. © 2010 Elsevier Ltd. All rights reserved.

**Keywords:** Flow-induced vibration; Suppression; Drag reduction; Parallel plates; Helical strakes; Tandem circular cylinders

---

## 1. Introduction

The response of an elastically mounted single cylinder under vortex-induced vibration (VIV) is well known and has been reviewed in detail by Sarpkaya (1979, 2004), Bearman (1984) and Williamson and Govardhan (2004), to cite only a few. However, an additional phenomenon appears when an elastically mounted cylinder is immersed in the wake of another identical cylinder placed upstream. The response of the cylinder with flow interference is very different from the typical one observed for VIV. The wake generated by the upstream body interacts with the flow around the downstream cylinder generating fluid forces that excite the structure into even higher amplitudes of vibration. This fluid-elastic mechanism, known as *wake-induced vibration* (WIV), occurs whenever one or more cylinders are immersed in the interference region of a bluff body wake.

Recently, the main motivation for studying this phenomenon is found in the offshore oil industry. A single floating platform is able to accommodate a number of production risers in complex arrangements together with many other

---

\*Corresponding author. Now at: Department of Naval Architecture and Ocean Engineering, POLI, University of São Paulo, São Paulo - SP, 05508-900, Brazil. Tel.: +55 11 30915646; fax: +55 11 30915642.

E-mail address: [g.assi@usp.br](mailto:g.assi@usp.br) (G.R.S. Assi).

cylindrical structures. Long drilling risers also suffer wake-interference from other structures attached to floating platforms. As the ocean current changes its direction through the sea depth it becomes practically impossible to avoid flexible structures from falling in the wakes of each other. This results in the probability of pipes developing severe WIV and increases the risk of damage due to structural fatigue as well as clashing.

Attempts to understand flow-induced vibration with flow interference are found in the literature. Blevins (1990) explains how a cylinder free to respond in two degrees of freedom (2-dof) can be excited into wake flutter when it is placed downstream of a fixed cylinder but laterally displaced from the centreline of the wake (the so called staggered arrangement). He shows how the mean velocity profile can input energy into the system as the cylinder oscillates in an elliptical orbit. When the gap between the cylinder is in the order of a few diameters Zdravkovich (1977) proposes another mechanism, called gap-flow-switching, which is able to excite cylinders in close proximity. If the separation between the cylinders is smaller than a critical value – which varies with turbulence and Reynolds number (Zdravkovich and Pridden, 1977) – the shear layers from the first cylinder may reattach on the second body and a vortex wake may not develop in the gap. However, in the present work we are particularly interested in studying a type of WIV that is different from the two mechanisms described above. We will focus on WIV that occurs when a pair of circular cylinders is initially aligned with the direction of the flow (Fig. 1) with enough space between them for a vortex wake to develop in the gap. In this arrangement the vortices from the front cylinder impinging on the second cylinder play a significant role in causing the rear cylinder to vibrate.

Most of the related works found in the literature present data for the response of flexible cylinders in various tandem and staggered configurations (King and Johns, 1976; Laneville and Brika, 1999). Bokaian and Geoola (1984), Hover and Triantafyllou (2001) and Assi et al. (2006), on the other hand, present studies of the cross-flow response of a flexibly mounted, rigid downstream cylinder in a tandem arrangement. While Bokaian and Geoola (1984) relate the dependency of WIV on structural parameters such as mass and damping, very few works investigate the fluid mechanism causing the excitation. A better understanding of the physical mechanism behind WIV has emerged from our recent study of tandem cylinders (Assi et al., 2010; Assi, 2009); the main findings being that the excitation of the downstream body is sustained by the unsteady force fluctuations caused by the vortices shed from the upstream body interacting with the shedding from the downstream one.

We believe that only with a clear phenomenological understanding of the nature of the excitation will be possible to start the development of suppressors that effectively reduce WIV. In this context, we present an experimental study that is aimed at developing more efficient suppressors for cylinders in tandem arrangements under flow interference.

### 1.1. Suppression of VIV with control plates

A widely used method for suppressing VIV of long slender bodies of circular cross-section is the attachment of helical strakes. Developed originally in the wind engineering field, strakes suffer from two major problems: the first being that they increase drag and the second that, for a given strake height, their effectiveness reduces with decrease in the response parameter  $m^*\zeta$  (where  $m^*$  is the ratio of structural mass to the mass of displaced fluid and  $\zeta$  is the structural damping expressed as a fraction of critical damping). Whereas a strake height of 10% of cylinder diameter is usually sufficient to suppress VIV in air, at least double this amount is often required in water, and this increase in height is accompanied by a corresponding further increase in drag. For a fixed cylinder it is known that if regular vortex shedding is eliminated, say by

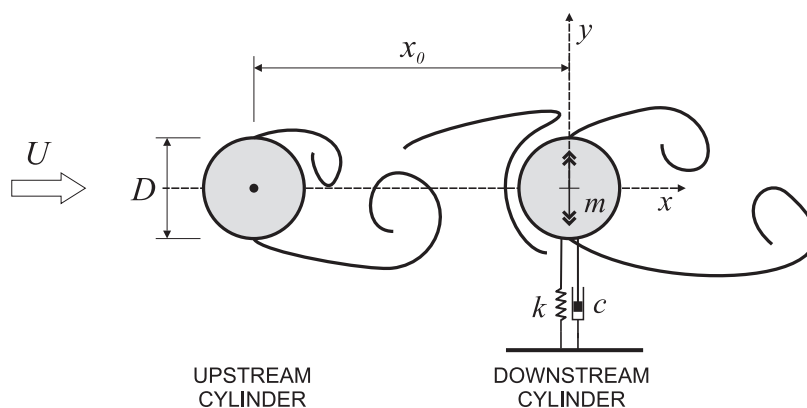


Fig. 1. Representation of two circular cylinders aligned in the flow direction (tandem arrangement). Upstream cylinder is fixed and the downstream one is free to oscillate in the cross-flow direction ( $y$ -axis).



the use of a long splitter plate, then drag is reduced. Hence in theory an effective VIV suppression device should be able to reduce drag rather than increase it. This idea underlies the work presented in this paper.

According to Bearman (1984), for example, a simple analysis for a linear oscillator model of VIV, assuming harmonic forcing and harmonic motion, shows that response is inversely proportional to the product of  $m^*$  and  $\zeta$ . Hence the most rigorous way to test the effectiveness of a VIV suppression device is to work at low mass and damping. In the experiments to be described in this paper the parameter  $m^*\zeta$  was equal to 0.014. As concluded by Assi et al. (2009), it seems that three-dimensional solutions like strakes or bumps are unlikely to provide the required combination of VIV suppression and low drag.

In previous works (Assi and Bearman, 2008; Assi et al., 2009) we have investigated the efficiency of pivoting control plates as VIV suppressors for a single cylinder. We concluded that suppression of cross-flow and in-line vibration of a circular cylinder, with resulting drag coefficients less than that for a fixed plain cylinder, is achievable using two-dimensional control plates. This has been accomplished at values of the combined mass and damping parameter down to at least 0.014, showing that the method has potential applications in the offshore industry, for example. The lowest drag coefficient of  $\overline{C}_x = 0.63$ , equivalent to a drag reduction of about 38% interference to a static cylinder, occurred when free-to-rotate (f-t-r) parallel plates were installed on the cylinder. A f-t-r splitter plate was also found to suppress VIV but the plate adopted a mean deflection angle and this configuration developed a mean transverse force towards the side to which the plate had deflected. This force could be eliminated by using a pair of splitter plates arranged so that the shear layers that spring from the cylinder attach to the tips of the plates. Because the parallel plates were found to be the most drag-efficient device to suppress VIV it became the focus of the present investigation.

In Assi et al. (2009) we have highlighted the importance of torsional resistance in stabilising f-t-r suppressors. Torsional friction “needs to be high enough to hold the devices in a stable position, while still allowing them to realign if the flow direction changes. Devices with torsional friction below a critical value oscillate themselves as the cylinder vibrates, sometimes increasing the amplitude of cylinder oscillation higher than that for a plain cylinder.” In the present work we kept the same parameters employed in that study to guarantee that our suppressor is working above the critical value of torsional resistance.

## 1.2. WIV suppression of a pair of cylinders

Very few works investigated suppression of flow-induced vibration for bluff bodies with interference. Zdravkovich (1974), whose study is probably the closest to the present one, presents a wind tunnel investigation of WIV suppression employing an axial-rod shroud. His level of  $m^*\zeta$  was rather high, but the shrouds showed some effect in reducing WIV of the second cylinder. It is interesting to note that the most effective suppression was achieved when both cylinders were fitted with shrouds. This is evidence that the current understanding of the excitation mechanism, discussed in Assi et al. (2010), is satisfactory. It is important to disrupt the coherent vortices coming from the upstream cylinder so as to reduce the interaction with the downstream body. This is exactly what the shrouds accomplished in his experiments.

But it was in another paper that Zdravkovich (1988) brought further insight about VIV suppressors being used in WIV. He wrote: “A wide variety of means for suppressing the vortex-shedding-induced oscillations [VIV] has been developed in the past. These means might not only be ineffective for the interference-induced oscillations [WIV] but even detrimental.” To cite an example, Korkischko et al. (2007) showed that helical strakes typically effective in reducing VIV for an isolated cylinder are no longer successful if the body is immersed in the wake interference region.

Building up understanding from previous research we set out to explore new solutions that not only are successful in suppressing VIV but also act on the vortex-structure interaction that drives WIV. It was not our intention to perform a parametric study of all geometric and structural properties of potential suppressors, but rather to verify if a family of solutions proven to be effective in suppressing VIV is a potential candidate for suppressing WIV. In addition, one of our objectives is to find an effective WIV suppressor that is functional and does not incur a drag penalty, preferably it should reduce drag.

## 2. Experimental arrangement

Experiments were conducted in the Hydrodynamics Laboratory of the Department of Aeronautics at Imperial College London. Tests were carried out in a recirculating water channel with a free surface and a test-section 0.6 m wide, 0.7 m deep and 8.0 m long. The sidewalls and bottom of the section were made of glass, allowing a complete view of the models for flow visualisation purposes. The free stream flow speed ( $U$ ) was continuously variable and flow with turbulence intensity less than 3% could be obtained up to at least 0.6 m/s. The circular cylinder models were constructed from 50 mm diameter perspex tube, giving a maximum Reynolds number of approximately 30 000 (based on cylinder

diameter  $D$  and  $U$  incident on the upstream cylinder). The models were mounted vertically and passed through the free water surface down to almost the full depth of the section. The downstream cylinder was mounted such that there was a 2 mm gap between the lower end of the cylinder and the glass floor of the test section. With a wet-length of 650 mm (total length below water level) the resulting aspect ratio of the model was 13.

### 2.1. Elastic rig and cylinder models

The upstream cylinder was rigidly attached to the structure of the channel preventing displacements in any direction, while the downstream cylinder was fixed at its upper end to an elastic mounting. Fig. 2 shows a schematic representation of the apparatus and helps in describing the operation of the system. The support system is firmly installed on the channel structure and the sliding cylindrical guides are free to move in the transverse direction, defined by the  $y$ -axis. A load cell connects the moving parts of the base to the top end of the model and is able to measure instantaneous fluid forces acting on the cylinder in the cross-flow and streamwise directions.

A pair of coil springs connecting the moving base to the fixed supports provides the restoration force for the system, setting the natural frequency of oscillation ( $f_0$ ). All the moving parts of the elastic base contribute to the effective mass, resulting in a mass ratio of  $m^* = 2.0$  defined as the ratio of the total oscillating mass to the mass of displaced fluid. An optical positioning sensor was installed to measure the  $y$ -displacement of the cylinder without introducing extra friction to damp the oscillations. Thus, the cylinder is free to oscillate only in the  $y$ -direction with a very low structural damping  $\zeta = 0.7\%$  (calculated as the percentage of the critical damping obtained from free decay oscillations performed in air) giving a value of the product of mass ratio and damping of only  $m^*\zeta = 0.014$ . Measurements were made using one set of springs and the reduced velocity range covered was from 1.5 to 30, where reduced velocity ( $U/Df_0$ ) is defined using the cylinder natural frequency  $f_0$  measured in air. As shown in Fig. 1, the cylinders are aligned one behind the other in the direction of the flow (known as tandem arrangement) with a longitudinal separation, measured from the centre of one model to the centre of the other, kept at  $x_0/D = 4.0$ .

Throughout the study, cylinder displacement amplitude ( $\hat{y}/D$ ) was found by measuring the root-mean-square value of response and multiplying by  $\sqrt{2}$ . This is likely to give an underestimation of the maximum peak response but, since it offers a good measure of the overall amplitude for many cycles of vibration, it appeared to be suitable for assessing the general effectiveness of suppression devices. The same method has been successfully employed by Assi et al. (2006, 2009) and others. The experimental set-up was validated by carrying out measurements of VIV for a single cylinder and the results were found to be in very good agreement with other works in the literature. Further details about the facilities, apparatus and validation can be found in Assi (2009).

### 2.2. Free-to-rotate parallel plates

The suppression device studied was inspired by the early work of Grimminger (1945) related to suppressing VIV of submarine periscopes, and its application to a single cylinder has been studied by Assi et al. (2009). It consists of two

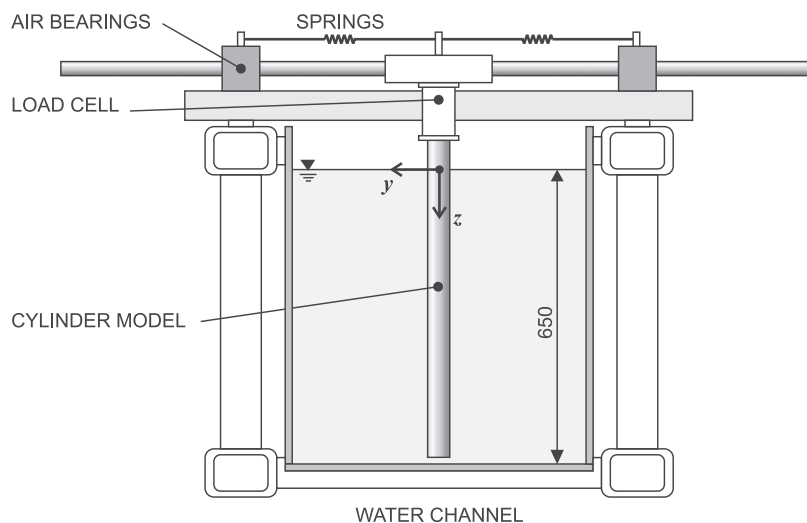


Fig. 2. Illustration of the test-section. The flow is moving perpendicular to the page plane and the cylinder is allowed to oscillate in the transverse direction ( $y$ -axis).

parallel plates running along the whole span of the cylinder. Starting at the  $\pm 90^\circ$  points each plate is 3 mm thick (about  $0.06D$ ) and trails back  $1D$  from the base of the cylinder (Fig. 5). The plates were mounted flush with the side of the cylinder, as close as possible to the cylinder wall, leaving only a small gap of less than 1 mm to allow for contactless rotation. Both plates were held together and kept parallel to each other by a supporting arm mounted on ball bearings at the extremities of the cylinder, freely rotating as one body around the centre of the cylinder.

The downstream cylinder, which was mounted on the elastic rig, could be fitted with free-to-rotate (f-t-r) plates. The upstream cylinder was kept fixed and could be fitted with an identical pair of fixed parallel plates. In addition to the reference configuration of two plain cylinders, three configurations with f-t-r plates were tested: plates fitted to both cylinders and plates fitted to either the upstream or downstream cylinder.

### 3. Preliminary results: attempt to suppress WIV with helical strakes

In order to verify the results presented by Korkischko et al. (2007) and to generate data for comparison we performed a series of tests with the most widespread of the VIV suppressors, helical strakes. The model had a diameter of 68 mm, a strake height of  $0.1D$  and a helical pitch of  $5D$ . While this geometry does not match strake geometries currently employed by the offshore industry, it provides some insight into the ineffectiveness of strakes in reducing vibrations when there is flow interference from an upstream wake. Separation was kept at  $x_0/D = 4.0$  and only the downstream cylinder was fitted with strakes as shown in Fig. 3(f). The upstream cylinder was left plain in order to generate a correlated vortex wake in the gap and represent the worst scenario for WIV excitation.

Fig. 4 presents the results compared to the reference VIV and WIV curves for plain cylinders. First, we note that this configuration of strakes installed on a single cylinder is able to reduce VIV amplitude by 44% at the resonance peak when compared to the plain cylinder response. The level of vibration remains fairly low around  $\hat{y}/D = 0.1$  up to reduced velocity 10, after which vibration builds up again reaching amplitudes around 0.4 at  $U/Df_0 = 23$ . This increasing response is an effect of random fluctuations in lift generated by the disruption of the flow by the strakes. The energy content of the force fluctuations increases with flow speed, and so does the random response. These VIV results are in good agreement with Bearman and Brankovic (2004), who found an almost 50% reduction of response at the resonance peak for a similar cylinder mounted with helical strakes (strake height:  $0.12D$ ; pitch:  $5D$  and  $Re = 10^3$ – $10^4$ ).

Once a plain cylinder is placed  $4D$  upstream of the straked cylinder the response changes significantly. The amplitude returns to  $\hat{y}/D = 0.8$  at the VIV resonance peak; it then falls slightly as reduced velocity is increased, but remains at a comparatively high level of around  $\hat{y}/D = 0.5$  for the rest of the reduced velocity range. As we can see, the response does not reach the high values of WIV found for plain cylinders, but still the significant level of response is enough to conclude that the strake loses efficiency when flow interference is present. In Fig. 4 we can also see the level of drag on the cylinder generated by the device. On average, the cylinder with strakes showed a 26% increase in the drag coefficient when compared to a static plain cylinder. The downstream cylinder with strakes also presented a higher drag coefficient relative to a static cylinder in tandem. It should be noted that drag coefficients for all configurations are defined throughout using the plain cylinder diameter and the undisturbed free stream velocity on the upstream cylinder.

Based on our current understanding of the WIV mechanism (Assi et al., 2010), we are able to conclude that the unsteady wake from upstream is still able to interact with the downstream body and enhance the response even if it is fitted with strakes. An ideal WIV suppressor has to work not only in disrupting the vortex formation from its own cylinder, but also avoiding the vortex-structure interference coming from the upstream wake. In principle, if WIV suppression with drag reduction is to be achieved the helical strake is not a family of solutions to be followed.

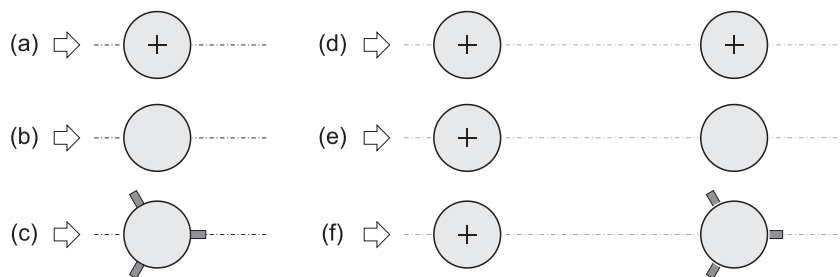


Fig. 3. Configurations tested as reference and to investigate strake effectiveness. Cylinders marked with a cross are not free to oscillate. (a) Static single; (b) VIV plain; (c) VIV with strakes; (d) static tandem; (e) WIV plain; (f) WIV with strakes. Results are presented in Fig. 4.

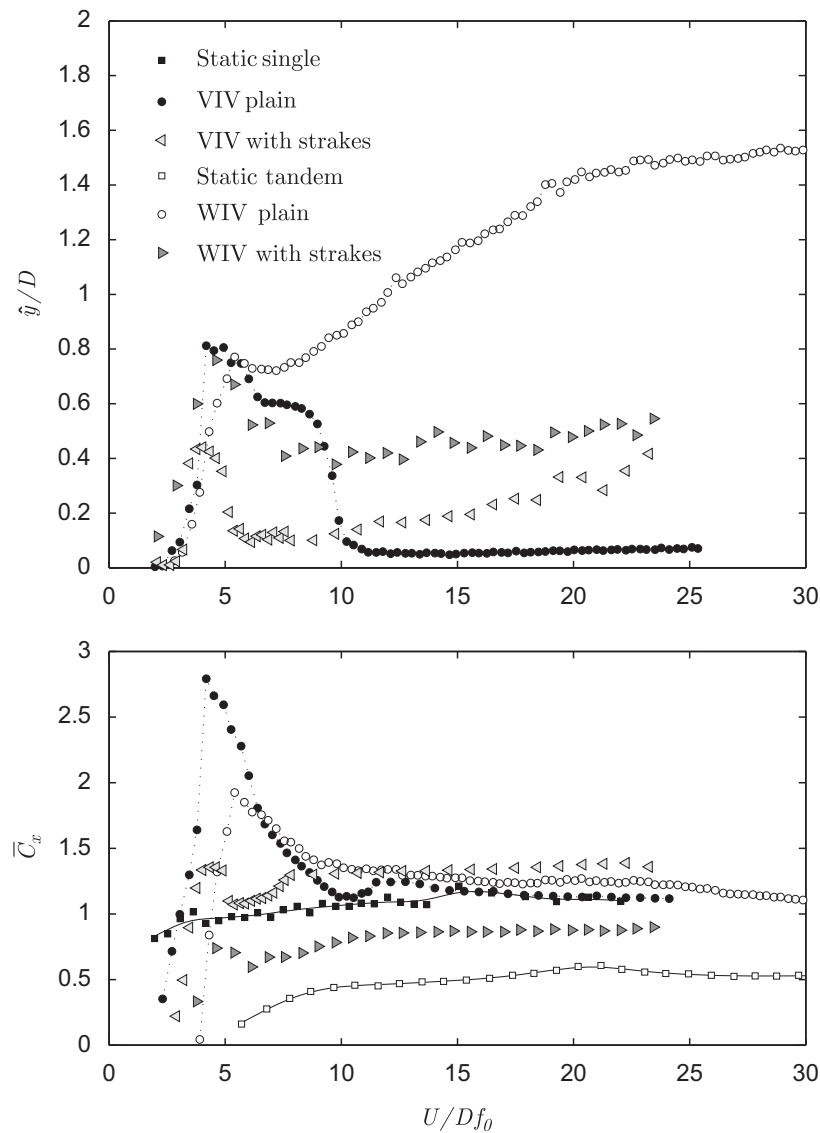


Fig. 4. WIV response (top) and mean drag coefficient (bottom) for cylinders fitted with strakes. Measurements are for the downstream cylinder of the tandem pair. Configurations as shown in Fig. 3.

#### 4. Results and discussion: WIV suppression with f-t-r parallel plates

Assi et al. (2009) have shown that two-dimensional control plates are very successful in suppressing VIV of a single cylinder. The cylinder responds with vibration below  $0.1D$  and a 38% drag coefficient reduction is achieved with reference to a static cylinder. Hence, we selected the most effective configuration presented in that work, the parallel plates, to investigate its effectiveness in suppressing WIV. Knowing that the WIV response decreases with increasing  $x_0$  we tested devices at  $x_0/D = 4.0$ , where we have found the most vigorous WIV response for a pair of plain cylinders (Assi et al., 2010).

The downstream cylinder, which was mounted on the elastic rig, could be fitted with f-t-r plates. The upstream cylinder was kept fixed and could be fitted with an identical pair of fixed parallel plates, resulting in three different configurations presented in Fig. 5.

##### 4.1. Preliminary results: upstream elastic cylinder

We started our investigation by fitting an elastically mounted cylinder with parallel plates but placing the static plain cylinder downstream; similar to configuration Config. I in Fig. 5, but with the upstream cylinder being the one free to

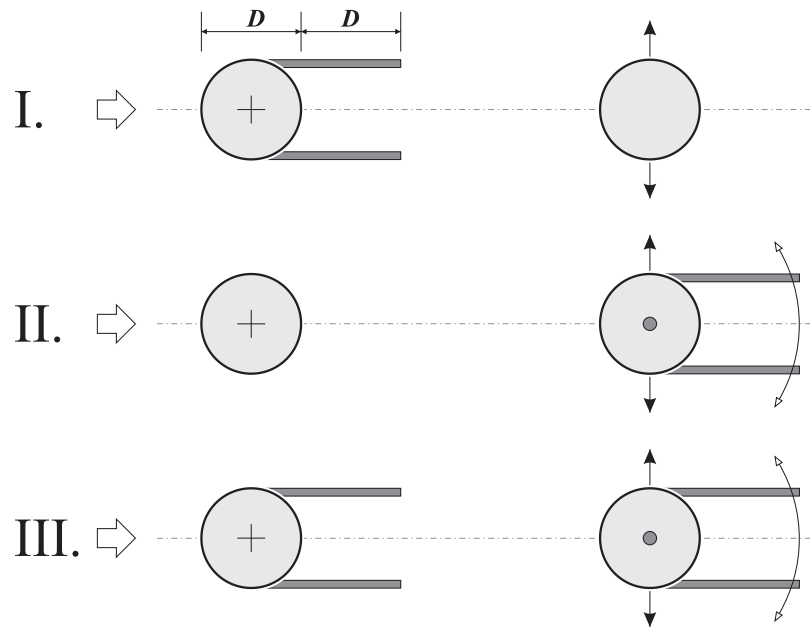


Fig. 5. Configurations of downstream and upstream cylinders fitted with f-t-r parallel plates. Centre-to-centre separation is  $x_0/D = 4.0$ . Cylinders marked with a cross are not free to oscillate.

oscillate. We observed that the presence of the downstream cylinder at  $x_0/D = 4.0$  did not interfere with the response of the upstream cylinder, i.e., when the second cylinder was positioned downstream of the cylinder mounted with the suppressor the latter remained motionless in a stable condition confirming the effectiveness of the suppressor in that configuration. This was important to validate our hypothesis that an upstream cylinder fitted with f-t-r parallel plates would behave as a static cylinder due to the effectiveness of the suppressor, at least for  $x_0/D \geq 4.0$ . This being true, we could replace the upstream cylinder by a fixed cylinder fitted with fixed parallel plates and concentrate our attention on the response of the downstream cylinder.

#### 4.2. WIV response of the downstream cylinder

Results are presented in Fig. 6. The first set shows the response for a plain downstream cylinder when the upstream cylinder is fitted with fixed plates (Config. I in Fig. 5). We know that WIV is related to the unsteady vortices from the upstream cylinder and we believe the amplitude of vibration is directly related to the dynamics of the vortices that are able to form in the gap between the cylinders (Assi, 2009). We also know that the parallel plates work by delaying the interaction between the two shear layers, thus delaying the formation of vortices and weakening the wake in the gap (Assi et al., 2009). (The fact that the drag on a single cylinder fitted with parallel plates is less than the drag on a plain fixed cylinder indicates that the wake being generated is weaker.) Therefore, since the plates do not suppress the formation of vortices from the first cylinder, but weaken them, the amplitude of vibration of the downstream cylinder is expected to be less than that observed for a pair of plain cylinders under WIV. This is exactly what we see in Fig. 6. If the upstream cylinder is the only one fitted with parallel plates (Config. I) the downstream cylinder still experiences WIV, although with a reduced amplitude level.

Now, in Config. II (Fig. 5) the cylinder fitted with f-t-r plates is positioned downstream of a plain static cylinder and Fig. 6 presents a remarkable result. The WIV of the downstream cylinder was suppressed to levels around 10% of a diameter, the same level of residual vibration measured for a single cylinder under VIV for reduced velocities after the synchronisation region. This amplitude of vibration is considered to be low and we could say that the parallel plates have successfully suppressed vibration to an acceptable level. We know that the upstream cylinder in Config. II is shedding vortices in a similar way to an isolated cylinder (Assi et al., 2010); and hence, the wake coming from the upstream cylinder will be similar to that found between two plain cylinders in a tandem arrangement. Therefore the parallel plates must be acting not only on the vortex shedding mechanism of the downstream cylinder, but also on the vortex-structure interaction this body encounters with the approaching flow. As a result, the vigorous type of WIV is suppressed.

The mass and damping parameters of the system play an important role and may reduce WIV for certain critical values (Bokaian and Geoola, 1984; Zdravkovich and Medeiros, 1991). One might suggest that the presence of two long

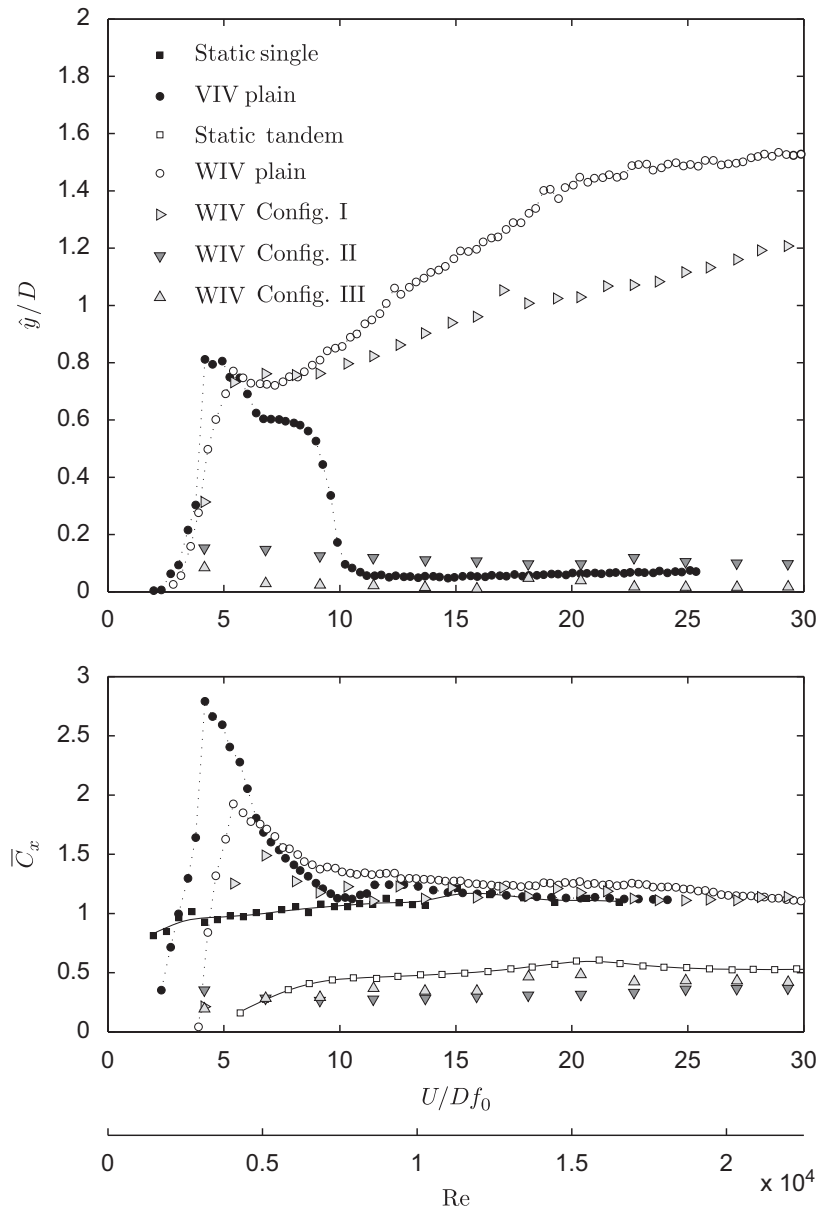


Fig. 6. WIV response in 1-dof (top) and mean drag coefficient (bottom) for cylinders fitted with parallel plates. Measurements are for the downstream cylinder of the tandem pair. Refer to Figs. 5 and 3.

plates along the cylinder axis may increase the hydrodynamic added mass and fluid damping in the direction of movement. Although this change could be the responsible for reducing the response it is probably not enough to suppress the vibration completely. Therefore we believe the plates are acting directly on the WIV excitation mechanism and not simply changing the dynamic characteristics of the system.

Finally, in Config. III we note the response of the downstream cylinder being suppressed to even lower levels. In this configuration the unsteadiness of the wake in the gap is also attenuated by the presence of parallel plates installed upstream and the response of the second body is further reduced. From this series of experiments we conclude that it is essential to install parallel plates on the downstream cylinder to suppress WIV, but if plates are also installed on the upstream cylinder the result is further improved.

#### 4.3. Drag reduction

We know that the mean flow profile that reaches the second cylinder of a tandem pair has a deficit in velocity compared to the free stream flow. Hence, the second cylinder of a tandem pair experiences a lower drag than the first



Table 1  
Drag reduction for WIV in 1-dof.

|   | Model  | $\overline{C}_x$ | Drag reduction |
|---|--|------------------|----------------|
| ■ | Static, plain single cylinder (Assi et al., 2009)        | 1.03             | Reference      |
|   | Single cylinder with parallel plates (Assi et al., 2009) | 0.63             | 38%            |
| □ | Static, plain tandem cylinders $x_0/D = 4.0$             | 0.49             | Reference      |
|   | Tandem cylinders: Parallel plates Config. II             | 0.33             | 33%            |
| △ | Tandem cylinders: Parallel plates Config. III            | 0.38             | 22%            |

$\overline{C}_x$  averaged in the range  $Re = 2 \times 10^3 - 1.8 \times 10^4$ . The lower three rows pertain to the downstream cylinder of the tandem pair. Symbols as in Fig. 6.

cylinder, which is exposed to the incident free stream  $U$  (Zdravkovich, 1977; Assi et al., 2010). However, as the body oscillates in and out of the wake interference region, this shielding effect is reduced and the mean drag ( $\overline{C}_x$ ) is increased, as shown in Fig. 6.

Fig. 6 also shows two reference sets of results for drag coefficients on static cylinders: one measured for a single cylinder and the other for the downstream cylinder of a tandem pair. We clearly see that the level of  $\overline{C}_x$  for the rear cylinder is half of that found for a single static cylinder. Therefore, a correct evaluation of drag reduction for WIV suppressors must take the averaged  $\overline{C}_x = 0.49$  as a reference and not  $\overline{C}_x$  around unity. Both configurations that successfully suppressed WIV (Configs. II and III) also reduced drag when compared to a fixed cylinder in a tandem arrangement. Table 1 summarises the data plotted in Fig. 6 averaging drag for the whole  $Re$  range.

In Assi et al. (2009) we have shown that the parallel plates act to delay the interaction between the shear layers and form in effect a cavity behind the cylinder resulting in weaker vortices in the wake. This was clearly noted by a reduction in the drag coefficient in relation to the cylinder without the plates. With weaker vortices coming from the upstream cylinder in Config. II the WIV response of the downstream cylinder is reduced—this is in agreement with the explanation for the WIV mechanism presented in Assi et al. (2010)—however it does not have as large an effect in reducing the drag of the downstream cylinder. The upstream cylinder fitted with parallel plates generates a wake that reaches the second cylinder with less of a mean velocity deficit than that for a plain cylinder, hence as a result the downstream body experiences more drag with plates on the upstream cylinder. While Config. II produced a 33% reduction in drag ( $\overline{C}_x = 0.33$ ) in relation to a downstream static cylinder ( $\overline{C}_x = 0.49$ ), the drag reduction in Config. III was limited to 22% ( $\overline{C}_x = 0.38$ ).

## 5. Single splitter plate as a WIV suppressor

Knowing that parallel plates are effective in suppressing both VIV and WIV, we might investigate if a single, 1D-long splitter plate is able to suppress WIV of cylinder arrays. The effectiveness of a f-t-r splitter plate was reported by Assi et al. (2009) who showed that a f-t-r splitter plate requires a stable deflected position in order to suppress VIV, resulting in a steady lift force being generated towards the side the plate has deflected. If the plate is not able to stabilise, say by some interference in the flow or by having very low torsional resistance, it will wobble from one side to the other as the cylinder oscillates.

The wake coming from the upstream cylinder contains coherent vortices that are responsible for the WIV excitation. This leads to the question: With unsteady forcing coming from the upstream wake, is it possible for a f-t-r splitter plate fitted on the downstream cylinder to find a stable position? In order to investigate this possibility, we performed an experiment replacing the parallel plates in Config. II by a single f-t-r splitter plate (1D-long, aligned with the centre of the cylinder) similar to the one employed in Assi et al. (2009). The result is presented in Fig. 7.

The plate was installed with a torsional friction above the critical value found for VIV suppression in Assi et al. (2009). We found that the single splitter plate did not stabilise in a deflected position, but oscillated vigorously as the cylinder responded with amplitudes between  $\hat{y}/D = 0.6$  and 1.0 for the whole range of reduced velocities. It appeared that the vortex-structure interaction present in the wake was indeed acting on the plate to prevent it from finding a stable angle.

The WIV excitation mechanism becomes more complex when a splitter plate is pivoting around the cylinder. During WIV, the lift force acting on the downstream cylinder is enhanced or diminished by the interaction with vortices shed from the upstream cylinder. Assi et al. (2010) has shown that strong vortex-structure interactions are necessary to



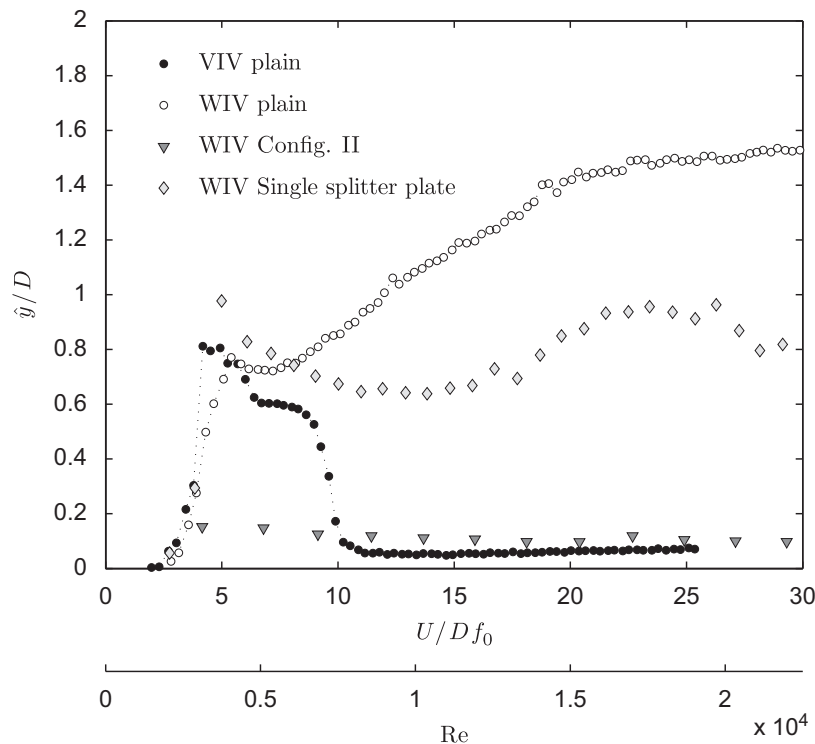


Fig. 7. WIV suppression with f-t-t splitter plate and parallel plates. Measurements are for the downstream cylinder of the tandem pair.

sustain the vibration. Nevertheless, vortices from the upstream wake will also induce fluctuating forces on the f-t-r splitter plate preventing it from finding a stable deflected position. Assi et al. (2009) showed that if a f-t-r splitter plate is not able to stabilise around a single cylinder (say by not having enough torsional friction, for example) the system will respond with vigorous vibrations with displacements higher than typical VIV. Now, for tandem cylinders, if a f-t-r splitter plate on the downstream cylinder develops a flapping movement due to strong vortex-structure interactions it will increase the response of the cylinder instead of suppressing it.

In Assi et al. (2009) we have shown that for a splitter plate to be effective suppressing VIV of a single cylinder, its length needed to be between 0.25 and 1.5 diameters. This was necessary so that the shear layer from one side of the cylinder could reattach to the tip of the plate allowing it to find a stable deflected position. Since the WIV mechanism with strong plate-vortex interaction prevents the plate from finding a suppressing configuration, we believe increasing or reducing the length of the plate would have no effect on suppressing WIV. It is necessary that an effective WIV suppressor would withstand the plate-vortex interaction without falling into a destabilising configuration.

Now, consider the flow field obtained with PIV measurements in Fig. 8 as an example (a sketch is presented in Fig. 8(c) for clarity). At this instant the cylinder is returning from its outermost displacement, still with low cross-flow velocity. The splitter plate shows a small outward deflection angle that will change as the body plunges across the wake. The resultant lift on the cylinder has a component induced by the interaction with upstream vortices and another due to the relative deflection of the splitter plate (as expressed by the arrows in opposite directions in Fig. 8(c)). We cannot tell these components apart based on the flow fields alone; from measurements of lift on the cylinder we can only infer the direction and magnitude of the resultant force. But the instantaneous competition between the two components contribute to increase the WIV response of the system, i.e., a small vortex impulse changing the angle of the plate may result in a substantial lift force exciting the vibration. In fact, we now have two oscillators – the first being the 1-dof cylinder and the second being the f-t-r splitter plate – and the force generated by their relative motion prevent the system from finding a stable condition, inputting energy to sustain the vibrations.

The force induced on the system is instantaneously changing as the cylinder vibrates across the wake and vortices from the upstream cylinder induce both the displacement of the cylinder and the deflection of the splitter plate. But by applying the concepts discussed in Zdravkovich (1977) and Assi et al. (2009) we could think of a simplified quasi-steady mechanism to model the dynamics of this system. Zdravkovich (1977) and others have shown that a static cylinder held at an offset position from the centreline of the wake will experience a steady lift force acting towards the centreline. From Assi et al. (2009) we also know that a f-t-r splitter plate generates a steady lift towards the side it is deflected. Depending on the relative position of the cylinder across the wake and the deflection of the plate the cylinder can

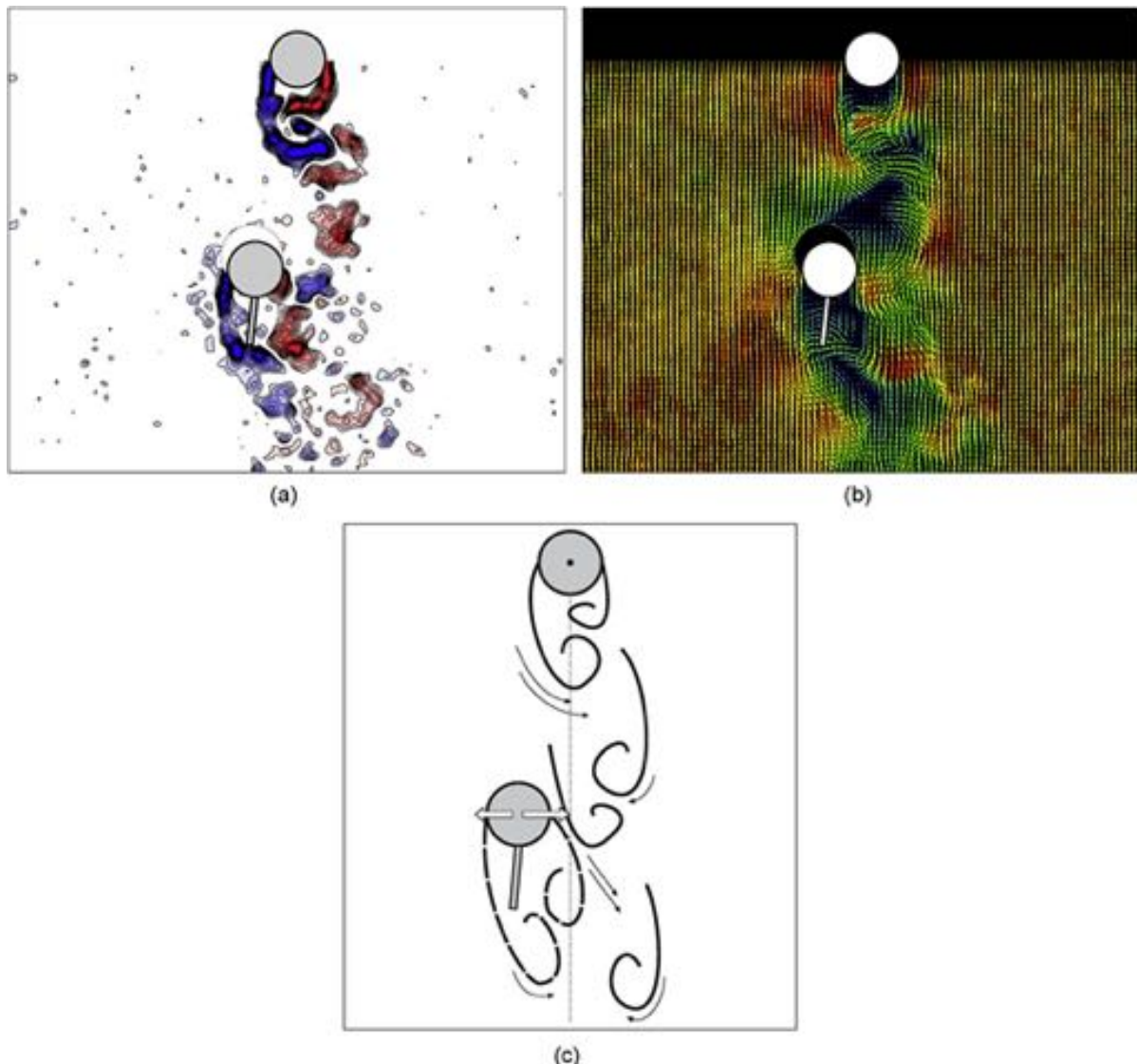


Fig. 8. Instantaneous vorticity contours (a) and velocity vectors (b) for a f-t-r splitter plate under WIV at  $U/Df_0 = 6.0$ . PIV measurements at  $Re = 4500$ ;  $x_0/D = 4.0$ . (c) Sketch of possible competition between components of lift generated by wake interaction with a f-t-r splitter plate under WIV.

experience an amplification or reduction of the steady lift force. A positive energy transfer from the flow to the structure may occur if the deflection of the splitter plate is able to alter the resultant force so that a favourable phase lag exists between the displacement of the cylinder and lift.

Both unsteady and quasi-steady explanations given above could produce enough excitation to sustain the vibrations. All that is required is that the relative motion between the f-t-r plate and the cylinder favours the WIV mechanism. This was certainly the case in our experiments, as the response curve shows, since a f-t-r splitter plate developed flapping motion under vortex interaction with the upstream wake. We suggest that devices requiring an asymmetric stable deflection position will not be effective in suppressing WIV. The parallel plates are successful because they do not depend in a deflected position to interact with the shear layers nor do they generate a destabilising lift force.

## 6. Conclusion

At the outset, parallel plates or any other device from this family of suppressors needs to be omni-directional in order to be employed in practical offshore application. Hence f-t-r plates were considered as project requirement. In the case of single splitter plates, this led to the discovery that a deflection angle was necessary for effective VIV suppression,

otherwise a rigid plate would induce the cylinder to gallop (Assi et al., 2009). However, when a f-t-r splitter plate was tested as a WIV suppressor it was found that no stable, deflected position of the plate existed due to the interference effect coming from the upstream wake, therefore single splitter plates were discarded. On the other hand, a pair of parallel plates does not require a deflection angle due to its symmetric configuration, thus it appeared as a potential suppressor for both VIV and WIV.

Cross-flow WIV suppression with drag reduction was achieved when f-t-r parallel plates were installed on the downstream cylinder of a pair. Response below  $\hat{y}/D = 0.1$  was achieved at a value of the  $m^*\zeta < 2 \times 10^{-2}$  for subcritical Reynolds numbers. If both cylinders are fitted with suppressors, which should be the case for an offshore installation, the drag coefficient can be as low as  $\overline{C}_x = 0.38$ , what amounts a 22% reduction compared to a downstream static cylinder in tandem arrangement. If only the downstream cylinder is fitted with parallel plates the drag reduction is around 33%.

The results presented in the present work refer only to a separation of  $x_0/D = 4.0$ . We already know that the excitation mechanism may change as  $x_0$  is reduced below a critical separation (Zdravkovich and Pridden, 1977; Assi, 2009). We also know that the plates require a minimum length to be effective (Assi et al., 2009). By reducing the gap or enlarging the plates we will enter the gap-flow-switching range (Zdravkovich, 1977) and a vigorous response may return. Nevertheless, the study proves that suppressors based on parallel plates have great potential to suppress VIV and WIV with substantial drag reduction.

It has been demonstrated that helical strakes, at least the configuration tested here, also lose their suppression efficiency when unsteady excitation is present in the upstream wake.

The present work was concerned with validating a concept of f-t-r parallel plates in suppressing WIV, therefore a 1D-long plate was chosen as the first trial. In Assi et al. (2009) we have tested the effect of plate length for a single splitter plate employed to suppress VIV in a single cylinder. It is our intention to perform similar tests with parallel plates as this would be the obvious step following from this piece of research. Future work should concentrate on optimising the devices in respect of overall length and geometry. Also, a more detailed parametric investigation of the effects of rotational inertia and torsional resistance should be carried out.

## Acknowledgements

The authors wish to thank BP Exploration Operating Company Ltd. and BP America Production Company for their support of this research. G.R.S. Assi was in receipt of a Ph.D. scholarship from CAPES, the Brazilian Ministry of Education.

## References

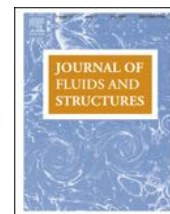
- Assi, G., 2009. Mechanisms for flow-induced vibration of interfering bluff bodies. Ph.D. Thesis, Imperial College London, London, UK, available from [www.ndf.poli.usp.br/~gassi](http://www.ndf.poli.usp.br/~gassi).
- Assi, G., Bearman, P., 2008. VIV suppression and drag reduction with pivoted control plates on a circular cylinder. In: Proceedings of OMAE2008—27th International Conference on Offshore Mechanics and Arctic Engineering, Estoril, Portugal.
- Assi, G., Bearman, P., Kitney, N., 2009. Low drag solutions for suppressing vortex-induced vibration of circular cylinders. *Journal of Fluids Structures* 25, 666–675.
- Assi, G., Bearman, P., Meneghini, J., 2010. On the wake-induced vibration of tandem circular cylinders: the vortex interaction excitation mechanism. *Journal of Fluid Mechanics*, doi:10.1017/S0022112010003095.
- Assi, G., Meneghini, J., Aranha, J., Bearman, P., Casaprima, E., 2006. Experimental investigation of flow-induced vibration interference between two circular cylinders. *Journal of Fluids Structures* 22, 819–827.
- Bearman, P., 1984. Vortex shedding from oscillating bluff bodies. *Annual Review of Fluid Mechanics* 16, 195–222.
- Bearman, P., Brankovic, M., 2004. Experimental studies of passive control of vortex-induced vibration. *European Journal of Mechanics B Fluids* 23, 9–15.
- Blevins, R., 1990. *Flow-induced Vibration*, second ed. Van Nostrand Reinhold.
- Bokaian, A., Geoola, F., 1984. Wake-induced galloping of two interfering circular cylinders. *Journal of Fluid Mechanics* 146, 383–415.
- Grimminger, G., 1945. The effect of rigid guide vanes on the vibration and drag of a towed circular cylinder. Technical Report 504, David Taylor Model Basin.
- Hover, F., Triantafyllou, M., 2001. Galloping response of a cylinder with upstream wake interference. *Journal of Fluids Structures* 15, 503–512.
- King, R., Johns, D., 1976. Wake interaction experiments with two flexible circular cylinders in flowing water. *Journal of Sound and Vibration* 45, 259–283.

- Korkischko, I., Meneghini, J., Casaprima, E., Franciss, R., 2007. An experimental investigation of the flow around isolated and tandem straked cylinders. In: *BBVIV5 5th Conference on Bluff Body Wakes and Vortex-Induced Vibrations*, Brazil.
- Laneville, A., Brika, D., 1999. The fluid and mechanical coupling between two circular cylinders in tandem arrangement. *Journal of Fluids Structures* 13, 967–986.
- Sarpkaya, T., 1979. Vortex-induced oscillations, a selective review. *Journal of Applied Mechanics* 46, 241–258.
- Sarpkaya, T., 2004. A critical review of the intrinsic nature of vortex-induced vibrations. *Journal of Fluids and Structures* 19, 389–447.
- Williamson, C., Govardhan, R., 2004. Vortex-induced vibrations. *Annual Review of Fluid Mechanics* 36, 413–455.
- Zdravkovich, M., 1974. Flow-induced vibrations of two cylinders in tandem and their suppression. In: Naudascher, E. (Ed.), *Flow Induced Structural Vibrations*. Springer-Verlag, Berlin, pp. 631–639.
- Zdravkovich, M., 1977. Review of flow interference between two circular cylinders in various arrangements. *ASME Journal of Fluids Engineering*, 618–633.
- Zdravkovich, M., 1988. Review of interference-induced oscillations in flow past two circular cylinders in various arrangements. *Journal of Wind Engineering and Industrial Aerodynamics* 28, 183–200.
- Zdravkovich, M., Medeiros, E., 1991. Effect of damping on interference-induced oscillations of two identical circular cylinders. *Journal of Wind Engineering and Industrial Aerodynamics* 38, 197–211.
- Zdravkovich, M., Pridden, D., 1977. Interference between two circular cylinders: series of unexpected discontinuities. *Journal of Wind Engineering and Industrial Aerodynamics* 2, 255–270.



Contents lists available at ScienceDirect

## Journal of Fluids and Structures

journal homepage: [www.elsevier.com/locate/jfs](http://www.elsevier.com/locate/jfs)

# Computational simulation of the flow-induced vibration of a circular cylinder subjected to wake interference

Bruno S. Carmo<sup>a,\*</sup>, Gustavo R.S. Assi<sup>b</sup>, Julio R. Meneghini<sup>a</sup><sup>a</sup> Department of Mechanical Engineering, Poli, University of São Paulo, Av. Prof. Melo Moraes, 2231, Cidade Universitária, São Paulo 05508-030, SP, Brazil<sup>b</sup> Department of Naval Engineering, Poli, University of São Paulo, Brazil

## ARTICLE INFO

## Article history:

Received 30 March 2012

Received in revised form

14 January 2013

Accepted 3 February 2013

Available online 22 March 2013

## Keywords:

Flow-induced vibration

Numerical simulation

Flow interference

## ABSTRACT

In this work, we considered the flow around two circular cylinders of equal diameter placed in tandem with respect to the incident uniform flow. The upstream cylinder was fixed and the downstream cylinder was completely free to move in the cross-stream direction, with no spring or damper attached to it. The centre-to-centre distance between the cylinders was four diameters, and the Reynolds number was varied from 100 to 645. We performed two- and three-dimensional simulations of this flow using a Spectral/hp element method to discretise the flow equations, coupled to a simple Newmark integration routine that solves the equation of the dynamics of the cylinder. The differences of the behaviours observed in the two- and three-dimensional simulations are highlighted and the data is analysed under the light of previously published experimental results obtained for higher Reynolds numbers.

© 2013 Elsevier Ltd. All rights reserved.

## 1. Introduction

The flow around circular cylinders has been extensively studied due to its practical importance in engineering and scientific relevance in fluid mechanics. When circular cylinders are grouped in close proximity, the flow field and the forces experienced by the cylinders can be entirely different from those observed when the bodies are isolated in the fluid stream. The effect of the presence of other bodies in the flow is called *flow interference*. One of the most severe types of interference, and the type on which this paper focuses, is *wake interference*, which happens when the cylinder is immersed or in close proximity to the wake of another bluff body. In such situations, the flow impinging on the cylinder is usually totally different from the free-stream. Given the number of differences observed in the forces exerted on cylinders subjected to wake interference when compared to the single cylinder case, one expects that the flow-induced vibrations (FIV) experienced by a flexible cylinder or a compliantly mounted rigid cylinder will also be different depending whether the cylinder is immersed in a vortex wake or not.

A few papers on this matter have been published, most of them were concerned with vibrations within the synchronisation range, i.e. when the vortex shedding is synchronised with the cylinder vibration. King and Johns (1976) investigated the vibration of two flexible cylinders in tandem by performing experiments in a water channel. Bokaian and Geoola (1984) carried out experiments on the flow around circular cylinders in tandem and staggered arrangements, the upstream cylinder being fixed and the downstream one being rigid and mounted on an elastic base that allowed

\* Corresponding author. Tel.: +55 11 3091 9882; fax: +55 11 3091 5642.

E-mail addresses: [bruno.carmo@usp.br](mailto:bruno.carmo@usp.br) (B.S. Carmo), [g.assi@usp.br](mailto:g.assi@usp.br) (G.R.S. Assi), [jmeneg@usp.br](mailto:jmeneg@usp.br) (J.R. Meneghini).

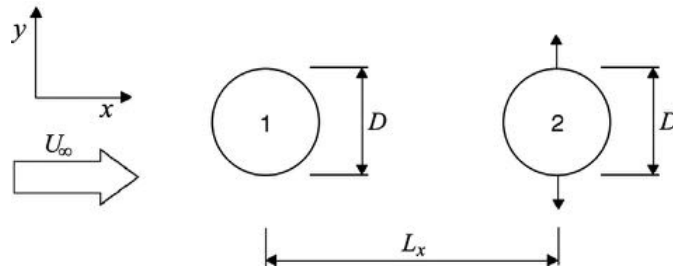


Fig. 1. Schematic drawing of arrangement studied.

cross-stream displacement. Zdravkovich (1985) investigated the behaviour of two flexible circular cylinders placed in diverse arrangements using a wind tunnel. Brika and Laneville (1999) utilised wind tunnel experiments to study the flow induced vibrations of a flexible circular cylinder, allowed to vibrate in one plane only, immersed in the wake of a rigid cylinder. Assi et al. (2006) performed experiments on the FIV of a elastically mounted rigid cylinder in the wake of a fixed identical cylinder, using a water channel. Recently, there has also been a few computational studies on FIV of two circular cylinders in tandem. Examples of this type of work are Mittal and Kumar (2001), Jester and Kallinderis (2004) and Papaioannou et al. (2008). In all these papers, the computations were two-dimensional and focused on reduced velocities within the synchronisation range. In general terms, they confirmed the main conclusions of previously published experimental data: the wake interference led to a wider synchronisation range and within this range the amplitude of response was larger than that observed in the response of an isolated cylinder with the same structural parameters.

However, some papers have also reported that cylinders subjected to wake interference also experienced vibrations with high amplitudes for higher reduced velocities, outside the synchronisation range (Bokaian and Geoola, 1984; Brika and Laneville, 1999; Hover and Triantafyllou, 2001; Zdravkovich, 1985). In most cases, the amplitude levels were even higher than those observed in the lock-in. Although the reduced velocity for which this peculiar type of response starts to be significant seems to depend on various aspects, such as the separation between the cylinders and the mass ratio, all the papers agree on the fact that an upper reduced velocity limit for which these vibrations would cease does not seem to exist.

In this paper, we investigate the limit case of this phenomenon by removing the springs and the damper attached to the downstream cylinder, i.e. making the reduced velocity equal to infinity. The arrangement is illustrated in Fig. 1: both cylinders have the same diameter, the upstream cylinder is fixed and the downstream cylinder is allowed to move in the cross-stream direction without any type of constraint. We limit our investigation to the case in which the centre-to-centre separation,  $L_x$ , is equal to  $4D$ , and study the influence of the Reynolds number in the range  $100 \leq Re \leq 645$ , employing two- and three-dimensional numerical simulations.

## 2. Numerical method

The computational results were obtained by coupling the solution of the flow with the solution of the structural response. The flow is governed by the incompressible Navier–Stokes equations, which can be written in non-dimensional form as

$$\frac{\partial \mathbf{u}}{\partial t} = -(\mathbf{u} \cdot \nabla) \mathbf{u} - \nabla p + \frac{1}{Re} \nabla^2 \mathbf{u}, \quad (1)$$

$$\nabla \cdot \mathbf{u} = 0. \quad (2)$$

The cylinder diameter  $D$  is the reference length and the free-stream speed  $U_\infty$  is the reference speed used in the non-dimensionalisation.  $\mathbf{u} \equiv (u, v, w)$  is the velocity field,  $t$  is the time,  $p$  is the static pressure,  $Re = \rho U_\infty D / \mu$  is the Reynolds number and  $\mu$  is the dynamic viscosity of the fluid. The pressure was assumed to be scaled by the constant density  $\rho$ . The numerical solution of these equations was calculated using a Spectral/hp discretisation as described in Karniadakis and Sherwin (2005).

On the structural side, we assumed that the moving cylinder was rigid and free to move in only one direction. The response of the cylinder to an external force is governed by Newton's second law, written in non-dimensional form as

$$\frac{\pi m^*}{4} \ddot{y}_c^* = F_y^*(\dot{y}_c^*, y_c^*, t^*). \quad (3)$$

In this equation,  $m^* = 4M / (\rho \pi D^2 L)$  is the mass ratio,  $F_y^* = C_L / 2 = F_y / (\rho U_\infty^2 DL)$  is the non-dimensional force imposed by the fluid in the direction of motion.  $L$  is the (axial) length of the cylinder and  $C_L$  is the lift coefficient. The variables  $\ddot{y}_c^*$ ,  $\dot{y}_c^*$ ,  $y_c^*$  are the non-dimensional acceleration, velocity and displacement of the body, respectively, and  $t^*$  is the non-dimensional time.



These variables are non-dimensionalised according to the expressions

$$\ddot{y}_c^* = \frac{\ddot{y}_c D}{U_\infty^2}, \quad \dot{y}_c^* = \frac{\dot{y}_c}{U_\infty}, \quad y_c^* = \frac{y_c}{D}, \quad t^* = \frac{t U_\infty}{D}.$$

The structural equation was integrated using [Newmark's \(1959\)](#) scheme.

The fluid–structure interaction problem this paper is concerned with comprises the flow around two bodies, with one of them being allowed to move independently of the other. The computational code used to simulate the flow had to provide support for that, thus an Arbitrary Lagrangian–Eulerian (ALE) formulation was employed. The ALE formulation consists basically in incorporating arbitrary displacements of the mesh into the equations being solved, so the movement of the bodies and the mesh deformations necessary to maintain an adequate spatial discretisation can be taken into account. This can be achieved by doing a simple modification in the advection term of the incompressible Navier–Stokes equations (1) and (2),

$$\frac{\partial \mathbf{u}}{\partial t} = -(\mathbf{u} - \mathbf{m}) \cdot \nabla \mathbf{u} - \nabla p + \frac{1}{\text{Re}} \nabla^2 \mathbf{u}, \quad (4)$$

$$\nabla \cdot \mathbf{u} = 0, \quad (5)$$

where  $\mathbf{m}$  is the velocity of the mesh. The velocity of the mesh on the cylinder walls was given by the velocity of the bodies and was zero on the other boundaries of the domain. The velocity of the mesh in the interior of the domain was calculated in an automated way following the scheme presented by [Batina \(1990\)](#). Eqs. (4) and (5) are the Arbitrary Lagrangian–Eulerian form of the Navier–Stokes equations.

Eqs. (3)–(5) have to be solved in a coupled manner. The fluid load  $F_y^*$  in Eq. (3) is calculated from the solution of the flow (4) and (5), and the motion of the boundaries, which are necessary for the solution of Eqs. (4) and (5), is determined by the solution of the structure Eq. (3). The equations were integrated in time employing a modified version of the algorithm described in [Carmo et al. \(2011\)](#). The modification consisted in the effectuation of sub-iterations so as to make the algorithm tightly coupled. In other words, sub-iterations were performed in order to assure that the body displacement and fluid force were consistent within the time-step. This measure made the code to run slower but was necessary to the integration to converge, since the increase in Reynolds number appears to make the simulation more sensitive to the low mass-ratio instability that takes place in flow–structure interaction calculations ([Causin et al., 2005](#); [Förster et al., 2007](#)).

### 3. Numerical simulations

Two- and three-dimensional simulations were performed for the tandem arrangement with centre-to-centre separation  $L_x/D = 4$ . This separation was chosen because we were interested in investigating flows in which there is a complete wake in the region between the cylinders (the WG regime described in [Carmo et al., 2010a](#)) with high vibration amplitude, and previous tests with fixed cylinders showed that this configuration exhibited the desired shedding regime with high lift coefficient amplitude. The mesh employed for all the simulations is shown in [Fig. 2](#). It extended  $36D$  upstream of the upstream cylinder, the lateral boundaries were located  $50D$  from the upstream cylinder centre and the outflow boundary located  $45D$  from the downstream cylinder. No-slip boundary conditions were enforced on the cylinder walls, essential boundary conditions  $(u, v) = (1, 0)$  were enforced on the lateral and upstream boundaries, and outflow

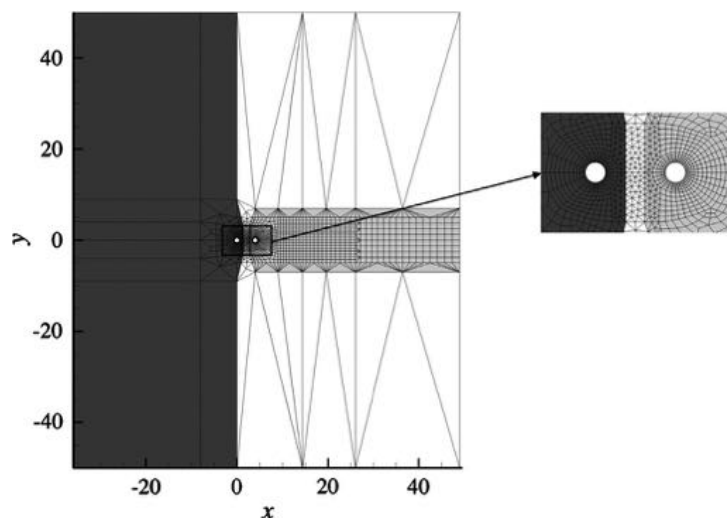


**Fig. 2.** Example of a mesh used with the ALE formulation, showing also the detail of the discretisation close to the cylinders. The dark grey region remains fixed, the elements in the light grey region move rigidly with the downstream cylinder and the elements in the white region deform to comply with the movement of the cylinder.

boundary conditions  $(\partial u/\partial \mathbf{n}, \partial v/\partial \mathbf{n}) = (0, 0)$  were employed on the downstream boundary. The high-order pressure boundary conditions were enforced on the cylinder walls, upstream and lateral boundaries, while the pressure was fixed to  $p=0$  on the downstream boundary. For the three-dimensional simulations, the spanwise length of the domain was  $15D$  discretised with 64 Fourier modes, and periodic boundary conditions were employed on the planes that crossed the ends of the cylinder. The mass ratio was  $m^* = 2.0$  for all calculations.

The Reynolds numbers tested varied between 90 and 645 for the two-dimensional simulations and between 300 and 600 for the three-dimensional simulations. The polynomial order of the basis functions varied from 3 (lowest Reynolds numbers) to 9 (highest Reynolds numbers) for the two-dimensional simulations and from 4 to 6 for the three-dimensional simulations. We also used different time-steps according to the Reynolds number, varying from  $\Delta t = 7.4 \times 10^{-3}$  for  $Re = 90$  to  $\Delta t = 7.6 \times 10^{-4}$  for  $Re = 645$ .

## 4. Results

### 4.1. Two-dimensional simulations

Fig. 3 shows the amplitude of response (rms of the amplitude signal multiplied by  $\sqrt{2}$ ) obtained with the numerical simulations. It is possible to identify three different regimes in the curve relative to the two-dimensional simulations.

The first regime shows a monotonically decreasing amplitude with increasing Reynolds number, comprising the range  $90 \leq Re \leq 165$ . It is interesting to note that for this Reynolds number range, the flow around a tandem arrangement with fixed cylinders with  $L_x/D = 4$  is basically two-dimensional – the critical Reynolds number regarding three-dimensional instabilities for this arrangement is  $Re = 163.5$  (Carmo et al., 2010b). Fig. 5(a) shows the time history of the downstream cylinder lift coefficient and displacement. It can be seen that both the force and the displacement are harmonic, with no amplitude modulation for neither quantity. The displacement signal is always in anti-phase with respect to the force signal. Comparing the power spectral density (PSD) of the force on the upstream cylinder (Fig. 4(a)) to the PSD of the downstream cylinder displacement (Fig. 4(b)), it can be seen that the power of these two signals is concentrated at the same frequency, i.e. the displacement of the downstream cylinder is synchronised with the shedding of the upstream cylinder. The vorticity contours depicted in Fig. 5(b) show that the vortices shed from the downstream cylinder form two separated rows of vortices that interact only far downstream, more than  $8D$  away from the downstream cylinder (therefore, not visible in the figure).

The second regime starts at  $Re \approx 180$  and is observed for Reynolds numbers up to 360. The amplitude of vibration for this regime exhibits significant scatter, as can be seen in Fig. 3. The displacement time history for this regime displays a slow modulation, as shown in Fig. 6(a). Nonetheless, the downstream cylinder displacement and upstream cylinder lift coefficient signals remain synchronised, as shown in Fig. 4. It can be seen in the vorticity contours in Fig. 6(b) that the vortices in the wake of the downstream cylinder interact in a region approximately  $6D$  away from the downstream body, i.e. much closer to the bodies than for the first regime (at lower Reynolds numbers).

There is a gradual transition between the second and third regimes, happening for  $360 \leq Re \leq 405$ . The third regime then extends up to the highest Reynolds number tested. For this regime, Fig. 3 shows that the amplitude grows monotonically with the Reynolds number. The PSD contours of the displacement of the downstream cylinder (Fig. 4(b)) shows that for this regime there is a strong component at low frequencies and this component does not have

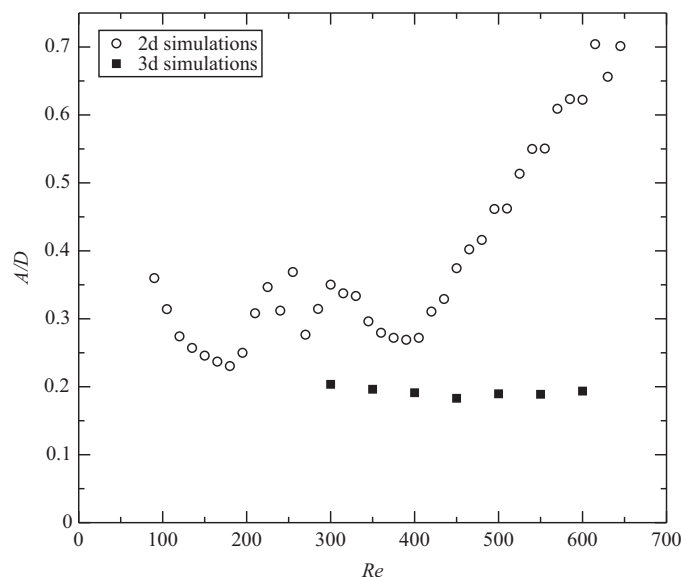
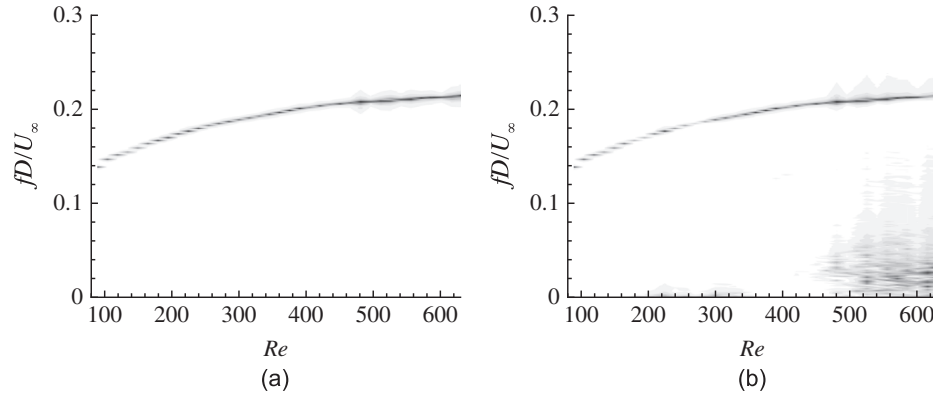
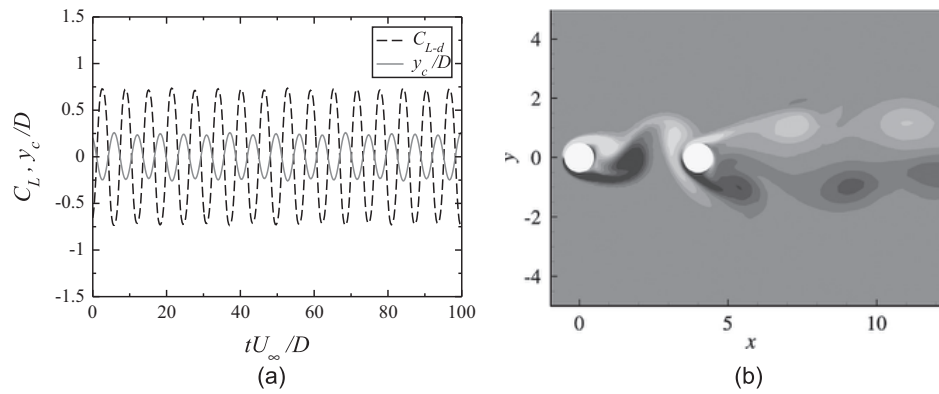


Fig. 3. Response amplitude obtained from two- and three-dimensional simulations at different Reynolds numbers.



**Fig. 4.** Contours of normalised power spectral density of the upstream cylinder lift coefficient and downstream cylinder displacement, as functions of the Reynolds number; two-dimensional simulations. (a) Upstream cylinder  $C_L$ . (b) Downstream cylinder  $y_c$ .



**Fig. 5.** Downstream cylinder lift coefficient and displacement time series (a) and instantaneous vorticity contours (b);  $Re = 150$ , two-dimensional simulations.

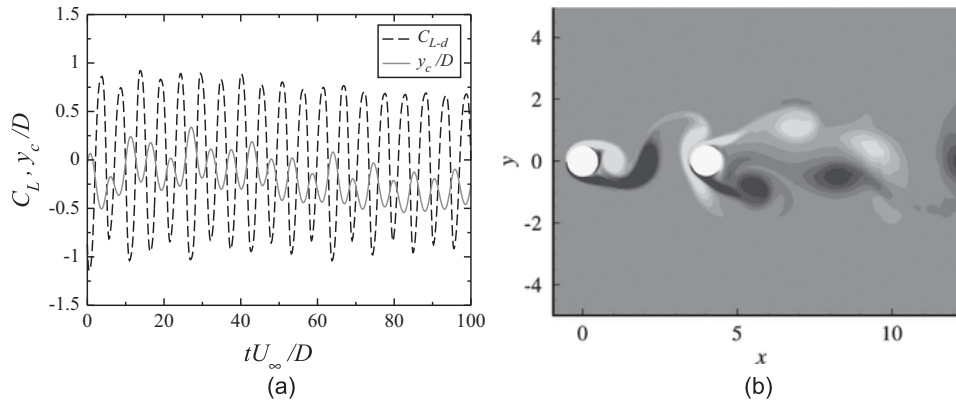


**Fig. 6.** Downstream cylinder lift coefficient and displacement time series (a) and instantaneous vorticity contours (b);  $Re = 300$ , two-dimensional simulations.

a corresponding match in the PSD contours of the lift of the upstream cylinder (Fig. 4(a)). The time history of the lift coefficient and displacement of the downstream cylinder, shown in Fig. 7(a), exhibit a very erratic behaviour. We see in Fig. 7(b) that the vortices in the near wake of the downstream cylinder, more precisely between the base region of the cylinder up to  $4D$  downstream, but without a regular pattern.

In order to better understand why in the third regime the downstream cylinder exhibits a significant part of its oscillation power at low frequencies, let us analyse the response of a mass-spring-damper system to a oscillatory force. In this case, the motion of the body is governed by the equation,

$$\ddot{y}_c + 2\zeta\omega_0\dot{y}_c + \omega_0^2 y_c = \frac{F_0 \sin(\omega t)}{M},$$

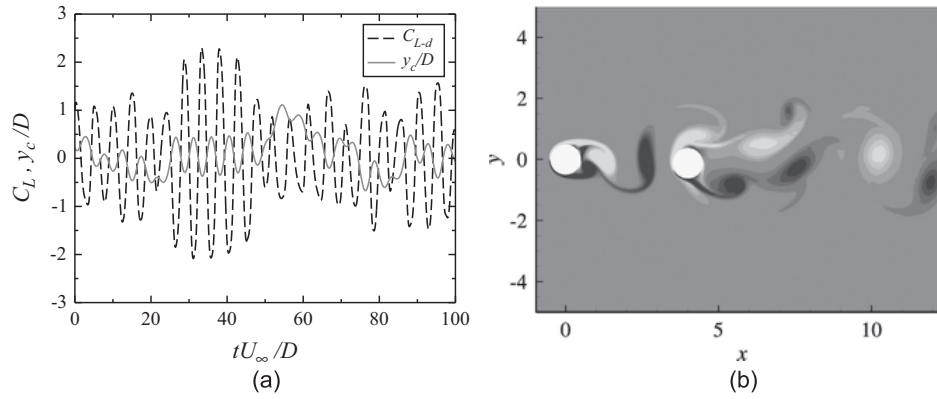


**Fig. 7.** Downstream cylinder lift coefficient and displacement time series (a) and instantaneous vorticity contours (b);  $Re = 540$ , two-dimensional simulations.

where  $\omega_0 = \sqrt{k/m}$  is the natural frequency of the structure in vacuum and  $F_0$  and  $\omega$  are the force amplitude and frequency, respectively. After the initial transient is finished, the structure will respond according to

$$y_c(t) = \frac{F_0}{M\omega \sqrt{\left(\frac{C}{M}\right)^2 + \frac{(\omega_0^2 - \omega^2)^2}{\omega^2}}} \sin(\omega t + \phi),$$

with

$$\phi = \arctan\left(\frac{2\omega\omega_0\zeta}{\omega^2 - \omega_0^2}\right).$$

Considering that our system does not have a spring ( $k=0$ ), so  $\omega_0 = 0$ , nor a damper ( $C=0$ ), the response amplitude obeys the equation

$$A = \frac{F_0}{M\omega^2}, \quad (6)$$

from this we conclude that the amplitude of vibration of the structure will be larger if the frequency of the force is low. A generic force can be decomposed into its Fourier components and the system will respond with larger amplitudes to that components with low frequency.

The spectra of the downstream cylinder lift coefficient and displacement for diverse Reynolds numbers are plotted in Fig. 8. It can be seen that at the laminar regime (Fig. 8(a)), the force signal is harmonic, showing a very clean spectrum, so the response of the structure is also harmonic, displaying peaks only at the shedding frequency and its third harmonic. If the Reynolds number is increased (Figs. 8(b)–(d)), the signal of the force on the downstream cylinder starts to show a multitude of components due to the now turbulent wake that impinges on the downstream cylinder, although a very clear peak is still observed at the shedding frequency. Consequently, the structure then responds with larger amplitudes at the low frequency range of the spectrum, and this is basically the reason why a significant part of the power is concentrated at the low frequencies for higher Reynolds numbers, as shown in Fig. 4(b).

The origin of the third harmonic can be understood by considering that a periodic function  $f(t)$  of zero mean value and period  $T$  can be represented by a Fourier series of the form:

$$f(t) = \sum_{n=1}^{\infty} a_n \sin(n\omega t) + b_n \cos(n\omega t).$$

The terms  $a_n$  and  $b_n$  of this series are given by

$$a_n = \frac{2}{T} \int_0^T f(t) \sin(n\omega t) dt \quad b_n = \frac{2}{T} \int_0^T f(t) \cos(n\omega t) dt.$$

By choosing the initial time appropriately, the function can be made odd, that is  $f(-t) = -f(t)$ . For odd functions,  $b_n = 0$  for every  $n$ . Furthermore,  $f(t) = -f(t+T/2)$ , hence  $a_n = 0$  for even values of  $n$ . Therefore, the function  $f(t)$  can be represented by

$$f(t) = a_1 \sin(\omega t) + a_3 \sin(3\omega t) + a_5 \sin(5\omega t) + \dots, \quad (7)$$

and the number of harmonics necessary to represent  $f(t)$  depends on how different from a sinusoidal function  $f(t)$  is. In the cases investigated in this paper (two- and three-dimensional), both the displacement and the force signals are periodic with zero mean, but they are not perfectly sinusoidal. So Eq. (7) indicates that the odd numbered harmonics should be strong in the spectra, and this is what we observe.

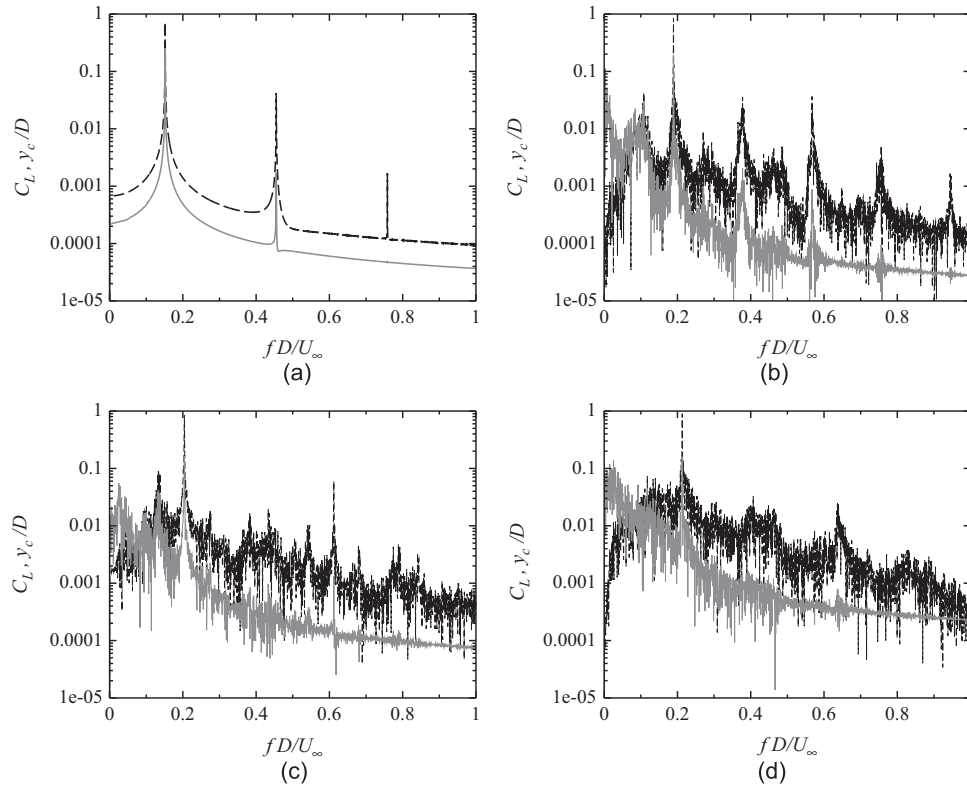


**Fig. 8.** Spectra for the downstream cylinder lift coefficient (dashed black lines) and displacement (solid grey lines) for various Reynolds numbers, obtained from two-dimensional simulations. (a)  $Re=120$ , (b)  $Re=300$ , (c)  $Re=420$  and (d)  $Re=600$ .

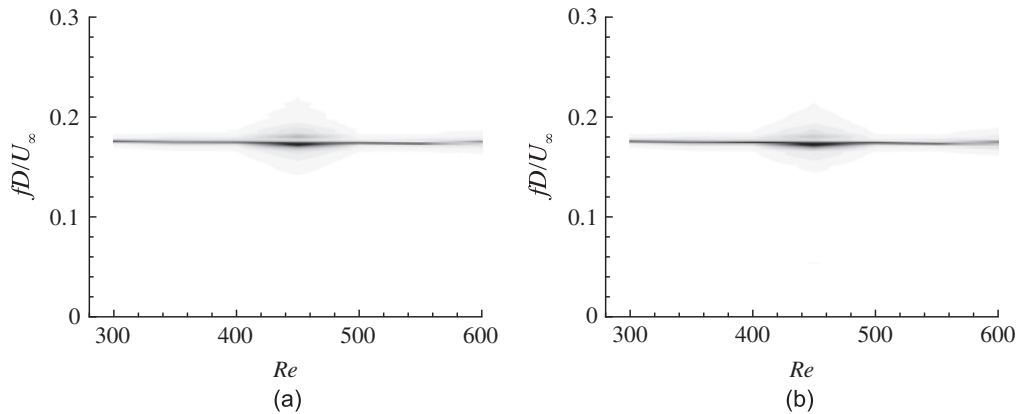
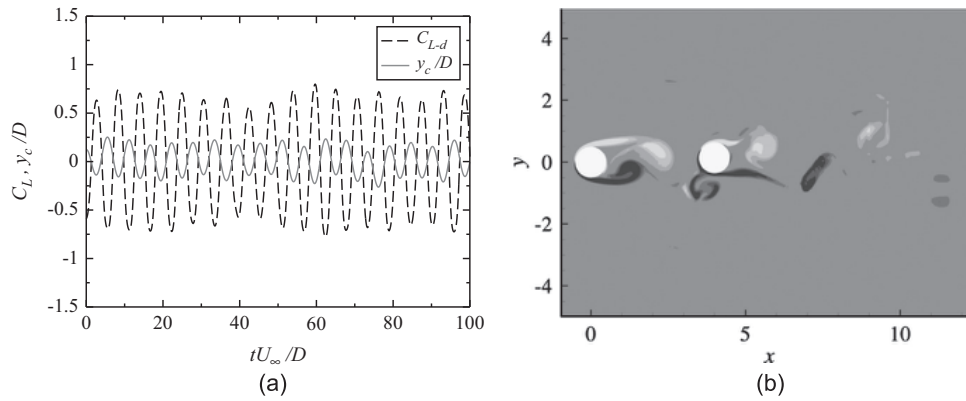


**Fig. 9.** Contours of normalised power spectral density of the upstream cylinder lift coefficient and downstream cylinder displacement, as functions of the Reynolds number; three-dimensional simulations. (a) Upstream cylinder  $C_L$ . (b) Downstream cylinder  $y_c$ .

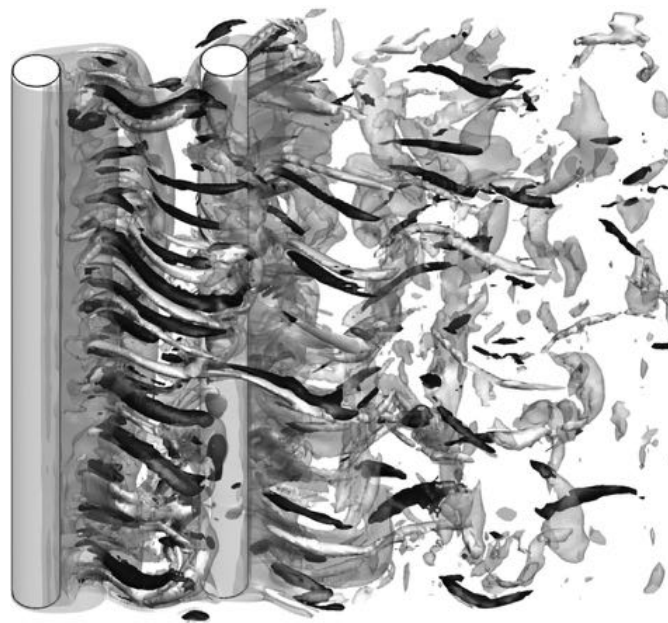
#### 4.2. Three-dimensional simulations

Fig. 3 shows that the amplitude of vibration varies very little for the three-dimensional simulations, within the Reynolds number range tested. The same can be said regarding the frequency of vibration: Fig. 9 shows that the frequency of vibration of the downstream cylinder and the frequency of shedding of the upstream cylinder are basically constant and have the same value for the entire Reynolds number range.

The time history of the downstream cylinder lift and displacement and the vorticity contours observed in the results of the three-dimensional results display very similar behaviour. Fig. 10 illustrates this behaviour by displaying these plots for  $Re=400$ . The time histories in Fig. 10(a) show that both the lift coefficient and displacement signals exhibit a little modulation in their amplitudes. This amplitude is less strong than those observed for the second and third regimes of the two-dimensional result, and for every cycle the cylinder crosses the line  $y=0$ , which is not the case for the two-dimensional simulations (see Figs. 6(a) and 7(a)). Fig. 10(b) shows clearly that the spanwise vortices diffuse much more quickly if three-dimensional flow is considered. It can be seen in Fig. 11 that the wake is strongly three-dimensional, with considerable streamwise vorticity present both in the region between the cylinders and in the wake of the downstream



**Fig. 10.** Downstream cylinder lift coefficient and displacement time series (a) and instantaneous vorticity contours at  $z/D = 7.5$  (b);  $Re = 400$ , three-dimensional simulations.



**Fig. 11.** Instantaneous iso-surfaces of spanwise vorticity (translucent surfaces) and streamwise vorticity (solid surfaces) for  $Re = 400$ , three-dimensional simulation. Solid light grey and dark grey surfaces represent iso-surfaces of negative and positive  $\omega_x$ , respectively.

cylinder. This weakening of the spanwise vortices seems to be the main responsible for the fact that the amplitudes observed in the three-dimensional results are smaller than those observed in the two-dimensional results, for the same Reynolds numbers. Besides that, it is interesting to highlight that the amplitude level obtained from the three-dimensional calculations stays at roughly the same level, while experimental results for subcritical Reynolds numbers show growing values with increasing Reynolds numbers (Assi, 2009). We suggest that this disparity of behaviours is due to fundamental differences in the flow regimes. Once the wake is three-dimensional, an increase of Reynolds number causes two opposite effects. The first is an increase of the vortex strength, due to an increase of the vorticity magnitude of the boundary layers and consequently of the free shear layers. The second is the intensification of the three-dimensional character of the flow and turbulence in the wake, which contributes for a faster diffusion of the spanwise vorticity. The work by Noca et al. (1998) indicates that the second effect prevails over the first for  $Re \lesssim 1500$  and the first effect prevails over the second for  $Re \gtrsim 1500$ . Since the forces on the downstream cylinder are directly linked to the strength of the vortices reaching the body, it is expected that the amplitude will only grow if the strength of the vortices shed by the upstream cylinder increases, i.e. if the Reynolds number is increased beyond the threshold  $Re \approx 1500$ .

As the structural parameters did not change from the two-dimensional simulations, we still expect that the amplitude of response will be given by Eq. (6). In order to analyse the three-dimensional results using this equation, the spectra of the downstream cylinder lift coefficient and displacement were plotted for a number of different Reynolds numbers in Fig. 12. The graphs show that for all the cases the force is composed by diverse components, but the peaks at the shedding frequency and its third harmonic are clearly dominant and more pronounced than in the two-dimensional results (Fig. 8). It is important to note that the turbulent diffusion is higher in the three-dimensional simulations, because in these calculations all the components of the Reynolds stresses, combining the three velocity components, are taken into account,



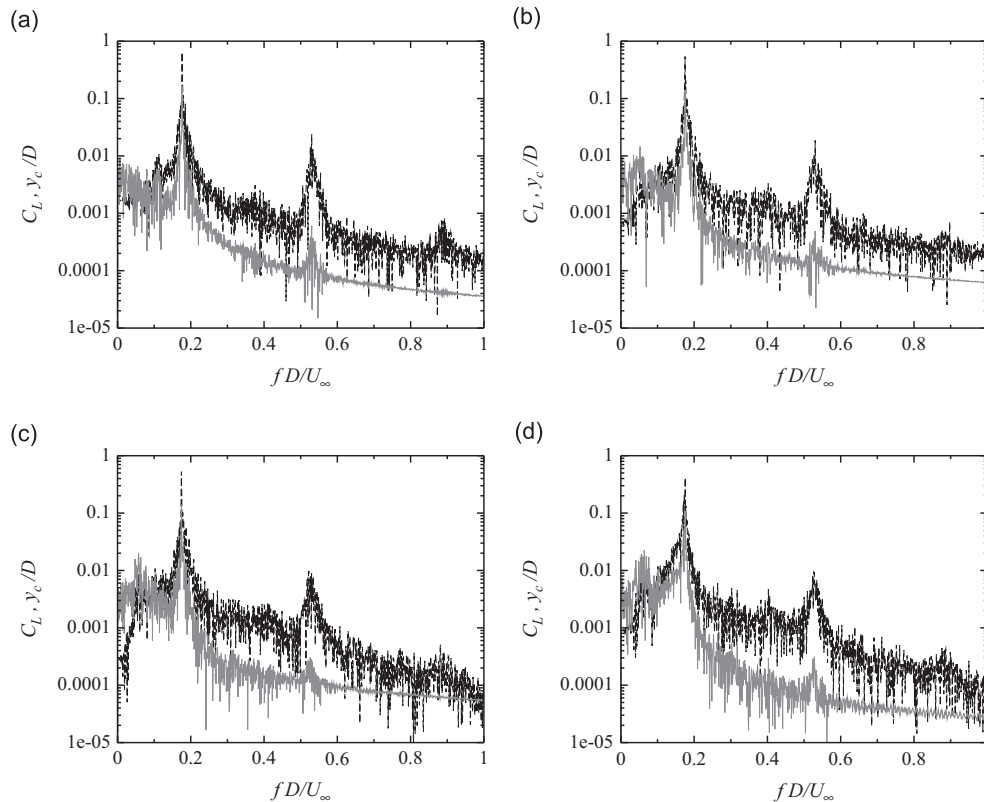


**Fig. 12.** Spectra for the downstream cylinder lift coefficient (dashed black lines) and displacement (solid grey lines) for various Reynolds numbers, obtained from three-dimensional simulations. (a)  $Re = 300$ , (b)  $Re = 400$ , (c)  $Re = 500$  and (d)  $Re = 600$ .

as well as vortex stretching and vortex tilting. As a result, the flow reaching the downstream cylinder has less energy at the lower frequencies. As a consequence of these characteristics of the force signal, the cylinder response also shows marked peaks at the shedding frequency and its third harmonic. However, it is also clear that a significant part of the displacement energy is concentrated at the lower frequencies, and the importance of this part of the spectrum increases with the Reynolds number. This trend is consistent with what is observed in the experiments performed at moderate Reynolds numbers (Assi, 2009), in which most of the energy is concentrated at low frequencies of vibration.

## 5. Conclusion

In this paper, we have investigated the flow-induced vibration of a circular cylinder subjected to wake interference, at infinite reduced velocities. The results confirm that the presence of the wake upstream of the cylinder lead to higher amplitudes of vibration when compared to vortex-induced vibration (VIV). Furthermore, it was shown that, differently than what is observed for VIV with mass ratios above the critical value found by Govardhan and Williamson (2002), there is not a delimited range of reduced velocities for which the vibration occurs with significant amplitude. We have highlighted the differences between the results obtained with two- and three-dimensional simulations and suggested explanations for the behaviours observed. In the near future, we will try to stretch the Reynolds number range to reach values up to 2000, so as to have a more complete picture of the response of the cylinder from the onset of the transition in the wake ( $Re \approx 150$ ) until the end of the crisis in the lift coefficient ( $Re \approx 2000$ ).

## Acknowledgment

Bruno S. Carmo would like to acknowledge the support from FAPESP through grant 2011/00131-2.

## References

- Assi, G.R.S., 2009. Mechanisms for Flow-Induced Vibration of Interfering Bluff Bodies. Ph.D. Thesis, Imperial College London.
- Assi, G.R.S., Meneghini, J.R., Aranha, J.A.P., Bearman, P.W., Casaprima, E., 2006. Experimental investigation of flow-induced vibration interference between two circular cylinders. *Journal of Fluids and Structures* 22, 819–827.
- Batina, J.T., 1990. Unsteady euler airfoil solutions using unstructured dynamic meshes. *AIAA Journal* 28, 1381–1388.
- Bokaian, A., Geoola, F., 1984. Wake-induced galloping of two interfering circular cylinders. *Journal of Fluid Mechanics* 146, 383–415.

- Brika, D., Laneville, A., 1999. The flow interaction between a stationary cylinder and a downstream flexible cylinder. *Journal of Fluids and Structures* 13, 579–606.
- Carmo, B.S., Meneghini, J.R., Sherwin, S.J., 2010a. Possible states in the flow around two circular cylinders in tandem with separations in the vicinity of the drag inversion spacing. *Physics of Fluids* 22, 054101.
- Carmo, B.S., Meneghini, J.R., Sherwin, S.J., 2010b. Secondary instabilities in the flow around two circular cylinders in tandem. *Journal of Fluid Mechanics* 644, 395–431.
- Carmo, B.S., Sherwin, S.J., Bearman, P.W., Willden, R.H.J., 2011. Flow-induced vibration of a circular cylinder subjected to wake interference at low Reynolds number. *Journal of Fluids and Structures* 27, 503–522.
- Causin, P., Gerbeau, J., Nobile, F., 2005. Added-mass effect in the design of partitioned algorithms for fluid–structure problems. *Computer Methods in Applied Mechanics and Engineering* 194, 4506–4527.
- Förster, C., Wall, W.A., Ramm, E., 2007. Artificial added mass instabilities in sequential staggered coupling of nonlinear structures and incompressible viscous flows. *Computer Methods in Applied Mechanics and Engineering* 196, 1278–1293.
- Govardhan, R., Williamson, C.H.K., 2002. Resonance forever: existence of a critical mass and an infinite regime of resonance in vortex-induced vibration. *Journal of Fluid Mechanics* 473, 147–166.
- Hover, F.S., Triantafyllou, M.S., 2001. Galloping response of a cylinder with upstream wake interference. *Journal of Fluids and Structures* 15, 503–512.
- Jester, W., Kallinderis, Y., 2004. Numerical study of incompressible flow about transversely oscillating cylinder pairs. *Journal of Offshore Mechanics and Arctic Engineering—Transactions of the ASME* 126, 310–317.
- Karniadakis, G.E., Sherwin, S.J., 2005. *Spectral/hp Element Methods for Computational Fluid Dynamics*, 2nd edition Oxford University Press, Oxford, UK.
- King, R., Johns, D.J., 1976. Wake interaction experiments with two flexible circular cylinders in flowing water. *Journal of Sound and Vibration* 45, 259–283.
- Mittal, S., Kumar, V., 2001. Flow-induced oscillations of two cylinders in tandem and staggered arrangements. *Journal of Fluids and Structures* 15, 717–736.
- Newmark, N.M., 1959. A method of computation for structural dynamics. *Journal of the Engineering Mechanics Division of ASCE* 85, 67–94.
- Noca, F., Park, H.G., Gharib, M., 1998. Vortex formation length of a circular cylinder ( $300 < Re < 4000$ ) using DPIV. In: Bearman, P.W., Williamson, C.H.K. (Eds.), *Proceedings of Bluff Body Wakes and Vortex-Induced Vibration*, ASME Fluids Engineering Division, Washington, DC, pp. 46.
- Papaioannou, G.V., Yue, D.K.P., Triantafyllou, M.S., Karniadakis, G.E., 2008. On the effect of spacing on the vortex-induced vibrations of two tandem cylinders. *Journal of Fluids and Structures* 24, 833–854.
- Zdravkovich, M.M., 1985. Flow-induced oscillations of two interfering circular cylinders. *Journal of Sound and Vibration* 101, 511–521.

# The role of wake stiffness on the wake-induced vibration of the downstream cylinder of a tandem pair

G. R. S. Assi<sup>1,†</sup>, P. W. Bearman<sup>2</sup>, B. S. Carmo<sup>3</sup>, J. R. Meneghini<sup>3</sup>,  
S. J. Sherwin<sup>2</sup> and R. H. J. Willden<sup>4</sup>

<sup>1</sup>Department of Naval Architecture and Ocean Engineering, University of São Paulo, São Paulo, 05508-030, Brazil

<sup>2</sup>Department of Aeronautics, Imperial College, London SW7 2AZ, UK

<sup>3</sup>Department of Mechanical Engineering, University of São Paulo, São Paulo, 05508-030, Brazil

<sup>4</sup>Department of Engineering Science, University of Oxford, Oxford OX1 3PJ, UK

(Received 22 March 2012; revised 23 October 2012; accepted 3 December 2012;  
first published online 8 February 2013)

When a pair of tandem cylinders is immersed in a flow the downstream cylinder can be excited into wake-induced vibrations (WIV) due to the interaction with vortices coming from the upstream cylinder. Assi, Bearman & Meneghini (*J. Fluid Mech.*, vol. 661, 2010, pp. 365–401) concluded that the WIV excitation mechanism has its origin in the unsteady vortex–structure interaction encountered by the cylinder as it oscillates across the wake. In the present paper we investigate how the cylinder responds to that excitation, characterising the amplitude and frequency of response and its dependency on other parameters of the system. We introduce the concept of *wake stiffness*, a fluid dynamic effect that can be associated, to a first approximation, with a linear spring with stiffness proportional to  $Re$  and to the steady lift force occurring for staggered cylinders. By a series of experiments with a cylinder mounted on a base without springs we verify that such wake stiffness is not only strong enough to sustain oscillatory motion, but can also dominate over the structural stiffness of the system. We conclude that while unsteady vortex–structure interactions provide the energy input to sustain the vibrations, it is the wake stiffness phenomenon that defines the character of the WIV response.

**Key words:** flow-structure interactions, vortex streets, wakes/jets

## 1. Introduction

*Wake-induced vibration* (WIV) is a fluid-elastic mechanism able to excite into transverse oscillatory motion a bluff body immersed in a wake generated from another body positioned upstream. In the present study we are concerned with the WIV of the downstream cylinder of a tandem pair. WIV differs from the well-studied phenomenon of *vortex-induced vibration* (VIV) in the sense that the excitation is not

<sup>†</sup> Present address: NDF Research Group, Dept. Eng. Naval e Oceânica, Escola Politécnica da Universidade de São Paulo, Av. Professor Mello Moraes 2231, 05508-030, São Paulo, SP, Brazil. Email address for correspondence: [g.assi@usp.br](mailto:g.assi@usp.br)

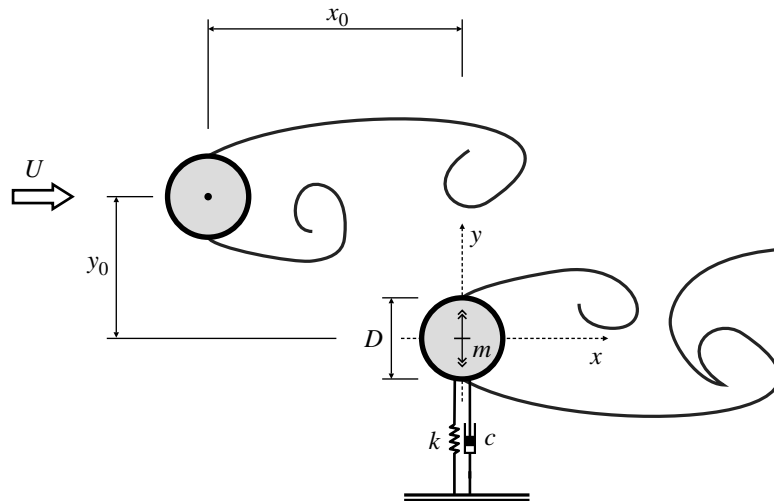


FIGURE 1. Arrangement of a pair of cylinders. The static upstream cylinder may be removed during experiments with a single cylinder. Solid lines represent hypothetical interaction between shear layers.

generated in the vortex shedding mechanism of the body itself, but it comes from the interaction with a wake developed farther upstream. In addition to that, while VIV is a resonant phenomenon, WIV does not depend on the fluid excitation matching the natural frequency of the structure. This will be explained in detail later.

In the past literature, WIV has also been referred to as: ‘interference galloping’ (Ruscheweyh 1983), ‘wake-induced galloping’ (Bokaian & Geoola 1984) and ‘wake-displacement excitation’ (Zdravkovich 1988). Nevertheless, later in the present work it will become clear why we hold to the WIV terminology.

In order to investigate the fundamental physics behind the phenomenon we study the simplest case consisting of two circular cylinders with the same diameter initially aligned with the flow. The basic arrangement is illustrated in figure 1, where  $x_0$  and  $y_0$  define the initial geometry of the pair. In the present work, the upstream cylinder is always static while the downstream cylinder is allowed to respond with oscillations in one degree of freedom (1-dof) in the cross-flow direction only.

Previous works found that the typical WIV response is characterized by an asymptotic build-up of amplitude with increasing reduced velocity. In one of them, Assi, Bearman & Meneghini (2010) investigated the origin of the fluid force involved in the excitation of the second cylinder. It has been concluded that WIV is indeed a wake-dependent type of *flow-induced vibration* (FIV), yet it was found that the unsteadiness of the wake plays a critical role in the WIV excitation mechanism and not simply the displacement of a steady flow field. It has been suggested that the WIV mechanism is sustained by unsteady vortex–structure interactions that input energy into the system as the downstream cylinder oscillates across the upstream wake. It has been shown that, in WIV, the upstream static body sheds vortices as an isolated cylinder while the downstream elastic body responds with oscillations at a different frequency. For flow velocities far beyond the typical VIV resonance the upstream vortex shedding frequency ( $f_s$ ) can be many times the natural frequency ( $f_0$ ), and yet the body will respond with severe vibrations.

Assi *et al.* (2010) showed that WIV is not a resonant phenomenon. Coherent vortices impinging on the second cylinder and merging with its own vortices induce fluctuations in lift that are not synchronized with the motion. While VIV finds

its maximum amplitude of vibration at the resonance when  $f_s \approx f_0$ , WIV response keeps increasing even when  $f_s$  is much higher than  $f_0$ . Nonetheless, for the sake of classification, WIV is essentially a type of vortex-induced mechanism in the sense that it requires the interaction of the structure with vortices, even though these vortices are coming from an upstream wake.

So far, this is what is known from previous research efforts as recently highlighted in Assi *et al.* (2010). In the present paper we will concentrate our attention on what we call the ‘character’ of the vibration. In other words, once we have understood why vibrations are excited and sustained (Assi *et al.* 2010), we are able to investigate how the cylinder responds to that excitation. Our objective is to characterize the response (amplitude and frequency) and its dependence on other parameters of the system, such as Reynolds number,  $x_0$  separation, structural stiffness and structural damping. Thus, the present paper is a continuation of the work presented in Assi *et al.* (2010).

### 1.1. WIV response of the downstream cylinder

Reflecting a need from the heat-exchanger industry, the earliest experiments to measure the response due to WIV of a pair of cylinders were performed with flexible tubes in order to supply data to design engineers. A more complete understanding of the fluid mechanics of the phenomenon was gradually developed when researchers started to limit the number of variables, performing tests with rigid cylinders in 2-dof. A further step was to simplify even more and allow a rigid cylinder only to vibrate either in the in-line or in the cross-flow direction. First, let us present some previous data found in the literature (including figures reproduced in this paper) that will be useful to support our conclusions.

King & Johns (1976) performed experiments in water ( $Re = 10^3$ – $2 \times 10^4$ ) with two flexible cylinders for separations in the range  $x_0/D = 0.25$ – $6.0$ . They observed that for  $x_0/D = 5.5$  the upstream cylinder responded with a typical VIV curve reaching amplitudes around  $\hat{y}/D = 0.45$  at the resonance peak, comparable to their tests with a single cylinder at same  $Re$ . On the other hand the downstream cylinder also started to build up oscillations together with the upstream one, but instead of the oscillations disappearing after the synchronization range they remained at roughly the same level for reduced velocities up to the highest tested. They identified the response of the second cylinder as a type of buffeting, since it originated from the wake interference coming from the upstream cylinder.

Brika & Laneville (1999) performed tests with a pair of long tubes in a wind tunnel with a flexible cylinder positioned from 7 to 25 diameters downstream of a rigid cylinder for Reynolds number between 5000 and 27 000. A series of curves for different separations reveal that as  $x_0$  increases the interference effect from the upstream wake is reduced until the response resembles that of a single cylinder without any (or with very little) interference. It is interesting to note that even between separations of 16 and 25 diameters the authors were still able to identify some change in the interference effect with the second cylinder positioned so far downstream. Because their experiment was performed in air, the mass ratio  $m^*$  (the ratio between the mass of the structure and the mass of displaced fluid) was two orders of magnitude higher than other experiments in water. Yet their damping parameter  $\zeta$  was extremely low, resulting in a combined mass-damping of only  $m^*\zeta = 0.068$ .

Moving from flexible to rigid cylinders, we recall experiments performed by Zdravkovich (1985) with two rigid cylinders free to respond in 2-dof mounted in a wind tunnel ( $Re = 1.5 \times 10^4$ – $9.5 \times 10^4$ ,  $m^* = 725$  and  $\zeta = 0.07$ ). Due to a very high mass-damping parameter of  $m^*\zeta = 50$ , Zdravkovich was only able to observe



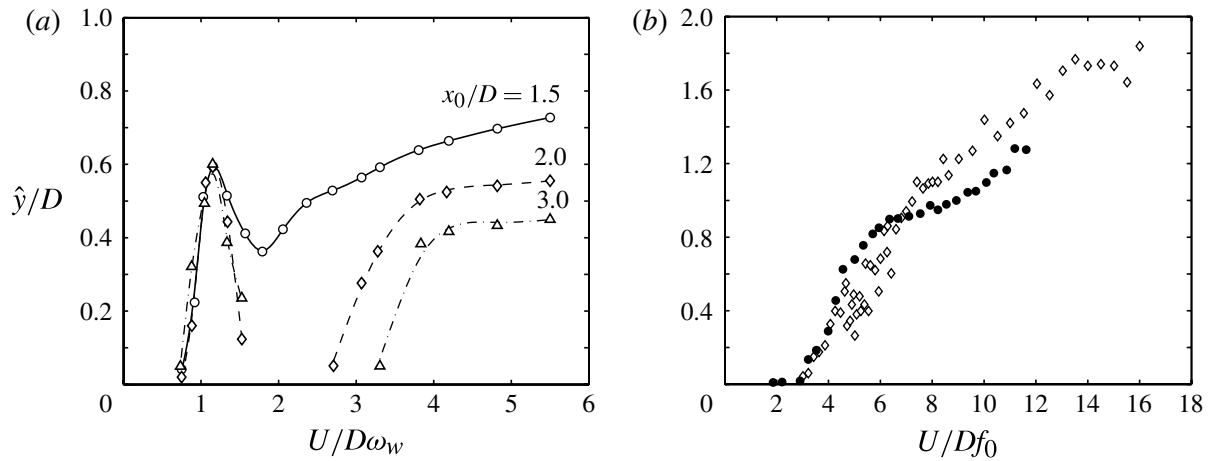


FIGURE 2. Response in the cross-flow direction of the downstream cylinder under WIV. (a) Varying  $x_0$ ,  $m^* = 8.4$ ,  $\zeta = 0.013$ ,  $Re = 700$ – $2000$ ,  $\omega_w$  is the natural frequency in radians per second measured in still water (Bokaian & Geoola 1984). (b)  $\diamond$ ,  $x_0/D = 4.75$ ,  $m^* = 3.0$ ,  $\zeta = 0.04$ ,  $Re = 3 \times 10^4$  (Hover & Triantafyllou 2001);  $\circ$ ,  $x_0/D = 4.0$ ,  $m^* = 1.9$ ,  $\zeta = 0.007$ ,  $Re = 3000$ – $13\,000$  (Assi *et al.* 2006).

a build-up of oscillations at  $x_0/D = 4.0$  for reduced velocities beyond  $U/Df_0 = 50$ , asymptotically reaching a maximum of  $\hat{y}/D = 1.7$  for the last point of his experiments at around reduced velocity 80. Nevertheless, he has also recorded a monotonically increasing branch of response that was qualitatively very similar to those results later presented by Brika & Laneville (1999). In a subsequent study of the effect of mass and damping, Zdravkovich & Medeiros (1991) performed similar 2-dof tests in a wind tunnel varying  $m^*\zeta$  between 6 and 200 ( $Re = 5 \times 10^3$ – $1.4 \times 10^5$ ). Once more, the cross-flow vibrations presented the same monotonic-asymptotic behaviour with the amplitude increasing with the reduced velocity. Their results revealed a strong dependence of the response on  $m^*\zeta$ , but more importantly showed that very high values of mass-damping are required to inhibit WIV of the second cylinder. Maximum amplitude was obtained at a maximum reduced velocity of 120, but in order to reduce the amplitude  $\hat{y}/D$  by half (from 2.2 to 1.1) it was required to increase  $m^*\zeta$  ten times (from 6.4 to 64).

Going one step further in the simplification of the problem, we find a few results from Bokaian & Geoola (1984) who performed experiments for two rigid cylinders in tandem responding only in 1-dof in a water channel. The upstream cylinder was fixed while the downstream cylinder was elastically mounted on air bearings and free to respond only in the cross-flow direction. They varied centre-to-centre separation in the range of  $x_0/D = 1.09$ – $5.0$ . Results for amplitude of response versus reduced velocity (with  $\omega_w$  being the natural frequency in radians per second measured in still water) are presented in figure 2(a) for three values of  $x_0$  tested. A vigorous build-up of oscillations with increasing flow speed is observed for all flow speeds greater than a critical threshold velocity. Such a severe 1-dof vibration was observed to resemble the response of classical galloping of non-circular bodies; therefore it was referred to as ‘wake-induced galloping’. They noted that ‘galloping carries the strong connotation of a negatively damped single degree of freedom oscillation, and its use to describe the problem under study is only because of the many similarities between the two kinds of instability’. However, elsewhere in their work Bokaian & Geoola (1984) stated that ‘whilst some characteristics of *wake-excited galloping* were found to be similar to those of galloping of sharp-edged bodies, others were observed to be fundamentally



different'. The authors concluded that depending on  $x_0$ ,  $m^*$  and  $\zeta$  the downstream cylinder 'exhibited a vortex-resonance, or a galloping, or a combined vortex-resonance and galloping, or a separated vortex-resonance and galloping' response. In figure 2(a) two examples of these different responses are found: results for  $x_0/D = 1.5$  present a vortex resonance that is followed by (or combined with) a 'galloping' response at about reduced velocity 2; results for  $x_0/D = 2.0$  and 3.0 present separated vortex-resonance and 'galloping' regimes. A pure vortex resonance is not shown in figure 2(a) but this would be similar to what we understand as a typical VIV response.

Hover & Triantafyllou (2001) measured displacements of and forces on rigid cylinders under WIV in a water towing tank at a constant Reynolds number. They made use of a closed-loop control system that forces the oscillation of the cylinder in response to a measured and integrated fluid force. In this way they cleverly tuned the mass, damping and stiffness parameters ( $m$ - $c$ - $k$ ) in an equation of motion in order to generate any artificial combination of  $f_0$ ,  $m^*$  and  $\zeta$ . As a result, their curve presented in figure 2(b) was obtained for  $Re = 3 \times 10^4$  adjusting  $f_0$  in order to vary the reduced velocity from 3 to 12. The resulting parameter  $m^*\zeta = 0.12$  is very close to  $m^*\zeta = 0.11$  obtained by Bokaian & Geoola (1984) in figure 2(a); however the difference in the level of amplitude might be related to a difference of one order of magnitude in  $Re$ , as will be discussed later. For a separation of  $x_0/D = 4.75$ , Hover & Triantafyllou (2001) observed one single branch of response that builds up monotonically reaching amplitudes of  $[\hat{y}/D]_{max} = 1.9$  for reduced velocities around 17 (their curve represents an average of the 10% highest peaks of displacement). Although they referred to the branch of high amplitude as an 'upward extension of the frequency lock-in branch' that occurs for the VIV response of a single cylinder, there is no evidence that the vortex shedding frequency of either cylinder is synchronized with the frequency of oscillation; on the contrary, their results reveal that vibrations occur 'without any clear signature of vortex resonance'.

More recently, Assi *et al.* (2006) performed 1-dof experiments with two rigid cylinders in a recirculating water channel ( $Re = 3 \times 10^3$ – $1.3 \times 10^4$ ). Their results, also presented in figure 2(b), are comparable to those of Hover & Triantafyllou (2001) since they have a similar  $Re$  range; however Assi *et al.* (2006) employed a very low-damping elastic system resulting in  $m^*\zeta = 0.013$ , one order of magnitude lower. Both curves are in good agreement showing an expected branch of high-amplitude oscillation building up as the reduced velocity is increased. In addition, the data points from Assi *et al.* (2006) also reveal a smooth hump corresponding to a local vortex-resonance response around  $U/Df_0 = 6.0$ .

Later in this paper we shall return to some of these results in order to compare our data and support our conclusions.

### 1.2. Steady fluid forces on staggered cylinders

It is known that the downstream cylinder of a staggered pair experiences a steady lift force even if the bodies are held static in the flow (Price 1976; Bokaian & Geoola 1984). Zdravkovich (1977) presents a map of steady fluid forces acting on a cylinder across the wake for separations as large as  $x_0/D = 5.0$ . His results, which are in agreement with many other maps in the literature, clearly show that the steady lift always points towards the centreline of the wake, i.e. as restoring the staggered downstream cylinder back to the tandem configuration. The steady lift is zero on the centreline of the wake, increases as the second cylinder is displaced towards the wake interference boundary and is reduced as the body is positioned farther out of the wake. Assi *et al.* (2010) have suggested that such a strong steady lift is induced

by the unsteady interaction of vortices present in the wake coming from the upstream cylinder. In a controlled experiment, the periodic unsteadiness associated with vortex shedding was removed from the upstream wake, leaving only a steady shear profile generated by a set of screens. It was shown that the steady lift acting on a static downstream cylinder was considerably reduced if coherent vortices were not present in the upstream wake.

Igarashi (1981) and others have identified two distinct regimes in the wake formed in the gap between tandem cylinders. The first regime occurs when the proximity of the cylinders allows the shear layers that separate from the upstream cylinder to reattach to the second body and a vortex street is not developed in the gap. The second regime, which normally occurs for larger separations, is characterized by the existence of a developed vortex wake in the gap. The force map presented by Zdravkovich (1977) shows that distinct regimes also appear for staggered arrangements and a steady lift force presents two prominent regions associated with different wake regimes. In the present work we are only interested in the second regime, i.e. the force field and vibration generated when a developed wake is present in the gap. The transition from the first to the second regime has a small influence of  $Re$ , but most of the investigations agree that the critical separation is between  $x_0/D = 3.0$  and  $4.0$ .

Bokaian & Geoola (1984) presented more detailed measurements of the steady lift  $\bar{C}_y$  acting across the wake for three separations of 3.0, 4.0 and 5.0 diameters and  $Re = 5900$ . Their measurements made it clear that the maximum lift towards the centreline decreases as the second cylinder moves farther downstream. While the steady drag  $\bar{C}_x$  is minimum on the centreline, due to the shielding effect of the upstream wake,  $\bar{C}_y$  is minimum around  $y_0/D = 1.0$ . This brings us back to the definition of interference regions proposed by Zdravkovich (1977). He says that ‘the wake boundary is a line along which the (mean) velocity becomes the same as the free stream one. The (wake) interference boundary is the line along which (the mean) lift force becomes zero or negligible’. These two lines do not necessarily coincide, but the wake interference boundary is always outside the wake boundary. It will become clearer later that the interaction between flow and structure occurring within the wake boundary is fundamental to WIV.

### 1.3. Vortex-induced vibration of a single cylinder

Before starting our analysis of WIV, we briefly review the modelling employed to understand other types of flow-induced vibrations, especially vortex-induced vibration (VIV), which has its origin in the cyclic loads generated by vortices shed from a bluff body. It has been extensively reviewed in the literature (Sarpkaya 1979; Bearman 1984; Parkinson 1989; Blevins 1990; Zdravkovich 1997; Williamson & Govardhan 2004), but some of the basic modelling is mentioned here since it will be employed to model WIV later in this paper.

An elastic cylinder will be modelled by its structural properties: mass ( $m$ ), stiffness ( $k$ ) and damping ( $c$ ). Allowing for displacements only in one degree of freedom (1-dof) in the  $y$ -axis, the equation of motion per unit length becomes

$$m\ddot{y} + c\dot{y} + ky = \frac{1}{2}\rho U^2 D \left[ \bar{C}_y + \hat{C}_y \sin(2\pi ft + \phi) \right], \quad (1.1)$$

where  $y$ ,  $\dot{y}$  and  $\ddot{y}$  are respectively the displacement, velocity and acceleration of the body, leaving the term on the right-hand side of the equation to represent the time-dependent fluid force in the cross-flow direction. As proposed by Bearman (1984) and others, the displacement of a cylinder under VIV may be expressed by the harmonic

response

$$y(t) = \hat{y} \sin(2\pi ft), \quad (1.2)$$

where  $\hat{y}$  and  $f$  represent the harmonic amplitude and frequency of oscillation. For large-amplitude oscillation under a steady-state regime of VIV the fluid force and the body response oscillate at the same frequency  $f$ , which is usually close to the natural frequency of the system. According to this ‘harmonic forcing and harmonic motion’ hypothesis the fluid force can be divided into a time-average term  $\bar{C}_y$  and a transient term modelled as a sine wave with amplitude  $\hat{C}_y$  and frequency  $f$ . For body excitation to occur, the phase angle between  $y(t)$  and  $C_y(t)$  must be between  $\phi = 0$  and  $180^\circ$ .

A second-order oscillator presents an undamped natural frequency that only takes into account the structural stiffness and mass of the system ( $f_0 = \sqrt{k/4\pi^2 m}$ ). The structural damping is generally expressed by a damping ratio  $\zeta$ , defined as a fraction of the critical damping ( $\zeta = c/\sqrt{4km}$ ). If  $\zeta$  is kept sufficiently low, the damped natural frequency can be considered approximately equal to  $f_0$ . It is useful to present the flow speed in terms of a reduced velocity  $U/Df_0$ . The reduced velocity for maximum VIV response occurs around  $U/Df_s$  (the inverse of the Strouhal number), that is at the resonance where the vortex shedding frequency  $f_s$  is equal to  $f_0$ .

According to Bearman (1984) the VIV response is inversely proportional to the product of  $m^*$  and  $\zeta$ , yielding the non-dimensional amplitude of vibration as

$$\frac{\hat{y}}{D} = \frac{1}{4\pi^3} \hat{C}_y \sin \phi \left( \frac{U}{Df_0} \right)^2 \left( \frac{1}{m^* \zeta} \right) \left( \frac{f_0}{f} \right). \quad (1.3)$$

Bearman (1984) states that ‘It is clear that the phase angle  $\phi$  plays an extremely important role. The amplitude response does not depend on  $\hat{C}_y$  alone but on that part of  $\hat{C}_y$  in phase with the body velocity. Hence, measurements of just the sectional fluctuating lift coefficient on a range of stationary bluff-body shapes will give little indication of the likely amplitudes of motion of similar bodies flexibly mounted’. Therefore, the combined  $\hat{C}_y \sin \phi$  term is fundamental in an unsteady analysis of the phenomenon.

## 2. Experimental set-up and validation with a single cylinder

The experimental set-up employed in the present study is exactly the same as that described in Assi *et al.* (2010). For further details, refer to Assi (2009). It is worth recalling here that a pair of coil springs connecting the moving base to the fixed supports provided the restoration force of the system. All the moving parts of the elastic base contributed to the effective mass oscillating along with the cylinder resulting in a mass ratio of  $m^* = 2.6$  (calculated as the total oscillating mass divided by the mass of water displaced by the cylinder). By carrying out free decay tests in air it was also possible to estimate the structural damping of the system as  $\zeta = 0.7\%$ , calculated as a percentage of the critical damping. Therefore, the mass-damping parameter was  $m^* \zeta = 0.018$  for the majority of the experiments.

In order to validate the experimental set-up and obtain reference data for comparison, a preliminary experiment was performed with a single cylinder free to oscillate in 1-dof in a uniform flow. These results have been discussed in more detail in Assi *et al.* (2010); therefore they will be presented very briefly here to allow comparison with the main WIV data to be discussed later.

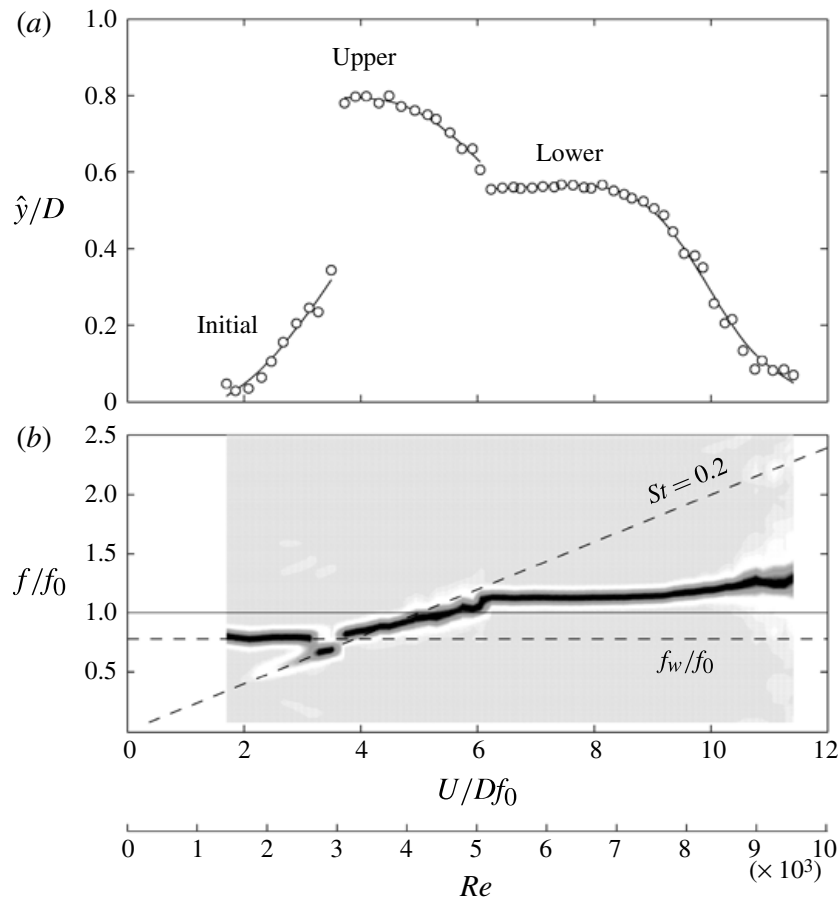


FIGURE 3. VIV response of a single cylinder free to oscillate in the cross-flow direction. Reproduced from Assi *et al.* (2010).

The typical VIV response, in terms of amplitude and frequency of oscillation, is presented in figure 3 and shows a good agreement with the results reviewed by Williamson & Govardhan (2004). The three typical branches of response, *initial*, *upper* and *lower*, are clearly identified in the displacement curve. Fluid force measurements (not presented in this paper) were in good agreement with the results presented by Khalak & Williamson (1999) and can be found in Assi *et al.* (2010). Figure 3 also shows the frequency response normalized by the natural frequency ( $f/f_0$ ); variation from light to dark grey represents higher peaks in the normalized power spectral density (PSD) of the frequency of oscillation (refer to Assi 2009 for more details). (The  $f_w/f_0$  line will be explained later.)

Throughout the study, the cylinder displacement amplitude normalized by the cylinder diameter ( $\hat{y}/D$ ) was found by measuring the r.m.s. value of response and multiplying by  $\sqrt{2}$ . Such a harmonic amplitude assumption is likely to give an underestimation of maximum response but was judged to be perfectly acceptable for assessing the average amplitude of response for many cycles of steady-state oscillations. The same procedure was employed to determine the magnitude of all other fluctuating variables, such as  $\hat{C}_y$  and  $\hat{C}_x$ .

### 3. Results: WIV response of the downstream cylinder

The characteristic build-up of response for higher reduced velocities, reported in previous works, is clearly observed in figure 4 and contrasts with the typical VIV

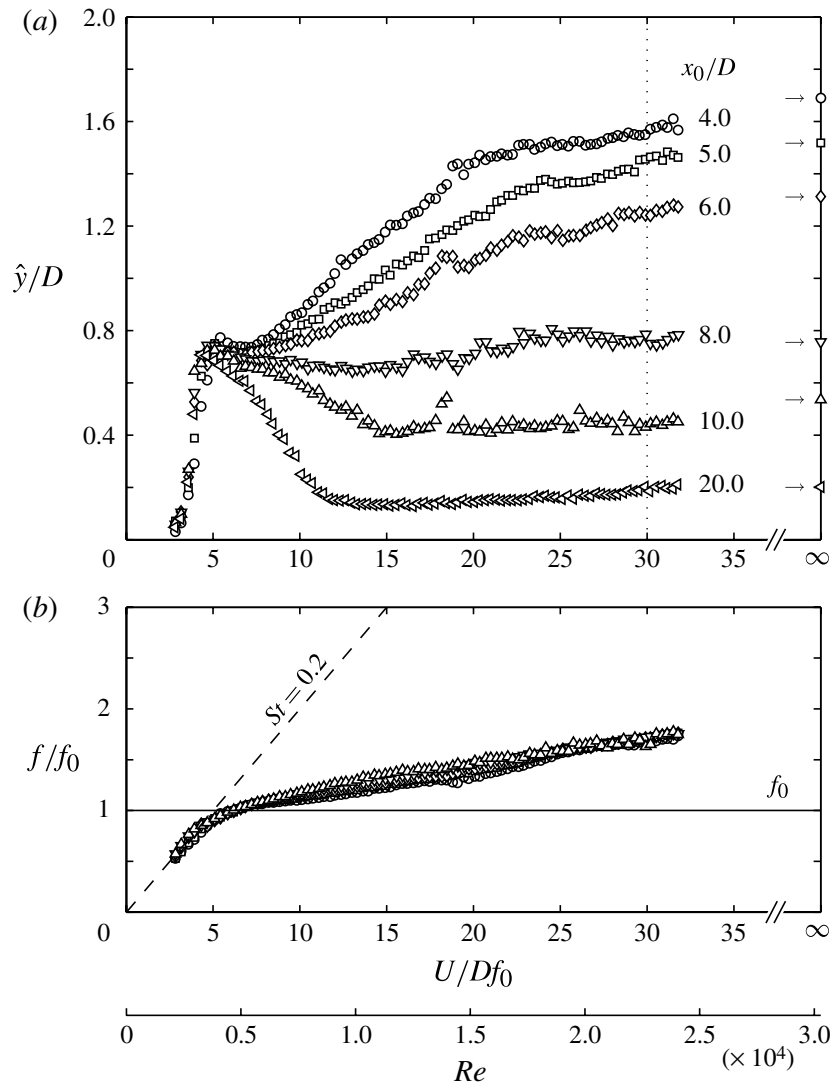


FIGURE 4. WIV response of the downstream cylinder for various  $x_0$  separations: (a) displacement; (b) dominant frequency of oscillation.

response obtained for a single cylinder in figure 3. A discrete hump is found to occur for all centre-to-centre separations at around  $U/Df_0 = 5.0$  and corresponds to the local peak of VIV resonance, although this happens slightly later in the reduced velocity scale due to the shielding effect of the wake that reaches the downstream cylinder. Beyond that, for higher reduced velocities, a branch of monotonically increasing amplitude starts to build up showing different levels of vibration for each separation. As expected, it reveals that displacement amplitude is inversely proportional to the separation  $x_0$ . As the downstream cylinder is moved farther away, the effect of WIV is reduced until the response curve eventually resembles that of VIV of an isolated cylinder. While at  $x_0/D = 4.0$  the cylinder reaches displacement amplitudes around  $\hat{y}/D = 1.6$ , a cylinder at  $x_0/D = 20$  shows only the VIV peak with levels of  $\hat{y}/D$  around 0.2 for the rest of the regime. The curve for  $x_0/D = 8.0$  is a particularly interesting one because the intensity of the WIV effect is just enough to sustain the same level of response observed for VIV through the whole range of reduced velocities. Nevertheless, all presented cases show some type of combined VIV and WIV response, with the maximum amplitude of VIV at  $U/Df_0 = 5.0$  showing a minor dependence on  $x_0$ .



Since WIV has its origin in the wake developed in the gap between the cylinders, it is expected that the centre-to-centre separation between a tandem pair has a major effect on the response of the downstream body. In Assi *et al.* (2010) we have suggested that as  $x_0/D$  is increased the fluid force induced by upstream vortices is reduced due to diffusion of vorticity and increasing flow three-dimensionality. This theory is supported by the results presented in figure 4 showing that the response curve has indeed a strong dependence on  $x_0$ . Our results are in good qualitative agreement with those of Laneville & Brika (1999) even though they have performed tests with flexible tubes.

Figure 4(b) shows the dominant frequency of oscillation for each case plotted above. At first sight it is remarkable that all data points collapse over the range of separations investigated. During the beginning of the VIV regime the frequency curve follows closely the  $St = 0.2$  line until  $f = f_0$ , but later it departs from this line to follow the lock-in behaviour observed for a single cylinder within the synchronization regime. But where the typical VIV regime would have finished for a single cylinder, say for  $U/Df_0 > 15$ , the  $f/f_0$  curve remains on the same trend as before, which is distinctively lower than  $St = 0.2$ . Even for larger separations of  $x_0/D = 20$ , in which the response resembles that of simple VIV, the dominant frequency is observed not to return to  $St = 0.2$  after the end of the supposed synchronization, but instead it remains at a much lower level for the rest of the reduced velocity range with  $\hat{y}/D$  around 0.2.

This is the first evidence that there must be a fluid force with a lower frequency that sustains the response – a frequency that is lower than the vortex shedding frequency of both cylinders. The frequency of this fluid force appears not to vary with  $x_0$  and shows only a small dependence on reduced velocity or Reynolds number when compared to the  $St = 0.2$  line, for example.

### 3.1. WIV response of the downstream cylinder at $x_0/D = 4.0$

In order to investigate the mechanism behind WIV we will now concentrate our attention on a single separation; later we shall return to the effect of  $x_0/D$  on the response. A separation of  $x_0/D = 4.0$  was chosen for various reasons: (i) it was beyond the critical separation where a bistable reattachment of the shear layers may occur, therefore a developed wake was observed to be present in the gap for all flow speeds; (ii) it gave a WIV response that is qualitatively consistent with other larger separations, being the most energetic behaviour observed; (iii) the cylinder displacement and magnitude of fluid forces were rather large and provided accurate measurements with the load cell; (iv) and the separation was not too large to fit in the particle image velocimetry (PIV) field of view.

Figure 5 presents the WIV response of the downstream cylinder of a pair, initially in tandem, with  $x_0/D = 4.0$ . The same pair of springs was employed during the whole experiment and the velocity of the flow in the test section was varied in order to cover a large range of reduced velocity, therefore yielding  $Re = 2000$ – $25\,000$ . Figure 5(a) plots displacement versus reduced velocity with  $\hat{y}/D$  being the harmonic amplitude of displacement. Although it gives a good idea of the average amplitude of vibration for many cycles of oscillation,  $\hat{y}/D$  does not offer a good estimation of the maximum amplitude the cylinder might reach if displacement is varying from cycle to cycle. By actually counting individual peaks of oscillation it was possible to estimate a maximum and a minimum peak amplitude taking an average of the 10 % highest and 10 % lowest peaks of the whole series, yielding  $[\hat{y}/D]_{max}$  and  $[\hat{y}/D]_{min}$  respectively. Therefore we can say that for a certain reduced velocity the cylinder oscillates on average with  $\hat{y}/D$  but reaches the maximum and minimum limits given



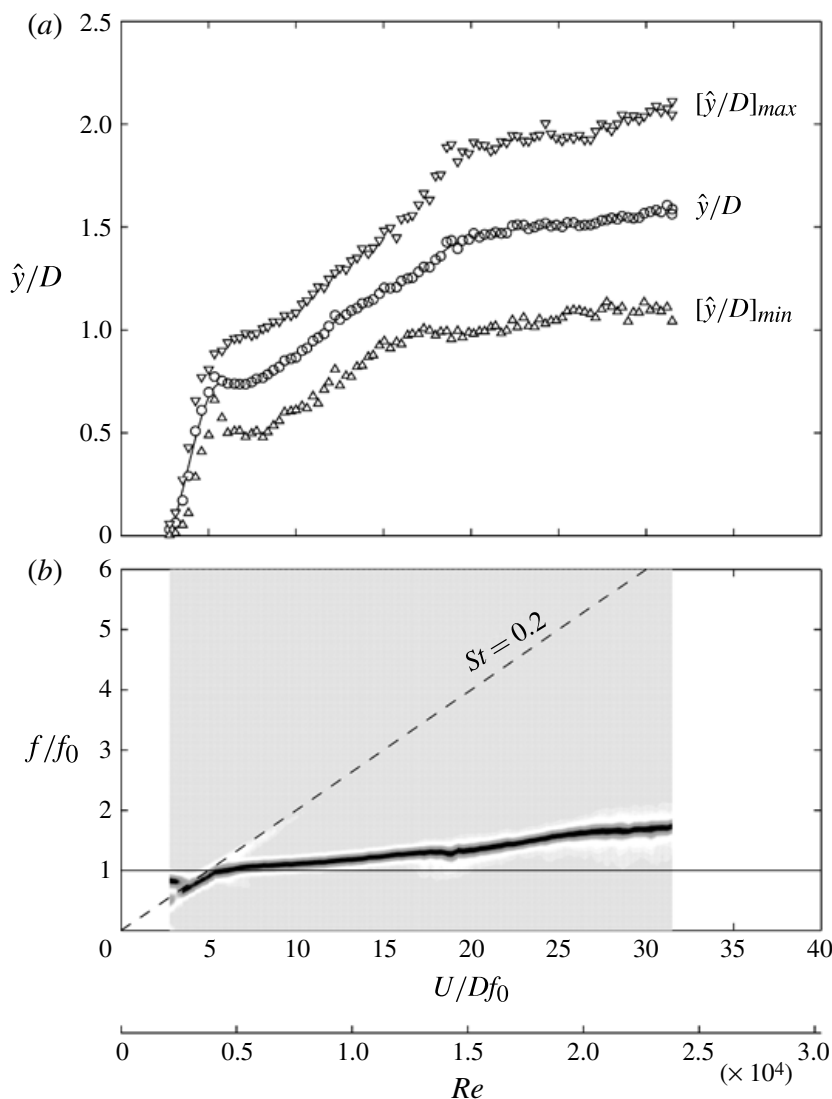


FIGURE 5. WIV response of the downstream cylinder at  $x_0/D = 4.0$ : (a) average displacement and average of maximum and minimum peaks; (b) normalized PSD of frequency of oscillation.

by the other two curves. This brings considerable new information about the response since it shows that  $\hat{y}/D$  is not only building up with reduced velocity, but also the deviation from the average amplitude is increasing, i.e. the width of the envelope is also increasing.

Figure 5(b) shows the frequency of oscillation versus reduced velocity, the same data presented for  $x_0/D = 4.0$  in figure 4 but now plotted as normalized PSD. It shows that  $f$  indeed follows a branch with values greater than  $f_0$  but still not related to  $St = 0.2$ . However, the PSD contours also reveal that any other secondary frequency or harmonic present in the spectrum of oscillation is much smaller than the single dominant branch that is evident across the reduced velocity range. That is to say that there is no significant trace of a frequency branch associated with  $St = 0.2$  beyond reduced velocity 10, with only a hint appearing between 5 and 10 (represented by white shading around the dashed line).

In Assi *et al.* (2010) we discussed in detail the behaviour of the lift force acting on both cylinders. For now it is enough to remember that the upstream cylinder

is shedding vortices as a single static body with  $St \approx 0.2$ . This was evident from measurements of lift as well as velocity fluctuation in the wake of the upstream cylinder. On the other hand, the lift force on the downstream cylinder has shown two clear branches bifurcating from the VIV resonance point (refer to figure 10 in Assi *et al.* 2010). The lowest branch corresponds to the frequency of oscillation in figure 5, but the highest branch is clearly associated with a vortex shedding frequency that follows the  $St = 0.2$  line. This frequency may originate in the vortex shedding mechanism occurring on the upstream cylinder, or on the downstream cylinder, or on both.

Looking again at the response curve in figure 5 it is quite apparent that three different regimes can be identified and related to different inclinations of the displacement curve: (i) a VIV resonance hump (upper branch) around  $U/Df_0 = 5$ ; (ii) a combined VIV (lower branch) and WIV regime roughly in the range  $U/Df_0 = 5$ –17; and (iii) a WIV regime for  $U/Df_0 > 17$ .

We conclude that the WIV response of the downstream cylinder of a pair is distinctively different from the VIV response of a single cylinder. Although some aspects are common to both types of FIV, especially those related to the overlap of VIV regime in the WIV response, others are very different. So far, it is clear that the low frequency of response observed for high reduced velocities is not directly associated with the vortex shedding mechanism of either cylinder.

#### 4. Results: steady fluid forces on static cylinders

Traditionally, quasi-steady theory has been employed in an attempt to model various fluid-elastic phenomena. Therefore, we have also performed experiments with a pair of static cylinders in order to evaluate the behaviour of fluid forces acting on the downstream body in various staggered arrangements. Measurements were obtained by holding the upstream cylinder fixed and traversing the downstream cylinder across 160 stations (each marked by a small cross in figure 6) in and out of the wake interference region at  $Re = 19\,200$ .

Figure 6(a) presents the map of steady lift (or mean lift) acting on the downstream cylinder for different regions of wake interference. A negative value of  $\bar{C}_y$  indicates lift force acting towards the centreline. As expected, the first evident observation is that the steady lift force points in the direction of the centreline for all configurations investigated. The  $\bar{C}_y$  map reveals two regions of intense steady lift as high as  $-0.8$ . The first region between  $x_0/D = 1.5$ –2.5 is associated with the gap-flow-switching mechanism (described in Zdravkovich 1977) occurring in the first wake-interference regime, i.e. when fully developed vortices do not form in the gap. The second region with intense lift occurs for larger lateral separations around  $y_0/D = 0.8$ . Beginning around  $x_0/D = 2.5$ –3.0 with  $\bar{C}_y \approx -0.8$ , it develops into a trend of maximum  $\bar{C}_y$  (indicated by the dash-dotted line) that decreases in intensity as the second cylinder moves farther downstream. For  $x_0/D > 3.0$ , it is observed that the magnitude of  $\bar{C}_y$  continually decreases on increasing the separation, but the transverse extent of the force field increases farther downstream as the wake widens. This second region is associated with the second interference regime in which the upstream shear layers are not able to reattach to the downstream cylinder but roll up to form a developed vortex wake in the gap, i.e. what we are calling WIV.

In the steady drag map presented in figure 6(b) positive contours of  $\bar{C}_x$  denote drag in the streamwise direction. Dotted lines represent contours of zero or negative drag that occur when the cylinders are close enough for the gap flow to be enclosed

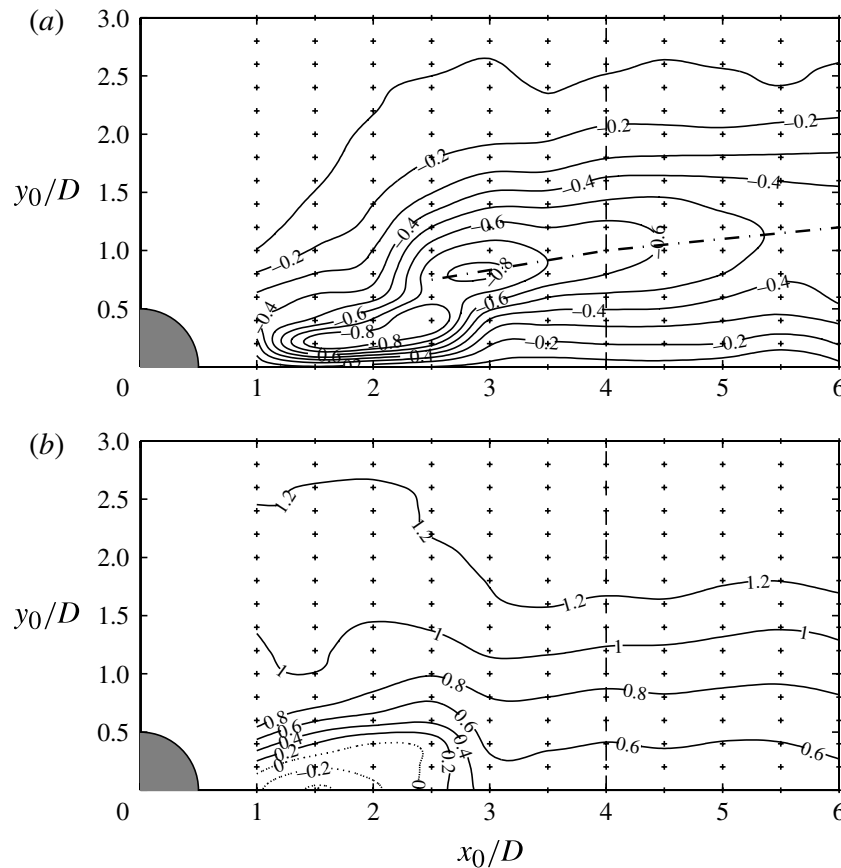


FIGURE 6. Contours of (a) steady lift ( $\bar{C}_y$ ) and (b) steady drag ( $\bar{C}_x$ ) on the downstream cylinder of a static pair.  $Re = 19\,200$ .

by the reattaching shear layers. For  $x_0/D > 2.5$  the downstream cylinder in tandem arrangement only experiences positive drag indicating that a developed wake can now be formed in the gap. This critical separation coincides with the overlap of the two trends of maximum  $\bar{C}_y$  presented in figure 6(a). While the downstream cylinder is immersed in the wake of the upstream cylinder the steady drag will be lower than that expected for a single cylinder exposed to a free stream. Only for lateral separations greater than  $y_0/D = 1.5$  does this shielding effect disappear and  $\bar{C}_x$  reaches values above 1.0. Our experimental results for the steady components are in very good agreement with other works found in the literature, including the maps produced by Zdravkovich (1977) and Bokaian & Geoola (1984).

#### 4.1. Detailed map for $x_0/D = 4.0$

Since we are concentrating our attention on  $x_0/D = 4.0$  we present a more detailed investigation of the steady fluid forces acting on the downstream cylinder for this separation. These results will be the basis for the discussion that will follow.

Starting from the  $\bar{C}_y$  and  $\bar{C}_x$  maps above, we can keep the downstream cylinder at  $x_0/D = 4.0$  and traverse it in small steps across the wake along the vertical dashed line plotted in figure 6. If we now vary  $Re$  for each one of these stations we have the detailed curves presented in figure 7. Once more, it shows that the steady lift acting on the downstream cylinder points towards the centreline of the wake for all  $y_0/D$  separations. An almost linear behaviour is observed for the range  $-1.0 < y_0/D < 1.0$  with a maximum of absolute  $\bar{C}_y = 0.65$  found just past  $y_0/D = -1.0$ . Beyond that

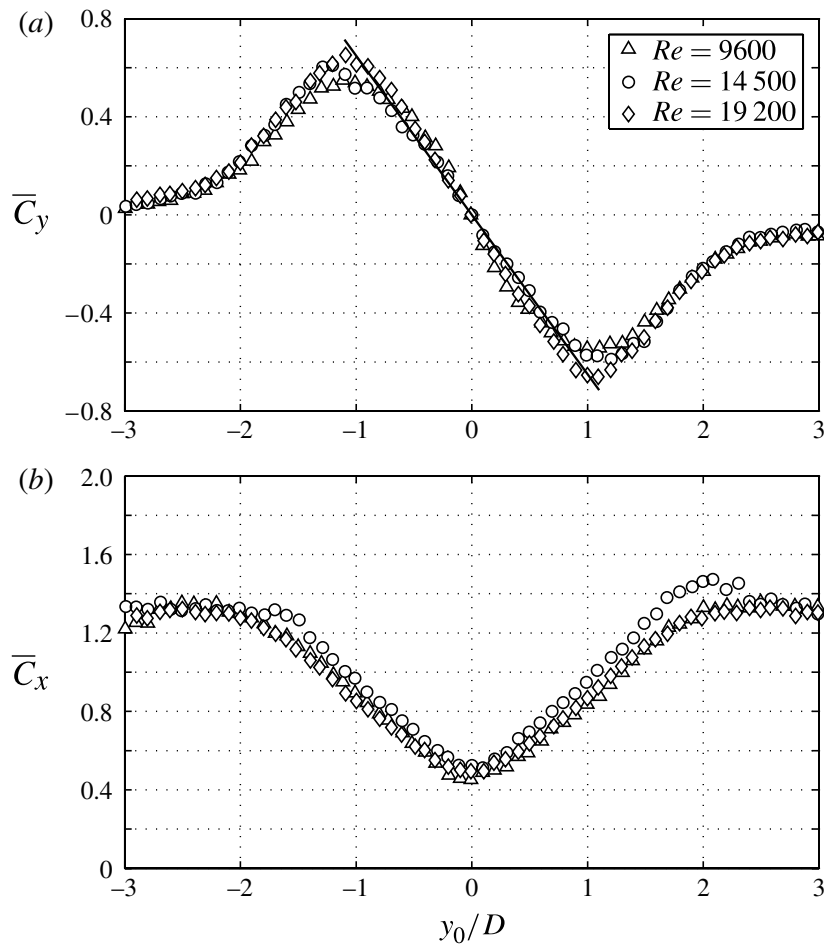


FIGURE 7. Steady fluid forces on a static downstream cylinder at  $x_0/D = 4.0$  and various staggered positions.

separation the steady lift gradually reduces until it is beyond the influence of the wake and reaches zero around  $y_0/D = 3.0$ .

In figure 7(b) the steady drag curve reveals the shielding effect of the wake by showing an almost 60 % reduction in drag at the centreline; however the mean drag never attains negative values (drag inversion) for this separation. Bokaian & Geoola (1984) observed that the distribution of the drag coefficient is insensitive to a limited increase of  $Re$  from 2600 to 5900. Price (1975) also observed the same independence from  $Re$  for a range one order of magnitude higher. We also conclude that the steady fluid forces, lift and drag, do not vary with  $Re$  for the range of the experiments ( $Re = 2000\text{--}25\,000$ ). In fact, several  $Re$  within this range were analysed but only three are plotted in figure 7 for clarity. This explains why our maps from figure 6 for  $Re = 1.9 \times 10^4$  are in good agreement with Zdravkovich's (1977) for  $Re = 6 \times 10^4$ .

## 5. Experiment without springs: $f_0 = 0$

In Assi *et al.* (2010) we performed an idealized experiment by removing the unsteadiness of the upstream wake generated by vortices being shed from the upstream cylinder. In that case we made  $f_s = 0$  and concluded that a cylinder immersed in such a steady wake would not develop WIV. We were convinced that the interaction between the oscillating cylinder and the unsteady wake from upstream is crucial to sustain the WIV mechanism. The necessary phase lag that drives and maintains the

excitation was shown to originate in this complex vortex–structure interaction. But one question was still left unanswered: Why is the cylinder oscillating at a frequency that is distinctively different from both the upstream vortex shedding frequency ( $f_s$ ) and the natural frequency of the system ( $f_0$ )? WIV turned out to be understood as a non-resonant mechanism with the amplitude of response increasing far beyond any synchronization range. The fact that the excitation mechanism is not dependent on the forcing frequency matching  $f_0$  gave us the idea of removing yet another fundamental frequency of the system. In the previous experiment we made  $f_s = 0$  by generating a steady shear profile without vortices; now we make  $f_0 = 0$  by removing the springs of the oscillator.

The same experimental set-up was employed. While mass ( $m$ ) and damping ( $c$ ) remained unchanged, the pair of springs was removed from the system so that  $k = 0$  and  $f_0 = 0$ . Therefore, for the downstream cylinder immersed in still water there was no structural stabilizing force whatsoever to keep it in position. Cylinders were initially aligned in tandem, but the downstream body would drift away from the centreline, responding to any perturbation coming from the flow or from the rig.

We found no other works on WIV of cylinders where all stiffness had been removed. Zdravkovich (1974) performed experiments with a downstream cylinder mounted on a horizontal swinging arm without springs, but he was left with a restoration force generated by the steady flow. The drag acting on the cylinder generated a stabilizing force component towards the centreline – in the same way that the weight stabilizes a vertical pendulum in free oscillation – resulting in an equivalent stiffness generated by the flow. Most of his experiments were concerned with the gap-flow-switching mechanism, hence were concentrated in the proximity interference region. For  $x_0/D < 3.5$  he observed severe vibrations with a clear dominant frequency; yet the response was abruptly reduced for separations between  $x_0/D = 3.5$ – $7.0$  with no clear dominant frequency being identified. Beyond that critical separation the downstream cylinder was not prone to gap flow switching any longer but on entering the WIV region still the expected build-up of response was not observed. Zdravkovich's experiment was performed in air and his elastic rig presented a very high damping factor of  $\zeta = 0.24$ . Probably, we believe, a high value of combined  $m^*\zeta$  was enough to suppress WIV but not gap flow switching, only proving that the content of energy in the first mechanism is lower than in the latter. Apart from this experiment we have not seen any other WIV investigation on cylinders mounted without springs – and even in this case there was still a remaining stabilizing force left due to resolved drag.

### 5.1. WIV response without springs

In the WIV response with springs we found that a VIV resonance peak always occurred around  $U/Df_0 = 5.0$ , before a pure WIV mechanism could prevail. A hypothesis is that the cylinder was being excited by VIV up to a condition of motion (coupled displacement and frequency) from which WIV could eventually take over. But now, once the springs are removed, we do not expect to see the local peak of VIV appearing, consequently the cylinder may not be excited into the critical motion for WIV to start. Would it still be possible to obtain a WIV response without first passing through a VIV resonance peak?

We already know that a static downstream cylinder in a staggered arrangement experiences a steady lift force towards the centreline. Keeping this stabilizing effect in mind, we expect that a free downstream cylinder mounted without springs would respond in one of the three possible ways.



(i) *Drift sideways*: the impulse generated by the vortex–structure interaction would be strong enough to overcome  $\bar{C}_y$  towards the centreline; the cylinder would drift away beyond the wake-interference region (static divergence) and no oscillatory motion would be sustained.

(ii) *Remain stable on the centreline*: the impulse generated by the vortex–structure interaction when the cylinder is on the centreline would be too weak to displace the cylinder and initiate any WIV; the cylinder would find a stable position on the centreline due to a strong  $\bar{C}_y$  field and no oscillatory motion would be sustained.

(iii) *Develop oscillatory motion*: the impulse generated by the vortex–structure interaction would be strong enough to displace the cylinder, but the stabilizing  $\bar{C}_y$  would restore the cylinder towards the centreline. A phase lag between force and displacement would appear to build up the WIV mechanism and sustain oscillatory motion even without springs.

In principle it appears that the existence of oscillatory motion depends on the balance between the impulse force from the vortex–structure interaction and the stabilizing lift towards the centreline, at least in a system without springs. But since both force components depend on the unsteady wake configuration and motion of the body we cannot predict *a priori* if the system will respond with sustainable oscillatory motion – and even if some oscillation is developed there is no indication that it would resemble the WIV response obtained when springs were present.

Figure 8 presents the WIV response for the downstream cylinder mounted without springs compared with the curve already presented for a cylinder with springs. Both curves were obtained for the same variation of the flow speed; therefore both data sets share the same Reynolds number scale. But because the system without springs has no inherent  $f_0$  it does not make sense to plot this curve with a reduced velocity axis. In fact, by making  $f_0 = 0$  we are effectively making  $U/Df_0 = \infty$  for all points of the response without springs; the variation of flow speed can only be represented by  $Re$  in this case.

From among the three hypotheses presented above, the response certainly agrees with the third one concerned with sustainable oscillatory motion. Not only was the cylinder able to sustain oscillations, but most surprisingly the amplitude of response was remarkably similar to the case with springs. As far as the amplitude of response is concerned, it appears that the absence of springs is insignificant for the WIV mechanism. As expected, the local peak of VIV around  $U/Df_0 = 5.0$  disappeared once the resonance  $f_s = f_0$  was eliminated by removing the springs. However, the overall response for both cases, with and without springs, is notably similar. The fact that  $\hat{y}/D$  increases with flow speed is not an effect of reduced velocity; in other words, the increase in WIV response observed for a cylinder without springs cannot be related to any structural stiffness. Instead, it seems that the response reveals some dependence simply on Reynolds number. Since both curves are essentially very similar, we suggest that an independence of response from reduced velocity and a dependence on  $Re$  might also be occurring for the cylinder mounted with springs. We shall return to this subject later on.

Let us turn now to the frequency of response presented in figure 8(b). Since  $f_0$  is not defined for the case without springs, we can only compare both curves if they are plotted in dimensional form ( $s^{-1}$ ). The response with springs was analysed above, but it is convenient to summarize it here once more:  $f$  follows the  $St = 0.2$  line up to the VIV resonance; then follows close to  $f_0$  through a distorted synchronization range, but eventually continues on a distinct branch dominated by pure WIV. On the other hand, the frequency of response without springs shows no effect of VIV synchronization



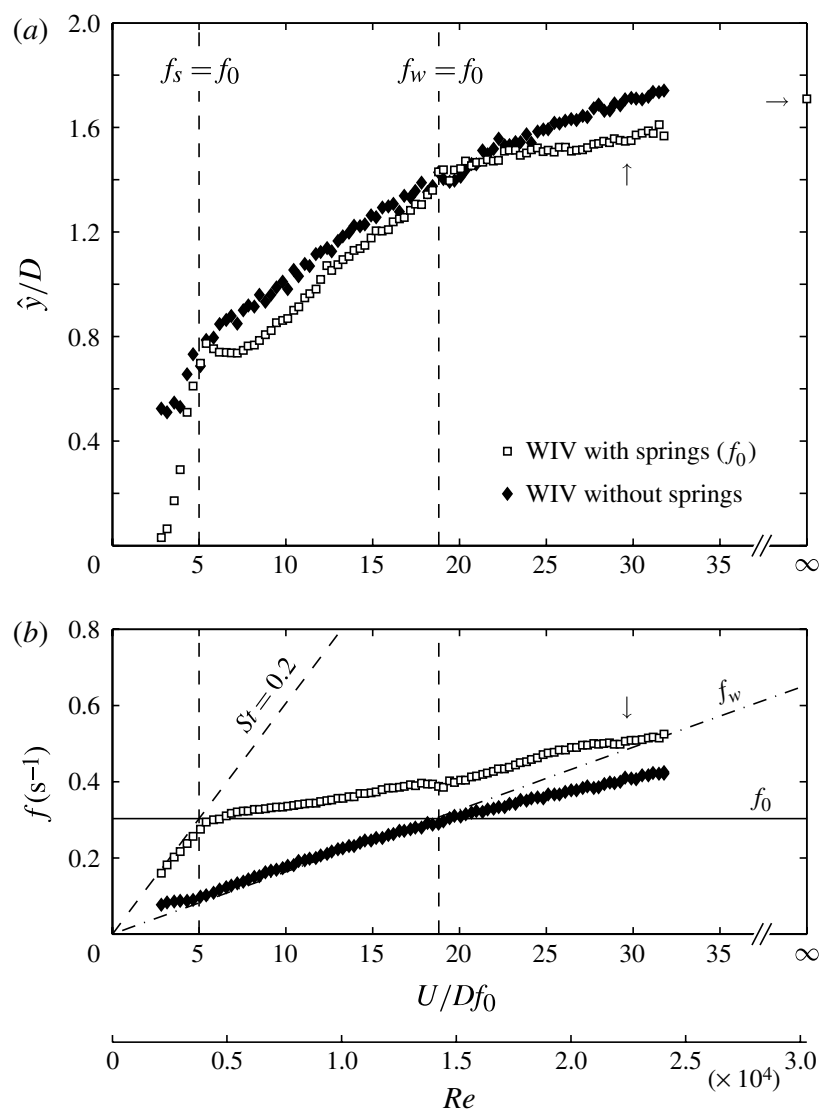


FIGURE 8. WIV response of a downstream cylinder mounted with and without springs at  $x_0/D = 4.0$ : (a) displacement; (b) dominant frequency of oscillation.

– that is obvious since there is no  $f_0$  for it to be synchronized with – but follows an almost straight line as the flow speed is increased. In fact, we note that it follows very closely the dash-dotted line marked as  $f_w$ , which shall be explained later. Another way to analyse this result is to create a non-dimensional parameter  $fD/U$ , a type of Strouhal number, plotted in figure 9. This way, the  $St = 0.2$  line presented in figure 8 becomes a constant in figure 9 and all the data are distorted to incorporate the effect of  $U$  varying in both axes. We shall return to this graph after some analytical modelling that will follow in the next sections. Before that, we will look at the time series of displacement and lift.

Figure 10 shows three examples of time series for the WIV response without springs. The flow speed in each case, represented by  $Re$ , would correspond to a reduced velocity of  $U/Df_0 = 10, 20$  and  $30$  for the cylinder mounted with springs (which can be compared with the plots in Assi *et al.* 2010). The displacement plots on the left (a,c,e) show that the system is indeed responding with oscillatory motion. Although the frequency of response seems to be rather regular, it is evident that the envelope of amplitude varies from cycle to cycle throughout the series.

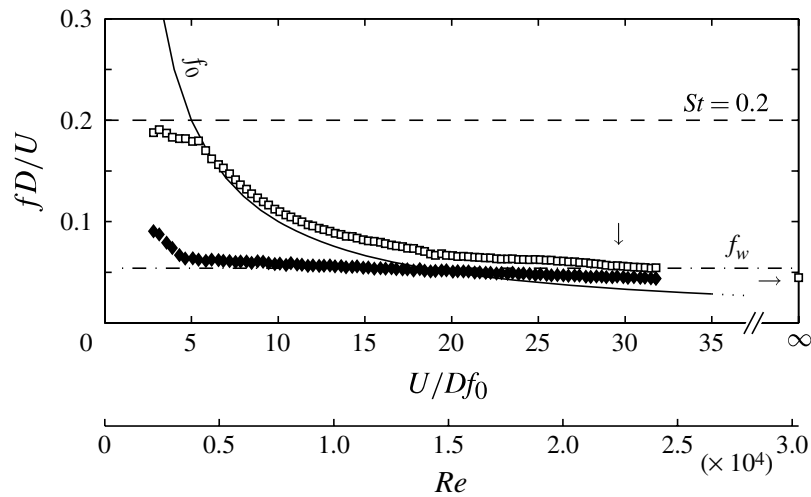


FIGURE 9. Non-dimensionalized dominant frequency of oscillation of a downstream cylinder mounted with and without springs. See figure 8 for key.

Figure 10(b,d,f) presents superimposed plots of displacement and lift for similar cycles around the average value of  $\hat{y}/D$  given in figure 8.

A considerable variation in displacement is evident from the deviation of dark-grey lines from the average cycle represented in black. Nevertheless, it is the irregularity of the lift force that really catches the attention. A clutter of light-grey lines reveals that almost no cycle is identical to any other and an abundance of higher frequencies induce  $C_y$  to present significant fluctuations within a single cycle of displacement. Once more we can note that intense, high-frequency fluctuations in lift, a consequence of the instantaneous interaction between cylinder and wake, may have a similar effect as generating the phase lag between  $y$  and  $C_y$  that is necessary to transfer energy from the flow to the structure. However, by looking at the average cycle of lift, given by a dashed-black line, we can still note a lower frequency component almost, but not exactly, out of phase with the displacement. This term must have some inertia component reacting against the acceleration of the body; part must be related to the flow excitation, but part must also be related to the steady  $\bar{C}_y$  field acting towards the centreline.

Analysing the PSD of  $C_y$  of both cylinders (figure 11) we note that the upstream cylinder (figure 11a) is shedding vortices as an isolated body, with no interference from the motion of the second cylinder propagating upstream. This was also observed for the case with springs and there is no reason to expect that it would be different for the same separation. On the other hand, the PSD of lift on the downstream cylinder shows two distinct branches of frequency: the higher  $f(C_y)$  branch is clearly an effect of vortex shedding from the upstream cylinder; whereas the lower  $f(C_y)$  branch is promptly identified with that frequency of response observed in figure 8. It is important to note that in this case there is no  $f_0$  defined by springs (that is why  $f(C_y)$  has a dimension of  $s^{-1}$ ), hence the fact that  $f(C_y)$  presents a lower branch is not associated with any structural stiffness. It is only at the very beginning of the scale, for  $Re < 0.3 \times 10^4$ , that we see the vortex shedding branch having more energy than the lower one; otherwise, for the rest of the response curve, the lower frequency branch clearly dominates the character of  $C_y$ . Now, with such a clear preponderance of the lower  $f(C_y)$  branch it is not surprising that the dominant frequency of response matches this major excitation.

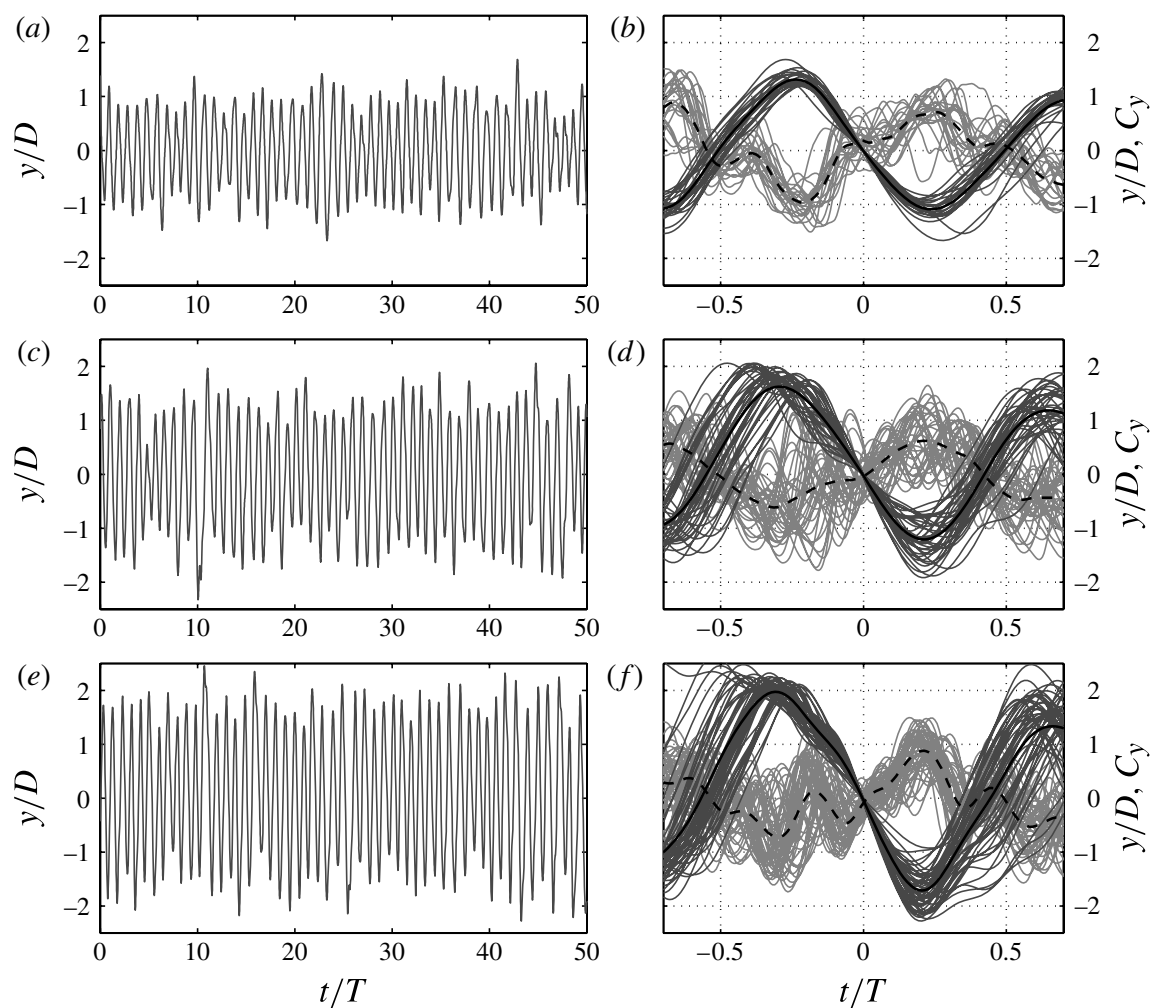


FIGURE 10. Three examples of time series for WIV without springs. (a,c,e) Displacement signal for around 50 cycles of oscillation. (b,d,f) Superimposed plots of similar cycles:  $y/D$  in dark grey and  $C_y$  in light grey with average cycle in black. (a,b)  $Re = 0.8 \times 10^4$ , (c,d)  $Re = 1.5 \times 10^4$ , (e,f)  $Re = 2.3 \times 10^4$ .

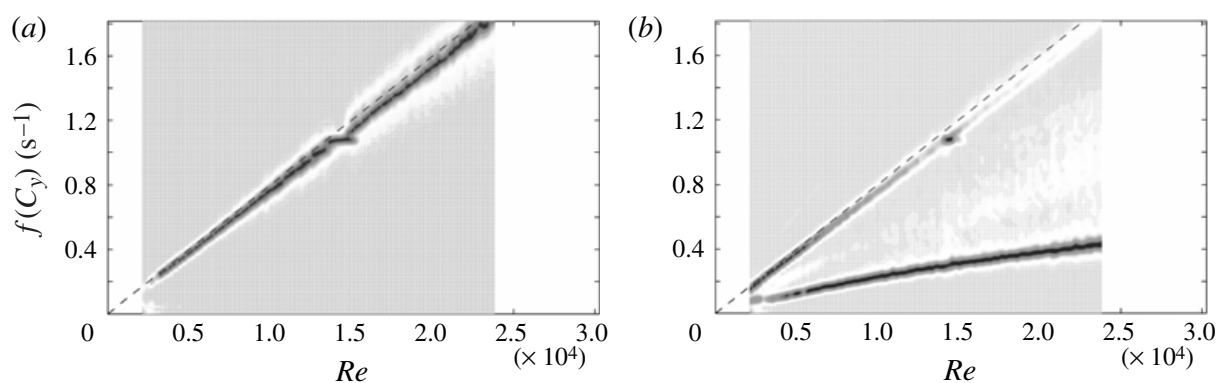


FIGURE 11. Normalized PSD of lift force acting on the (a) upstream static cylinder and (b) downstream cylinder without springs.

The body is able to sustain oscillatory motion even without any springs to create structural stiffness and we are still left with the question about the origin of a lower

frequency force that is not related to either  $f_s$  or  $f_0$ . The only possibility left is that there must be another force acting to restore the body to equilibrium. Since the body is essentially without any structural stiffness, such a stabilizing force has to be coming from the flow itself. That is to say that there must be a fluid force playing the role of the stiffness in the oscillator, otherwise no oscillatory motion would be observed. So we turn our attention once more to the steady lift generated in staggered arrangements.

## 6. The wake-stiffness concept

Now that we have observed that the WIV response without springs indeed presented oscillatory motion – with amplitude increasing with Reynolds number and a frequency distinct from  $f_s$  or any  $f_0$  – we should model the problem of a cylinder with no structural stiffness. The equation of motion (1.1) has the stiffness term removed if we make  $k = 0$  for a downstream cylinder without springs, resulting in

$$m\ddot{y} + c\dot{y} = C_y \frac{1}{2} \rho U^2 D, \quad (6.1)$$

where all forces are per unit length of cylinder.

Applying the same ‘harmonic forcing and harmonic motion’ assumption, where  $y = \hat{y} \sin(2\pi ft)$  and  $C_y = \hat{C}_y \sin(2\pi ft + \phi)$ , results in

$$\frac{\hat{y}}{D} = \frac{1}{4\pi} \hat{C}_y \sin \phi \frac{\rho U^2}{cf}. \quad (6.2)$$

Notice that neither the mass nor any stiffness comes into the equation, but the excitation is simply balancing the structural damping of the system given by  $c$  (friction damping per unit length of cylinder). Rearranging (6.2) into non-dimensional groups results in

$$\frac{\hat{y}}{D} = \frac{1}{4\pi} \hat{C}_y \sin \phi \left( \frac{U}{Df} \right) \left( \frac{\rho UD}{\mu} \right) \left( \frac{\mu}{c} \right). \quad (6.3)$$

Knowing that the dynamic viscosity  $\mu$  is a physical property of the fluid and assuming that viscous damping per unit length  $c$  is only based on the friction of the air bearings, we conclude that  $\mu/c$  does not vary with Reynolds number. We are left with three non-dimensional groups: (i)  $C_y \sin \phi$  is associated with the excitation force, we call it the vortex-impulse term and will consider it later; (ii)  $U/Df$  represents the inverse of a non-dimensional frequency of oscillation; (iii)  $\rho UD/\mu$  is the Reynolds number.

### 6.1. Frequency of oscillation and natural frequency of wake stiffness

Let us first investigate the behaviour of the non-dimensional oscillation frequency ( $fD/U$ ). If we consider the map of steady lift across the wake for  $x_0/D = 4.0$  presented in figure 7 we note that  $\bar{C}_y$  acting towards the centreline has a rather good linear behaviour between  $-1.0 \leq y_0/D \leq 1.0$  and does not vary within the  $Re$  range. Of course nonlinearities appear for larger separations, but we can estimate the slope

$$\left| \frac{\partial \bar{C}_y}{\partial (y_0/D)} \right| \equiv \Delta_{\bar{C}_y} \approx 0.65 \quad (6.4)$$

with 95 % confidence inside the wake interference region (considered to be  $-1.0 \leq y_0/D \leq 1.0$  in this analysis). For convenience, we shall refer to this slope simply as  $\Delta_{\bar{C}_y}$  from now on.

We know that this steady lift works as a restoring force towards the centreline. Similarly to the stiffness generated by a spring, the magnitude of  $\bar{C}_y$  increases linearly with transverse displacement of the cylinder, at least within the wake interference region. For that reason, the  $\bar{C}_y$  field can be understood as a ‘fluid-dynamic spring’ generated by the flow; such an effect will be referred to as *wake stiffness* from now on.

The equivalent spring constant per unit length ( $k_w$ ) that would generate such a flow effect is

$$k_w = \Delta \bar{C}_y \frac{1}{2} \rho U^2; \quad (6.5)$$

thus an equivalent natural frequency  $f_w$  could also be associated with the wake stiffness as

$$f_w = \frac{1}{2\pi} \sqrt{\frac{k_w}{(m^* + C_a) \rho \frac{\pi D^2}{4}}}, \quad (6.6)$$

where  $C_a$  denotes the potential added mass coefficient to take into account the effect of the added inertia of the displaced water.

Since wake stiffness is a fluid-dynamic force, its effect would be equivalent to a spring with a  $k_w$  that increases with  $U^2$ , as seen in (6.5); hence the associated natural frequency  $f_w$  increases linearly with  $Re$ . Replacing (6.5) in (6.6) and multiplying it by  $D/U$  results in a Strouhal-type non-dimensional parameter

$$\frac{f_w D}{U} = \frac{1}{2\pi} \sqrt{\frac{2}{\pi} \frac{\Delta \bar{C}_y}{(m^* + C_a)}}. \quad (6.7)$$

We already know that  $\Delta \bar{C}_y$  is invariant with  $Re$ . Since  $C_a$  cannot vary with  $Re$  either, we conclude that  $f_w D/U$  is a constant irrespective of  $Re$ .

Turning back to figure 8 we note that the frequency of oscillation  $f$  for a cylinder without springs presents a remarkable linear behaviour that grows with  $Re$ , which is represented by an almost constant curve far from  $St = 0.2$  in figure 9. This suggests that there must be a preferred frequency lower than  $f_s$  dominating the response. Note that this characteristic frequency cannot be related to  $f_0$  because the system has no springs. Therefore we are left with the possibility that this restoration is indeed coming from the  $\bar{C}_y$  field, hence it must be related to  $\Delta \bar{C}_y$ .

Now if we substitute the numerical values  $\Delta \bar{C}_y = 0.65$ ,  $m^* = 2.6$  and  $C_a = 1.0$  in (6.7) we find that  $f_w D/U = 0.054$ , which is represented by the  $f_w$  dot-dashed line in figures 8 and 9. The agreement between  $f_w$  and the WIV response without springs is remarkable. This is evidence that a cylinder without springs may also be responding to the wake stiffness with  $f = f_w$  for the whole range of  $Re$ . That is to say that the excitation frequency identified in the lower branch of  $f(C_y)$  in figure 11 – the one that matches the response frequency  $f$  in figure 8 – is actually governed by the wake stiffness effect described in (6.5) to (6.7).

If it is true that  $f = f_w$ , (6.7) tells us that  $fD/U$  is also a constant and the cylinder indeed oscillates with  $f$  that increases linearly with  $Re$ . In figure 8 we note that  $f$  closely follows  $f_w$  up to around  $Re = 1.5 \times 10^4$  when the response amplitude reaches about  $\hat{y}/D = 1.4$ . Beyond this point the amplitude grows towards values around  $\hat{y}/D = 1.8$  meaning that the cylinder is oscillating further out of the wake interference region. From the  $\bar{C}_y$  map for  $x_0/D = 4.0$  (figure 7) we know that the



steady lift grows linearly with lateral separation up to around  $y_0/D = 1.0$ . Beyond that, nonlinear effects start to appear and the wake stiffness is not able to be represented simply by the slope  $\Delta\bar{c}_y$ , but would gradually be reduced. This is exactly what is observed as the frequency curve begins to depart from the  $f_w$  line as  $\hat{y}/D$  increases. Of course some effect in reducing  $f$  must be coming from the fact that secondary effects in the effective added mass of fluid may appear as the cylinder moves in and out of the wake interference region. But even considering that the effective added mass is constant throughout  $Re$  the agreement is still very good.

Although it is very helpful to think of the wake stiffness effect as a linear spring, a quasi-static lift map still is an oversimplification of the problem. If the restoring fluid force towards the centreline is induced by complex vortex–structure interactions – as proposed in Assi *et al.* (2010) – it should also present unsteady variations as the cylinder moves across the wake. However, we can still imagine that if the cylinder is displaced farther away from the wake interference region ( $y/D \gg 1.0$ ) the induced force at that instant must be reduced. On the other hand, if in another instant the cylinder is located closer to the wake boundary the vortex-induced force can be amplified. For that reason we could suggest that the total excitation force must be composed of two fluctuating terms with distinct frequencies: one term is associated with the wake stiffness, which obviously depends on the position of the body across the wake and is related to  $f$ ; the other is associated with the impulse vortex-force induced on the cylinder, which also depends on the lateral position of the cylinder and is thus related to  $f_s$ . We believe that while a series of vortices streaming along the wake induces a steady force towards the centreline, each vortex also induces an instantaneous force fluctuation (an impulse) on the cylinder. The magnitude of both *wake-stiffness* and *vortex-impulse* terms will depend on the relative position of the body and a particular interaction with the wake.

## 6.2. VIV and WIV resonances: $f_s = f_0$ and $f_w = f_0$

If the wake-stiffness is dominant over the vortex-impulse term it is straightforward to predict that the cylinder should respond with  $f = f_w$  and not  $f = f_s$ . As we have seen so far  $f_w D/U$  does not vary with flow speed, thus  $f_w$  increases linearly with  $Re$ . Since  $f_0$  is a constant defined by the springs, there must be a critical point where the wake stiffness has the same intensity as the spring stiffness, i.e.  $k_w = k$  and  $f_w = f_0$ . This occurs in figures 8 and 9 where  $f_w$  crosses the  $f_0$  line at  $Re = 1.2 \times 10^4$  (equivalent to  $U/Df_0 = 18.8$  for the case with springs). We know the present set of coil springs provides the system with a measured stiffness of  $k = 11.8 \text{ N m}^{-1}$ . But considering the steady lift map with  $\Delta\bar{c}_y = 0.65$  in (6.5) we see that the wake stiffness can reach values as high as  $k_w = 34 \text{ N m}^{-1}$  at the end of the  $Re$  range of the experiments.

For the case with springs we find  $f$  following closer to the  $f_0$  line during the range where VIV is relevant, with the lock-in peak occurring around the intersection of  $f$  with both  $f_0$  and  $St = 0.2$  lines. This first VIV resonance is marked by the vertical line  $f_s = f_0$  in figure 8. At this point  $k_w = 1.8 \text{ N m}^{-1}$  is only 15 % of  $k$  provided by the springs. As the flow speed is increased the VIV synchronization tends to disappear as  $St = 0.2$  moves away from  $f_0$ . At the same time the wake stiffness is also getting stronger until both  $k_w$  and  $k$  have the same value. As we saw, this occurs for  $U/Df_0 = 18.8$  and is marked by the second WIV resonance line  $f_w = f_0$ , beyond which  $k_w$  is greater than  $k$ .

The two resonance lines divide the response for a cylinder with springs into three regimes that are best identified in figure 8. (i) Before  $f_s = f_0$ , when  $St = 0.2$  is



approaching  $f_0$ , the displacement resemble an initial branch of VIV and  $f$  follows the Strouhal line up to the resonance peak. (ii) The second regime, between  $f_s = f_0$  and  $f_w = f_0$ , is marked by a steep slope in the displacement curve;  $f$  remains rather close to  $f_0$  as the VIV synchronization range gradually gives way to a wake stiffness that is growing stronger with  $Re$ . (iii) The third regime, beyond the second resonance  $f_w = f_0$  is characterized by a change of slope in both the displacement and frequency curves. With  $k_w > k$  the WIV response is established and dominates alone for the rest of the  $Re$  range.

The system works as if the set of springs were important only in the first regime before the  $f_w = f_0$  resonance, but the system completely overlooks its small structural stiffness given by  $f_0$  as  $k_w$  gets relatively stronger. It appears that away from the resonances  $f_s = f_0$  and  $f_w = f_0$  the spring acts against the WIV excitation with the effect of reducing the amplitude of vibration. This idea is in agreement with the classical theory of linear oscillators; if the excitation force is outside the resonance of the system the response will not be as high as the resonance peak.

Various experiments have investigated the flux of energy in the system for a cylinder oscillating in forced vibrations in a flow. Recently, Morse & Williamson (2009) have presented a detailed energy map for VIV of a single cylinder. If we take values of displacement and frequency from our own WIV curves and plot them in their VIV energy map we will see that the structure is actually losing energy to the flow. If we assume that the major forcing term is coming from the WIV mechanism governed by wake stiffness, the VIV part governed by spring stiffness is contributing to dissipate energy and reduce the vibration. That is why the response curve with springs shows reduced amplitude away from the two resonance lines when compared with the case without springs. Because our excitation force is believed to have a wake-stiffness and a vortex-impulse component, each related to one characteristic frequency, the response will be slightly accentuated when  $f_s = f_0$  (VIV resonance) and  $f_w = f_0$  (WIV resonance).

One could ask if it would be possible to have a third resonance  $f_s = f_w$ , potentially occurring also for a cylinder without springs. Since both  $St = 0.2$  and  $f_w$  are dependent on Reynolds number, they would have to be equal throughout the whole  $Re$  range. Starting from (6.7) and considering that the Strouhal number of a cylinder is roughly constant with  $Re$ , there are only two ways to bring both  $St = 0.2$  and  $f_w$  lines together.

Firstly, fixing the mass of the system we would have to generate a steady lift field with  $\Delta\bar{C}_y = 8.9$  which is one order of magnitude higher than the maximum value measured for staggered cylinders. Now, if the steady lift towards the centreline has its origin in the unsteady vortex–structure interaction, both  $f_s$  and  $f_w$  originate in the same phenomenon and have to coexist within physical boundaries. By this we mean that the wake structure required to generate such an intense steady field would have to be very different from the vortex shedding mechanism that we know. Therefore we do not expect  $f_s = f_w$  due to such an intense  $\bar{C}_y$  field.

Secondly, knowing that  $\Delta\bar{C}_y$  is invariant with  $Re$ , we can change the mass of the system in order to change the natural frequency  $f_w$ . Keeping  $\Delta\bar{C}_y = 0.65$  and  $C_a = 1.0$  constant in (6.7) and equating the right-hand side to  $St = 0.2$  results in  $m^* = -0.74$ . Since this result is impossible in a physical system we can affirm that  $St = 0.2$  and  $f_w$  will never overlap.

In fact, since we know the cylinder is responding to WIV with  $f = f_w$ , to have  $f_w = f_s$  means that the cylinder would be oscillating at the frequency of vortex shedding for the whole  $Re$  range. This is the WIV equivalent of the phenomenon

described by Govardhan & Williamson (2002) for VIV of a single cylinder. They verified that for  $m^*$  below a critical value around 0.54 the VIV response would persist for an infinite regime as if the lower branch were extended indefinitely. It was observed that the frequency of oscillation  $f$  would follow the vortex shedding frequency  $f_s$ , linearly increasing with reduced velocity, sustaining a regime they called ‘resonance forever’. Although this appears to be physically impossible in our case, we hypothesize that if we could artificially bring both  $St = 0.2$  and  $f_w$  lines together – in a force feedback system this would be possible – the cylinder would vibrate indefinitely with both VIV and WIV perfectly combined.

### 6.3. Response without springs in a shear flow

In Assi *et al.* (2010) we have seen that the unsteadiness of the wake was necessary to excite WIV; a cylinder immersed in an artificial wake without vortices did not respond with WIV. In the present paper we investigated the importance of the wake-stiffness effect in sustaining the vibration of a cylinder mounted without springs. Finally, we can combine the two concepts of wake stiffness and vortex impulse in the response of a cylinder immersed in a shear flow (without unsteady vortices) but also without springs (without structural stiffness). This experiment was performed and the result was that no vibration was observed.

Although some small wake-stiffness effect was left in the shear flow after vortices were removed –  $\Delta \bar{C}_y \approx 0.2$  could be estimated from the steady lift field in Assi *et al.* (2010) – it was not strong enough to sustain oscillatory motion and the cylinder did not respond with vibrations. If our theory is correct, we need to bring the excitation term from the vortex–structure interaction acting together with the wake-stiffness effect in order to produce a WIV response. Removing the unsteadiness of the upstream wake we are essentially left without the WIV excitation term, therefore the response will be that of VIV. But, by removing both the unsteadiness of the wake and the springs at the same time we are left with no response at all.

## 7. Dependence on Reynolds number

Returning to (6.3), we can now analyse the behaviour of the non-dimensional parameter  $\hat{C}_y \sin \phi$  (that we are calling the vortex–impulse term) with respect to Reynolds number. We already know that the cylinder is responding with  $f = f_w$ , a dominant frequency produced by the wake stiffness effect. In the harmonic assumption applied in (6.1) we consider that the fluid force is represented by only a single dominant frequency and phase angle. However, in figures 10 and 11 we clearly see that  $C_y$  in fact presents two significant frequencies: a lower branch associated with wake stiffness and a higher branch associated with vortex–impulse from the upstream wake.

Retaining the harmonic hypothesis we could split the actual effect of  $C_y$  into two parts. Because  $f_w$  is clearly dominant over  $f_s$  let us consider that the magnitude of  $\hat{C}_y$  is only produced by the wake stiffness effect and has very little influence from vortex–impulse fluctuations. Consequently, the fluid force would have a dominant component  $f = f_w$ , with magnitude depending only on  $\Delta \bar{C}_y$  and acting out of phase with the displacement (again we are entering quasi-static territory, but at least now we are supported by having  $U/Df_0 = \infty$ ). On the other hand, we need to account for the phase lag necessary to sustain the vibration. We have already proposed (Assi *et al.* 2010) that it is generated by the complex vortex–structure interaction as the body

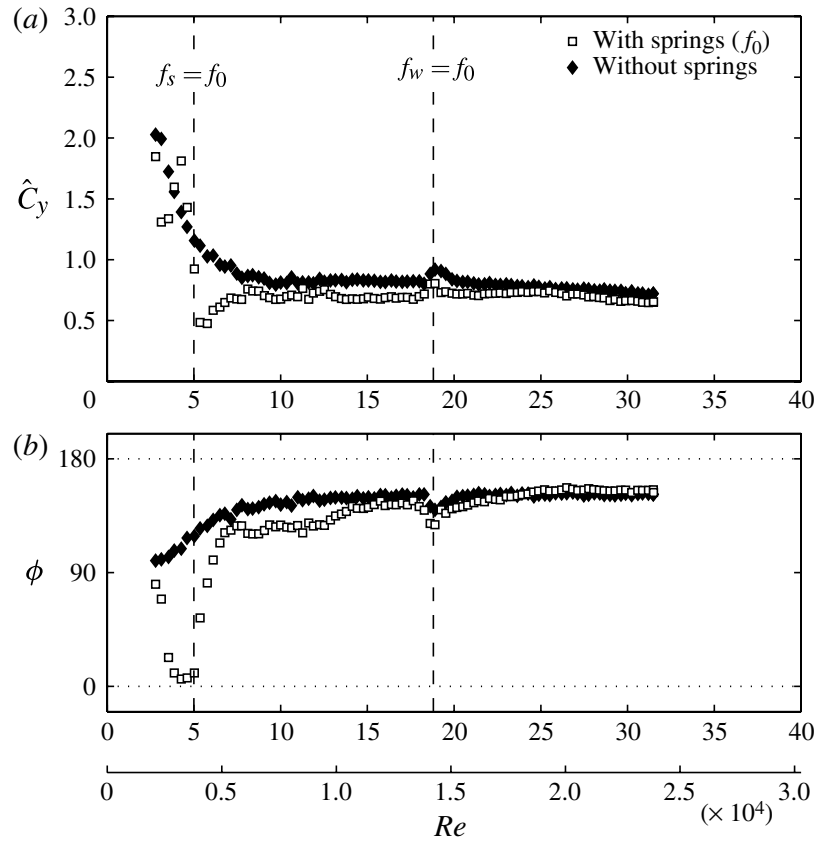


FIGURE 12. Comparison between lift coefficient (a) and phase angle (b) for the WIV response of a cylinder with and without springs at  $x_0/D = 4.0$ .

crosses the wake, therefore we could attribute the existence of  $\phi$  to the vortex–impulse fluctuations operating at  $f_s$ .

We have shown that  $\Delta \bar{C}_y$  does not vary with  $Re$ , therefore  $\hat{C}_y$  should also be invariant. However, we have also demonstrated that, due to fluctuations caused by vortex–impulse, the phase angle varies from cycle to cycle as the cylinder interacts with different wake configurations. Albeit not being very strong, this supposition finds some support in the time series presented in figure 10. Therefore, let us now investigate  $\hat{C}_y$  and  $\phi$  independently.

Figure 12(a) compares the total lift coefficient for WIV responses both with and without springs. An abrupt reduction in  $\hat{C}_y$  for the case with springs is characteristic of the VIV phase shift and occurs at the  $f_s = f_0$  resonance. We can still note some differences between the cases while VIV is losing strength between the resonances, but yet it is beyond the resonance  $f_w = f_0$  that WIV clearly dominates and both curves follow each other closely for the rest of the  $Re$  range. Apart from a small range of  $Re < 0.5 \times 10^4$ ,  $\hat{C}_y$  without springs shows a fairly constant behaviour with a small negative slope. Figure 12(b) compares average values of  $\phi$  for WIV responses with and without springs. Each data point was obtained by employing the Hilbert transform to calculate instantaneous values of phase angles and then averaging  $\phi$  for more than 500 cycles of oscillation (refer to Assi 2009 for more details). The curve shows that  $\phi$  without springs presents a relatively constant value around  $153^\circ$  for  $Re > 0.5 \times 10^4$ .

Although both  $\hat{C}_y$  and  $\phi$  appear to be fairly invariant with  $Re$ , we cannot forget that values plotted in figure 12 are averaged for as many as 500 cycles of oscillations.

We have already seen in figure 10 how irregular  $C_y$  can be from cycle to cycle. Variations within the present  $Re$  range are also expected to occur due to the complex characteristic of the wake. For example, it is known that the vortex formation length presents a strong variation with  $Re$  (Norberg 1998; Assi *et al.* 2006); and the three-dimensionality of the wake may also present some  $Re$  dependence. Nevertheless, although  $\hat{C}_y$  and  $\phi$  cannot be confirmed as strictly constant we are able to conclude that, to a first approximation, the non-dimensional term  $\hat{C}_y \sin \phi$  should be roughly invariant with  $Re$ , at least within the subcritical  $Re$  range of the experiments.

Turning back to (6.3), we can now verify that  $\mu/c$ ,  $U/Df$  and  $\hat{C}_y \sin \phi$  are approximately invariant with  $Re$ , leaving only the Reynolds number term itself on the right-hand side of the equation. As a result it is evident from this analysis that  $\hat{y}/D$  is linearly dependent on  $Re$  and the WIV response should increase with flow speed up to a critical amplitude. Once the cylinder starts to be displaced out of the wake interference region nonlinear effects become important, limiting the response to an asymptotic value. Secondary effects may be acting on  $U/Df$  and  $\hat{C}_y \sin \phi$  conferring on the response the curved shape presented in figure 8. The analysis developed above is in good agreement with displacement curves presented for both cases (with and without springs). Therefore we conclude that the mechanism that is building up the amplitude of vibration in WIV is definitely not a consequence of reduced velocity but a direct effect of Reynolds number.

Picking a displacement point from the curve without springs at an arbitrary value of  $Re = 2.3 \times 10^4$  (the location represented by a vertical arrow in figure 8) we are able to estimate the limiting value the response is asymptotically approaching as  $U/Df_0 \rightarrow \infty$  for that specific  $Re$ . Of course this is the data point from the curve without springs immediately above the vertical arrow, but it can also be represented on the right-hand axis for  $U/Df_0 = \infty$  (this will be useful later when comparing different  $x_0/D$  separations).

Such a strong  $Re$  dependence turned out to be a rather unexpected result. It took us some time to comprehend how a fluid-elastic system could show large variations over such a short  $Re$  range. However, if we consider that our system actually possesses a fluid-dynamic spring that increases stiffness with  $U^2$ , as seen in (6.5), we are left with the only conclusion that  $\hat{y}/D$  must indeed vary with  $Re$ .

### 7.1. Experiments with constant $Re$

At this point one may recall the results from Hover & Triantafyllou (2001), presented in figure 2(b), who measured the WIV response of a cylinder at  $x_0/D = 4.75$  and constant  $Re = 3 \times 10^4$ . They achieved this by varying the spring stiffness of a force-feedback system. In spite of operating at a fixed Reynolds number, they were able to measure a build-up of response that increased with reduced velocity. In principle, this seems to contradict our theory that the WIV response is not affected by reduced velocity.

Considering that their separation of  $x_0/D = 4.75$  must provide a wake-stiffness effect in the order of  $\Delta \bar{C}_y \approx 0.55$  (based in our figure 6), we can estimate that the critical reduced velocity at which the wake stiffness equals the spring stiffness ( $k_w = k$ ) is as high as  $U/Df_0 = 21$  (based in our  $\bar{C}_y$  map of figure 6,  $C_a = 1.0$  and their value of  $m^* = 3.0$ ). However, the maximum reduced velocity achieved in their experiment is only around 17. Hence the regime Hover & Triantafyllou (2001) observed was still between the resonances  $f_s = f_0$  and  $f_w = f_0$ , a region where VIV still has some significance.

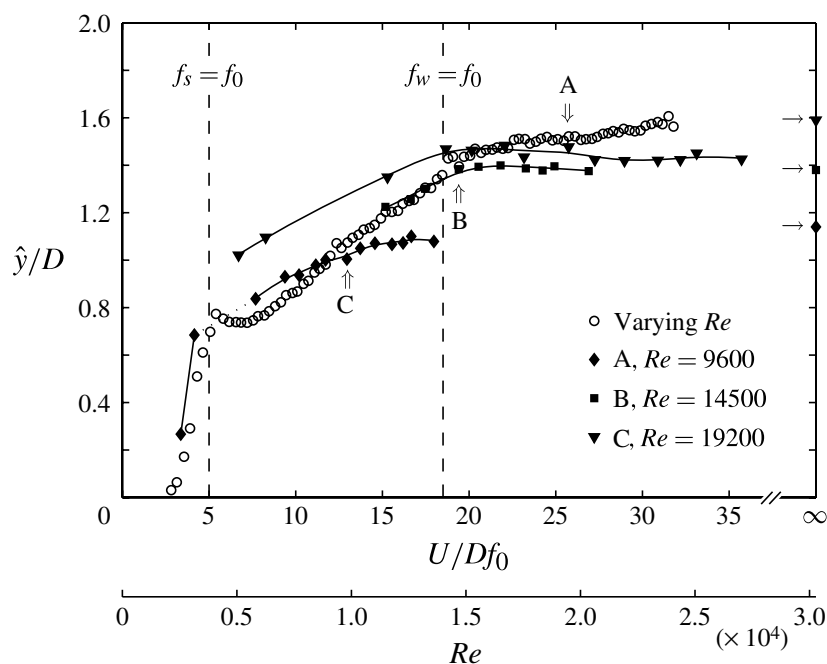


FIGURE 13. WIV response at constant  $Re$  for  $x_0/D = 4.0$ . Reduced velocity varied by changing the springs, compared to our reference cylinder with fixed springs and varying  $U/Df_0$  by varying flow speed (the secondary axis of  $Re$  refers to this curve only).

According to our theory, we would expect their results to reach an asymptotic value around  $\hat{y}/D = 1.5$  for  $Re = 3 \times 10^4$ , which is in good agreement with their curve reproduced in the present work (figure 2*b*). Note, however, that Hover & Triantafyllou (2001) do not plot  $\hat{y}/D$  but an average of the 10 % highest peaks of displacement. As we have seen in figure 5 the maximum displacement of the cylinder can be considerably greater than the averaged  $\hat{y}/D$  that we usually employ. The same observation is also true for the results obtained by Assi *et al.* (2006) also presented in figure 2*b*). Even though  $k$  was constant, they could not reach the regime above the WIV resonance  $f_w = f_0$  due to a limitation in the maximum flow speed.

In order to verify this phenomenon, we carried out a series of experiments for three constant Reynolds numbers at  $x_0/D = 4.0$ . The flow speed was fixed and reduced velocity was varied by changing the set of springs and, consequently, changing  $f_0$ . Figure 13 presents the results compared to our reference WIV response of a cylinder with fixed springs and varying  $U/Df_0$  by varying flow speed (the secondary axis of  $Re$  refers to this curve only).

Three vertical arrows (A, B, C), one for each  $Re$  curve, mark the condition where the stiffness of the varying wake spring matches the fixed spring  $k$ . Hence all data points to the right of these arrows have a spring that is softer than our reference curve (and stiffer to the left). None of the curves was able to span the three regimes defined by the resonance lines  $f_s = f_0$  and  $f_w = f_0$ , but considering the results of all three curves we are able to understand the general behaviour of the response at a constant  $Re$ .

The curve for  $Re = 9600$  does not have enough data points to reveal a local peak of VIV at  $f_s = f_0$ , but the majority of the points fall within the first regime between the resonances, where VIV is gradually losing its influence to WIV. In our experiment with varying  $Re$  we have noticed that the amplitude of response generally presents a positive slope in this first regime; this is verified now for a constant  $Re$  as well. As we have discussed above, Hover & Triantafyllou (2001) also found increasing response



for a constant  $Re$  in this regime. Our data agree with theirs in showing a build-up of response between  $f_s = f_0$  and  $f_w = f_0$ . Such an effect is also observed for our curve at  $Re = 19\,200$ .

Let us move on to the other curves at  $Re = 14\,500$  and  $19\,200$  that cross  $f_w = f_0$  and enter the second regime where WIV dominates. Now that the wake stiffness is greater than the spring stiffness we see that the response is not influenced by reduced velocity anymore, but presents a rather constant level of amplitude for each fixed value of  $Re$ . Even if the reduced velocity is increased from 20 to 35 the amplitude of response seems not to be much affected and the data points appear to follow the same trend as long as  $Re$  is kept constant. Going back to the curve without springs in figure 8 we are able to find a displacement amplitude for each of our  $Re$  curves at  $U/Df_0 = \infty$  towards which the data points should be converging. We note that they are slightly higher than the level of amplitude the curves are reaching beyond  $f_w = f_0$ , but we have to remember that we are still operating with springs, although soft ones, that might be contributing to reduce the response away from the resonance lines.

While on the one hand the VIV peak at  $f_s = f_0$  seems to always reach  $\hat{y}/D$  around 1.0 (for this value of  $m^*\zeta$ ), the amplitude at the end of the first regime, at  $f_w = f_0$ , varies with the intensity of the wake-stiffness effect. Because  $k_w$  increases with  $Re$  the amplitude at  $f_w = f_0$  must also increase with  $Re$ . This level of amplitude is already very close to the asymptotic value predicted by the experiments without springs; hence, as the spring stiffness gets less important beyond  $f_w = f_0$ , we expect the curves to be converging towards the values plotted at  $U/Df_0 = \infty$ .

This series of experiments at constant  $Re$  proved that while the response below  $f_w = f_0$  is dependent on both  $Re$  and reduced velocity, the response for  $f_w > f_0$  is clearly governed by  $Re$  only. In other words, we conclude that in the first regime where both VIV and WIV are competing (or cooperating) the response increases due to a combination of spring and wake-stiffness effects. Even with constant  $Re$  we note a build-up of response while the ratio between  $k$  and  $k_w$  makes reduced velocity an important parameter. But once the wake stiffness becomes dominant over the springs the response is not affected by the structural stiffness and is only governed by wake stiffness. Now this second regime is clearly dominated by a Reynolds number effect.

## 7.2. Equivalent damping

Another way to comprehend the behaviour of the amplitude of response is to think in terms of an equivalent damping ratio. We can define  $\zeta$  by the ratio between  $c$  and a critical damping:

$$\zeta = \frac{c}{4\pi f_0 m}. \quad (7.1)$$

Note that the natural frequency and the mass of the system are present in the denominator. Apart from removing the pair of springs we keep exactly the same set-up from previous experiments, therefore we assume all other parameters are kept constant including the structural damping  $c$ . In other words, we presuppose the friction in the air bearings was kept the same; hence the system would dissipate the same amount of energy for a similar velocity of the cylinder. However, now that the springs are removed we do not have  $f_0$  that can be used to non-dimensionalize  $\zeta$  as expressed in (7.1).

Govardhan & Williamson (2002) encountered a similar problem to define a suitable damping ratio when performing experiments with a cylinder mounted on air bearings without springs. They also wanted to investigate the VIV response for  $U/Df_0 \rightarrow \infty$



and achieved that by removing the springs from the elastic system, making  $k = 0$  and  $f_0 = 0$ . In their experiment  $f$  followed the shedding frequency throughout the oscillatory regime, therefore they employed an equivalent damping ratio non-dimensionalized by  $f_s$  instead of  $f_0$ . But in the present WIV investigation  $f$  was observed not to follow  $f_s$ ; instead it increases linearly with flow speed following  $f_w$  – the natural frequency given by wake stiffness – as demonstrated above. Therefore, unlike in Govardhan & Williamson (2002), it does not make sense to define an equivalent damping ratio based on the shedding frequency  $f_s$ , but based it on the oscillation frequency  $f = f_w$  instead:

$$\zeta_w = \frac{c}{4\pi f_w m}. \quad (7.2)$$

According to this definition of  $\zeta_w$  the damping ratio varies with flow speed since  $f_w$  is also varying with  $U$ , as seen in (6.6). The same occurred for Govardhan & Williamson (2002), where their damping ratio was based on  $f_s$  which also varies with  $U$  according to the Strouhal law. (This was not the case with the traditional  $\zeta$ , which is invariant with  $U$  given a constant natural frequency  $f_0$  defined by structural stiffness.) Now, substituting  $c$  from (7.2) into (6.3) results in

$$\frac{\hat{y}}{D} = \frac{1}{4\pi} \hat{C}_y \sin \phi \left( \frac{U}{Df} \right)^2 \left( \frac{1}{m^* \zeta_w} \right), \quad (7.3)$$

with a combined  $m^* \zeta_w$  parameter appearing in the denominator.

We now observe that the amplitude of response should be inversely proportional to this new  $m^* \zeta_w$ . However, now the combined mass-damping parameter is not constant but incorporates a variation with flow speed. Because  $f_w$  increases with  $Re$ ,  $\zeta_w$  decreases with flow speed and, thinking about an equivalent damping term, we reach the same conclusion that the response should in fact increase with  $Re$ .

## 8. Wake stiffness for other separations

Now that we have analysed the WIV response for a pair of cylinders at  $x_0/D = 4.0$  we can bring the wake-stiffness concept back to our starting point and investigate the effect it has on other separations. We already know that moving the second cylinder farther downstream does not affect the wake formed in the gap, i.e. the upstream vortex shedding process is not affected if the separation changes from  $x_0/D = 4.0$  up to 20.0, the highest case investigated in the present work.

The development of a von Kármán wake from a static cylinder has been diligently studied in the literature. Schaefer & Eskinazi (1958) performed experiments in a wind tunnel in order to model the effect of fluid viscosity in diffusing a vortex from the instant it is shed from the cylinder. The core of concentrated circulation expands with time as vortices travel downstream towards the second body, so if the cylinder is farther away we expect weaker vortices (at least with less concentrated vorticity) to reach that specific position of the wake. Weaker vortices induce weaker fluid forces, therefore we would expect both wake-stiffness and vortex-impulse terms to decrease with increasing  $x_0$ .

Looking back at the steady lift map presented in figure 6 we see that the maximum  $\overline{C_y}$  is indeed decreasing for larger separations, consequently  $\Delta \overline{C_y}$  is also reduced with increases in  $x_0$ . To a certain extent it is straightforward to think that the wake-stiffness effect is inversely proportional to  $x_0$  and results in lower values of  $f_w D/U$  for larger separations. As a consequence, the frequency of oscillation should also be reduced.

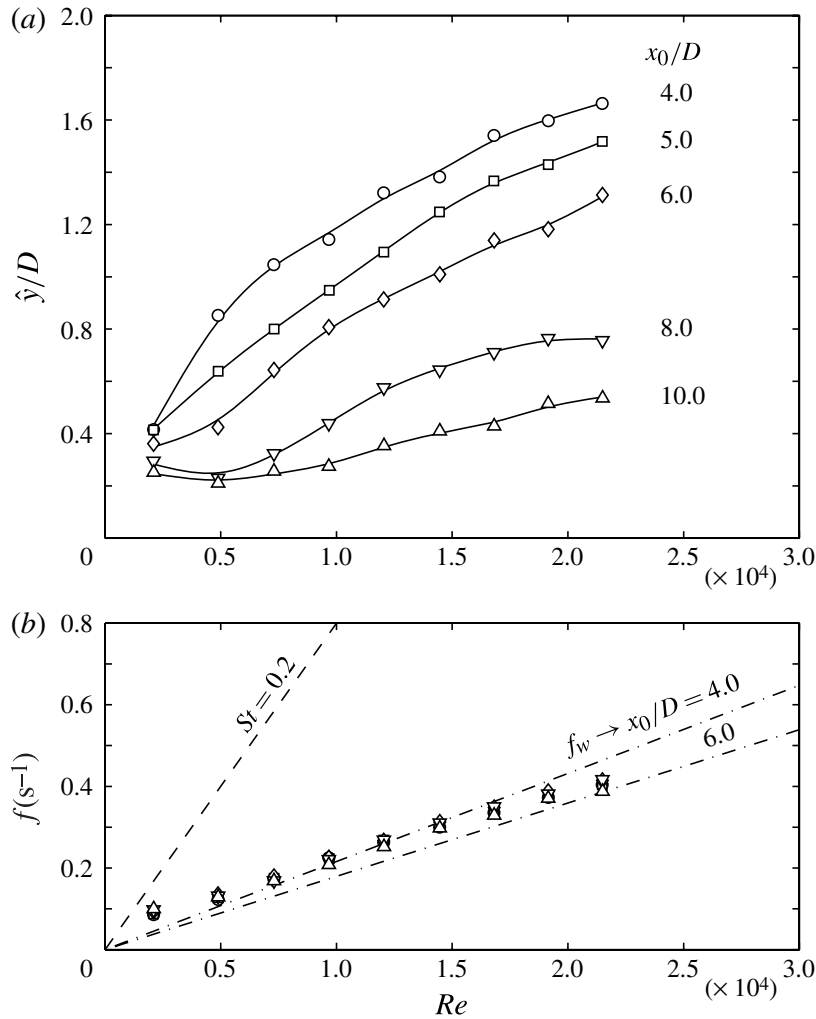


FIGURE 14. WIV response of a downstream cylinder mounted without springs at various  $x_0$  separations: (a) displacement; (b) dominant frequency of oscillation.

However, (6.3) tells us that the amplitude must increase if  $fD/U$  is reduced and all other terms are kept constant. This is clearly not observed in the response with springs presented in figure 4. Instead  $\hat{y}/D$  for the WIV regime is seen to be reduced with increasing  $x_0$ , up to a separation where no effect from the upstream wake can be sensed by the downstream cylinder and it returns to a simple VIV regime. Therefore, some other non-dimensional terms in (6.3) must be dominating over the effect of  $fD/U$  to reduce the response as  $x_0$  is increased.

Figure 14 presents the effect of  $x_0$  on the response of a cylinder mounted without springs. In accordance with (6.3), the amplitude of displacement should increase with Reynolds number for a fixed separation, while  $\hat{y}/D$  should be reduced for larger separations if  $Re$  is kept constant. Although this plot is not as densely populated with data points as figure 4, it can still reveal the overall behaviour of the response in relation to  $Re$  and  $x_0$ . The main difference now is that no VIV resonance peak is identified because the system lacks any  $f_0$  conferred by springs, but still the WIV response seems to diminish as the second cylinder is moved farther downstream.

Remember that every point in figure 14 represents an infinite reduced velocity. Therefore, variations observed in the curves are an effect of  $Re$  and  $x_0$  only. We can pick one data point from each  $x_0/D$  curve at  $Re = 2.3 \times 10^4$  in figure 14 and plot

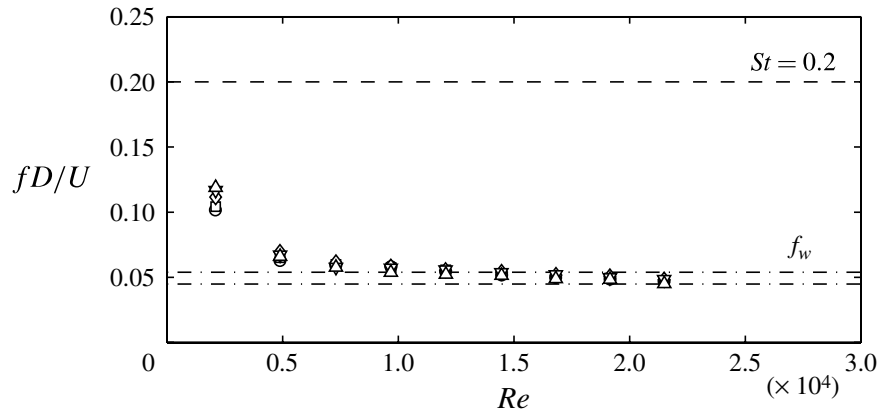


FIGURE 15. Non-dimensionalized dominant frequency of oscillation of a downstream cylinder mounted without springs at various  $x_0$  separations. See figure 14 for key.

them back in figure 4 at  $U/Df_0 = \infty$ . Every point plotted there (on the right-hand axis) represents the asymptotic value the response would reach if  $Re$  were kept constant beyond the vertical dashed line of  $Re = 2.3 \times 10^4$ . This agreement confirms that beyond the flow speed range in which VIV is important reduced velocity has no effect on the WIV response and the cylinder is expected to sustain a constant level of vibration for the rest of the  $Re$  range. It is also verified that the asymptotic value that limits  $\hat{y}/D$  is indeed a function of  $Re$  and  $x_0$  alone and must be related to the actual configuration of the wake at those conditions.

As we saw in figure 8 for  $x_0/D = 4.0$  the frequency of oscillation shows a fairly linear behaviour with  $Re$ , which is represented by a constant line when plotted non-dimensionally as  $fD/U$  in figure 9. Interestingly, we know that as far as the separation is concerned  $\Delta\bar{C}_y$  decreases with  $x_0$ . However, when this effect is reflected into  $f_w$  it seems to cause only a small variation in the frequency of response, making all frequency curves for different  $x_0$  collapse onto each other. A similar result was observed in figure 4 for the response with springs, where, differently from the displacement,  $f/f_0$  did not show much variation with  $x_0$ .

Considering our smallest separation of  $x_0/D = 4.0$  we saw that the steady lift field generates, to a first approximation, a wake stiffness effect proportional to  $\Delta\bar{C}_y = 0.65$  (figure 7). Again we can plot  $f_w$  from (6.6) associated with this steady field as a dot-dashed line in figure 14(b). However, on moving the second cylinder farther downstream in the wake we saw that  $\Delta\bar{C}_y$  is reduced. Considering the maximum separation measured in the  $\bar{C}_y$  map of figure 6 we can estimate a wake-stiffness effect proportional to  $\Delta\bar{C}_y = 0.45$  for  $x_0/D = 6.0$ . If we then plot  $f_w$  associated with this weaker wake stiffness in figure 14(b) we are able to verify that the expected variation of  $f$  between both separations is actually rather small. This is made even clearer when the data are plotted in the non-dimensional form of  $fD/U$  in figure 15.

Turning back to our analysis of (6.3) regarding separation, we conclude that the variation of  $fD/U$  versus  $x_0$  may be rather small and unlikely to dominate over other non-dimensional groups, leaving us with the vortex-impulse term  $\hat{C}_y \sin \phi$  that might present some significant variation with  $x_0$ .

As suggested above, the diffusion of vortices in the wake may be responsible for the reduction of the wake stiffness effect observed in figure 6. But, since we argue that

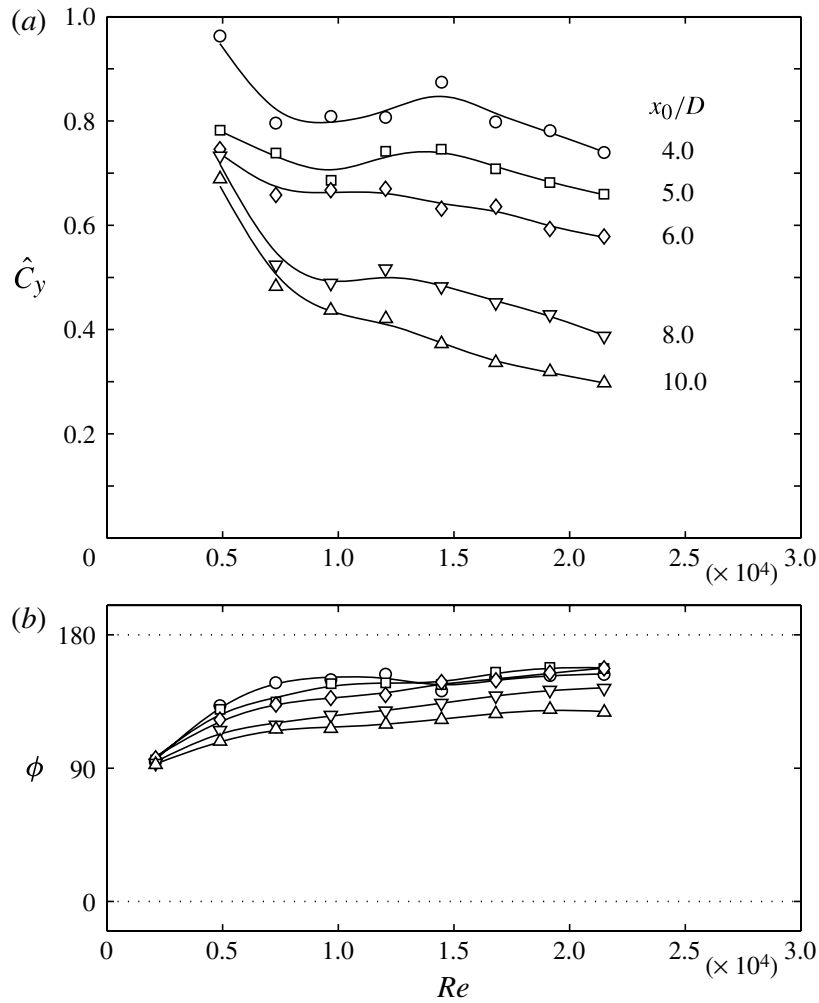


FIGURE 16. Fluctuating lift coefficient (a) and phase angle (b) for WIV responses without springs at various  $x_0$  separations.

both wake-stiffness and vortex-impulse terms originate in the same phenomenon, we believe that vortex diffusion may also be responsible for changes in  $\hat{C}_y \sin \phi$  versus  $x_0$ .

Figure 16 presents the variation of  $\hat{C}_y$  and  $\phi$  with both  $Re$  and  $x_0$ . We have shown that  $\hat{C}_y$  has a small dependence on  $Re$ , resulting in a mildly decreasing slope for  $x_0/D = 4.0$ . However, as separation is increased in figure 16 we observe that not only is the overall level of  $\hat{C}_y$  reduced, but also that the negative slope with  $Re$  is accentuated. On the other hand, figure 16(b) shows that although  $\phi$  is roughly constant with  $Re$  it is also reduced for larger  $x_0$ . Now, depending on the combination of both terms,  $\hat{C}_y \sin \phi$  can show significant variation with  $x_0$ , as much as to dominate over  $fD/U$  and govern the behaviour of the response versus separation.

## 9. Conclusions

The experiment without springs was crucial in the understanding of the WIV phenomenon. It not only revealed the existence of a dominant wake-stiffness effect that can sustain vibrations even if springs are removed, but also helped to explain different regimes of the response when springs are present. We proved that  $\bar{C}_y$  towards

the centreline not only provides some restoration for a quasi-static system but is in fact responsible for the characteristic WIV response of a cylinder that is free to vibrate.

The wake-stiffness concept does not explain the excitation mechanism but it predicts rather well the characteristic signature of the WIV response both in terms of displacement and frequency. We can say that while unsteady vortex–structure interactions provide the energy input to sustain the vibrations (Assi *et al.* 2010), it is the wake-stiffness phenomenon that defines the character of the WIV response.

We conclude that the restoration force provided by wake stiffness is strong enough to balance the flow excitation and produce oscillatory motion for a system without structural stiffness. The cylinder was not observed to drift away from the centreline, but presented WIV throughout the  $Re$  range of the experiments. The analytical modelling for a system without springs revealed that the amplitude of response should increase with Reynolds number. This was verified by experimental data. However, a simple model that did not account for nonlinear effects in the fluid force was not able to predict the correct level of amplitude. We found that the WIV response should converge to an asymptotic value that depends on  $Re$  but not on reduced velocity.

As  $\hat{y}/D$  is increased beyond a certain limit, the cylinder starts to reach amplitudes outside the wake interference region. The wake-stiffness effect cannot be represented by a linear spring anymore, but the overall stiffness tends to be reduced. This effect was in agreement with cases with and without springs and also with various  $x_0$  separations. A simple linear model was able to predict the frequency of response rather well. It was confirmed that the cylinder without springs does not respond following the vortex shedding frequency  $f_s$ . Instead the response matches the frequency branch  $f_w$  associated with wake stiffness, which was well predicted by the model. A cylinder with springs responds with a frequency that combines influences from  $f_w$  and  $f_0$ , yet is different from both.

In our experiments we observed a gradual transition from an initial VIV regime to a dominating WIV regime as flow speed was increased. The boundaries between them were found to be related to two resonances:  $f_s = f_0$  and  $f_w = f_0$ . The first regime has a clear VIV character, with a local peak of displacement occurring at  $f_s = f_0$ . The wake stiffness is still smaller than the spring stiffness, making  $U/Df_0$  a significant parameter. The amplitude of the VIV peak is in agreement with the response curve for a single cylinder and showed no noticeable dependence on  $Re$  for the range of the experiments. The second regime is characterized by an established WIV response that experiences no influence of VIV. Beyond  $f_w = f_0$  the wake-stiffness effect is dominant over the spring stiffness and reduced velocity becomes irrelevant.

During the transition between the regimes we find an intermediate condition in which VIV is losing strength and WIV is taking control. Between the resonances  $f_s = f_0$  and  $f_w = f_0$  the response leaves the VIV peak until it reaches a characteristic value at  $f_w = f_0$  that is dependent on  $Re$ . During the transition, reduced velocity gradually loses its influence until the WIV response is only dominated by  $Re$  as it enters the second regime. The total stiffness of the system is not only caused by either the wake stiffness ( $k_w$ ) or the spring stiffness ( $k$ ) alone, but it is a combination of both;  $k$  is very relevant in the first regime, but  $k_w$  becomes dominant in the second. Nevertheless, both  $k$  and  $k_w$  contribute in part to the characteristic displacement and frequency responses.

As expected, the  $x_0$  separation between the two cylinders was confirmed to have a significant effect on the response. We suggest this effect is related to an increase in vortex diffusion and flow three-dimensionality as the gap is enlarged. The WIV response changed as the second cylinder was moved farther downstream. The first VIV



regime experienced no influence of  $x_0$  and the local resonance peak kept the same level of displacement for all separations between  $4D$  and  $20D$ . On the other hand, the second WIV regime showed a strong influence of the separation. The characteristic WIV branch of response gradually disappeared with increasing  $x_0$  until the response resembled only that of a typical VIV phenomenon. In contrast with the displacement, the frequency of oscillation showed only a small variation with  $x_0$ , with curves for all separations collapsing onto the value predicted by the wake-stiffness effect, especially for the case without springs. Such a strong  $x_0$  dependence was associated with the fact that vortices from the upstream cylinder have more time to diffuse as they travel to reach a cylinder located farther downstream. Together with that is the fact that increasing three-dimensionality of the flow also weakens the coherent wake. Weaker vortices induced weaker forces. Both the wake-stiffness effect (proportional to  $\Delta\bar{C}_y$ ) and the vortex-impulse term (related to  $\hat{C}_y \sin \phi$ ) are affected.

By modelling a second-order oscillator without springs but incorporating the stiffness as a consequence of the fluid force (wake stiffness) we were able to predict the frequency behaviour rather well. But no matter how good this approach was in regard to the frequency response, the displacement response is somewhat more complex and is not fully captured by this first approximation. We believe this is due to the simplicity in modelling the term  $\hat{C}_y \sin \phi$ . Even though in some analysis we have considered  $\hat{C}_y$  and  $\phi$  to be independently related to the wake-stiffness and vortex-impulse terms, we are fully aware that this decomposition is not ideal and must overlook significant secondary effects.

A simple harmonic model such as the one we have employed cannot account for nonlinear effects that might be important to the system. It will not be able, for example, to predict the asymptotic effect that is limiting the displacement. The complex interaction between body and wake causes  $\Delta\bar{C}_y$  and  $\hat{C}_y \sin \phi$  to be coupled in such a way that we cannot simply analyse them independently. Since we believe both wake-stiffness and vortex-impulse terms originate in the same fluid-mechanic phenomenon, we are not able to uncouple and isolate their effects into linear concepts. We argue that an improved, nonlinear model is necessary to account for more complex fluid-dynamic phenomena that we have identified to exist but were not considered in our model.

In Assi *et al.* (2010) we have discussed the idea that WIV could not be predicted by the classical galloping theory. Remember that, in the literature, WIV had been referred to as a type of galloping mostly because the typical response presents a build-up of amplitude for higher reduced velocities. But now we know that the response is increasing due to the wake-stiffness effect as a function of Reynolds number. We have argued that quasi-steady assumptions commonly employed by the classical galloping theory would not fit the WIV phenomenon nor help to understand the real flow-structure mechanism. For that reason we have insisted on a dissociation of WIV from the classical galloping idea. In the present work we have shown that WIV is indeed a wake-dependent type of flow-induced vibration. Remember that according to the classical galloping theory the oscillations of the body are dependent on the structural stiffness of the system to provide the restoration force, even more for the wake-flutter phenomenon of interfering cylinders, where structural stiffness in 2-dof is required. In our case, however, we showed that a body without any structural stiffness can be excited into flow-induced vibration. If some stiffness is provided by the flow, the body is able to be excited and sustained into oscillatory motion. The concept of wake stiffness is a powerful one but it also requires the existence of an unsteady



vortex wake present in the gap to generate the excitation. Therefore we continue to propose that WIV is not to be understood as a type of classical galloping, but must be interpreted as a wake-excited and wake-sustained FIV mechanism.

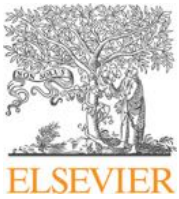
### Acknowledgements

G.R.S. and B.S.C wish to thank CAPES, Brazilian Ministry of Education, for their PhD scholarships. J.R.M. is grateful to CNPq for a research scholarship.

### REFERENCES

- ASSI, G. R. S. 2009 Mechanisms for flow-induced vibration of interfering bluff bodies. PhD thesis, Imperial College London, London, UK. available from [www.ndf.poli.usp.br/~gassi](http://www.ndf.poli.usp.br/~gassi).
- ASSI, G. R. S., BEARMAN, P. W. & MENEGHINI, J. R. 2010 On the wake-induced vibration of tandem circular cylinders: the vortex interaction excitation mechanism. *J. Fluid Mech.* **661**, 365–401.
- ASSI, G. R. S., MENEGHINI, J. R., ARANHA, J. A. P., BEARMAN, P. W. & CASAPRIMA, E. 2006 Experimental investigation of flow-induced vibration interference between two circular cylinders. *J. Fluids Struct.* **22**, 819–827.
- BEARMAN, P. W. 1984 Vortex shedding from oscillating bluff bodies. *Annu. Rev. Fluid Mech.* **16**, 195–222.
- BLEVINS, R. D. 1990 *Flow-Induced Vibration*, 2nd edn. Van Nostrand Reinhold.
- BOKAIAN, A. & GEOOLA, F. 1984 Wake-induced galloping of two interfering circular cylinders. *J. Fluid Mech.* **146**, 383–415.
- BRIKA, D & LANEVILLE, A. 1999 The flow interaction between a stationary cylinder and a downstream flexible cylinder. *J. Fluids Struct.* **13**, 579–606.
- GOVARDHAN, R. & WILLIAMSON, C. H. K. 2002 Resonance forever: existence of a critical mass and an infinite regime of resonance in vortex-induced vibration. *J. Fluid Mech.* **473**, 147–166.
- HOVER, F. S. & TRIANTAFYLLOU, M. S. 2001 Galloping response of a cylinder with upstream wake interference. *J. Fluids Struct.* **15**, 503–512.
- IGARASHI, T. 1981 Characteristics of the flow around two circular cylinders arranged in tandem. *Bull. Japan Soc. Mech. Engrs* **24**, 323–331.
- KHALAK, A. & WILLIAMSON, C. H. K. 1999 Motions, forces and mode transitions in vortex-induced vibrations at low mass-damping. *J. Fluids Struct.* **13**, 813–851.
- KING, R. & JOHNS, D. J. 1976 Wake interaction experiments with two flexible circular cylinders in flowing water. *J. Sound Vib.* **45**, 259–283.
- LANEVILLE, A. & BRIKA, D. 1999 The fluid and mechanical coupling between two circular cylinders in tandem arrangement. *J. Fluids Struct.* **13**, 967–986.
- MORSE, T. L. & WILLIAMSON, C. H. K. 2009 Prediction of vortex-induced vibration response by employing controlled motion. *J. Fluid Mech.* **634**, 5–39.
- NORBERG, C. 1998 LDV-measurements in the near wake of a circular cylinder. In *Advances in Understanding of Bluff Body Wakes and Flow-Induced Vibration* (ed. C. H. K. Williamson & P. W. Bearman). pp. 1–12. ASME.
- PARKINSON, G. V. 1989 Phenomena and modelling of flow-induced vibrations of bluff bodies. *Prog. Aeronaut. Sci.* **26**, 169–224.
- PRICE, S. J. 1975 Wake-induced flutter of power transmission conductors. *J. Sound Vib.* **38**, 125–147.
- PRICE, S. J. 1976 The origin and nature of the lift force on the leeward of two bluff bodies. *Aeronaut. Q.* **26**, 1154–1168.
- RUSCHEWEYH, H. P. 1983 Aeroelastic interference effects between slender structures. *J. Wind Engng Ind. Aerodyn.* **14**, 129–140.
- SARPKAYA, T. 1979 Vortex-induced oscillations, a selective review. *J. Appl. Mech.* **46**, 241–258.
- SCHAEFER, J. W. & ESKINAZI, S. 1958 An analysis of the vortex street generated in a viscous fluid. *J. Fluid Mech.* **6**, 241–260.

- WILLIAMSON, C. H. K. & GOVARDHAN, R. 2004 Vortex-induced vibrations. *Annu. Rev. Fluid Mech.* **36**, 413–455.
- ZDRAVKOVICH, M. M. 1974 Flow-induced vibrations of two cylinders in tandem and their suppression. In *International Symposium of Flow Induced Structural Vibrations* (ed. E. Naudascher). pp. 631–639. Springer.
- ZDRAVKOVICH, M. M. 1977 Review of flow interference between two circular cylinders in various arrangements. *Trans. ASME: J. Fluids Engng* **99**, 618–633.
- ZDRAVKOVICH, M. M. 1985 Flow induced oscillations of two interfering circular cylinders. *J. Sound Vib.* **101**, 511–521.
- ZDRAVKOVICH, M. M. 1988 Review of interference-induced oscillations in flow past two circular cylinders in various arrangements. *J. Wind Engng Ind. Aerodyn.* **28**, 183–200.
- ZDRAVKOVICH, M. M. 1997 *Flow Around Circular Cylinders*, vol. 1. 1st edn. Oxford University Press.
- ZDRAVKOVICH, M. M. & MEDEIROS, E. B. 1991 Effect of damping on interference-induced oscillations of two identical circular cylinders. *J. Wind Engng Ind. Aerodyn.* **38**, 197–211.



Contents lists available at ScienceDirect

## Journal of Fluids and Structures

journal homepage: [www.elsevier.com/locate/jfs](http://www.elsevier.com/locate/jfs)

# Wake-induced vibration of tandem cylinders of different diameters

Gustavo R.S. Assi

Department of Naval Architecture &amp; Ocean Engineering, University of São Paulo, NDF, Escola Politécnica, 05508-030 São Paulo, Brazil



## ARTICLE INFO

## Article history:

Received 3 February 2014

Accepted 2 July 2014

Available online 22 August 2014

## Keywords:

Wake-induced vibration

Circular cylinders

Vortex wake

Flow interference

## ABSTRACT

The wake-induced vibration (WIV) of the downstream cylinder of a tandem pair is investigated for different diameter ratios of  $D_1/D_2 = 1/1$ ,  $1/2$  and  $1/3$ , where  $D_1$  and  $D_2$  refer to the upstream and downstream cylinders, respectively. The streamwise separation between the cylinders was  $L/D_1 = 3.5$ ,  $7.0$  and  $6.5$ , respectively, measured from the centre of the upstream cylinder to the forward stagnation point of the downstream cylinder. Experiments with low mass-damping cylinders have been conducted in a water channel at around  $Re = 25\,000$ . The dynamic response showed that the downstream cylinder experienced WIV for all diameter ratios investigated, with displacement amplitudes reaching more than 1.5 diameters for higher reduced velocities beyond the vortex resonance range. The frequency response showed a similar behaviour for all three configurations, giving hints that a type of wake-stiffness mechanism might be governing the frequency of oscillation for all diameter ratios. The response was found to be dependent on both  $D_1/D_2$  and  $L/D_1$ . In all cases, the static upstream cylinder was found to shed vortices as an isolated cylinder, not influenced by the presence or movement of the downstream body. Lift and drag coefficients as well as measurements of velocity fluctuations in both wakes are presented for all cases.

© 2014 Elsevier Ltd. All rights reserved.

## 1. Introduction

When an elastic bluff body, like a circular cylinder, is immersed in the wake developed from an upstream body it will dynamically respond with *wake-induced vibrations* (WIVs). This hydroelastic mechanism has also been referred to as ‘wake-induced galloping’, ‘interference galloping’ or ‘wake-displacement excitation’ (Ruscheweyh, 1983; Bokaian and Geoola, 1984; Zdravkovich, 1988) and consists of the excitation of the downstream body by the interference of vortices developed in an unsteady wake generated upstream. The response of the downstream cylinder of a tandem pair is known to be severely increased by WIV when compared with that of an isolated cylinder under the resonant phenomenon of *vortex-induced vibration* (VIV).

Assi et al. (2010) reported on the effect of flow interference in the response of two identical cylinders aligned with the flow with centre-to-centre separations as large as 20 diameters. They have shown that vortices in the upstream wake play an essential role in driving the high-amplitude vibrations of the downstream cylinder. In fact, they performed an idealised experiment in which the unsteady vortex wake was replaced by a steady shear flow of equivalent mean velocity profile. They showed that the downstream cylinder immersed in that shear flow responded with a distorted type VIV but not with

E-mail address: [g.assi@usp.br](mailto:g.assi@usp.br)

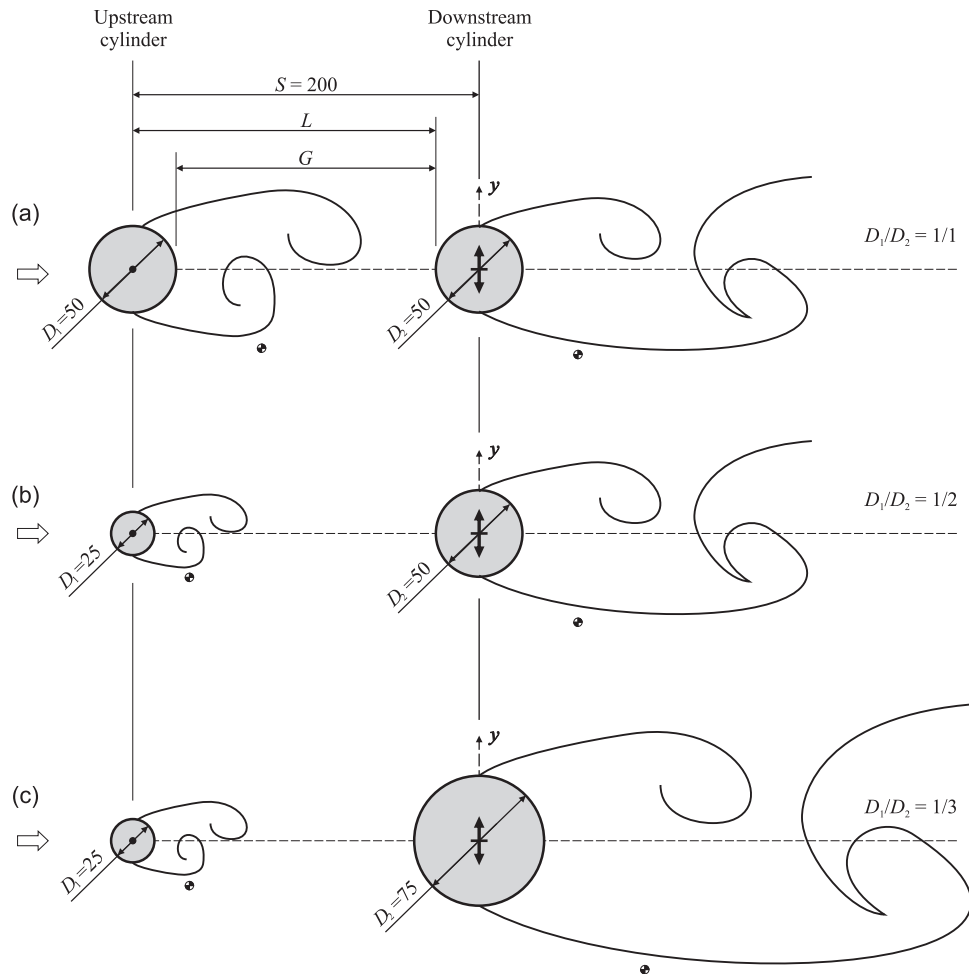


**Fig. 1.** Tandem configurations varying cylinders diameters. (a)  $D_1/D_2 = 1/1$ , (b)  $1/2$  and (c)  $1/3$ . Dimensions are in millimetres. Sketches drawn to scale.

high-amplitude WIV. Their conclusion was that the unsteady interaction of coherent and periodic vortices from the upstream wake was necessary to input energy into the system and sustain the vibration.

The present work is a step further in the direction of understanding the vortex–structure interferences driving WIV of two bodies. This time we are concerned with varying the length and time scales of the wake involved in this kind of fluid–structure interaction. The downstream cylinder of a tandem pair is immersed in the wake developed from an upstream cylinder with smaller diameter. Consequently, the length and the time scales of the vortices that come from the upstream wake and reach the downstream cylinder vary proportionally. Three tandem configurations with the smaller cylinder positioned upstream are investigated in the present study, as illustrated in Fig. 1. The subscripts 1 and 2 will always refer to the upstream and downstream cylinders, hence  $D_1$  and  $D_2$  represent the respective cylinder diameters. Three diameter ratios of  $D_1/D_2 = 1/1, 1/2$  and  $1/3$  were chosen for the experiments and the centre-to-centre separation was kept constant at 200 mm in order to allow for the upstream wake to develop in the gap with no interference from the second body. As a consequence, the wake reaching the second cylinder will be proportionately different in each case due to the scale of the upstream vortex shedding mechanism and wake diffusion in the gap.

(Note: The subscripts in the non-dimensional numbers follow the same convention. Reynolds numbers ( $Re_1$  and  $Re_2$ ) take the diameter of the specified cylinder and Strouhal numbers are calculated employing the vortex shedding frequency ( $f_s$ ) and the diameter of the referred cylinder, i.e.  $St_1 = f_{s1}D_1/U$  for the upstream cylinder and  $St_2 = f_{s2}D_2/U$  for the downstream cylinder.)

### 1.1. Flow interference between cylinders

Zdravkovich (1988) proposed a map of wake interference for two static cylinders with the same diameter arranged in several tandem and staggered configurations. The boundaries for each wake-interference zone clearly depend on the diameter of the two cylinders involved. It is expected that a smaller cylinder in the wake of a larger one will have to move many diameters across the wider wake before being free from any flow interference from upstream. The opposite might also happen for a larger cylinder moving across the narrower wake of a smaller body; the wake-interference zone might be reduced. Hence, the wake-interference map proposed by Zdravkovich (1988) will probably be different for each diameter

ratio illustrated in Fig. 1. However, this thought exercise might only be valid for the wake-interference of two static cylinders. Based on the results of Assi et al. (2010) we expect minute vortex impulses from upstream to have a considerable effect on the excitation of the downstream cylinder, especially if it presents low structural mass and damping. Even the wake of a smaller cylinder placed upstream (with smaller vortices at a higher frequency) might be sufficient to induce severe WIV of the second larger body. Assi (2014) showed that the flow interference from the upstream wake will have an effect even if the downstream cylinder is initially positioned further out of the centreline of the wake, in what is called a staggered arrangement. An effect on the response of the downstream cylinder was observed for lateral separations up to 3 diameters when  $S/D=4$  (both cylinders having the same diameter).

Most of the studies concerning interference of cylinders with different diameters are focussed on the effect that the wake of a smaller cylinder has on the flow behaviour around a larger body. Studies of this kind can be classified as flow control experiments and some will go as far as to consider both the small and large cylinders as a coupled pair able to respond to flow-induced vibrations. Rahmanian et al. (2012) performed numerical simulations of the flow around two interfering cylinders with  $D_1/D_2=0.1$ . The pair was mechanically coupled and able to respond to flow-induced vibrations in two degrees of freedom, thus the investigation was aimed at understanding the interference effect of the smaller cylinder on the larger one as the gap and the angular position were varied between them. Their main finding was that the maximum vibration observed for the coupled pair occurred when the cylinders were arranged in staggered configuration and not aligned with the flow. Tsutsui et al. (1997) also presented an experimental and numerical investigation employing a similar arrangement of a very small cylinder positioned about the main body. But their investigation with static cylinders only showed that the wake structure and fluid forces were strongly affected by the position of the small cylinder. Zhao et al. (2005) and Zhao and Yan (2013) both presented numerical investigations in the same lines.

The present investigation, however, is not concerned with the flow interference between a very small cylinder positioned in the vicinity or about a main body nor it is concerned with a mechanically coupled pair. In the present work we will investigate the flow interference from a fully developed upstream wake on the response of the downstream cylinder of a tandem pair with relatively similar diameters. Thus, we are truly concerned with the effect that wakes of different scales will have on the wake-induced vibration of the downstream body. The upstream cylinder is always static and only responsible for generating a vortex wake that reaches the second body. The downstream cylinder is free to respond with flow-induced vibrations only one degree of freedom (1-dof) in the cross-flow direction. The in-line separation between the cylinders is kept constant at all times.

In our experiments, the upstream cylinder is always smaller than the downstream one. Nevertheless, it is worth mentioning the work done by Huang and Sworn (2011), in which they investigated the WIV of a cylinder when a larger body was placed upstream. In their experiments, performed in a water flume at subcritical  $Re$ , they employed a pair of rigid cylinders in tandem with  $D_1/D_2=2.0$  and in-line spacing varying between  $S/D_1=1$  and 10. Both cylinders were elastically supported in a low-damping system, free to respond in both the cross-flow and streamwise directions. They observed that the signature of lift measured on the downstream cylinder had the frequency components from the upstream vortex shedding as well as from its own vortex shedding, with predominance depending on the in-line spacing. Independently of the separation, they observed that the upstream cylinder always showed a typical VIV response, while the downstream cylinder presented WIV response reaching cross-flow displacements as high as 1.5 diameters in amplitude. In a later study, Huang and Sworn (2013) employed cylinders with  $D_1/D_2=1, 2$  and 4 and varied the in-line spacing between  $S/D_1=1$  and 15 to reach similar conclusions. As expected, when both cylinders were held static, the average drag measured on the downstream cylinder showed the effect of a slower mean flow coming from the upstream body, which in turn was dependent on the diameter ratio and the in-line separation.

Alam and Zhou (2008) performed wind-tunnel experiments with a pair of static cylinders with different diameters to measure forces and flow structures of the interfering flow. The diameter ratio varied between  $D_1/D_2=0.24$  and 1.0 and the in-line spacing was fixed at  $L/D_1=5.5$ , providing that a fully developed wake was generated in the gap for the range of  $Re_2=0.6 \times 10^4$ – $2.7 \times 10^4$ . The authors found two distinct frequencies of vortex shedding coexisting in the wake downstream of the pair, which were attributed to the vortex shedding mechanisms of each of the cylinders. This was only verified for certain diameter ratios for static cylinders.

In a recent study, Alam and Zhou (2014) investigated the flow-induced response of a similar pair of cylinders at  $Re_2=2.7 \times 10^4$ . The smaller, static cylinder was placed upstream of a cantilevered cylinder, with the ratio between the two diameters also varying between  $D_1/D_2=0.24$  and 1.0. This time the tandem cylinders were arranged in close proximity, with in-line separation being set at  $L/D_2=1.0$  and 2.0. Interestingly, Alam and Zhou (2014) only observed severe vibrations of the downstream cylinder for  $D_1/D_2=0.24$ –0.8 (considering both in-line separations tested) and not for cylinders with the same diameter. In addition, vibrations were observed for reduced velocities in the range of 13–22.5, too high to be regarded as a result of resonant VIV. They explained that the smaller cylinder placed upstream would generate a narrower wake capable of exciting vibrations as the shear layers flipped from one side to the other during the cross-flow displacement of the downstream body. For cylinders of equal diameters at close proximity, on the other hand, the wider upstream wake would engulf the downstream cylinder making the side-to-side flipping mechanism rather difficult to occur. We believe these vibrations are better described by the ‘gap-flow switching’ mechanism explained in Zdravkovich (1988), since the close proximity of the bodies prevents a developed wake to form in the gap. The fact that the downstream cylinder was mounted as a cantilever may result that not its entire length is being excited by the same mechanism, especially knowing that ‘gap-flow switching’ requires a considerable amount of transverse displacement to occur.



2. Method

At first sight it seems rather simple to find a parameter to represent the in-line separation between the cylinders, but one must not be mistaken by the effect that the apparent simplicity of the geometries in Fig. 1 has on the hydrodynamic mechanisms involved. Since both cylinders vary in diameter, the effective gap between the bodies changes from case to case. For example, to consider the centre-to-centre separation  $S$  to be the characteristic in-line distance of the problem will make the gap between cylinders in Fig. 1(b) to appear larger than in the other two cases. Another way to interpret the actual length scale affecting the flow interference would consider the gap  $G$  measured between the cylinder walls, thus making the cylinders in Fig. 1(a) to look closer than the others. One can see that there are several ways to organise and interpret the data. The physical characteristics of the wake interference phenomena must not be forgotten. On top of that, there is the problem of choosing which diameter should be the reference for normalisation: that of the static upstream cylinder ( $D_1$ ), where the wake is generated, or that of the oscillatory downstream cylinder ( $D_2$ ), the object of WIV.

Perhaps the most reasonable interpretation would consider the distance measured from the centre of the upstream cylinder to the wall (or forward stagnation point) of the downstream cylinder, defined by  $L$  in Fig. 1. Such an interpretation might be possible because the separation points on the upstream cylinder are practically aligned with the centre of the cylinder; hence at roughly the same location for all three configurations independently of the dimension  $D_1$ . The interference effect of the wake on the downstream cylinder, on the other hand, depends on  $D_2$  and the position of the forward stagnation point. Therefore, as far as wake interference is concerned, the most appropriate parameter to be employed in the study appears to be  $L/D_1$ , non-dimensionalised by the diameter of the upstream cylinder, where the upstream wake is being generated.

Table 1 presents all geometrical parameters and respective normalisations as explained in the paragraphs above. All possible normalisations of  $S$ ,  $G$  and  $L$  were kept in the table to illustrate the variety of ways that could be employed in interpreting the in-line separation. In the present work, however,  $L/D_1$  is considered to be the length scale representative of the wake interference phenomenon, thus special attention will be given to the penultimate column.

2.1. Experimental setup

Experiments were performed during a test campaign in the Department of Aeronautics at Imperial College, London. Tests were carried out in a recirculating water channel with a free surface and a test section 0.6 m wide, 0.7 m deep and 8.0 m long. Flow speed was continuously variable up to  $U=0.6$  m/s and free stream turbulence intensity was around 3%. Circular cylinder models were made from acrylic tubes, giving a maximum  $Re=30\,000$  based on a cylinder diameter of 50 mm.

The downstream cylinder was fixed at its upper end to a 1-dof elastic mounting represented in Fig. 2. The model was aligned in the vertical direction passing through the free surface and mounted such that there was a 2 mm gap between the

**Table 1**  
Geometrical parameters for the tandem configurations illustrated in Fig. 1. Dimensional terms in columns 2–6 are in millimetres.

| $D_1/D_2$ | $D_1$ | $D_2$ | $S$ | $G$   | $L$   | $S/D_1$ | $S/D_2$ | $G/D_1$ | $G/D_2$ | $L/D_1$ | $L/D_2$ |
|-----------|-------|-------|-----|-------|-------|---------|---------|---------|---------|---------|---------|
| 1/1       | 50    | 50    | 200 | 150   | 175   | 4.0     | 4.0     | 3.0     | 3.0     | 3.5     | 3.5     |
| 1/2       | 25    | 50    | 200 | 162.5 | 175   | 4.0     | 4.0     | 6.5     | 3.25    | 7.0     | 3.5     |
| 1/3       | 25    | 75    | 200 | 150   | 162.5 | 8.0     | 2.7     | 6.0     | 2.0     | 6.5     | 2.17    |

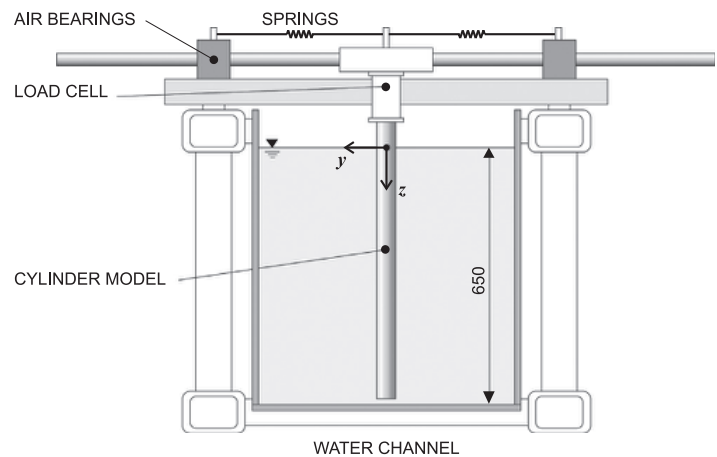


**Fig. 2.** Representation of the downstream cylinder mounted on the 1-dof rig in the test section of the water channel. View of the cross-section. Dimensions are in millimetres.



**Table 2**  
Structural properties for the downstream cylinder.

| $D_1/D_2$ | $m^*$ | $\zeta(\%)$ | $m^*\zeta$ |
|-----------|-------|-------------|------------|
| 1/1       | 2.6   | 0.35        | 0.0091     |
| 1/2       | 2.6   | 0.35        | 0.0091     |
| 1/3       | 1.2   | 0.35        | 0.0041     |

lower end of the cylinder and the floor of the test section. It was judged preferable not to install end plates on the cylinder in order not to increase the fluid damping in the system. The support was firmly attached to the channel structure and sliding cylindrical guides were free to move in the transverse direction ( $y$ -axis) through air bearings. A pair of coil springs connecting the moving base to the fixed supports provided the restoration force for the system.

It is known that the dynamic response of a cylinder is extremely sensitive to the structural characteristics of the system; therefore extra care was taken to determine the precise value of natural frequency, mass and damping of the structure. The air bearings proved to be an effective way to reduce damping without compromising the stiffness of the structure, especially in resisting drag loads for higher flow speeds. By carrying out free decay tests in air it was possible to estimate the natural frequency ( $f_0$ ) and the structural damping parameter of the system ( $\zeta$ , calculated as a percentage of the critical damping). They are presented in Table 2 along with the mass ratio ( $m^*$ , calculated as the total mass divided by the mass of displaced water), for the configurations tested.

A load cell was installed between the model and the platform to measure hydrodynamic forces acting on the cylinder (inertial components have been subtracted from the total force acquired by the load cell). An optical positioning sensor measured the  $y$ -displacement without adding damping. Two hot-film probes were employed to measure velocity fluctuation in the wake of both cylinders in order to capture the frequency of vortex shedding close to the vortex formation regions. Probes were positioned at roughly  $1D$  downstream of the cylinder centre and  $1D$  to the side of the centreline; locations are marked by quartered-circle symbols in Fig. 1. More details about the apparatus, flow quality, design of the load cell and operation of the 1-dof rig can be found in Assi (2009).

Measurements were made using one set of springs and the reduced velocity range covered was from  $U/D_2f_0 = 2$  to 30, where reduced velocity is defined using  $f_0$  measured in air. The only flow variable changed during the course of the experiments was  $U$ , which alters both the reduced velocity and the Reynolds number. Throughout the study, cylinder displacement amplitudes ( $\hat{y}/D_2$ ) were found by measuring the root mean square (r.m.s.) value of response and multiplying by  $\sqrt{2}$  (the so-called harmonic amplitude). Displacements were non-dimensionalised by dividing by the downstream cylinder diameter.

### 3. Results and discussion

Fig. 3 presents the WIV response for the tandem configurations versus reduced velocity. Displacement and frequency curves are compared with the response of a single cylinder with  $D=50$  mm, which will serve as a reference for the discussion that follows. During the typical single-cylinder VIV excitation, as  $U$  increases, the frequency of vortex-shedding ( $f_s$ ) gets close enough to the body's natural frequency of oscillation ( $f_0$ ) in a way that the unsteady pressure fluctuation in the near wake induces the body to respond in resonance. Once the cylinder starts to oscillate, high-amplitude movements will control the vortex formation and  $f_s$  will be *locked in* the response frequency ( $f$ ) near  $f_0$ . If  $U$  continues to increase the typical vortex-shedding frequency will move far away from the natural frequency of the system, i.e.  $f_s$  and  $f$  will be uncoupled again. Refer to Bearman (1984) and Williamson and Govardhan (2004) for a detailed description of the VIV mechanism and typical responses.

Since reduced velocity was increased by changing  $U$  in the channel an extra horizontal axis has been introduced to indicate the equivalent Reynolds number scale calculated for a cylinder with  $D=50$  mm. All three experiments were performed until the maximum flow speed was reached in the channel, making the third dataset look shorter in the reduced velocity scale; hence the Re scale is not true for the  $D_1/D_2 = 1/3$  curve.

Fig. 3(a) presents the harmonic amplitude of vibration of the downstream cylinder. It is evident that all three configurations present the build-up of displacement for higher reduced velocities that are characteristic of WIV. For  $U/D_2f_0 = 4$ –7 all tandem configurations present a local peak of vibration related to the resonance of vortex shedding; this is equivalent to the upper branch registered for the single cylinder under VIV. But for  $U/D_2f_0 > 12$  it becomes clear that the responses are not driven by resonance any longer, but sustained by the WIV mechanism.

The case  $D_1/D_2 = 1/1$  (with  $L/D_1 = 3.5$ ) reaches a maximum  $\hat{y}/D_2 = 1.8$  at  $U/D_2f_0 \approx 30$ . For  $D_1/D_2 = 1/2$  the maximum response reaches  $\hat{y}/D_2 = 1.3$  at around the same reduced velocity, but the effective separation is now  $L/D_1 = 7.0$ , twice as much as the previous case. Between the first two cases there is no variation of Reynolds number, so the decrease in the level of response must be related to decreasing the diameter ratio and/or doubling the effective in-line separation.

On the other hand, when the diameter ratio was made even smaller in the  $D_1/D_2 = 1/3$  configuration the response increased when compared with the  $D_1/D_2 = 1/2$  case. A maximum  $\hat{y}/D_2 = 1.4$  was reached for the maximum reduced

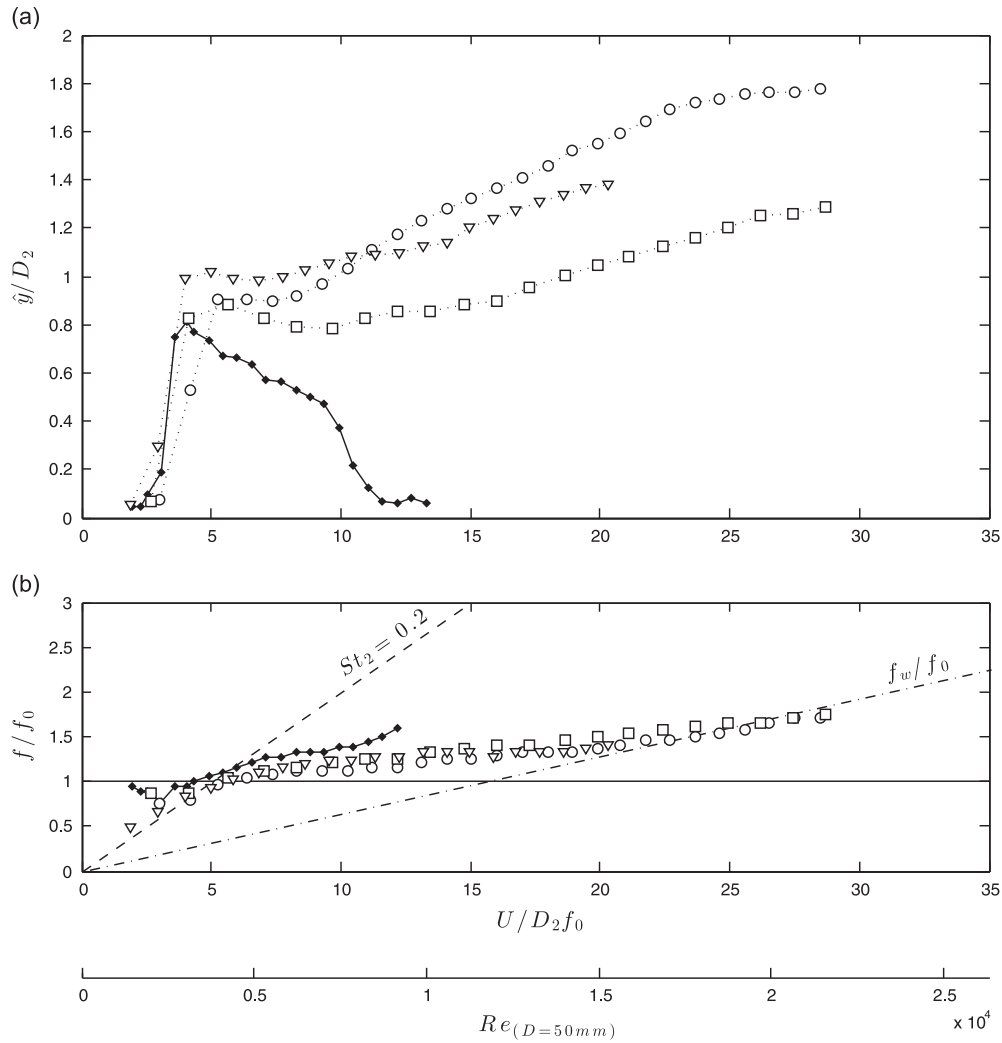


**Fig. 3.** WIV response of cylinders with different diameters. (a) Displacement and (b) frequency of vibration versus reduced velocity. Key:  $\blacklozenge$ , single cylinder VIV;  $\circ$ ,  $D_1/D_2 = 1/1$ ;  $\square$ ,  $D_1/D_2 = 1/2$ ;  $\nabla$ ,  $D_1/D_2 = 1/3$ .

velocity, now just above 20, but an amplification of the response was clear to be occurring for the whole range of reduced velocities tested. In this case, decreasing  $D_1/D_2$  produced stronger vibration of the downstream cylinder, which might be related to the fact that the effective in-line separation decreased to  $L/D_1 = 6.5$  when compared with the previous tandem configuration (it must be noted that  $Re$  has also increased).

Comparing the three response curves in Fig. 3(a) we may conclude that both the diameter ratio and the effective in-line separation have a strong effect on the WIV response of the downstream cylinder. Nevertheless it is interesting to note that even the smallest upstream cylinder with  $D_1/D_2 = 1/3$  is capable of inducing vibrations on the downstream body of comparable amplitude as a configuration with cylinders with equal diameters.

The mass ratio, however, might still be another factor playing some role in the amplification of response from case  $D_1/D_2 = 1/2$  to  $1/3$ . As seen in Table 2, the  $D_1/D_2 = 1/3$  case presents  $m^* = 1.2$ , less than half of the  $m^* = 2.6$  for the other two configurations due to the larger diameter of the cylinder. Probably a relatively lighter cylinder would be more vulnerable to the upstream excitation even though it comes from a much smaller cylinder. This could produce higher amplitudes of response during the VIV resonance range, as it is known to occur for a single-cylinder VIV. Past the VIV range, say for reduced velocities above 15, the response for  $D_1/D_2 = 1/3$  is lower than that for  $D_1/D_2 = 1$ . We suspect this is related to the width of the upstream wake relative to  $D_2$ . In this case, the downstream cylinder moves out of the upstream wake at smaller displacements and the unsteady excitation mechanism proposed in Assi et al. (2010) is therefore weakened.

The dominant frequency of response of the downstream cylinder normalised by the natural frequency of vibration ( $f/f_0$ ) is presented in Fig. 3(b). An inclined dashed line indicates that the frequency associated with the vortex shedding of the downstream cylinder was it to follow a typical Strouhal number of 0.2. Between  $U/D_2 f_0 = 2$  and 7, in the region associated with the stronger VIV resonance, all configurations vibrate with dominant frequency following close to the  $St_2 = 0.2$  line, as well as the single cylinder under VIV. As flow speed is increased towards the end of the VIV synchronisation range, the dominant frequencies for all cases depart from the  $St_2 = 0.2$  towards the horizontal line of  $f/f_0 = 1$ . Eventually, for even higher reduced velocities past the VIV influence, the frequency curves tend towards another dot-dashed line identified as

$f_w/f_0$ . Surprisingly, this line represents the frequency of wake stiffness introduced by Assi et al. (2013) as the characteristic WIV frequency of vibration of the downstream cylinder of a pair with equal diameters. (Note that the slope of this line was determined in Assi et al., 2013 and is only valid for  $D_1 = D_2$ .)

The wake-stiffness concept explains that there is a natural frequency of oscillation of hydrodynamic nature ( $f_w$ ) dominating over the response of the cylinder immersed in the upstream wake (Refer to Assi et al., 2013 for details on the estimation of  $f_w$ ). We believe  $f_w$  to be strongly dependent on the vortex interaction occurring in the wake, thus depending on the width of the upstream wake as well as the length and time scales of the vortices being shed (wake topology). Tandem pairs with different diameter ratios would probably produce different values of  $f_w$ , but this was not measured in the present investigation. What is surprising here is that the frequency of response for  $D_1/D_2 = 1/2$  was not expected to follow the  $f_w/f_0$  line previously determined for  $D_1/D_2 = 1/1$ , but as a matter of fact it falls very close to it. Unfortunately the response curve for  $D_1/D_2 = 1/3$  does not go much further than  $U/D_2 f_0 = 20$ , but up to that point it follows the other two curves pretty well. If wake stiffness is a function of wake topology and geometry, as believed, it is not a strong dependency as to make significant difference in these response curves, at least not in the present range of  $D_1/D_2$  and  $L/D$ .

In summary, even with considerable variations of  $D_1/D_2$ ,  $L/D_1$  and  $m^*$  the frequency signatures of WIV for all tandem cases are remarkably similar and follow very closely the behaviour governed by the wake stiffness of WIV introduced by Assi et al. (2013) for  $D_1 = D_2$ . More striking is the fact that the dominant frequency of vibration of the downstream cylinder is higher than the structural natural frequency of the system (line for  $f/f_0 = 1$ ), clearly different from the expected vortex shedding frequency of the cylinder (line for  $St_2 = 0.2$ ) and probably very different from the expected shedding frequency of the upstream cylinder, which has a smaller diameter. In order to clarify that, we shall turn to the frequency signature measured in both wakes and derived from the forces acting on the cylinders.

### 3.1. Frequency signatures of lift and wakes

Fig. 4 presents a series of contour plots representing the power spectrum signature of wakes and forces for the configuration  $D_1/D_2 = 1/1$ . Each plot shows the frequency scale non-dimensionalised by  $f_0$  in the vertical axis versus reduced velocity in the horizontal axis. The intensity of the colour shade represents the power content for either velocity fluctuation in the wake or fluctuating force on the cylinder. Power spectra were normalised for each reduced velocity in order to make it possible to follow through branches of dominant frequency along the horizontal axis. The dominant frequency of oscillation presented in Fig. 3(b) is repeated as data points in each plot as a reference of the response.

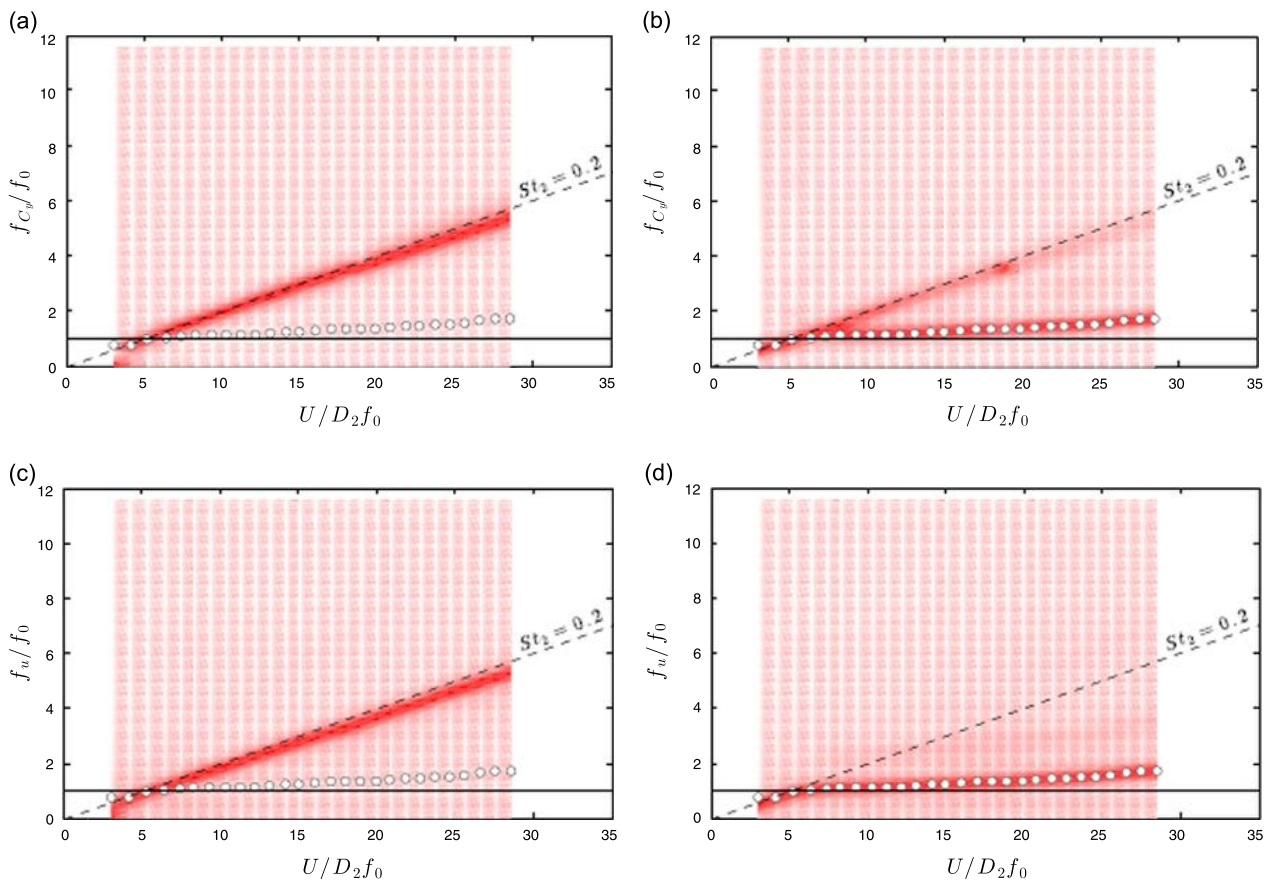


**Fig. 4.** Power spectra for configuration  $D_1/D_2 = 1/1$ . Frequency of lift on the (a) upstream and (b) downstream cylinders. Frequency of velocity fluctuation in the wake of the (c) upstream and (d) downstream cylinders.

The frequency signature of lift measured on the upstream cylinder ( $f_{C_y}/f_0$ ) is presented in Fig. 4(a), revealing that the upstream static cylinder is shedding vortices as an isolated cylinder following the typical  $St_2 = 0.2$  dashed line (in this case  $D_1 = D_2$ ). As seen in Fig. 4(c), the behaviour is confirmed by the signature of velocity fluctuation in the wake ( $f_u/f_0$ ) measured by a hot-film probe downstream of the upstream cylinder. Hence, the upstream cylinder is shedding vortices as an isolated cylinder and no traces of the frequency of oscillation of the downstream cylinder are noticeable in the spectra of the wake or lift.

The spectrum of lift ( $f_{C_y}/f_0$ ) on the downstream cylinder, presented in Fig. 4(b), reveals that the second body indeed experiences lift at the frequency of shedding coming from the upstream cylinder. This is a result of vortices impinging on the downstream cylinder as it moves across the wake. However, a much stronger branch appears to dominate the spectrum, one which is associated with the frequency of vibration represented by the data points. Now, one cannot tell how much of the power in that strong branch is a result of the unsteady flow excitation or simply the hydrodynamic inertia measured by the load cell as the cylinder moves across the wake. Perhaps it is a combination of both. A branch at that frequency would also appear if the cylinder were vibrating with  $f$  in still water. The fact is that this is the preferred frequency of vibration for the downstream cylinder, the one associated with the wake stiffness. This happens to be the only frequency branch identified in the wake of the downstream cylinder, as seen in Fig. 4(d), and no traces of vortex shedding following the Strouhal line were registered. Again, this might be the effect of the movement of the downstream cylinder dominating over the velocity fluctuations measured by the hot-film probe in the wake.

Moving on to the  $D_1/D_2 = 1/2$  configuration presented in Fig. 5, we notice that the frequency signature of lift on the downstream cylinder ( $f_{C_y}/f_0$ ), shown in Fig. 5(a), also presents a clear dominant branch coinciding with the frequency of oscillation, as expected. Other secondary frequency branches, nonetheless, can be seen to occur at the shedding frequencies of both cylinders, i.e. following the  $St_1 = 0.2$  and  $St_2 = 0.2$  dashed lines (represented by very light shades of colour in the contour plots). Looking at the wake signature of the upstream cylinder in Fig. 5(b) it becomes clear that the first body is shedding vortices as an isolated static cylinder and no significant traces of the downstream oscillation are being propagated upstream either. Once more, the wake signature ( $f_u/f_0$ ) of the downstream cylinder in Fig. 5(c) only captures weak traces of these higher frequencies, with the dominant frequency branch being associated with the frequency of vibration. As noted before, Alam and Zhou (2008) verified the existence of higher frequencies associated with the upstream shedding for two static cylinders. We believe that when the downstream cylinder is free to oscillate the frequency of oscillation will dominate over the shedding frequencies of the upstream body and the latter will not be very clear in the spectrum plots of the downstream wake.

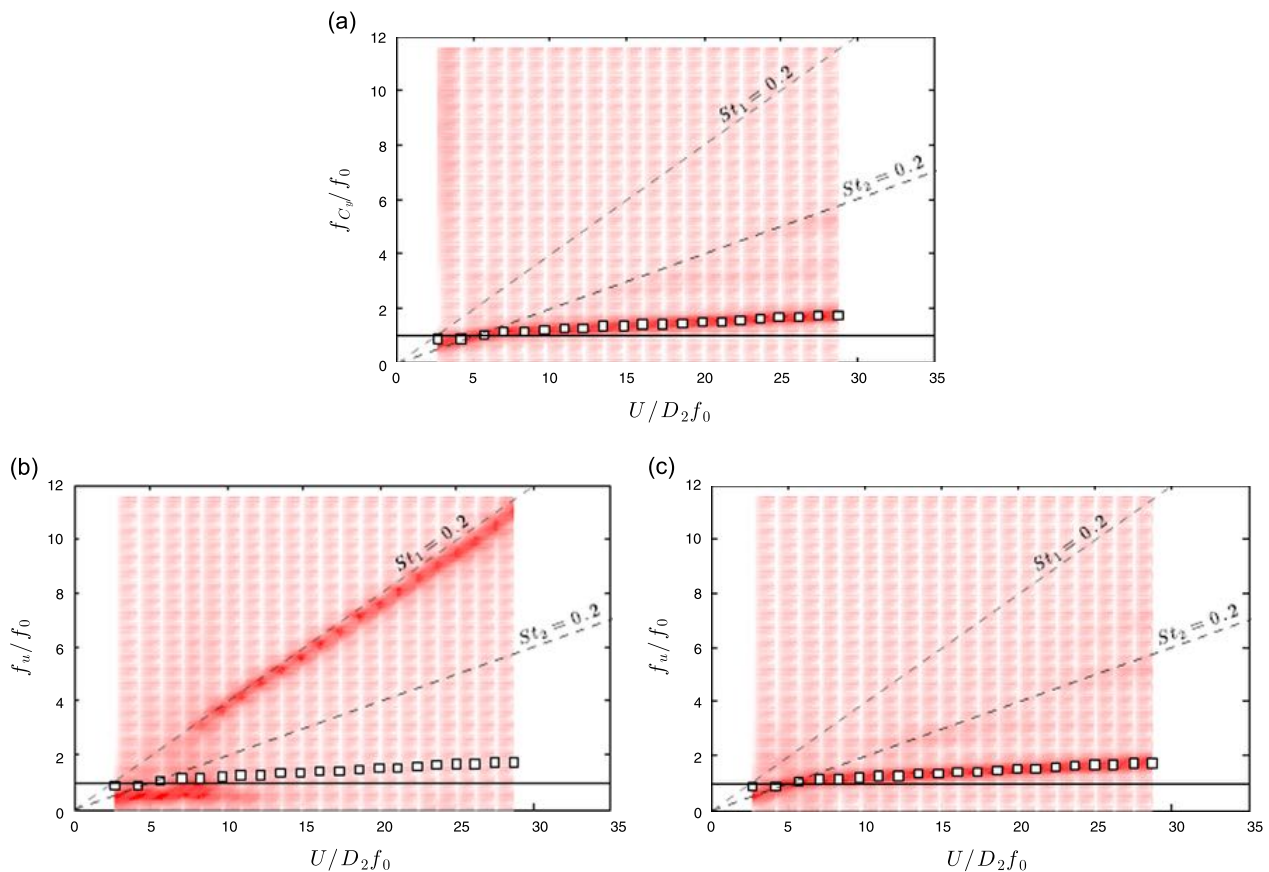


**Fig. 5.** Power spectra for configuration  $D_1/D_2 = 1/2$ . (a) Frequency of lift on the downstream cylinder. Frequency of velocity fluctuation in the wake of the (b) upstream and (c) downstream cylinders.



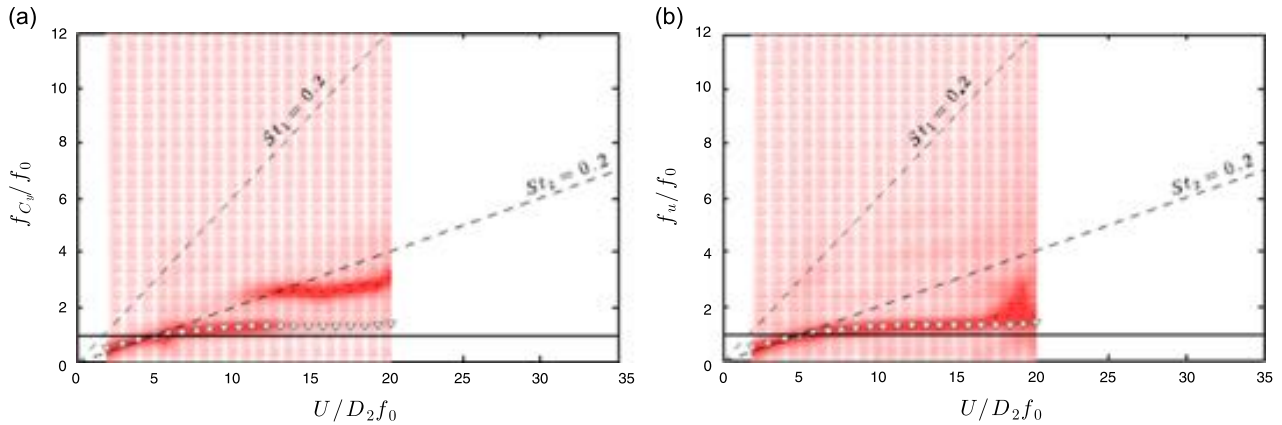


**Fig. 6.** Power spectra for configuration  $D_1/D_2 = 1/3$ . (a) Frequency of lift on the downstream cylinder and (b) frequency of velocity fluctuation in the wake of the downstream cylinder.

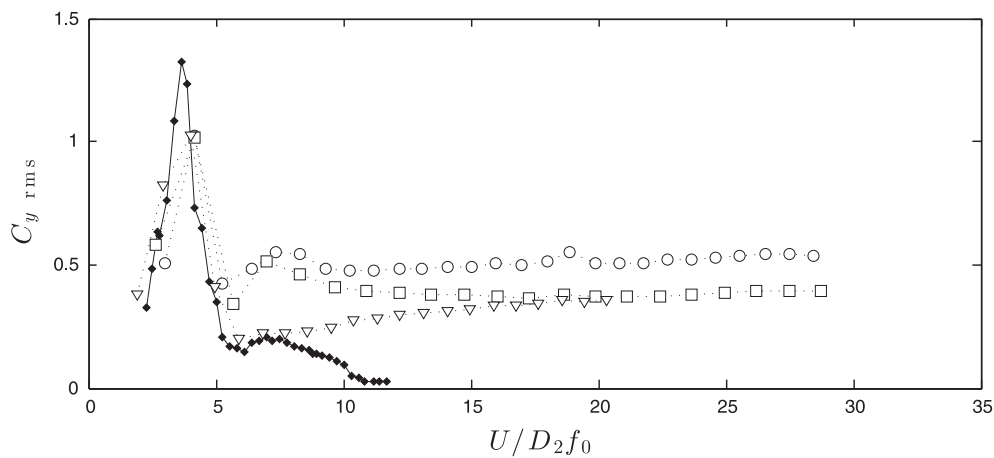


**Fig. 7.** Lift coefficient (r.m.s.) versus reduced velocity. Key:  $\blacklozenge$ , single cylinder VIV;  $\circ$ ,  $D_1/D_2 = 1/1$ ;  $\square$ ,  $D_1/D_2 = 1/2$ ;  $\nabla$ ,  $D_1/D_2 = 1/3$ .

Finally, for the  $D_1/D_2 = 1/3$  configuration presented in Fig. 6(a) we observe that traces of the vortex shedding frequency of the upstream cylinder (occurring at  $St_1 = 0.2$ ) are barely noticeable in the lift signature of the downstream cylinder. The lower branch associated with the frequency of vibration still dominates over the spectrum, however a second branch of  $f_{Cy}/f_0 \approx 3$  appears for  $U/D_2f_0 > 12$ . It is not clear what mechanism this higher frequency represents. In the wake spectrum presented in Fig. 6(b) we do not observe other significant frequency branches other than the actual dominant frequency of vibration.

Based on the spectrum plots presented in Figs. 4–6 we conclude that the separation of  $S=200$  mm (resulting in  $L/D_1 = 3.5$ ,  $7.0$  and  $6.5$  for each respective configuration) was sufficiently large to prevent any interference from the downstream wake or vibration from propagating upstream to affect the vortex shedding mechanism of the first cylinder. The upstream cylinder behaved as an isolated static cylinder for all cases and the higher frequency associated with the upstream shedding reached the downstream cylinder and was captured by the lift spectrum for all cases. This is similar to what was observed by Huang and Sworn (2011) with the larger cylinder placed upstream. However, the vibration of the downstream body was not directly associated with that frequency of excitation, but it responded in a much lower frequency closely related to the frequency of wake stiffness ( $f_w$ ) proposed by Assi et al. (2013).

### 3.2. Hydrodynamic force coefficients

In the response curves presented in Fig. 3 we observed that different levels of amplitude of vibration were reached by each  $D_1/D_2$  case. We also noticed in the spectrum plots of Figs. 4–6 that the WIV excitation is indeed coming from the fully developed wakes of the upstream cylinders, which produce vortices with different strengths, lengths and time scales due to variations in  $D_1/D_2$  and  $L/D_1$ . Now, in order to investigate how the amplitude of response is correlated with the upstream excitation we will turn to measurements of lift on the downstream cylinder.

Fig. 7 presents the r.m.s. of lift coefficient ( $C_{y \text{ rms}}$ ) measured on the downstream cylinder compared with  $C_{y \text{ rms}}$  measured on a single cylinder under VIV, the latter being in good agreement with the experimental data presented by Khalak and Williamson (1999). As expected, all tandem configurations present a peak of  $C_{y \text{ rms}}$  corresponding to the local resonance of VIV at  $U/D_2f_0 \approx 4$ . After that, when  $C_{y \text{ rms}}$  associated with VIV starts to diminish with the end of the synchronisation range,

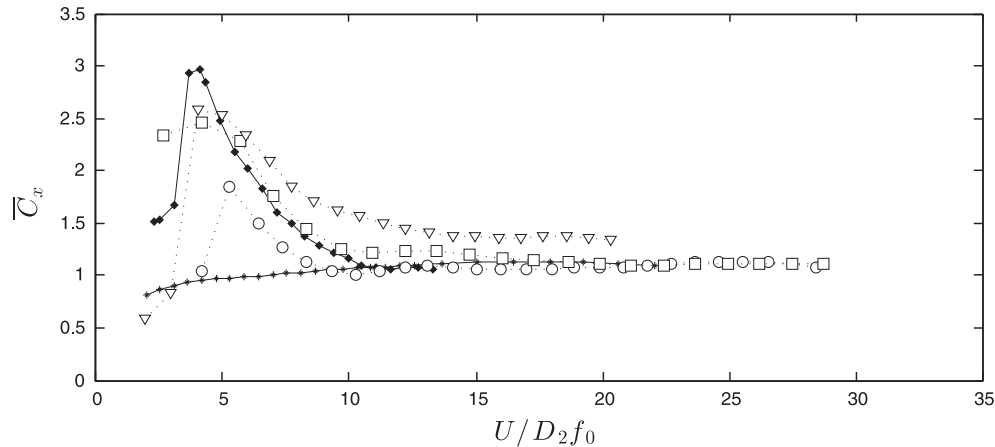


**Fig. 8.** Mean drag coefficient versus reduced velocity. Key: \*, single static cylinder; ♦, single cylinder VIV; ○,  $D_1/D_2 = 1/1$ ; □,  $D_1/D_2 = 1/2$ ; ▽,  $D_1/D_2 = 1/3$ .

$C_{y \text{ rms}}$  for the tandem cases increases to a much higher level, which is sustained until the end of the reduced velocity range tested.

Lift coefficient for  $D_1/D_2 = 1/1$  remains at  $C_{y \text{ rms}} \approx 0.5$  while the other two cases find levels slightly below that, with  $D_1/D_2 = 1/3$  showing the lowest  $C_{y \text{ rms}}$  level. It appears that the level of  $C_{y \text{ rms}}$  is more dependent on  $D_1/D_2$  rather than on  $L/D_1$ . The amplitude of response ( $\hat{y}/D_2$ ), on the other hand, seems to be more dependent on  $L/D_1$  rather than on  $D_1/D_2$ , with  $D_1/D_2 = 1/3$  reaching amplitudes higher than  $D_1/D_2 = 1/2$ . Nevertheless, as suggested before, this could also be related to the fact that  $D_1/D_2 = 1/3$  presents half of the  $m^*$  of the other two cases.

We have seen that the lift on the downstream cylinder will act at the frequency of wake stiffness ( $f_w$ ) and those of vortex shedding ( $f_s$ ), which will be sustained for an indefinite range of reduced velocities during the WIV mechanism. Assi et al. (2010) explained how this excitation mechanism depends on the unsteady interaction of the vortices coming from the upstream wake and the downstream cylinder. Therefore, the topology of the wake (width, vortex strength, length, time scales, etc.) modified by an upstream cylinder of smaller diameter must be playing a fundamentally different role in the excitation mechanism.

Mean drag coefficients ( $\bar{C}_x$ ) on the downstream cylinder are presented in Fig. 8. The drag curve for a single cylinder reveals the amplification of drag normally observed during the synchronisation range of VIV, which agrees well with the results presented by Khalak and Williamson (1999). A curve for the drag of a static single cylinder has also been added as a reference.

All tandem configurations present a similar amplification of drag during the resonance range of VIV. Past the synchronisation range,  $\bar{C}_x$  due to WIV remains at slightly higher levels, but very close to the drag measured for a static single cylinder. In general,  $\bar{C}_x$  decreases as  $D_1/D_2$  increases, perhaps due to the deficit of mean velocity in the wake coming from the upstream cylinder; i.e. a smaller  $D_1$  will create a wake with higher streamwise velocity reaching the second cylinder.

#### 4. Conclusion

In the present work we investigate the WIV response of the downstream cylinder of a pair with diameter ratios  $D_1/D_2 = 1/1, 1/2$  and  $1/3$ . For all tandem configurations, the static upstream cylinder appears to be shedding vortices as an isolated cylinder, not being affected by the presence or movement of the downstream body. This is true for effective separations of  $L/D_1 = 3.5, 7.0$  and  $6.5$ , respectively.

The overall WIV response turned out to be dependent on several parameters: wake topology (Re), arrangement geometry (both  $D_1/D_2$  and  $L/D_1$ ) and system dynamics ( $m^*$ ). Other dimensionless representations of the separation parameter can lead to different interpretations of the data. In the present work, the effective separation  $L/D_1$  was chosen as a representative of the effect of the upstream wake impinging on the downstream body.

The frequency response, on the other hand, turned out to be rather independent of both  $D_1/D_2$  and  $L/D_1$ . In fact, a mechanism similar to the wake stiffness proposed by Assi et al. (2013) might be occurring for different diameter ratios but with different intensities. Nevertheless, all frequency responses appeared to be very close to the wake stiffness frequency previously characterised for cylinders of equal diameters.

It is not clear from the present investigation if the enhanced response of  $D_1/D_2 = 1/3$  in relation to  $D_1/D_2 = 1/2$  is due to the decrease of the effective separation  $L/D_1$ , the decrease of  $m^*$  or the increase of Re. Assi et al. (2010) have already shown that Reynolds number plays a very important role in WIV. Maybe increasing the diameter of the downstream cylinder from 50 mm to 75 mm from case  $D_1/D_2 = 1/2$  to  $1/3$  may include such a Re effect. Future experiments should be able to isolate some of these parameters in order to achieve a better understanding of the phenomenon.



## Acknowledgements

The author is grateful to the advice of Prof. Peter Bearman and the support from Imperial College (Dept. of Aeronautics) and CAPES (2668-04-1) at the time of the experiments. He also wishes to acknowledge the recent support from FAPESP (2013/07335-8) and CNPq (308916/2012-3) that allowed him time to revisit the data and write this manuscript.

## References

- Alam, M.M., Zhou, Y., 2008. Strouhal numbers, forces and flow structures around two tandem cylinders of different diameters. *Journal of Fluids and Structures* 24, 505–526.
- Alam, M.M., Zhou, Y., 2014. Flow-induced vibrations of a circular cylinder interacting with another of different diameter. In: Zhou, Y., Liu, Y., Huang, L., Hodges, D.H. (Eds.), *Fluid–Structure–Sound Interactions and Control. Lecture Notes in Mechanical Engineering*, Springer, Berlin, Heidelberg, pp. 385–390.
- Assi, G.R.S., 2009. Mechanisms for Flow-Induced Vibration of Interfering Bluff Bodies (Ph.D. thesis). Imperial College London, London, UK, available from [www.ndf.poli.usp.br/~gassi](http://www.ndf.poli.usp.br/~gassi).
- Assi, G.R.S., 2014. Wake-induced vibration of tandem and staggered cylinders with two degrees of freedom. *Journal of Fluids and Structures*, <http://dx.doi.org/10.1016/j.jfluidstructs.2014.07.002>, in press.
- Assi, G.R.S., Bearman, P.W., Carmo, B., Meneghini, J., Sherwin, S., Willden, R., 2013. The role of wake stiffness on the wake-induced vibration of the downstream cylinder of a tandem pair. *Journal of Fluid Mechanics* 718, 210–245.
- Assi, G.R.S., Bearman, P.W., Meneghini, J., 2010. On the wake-induced vibration of tandem circular cylinders: the vortex interaction excitation mechanism. *Journal of Fluid Mechanics* 661, 365–401.
- Bearman, P.W., 1984. Vortex shedding from oscillating bluff bodies. *Annual Review of Fluid Mechanics* 16, 195–222.
- Bokaian, A., Geoola, F., 1984. Wake-induced galloping of two interfering circular cylinders. *Journal of Fluid Mechanics* 146, 383–415.
- Huang, S., Sworn, A., 2011. Some observations of two interfering VIV circular cylinders of unequal diameters in tandem. *Journal of Hydrodynamics* 23, 535–543.
- Huang, S., Sworn, A., 2013. Interference between two stationary or elastically supported rigid circular cylinders of unequal diameters in tandem and staggered arrangements. *J. Shore Mech. Arctic Eng.* 135, 021803. (February 25, 2013) (10).
- Khalak, A., Williamson, C.H.K., 1999. Motions, forces and mode transitions in vortex-induced vibrations at low mass-damping. *Journal of Fluids and Structures* 13, 813–851.
- Rahmanian, M., Zhao, M., Cheng, L., Zhou, T., 2012. Two-degree-of-freedom vortex-induced vibration of two mechanically coupled cylinders of different diameters in steady current. *Journal of Fluids and Structures* 35, 133–159.
- Ruscheweyh, H.P., 1983. Aeroelastic interference effects between slender structures. *Journal of Wind Engineering and Industrial Aerodynamics* 14, 129–140.
- Tsutsui, T., Igarashi, T., Kamemoto, K., 1997. Interactive flow around two circular cylinders of different diameters at close proximity. *Experiment and numerical analysis by vortex method. Journal of Wind Engineering and Industrial Aerodynamics* 69–71, 279–291.
- Williamson, C.H.K., Govardhan, R., 2004. Vortex-induced vibrations. *Annual Review of Fluid Mechanics* 36, 413–455.
- Zdravkovich, M.M., 1988. Review of interference-induced oscillations in flow past two circular cylinders in various arrangements. *Journal of Wind Engineering and Industrial Aerodynamics* 28, 183–200.
- Zhao, M., Cheng, L., Teng, B., Liang, D., 2005. Numerical simulation of viscous flow past two circular cylinders of different diameters. *Applied Ocean Research* 27, 39–55.
- Zhao, M., Yan, G., 2013. Numerical simulation of vortex-induced vibration of two circular cylinders of different diameters at low Reynolds number. *Physics of Fluids* 25, 083601, <<http://dx.doi.org/10.1063/1.4816637>>.



Contents lists available at ScienceDirect

## Journal of Fluids and Structures

journal homepage: [www.elsevier.com/locate/jfs](http://www.elsevier.com/locate/jfs)

# Wake-induced vibration of tandem and staggered cylinders with two degrees of freedom



Gustavo R.S. Assi

Department of Naval Architecture &amp; Ocean Engineering, University of São Paulo, NDF, Escola Politécnica, 05508-030 São Paulo, Brazil

## ARTICLE INFO

## Article history:

Received 3 February 2014

Accepted 2 July 2014

Available online 22 August 2014

## Keywords:

Wake-induced vibration

Circular cylinders

Vortex wake

Flow interference

## ABSTRACT

The wake-induced vibration (WIV) of two staggered cylinder with two degrees of freedom (2-dof) has been investigated by experiments in a water channel for Reynolds number between 2000 and 25 000. The streamwise separation was fixed to 4 diameters and the lateral separation varied between 0 and 3 diameters for tandem and staggered configurations. Results are presented in the form of trajectories of motion and dynamic response curves of displacements, frequencies and force coefficients. Excitation caused by the WIV mechanism is found to get weaker as the initial position of the downstream cylinder is increased from the centreline of the wake (tandem arrangement) towards the sides. For a lateral separation of 3 diameters wake interference was already found to be negligible. Evidence of a type of wake-stiffness concept is also observed to occur for 2-dof WIV in tandem arrangement, especially for higher reduced velocities. A similar mechanism may also be occurring for staggered arrangements around the centreline.

© 2014 Elsevier Ltd. All rights reserved.

## 1. Introduction

The topic of *wake-induced vibration* (WIV) of a pair of interfering cylinders is a fundamental subject in fluid–structure interaction that still draws the attention of many researches. In a few words, WIV is a fluid–elastic mechanism able to excite into oscillatory motion a bluff body immersed in the wake generated from another body positioned upstream. At first sight it appears to be a very simple phenomenon, but careful investigations have uncovered complex mechanisms that can only be understood through the lenses of unsteady fluid–elasticity. In the present study we are concerned with the WIV of the downstream cylinder of a pair arranged in tandem and staggered configurations, i.e. in staggered arrangements the cylinders are not aligned with the flow but offset from the centreline. WIV differs from the well studied phenomenon of *vortex-induced vibration* (VIV)—reviewed by Bearman (1984), Williamson and Govardhan (2004) and others—in the sense that the excitation is not generated in the vortex shedding mechanism of the body itself, but it comes from the interaction of the body with a wake developed further upstream.

It is not difficult to be carried away by the apparent simplicity of the problem and plan or design experiments without considering the number of parameters involved. For example, take two cylinders modelled as rigid bodies with two degrees of freedom (2-dof) each. To start with geometric parameters, there will be two diameters and a streamwise and a cross-flow separation, which will distinguish the tandem from the staggered arrangements. On the structural properties side, there will be different parameters of mass for each cylinder as well as damping and stiffness regarding each direction of motion. After all, a pair of rigid cylinders oscillating in 2-dof will present a dozen of different possible combinations of geometric and

E-mail address: [g.assi@usp.br](mailto:g.assi@usp.br)

structural parameters to be considered, not to mention experiments with long flexible cylinders with several modes of vibration. In addition, one may include flow parameters such as speed, velocity profiles and turbulence intensity on the free stream. For this reason, only a few studies that managed to vary one or two parameters at a time were able to contribute to the understanding of the WIV excitation mechanisms and tell it apart from other types of flow-induced vibration of bluff bodies.

Nevertheless, WIV has been revisited by quite a few papers in the recent years. In addition to the papers pointed out along this text, one should refer to the book of [Paidoussis et al. \(2011\)](#) and the comprehensive review paper published by [Sumner \(2010\)](#) as a means to finding old and new literature on the topic of wake interaction. WIV has also been referred to by different names in the past literature, such as ‘wake-induced galloping’ ([Bokaian and Geoola, 1984](#)) and ‘wake-displacement excitation’ ([Zdravkovich, 1988](#)). But we shall follow [Assi et al. \(2010\)](#) and keep the terminology *wake-induced vibration* not to mistake it by 1-dof vibrations normally associated with classical galloping of non-axisymmetric cross-sections.

[Bokaian and Geoola \(1984\)](#) and [Assi et al. \(2010, 2013\)](#) have studied the flow-induced vibration of the downstream cylinder moving only in the cross-flow direction in water channels. [Simpson \(1977\)](#), on the other hand, has investigated the streamwise instabilities of a pair of tandem cylinders in a wind tunnel. Several models have been developed to capture the mechanisms behind this type of flow-induced vibration, most of them starting from quasi-steady assumptions but adding time delays to account for the unsteady effects of the wake–structure interaction (a review of these models is found in [Price, 1995](#)). [Simpson and Flower \(1977\)](#) enhanced the quasi-steady model including movements of the upstream cylinder. [Tsui and Tsui \(1980\)](#) further developed an instability analysis for when the cylinders are mechanically coupled. And the nonlinear analysis performed by [Price and Abdallah \(1990\)](#) revealed interesting results about the effect of damping and frequency detuning on the response. Most of these works have been concerned with the vibration of the downstream cylinder undergoing a type of mechanism called ‘wake flutter’, in which the cylinder is able to extract energy from the flow as it oscillates in an elliptical orbit within the upstream wake. [Price \(1975\)](#), [Price and Abdallah \(1990\)](#) and [Naudascher and Rockwell \(1994\)](#) offer clear descriptions with illustrated explanations of this mechanism.

[Fig. 1](#) presents the velocity field obtained with PIV (particle-image velocimetry) around two static cylinders in staggered arrangements. PIV was performed at mid length to characterise steady wake topology; details on the set-up are presented in [Assi \(2009\)](#). As the downstream cylinder moves away from the centreline, the wake interference from the upstream cylinder is reduced. For the tandem arrangement, in [Fig. 1\(a\)](#), the upstream wake is symmetrically split around the downstream body, while for the staggered configurations in (b) and (c) the upstream wake interferes with the inner side of the second cylinder. Streamlines show that the steady wake of the upstream cylinder is displaced by the presence of the second body. For a lateral separation of  $y_0/D = 3.0$  the downstream cylinder appears to be so far out of the upstream wake that its wake symmetry is almost recovered.

We believe [Fig. 1](#) illustrates rather well the phenomenon described by [Zdravkovich \(2003\)](#) as ‘wake-displacement’ when he writes that “the downstream cylinder is not *immersed* in the upstream cylinder wake but *displaces* it instead”. However, as shown by [Assi et al. \(2013\)](#), the unsteady flow field around a static downstream cylinder is quite different from that around a cylinder that is not moving across the wake. In fact, the unsteady wake interference was found to be fundamental to excite WIV. [Assi et al. \(2010\)](#) showed how the instantaneous vortex interference may enhance or diminish lift depending on the wake pattern. Hence the time-averaged flow fields in [Fig. 1](#) are very limited in terms of information they provide for an investigation of the unsteady phenomenon. Nevertheless, they show how far out of the centreline the downstream cylinder needs to be in order for wake interference to become insignificant, setting the boundaries for the present study.

## 2. Method

The present paper is a follow-up on the previous works of [Assi et al. \(2010, 2013\)](#) so, in order to avoid unnecessary lengthy repetition, the reader will be constantly referred to those papers. In those previous works we kept constant as many parameters as possible in order to investigate the intricate mechanisms of wake interference. Only allowing for the downstream cylinder of a tandem pair to respond to flow excitation in the cross-flow direction made it possible to identify the complex unsteady excitation mechanism by vortex–structure interaction and the powerful concept of wake stiffness. Now, in the present study, we shall release some constraints adding new parameters to the investigation.

The basic arrangement is illustrated in [Fig. 2](#). The initial position of the downstream cylinder can be varied from the tandem arrangement (in which both cylinders are aligned with the flow direction) to staggered configurations changing the lateral spacing between the bodies, hence  $x_0$  and  $y_0$  define the initial geometry of the pair. The streamwise separation, measured from centre to centre, was kept fixed at  $x_0/D = 4.0$  at all times and  $y_0/D$  was varied between 0 and 3. The upstream cylinder was always static while the downstream cylinder was allowed to respond with oscillations in 2-dof in the cross-flow ( $y$ ) and streamwise ( $x$ ) directions. Although this represents only a sample of the multi-parametric universe, by testing the system on these conditions we may identify some general characteristic behaviours. For example, we will be able to notice the decreasing effect of the WIV mechanism as the downstream cylinder moves away from the centreline of the wake and we will see evidence for the existence of ‘wake-stiffness’ for configurations other than the tandem arrangement (to be described later).

[Fig. 3](#), reproduced from [Assi et al. \(2010\)](#), presents the WIV response of the downstream cylinder of a tandem pair free to respond in one degree of freedom (1-dof) in the cross-flow direction. The top graph shows the variation of the amplitude of

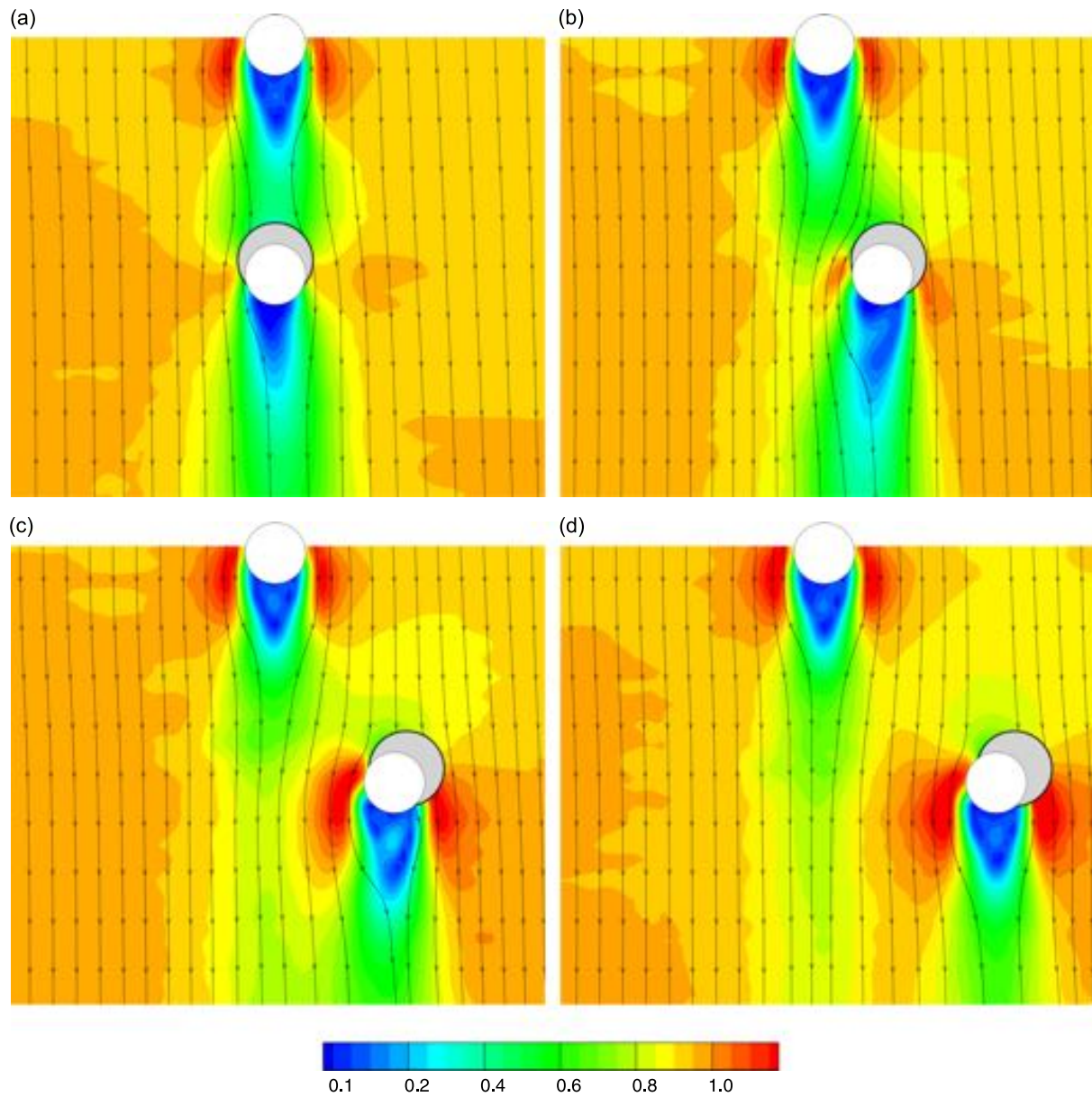


**Fig. 1.** Steady flow velocity field around a pair of static cylinders. Contours of velocity magnitude normalised by free stream velocity.  $Re = 19\,200$ ,  $x_0/D = 4.0$  and (a)  $y_0/D = 0.0$ , (b)  $y_0/D = 1.0$ , (c)  $y_0/D = 2.0$ , (d)  $y_0/D = 3.0$ .

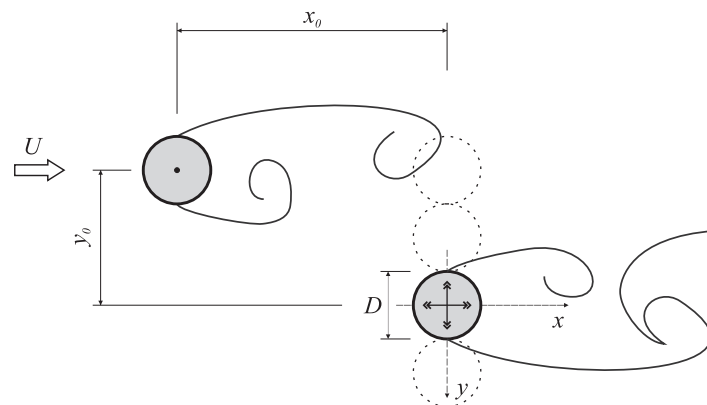


**Fig. 2.** Arrangement for a pair of tandem and staggered cylinders. The initial streamwise spacing was fixed at  $x_0/D = 4.0$  and the lateral spacing varied between  $y_0/D = 0.0, 1.0, 2.0$  and  $3.0$ . Solid lines represent hypothetical interaction between the shear layers.

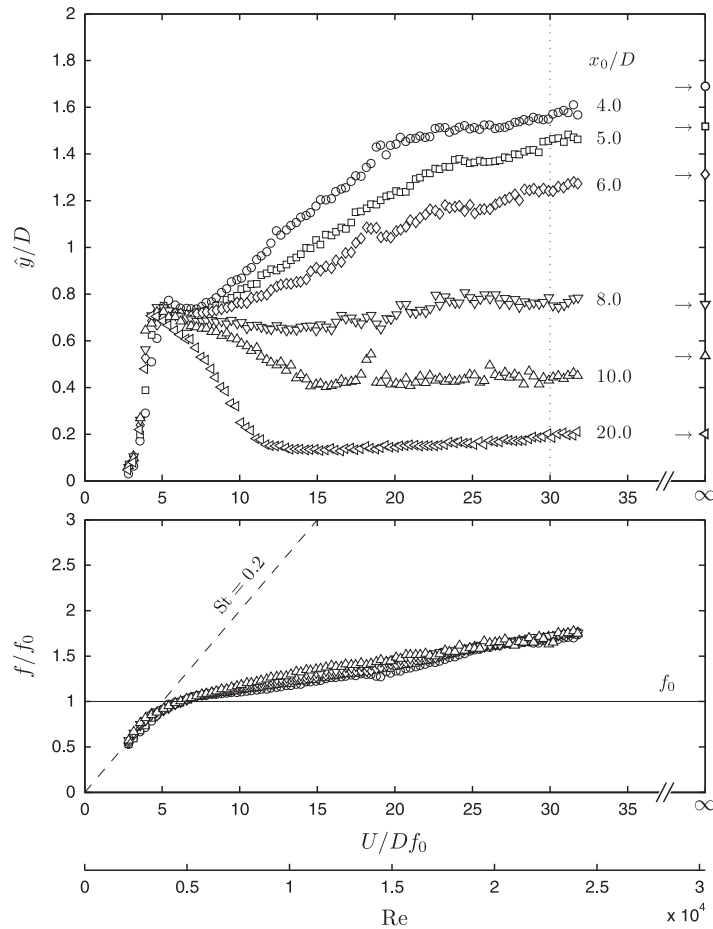


**Fig. 3.** WIV response of the downstream cylinder with 1-dof for various  $x_0/D$  separations. (top) Displacement and (bottom) dominant frequency of oscillation. Reproduced from Assi et al. (2010).

vibration for various tandem separations ( $x_0/D$ ) between 4 and 20 diameters. One immediately notices that the interference effect from the upstream wake reduces as the second cylinder is moved further downstream. But it is interesting to note that even for a large gap of  $x_0/D = 10$  the vibration of the downstream cylinder still is influenced by the upstream wake. It was only for  $x_0/D = 20$  that the typical WIV response of an isolated cylinder was recovered.

Another interesting aspect of WIV lies in the frequency signature of the response. In the bottom graph of Fig. 3 it becomes evident that, independently of the separation, the downstream cylinder presents a rather well behaved and predictable frequency of vibration. Assi et al. (2013) later pointed out that this response frequency is a signature of the WIV mechanism and could be associated with the concept of wake stiffness, which dominates over the structural stiffness for higher reduced velocities. They argued that the wake–structure interaction creates a restoring force of hydrodynamic nature that confers the system a kind of characteristic frequency of vibration.

Now, if the initial position of the cylinders is altered to staggered configurations it is expected that the WIV response will also change, since the downstream cylinder will oscillate in regions of different wake interferences. Zdravkovich (1988) mapped the wake downstream of the first static cylinder regarding the wake interference on the second static body and Sumner et al. (2000) investigated the flow patterns of the wake around several staggered configurations. Fig. 4 identifies a region of ‘proximity interference’ for various staggered arrangements when the streamwise separation is less than a critical value around  $x_0/D = 3.5$ . Flow-induced vibration in this region is driven by different mechanisms other than WIV and will not be covered in the present study. For an investigation of ‘interference galloping’ of the cylinder at close proximity the reader should refer to Ruscheweyh (1983), who performed tests with an elastic cylinder in a wind tunnel to explain the excitation from hysteretic flow-switching in the gap between the cylinders (later verified in waterchannel experiments by Ruscheweyh and Dielen, 1992). A second region identified as ‘wake interference’ appears for tandem and staggered configurations up to  $y_0/D \approx 1.5$  independently of streamwise separation. In this region the WIV mechanism described in Assi et al. (2010, 2013) takes place. Finally, another region identified as ‘no interference’ appears when the downstream cylinder is located out of the reach of the upstream wake for  $y_0/D > 1.5$ .

In the present study we shall focus on the response of the downstream cylinder in 2-dof at  $x_0/D = 4.0$  in order to avoid close ‘proximity interference’ and a response excited by ‘interference galloping’. Four lateral separations will vary between  $y_0/D = 0$  and 3. According to the static map of Zdravkovich (1988) the cylinder should move from the strongest ‘wake



interference' region out of the upstream wake to the 'no interference' region without passing through the 'proximity interference' region.

### 3. Experimental setup

Experiments were performed in the Department of Aeronautics at Imperial College, London, in a recirculating water channel with a test section 0.6 m wide, 0.7 m deep and 8.4 m long. Flow speed,  $U$ , could be continuously varied up to 0.6 m/s with free stream turbulence intensity around 3%. The actual flow quality was proved to be adequate to perform flow-induced vibration tests and preliminary results were validated in Assi et al. (2010) against other experiments presented in the literature. A pair of cylinders was arranged in the test section, as illustrated in Fig. 2, at  $x_0/D = 4.0$  and  $y_0/D = 0.0, 1.0, 2.0$  and 3.0. Measurements of displacement were taken in relation to the initial position of the downstream cylinder, i.e. the origin of the  $x$  and  $y$  axes in Fig. 2.

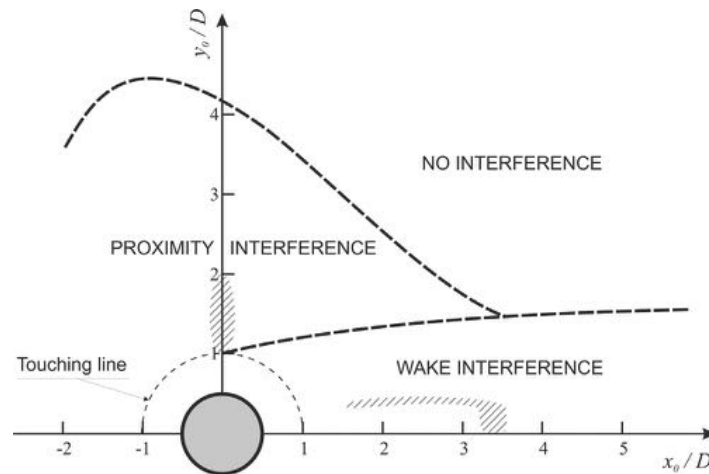


Fig. 4. Sketch of interference regions for static cylinders. Hatched areas mean bistable flow regions. Adapted from Zdravkovich (1988).

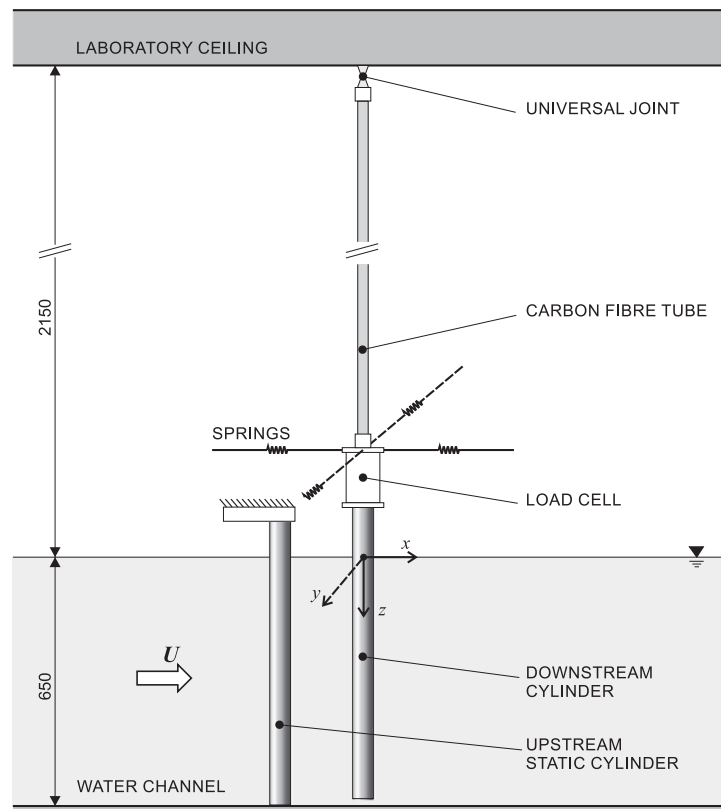
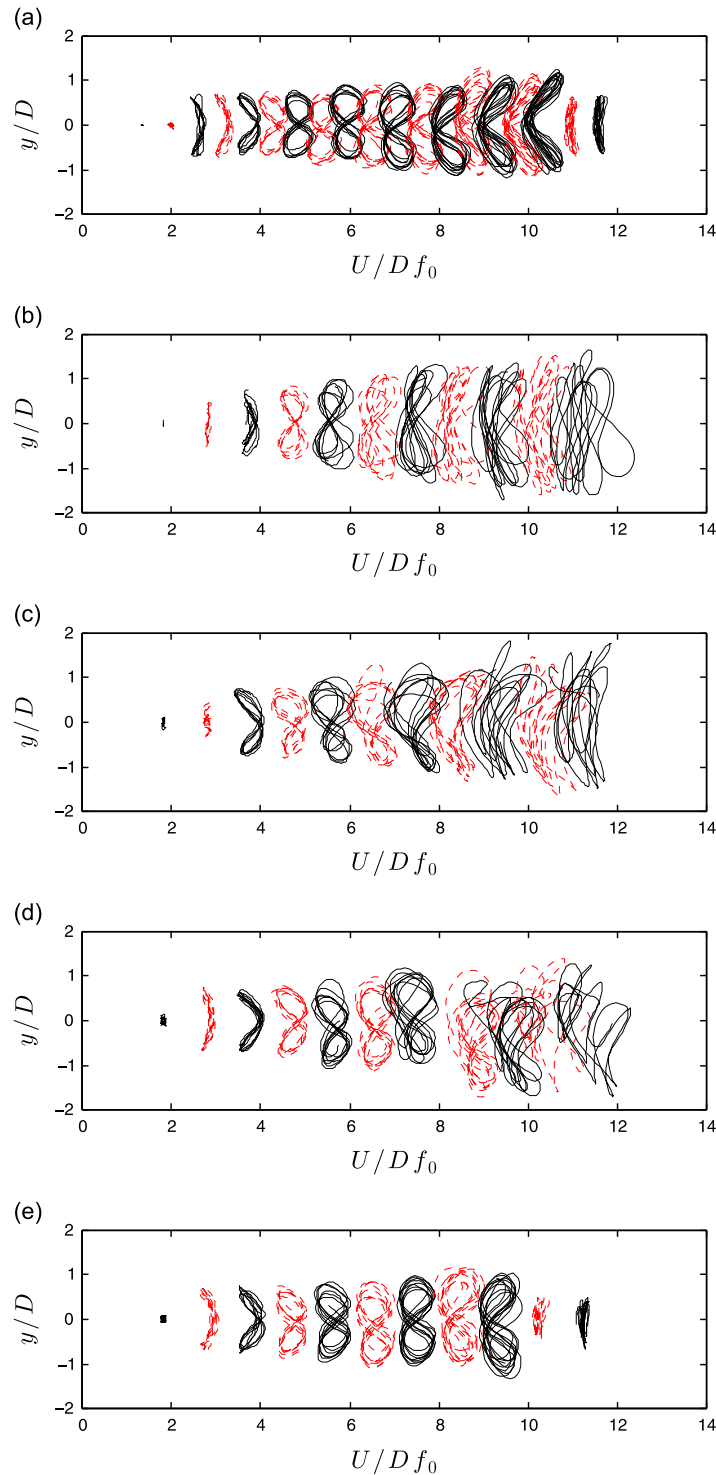


Fig. 5. Schematic representation of the experimental setup with the 2-dof pendulum rig holding the downstream cylinder. (Units are in millimetres.)



A schematic representation of the experimental setup is shown in Fig. 5. Circular cylinder models were made from a 50 mm-diameter acrylic tube, giving a maximum Reynolds number of approximately 30 000, based on cylinder diameter,  $D$ , at  $U=0.6$  m/s. With a wet-length of 650 mm, the resulting aspect ratio of the model was 13. The upstream cylinder was rigidly attached to the structure of the channel preventing displacements in any direction, while the downstream cylinder was fixed from its upper end to a 2-dof elastic rig that allowed the cylinder to freely respond in both cross-flow and streamwise directions. The downstream cylinder was mounted at the lower end of a long carbon-fibre tube which formed the arm of a rigid pendulum and was connected to a universal joint fixed at the ceiling of the laboratory.

A small gap of 2 mm was left between the bottom of the downstream cylinder and the floor of the test section. Although end conditions were different at the extremities of the cylinder, flow visualisations showed that vortex shedding remained



**Fig. 6.** Trajectories of motion versus reduced velocity for (a) a single cylinder and the downstream cylinder of a pair at  $x_0/D=4.0$ , (b)  $y_0/D=0.0$ , (c)  $y_0/D=1.0$ , (d)  $y_0/D=2.0$ , (e)  $y_0/D=3.0$ .

parallel to the cylinder for all flow speeds. The distance between the bottom of the cylinder and the pivoting point of the universal joint was 2800 mm, hence for a displacement equal to 1 diameter the inclination angle of the cylinder was only just over 1 degree from the vertical. Two independent optical sensors were employed to measure displacements in the  $x$  and  $y$ -directions; all displacement amplitudes presented for 2-dof measurements are for a location at the mid-length of the model.

Two pairs of coil springs were installed in the  $x$  and  $y$ -axes allowing the setting of different natural frequencies in the cross-flow and streamwise directions,  $f_{0y}$  and  $f_{0x}$ , respectively. Although the cylinder was initially aligned in the vertical position, in flowing water the mean drag displaced the cylinder from its original location. To counteract this effect the in-line pair of springs was attached to a frame that could be moved back and forth in the direction of the flow. For each flow speed there was a position of the frame that maintained the mean position of the cylinder within 10% of a diameter from the original vertical arrangement, balancing the drag force with the displacement of the springs. This was more difficult to achieve for higher reduced velocities due to the unsteady nature of the phenomenon, as will be explained later. It was a compromise in either altering the mean position or allowing the cylinder to freely respond. In the end it was preferable to

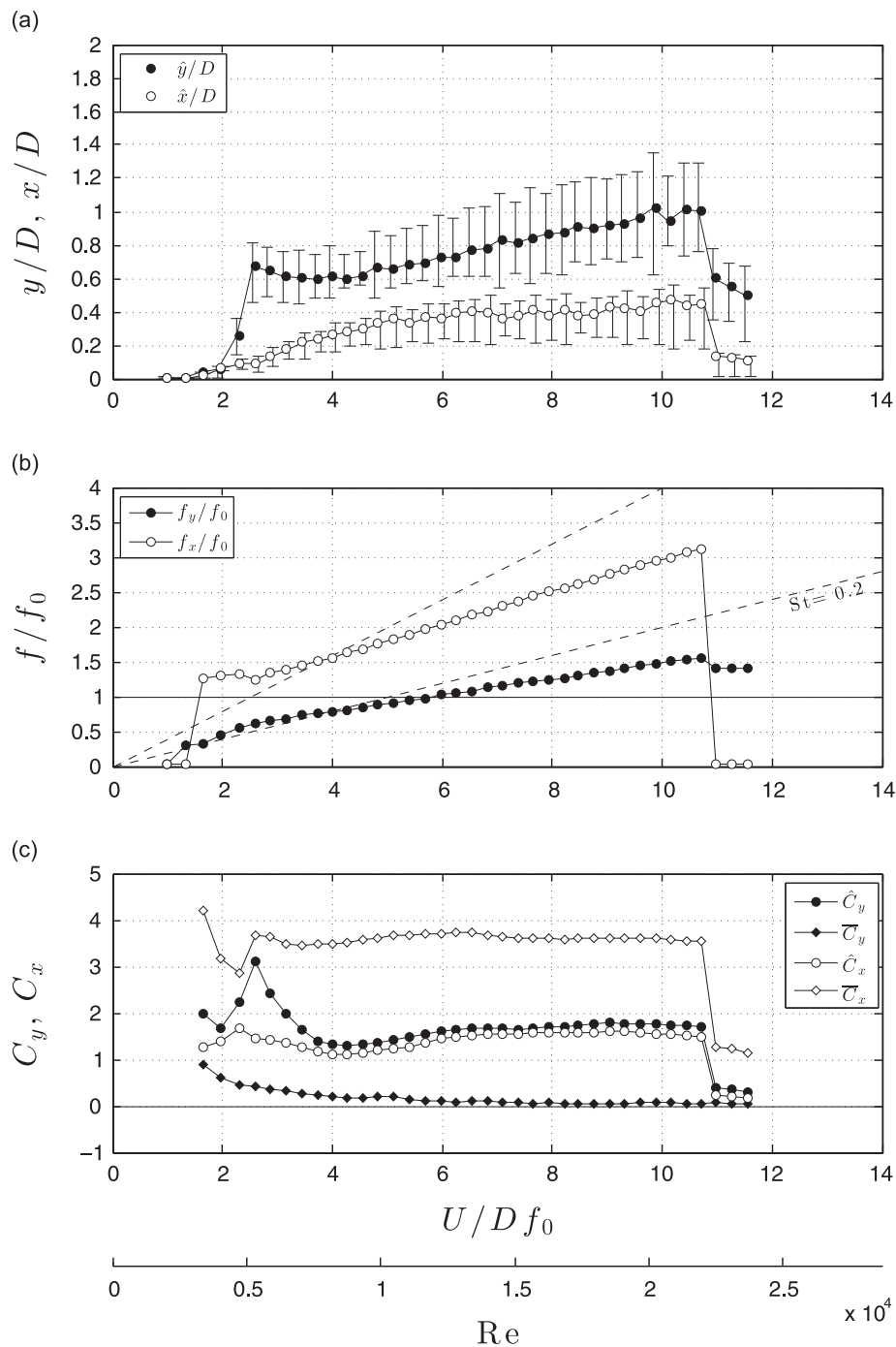


Fig. 7. VIV dynamics response of an isolated cylinder. (a) Displacement and (b) frequency of vibration and (c) force coefficients.

keep the parameter  $x_0$  constant, thus favouring parametric analyses. Using two pairs of springs perpendicular to each other resulted in nonlinear spring constants for large displacements in the transverse and in-line directions. Movement in the transverse direction will cause a lateral spring deflection in the in-line direction and vice versa. This nonlinearity was minimised by making the springs as long as possible, hence the in-line springs were installed at the end of 4 m-long wires fixed at the extremities of the frame.

It is known that during the cycle of vortex shedding from bluff bodies the fluctuation of drag has double the frequency of the fluctuation of lift. Hence a particularly severe vibration might be expected to occur if the hydrodynamic forces in both directions could be in resonance with both in-line and transverse natural frequencies at the same time. For this reason, we set  $f_{0x}$  to be close to twice of  $f_{0y}$  by adjusting the stiffness of both pairs of springs. Values for  $f_{0x}$ ,  $f_{0y}$  and  $\zeta$  were determined by measuring free oscillations in air in both directions. In fact, the actual value turned out to be  $f_{0x}/f_{0y} = 1.9$ . In the reduced velocity parameter,  $U/Df_0$ , the frequency  $f_0$  is the natural frequency in the cross-flow direction  $f_{0y}$ . The mass ratio was found to be  $m^* = 1.6$ , defined as the ratio between the total oscillating mass to the mass of displaced fluid. The structural damping  $\zeta = 0.3\%$ , represented as a fraction of the critical damping, was practically the same for both directions of motion.

A load cell was attached at each cylinder to measure instantaneous and time-averaged hydrodynamic forces—inertial components have been subtracted from the total force acquired by the load cell, find details in Assi et al. (2009). Total lift was divided into mean ( $\bar{C}_y$ ) and r.m.s. ( $\hat{C}_y$ ) components. The same applied to the drag coefficient ( $\bar{C}_x$  and  $\hat{C}_x$ ). Each data point presented in the following section is composed of more than 200 cycles of vibration on that specific reduced velocity.

#### 4. Results and discussion

Results are presented in the form of trajectories of motion and curves of the dynamic response of displacement and frequency. Hydrodynamic force coefficients are also presented for all configurations compared with those for an isolated cylinder.

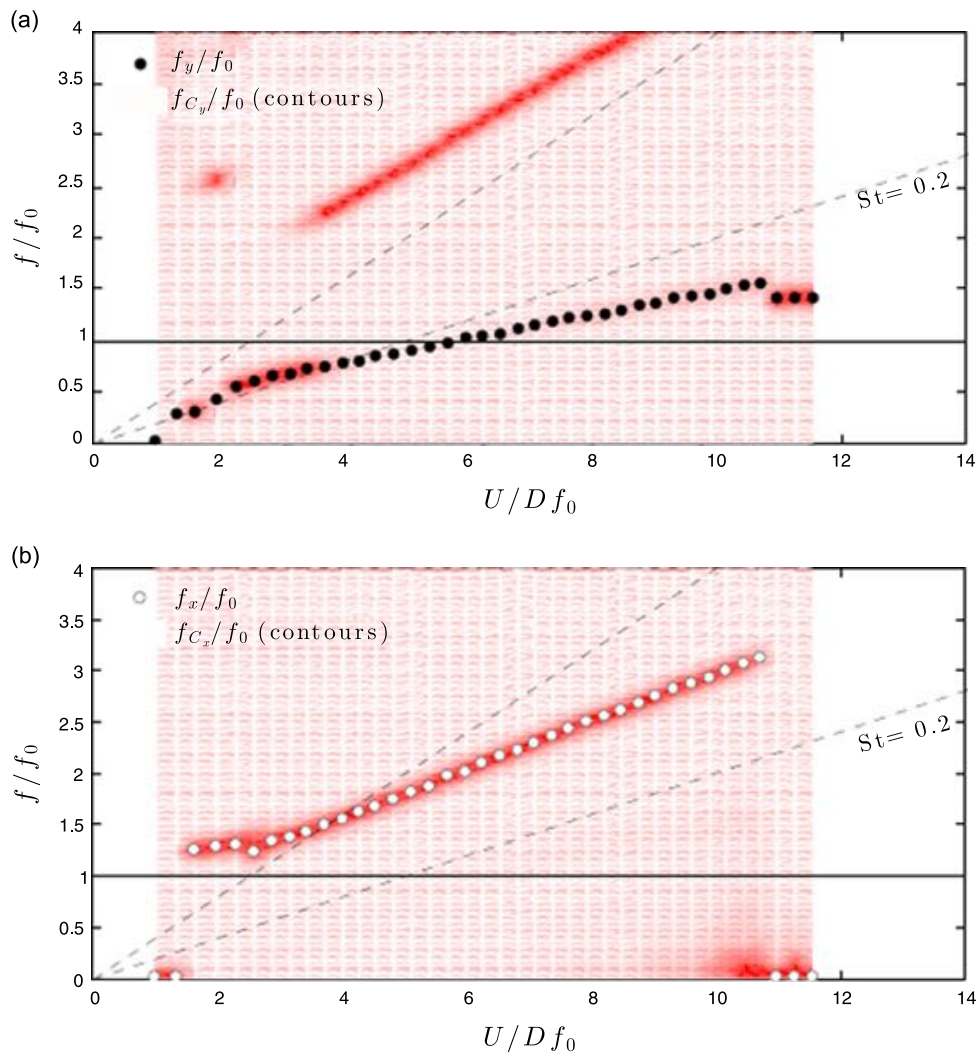


**Fig. 8.** Dominant frequency of vibration (symbols) and power spectrum (background red contours) of (a) lift and (b) drag for an isolated cylinder. (For interpretation of the references to colour in this figure caption, the reader is referred to the web version of this paper.)

#### 4.1. Trajectories of motion

Before going into the details of the response for all staggered configurations we shall start by an overall qualitative comparison between the response of an isolated cylinder under VIV and the tandem and staggered cases under WIV. Fig. 6 compares 2-dof trajectories of motion versus reduced velocity for all investigated cases. The  $x$ -axis for displacement is not shown in the figure for clarity, but it has the same scale as the  $y$ -axis. Also, trajectories alternate in colour and line style for clarity.

Fig. 6(a) presents the typical trajectories of motion for a single cylinder under 2-dof VIV in which the  $f_{0x}$  is almost twice as  $f_{0y}$ . As reduced velocity is increased vibrations start to build up in a 'C' shape, changing into '8'-shaped curves until the end of the synchronisation range at around reduced velocity 12. The overall response was found to be in good agreement with results found for  $f_{0x}/f_{0y} = 1.9$  in Fig. 4 of Dahl et al. (2006) and those of Assi et al. (2009).

The 2-dof response of the downstream cylinder of a tandem pair is presented in Fig. 6(b). As expected, trajectories are very different from those of the typical VIV response of an isolated cylinder due to the interference effect of the upstream wake. It is evident that both streamwise and cross-flow displacements are increased when compared to Fig. 6(a), but one may also note that the cycles of WIV are not as repeatable as those for VIV, especially for reduced velocities above 6 when the WIV mechanism dominates over VIV. One may argue about the non-existence of harmonic motion in WIV, but the fact is that each cycle of vibration will be the result of interference with different wake patterns (as proposed by Assi et al., 2010), resulting in a unique trajectory at each cycle but with overall periodic characteristics.

In Fig. 6(c) we find the response of a staggered cylinder initially dislocated from the centreline of the upstream wake by 1D. The trajectories manage to capture the asymmetry in the wake interference by showing one loop of the '8' shapes larger than the other. For reduced velocities above 9 the '8'-shaped cycles tend to disappear and the trajectories take the form of periodic orbits that could be associated with 'wake flutter' (to be discussed later).

The wake interference effect is further reduced as the cylinder moves out of the upstream wake, as observed in Fig. 6(d) for a staggered configuration of  $y_0/D = 2.0$ . The asymmetry in motion is still perceived, but rather weakened when compared to Fig. 6(c). For the last staggered arrangement of  $y_0/D = 3.0$ , presented in Fig. 6(e), the downstream cylinder finds itself too far out of the upstream wake that almost no interference is observed in the response. The trajectories resemble that of an isolated cylinder in VIV, not quite like those observed in Fig. 6(a), but still very different from Fig. 6(b)–(d).

According to Zdravkovich (1988), somewhere between  $y_0/D = 1.0$  and  $2.0$  a static downstream cylinder should cross the boundary from the 'wake interference' to the 'no interference' region (Fig. 4). However, when the downstream cylinder is oscillating with high amplitudes of motion it is expected that wake interference will occur for initial separations further out of the centreline, since the cylinder moves in and out of the 'wake interference' zone. This is made clear by the fact that a significant change in the response seen in Fig. 6(d) and (e) was only achieved when the downstream cylinder was moved from  $y_0/D = 2.0$  to  $3.0$ .

#### 4.2. Displacement, frequency and force coefficients

Moving on to a more detailed analysis involving displacements, frequencies and hydrodynamic forces we come to Fig. 7, which will serve as a reference presenting the response of an isolated cylinder in 2-dof VIV.

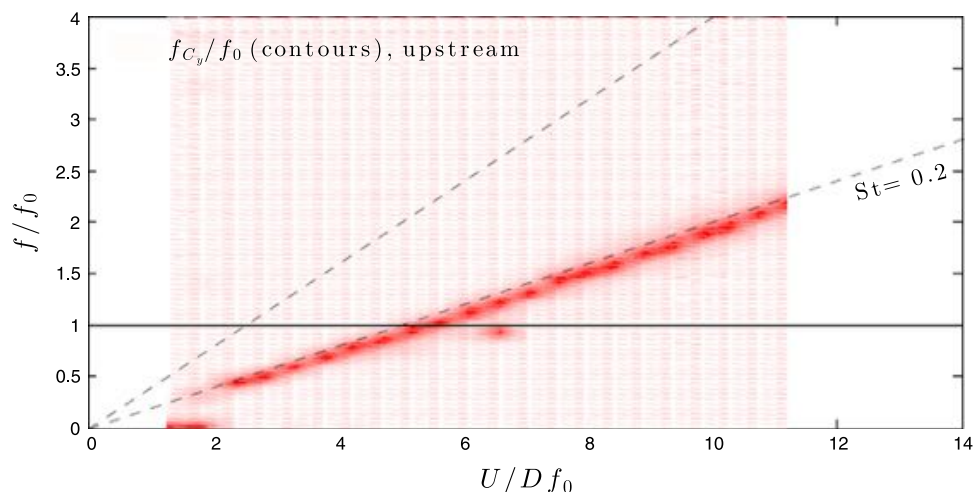
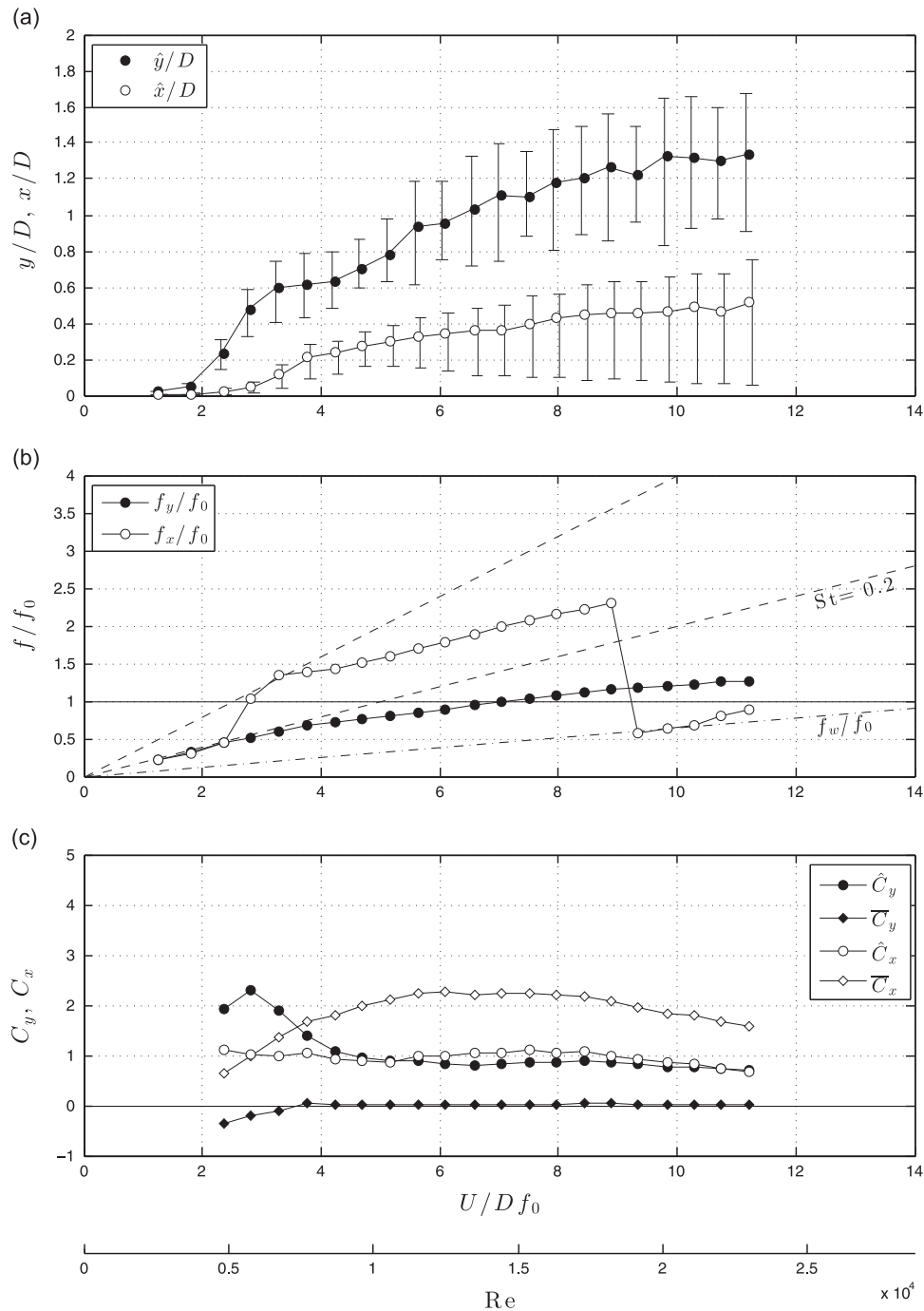


Fig. 9. Power spectrum (red contours) of lift for the upstream cylinder of a tandem pair. Identical plots were obtained for all staggered arrangements. (For interpretation of the references to colour in this figure caption, the reader is referred to the web version of this paper.)

#### 4.2.1. Isolated cylinder

Fig. 7(a) presents the amplitudes of displacement in the cross-flow ( $\hat{y}/D$ ) and streamwise ( $\hat{x}/D$ ) directions nondimensionalised by the cylinder diameter. The amplitudes  $\hat{y}$  and  $\hat{x}$  represent the so called harmonic amplitude of motion, calculated as the r.m.s. of the signal multiplied by  $\sqrt{2}$ . Vertical bars associated with each data point represent an estimation of the maximum and minimum peaks of vibration achieved for each reduced velocity. In fact, the bars have been calculated taking an average of the 25% highest and lowest peaks for each time series constituted of more than 200 cycles of oscillation. Therefore, for a given reduced velocity it is possible to evaluate the average amplitude of vibration as well as variations in the envelope of vibration through time. Larger bars mean that the displacement presents considerable variation from cycle to cycle.

In Fig. 7(a) the synchronisation range of VIV is clearly identified by a rise in amplitude in both  $\hat{y}/D$  and  $\hat{x}/D$  roughly between reduced velocities 2 and 11. A maximum amplitude of  $\hat{y}/D \approx 1.0$  is achieved at the end of the synchronisation



**Fig. 10.** WIV dynamic response of the downstream cylinder in tandem arrangement,  $x_0/D = 4.0$  and  $y_0/D = 0.0$ . (a) Displacement and (b) frequency of vibration and (c) force coefficients.



range, just before a sudden drop in response in both directions. This is typical of the 2-dof VIV response of a single cylinder with  $f_{0x}/f_{0y} \approx 2$  and has been reported by Dahl et al. (2006) and Assi et al. (2009), among others.

The dominant frequencies of vibration nondimensionalised by  $f_0$  are plotted in Fig. 7(b). Both  $f_y/f_0$  and  $f_x/f_0$  follow clear trends in which the streamwise vibration shows double the frequency of the cross-flow direction, as expected. Two dashed lines mark the equivalent frequency for a hypothetical Strouhal number of 0.2 and twice as that. Fig. 8 presents the same frequency data in a slightly different manner. The same dominant frequency data points are plotted over the normalised power spectrum of the hydrodynamics force associated to each direction. Darker areas represent peaks in the spectrum. So, in Fig. 8(a) it becomes clear that although the preferred frequency of oscillation follows very closely the  $St=0.2$  line, the lift force measured on the cylinder presents clear evidence of the third harmonic. In Fig. 8(b) only one single branch is identified in the spectral signature of drag, which obviously corresponds to the dominant  $f_x/f_0$ . For details about how the spectrum plots were created refer to Assi (2009).

Returning to Fig. 7(c), the mean and fluctuating components of lift and drag are presented for almost the whole range of reduced velocities. A few data points for the lowest reduced velocities have been excluded due to the high experimental uncertainty in measuring minute hydrodynamic forces caused by very low flow speeds; data points for  $U/Df_0 < 2$  were kept in the figures but must be considered with caution since uncertainties are still high. Nevertheless, the typical amplification of  $\bar{C}_x$  and  $\hat{C}_y$  is observed to occur during the synchronisation range. It is difficult to find similar measurements in the literature, but our results show some agreement with those of Jauvtis and Williamson (2004), at least as far as orders of magnitude are concerned.

#### 4.2.2. Tandem arrangement

The spectrum of lift on the upstream static cylinder has also been measured in a similar way, as presented in Fig. 9 for when the cylinders are arranged in tandem ( $y_0/D=0.0$ ). It reveals that the upstream cylinder is shedding vortices as an

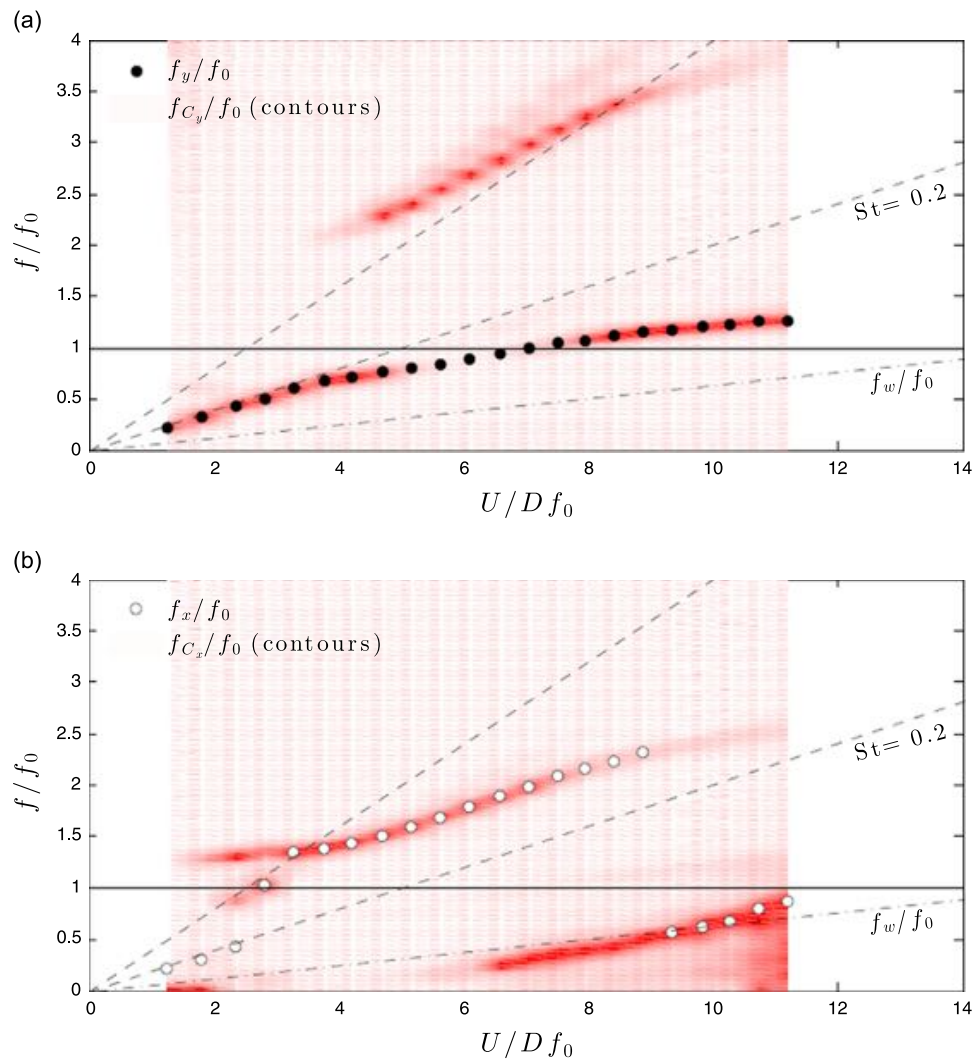


**Fig. 11.** Dominant frequency of vibration (symbols) and power spectrum (background red contours) of (a) lift and (b) drag for the downstream cylinder of a tandem pair:  $x_0/D = 4.0$  and  $y_0/D = 0.0$ . (For interpretation of the references to colour in this figure caption, the reader is referred to the web version of this paper.)



isolated cylinder, with the frequency of lift clearly following the  $St=0.2$  line. Identical plots were obtained for the upstream cylinder for all tandem and staggered configurations, thus not repeated here for brevity. We conclude that the upstream cylinder (or its vortex shedding mechanism, to be precise) is not affected by the presence or movement of the downstream cylinder in any of the four tested arrangements if  $x_0/D \geq 4.0$ .

Fig. 10(a) presents the WIV response for the downstream cylinder in tandem arrangement ( $y_0/D = 0.0$ ). As seen in the trajectories of motion in Fig. 6, the displacements are very different from the VIV of a single cylinder due to wake interference. Similar to what was observed for 1-dof WIV of tandem cylinders (Assi et al., 2010), there is no synchronisation range in the WIV excitation, but both  $\hat{y}/D$  and  $\hat{x}/D$  increase in amplitude with increasing reduced velocity. The variation between maximum and minimum peaks also increases for both cross-flow and streamwise vibrations.

The dominant frequency plot in Fig. 10(b) shows an interesting result. Once more  $f_y/f_0$  and  $f_x/f_0$  seem to follow clear lines that are multiples of each other for most of the reduced velocity range. However, close to the end of the experiments at around  $U/Df_0 = 9.0$ , the dominant  $f_x/f_0$  jumps to a much lower frequency branch and remains there until the end of the

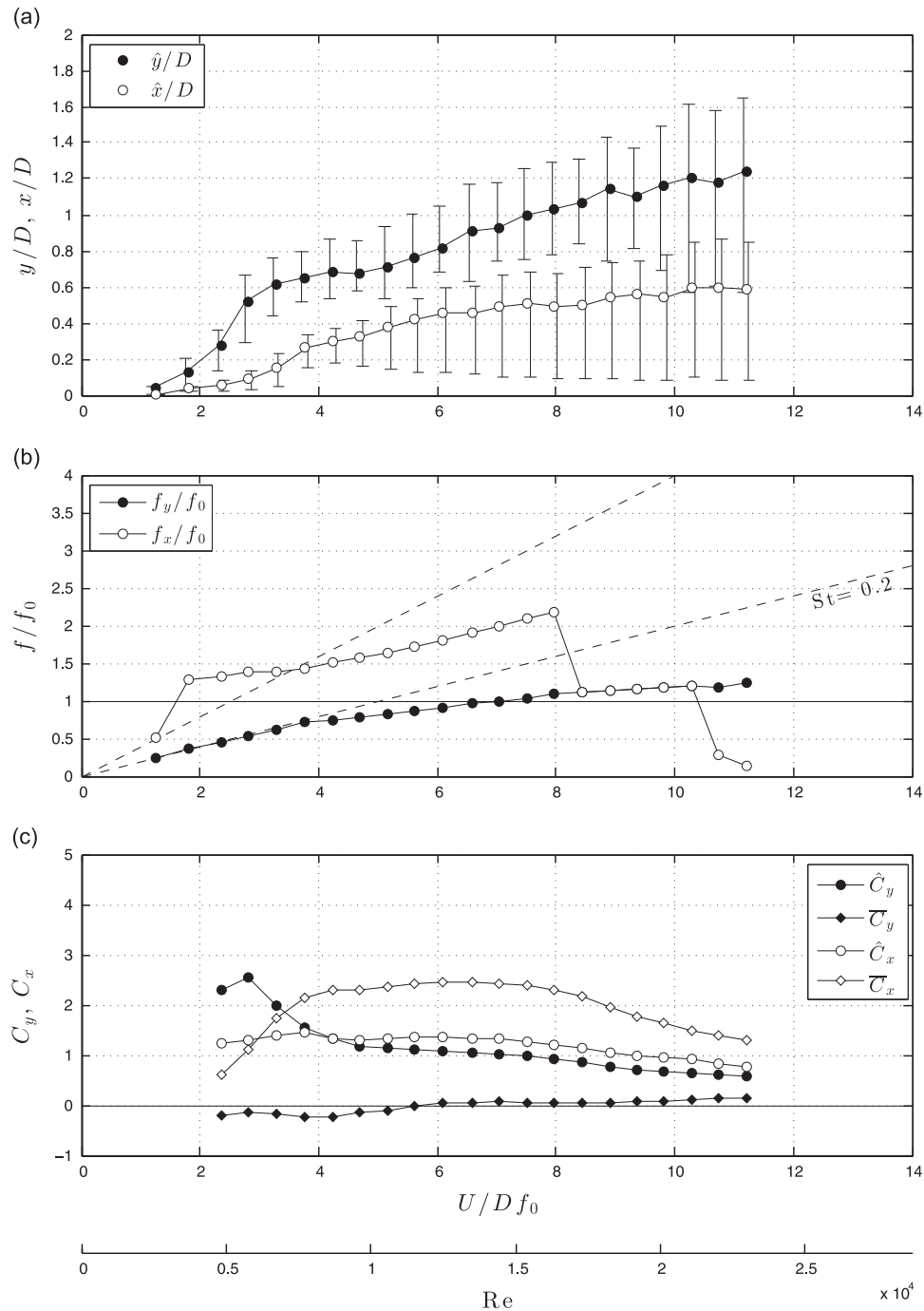


**Fig. 12.** WIV dynamic response of the downstream cylinder in staggered arrangement,  $x_0/D = 4.0$  and  $y_0/D = 1.0$ . (a) Displacement and (b) frequency of vibration and (c) force coefficients.

reduced velocity range. Looking at the power spectrum of lift and drag in Fig. 11, we verify two branches in Fig. 11(a) for the lift signature (the highest corresponding to the third harmonic), and two branches in Fig. 11(b) for drag. Now, the lowest branch in the drag signature is the one that dominates the frequency of response for reduced velocities above 9. If we take the concept of wake stiffness developed by Assi et al. (2013) for tandem cylinders at  $x_0/D = 4.0$  and plot the corresponding wake-stiffness frequency as a dash-dotted line  $f_w/f_0$  in the frequency plots we find that the lowest branch observed in the drag spectrum is indeed very close to  $f_w/f_0$ . The same dash-dotted line was added to Fig. 10(b).

We know that for higher reduced velocities around 9 or 10 the resonant effect of VIV is getting weaker as we approach the end of the synchronisation range (Assi et al., 2013). So, for higher reduced velocities the response is totally governed by WIV, hence the wake stiffness could be playing some role in the response, even though the system now has 2-dof. If it is not a coincidence that the dominant  $f_x/f_0$  is so close to  $f_w/f_0$ —it might as well be the case—we are left with an open question: why do traces of ‘wake-stiffness’ frequency appear for vibrations in the streamwise direction rather than in the cross-flow direction? Further investigation, perhaps restraining the cross-flow degree of freedom, may be required for an answer.

The hydrodynamic coefficients in Fig. 10(c) show the amplification of  $\bar{C}_x$  due to vibration but with a reduction caused by the shading effect of the upstream wake, as expected.  $\bar{C}_y$  is very close to zero (within the experimental uncertainty for force measurements) as a result of a symmetric wake interference.

#### 4.2.3. Staggered arrangements

Fig. 12 presents the WIV response for the downstream cylinder in staggered arrangement with  $y_0/D = 1.0$ . The overall displacements in Fig. 12(a) are not very different from the tandem configuration, showing that the downstream cylinder is still under a similar interference effect of the upstream wake. The top amplitude of  $\hat{y}/D \approx 1.2$  obtained for the highest

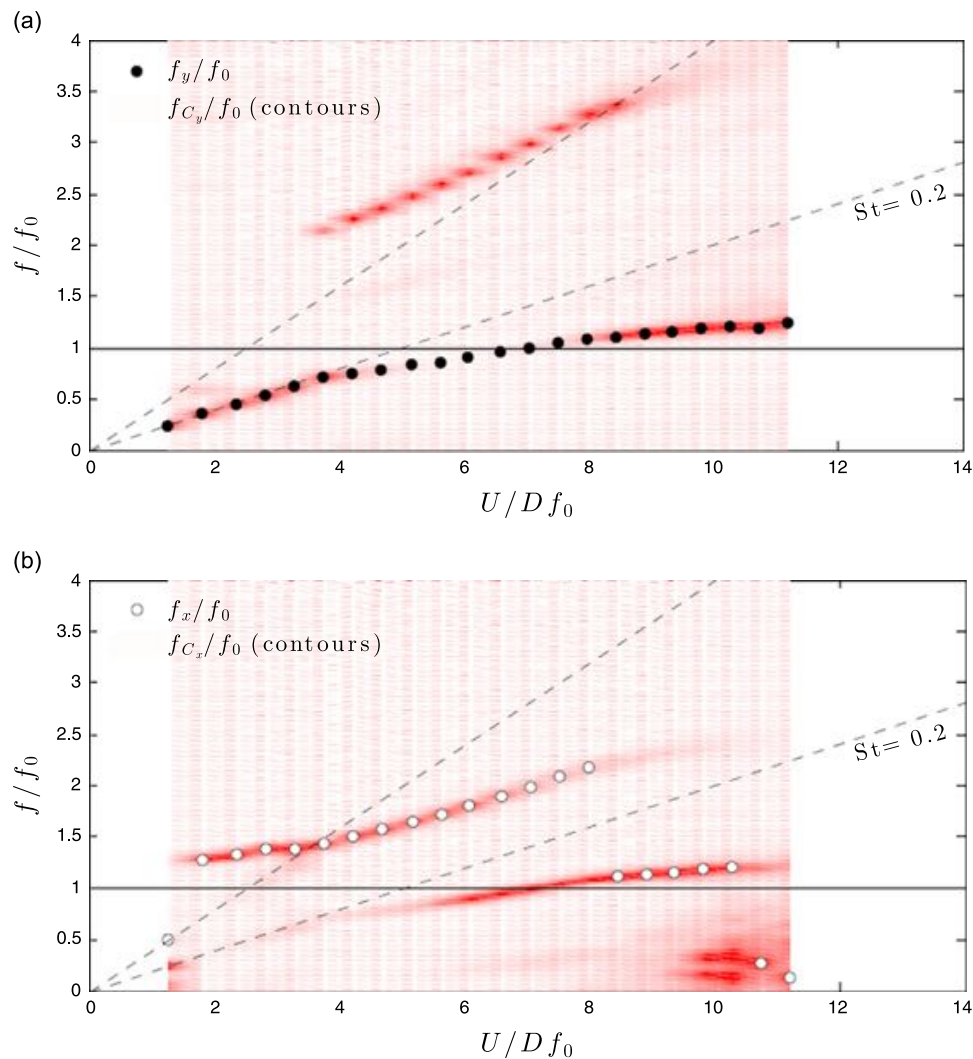


**Fig. 13.** Dominant frequency of vibration (symbols) and power spectrum (background red contours) of (a) lift and (b) drag for the downstream cylinder of a tandem pair:  $x_0/D = 4.0$  and  $y_0/D = 1.0$ . (For interpretation of the references to colour in this figure caption, the reader is referred to the web version of this paper.)

reduced velocity is slightly reduced when compared to the tandem case. On the other hand, the maximum  $\hat{x}/D$  is increased to 0.6. The vertical bars indicate that the envelope of vibration shows an even greater peak variation between cycles.

Again, the frequency curves in Fig. 12(b) bring the most interesting results. Up to reduced velocity 8 both  $f_y/f_0$  and  $f_x/f_0$  are very similar to the tandem case. But for higher reduced velocities the cylinder vibrates with the same frequency in both directions, at least up to  $U/Df_0 \approx 10.5$ . This congruence of frequencies results in the kind of orbit trajectories seen in Fig. 6(c). In fact, the response for high reduced velocities at this  $y_0/D = 1.0$  separation might be governed by ‘wake flutter’ on top of WIV. Theoretically, ‘wake flutter’ can be excited in spite of the unsteadiness of the flow, being sustained only by the steady fluid forces present in the wake. Force maps presented in Price (1975) and Assi et al. (2010) show that a static downstream cylinder will be subjected to changes in the steady fluid forces for considerably large separations. A reduced drag force has minimum values on the centreline of the wake and a steady lift force develops maximum values close to the wake interference boundary around  $y_0/D = 1.0$ . If the downstream cylinder is able to respond in two degrees of freedom (as is the case here) following an elliptical orbit it will move across different gradients of steady lift and drag. A counter-clockwise orbit on the starboard side of the wake extracts energy from the flow to sustain the oscillations.

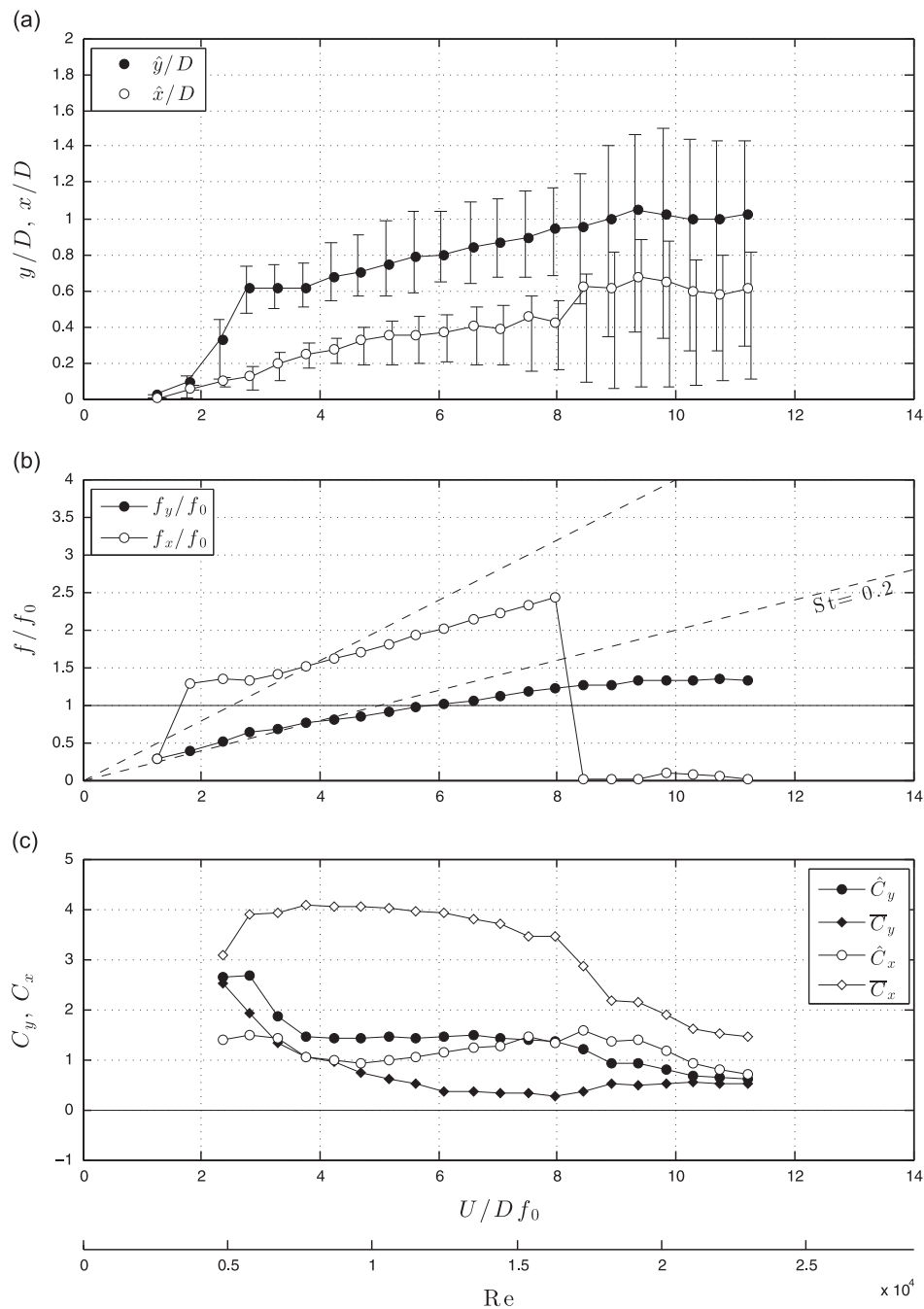


**Fig. 14.** WIV dynamic response of the downstream cylinder in staggered arrangement,  $x_0/D = 4.0$  and  $y_0/D = 2.0$ . (a) Displacement and (b) frequency of vibration and (c) force coefficients.

This quasi-steady approach does not take into account the vortex wake from upstream, but only the steady effect of lift and drag. Also, this mechanism would not excite systems with 1-dof, since it requires an orbit in  $x$  and  $y$  for a positive input of energy. Naudascher and Rockwell (1994) comment that wake flutter, like other coupled instabilities, occurs only if the natural frequencies in the  $x$  and  $y$  directions are reasonably close, which is not the case for this experiment. But perhaps for a reduced range of reduced velocities, the WIV mechanism is able to bring both oscillation frequencies close together, as seen in Fig. 12(b), and extract energy from the flow in such a manner. (Note: Wake flutter has been called ‘wake galloping’ by Zdravkovich, 1997 and Blevins, 1990, but we prefer to stick to the terminology ‘wake flutter’ since it requires response in 2-dof to be sustained.)

Elliptical vibrations can happen in different regions of the wake wherever the steady velocity profile is favourable. The amplitude of the oscillation is directly related to the intensity of the lift and drag gradient in the wake, hence oscillations are reduced for larger separations as the steady force profiles get attenuated. Bokaian and Geoola (1984) and Assi et al. (2010) correctly noted that the fluid–elastic instability reported in their work was not be mistaken by the wake-flutter mechanism described above, since their experiment presented only a single degree of freedom.

For  $y_0/D = 1.0$  we cannot directly employ the same wake-stiffness concept as we did for the tandem case. Assi et al. (2013) showed that the ‘wake spring’ in the ‘wake-stiffness’ concept is only considered to be linear for around  $\pm 1D$  away from the centreline. Nevertheless, a close look in the spectrum of drag in Fig. 13 reveals the existence of two branches in the  $C_x$  signature. Perhaps there is a similar ‘wake stiffness’ effect acting for oscillations around  $y_0/D = 1.0$  as well, which we cannot determine in the present work.

Hydrodynamic coefficients in Fig. 12(c) show a very similar behaviour to the tandem case, except for a small variation in  $\bar{C}_y$  due to the asymmetric characteristic of wake interference. The presence of a steady force pushing the cylinder towards the centreline of the upstream wake is also noticeable in a small lateral drift in the trajectories of Fig. 6(c).

As we move further out of the centreline to the staggered arrangement with  $y_0/D = 2.0$  the interference effect of the wake starts to weaken. Fig. 14(a) shows that the maximum cross-flow displacement for the reduced velocity range is now

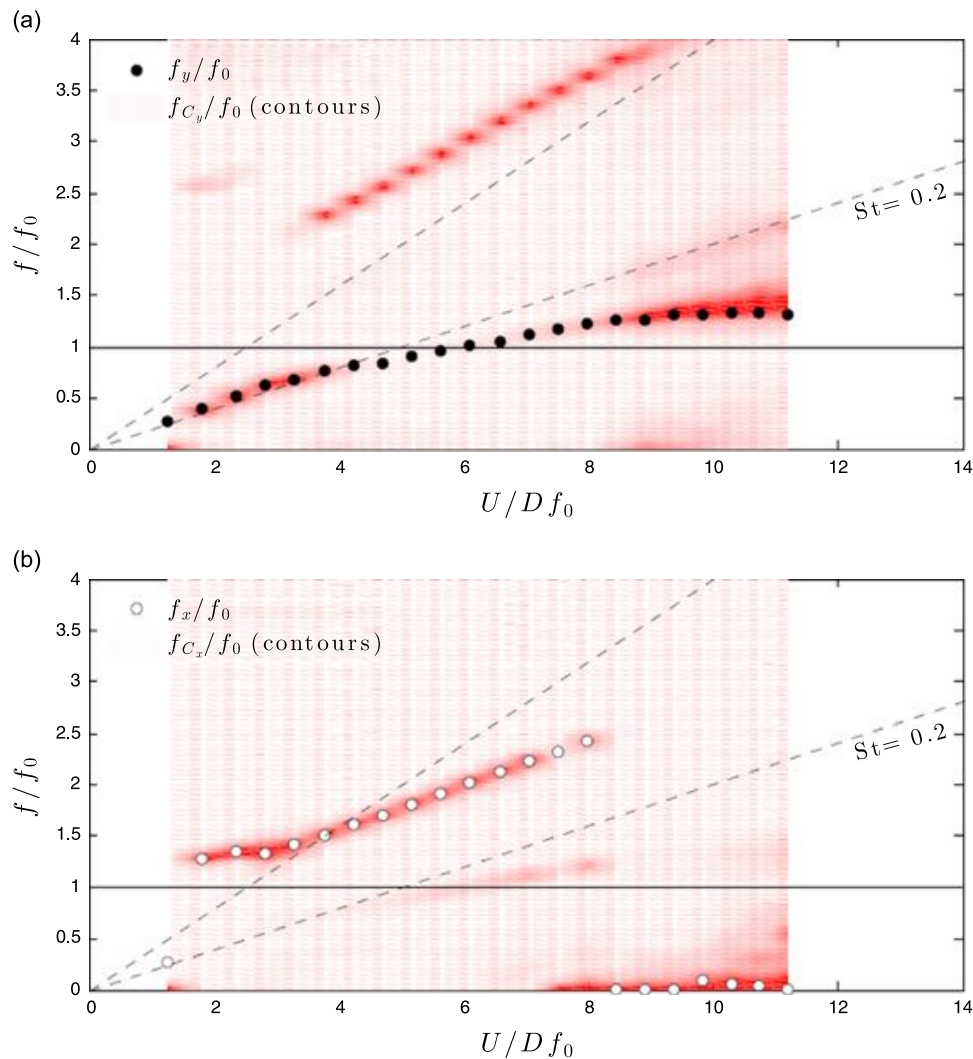
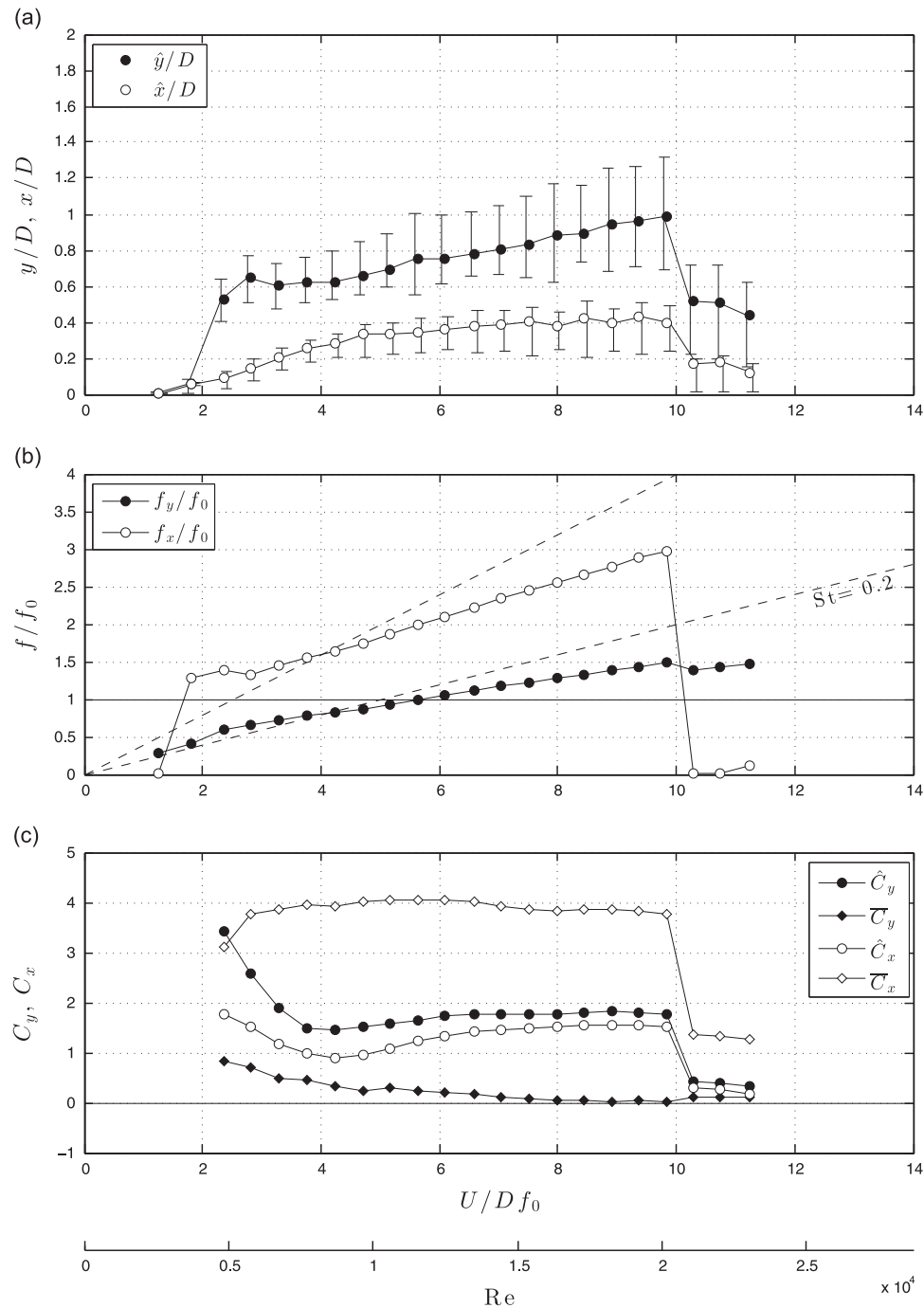


**Fig. 15.** Dominant frequency of vibration (symbols) and power spectrum (background red contours) of (a) lift and (b) drag for the downstream cylinder of a tandem pair:  $x_0/D = 4.0$  and  $y_0/D = 2.0$ . (For interpretation of the references to colour in this figure caption, the reader is referred to the web version of this paper.)

reduced to  $\hat{y}/D \approx 1.0$ , even though  $\hat{x}/D$  still shows the same levels as the previous separation. Vertical bars now decrease revealing a more well behaved envelope of vibration.

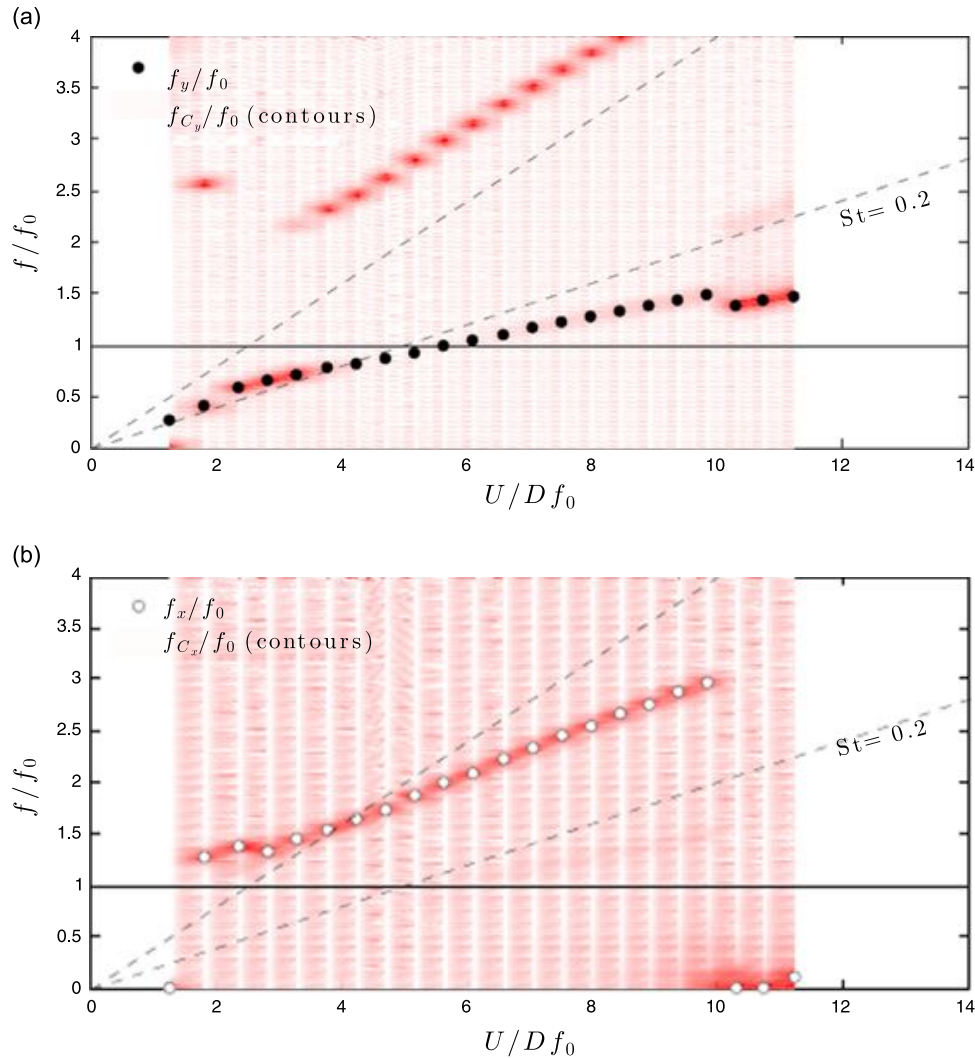
Fig. 14(b) shows that  $f_y/f_0$  still follows a well behaved trend, also identified as the lowest branch in the  $C_y$  spectrum of Fig. 15(a). However,  $f_x/f_0$  only shows a dominant frequency during the reduced velocity range in which resonant VIV is effective. After the end of the synchronisation region, for  $U/Df_0 > 8$ , no clear dominant frequency is identified in the streamwise motion, only slow drift and random vibrations as observed in Fig. 6; nevertheless they do amount to a significant amplitude of displacement. Also, no clear inferior branch is found in the  $C_x$  spectrum in Fig. 15(b), especially none related to the ‘wake stiffness’ concept.

Fig. 14(c) shows that  $\overline{C}_x$  has increased as the cylinder moved out of the protected, low-speed region of the wake. But the most interesting result lies in the variation of  $\overline{C}_y$  versus reduced velocity. One can imagine that as the cylinder oscillates with higher amplitudes it enters the region with stronger interference of the upstream wake. A lateral force will develop to



**Fig. 16.** WIV dynamic response of the downstream cylinder in staggered arrangement,  $x_0/D = 4.0$  and  $y_0/D = 3.0$ . (a) Displacement and (b) frequency of vibration and (c) force coefficients.





**Fig. 17.** Dominant frequency of vibration (symbols) and power spectrum (background red contours) of (a) lift and (b) drag for the downstream cylinder of a tandem pair:  $x_0/D = 4.0$  and  $y_0/D = 3.0$ . (For interpretation of the references to colour in this figure caption, the reader is referred to the web version of this paper.)

draw the cylinder towards the centreline, thus changing the mean lift  $\bar{C}_y$ . However, this phenomenon turned out to be stronger for  $y_0/D = 2.0$  and not the smaller separation.

Finally, Fig. 16 presents the results for the furthest staggered case of  $y_0/D = 3.0$ . We will limit to comment that at this lateral separation the downstream cylinder is too far out of the centreline to encounter significant interference from the upstream wake. Displacements, frequencies and forces all come back to be similar to the isolated cylinder case in VIV. Also, no signs of wake interference are noticeable in the spectrum of  $C_y$  and  $C_x$  in Fig. 17 either. With the exception of a small variation in  $\bar{C}_y$ , that should appear as the cylinder gets closer to the ‘wake interference’ region during vibration, the response seems to be driven by VIV and not WIV any longer.

## 5. Conclusion

In the present work we observed that the downstream cylinder of a pair is able to undergo 2-dof WIV for lateral separations between  $y_0/D = 0.0$  and  $2.0$ . For a larger separation of  $y_0/D = 3.0$  the cylinder was found to respond in a typical VIV behaviour.

For reduced velocities in the range between  $1.5$  and  $12$ , the response was found to pass through a synchronisation range in which VIV is important. If reduced velocity is increased beyond this range, the WIV mechanism will dominate the 2-dof response in pretty much the same way it dominates 1-dof vibrations.

The WIV response in 2-dof is not qualitatively different from that observed for 1-dof systems oscillating in the cross-flow direction. Of course the branches of response take a different shape, but apart from that the general behaviour is monotonically increasing amplitude of displacement for increasing reduced velocity (or Reynolds number) was observed once more. The typical wake-flutter response, showing elliptical orbits, was not observed during the experiments, maybe



due to the frequency ratio being different from 1. For some specific flow speeds for  $y_0/D = 1.0$  we might consider that wake-flutter was acting together with WIV

We have found evidence for a mechanism of ‘wake stiffness’ to be occurring for the 2-dof tandem arrangement and traces of it for  $y_0/D = 1.0$ . Further investigation is required to understand how the ‘wake-stiffness’ concept in 2-dof would differ from the 1-dof case.

Postscript: At the time of this paper going to print, Chaplin and Batten (2014) published a very interesting work concerning WIV of two cylinders with four degrees of freedom, two in each direction of motion. This is probably the work most similar to the present investigation and deserve the attention of the reader interested in WIV.

## Acknowledgements

We are thankful to the kind contribution of Prof. Peter W. Bearman and the support from Imperial College (Dept. of Aeronautics) and CAPES Brazilian Ministry of Education (2668-04-1) at the time of the experiments. The author also acknowledges support from FAPESP (2013/07335-8) and CNPq (308916/2012-3) that allowed him time to revisit the data and write this manuscript.

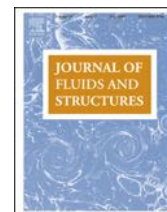
## References

- Assi, G.R.S., 2009. Mechanisms for Flow-Induced Vibration of Interfering Bluff Bodies (Ph.D. thesis). Imperial College London, London, UK. Available from ([www.ndf.poli.usp.br/~gassi](http://www.ndf.poli.usp.br/~gassi)).
- Assi, G.R.S., Bearman, P.W., Carmo, B., Meneghini, J., Sherwin, S., Willden, R., 2013. The role of wake stiffness on the wake-induced vibration of the downstream cylinder of a tandem pair. *Journal of Fluid Mechanics* 718, 210–245.
- Assi, G.R.S., Bearman, P.W., Kitney, N., 2009. Low drag solutions for suppressing vortex-induced vibration of circular cylinders. *Journal of Fluids Structures* 25, 666–675.
- Assi, G.R.S., Bearman, P.W., Meneghini, J., 2010. On the wake-induced vibration of tandem circular cylinders: the vortex interaction excitation mechanism. *Journal of Fluid Mechanics* 661, 365–401.
- Bearman, P.W., 1984. Vortex shedding from oscillating bluff bodies. *Annual Review of Fluid Mechanics* 16, 195–222.
- Blevins, R., 1990. *Flow-Induced Vibration*, 2nd edition. Van Nostrand Reinhold, New York.
- Bokaian, A., Geoola, F., 1984. Wake-induced galloping of two interfering circular cylinders. *Journal of Fluid Mechanics* 146, 383–415.
- Chaplin, J.R., Batten, W.M.J., 2014. Simultaneous wake- and vortex-induced vibrations of a cylinder with two degrees of freedom in each direction. *Journal of Offshore Mechanics and Arctic Engineering* 136. Page numbers TBA.
- Dahl, J., Hover, F., Triantafyllou, M., 2006. Two-degree-of-freedom vortex-induced vibrations using a force assisted apparatus. *Journal of Fluids Structures* 22, 807–818.
- Jauvtis, N., Williamson, C.H.K., 2004. The effect of two degrees of freedom on vortex-induced vibration at low mass and damping. *Journal of Fluid Mechanics* 509, 23–62.
- Naudascher, E., Rockwell, D., 1994. *Flow-Induced Vibrations. An Engineering Guide*, 1st edition. A.A. Balkema, Rotterdam.
- Paidoussis, M., Price, S., deLangre, E., 2011. *Fluid-Structure Interactions: Cross-Flow-Induced Instabilities*, 1st edition. Cambridge University Press, New York.
- Price, S., 1995. A review of theoretical models for fluid–elastic instability of cylinder arrays in crossflow. *Journal of Fluids Structures* 9, 463–518.
- Price, S.J., 1975. Wake induced flutter of power transmission conductors. *Journal of Sound Vibration* 38, 125–147.
- Price, S.J., Abdallah, R., 1990. On the efficacy of mechanical damping and frequency detuning in alleviating wake-induced flutter of overhead power conductors. *Journal of Fluids Structures* 4, 1–34.
- Ruscheweyh, H.P., 1983. Aeroelastic interference effects between slender structures. *Journal of Wind Engineering and Industrial Aerodynamics* 14, 129–140.
- Ruscheweyh, H.P., Dielen, B., 1992. Interference galloping-investigations concerning the phase lag of the flow switching. *Journal of Wind Engineering and Industrial Aerodynamics* 43, 2047–2056.
- Simpson, A., 1977. In-line flutter of tandem cylinders. *Journal of Sound Vibration* 54, 379–387.
- Simpson, A., Flower, J.W., 1977. An improved mathematical model for the aerodynamic forces on tandem cylinders in motion with aeroelastic applications. *Journal of Sound Vibration* 51, 183–217.
- Sumner, D., 2010. Two circular cylinders in cross-flow: a review. *Journal of Fluids Structures* 26, 849–899.
- Sumner, D., Price, S., Paidoussis, M., 2000. Flow-pattern identification for two staggered circular cylinders in cross-flow. *Journal of Fluid Mechanics* 411, 263–303.
- Tsui, Y.T., Tsui, C.C., 1980. Two dimensional stability analysis of two coupled conductors with one in the wake of the other. *Journal of Sound Vibration* 69, 361–394.
- Williamson, C.H.K., Govardhan, R., 2004. Vortex-induced vibrations. *Annual Review of Fluid Mechanics* 36, 413–455.
- Zdravkovich, M.M., 1988. Review of interference-induced oscillations in flow past two circular cylinders in various arrangements. *Journal of Wind Engineering and Industrial Aerodynamics* 28, 183–200.
- Zdravkovich, M.M., 1997. *Flow Around Circular Cylinders*, vol. 1, 1st edition. Oxford University Press, Oxford.
- Zdravkovich, M.M., 2003. *Flow Around Circular Cylinders*, vol. 2, 1st edition. Oxford University Press, Oxford.



Contents lists available at ScienceDirect

## Journal of Fluids and Structures

journal homepage: [www.elsevier.com/locate/jfs](http://www.elsevier.com/locate/jfs)

# Experimental investigation of the flow-induced vibration of a curved cylinder in convex and concave configurations

Gustavo R.S. Assi<sup>a,\*</sup>, Narakorn Srinil<sup>b</sup>, Cesar M. Freire<sup>c</sup>, Ivan Korkischko<sup>c,1</sup><sup>a</sup> Department of Naval Architecture and Ocean Engineering, University of São Paulo, São Paulo, Brazil<sup>b</sup> Department of Naval Architecture and Marine Engineering, University of Strathclyde, Glasgow, UK<sup>c</sup> Department of Mechanical Engineering, University of São Paulo, São Paulo, Brazil

## ARTICLE INFO

## Article history:

Received 8 April 2013

Accepted 10 October 2013

Available online 6 November 2013

## Keywords:

Vortex-induced vibration

Cross-flow and in-line motion

Curved cylinder

Particle image velocimetry

## ABSTRACT

Experiments have been conducted to investigate the two-degree-of-freedom vortex-induced vibration (VIV) response of a rigid section of a curved circular cylinder with low mass-damping ratio. Two curved configurations, a concave and a convex, were tested regarding the direction of the flow, in addition to a straight cylinder that served as reference. Amplitude and frequency responses are presented versus reduced velocity for a Reynolds number range between 750 and 15 000. Results for the curved cylinders with concave and convex configurations revealed significantly lower vibration amplitudes when compared to the typical VIV response of a straight cylinder. However, the concave cylinder showed relatively higher amplitudes than the convex cylinder which were sustained beyond the typical synchronisation region. We believe this distinct behaviour between the convex and the concave configurations is related to the wake interference taking place in the lower half of the curvature due to perturbations generated in the horizontal section when it is positioned upstream. Particle-image velocimetry (PIV) measurements of the separated flow along the cylinder highlight the effect of curvature on vortex formation and excitation revealing a complex fluid–structure interaction mechanism.

© 2013 Elsevier Ltd. All rights reserved.

## 1. Introduction

Ongoing deep-sea exploration, installation and production of hydrocarbon energy need the development of new viable technologies. One of these is the requirement of a robust and reliable analysis tool for the prediction of vortex-induced vibration (VIV) of marine structures exposed to ocean currents. Because VIV can cause high cyclic-loading fatigue damage of structures, it is now widely accepted to be a crucial factor that should be taken into account in the preliminary analysis and design. However, many insightful VIV aspects are still unknown and far from fully understood; these render the structural design quite conservative with the use of a large factor of safety. For offshore structures with initial curvatures and high flexibility such as catenary risers, mooring cables and free-spanning pipelines, the theoretical, numerical or experimental VIV research is still very lacking.

\* Corresponding author. Current address: PNV Dept. Eng. Naval e Oceanica, Escola Politécnica da Universidade de São Paulo, Av. Prof Mello Moraes 2231, 05508-030, São Paulo - SP, Brazil. Tel.: +55 11 30915646; fax: +55 11 30915642.

E-mail addresses: [g.assi@usp.br](mailto:g.assi@usp.br), [gustavo.assi@gmail.com](mailto:gustavo.assi@gmail.com) (G.R.S. Assi).

URL: <http://www.ndf.poli.usp.br> (G.R.S. Assi).

<sup>1</sup> Now at the Institute of Aerodynamics and Flow Technology, German Aerospace Center (DLR), Göttingen, Germany.

| Nomenclature |   |           |  |
|--------------|---|-----------|--|
|              |   | $m^*$     | mass ratio                                 |
|              |   | Re        | Reynolds number                            |
|              |   | $U$       | flow speed                                 |
| $D$          | cylinder external diameter                    | $U/Df_0$  | reduced velocity                           |
| $f_0$        | natural frequency in air                      | $\hat{x}$ | streamwise harmonic amplitude of vibration |
| $f_x$        | streamwise oscillation frequency              | $\hat{y}$ | cross-flow harmonic amplitude of vibration |
| $f_y$        | cross-flow oscillation frequency              | $\zeta$   | structural damping ratio                   |
| $h$          | cylinder vertical length below the water line |           |  |

Risers are very long pipes used to carry oil from the sea bed to offshore platforms floating on the water surface. Under the effect of sea currents, these flexible structures are especially susceptible to flow-induced vibrations, particularly since they have a relatively low mass compared to the mass of the displaced fluid. Generally, an offshore floating platform accommodates several riser pipes together with many other cylindrical structures. The interaction of these flexible structures can produce an even more complex problem, resulting in vibrations with rather unexpectedly higher amplitudes (Assi et al., 2010a). Flow interference from the platform hull, the soil on sea bed and the pipe itself can also increase the complexity of the flow, generating complex responses.

The riser may respond with different amplitudes and frequencies depending on the flow excitation and structural stiffness along the length of the pipe. Consequently, several modes of vibration with varying curvature appear along the span resulting in a very rich fluid–structure interaction mechanism (Srinil, 2010). In addition to that, flexible risers can be laid out in a catenary configuration which results in high curvature close to the region where it touches the bottom of the ocean, called the touchdown point.

In an attempt to understand and model the fluid-dynamic behaviour around curved sections of risers we have performed experiments with a curved, rigid circular cylinder in a water channel. This idealised experiment is far from reproducing the real conditions encountered in the ocean; nevertheless it should throw some light on understanding how the vortex shedding mechanism is affected by the curvature of the pipe. In addition to the phenomenological aspects, the present work may also serve as reference for validation and benchmarking of numerical simulations of fluid–structure interaction.

An investigation into the vortex shedding patterns and the fundamental wake topology of the flow past a stationary curved circular cylinder has been carried out by Miliou et al. (2007) and de Vecchi et al. (2008, 2009) based on computational fluid dynamics studies. As a result of pipe initial curvatures, flow visualisations highlight different kinds of wake characteristics depending on the pipe (convex or concave) configuration and its orientation with respect to (aligned with or normal to) the incoming flow. When the flow is uniform and normal to the curvature plane, the cross-flow wake dynamics of curved pipes behave qualitatively similar to those of straight pipes. This is in contrast to the case of flow being aligned with the curvature plane where wake dynamics change dramatically. However, these scenarios are pertinent to a particular stationary cylinder case in a very low-Reynolds number range. The VIV behaviour will further transform if the structure oscillates and interacts with the fluid wakes, depending on several fluid–structure parameters.

## 2. Experimental arrangement

Experiments have been carried out in the Circulating Water Channel of the NDF (Fluids and Dynamics Research Group) at the University of São Paulo, Brazil. The NDF-USP water channel has an open test section 0.7 m wide, 0.9 m deep and 7.5 m long. Good quality flow can be achieved up to 1.0 m/s with turbulence intensity less than 3%. This laboratory has been especially designed for experiments in flow-induced vibrations and more details about the facilities are described in Assi et al. (2006).

A rigid section of a curved circular cylinder, with an external diameter of  $D=32$  mm, was made of ABS plastic and Perspex tubes according to the dimensions shown in Fig. 1. The curved cylinder was composed of a horizontal section with  $10D$  in length, a curved section with a  $10D$  radius and a vertical section with length  $h/D$  that could be varied with reference to the water line. The water level was set to 700 mm from the floor of the channel, which meant that the  $10D$ -long horizontal part of the cylinder was not close enough to the floor to suffer interference from the wall.

The model was connected by its upper end to a long pendulum rig (length  $H=3.0$  m) that allowed the system to oscillate in two degrees of freedom (2-dof) in the cross-flow and streamwise directions. The model was attached to two pairs of coil springs that provided the stiffness of the system. The springs were set to provide the same natural frequency ( $f_0$ , measured in air) in both the cross-flow and streamwise directions. The design and construction of the pendular elastic rig was made by Freire and Meneghini (2010) based on a previous idea employed by Assi et al. (2009, 2010b) for experiments with VIV suppressors. The present apparatus has been validated for VIV experiments by Freire et al. (2009, 2011).

Two laser sensors measured the cross-flow and streamwise displacements of the pendulum referring to the displacement of the bottom tip of the models. A load cell was installed before the springs to allow for instantaneous measurements of lift and drag acting on the cylinder. (Hydrodynamic forces will not be discussed in this paper.) A particle-image velocimetry (PIV) system was employed to analyse the instantaneous wake patterns along the cylinder span.

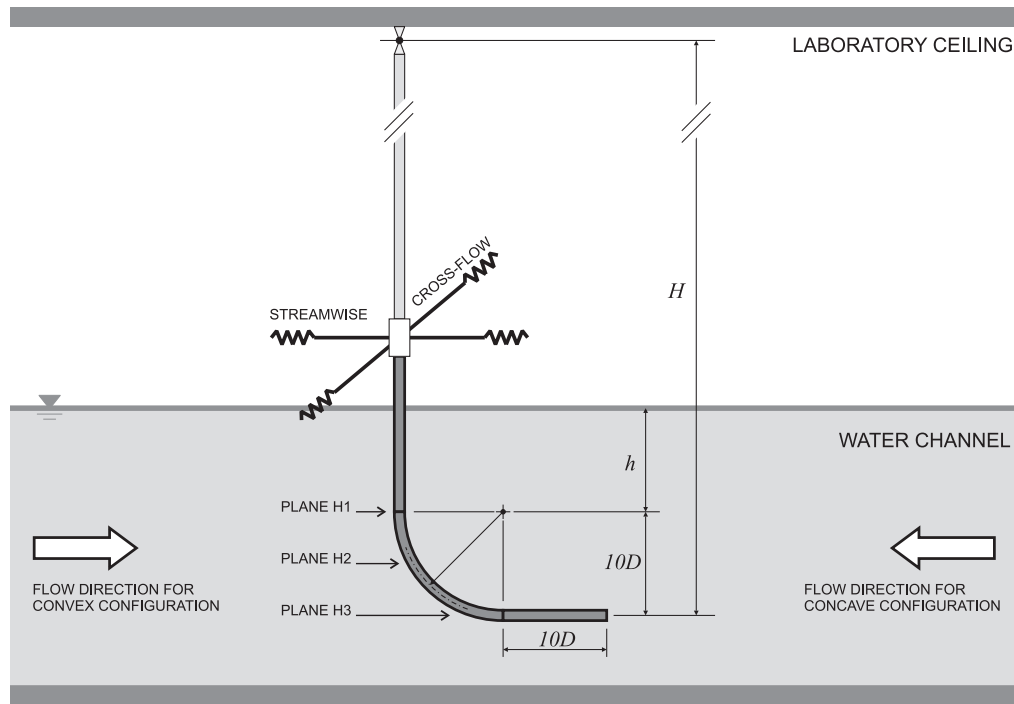


**Fig. 1.** Experimental arrangement in the NDF-USP circulating water channel. The cylinder was rotated by 180 degrees to arrange concave and convex configurations.

**Table 1**  
Structural properties.

| Model             | $m^*$ | $\zeta$ (%) | $m^*\zeta$ |
|-------------------|-------|-------------|------------|
| Straight cylinder | 2.8   | 0.2         | 0.0056     |
| Curved cylinders  | 2.1   | 0.2         | 0.0042     |

Regarding the flow direction, two orientations were investigated: a convex and a concave configuration according to the direction of the flow approaching the curvature. The flow direction in the test section of the water channel was not changed; naturally the curved cylinder was rotated by 180 degrees to allow for both concave and convex arrangements. This is also illustrated in Fig. 1.

Decay tests have been performed in air in order to determine the natural frequencies of the system in both directions as well as the level of structural damping. The apparatus with one universal joint and four springs turned out to present a very low structural damping of  $\zeta = 0.2\%$ , measured as a fraction of the critical damping. The total oscillating mass of the system was measured in air, resulting in a non-dimensional mass ratio  $m^*$ , defined as the ratio between the total mass and the mass of displaced fluid. Consequently, the mass-damping parameter  $m^*\zeta$  of the system was kept to the lowest possible value in order to amplify the amplitude of response.

Table 1 presents a summary of the structural parameter for both the straight and curved cylinder.

### 3. Results for a straight cylinder

A preliminary VIV experiment was performed with a straight cylinder in order to validate the set-up and generate data for comparison. The same pendulum rig was employed, only replacing the curved model by a straight cylinder with the same diameter. This time, the straight cylinder was long enough to reach the bottom wall only leaving a 3 mm clearance to allow for free movement of the pendulum in any direction.

The dynamic response of the straight cylinder covered a reduced velocity range from 1.5 to 12, where reduced velocity ( $U/Df_0$ ) is defined using the cylinder natural frequency of oscillation measured in air. The only flow variable changed during the course of the experiments was the flow velocity  $U$ , which, as for full-scale risers, alters both the reduced velocity and the Reynolds number between 750 and 15 000 for a maximum reduced velocity of 20.

The flow around a smooth, straight circular cylinder in the considered Reynolds number range (identified as sub-critical) is generally expected to be three-dimensional, with a laminar boundary layer over the cylinder surface and turbulent vortex wake. However, in the case of curved cylinder, the curvature plays a significant role in modifying the wake dynamics, which

depends on the leading geometry facing the approaching flow. This entails both the normal and axial flow components along the cylinder curved section, further complicating the spatio-temporal vortex shedding mechanisms, associated forces and frequencies. This has been exemplified by [Miliou et al. \(2007\)](#) for  $Re = 500$ .

Throughout the study, cylinder displacement amplitudes ( $\hat{x}/D$  for the streamwise and  $\hat{y}/D$  for the cross-flow directions) were found by measuring the root mean square value of response and multiplying by the square root of 2 (the so called harmonic amplitude). This is likely to give an underestimation of maximum response but was judged to be perfectly acceptable for assessing the general behaviour of VIV, since the response is mostly harmonic. Results presented in the present study correspond to the displacement of the lowest point of the model, i.e., the end of the cylinder closer to the section floor, thus representing the maximum displacement developed by each model. Consequently, the equivalent amplitude at the water surface for the cylinder with a  $10D$  vertical section is 20% smaller than the amplitude indicated in the results. Applying similar corrections, amplitudes are 16% smaller for the cylinder with a  $5D$  vertical section and 11% smaller for the cylinder with no vertical section.

Displacements are non-dimensionalised by the cylinder diameter  $D$ . The dataset for the straight cylinder is repeated in [Figs. 2–5](#) to serve as reference.

[Figs. 2 and 4](#) compare the reference cross-flow and streamwise responses obtained from two different runs with the straight cylinder. In the first one, the flow speed ( $U$ ) was increased in 30 steps from zero to a maximum, while in the second it was decreased from the maximum to zero. Both data sets overlap rather well for all the reduced velocity range except for a region around  $U/Df_0 = 6$  where the well-known phenomenon of hysteresis in the VIV response has been observed. The streamwise VIV response also seems to occur in two resonance ranges ( $U/Df_0 = 2$  and  $6$ ), the so-called second and third instability ranges involving asymmetric vortices ([Bearman, 1984](#)).

Although the observed peak amplitude of  $\hat{y}/D = 1.5$  around  $U/Df_0 = 6$  is slightly higher than other results found in the literature for similar values of  $m^*\zeta$  (for example, [Assi et al., 2009](#)) the general behaviour of both curves shows a typical response for 2-dof VIV. The higher amplitude found here could be explained by the very low mass-damping characteristics of the system and the geometric projection of the amplitude at the tip of the model and not at mid-length as usual.

Although the cylinder was initially aligned in the vertical position, in flowing water the mean drag displaces the cylinder from its original location reaching a slightly inclined configuration from the vertical. This was judged not to be detrimental to the experiment; hence the inclination of the cylinder was not corrected between each step. The same procedure was adopted for the curved cylinder.

[Figs. 3 and 5](#) present the dominant frequency of response versus reduced velocity. Two dashed lines inclined with different slopes represent the region for a Strouhal number of 0.2 and 0.4, i.e., an estimation of the vortex shedding frequency for a straight cylinder in the cross-flow and streamwise direction respectively. It is clear that the straight cylinder

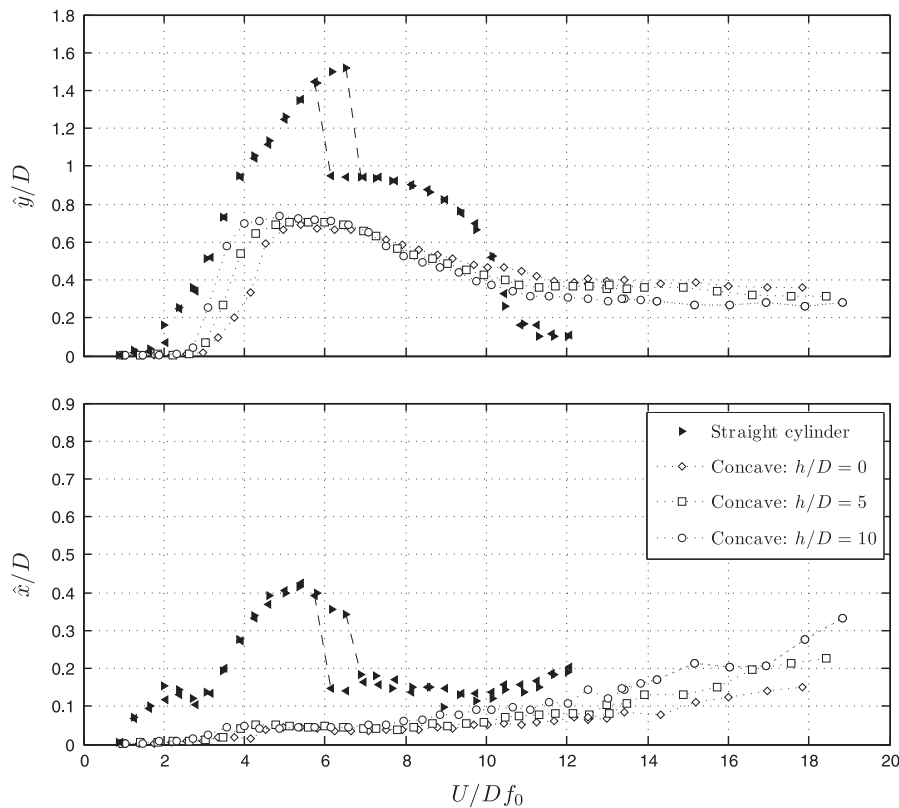


**Fig. 2.** Cross-flow ( $\hat{y}/D$ ) and streamwise ( $\hat{x}/D$ ) amplitude of vibration versus reduced velocity for a straight cylinder and concave configurations varying the vertical section length ( $h/D$ ). Symbols ▶ are for runs with increasing flow speed, while ◀ are for decreasing.

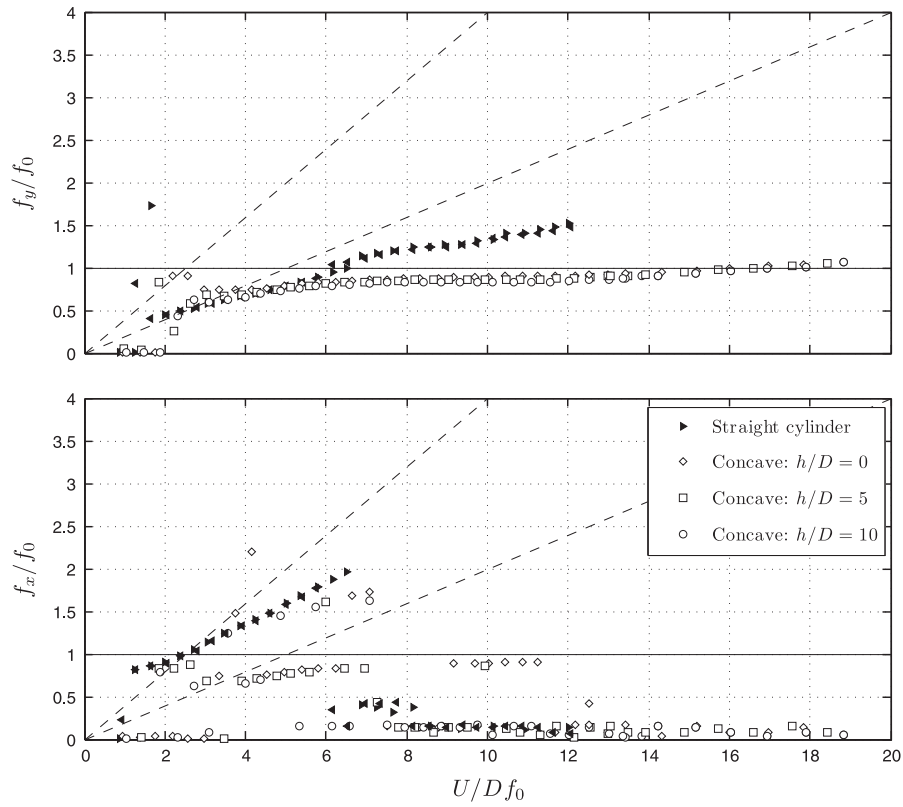


**Fig. 3.** Cross-flow ( $\hat{y}/D$ ) and streamwise ( $\hat{x}/D$ ) dominant frequency of response versus reduced velocity for a straight cylinder and curved concave configurations varying the vertical section length ( $h/D$ ). Symbols  $\blacktriangleright$  are for runs with increasing flow speed, while  $\blacktriangleleft$  are for decreasing.

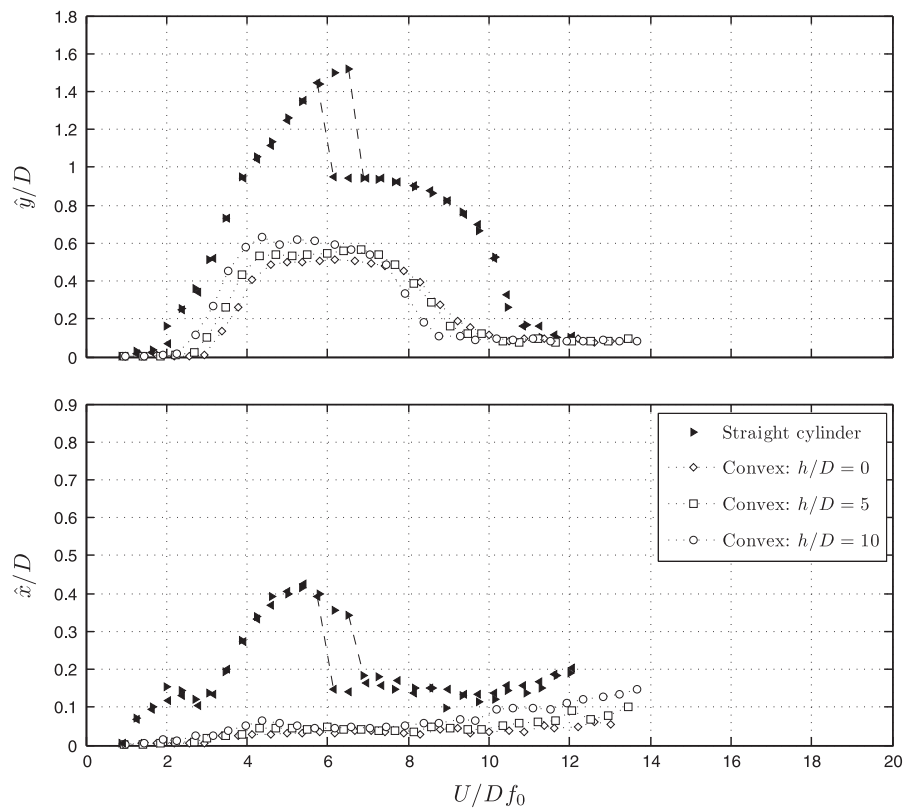


**Fig. 4.** Cross-flow ( $\hat{y}/D$ ) and streamwise ( $\hat{x}/D$ ) amplitude of vibration versus reduced velocity for a straight cylinder and convex configurations varying the vertical section length ( $h/D$ ). Symbols  $\blacktriangleright$  are for runs with increasing flow speed, while  $\blacktriangleleft$  are for decreasing.



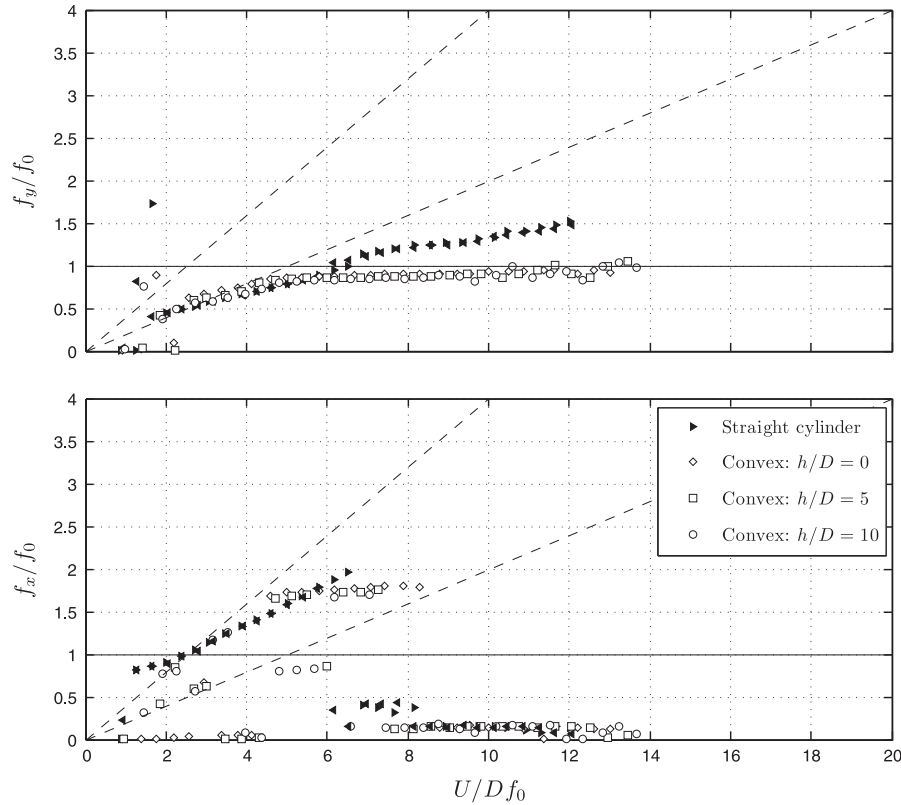


**Fig. 5.** Cross-flow ( $\hat{y}/D$ ) and streamwise ( $\hat{x}/D$ ) dominant frequency of response versus reduced velocity for a straight cylinder and curved convex configurations varying the vertical section length ( $h/D$ ). Symbols  $\blacktriangleright$  are for runs with increasing flow speed, while  $\blacktriangleleft$  are for decreasing.

presents a typical VIV response oscillating in the cross-flow direction with a frequency following the  $St = 0.2$  line up to the beginning of the upper branch. Eventually,  $f_y/f_0$  departs from  $St = 0.2$  towards the unity value around  $U/Df_0 = 6$ . The behaviour observed for the streamwise vibration is also typical of VIV with the difference that the frequency of response is twice as that for the cross-flow direction during much of the synchronisation range.

#### 4. Response of the curved cylinder

As mentioned above, experiments with the curved cylinder were performed taking into account two distinct configurations as far as the flow direction is concerned. In the concave configuration the flow approaches the model reaching first the horizontal section. As opposed to that, in the convex configuration the horizontal section is placed downstream of the curved and vertical parts.

##### 4.1. Amplitude of vibration

In general terms, as presented in Figs. 2 and 4, the curved cylinders showed significantly less vibration for both concave and convex configurations when compared to the typical VIV response of the straight cylinder. Such a reduction is noticeable in both the cross-flow and streamwise responses. This clearly shows that the curvature of the cylinder modifies the vortex shedding mechanism in a manner that the structure extracts less energy from the flow. We shall return to this point when investigating the velocity flow field with PIV.

For each concave and convex configuration, the vertical section of the cylinder close to the free surface was varied in three different lengths:  $h/D = 0, 5$  and  $10$ . The overall response for the three values of  $h/D$  is very similar, showing only minor differences at the beginning of the synchronisation range between  $U/Df_0 = 3.0$  and  $5.0$ . Apart from that, no distinct behaviour was observed as far as a variation in  $h/D$  is concerned for both concave and convex configurations.

The cross-flow displacement does not reveal distinct upper and lower branches of vibration such as those observed for a straight cylinder, but it produces a smooth curve that spans the whole synchronisation region with maximum amplitude around  $\hat{y}/D = 0.75$  for the concave and  $0.65$  for the convex configurations. No hysteresis is found.

However, the most interesting feature of such a behaviour is found when the convex response is compared to the concave one (Figs. 2 and 4). While the convex curve for  $\hat{y}/D$  drops immediately between  $U/Df_0 = 8$  and  $10$  to a level of  $\hat{y}/D \approx 0.1$ , the response for the concave case does not diminish, but is sustained for higher reduced velocities around  $\hat{y}/D = 0.3$  until the end of the experiment. Apparently there must be a fluid-elastic mechanism occurring for reduced

velocities above 8.0 for the concave configuration capable of extracting energy from the flow to sustain vibrations around  $\hat{y}/D = 0.3$ . We shall discuss this point later while analysing the PIV flow fields.

In the streamwise direction the responses of the curved cylinders are different from the typical VIV developed by the straight cylinder. Streamwise vibrations in the first and second resonance regions are totally suppressed, probably owing to the hydrodynamic damping effect induced by the cylinder's horizontal part. At the same time, the streamwise vibration  $\hat{x}/D$  for the concave case also shows increasing amplitude beginning at reduced velocities higher than 10 and reaching  $\hat{x}/D \approx 0.35$  for the highest flow speed. It coincides with the increased amplitude observed in the cross-flow direction and should be related to the same excitation mechanism. Once more, no distinct difference in the streamwise response was observed while varying  $h/D$ .

#### 4.2. Frequency of vibration

Figs. 3 and 5 present the dominant frequency of oscillation non-dimensionalised by the natural frequency for both cross-flow and streamwise directions of motion. Results for the curved cylinder show a consistent behaviour in the cross-flow direction, with data points following the Strouhal line up to the upper branch peak but remaining closer to  $f_y/f_0 = 1.0$  for the rest of the reduced velocity range. In the streamwise direction, we find data points following both Strouhal lines and also very low frequencies indicating random drifts instead of periodic oscillations. Since the displacements in the streamwise direction are much smaller for the curved cylinder than the straight one, we should expect broader frequency spectra dominating over the response.

One might remember that the straight and curved cylinder should have very similar values of added mass in the cross-flow direction, but slightly different values in the streamwise direction due to the geometric properties relative to the flow. We have not taken such effect into account in this paper, but it might be playing an important role defining the frequencies of oscillation in water.

#### 4.3. Trajectories of motion

Fig. 6 qualitatively compares samples of displacement trajectories obtained for three experiments performed with the straight cylinder and the curved cylinders with  $h/D = 10$ . The straight cylinder presents distinct eight-shape figures typical of 2-dof VIV owing to the 2:1 ratio on the streamwise to cross-flow frequency of excitation. On the other hand, trajectories for both configurations of the curved cylinder reveal that the streamwise displacement is greatly reduced when compared to the straight cylinder. Both concave and convex cases show very little movement in the streamwise direction for the whole range of reduced velocity.

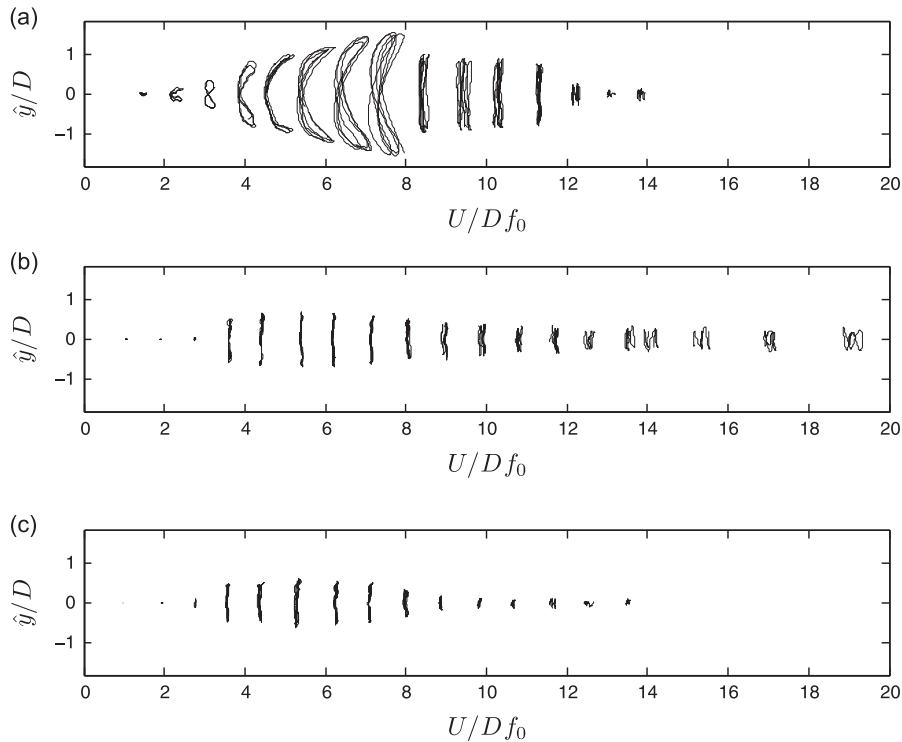


**Fig. 6.** Response trajectories of motion for a (a) straight cylinder and a curved cylinder in (b) concave and (c) convex configurations. Each trajectory was taken at the reduced velocity indicated in the horizontal axis. (a) Straight cylinder, (b) curved cylinder, concave configuration,  $h/D = 10$ , and (c) curved cylinder, convex configuration,  $h/D = 10$ .

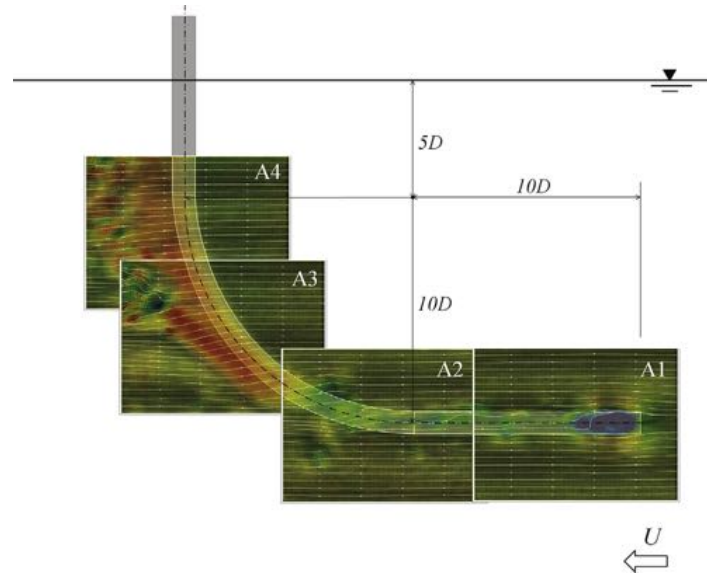


Fig. 7. Composition of instantaneous PIV velocity fields for concave configuration with  $h/D = 5$ .

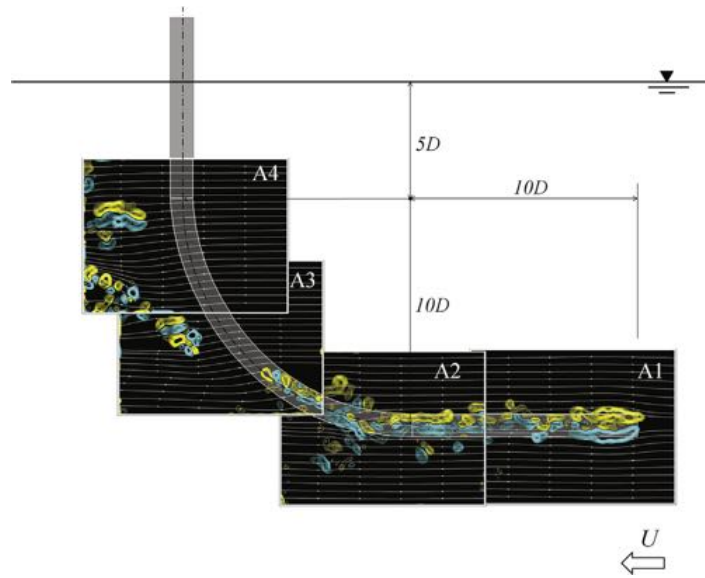


Fig. 8. Composition of instantaneous PIV vorticity fields for concave configuration with  $h/D = 5$ .

Another interesting observation relates to the movement of both curved cylinders. It is clear that for reduced velocities greater than 10 the convex cylinder shows small displacements in both directions, while vibrations are sustained until the end of the experiment for the concave case as shown in Figs. 2 and 4.

## 5. Velocity and vorticity fields of stationary cylinders

Two dimensional PIV (particle image velocimetry) measurements of the flow around the cylinder were performed, for both concave and convex configurations, on a vertical plane parallel to the plane of curvature. In addition, PIV measurements were also performed on three horizontal planes (marked H1, H2 and H3 in Fig. 1 across the cylinder diameter.

All PIV measurements were taken for  $Re = 1000$  in the sub-critical Reynolds number regime found for a straight circular cylinder. According to Williamson (1996), the particular flow is in the shear-layer transition regime, characterised by an increase on the base suction, a gradual decrease in the Strouhal number and a decrease in the formation length of the mean recirculation region. These trends are caused by the developing instability of the separating shear layers from the sides of the body. The flow around a curved cylinder, which presents different elliptical cross-sections along the span, may behave slightly different from the above description. Further investigation is necessary in order to evaluate that.

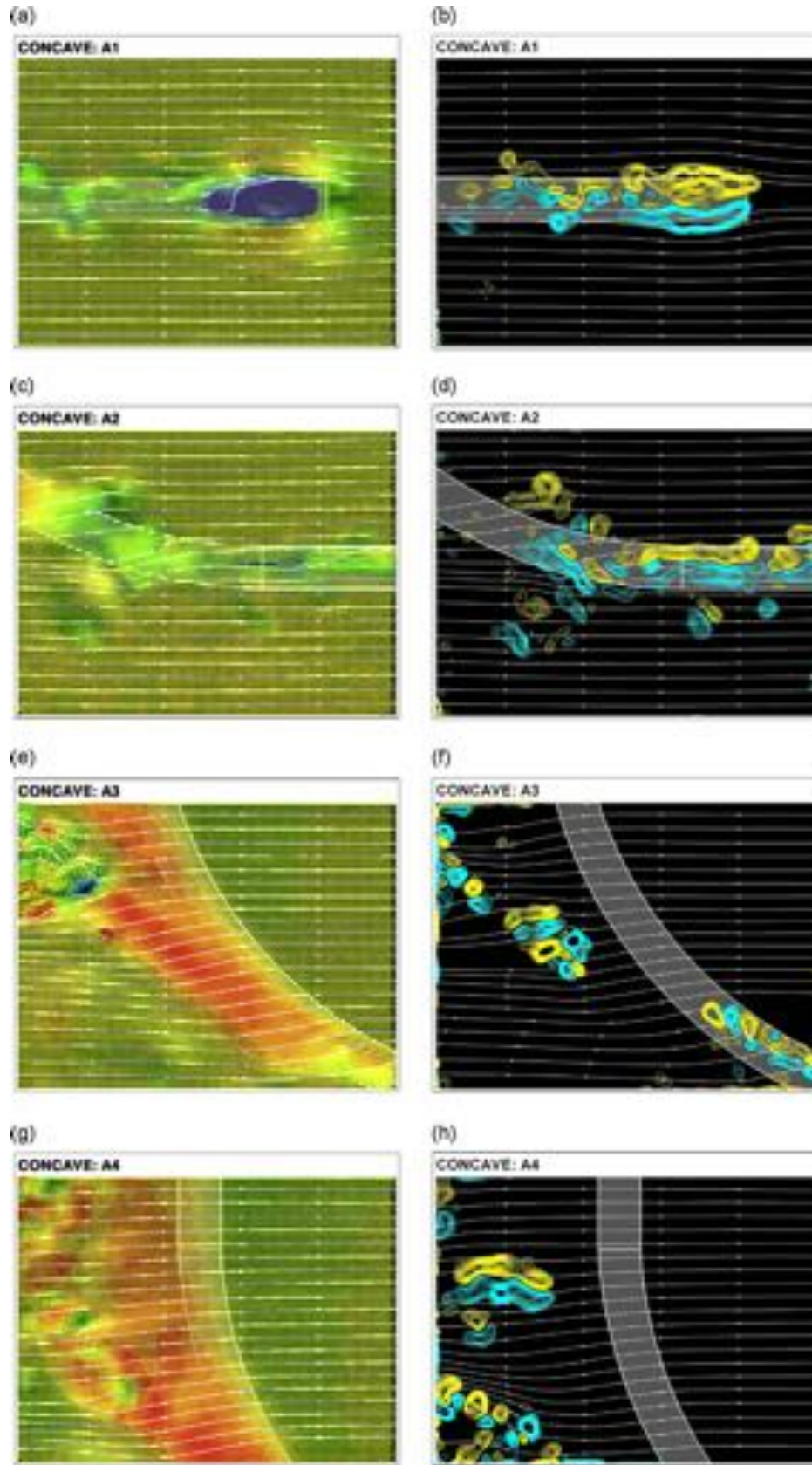


**Fig. 9.** Detailed velocity and vorticity fields from Figs. 7 and 8. Flow direction is from right to left.  $Re = 1000$ . Colour scale for velocity magnitude is from 0.004 m/s (blue) to 0.05 m/s (red). Colour scale for vorticity contours in the range  $\pm 0.004 \text{ s}^{-1}$ . (Velocity fields do not correspond to the vorticity fields in time.). (a) Velocity magnitude, A1, (b) vorticity contours, A1, (c) velocity magnitude, A2, (d) vorticity contours, A2, (e) velocity magnitude, A3, (f) vorticity contours, A3, (g) velocity magnitude, A4, and (h) vorticity contours, A4. (For interpretation of the references to color in this figure caption, the reader is referred to the web version of this article.)

### 5.1. Vertical plane

We shall start discussing the results obtained from the vertical plane, as presented in Figs. 7–12. Four visualisation areas for each configuration, labelled A1–A4, were conveniently distributed along the length of the cylinder in order to evaluate as much as possible to the flow pattern around the body. All four areas are in the same plane illuminated by the laser, which is parallel to the plane of curvature only dislocated by  $1D$  from the centre of the cylinder towards the camera in order to capture the highest velocities induced by the vortex tubes. Figs. 9 and 12 show the location of each area composing the flow field along the cylinder. It is important to note that each velocity field was obtained from a different acquisition instant; hence A1, A2, A3 and A4 are not correlated in time.

All PIV measurements were performed for a static cylinder at  $Re \approx 1000$ . Of course the wake pattern for the static cylinder is expected to be different from the wake of an oscillating cylinder, but even an analysis of a fixed body can contribute to the understanding of the complex vortex–structure interaction occurring during the response. A similar approach was employed by Miliou et al. (2007) who performed numerical simulations for a static, curved cylinder between  $Re = 100$  and  $500$ . The same colour scales have been employed from Figs. 7 to 12 to allow for direct comparison of velocity magnitude and vorticity contours.

With that in mind, let us analyse first the flow pattern around the concave configuration in Figs. 7–12. The overall flow around the body can be divided into two parts:

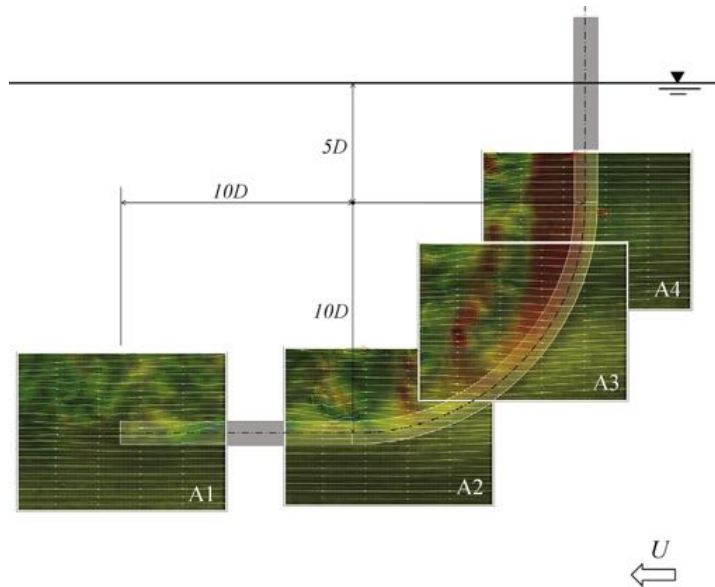


Fig. 10. Composition of instantaneous PIV velocity fields for convex configuration with  $h/D = 5$ .

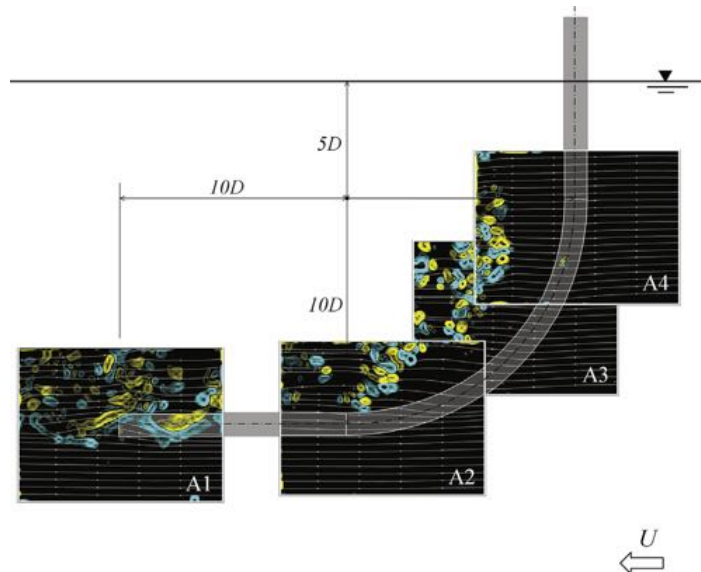
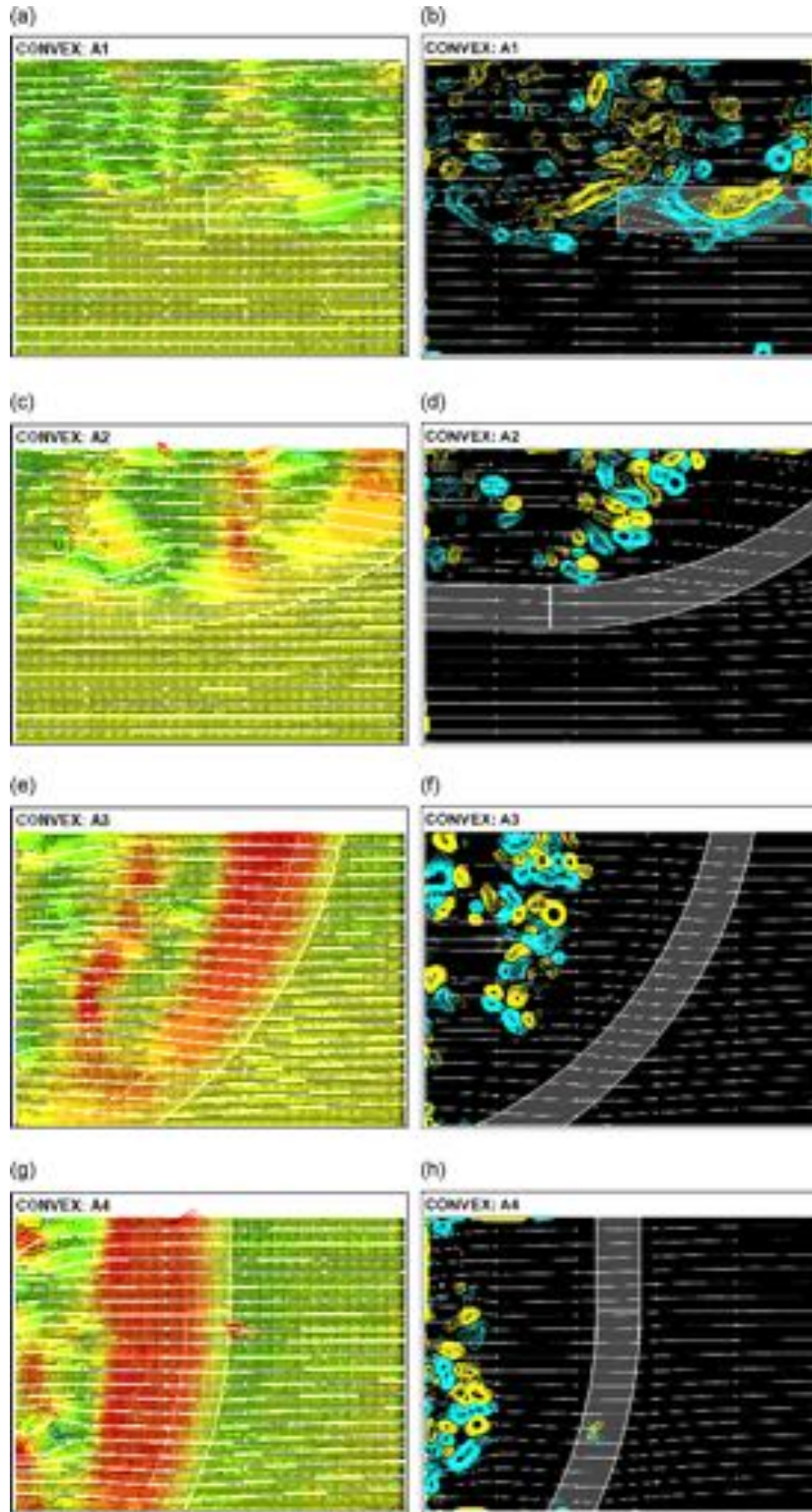


Fig. 11. Composition of instantaneous PIV vorticity fields for convex configuration with  $h/D = 5$ .





**Fig. 12.** Detailed velocity and vorticity fields from Figs. 10 and 11. Flow direction is from right to left.  $Re = 1000$ . Colour scale for velocity magnitude is from 0.004 m/s (blue) to 0.05 m/s (red). Colour scale for vorticity contours in the range  $\pm 0.004 \text{ s}^{-1}$ . (Velocity fields do not correspond to the vorticity fields in time.). (a) Velocity magnitude, A1, (b) vorticity contours, A1, (c) velocity magnitude, A2, (d) vorticity contours, A2, (e) velocity magnitude, A3, (f) vorticity contours, A3, (g) velocity magnitude, A4, and (h) vorticity contours, A4. (For interpretation of the references to color in this figure caption, the reader is referred to the web version of this article.)



- (I) Areas A1 and A2 show the region where the flow is mostly parallel to the axis of the cylinder. Therefore, no clear vortex tubes are observed with concentrated axial vorticity. Instead, the flow along the horizontal length is disturbed by the separation occurring at the tip of the cylinder. Area A1 shows the flow approaching the disk facing upstream and separating into a recirculation bubble. The periodicity of the shedding associated with this region is also related to the flow speed and the diameter  $D$ , but no coherent vortices parallel to the cylinder are able to form. As a consequence, a cascade of small vortices is convected downstream along the horizontal length (see area A2) reaching the beginning of the curved section.
- (II) Areas A3 and A4 show the region where the flow is mainly perpendicular to the axis of the cylinder. Coherent vortex tubes tend to form following the curvature of the body, but further downstream they are stretched and rapidly breakdown into smaller vortices that are convected by the flow. Area A3 shows the instant when a vortex tube is shed almost tangent to the curvature, while area A4, around the vertical section, reveal a formation region more or less aligned with the axis of the cylinder. Streamlines drawn in areas A3 and A4 reveal a non-negligible velocity component deflecting the flow downwards immediately after the vortex formation region. As we move along the cylinder towards the water line from A3 to A4 the downward component is gradually reduced until it eventually disappears towards the upper half of A4. This region marks the competition between two wake modes existent along the transition from curved to straight cylinder. This looks similar to Fig. 15 in Miliou et al. (2007), with  $Re = 100$ , although without the cylinder horizontal section therein.

Analysing the flow pattern for the convex configuration in Figs. 10–12 we notice two striking differences:

Firstly, because the flow approaching the convex body does not encounter a blunt disk facing upstream, no strong separation or recirculation bubble is formed. As a consequence, the horizontal section seen in areas A1 and A2 is not exposed to a disturbed, unsteady flow parallel to the axis of the cylinder. In fact, A1 and A2 reveal that the upper half of the horizontal length is exposed to a periodic flow formed by a regular wake, while the bottom half experiences almost no perturbation, with streamlines showing a well behaved flow field parallel to the axis.

Secondly, looking at the upper half of the body (A3 and A4) we notice much stronger and coherent vortex tubes when compared to the flow around the concave configuration. Area A3 reveals some kind of vortex dislocation after a formation region that increases in length as we move upwards. Because the convex geometry does not encourage the vortex tubes to stretch and break, a periodic wake seems to be sustained farther downstream. In contrast with the flow around the concave configuration, the velocity field around the curved section has a non-negligible vertical component upwards. It is stronger in A2 and is gradually reduced as we move upwards along the curvature in A3. This looks similar to Fig. 3 in Miliou et al. (2007) for  $Re = 100$ .

Gallardo et al. (2011) stated that there is a certain degree of alignment of the flow structures with the axial curvature of the cylinder, which tilts the flow structures with respect to the vertical direction. Fig. 12(e) and (f) captures this behaviour, also recognised in Fig. 2 of Gallardo et al. (2011) and Fig. 8 of Miliou et al. (2007).

## 5.2. Horizontal planes

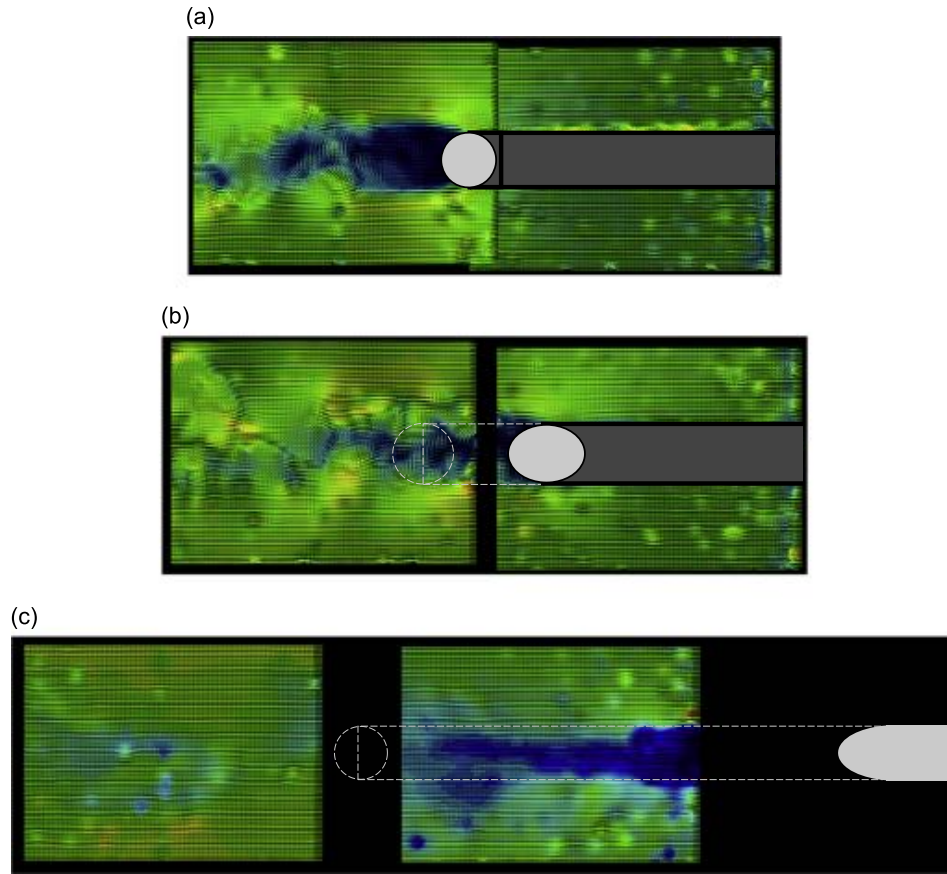
Figs. 13 and 14 present PIV velocity fields for the three horizontal planes indicated by H1, H2 and H3 in Fig. 1. All measurements were performed with  $h/D = 5$ . Plane H1 was positioned at the transition from the straight to the curved section of the model, i.e.,  $5D$  below the water line. Plane H2 was located  $5D$  below that position and plane H3 another  $5D$  down towards the floor.

Fig. 13 presents results for the concave configuration. The two cameras were positioned underneath the model as viewing from the bottom through the glass floor. A light grey circle or ellipse marks the cross section of the cylinder at the illuminated plane. A dark grey rectangle represents the part of the curved model in front of the laser plane, while a dashed line illustrates the projection of the model behind the plane. Each image is composed of two PIV areas taken simultaneously; for some cases they overlap, for others they are apart.

In Fig. 13(a), for the horizontal plane at the transition from the straight to the curved section, we notice a wider wake with a longer formation region that generates stronger vortices. This formation is related to the strong vortex tubes parallel to the straight section presented in Fig. 9(g). Moving down to plane H2, the cross section of the cylinder turns into an ellipse. The wake becomes much narrower with a short formation length and no strong vortices are distinguishable in the downstream flow. Fig. 9(e) also showed that an oblique vortex tube would form closer to the cylinder with vortices breaking apart into smaller eddies. Farther down to plane H3, the cross section illuminated by the laser plane now shows the beginning of the horizontal portion of the model. No vortex wake is identified, but only a region of disturbed flow which agrees with pattern shown in Fig. 9(c).

Results for the convex configuration in Fig. 14 were obtained in the same way as the concave, the only difference being that the cameras were installed above the channel, viewing from the top through the free surface. As a consequence, plane H3 does not result in any useful velocity field once the flow that separates from the cylinder follows attached to the horizontal portion of the model, as seen in Fig. 12(c).

Fig. 14(a) presents velocity fields for the first plane H1 at the transition region. A rather wide wake with strong vortical structures is noticeable through high induced velocities. Again, the same pattern was captured on the vertical PIV shown in Fig. 12(g). Moving down to plane H2 we notice that an organised wake may still exist, even though the cross section of the cylinder turned into an ellipse. Vortex tubes were also verified to persist further downstream in Fig. 12(c) and (e) as



**Fig. 13.** Velocity fields for horizontal planes across the concave configuration. Refer to Fig. 1 for positions. Flow direction is from right to left.  $Re = 1000$ . Colour scale for velocity magnitude is from 0.004 m/s (blue) to 0.05 m/s (red). (a) Plane H1, (b) plane H2, and (c) plane H3. (For interpretation of the references to color in this figure caption, the reader is referred to the web version of this article.)

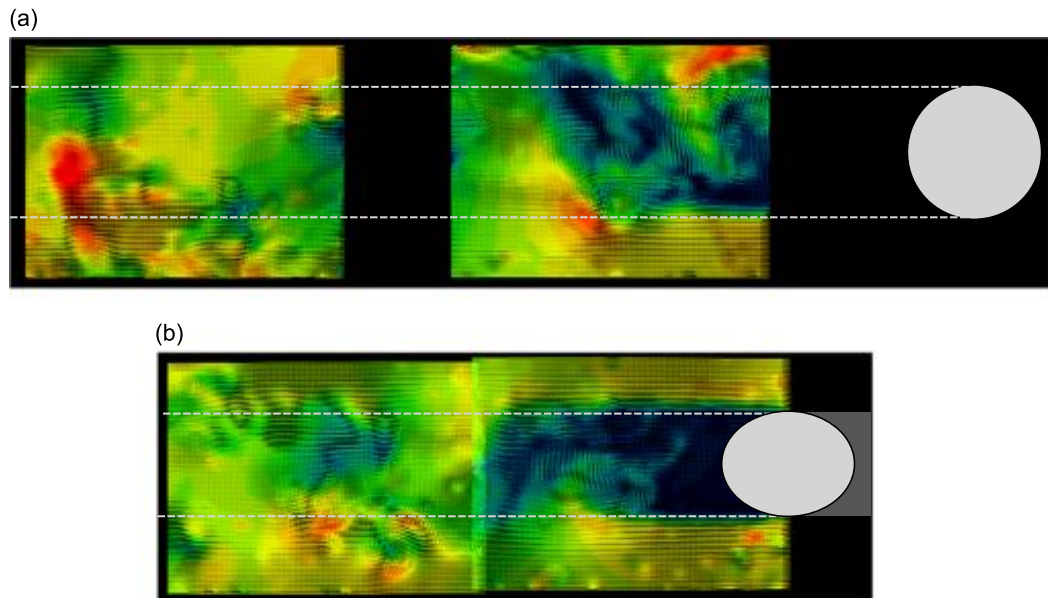


**Fig. 14.** Velocity fields for horizontal planes across the convex configuration. Refer to Fig. 1 for positions. Flow direction is from right to left.  $Re = 1000$ . Colour scale for velocity magnitude is from 0.004 m/s (blue) to 0.05 m/s (red). (a) Plane H1 and (b) plane H2. (For interpretation of the references to color in this figure caption, the reader is referred to the web version of this article.)

coherent flow structures appeared periodically downstream of the cylinder in the flow fields. Similar vortex structures were verified by Miliou et al. (2007) and Gallardo et al. (2011). This proves that the convex configuration is more prone to produce correlated vortex tubes along the curved length of the cylinder, while in the concave configuration vortices soon break apart as they are convected downstream.

Based on the results of Gallardo et al. (2011) for the convex configuration, one can observe that the interaction of the shear layers and thus the vortex formation length is a function of the cross-sectional shape being circular or elliptical, here represented by different planes along the cylinder span as can be seen in Fig. 14 and also in Fig. 3 of Gallardo et al. (2011).

Plane H1 in Fig. 14(a), which corresponds to plane  $z/D = 16$  in Gallardo et al. (2011), shows that the shear layers interact in a farther downstream position from the body and the wake is wider compared to a horizontal position of the H2 plane in Fig. 14(b) where the cross-section of the cylinder is elliptical. In the latter case, seen also at the  $z/D = 8$  plane in Gallardo et al. (2011), there are vortices produced within the recirculation region exhibiting the wavier shear layers.

## 6. The excitation mechanism

The main question to be answered by the present study is concerned with the fact that the amplitude in the cross-flow direction for the convex configuration is able to drop down to 0.1 for high reduced velocities while the concave configuration sustains vibration around 0.35. We believe this distinct behaviour between the convex and the concave configurations is related to the wake interference happening in the lower half of the cylinder due to perturbations generated in the horizontal section when it is positioned upstream.

In the concave configuration the horizontal part of the cylinder is located upstream of the curved and vertical parts. The approaching flow encounters a circular blunt leading edge with a clear separation region around the circumference (Fig. 9(a)). The flow that separates at the leading edge tends to create a separation bubble and latter reattaches along the horizontal section of the cylinder. Because the cylinder already presents cross-flow and streamwise vibrations, the three-dimensional separation bubble will not find a stable configuration nor a definite reattachment region, instead it will develop a periodic behaviour that may result in three-dimensional vortices being shed downstream, reaching the other parts of the cylinder. This is very clear in areas A1 and A2 of Figs. 7 and 9 for the static cylinder.

The fluid-elastic mechanism behind the response may be a composition of different phenomena acting at the same time. We believe this interaction between the disturbed flow from the upstream horizontal part with the curved and vertical parts is responsible for sustaining the level of vibration around  $\hat{y}/D = 0.35$  and  $\hat{x}/D = 0.35$ . We suggest such an interaction may be occurring in the following forms:

- (i) Vortices generated along the horizontal section may impinge on the curved part generating impulses in the same manner that large eddies of turbulence induce buffeting on elastic structures. Because the concave configuration has a longer section immersed in such a disturbed wake it is more susceptible to buffet. Evidence that a buffeting-like phenomenon might be occurring is that the streamwise vibration shows a considerable increase in amplitude with increasing flow speed further out of the synchronisation range. Fig. 6(b) also reveals that these vibrations are not harmonic and may even be chaotic, another evidence supporting the buffeting-excitation hypothesis.
- (ii) The disturbed flow from the horizontal part may be disturbing and disrupting the vortex shedding mechanism from the curved and vertical sections, for example uncorrelating the vortex shedding mechanism in a curved region of the cylinder near the horizontal part. Also, the vortex wake along the curved-vertical half of the concave cylinder showed less correlation along the span, resulting in a lower peak of vibration during the synchronisation range.
- (iii) Because the concave configuration has a fixed separation ring at the circle facing upstream, there might be some galloping-like instability related to the separation and reattachment of the three-dimensional bubble. This could generate non-resonant forces that could sustain some level of vibration for reduced velocities above the synchronisation range.
- (iv) Finally, the concave configuration might experience some kind of instability related to the geometric arrangement of the experiment. Because the centre of pressure is located upstream of the vertical axis of the pendulum a minute deflection of the cylinder may result in a resolved force that will increase displacement. The opposite is true for the convex configuration in which the centre of pressure downstream of the vertical axis of the pendulum can only generate stabilising forces.

Of course all four mechanisms suggested above may also be occurring simultaneously or it may not even be possible to explain them separately. In addition, they might as well be very dependent on Reynolds number and amplitude of vibration.

## 7. Conclusions

We have experimentally investigated the two-degree-of-freedom VIV response of a rigid, curved circular cylinder with a low mass-damping ratio. With regard to the approaching flow (Reynolds number is in the range of 750–15 000) both concave and convex configurations were considered and the measured responses were compared with those of a typical straight cylinder. In summary, we conclude that:

- (i) In general terms, a curved cylinder presents a lower peak of amplitude of vibration in both the cross-flow and streamwise direction when compared to a straight cylinder. Nevertheless, a considerable level of streamwise vibration, not attributed to VIV, was observed for reduced velocity as high as 18.

- (ii) Although the peak amplitude is reduced, a curved cylinder may present a significant level of vibration that is sustained for higher values of reduced velocity beyond the end of the typical synchronisation range.
- (iii) The concave configuration shows a considerable level of cross-flow vibration around  $\hat{y}/d = 0.35$  up to the highest reduced velocity performed in this experiment.
- (iv) The overall response showed little dependency on the vertical length immediately below the water line, at least for a section varying between  $h/D = 0$  and 10.
- (v) From the PIV study on a stationary curved cylinder, we suggest that the flow–structure interaction mechanism that differentiates the concave from the convex cylinder response may have its origin in the disturbed flow that separates from the horizontal part located upstream. This could be related to buffeting, galloping, disturbed VIV or geometric instabilities.

Future work should concentrate on correlated PIV analyses of the vortex formation along the curvature as well as on measurements of the flow field on planes perpendicular to the plane of curvature. An investigation of the interference effect generated by the separation at the tip of the horizontal section could also help towards understanding the response. PIV and instantaneous force measurements for an oscillating cylinder, especially at high reduced velocities, could throw some light into the actual mechanism of excitation.

### Acknowledgements

G.R.S. Assi wishes to acknowledge the support of CNPq (308916/2012-3) and FAPESP (11/00205-6). C.M. Freire acknowledges support from FAPESP (10/00053-9). N. Srinil is grateful to the “Sir David Anderson Award” from the University of Strathclyde and the “Early Career Researcher International Exchange Award” supported by The Scottish Funding Council.

### References

- Assi, G.R.S., Meneghini, J.R., Aranha, J.A.P., Bearman, P.W., Casaprima, E., 2006. Experimental investigation of flow-induced vibration interference between two circular cylinders. *Journal of Fluids and Structures* 22, 819–827.
- Assi, G.R.S., Bearman, P.W., Kitney, N., 2009. Low drag solutions for suppressing vortex-induced vibration of circular cylinders. *Journal of Fluids and Structures* 25, 1–10.
- Assi, G.R.S., Bearman, P.W., Meneghini, J.R., 2010a. On the wake-induced vibration of tandem circular cylinders: the vortex interaction excitation mechanism. *Journal of Fluid Mechanics* 661, 365–401.
- Assi, G.R.S., Bearman, P.W., Kitney, N., Tognarelli, M.A., 2010b. Suppression of wake-induced vibration of tandem cylinders with free-to-rotate control plates. *Journal of Fluids and Structures* 26, 1045–1057.
- Bearman, P.W., 1984. Vortex shedding from oscillating bluff bodies. *Annual Review of Fluid Mechanics* 16, 195–222.
- Freire, C.M., Korkischko, I., Meneghini, J.R., 2009. Development of an elastic base with two degrees of freedom for VIV studies. In: *Proceedings of COBEM 2009 – 20th International Congress of Mechanical Engineering*, 2009, Gramado, Brazil.
- Freire, C.M., Meneghini, J.R., 2010. Experimental investigation of VIV on a circular cylinder mounted on an articulated elastic base with two degrees-of-freedom. In: *Proceedings of BBVIV6 – IUTAM Symposium on Bluff Body Wakes and Vortex-Induced Vibrations*, 2010, Capri, Italy.
- Freire, C.M., Korkischko, I., Meneghini, J.R., 2011. Defining a parameter of effectiveness for the suppression of vortex-induced vibration. In: *Proceedings of OMAE2011 – 30th International Conference on Ocean, Offshore and Arctic Engineering*, 2011, Rotterdam, The Netherlands.
- Gallardo, J.P., Pettersen, B., Andersson, H.I., 2011. Dynamics in the turbulent wake of a curved circular cylinder. *Journal of Physics: Conference Series* 318, 062008.
- Miliou, A., De Vecchi, A., Sherwin, S.J., Graham, M.R., 2007. Wake dynamics of external flow past a curved circular cylinder with the free stream aligned with the plane of curvature. *Journal of Fluid Mechanics* 592, 89–115.
- Srinil, N., 2010. Multi-mode interactions in vortex-induced vibrations of flexible curved/straight structures with geometric nonlinearities. *Journal of Fluids and Structures* 26, 1098–1122.
- de Vecchi, A., Sherwin, S.J., Graham, J.M.R., 2008. Wake dynamics of external flow past a curved circular cylinder with the free-stream aligned to the plane of curvature. *Journal of Fluids and Structures* 24, 1262–1270.
- de Vecchi, A., Sherwin, S.J., Graham, J.M.R., 2009. Wake dynamics past a curved body of circular cross-section under forced cross-flow vibration. *Journal of Fluids and Structures* 25, 721–730.
- Williamson, C.H.K., 1996. Vortex dynamics in the cylinder wake. *Annual Review of Fluid Mechanics* 28, 477–539.



# Investigation on the Stability of Parallel and Oblique Plates as Suppressors of Vortex-Induced Vibration of a Circular Cylinder

**Gustavo R. S. Assi<sup>1</sup>**

Assistant Professor  
Department of Naval Architecture  
and Ocean Engineering,  
University of São Paulo,  
São Paulo 05508-030, Brazil  
e-mail: g.assi@usp.br

**Guilherme S. Franco**

Department of Naval Architecture  
and Ocean Engineering,  
University of São Paulo,  
São Paulo 05508-030, Brazil

**Michaelli S. Vestri**

Department of Naval Architecture  
and Ocean Engineering,  
University of São Paulo,  
São Paulo 05508-030, Brazil

*Experiments have been carried out with models of free-to-rotate parallel and oblique plates fitted to a rigid section of circular cylinder to investigate the effect of plate length and oblique angle on the stability of this type of vortex-induced vibration (VIV) suppressor. Measurements of the dynamic response and trajectories of motion are presented for models with low mass and damping which are free to respond in the cross-flow and streamwise directions. It is shown that, depending on a combination of some geometric parameters, the devices might not be able to completely suppress VIV for the whole range of reduced velocities investigated. Plates with larger oblique angles turned to be less stable than parallel plates and induced high-amplitude vibrations for specific reduced velocities. Systems may present streamwise vibration due to strong flow separation and reattachment on the outer surface of plates with large oblique angles. Large angles may also increase drag. Experiments with a plain cylinder in the Reynolds number range from 3000 to 20,000 have been performed to serve as reference. Reduced velocity was varied between 2 and 13. Two-dimensional numerical simulation of static systems at  $Re = 10,000$  revealed that complex and fully separated flow regimes exist for almost all investigated cases. There is a good chance that systems with such geometric characteristics will be unstable unless other structural parameters are positively verified. [DOI: 10.1115/1.4027789]*

**Keywords:** VIV suppression, stability, free-to-rotate suppressors, parallel and oblique plates

## 1 Introduction

This paper reports on new fundamental studies regarding a pair of free-to-rotate plates acting as suppressors for the VIV of a circular cylinder. The development of new suppressors of flow-induced vibration (FIV) of offshore structures is a topic that became frequent in the literature in the past years. As previously discussed in Refs. [1–3], with the advancement of offshore oil exploration, research on FIV suppressors was pushed to a new level. “The industry demands suppressors that are not only efficient for low mass-damping systems but also that could be installed under harsh environmental conditions; such is the case for offshore risers” [3].

The present work contributes to the understanding of the dynamic stability and hydrodynamic phenomena behind a type of free-to-rotate device made of a pair of rigid plates attached to a cylinder. Suppressors employing parallel plates are already available as viable commercial solutions [4,5] for offshore drilling risers. Drilling risers are not in operation for as long as production risers; therefore, fatigue damage is not as important a concern as the loads caused by strong currents. Therefore, besides suppressing FIV, suppressors must contribute to reduce drag, consequently reducing pipe bend during drilling operation. A real drilling riser in the field is not a rigid structure, but responds the flow excitation in several modes of vibration with different frequencies. Testing free-to-rotate devices on a rigid section of a finite cylinder, as is the case in this fundamental investigation, elucidates the local fluid–structure interaction associated with the suppression

mechanism occurring in different sections along the riser, but is limited to capture the complex three-dimensional phenomena along the pipe. Small variations in the angle between the plates may affect the flow behavior around the suppressor, enhancing efficiency in suppression and potentially drag reduction. However, an opposite effect may also occur and plates with oblique angles may produce hydrodynamically unstable systems. The present study sets out to investigate these possibilities.

It is known that free-to-rotate suppressors may experience hydrodynamic instabilities that will not only cause a substantial increase in drag but also prevent it from suppressing vibrations [1]. Actually, an unstable free-to-rotate suppressor may induce the structure into more vigorous vibrations excited by a type of flutter mechanism. Assi et al. [1,3] have shown that the instability of free-to-rotate suppressors is directly related to the level of rotational resistance encountered in the system as well as geometric parameters such as plate length. They performed experiments in laboratory scale and showed that a free-to-rotate suppressor formed by a single splitter plate may need a minimum rotational resistance (or be above a critical rotational friction) to enable a stable configuration with effective suppression. The same was verified for free-to-rotate suppressors composed of two parallel plates [6], revealing that a minimum rotational resistance is necessary to stabilize the devices.

Assi et al. [1,2] have already shown that 1D-long parallel plates can be very efficient in suppressing both VIV and wake-induced vibration (WIV). WIV occurs when the downstream body of a set is excited by the unsteady wake generated from another body placed upstream [7,8]. In the present work, we set out to investigate if free-to-rotate oblique plates are able to find stable configurations and suppress VIV for various plate lengths and oblique angles. The installation of free-to-rotate suppressors on offshore risers requires fitting bearings or sliding components around the

<sup>1</sup>Corresponding author.

Contributed by the Ocean, Offshore, and Arctic Engineering Division of ASME for publication in the JOURNAL OF OFFSHORE MECHANICS AND ARCTIC ENGINEERING. Manuscript received September 26, 2013; final manuscript received May 23, 2014; published online June 19, 2014. Assoc. Editor: Antonio C. Fernandes.

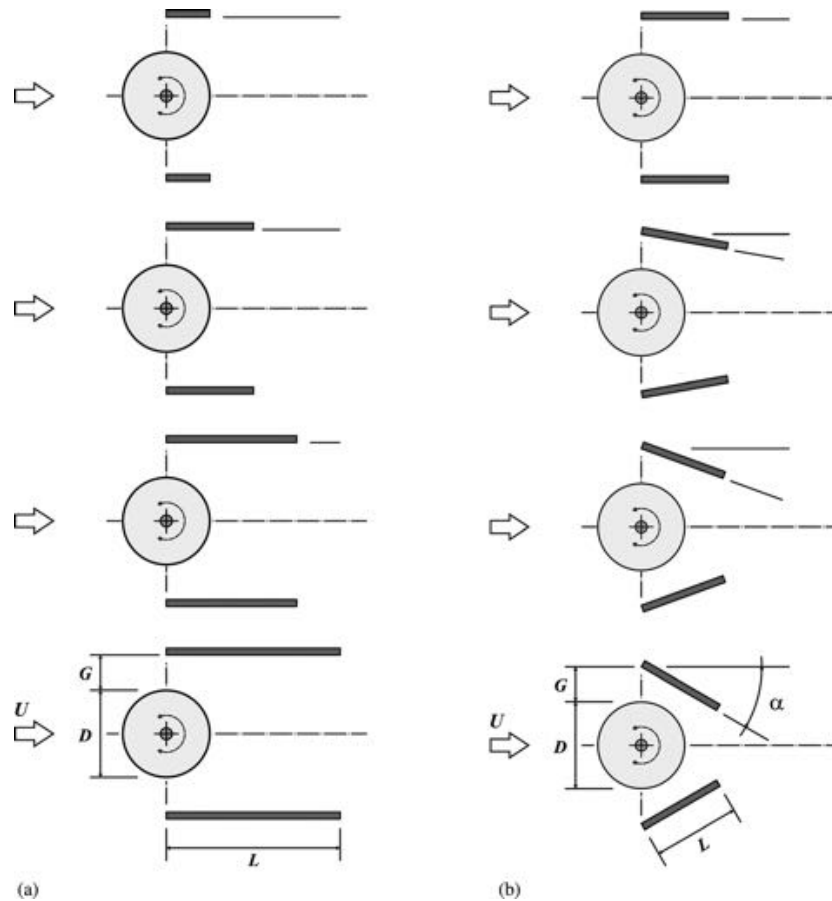


**Fig. 1 (a) First experiment: Free-to-rotate parallel plates. Fixed  $G/D = 0.4$  and  $\alpha = 0$  deg, varying  $L/D = 0.5, 1.0, 1.5$ , and  $2.0$  from top to bottom. (b) Second experiment: Free-to-rotate oblique plates. Fixed  $G/D = 0.4$  and  $L/D = 1.0$ , varying  $\alpha = 0$  deg,  $10$  deg,  $20$  deg, and  $30$  deg from top to bottom.**

pipe that may be vulnerable to fatigue or deteriorate due to the marine environment. The present study is limited to a fundamental investigation of a concept as far as the stability of the system is concerned; hence, it will not discuss the devices in a deeper technological level.

## 2 Parallel and Oblique Plates

Variations on the concept of double plates, some inspired by the early work of Grimminger [9] related to suppressing VIV of submarine periscopes, were the inspiration for previous works that employed a similar apparatus [1–3,6,10,11]. In Grimminger's experiments, the plates were fixed since the direction of the flow around a submarine is known, but in the investigations mentioned above the plates were free to rotate according to the flow orientation.

Based on the previous investigations [1], we believe that parallel plates and splitter plates are able to suppress VIV based on the same fluid-dynamic mechanism. Free-to-rotate parallel plates are not a "fairing" in the strict sense of the term, i.e., they do not make the cylinder a streamlined body. For this to occur, the length of the fairing would have to be many times the diameter of the cylinder (as shown in Refs. [12–14]). In essence, parallel plates act in the near wake with fully separated flow, avoiding the interaction between the shear layers and delaying vortex formation and shedding, hence the same mechanism as splitter plates and short-tail (or teardrop) fairings [1,3].

In a previous work [6], we have investigated if free-to-rotate parallel plates would be able to find stable configurations and suppress VIV for various plate lengths. In that configuration, the

leading edge of the plate was practically touching the cylinder wall, creating a chamber of almost stagnant flow downstream of the cylinder and in between the plates. That configuration did not allow any flow to "ventilate" the near wake. The longer the plates, the larger would become the region of stagnant flow. In the present study, we want to investigate if a small vent in the form of a gap between the plates and the cylinder would possibly allow high-speed flow to feed momentum into the near wake, creating a more streamlined body by disrupting the interaction between the shear layers that generate vortices.

We chose to vary three geometric parameters to characterize the suppressors, as seen in Figs. 1(a) and 1(b): Plate length normalized by the diameter,  $L/D$ ; plate angle,  $\alpha$ , that defines the oblique configurations ( $\alpha = 0$  deg means parallel plates); and the normalized gap,  $G/D$ , measured between the leading edge of the plate and the cylinder wall. Both plates are installed so that their leading edge is aligned with the center of the cylinder. Plates cannot move in relation to each other, but the pair is free to rotate about the center of the cylinder. Plate thickness  $t/D = 0.06$  was kept constant in the present study, even though it was thought to be a relevant parameter for investigation.

It is intuitive to think that if we held  $L/D$  fixed, only varying the other two geometrical parameters, we could already produce several different flow patterns.  $G/D$  is directly related to the flow intake into the near wake, especially related to the flow behavior in the boundary layers. Increasing  $\alpha$  directs momentum inward (toward the centerline), but it is also directly related to strong flow separation that may occur on the outer surface of the plates. Minor variations in both  $G$  and  $\alpha$  would be enough to modify the flow behavior. Actually, it is not difficult to imagine that an optimum



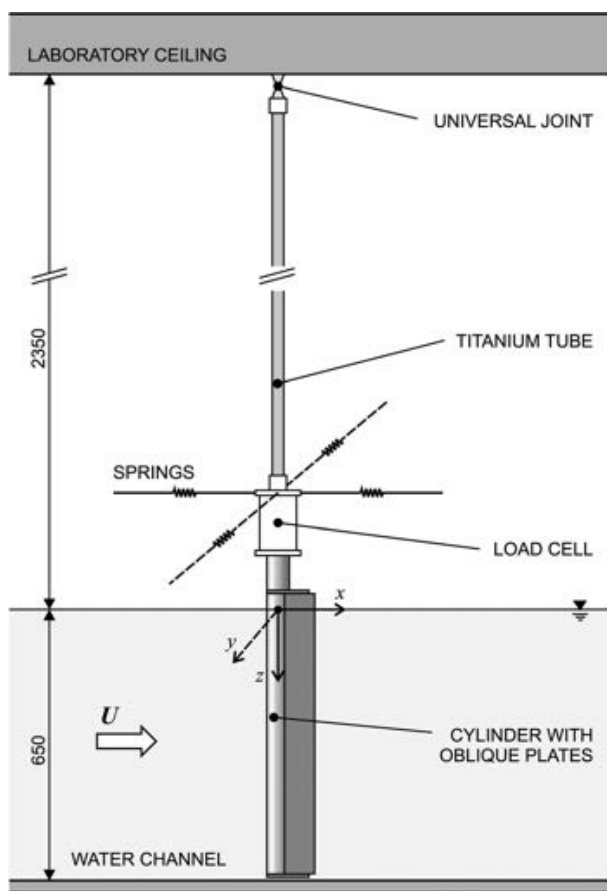


**Fig. 2 Experimental setup: cylinder with parallel plates mounted on the two-degrees of freedom rig in the test section of the NDF-USP water channel**

solution to minimize vibration and reduce drag would have a small gap and a minute oblique angle with almost no separation.

The present investigation is not intended as a study of optimization, but it aims on the understanding of the overall behavior of the system for larger variations of  $G/D$ ,  $L/D$ , and  $\alpha$ , much larger than the intuitive geometries. At the moment, we are more concerned with the overall stability of the system rather than with optimum proportions. Therefore, our parameters will vary in large steps as follows:  $L/D = 0.5, 1.0, 1.5, 2.0$  and  $\alpha = 0$  deg, 10 deg, 20 deg, 30 deg with  $G/D = 0.4$  kept constant. Overall, our broader study results from 80 different tested configurations. This paper will focus on the eight most interesting cases, not necessarily the ones that produced effective suppression and drag reduction, but especially on those that showed surprising results. The study was divided into two experiments. In the first experiment, with parallel plates shown in Fig. 1(a),  $G/D = 0.4$  and  $\alpha = 0$  deg were kept constant while  $L/D$  was varied in four steps. In the second experiment, with oblique plates shown in Fig. 1(b),  $G/D = 0.4$  and  $L/D = 1.0$  were kept constant while  $\alpha$  was varied in four steps. Varying one parameter at a time was thought to help the parametric analysis that will follow.

### 3 Experimental Arrangement

Experiments have been carried out in the circulating water channel of NDF Fluids and Dynamics Research Group at the University of São Paulo, Brazil. The NDF-USP water channel has an open test section which is 0.7 m wide, 0.9 m deep, and 7.5 m long. Good quality flow can be achieved up to 1.0 m/s with turbulence intensity less than 3%. This laboratory has been especially

**Table 1 Structural properties**

|                      | $m^*$ | $\zeta$ (%) | $m^*\zeta$ |
|----------------------|-------|-------------|------------|
| Plain cylinder       | 1.90  | 0.2         | 0.0038     |
| Cylinder with plates |       |             |            |
| $L/D = 0.5$          | 2.10  | 0.2         | 0.0042     |
| $L/D = 1.0$          | 2.17  | 0.2         | 0.0043     |
| $L/D = 1.5$          | 2.24  | 0.2         | 0.0045     |
| $L/D = 2.0$          | 2.30  | 0.2         | 0.0046     |

designed for experiments in FIV; further details about the facilities are described in Ref. [15].

A rigid section of circular cylinder with an external diameter of  $D = 50$  mm was made of a perspex tube (please refer to Figs. 1 and 2 for details). Four pairs of rigid perspex plates were manufactured varying in length in four steps of  $L/D = 0.5, 1.0, 1.5$ , and 2.0. The plates were mounted on ball bearings at the extremity of the cylinder and could not move in relation to each other, i.e., the angle between the plates was kept constant at all times. The leading edge was kept at the same vertical alignment as the center of the cylinder so that plates were oriented at the  $\pm 90$  deg points in relation to the incoming flow. The oblique angle of the plates  $\alpha$  in Fig. 1(b) (defined as the actual angle of attack for each flat plate) was adjusted in four steps of  $\alpha = 0$  deg, 10 deg, 20 deg, and 30 deg. As a result, the pair of parallel or oblique plates would freely rotate as one body around the center of the cylinder. The gap between the leading edge of the plates and the cylinder wall was kept constant at  $G/D = 0.4$ . As far as the boundary layer thickness is concerned, this is considered to be a large gap relative to the cylinder diameter, at least large enough for the plate not to interact with the laminar boundary layers around the natural separation points. A schematic representation of all the considered geometries is presented in Fig. 1. Rotational friction was not measured in this study, instead it was simply verified if the actual level of rotational friction in the bearings was high enough to stabilize the 1D-long plates around the expected peak of response for VIV.

Models were mounted on a low-damping rig that allowed the cylinder to freely respond in both cross-flow and streamwise directions, as seen in Fig. 2. The cylinder model was mounted at the lower end of a long titanium tube forming the arm of a rigid pendulum connected to a universal joint fixed at the ceiling of the laboratory. The water channel was filled up to 650 mm, resulting in a submerged length to diameter ratio of 13. The design and construction of the pendular elastic rig were made by Freire and Meneghini [16] based on a previous idea employed by Assi et al. [1,2] for experiments with VIV suppressors. Two independent optical sensors were employed to measure displacements in the  $x$  and  $y$  directions at the midlength of the model. It should be noted that for a displacement equal to one diameter the inclination angle of the cylinder was only just over 1 deg from the vertical. Two pairs of springs were installed in the  $x$  and  $y$  axes to set the natural frequencies in both directions of motion. The springs were chosen to provide the same natural frequency ( $f_0$ ) measured in air in both the cross-flow and streamwise directions.

Decay tests have been performed in air in order to determine the natural frequencies of the system in both direction as well as the level of structural damping. The apparatus with one universal joint and four springs turned out to present a very low structural damping of  $\zeta = 0.20\%$ , measured as a fraction of the critical damping. The total oscillating mass of the system was measured in air, resulting in a nondimensional mass parameter of  $m^* \approx 2.0$ , defined as the ratio between the total mass and the mass of displaced fluid. Consequently, the mass-damping parameter  $m^*\zeta$  of the system was kept to the lowest possible value in order to amplify the amplitude of response. Preliminary tests have been performed with a plain cylinder to serve as reference for comparison. Table 1 summarizes the structural parameter for both the plain cylinder and the cylinders fitted with plates of various

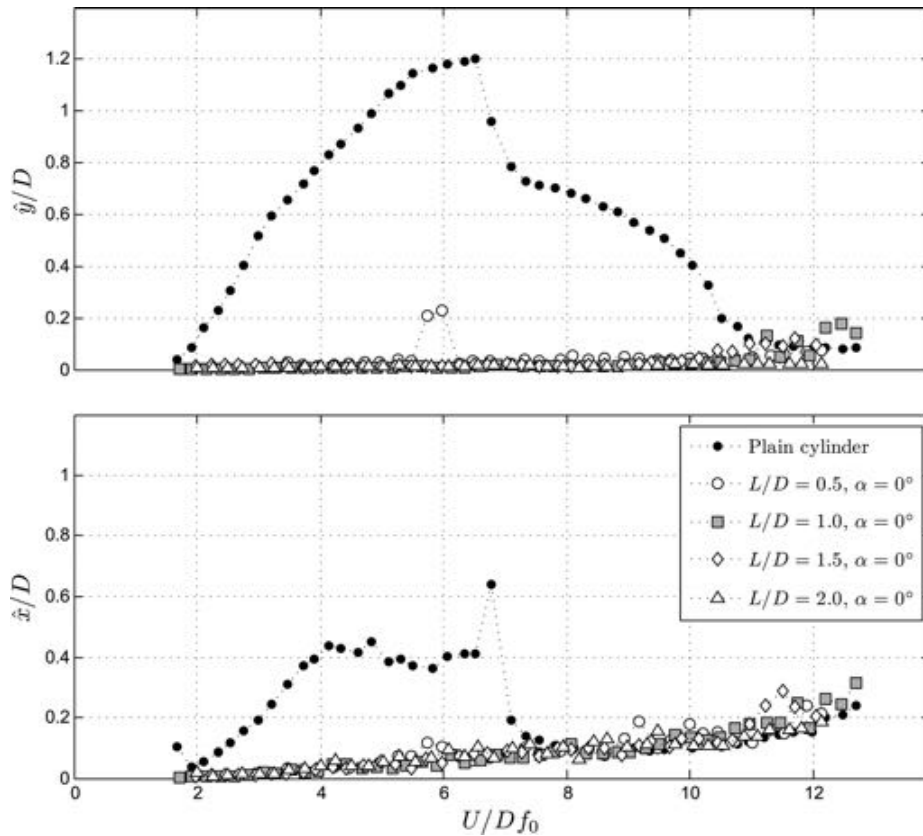


**Fig. 3 First experiment: cross-flow ( $\hat{y}/D$ ) and streamwise ( $\hat{x}/D$ ) amplitude of vibration versus reduced velocity for a plain cylinder compared to cylinders fitted with parallel plates of various lengths**

lengths. Notice that  $m^*$  varies slightly from model to model due to the mass variation of the installed plates.

Measurements were made using a fixed set of springs and the reduced velocity range covered was up to 13, where reduced velocity,  $U/Df_0$ , is defined using the cylinder natural frequency of oscillation in the cross-flow direction measured in air. The only flow variable changed during the course of the experiments was the flow velocity,  $U$ , which alters both the reduced velocity and the Reynolds number between 3000 and 20,000. Throughout the present study, cylinder displacement amplitudes nondimensionalized by the plain cylinder diameter ( $\hat{x}/D$  for streamwise and  $\hat{y}/D$  for cross-flow directions) were found by measuring the root mean square value of response and multiplying by the square root of 2 (the so called equivalent harmonic amplitude). This is likely to give an underestimation of maximum response but was judged to be perfectly acceptable for assessing the effectiveness of VIV suppression devices.

#### 4 Preliminary Results for a Plain Cylinder

A preliminary VIV experiment was performed with a plain cylinder in order to validate the setup and methodology. The same pendulum rig was employed, only replacing the model with parallel plates by a plain cylinder with the same diameter. Figures 3 and 4 will compare the reference cross-flow and streamwise responses obtained for the plain cylinder with those obtained for each suppression device. As far as the plain cylinder is concerned, the observed peak amplitude of  $\hat{y}/D = 1.2$  between  $U/Df_0 = 6.0$  and 7.0 is in good agreement with other results presented in the literature [1,17]. The general behavior of the cross-flow response confirms the typical response for the two-degrees of freedom VIV of a system with the same natural frequency in both directions.

The recorded streamwise response presented a peculiar feature. Around reduced velocity of 7.0, corresponding to the transition from the upper to the lower branch in the cross-flow response, we observed high-amplitude vibration above  $\hat{x}/D = 0.6$ . At first sight, one might conclude that such a distinct peak could be related to a local resonance between the streamwise excitation and a higher harmonic in that direction. However, this idea was discarded once the time series for the displacement signal was analyzed. In fact, it occurred that the cylinder experienced an unstable transition from the upper to the lower mode in the cross-flow oscillations, jumping back and forth from one mode to the other. This alternation between two different levels of amplitude had an effect on the streamwise response due to fluctuations on the mean drag induced by the cross-flow vibrations. As a result, the response appeared as if the cylinders were oscillating with  $\hat{x}/D > 0.6$  around a mean position, but in fact it was alternating between two branches of vibration as long as the transition was not completed.

Although the cylinder was initially aligned in the vertical position, in flowing water, the mean drag displaces the cylinder from its original location reaching a slightly inclined configuration from the vertical. This was judged not to be detrimental to the experiment, hence the inclination of the cylinder was not corrected between each step of increasing flow speed. The same procedure was adopted for the cylinders fitted with plates.

#### 5 Results for Cylinders With Plates

Figures 3 and 4 also present two sets of data with cross-flow and streamwise response curves for the suppressors tested in the first and second experiments, respectively. We shall start discussing results from the first experiment.

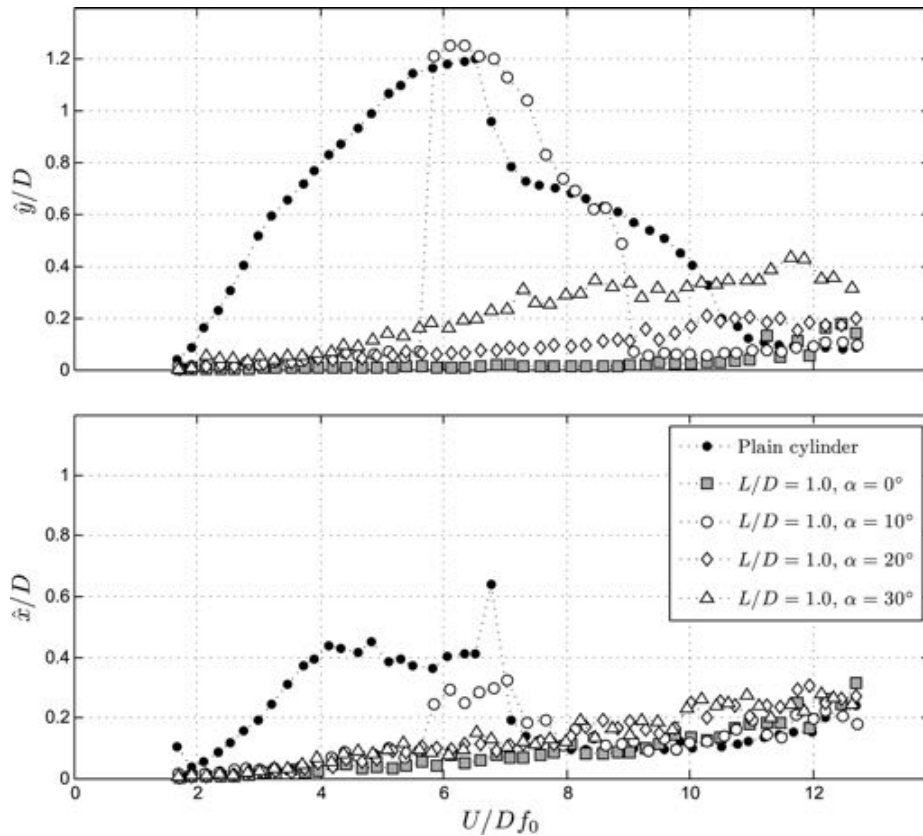


**Fig. 4 Second experiment: cross-flow ( $\hat{y}/D$ ) and streamwise ( $\hat{x}/D$ ) amplitude of vibration versus reduced velocity for a plain cylinder compared to cylinders fitted with oblique plates of various angles**

**5.1 First Experiment: Varying  $L/D$ .** The first experiment presents only parallel plates varying in length. These configurations differ from those of Assi et al. [6] in the existence of a lateral gap of  $G/D = 0.4$  between the cylinder and the plate; nevertheless, the overall behavior of the free-to-rotate devices is very similar in both studies. The general behavior of all free-to-rotate parallel plates shows a remarkable reduction in vibration in both directions for most of the reduced velocity range investigated (Fig. 3). Given the minimum level of rotational friction provided by the bearings, all parallel plates were found to be reasonably stable for the whole range of reduced velocities.

Except for two data points for the shorter plates of  $L/D = 0.5$  around reduced velocity of 6.0, most plates were able to practically mitigate vibrations below  $\hat{y}/D = 0.2$  for the whole range of reduced velocities, even during the cross-flow and streamwise resonances. This localized amplification of the response around  $U/Df_0 = 6.0$  is attributed to a minor resonance of the vortex-shedding mechanism altered by the presence of the short plates. For reduced velocities greater than ten, random vibration associated with turbulence buffeting appeared for all suppressors as well as for the plain cylinder, reaching  $\hat{y}/D \approx 0.1$ . The increase of amplitude is even more pronounced for the streamwise motion, monotonically building up from reduced velocity of 8.0 and reaching  $\hat{x}/D \approx 0.3$  for the maximum flow speed. A qualitative analysis of trajectory plots (Fig. 6) reveals a nonperiodic motion, supporting the buffeting hypothesis. We shall return to this point when discussing the trajectories in Sec. 6.

Based on the first experiment, we cannot tell which plate length presented the most efficient suppression. We cannot affirm that all plates are perfectly stable either, since we have observed some distinct vibration for  $L/D = 0.5$ . One can only infer that shorter plates around  $L/D = 0.5$  may be more prone to instability than the others. There is a possibility that other plates may present

unstable regimes as well, especially if plate length is increased beyond  $L/D = 2.0$ . Results obtained for the 1D-long parallel plates are in good agreement with the previous experiments reported by Assi et al. [1,10,11]. Although their parallel plates had a slightly different geometry than the ones tested in this experiment, the general behavior agrees quite well.

Assi et al. [6] showed that parallel plates with no gap ( $G/D = 0.0$ ) were able to suppress VIV because they inhibited the interaction between the free shear layers, delaying vortex formation and consequent excitation. For a geometry with  $G/D = 0.0$ , the boundary layers do not separate, but the shear layers flow alongside the outer surface of the plates. Now, in the present study with a large gap of  $G/D = 0.4$ , the flow separates around the cylinder and the free shear layers flow downstream along the inner side of the parallel plates. Hence, there is no obstruction to the interaction of the shear layers and, in principle, the vortex-shedding mechanism occurs confined in between the plates. Even with vortices being shed in between the plates, VIV is still suppressed by parallel plates with  $G/D = 0.4$ .

**5.2 Second Experiment: Varying  $\alpha$ .** The second experiment presents 1D-long plates varying only the oblique angle  $\alpha$ . These are new results for which we found no references in the literature to be compared with. Case  $L/D = 1.0$  and  $\alpha = 0$  deg (marked with gray squares in Figs. 3 and 4) is repeated in both experiments. Differently from the first experiment, variation in  $\alpha$  showed an interesting effect over the response, especially in the cross-flow displacement of the cylinder. As seen,  $\alpha = 0$  deg suppressed vibration below  $\hat{y}/D = 0.1$  for most of the velocity range tested. Now, as  $\alpha$  is increased in steps of 10 deg the cross-flow response curves reach higher levels of monotonically increasing amplitude.

The only exception was found for the case for  $\alpha = 10$  deg in which the system presented resonant behavior for reduced

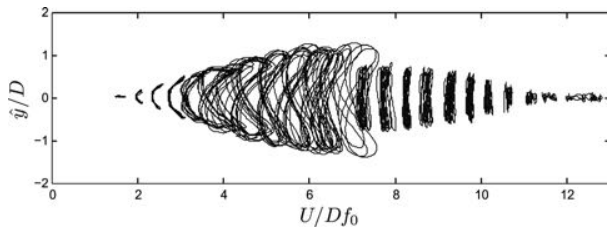


Fig. 5 Reference experiment: trajectories of motion for a plain cylinder

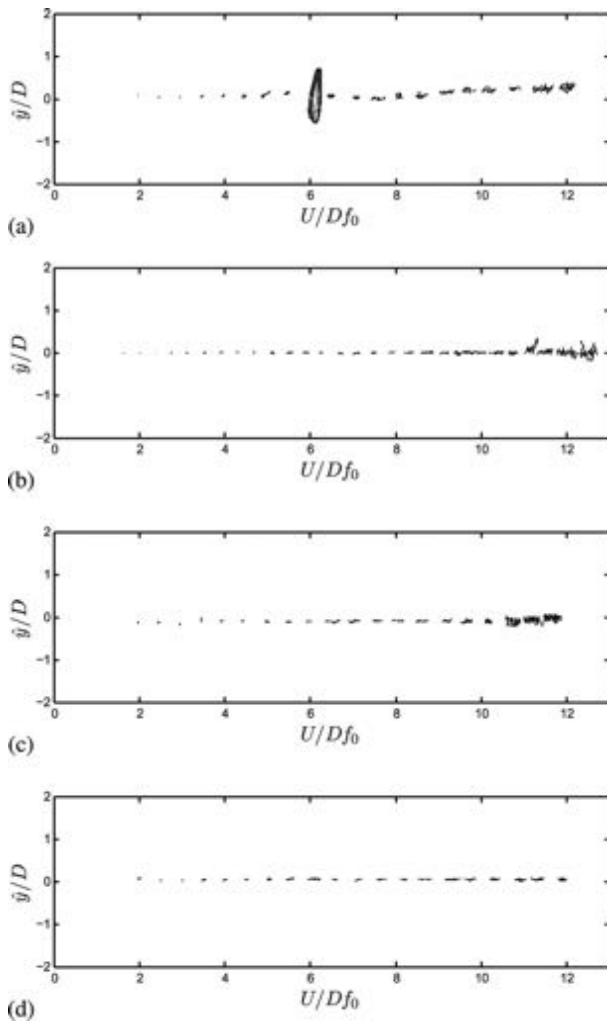


Fig. 6 First experiment: trajectories of motion for a cylinder fitted with parallel plates of different lengths

velocities between 6.0 and 9.0. During this interval, the amplitude of response practically followed the response curve obtained for a plain cylinder reaching almost  $\hat{y}/D = 1.3$  for reduced velocity of 6.0. At the same time, streamwise vibration was also increased to  $\hat{x}/D \approx 0.3$  for a shorter resonant range between reduced velocities of 6.0 and 7.0. Periodic motion registered in the trajectory plot of Fig. 7(b) supports the hypothesis of resonant vibration within a limited range of reduced velocity. Apart from that, all other cases showed vibration that is associated with turbulence buffeting rather than a resonant phenomenon such as VIV. Of course, other excitation mechanisms may also be occurring for highly oblique

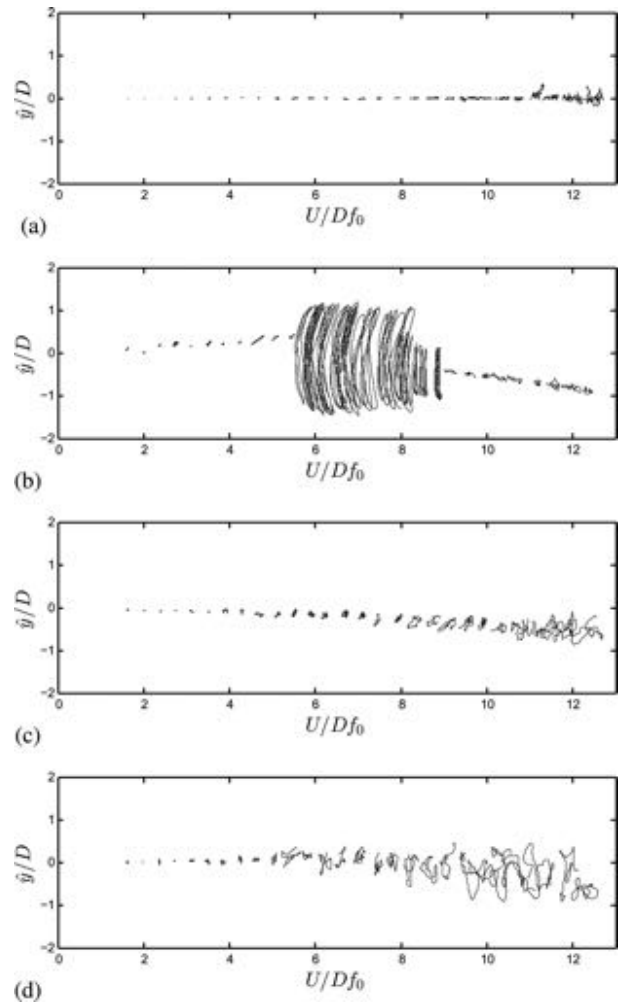


Fig. 7 Second experiment: trajectories of motion for a cylinder fitted with oblique plates of different angles

plates. It is not difficult to imagine that large values of  $\alpha$  generate strong separated flow around the plates and the cylinder. The interaction between unstable reattachment bubbles and small-scale vortices may be driving the cylinder into vibrations of a different nature. Minute variations of  $\alpha$  may drastically alter the flow behavior in the region in between the plates. It is interesting to know if there is a value of  $\alpha$  (as well as the other geometric parameters) to permit maximum “ventilation” of the near wake with minimum flow separation around the plates and consequent VIV suppression with drag reduction.

## 6 Trajectories of Motion

Trajectory figures are a simple and qualitative manner to analyze the responses presented in Figs. 3 and 4. Samples of displacement trajectories obtained for the plain cylinder (Fig. 5) are compared with those for the suppressors for the first and second experiments (Figs. 6 and 7). The same scale was kept in all figures to allow for direct comparison between them and a few trajectory lines have been suppressed for clarity. The plain cylinder response in Fig. 5 presents characteristic figures typical of VIV in two degrees of freedom. A C-shaped trajectory, at the initial branch, progressively changes into an eight-shaped trajectory up to the peak amplitude at the upper branch. When the response changes from the upper to the lower branch, after reduced velocity of 6.0, the trajectories immediately take a flatter shape with reduced displacement in the streamwise direction.



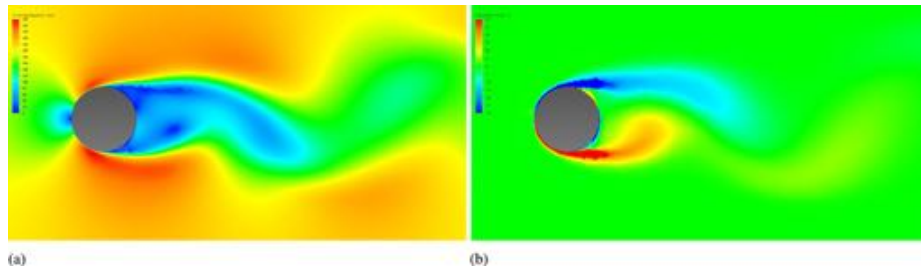


Fig. 8 Reference simulation: wake of a plain cylinder

Trajectories for the suppressors investigated in both experiments are very different from those of the plain cylinder in Fig. 5. In general terms, the cylinders fitted with free-to-rotate plates present small movement around a mean position for most of the reduced velocity range, except for a few points as seen in Figs. 6(a) and 7(b). A distinct behavior was observed for a parallel plate with  $L/D = 0.5$  around reduced velocity 6.0, as seen in Fig. 6(a) and registered in Fig. 3. Sometimes, the plates were unable to stabilize for a range of reduced velocities and periodic vibrations were registered for a few cycles, as illustrated in Fig. 4 for  $L/D = 1.0$ ,  $\alpha = 10^\circ$  and reduced velocity between 6.0 and 9.0. Such vibrations are normally associated with resonant mechanisms, such as VIV, but they can also be an effect of a flutter type of excitation due to the rotational movement of the plate.

Almost all trajectory plots of Figs. 6 and 7 show random vibrations for the higher reduced velocities. Figure 7(d) particularly shows nonperiodic vibrations for most of flow speeds. In addition, Figs. 7(b)–7(d) clearly show that the cylinder drifted to one side as the flow speed was increased. Oblique plates, especially those with high angles, tend to be more difficult to align with the flow, thus stabilizing at a small deflected position from the centerline. As a consequence, a steady lift force drives the cylinder toward the side the plate has deflected. Assi et al. [1,3] showed that such a drift is due to occur for a single splitter plate that finds a deflected but stable position to one of the sides while suppressing VIV. Assi et al. [6] showed a similar behavior for parallel plates longer than  $L/D = 1.0$ . Now, a similar behavior has been observed for oblique plates.

## 7 Numerical Simulations of the Flow

In order to gain insight into the flow around the cylinder and devices, numerical simulations have been performed for the four geometries of oblique plates investigated in the second experiment. Keeping  $G/D = 0.4$  and  $L/D = 1.0$  fixed,  $\alpha$  was varied in the four steps studied above. Such numerical simulations are presented here to illustrate and contribute to our understanding of the flow characteristics around the devices. It is evident that the main body of work presented in this paper is concerned with the experimental results obtained for free-to-rotate systems. In the numerical study, the cylinder and the plates are all static, i.e., they cannot move in relation to one another nor can the system respond with FIV. Nevertheless, we believe that even a qualitative analysis of the flow around a static system is able to elucidate some interesting points.

The commercial code AUTODESK SIMULATION Computational Fluid Dynamics (CFD) was employed in the study. Each two-dimensional mesh was composed of around 8000 elements with particular care taken into refining the mesh around the walls and in the gap between the cylinder and the plates. The unsteady Reynolds-Averaged Navier–Stokes equations were solved for an incompressible flow employing a segregated upwind, finite element method. The two-dimensional domain extended for  $5D$  upstream,  $15D$  downstream, and  $5D$  to each side of the cylinder. Reynolds number was set to 10,000 and the k- $\omega$  shear-stress transport (SST) turbulence model was employed. Each simulation

was performed for at least 100 cycles of vortex shedding after a steady wake regime had been reached.

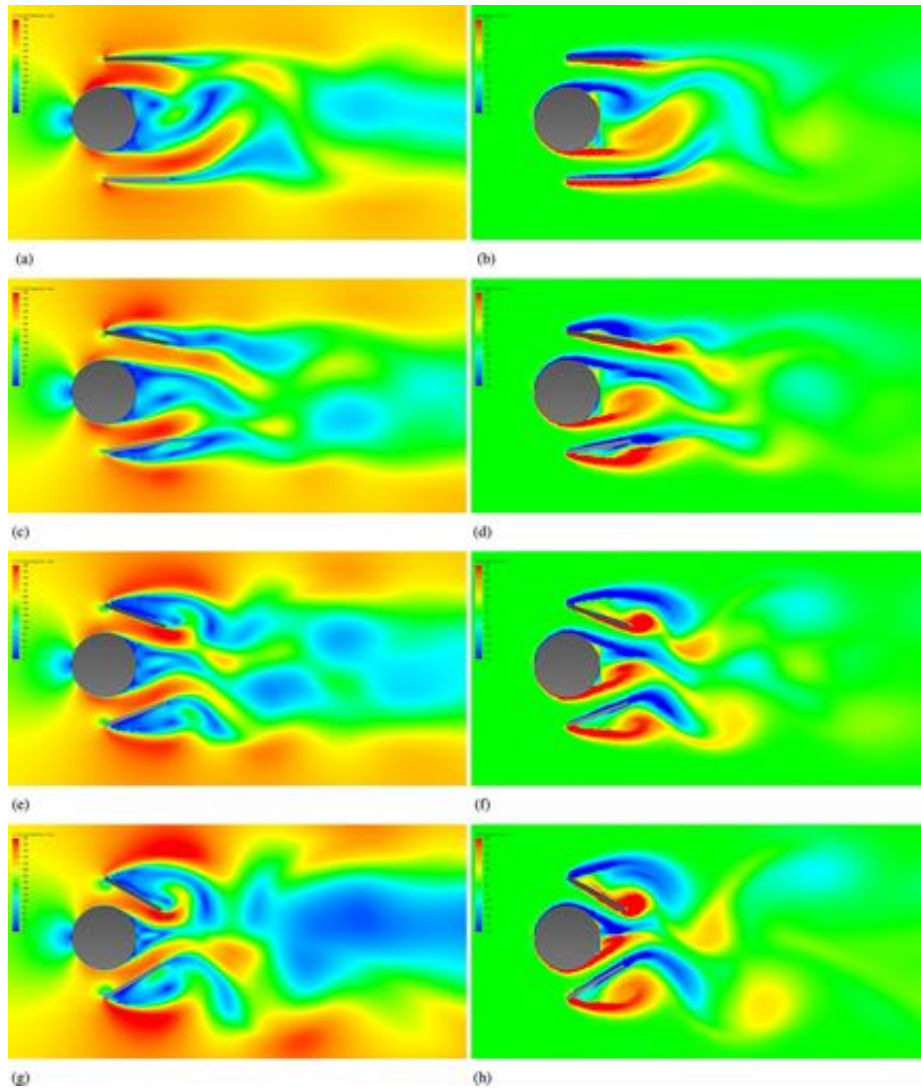
The results discussed below focus on the vortex formation region and the near wake in order to observe flow structures around the plates and in the gap between plates and cylinder. Velocity and vorticity fields are both presented side by side for the same instant in time for each configuration. The flow around a single cylinder without plates has been computed as a reference and is presented in Fig. 8. As expected, a classic von Karman wake was obtained. The color scales for velocity magnitude and vorticity is the same in all figures to allow for direct comparison of the wakes.

Figure 9 presents the results for the cylinders fitted with plates. In Figs. 9(a) and 9(b), we observe that the two parallel plates spaced from the cylinder barely interfere with the vortex formation mechanism. A typical vortex wake is formed and confined between them, but only farther downstream the vorticity generated on the plates will interact with the vortices shed from the cylinder. The result is a rather typical vortex street with minor interference from the external vorticity from the plates. Nevertheless, even this minor effect might be responsible for the suppression achieved by this geometry through the whole range of reduced velocities, as observed in the experimental results in Fig. 7(a).

Once the oblique angles are changed, the flow around the cylinder and plates changes drastically. Figures 9(c) and 9(d) show that even the smallest angle of attack of  $\alpha = 10^\circ$  already causes considerable separation of the flow on the outer surface of the plates. One may argue that  $\alpha = 10^\circ$  is not a small angle of attack and one should not expect anything different from the separated flow around a flat plate; we agree with that. The vortex formation region is confined between the plates and forced toward the centerline by the high-speed flow coming through the gap. Vortices are shed with higher frequency in this narrower wake and then combined with other small vortices shed from the plates. The result is a periodic wake with a frequency signature different from the typical Strouhal number of a plain cylinder. Experimental results in Fig. 7(b) have shown that this configuration can become very unstable and induce severe vibrations to the level of the VIV response of a plain cylinder.

For  $\alpha = 20^\circ$ , shown in Figs. 9(e) and 9(f), the high-speed flow ventilated through the gaps forces a much narrower wake behind the cylinder, with the contribution of the two plates closing the gap as the vortices are shed downstream. The overall wake is now dominated by the two large vortex systems shed from each of the oblique plates. They interfere further downstream merging with the small vortices formed behind the cylinder near the centerline.

The final configuration with  $\alpha = 30^\circ$ , presented in Figs. 9(g) and 9(h), shows that the flow behavior has changed completely from a wake dominated by vortices shed from the cylinder to a wake dominated by vortices shed from the plates. While for  $\alpha = 10^\circ$  and  $20^\circ$ , we could say that vortices from the cylinder and from the plates had roughly the same scale and intensity, we observe now for  $\alpha = 30^\circ$  that the wake is completely dominated by vortices shed from the plates. The vortex formation region behind the cylinder is practically nonexistent and only a symmetrical bubble is observed to survive between the jets from



**Fig. 9 Wake of a cylinder with oblique plates: fixed  $G/D = 0.4$  and  $L/D = 1.0$ , varying  $\alpha = 0$  deg, 10 deg, 20 deg, and 30 deg from top to bottom**

the gaps through the confinement of the plates. The overall wake is a result of the interference of the wakes of mainly two bluff bodies, i.e., the plates.

Of course numerical simulations of this sort are very limited in modeling the fluid–structure interaction occurring in the free-to-rotate experiments. But it becomes clear that systems with so many regions of separated flow, with severe wake interactions and gaps with accelerated flow in the form of jets have all the ingredients to produce unstable dynamics. In fact, we can conclude that suppressors with such geometric characteristics will rarely help to streamline the flow around a cylinder; on the contrary, the system will behave as a distinct bluff body with several separation regions and wake interferences. Stability becomes very difficult to achieve with such configurations and will require other structural parameters such as damping and inertia to be precisely adjusted.

## 8 Conclusions

Although being a fundamental study in laboratory scale, the present investigation throws some light in the technological development of new geometries for VIV suppressors. Results showed that free-to-rotate parallel and oblique plates with  $G/D = 0.4$  may present hydrodynamically unstable behavior depending on  $L/D$  and  $\alpha$ . Nevertheless, most of the tested configurations were able to

suppress vibrations down to  $\hat{y}/D \approx 0.2$  and  $\hat{x}/D \approx 0.2$  for most of the reduced velocity range, given the level of rotational friction of the system. In summary, we conclude that:

- (i) The gap between plates and cylinder is thought to act as a vent, directing the flow toward the near wake and injecting momentum into the vortex formation region. However, large gaps, such as the one studied in the present paper, may cause the plate to act as a strong lifting surface detached from the cylinder.
- (ii) Systems may present streamwise vibration due to strong flow separation and reattachment on the outer surface of the plates, particularly for larger oblique angles. Consequently, large values of  $\alpha$  also increase drag.
- (iii) An undesirable lateral force appeared to act on the system for plates with high oblique angles causing the cylinder to drift to one side. This is being caused by a small deflection of the plates (although such a deflection angle was too small to be noticeable or measured in the present work) or nonsymmetric flow separation around the cylinder.
- (iv) Numerical simulation of the flow around static systems revealed that complex and fully separated flow regimes exist for almost all investigated cases. The wake of the cylinder is severely affected by the wakes generated on the plates and the wake of a distinct bluff body is what



remains farther downstream. Systems with such flow characteristics will have a tendency to become unstable unless other structural parameters are adequately adjusted.

### Acknowledgment

The authors wish to acknowledge the support of FAPESP São Paulo Research Foundation (No. 2011/00205-6). G.R.S.A. is thankful to CNPq (No. 308916/2012-3). G.S.F. is in receipt of a undergraduate research grant from ANP Agência Nacional do Petróleo, Gás Natural e Biocombustíveis (PRH-19).

### Nomenclature

$D$  = cylinder external diameter  
 $f_0$  = natural frequency in air  
 $G$  = gap between plate edge and cylinder wall  
 $L$  = plate length  
 $m^*$  = mass ratio  
 $Re$  = Reynolds number  
 $U$  = flow speed  
 $U/Df_0$  = reduced velocity  
 $\hat{x}$  = streamwise harmonic amplitude of vibration  
 $\hat{y}$  = cross-flow harmonic amplitude of vibration  
 $\alpha$  = plate oblique angle  
 $\zeta$  = structural damping ratio

### References

- [1] Assi, G. R. S., Bearman, P. W., and Kitney, N., 2009, "Low Drag Solutions for Suppressing Vortex-Induced Vibration of Circular Cylinders," *J. Fluids Struct.*, **25**, pp. 666–675.
- [2] Assi, G. R. S., Bearman, P. W., Kitney, N., and Tognarelli, M., 2010, "Suppression of Wake-Induced Vibration of Tandem Cylinders With Free-to-Rotate Control Plates," *J. Fluids Struct.*, **26**, pp. 1045–1057.
- [3] Assi, G. R. S., Bearman, P. W., Rodrigues, J. R., and Tognarelli, M., 2011, "The Effect of Rotational Friction on the Stability of Short-Tailed Fairings Suppressing Vortex-Induced Vibrations," 30th International Conference on Ocean, Offshore and Arctic Engineering, *OMAE2011*, Rotterdam, The Netherlands, June 19–24.
- [4] Schaudt, K., Wajnikonis, C., Spencer, D., Xu, J., Leverette, S., and Masters, R., 2008, "Benchmarking of VIV Suppression Systems," 27th International Conference on Offshore Mechanics and Arctic Engineering, *OMAE2008*, Estoril, Portugal, June 15–20.
- [5] Taggart, S., and Tognarelli, M., 2008, "Offshore Drilling Riser VIV Suppression Devices? What is Available to Operators?," 27th International Conference on Offshore Mechanics and Arctic Engineering, *OMAE2008*, Estoril, Portugal, June 15–20.
- [6] Assi, G. R. S., Rodrigues, J. R., and Freire, C., 2012, "The Effect of Plate Length on the Behaviour of Free-to-Rotate VIV Suppressors With Parallel Plates," 31st International Conference on Ocean, Offshore and Arctic Engineering, *OMAE2012*, Rio de Janeiro, Brazil, July 1–6.
- [7] Assi, G. R. S., Bearman, P. W., and Meneghini, J. R., 2010, "On the Wake-Induced Vibration of Tandem Circular Cylinders: The Vortex Interaction Excitation Mechanism," *J. Fluid Mech.*, **661**, pp. 365–401.
- [8] Assi, G. R. S., Bearman, P. W., Carmo, B. S., Meneghini, J. R., Sherwin, S. J., and Willden, R. H. J., 2013, "The Role of Wake Stiffness on the Wake-Induced Vibration of the Downstream Cylinder of a Tandem Pair," *J. Fluid Mech.*, **718**, pp. 210–245.
- [9] Grimmering, G., 1945, "The Effect of Rigid Guide Vanes on the Vibration and Drag of a Towed Circular Cylinder," David Taylor Model Basin, Technical Report No. 504.
- [10] Assi, G. R. S., and Bearman, P. W., 2008, "VIV Suppression and Drag Reduction With Pivoted Control Plates on a Circular Cylinder," 27th International Conference on Offshore Mechanical and Arctic Engineering, *OMAE2008*, Estoril, Portugal, June 15–20.
- [11] Assi, G. R. S., and Bearman, P. W., 2009, "VIV and WIV Suppression With Parallel Control Plates on a Pair of Circular Cylinders in Tandem," 28th International Conference on Ocean, Offshore and Arctic Engineering, *OMAE2009*, Honolulu, HI, May 31–June 5.
- [12] Henderson, J., 1978, "Some Towing Problems With Faired Cables," *Ocean Eng.*, **5**, pp. 105–125.
- [13] Wingham, P., 1983, "Comparative Steady State Deep Towing Performance of Bare and Faired Cable Systems," *Ocean Eng.*, **10**, pp. 1–32.
- [14] Packwood, A., 1990, "Performance of Segmented Swept and Unswept Cable Fairings at Low Reynolds Numbers," *Ocean Eng.*, **17**, pp. 393–407.
- [15] Assi, G. R. S., Meneghini, J. R., Aranha, J., Bearman, P. W., and Casaprima, E., 2006, "Experimental Investigation of Flow-Induced Vibration Interference Between Two Circular Cylinders," *J. Fluids Struct.*, **22**, pp. 819–827.
- [16] Freire, C., and Meneghini, J. R., 2010, "Experimental Investigation of VIV on a Circular Cylinder Mounted on an Articulated Elastic Base With Two Degrees-of-Freedom," BBVIV6–IUTAM Symposium on Bluff Body Wakes and Vortex-Induced Vibrations, Capri, Italy.
- [17] Williamson, C., and Govardhan, R., 2004, "Vortex-Induced Vibrations," *Annu. Rev. Fluid Mech.*, **36**, pp. 413–455.



Contents lists available at ScienceDirect

## Ocean Engineering

journal homepage: [www.elsevier.com/locate/oceaneng](http://www.elsevier.com/locate/oceaneng)

# On the stability of a free-to-rotate short-tail fairing and a splitter plate as suppressors of vortex-induced vibration

Gustavo R.S. Assi<sup>a,\*</sup>, Peter W. Bearman<sup>b</sup>, Michael A. Tognarelli<sup>c</sup><sup>a</sup> Dept. of Naval Arch. and Ocean Eng., University of São Paulo, São Paulo, Brazil<sup>b</sup> Department of Aeronautics, Imperial College, London, UK<sup>c</sup> BP America Production Company, Houston, USA

## ARTICLE INFO

## Article history:

Received 10 December 2013

Accepted 20 October 2014

Available online 6 November 2014

## Keywords:

Vortex-induced vibration

Galloping

Suppression

Splitter plate

Short-tail fairing

Offshore risers

## ABSTRACT

Experiments in the Reynolds number range of 1000 to 12,000 have been carried out on a free-to-rotate short-tail fairing fitted to a rigid length of circular cylinder to investigate the effect of rotational friction on the stability of this type of VIV suppressor. Measurements of the dynamic response are presented for models with low mass and damping which are free to respond in the cross-flow and streamwise directions. It is shown how vortex-induced vibration can be reduced if the rotational friction between the cylinder and the short-tail fairing exceeds a critical limit. In this configuration the fairing finds a stable position deflected from the flow direction and a steady lift force appears towards the side to which the fairing has deflected. The fluid-dynamic mechanism is very similar to that observed for a free-to-rotate splitter plate of equivalent length. A non-rotating fairing as well as splitter plates is shown to develop severe galloping instabilities in 1-dof experiments.

© 2014 Elsevier Ltd. All rights reserved.

## 1. Introduction

Efficient suppression of flow-induced vibration (FIV) of slender submarine structures is a challenging and interesting problem for the offshore industry and the scientific community. Various methods for suppressing vortex-induced vibrations (VIV) of bluff bodies have been investigated over the past decades. With the advancement of offshore oil exploration, research on VIV suppressors was pushed to a new level. The industry demands suppressors that are not only efficient for low mass-damping systems but also that could be installed under harsh environmental conditions; such is the case for offshore risers. Zdravkovich (1981) and Every et al. (1982) present comprehensive reviews of solutions varying from the simple attachment of ribbons to quite expensive devices such as helical strakes and fairings. Drilling risers may typically be inspected more often than production risers, therefore fatigue damage is not as important a concern as the steady loads caused by strong currents. Therefore, besides suppressing FIV, suppressors must reduce drag consequently reducing pipe bend and wear risk during drilling operations.

It is known that free-to-rotate suppressors may experience hydrodynamic instabilities that will not only cause a substantial increase in drag but also prevent them from suppressing vibrations (Assi et al., 2009). Actually, an unstable free-to-rotate suppressor may induce more vigorous structural vibrations excited by a type of flutter mechanism. Assi et al. (2009) have shown that the instability of free-to-rotate suppressors is directly related to the level of rotational resistance encountered in the system as well as geometric parameters such as plate length. They performed experiments in laboratory scale and showed that a free-to-rotate suppressor formed by a single splitter plate may need a minimum rotational resistance (or be above a critical rotational friction) to enable a stable configuration with effective suppression. The same was verified for free-to-rotate suppressors composed of two parallel plates (Assi et al., 2012), revealing that a minimum rotational resistance is necessary to stabilise the devices. Assi et al. (2009, 2010a) have also shown that 1D-long parallel plates can be very efficient in suppressing both VIV and WIV (wake-induced vibration). WIV occurs when the downstream body of a set is excited by the unsteady wake generated from another body placed upstream (Assi et al., 2010b, 2013a).

In the present work we contribute to the understanding of the hydrodynamic mechanism behind a type of free-to-rotate device known as the short-tail fairing compared with a cylinder associated with a simple geometry of a splitter plate. We focus on the dynamic stability and hydrodynamic phenomena that cause the

\* Correspondence to: PNV Dept. Eng. Naval e Oceânica, Escola Politécnica da Universidade de São Paulo, Av. Prof Mello Moraes 2231, 05508-030 São Paulo – SP, Brazil.

E-mail address: [g.assi@usp.br](mailto:g.assi@usp.br) (G.R.S. Assi).

URL: <http://www.ndf.poli.usp.br> (G.R.S. Assi).

## Nomenclature

|                   |  |
|-------------------|--|
| $\bar{C}_x$       | mean drag coefficient                        |
| $D$               | cylinder external diameter                   |
| $f_{0x}$          | streamwise natural frequency measured in air |
| $f_{0y}$ or $f_0$ | cross-flow natural frequency measured in air |
| $f_x$             | streamwise oscillation frequency             |
| $f_y$             | cross-flow oscillation frequency             |
| $L/D$             | non-dimensional length of the splitter plate |
| $m^*$             | mass ratio                                   |
| Re                | Reynolds number                              |
| St                | Strouhal number                              |

|             |  |
|-------------|--|
| $U$         | flow speed   |
| $U/Df_0$    | reduced velocity   |
| $\hat{x}/D$ | non-dimensional streamwise harmonic amplitude of vibration |
| $\hat{y}/D$ | non-dimensional cross-flow harmonic amplitude of vibration |
| $\delta$    | stable angular position of a free-to-rotate suppressor     |
| $\rho$      | specific mass of water                                     |
| $\tau_f$    | torque due to rotational friction                          |
| $\tau_f^*$  | non-dimensional torque due to rotational friction          |
| $\zeta$     | structural damping ratio                                   |

fairing and the splitter plate to behave in quite the same way. A parametric investigation of the geometry of suppressors, in special the splitter plate, is not the concern of the present work. For that matter, the reader may refer to other works of the same authors (Assi et al., 2012, 2013b; Assi and Franco, 2013).

## 2. Free-to-rotate suppressors

It is known that if vortex shedding from a fixed cylinder is eliminated, say by the use of a long splitter plate (Cimbala and Garg, 1991), then drag is reduced. Hence conceptually an effective VIV suppression device should be able to reduce drag rather than increase it. This simple idea was the motivation for the development of suppressors such as splitter plates and fairings that act primarily by disrupting the vortex shedding mechanism on the near wake of bluff bodies by delaying the interaction between the separated shear layers.

Assi et al. (2009) have shown that suppression of cross-flow and in-line VIV of a circular cylinder, with resulting drag coefficients less than that for a fixed plain cylinder, has been achieved using two-dimensional control plates in low mass-damping systems. A free-to-rotate splitter plate was also found to suppress VIV but instead of remaining aligned with the flow on the centreline of the wake the plate adopted a stable but deflected position when it was released. VIV was suppressed, throughout the range of reduced velocity investigated, and drag reduced below that of a plain cylinder. Cimbala and Garg (1991) had also observed this bi-stable behaviour for a free-to-rotate cylinder fitted with a splitter plate.

Particle-image velocimetry (PIV) measurements performed by Assi et al. (2009) showed that on the side to which the plate deflected the separating shear layer from the cylinder appeared to attach to the tip of the plate and this had the effect of stabilising the near wake flow. Vortex shedding was visible downstream but this did not feed back to cause vibrations. An unwanted effect was that a steady transverse lift force developed on the cylinder towards the side to which the splitter plate deflected. This steady lift could be eliminated by using a pair of splitter plates arranged so that the shear layers that spring from both sides of the cylinder attach to the tips of the plates. The maximum suppression and drag reduction occurred with a pair of free-to-rotate parallel plates installed on the sides of the cylinder.

Assi et al. (2009) also found that the level of rotational friction between the free-to-rotate plate and the cylinder plays a fundamentally important role, needing to be “high enough to hold the device in a stable position, while still allowing them to realign if the flow direction changes. Devices with rotational friction below a critical value oscillate themselves as the cylinder vibrates, sometimes increasing the amplitude of cylinder oscillation higher

than that for a plain cylinder”. All devices with rotational friction above a critical value appeared to suppress VIV and reduce drag. However, if the rotational resistance was above a limiting threshold the suppressors could not rotate and an undesired galloping response was initiated.

In the present study we set out with the hypothesis that short-tail fairings and short splitter plates are able to suppress VIV based on the same fluid-dynamic mechanism. Short-tail fairings are not “fairings” in the strict sense of the term, meaning that they do not make a streamlined body. For this to happen the length of the fairing would have to be many times the diameter of the cylinder, as shown in Henderson (1978), Wingham (1983) and Packwood (1990). In essence, we believe a short-tail fairing acts in the near wake with fully separated flow avoiding the interaction between the shear layers and delaying vortex shedding, therefore the same mechanism as the splitter plate.

If this is true, we expect short fairings to find stable but deflected positions towards one of the sides of the cylinder instead of aligning itself with the flow. In the same manner as splitter plates, the stability of short fairings might also depend on a minimum level of rotational friction in order to suppress VIV. The effect of rotational friction on the stability of a short-tail fairing is what this present study sets out to investigate. However, if friction is too high the suppressor may not find itself free to rotate around the cylinder, but stuck with no angular movement. If this is the case, the system becomes susceptible to galloping, which may cause severe vibrations in a very different fashion from VIV.

## 3. Experimental arrangement

Two types of suppressors were tested in this experimental campaign: a free-to-rotate splitter plate and a short-tail fairing. Fig. 1(a) presents the geometric parameters for the splitter plate. Plate length  $L/D$  could be varied by changing the plate made out of acrylic plastic. The short-tail fairing was made of a triangular

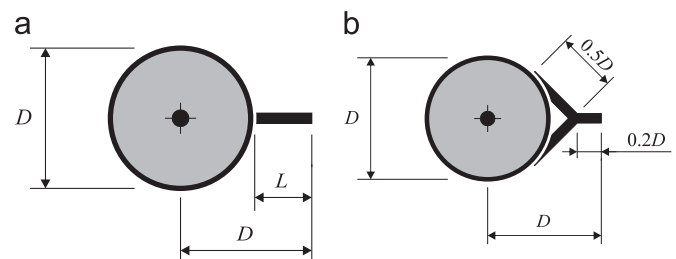


Fig. 1. Geometries for splitter plates and a short-tailed fairing. (a) Short splitter plate; (b) Short-tail fairing.

fairing with a flat tail piece as shown in Fig. 1(b). Devices with a similar geometry are used by the offshore industry following its appearance as a commercial solution to reduce VIV (Allen and Henning, 1995). The geometry adopted in this work was based on the proportions found in Pontaza and Chen (2006). It consisted of two perpendicular plates of  $0.5D$  in length joined at the tip to a short  $0.2D$ -long tail plate. The characteristic length of the fairing was  $0.5D$  if measured from the base of the cylinder, thus of the same order as the  $L/D=0.5$  splitter plate.

Suppressors were supported by two rotating arms at each end mounted on low-friction ball bearings. Plates were kept at a small distance from the cylinder wall in order to allow the devices to freely rotate about the centre of the cylinder. Control of the rotational friction was achieved by adjusting a screw pushing a small brake plate between the rotating parts. The same system was employed by Assi et al. (2009).

Experiments were carried out on devices fitted to a rigid length of a circular cylinder free to respond to VIV. The investigation was performed during a test campaign in 2007 in a recirculating water channel in the Department of Aeronautics, Imperial College, London. The parallel test section was  $0.6$  m wide,  $0.7$  m deep and  $8.0$  m long. The flow speed  $U$  was continuously variable and good quality flow could be obtained up to at least  $0.6$  m/s. The cylinder model was constructed from  $50$  mm diameter acrylic tube, giving a maximum Reynolds number of approximately  $30,000$ , based on cylinder diameter  $D$ .

Models could be mounted in two different elastic rigs, one that allowed one-degree-of-freedom (1-dof) motion in the cross-flow direction and another that allowed two-degrees-of-freedom (2-dof) motion in the cross-flow and streamwise directions. The 2-dof rig allowed for motion that is closer to the real application of suppressors in offshore risers, hence most of the results discussed in the present study were obtained from experiments in this rig. Also, 2-dof experiments proved to be rather important to evaluate the stability of free-to-rotate suppressors due to the effect of streamwise movement over the rotation of the plates. Of course the rotation of the plate could be thought of as a third dof in the dynamic system, but in the present work we shall only consider the response of the cylinder in the cross-flow and streamwise directions.

For the 2-dof experiments, models were mounted on a very low damping rig shown in Fig. 2. The cylinder model was mounted at the lower end of a long carbon fibre tube which formed the arm of a rigid pendulum. The top end of the arm was connected to a universal joint fixed at the ceiling of the laboratory so that the cylinder model was free to oscillate in any direction in a pendulum motion.

The cylinder was vertically aligned at the centre of the test section, distant  $300$  mm from each of the side walls. A total blockage of  $8.3\%$  was judged not to affect the overall response based on the study of Brankovic (2004). A small gap of  $2$  mm was left between the bottom end of the cylinder and the floor. Also

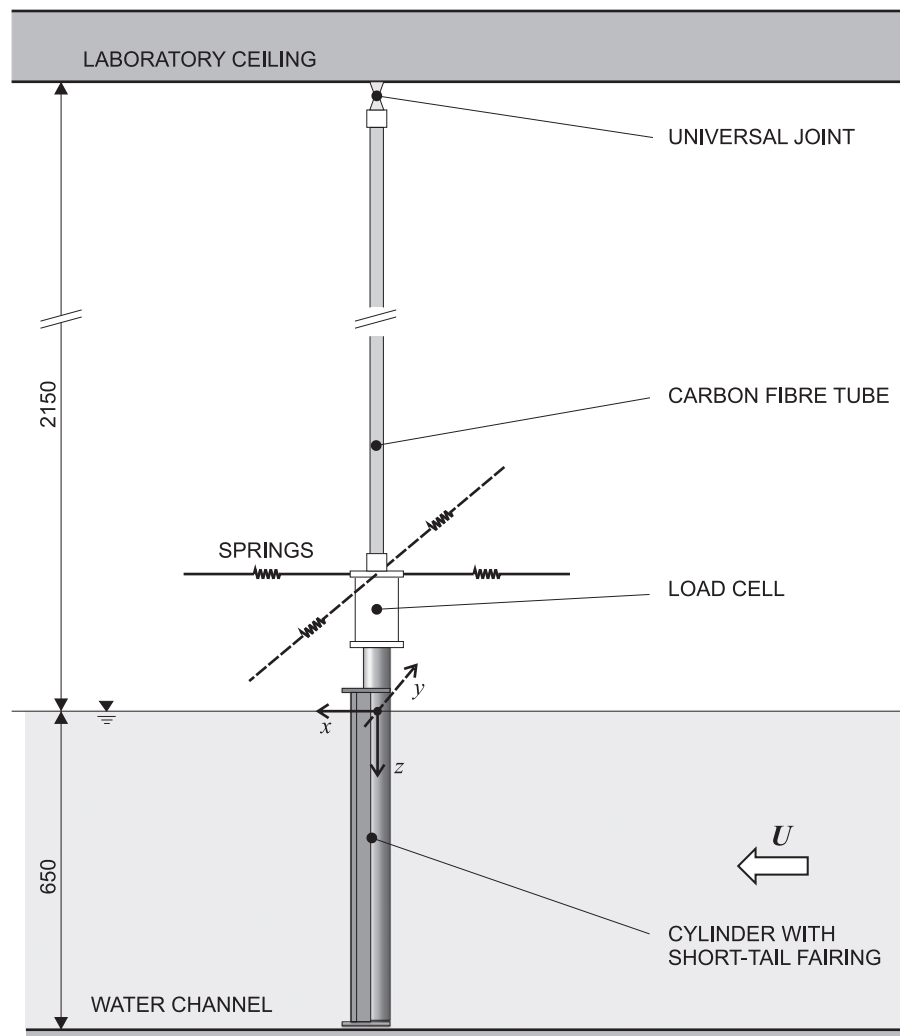


Fig. 2. Representation of the cylinder with a short-tail fairing mounted on the 2-dof rig in the test section of the water channel. Dimensions are in millimetres.

based on previous studies employing the same set-up (Assi et al., 2009, 2010b, for example), the different end conditions at the free surface and the bottom of the cylinder did not affect the overall behaviour of the system as far as flow-induced vibration is concerned.

Two independent optical sensors were employed to measure displacements in the  $x$ - and  $y$ -directions at the mid-length of the model. It should be noted that for a displacement equal to 1 diameter the inclination angle of the cylinder was only just over  $1^\circ$  from the vertical. Two pairs of springs were installed in the  $x$ - and  $y$ -axes to set the natural frequencies in both directions of motion allowing different natural frequencies to be set for each direction.

Although the cylinder was initially aligned in the vertical position, in flowing water the mean drag displaces the cylinder from its original location. To counteract this effect, both pairs of springs were attached to a frame that could be moved back and forth in the direction of the flow. For each flow speed there was a position of the frame that maintained the mean position of the cylinder in the vertical alignment. By using two pairs of springs perpendicular to each other, the assembly has nonlinear spring constants in the transverse and in-line directions for large displacements. Movement in the transverse direction will cause a lateral spring deflection in the in-line direction and vice versa. This nonlinearity is minimised by making the springs as long as possible, hence the in-line springs were installed at the end of 4 m-long wires, fixed at the extremities of the frame.

It is known that during the cycle of vortex shedding from bluff bodies the fluctuation of drag has double the frequency of the fluctuation of lift. Hence a particularly severe vibration might be expected to occur if the hydrodynamic forces in both directions could be in resonance with both in-line and transverse natural frequencies at the same time. For this reason, we set the streamwise natural frequency ( $f_{0x}$ ) to be close to twice the cross-flow frequency ( $f_{0y}$ ) or simply  $f_0$  by adjusting the stiffness of both pairs of springs. The structural damping of the 2-dof rig was  $\zeta=0.3\%$  (measured in air), defined as a fraction of critical damping, practically the same for both principal directions of motion. A load cell was attached between the cylinder and the support system to deduce the instantaneous and time-averaged hydrodynamic forces on the cylinder model. The mass ratio  $m^*$ , defined

as vibrating mass divided by the displaced mass of water, was kept to the lowest possible value. Preliminary tests have been performed with a plain cylinder to serve as reference for comparison. Table 1 presents the structural parameters for the arrangements of cylinder and suppression device tested.

Measurements were made using a fixed set of springs and the reduced velocity range covered was from 1.5 to 13, where reduced velocity ( $U/Df_0$ ) is defined using the cylinder natural frequency of oscillation in the cross-flow direction measured in air. The only flow variable changed during the course of the experiments was the flow velocity  $U$ , which, as for full-scale risers, alters both the reduced velocity and the Reynolds number. Throughout the study, cylinder displacement amplitudes ( $\hat{x}/D$  for streamwise and  $\hat{y}/D$  for cross-flow) were found by measuring the root mean square value of response and multiplying by the square root of 2 (the so called harmonic amplitude). This is likely to give an underestimation of maximum peak response but was judged to be perfectly acceptable for assessing the effectiveness of VIV suppression devices. Displacements were nondimensionalised by dividing by the plain cylinder diameter  $D$ .

The 1-dof rig has been employed for several VIV experiments and is described in detail in Assi et al. (2010a). For brevity, we will limit ourselves to comment that the 1-dof rig consisted of a rigid support table, mounted on two carbon fibre tubes, sliding through air bearings in the cross-flow direction. Restoration was achieved by one pair of coil springs. Mass and damping were also kept to a minimum, resulting in  $m^* \approx 2.6$  and  $\zeta=0.7\%$  (with a combined parameter  $m^*\zeta \approx 0.0182$ ) for all the 1-dof experiments. The 1-dof rig was only employed for experiments in which the suppressors were not free to rotate, as will be presented below.

#### 4. Results and discussion

Preliminary experiments performed with a plain cylinder (previously presented in Assi et al., 2009) will serve as reference for the discussion that follows. Fig. 3 presents the typical trajectories of motion for a single cylinder under 2-dof VIV in which  $f_{0x}$  is almost twice as  $f_{0y}$ . The  $x$ -axis for displacement is not shown in Fig. 3 for clarity, but it has the same scale as the  $y$  axis. As reduced velocity is increased, vibrations start to build up in a 'C' shape, then changing into '8'-shaped curves until the end of the synchronisation range at around reduced velocity 12. The overall response was found to be in good agreement with results from Jauvtis and Williamson (2004) (even though they had  $f_{0x}=f_{0y}$ ) and Dahl et al. (2006). Figs. 4 and 5 both repeat the same 2-dof response for a plain cylinder projected in the cross-flow ( $\hat{y}/D$ ) and streamwise ( $\hat{x}/D$ ) directions, revealing a different behaviour from the typical cross-flow VIV response in 1-dof. Initial, upper and lower branches are not clearly identified but instead 2-dof vibrations build up in the form of a single branch during the synchronisation range.

**Table 1**  
Structural properties.

| Model                    | $m^*$ | $\zeta$ (%) | $m^*\zeta$ | $f_{0x}/f_{0y}$ |
|--------------------------|-------|-------------|------------|-----------------|
| Plain cylinder           | 1.6   | 0.3         | 0.0047     | 1.93            |
| Splitter plate $L/D=0.5$ | 1.7   | 0.3         | 0.0051     | 1.90            |
| Splitter plate $L/D=1.0$ | 1.7   | 0.3         | 0.0051     | 1.90            |
| Short-tail fairing       | 1.7   | 0.3         | 0.0051     | 1.90            |

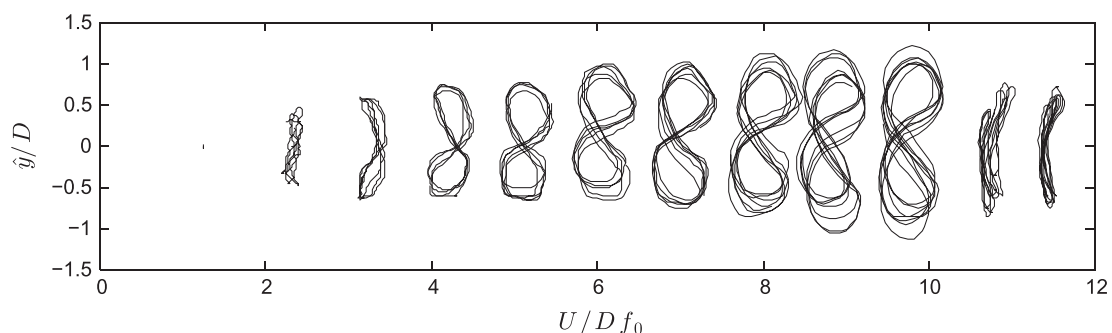


**Fig. 3.** Trajectories of motion for a plain cylinder.

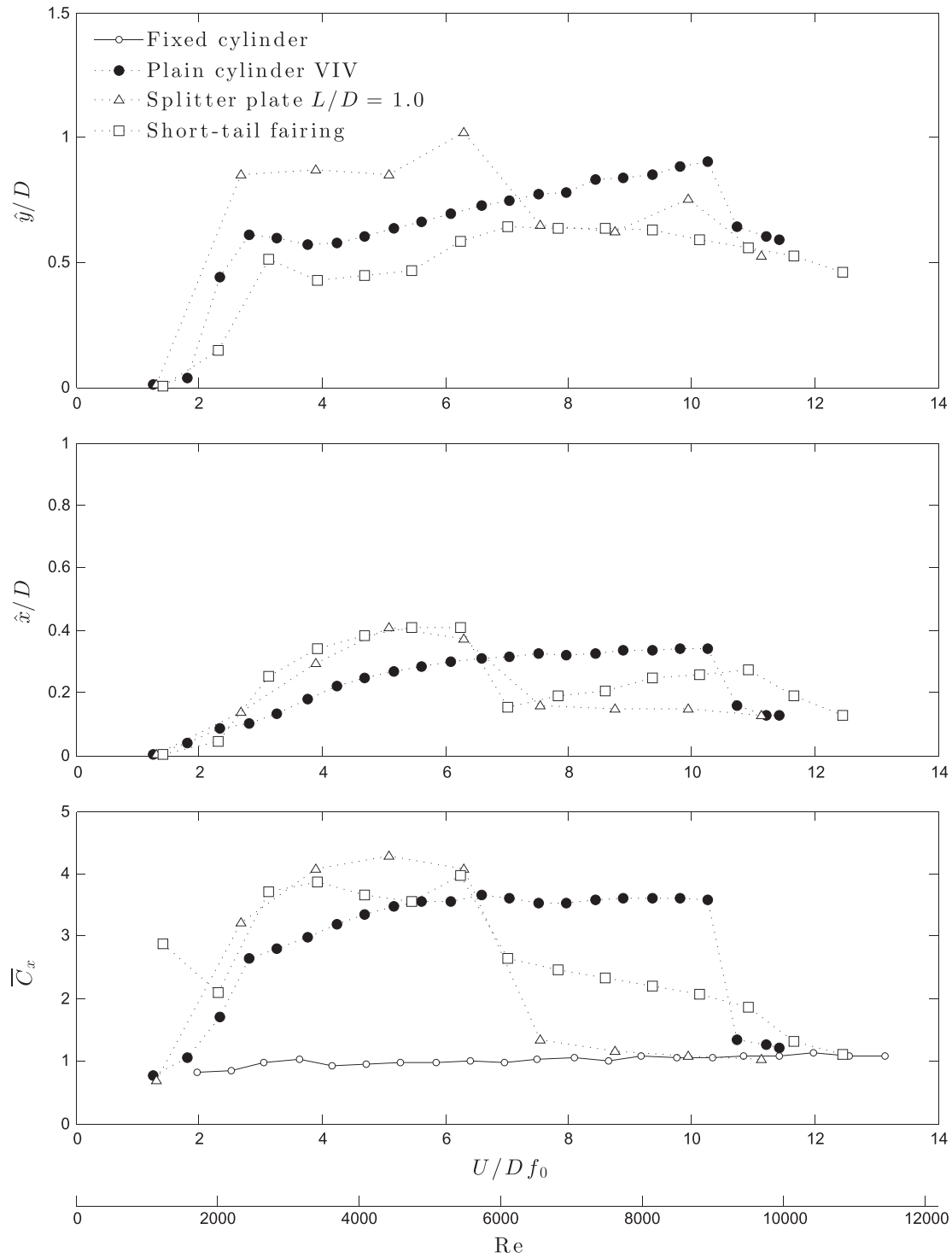


**Fig. 4.** 2-dof response of cylinder fitted with free-to-rotate devices with low friction ( $\tau_f = 0.009 \text{ Nm/m}$ ). Displacement (*top*) and frequency (*middle*) of vibration and mean drag coefficient (*bottom*) versus reduced velocity.

#### 4.1. Free-to-rotate suppressors in 2-dof

In order to investigate the rotation stability of free-to-rotate splitter plates and short-tail fairings models were prepared with two values of rotational friction  $\tau_f$ . Low friction ( $\tau_f = 0.009 \text{ Nm/m}$ ) and a high friction ( $\tau_f = 0.035 \text{ Nm/m}$ ) cases were chosen based on the results obtained for a splitter plate presented in Assi et al. (2009). In that same paper,  $\tau_f$  was measured in torque per unit length and could be rewritten as a non-dimensional friction torque

parameter

$$\tau_f^* = \frac{\tau_f}{\rho U^2 D^2}, \quad (1)$$

which represents the ratio of structural torsional resistance to a hydrodynamic torque, thus varying with flow speed squared.

Similar to what was observed for a splitter plate in Assi et al. (2009), neither the splitter plate ( $L/D=1.0$ ) nor the short-tail fairing with low friction ( $\tau_f = 0.009 \text{ Nm/m}$ ) came to a stable



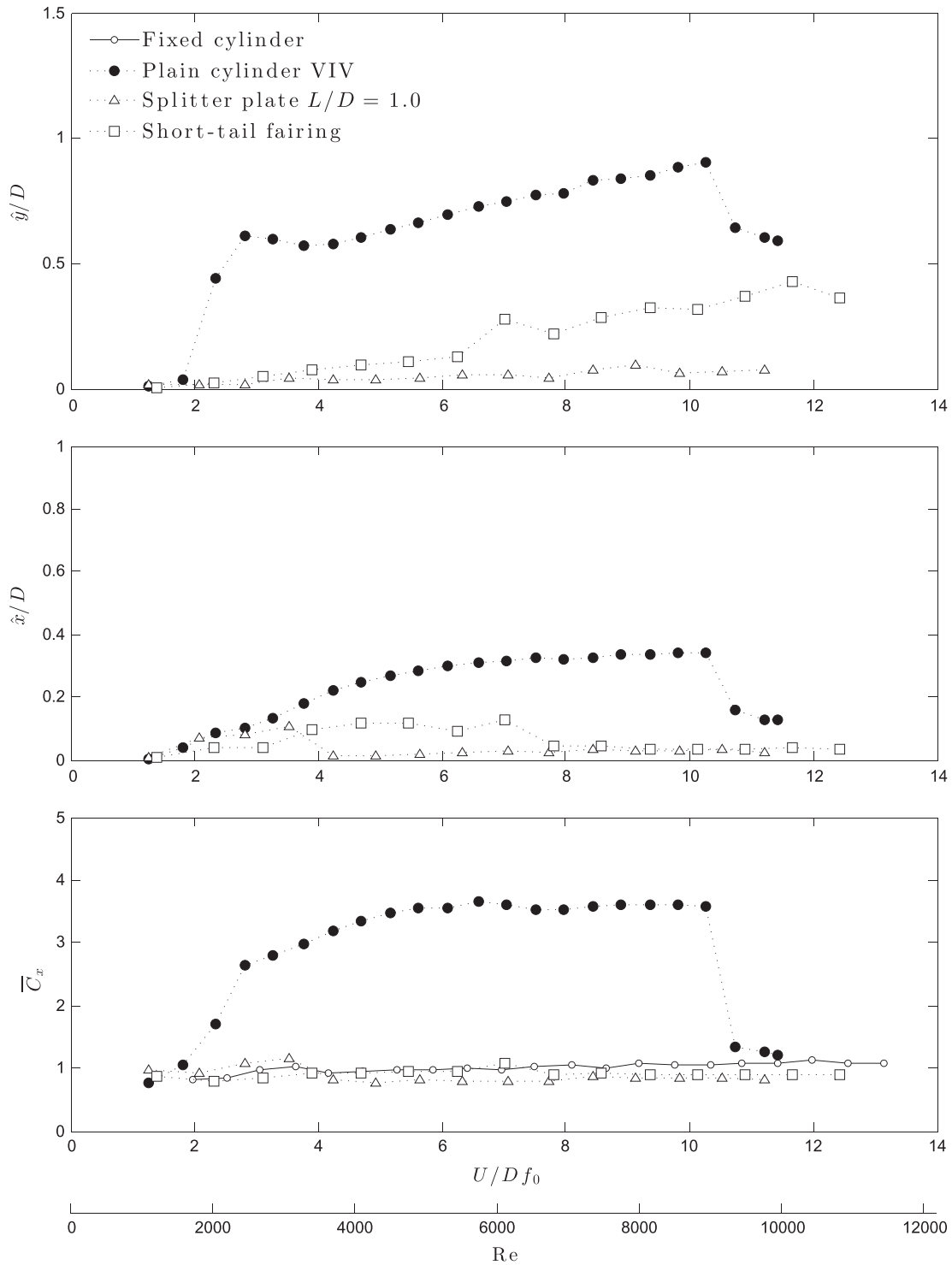


**Fig. 5.** 2-dof response of cylinder fitted with free-to-rotate devices with high friction ( $\tau_f = 0.035 \text{ Nm/m}$ ). Displacement (top) and frequency (middle) of vibration and mean drag coefficient (bottom) versus reduced velocity.

angular position about the centre of the cylinder wake, instead they oscillated from side to side as the cylinder responded with VIV. The trajectories of motion presented in Figs. 6(a) and 7(a) also resemble a deformed '8' shape with amplitudes of vibration almost as high as those observed for a plain cylinder (Fig. 3) for the whole range of reduced velocities.

This effect can also be seen in Fig. 4 for cross-flow and streamwise directions in contrast with the response of the single cylinder. It reveals that while the cross-flow response of the short-tail fairing falls just below the curve for the single cylinder, the

1.0D-long splitter plate actually enhances vibration. One has to bear in mind that the characteristic length of this specific splitter plate is twice that of the short-tail fairing, thus inducing more severe oscillations when the device rotates. Streamwise responses are rather similar to both suppressors.

In contrast, both the splitter plate and the short-tail fairing presented a distinct behaviour when rotational friction was increased from  $\tau_f = 0.009 \text{ Nm/m}$  to  $0.035 \text{ Nm/m}$ , as shown in Figs. 6 and 7. Both devices came to a stable position at a deflected angle (which was different for each suppressor) about the axis of

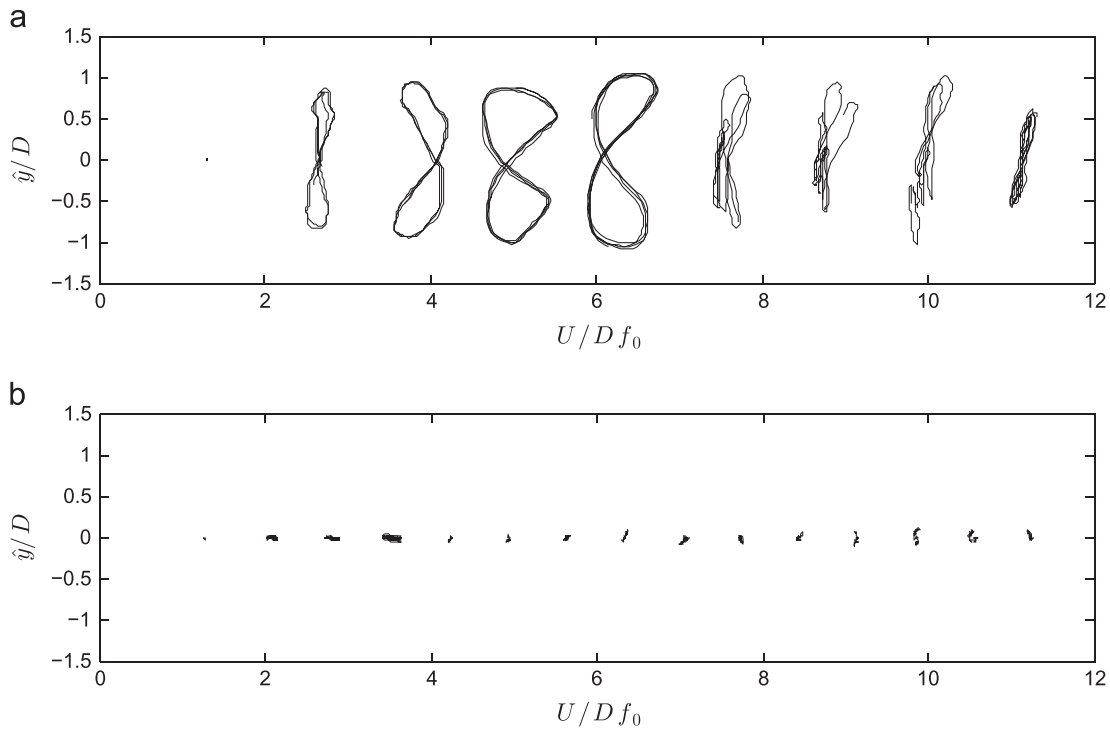


**Fig. 6.** Trajectories of motion for a splitter plate with  $L/D=1.0$ . (a) Low friction ( $\tau_f = 0.009$  Nm/m); (b) High friction ( $\tau_f = 0.035$  Nm/m).

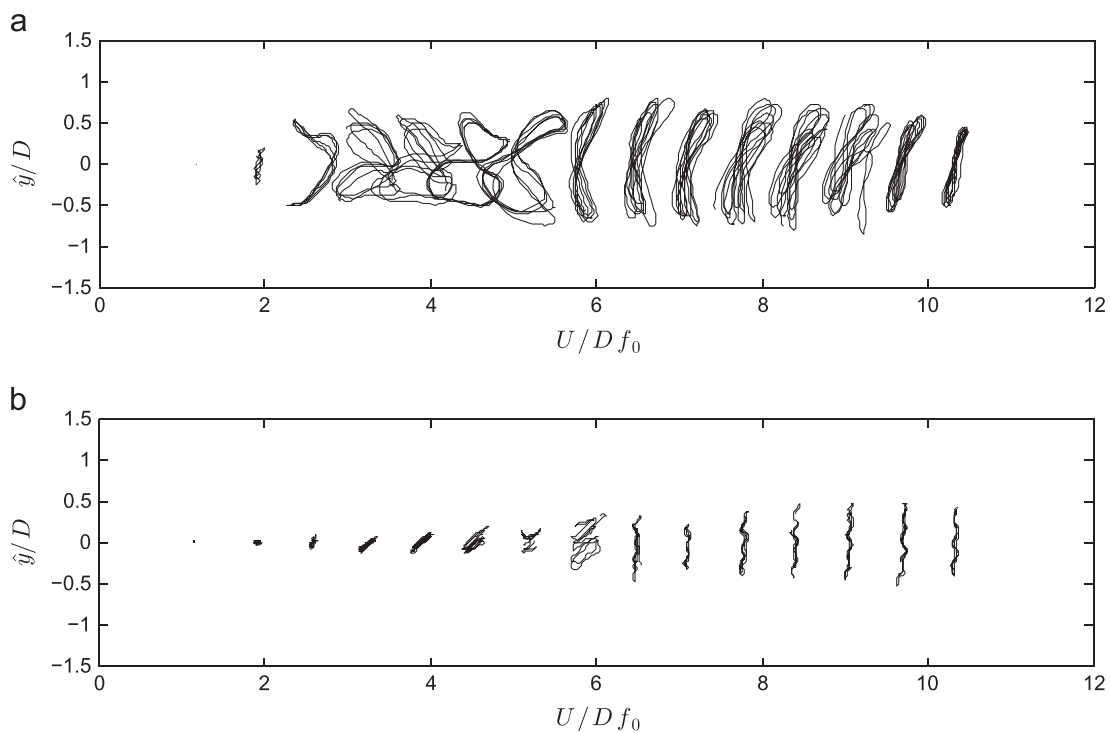


**Fig. 7.** Trajectories of motion for a short-tail fairing. (a) Low friction ( $\tau_f = 0.009$  Nm/m); (b) High friction ( $\tau_f = 0.035$  Nm/m).

the cylinder and, similar to what was observed for the splitter plate in Assi et al. (2009), VIV was reduced. In this angular configuration the short-tail fairing was successful in suppressing VIV, though not completely.

Fig. 5 shows that the maximum amplitude of vibration was  $\hat{y}/D \approx 0.45$  in the cross-flow and  $\hat{x}/D \approx 0.15$  in the streamwise directions within the synchronisation range. Significant vibration might still appear for higher reduced velocities because the fairing is not long enough to sufficiently delay the interaction of the shear

layers downstream of the body, thus vortices are feeding back and exciting the cylinder. The 1.0D-long splitter plate, on the other hand, seems to be playing this role rather well. Cross-flow and streamwise vibrations are considerably reduced and kept to a minimum through the whole range of reduced velocities investigated.

As far as drag reduction is concerned, Fig. 4 shows that both suppressors with low rotational friction presented drag coefficients higher than that of a plain cylinder under VIV for a good

part of the synchronisation range. On the other hand, once the devices were able to stabilise with high friction, the level of drag dropped to values comparable to a static plain cylinder, as presented in Fig. 5, with the 1.0D-long splitter plate being the most efficient in terms of drag reduction. The short-tail fairing did not show such a large a drag reduction as the splitter plate or other devices studied in Assi et al. (2009), but achieved an average reduction of 6% compared to a fixed cylinder if the whole range of reduced velocity (or Reynolds number) is considered.

A stable angle of deflection  $\delta$  of around  $25^\circ$  was observed for the short-tail fairing and was very close to that found for a 0.5D-long splitter plate by Assi et al. (2009). As illustrated in Fig. 8, this angle is related to the characteristic length of the suppressor and its capacity to encounter and reattach one of the separated shear layers (Assi et al., 2009), thus we expect the short-tail fairing and a 0.5D-long splitter plate to find similar stable angular deflections.

We have observed that, likewise the splitter plate, a short-tail fairing requires a deflected position in order to stabilise and disrupt the communication between the shear layers, consequently delaying vortex shedding and suppressing VIV. However, as a consequence of this new asymmetric configuration, the fairing also generates a mean lift force towards the side to which it has deflected. In practise, long risers are fitted with a series of fairings mounted along the span of the pipe. It is possible, therefore, that some fairings might randomly deflect to one side whereas others deflect to the opposite side, in a way that the resultant lift force generated on the entire riser is neutralised. This prediction was not verified in our experiments, but operators have reported this behaviour.

#### 4.2. Fixed suppressors in 1-dof

Now, if a deflected position is capable of generating steady lift, this lateral force might become a problem for a device that got stuck at a fixed position about the cylinder. Experiments with fixed suppressors (not free to rotate) were designed to verify this. Devices were fixed at  $180^\circ$  in relation to the flow direction (as shown in Fig. 1) by locking the rotating arms about the cylinder. In addition to the short-tail fairing, two splitter plates of length  $L/D=0.5$  and  $1.0$  were tested in the 1-dof rig (cross-flow direction only). Responses are compared against the typical VIV response of a plain cylinder with 1-dof from Assi et al. (2010a).

As shown in Fig. 9, the response is very different from that obtained for free-to-rotate suppressors. Both splitter plates and the short-tail fairing presented a very vigorous transverse galloping oscillation that, with increasing reduced velocity, would apparently

increase without limit. In this 1-dof experiment the maximum amplitude of the rig for cross-flow oscillation was limited to about 2D and this was reached by the splitter plates at reduced velocity of about 10. The same behaviour has been observed for the short-tail fairing in the present work. The fairing was allowed to vibrate for higher reduced velocities and the response presented an abrupt decrease in displacement at  $U/Df_0 \approx 14$ . Stappenbelt (2010) performed experiments with low aspect ratio cylinders fitted with splitter plates with  $L/D \leq 4$  and noticed the same behaviour for  $L/D \leq 1.0$ .

The middle graph of Fig. 9 shows the dominant frequency signature of the response. The plain cylinder follows the typical frequency behaviour expected for 1-dof VIV, following the dot-dashed line indicating  $St=0.2$  and slightly departing from the natural frequency during the synchronisation range. The cylinder fitted with fixed devices, on the other hand, adopts much lower frequencies of vibration, not related to the vortex shedding mechanism. In addition, the bottom graph of Fig. 9 reveals no drag amplification for the suppressors through the synchronisation range would be expected if they were vibrating due to VIV. The steep ramp in the displacement curve, the low-frequency signature and no amplification of drag are all evidence that the system is indeed being driven by a 1-dof galloping mechanism. In fact, Assi et al. (2009) showed that the origin of the lift force causing galloping is that of the mean lift that appears for free-to-rotate devices with an angular deflection.

Flow visualisation and PIV measurements were carried out to investigate the interaction between the wake and the fixed devices. Figs. 10–12 present instantaneous vorticity fields for three different reduced velocities of 3.0, 5.0 and 7.3, identified with a (\*) in the axis of Fig. 9 (top) for convenience. The data was acquired when the cylinder was crossing the centreline from left to right, therefore presenting maximum cross-flow velocity; flow direction is from top to bottom. A key for colour contours is not presented in these figures because the objective is only the qualitative comparison of the wake.

Fig. 10 presents vorticity contours of the wake of a plain cylinder under VIV for reference. For reduced velocity 3.0 in Fig. 10(a) the cylinder presents small vibration with a typical 2S-mode wake being shed (refer to Williamson and Govardhan, 2004 for a description of wake modes). For reduced velocity 5.0 in Fig. 10(b), close to the peak of resonance, the wake appears much wider due to the high-amplitude movement of the cylinder. The wake mode will change again in the lower branch of vibration as it appears for reduced velocity 7.3 in Fig. 10(c). For all cases in Fig. 10 the interaction of the separated shear layers in the vortex-formation mechanism is quite evident.

Figs. 11 and 12 present vorticity contours for a cylinder fitted with non-rotating splitter plates of lengths  $L/D=0.5$  and  $1.0$ , respectively. For both plate lengths and for almost all reduced velocities the shear layer that separates from the right-hand side of the cylinder reattaches to the tip of the plate. An exception is the short plate at reduced velocity 3.0 in Fig. 11(a), where the vortices are able to form downstream of the plate without any reattachment. As explained in Assi et al. (2009), the reattachment of the shear layer on the right-hand side will create a lift force towards that side, which is in phase with the velocity of the cylinder. This galloping excitation is observed to occur for both plate lengths. Although one may think that the 1D-long plate would be able to extract more energy from the flow during the galloping mechanism, the response of both plates in Fig. 9 (top) is rather similar.

An identical galloping mechanism appears to occur with the non-rotating short-tail fairing, as presented in Fig. 13. For reduced velocity 3.0 in Fig. 13(a) the vortex shedding mechanism is not affected by the presence of the fairing in quite the same way the

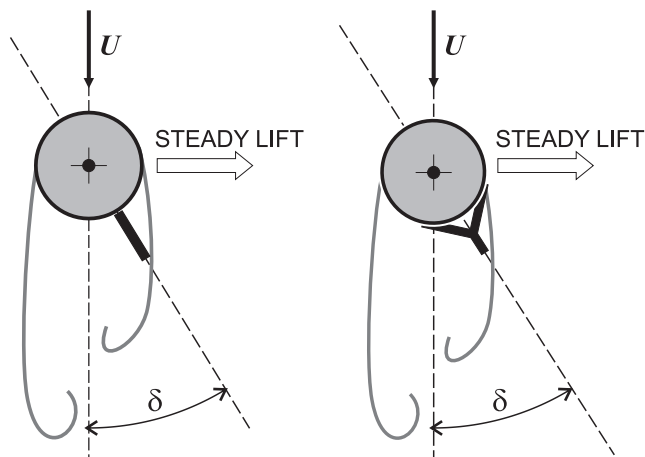
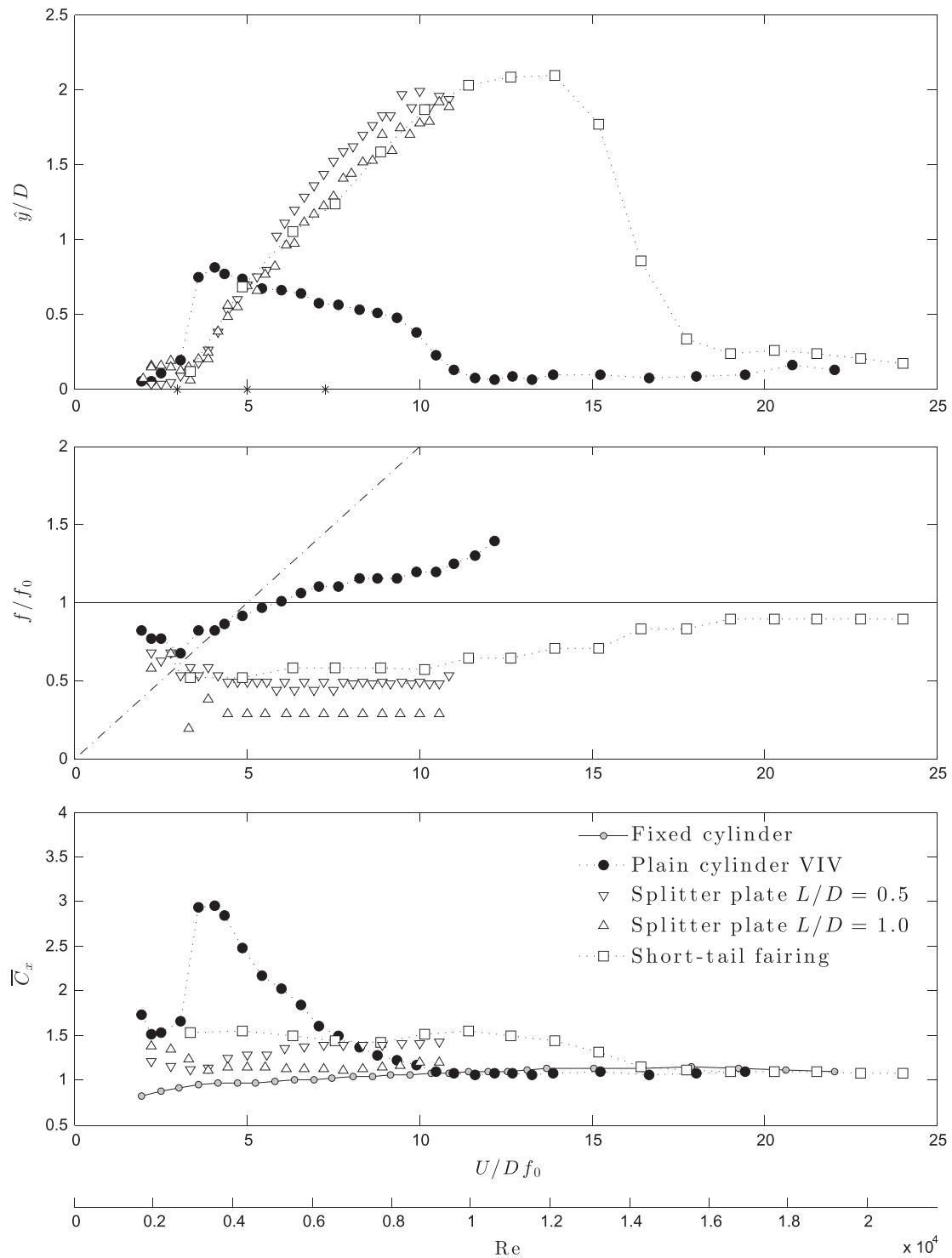


Fig. 8. Steady lift generated on the cylinder due to the deflection of the suppressors.



**Fig. 9.** 1-dof galloping response of cylinder fitted with non-rotating devices. Displacement (*top*) and frequency (*middle*) of vibration and mean drag coefficient (*bottom*) versus reduced velocity.

short plate is unnoticed by the flow in Fig. 11(a). As reduced velocity (and Reynolds number) is increased the vortex formation length is reduced and the reattachment of the shear layer due to the relative motion of the fairing is achieved. All three cases illustrated in Fig. 13 are essentially identical to those for the short plate in Fig. 11. In fact, the responses of these short suppressors are not at all different, as seen in Fig. 9. We believe this explains how a non-rotating short-tail fairing can undergo galloping instabilities in the same way as a splitter plate with equivalent characteristic length. Again, Fig. 8 summarises the idea that the origin of the

steady lift on a free-to-rotate but deflected suppressor is the same as that to cause galloping in a non-rotating fairing.

Once the devices were allowed to rotate about the centre of the cylinder the 1-dof responses were completely different. The plates and the fairing tilted to an inclined position and the low-amplitude levels of displacement proved that they successfully suppressed VIV. The previous work of Assi et al. (2009) showed that rotary inertia is not an important parameter for stability, at least not as important as rotary friction (in the form of rotary damping). Marine growth, for example, would certainly affect

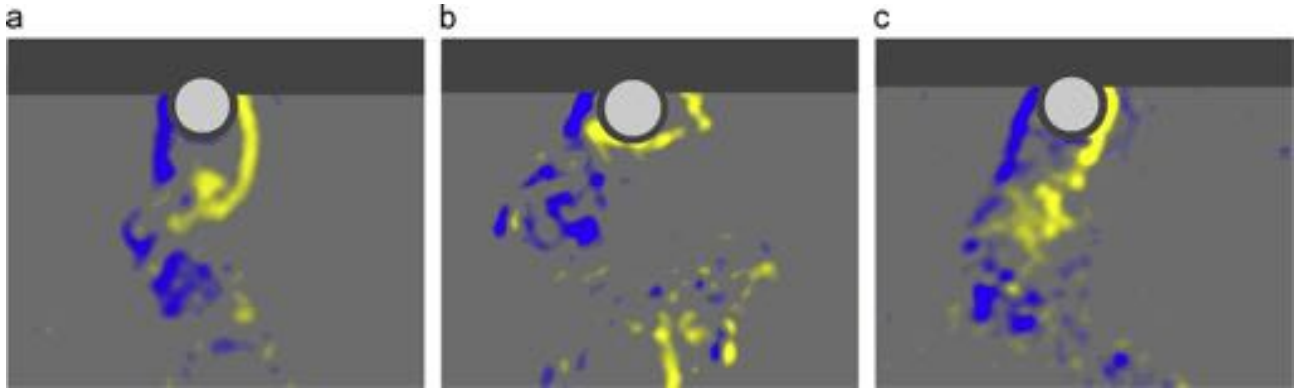


**Fig. 10.** Vorticity contours for a single cylinder. (a)  $U/Df_0 = 3.0$ ; (b)  $U/Df_0 = 5.0$ ; (c)  $U/Df_0 = 7.3$ . (For interpretation of the references to color in this figure legend, the reader is referred to the web version of this article.)

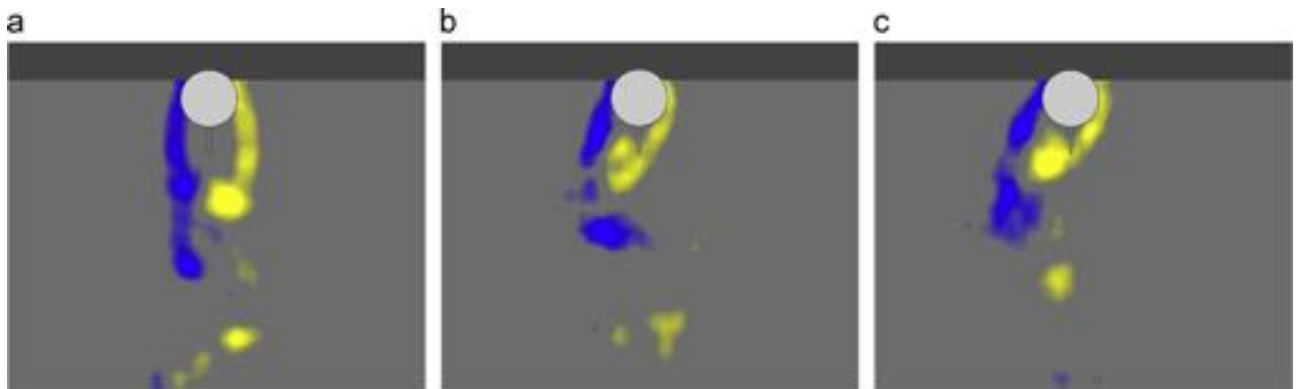


**Fig. 11.** Vorticity contours for a non-rotating splitter plate  $L/D=0.5$ . (a)  $U/Df_0 = 3.0$ ; (b)  $U/Df_0 = 5.0$ ; (c)  $U/Df_0 = 7.3$ . (For interpretation of the references to color in this figure legend, the reader is referred to the web version of this article.)

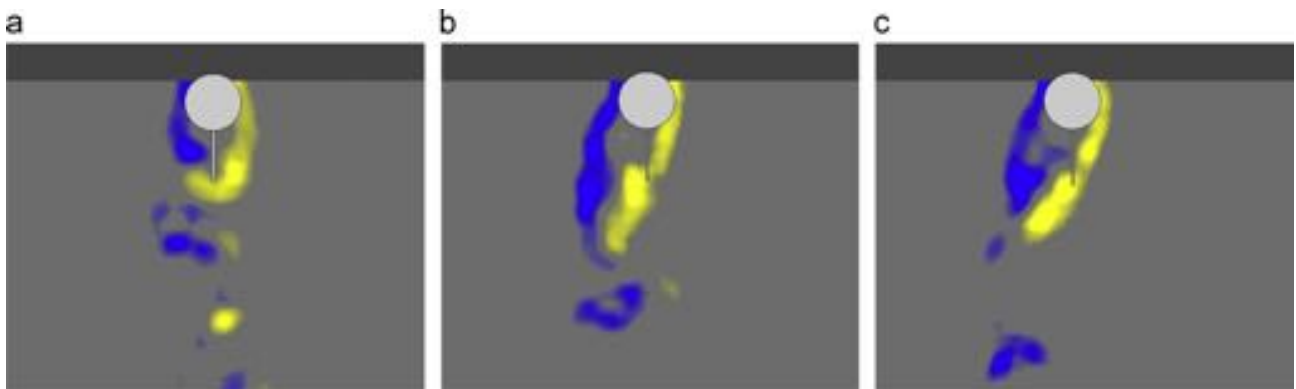


**Fig. 12.** Vorticity contours for a non-rotating splitter plate  $L/D=1.0$ . (a)  $U/Df_0 = 3.0$ ; (b)  $U/Df_0 = 5.0$ ; (c)  $U/Df_0 = 7.3$ . (For interpretation of the references to color in this figure legend, the reader is referred to the web version of this article.)

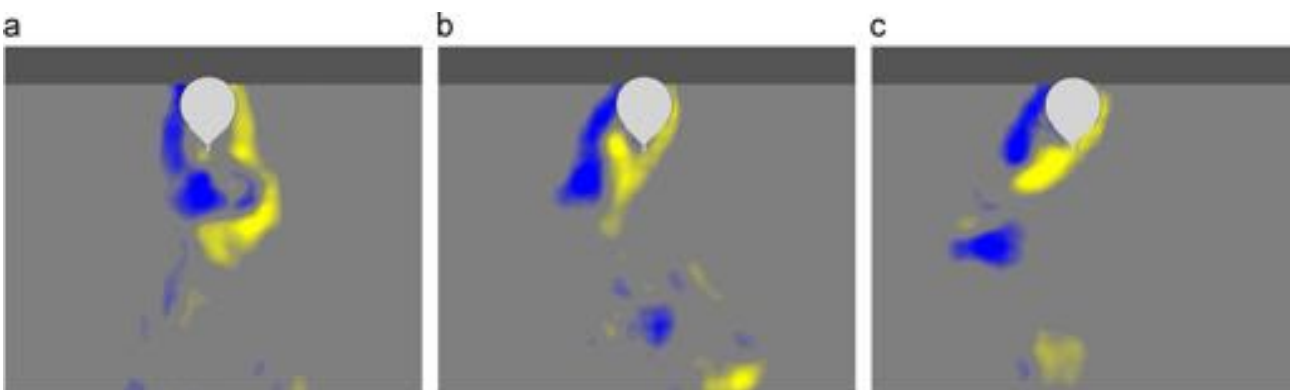


**Fig. 13.** Vorticity contours for a non-rotating short-tail fairing. (a)  $U/Df_0 = 3.0$ ; (b)  $U/Df_0 = 5.0$ ; (c)  $U/Df_0 = 7.3$ . (For interpretation of the references to color in this figure legend, the reader is referred to the web version of this article.)

rotary friction, thus altering the stability of the system. Although fairings are being used to suppress VIV in practical offshore applications, our results show that a non-rotating fairing (for example, a fairing that got stuck) can cause severe galloping over a considerable range of flow speeds.

## 5. Conclusions

Following this study we have achieved a better understanding of the hydroelastic principles behind the way short-tail fairings work to reduce VIV. It appears that the short-tail fairing behaves in a similar manner to a single splitter plate of equivalent characteristic length.

Although the critical value of rotational friction has not been determined for a short-tail fairing, our results suggest that a critical value exists between the low and the high friction cases presented here. It seems likely that different suppressors might have different stability boundaries for rotational resistance, but there is clearly a range of  $\tau_f$  within which VIV suppression would be achieved with short-tail fairings.

Short-tail fairings with a characteristic length of  $0.5D$  proved to reduce amplitude levels (at the expense of a mean transverse force) but were not as efficient as other longer suppressors reported in Assi et al. (2009). Rather than reducing drag for the entire range of reduced velocities tested, the fairing increased it for certain velocities. As a result, the average drag has a similar level to that of a plain fixed cylinder, offering a slight reduction of 6% throughout the Reynolds number range.

Non-rotating splitter plates produced severe galloping response in 1-dof, reaching the limiting amplitude for the apparatus ( $\hat{y}/D = 2$ ) at reduced velocity 10. The non-rotating short-tail fairing presented similar behaviour, but an abrupt decrease in the response was observed for reduced velocity 14. PIV measurements revealed the behaviour of the flow inducing the galloping instability.

As with all circular cylinder flows, undoubtedly Reynolds number plays a role and hence some caution may need to be exercised in extrapolating the results presented here to full-scale risers. However, the underlying flow physics is not expected to change and the devices described in this study are likely to be effective at suppressing VIV when applied to full-scale risers.

## Acknowledgements

The authors wish to acknowledge the support of BP Exploration Operating Company and BP America Production Company. GRSA is

grateful to the support of CAPES Brazilian Ministry of Education (2668-04-1) at the time of the experiments and acknowledges the support of FAPESP (2013/07335-8) and CNPq (308916/2012-3) that allowed him the time to revisit the data and prepare this paper.

## References

- Allen, D.W., Henning, D., May 1995. Small fixed teardrop fairings for vortex induced vibration suppression. United States Patent (number 5,410,979).
- Assi, G.R.S., Bearman, P.W., Carmo, B., Meneghini, J., Sherwin, S., Willden, R., 2013a. The role of wake stiffness on the wake-induced vibration of the downstream cylinder of a tandem pair. *J. Fluid Mech.* 718, 210–245.
- Assi, G.R.S., Bearman, P.W., Kitney, N., 2009. Low drag solutions for suppressing vortex-induced vibration of circular cylinders. *J. Fluids Struct.* 25, 666–675.
- Assi, G.R.S., Bearman, P.W., Kitney, N., Tognarelli, M., 2010a. Suppression of wake-induced vibration of tandem cylinders with free-to-rotate control plates. *J. Fluids Struct.* 26, 1045–1057.
- Assi, G.R.S., Bearman, P.W., Meneghini, J., 2010b. On the wake-induced vibration of tandem circular cylinders: the vortex interaction excitation mechanism. *J. Fluid Mech.* 661, 365–401.
- Assi, G.R.S., Franco, G.S., 2013. Experimental investigation on the stability of parallel and oblique plates as suppressors of vortex-induced vibration. In: *Proceedings of OMAE2013, Thirty-second International Conference on Ocean, Offshore and Arctic Engineering*, 2013, Nantes, France.
- Assi, G.R.S., Franco, G.S., Vestri, M.S., 2013b. Instability and Control of Massively Separated Flows. Springer (Ch. Notes on the stability of free-to-rotate plates suppressing the vortex-induced vibration of a circular cylinder).
- Assi, G.R.S., Rodrigues, J., Freire, C., 2012. The effect of plate length on the behaviour of free-to-rotate VIV suppressors with parallel plates. In: *Proceedings of OMAE2012, Thirty-first International Conference on Ocean, Offshore and Arctic Engineering*, Rio de Janeiro, Brazil.
- Brankovic, M., 2004. Vortex-induced Vibration Attenuation of Circular Cylinders with Low Mass and Damping (Ph.D. thesis). Imperial College, London, UK.
- Cimbala, J., Garg, S., 1991. Flow in the wake of a freely rotatable cylinder with splitter plate. *AIAA J.* 29, 1001–1003.
- Dahl, J., Hover, F., Triantafyllou, M., 2006. Two-degree-of-freedom vortex-induced vibrations using a force assisted apparatus. *J. Fluids Struct.* 22, 807–818.
- Every, M., King, R., Weaver, D., 1982. Vortex-excited vibrations of cylinders and cables and their suppression. *Ocean Eng.* 9 (2), 135–157.
- Henderson, J., 1978. Some towing problems with faired cables. *Ocean Eng.* 5, 105–125.
- Jauvtis, N., Williamson, C.H.K., 2004. The effect of two degrees of freedom on vortex-induced vibration at low mass and damping. *J. Fluid Mech.* 509, 23–62.
- Packwood, A., 1990. Performance of segmented swept and unswept cable fairings at low Reynolds numbers. *Ocean Eng.* 17, 393–407.
- Pontaza, J., Chen, H., 2006. Numerical simulations of circular cylinders outfitted with vortex-induced vibrations suppressors. In: *ISOPE Int. Soc. Offshore and Polar Eng.*
- Stappenbelt, B., 2010. Splitter-plate wake stabilisation and low aspect ratio cylinder flow-induced vibration mitigation. *Int. J. Offshore Polar Eng.* 20 (3), 1–6.
- Williamson, C.H.K., Govardhan, R., 2004. Vortex-induced vibrations. *Annu. Rev. Fluid Mech.* 36, 413–455.
- Wingham, P., 1983. Comparative steady state deep towing performance of bare and faired cable systems. *Ocean Eng.* 10, 1–32.
- Zdravkovich, M.M., 1981. Review and classification of various aerodynamic and hydrodynamic means for suppressing vortex shedding. *J. Wind Eng. Ind. Aerodyn.* 7, 145–189.





Contents lists available at ScienceDirect

## Journal of Fluids and Structures

journal homepage: [www.elsevier.com/locate/jfs](http://www.elsevier.com/locate/jfs)

# Transverse galloping of circular cylinders fitted with solid and slotted splitter plates

Gustavo R.S. Assi<sup>a,\*</sup>, Peter W. Bearman<sup>b</sup><sup>a</sup> Dept. of Naval Arch. & Ocean Eng., University of São Paulo, São Paulo, Brazil<sup>b</sup> Department of Aeronautics, Imperial College, London, UK

## ARTICLE INFO

## Article history:

Received 8 May 2014

Accepted 1 November 2014

Available online 6 December 2014

## Keywords:

Flow-induced vibration

Galloping

Circular cylinder

Splitter plate

## ABSTRACT

The galloping response of a circular cylinder fitted with three different splitter plates and free to oscillate transverse to a free stream has been investigated considering variations in plate length and plate porosity. Models were mounted in a low mass and damping elastic system and experiments have been carried out in a recirculating water channel in the Reynolds number range of 1500 to 16 000. Solid splitter plates of 0.5 and 1.0 diameter in length are shown to produce severe galloping responses, reaching displacements of 1.8 diameters in amplitude at a reduced velocity of around 8. Fitting a slotted plate with a porosity ratio of 30% also caused considerable vibration, but with a reduced rate of increase with flow speed. All results are compared with the typical vortex-induced vibration response of a plain cylinder. Force decomposition in relation to the body velocity and acceleration indicates that a galloping mechanism is responsible for extracting energy from the flow and driving the oscillations. Visualisation of the flow field around the devices performed with PIV reveal that the reattachment of the free shear layers on the tip of the plates is the hydrodynamic mechanism driving the excitation.

© 2014 Elsevier Ltd. All rights reserved.

## 1. Introduction

The study of bluff bodies fitted directly with splitter plates or in the presence of splitter plates is not new. Experiments performed by Roshko (1954), Bearman (1965) and Gerrard (1966) with a variety of bluff bodies report significant changes in base pressure, vortex formation length and Strouhal number depending on the length of a splitter plate and the distance it is positioned downstream of the body. From the attenuation of vibration of offshore risers to the reduction of noise from an aeroplane's landing gear, previous studies are mainly concerned with the suppression of vortex shedding.

The present investigation was motivated by the use of a splitter plate as a means to suppress vortex-induced vibration (VIV) of offshore risers, which are characterised by highly flexible pipes with relatively low mass and damping susceptible to excitation by ocean currents. In contrast, if the purpose is to enhance vibrations of a low mass-damping system (Chang et al., 2011, for example), the addition of splitter plates may produce considerable improvement in the response for the same range of flow speeds. Cylinders with splitter plates or fitted with other devices prone to galloping may be useful if employed to harvest energy from the flow.

\* Correspondence to: NDF Research Group – Dept. Eng. Naval e Oceânica, Escola Politécnica da Universidade de São Paulo, Av. Prof Mello Moraes 2231, 05508-030, São Paulo – SP, Brazil.

E-mail address: [g.assi@usp.br](mailto:g.assi@usp.br) (G.R.S. Assi).

URL: <http://www.ndf.poli.usp.br> (G.R.S. Assi).

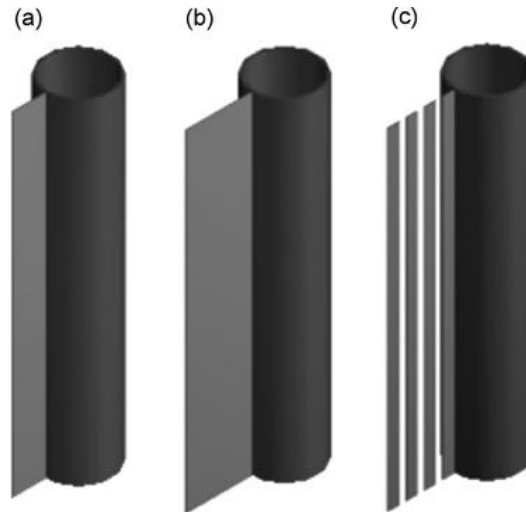


Fig. 1. Representation of tested devices: (a) solid splitter plate  $L/D=0.5$ , (b) solid splitter plate  $L/D=1.0$  and (c) slotted splitter plate  $L/D=1.0$ .

It is known that if vortex shedding from a fixed cylinder is eliminated, say by the use of a long splitter plate (Cimbala and Garg, 1991), then drag is reduced. Hence conceptually an effective VIV suppression device should be able to reduce drag rather than increase it. Assi et al. (2009) have shown that suppression of cross-flow and streamwise VIV of a circular cylinder, with resulting drag coefficients less than that for a fixed plain cylinder, can be achieved using two-dimensional control plates in low mass-damping systems. A free-to-rotate splitter plate was found to suppress VIV, but instead of remaining aligned with the flow on the centreline of the wake the plate adopted a stable but deflected position when it was released. Cimbala and Garg (1991) had also observed such a bi-stable behaviour of the plate for a free-to-rotate cylinder fitted with a splitter plate.

Successful VIV suppression has been achieved with splitter plates for systems with one and two degrees of freedom as reported by Assi et al. (2009, 2010a). In their experiments the plate was free to rotate to allow for the device to realign itself with the incoming flow, thus producing an omni-directional suppressor. However, when non-rotating splitter plates (among other devices) were investigated it was found that they induced the system into severe galloping-type responses instead of suppressing VIV. Although a failure in VIV suppression, we find such behaviour very interesting and worthy of a detailed investigation.

Therefore, the present study will focus on the comparison between the flow-induced vibration (FIV) of a plain circular cylinder and a cylinder fitted with non-rotating splitter plates with different lengths and porosities, as illustrated in Fig. 1.

### 1.1. Classical galloping of non-circular cross sections

The term *galloping* has been generally employed to describe a specific type of FIV mechanism that occurs for bodies moving in one degree of freedom (1-dof) with non-circular cross sections. Comprehensive reviews of the classical theory of galloping have been written by Parkinson (1971, 1989), Blevins (1990), Naudascher and Rockwell (1994) and Paidoussis et al. (2011). Classical galloping of non-circular cylinders (the square section being the classic example) is caused by a fluid-dynamic instability of the cross section of the body such that the motion of the structure generates forces which increase the amplitude of vibration (Bearman et al., 1987).

We will argue that a galloping mechanism similar to that occurring in a square cross-section takes place when an elastically mounted cylinder with a non-rotating splitter plate is placed in an oncoming flow.

If a perturbation displaces the body from rest the relative velocity of the flow will be the vectorial sum of the oncoming flow speed,  $U$ , and the body's velocity,  $\dot{y}$ , defining an angle of incidence,  $\alpha$ , in relation to the free stream. As depicted in Fig. 2, the upper shear layer approaches the body surface whereas the lower shear layer moves away. Depending on plate length and the body's movement, the separated shear layers will tend to reattach to the tip of the plates as the cylinder oscillates. This generates a decrease in pressure on the upper surface and an increase on the lower surface leading to a transverse fluid force,  $F_y$ , acting in the same direction as the motion and causing an increase in the displacement. The stiffness of the spring will eventually act to restore the body back to its original position. When the body reaches its maximum displacement and  $\dot{y}$  then changes direction the process is inverted, though with  $F_y$  still acting in the same direction as  $\dot{y}$ . Therefore, in the classical galloping mechanism the cross-flow fluid force is *in phase* with the body's velocity, acting as a negative damping term in the equation of motion, hence classical galloping is classified as a damping-controlled fluid-elastic mechanism. The magnitude of  $F_y$  increases with  $\alpha$ , which itself increases with  $\dot{y}$ , resulting in a continuous increase in the steady state amplitude of vibration with increasing flow speed.

"For while VIV is typically limited to amplitudes less than  $1D$ , galloping amplitudes can be many times  $D$ " (Parkinson, 1971). Of course a vortex wake will develop further downstream of a square section or a cylinder with splitter plate as in any

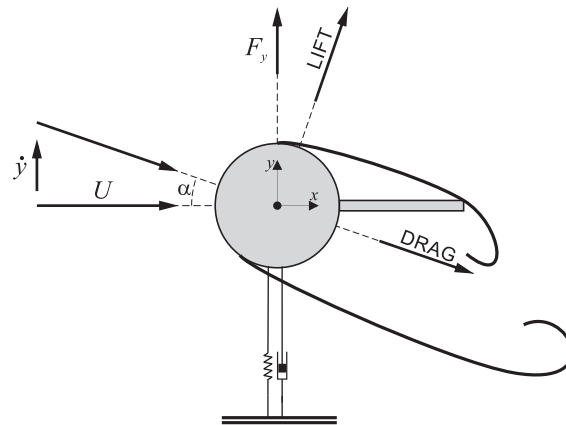


Fig. 2. Proposed sketch of flow and hydrodynamic forces for galloping of a cylinder with splitter plate.

other bluff body, but the galloping instability is not a resonant mechanism that depends on matching values of natural frequency,  $f_0$ , and the vortex shedding frequency,  $f_s$ . For this reason classical galloping allows for modelling with a quasi-steady approach considering that the fluid force on the structure is assumed to be determined solely by the instantaneous relative velocity. “The quasi-steady assumption is valid only if the frequency of periodic components of fluid force, associated with vortex shedding or time-lag effects, is well above the vibration frequency of the structure ( $f_s \gg f_0$ )” (Blevins, 1990). This is generally the case for high values of reduced velocity, defined as the flow speed non-dimensionalised by cylinder diameter and natural frequency. Of course a square section bluff body is also susceptible to VIV at low reduced velocities, however this may be combined with a galloping excitation which will persist for velocities above the resonant range for VIV. “While vortex-induced oscillations occur only in discrete ranges of [flow] speed, galloping will occur at all flow speeds above a critical value determined by the structural damping” (Parkinson, 1971).

Parkinson (1971), referring to den Hartog (1956), presents a simplified quasi-steady analysis that is very useful in predicting the stability of a 1-dof system to classical galloping. The so called ‘galloping stability criterion’ is evaluated by measuring force coefficients on the body for various incidence angles in a steady flow. The reader is encouraged to read Paidoussis et al. (2011) and the above references for further details.

By balancing the negative damping generated by  $F_y$  and the structural damping it is possible to determine the critical reduced velocity for the onset of galloping. Depending on the parameters of mass ratio ( $m^*$ , defined as the ratio of structural mass to the mass of displaced fluid) and damping ( $\zeta$ , calculated as a fraction of critical damping), galloping instability can appear for relatively low reduced velocities, overlapping with the VIV range.

Blevins (1990) writes that “the major limitation of the [classical] galloping theory is that the aerodynamic coefficients are assumed to vary only with angle of attack, but experience shows that the coefficients are affected by turbulence and vortex shedding.” He states that the quasi-steady assumption employed in this analysis requires that the vortex shedding frequency be well above the natural frequency so that “the fluid responds quickly to any structural motion”. Based on experimental works found in the literature he concluded that “the reduced velocity must exceed 20 and the amplitude of vibration should not exceed 0.1 to 0.2D for application of the quasi-steady theory.” This conclusion was also reached by Nakamura et al. (1994). Since this is not the case in the present investigation, the classical galloping criterion will not be verified in the present work.

## 1.2. Previous experiments of cylinders with splitter plates

A few experiments with static cylinders fitted with splitter plates have been performed in the past and could throw some light in the hydrodynamic mechanisms behind this investigation.

Apelt et al. (1973) performed experiments with a static cylinder fitted with a splitter plate of  $L/D \leq 2.0$  (ratio of plate length to the cylinder diameter) in a water tunnel in the range of  $Re = 10^4$  to  $5 \times 10^4$ . They showed that the overall behaviour of the wake can be greatly affected when a splitter plate is placed in the near wake along the centreline. If separation points are stabilised, drag may be considerably reduced and a wake narrower than that for a plain cylinder is produced. They reported that minimum drag and Strouhal number were obtained when  $L/D = 1.0$  and increased for other plate lengths. Later, the work was extended to plates with  $L/D$  between 2 and 7 in the same  $Re$  range (Apelt and West, 1975), with results indicating that no further changes are likely to be produced by lengthening the splitter plates beyond the limits tested. Bluff bodies other than circular cylinders have also been considered by Apelt and West (1975).

Unal and Rockwell (1987) performed experiments in the range of  $Re = 140$  to 3600 to investigate the control of the wake by the proximity of a splitter plate to the bluff body. The length of the plate was many times the diameter ( $L/D = 24$ ), yielding only the gap between the cylinder and the plate as the governing parameter. The plate was not attached to the cylinder nor was the system free to respond with flow-induced vibrations, however this fine experiment clearly illustrated the sensitivity of the vortex formation mechanism to the interference of a plate positioned downstream of the near wake.

Suppressors that are free to rotate about the cylinder have the advantage of being omnidirectional, realigning their orientation as flow direction changes. They mitigate vibrations and reduce drag if a stable configuration is found. Particle-image velocimetry (PIV) measurements from Assi et al. (2009) showed that the shear layer separated from the cylinder appeared to attach to the tip of the plate on the same side to which the plate had deflected and this had the effect of stabilising the near-wake flow. Vortex shedding was visible downstream but this did not feed back to cause vibrations. An unwanted effect was the appearance of a steady transverse force on the cylinder towards the side to which the splitter plate had deflected. This steady lift could be eliminated by using a pair of splitter plates arranged so that the shear layers springing from both sides of the cylinder could attach to the tips of both plates. However, it is known that free-to-rotate splitter plates may experience hydrodynamic instabilities that will not only cause a substantial increase in drag but also prevent them from suppressing vibrations (Assi et al., 2009). Actually, an unstable free-to-rotate suppressor may induce the structure into very vigorous vibrations excited by a type of flutter mechanism. Assi et al. (2009, 2011) have shown that the instability of free-to-rotate suppressors is directly related to the level of rotational resistance encountered in the system as well as geometric parameters such as plate length. “Devices with rotational friction below a critical value oscillate themselves as the cylinder vibrates, sometimes increasing the amplitude of cylinder oscillation higher than that for a plain cylinder”. On the other hand, if the rotational resistance is above a limiting threshold the suppressor cannot rotate and an undesired galloping response is initiated.

Free vibration experiments performed by Stappenbelt (2010) for a low aspect ratio cylinder fitted with splitter plates with  $L/D \leq 4$  registered galloping response for a reduced velocity range between 3 and 60. For small  $L/D$  the response of the cylinder appeared to be strongly influenced by vortex shedding and an abrupt decrease in the galloping response occurred at higher reduced velocities. With increasing plate length “there appears to be a smooth transition from pure VIV to a galloping-type response heavily influenced by the vortex shedding at low reduced velocity and a predominantly galloping response at high reduced velocity”. This is in agreement with experiments with splitter plates and other suppressors reported in Assi et al. (2011, 2014).

Nakamura et al. (1994) experimented with spring supported circular cylinders fitted with long splitter plates from  $L/D = 4.2$  to 31.3 in the range of  $Re = 0.6 \times 10^4$  to  $4.2 \times 10^4$  to show that plate length had a significant effect on the galloping instability. Plots of response amplitude versus reduced velocity were not obtained since they were more concerned with the onset of galloping by measuring small amplitudes and the growth rate of oscillation. Nevertheless, they highlighted the inapplicability of the quasi-steady theory of classical galloping to a cylinder fitted with a long splitter plate. Plotting static force coefficients versus incidence angle they found that  $L/D = 20.8$  produced a stable system. This was very different from the unstable behaviour observed during free vibration experiments. For a splitter plate with  $L/D = 4.2$  they found a stable system according to the galloping criterion, but still the classical quasi-steady theory could not predict the correct velocity for the onset of galloping. Similar results have been observed for a rectangular cylinder reported in Nakamura et al. (1991). Both papers together conclude that bluff bodies, with or without sharp edges, may gallop in the presence of a splitter plate.

In the present work we are concerned with the flow-induced response of cylinders fitted with much shorter plates of around  $L/D = 1$ . This is the characteristic length for a device that could be employed in the suppression of flow-induced vibration of offshore structures, for example.

## 2. Experimental arrangement

Experiments were performed in the Department of Aeronautics at Imperial College using a recirculating water channel with a free surface and a test section 0.6 m wide, 0.7 m deep and 8.0 m long. Flow speed was continuously variable up to  $U = 0.6$  m/s and free stream turbulence intensity across the section was around 3%. Circular cylinder models were made from a 50 mm diameter acrylic tube, giving a maximum  $Re = 30\,000$ , based on cylinder diameter  $D$ . With a wet-length of 650 mm

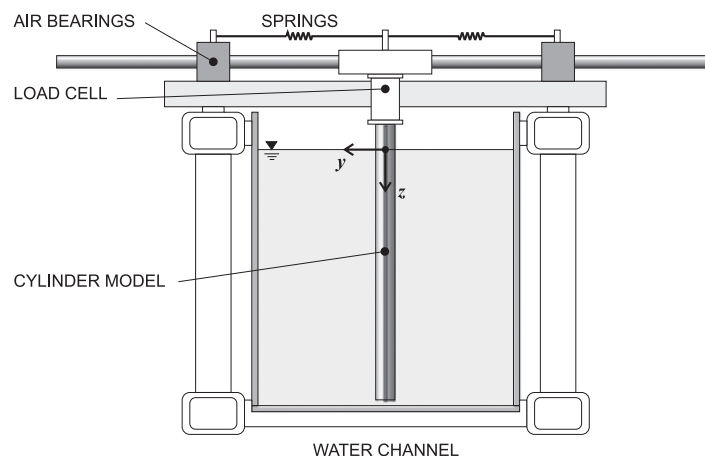
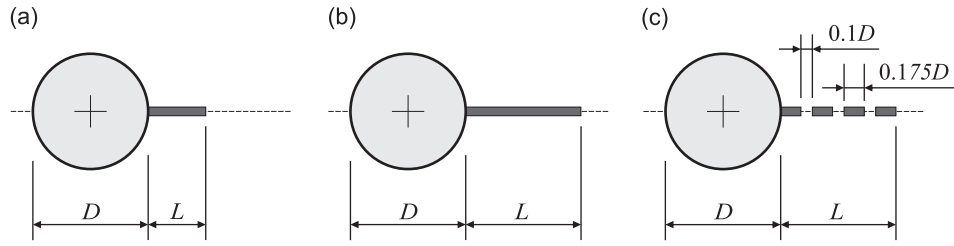
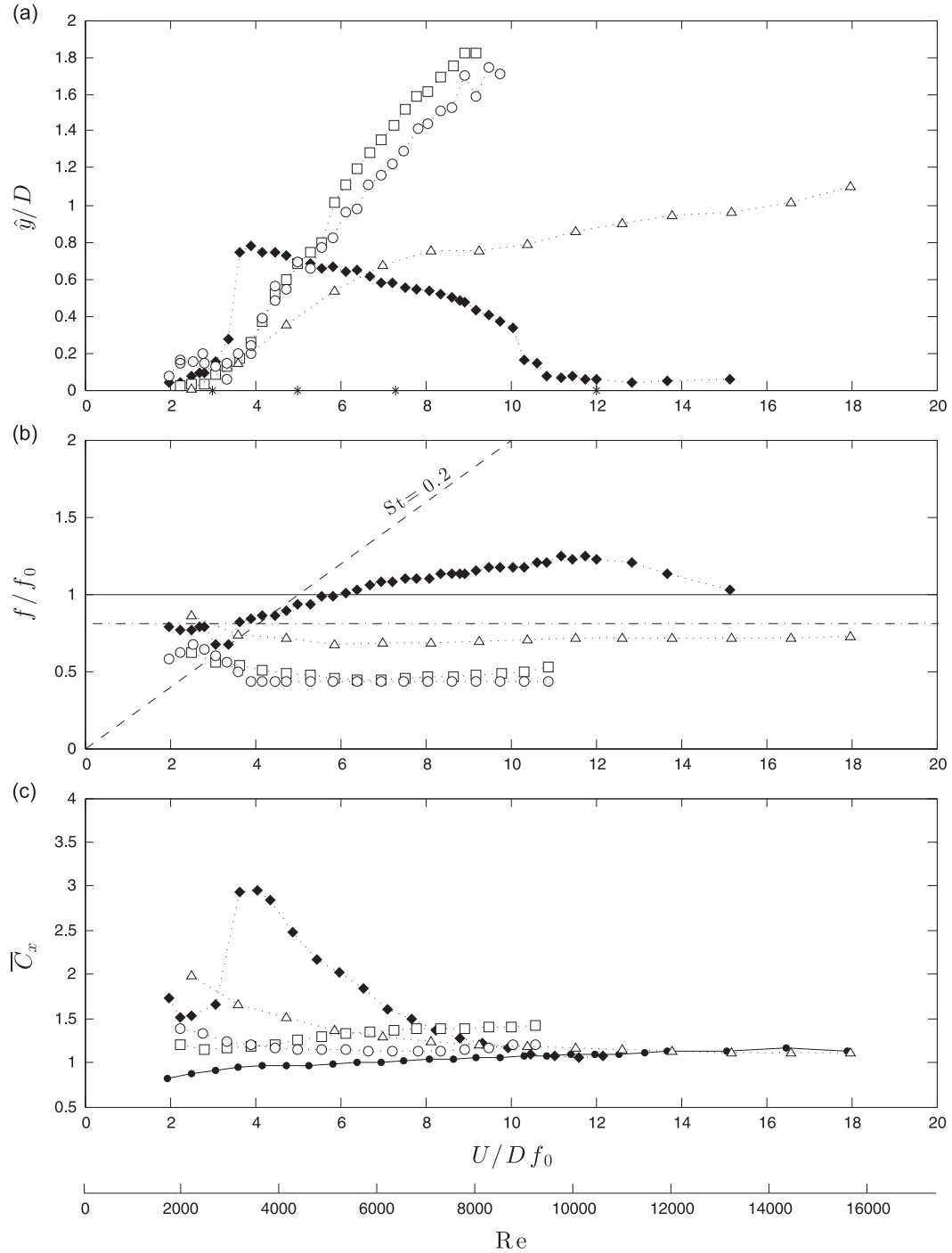


Fig. 3. Representation of the cylinder fitted with a splitter plate mounted on the 1-dof rig in the test section of the water channel. View of the cross-section.



**Fig. 4.** Geometric parameters of tested devices: (a) solid splitter plate  $L/D=0.5$ , (b) solid splitter plate  $L/D=1.0$  and (c) slotted splitter plate  $L/D=1.0$ .



**Fig. 5.** Galloping response of cylinder fitted with non-rotating devices. (a) Displacement, (b) frequency and (c) mean drag coefficient versus reduced velocity. Key:  $\bullet$  static cylinder,  $\diamond$  plain cylinder VIV,  $\square$  solid splitter plate  $L/D=0.5$ ,  $\circ$  solid splitter plate  $L/D=1.0$ ,  $\triangle$  slotted plate  $L/D=1.0$ .



(total length below water level), the resulting aspect ratio of the model was 13. The cylinder was fixed at its upper end to a 1-dof (degree of freedom) elastic mounting represented in Fig. 3. The model was aligned in the vertical direction passing through the free surface and mounted such that there was a 2 mm gap between the lower end of the cylinder and the glass floor of the test section. It was judged preferable not to install end plates on the cylinder in order not to increase the fluid damping in the system. The support was firmly attached to the channel structure and sliding cylindrical guides were free to move in the transverse direction ( $y$ -axis) through air bearings. A pair of coil springs connecting the moving base to the fixed supports provided the restoration force for the system. The present setup has already been employed and validated in previous experiments (Assi et al., 2010a, 2010b, 2013; Assi, 2014a, 2014b).

It is known that the dynamic response of a cylinder is extremely sensitive to the structural characteristics of the system, so extra care was taken to determine the precise values of natural frequency, mass and damping of the structure. All moving parts of the elastic base contributed to the effective mass oscillating with the cylinder, resulting in a mass ratio of  $m^* = 2.6$  (calculated as the total mass divided by the mass of displaced water). The air bearings proved to be an effective way to reduce damping without compromising the stiffness of the structure, especially in resisting drag loads for higher flow speeds. By carrying out free decay tests in air it was also possible to estimate the structural damping of the system resulting in  $\zeta = 0.7\%$ , calculated as a percentage of the critical damping, yielding the product  $m^*\zeta = 0.018$ .

A load cell was installed between the model and the platform to measure hydrodynamic forces acting on the cylinder and an optical positioning sensor measured the  $y$ -displacement without adding damping. A PIV system was employed to map velocity fields. More details about the experimental setup, flow quality, the design of the load cell and operation of the 1-dof rig can be found in Assi (2009).

Measurements were made using one set of springs and the reduced velocity range covered was from  $U/Df_0 = 2$  to 20, where reduced velocity is defined using the cylinder natural frequency of oscillation,  $f_0$ , measured in air. The only flow variable changed during the course of the experiments was  $U$ , which alters both the reduced velocity and Reynolds number. Throughout the study, cylinder displacement amplitudes,  $\hat{y}/D$ , were found by measuring the root mean square value of response and multiplying by  $\sqrt{2}$  (the so called harmonic amplitude). Displacements were nondimensionalised by dividing by  $D$ .

Three splitter plates were built out of acrylic plastic and installed on the cylinder model following the geometric parameters in Fig. 4. Two solid splitter plates with  $L/D = 0.5$  and 1.0, shown in Fig. 4(a) and (b), were employed to evaluate the dependency of the response on plate length. A slotted plate with  $L/D = 1.0$ , shown in Fig. 4(c), was built in order to investigate the effect of plate porosity (or permeability) on the response. Parallel slots were cut out of the plate material creating 0.1D-wide continuous gaps in the vertical direction along the whole span of the cylinder (refer to Fig. 1(c)). The slotted plate presented 70% of the area of a completely solid plate of the same length, thus defining a porosity ratio of 30%. Plates were rigidly attached to the cylinders and aligned with the incoming flow direction, which is from left to right in Fig. 4. Plates were 3 mm thick ( $0.06D$ ) and did not bend with the flow; their installation did not significantly alter  $m^*$ .

### 3. Results and discussion

Preliminary experiments performed with a plain cylinder will serve to serve the experimental setup and as a reference for the discussion that follows. During the typical VIV excitation, as  $U$  increases, the frequency of vortex-shedding,  $f_s$ , gets close enough to  $f_0$  such that the unsteady pressure fluctuations in the near wake induce the body to respond. Once the cylinder starts to oscillate, the vibrations will control the vortex formation process and  $f_s$  becomes *locked in* to the response frequency,  $f$ , near  $f_0$ . If the velocity continues to increase  $f_s$  moves away from  $f_0$  so that vortex shedding becomes uncoupled with the cylinder frequency. Refer to Williamson and Govardhan (2004) for a detailed description of the VIV mechanism and typical responses.

Depending on the mass of the system and the specific mass of the fluid in which the cylinder is immersed, the frequency of oscillation can be significantly influenced by the additional mass of fluid that is accelerated with the body. For this reason, the reduced mass parameter,  $m^*$  is relevant for the response of light cylinders immersed in water and, consequently,  $f_0$  measured in air will be different from the natural frequency in still water,  $f_w$ . As expected, the response of a forced linear oscillator will be inversely proportional to the product of  $m^*$  and  $\zeta$  (Bearman, 1984).

The typical VIV response of a plain cylinder, in terms of amplitude and frequency of oscillation, is presented in Fig. 5 and shows a good agreement with the results reviewed by Williamson and Govardhan (2004). Fig. 5(a) shows the typical resonant response of VIV in the displacement curve, with vibration building up in the synchronisation range between  $U/Df_0 \approx 3.0$  and 11 and a maximum response of  $\hat{y}/D = 0.8$  at  $U/Df_0 \approx 4.0$ . Fig. 5(b) shows the dominant frequency of response,  $f$ , normalised by  $f_0$ . The inclined dashed line represents a Strouhal number of 0.2, approximately equivalent to the vortex shedding frequency for a static cylinder. The horizontal dot-dashed line represents the natural frequency of the system measured in still water ( $f_w/f_0 \approx 0.8$ ). Frequency measurements for  $U/Df_0 > 11$  are kept in the plot but must be treated with caution, since beyond the end of the synchronisation range displacements are very small (below  $\hat{y}/D = 0.1$ ) and the frequency spectrum becomes quite broad. Mean drag coefficient ( $\bar{C}_x$ ) in Fig. 5(c) reveals the amplification of drag normally observed during the synchronisation range for VIV. A curve for the drag of a fixed cylinder (static) has also been added as a reference. Fluid force measurements are in good agreement with the results presented by Khalak and Williamson (1999).



### 3.1. Displacement, frequency and drag

Results for the cylinders fitted with splitter plates are presented together with results for the plain cylinder in Fig. 5. The first distinct difference, when compared against the plain cylinder VIV, is observed in the displacement curves in Fig. 5(a). All cylinders fitted with splitter plates show a continuous increase in response as flow speed is increased. Cylinders with solid splitter plates show a steeper response curve when compared with the slotted plate, but none respond with the resonant behaviour typical of VIV. In fact, the response curves for the two solid splitter plate cases are not very different,

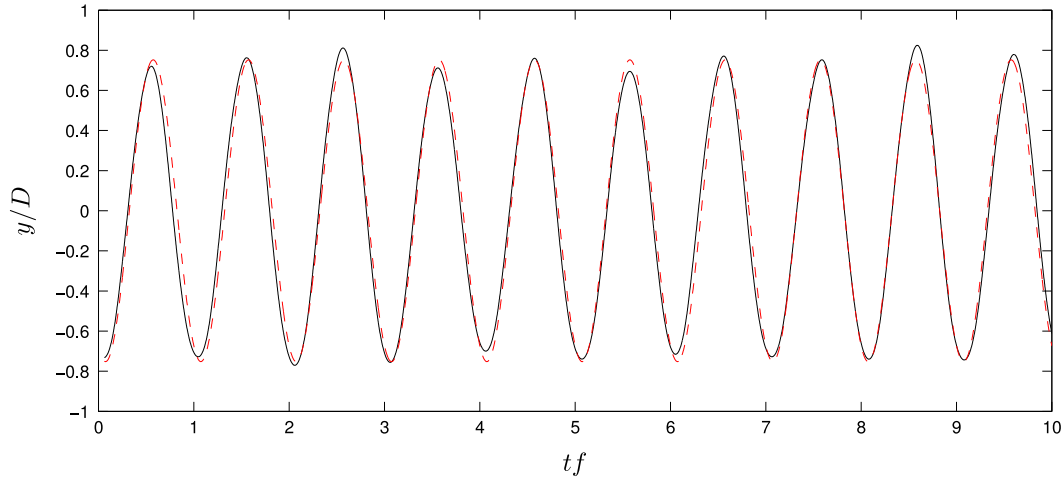


**Fig. 6.** Sample of displacement time series (continuous line) compared with a harmonic curve  $y(t) = \hat{y} \sin(2\pi f t)$  (dashed line) for a cylinder fitted with a solid splitter plate with  $L/D=1.0$  at  $U/Df_0 = 8.1$ .

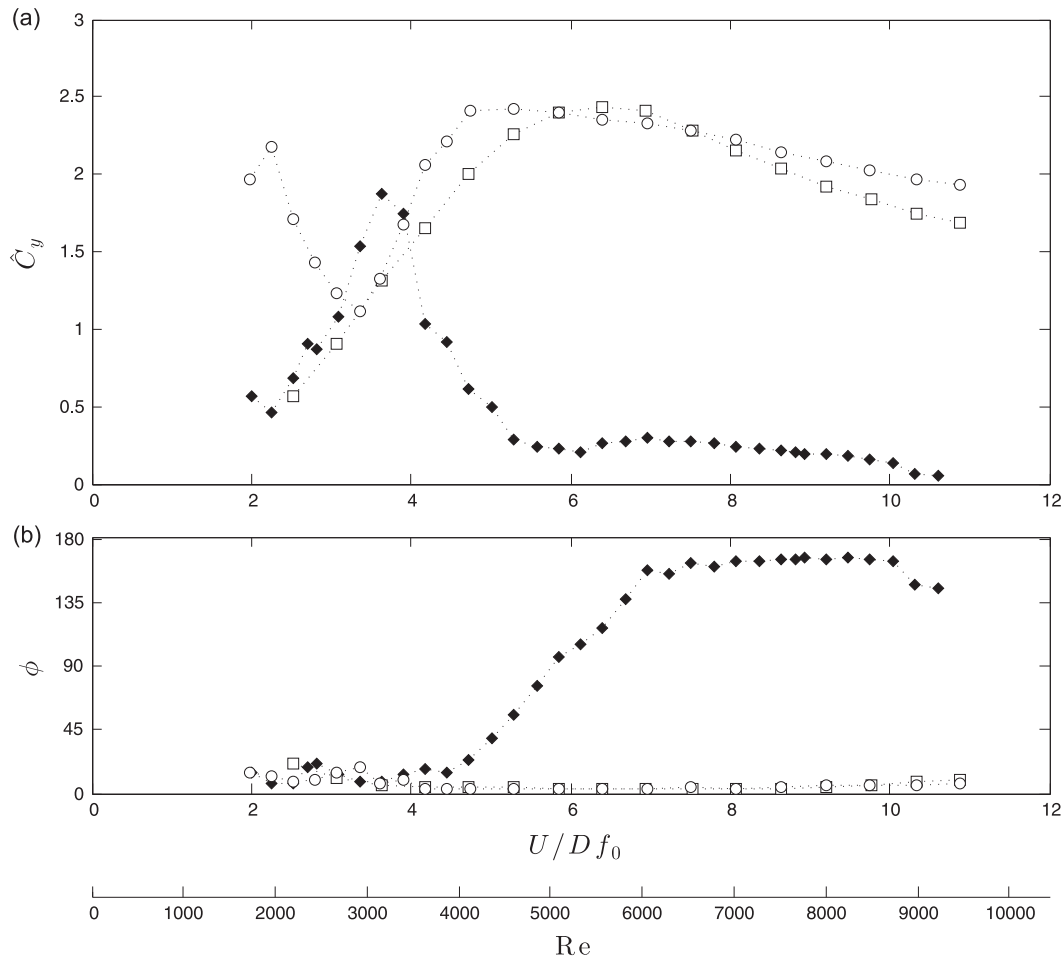


**Fig. 7.** (a) Amplitude of fluctuating lift coefficient and (b) phase angle versus reduced velocity. Key:  $\diamond$  plain cylinder VIV,  $\square$  solid splitter plate  $L/D=0.5$ ,  $\circ$  solid splitter plate  $L/D=1.0$ .

with the  $L/D=1.0$  showing a slightly lower response than the shorter plate. Displacement was physically limited to  $\hat{y}/D=2.0$  by a stop in the rig; this was reached at around a reduced velocity 9 for the solid plates. Two runs have been performed for each solid device to verify repeatability, producing a small scatter in the data points for the highest amplitudes. The response of the slotted plate is qualitatively similar in the sense that no VIV was observed. However, the slope of the response versus reduced velocity is lower than that of the solid plates with  $\hat{y}/D$  monotonically increasing with reduced velocity until  $\hat{y}/D \approx 1.1$  is reached at the highest reduced velocities achieved in the experiments, a reduced velocity of almost 18.

Stappenbelt (2010) presents comparable results covering a wider range of plate lengths between  $L/D=0.34$  and 4.0. He verified that the galloping response for splitter plates with  $L/D < 0.5$  terminated abruptly as reduced velocity was increased. In his investigation the maximum galloping response for  $L/D=0.34, 0.44$  and  $0.5$  was  $\hat{y}/D \approx 1.8, 2.5$  and  $3.4$  achieved for reduced velocities 15, 20 and 30, respectively. Stappenbelt also found that the slope of the initial response was not very different between splitter plates with  $L/D=0.5$  and  $1.0$ . This phenomenon has also been observed by Assi et al. (2014) to be occurring with other VIV suppressors with similar characteristic length.

The frequency responses in Fig. 5(b) also show that the cylinders fitted with splitter plates are not responding with VIV. Apart from a range of  $U/Df_0 < 4$  the dominant frequencies of vibration for all devices are constant and significantly lower than that observed for the plain cylinder. The frequencies do not follow the Strouhal line for the plain cylinder during the typical upper branch of VIV. The solid plates appear to oscillate at more or less the same frequency, which is lower than that of the slotted plate; we shall return to this point later when discussing added mass.

The mean drag curves in Fig. 5(c) show no drag amplification for the cylinders with splitter plates during the equivalent synchronisation range of VIV. Although vibrating with much larger displacements, the splitter plates seem to keep drag below that observed during VIV of a plain cylinder. Results for the solid splitter plates show the same levels of drag as those reported by Stappenbelt (2010). The solid and the slotted plates, both having  $L/D=1.0$ , managed to reduce drag down to  $\bar{C}_x \approx 1.0$  for the whole of the reduced velocity range. It is surprising that such large vibrations present considerably low drag; we shall return to this when discussing force decomposition. Stappenbelt (2010) also reports that drag continues to drop with increasing plate length for solid plates with  $L/D > 1.0$ .

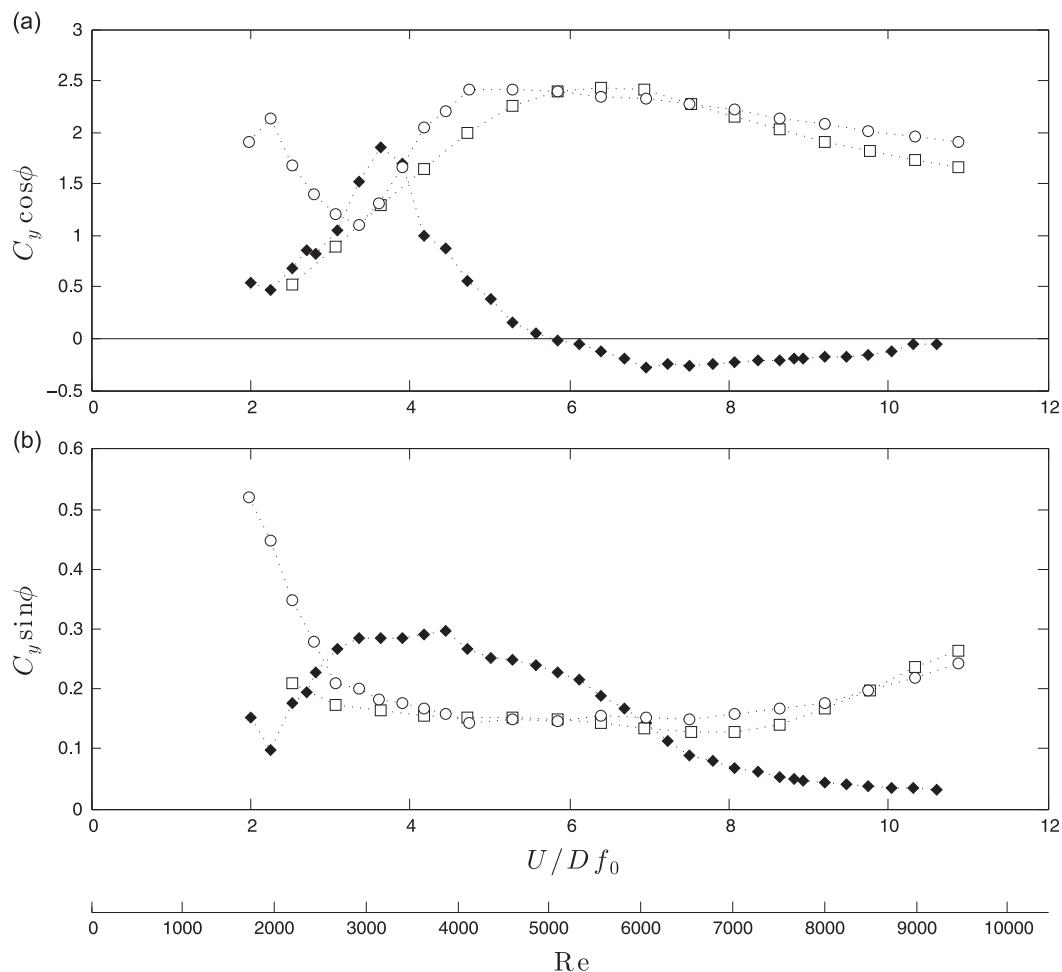


**Fig. 8.** Decomposition of lift coefficient in phase with (a) acceleration and (b) velocity. Key:  $\diamond$  plain cylinder VIV,  $\square$  solid splitter plate  $L/D=0.5$ ,  $\circ$  solid splitter plate  $L/D=1.0$ .

### 3.2. Harmonic motion hypothesis: lift and phase angle

A careful analysis of the data acquired during each run revealed that response of the cylinder is quite well behaved, with a single dominant peak in the frequency spectrum and a fairly constant envelop of displacement. Fig. 6 presents a sample of the time series of displacement for a cylinder fitted with a  $L/D=1.0$  splitter plate at  $U/Df_0=8.1$ . The continuous line represents the recorded displacement of the cylinder over time ( $t$ ), while the dashed line represents a sine function with the corresponding frequency,  $f$ , and amplitude,  $\hat{y}/D$ , determined experimentally. It is clear that the movement of the cylinder can be approximated by such a simple harmonic function; the same was verified to occur for all plate configurations at all reduced velocities. Hence, a harmonic hypothesis for the movement is quite adequate.

Now, following the hypothesis for harmonic forcing and harmonic motion employed by Bearman (1984) and others, cross-flow displacement of the cylinder can be written simply as a sine function of time

$$y(t) = \hat{y} \sin(2\pi ft), \quad (1)$$

where  $\hat{y}$  and  $f$  represent the harmonic amplitude and frequency of oscillation, respectively. The equation of motion for the second order harmonic oscillator is then

$$m\ddot{y} + c\dot{y} + ky = \left[ \bar{C}_y + \hat{C}_y \sin(2\pi ft + \phi) \right] \frac{1}{2} \rho U^2 D, \quad (2)$$

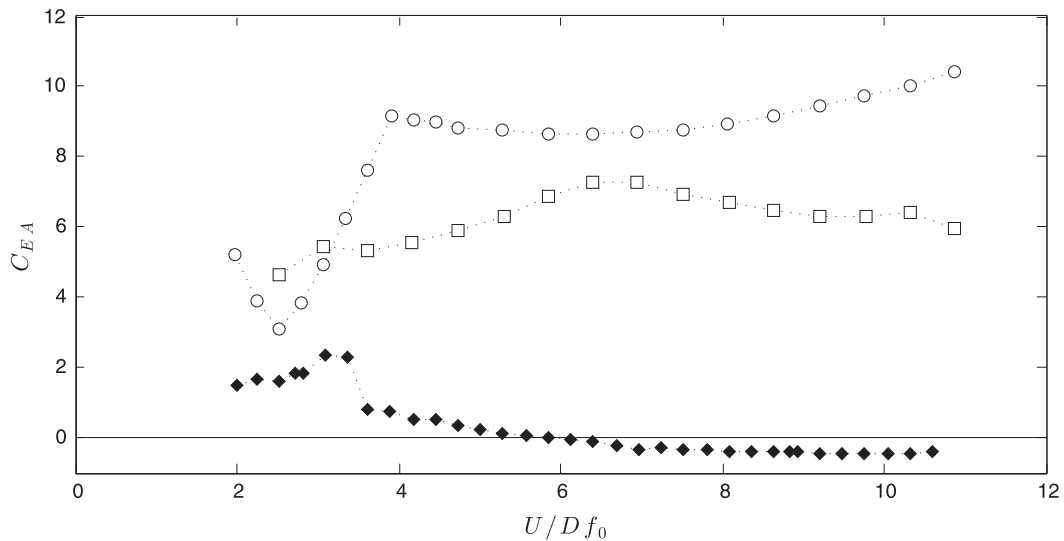


Fig. 9. Coefficient of effective added mass. Key:  $\diamond$  plain cylinder VIV,  $\square$  solid splitter plate  $L/D=0.5$ ,  $\circ$  solid splitter plate  $L/D=1.0$ .

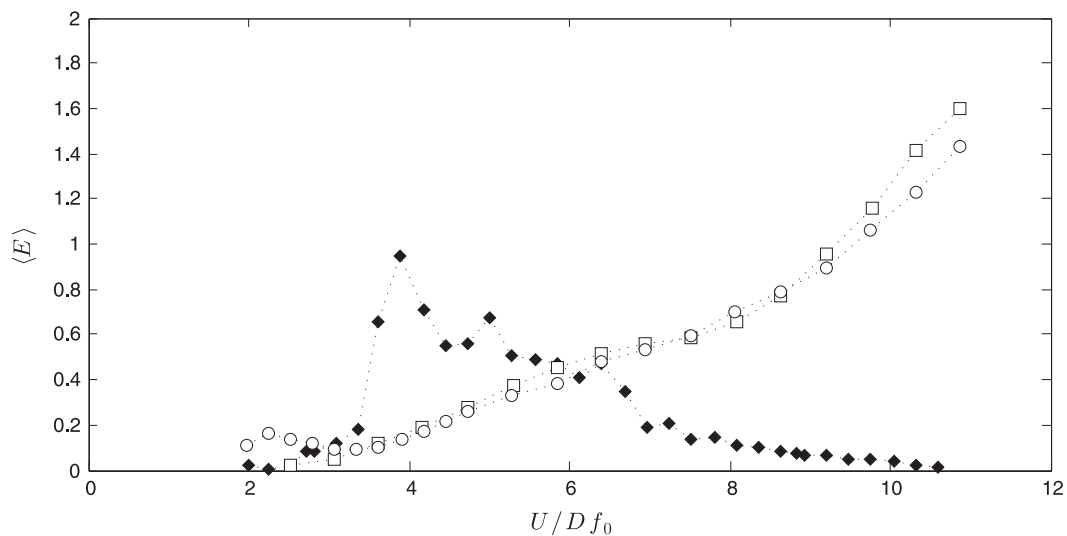
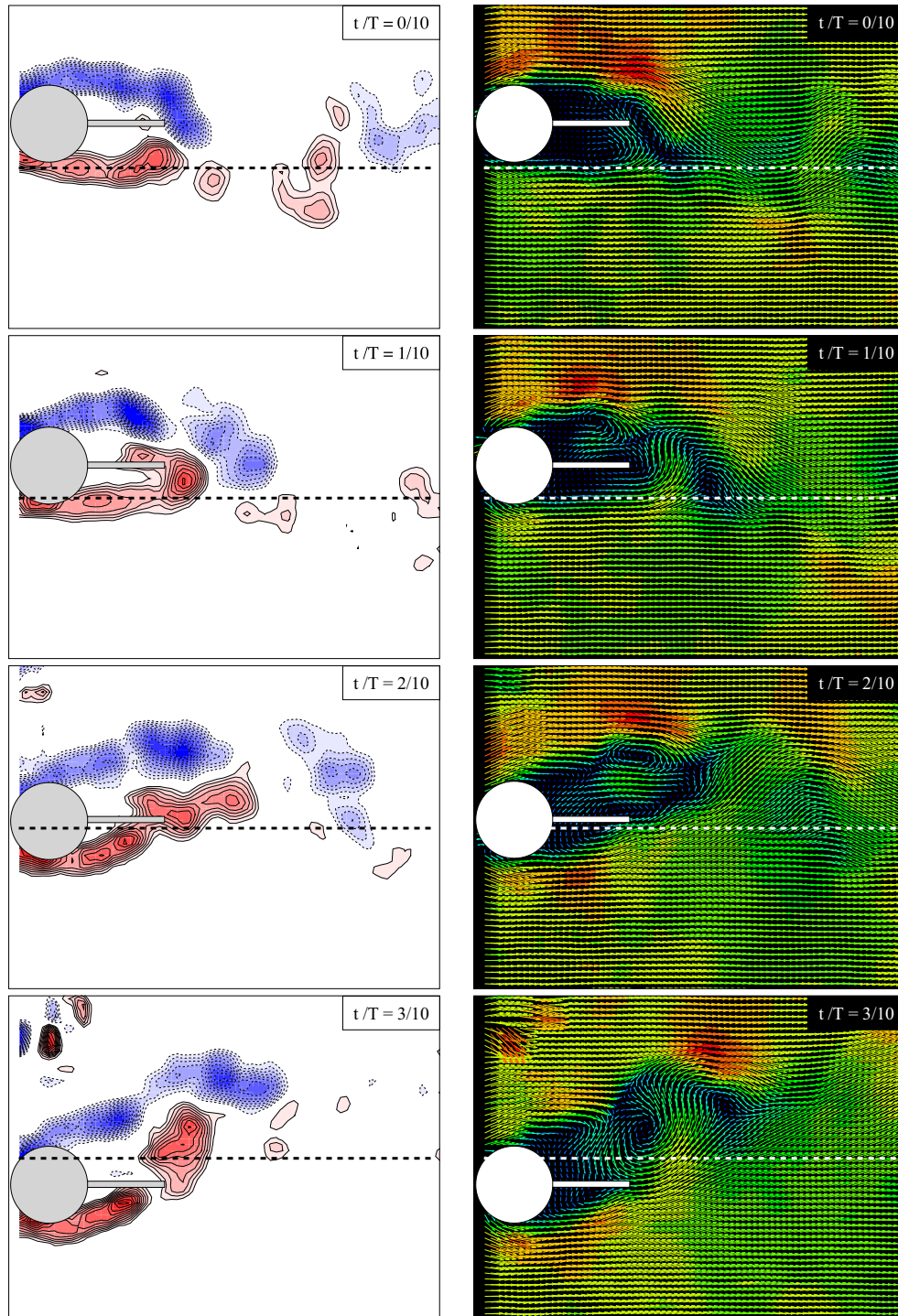


Fig. 10. Energy transferred from the flow to the body during one cycle of oscillation. Key:  $\diamond$  plain cylinder VIV,  $\square$  solid splitter plate  $L/D=0.5$ ,  $\circ$  solid splitter plate  $L/D=1.0$ .

with the respective structural parameters of mass,  $m$ , stiffness,  $k$ , and damping,  $c$ . Displacement,  $y$ , velocity,  $\dot{y}$ , and acceleration,  $\ddot{y}$  of the body and fluid force coefficients are time dependent and all terms are expressed per unit length of the cylinder. The fluid force and the body response oscillate at the same frequency  $f$  under a steady-state regime.

The total fluid force, on the right-hand side of Eq. (2) can then be divided into a time-average term  $\bar{C}_y$  (usually equal to zero for symmetric cross sections) and a transient term modelled as a sine wave with amplitude  $\hat{C}_y$  and frequency  $f$ , with  $\phi$  representing the phase angle between displacement and force. In the present work  $\hat{C}_y$  was determined by taking the r.m.s. of lift and multiplying it by  $\sqrt{2}$ , while  $\phi$  was determined by means of a Hilbert transform applied to the time series of force and displacement, as explained in Khalak and Williamson (1999) and Assi (2009).

For body excitation to occur  $\phi$  must be between  $0^\circ$  and  $180^\circ$ . A phase angle equal to either  $0^\circ$  or  $180^\circ$  means that no energy is transferred from the flow to the structure to excite any vibration. As far as the excitation is concerned, Bearman



**Fig. 11.** Instantaneous fields of (left column) vorticity contours coloured by intensity and (right column) velocity vectors coloured by magnitude during one cycle of oscillation.  $U/Df_0 = 6.4$  and  $Re = 4800$ . A horizontal dashed line represents the centreline of the wake.



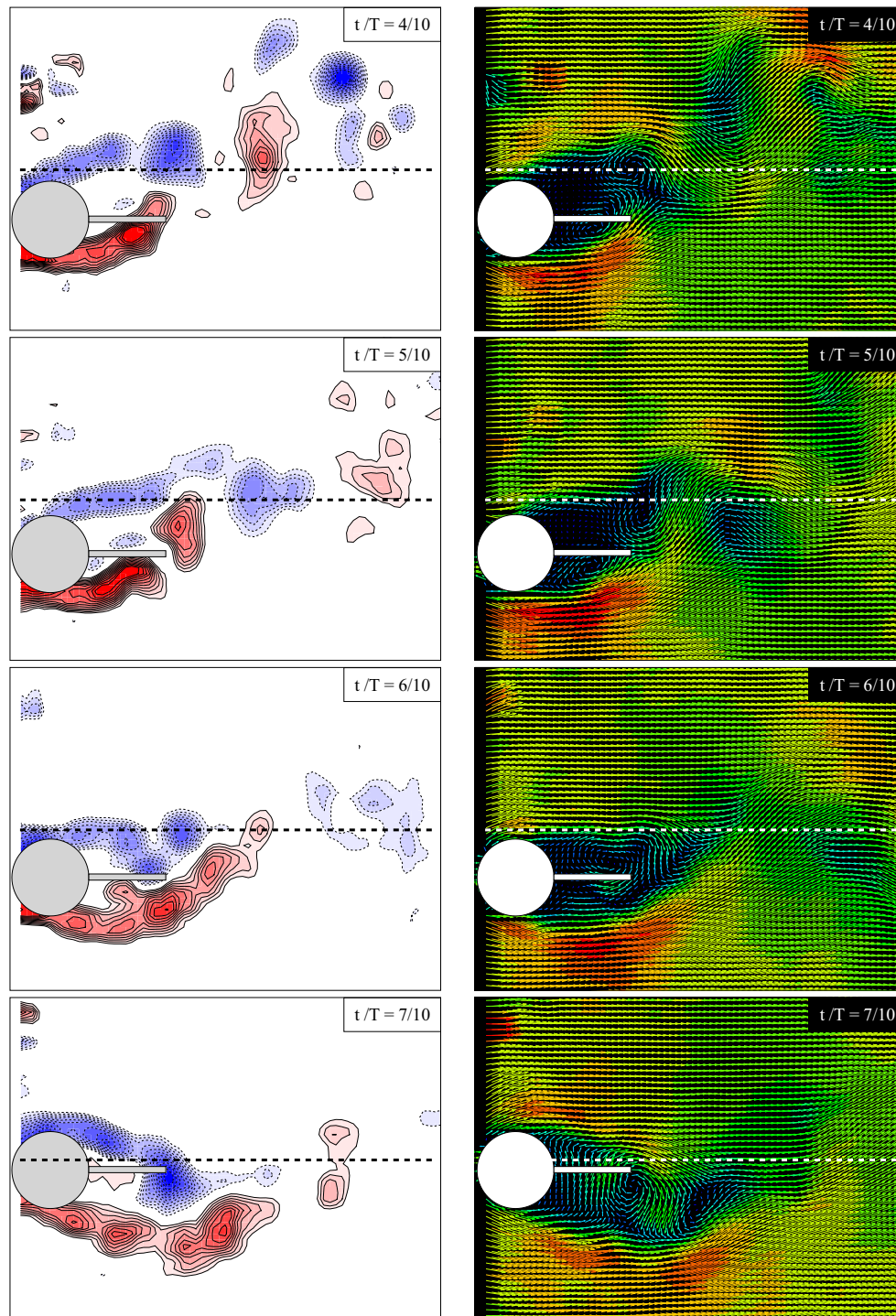


Fig. 11. (continued)

(1984) explains that “it is clear that the phase angle  $\phi$  plays an extremely important role. The amplitude response does not depend on  $\hat{C}_y$  alone but on that part of  $\hat{C}_y$  in phase with the body velocity. Hence, measurements of the sectional fluctuating lift coefficient on a range of stationary bluff-body shapes will give little indication of the likely amplitudes of motion of similar bodies flexibly mounted”. With VIV excitation, when reduced velocity is increased,  $\phi$  shifts from almost  $0^\circ$  to almost  $180^\circ$  as the response passes through resonance. Khalak and Williamson (1999) clearly show, for a plain circular cylinder, how this phase shift is related to different wake modes and transitions between branches of response.

Fig. 7(a) presents results for  $\hat{C}_y$  for the plain cylinder compared with the cylinder fitted with solid splitter plates. During the typical VIV response we notice the plain cylinder experiences a lift amplification close to the peak of resonance (at  $U/Df_0 \approx 4$ ) before a considerable drop in  $\hat{C}_y$  that remains for the rest of the synchronisation range. The cylinders with splitter plates, on the other hand, show a build-up of  $\hat{C}_y$  at low values of reduced velocity, reaching a maximum of  $\hat{C}_y \approx 2.5$  and then reducing slowly for  $U/Df_0 > 6$ . (Note: Uncertainties for force measurements are larger at low Re due to the small

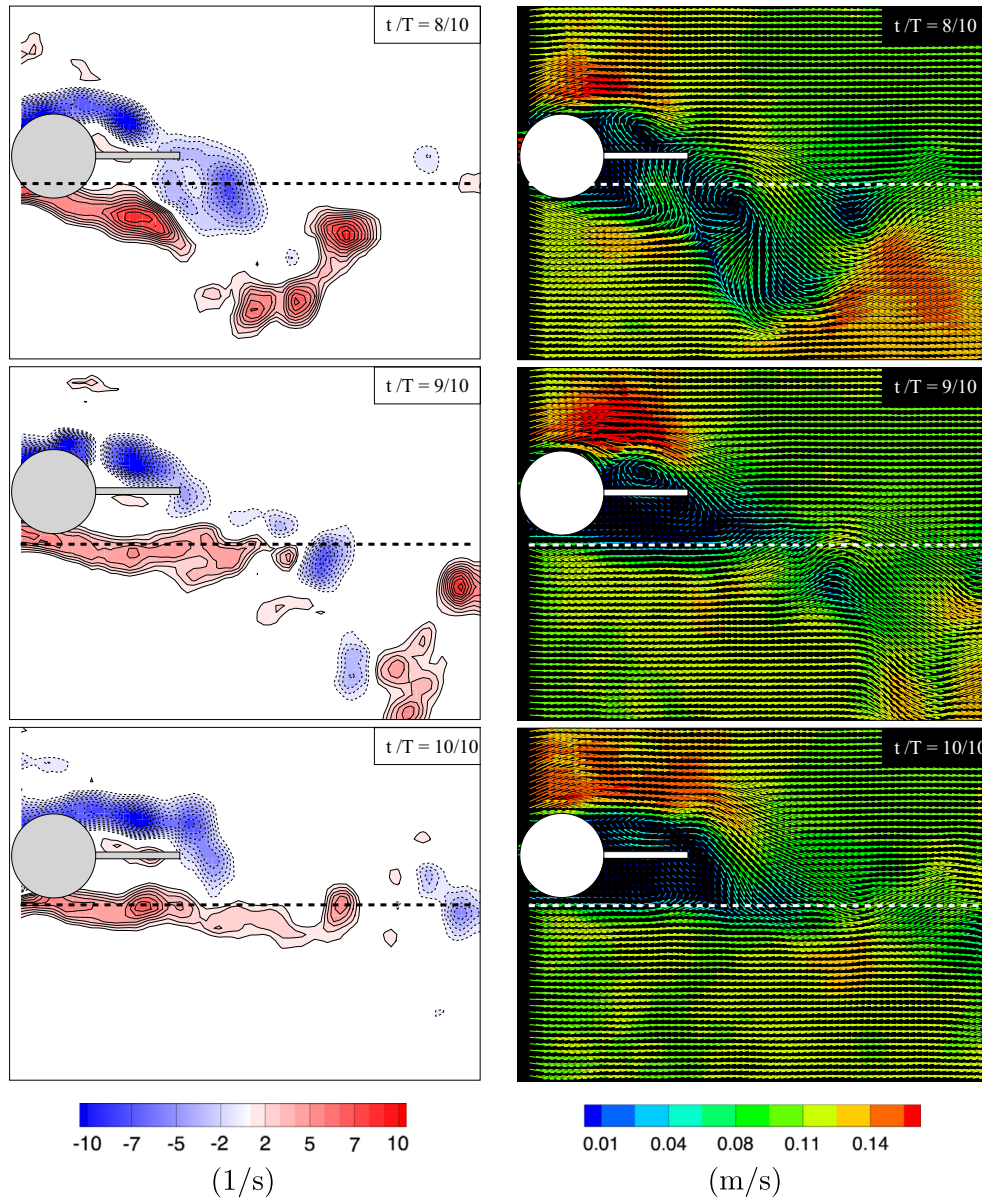


Fig. 11. (continued)

magnitude of measured forces, thus results for  $\hat{C}_y$  and  $\phi$  must be taken with caution for  $U/Df_0 < 3$ . To offer an estimate, uncertainties in  $\hat{C}_y$  vary in approximate bands of: 15% for  $U/Df_0 < 3$ ; 5% for  $3 < U/Df_0 < 6$ ; and 1% for  $U/Df_0 > 6$ .) It is evident that the  $\hat{C}_y$  curve for the resonant mechanism of VIV is qualitatively different from those for the hydrodynamic instability of galloping, but the difference between the phenomena is made clearer from measurements of  $\phi$  presented in Fig. 7(b).

While the resonant response of VIV presents a phase shift of almost  $180^\circ$  when the response crosses the resonance peak (between  $U/Df_0 = 4$  and 7). The galloping response of the solid plates experiences no such shift in  $\phi$ , proving that the excitation mechanism is not of a resonant type. For the solid splitter plates  $C_y$  was not found to be *in phase* with velocity, otherwise  $\phi$  would have been at values close to  $90^\circ$  in Fig. 7. Instead,  $\phi$  remains at low values for the whole of the galloping response range with lift leading the movement of the cylinder by a very small time lag. This small value of  $\phi$ , coupled with high values of  $C_y$ , provides the excitation to overcome the very-low structural damping of the system and induces high-amplitude galloping vibrations.

### 3.3. Added mass and energy transfer

In order to investigate further the system dynamics and the energy transfer from the flow to the body we calculate the components of the fluid lift force in phase with  $\dot{y}$  and in phase with  $\ddot{y}$ . Fig. 8(a) presents  $C_y \cos \phi$ , the portion of the fluid force in phase with acceleration; as discussed in detail by Sarpkaya (2004) this takes the form of inertia and can also be considered as being directly related to the added mass of fluid. For a body subjected to FIV the *effective* added mass will be



different from the potential added mass (equal to the mass of displaced fluid for a circular cross section) or even the measured added mass of a cylinder in still water. For the VIV response of a plain cylinder it is known (Bearman, 1984) that the added mass coefficient will find its maximum at the resonance peak and become negative as the response passes through the synchronisation range as shown in Fig. 8(a). This will have an effect on the frequency response signature of VIV. However,  $C_y \cos \phi$  for the splitter plates shows a different behaviour reaching much higher values and never becoming negative, once more demonstrating the absence of a resonant VIV-type mechanism. Khalak and Williamson (1999), for example, suggested that this effective added mass coefficient can be represented by

$$C_{EA} = \frac{1}{2\pi^3} \frac{C_y \cos \phi}{\hat{y}/D} \left[ \frac{U}{Df} \right]^2, \quad (3)$$

taking into account the reduced velocity, amplitude and frequency of vibration. (Note that Khalak and Williamson (1999) define  $C_{EA}$  with a natural frequency measured in still water, which is cancelled out in the equation above.)

Values of  $C_{EA}$  are presented in Fig. 9. It is clear that the effective added mass coefficients of galloping cylinders with splitter plates are significantly greater than that of a plain cylinder in VIV. The splitter plate with  $L/D=1.0$  presents higher  $C_{EA}$  than the shorter one, and this is consistent with the lower frequencies of response observed for the galloping cylinder with splitter plates in Fig. 5(b).

Fig. 8(b) presents  $C_y \sin \phi$ , the portion of the fluid force in phase with velocity, which gives an idea of the excitation (or energy transfer) in the system. The VIV response exhibits positive values of  $C_y \sin \phi$  during the synchronisation range, again with a maximum value found at the peak of resonance ( $U/Df_0 \approx 4$ ). The galloping responses, on the other hand, show a very different behaviour with a broad minimum around  $U/Df_0 = 5$  and increasing  $C_y \sin \phi$  as reduced velocity is further increased. Based on the theory of second order oscillators, one can present the average non-dimensionalised energy transferred from the flow to the body during one cycle of oscillation,  $\langle E \rangle$ , as

$$\langle E \rangle = \pi \frac{\hat{y}}{D} C_y \sin \phi, \quad (4)$$

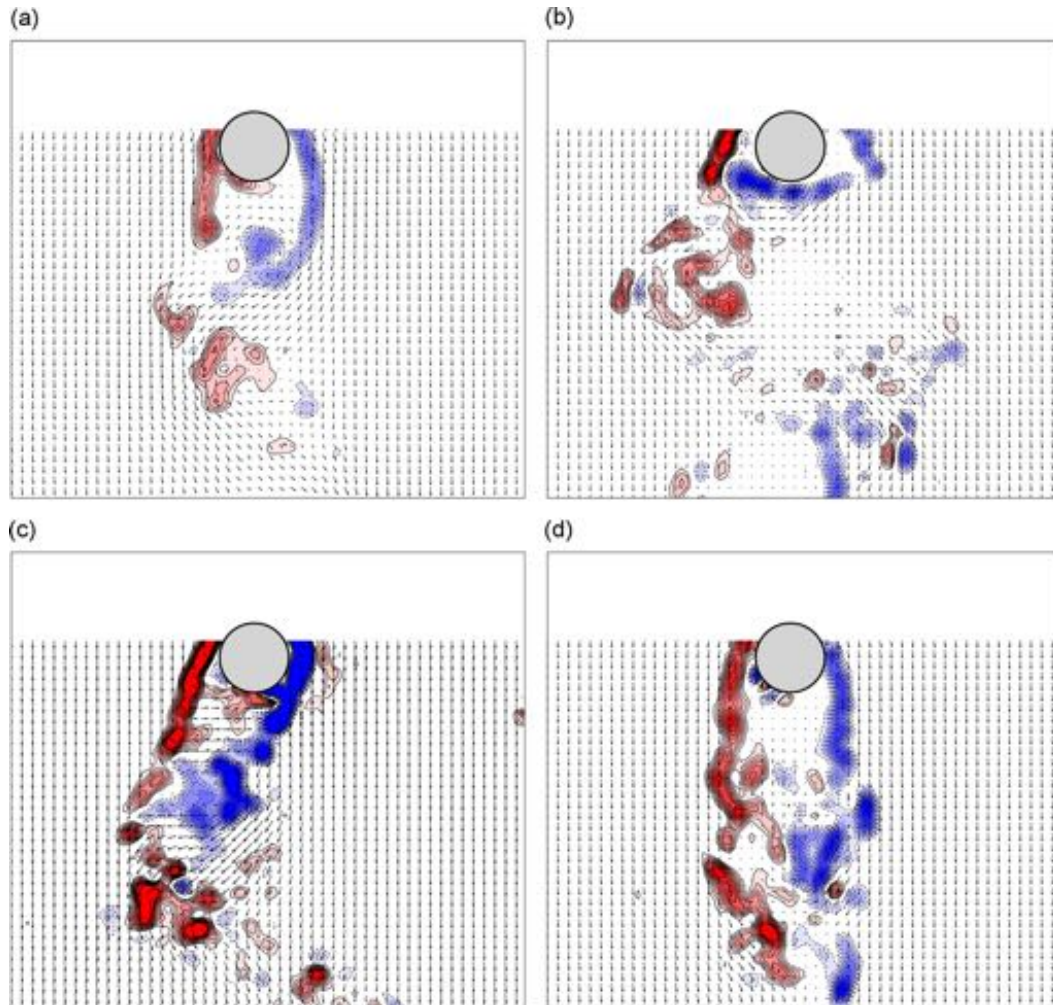


Fig. 12. Instantaneous vorticity contours and velocity vectors for a single cylinder at various reduced velocities: (a)  $U/Df_0 = 3.0$ , (b) 5.0, (c) 7.3 and (d) 12.

i.e. the work done by the non-dimensional hydrodynamic force in phase with velocity ( $C_y \sin \phi$ ) during one cycle of non-dimensional displacement ( $\hat{y}/D$ ). Results for  $\langle E \rangle$  presented in Fig. 10 show that the plain cylinder VIV has its maximum energy transfer during synchronisation, as expected, but for the cylinder with splitter plates the energy transfer builds up as reduced velocity is further increased. It becomes evident that adding the splitter plates to the cylinder produces a much more energetic mechanism for vibration that is not of a resonant kind.

Due to a technical fault  $C_y$  was not measured for the cylinder with a slotted plate. Nevertheless, one may expect that the porosity of the plate will have an effect on the added mass and also the hydrodynamic damping which will influence the hydrodynamic excitation. Theoretically, the ideal-flow added mass coefficient for a slotted plate in still water should fall between values for the short and the long solid plates. The solidity of the plate is also expected to have an effect on flow behaviour in the near wake. Although communication between the shear layers might be inhibited, some flow between the two sides of the near wake is permitted through the slots. The slots on the plate may also help to dissipate energy as the flow is forced to pass through the narrow passages as the body oscillates. Flow visualisations presented in the next section will help to clarify various conjectures regarding the flow with solid and slotted splitter plates. However, the main conclusion is that the galloping response of the slotted plate is different from that of the solid plate of similar length, showing, for a given reduced velocity, lower amplitude of vibration at a higher frequency of oscillation (Fig. 5).

#### 4. Flow field measurements

Measurements of the velocity field by PIV were taken on a horizontal plane at mid-length of the cylinder. The objective was to investigate the separated shear layers reattaching on the splitter plates as the cylinder moved across the flow. First we shall focus on the detailed visualisations of the flow around a solid splitter plate with  $L/D=1.0$  before comparing velocity fields for the various plates.

Fig. 11 presents the evolution in time of the flow around a cylinder fitted with a solid splitter plate of  $L/D=1.0$  during one cycle of oscillation at  $U/Df_0 = 6.4$ . The sequence is composed of 11 instantaneous flow fields identified in time by  $t/T$ , where  $T = 1/f$  is the period of oscillation for that specific reduced velocity. The left column presents vorticity contours coloured by

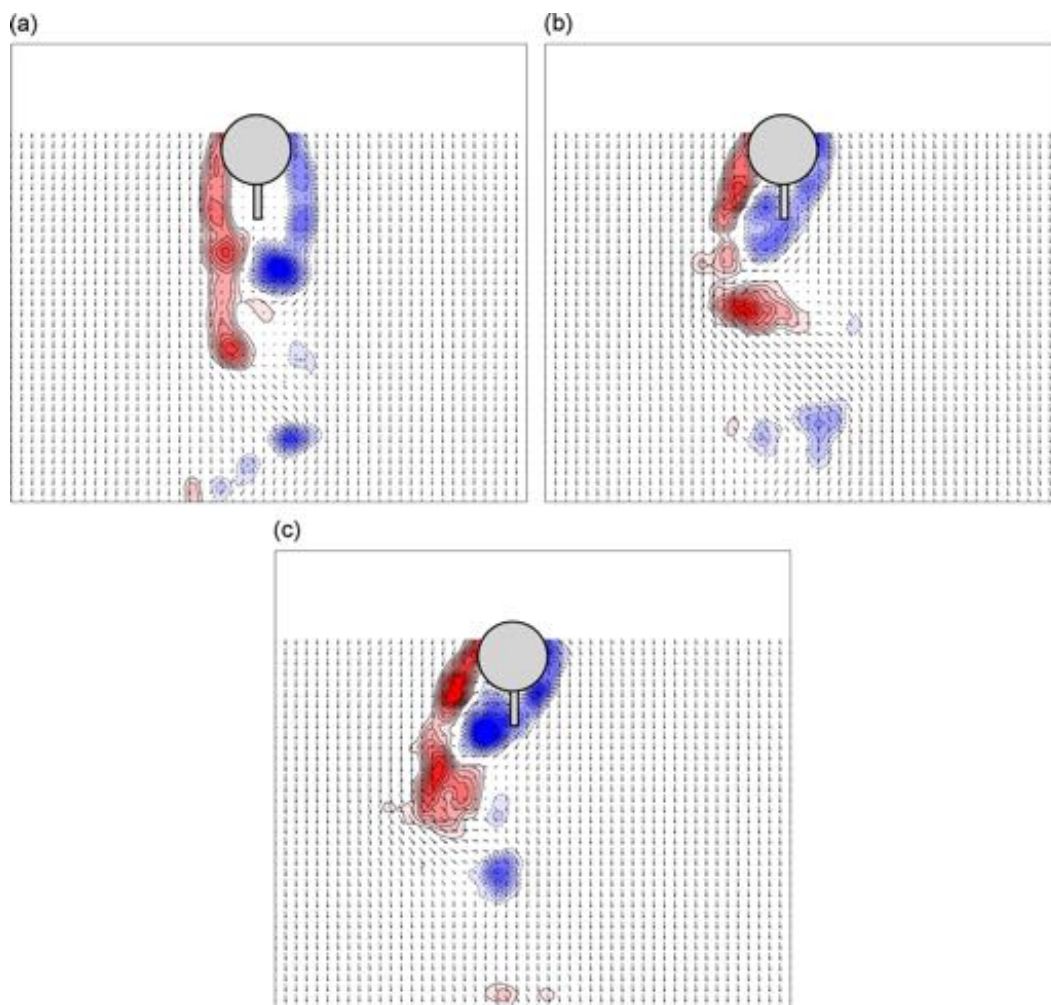


**Fig. 13.** Instantaneous vorticity contours and velocity vectors for a cylinder with a solid splitter plate  $L/D=0.5$  at various reduced velocities: (a)  $U/Df_0 = 3.0$ , (b) 5.0 and (c) 7.3.

vorticity magnitude and the right column shows the corresponding velocity vectors coloured by velocity magnitude. At  $t/T = 0/10$  the cylinder is in its uppermost position with  $\dot{y} \approx 0$ . The separated shear layers seem to be equally aligned with the flow direction, but relatively high speed flow is noticeable at the upper side of the cylinder (probably resulting from the previous cycle of oscillation). As time progresses, the cylinder moves down across the flow passing through the centreline with maximum  $\dot{y}$  between  $t/T = 2/10$  and  $3/10$ . At this moment the shear layer on the lower side is drawn closer to the body and reattaches to the tip of the plate. The corresponding velocity field shows a recirculation bubble developed from the separation point on the cylinder to the reattachment point on the tip of the plate. This flow configuration generates a lift force in the same direction as the body movement, thus providing the excitation for galloping. A lift force with the same hydrodynamic origin was reported by Assi et al. (2009) in experiments with a free-to-rotate splitter plate. The cylinder reaches its lowermost position with  $\dot{y} \approx 0$  at  $t/T = 6/10$  when the reattaching shear layer seem to recover symmetry. On the way up, the cylinder crosses the centreline with maximum  $\dot{y}$  between  $t/T = 7/10$  and  $8/10$ . The reattachment of the upper shear layer is now made possible by the strong  $\dot{y}$ .

During this cycle the cylinder is able to extract energy from the flow due to the reattachment of the shear layers on the plate, thus supporting the flow sketch proposed in Fig. 2. Vortex shedding is observed to occur downstream of the plate throughout the cycle, which might have an effect on the amount of lift generated on the body as well as the phase lag between the force and movement. The flow behaviour will vary as reduced velocity (and Reynolds number) is varied, especially as the reduced velocity moves away from the VIV synchronisation range in which vortex shedding may have a considerable influence.

Similar PIV measurements were carried out to investigate the flow around the cylinder with other plates. For brevity, we will only present results for the instant when the cylinder crosses the centreline for various reduced velocities. But first, Fig. 12 presents vorticity contours of the instantaneous wake generated around a plain cylinder in VIV to serve as a reference. (Note: Vorticity contours presented in the next figures are intended to offer a qualitative interpretation of the wake, therefore key for the colour scales, which vary with flow speed, is not necessary. The same applies to the velocity vectors.)

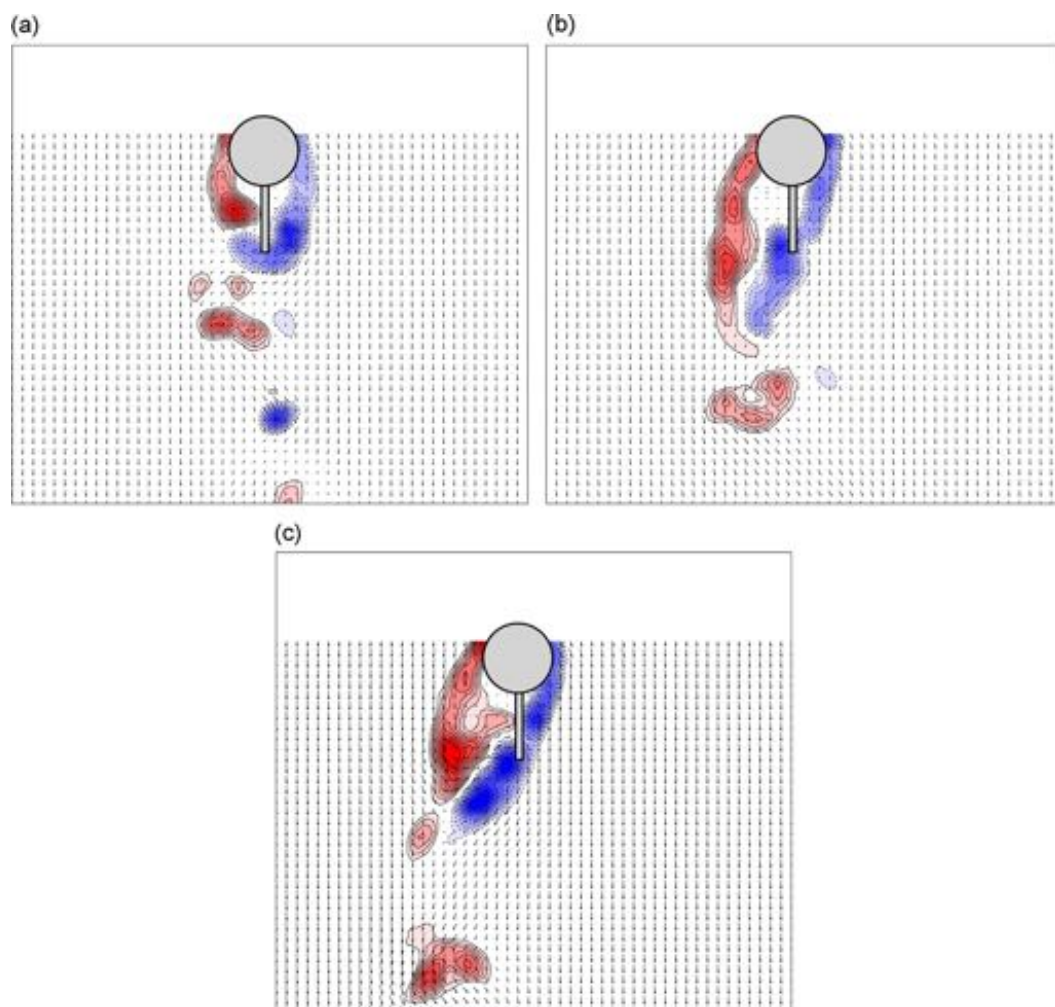


**Fig. 14.** Instantaneous vorticity contours and velocity vectors for a cylinder with a solid splitter plate  $L/D = 1.0$  at various reduced velocities (a)  $U/Df_0 = 3.0$ , (b) 5.0 and (c) 7.3.



Reduced velocities of  $U/Df_0 = 3.0$ , 5.0, 7.3 and 12 are located within and just beyond the synchronisation range (identified with an asterisk in the axis of Fig. 5(a), for convenience). Data was acquired when the cylinder was crossing the centreline from left to right, therefore presenting maximum cross-flow velocity. It is possible to observe the evolution of the wake for the different branches of the VIV response. For reduced velocity 3.0 in Fig. 12(a) the cylinder presents small  $\dot{y}/D$  with a typical '2S'-mode vortex wake being shed (Refer to Williamson and Govardhan, 2004 for a description of wake modes.) For reduced velocity 5.0 in Fig. 12(b), close to the peak of resonance, the '2P' wake appears much wider due to the high-amplitude movement of the cylinder. This wake changes mode again in the lower branch of vibration as shown for reduced velocity 7.3 in Fig. 12(c). For  $U/Df_0 = 12$  the cylinder is no longer experiencing VIV excitation. For all cases in Fig. 12 the interaction of the separated shear layers in the vortex-formation mechanism is quite evident.

Fig. 13 presents the flow field around a cylinder with a solid splitter plate with  $L/D = 0.5$  for the same reduced velocities as presented for the plain cylinder. At  $U/Df_0 = 3.0$  the cylinder experiences very small movement across the flow and the galloping mechanism has not developed yet. But for the higher reduced velocities, the shear layer on the right-hand side of the cylinder is drawn closer to the plate as the cylinder moves with maximum  $\dot{y}$  to the right; consequently, galloping is sustained. For the longer solid plate of  $L/D = 1.0$ , presented in Fig. 14, the separated shear layers manage to reattach to the tip of the plate for all three reduced velocities investigated. Galloping is incipient at  $U/Df_0 = 3.0$  but it dominates the response for the higher reduced velocities. The instants captured in Fig. 14 are equivalent to  $t/T = 2/10$  and  $8/10$  in Fig. 11. Although one may think the 1D-long plate would be able to extract more energy from the flow during the galloping mechanism it should be recalled that the responses of both plates in Fig. 5(a) are rather similar.

Results for the slotted splitter plate with  $L/D = 1.0$  are not conceptually different from the others, as seen in Fig. 15. For  $U/Df_0 = 3.0$  the vortex formation length is certainly extended due to the presence of the plate, but no reattachment of the shear layers on the plate is observed. For reduced velocities 5.0 and 7.3 a clear deflection of the wake is noticeable due to  $\dot{y}$  and the shear layer on the right-hand side reattaches to the tip of the plate. The reduced rate of increase of response with reduced velocity allowed PIV measurements to be taken up to  $U/Df_0 = 12$ , where the same behaviour was observed. In summary, from Fig. 15 it becomes clear that a similar galloping mechanism is also driving the response of the slotted plate.

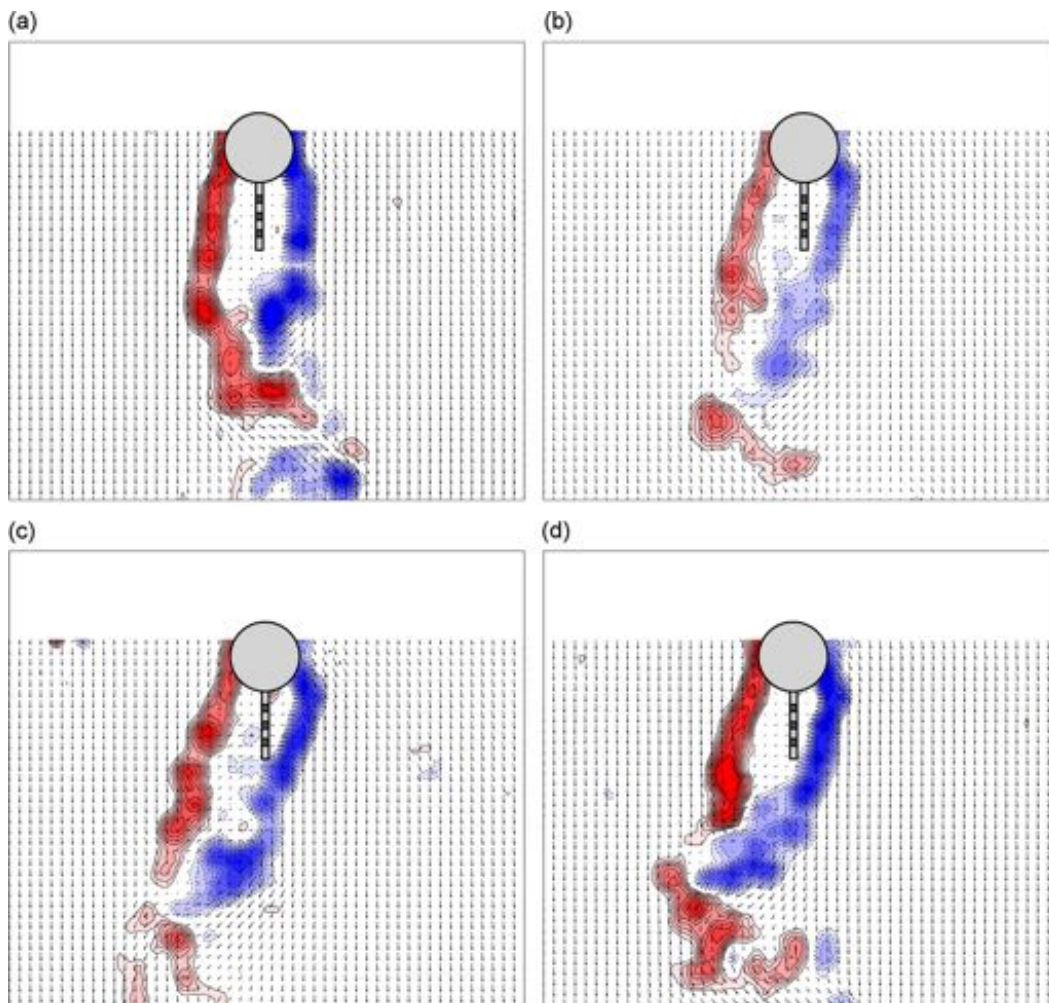
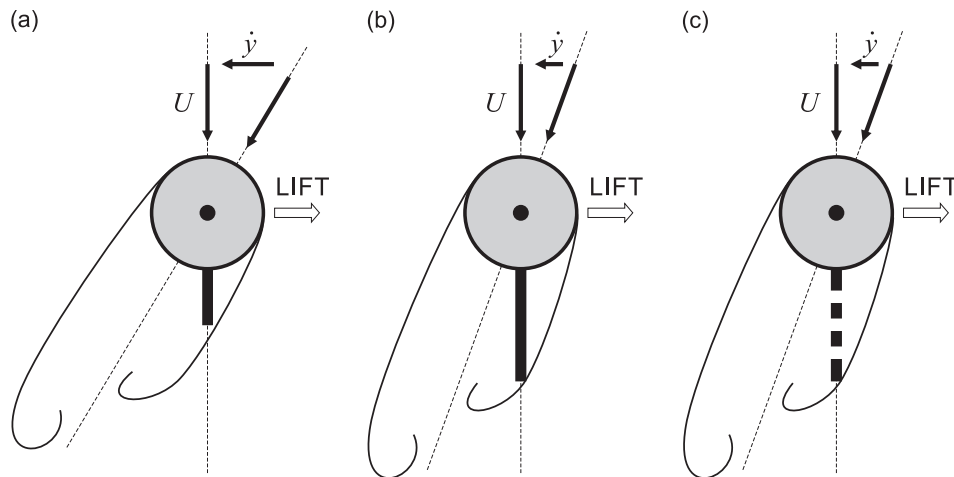


Fig. 15. Instantaneous vorticity contours and velocity vectors for a cylinder with a slotted splitter plate  $L/D = 1.0$ . (a)  $U/Df_0 = 3.0$ , (b) 5.0, (c) 7.3 and (d) 12.



**Fig. 16.** Sketches of the hydrodynamic mechanism leading to the galloping instability of a cylinder with (a) a solid short splitter plate  $L/D=0.5$ , (b) a solid long splitter plate  $L/D=1.0$  and (c) a slotted splitter plate  $L/D=1.0$ .

Note that the PIV measurements performed in the present work were not aimed at capturing the small flow scales within the recirculation bubble or through the slots. Also, flow fields presented in Figs. 12–15 were taken for the same reduced velocities, but the cylinders are oscillating at different frequencies for each case.

Independently of plate length or porosity, the general flow pattern that induces galloping is found to be the same, as summarised for all geometries in Fig. 16. At small amplitudes one shear layer moves close to the splitter plate while the opposing one moves away, hence producing a pressure difference across the plate. For larger amplitudes the shear layers intermittently reattach to the tip of a plate as the body oscillates. This reattachment sustains a pressure difference across the splitter plate feeding the excitation. In all cases, lift is generated on the cylinder/splitter plate combination.

Future investigations could focus on the plate solidity ratio to evaluate its effect on the response of bluff bodies with permeable structures in between the separated shear layers. Such a configuration may be useful for many engineering applications if shown that porous plates may be effective in suppressing vortex shedding and reducing drag without being prone to severe galloping, at least for moderate flow speeds.

## 5. Conclusion

In the present work we have investigated the FIV response of circular cylinders fitted with three different geometries of splitter plate. Hydrodynamic force decompositions together with PIV measurements of the flow field around the plates confirm that a transverse galloping mechanism is responsible for driving the cylinders with splitter plates into high-amplitude vibrations.

Firstly, this conclusion is supported by the overall behaviour of the response concerning a non-axisymmetric cross-section vibrating in 1-dof with displacements that monotonically increase with flow speed. Besides that, the driving mechanism is not resonant, since no phase shift between movement and forcing was observed as the frequency of vibration passes through the natural frequency of the system. Finally, flow visualization of the separated shear layers reattaching on the tip of the plates reveal the hydrodynamic mechanism that produces a transverse force in phase with the body's velocity.

Solid plates with  $L/D=0.5$  and  $1.0$  showed a much larger increase in response with increasing reduced velocity than the slotted plate, indicating that they can extract more energy from the flow. The effect of the slots on excitation is thought to be twofold: they increase hydrodynamic damping and reduce the pressure difference across the splitter plate, but this requires further confirmation. Independently of plate length or porosity, the general flow pattern that induces galloping is found to be the same.

The validity of the quasi-steady theory of galloping has not been verified in the present study. Nakamura et al. (1994) have already pointed out that it might not hold true for circular cylinders fitted with long splitter plates. Simply modelling the lift force as an harmonic function may not be the most accurate approach, but it reveals distinct features of lift, phase angle, added mass and energy transfer, clearly isolating the nature of the galloping instability from the VIV response of a plain cylinder.

## Acknowledgments

The authors wish to acknowledge the support of CAPES (2668-04-1) at the time of the experiments. GRSA is grateful to FAPESP (2013/07335-8) and CNPq (308916/2012-3) that allowed him time to revisit the data and write this paper.

## References

- Apelt, C.J., West, G.S., 1975. The effects of wake splitter plates on bluff-body flow in the range  $10^4 < R < 5 \times 10^4$ . Part 2. *Journal of Fluid Mechanics* 71, 145–160.
- Apelt, C.J., West, G.S., Szewczyk, A., 1973. The effects of wake splitter plates on the flow past a circular cylinder in the range  $10^4 < R < 5 \times 10^5$ . *Journal of Fluid Mechanics* 61, 187–198.
- Assi, G.R.S., 2009. Mechanisms for Flow-induced Vibration of Interfering Bluff Bodies (Ph.D. thesis). Imperial College London, London, UK, available from [www.ndf.poli.usp.br/~gassi](http://www.ndf.poli.usp.br/~gassi).
- Assi, G.R.S., 2014a. Wake-induced vibration of tandem and staggered cylinders with two degrees of freedom. *Journal of Fluids and Structures* 50, 329–339.
- Assi, G.R.S., 2014b. Wake-induced vibration of tandem cylinders of different diameters. *Journal of Fluids and Structures* 50, 340–357.
- Assi, G.R.S., Bearman, P.W., Carmo, B., Meneghini, J., Sherwin, S., Willden, R., 2013. The role of wake stiffness on the wake-induced vibration of the downstream cylinder of a tandem pair. *Journal of Fluid Mechanics* 718, 210–245.
- Assi, G.R.S., Bearman, P.W., Kitney, N., 2009. Low drag solutions for suppressing vortex-induced vibration of circular cylinders. *Journal of Fluids and Structures* 25, 666–675.
- Assi, G.R.S., Bearman, P.W., Kitney, N., Tognarelli, M., 2010a. Suppression of wake-induced vibration of tandem cylinders with free-to-rotate control plates. *Journal of Fluids and Structures* 26, 1045–1057.
- Assi, G.R.S., Bearman, P.W., Meneghini, J., 2010b. On the wake-induced vibration of tandem circular cylinders: the vortex interaction excitation mechanism. *Journal of Fluid Mechanics* 661, 365–401.
- Assi, G.R.S., Bearman, P.W., Rodrigues, J., Tognarelli, M., 2011. The effect of rotational friction on the stability of short-tailed fairings suppressing vortex-induced vibrations. in: *Proceedings of OMAE2011, 30th International Conference on Ocean, Offshore and Arctic Engineering*, Rotterdam, The Netherlands.
- Assi, G.R.S., Bearman, P.W., Tognarelli, M., 2014. On the Stability of a Free-To-Rotate Short-Tail Fairing and a Splitter Plate as Suppressors of Vortex-Induced Vibration. *Ocean Engineering*, TBA.
- Bearman, P.W., 1965. Model with a blunt trailing edge and fitted with splitter plates. *Journal of Fluid Mechanics* 21, 241–255.
- Bearman, P.W., 1984. Vortex shedding from oscillating bluff bodies. *Annual Review of Fluid Mechanics* 16, 195–222.
- Bearman, P.W., Gartshore, I.S., Maull, D.J., Parkinson, G.V., 1987. Experiments on flow-induced vibration of a square-section cylinder. *Journal of Fluids and Structures* 1, 19–34.
- Blevins, R., 1990. *Flow-Induced Vibration*, second edition Van Nostrand Reinhold, New York.
- Chang, C.-C., Kumar, R., Bernitsas, M.M., 2011. VIV and galloping of single circular cylinder with surface roughness at  $3.0 \times 10^4 \leq Re \leq 1.2 \times 10^5$ . *Ocean Engineering* 38 (16), 1713–1732.
- Cimbala, J., Garg, S., 1991. Flow in the wake of a freely rotatable cylinder with splitter plate. *AIAA Journal* 29, 1001–1003.
- den Hartog, J., 1956. *Mechanical Vibrations*, fourth edition McGraw Hill, New York.
- Gerrard, J., 1966. The mechanics of the formation region of vortices behind bluff bodies. *Journal of Fluid Mechanics* 25, 401–413.
- Khalak, A., Williamson, C.H.K., 1999. Motions, forces and mode transitions in vortex-induced vibrations at low mass-damping. *Journal of Fluids and Structures* 13, 813–851.
- Nakamura, Y., Hirata, K., Kashima, K., 1994. Galloping of a circular cylinder in the presence of a splitter plate. *Journal of Fluids and Structures* 8, 355–365.
- Nakamura, Y., Hirata, K., Urabe, T., 1991. Galloping of rectangular cylinders in the presence of a splitter plate. *Journal of Fluids and Structures* 5, 521–549.
- Naudascher, E., Rockwell, D., 1994. In: Balkema, A.A. (Ed.), *Flow-Induced Vibrations, An Engineering Guide*, Rotterdam. 1st Edition.
- Paidoussis, M., Price, S., deLangre, E., 2011. *Fluid-Structure Interactions: Cross-Flow-Induced Instabilities*, 1st Edition Cambridge University Press, New York.
- Parkinson, G., 1971. Wind-induced instability of structures. *Philosophical Transactions of the Royal Society* 269, 395–413.
- Parkinson, G., 1989. Phenomena and modelling of flow-induced vibrations of bluff bodies. *Progress in Aerospace Sciences* 26, 169–224.
- Roshko, A., 1954. On the Drag and Shedding Frequency of Two-dimensional Bluff Bodies. Technical Report. TN-3169, NACA.
- Sarpkaya, T., 2004. A critical review of the intrinsic nature of vortex-induced vibrations. *Journal of Fluids and Structures* 19, 389–447.
- Stappenbelt, B., 2010. Splitter-plate wake stabilisation and low aspect ratio cylinder flow-induced vibration mitigation. *International Journal of Offshore and Polar Engineering* 20 (3), 1–6.
- Unal, M., Rockwell, D., 1987. On vortex formation from a cylinder. Part 2. Control by splitter-plate interference. *Journal of Fluid Mechanics* 190, 513–529.
- Williamson, C.H.K., Govardhan, R., 2004. Vortex-induced vibrations. *Annual Review of Fluid Mechanics* 36, 413–455.





Contents lists available at ScienceDirect

Applied Ocean Research

journal homepage: [www.elsevier.com/locate/apor](http://www.elsevier.com/locate/apor)

# Experiments with flexible shrouds to reduce the vortex-induced vibration of a cylinder with low mass and damping

M.M. Cicolin, G.R.S. Assi<sup>\*,1</sup>

Department of Naval Architecture &amp; Ocean Engineering, EPUSP, University of São Paulo, São Paulo, SP, Brazil

## ARTICLE INFO

### Article history:

Received 23 December 2016

Accepted 3 April 2017

Available online 9 May 2017

### Keywords:

Vortex-induced vibration

Suppression

Flexible shroud

Drag reduction

Ventilated trousers

## ABSTRACT

Experiments employing a low-mass-damping cylinder have been conducted to determine the vortex-induced vibration (VIV) response of four suppressors of the flexible-shroud family. The VIV suppressors were inspired in the concept of the *Ventilated Trousers* (VT), a flexible shroud composed of a flexible net fitted with three-dimensional bobbins. Reynolds number varied between  $5 \times 10^3$  and  $25 \times 10^3$ , while reduced velocity varied from 2 to 26. The VIV dynamic response showed that the VT suppressed the peak amplitude of vibration down to 40% of that of a bare cylinder. Other flexible shrouds also achieved suppression, but not as efficiently. Drag was reduced during the VIV synchronization range, but remained above the value for a bare static cylinder thereafter. Spectral analysis of displacement and lift revealed that, depending on the geometry and distribution of the bobbins, the flexible shroud can develop an unstable behavior, capturing energy from the wake and sustaining vibrations for higher reduced velocities. PIV measurements of the wake revealed that the entrainment flow through the mesh is necessary to extend the vortex-formation length of the wake; this mechanism only occurs for the VT mesh.

© 2017 Elsevier Ltd. All rights reserved.

## 1. Introduction

The vibration induced by the external flow past slender structures poses a problem to submarine and offshore cables, flexible pipes, drilling and production risers and other elastic structures exposed to sea currents. The excitation has its origin in the shedding mechanism of alternating vortices occurring in the wake of bluff bodies, so the hydroelastic phenomenon is called vortex-induced vibration (VIV). Flexible lines exposed to vibrations for a long time may be damaged by structural fatigue [1]. The amplification of drag due to the vibration of the body is also of considerable concern, since it increases static and dynamic loads at the joints, platform and other fixtures.

One way to mitigate the effects of VIV is the installation of suppressors along the riser, or at least on the length of the line where currents are most intense. Helical strakes and fairings, for example, have been widely employed by the industry as VIV suppressors [2]. On one hand, significant VIV suppression of light structures requires wider strakes, which increases drag. Fairings, on the other

hand, tend to be more efficient in suppression as far as drag is concerned, but may suffer from hydroelastic instabilities [3]. With the improvement of molded plastic, helical strakes and fairings have indeed become sturdy contraptions, but they still take considerable time to install and occupy large areas on the deck. Other devices based on the disruption of the wake by interfering control surfaces (as explored by Silva-Ortega and Assi [4], for example) may suffer from the same problem.

During the last decades many devices have been investigated and offered as commercial products. Following the industry demand for more efficient, robust and easy-to-install devices, the technological development for suppressing VIV has been under pursuit by both the scientific and industrial communities.

In this context, All Brown Universal Components, a technology company based in the UK, created an interesting new device for suppressing VIV of drilling risers called the *Ventilated Trousers*, or simply VT [5]. Composed of a net of flexible cables holding an orthogonal array of bobbins (solid elements fitted on the net), the VT suppressor is, in the words of the inventors, “a loose fitting sleeve in the form of a light flexible net with integral bobbins in a special arrangement. It is omni-directional, rugged, and made from materials compatible with the offshore environment” [6]. Essentially, the VT is an improvement on the idea of wrapping the drilling riser in a type of flexible cover able to deform with the flow, interact with the wake and mitigate the response to hydrodynamic loads.

<sup>\*</sup> Corresponding author.

E-mail address: [g.assi@usp.br](mailto:g.assi@usp.br) (G.R.S. Assi).

<sup>1</sup> Currently a Visiting Associate in Aerospace at GALCIT, California Institute of Technology.

The suppression effectiveness of the VT and its efficiency concerning drag reduction have been studied over the last years with promising results [7,6,8]. Brown and King [7], for example, performed experiments in a laboratory scale with flexible cylinders showing a 90% reduction of the VIV peak amplitude of displacement at a Reynolds number ( $Re$ ) of approximately  $1.4 \times 10^5$ . So far, all known experiments have been performed either with flexible pipes or near real conditions at sea, especially regarding the range  $Re = 3.7 \times 10^4$  to  $1.2 \times 10^6$  and the structural properties of a riser [7,6]. Although this kind of experiment verifies the potential of such a device in practical applications (for being performed closer to real conditions), they are not designed to reveal the intricate hydrodynamic mechanisms by which the VT is able to achieve suppression.

### 1.1. Objective

In the present work we set out to understand the behavior of the VT and other similar suppressors in idealized laboratory conditions. It could be said that the VT is part of a larger family of suppressors, here called the *flexible shrouds* (also called *permeable meshes* in our previous investigations). We believe that exploring geometric variations based on the VT concept will produce siblings that could thus reveal the fundamental physical mechanisms behind the suppression.

Purely motivated by the scientific interest on the topic, the present work is part of an investigation to study the behavior of this family of suppressors at moderate  $Re$ , low mass and very low damping conditions. We are particularly concerned with the scientific investigation of the hydrodynamic and hydroelastic mechanisms that will explain us how this family of VIV suppressors works.

We will characterize the VIV response of the VT and three other simpler flexible shrouds derived from it. In idealized laboratory conditions all variables are under control and crucial parameters are reduced to enhance the response. The idea is to test the suppression device in the most undisturbed condition, indeed different for the real application in the ocean, but free from most of the interference that could mask the understanding of the fundamental physical phenomena. As will become clearer shortly, the differences between the models emerge from variations on the geometric parameters of the original VT, taking us step by step in understanding the physical principles.

## 2. Experimental method

Experiments have been carried out in the recirculating water channel of NDF Fluids and Dynamics Research Group at the University of São Paulo, Brazil. The water channel has a test section 0.7 m wide, 0.9 m deep and 7.5 m long. The flow speed ( $U$ ) is variable up to 1 m/s, allowing for tests with different values of Reynolds number, with a turbulence intensity of less than 3%.

Models were attached to a one-degree-of-freedom rig which allowed the model to oscillate freely in the cross-flow direction ( $y$ ), as shown in Fig. 1. The platform was mounted on air bearings to reduce friction within the system, thus ensuring very low structural damping and maximum response. A load cell installed between the cylinder and the rig measured instantaneous lift and drag forces acting on the cylinder. A pair of coil springs provided the restoration force to the system and an optical sensor measured the displacement without adding extra damping. For further details on the elastic rig, other VIV experiments employing the rig and information on the facilities please refer to [9,10].

Tests were performed with a rigid section of a circular cylinder (external diameter  $D = 50$  mm, submerged length  $L = 650$  mm) fitted with four different flexible shrouds. Variations of the meshes

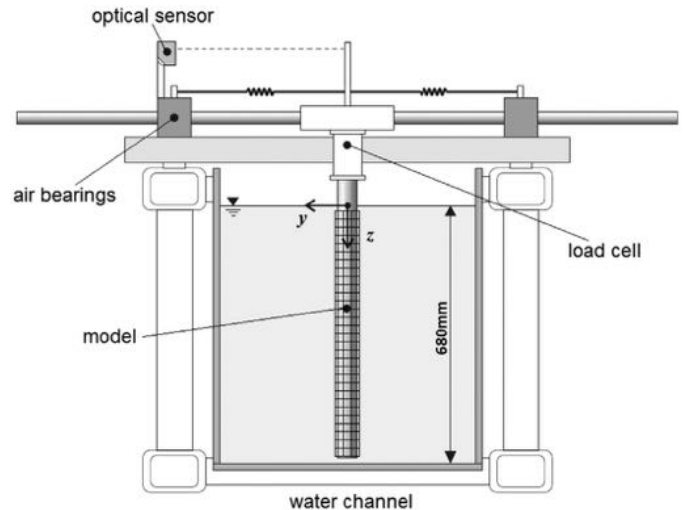


Fig. 1. Cross-view of the test section showing the elastic rig and cylinder in the water channel.

concerned the geometry of the bobbins, focusing on the main length scales of the original bobbin, and their distribution on the net.

The first model is a pure reproduction of the VT device. Its main properties are the perimeter ( $p$ ), the width of the mesh element ( $w$ ) and a characteristic dimension of the bobbin ( $d$ ), as can be seen in Fig. 2. Brown [5] provides a guide for the geometric definition of the mesh, allowing some variations on its properties: the diameter ratio, for example, must vary between  $d/D = 0.08$  and  $0.125$ . Besides that, in a previous work, Brown and King [7] verified that a mesh element width of 5 times the bobbin characteristic dimension ( $w = 5d$ ) resulted in a more effective VT than one in which  $w = 3d$ . They also reported that the net perimeter must be between  $p = 4D$  and  $4.71D$ . Following these guidelines and considering that the parameters are not completely independent, the largest possible mesh was built respecting the restrictions and recommendations proposed by Brown [5]. The final dimensions of the VT model employed in the present work are shown in Table 1.

Based on the VT mesh, presented in Fig. 3a, three other meshes with simpler geometries have been built altering the VT bobbin geometry and distribution, but keeping the same  $w$  and  $p$ . The *thick-sparse mesh*, shown in Fig. 3b, had different bobbins formed by only one circular cylinder with an external diameter of  $d_{ext} = 3d$ , corresponding to the outer diameter of the VT bobbin. On the other hand, the bobbin of the *thin-sparse mesh* shown in Fig. 3c, was made with a single cylinder with external diameter  $d_{ext} = d$ , resulting in a mesh following the thinner elements of the VT bobbin.

The VT, the thick-sparse and the thin-sparse meshes all had the same bobbin distribution, with bobbins fitted on every other mesh element. Now, the third variation resulted in the *thin-dense mesh* shown in Fig. 3d. It was built with the same bobbins used in the thin-sparse mesh, but fitting bobbins in every element of the net, resulting in a different distribution of bobbins.

In summary, all three bobbins have the same height of  $5d$ , but they vary in shape and how they are distributed on the mesh, as illustrated in Fig. 3 and Table 1. Again, all new bobbins are based on the main length scales found in the VT bobbin: height  $5d$  and diameters  $d$  or  $3d$ .

By keeping the net perimeter ( $p$ ) constant for all meshes and varying the outer diameter of the bobbins, the thin meshes presented a loose fit around the cylinder when compared with the other two. At first, this was not intentional, since we believed that keeping  $p$  constant would support the direct comparison of the results. However, as will be discussed later, the loose meshes had quite a significant and interesting effect in the response.

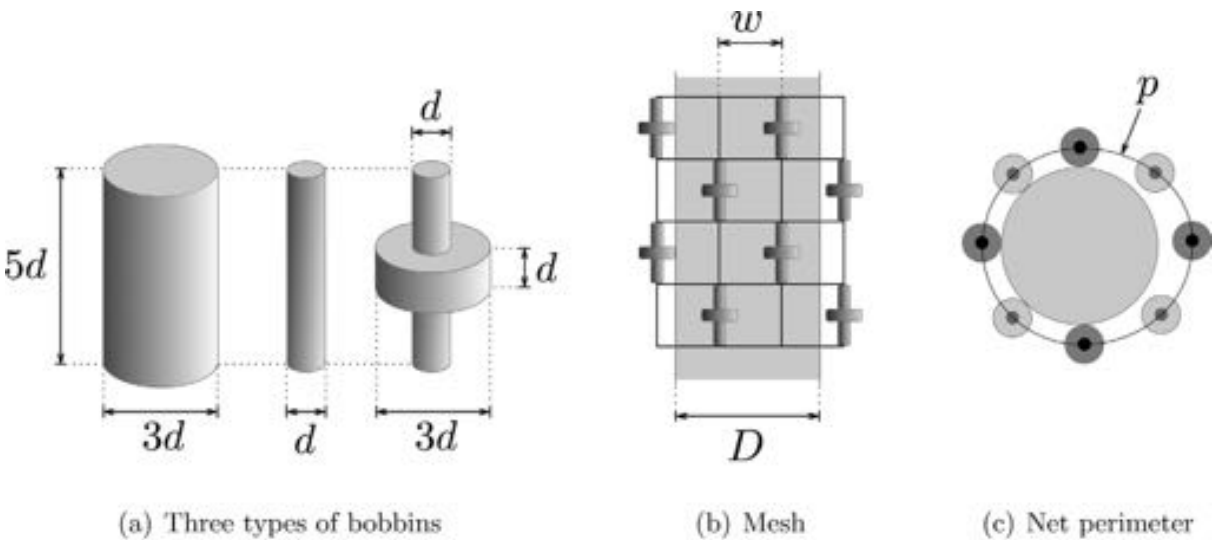


**Fig. 2.** Geometric properties and dimensions. (a) Three types of bobbins: thick cylinder, thin cylinder and VT bobbin. (b) Mesh distribution. (c) Net perimeter.

**Table 1**  
Model properties.

| Model             | Bobbin     | Distribution  | $d$     | (mm)  | $d_{ext}$ | $w$  | $p$     |
|-------------------|------------|---------------|---------|-------|-----------|------|---------|
| VT mesh           | VT bobbin  | Skip one cell | $0.11D$ | (5.8) | $3d$      | $5d$ | $4.64D$ |
| Thick-sparse mesh | Thick cyl. | Skip one cell | $0.11D$ | (5.8) | $3d$      | $5d$ | $4.64D$ |
| Thin-sparse mesh  | Thin cyl.  | Skip one cell | $0.11D$ | (5.8) | $d$       | $5d$ | $4.64D$ |
| Thin-dense mesh   | Thin cyl.  | Every cell    | $0.11D$ | (5.8) | $d$       | $5d$ | $4.64D$ |

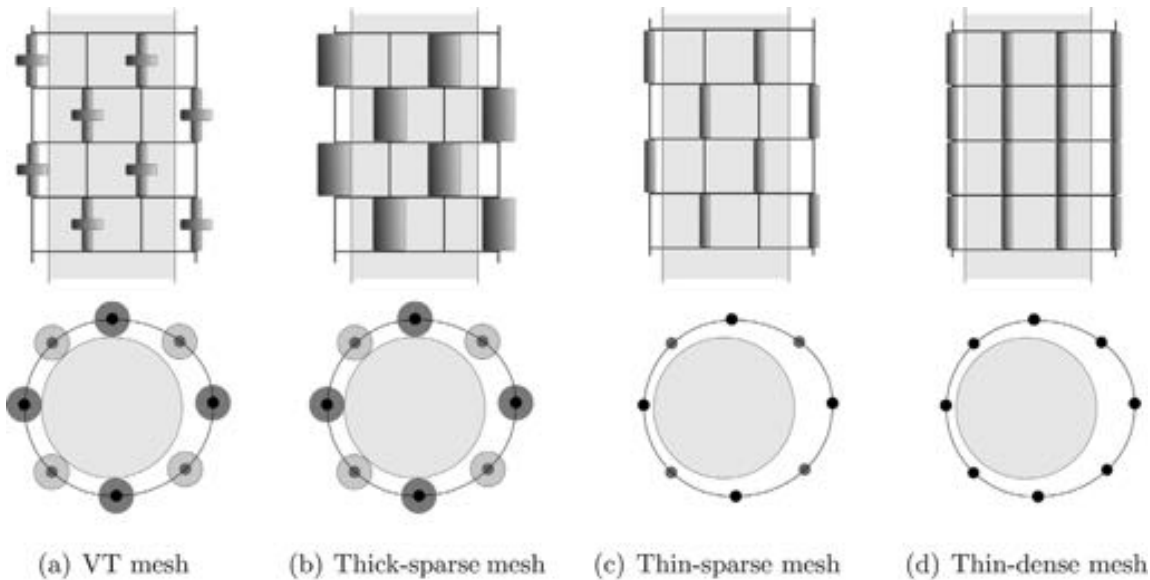


**Fig. 3.** Different configurations of the flexible shrouds. (a) VT mesh. (b) Thick-sparse mesh. (c) Thin-sparse mesh. (d) Thin-dense mesh.

**3. Results and discussion**

**3.1. Preliminary results with static models**

Preliminary experiments with fixed models have been performed as a reference for the hydrodynamic loads on a static body. The models were attached to the load cell on a fixed rig while measurements of drag and lift were taken. Hydrodynamic loads are presented in terms of force coefficients per unit length of cylinder, i.e. dividing lift and drag by  $\frac{1}{2}\rho DU^2$ , where  $\rho$  is the density of water and  $U$  is the free stream velocity.

Fig. 4a presents the mean drag ( $\bar{C}_D$ ) and mean lift ( $\bar{C}_L$ ) coefficients versus  $Re$  for all meshes compared with those for a bare cylinder. The bare cylinder presented  $\bar{C}_D \approx 1.15$ , which is in agreement with the results found in the literature for this range of  $Re$  [11,12]. All the meshes increased  $\bar{C}_D$  when compared to that of the bare cylinder: an approximate increase of 30% for the VT mesh, 65% for the thick-sparse mesh, 40% for the thin-sparse mesh and 60% for the thin-dense mesh. Since drag was increased, the shrouds must increase the amount of kinetic energy lost to the wake. All flexible shrouds not only enlarge the frontal area exposed to the flow but also increase the kinetic loss due

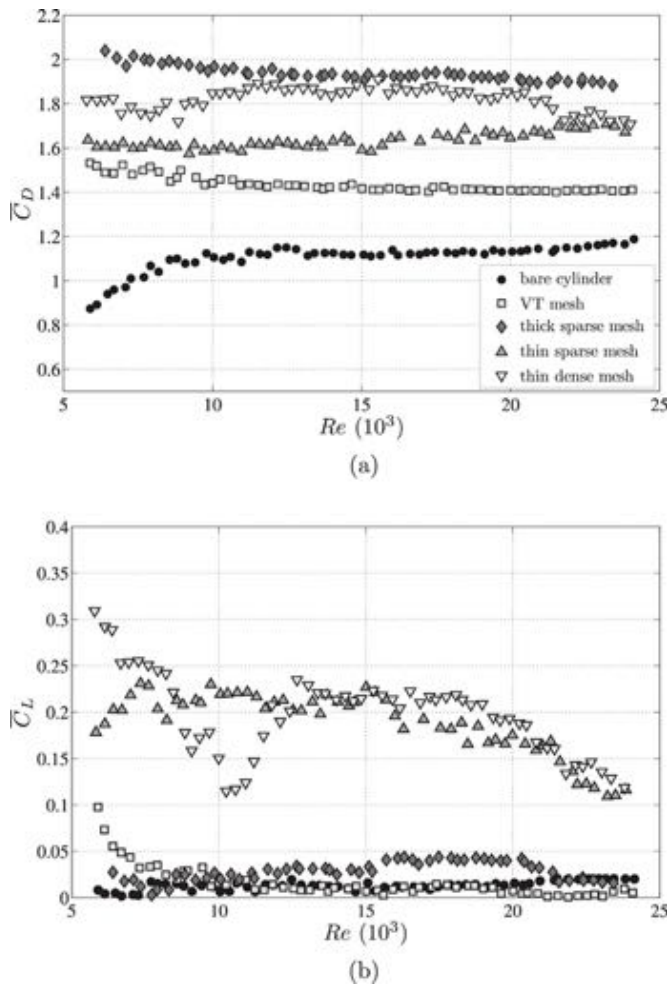


Fig. 4. Coefficients of (a) mean drag and (b) mean lift for static models versus  $Re$ .

to friction and locally-separated flow around the bobbins and net.

The mean lift coefficients presented in Fig. 4b, however, tell an interesting story. While the VT and the thick-sparse mesh have shown  $\bar{C}_L$  very close to zero (and also the bare cylinder, as expected for symmetric bodies), the thin-sparse and the thin-dense meshes presented  $\bar{C}_L$  distinctly higher for most of the  $Re$  range. It must be pointed out that even though the system (cylinder and load cell) was kept fixed, the flexible meshes were able to wobble around the cylinder responding to the unsteady flow. Because the VT and the thick-sparse mesh were tighter around the cylinder (compared to the other two loose meshes) they remained fairly static, while the thin meshes had more room to oscillate. Even though all meshes had the same perimeter, the larger size of the bobbins reduced the clearance between the devices and the main cylinder.

Now, both loose meshes tended to accommodate towards one of the sides of the cylinder, creating an effective asymmetry of the body, hence producing a residual mean lift. The meshes could randomly find stable positions on either side of the cylinder (in a kind of bifurcation), generating steady lift to either side. A very similar mechanism has been reported by Assi et al. [13] when investigating the dynamics of a cylinder fitted with free-to-rotate splitter plates. Of course in the present case the interfering body is not a solid plate, but a loose, flexible shroud interacting within the vortex formation region of the wake.

Fig. 5a presents the fluctuation of lift ( $C_L'$ ), calculated as the RMS (root mean square) of the lift signal. The reference case for the bare cylinder shows a scatter of points around  $C_L' = 0.2$ , as expected for

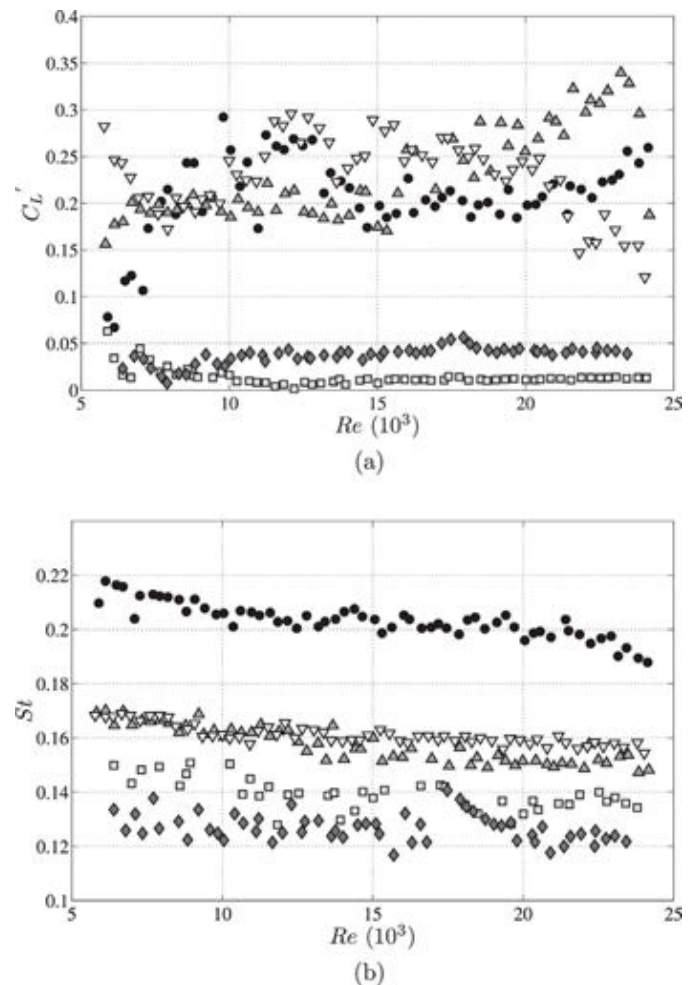


Fig. 5. (a) RMS of lift coefficient and (b) Strouhal number for static models versus  $Re$ . Key: please refer to Fig. 4.

this  $Re$  range and in agreement with Williamson [14]. Similar to the mean lift discussed above,  $C_L'$  also reveals a different behavior for the thin meshes, with the same level of  $C_L'$  as that of the bare cylinder. This fluctuation is generated by the loose meshes oscillating towards one of the sides of the cylinder. The VT and the thick-sparse mesh, however, present very low  $C_L'$ , showing that they might be effectively disrupting the vortex shedding mechanism in the near wake region.

The Strouhal number ( $St = f_s D / U$ , where  $f_s$  is the frequency of vortex shedding) was estimated from the frequency of fluctuation of the lift signal and is presented in Fig. 5b. As expected, the bare cylinder shows a typical value close to  $St = 0.2$ , in agreement with Norberg [15] for this range of  $Re$ . All meshes presented lower Strouhal numbers when compared to the bare cylinder, which means that their vortex-shedding frequencies are smaller due to a wider wake or a wake with weaker vortices.

Flow separation for these models is made very complex by the three-dimensional interference of the shrouds. Separation might be occurring from the various regions of the bobbins, from the cables of the net and ultimately from the wall of the main cylinder. The actual distance between the separated shear layers (to define the characteristic length in  $St$ ) is not so clear, therefore we chose to non-dimensionalize  $St$  by the external diameter of the main cylinder ( $D$ ). Now, the flexible shrouds are indeed enlarging the effective diameter of the body, but it is interesting to note that the thick-sparse mesh produced the lowest  $St$  (or shedding frequency) of them all. If the effective external diameter of the body were to



**Table 2**  
Dynamic properties for the VIV series.

| Model             | $m^*$ | First VIV series |       |               |                 | Second VIV series |       |               |                 |
|-------------------|-------|------------------|-------|---------------|-----------------|-------------------|-------|---------------|-----------------|
|                   |       | $f_{N_{air}}$    | $f_N$ | $\zeta_{air}$ | $\zeta_{water}$ | $f_{N_{air}}$     | $f_N$ | $\zeta_{air}$ | $\zeta_{water}$ |
| Bare cylinder     | 2.8   | 0.67             | 0.58  | 0.3%          | 1.6%            | 0.40              | 0.35  | 0.6%          | 2.0%            |
| VT mesh           | 2.9   | 0.66             | 0.55  | 0.3%          | 6.0%            | 0.39              | 0.33  | 0.6%          | 7.5%            |
| Thick-sparse mesh | 2.9   | 0.67             | 0.50  | 0.3%          | 10.6%           | 0.39              | 0.31  | 0.6%          | 12.0%           |
| Thin-sparse mesh  | 2.8   | 0.67             | 0.57  | 0.4%          | 3.6%            | 0.41              | 0.33  | 0.6%          | 6.1%            |
| Thin-dense mesh   | 2.8   | 0.67             | 0.58  | 0.4%          | 4.0%            | 0.39              | 0.33  | 0.6%          | 8.8%            |

be approximated, say by adding the size of the bobbins to  $D$ , then the true value of  $St$  would be very close to 0.2 for all cases.

### 3.2. VIV response

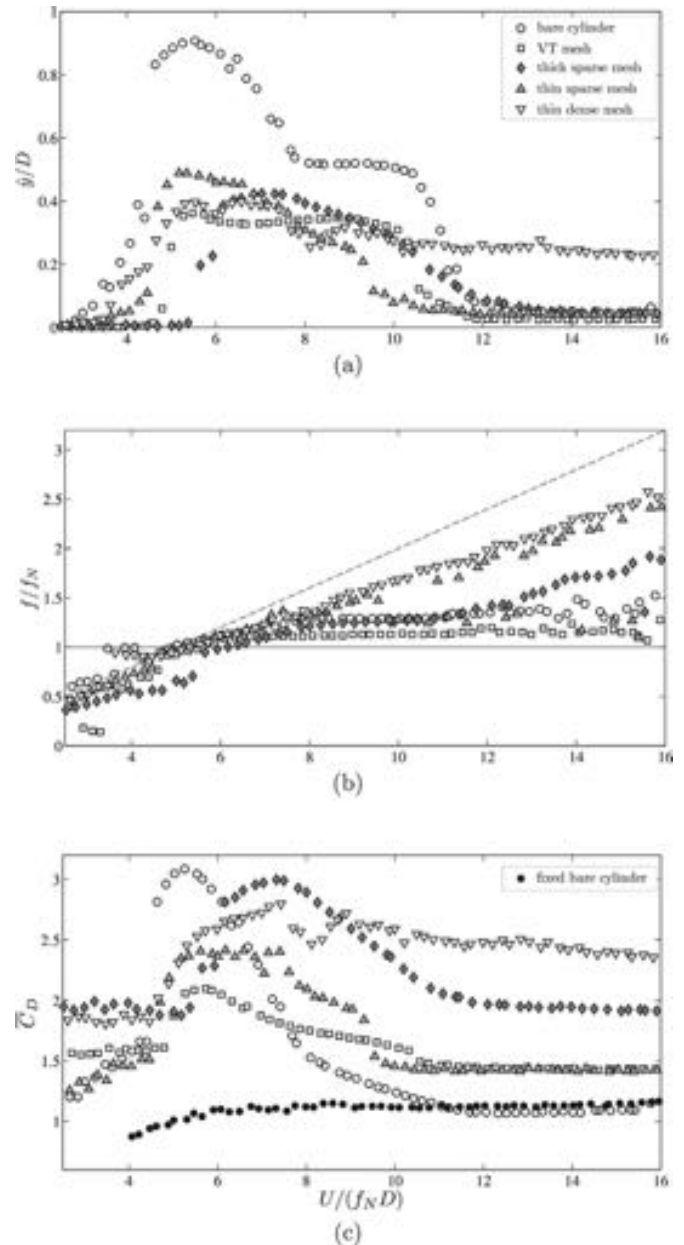
Tests to determine the VIV response for the models were carried out by installing the cylinders on the elastic rig, which allow for free vibrations only in the cross-flow direction ( $y$ ). The pair of coil springs that conferred the stiffness to the system was changed twice, resulting in two ranges of reduced velocity ( $U/f_N D$ ) covering the same  $Re$  range. Thus the experimental results are divided in two series.

Table 2 presents the main structural properties for both series. The reduced mass ( $m^*$ , defined as the ratio of structural mass to the mass of displaced fluid) was approximately 2.9 for all models, which is close to the values found in real offshore applications. Free-decay tests were performed in air in order to determine the natural frequency ( $f_{N_{air}}$ ) and the structural damping of the system ( $\zeta_{air}$ , defined as a percentage of the critical damping). Additional decay tests performed in still water yielded the natural frequencies in water ( $f_N$ ) and the total (structural plus hydrodynamic) damping ( $\zeta_{water}$ ) of the system. The reduced velocity was normalized using the natural frequency measured in still water ( $f_N$ ).

#### 3.2.1. First VIV series: reduced velocity up to 16

Fig. 6 presents the VIV response of all models with flexible shrouds compared with that of the bare cylinder as a reference. The displacement curve ( $\hat{y}/D$ , where  $\hat{y}$  is calculated as the RMS of the displacement signal multiplied by  $\sqrt{2}$ ) shown in Fig. 6a reveals the typical VIV response for the bare cylinder, with the initial, upper and lower branches of vibration clearly identified for a low- $m^* \zeta$  system. A peak amplitude of  $\hat{y}/D \approx 0.9$  is found around reduced velocity 5, with synchronization occurring roughly between  $U/(f_N D) = 4.5$  and 11.5. Within this range, the frequency of oscillation ( $f$ , calculated from the spectrum of displacement) is synchronized with the frequency of vortex shedding and both remain very close to the natural frequency of the system, as presented in Fig. 6b. Also for the bare cylinder, Fig. 6c highlights the amplification of mean drag, reaching a maximum of  $\bar{C}_D \approx 3.1$ , occurring in the synchronization range. Past reduced velocity 12,  $\bar{C}_D$  returns to the value for a fixed cylinder of approximately 1.1, as the cylinder stops responding to VIV. Reference results for the bare cylinder are in good agreement with Williamson and Govardhan [16].

Now we shall turn to the VIV response of the cylinder fitted with the flexible shrouds. In general, Fig. 6a shows that all meshes managed to reduce the peak amplitude of displacement within the synchronization range. The VT reached a maximum amplitude of  $\hat{y}/D \approx 0.38$ , accounting for a 60% reduction when compared to the peak amplitude of the bare cylinder. The synchronization range has also been shortened by the VT. The frequency signature of the response, shown in Fig. 6b, is not much different from that observed for the bare cylinder. Peak  $\bar{C}_D$ , on the other hand, presented a 30% reduction during the synchronization range, but remained slightly higher ( $\bar{C}_D \approx 1.45$ ) than that of the static bare cylinder by the end of the experiment. That is to say that the VT indeed suppresses



**Fig. 6.** Dynamic response of VIV versus reduced velocity: (a) amplitude of displacement, (b) dominant frequency of oscillation and (c) mean drag coefficient.

VIV and reduces the maximum drag amplified by the vibration, but once the vibration ceases, after the synchronization, the mean drag is higher than that of a bare cylinder.

The thick-sparse mesh follows the trend of VT, but is not as successful in reducing the peak amplitude of displacement. The response peak is shifted as the whole synchronization range is delayed in relation to the bare cylinder, starting at  $U/(f_N D) = 5.5$  and

ending at 12. This is due to a significant increase in the effective diameter of the body, caused by the larger diameter of the bobbins. The maximum mean drag is almost as high as that of the bare cylinder during synchronization, but it remains approximately 70% higher once the vibration terminates. Again, this might be due to the enlarged size of the bobbins. The frequency signature is very similar to the other two previous cases.

The thin-sparse mesh follows the same behavior, reaching the highest peak of displacement of all the flexible shrouds (only a 40% reduction compared to the bare cylinder). The synchronization range is not dislocated to higher reduced velocities since the smaller size of the bobbins tend not to enlarge much the effective diameter of the body. The frequency response, however, shows a different behavior from the previous cases, with the dominant frequency of oscillation following just under the frequency of vortex shedding for the whole range of reduced velocity (the inclined dashed line in Fig. 6b corresponds to  $St = 0.2$ ).  $\bar{C}_D$  is reduced during the synchronization, but remains higher than that of a bare static cylinder when no vibration exists.

Finally, the thin-dense mesh shows the most interesting behavior of them all. While the peak displacement shows the same level as that for the VT during synchronization, the vibration does not die out as expected after resonance. For higher reduced velocities a steady value of  $\hat{y}/D > 0.2$  is sustained until the end of the experiment. The frequency of response shows that the cylinder with a thin-dense mesh is persistently oscillating at the vortex-shedding frequency for the whole range of reduced velocities. As a consequence, the mean drag coefficient is also sustained at  $\bar{C}_D \approx 2.5$  until

the end of the experiment, while all the other models returned to their values obtained during the static-models experiments (Fig. 4).

The thin-dense mesh is able to capture energy from the vortex shedding mechanism, sustaining considerable vibration at the shedding frequency beyond the VIV synchronization. In fact, looking at the mesh during the experiments, we were able to note that the loose thin-dense mesh could wobble from side to side as the cylinder oscillated. The thin-sparse mesh would be as loose around the cylinder as the thin-dense mesh, but the latter was less permeable to the flow and able to interact with the unsteady wake. The concentration of bobbins on the thin-dense mesh together with its loose fit around the cylinder helped it to work as a sail, oscillating with the body (including a visible phase lag in the movement), interacting with the wake and thus exciting the cylinder into sustained oscillations.

Due to the distinct frequency response of the thin meshes, and especially due to the displacement response of the thin-dense mesh, we were motivated to extend the VIV experiments into a second series, this time changing to a softer set of springs to allow for higher reduced velocities (Table 2).

### 3.2.2. Second VIV series: reduced velocity up to 26

The results for the second VIV series will concentrate on the frequency signature of the response and the excitation, therefore we will be looking at the frequency signature of both displacement and lift.

The typical displacement response for the bare cylinder is shown again in Fig. 7, this time for reduced velocities up to 26. The

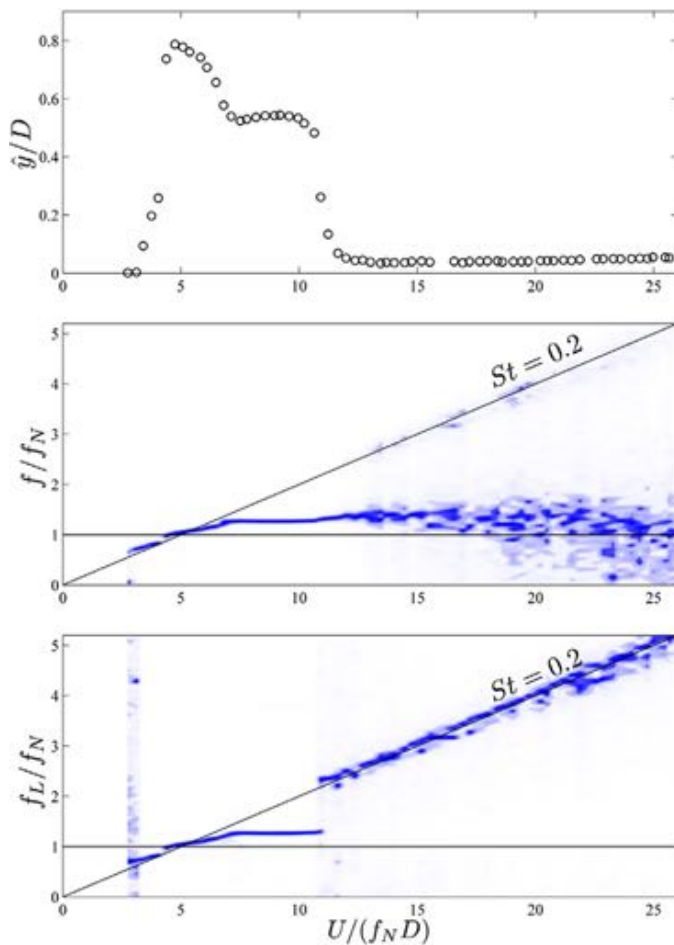


Fig. 7. (a) Amplitude of displacement, (b) spectrum of displacement and (c) spectrum of lift for a bare cylinder responding to VIV.

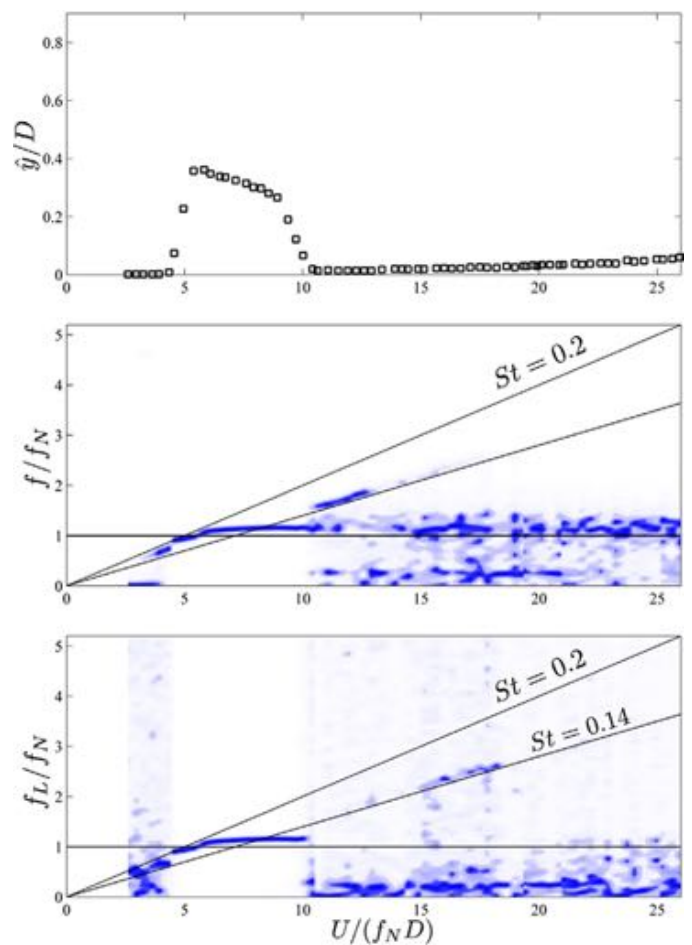


Fig. 8. (a) Amplitude of displacement, (b) spectrum of displacement and (c) spectrum of lift for a cylinder fitted with the VT responding to VIV.



frequency of oscillation ( $f/f_N$ ) is not shown as points representing the dominant frequency of the spectrum (as in Fig. 6), but instead it shows the whole spectrum in different shades for each reduced velocity. Darker shades of color represent higher peaks in the frequency spectrum. This way we are able to follow concurrent branches in the frequency signature that would otherwise be hidden. While the second plot ( $f/f_N$ ) in Fig. 7 shows the spectrum of displacement (the response), the third plot ( $f_L/f_N$ ) shows the spectrum of lift (the excitation).

The spectrum of  $f/f_N$  shows a clear branch of dominant frequency during the synchronization range (between  $U/(f_N D) = 5$  and 11), which is then dispersed in a much broader signature with no dominant frequency at the end of resonance. One may note that the bare cylinder is vibrating with very small amplitudes of displacement in a broader range of frequencies close to the natural frequency. This is a typical indication of turbulence buffeting. A faint frequency branch is barely noticeable matching the  $St = 0.2$  line, which is reminiscent of the vortex shedding that is now occurring from the almost-static body. The same branch can be traced in the  $f_L/f_N$  plot, showing that at the end of the synchronization the vortex shedding mechanism returns to its “natural” regime. The magnitude of lift due to vortex-shedding, though, is not strong enough to overcome the damping of the system, that responds predominantly by buffeting.

We shall now perform the same analysis for the models with flexible shrouds. Fig. 8 shows the results for the VT, again showing a synchronization range until reduced velocity 10. Both spectra for displacement and lift show a clear dominant peak during resonance. For higher reduced velocities the spectrum of  $f/f_N$  reveals that the small vibrations are around the natural frequency, while no clear branch of lift is distinguishable, again a clear indication of turbulence buffeting. A different faint branch is noticeable in both spectra, revealing the predominant frequency of vortex shedding for the static cylinder with the VT to be lower than that of the bare cylinder. The resulting  $St$  was calculated to be approximately 0.14, which is in good agreement with Fig. 5b. (Please bear in mind that very low frequencies in the spectrum plots represent low-frequency drifts of the cylinder.)

The frequency signature for the thick-sparse mesh is presented in Fig. 9. Similarly, the synchronization range is clearly identified in both spectra, but with a little shift towards higher reduced velocities when compared to the bare cylinder (as explained before). The residual low-amplitude vibrations at higher reduced velocities is due to turbulence buffeting. This time, the frequency branch representing the vortex shedding frequency for a static model results in  $St = 0.13$ , as expected from Fig. 5b.

Now, the models fitted with thin meshes are the ones with a different behavior. The frequency signature for the thin-sparse mesh is

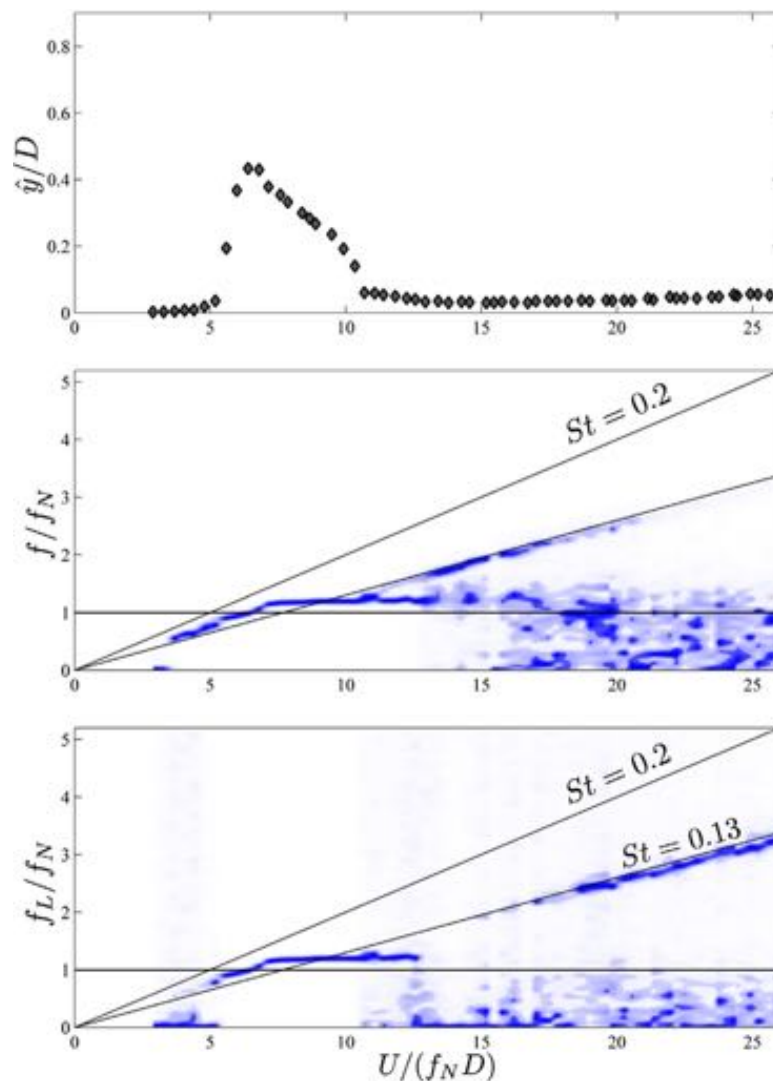
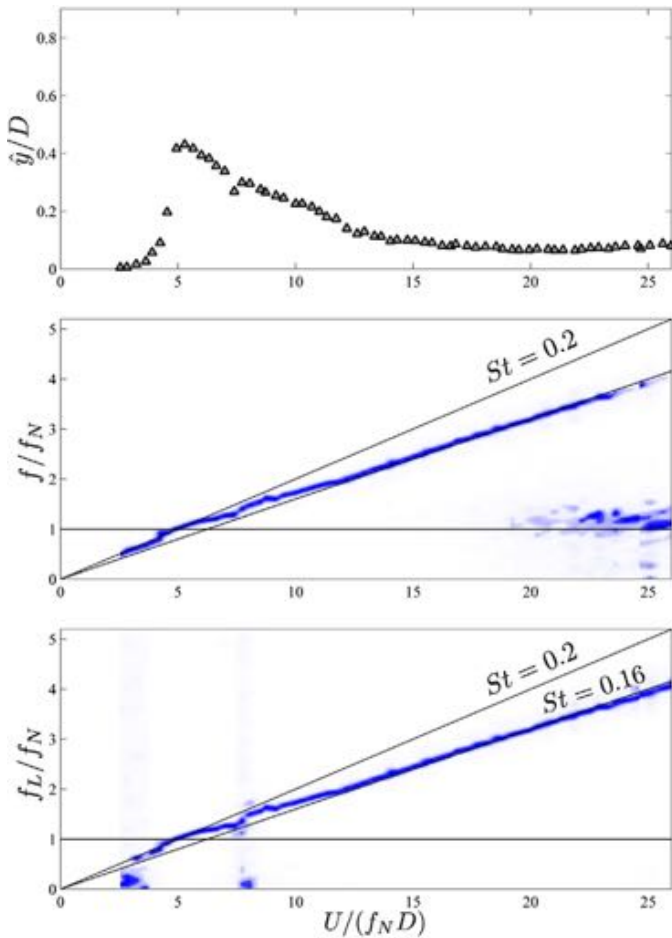


Fig. 9. (a) Amplitude of displacement, (b) spectrum of displacement and (c) spectrum of lift for a cylinder fitted with the thick-sparse mesh responding to VIV.



**Fig. 10.** (a) Amplitude of displacement, (b) spectrum of displacement and (c) spectrum of lift for a cylinder fitted with the thin-sparse mesh responding to VIV.

shown in Fig. 10. This time, the spectrum of  $f/f_N$  shows a clear branch of response following the vortex-shedding frequency. The same branch is identified in the spectrum of the excitation in  $f_L/f_N$ , yielding  $St = 0.16$  for the thin-sparse mesh as in Fig. 5b. The fact that the shedding frequency is not locked-in by the oscillation frequency is rather curious. A clear resonant peak is evident in the displacement curve, but the typical synchronization range expected for classical VIV is seen not to be occurring. A region of scattered  $f/f_N$  around the natural frequency reveals the presence of turbulence buffeting for higher reduced velocities. In fact, as shown by the points of dominant frequency in Fig. 6b, both mechanisms of buffeting and harmonic vortex excitation are competing throughout the whole range of reduced velocities.

The behavior for the thin-dense mesh is similar, but intensified (Fig. 11). The spectrum of  $f/f_N$  shows a single dominant branch following the  $St = 0.16$  line, also evident from  $f_L/f_N$ .  $St$  for both thin meshes are very similar because the effective diameters of the bodies are the same. The clear difference lies in the  $\hat{y}/D$  curve showing that the cylinder with a thin-dense mesh shows no sign of reducing the amplitude of vibration for higher reduced velocities. Again, a non-negligible amplitude of  $\hat{y}/D \approx 0.3$  is observed to occur until the end of the experiment. The cylinder does not present turbulence buffeting, but a prominent vortex-excitation mechanism dominates over the response.

As mentioned before, the clearance between the model and the thin meshes allows them to oscillate independently of the motion of the cylinder, showing movements similar to a sail. The thin-sparse mesh is as loose as the thin-dense mesh. Nevertheless, the

increased number of bobbins might make the thin-dense mesh just dense enough to reduce its permeability to the flow, interact with the wake and capture more energy from the vortices. Consequently, the vortex-excitation mechanism dominates over turbulence buffeting for the whole range of reduced velocities.

Once more, it is worth highlighting that the thin meshes were seen to oscillate from side to side (more or less like a sail) as the cylinder responded to VIV. We believe this phenomenon is not much different from the hydrodynamic mechanism driving the oscillations of a cylinder fitted with a long splitter plate (with low friction) that is free to rotate around the body, as presented by Assi et al. [13].

#### 4. Investigation of the wake

Particle image velocimetry (PIV) measurements of the wakes have been taken for static models at  $Re = 9000$ . A horizontal plane illuminated the flow at mid length of the models. Two cameras were positioned side by side below the test section in order to compose a vector field wide enough to evaluate the larger flow structures in the wake. Instantaneous velocity fields were taken at a rate of 15 vector fields per second, thus producing a time-resolved analysis of 300 vector fields with almost 20 snapshots for each cycle of vortex shedding (considering  $f_s$  of the bare cylinder). Fig. 12 presents velocity vectors and vorticity contours for all the models except the thick-sparse mesh. The dashed white circle represents the masked region shadowed by the meshes. Each image is a composition of at least five instantaneous fields phase-averaged in time.

Fig. 12a shows that the bare cylinder is shedding a typical Karman wake of vortices with two single vortices per cycle. On the other hand, Fig. 12b reveals a different vortex shedding behavior for the cylinder with VT. Coherent vortex structures are indeed present in the wake, but vortices form much further downstream of the cylinder. Fig. 12c and d shows that, although the wakes of the cylinder with thin-sparse mesh and thin-dense mesh are affected by the presence of the flexible shrouds, the overall vortical structures are much more similar to that of the bare cylinder rather than that of the VT.

Examining the mean flow averaged in time from 300 images, presented in Fig. 13, one may note that the cylinder with VT (Fig. 13b) produces an extended region of velocity deficit near the base of the cylinder. Again, the mean flow in the wake of the cylinder fitted with the thin-sparse and thin-dense meshes are not much different from that in the wake of the bare cylinder.

From Figs. 12 and 13 we can conclude that the shrouds are not preventing the formation of a wake with organized vortices. They do not work to streamline the body either. In fact, a Karman wake associated with the typical flow around bluff bodies is clearly identified for all cases. The flexible shrouds do not prevent the communication of the separated shear layers, hence they are able to disrupt and modify the wake formation mechanism, but not to eliminate it altogether.

In Fig. 14 we have a quantitative view of how the wake is being modified. Measurement of the vortex-formation length are presented with streamlines of the mean flow. The color contours represent the fluctuation of the cross-flow component of velocity in the wake ( $v_{rms}$  is the root-mean-square of  $v$ , normalized by the maximum value obtained in the whole field). The locus of maximum velocity fluctuation defines the vortex formation length ( $L_F$ ) indicated by a white target in each figure.

Fig. 14a shows that the Karman wake for the bare cylinder has a vortex formation length of  $L_F/D = 1.5$ , in agreement with the literature (please note that  $L_F$  is strongly dependent on  $Re$  [17]). Fig. 14c and d shows that the vortex formation lengths in the wake produced by the thin-sparse and thin-dense meshes

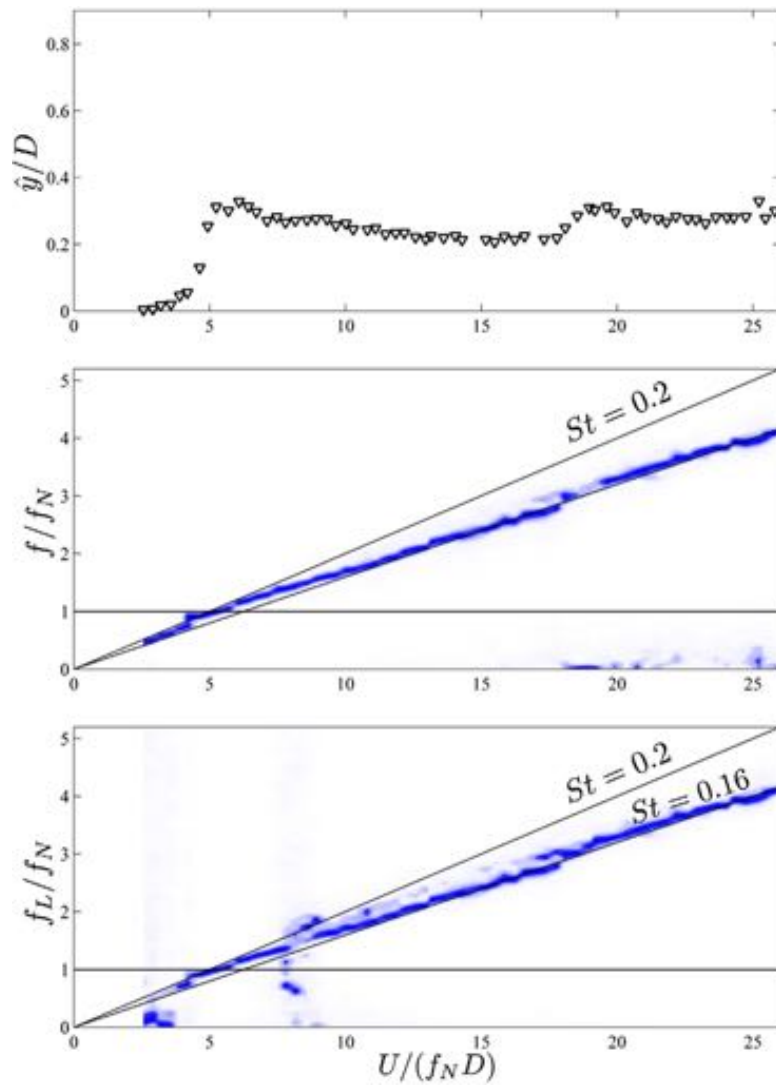


**Fig. 11.** (a) Amplitude of displacement, (b) spectrum of displacement and (c) spectrum of lift for a cylinder fitted with the thin-dense mesh responding to VIV.

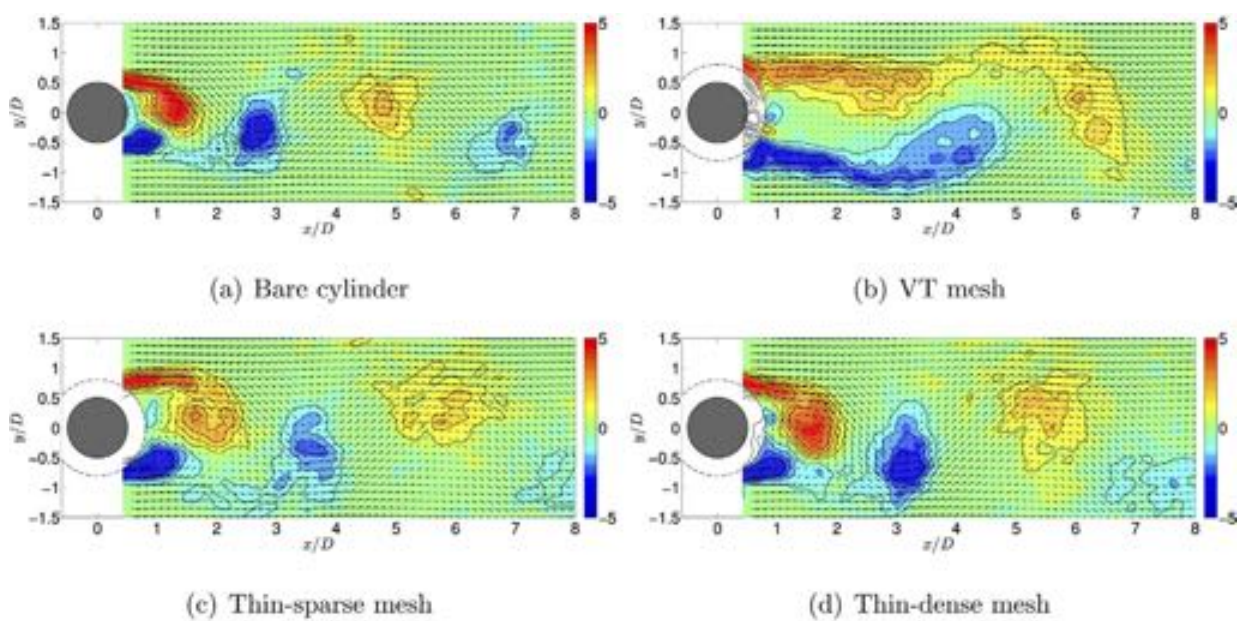


**Fig. 12.** Instantaneous velocity vectors and vorticity contours colored by vorticity magnitude (unit is 1/s). (a) Bare cylinder. (b) VT mesh. (c) Thin-sparse mesh. (d) Thin-dense mesh.



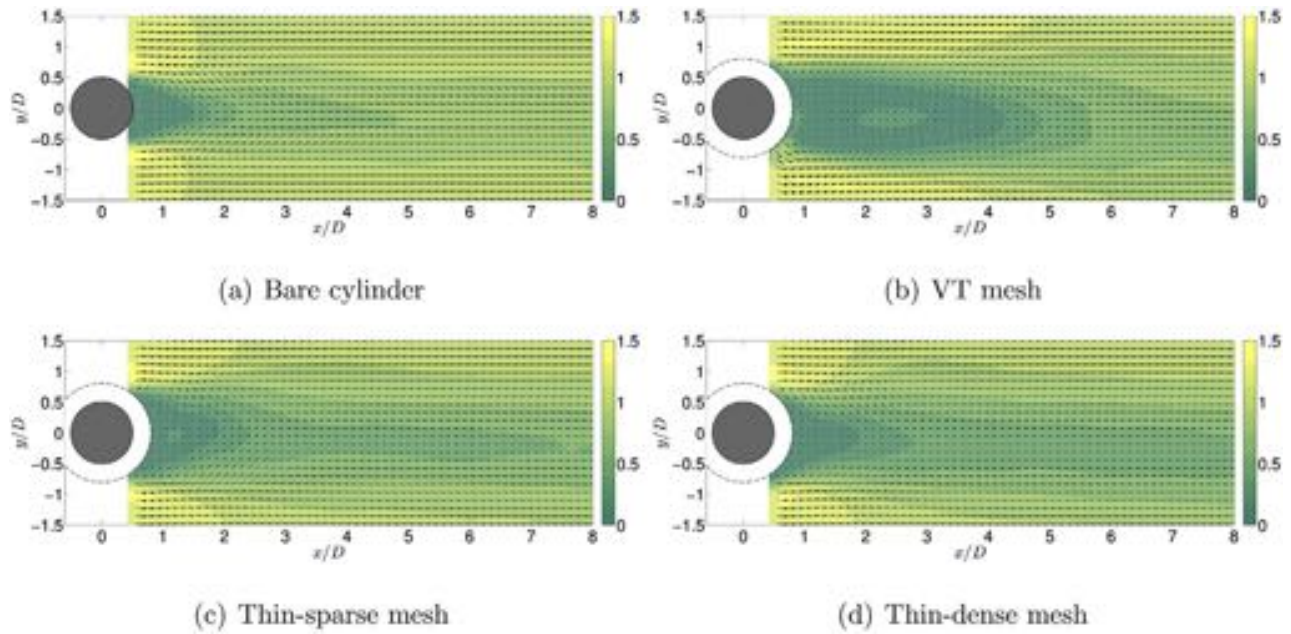


**Fig. 13.** Mean velocity field colored by velocity magnitude (normalized by  $U$ ). (a) Bare cylinder. (b) VT mesh. (c) Thin-sparse mesh. (d) Thin-dense mesh.

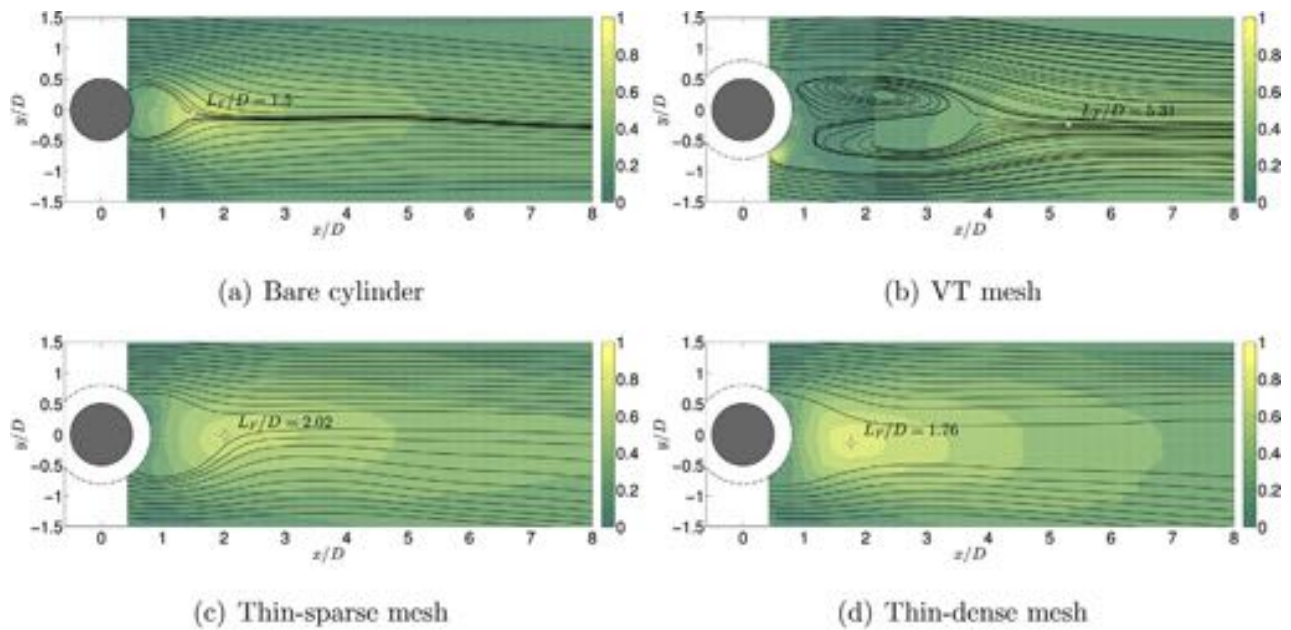


**Fig. 14.** RMS of the cross-flow component of velocity.  $v_{rms}$  is normalized by the maximum value found in each field. (a) Bare cylinder. (b) VT mesh. (c) Thin-sparse mesh. (d) Thin-dense mesh.

are not very different from that of the bare cylinder, being respectively  $L_F/D=2.02$  and  $1.76$ . The case for the VT, however, shows a completely different behavior. Fig. 14b reveals a much longer vortex formation length of  $L_F/D=5.31$  in the wake of the VT.

We argue that the longer formation length found for the VT is responsible for a decrease in the fluctuating lift feeding back to excite the cylinder into VIV. A longer  $L_F$  is also related to a decrease in the mean drag. Therefore, while most of the flow is separated from the outer surfaces of the bobbins, the entrainment of flow that permeates the VT mesh bleeds through to feed the near wake region, extending the vortex-formation length and increasing the base pressure (thus reducing drag). This mechanism, illustrated in

Fig. 15, is only possible due to the peculiar geometry of the VT bobbins, which is not matched by the other meshes. The outer ring of the VT bobbin separates the vertical cylindrical elements from the wall of the main cylinder, allowing for entrained fluid to flow through the mesh.

Please be aware that the PIV measurements have been performed for static cylinders in order to investigate the dominant flow structures produced by the flexible shrouds. We understand that the wake dynamics for the oscillating cylinders could be quite different from the results presented in this section. Nevertheless, the investigation of the wakes of static models has already clarified some interesting points regarding the underlying hydrodynamic mechanisms.

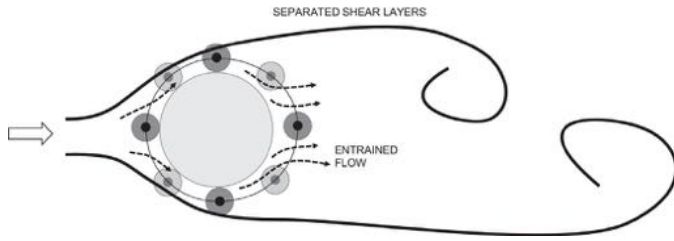


Fig. 15. Illustration of the flow around the VT mesh.

## 5. Concluding remarks

The preliminary experiments with fixed models revealed that all meshes increase drag for a static body. This is expected, since all meshes enlarge the area exposed to the flow and  $\bar{C}_D$  is obtained using just the diameter  $D$  of the bare cylinder. The thick-sparse mesh, for instance, increases more than 30% the frontal area compared to that of the bare cylinder. Besides that, the net and bobbins increase significantly the surface area and, consequently, the friction drag. The effect of an enlarged body is also responsible for reducing the Strouhal number of the shrouds, verified in Fig. 5b.

The fluctuation of lift presented in Fig. 4 reveals that the VT and the thick-sparse mesh reduce  $C_L'$  to values close to zero. Since the integral force is acquired at the top of the models, it is reasonable to infer that the meshes could either mitigate the sectional force, or uncorrelate lift along the span of the cylinder, or both. The most surprising result for the fixed-models experiments was the mean lift different from zero for the thin meshes. During the tests, it was verified that the meshes oscillated like a sail, breaking the body symmetry and generating a net lift force.

Observing the decay tests (Table 2), all five models have practically the same values of  $m^*$  and  $\zeta_{air}$ , hence the different behaviors are related to hydrodynamic effects. From the decay tests in still water, it is verified that all models increased the hydrodynamic damping and the effective added mass. It is known that there is a strong relationship between a decrease in the peak response and an increase in  $m^* \zeta$  [18,19]. Fig. 6 shows that all meshes reduced the peak response, and part of this suppression could be credited to the increase of hydrodynamic damping generated by the shrouds. On the other hand, an increase of hydrodynamic damping must not be solely the only mechanism responsible for all the suppression. For instance, the VT presents lower  $\zeta_{water}$  than the thick-sparse mesh, but it is more efficient in suppressing the peak amplitude of response. As a conclusion, the geometry of the bobbin is significant, since it produces a particular change in flow, leading to different responses.

The spectrum of the VT (Fig. 8) shows that the VT is more efficient in disrupting the wake than the other meshes. After the synchronization range, the oscillation frequency of the VT remains close to  $f_N$  while the  $f_L$  shows no clear trace. The thick-sparse mesh, on the other hand, even for very small oscillations, shows a typical trace of the Strouhal frequency for both oscillation and lift frequencies. This indicates that, in spite of reducing the oscillations, the thick-sparse mesh does not eliminate coherent vortex-shedding, while the VT disrupts it better. Since their distribution is the same, the differences between the two meshes can be attributed to their bobbin geometry.

As seen from the fixed-models experiments, the thin meshes had a distinctive behavior, showing a fashion for oscillating as a sail with the wake independently of the motion of the cylinder. As shown in Figs. 6, 3(c) and (d), there is no clear synchronization range because these models always oscillate in the same frequency of vortex-shedding. In the case of thin-dense mesh, not only the oscillation continues for higher reduced velocities, but it also reaches

another peak of response around reduced velocity of 20, which indicates the system is excited by another resonant frequency. The sail effect made the thin meshes extract more energy and in a wider range of frequencies than a mesh tightly attached to the cylinder; this mechanism is not associated with pure VIV.

This sail effect occurs because there is a larger clearance between the loose, thin meshes and the cylinder. Since the VT and the thick-sparse mesh have wider bobbins, their clearance is lower and the sail effect was not observed. In previous studies, Brown and King [7] noted the possibility of a "tail effect" due to the influence of mesh perimeter for VIV suppression. In the same work, they recommend a maximum value of  $\frac{3}{2}\pi D$  for this parameter. As it happened, all meshes in the present study have the same perimeter, which was below that limit. Therefore we suggest that the clearance is more relevant to predict the sail phenomenon rather than the perimeter itself (because it considers the influence of bobbin size).

The only difference between the thin-sparse and the thin-dense meshes is the bobbin distribution. The thin-sparse mesh extract less energy from the flow. Therefore, we may conclude that the hydrodynamic permeability of the mesh as well as the alternating distribution of the bobbins are important parameters (the latter due to the loss of three-dimensional correlation along the span).

PIV investigation of the wake for static models revealed that the cylinder fitted with the VT mesh produces a larger vortex-formation length, indeed much larger than that for the bare cylinder. We believe the suppression efficiency of the VT is related to the weakening of the feedback mechanism of the fluctuating lift force associated with vortex shedding. We have proposed that the entrainment of the flow between the bobbins and the wall that feeds through to the near wake is necessary to extend the vortex-formation length. This mechanism is only possible to occur with the VT mesh.

Finally, it is worth highlighting that these experiments have been conducted at relatively low mass-damping systems in order to enhance the vibration. We are not saying that all devices will present the same suppression efficiency at higher  $Re$ , or in systems with higher damping. Experiments in an idealized laboratory condition with a rigid cylinder, with low- $m^* \zeta$ , restricted to oscillate in one degree of freedom, will serve to establish the basic working principles of this family of suppressors and offer guidelines for further development.

## Acknowledgements

MMC is thankful to the support of ANP Brazilian Agency of Petroleum, Natural Gas and Biofuels. GRSA is grateful to FAPESP (2011/00205-6, 2014/50279-4), CNPq (306917/2015-7) and the Brazilian Navy.

## References

- [1] M. Tognarelli, S. Taggart, M. Campbell, Actual VIV fatigue response of full scale drilling risers: with and without suppression devices, in: *Proceedings of the 27th International Conference on Ocean, Offshore and Arctic Engineering* (ASME-OMAE 2008), 2008, p. 57046.
- [2] S. Taggart, M. Tognarelli, Offshore drilling riser VIV suppression devices – what's available to operators? in: *Proceedings of the 27th International Conference on Ocean, Offshore and Arctic Engineering* (ASME-OMAE 2008), 2008, p. 57047.
- [3] G.R. Assi, P.W. Bearman, M.A. Tognarelli, On the stability of a free-to-rotate short-tail fairing and a splitter plate as suppressors of vortex-induced vibration *Ocean Eng.* 92 (2014) 234–244, <http://dx.doi.org/10.1016/j.oceaneng.2014.10.007>.
- [4] M. Silva-Ortega, G. Assi, Flow-induced vibration of a circular cylinder surrounded by two, four and eight wake-control cylinders, *Exp. Therm. Fluid Sci.* 85 (2017) 354–362, <http://dx.doi.org/10.1016/j.expthermflusci.2017.03.020>.
- [5] A. Brown, Device and Method for Suppressing Vortex-Induced Vibrations, Tech. Rep., United States Patent Application Publication; 2010.



- [6] R. King, A. Brown, H. Braaten, M. Russo, R. Baarholm, H. Lie, Suppressing full scale riser VIV with the VT suppressor, in: *Proceedings of the 32nd International Conference on Ocean, Offshore and Arctic Engineering (ASME-OMAE 2008)*, 2013, p. 11642.
- [7] A. Brown, R. King, Tests with flexible quasi-fairing to reduce riser drag, suppress VIV and limit drilling down-time, in: *Offshore Technology Conference (OTC 2008)*, 2008, p. 19161.
- [8] M. Cicolin, C. Freire, G. Assi, VIV response and drag measurements of circular cylinders fitted with permeable meshes, in: *A.S. of Mechanical Engineers (ASME) (Ed.), 34th International Conference on Ocean, Offshore and Arctic Engineering (OMAE 2015)*, 2015, p. 42278.
- [9] M. Cicolin, *Suppression of the Vortex-Induced Vibration of Circular Cylinders With Permeable Meshes* (Master's thesis), Escola Politécnica, University of São Paulo, 2015, Available in Portuguese from [www.teses.usp.br](http://www.teses.usp.br).
- [10] G.R.S. Assi, P.W. Bearman, B.S. Carmo, J.R. Meneghini, S.J. Sherwin, R.H.J. Willden, The role of wake stiffness on the wake-induced vibration of the downstream cylinder of a tandem pair, *J. Fluid Mech.* 718 (2013) 210–245, <http://dx.doi.org/10.1017/jfm.2012.606>.
- [11] M. Zdravkovich, Review and classification of various aerodynamic and hydrodynamic means for suppressing vortex shedding, *J. Wind Eng. Ind. Aerodyn.* 7 (1981) 145–189.
- [12] M. Zdravkovich, *Flow Around Circular Cylinders: Vol. 1 – Fundamentals*, 1st ed., Oxford Science Publications, 1997.
- [13] G.R.S. Assi, P.W. Bearman, N. Kitney, Low drag solutions for suppressing vortex-induced vibration of circular cylinders, *J. Fluids Struct.* 25 (2009) 666–675.
- [14] C. Williamson, Three-dimensional wake transition, *J. Fluid Mech.* 328 (1996) 345–407.
- [15] C. Norberg, Fluctuating lift on a circular cylinders: review and new measurements, *J. Fluids Struct.* 17 (2003) 57–96.
- [16] C. Williamson, R. Govardhan, Vortex-induced vibrations, *Annu. Rev. Fluid Mech.* 36 (2004) 413–455.
- [17] M.F. Unal, D. Rockwell, On vortex formation from a cylinder. Part 1. The initial instability, *J. Fluid Mech.* 190 (1988) 491–512, <http://dx.doi.org/10.1017/S0022112088001429>.
- [18] R. Govardhan, C. Williamson, Defining the modified Griffin plot in vortex-induced vibration: revealing the effect of Reynolds number using controlled damping, *J. Fluid Mech.* 561 (2006) 147–180.
- [19] P.W. Bearman, Vortex shedding from oscillating bluff bodies, *Annu. Rev. Fluid Mech.* 16 (1984) 195–228.



Contents lists available at ScienceDirect

## Experimental Thermal and Fluid Science

journal homepage: [www.elsevier.com/locate/etfs](http://www.elsevier.com/locate/etfs)

## Flow-induced vibration of a circular cylinder surrounded by two, four and eight wake-control cylinders

M. Silva-Ortega<sup>1</sup>, G.R.S. Assi<sup>\*,2</sup>

Department of Naval Architecture &amp; Ocean Engineering, EPUSP University of São Paulo, São Paulo, SP, Brazil

## ARTICLE INFO

## Article history:

Received 24 October 2016

Received in revised form 13 March 2017

Accepted 13 March 2017

Available online 18 March 2017

## Keywords:

Vortex-induced vibration

Galloping

Suppression

Wake control

Drag reduction

## ABSTRACT

The present work investigates the use of a polar array of 2, 4 and 8 wake-control cylinders as a means to suppress the vortex-induced vibration (VIV) of a larger circular cylinder. The diameter of the control cylinders and the gap between their walls have been varied in 27 different configurations. Experiments have been performed in water at Reynolds numbers between 5000 and 50,000. Cross-flow amplitude of displacement, frequency of vibration, mean drag and fluctuating lift coefficients are presented. While some configurations of control cylinders suppressed VIV, others produced a galloping-like response. The best VIV suppressor was composed of 8 control cylinders and mitigated 99% of the peak amplitude of vibration when compared to that of a plain cylinder; mean drag was increased by 12%. A polar array of 4 control cylinders was the most efficient configuration to minimize the mean drag, but the system developed severe vibrations combining VIV and a galloping-like response. The system appeared to be very sensitive to the parameters investigated; small variations in the size and position of the control cylinders produced unexpected responses.

© 2017 Elsevier Inc. All rights reserved.

## 1. Introduction

The vortex-shedding mechanism of a circular cylinder can be controlled, at least in theory, by the interference of small wake-control cylinders positioned around the circumference of the main body. Strykowski and Sreenivasan [18] and others have showed that this strategy is possible for low Reynolds numbers. Such control cylinders interact with the boundary layer and/or the separated shear layers, disrupting the formation of vortices that are convected downstream to form a vortex wake. As a consequence, the periodic hydrodynamic forces feeding back from the vortex-shedding mechanism are considerably reduced, if not completely suppressed. In theory, the mean drag acting on the body is also reduced if suppression of the vortex wake is achieved [3,1]. Therefore, the development of passive devices to control the wake of a bluff body has called the attention of not only the scientific community, but also of the industry. Applications may vary from reduction of vortex-generated noise in the field of aeroacoustics to the mitigation of hydrodynamic loads on floating platforms in the field of offshore engineering. The suppression of the flow-

induced motion of offshore risers or of a monocolumn platform are good examples [15].

Placing a smaller control rod upstream of the main cylinder is also a well-established strategy for drag reduction [10]. But Strykowski and Sreenivasan [18] have proved that if the small control cylinder is placed within a defined region in the near-wake (downstream) of the main cylinder, coherent vortices could be effectively suppressed at a Reynolds number of  $Re = 80$ . Hwang and Choi [4] showed that the flow instability leading to the formation of a vortex street could be delayed by employing even smaller control cylinders at specific locations in the wake. Later, Kuo et al. [9] and Kuo and Chen [8] proved that, even if a vortex-wake is formed, the wake pattern could be altered by the presence of two control cylinders positioned in the near wake region.

Previous investigations positioning control cylinders in various arrangements around a bluff body have been performed through experiments and numerical simulations. Mittal [11] investigated the flow around a static cylinder with two wake-control cylinders positioned at  $\pm 90^\circ$  in relation to the incoming flow at  $Re = 10^2$  to  $10^4$ . He found that vortex shedding could be suppressed only if the control cylinders (at that specific  $\pm 90^\circ$  location) were rotating above a critical spinning ratio. Sakamoto and Haniu [16] also investigated the control of a vortex-wake by varying the position of a smaller cylinder around the main body. They observed that, for certain positions, the control cylinder could produce the useful

\* Corresponding author.

E-mail address: [g.assi@usp.br](mailto:g.assi@usp.br) (G.R.S. Assi).<sup>1</sup> Now at the Dept. Naval Architecture, Universidad Veracruzana, Mexico.<sup>2</sup> Currently a Visiting Associate in Aerospace at GALCIT, California Institute of Technology, USA.

effect of reducing the hydrodynamic forces experienced by the main body at  $Re = 6.5 \times 10^4$ .

Recently, Silva-Ortega [17] has shown that a polar array of 2, 4 and 8 control cylinders equally spaced around a static body could be developed into an effective device to suppress vortex shedding from a larger circular cylinder at  $Re = 5000$  to  $50,000$ . Fundamental parameters (such as the number of control cylinders, their diameter and their distance from the main body) have been shown to play a significant role in the wake-control mechanism. As consequence, a reduction of hydrodynamic forces has been achieved.

### 1.1. Suppression of flow-induced vibration

In the present work, we move from controlling the wake of static bluff bodies to the field of hydroelasticity. This time we investigate the effectiveness of a polar array of control cylinders in suppressing the vortex-induced vibrations (VIV) of a circular cylinder that is free to respond to the excitation of the incoming flow. Our investigation is limited to vibrations in one degree of freedom in the cross-flow direction.

VIV is a fluid-structure interaction phenomenon that occurs when the frequency of vortex shedding resonates with one of the natural frequencies of an elastic bluff body. Please refer to Williamson and Govardhan [19] for a comprehensive review of the phenomenon. In principle, if a device is able to suppress the formation of coherent vortices, VIV is eliminated at its root and vibrations do not develop. Now, it is one thing to disrupt or control the wake of a bluff body when the body is static, but it is another to control the wake of a body that is free to respond to the flow. Sometimes an efficient device for the control of vortex-shedding is not as efficient in suppressing VIV. Various examples of VIV suppressors are found in the literature, for example, in the review by Zdravkovich [22].

Korkischko and Meneghini [7] have performed VIV experiments with a circular cylinder free to oscillate in the cross-flow direction and fitted with two wake-control cylinders in the range of  $Re = 7500$ . They found that the two non-rotating control cylinders positioned at  $\pm 90^\circ$  were not effective in suppressing VIV of the main body. In fact, they only reduced the peak amplitude of response by 17%, when compared to that of a plain cylinder. However, when they applied enough rotation to the small cylinders, the vortex wake was stabilized and VIV was suppressed.

Zhu et al. [23] performed numerical simulations of the flow at  $Re = 2000$  and showed that the two-degree-of-freedom vibration of an elastic cylinder could be reduced by 89% when two control cylinders were positioned at  $\pm 135^\circ$  from the frontal stagnation point of the cylinder. Again, when the two control cylinders were forced to rotate, an ever better suppression was obtained. Similar results were obtained by Muddada and Patnaik [13], who performed two-dimensional numerical simulations of the flow around a cylinder fitted with two control cylinders located at  $\pm 120^\circ$  in the range of  $Re = 100$ – $300$ .

Wu et al. [21] tested the VIV suppression of a long flexible cable with a circular cross section fitted with four flexible control rods positioned parallel to the axis of the cylinder. At  $Re \approx 10^3$ , they observed that the dynamic response of the cable was substantially altered by the hydrodynamic interaction of the flow-control rods. In their experimental arrangement, the distribution of the control rods was such that there was always one rod aligned with the incoming flow. In another study, Wu et al. [20] investigated the effect of rotating the array of control rods around the main cylinder.

### 1.2. Objective

In the present study, we start with the polar arrays of 2, 4 and 8 control cylinders proposed by Silva-Ortega [17] to reduce the

hydrodynamic loads on a static cylinder and employ them as a means to suppress the cross-flow VIV of a larger elastic circular cylinder. The dynamic response due to VIV, as well as the hydrodynamic loads acting on the cylinder, are presented for a wide range of flow speeds.

We will conclude that the VIV of a circular cylinder can be mitigated by specific arrangements of wake-control cylinders in the range of Reynolds number between 5000 and 50,000. On the other hand, a few arrangements may cause the system to develop severe vibrations associated with a galloping-like excitation, showing that the dynamic response of the system is very sensitive to small variations in the geometrical parameters.

## 2. Experimental setup

Experiments have been carried out in the Circulating Water Channel of NDF (Fluids and Dynamics Research Group) at the University of São Paulo, Brazil. The water channel has an open test section which is 0.7 m wide, 0.9 m deep and 7.5 m long. Good quality flow can be achieved up to 1.0 m/s with turbulence intensity less than 3%. For further details on the apparatus, other VIV experiments employing the elastic rig and information on the facilities please refer to Silva-Ortega [17] or Assi et al. [2].

A rigid section of a smooth circular cylinder was made of a perspex tube of external diameter  $D = 100$  mm. Two, four or eight identical wake-control cylinders of diameter  $d_c$  were made of perspex rods and supported by rings attached to the ends of the main cylinder. The distribution of the control cylinders about the main cylinder is presented in Fig. 1, in which the arrow indicates the direction of the incoming flow. The position of the  $N$  control cylinders was chosen so that they are equally spaced around the main cylinder, but keeping a symmetric distribution in relation to the streamwise axis, with no cylinder at the frontal stagnation point.

It is worth noting that our cylinder fitted with 2 control cylinder is similar to other arrangements found in the literature ([7,11] for example). Our arrangement with 4 control cylinder is not similar to that of Wu et al. [21], since they always kept one control cylinder facing the incoming flow. We are not aware of other works that have employed an array of  $N = 8$  wake-control cylinders.

The axes of the control cylinders were parallel to the axis of the main cylinder, spanning the whole immersed length of the model ( $L = 700$  mm). Two extra supporting rings were installed at  $L/3$  and  $2L/3$  positions to hold the control cylinders in place and prevent them from vibrating by reducing their free span. The control cylinders did not present significant deflections nor vibrations due to their own VIV in the course of the experiments.

Inspired by the experimental results of Korkischko and Meneghini [7] and based on the parametric variation of Silva-Ortega [17], the diameter of the control cylinders was varied in three steps of  $d_c/D = 0.04$ ,  $0.06$  and  $0.08$ . The gap measured between the wall of the control cylinders and the wall of the main cylinder was set to  $G/D = 0.05$ ,  $0.10$  and  $0.15$ . A total of 27 geometric variations employing the wake-control cylinder have been tested, in addition to the case of a plain cylinder (without control cylinders) that served a reference.

Models were mounted on a especially built load cell attached to a sliding frame and supported by air bearings. A pair of coil springs provided the restoration force to the system, which was free to oscillate only in the cross-flow direction, as shown in Fig. 2. An optical sensor measured the displacement ( $y$ ) of the cylinder, keeping structural mass and damping to a minimum. The product between the mass ratio ( $m^*$ , calculated as the ratio between the total oscillating mass and the mass of displaced water) and the damping ratio ( $\zeta$ , measured as a percentage of the critical damping) was  $m^*\zeta = 0.066$ . The natural frequency of the system ( $f_0$ ) as well

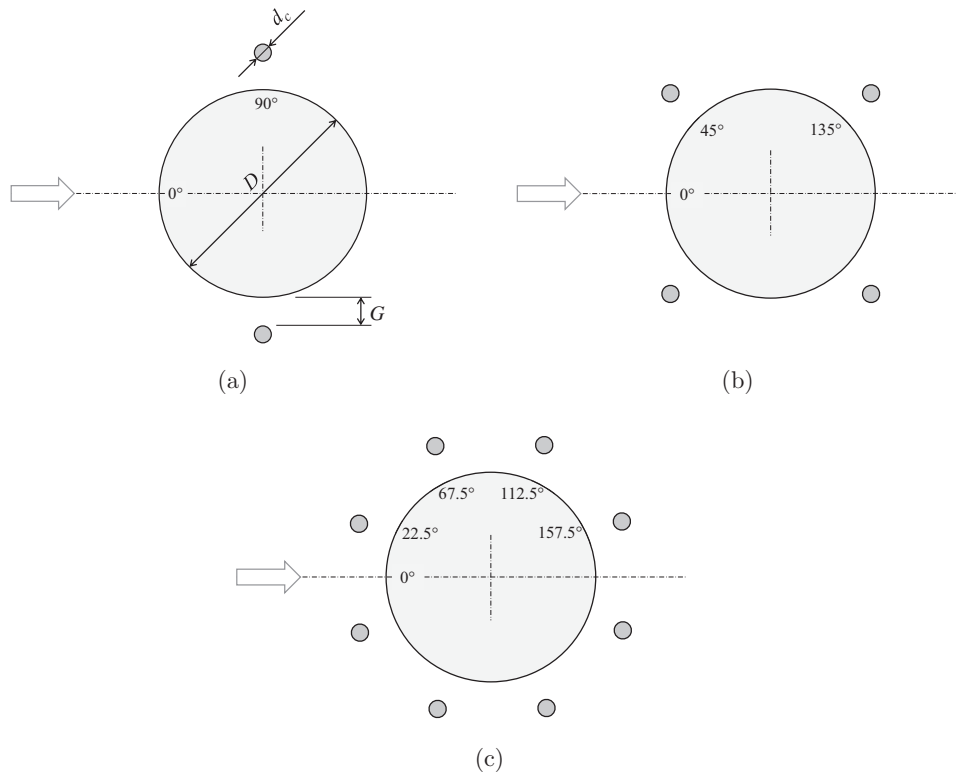


**Fig. 1.** Geometrical parameters for the main cylinder with (a) two, (b) four and (c) eight control cylinders (figures drawn not to scale). Incoming flow direction marked by the arrow.

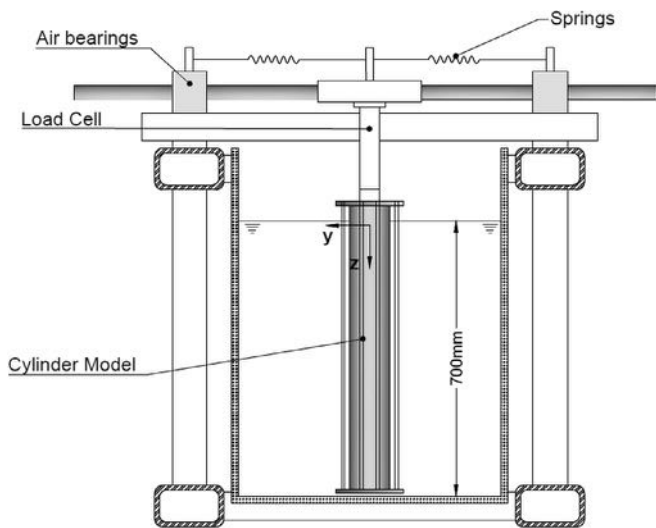


**Fig. 2.** Cross view of the experimental setup: elastic rig mounted on the test section.

as the damping ratio ( $\zeta$ ) were determined by decay tests performed in air.

The only flow variable changed during the course of the experiments was the flow speed ( $U$ ), which altered  $Re = UD/\nu$  between 5000 and 50,000 (where  $\nu$  is the dynamic viscosity of water) and the reduced velocity  $U_R = U/(Df_0)$  in the range of 2 to 20. A summary of all the parameters investigated in the experiment is presented in Table 1.

The dynamic responses due to VIV are analyzed across the  $U_R$  range by comparing the normalized amplitude of displacement

$\hat{y}/D$ , where  $\hat{y}$  is the RMS of  $y$  times  $\sqrt{2}$  (also called harmonic amplitude). The dominant frequency of oscillation normalized by the natural frequency ( $f/f_0$ ) was obtained from the spectrum of displacement with a non-dimensional resolution of 0.02. The mean drag coefficient ( $\bar{C}_D$ ) and the RMS of the lift coefficient ( $\hat{C}_L$ ) were obtained by reducing the force measurement of the load cell with the product  $\frac{1}{2}\rho U^2 D$ , per unit length of the cylinder (where  $\rho$  is the specific mass of the water). The experimental uncertainties for the measurements of all variables and parameters are specified in Table 1.

### 3. Results and discussion

Preliminary VIV results were obtained for a plain cylinder to validate the setup and serve as reference for comparison. Fig. 3a presents the amplitude of displacement ( $\hat{y}/D$ ) compared to the results of Khalak and Williamson [6], who performed VIV experiments with low damping at  $m^* = 2.4$  and 3.3. The peak amplitude of response is almost  $\hat{y}/D = 1$  around  $U_R = 4$  and the typical three branches of response (initial, upper and lower) are clearly identified in both datasets. The wider synchronization range observed in the present data, extending from  $U_R = 3$  to almost 15, is due to our lower value of  $m^* = 1.09$ .

While Khalak and Williamson [6] normalized  $U_R$  employing the natural frequency of the system immersed in still water ( $f_N$ , in their notation), their previous work [5] had presented the same data non-dimensionalizing  $U_R$  by the natural frequency measured in air ( $f_0$ ). In the present paper we have recalculated the  $U_R$  axis from Khalak and Williamson [6] based on their data presented in 1996 to allow for a direct comparison of the data. Even though there are small differences in  $m^*$  and  $\zeta$ , the agreement is very good.

Fig. 3b shows the dominant frequency of vibration ( $f/f_0$ ). The inclined line represents a nominal Strouhal number  $St = 0.2$ , which

**Table 1**

Parameters and variables employed in the present investigation.

| Parameter or Variable              | Symbol      | Variation                       | Uncertainty (%) |
|------------------------------------|-------------|---------------------------------|-----------------|
| Number of control cylinders        | $N$         | 0, 2, 4, 8                      |                 |
| Diameter of control cylinders      | $d_c/D$     | 0.04, 0.06, 0.08                | $\pm 5$         |
| Gap between cylinders              | $G/D$       | 0.05, 0.10, 0.15                | $\pm 5$         |
| Reynolds number                    | $Re$        | $5 \times 10^3 - 5 \times 10^4$ | $\pm 5$         |
| Reduced velocity                   | $U_R$       | 2–20                            | $\pm 5$         |
| Mass ratio                         | $m^*$       | 1.09                            | $\pm 5$         |
| Damping ratio                      | $\zeta$     | 0.0061                          | $\pm 7$         |
| Harmonic amplitude of displacement | $\hat{y}/D$ |                                 | $\pm 3$         |
| Dominant frequency of oscillation  | $f/f_0$     |                                 | $\pm 5$         |
| Mean drag coefficient              | $\bar{C}_D$ |                                 | $\pm 3$         |
| RMS of lift coefficient            | $\hat{C}_L$ |                                 | $\pm 5$         |

is expected for a plain, static cylinder in this  $Re$  range. Both curves show the synchronization range within which the frequency of vortex-shedding is locked by the frequency of oscillation ( $f$ ). The curves depart from the  $St = 0.2$  line and follow closer to  $f/f_0 = 1$ . Even though the present data only shows the dominant frequencies of response – and not concurrent frequency branches along the  $U_R$  range – the overall trend is in agreement with the reference.

Fig. 3c shows the mean drag ( $\bar{C}_D$ ) as a function of  $U_R$ , revealing the amplification of drag during the synchronization range. The maximum  $\bar{C}_D \approx 4$  is consistent in both curves. The fluctuating lift coefficients, presented in Fig. 3d, also show good agreement with the results of Khalak and Williamson [6]. Even though our results show a local amplification of  $\hat{C}_L$  between  $U_R = 7$  and 10, corresponding to the transition from the upper to the lower branch of response, the maximum values of  $\hat{C}_L \approx 2.5$  are in very good agreement.

### 3.1. VIV response with 2 control cylinders

Fig. 4a presents the VIV response for the case with 2 control cylinders compared with that of a plain cylinder. In general, all cases with 2 control cylinders presented peak amplitudes of vibration at resonance ( $U_R \approx 4$ ) lower than that experienced by the plain cylinder. But while the end of the VIV synchronization range was clearly noticeable for the plain cylinder at  $U_R = 15$ , all systems with 2 control cylinders sustained greater  $\hat{y}/D$  for the higher reduced velocities.

The results obtained by Korkischko and Meneghini [7] for a system with two control cylinders are also presented in Fig. 4a for comparison. In their experiment,  $Re$  was varied between 1600 and 7500 and the geometrical parameters were  $[d_c/D, G/D] = [0.06, 0.07]$ , which fits in between our two cases with  $[d_c/D, G/D] = [0.06, 0.05]$  and  $[0.06, 0.10]$ . Their response curve revealed a single branch of considerable vibration extending until the end of the  $U_R$  range. While their maximum  $\hat{y}/D \approx 0.6$  was not too far from our results (which showed  $\hat{y}/D \approx 0.7$ ), their system did not develop severe vibrations for the higher reduced velocities. On the other hand, our results showed a considerable build-up of response with increasing flow speeds, with  $[d_c/D, G/D] = [0.06, 0.10]$  reaching  $\hat{y}/D \approx 1.3$  at  $U_R = 17$ . Korkischko and Meneghini [7] concluded that their system did not respond due to a galloping instability even though their control cylinders broke the axial-symmetry of the body, making it, at least in theory, susceptible to galloping.

This fundamental difference in the responses may suggest that  $Re$  could play an important role in the dynamics of the system. The

difference of  $Re$  between the two experiments was only of one order of magnitude, but it might have been that different regimes of separated flow could have sustained galloping-like oscillations for higher reduced velocities in our case. Another possible explanation – and perhaps a more probable one – regards the difference in the level of structural damping of both systems. Since Korkischko and Meneghini [7] reported a  $\zeta = 0.01$  (one order of magnitude higher than in the present work), it might be that the responses from both experiments are due to the same hydrodynamic mechanisms, but balancing different levels of structural damping.

In general, the behavior of the cases with 2 control cylinders could be divided into two groups. The difference might not be noticeable from the  $\hat{y}/D$  alone, but requires a close look in the frequency signatures presented in Fig. 4b. Three cases made a group of distinct response showing  $f/f_0$  following closer the  $St = 0.2$  line as  $U_R$  was increased. They were  $[d_c/D, G/D] = [0.04, 0.15]$ ,  $[0.06, 0.15]$  and  $[0.08, 0.05]$ . They did not show the highest  $\hat{y}/D$ , but their frequency signature was rather distinct from the other cases. Somehow, the size and position of the two control cylinders made the system increase  $f/f_0$  with  $U_R$  following the frequency of vortex shedding. As a result, considerable vibration with  $\hat{y}/D \approx 0.4$  to 0.7 were sustained for higher reduced velocities at a clearly distinct frequency trend. On top of that, one has to bear in mind that such a low- $m^*\zeta$  system may also present a non-negligible residual vibration due to turbulence buffeting, especially for high flow speeds.

All other cases, apart from the three identified above, showed considerable  $\hat{y}/D$  (which increases with  $U_R$ ), but with a periodic response at a much lower  $f/f_0$  signature, most of the time lower than  $f/f_0 = 1$ . Also, sudden jumps between different levels of dominant  $f/f_0$  suggest a broader spectrum of vibration, with not a single branch of  $f/f_0$  dominating over the  $U_R$  range. For some cases,  $f/f_0$  was so low that it might indicate a slow lateral drift of the cylinder.

We believe that the build-up of  $\hat{y}/D$  with increasing  $U_R$  combined with a low frequency signature suggests a galloping-like excitation. The most significant cases were  $[d_c/D, G/D] = [0.06, 0.10]$ ,  $[0.08, 0.10]$  and  $[0.08, 0.15]$ . Of course a detailed analysis of the lift signal would be necessary to identify the phenomenon (what is beyond the scope of this paper). Nevertheless, inspired by the classical galloping theory presented by Parkinson [14], it might be that different combinations of  $d_c/D$  and  $G/D$  for 2 control cylinders produced different amounts of lift in phase with the transverse velocity of the body to overcome the actual level of  $\zeta$ . In a future investigation, visualization of the flow around the control cylinders will be required to determine if flow regimes of a different nature were in action.

Turning now to Fig. 4c,  $\bar{C}_D$  curves show that all cases with 2 control cylinders presented the amplification of mean drag during and beyond the VIV synchronization range, with  $\bar{C}_D$  remaining higher than that measured for the plain cylinder for higher  $U_R$ . Interestingly, the cases with the highest  $\hat{y}/D$  for the higher  $U_R$  were not the ones that presented the highest  $\bar{C}_D$ . On the contrary, the three cases mentioned above (following the vortex-shedding frequency) presented the lowest mean drag for the widest range of  $U_R$ . The highest  $\bar{C}_D$  were found for  $[d_c/D, G/D] = [0.08, 0.05]$  and the other two cases governed by that distinct mechanism.

Finally, Fig. 4d does not reveal a distinct behavior that separates the cases with 2 control cylinders. Perhaps the only thing to highlight is that the highest  $\hat{C}_L$  were observed for those cases whose frequency signatures followed the  $St = 0.2$  line for longest. When the response was tuned in the vortex-shedding frequency, the system was able to extract more energy from the flow, thus resulting in higher  $\hat{C}_L$ .



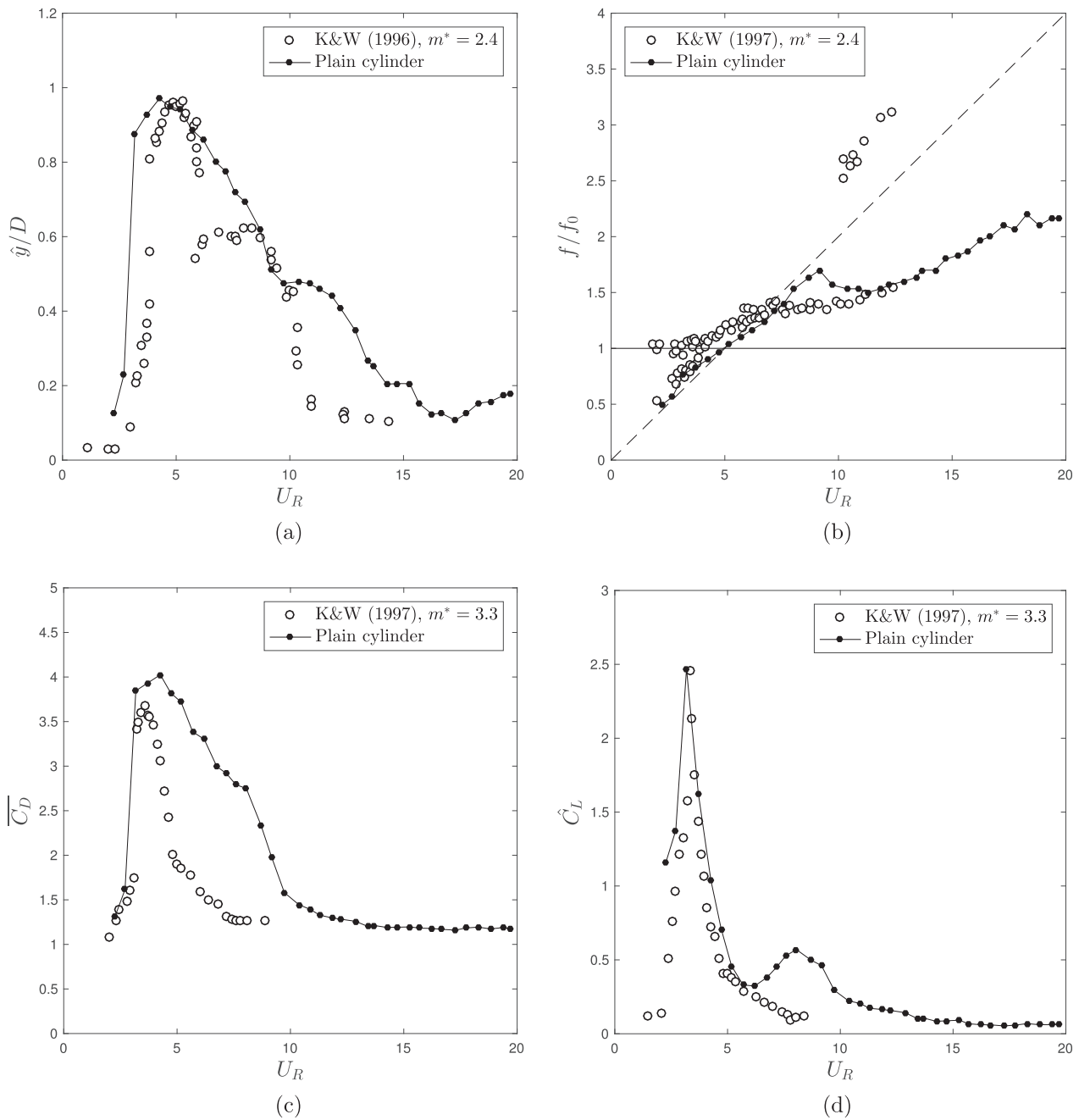


**Fig. 3.** Validation of the VIV response of a plain circular cylinder with  $m^* = 1.09$  and  $m^*\zeta = 0.066$ : (a) amplitude of displacement, (b) frequency of vibration, (c) mean drag coefficient and (d) RMS of lift coefficient. Data for comparison is from Khalak and Williamson [5,6], with  $m^*\zeta = 0.013$ .

### 3.2. VIV response with 4 control cylinders

The responses are considerably different when 4 control cylinders were fitted around the main body; Fig. 5a presents  $\hat{y}/D$  for all nine variations. In general, the three cases with the smallest control cylinders ( $d_c/D = 0.04$ ) presented a reduced peak of vibration when compared to the response of the plain cylinder;  $\hat{y}/D$  was also considerably reduced by the end of the synchronization range around  $U_R = 14$ . It appeared that these three cases were indeed responding under the influence of VIV. The best case with  $[d_c/D, G/D] = [0.04, 0.05]$  reduced the peak  $\hat{y}/D$  by 50%.

When  $d_c/D$  was increased to 0.06,  $[d_c/D, G/D] = [0.06, 0.05]$  and  $[0.06, 0.10]$  presented a suppressed response. But the clear distinct response was observed for the case  $[d_c/D, G/D] = [0.06, 0.15]$ , with

a local resonant peak of VIV at  $U_R \approx 4$ , followed by a galloping-like response characterized by rapidly increasing amplitudes for  $U_R > 10$ . The frequency signature for  $[d_c/D, G/D] = [0.06, 0.15]$ , presented in Fig. 5b, showed that  $f/f_0$  followed a clear dominant trend below 1 for the entire response. Again, it might be that a specific pair  $[d_c/D, G/D]$  for 4 control cylinders was able to interact with the separated flow generating lift in phase with the transverse velocity of the body. This galloping-like mechanism is possible to occur for non-circular geometries and might have occurred for this specific case of  $N = 4$  control cylinders.

The best VIV suppression for 4 control cylinders was found for  $[d_c/D, G/D] = [0.08, 0.05]$ , with a maximum peak of only  $\hat{y}/D = 0.25$  at the VIV resonance ( $U_R = 4$ ) and  $\hat{y}/D < 0.2$  for the rest of the reduced velocity range. In contrast, the case  $[d_c/D, G/D] =$

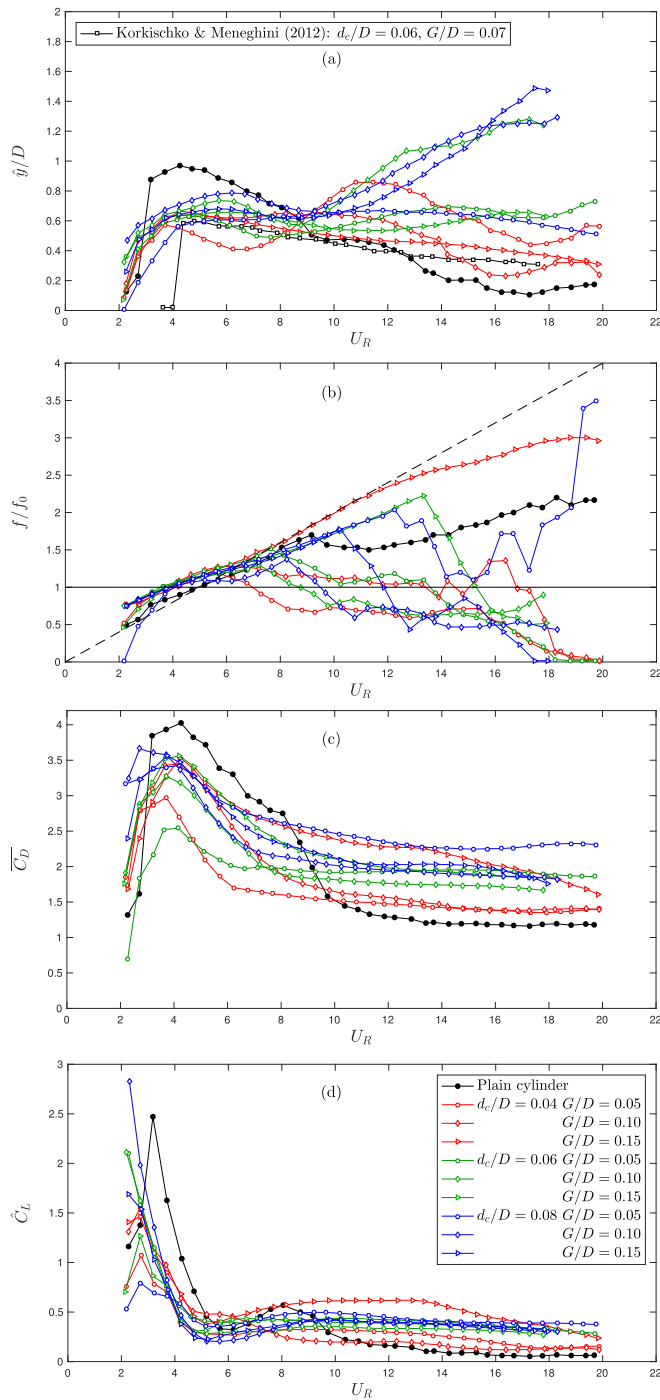


**Fig. 4.** VIV response for a circular cylinder with  $N=2$  control cylinders: (a) amplitude of displacement, (b) frequency of vibration, (c) mean drag coefficient and (d) RMS of lift coefficient.

[0.08, 0.15] responded with a very distinct behavior, with local peaks of vibration at  $U_R = 4, 11$  and  $16$ . Its frequency signature also remained below  $f/f_0 = 1$ , suggesting that a galloping-like excitation was present but could not be sustained until the highest reduced velocity.

It is interesting to note in Fig. 5c that almost all cases presented  $\bar{C}_D$  below that for a plain cylinder. Case  $[d_c/D, G/D] = [0.06, 0.05]$ , which presented a good suppression, achieved the lowest mean drag for most of the reduced velocity range. As expected, the case  $[d_c/D, G/D] = [0.06, 0.15]$ , with the highest response, also presented the highest  $\bar{C}_D$ .

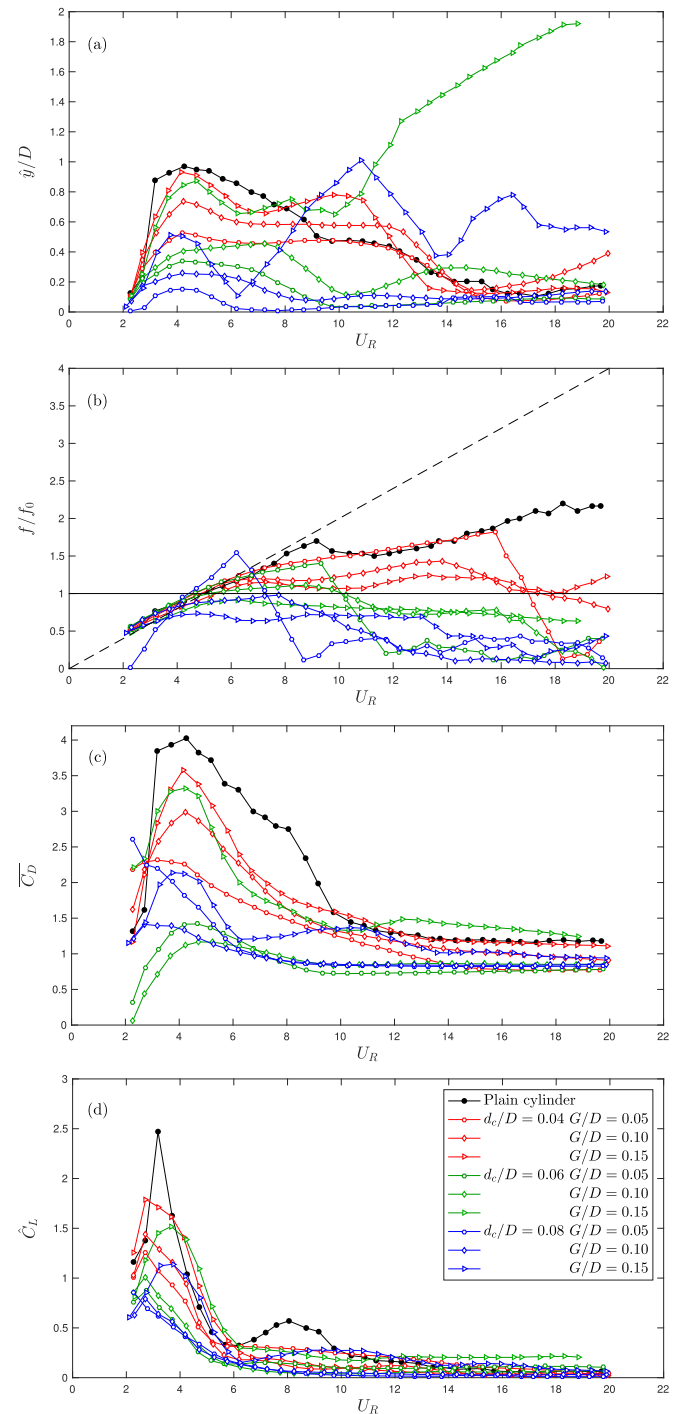


**Fig. 5.** VIV response for a circular cylinder with  $N=4$  control cylinders: (a) amplitude of displacement, (b) frequency of vibration, (c) mean drag coefficient and (d) RMS of lift coefficient.

### 3.3. VIV response with 8 control cylinders

First of all, no galloping-like responses were observed for the systems with 8 control cylinders, as seen in Fig. 6a, probably because the apparent axial-symmetry of the body is somewhat recovered with the distribution of more control cylinders. Almost all cases presented  $y-hat/D$  under the response curve of the plain cylinder, with only a few exceptions. Cases with  $[d_c/D, G/D] = [0.04, 0.10]$  and  $[0.04, 0.15]$  presented the highest responses, with  $y-hat/D \approx 0.4$  being sustained for higher  $U_R$  beyond

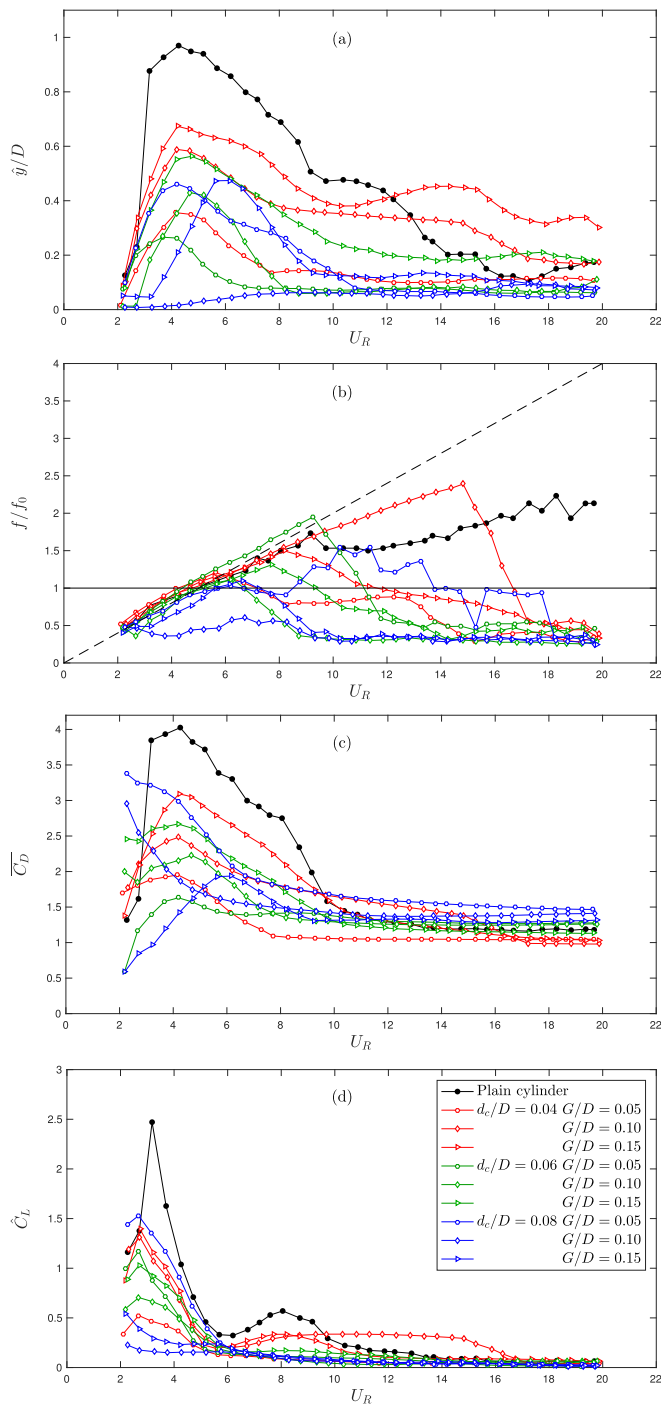


**Fig. 6.** VIV response for a circular cylinder with  $N=8$  control cylinders: (a) amplitude of displacement, (b) frequency of vibration, (c) mean drag coefficient and (d) RMS of lift coefficient.

the synchronization range of the plain cylinder. The frequency signatures for these two cases, shown in Fig. 6b, remained below  $f/f_0 = 1$ , suggesting that a mechanism other than VIV was driving the vibrations.

The best suppression was achieved by the largest control cylinders, in special by the case  $[d_c/D, G/D] = [0.08, 0.10]$ , that showed almost no response (in fact, a reduction by 99%) near the VIV resonance and minimum  $\hat{y}/D < 0.1$  for the wider range of  $U_R$ . This case, however, did not present the lowest mean drag, which was increased by 12% when compared to that of a plain cylinder. The lowest mean drag of all was recorded for the case  $[d_c/D, G/D] =$

$[0.04, 0.05]$ , as seen in Fig. 6c. Very few cases with 8 control cylinders managed to reduced the mean drag below that of the plain cylinder for the wide range of  $U_R$ . Finally, the highest  $\hat{C}_L$  was achieved by  $[d_c/D, G/D] = [0.04, 0.10]$ , apparently responding with  $f/f_0$  following the frequency of vortex-shedding, as seen in Fig. 6d.

#### 4. Further discussion

As seen above, the responses showed a variety of different behaviors, making it a rather difficult task to find a general governing principle with the parameters we had in hand. Sometimes, a small variation in one of the parameters produced a totally different response. In an attempt to find a general geometric parameter governing the response behavior, one could propose to add the diameter of the control cylinder to the gap between the walls, thus creating  $(G + d_c)/D$ . This new parameter simply represents the outermost radial distance of the control cylinders from the wall of the main cylinder, in a way suggesting how far into the flow the control cylinders could interfere.

Table 2 presents the parameter  $(G + d_c)/D$  calculated for the nine parametric variations for each  $N$  control cylinders. One can easily note that  $(G + d_c)/D$  more than doubles from the first to the last case. Also, one could expect that small variations in this parameter, say from  $(G + d_c)/D = 0.13$  to  $0.14$ , would not produce qualitatively different responses. Indeed, cases  $[d_c/D, G/D] = [0.08, 0.05]$  and  $[0.04, 0.10]$  showed qualitatively similar responses for  $N = 2$  and  $4$ , but significantly different responses for  $N = 8$ . In summary, simply considering the outermost position of the control cylinders represented by  $(G + d_c)/D$  would not explain the complex hydrodynamic interference by grouping together similar response curves.

The most interesting general aspect is that all cases reduced maximum amplitude of vibration at the VIV resonance. Most of the cases also reduced  $\hat{y}/D$  for most of the synchronization range ( $3 < U_R < 13$ ). On the other hand, the behavior for higher reduced velocities, way past the synchronization range, appeared to have shown a complex phenomenology. Pure VIV, pure galloping-like and combined VIV and galloping-like excitations all appeared in the responses for higher values of  $U_R$ . The configurations with  $N = 4$  control cylinders, for example presented the most diverse response for the set of parameters investigated (Fig. 5). At the same time that they presented the lowest recorded mean drag, they also produced the highest amplitudes of vibration with the richest frequency signatures. A small variation on the radial position and size of the control cylinders produced unexpected responses.

The group with  $N = 2$  control cylinders have shown even higher levels of mean drag, the highest recorded in the investigation. Apart from the suppression of  $\hat{y}/D$  within the synchronization range, all cases produced responses higher than that of the plain cylinder for  $U_R > 8$ . This behavior can be associated with a galloping-like excitation, especially if the frequency signature is taken into account. Korkischko and Meneghini [7] performed experiments with a similar case with 2 control cylinders with  $[d_c/D, G/D] = [0.06, 0.07]$  and  $m^* = 1.8$ . They reported that the amplitude of response was completely different when compared to that of a plain cylinder. In fact, their peak response of

**Table 2**  
Parameter  $(G + d_c)/D$ .

|              | $d_c/D = 0.04$ | $d_c/D = 0.06$ | $d_c/D = 0.08$ |
|--------------|----------------|----------------|----------------|
| $G/D = 0.05$ | 0.09           | 0.11           | 0.13           |
| $G/D = 0.10$ | 0.14           | 0.16           | 0.18           |
| $G/D = 0.15$ | 0.19           | 0.21           | 0.23           |

$\dot{y}/D \approx 0.6$  at  $U_R = 4$  was similar to our case  $[0.04, 0.15]$ , for which the peak amplitude was  $\dot{y}/D \approx 0.7$ .

Four of our cases presented galloping-like instability: three cases for  $N = 2$  ( $[d_c/D, G/D] = [0.08, 0.10], [0.08, 0.15]$  and  $[0.06, 0.10]$ ); and one for  $N = 4$  ( $[d_c/D, G/D] = [0.06, 0.15]$ ). Based on the theory for classical galloping summarized by Parkinson [14], the position of the fixed control cylinders may have interacted with the separation points as the cylinders oscillated across the flow. The arrangement may have broken the body's axial-symmetry, generating lift in phase with the body's transverse velocity. Consequently, as we have observed, the amplitude of response presented a rapid increase for increasing flow speeds, with no sign of decrease, at least not in the range of the experiments.

For other cases, it appears that the high amplitudes of oscillations due to galloping are competing with or being disrupted by the resonant vibrations of VIV. This might be happening for the case with  $N = 4$  and  $[d_c/D, G/D] = [0.08, 0.15]$ , in which galloping and VIV appear to interchangeably occur along the reduced velocity range. The peak displacement initially achieved by VIV around  $U_R \approx 4$  could produce fast-enough vibrations to lead the system into galloping for the rest of the  $U_R$  range.

When the cylinder was surrounded by  $N = 8$  control cylinders, no galloping-like response was observed. Apparently, the evenly distribution of more control cylinder around the body helped it to restore its axial-symmetry, at least as far as the main flow structures are concerned. One should note that galloping is highly dependent on Reynolds number, free stream turbulence intensity and other secondary factors, therefore we cannot assert that a cylinder fitted with 8 control cylinders will never develop galloping under other flow circumstances. Zdravkovich [22] presented results of a cylinder fitted with an axial-rod shroud. Several parameters were varied in order to find an optimum configuration, such as the shroud diameter and porosity. The most effective shroud geometry had  $d_c/D = 1.25$  with a 63% porosity, hence this configuration was chosen to verify the optimal circumferential distribution by pulling out the rods. When the body was left with only 11 rods on each size (distributed around  $\pm 90^\circ$ ), the amplitude of oscillation was higher than that of a plain cylinder and resembled galloping. Our results, together with Zdravkovich [22], confirm that galloping-like excitation will be very sensitive to the position of the control cylinders (especially if they are located near the separation points), therefore hydrodynamic axial-symmetry must be pursued.

## 5. Conclusion

Amplitude of displacement, frequency of oscillations, mean drag and fluctuating lift coefficients have been measured for a cylinder surrounded by a polar array of  $N = 2, 4$  and 8 wake-control cylinders intended to act as VIV suppressors. The response showed that while some configurations suppressed the flow-induced oscillations, others enhanced them under a galloping-like mechanism.

Most of the configurations presented a VIV resonant response with a reduced amplitude of displacement when compared with that of a plain cylinder. The best case for response reduction was the configuration of 8 control cylinders with  $[d_c/D, G/D] = [0.08, 0.10]$ , which reduced about 99% of the peak amplitude for the whole range of reduced velocities. Consequently, mean drag was increased by 12% above the reference value for a plain cylinder beyond the synchronization range.

In a very brief summary: (i) A polar array of 8 control cylinders may achieve complete suppression of VIV without leading the system into galloping. Suppression is achieved at the cost of increas-

ing the mean drag. (ii) A polar array of 4 control cylinders may be the most efficient configuration to minimize the mean drag, but the system may develop severe vibrations combining VIV and galloping. (iii) The system is very sensitive to the parameters investigated ( $N, d_c/D$  and  $G/D$ ), therefore small geometric variations in the control cylinders may produce unexpected responses.

It is worth noting that the system approximates an omnidirectional device as the number of equally-spaced control cylinders is increased. In the limit, we should be able to recover the behavior of a cylinder fitted with shrouds (or axial rods) with equivalent density. In the present investigation, the arrangement with 8 control cylinders is the closest to an axial-symmetric system. Perhaps this is the reason why the device did not develop a galloping-like instability. An omnidirectional device would be very interesting for practical applications in engineering, since the response would be independent of the incoming flow direction.

Future research should focus on the hydrodynamic mechanisms that govern the response of the system to flow-induced vibrations. Visualization of the flow in the near wake and around the control cylinders should shed light on the flow regimes that produce the distinct responses observed above. The present investigation also paves the way for experiments with active-control devices, for example, with rotating (for example, as discussed by Modi [12]) or vibrating wake-control cylinders.

## Acknowledgments

MSO is grateful to CAPES Brazilian Ministry of Education. GRSA acknowledges the support of FAPESP (2011/00205-6, 2014/50279-4), CNPq (306917/2015-7) and the Brazilian Navy.

## References

- [1] G. Assi, P. Bearman, N. Kitney, Low drag solutions for suppressing vortex-induced vibration of circular cylinders, *J. Fluids Struct.* 25 (2009) 666–675.
- [2] G.R.S. Assi, P.W. Bearman, B.S. Carmo, J.R. Meneghini, S.J. Sherwin, R.H.J. Willden, The role of wake stiffness on the wake-induced vibration of the downstream cylinder of a tandem pair, *J. Fluid Mech.* 718 (2013) 210–245.
- [3] P.W. Bearman, Vortex shedding from oscillating bluff bodies, *Ann. Rev. Fluid Mech.* 16 (1984) 195–222.
- [4] Y. Hwang, H. Choi, Control of absolute instability by basic-flow modification in a parallel wake at low Reynolds number, *J. Fluid Mech.* 560 (Aug) (2006) 465–475.
- [5] A. Khalak, C.H.K. Williamson, Dynamics of a hydroelastic cylinder with very low mass and damping, *J. Fluids Struct.* 10 (1996) 455–472.
- [6] A. Khalak, C.H.K. Williamson, Fluid forces and dynamic of a hydroelastic structure with very low mass and damping, *J. Fluids Struct.* 11 (8) (1997) 973–982.
- [7] I. Korkischko, J.R. Meneghini, Suppression of vortex-induced vibration using moving surface boundary-layer control, *J. Fluids Struct.* 34 (2012) 259–270.
- [8] C.-H. Kuo, C.-C. Chen, Passive control of wake flow by two small control cylinders at Reynolds number 80, *J. Fluids Struct.* 25 (6) (2009) 1021–1028.
- [9] C.-H. Kuo, L.-C. Chiou, C.-C. Chen, Wake flow pattern modified by small control cylinders at low Reynolds number, *J. Fluids Struct.* 23 (2007) 938–956.
- [10] S.-J. Lee, S.-I. Lee, C.-W. Park, Reducing the drag on a circular cylinder by upstream installation of a small control rod, *Fluid Dynam. Res.* 34 (4) (2004) 233–250.
- [11] S. Mittal, Control of flow past bluff bodies using rotating control cylinders, *J. Fluids Struct.* 15 (2) (2001) 291–326.
- [12] V. Modi, Moving surface boundary-layer control: a review, *J. Fluids Struct.* 11 (6) (1997) 627–663.
- [13] S. Muddada, B. Patnaik, An active flow control strategy for the suppression of vortex structures behind a circular cylinder, *Eur. J. Mech.-B/Fluids* 29 (2) (2010) 93–104.
- [14] G. Parkinson, Phenomena and modelling of flow-induced vibrations of bluff bodies, *Prog. Aerospace Sci.* 26 (2) (1989) 169–224.
- [15] L.V.S. Sagrilo, M.Q. Siqueira, T.A.G. Lacerda, G.B. Ellwanger, E.C.P. Lima, E.F.N. Siqueira, VIM and wave-frequency fatigue damage analysis for SCRs connected to monocolumn platforms, in: ASME 2009 28th International Conference on Ocean, Offshore and Arctic Engineering, No. OMAE2009-79807, 2009, pp. 723–729.
- [16] H. Sakamoto, H. Haniu, Optimum suppression of fluid forces acting on a circular cylinder, *J. Fluids Eng.* 116 (2) (1994) 221–227.
- [17] M. Silva-Ortega, Suppression of vortex-induced vibration of a circular cylinder with fixed and rotating control cylinders Master's thesis, University of São Paulo, 2015, <[www.teses.usp.br](http://www.teses.usp.br)>.

- [18] P.J. Strykowski, K.R. Sreenivasan, On the formation and suppression of vortex shedding at low Reynolds numbers, *J. Fluid Mech.* 218 (1990) 71–107.
- [19] C.H.K. Williamson, R. Govardhan, Vortex-induced vibrations, *Ann. Rev. Fluid Mech.* 36 (2004) 413–455.
- [20] H. Wu, D. Sun, L. Lu, B. Teng, G. Tang, J. Song, Influence of attack angle on viv suppression by multiple control rods for long flexible riser model, in: *Proceedings of the 21st International Offshore and Polar Engineering Conference*, 2011, p. 1276.
- [21] H. Wu, D. Sun, L. Lu, B. Teng, G. Tang, J. Song, Experimental investigation on the suppression of vortex-induced vibration of long flexible riser by multiple control rods, *J. Fluids Struct.* 30 (2012) 115–132.
- [22] M. Zdravkovich, Review and classification of various aerodynamic and hydrodynamic means for suppressing vortex shedding, *J. Wind Eng. Indust. Aerodynam.* 7 (1981) 145–189.
- [23] H. Zhu, J. Yao, Y. Ma, H. Zhao, Y. Tang, Simultaneous {CFD} evaluation of {VIV} suppression using smaller control cylinders, *J. Fluids Struct.* 57 (2015) 66–80.





Contents lists available at ScienceDirect

## Journal of Fluids and Structures

journal homepage: [www.elsevier.com/locate/jfs](http://www.elsevier.com/locate/jfs)

# Suppression of the vortex-induced vibration of a circular cylinder surrounded by eight rotating wake-control cylinders

M. Silva-Ortega<sup>1</sup>, G.R.S. Assi<sup>\*,2</sup>

Department of Naval Architecture &amp; Ocean Engineering, EPUSP, University of São Paulo, São Paulo SP, Brazil

## ARTICLE INFO

## Article history:

Received 22 October 2016

Received in revised form 26 April 2017

Accepted 3 July 2017

Available online 20 July 2017

## Keywords:

Vortex-induced vibration

Suppression

Wake control

Drag reduction

## ABSTRACT

The present work investigates the use of a polar array of 8 wake-control cylinders as a means of suppressing the vortex-induced vibration (VIV) of a larger circular cylinder. The diameter of the control cylinders and their rotation speed were the main parameters investigated. Experiments have been performed in water at Reynolds numbers between 5000 and 50,000. The rotating cylinders suppressed the peak amplitude of displacement by around 70% when compared to that of a bare cylinder. A similar response was obtained even if the rotation speed of the control cylinders was kept constant in relation to the flow speed. A specific configuration with 8 non-rotating control cylinders achieved an even better 99% suppression. As a consequence of reduced vibrations, the fluctuation of lift and mean drag were not as amplified due to VIV. The results pave the way for further studies concerning system optimization and support the development of efficient VIV suppressors and dynamic positioning systems for large floating offshore platforms and other applications.

© 2017 Elsevier Ltd. All rights reserved.

## 1. Introduction

Offshore platforms built to explore oil and gas in ultra-deep waters have become large floating units employed in almost all the processes of drilling, production and storage. Platforms of the mono-column and spar types present hulls in the form of a circular cylinder or other cylindrical shapes of bluff bodies, as reported by Gonçalves et al. (2010, 2011). Ocean currents past the hull will not only generate steady drag but also drive the platform into flow-induced motions that may affect the efficiency of the processes being carried out on the deck. Vibrations may also pose a threat to the structural integrity of the platform, of its mooring lines and riser pipes underwater (Sagrilo et al., 2009).

This type of flow-induced motion has its origin in the vortex-shedding mechanism of the flow past bluff bodies, which starts at the interaction of the separated shear layers in the near wake. Alternating vortices generate cyclic fluid loads (lift and drag) that feed back on the body. If the frequency of vortex shedding is approximate one of the natural frequencies of the elastic cylinder ( $f_0$ ), the system will be excited into vortex-induced vibrations (VIV) for a wide range of flow speeds. Please refer to Bearman (1984) and Williamson and Govardhan (2004) for a detailed description of the phenomena involved.

Several strategies have been proposed to suppress VIV by disrupting the wake or avoiding the formation of vortices in the first place. Zdravkovich (1981) presented an introduction to some of those techniques, while Choi et al. (2008) reviewed different strategies to control the wake. With the advancement of control theory and its implementation, active strategies

\* Corresponding author.

E-mail address: [g.assi@usp.br](mailto:g.assi@usp.br) (G.R.S. Assi).

<sup>1</sup> Now at the Dept. Naval Architecture, Universidad Veracruzana, Mexico.

<sup>2</sup> Currently a Visiting Associate in Aerospace at GARCIT, California Institute of Technology, USA.

to suppress VIV appeared with the promise of higher efficiency. From a phenomenological point of view, these techniques have to deal with very interesting (and complex) problems of unsteady hydrodynamics.

### 1.1. Flow control with interfering cylinders

It is known that the vortex-shedding mechanism of a circular cylinder can be controlled by the interference of small cylinders positioned around the circumference of the main body (Strykowski and Sreenivasan, 1990; Hwang and Choi, 2006). These wake-control cylinders interact with the boundary layer and the separated shear layers disrupting the formation of vortices that are convected downstream to form the wake. As a consequence, the cyclic hydrodynamic forces feeding back from the vortex-shedding mechanism are considerably reduced, if not completely suppressed. The mean drag acting on the body is also reduced if wake suppression is achieved.

Placing a smaller control cylinder upstream of the main cylinder is also a well-established strategy for drag reduction (Lee et al., 2004). But Strykowski and Sreenivasan (1990) have shown that if the small control cylinder is now placed within a defined region in the near wake, the formation of vortices could be effectively suppressed at a Reynolds number of  $Re = 80$ . Previous investigations positioning control cylinders in various arrangements around a bluff body have been performed through experiments and numerical simulations. Mittal (2001) performed numerical simulations of a static cylinder with two control cylinders positioned at  $\pm 90^\circ$  in relation to the incoming flow. He found that vortex shedding was completely suppressed for a few arrangements at low  $Re$ .

Active open- and closed-loop control techniques have also received attention by the scientific community (Gad-El-Hak, 2000; Cattafesta and Sheplak, 2011; Schulmeister, 2012). Among them, the *moving surface boundary-layer control* (MSBC) method relies on the injection of momentum in the boundary layer by the rotation of small elements placed within or very near the boundary layer close to the separation points (Modi, 1997). Rotating elements are usually small circular cylinders placed inside or just above the wall. It is thought that the injection of momentum postpones the effects of the adverse pressure gradient, moving the separation points to a more advanced position. As a result, the wake becomes narrower and the recirculation region behind the body reduced. One of the most important control parameters directly associated with this technique is the ratio between the tangential velocity of the moving surface to the velocity of the free stream ( $U_c/U$ ).

MSBC can be applied either as an active open- or closed-loop control strategy. Patnaik and Wei (2002) numerically simulated the flow around a D-section cylinder with MSBC at  $Re = 200$  and  $400$  and verified a recirculation-free zone in the wake for  $U_c/U = 1.25$ . Muddada and Patnaik (2010) made further developments employing a cylinder fitted with two simple rotary type mechanical actuators located at  $120^\circ$  from the frontal stagnation point. The effectiveness of the MSBC in reducing drag was shown by all cases tested. Mittal and Raghuvanshi (2001) employed numerical simulations to observe that the control cylinders provided a local favorable pressure gradient in the wake region, thereby locally stabilizing the shear layers. Following that, Mittal (2001) applied the MSBC to control the flow around a circular cylinder in two-dimensional numerical simulations at  $Re = 100$  and  $10,000$ . At  $Re = 100$  and  $U_c/U = 5$ , the flow achieved a steady state; at  $Re = 10,000$  the wake did not reach a steady state, but it appeared highly organized and narrower when compared to the case without any control. The effect of the gap between the control cylinders and the wall of the main cylinder at  $Re = 10,000$  was later investigated by Mittal (2003).

Korkischko and Meneghini (2012) performed an experiment employing MSBC with two wake-control cylinders as a means to suppress VIV of an isolated cylinder free to oscillate in the cross-flow direction ( $Re \approx 7500$ ). They found that the two static control cylinders positioned at  $\pm 90^\circ$  were not effective in suppressing VIV of the main body. However, when they applied enough rotation to the small cylinders, the wake was stabilized and VIV suppressed.

### 1.2. Objective

MSBC with more than two control cylinders has already been experimentally tested as a means to suppress vortex shedding of static cylinders as well as VIV of oscillating bodies (Silva-Ortega, 2015). Recently, Silva-Ortega et al. (2014b, a) have shown that a polar array of 2, 4 and 8 control cylinders equally spaced around a static body may create an effective device to suppress vortex shedding from a larger circular cylinder at  $Re = 100$ . Fundamental parameters (such as the number of control cylinders, their diameter and their distance from the main body) have been shown to play a significant role in the wake-control mechanism. Silva-Ortega (2015) also showed that the same arrays of control cylinders would impact the hydrodynamic loads acting on a static cylinder at  $Re = 5000$ – $50,000$ .

In a previous study, we have investigated the flow-induced vibration of a cylinder surrounded by a polar array of 2, 4 and 8 control cylinders that were not rotating (Silva-Ortega and Assi, 2017). That configuration was similar in nature to the axial-rods suppressors described by Zdravkovich (1981). It was found that, depending on the geometric configuration, the system could respond with a combination of VIV and galloping. In the present study, we will take the polar array with 8 control cylinders proposed by Silva-Ortega and Assi (2017) to control the wake of a static cylinder and employ it as a means of suppressing the VIV of a larger circular cylinder. This time, the 8 wake-control cylinders will be rotating (as in the MSBC technique) and the whole system will be free to respond to the flow excitation in the cross-flow direction. In this experiment, we expect to probe the parameter space regarding the dynamic response of the system to VIV.

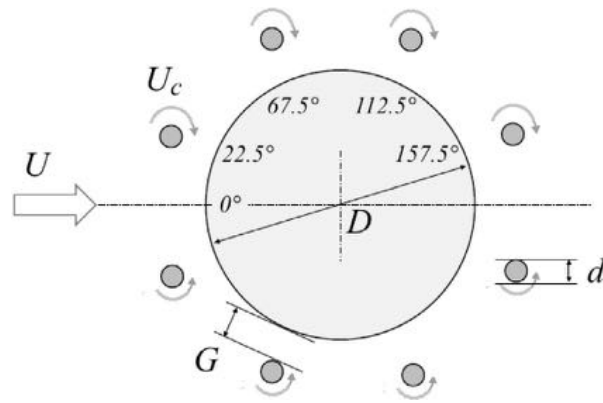


Fig. 1. Geometrical parameters for the main cylinder with eight control cylinders (figure not drawn to scale).

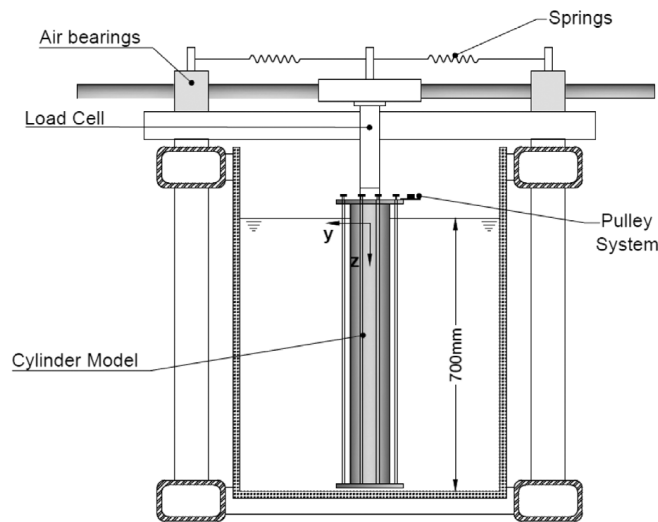


Fig. 2. Cross view of the experimental setup: elastic rig mounted on the test section.

## 2. Experimental setup

Experiments have been carried out in the Circulating Water Channel of NDF (Fluids and Dynamics Research Group) at the University of São Paulo, Brazil. The water channel has an open test section ( $0.7 \text{ m} \times 0.9 \text{ m} \times 7.5 \text{ m}$ ) and good quality flow can be achieved up to  $1 \text{ m/s}$  with turbulence intensity of less than 3%.

A rigid section of a smooth circular cylinder was made of an acrylic tube of external diameter  $D = 100 \text{ mm}$ . Two sets of 8 control cylinders with diameter  $d$  were made of acrylic rods and supported by rings attached to the ends of the main cylinder. Their distribution about the main cylinder is presented in Fig. 1, in which the arrow indicates the direction of the incoming flow with velocity  $U$ . The axes of the control cylinders were parallel to the axis of the main cylinder, spanning the whole length of the model (immersed length of  $700 \text{ mm}$ ). The diameter of the control cylinders was varied in two steps of  $d/D = 0.06$  and  $0.08$ , while the gap measured between the wall of the control cylinders and the wall of the main cylinder was set to  $G/D = 0.1$  in this study (based on the best results obtained by Silva-Ortega and Assi (2017)).

The top of the control cylinders was connected to a pulley system driven by an electric servo motor. All eight cylinders rotated at the same speed ratio  $U_c/U$ , where  $U_c$  is the tangential velocity on the wall of the control cylinders. As seen in Fig. 1, control cylinders at the top (starboard) rotated in the clockwise direction, while cylinders at the bottom (port) rotated in the opposite direction.

Models were mounted on a load cell attached to a sliding frame supported by air bearings, as shown in Fig. 2. A pair of coil springs provided the restoration force to the system, which was free to oscillate only in the cross-flow direction. An optical sensor measured the displacement ( $y$ ) of the cylinder, providing that structural mass and damping were kept to a minimum. The product between the mass ratio ( $m^*$ , calculated as the ratio between the total oscillating mass and the mass of displaced water) and the damping ratio ( $\zeta$ , measured as a percentage of the critical damping) was  $m^*\zeta = 0.066$ . The natural frequency of the system ( $f_0$ ) as well as the damping ratio were determined during decay tests performed in air.

The only flow variable changed during the course of the experiments was the flow velocity, which altered the Reynolds number between 5000 and 50,000 ( $Re = UD/\nu$ , where  $\nu$  is the kinematic viscosity of water) and the reduced velocity

**Table 1**  
Parameters.

|                               |         | 1st series | 2nd series   | 3rd series        |
|-------------------------------|---------|------------|--------------|-------------------|
| Number of control cylinders   | $N$     | 8          |              | 0, 8              |
| Diameter of control cylinders | $d/D$   |            | 0.06, 0.08   |                   |
| Gap between cylinders         | $G/D$   |            | 0.1          |                   |
| Rotation of control cylinders | $U_c/U$ | 1–10       | 0, 2, 2.5, 3 | $U_c = 0.266$ m/s |
| Reynolds number               | $Re$    | 10,500     |              | 5000–50,000       |
| Reduced velocity              | $U_R$   | 4.2        |              | 2–20              |
| Mass ratio                    | $m^*$   |            | 1.09         |                   |
| Damping ratio                 | $\zeta$ |            | 0.61%        |                   |

$U_R = U/(Df_0)$  in the range of 2 to 20. A summary of all the parameters investigated in the experiments is presented in Table 1. The dynamic responses to VIV are analyzed across the  $U_R$  range by comparing the normalized amplitude of displacement ( $\hat{y}/D$ , where  $\hat{y}$  is the RMS of  $y$  times  $\sqrt{2}$ ), the dominant frequency of oscillation normalized by the natural frequency ( $f/f_0$ ), the mean drag coefficient ( $\bar{C}_D$ ) and the RMS of the lift coefficient ( $\hat{C}_L$ ). In addition, preliminary tests have been performed with a bare cylinder (without control cylinders) to serve as reference for comparison.

### 2.1. Method

As reported by Silva-Ortega and Assi (2017), we have started this VIV research project testing 27 different cases varying the parameters  $N$ ,  $d/D$  and  $G/D$  for a cylinder surrounded by non-rotating control cylinders. Each case was run for a whole range of reduced velocities, resulting in a series of VIV response curves. Now, in order to investigate the effect of the rotating cylinders one needs to add the new parameter  $U_c/U$ . If  $U_c/U$  were to be varied in ten steps, say between 1 and 10, one would end up with another 270 cases to test over the same reduced velocity range.

To avoid an exhaustive investigation of the parametric space, our current work took the most effective case for VIV suppression with non-rotating control cylinders found by Silva-Ortega and Assi (2017) to investigate its behavior for rotating control cylinders. The chosen configuration had  $N = 8$  control cylinders,  $d/D = 0.08$  (with one extra variation) and  $G/D = 0.1$ . The present investigation was divided into three series of experiments concerning the most significant parameters expected to govern the phenomenon:

**1st series:** We chose configurations with  $d/D = 0.06$  and  $0.08$  to investigate the dependency of the peak response at the VIV resonance to the rotation speed of the control cylinders.  $U_c/U$  was varied in smaller intervals to probe which rotation speed would produce the most suppression at  $U_R = 4.2$ .

**2nd series:** We took the best case for peak suppression found in the first series and varied the whole range of  $U_R$  keeping  $U_c/U$  constant. Since  $U$  was increased to change  $U_R$ , the actual rotation of the control cylinders ( $U_c$ ) was also increased in order to keep  $U_c/U$  constant.

**3rd series:** We set out to investigate the effectiveness of VIV suppression if the actual rotation speed  $U_c$  was kept constant for the whole range of  $U_R$ , thus altering the ratio  $U_c/U$  for each step of  $U$ . For that matter, the value of  $U_c$  that produced the best peak suppression in the first series was employed.

## 3. Results and discussion

The parametric variation for each series of experiments is also presented in Table 1. We shall now turn to their results.

### 3.1. 1st series: peak amplitude at $U_R = 4.2$

In addition to the case with  $d/D = 0.08$ , one extra variation was tested with a smaller diameter of  $d/D = 0.06$  (both cases kept a radial separation of  $G/D = 0.1$ ). Numerical simulations of the flow performed by Silva-Ortega et al. (2014a) have shown that a rotation speed of  $U_c/U = 3$  was enough to control vortex shedding of a static cylinders for low  $Re$ . Based on that, we varied  $U_c/U$  in small intervals from 1 to 9. The reduced velocity was kept constant at  $U_R = 4.2$  (equivalent to  $Re = 10,500$ ), which corresponded to the point of maximum amplitude for the bare cylinder at the VIV resonance (to be discussed later).

Fig. 3 presents the peak amplitude of response versus  $U_c/U$  for both cases with  $d/D = 0.08$  and  $0.06$ . The lowest value of  $[\hat{y}/D]_{\text{peak}} \approx 0.2$  was found at  $U_c/U = 2.5$  for both cases. For lower and higher rotation speeds the peak response was considerably increased. Consequently,  $U_c/U = 2.5$  and its neighboring values of  $U_c/U = 2$  and  $3$  were chosen as the reference values to proceed to the second series of experiments.

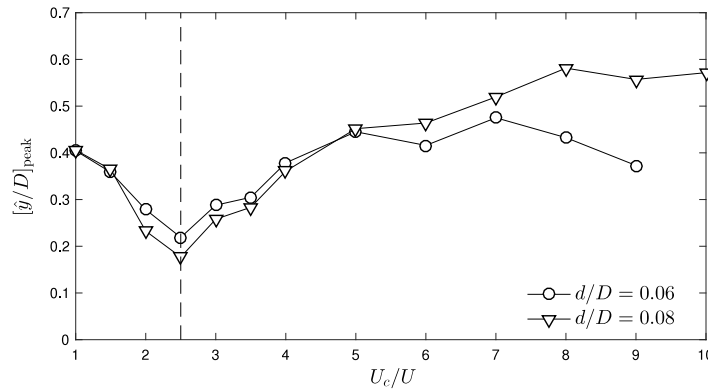


Fig. 3. Peak amplitude of response varying  $U_c/U$  at  $U_R = 4.2$  and  $Re = 10,500$ .

### 3.2. 2nd series: VIV response for $U_c/U = 2, 2.5$ and $3$

A preliminary experiment with a bare cylinder (without surrounding control cylinders) has been performed to validate the setup and generate the reference data for comparison. Fig. 4 shows the reference case obtained for reduced velocities up to 20. The results of VIV amplitude of displacement, frequency of oscillation, mean drag coefficient and fluctuating lift coefficient obtained for the bare cylinder are in good agreement with other experimental results collected by Williamson and Govardhan (2004), Norberg (2003) and Assi et al. (2013), who also employed the same apparatus. The reference results for a cylinder with 8 non-rotating control cylinders ( $U_c/U = 0$ ) have been extracted from Silva-Ortega and Assi (2017).

Fig. 4 shows the amplitude of displacement ( $\hat{y}/D$ ), frequency of oscillation ( $f/f_0$ ), mean drag coefficient ( $\bar{C}_D$ ) and RMS of lift coefficient ( $\hat{C}_L$ ) for the case with  $d/D = 0.08$  with varying  $U_c/U$  versus reduced velocity. The response curve for the bare cylinder is in clear contrast with the curves of the rotating cylinders (Fig. 4(a)). In general, all rotation speeds managed to reduce the amplitude of VIV in the initial, upper and lower branches (as defined by Williamson and Govardhan (2004)). At  $U_R = 4.2$ , the peak responses match those presented in Fig. 3. (Please note that the data points do not cover the whole range of  $U_R$  up to 20. Since the actual rotation speed ( $U_c$ ) of the control cylinders was increasing with  $U_R$ , the motor reached its maximum rotation speed limiting the experiment to  $U_R \approx 12$ .)

The case with  $U_c/U = 2.5$  presented the lowest response for the widest range of  $U_R$ , but the other two neighboring cases also showed similar responses. The striking result, however, came out when the responses were compared with that for 8 non-rotating cylinders: A cylinder surrounded by 8 non-rotating cylinders ( $U_c/U = 0$ ) appeared to offer considerably better suppression than the cases with rotating cylinders. For the whole range of  $U_R$ , the case with non-rotating cylinders rarely passed  $\hat{y}/D = 0.1$ , while the rotating cylinders reached  $\hat{y}/D \approx 0.25$  during the synchronization range. The non-rotating wake-control cylinders appear to be more efficient in suppressing VIV, at least for this set of parameters.

The frequency of response presented in Fig. 4(b) clearly shows that the bare cylinder and the cylinder with rotating cylinders all follow the expected behavior for VIV. The data points representing the dominant  $f/f_0$  follow closely the  $St = 0.2$  line (the inclined line representing the typical Strouhal number for a circular cylinder). The dominant frequency for  $U_c/U = 0$ , on the other hand, shows that the system only oscillated at very low frequencies, associated with slow drifts at small displacements.

As a consequence of the VIV suppression,  $\bar{C}_D$  presented in Fig. 4(c) shows considerably low values for the case with  $U_c/U = 0$ . When the control cylinders are rotating, mean drag is increased above the value found for the bare cylinder, considerably higher than the mean drag for the case with non-rotating cylinders. Fig. 4(d) also reveals that the rotating cylinders generate more lift driving the excitation, when compared with the results for the non-rotating cylinders.

The same experiment was repeated for smaller control cylinders with  $d/D = 0.06$ , as seen in Fig. 5. Again, the cases with rotating cylinders showed a considerable reduction of response when compared with that of the bare cylinder. Maximum response for the case with  $U_c/U = 2.5$  reached  $\hat{y}/D \approx 0.25$  during the synchronization range. The frequency response, as well as the curves of  $\bar{C}_D$  and  $\hat{C}_L$ , show a similar behavior.

The unexpected response now appeared for the case with non-rotating control cylinders. Instead of suppressing VIV for the whole range of  $U_R$ , the case with slightly smaller control cylinders ( $d/D = 0.06$ ) presented a peak response of  $\hat{y}/D \approx 0.5$  at the resonance. This is worse than the displacement measured for the cases with rotating cylinders. In fact, it appears that the VIV mechanism could not be suppressed as before, but only restricted to a shorter range of  $U_R$ . Fig. 5(b) shows a dominant frequency signature over the Strouhal line, indicating that the fundamental mechanisms are not different from VIV. In spite of reducing the peak amplitude of vibration, the rotating cylinders still presented  $\bar{C}_D$  higher than that of non-rotating cylinders for the whole  $U_R$  range; for most of the time it was also higher than that of a bare cylinder.



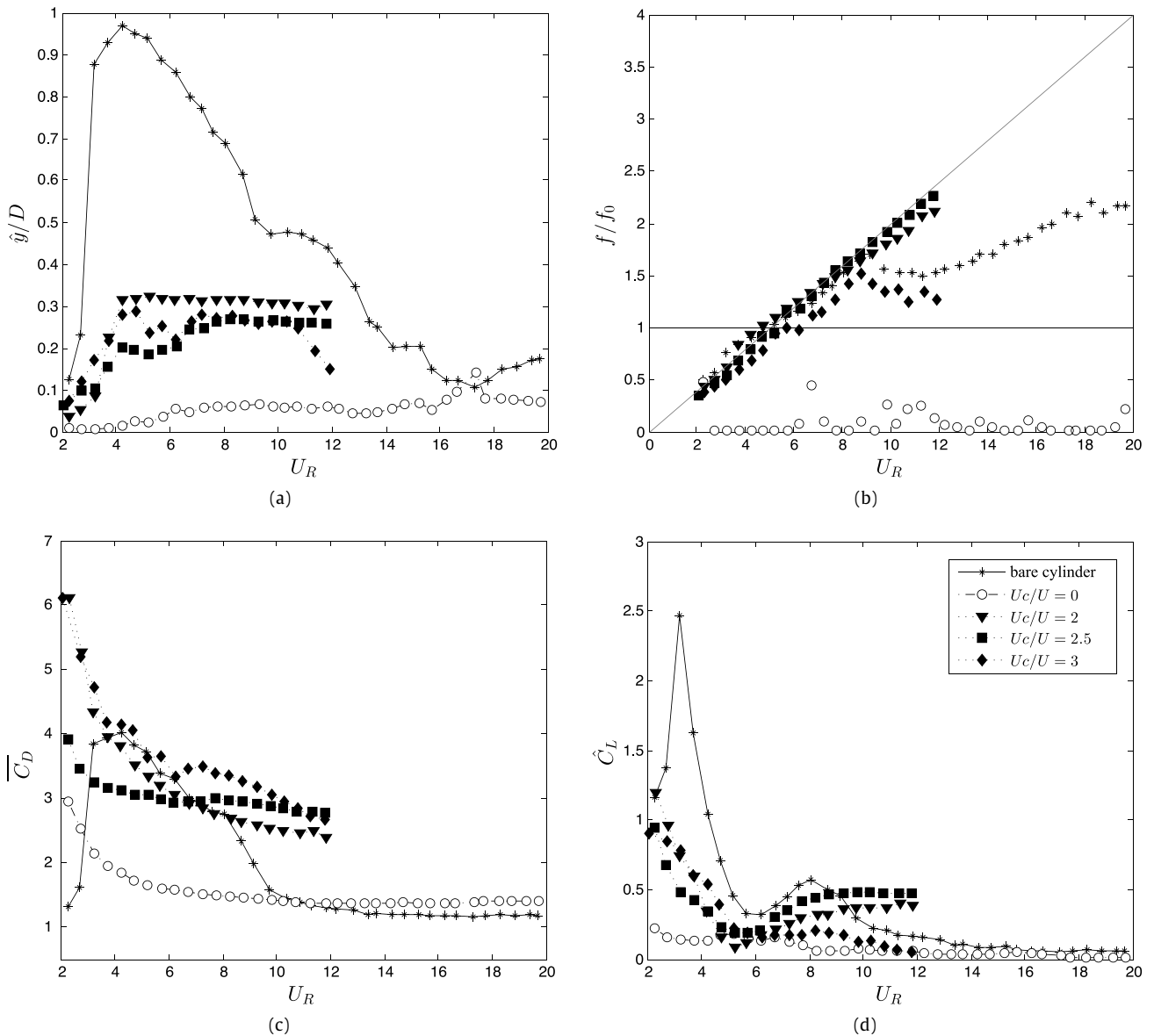


**Fig. 4.** VIV response for 8 control cylinders with  $d/D = 0.08$  at  $U_c/U = 0, 2, 2.5$  and  $3$ : (a) Amplitude of displacement, (b) frequency of oscillation, (c) mean drag and (d) RMS of lift coefficients.

### 3.3. 3rd series: VIV response for $U_c = 0.266$ m/s

In the third series, the actual rotation of the control cylinders ( $U_c$ ) was kept constant independently of the flow speed ( $U$ ), thus altering the ratio  $U_c/U$  as  $U_R$  was increased. The value of  $U_c = 0.266$  m/s was chosen because it was the actual rotation speed at the peak-amplitude during the first series of experiments; i.e.  $U_c = 0.266$  m/s resulted in  $U_c/U = 2.5$  for  $U_R = 4.2$ . Keeping  $U_c$  constant resulted in a variation of  $U_c/U = 5.25$ – $0.52$  for the range of  $U_R = 2$ – $20$ , since both parameters vary inversely to each other, but linearly with flow speed.

At a constant  $U_c$ , the reduced velocity range could now be extended up to  $U_R = 20$ . Results for both cases with  $d/D = 0.08$  and  $0.06$  are compared with those of the bare cylinder, the non-rotating control cylinders ( $U_c/U = 0$ ) and the rotating cylinders with  $U_c/U = 2.5$  discussed in the second series.

The amplitude of displacement presented in Fig. 6(a) reveals that both cases with rotating control cylinders managed to reduce the VIV response in the synchronization range. But the residual vibration of  $\hat{y}/D > 0.2$  is still worse than the suppression achieved by the non-rotating cylinders ( $U_c/U = 0$ ). (Please note that both curves match at  $U_R = 4.2$  in all plots of Fig. 6, as expected.)

With  $U_c = 0.266$  m/s,  $U_R$  was extended to 20, revealing a drop in the  $\hat{y}/D$  curve at  $U_R \approx 12$ , marking the end of the synchronization range (also noticeable in the frequency signature of Fig. 6(b)). It is important to note that the system was not induced into other types of vibration for higher flow speeds, such as galloping or turbulence buffeting.

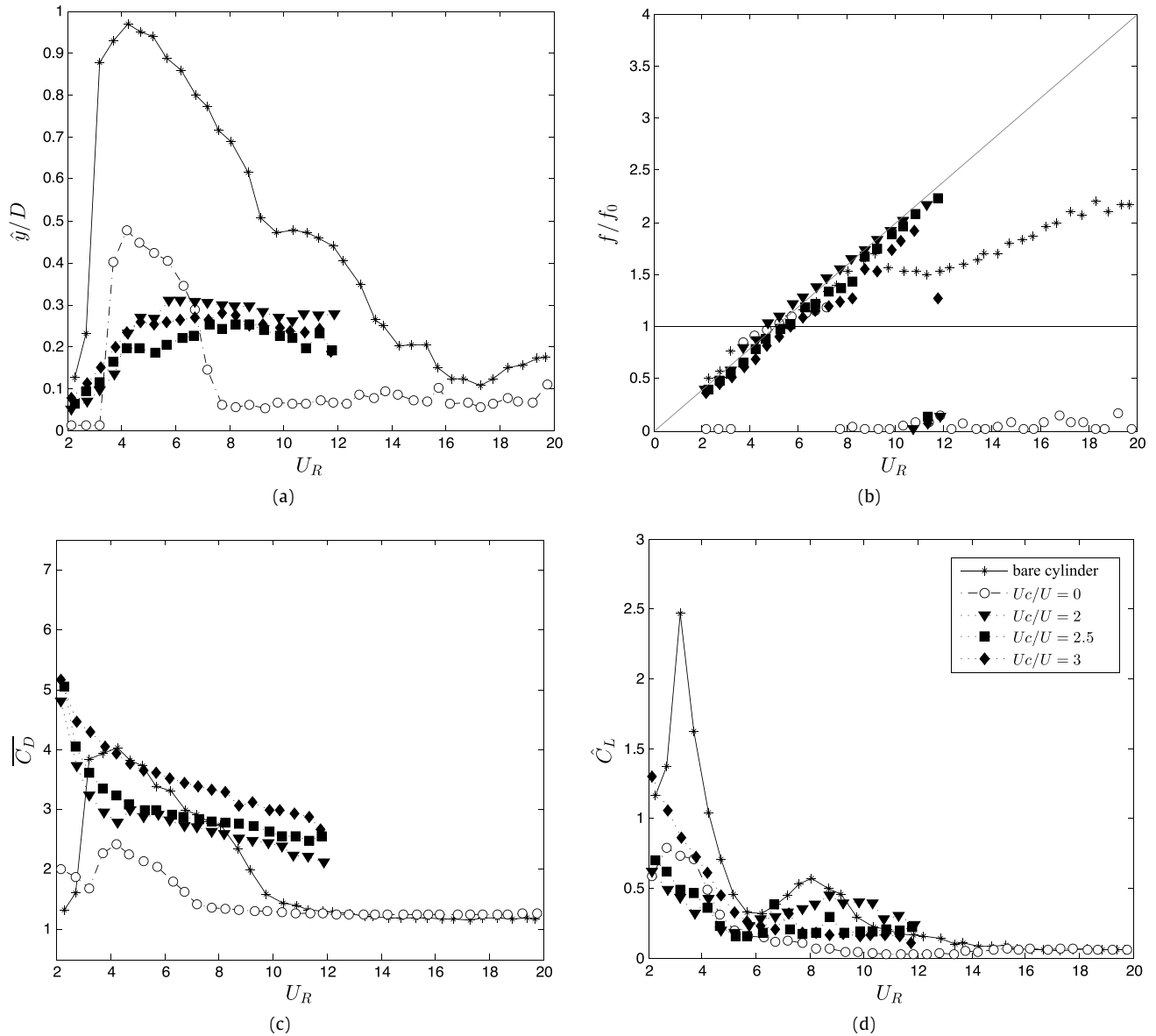


**Fig. 5.** VIV response for 8 control cylinders with  $d/D = 0.06$  at  $U_c/U = 0, 2, 2.5$  and  $3$ : (a) Amplitude of displacement, (b) frequency of oscillation, (c) mean drag and (d) RMS of lift coefficients.

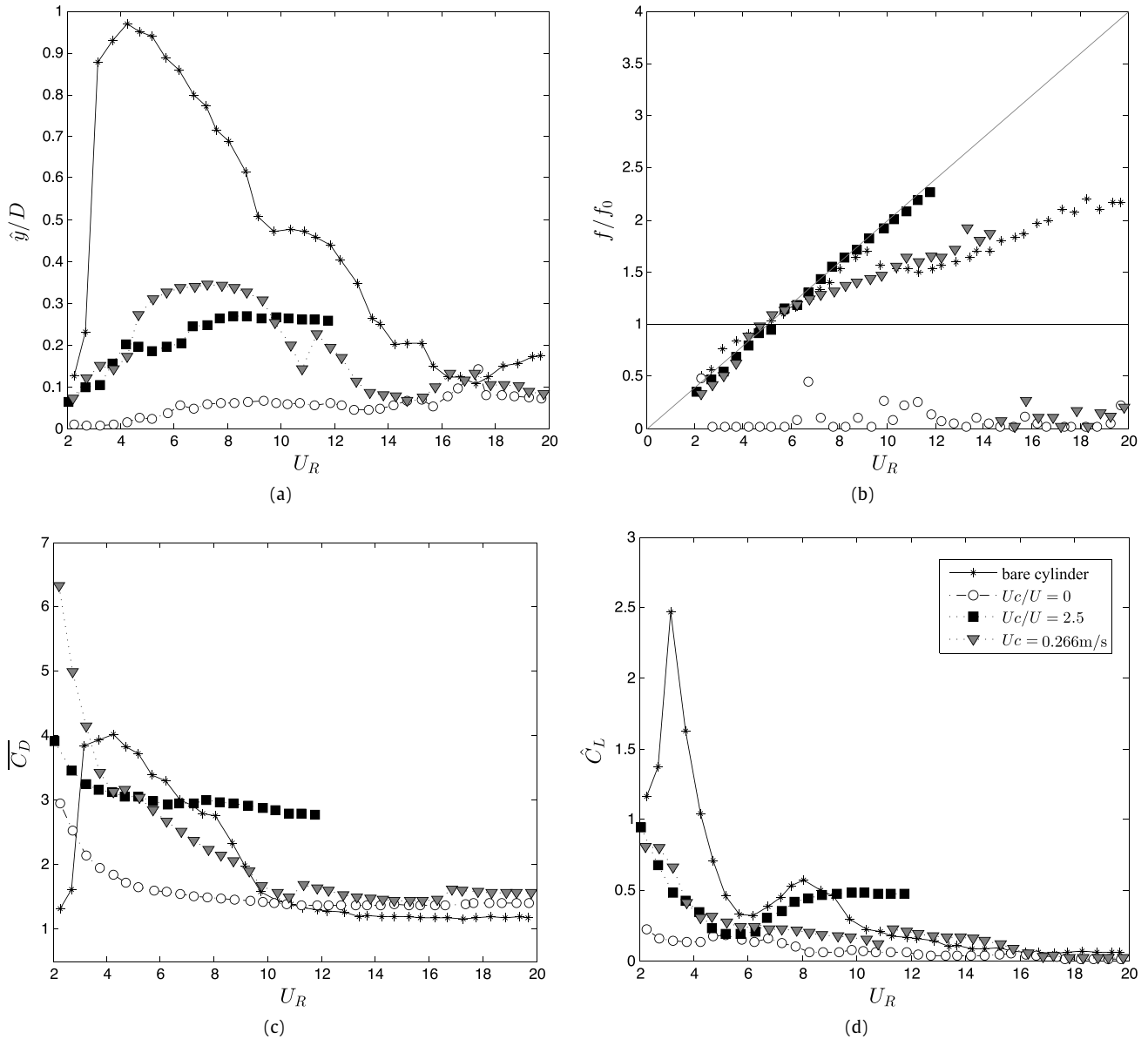
Mean drag and RMS of lift show the similar pattern seen before. Although the case with  $U_c = 0.266$  m/s presented a decrease in  $\bar{C}_D$  for higher reduced velocities (Fig. 6(c)), it did not reduce drag below the value measured for non-rotating control cylinders. As expected,  $\bar{C}_D$  was below that of a bare cylinder during synchronization, but larger thereafter.

Fig. 7 shows a slight improvement in the response if the control cylinders with  $d/D = 0.06$  are rotated at  $U_c = 0.266$  m/s, when compared with the previous case with  $d/D = 0.08$ : the synchronization range is shortened, but the maximum displacement is kept at the same level of  $\hat{y}/D \approx 0.35$  (Fig. 7(a)).

As happened before, the rotating control cylinders produced better suppression than the non-rotating cylinders ( $U_c/U = 0$ ), but with the cost of increasing drag for a wider range of reduced velocities (Fig. 7(c)). For  $U_R > 10$ , the cases with  $U_c/U = 0$  and  $U_c = 0.266$  m/s were able to reach the lowest values of mean drag recorded for the bare cylinder beyond the synchronization range ( $\bar{C}_D \approx 1.4$ ).

### 3.4. Discussion of all three series

As a first general comment, it is important to highlight that the VIV suppression achieved by an array of 8 non-rotating control cylinders ( $U_c/U = 0$ ) with  $d/D = 0.08$  was higher than any other case investigated in the present work. Consequently, mean drag was also reduced to the minimum observed value. Indeed, only by positioning the non-rotating control cylinders around the main cylinder was enough to achieve an almost 99% suppression of the peak amplitude of



**Fig. 6.** VIV response for 8 control cylinders with  $d/D = 0.08$  at  $U_c = 0.266$  m/s: (a) Amplitude of displacement, (b) frequency of oscillation, (c) mean drag and (d) RMS of lift coefficients.

displacement at resonance (Fig. 4). This arrangement, however, proved to be very sensitive to the position and the diameter of the control cylinders. A small reduction to  $d/D = 0.06$  would make the non-rotating cylinders suppress only roughly 50% of the peak amplitude of displacement (Fig. 5). This result invites further investigation of the hydrodynamic mechanisms between the control cylinders and the boundary layer.

Now, when the cylinders (with either  $d/D = 0.08$  or  $0.06$ ) were allowed to rotate, the system consistently reached approximately 70%–75% of VIV suppression at resonance, also becoming less susceptible to small variations in the  $d/D$  parameter. In brief, the rotating cylinders may not provide the very best performance, but certainly a more predictable suppression.

Differently from the results reported by Korkischko and Meneghini (2012), who employed two rotating control cylinders at  $\pm 90^\circ$  ( $d/D = 0.06$ ,  $G/D = 0.07$  and  $U_c/U = 5$ – $25$ ), our cases with 8 rotating cylinders did not achieve the same level of VIV suppression and drag reduction. Although Korkischko and Meneghini (2012) applied much higher rotation speeds to their cylinders, we do not believe that the total rotation (or sum of angular momentum transferred to the flow) is the only parameter to govern the suppression. The position and size of the control cylinders indeed play a significant role, as supported by previous studies on the sensibility of wakes (Strykowski and Sreenivasan, 1990; Patino et al., 2015, 2017) together with our results for  $U_c/U = 0$  (that managed to stabilize the wake with no rotation).

In general, the behavior of the response found when the 8 control cylinders were rotating was qualitatively the same for all configurations. Since the second series was based on the best results of the first series ( $U_c/U = 2.5$ ) – for higher and

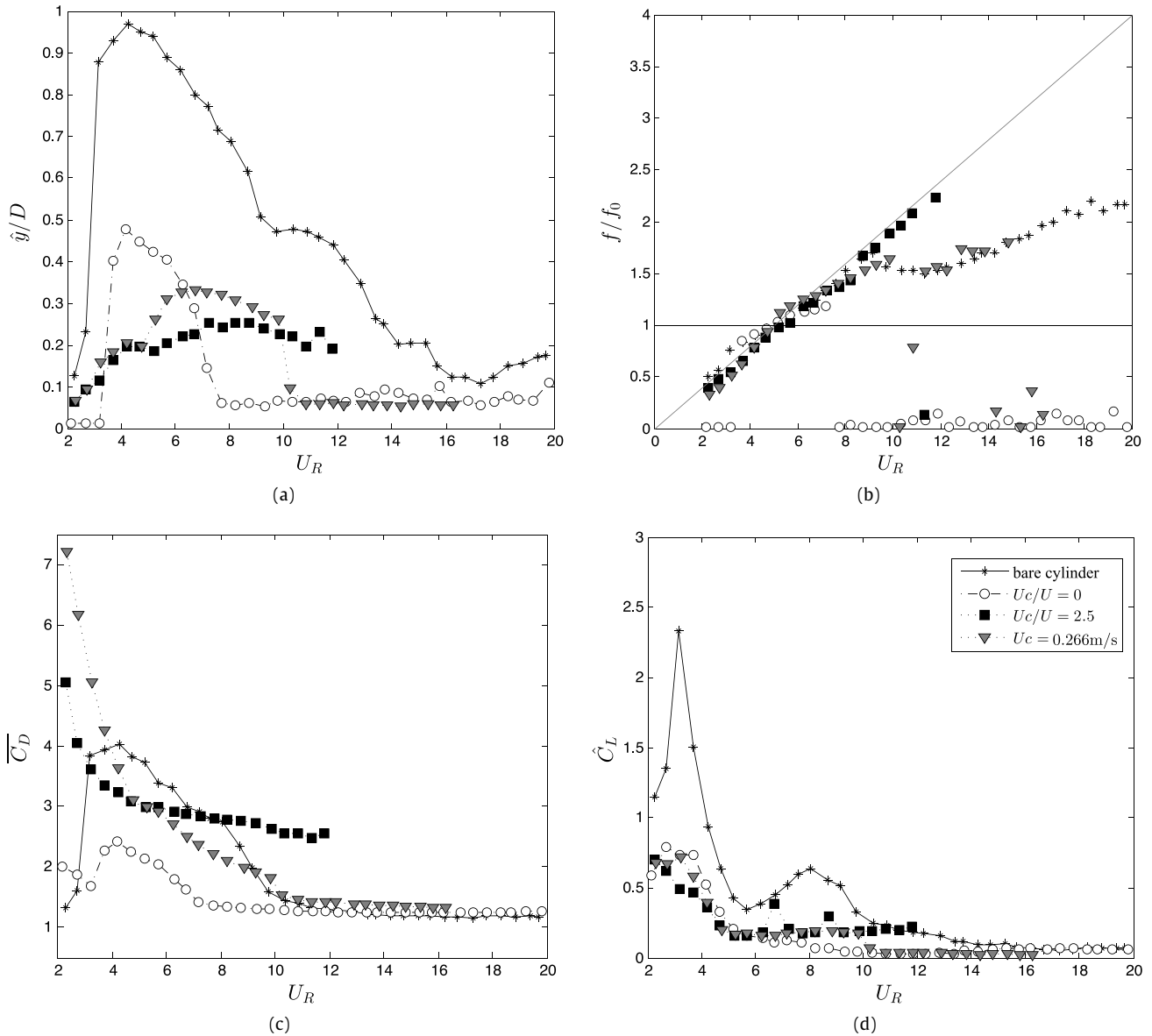


**Fig. 7.** VIV response for 8 control cylinders with  $d/D = 0.06$  at  $U_c = 0.266$  m/s: (a) Amplitude of displacement, (b) frequency of oscillation, (c) mean drag and (d) RMS of lift coefficients.

lower rotation speeds ( $U_c/U = 2$  and  $3$ ) the peak amplitude was found to be higher —, we believe that the response curves for rotating cylinders with  $U_c/U \neq 2.5$  should not produce better results, at least not for this range of  $Re$ .

If rotation is to be applied, the question would turn to the optimum rotation speed. The optimum  $U_c$  is most certainly a function of  $U$ , since the vortex shedding mechanism by which the cylinders are actuating depends on Reynolds number. But if it were not necessary to correct  $U_c$  for each flow speed, the control strategy for this kind of suppression device would be significantly simplified. Since this study is not concerned with optimization, we have limited the investigation to keeping a constant  $U_c$ .

As seen in Figs. 6 and 7, keeping a constant actual rotation of  $U_c = 0.266$  m/s (which corresponded to  $U_c/U = 2.5$  at  $U_R = 4.2$ ) did not change the response significantly. It is possible that an optimized rotation speed would produce better suppression at the new peak of response (around  $U_R = 7$  in Figs. 6(a) and 7(a)), but one is left to wonder if it would be worth implementing this kind of closed-loop control in a practical application. This is an interesting topic for further investigations.

#### 4. Further discussion and future work

The present investigation showed that the classical axial rods are not a bad suppressor after all, given that their geometry (density, distribution, etc.) is correct. For certain conditions, a simple array of non-rotating control cylinders in the form of axial rods might achieve satisfactory suppression. If the operator can live with the difference in peak amplitude between

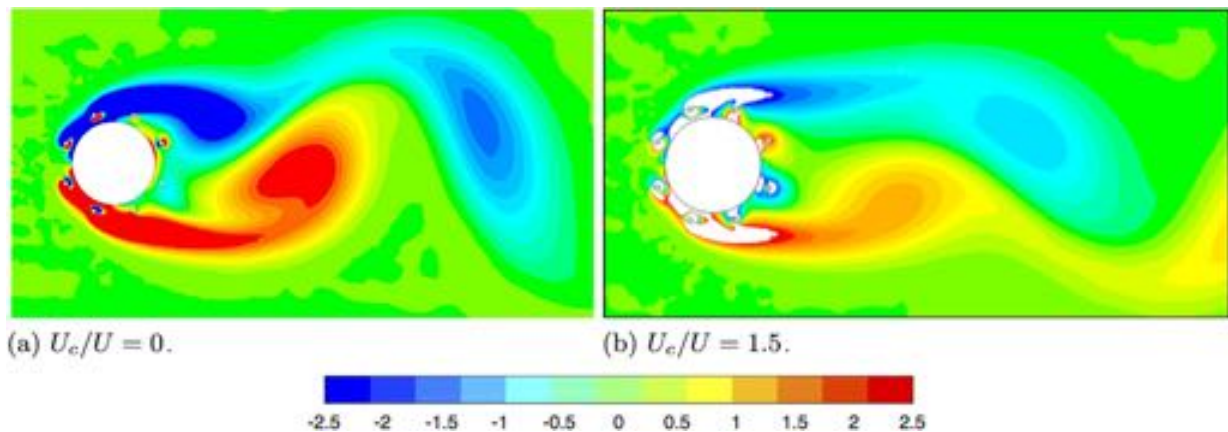


**Fig. 8.** Instantaneous vorticity contours ( $s^{-1}$ );  $d/D = 0.05$ ,  $G/D = 0.1$  and  $Re = 100$ .  
Source: Reproduced from [Silva-Ortega et al. \(2014a\)](#).

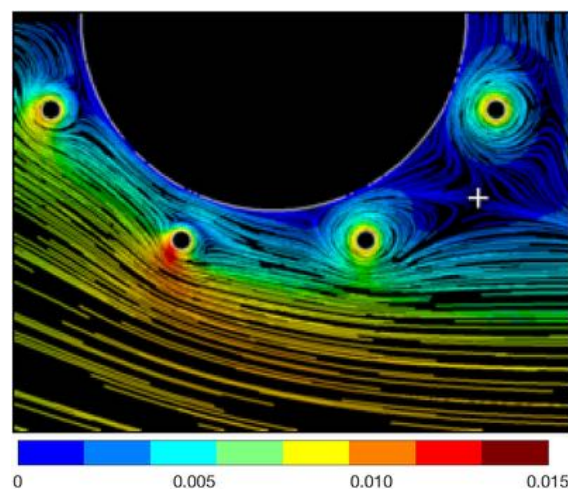


**Fig. 9.** Detail of the streamlines around the rotating control cylinders of Fig. 8(b). Flow is from left to right; colored by velocity magnitude (m/s). (For interpretation of the references to color in this figure legend, the reader is referred to the web version of this article.)  
Source: Reproduced from [Silva-Ortega et al. \(2014a\)](#).

0.25 and 0.5, it might be better to stick to the non-rotating cylinders as far as drag is concerned. Now if vibration is to be reduced at any drag cost, say to avoid fatigue damage or dynamic loads, then the rotating cylinders could be considered as an option. In a floating offshore platform with a bluff-body hull (a mono-column or a spar platform, for example), it might be desirable to mitigate vibration and the dynamic loads associated with it even if the mooring lines are to be loaded with extra drag.

If the main cylinder were a static body, the rotation of the control cylinders could help to suppress the wake and reduce loads due to vortex shedding, as shown by [Silva-Ortega \(2015\)](#). But rotating cylinders may not produce the expected result of VIV suppression with drag reduction if the cylinder is free to respond to the flow (this is true for this range of  $Re$ ). Again, this is proof that if a device appears to reduce hydrodynamic loads on a static body it does not necessary mean that it will make a good VIV suppressor, especially if the system presents low mass and damping. It might be the case that for a system with higher  $m^*\zeta$ , a suppressor with 8 rotating cylinders could present a qualitatively different response.

Of course there are infinite possibilities to arrange and drive the rotating control cylinders around the main cylinder. The present work was never intended to find an optimal solution to the problem, but simply to probe a finite parametric space. For a serious optimization study this space is so vast that a robust optimization method must be considered to tackle the problem, especially if each of the control cylinders had an independent  $U_c$ . So many possibilities make it a very exciting, non-linear optimization problem for future investigations.

The most interesting question about the hydrodynamic mechanisms caused by the 8 control cylinders remains unanswered. Some light has been shed from numerical simulations of the flow performed by [Silva-Ortega et al. \(2014a\)](#). Fig. 8 compares the results of two-dimensional numerical simulations of the flow around static cylinders with 8 rotating control cylinders with  $U_c/U = 0$  and 1.5 at  $Re = 100$ . Even though  $Re$  was significantly lower, it was possible to notice that the rotating control cylinders not only produced weaker vortices, but a narrower wake with an almost doubled vortex-formation



length. A closer look at the streamlines around the control cylinders on one of the sides (presented in Fig. 9) reveals the existence of reversed flow near the wall of the main cylinder. This might be causing the global separation point (marked by a cross on a saddle region of the streamlines) to offset from the wall of the main cylinder in between the third and the fourth control cylinders. The momentum transferred from the control cylinders might help the flow to better withstand the adverse pressure gradient, delaying separation.

The interaction between the control cylinders and the boundary layer must be strongly depend on  $Re$ , especially for  $Re$  approaching the transition from a laminar to a turbulent regime of the boundary layer. In the present experiments, for example, we were not able to evaluate if the control cylinders were immersed or outside of the boundary layer, as suggested by Silva-Ortega et al. (2014a) for  $Re = 100$ . In order to better evaluate the governing hydrodynamic mechanisms at higher  $Re$ , further investigations employing flow visualization and detailed PIV of the near wake and around the control cylinders are planned in the near future.

Finally, the behavior of the wake for oscillating cylinders under VIV is of particular interest, since the angle of attack of the incoming flow relative to the control cylinders will vary through the cycle of vibration. It is possible that the relative angle of attack due to the body's cross-flow velocity causes the frontal stagnation point to approach one of the control cylinders. If that occurs, say at an instant of the oscillation cycle, the wake could present unsteady variations in its dynamics. We believe that an arrangement that produces a control cylinder at the stagnation point would break the symmetry of the flow, resulting in a non-symmetric wake that could result in a steady lift force to one of the sides. This topic should be pursued in future experiments.

## 5. Conclusion

Amplitude of response, frequency of oscillations, mean drag and fluctuating lift coefficients were measured for two configurations of a device made with 8 rotating control cylinders employed to suppress the VIV of a main circular cylinder. Results were obtained for three different values of the rotation parameter ( $U_c/U$ ) and, finally, with a constant tangential velocity ( $U_c$ ) between  $Re = 5000$  and  $50,000$ .

Both configurations (with  $d/D = 0.08$  and  $0.06$ ) reduced the peak amplitude of response in about 70% when compared with that of a bare cylinder for a rotation speed of  $U_c/U = 2.5$ . A similar reduction was found when the tangential velocity remained constant at  $U_c = 0.266$  m/s across the range of reduced velocities. Nevertheless, as far as VIV suppression and drag reduction were concerned, the best case overall was found for the configuration with 8 non-rotating control cylinders, ( $d/D = 0.08$  with  $G/D = 0.10$  and  $U_c/U = 0$ ), achieving approximately a 99% suppression of the peak displacement at the VIV resonance.

In general, the RMS of lift was also minimized by all configurations. Measurements have shown that these configurations with 8 control cylinders do not reduce the mean drag coefficient as much as the case with 2 rotating control cylinders reported in the experimental investigation of VIV by Korkischko and Meneghini (2012) and in the numerical simulations of a static cylinder performed by Mittal (2001). In terms of efficiency, the case with a constant tangential velocity ( $U_c$ ) performed better than with a constant rotation ratio ( $U_c/U$ ) along the reduced velocity range. The peak amplitude of displacement was not very different between the two cases, but the constant  $U_c$  would require less energy to drive the 8 control cylinders as flow speed was increased.

An explanation for the hydrodynamic mechanisms around the control cylinders and in the near wake is still required.

## Acknowledgments

MSO is grateful to CAPES Brazilian Ministry of Education. GRSA acknowledges the support of FAPESP (2011/00205-6, 2014/50279-4), CNPq (306917/2015-7) and the Brazilian Navy.

## References

- Assi, G.R.S., Bearman, P.W., Carmo, B.S., Meneghini, J.R., Sherwin, S.J., Willden, R.H.J., 2013. The role of wake stiffness on the wake-induced vibration of the downstream cylinder of a tandem pair. *J. Fluid Mech.* 718, 210–245.
- Bearman, P.W., 1984. Vortex shedding from oscillating bluff bodies. *Ann. Rev. Fluid Mech.* 16, 195–222.
- Cattafesta, L.N., Sheplak, M., 2011. Actuators for active flow control. *Annu. Rev. Fluid Mech.* 43, 247–272.
- Choi, H., Jeon, W.-P., Kim, J., 2008. Control of flow over a bluff body. *Annu. Rev. Fluid Mech.* 40, 113–139.
- Gad-El-Hak, M., 2000. *Flow Control: Passive, Active, and Reactive Flow Management*. Cambridge University Press.
- Gonçalves, R.T., Fajarra, A.L.C., Rosetti, G.F., Nishimoto, K., 2010. Mitigation of vortex-induced motion (VIM) on a monocolumn platform: forces and movements. *J. Offshore Mech. Arctic Eng.* 132 (4), 041102.
- Gonçalves, R.T., Rosetti, G.F., Fajarra, A.C., Nishimoto, K., 2011. An overview of relevant aspects on VIM of spar and monocolumn platforms. *J. Offshore Mech. Arctic Eng.* 134 (1), 014501.
- Hwang, Y., Choi, H., 2006. Control of absolute instability by basic-flow modification in a parallel wake at low Reynolds number. *J. Fluid Mech.* 560, 465–475.
- Korkischko, I., Meneghini, J.R., 2012. Suppression of vortex-induced vibration using moving surface boundary-layer control. *J. Fluids Struct.* 34, 259–270.
- Lee, S.-J., Lee, S.-I., Park, C.-W., 2004. Reducing the drag on a circular cylinder by upstream installation of a small control rod. *Fluid Dyn. Res.* 34 (4), 233–250.
- Mittal, S., 2001. Control of flow past bluff bodies using rotating control cylinders. *J. Fluids Struct.* 15 (2), 291–326.
- Mittal, S., 2003. Flow control using rotating cylinders: effect of gap. *J. Appl. Mech.* 70 (5), 762–770.
- Mittal, S., Raghuvanshi, A., 2001. Control of vortex shedding behind circular cylinder for flows at low Reynolds numbers. *Internat. J. Numer. Methods Fluids* 35 (4), 421–447.

- Modi, V.J., 1997. Moving surface boundary-layer control: A review. *J. Fluids Struct.* 11 (6), 627–663.
- Muddada, S., Patnaik, B.S.V., 2010. An active flow control strategy for the suppression of vortex structures behind a circular cylinder. *Eur. J. Mech. B Fluids* 29 (2), 93–104.
- Norberg, C., 2003. Fluctuating lift on a circular cylinders: Review and new measurements. *J. Fluids Struct.* 17, 57–96.
- Patino, G., Silva-Ortega, M., Gioria, R.S., Assi, G.R.S., Meneghini, J.R., 2015. Investigation of circular-cylinder VIV passive-control device using flow sensitivity analysis. In: *Bifurcations and Instabilities in Fluid Dynamics, BIFD2015*, France.
- Patino, G.A., Gioria, R.S., Meneghini, J.R., 2017. Evaluating the control of a cylinder wake by the method of sensitivity analysis. *Phys. Fluids* 29 (4), 044103.
- Patnaik, B.S.V., Wei, G.W., 2002. Controlling wake turbulence. *Phys. Rev. Lett.* 88, 1–4.
- Sagrilo, L.V.S., Siqueira, M.Q., Lacerda, T.A.G., Ellwanger, G.B., Lima, E.C.P., Siqueira, E.F.N., 2009. VIM and wave-frequency fatigue damage analysis for SCRs connected to monocolumn platforms. In: *ASME 2009 28th International Conference on Ocean, Offshore and Arctic Engineering, OMAE2009-79807*, pp. 723–729.
- Schulmeister, J.C., 2012. *Flow Separation Control with Rotating Cylinders* (Master's thesis), Massachusetts Institute of Technology.
- Silva-Ortega, M., 2015. *Suppression of Vortex-Induced Vibration of a Circular Cylinder with Fixed and Rotating Control Cylinders* (Master's thesis), University of São Paulo, Available at [www.teses.usp.br](http://www.teses.usp.br).
- Silva-Ortega, M., Assi, G.R.S., 2017. Flow-induced vibration of a circular cylinder surrounded by two, four and eight wake-control cylinders. *Exp. Therm Fluid Sci.* 85, 354–362.
- Silva-Ortega, M., Orselli, R.M., Assi, G.R.S., 2014a. Control of rotating cylinders as suppressors of vortex-induced vibration of a bluff body. In: *Proceedings of SOBENA2014 the 25th Congress of the Brazilian Society of Naval Architects, SOBENA*.
- Silva-Ortega, M., Orselli, R.M., Assi, G.R.S., 2014b. Control of vortex shedding of a circular cylinder with two and four small rotating cylinders. In: *Proceedings of EPTT2014 the XI Spring School of Turbulence and Transition. ABCM*.
- Strykowski, P.J., Sreenivasan, K.R., 1990. On the formation and suppression of vortex shedding at low Reynolds numbers. *J. Fluid Mech.* 218, 71–107.
- Williamson, C.H.K., Govardhan, R., 2004. Vortex-induced vibrations. *Ann. Rev. Fluid Mech.* 36, 413–455.
- Zdravkovich, M.M., 1981. Review and classification of various aerodynamic and hydrodynamic means for suppressing vortex shedding. *J. Wind Eng. Ind. Aerodyn.* 7, 145–189.



Contents lists available at ScienceDirect

## Ocean Engineering

journal homepage: [www.elsevier.com/locate/oceaneng](http://www.elsevier.com/locate/oceaneng)

# Laboratory-scale investigation of the Ventilated-Trousers device acting as a suppressor of vortex-induced vibrations



M.M. Cicolin, G.R.S. Assi\*

Department of Naval Architecture &amp; Ocean Engineering, University of São Paulo, Brazil

## ARTICLE INFO

## Keywords:

Vortex-induced vibration  
Suppression  
Ventilated Trousers  
Circular cylinders

## ABSTRACT

Experiments have been carried out with circular cylinders fitted with a suppressor of vortex-induced vibrations called the *Ventilated Trousers* (VT). Tests were performed at laboratory scale in a free-surface water channel with fixed and free-to-respond models in one degree of freedom. The oscillating tests were performed with elastically mounted cylinders with low mass and damping ( $m^*\zeta < 0.009$ ). Reynolds number varied from 5000 to 25000 and reduced velocity varied between 2 and 15. Tests with fixed models showed that the VT increased the mean drag and practically eliminated the fluctuating lift force when compared to a bare fixed cylinder. Free-response tests showed that the VT was able to reduce 60% of the peak amplitude of vibration, thus reducing the maximum drag compared with that of a bare oscillating cylinder. Three hypotheses are proposed to explain the physical mechanism underlying the suppression by the VT: local disruption of vortex shedding; three-dimensional disruption of the near wake; and the increase of hydrodynamic damping.

## 1. Introduction

The phenomenon of vortex-induced vibration (VIV) may be associated with serious damage caused to offshore cables, flexible pipes and other slender structures such as drilling risers. In the pursuit of viable solutions, the technological development of novel devices for suppressing VIV has been a current topic in both scientific and industrial communities. During the last three decades many devices have been investigated and offered as commercial products, such as helical strakes, fairings, shrouds, etc. However, following the industry demand for more efficient, robust and easy-to-install devices, new ideas for VIV suppressors are still under investigation. Helical strakes, for example, may be the most widely employed suppression device of them all. Strakes became sturdy contraptions with the improvement of molded plastic, but they still reduce VIV with the cost of increasing drag, taking considerable time to install and occupying large areas on the deck.

In this context, Brown and King (Brown, 2010) created an interesting new device for suppressing VIV of drilling risers called the “*Ventilated Trousers*”, or simply VT in this paper. The VT is composed of a net of flexible cables through which an orthogonal array of bobbins (with a specific geometry) is fitted. In the words of its creators, the VT suppressor is “a loose fitting sleeve in the form of a light flexible net with integral bobbins in a special arrangement. It is omni-directional, rugged, and made from materials compatible with the offshore environment” (King et al., 2013). Essentially, the VT is an improve-

ment on the idea of wrapping the drilling riser in a type of flexible cover able to deform with the flow and mitigate the body response to the hydrodynamic loads.

The suppression efficiency of the VT has been studied over the last years with promising results. Brown and King (2008), for example, performed experiments in a laboratory scale with flexible cylinders at  $Re \approx 1.2 \times 10^6$ , showing a 90% reduction of the VIV peak amplitude of displacement. (Reynolds number is defined as  $Re = UD/\nu$ , where  $U$  is the flow speed,  $D$  is the cylinder diameter and  $\nu$  is the kinematic viscosity of water.) So far, all known experiments have been performed either with flexible pipes or near real conditions at sea, especially regarding the range of  $3.7 \times 10^4 < Re < 1.2 \times 10^6$  and the structural properties of the risers (Brown and King, 2008; King et al., 2013).

## 1.1. Objective

Although these results are important for revealing the suppressing potential of the device, they do not shed much light on the physical mechanisms by which the VT is able to suppress vibrations. The present work is part of an investigation to study the interaction between model and flow at moderate  $Re$  and very low damping conditions. We are concerned with the scientific investigation of the hydrodynamic and hydroelastic mechanisms that make this type of suppressor effectively work.

This paper characterizes the VIV response of the VT in idealized

\* Corresponding author.

E-mail address: [g.assi@usp.br](mailto:g.assi@usp.br) (G.R.S. Assi).<http://dx.doi.org/10.1016/j.oceaneng.2017.07.024>

Received 30 August 2016; Received in revised form 10 May 2017; Accepted 5 July 2017

Available online 14 July 2017

0029-8018/ © 2017 Elsevier Ltd. All rights reserved.

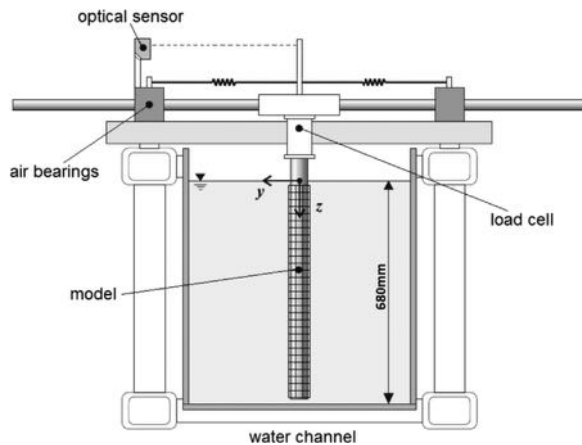


Fig. 1. Cross-section of the water channel showing the cylinder mounted on the elastic rig.

laboratory conditions, in which all variables were under control and crucial parameters were reduced to enhance response. The idea was to test the suppression device in the most pristine condition, indeed different from the real application in the ocean, but free from interference that could mask the understanding of the fundamental physical phenomena.

## 2. Experimental method

Experiments have been carried out in the free-surface water channel of NDF – Fluids and Dynamics Research Group – at the University of Sao Paulo, Brazil. The water channel has a test Section 0.7 m wide, 0.9 m deep and 7.5 m long. The flow speed  $U$  is variable up to 1 m/s, allowing for tests with different values of Reynolds number with a turbulence intensity less than 3%, obtained from velocity and turbulence profiles measured with hot-film anemometers by Assi (2005).

A rigid section of a circular cylinder was attached to a platform on a 1-degree-of-freedom rig, which allowed the model to oscillate freely in the transverse direction ( $y$ ), as shown in a cross-sectional view in Fig. 1. The platform was mounted on air bearings to reduce friction, thus ensuring very low structural damping and maximum response. A pair of coil springs was responsible for providing the stiffness of the system and an optical positioning sensor (employing laser triangulation) measured the displacements with a resolution of 0.2 mm without adding extra damping.

A load cell installed between the cylinder and the platform measured instantaneous lift and drag forces acting on the cylinder. Because the load cell moved with the cylinder, the inertial component due to the mass of the model being accelerated was subtracted from the total force measured by the sensor. Details on the manufacturing and operation of the load cell were presented by Assi (2009). For further details on the elastic rig, other VIV experiments employing the rig and information on the facilities please refer to Cicolin et al. (2015, 2014) and Assi et al. (2013, 2010a, 2010b, 2009). Drag and lift coefficients have been reduced by dividing the fluid forces measured by the load cell by  $\frac{1}{2}\rho U^2 DL$ , where  $\rho$  is the specific mass of water,  $D$  is the external diameter and  $L$  is the submerged length of the cylinder.

Visualization of the flow in the near wake has been performed by the emission of hydrogen bubbles from a thin wire stretched parallel to the axis of the cylinder at about  $1D$  upstream and  $1D$  to the side of the centerline of the wake. A laser sheet illuminated a plane near the region where the free shear layers separated and rolled up to form vortices. A camera positioned perpendicular to the laser plane captured a field of view of almost  $4D$  by  $4D$  in the  $xz$ -plane.

The circular cylinder was cut from a perspex tube with an external diameter of  $D = 50$  mm; the underwater aspect ratio was  $L/D = 13.4$ .

Table 1

Experimental parameters.

|                  | $m^*$ | $f_{N_{air}}$ (Hz) | $f_N \equiv f_{N_{water}}$ (Hz) | $\zeta_{air}$ | $\zeta_{water}$ |
|------------------|-------|--------------------|---------------------------------|---------------|-----------------|
| Bare cylinder    | 2.8   | 0.68               | 0.58                            | 0.3%          | 1.6%            |
| Cylinder with VT | 2.9   | 0.66               | 0.56                            | 0.3%          | 6.5%            |

The cylinder top end was attached to the load cell and the bottom end was closed to keep it watertight. Free-decay tests have been performed both in air and in water to determine the natural frequency and damping associated with the models. The natural frequencies were obtained from the power spectrum of displacement and the damping parameter from the logarithmic decrement of the decay response (values will be presented later when discussing the VIV response). Reduced mass  $m^*$  (defined as the ratio of total structural mass to the mass of displaced fluid) and structural damping  $\zeta_{air}$  (defined as a fraction of the critical damping) were kept to a minimum in order to enhance the response. All experimental parameters are presented in Table 1.

The VT device was built with a flexible net of common polymeric twisted threads. Dozens of bobbins were manufactured out of polymeric rods, drilled through and attached to the net. All materials employed in the construction have been carefully chosen to ensure the VT was neutrally buoyant when submerged. Fig. 2 illustrates the assembly as it was ready for tests.

Some considerations must be presented concerning the geometric parameters of the VT model: The description found in the patent (Brown, 2010) allows for some variations on bobbin dimensions. The reference tests presented by Brown and King (2008), however, have been performed employing a fixed ratio between geometric variables. To allow for comparison, the same proportions for the bobbins, mesh size and bobbin distribution found in that report have been kept in the present work, as shown in Fig. 3. The mesh element width ( $w$ ), net perimeter ( $p$ ) and the ratio between the cylinder and the characteristic size of the bobbin ( $d/D$ ) were specified.

Previously, Brown and King (2008) verified that a mesh element width of 5 times the bobbin characteristic dimension ( $w = 5d$ ) resulted in a more effective VT than one in which  $w = 3d$ . They also reported that the net perimeter must be between  $p = 4D$  and  $\frac{3}{2}\pi D$  (or  $4.71D$ ). Besides that, the patent recommended that the diameter ratio must vary between  $d/D = 0.08$  and  $0.125$ . Following this recipe and considering that the parameters are not completely independent, the largest possible mesh was built respecting the patent restrictions and recommendations. The final dimensions of the VT model employed in the present work are shown in Table 2.

## 3. Results

Preliminary experiments have been carried out with fixed models in flowing water in order to measure the hydrodynamic coefficients of drag (streamwise direction) and lift (cross-flow direction) acting on the cylinder with and without VT. The mean drag coefficient ( $\bar{C}_D$ ) obtained for the cylinder with and without VT are shown in Fig. 4(a). The bare cylinder presented  $\bar{C}_D \approx 1.1$  for the whole range of  $Re$ , as expected and in agreement with Zdravkovich (1997). On the other hand, the VT increased  $\bar{C}_D$  by approximately 25% when compared with that of a fixed bare cylinder, at least in the range  $10 \times 10^3 < Re < 25 \times 10^3$ . This result was expected, considering that the effective diameter of the cylinder with the VT is larger than the external diameter  $D$  of the bare cylinder, thus exposing a larger frontal area to the incoming flow. (Please note that  $\bar{C}_D$  was normalized employing  $D$  for both cases.) But the main observation is that the complex geometry of the VT increased the loss of kinetic energy to the wake as the flow passed around the body, at least as far as fixed cylinders were concerned.



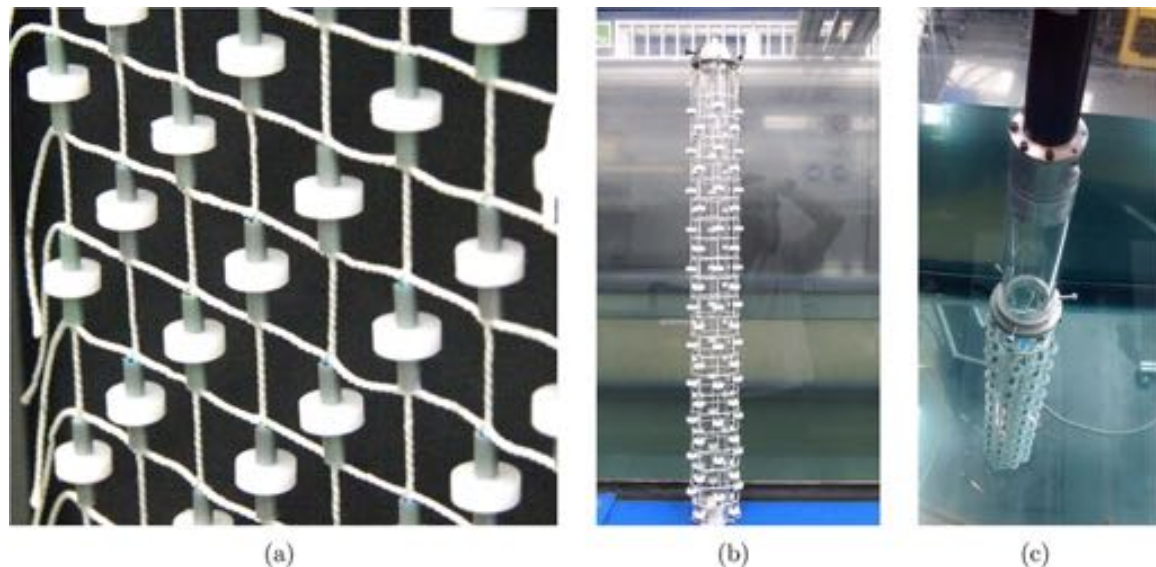


**Fig. 2.** (a) Details of the VT net with bobbins. (b) VT net fitted around the cylinder. (c) Cylinder with VT mounted on the rig and ready for tests in water.

Fig. 4(b) shows the magnitude of fluctuation of the lift force, calculated as the RMS of the lift signal.  $C'_L$  for a bare cylinder was near 0.2, showing considerable dispersion in this  $Re$  range. Norberg (2003) has already determined that such a dispersion occurs at this  $Re$  range due to the sensibility of the boundary conditions. Nevertheless, the results were in agreement with those obtained by Williamson (1996) for tests under similar conditions. In contrast with the increase in drag, the VT managed to almost completely reduce  $C'_L$  for the range of  $Re$  tested. This finding indicates that the VT indeed acts to considerably reduce the cyclic fluctuation of lift due to vortex shedding, at least for fixed cylinders.

The preliminary results obtained for the fixed cylinders do not guarantee that the VT will remain as effective in mitigating  $C'_L$  (and thus suppressing the force excitation) once the cylinder starts to oscillate. Previous studies have shown that three-dimensional suppressors that are effective in disrupting vortex shedding from fixed bodies, might not be so for oscillating bodies (for example, Kleissl and Georgakis, 2011; Owen et al., 2001; Bearman and Brankovic, 2004). Hence, experiments with free-to-respond models were necessary to evaluate the behavior of the VT while responding to VIV.

### 3.1. Cross-flow VIV

Free-to-respond experiments have been performed with cylinders

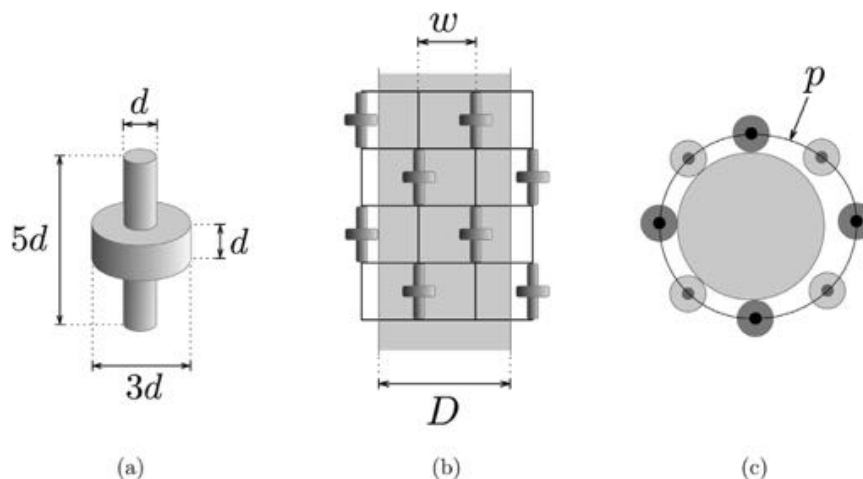
**Table 2**

Model parameters.

|                                 |     |        |         |
|---------------------------------|-----|--------|---------|
| Cylinder diameter               | $D$ | 50 mm  |         |
| Bobbin characteristic dimension | $d$ | 5.8 mm | $0.11D$ |
| Mesh element width              | $w$ | 29 mm  | $5d$    |
| Net perimeter                   | $p$ | 232 mm | $4.64D$ |
| Submerged length                | $L$ | 670 mm | $13.4D$ |
| VT dry mass                     |     | 161 g  |         |

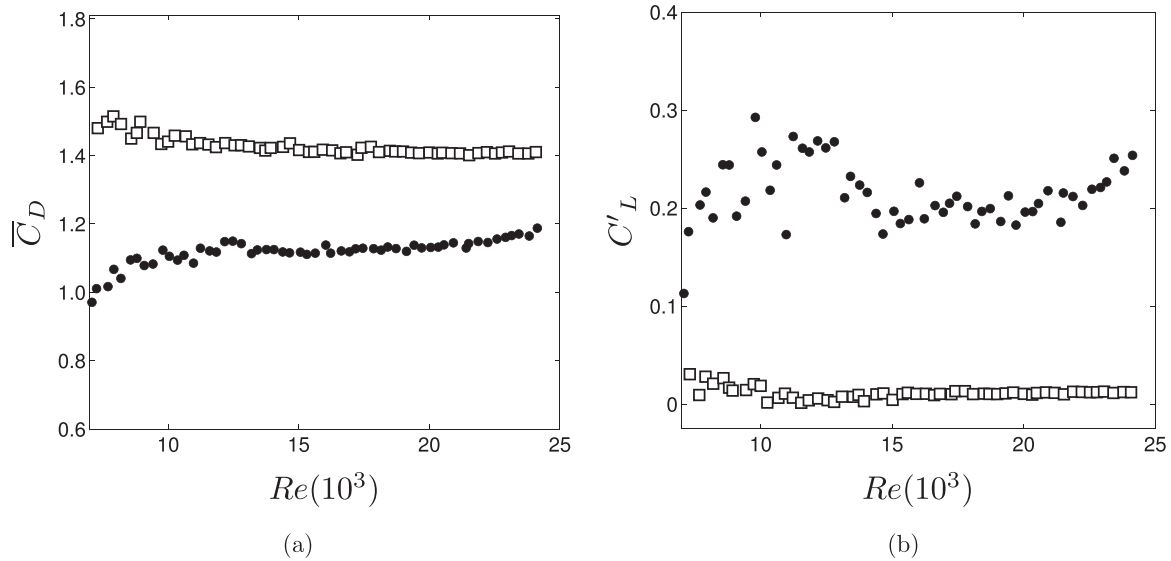
with and without the VT in the same range of  $Re$  as in the fixed tests. The objective was to characterize the cross-flow VIV response of the cylinder with VT compared to that of the bare cylinder. The pair of springs (setting the natural frequency  $f_N$  of the system) was chosen to ensure that the whole synchronization range of VIV fitted within the  $Re$  range of the experiment. As mentioned before,  $m^*$  and  $\zeta_{air}$  were kept to a minimum in order to enhance the response.

Fig. 5 presents the VIV response of the cylinder with VT compared to that of a bare cylinder for a wide range of reduced velocity ( $U/Df_N$ ). The non-dimensional amplitude of vibration  $\hat{y}/D$  (top plot) was obtained by multiplying the RMS of the displacement signal by  $\sqrt{2}$ , thus yielding the equivalent amplitude of a harmonic oscillation. The non-dimensional dominant frequency of oscillation  $f/f_N$  (bottom plot) was obtained by applying a fast Fourier transform on the displacement



**Fig. 3.** Geometric properties of the VT suppressor: (a) bobbin dimensions (b) mesh arrangement and (c) cross-section view of the model.





**Fig. 4.** Force coefficients for fixed models versus  $Re$ : (a) mean drag and (b) RMS of fluctuating lift. Key: • bare cylinder, □ cylinder with VT.

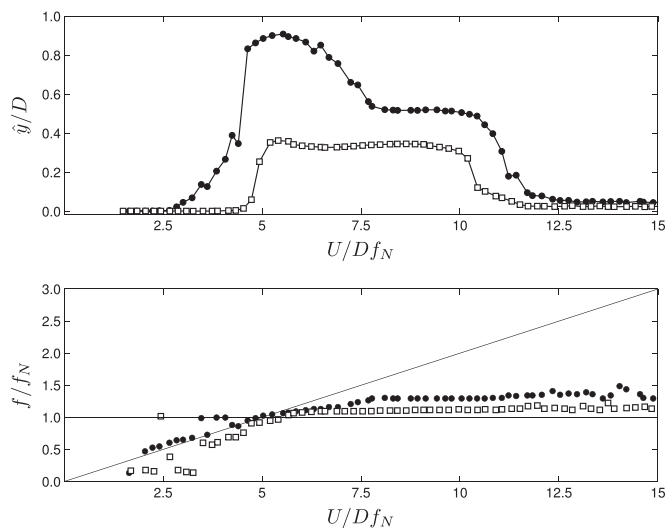


**Fig. 5.** Displacement (top) and frequency (bottom) responses versus reduced velocity for the cylinders under VIV. Key: • bare cylinder, □ cylinder with VT.

data. (Please remind that  $f_N$  was determined for the cylinder immersed in water.)

The bare cylinder presented a typical VIV response, in agreement with the results obtained by Williamson and Govardhan (2004). The peak response amplitude occurred at  $U/Df_N \approx 5$ , when the frequency of vortex shedding resonated with the natural frequency of the system. At around this point,  $f/f_N$  crossed the line representing  $f/f_N = 1$  and remained close to the natural frequency of the system until the end of the synchronization range. For  $U/Df_N > 12$  the response died out, marking the end of the VIV synchronization range. Please note that a residual vibration of insignificant amplitude and frequency near to the natural frequency remained for higher reduced velocities (higher  $Re$ ) due to turbulence buffeting.

At first sight, it is evident that the cylinder with the VT presents a suppressed response when compared to that of a bare cylinder. One may note that the displacement response curve for the VT actually “fits inside” the typical VIV curve for the bare cylinder, thus showing a reduced amplitude and synchronization range. The upper and lower branches of vibration, clearly identified for the bare cylinder, have now disappeared with the VT. A reminiscence of the upper branch still holds the peak amplitude of vibration at  $\hat{y}/D \approx 0.4$  close to  $U/Df_N \approx 5.5$ ,

resulting in a 60% reduction when compared with that of the bare cylinder. Interestingly the frequency signature of the cylinder with the VT is fairly similar to that of the bare cylinder, except for small variations due to differences in  $f_{Nwater}$  of both systems.

Fig. 6 compares examples of the time series of displacement for roughly 60 cycles of vibration ( $t$  is time) for a bare cylinder and a cylinder with VT during the VIV synchronization range. It becomes clear that both responses are indeed harmonic, each with a distinct dominant frequency for the entire sample. At  $U/Df_N = 6$ , in which the bare cylinder oscillated in the upper branch of response, the maximum  $y/D$  of the cylinder with VT was not only less than half of that of the bare cylinder, but also the envelope of displacement presented less variations in time. At  $U/Df_N = 9$ , near the end of the synchronization range, both envelopes became equally well behaved.

Drag measurements obtained during the VIV experiments are shown in Fig. 7(a). As expected, the mean drag coefficient of the bare cylinder increased significantly during the synchronization range, reaching  $\bar{C}_D \approx 3$  when the cylinder oscillated with the largest displacement. As the amplitude decreased towards the end of synchronization,

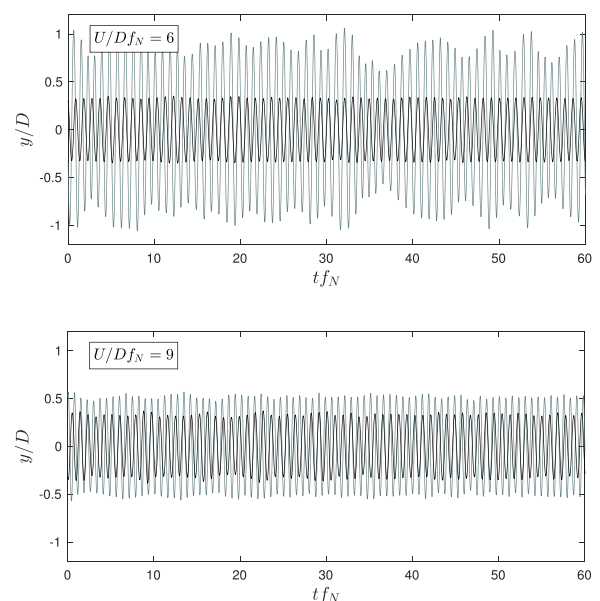


**Fig. 6.** Examples of time series of displacement during the VIV response for a bare cylinder (gray line) and a cylinder with VT (black line).

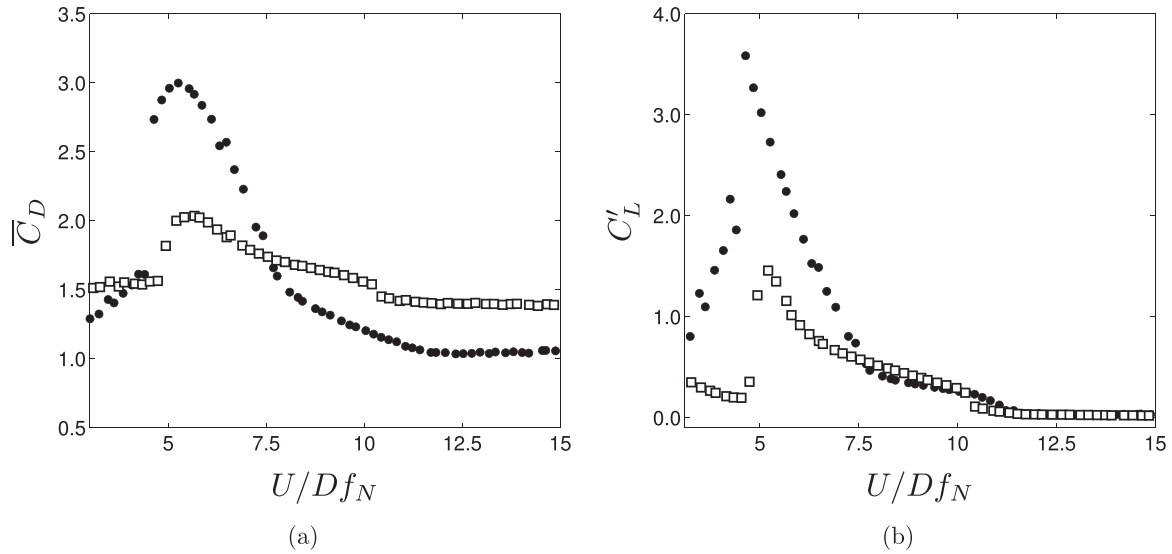


Fig. 7. (a) Mean drag and (b) RMS of lift coefficients versus reduced velocity for the cylinders under VIV. Key: • bare cylinder, □ cylinder with VT.

drag was restored to  $\bar{C}_D \approx 1$ , very close to the value found for the fixed cylinder. These results are in good agreement with those obtained by Williamson (1996) for similar tests. The cylinder with the VT showed the same behavior, presenting a maximum value when the displacement amplitude was the largest, then decreasing as the amplitude became smaller until it reached the value measured for a fixed cylinder with VT for  $U/Df_N > 12$ . It is worth noting that the maximum value of  $\bar{C}_D \approx 2$  was almost 30% lower than that found for the bare cylinder. But after the synchronization range,  $\bar{C}_D$  approximated to 1.4, which was practically the same value found for the fixed model, but larger than the  $\bar{C}_D$  of a bare cylinder.

RMS of lift coefficient presented in Fig. 7(b) shows that  $C'_L$  of a bare cylinder increased up to approximately 3.7 during VIV resonance, at  $U/Df_N \approx 5$ , when there was maximum energy transfer from the flow to the system. As the reduced velocity increased,  $C'_L$  decreased reaching values close to zero when the synchronization ended. As expected, there was a strong relationship between  $C'_L$  and  $\hat{\delta}/D$ , as explained by Williamson (1996). The RMS of lift coefficient of the cylinder with the VT followed a similar trend as that for the bare cylinder, but with values significantly lower. A maximum value of  $C'_L \approx 1.5$  was only 40% of that of the bare cylinder, showing that the VT is capable of reducing, to a certain extent, the magnitude of the fluctuating force exciting the cylinder also during VIV.

A detailed view of the frequency signature of the phenomenon is presented in Fig. 8. The top plot presents the VIV response as a reference. The middle plot presents color contours representing the power spectrum of displacement, highlighting the dominant frequencies ( $f/f_N$ ) versus reduced velocity. The bottom plot, presents a similar power spectrum, this time for the lift force acting on the body, in which the dominant frequency of lift ( $f_{CL}/f_N$ ) is noticeable. The highest peak in the spectrum for each reduced velocity resulted in the points plotted before in Fig. 5. Refer to Assi (2009) for details on how these plots have been made.

The  $f/f_N$  spectrum for the bare cylinder (Fig. 8(a)) shows the typical frequency signature for the VIV response. A single branch of dominant frequency remained near the natural frequency of the system during the lock-in range. Both displacement and lift showed the same signature, as expected. After the end of lock-in, for  $U/Df_N > 12$ , the cylinder presented minute vibrations due to turbulence buffeting and  $f_{CL}/f_N$  followed the  $St = 0.2$  line (indicated by the inclined solid line on the plot).

The frequency signature for the cylinder with VT (Fig. 8(b)) was essentially the same, with a single frequency branch dominating along the synchronization range. However, outside the lock-in range, we did

not see a significant component of  $f_{CL}/f_N$  following the  $St = 0.2$  (not even when the flow was more energetic at  $U/Df_N > 12$ ), but a broader lift spectrum instead. This explains the lower values of  $C'_L$  measured for a fixed cylinder and presented before in Fig. 4(b). While the three-dimensional geometry of the VT might be efficient in disrupting vortex shedding from fixed cylinders, a coherent wake may reappear as the cylinder is excited into cross-flow oscillations near its natural frequency.

#### 4. Discussion on the hydrodynamic mechanisms

The preliminary tests with fixed models revealed important features of the behavior of the VT suppressor. The increase in mean drag was not a surprise, since the installation of the VT around the cylinder simply increases the effective frontal area facing the incoming flow. The complex geometry of the net and bobbins also increased the surface area of the system, resulting in stronger separated flow around the net and bobbins as well as increased friction losses.

In another recent work (Cicolin and Assi, 2017) we have observed that the VT increases the vortex-formation length in the near wake. We argued that “the longer formation length found for the VT is responsible for a decrease in the fluctuating lift feeding back to excite the cylinder into VIV.” Particle-image velocimetry (PIV) measurements of the wake, reproduced here in Fig. 9, revealed that “while most of the flow is separated from the outer surfaces of the bobbins, the entrainment of flow that permeates the VT mesh bleeds through to feed the near wake region, extending the vortex-formation length and increasing the base pressure.” This mechanism, which interferes with the two-dimensional formation of vortices, was attributed to the peculiar geometry of the bobbins working like a shroud.

On the other hand, it was rather unexpected that the VT managed to reduce the RMS of lift to almost zero for the whole range of  $Re$ , hence we conclude that the VT successfully acted to weaken the vortex-excitation force. Considering that hydrodynamic loads were measured as an integral force at the top of cylinder, it is reasonable to hypothesize that the VT could either eliminate the sectional lift force, or uncorrelate it along the span of the cylinder. This is a clear indication that the three-dimensional geometry of the VT suppressor is important for its effectiveness.

In order to investigate three-dimensional flow structures along the span, flow visualization employing hydrogen bubbles has been performed for a fixed cylinder with and without VT at  $Re=7800$ . A curtain of bubbles was released from a thin wire and illuminated by a laser sheet on the  $xz$ -plane, parallel to the axis of the cylinder. Figs. 10–12

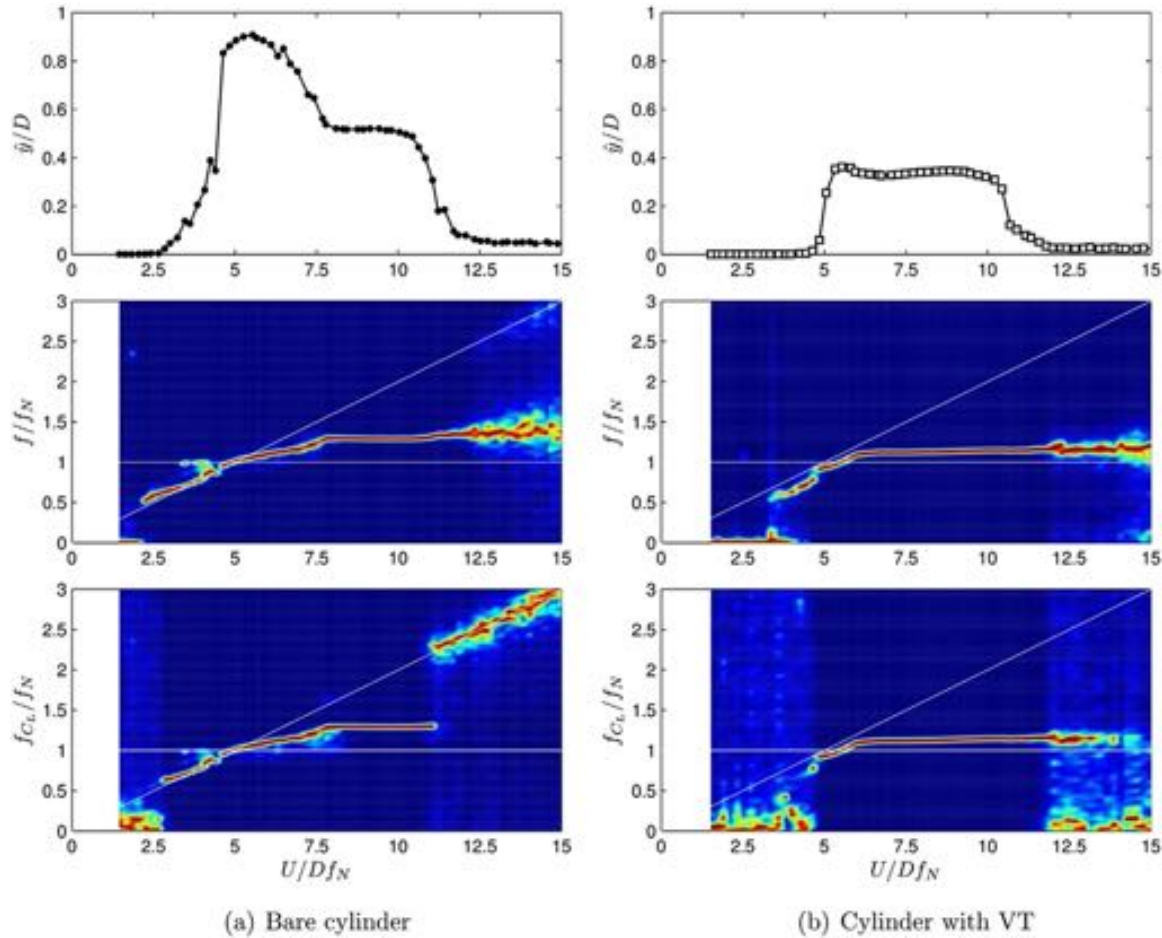


Fig. 8. Amplitude of displacement (top) and power spectra of displacement (middle) and lift (bottom) for both models.

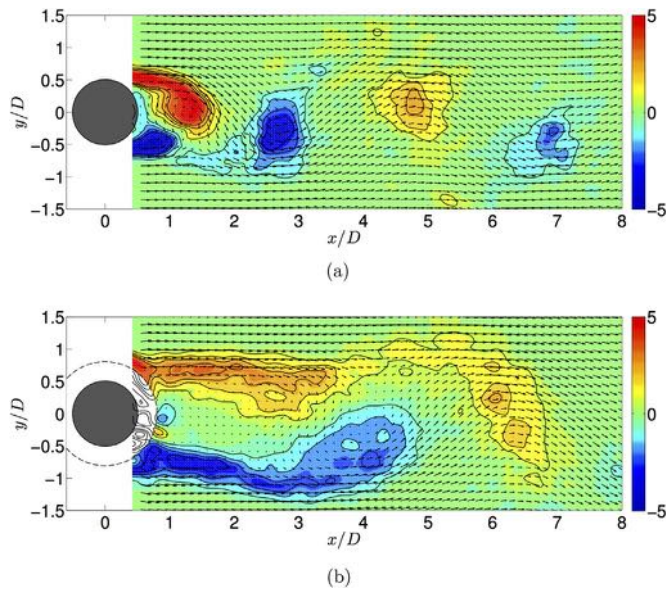


Fig. 9. Phase-averaged vorticity contours ( $s^{-1}$ ) in the near wake of (a) a bare cylinder and (b) a cylinder with VT.  $Re=9000$ . Reproduced from Cicolin and Assi (2017).

compare the three-dimensional wake structures along the span created by the VT with that of a bare cylinder.

Fig. 10 presents two examples of the three-dimensional wake structure downstream of a bare cylinder (the cylinder walls are represented by thick lines, while the center is marked by a dot-dashed line). A clear vortex filament parallel to the axis of the cylinder is seen

at its maximum extension. The estimated vortex-formation length is seen to be around  $1D$  and  $2D$  downstream of the cylinder center, which is in good agreement with other values found in the literature for this  $Re$  range, including the value of 1.5 measured by Cicolin and Assi (2017) for  $Re=9000$  and reproduced in Fig. 9.

The flow structures in the wake of a cylinder with VT are shown in Fig. 11. Distinct three-dimensionalities associate with the bobbins are visible in the near wake, specially for the first  $2D$  downstream of the cylinder center. The formation of a coherent vortex filament is not seen to be occurring within the plane illuminated by the laser sheet, which agrees with Cicolin and Assi (2017), who measured a vortex-formation length of 5.31 for  $Re=9000$  (Fig. 9(b)). A detailed view of the flow around the VT is seen in Fig. 12, confirming that complex three-dimensional flow structures generated at the scale of the bobbins dominate the flow in the near wake. We believe these flow structures enhance flow entrainment and mixing of the free shear layers, disrupting the formation of an organized vortex wake.

In essence, we believe that (i) the shrouding effect acting on the two-dimensional level proposed by Cicolin and Assi (2017) combined with (ii) the three-dimensional disruption of the near wake by the bobbins are the hydrodynamic mechanisms that weaken the vortex-shedding excitation force that drives VIV.

Nevertheless, other secondary effects might also be playing a role in reducing the response of a cylinder with VT. The decay tests performed in air and in water raised another important aspect associated with the VIV response. Although both cylinders were designed to present the same level of structural damping ( $\zeta_{air}$ ), the VT increased the hydrodynamic damping of the system when submerged:  $\zeta_{water}$  for the cylinder with VT is almost 5 times higher than that of the bare cylinder. This is due to the viscous loss of energy as the cylinder oscillates in still



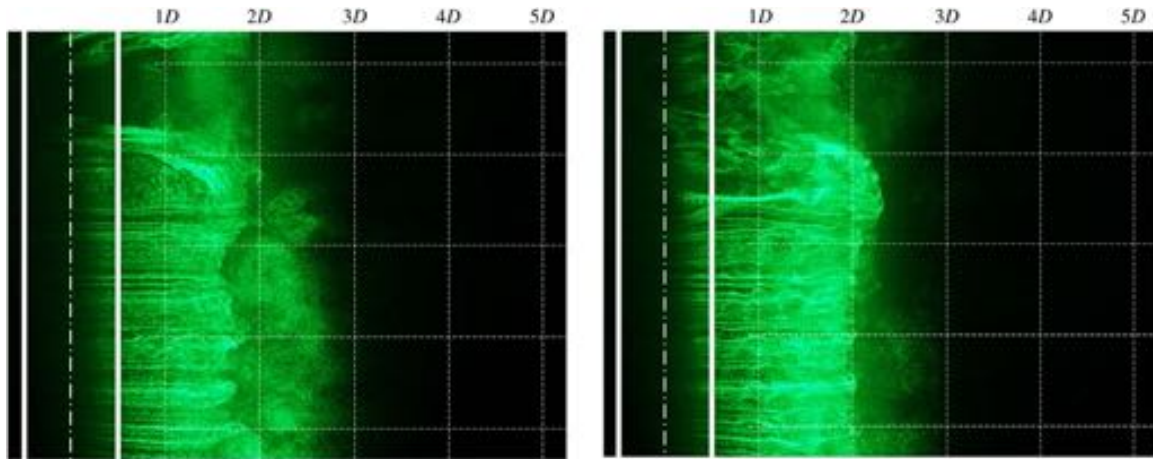


Fig. 10. Visualization of the near wake of a fixed bare cylinder. Two instants. Flow is from left to right.  $Re=7800$ .

water. Of course the interaction of the oscillating cylinder with its own wake will change its perception of the fluid loads (Vandiver, 2012, refer to), yet it is reasonable to think that the VT is likely to present lower amplitudes of vibration due to its increased non-linear hydrodynamic damping. A considerable number of works (Vikestad et al., 2000; Blevins, 2001, for example) show that the VIV response is very sensitive to damping, especially at low mass ratios.

Consequently, we believe that the suppression efficiency of the VT in real applications out in the ocean may be higher than that observed in this laboratory experiment performed in idealized conditions with low mass and damping. In real conditions at sea, structural damping reaches values ten times higher, while hydrodynamic damping may also be increased due to higher- $Re$  and higher-turbulence effects. In spite of increasing drag for non-oscillating models, the VT reduces drag when the maximum amplitude of vibration occurs. All facts combined make the VT an attractive solution as far as hydroelasticity is concerned (not to mention other criteria regarding storage and installation).

## 5. Conclusion

The cross-flow VIV response of a cylinder with VT was characterized through the synchronization range for  $Re=2 \times 10^3$  to  $25 \times 10^3$  and reduced velocities up to 15. Our main conclusion in the present work is that the VT suppressor is capable of reducing the VIV peak amplitude of displacement in 60%, with an increase of about 25% in drag, when compared to a bare cylinder under VIV. This was achieved for idealized conditions in the laboratory: at moderate Reynolds number, low mass ratio and extremely low-damping systems.

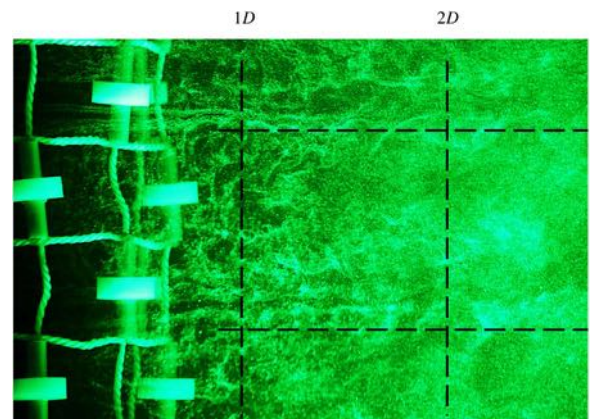


Fig. 12. Detail of the flow structures around the VT. Flow is from left to right.  $Re=7800$ .

Experiments with fixed models also confirmed that a cylinder with VT presents reduced RMS of lift, but increased drag when compared to a bare cylinder. While the three-dimensional geometry of the VT might be efficient in disrupting vortex shedding from fixed cylinders, a coherent wake may reappear as the cylinder is excited into cross-flow oscillations. Only a small lift force is required for that to occur with low-mass-damping systems under VIV.

Results helped us raise three hypotheses to explain the physical mechanism underlying the suppression by the VT: (i) local disruption of the two-dimensional vortex shedding mechanism and the formation of the wake; (ii) global changes in the three-dimensional flow structure

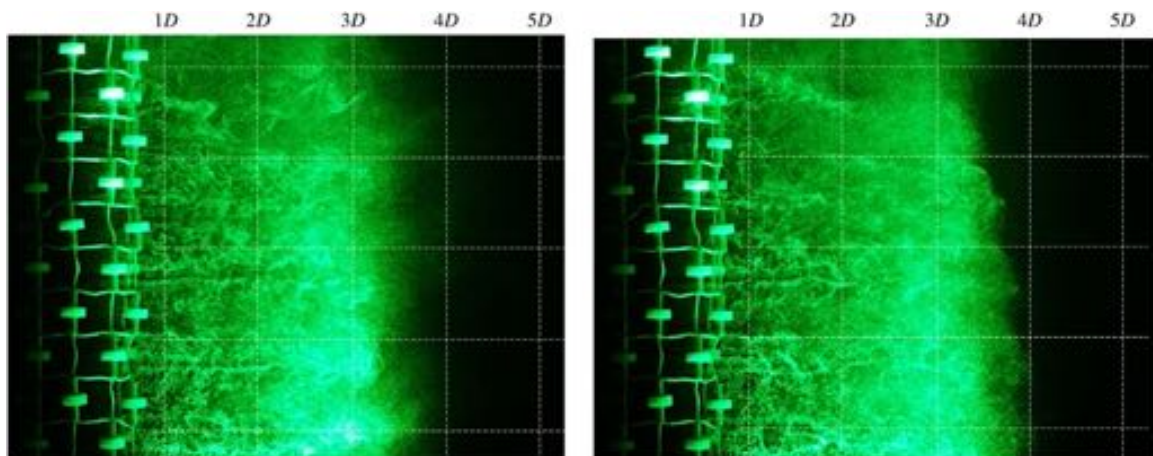


Fig. 11. Visualization of the near wake of a fixed cylinder with VT. Two instants. Flow is from left to right.  $Re=7800$ .

along the span of the cylinder caused by the flow around the bobbins; and (iii) the increase of hydrodynamic damping caused by the VT. Future works should try to isolate parameters to verify whether one or a combination of mechanisms is responsible for the suppression.

Finally, we would like to highlight that idealized experiments in laboratory scale are designed to allow for the control of the fundamental parameters involved in the investigation, thus shedding light on the physical mechanisms being studied. We cannot fully predict how the VT would behave in real applications at much larger scales. We can make reasonable assumptions knowing that Reynolds number, turbulence intensity, structural damping and other parameters will be significantly different. Data collected from large-scale field tests cannot be directly compared to the results presented in this paper without such considerations being made.

## Acknowledgements

MM Cicolin is thankful to the support of ANP Brazilian Agency of Petroleum, Natural Gas and Biofuels. GRS Assi is grateful to FAPESP (2011/00205-6, 2014/50279-4), CNPq (306917/2015-7) and the Brazilian Navy.

## References

- Assi, G.R.S., 2005. Experimental Study of the Flow Interference Effect around Aligned Cylinders (Master's thesis). University of São Paulo, São Paulo, Brazil, (in portuguese) Available from: [www.teses.usp.br](http://www.teses.usp.br).
- Assi, G.R.S., 2009. Mechanisms for Flow-induced Vibration of Interfering Bluff Bodies (Phd thesis). Imperial College London, Available from: [www.ndf.poli.usp.br/~gassi](http://www.ndf.poli.usp.br/~gassi).
- Assi, G.R.S., Bearman, P.W., Carmo, B.S., Meneghini, J.R., Sherwin, S.J., Willden, R.H.J., 2013. The role of wake stiffness on the wake-induced vibration of the downstream cylinder of a tandem pair. *J. Fluid Mech.* 718, 210–245, (3).
- Assi, G.R.S., Bearman, P.W., Kitney, N., 2009. Low drag solutions for suppressing vortex-induced vibration of circular cylinders. *J. Fluids Struct.* 25, 666–675.
- Assi, G.R.S., Bearman, P.W., Kitney, N., Tognarelli, M.A., 2010a. Suppression of wake-induced vibration of tandem cylinders with free-to-rotate control plates. *J. Fluids Struct.* 26, 1045–1057.
- Assi, G.R.S., Bearman, P.W., Meneghini, J.R., 2010b. On the wake-induced vibration of tandem circular cylinders: the vortex interaction excitation mechanism. *J. Fluid Mech.* 661, 365–401, (10).
- Bearman, P.W., Brankovic, M., 2004. Experimental studies of passive control of vortex-induced vibration. *Eur. J. Mech.- B/Fluids* 23 (1), 9–15.
- Blevins, R.D., 2001. *Flow-Induced Vibration* 2nd Ed.. Krieger Publishing Company.
- Brown, A., 2010. Device and Method for Suppressing Vortex-induced Vibrations. Tech. rep., United States Patent Application Publication.
- Brown, A., King, R., 2008. Tests with flexible quasi-fairing to reduce riser drag, suppress viv and limit drilling down-time. In: *Proceedings of the Offshore Technology Conference (OTC 2008)*. p. 19161.
- Cicolin, M.M., Assi, G.R.S., 2017. Experiments with flexible shrouds to reduce the vortex-induced vibration of a cylinder with low mass and damping. *Appl. Ocean Res.* 65, 290–301.
- Cicolin, M.M., Freire, C.M., Assi, G.R.S., 2014. Suppression of the vortex-induced vibration of a circular cylinder with permeable meshes. In: *Proceedings of the 4th Joint US-European Fluids Engineering Summer Meeting*.
- Cicolin, M.M., Freire, C.M., Assi, G.R.S., 2015. VIV response and drag measurements of circular cylinders fitted with permeable meshes. In: *Proceedings of the 34th International Conference on Ocean, Offshore and Arctic Engineering*.
- King, R., Brown, A., Braaten, H., Russo, M., Baarholm, R., Lie, H., 2013. Suppressinf full scale riser viv with the vt suppressor. In: *of Mechanical Engineers (ASME), A.S. (Ed.)*, *Proceedings of the 32th International Conference on Ocean, Offshore and Arctic Engineering (OMAE 2008)*. p. 11642.
- Kleissl, K., Georgakis, C., 2011. Aerodynamic control of bridge cables through shape modification: A preliminary study. *J. Fluids Struct.* 27 (7), 1006–1020.
- Norberg, C., 2003. Fluctuating lift on a circular cylinders: Review and new measurements. *J. Fluids Struct.* 17, 57–96.
- Owen, J.C., Bearman, P.W., Szewczyk, A.A., 2001. Passive control of VIV with drag reduction. *J. Fluids Struct.* 15, 597–605.
- Vandiver, J.K., 2012. Damping parameters for flow-induced vibration. *J. Fluids Struct.* 35, 105–119.
- Vikestad, K., Larsen, C.M., Vandiver, J.K., 2000. Norwegian deepwater program: damping of vortex-induced vibrations. In: *Proceedings of the Offshore Technology Conference*. No. OTC 11998.
- Williamson, C., 1996. Three-dimensional wake transition. *J. Fluid Mech.* 328, 345–407.
- Williamson, C., Govardhan, R., 2004. Vortex-induced vibrations. *Annu. Rev. Fluid Mech.* 36, 413–455.
- Zdravkovich, M., 1997. *Flow Around Circular Cylinders: Vol.1 – Fundamentals* 1st Ed.. Oxford Science Publications.





Contents lists available at ScienceDirect

## Ocean Engineering

journal homepage: [www.elsevier.com/locate/oceaneng](http://www.elsevier.com/locate/oceaneng)

## Hydrodynamic loads on a circular cylinder surrounded by two, four and eight wake-control cylinders

M. Silva-Ortega<sup>1</sup>, G.R.S. Assi<sup>\*</sup>

Department of Naval Architecture &amp; Ocean Engineering, Escola Politécnica, University of São Paulo, São Paulo, Brazil



## ARTICLE INFO

## Keywords:

Vortex shedding  
Wake control  
Drag reduction  
Axial rods  
Shrouds

## ABSTRACT

The hydrodynamic loads of mean drag and fluctuating lift are presented for a circular cylinder fitted with 2, 4 and 8 wake-control cylinders positioned around its circumference. The device is fitted around the body to interact with the flow in the near wake and control vortex shedding. The efficiency regarding lift suppression and drag reduction has been investigated for nine different cases varying the diameter of the control cylinders and their relative gap from the wall. All cases have been compared with the hydrodynamic forces of a plain cylinder. The configuration with 4 control cylinders, gap ratio of  $G/D = 0.05$  ( $G$  is the gap between the control cylinders and the main cylinder of diameter  $D$ ) and diameter ratio of  $d/D = 0.06$  ( $d$  is the diameter of the control cylinders) produced the lowest drag when compared to all other configurations: mean drag coefficient was 0.75, approximately 50% lower than that of a bare cylinder. Experiments have been conducted in a free-surface water channel at moderated Reynolds numbers between 5000 and 50,000.

## 1. Introduction

The periodic shedding of vortices downstream of a bluff body generates cyclic hydrodynamic loads that feed back on the body. Fluctuating lift will be at the frequency ( $f_s$ ) in which vortices are shed in the wake, while drag will be at double that frequency ( $2f_s$ ). With time, the cyclic loads may cause structural problems to the body, such as fatigue damage, a special concern for slender structures as riser pipes and submarine cables. Flexible structures with a bluff shape may be excited by this periodic load and respond with considerable oscillations. The motion of the structure interacts with the flow and develop into what is called vortex-induced vibrations (VIV).

Mitigating vortex shedding and VIV are important issues for many engineering applications, ranging from aeroacoustic problems in aviation to the vibration of a drilling riser in offshore exploration. Hence, the scientific community and the industry are constantly pursuing the development of new methods to control the wake and design novel VIV suppressors (devices attached to the body to mitigate the damaging effects of the vibration).

Wake-control mechanisms can be classified as passive or active systems (Choi et al., 2008), with the latter considering both open-loop and closed-loop control systems. Zdravkovich (1981) presents several passive-control devices, classifying them into three categories according

to the way they affect the vortex-shedding mechanism: (i) Surface protrusions, which affect separation lines and/or separated shear layers: they involve helical strakes, wires, fins, studs, or spheres, among others. (ii) Shrouds, that affect the entrainment layers around the body. The perforated shroud and the axial rods are two examples. (iii) Near-wake stabilizers, that affect the switch of the confluence point. Fairings and splitter plates, which prevents communication between the opposing shear layers of the wake, are common examples. These passive methods require no external energy supply and they act primarily disrupting the formation and development of an organized wake of vortices.

Among the various solutions for passive vortex-shedding and VIV suppression, the helical strakes are one of the most commonly used in air and water flows (Bearman and Brankovic, 2004; Korkischko and Meneghini, 2010). But despite the proven efficiency of the strakes in reducing fluctuating lift, they increase the mean drag (Korkischko and Meneghini, 2011; Zdravkovich, 1981), which is undesirable in a great number of applications.

Placing a smaller control rod upstream of the main cylinder is a well-established strategy for drag reduction (Lee et al., 2004). Strykowski and Sreenivasan (1990) proved that if the small control cylinder is otherwise placed within a defined region in the near-wake (downstream) of the main cylinder, the wake could be effectively suppressed at a Reynolds number of  $Re = 80$ . Suppression of the vortex street is associated with

<sup>\*</sup> Corresponding author.

E-mail address: [g.assi@usp.br](mailto:g.assi@usp.br) (G.R.S. Assi).

<sup>1</sup> Currently at Department of Naval Engineering, University Veracruzana, Mexico.

damping the instability in the near-wake region. In their investigation, the ratio between the diameter of the control cylinder to the diameter of the main cylinder varied between  $d/D = 1/3$  to  $1/20$ . They also showed that wake suppression is the most efficient when the small control cylinder is placed roughly around  $1D$  downstream of the cylinder center and  $1D$  to the side of the centerline of the wake for  $d/D = 0.05$  to  $0.07$ . Their experimental and numerical results also indicate that this region of effectiveness strongly depends on  $Re$  and  $d/D$ . For  $Re = 80$  to  $300$ , Kuo et al. (2007) showed detailed flow structures revealing the primary mechanism that led to significant lift and drag reduction without completely suppressing the shedding of a vortex street.

Zdravkovich (1981) presented results of an axial-rod shroud, following the concept that the shroud should break-up the flow into a large number of small vortices. Axial rods were fitted about the circular cylinder and several parameters were varied in order to find an optimum configuration for VIV suppression: the number of rods (varied between 4 and 218, defining the shroud porosity), the distance of the rods to the wall of the cylinder (gap) and their circumferential distribution. Tests were performed in a water channel and in a wind tunnel for  $Re \approx 10^3$ – $10^5$ . The most interesting result, as far as suppression was concerned, was obtained for a porosity of 63% (39 rods) when the rods were positioned with a gap of  $G/D \approx 0.25$  from the cylinder wall. But most surprisingly was the fact that the best suppression was achieved when the rods were not evenly distributed around the cylinder, but grouped close to the near wake, leaving an unshrouded portion (of about 90 degrees of the circumference) facing the free stream.

More recently, control of the wake of a cylinder with rotating control cylinders has been investigated experimentally (Korkischko and Meneghini, 2012) and numerically (Mittal, 2001; Silva-Ortega et al., 2014b). In a recent study, Silva-Ortega and Assi (2017) reported on VIV experiments performed with the same control cylinder discussed in the present work acting as VIV suppressors. They found that the best VIV suppressor was “composed of 8 control cylinders and mitigated 99% of the peak amplitude of vibration when compared to that of a plain cylinder; mean drag was increased by 12%”. They also concluded that “a polar array of 4 control cylinders was the most efficient configuration to minimize the mean drag, but the system developed severe vibrations combining VIV and a galloping-like response”.

The objective of the present work is to investigate a method of suppressing the vortex wake of a circular cylinder employing a passive control strategy. A rigid section of a circular cylinder of diameter  $D$  is surrounded by a polar array of  $N = 2, 4$  and  $8$  smaller control cylinders of diameter  $d$ , equally spaced about the circumference and separated by a gap  $G$  from the wall of the main cylinder. The ratios  $d/D$  and  $G/D$  are the control parameters of the experimental investigation. As seen above, previous results found in the literature indicate that there are many other significant parameters apart from the number and size of the control cylinders. Therefore, we have conducted an experimental investigation trying to probe the domain of only a few of those governing parameters.

The diameter of the control cylinders ( $d$ ) was varied in three steps around the size of the smaller cylinders reported by Strykowski and Sreenivasan (1990). Since the vortex-formation length tends to be reduced by an increase in  $Re$ , the region of effective wake control presented by Strykowski and Sreenivasan (1990) for  $Re = 80$  should be brought much closer to the base of the cylinder for our  $Re$  range. Inspired by the work of Zdravkovich (1981), the gap between the control cylinders and the wall of the main cylinder ( $G$ ) was also varied in three steps. In the present parametric study neither the main cylinder nor the control cylinders were allowed to move or respond to the flow, so the efficiency of the wake-control method was evaluated by measuring the hydrodynamic loads acting on the body.

## 2. Experimental method

Experiments have been carried out in the recirculating water channel

of NDF (Fluids and Dynamics Research Group) at the University of São Paulo, Brazil. The water channel has a free-surface test section which is  $0.7$  m wide,  $0.9$  m deep and  $7.5$  m long. Good quality flow can be achieved up to  $1.0$  m/s with turbulence intensity less than 3%. This laboratory has been especially designed for experiments with flow-induced vibrations. For further details the apparatus, validation and information on the facilities please refer to Assi et al. (2013, 2010a, 2010b).

A rigid section of a circular cylinder was made of a perspex tube of external diameter  $D = 100$  mm with a smooth surface. Two, four or eight identical control cylinders were made of perspex rods and supported by rings attached to the ends of the main cylinder. The distribution of the control cylinders about the main cylinder is presented in Fig. 1, in which the arrow indicates the direction of the incoming flow. The position of the  $N$  control cylinders was chosen so that they were equally spaced around the main cylinder, but keeping a symmetric distribution in relation to the streamwise axis, with no cylinder at the frontal stagnation point.

The axes of the control cylinders were parallel to the axis of the main cylinder, spanning the whole length of the model (immersed length of  $L = 700$  mm). Two extra supporting rings were installed at  $L/3$  and  $L2/3$  positions to hold the control cylinders in place and prevent them from vibrating by reducing their free span. The control cylinders did not present significant deflections nor vibrations due to their own VIV in the course of the experiments. The diameter of the control cylinders was varied in three steps of  $d/D = 0.04, 0.06$  and  $0.08$ . The gap measured between the wall of the control cylinders and the wall of the main cylinder could be set to  $G/D = 0.05, 0.10$  and  $0.15$ . The angular distribution of the control cylinders was kept constant for all cases while varying  $d/D$  and  $G/D$ . The models were the same employed by Silva-Ortega and Assi (2017).

Models were mounted on a especially built load cell (developed by Assi, 2009), rigidly attached to the frame of the test section to deduce the instantaneous and time-averaged hydrodynamic forces on the cylinder model. An illustration of the experimental setup is presented in Fig. 2. A summary of all the parameters investigated in the experiment is presented in Table 1, adding up to 27 different experimental configurations. In addition, preliminary tests have been performed with a bare cylinder (without control cylinders) to serve as a reference for comparison. The only flow variable changed during the course of the experiments was the flow velocity  $U$ , which alters the Reynolds number ( $Re = UD/\nu$ , based on the diameter  $D$  of the bare cylinder and the viscosity of water  $\nu$ ) between 5000 and 50,000.

## 3. Results

Measurements of lift and drag were made for each of the 27 configurations presented above. Results for a bare cylinder in the range  $Re = 5,000$  to  $50,000$  are presented as a reference and for validation. This  $Re$  range falls in the subcritical regime in which transition to turbulence occurs in the separated shear layers and a considerable scatter of lift and drag is found in the literature (Zdravkovich, 1997). The mean drag coefficient ( $\bar{C}_D$ ) and the RMS of the lift coefficient ( $\bar{C}_L$ ) are presented for a bare (or plain) cylinder in Fig. 3. In Fig. 3a, mean drag for the plain cylinder remains roughly around  $\bar{C}_D \approx 1.4$ , not too far but higher than the curve presented by Zdravkovich (1997), who summarized results from various sources.

It is worth highlighting that, in the present experiments, the top end of the cylinder pierced the free surface of the water, hence a small fraction of the drag is due to the generation of waves. The Froude number ( $Fr = U/\sqrt{gD}$ , where  $g$  is the acceleration of gravity) was rather small, varying between  $Fr = 0.05$  and  $0.5$  for a constant ratio of Reynolds number to Froude number of  $Re/Fr \approx 10^5$ . Chaplin and Teigen (2003), who measured the wave-resistance drag on a bare cylinder piercing a free surface at  $Re/Fr = 2.79 \times 10^5$ , concluded that an increase in drag due to the formation of waves is only significant for  $Fr$  around 1 and should not

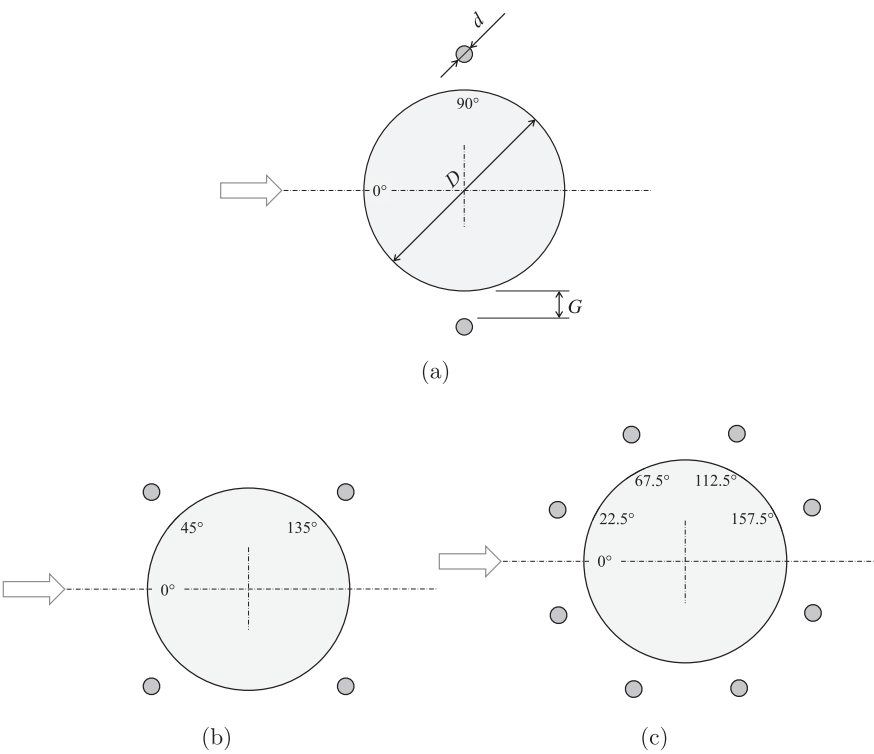


**Fig. 1.** Geometrical parameters for the main cylinder with (a) two, (b) four and (c) eight control cylinders. Flow approaching in the direction of the arrow.

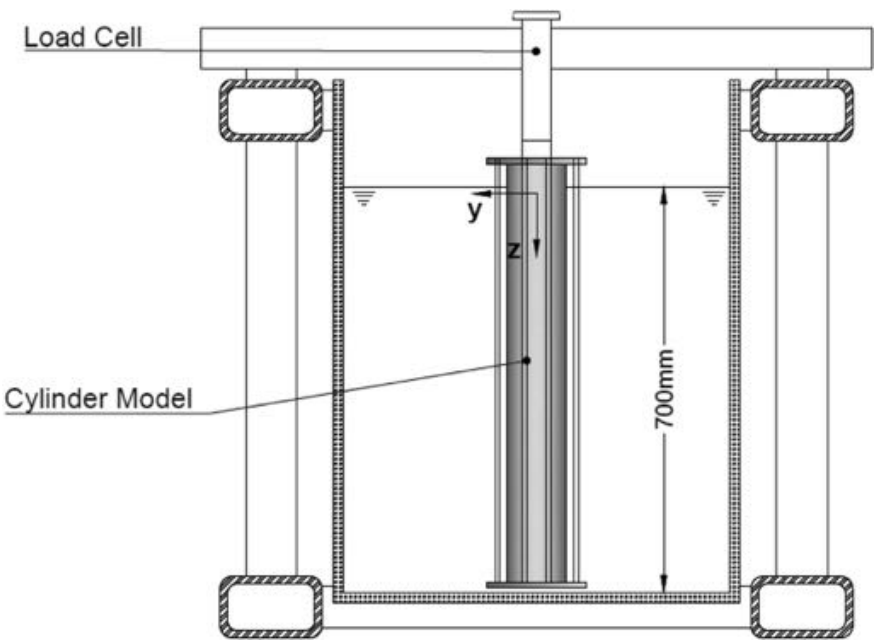


**Fig. 2.** Experimental setup: cylinder control cylinders mounted on the load cell.

**Table 1**  
Parameters for the present investigation.

|   |       |  |
|---|-------|--|
| Number of control cylinders             | $N$   | 0, 2, 4, 8                               |
| Diameter ratio of the control cylinders | $d/D$ | 0.04, 0.06, 0.08                         |
| Gap ratio between cylinders             | $G/D$ | 0.05, 0.10, 0.15                         |
| Reynolds number                         | $Re$  | $5 \times 10^3$ to $5 \times 10^4$       |
| Froude number                           | $Fr$  | $5 \times 10^{-2}$ to $5 \times 10^{-1}$ |

occur for the  $Fr < 0.5$ , which is the case in the present experiments. Other effects, due to free stream turbulence intensity (Bell, 1983) or

cylinder aspect ratio (Zdravkovich et al., 1989), for example, may contribute to change the mean drag from the canonical value expected for a two-dimensional body. Nevertheless, since all models have been measured under the same condition, the current value of  $\bar{C}_D$  for a plain cylinder will be taken as a reference for comparison in this study.

Fig. 3b compares the RMS of lift to the data collected by Norberg (2003). In our study, the overall force acting on the cylinder was measured with a load cell positioned on the top. Due to three-dimensional flow effects,  $\bar{C}_L \approx 0.3$  differs from that expected for a two-dimensional section of the cylinder. Norberg (2003) analyzed several experimental and numerical results at different conditions and

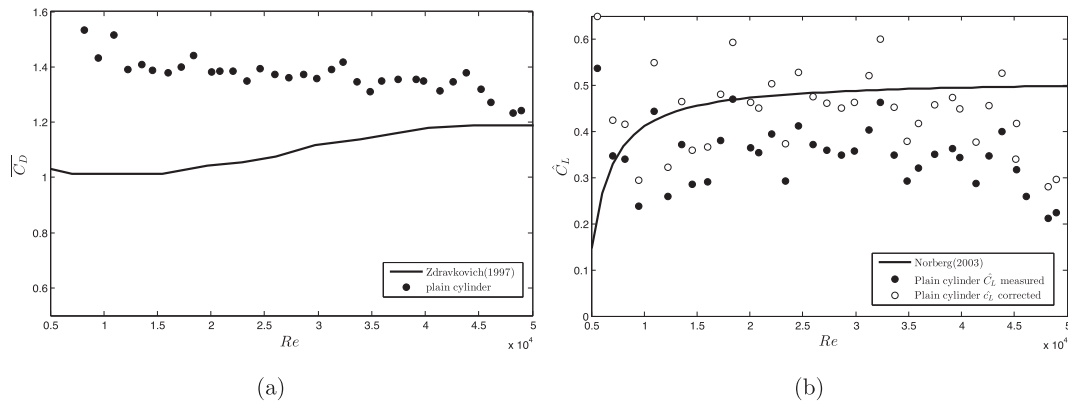


Fig. 3. (a) Mean drag coefficient and (b) RMS of lift coefficient versus  $Re$  for the bare cylinder. Results compared to Zdravkovich (1997) and Norberg (2003).

proposed an expression to convert three-dimensional lift ( $\hat{C}_L$ ) into sectional lift ( $\bar{C}_L$ ), taking into account  $Re$  and the aspect ratio of the body. Therefore, Fig. 3b also presents the corrected  $\hat{C}_L \approx 0.4$ , as proposed by Norberg (2003), which is in good agreement with the results collected in the literature.

Tests with  $N = 2, 4$  and  $8$  control cylinders with different diameters ( $d/D$ ), were performed for the same  $Re$  range of the bare cylinder. For each configuration,  $\bar{C}_D$  and  $\hat{C}_L$  were measured for 36 equally spaced values of  $Re$  as flow speed was increased. In order to evaluate the force coefficients, the cylinder diameter ( $D$ ), was employed as a standard dimension for all configurations. It is known that the effective external diameter of the system is slightly different depending on the distribution, diameter and gap of the control cylinders for each case. Silva-Ortega and Assi (2017) suggested the use of the combined parameter  $(G + d)/D$ , simply representing the “outermost radial distance of the control cylinders from the wall of the main cylinder, in a way suggesting how far into the flow the control cylinders could interfere.” In the present study,  $(G + d)/D$  varied between  $0.09$  and  $0.23$ . However, as far as hydrodynamic forces are concerned, the frontal area of the model did not change as  $G$  was increased for each  $d$ . Also, variations in  $d$  only slightly changed the frontal area. Therefore, we believe the main body's diameter ( $D$ ) is the most representative dimension to non-dimensionalize the hydrodynamic loads so that they could be compared against each other for each case.

Results are presented in three sets, grouped by the diameter of the control cylinders.

### 3.1. Control cylinders with $d/D = 0.04$

$\bar{C}_D$  for all cases with  $d/D = 0.04$  is shown in Fig. 4a. Apart from the lowest values of  $Re$ , the behavior of each case is quite clear. All cases with 2 control cylinders (2 cyl.) presented  $\bar{C}_D$  higher than that of the bare cylinder, with the case  $G/D = 0.15$  showing the highest  $\bar{C}_D \approx 1.8$ . The cases with 4 control cylinders (4 cyl.) presented the highest variations, with the great majority of points falling below  $\bar{C}_D$  for the bare cylinder. The case  $G/D = 0.05$ , in special, presented the lowest  $\bar{C}_D \approx 0.8$  of all cases for most of the  $Re$  range. All cases with 8 control cylinders (8 cyl.) presented values below  $\bar{C}_D$  for the bare cylinder; also showing the smaller dispersion within the group.

Fig. 4b shows  $\hat{C}_L$  for all cases with  $d/D = 0.04$ . Like before, all cases with 2 control cylinders tend to show  $\hat{C}_L$  higher than that of the bare cylinder. Cases with 4 control cylinders tend to show  $\hat{C}_L$  below the value for the bare cylinder. But more importantly, cases with 8 control cylinders showed the lowest values of  $\hat{C}_L$  for the  $Re$  range, with the cases  $G/D = 0.05$  and  $0.10$  presenting the RMS of lift very close to zero.

(Please note that the limits of the vertical axes in all figures were kept the same to allow for direct qualitative comparison between all figures in

the paper.)

### 3.2. Control cylinders with $d/D = 0.06$

Fig. 5a shows  $\bar{C}_D$  for all cases with  $d/D = 0.06$ . At first sight, one may realize that the larger diameter of the control cylinders has increased  $\bar{C}_D$  for all cases. For most cases this might be due to the increase of the effective diameter of the body. While all cases with 2 control cylinders produced the highest  $\bar{C}_D$ , all cases with 8 control cylinders now fall in the middle, but still with  $\bar{C}_D$  below that for the bare cylinder. With the lowest  $\bar{C}_D$ , now appears the group with 4 control cylinders, with the case  $G/D = 0.05$  showing the lowest  $\bar{C}_D \approx 0.75$  for most of the  $Re$  range.

Results of  $\hat{C}_L$  in Fig. 5b are not very different. All cases with 2 control cylinders produce the highest RMS of lift, above the value for the bare cylinder. On the other hand, all cases with 4 and 8 control cylinders managed to reduce  $\hat{C}_L$  below that of a bare cylinder for most of the  $Re$  range, highlighting cases 8 cyl. with  $G/D = 0.15$  and 4 cyl. with  $G/D = 0.05$  that produced almost zero  $\hat{C}_L$ .

### 3.3. Control cylinders with $d/D = 0.08$

Finally, Fig. 6a presents  $\bar{C}_D$  for cases with  $d/D = 0.08$ . With the largest control cylinders, almost all cases presented  $\bar{C}_D$  roughly equal or higher than that of the bare cylinder. The exception was the group with 4 control cylinders, which showed  $\bar{C}_D \approx 1$  for most of the  $Re$  range. This time, the cases with 4 control cylinders and  $G/D = 0.05$  and  $0.10$  presented the lowest  $\bar{C}_D$ .

The RMS of lift shown in Fig. 6b follows the same behavior seen before, with all cases with 2 control cylinders showing higher  $\hat{C}_L$  than that of the bare cylinder. Again, cases with 4 and 8 control cylinders reduced  $\hat{C}_L$  considerably, with cases  $N = 8$  with  $G/D = 0.10$  and  $N = 4$  with  $G/D = 0.05$  reaching almost zero  $\hat{C}_L$ .

## 4. Discussion

It is easy to get confused with so many response curves considering the variations in all three parameters:  $N$ ,  $d/D$  and  $G/D$ . The first general consideration to be made is that the position of the control cylinders in relation to the flow is indeed very important. The three parameters combined work to alter the influence of the control cylinders over the near wake, not to mention their influence over the flow before it separates from the body.

For example, for the case with  $N = 2$ , it is believed that the control cylinders are interfering with the flow near the separation points, since they are positioned at  $\pm 90^\circ$  in relation to the incoming flow. With 4 control cylinders, we can still suppose that the rear cylinders (located at

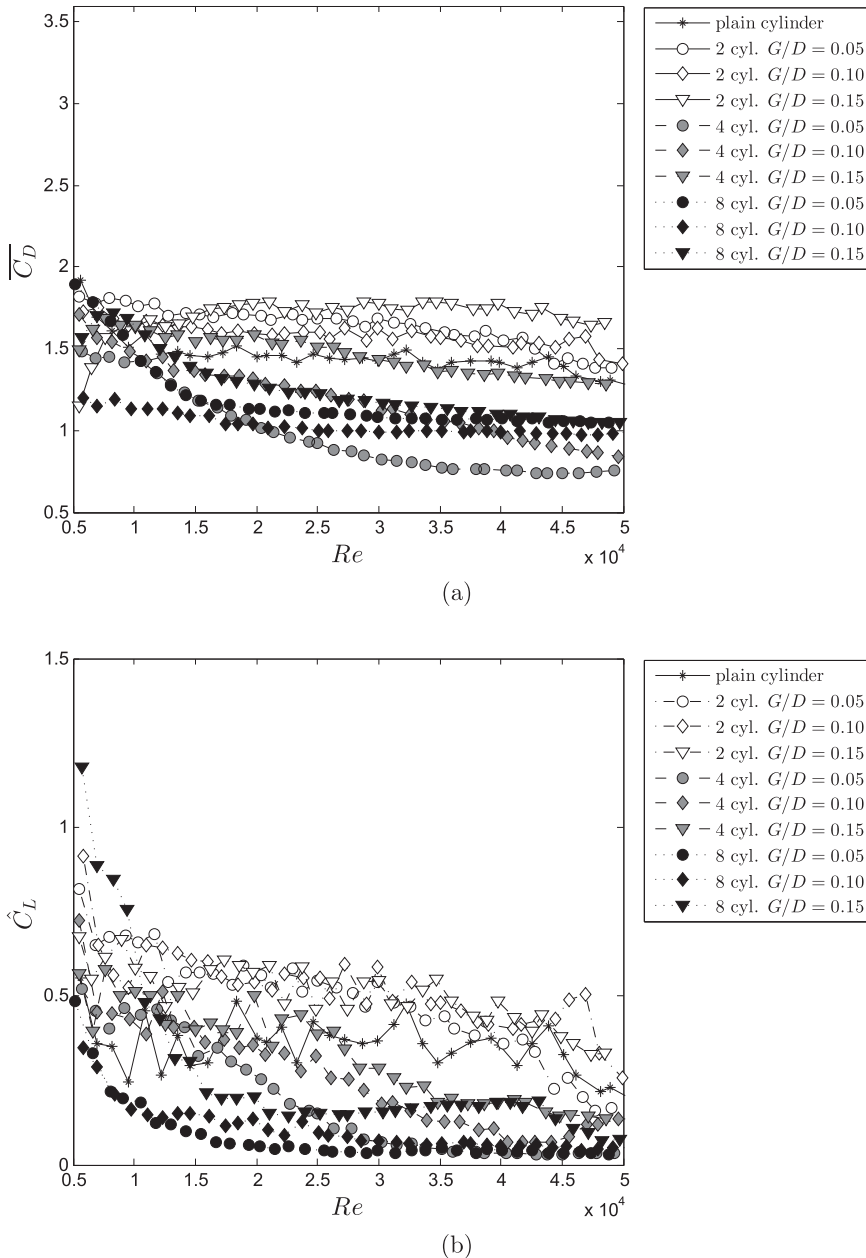


**Fig. 4.** (a) Mean drag coefficient and (b) RMS of lift versus  $Re$  for 2, 4 and 8 control cylinders with  $d/D = 0.04$  and varying gap.

$\pm 135^\circ$ ) interact with the separating flow and/or the separated shear layers in the near wake, but the front cylinders (located at  $\pm 45^\circ$ ) are most likely interacting with the attached boundary layers. The same must be happening with  $N = 8$ : while cylinders positioned at  $\pm 22.5^\circ$  and  $\pm 67.5^\circ$  are most likely interacting with the boundary layer, cylinders at  $\pm 112.5^\circ$  are located very near the natural separation points, while cylinders at  $\pm 157.5^\circ$  might be interacting with the near wake. This is supported by the flow visualization provided by the numerical simulations performed by Silva-Ortega et al. (2014a,b) at  $Re = 100$ .

The cases with 2 control cylinders have shown a behavior similar to that observed by Mittal (2001), who performed numerical simulation of the flow past a circular cylinder at  $Re = 10^4$ , with  $d/D = 0.05$  and  $G/D = 0.075$ . In their case, the numerical simulations allowed for a better understanding of the flow. In our study, among all experiments, the cases with  $N = 2$  consistently appeared as the worst arrangement to suppress  $\hat{C}_L$  and reduce  $\bar{C}_D$ . It actually increased drag above the value for a bare cylinder. On the other hand, the cases with 4 control cylinders with diameters  $d/D = 0.06$  and  $0.08$  presented a considerable reduction

of  $\hat{C}_L$  with the lowest  $\bar{C}_D$ .

Recently, motivated by the work of Strykowski and Sreenivasan (1990), Patino et al. (2015) performed flow sensibility analysis of the flow to study the effects of wake control with small cylinders located around the main cylinder with  $d/D = 0.06$  and  $G/D = 0.07$  at  $Re = 47$ . Changing the position of a single control cylinder around the main cylinder, they found that the wake became stable when the control cylinder was positioned at  $0^\circ$ – $50^\circ$ ,  $135^\circ$ – $225^\circ$  and  $310^\circ$ – $360^\circ$ , thus inhibiting the formation of vortices. Please note that their study suggested an effective control of the wake with control cylinder positioned at the front and at the back of the main body.

Of course the sensibility analysis conducted by Patino et al. (2015) was focusing at an extremely low  $Re$ , at the beginning of the hydrodynamic instability that leads to the formation of the vortex wake. Nevertheless, leaving the difference of  $Re$  aside, we cannot ignore the fact that, in our work, only the cases with  $N = 4$  and  $8$  have cylinders located within the regions highlighted by Patino et al. (2015). Those cases were precisely the ones to present the most reduction in  $\hat{C}_L$  and  $\bar{C}_D$ . It is worth



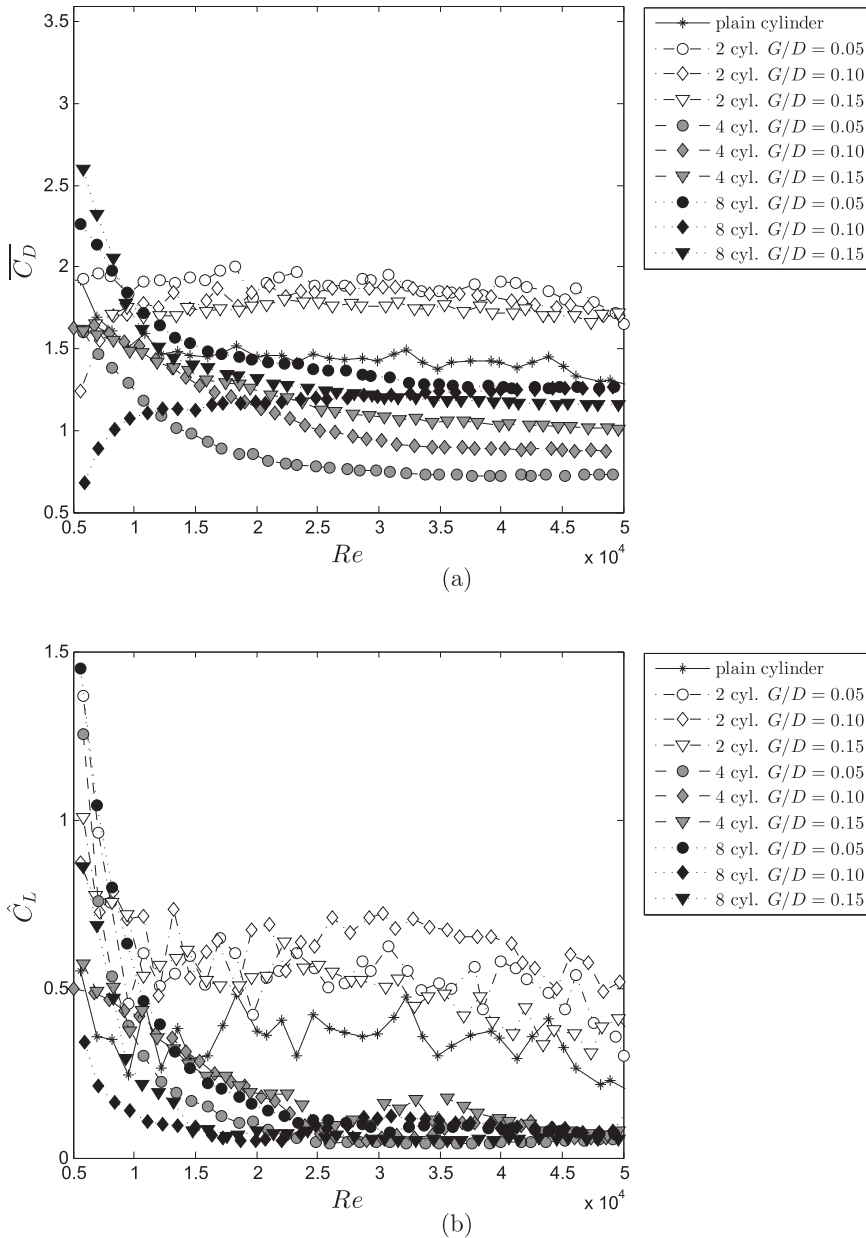


**Fig. 5.** (a) Mean drag coefficient and (b) RMS of lift versus  $Re$  for 2, 4 and 8 control cylinders with  $d/D = 0.06$  and varying gap.

noting that the case with 8 control cylinders is the closest to an omnidirectional system tested in this investigation, even though with discrete elements positioned  $45^\circ$  apart. Needless to say that an omnidirectional device would be very interesting for practical applications in engineering.

Finally, considering only the diameters of the control cylinders, cases with  $d/D = 0.06$  have shown a slight advantage in reducing  $\hat{C}_L$  and  $\bar{C}_D$  over the other cases. Interestingly,  $d/D = 0.06$  was not the smallest nor the largest of the tested diameters. Finally the  $G/D$  parameter showed the lowest influence on the results when compared to the effect of  $d/D$  and  $N$ . All this could tell us that there is an optimum value of  $d/D$  to suppress the wake and it would probably be dependent on  $Re$ , the distribution of control cylinders and weakly dependent on  $G/D$  (within the range of this investigation).

The current investigation does not provide information on the hydrodynamic interaction of the bodies, only presented the hydrodynamic loads experienced by the cylinder. Future studies should investigate the flow to look for the physical mechanisms in action. It is widely accepted that if the wake is controlled and the shedding of vortices is eliminated

the bluff body will not only generate considerably less drag but will also become invulnerable to vortex-induced vibrations.

## 5. Conclusion

We have presented the hydrodynamic loads of mean drag ( $\bar{C}_D$ ) and fluctuating lift ( $\hat{C}_L$ ) for a circular cylinder fitted with  $N = 2, 4$  and 8 control cylinders positioned around its circumference. The efficiency regarding the mitigation of  $\hat{C}_L$  and reduction of  $\bar{C}_D$  was investigated for 27 different cases varying the diameter of the control cylinders ( $d/D$ ) and their relative distance from the wall  $G/D$ . All cases have been compared with the hydrodynamic forces of a plain cylinder.

Cases with  $N = 4$  and 8 appeared to perform much better than the cases with 2 control cylinders. This might not be directly related to the total number of control cylinders ( $N$ ), but instead with the actual position of the cylinder around the main body. Having learnt from previous investigations (Strykowski and Sreenivasan, 1990; Patino et al., 2015), we believe the position of the control cylinders is crucial to the way they interfere with the flow to control the wake. For a future optimization

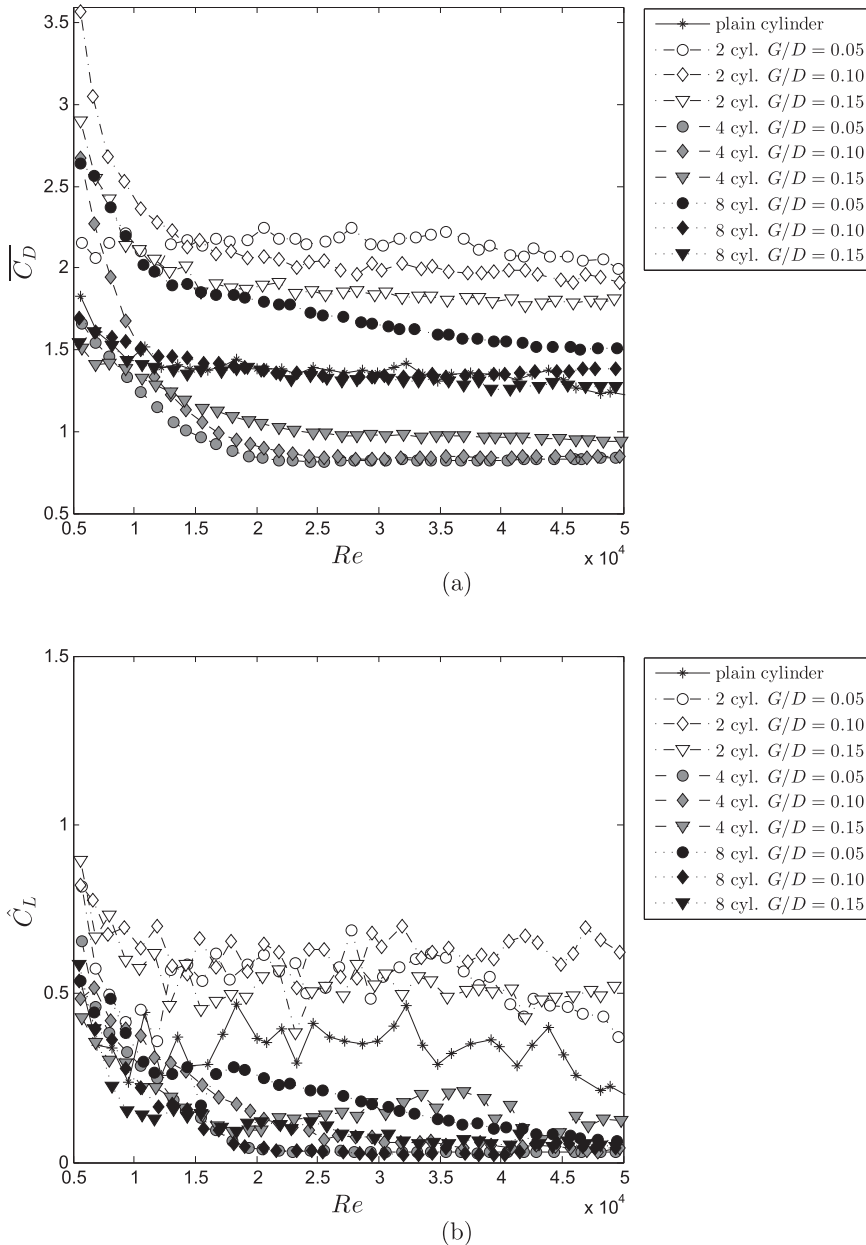


**Fig. 6.** (a) Mean drag coefficient and (b) RMS of lift versus  $Re$  for 2, 4 and 8 control cylinders with  $d/D = 0.08$  and varying gap.

study, the angular distribution of the control cylinders must be investigated with a much smaller step than the one we have employed in this work (especially when compared with the small variations performed in the  $d/D$  and  $G/D$  parameters).

The configuration with 4 control cylinders with  $G/D = 0.05$  and  $d/D = 0.06$  produced the lowest drag when compared to all other configurations:  $\bar{C}_D \approx 0.75$ , approximately 50% lower than that of a bare cylinder. For the configuration with 8 control cylinders with  $d/D = 0.04$ , all  $G/D$  ratios showed an average  $\bar{C}_D \approx 1$ , which corresponds to a 33% reduction. Only the configurations with 2 control cylinders showed a 10% increase in drag, with  $\bar{C}_D \approx 1.66$  on average.

There is no guarantee that a fixed cylinder with low  $\hat{C}_L$  will not oscillate due to VIV once it is free to respond, especially if a low mass-damping system is concerned. However, a suppressor that produces low  $\hat{C}_L$  in a fixed condition might produce a system with low VIV response, if not get VIV suppressed altogether. Not coincidentally, the

case with  $N = 8$ ,  $d/D = 0.08$  and  $G/D = 0.10$  that presented one of the lowest  $\hat{C}_L$  in the present work, was also the most successful in suppressing VIV in the work of [Silva-Ortega and Assi \(2017\)](#). Future work in this topic will also consider the rotation of the control cylinders, as we explore active-control methods.

Finally, the wave interaction between the control cylinders and the main cylinder produced rather interesting patterns that sometimes appeared to increase and other times to reduce the height of the waves being formed. The wave interaction between the various configurations of control cylinders and its effect on drag or VIV were not properly understood. Based on the principle that there might be an arrangement of control cylinders to suppress the formation of a vortex wake, it is possible that an arrangement of interacting control cylinder could be able to mitigate the formation of surface waves. This questions certainly appears as an interesting topic for future research.

## Acknowledgments

MSO is grateful to CAPES Brazilian Ministry of Education. GRSA acknowledges the support of FAPESP (2011/00205-6, 2014/50279-4), CNPq (306917/2015-7) and the Brazilian Navy.

## References

- Assi, G., Bearman, P., Kitney, N., Tognarelli, M., 2010a. Suppression of wake-induced vibration of tandem cylinders with free-to-rotate control plates. *J. Fluid Struct.* 26, 1045–1057.
- Assi, G.R.S., 2009. Mechanisms for flow-induced vibration of interfering bluff bodies. Phd thesis. Imperial College London.
- Assi, G.R.S., Bearman, P.W., Carmo, B.S., Meneghini, J.R., Sherwin, S.J., Willden, R.H.J., 2013. The role of wake stiffness on the wake-induced vibration of the downstream cylinder of a tandem pair, 3 *J. Fluid Mech.* 718, 210–245.
- Assi, G.R.S., Bearman, P.W., Meneghini, J.R., 2010b. On the wake-induced vibration of tandem circular cylinders: the vortex interaction excitation mechanism, 10 *J. Fluid Mech.* 661, 365–401.
- Bearman, P.W., Brankovic, M., 2004. Experimental studies of passive control of vortex-induced vibration. *Eur. J. Mech. B Fluid* 23, 9–15.
- Bell, W., 1983. Turbulence vs drag—some further considerations. *Ocean Eng.* 10 (1), 47–63.
- Chaplin, J., Teigen, P., 2003. Steady flow past a vertical surface-piercing circular cylinder. *J. Fluid Struct.* 18 (3), 271–285.
- Choi, H., Jeon, W.-P., Kim, J., 2008. Control of flow over a bluff body. *Annu. Rev. Fluid Mech.* 40, 113–139.
- Korkischko, I., Meneghini, J.R., 2010. Experimental investigation of flow-induced vibration on isolated and tandem circular cylinders fitted with strakes. *J. Fluid Struct.* 26 (4), 611–625.
- Korkischko, I., Meneghini, J.R., 2011. Volumetric reconstruction of the mean flow around circular cylinders fitted with strakes. *Exp. Fluid* 51, 1109–1122.
- Korkischko, I., Meneghini, J.R., 2012. Suppression of vortex-induced vibration using moving surface boundary-layer control. *J. Fluid Struct.* 34, 259–270.
- Kuo, C.-H., Chiou, L.-C., Chen, C.-C., 2007. Wake flow pattern modified by small control cylinders at low Reynolds number. *J. Fluid Struct.* 23, 938–956.
- Lee, S.-J., Lee, S.-I., Park, C.-W., 2004. Reducing the drag on a circular cylinder by upstream installation of a small control rod. *Fluid Dynam. Res.* 34 (4), 233–250.
- Mittal, S., 2001. Control of flow past bluff bodies using rotating control cylinders. *J. Fluid Struct.* 15 (2), 291–326.
- Norberg, C., 2003. Fluctuating lift on a circular cylinder: review and new measurements. *J. Fluid Struct.* 17, 57–96.
- Patino, G., Silva-Ortega, M., Gioria, R.S., Assi, G.R.S., Meneghini, J.R., 2015. Investigation of circular-cylinder VIV passive-control device using flow sensitivity analysis. In: *Bifurcations and Instabilities in Fluid Dynamics*. BIFD2015, France.
- Silva-Ortega, M., Assi, G., 2017. Flow-induced vibration of a circular cylinder surrounded by two, four and eight wake-control cylinders. *Exp. Therm. Fluid Sci.* 85, 354–362.
- Silva-Ortega, M., Orselli, R.M., Assi, G., 2014a. Control of rotating cylinders as suppressors of vortex-induced vibration of a bluff body. In: *Proceedings of SOBENA2014 the 25th Congress of the Brazilian Society of Naval Architects*. SOBENA.
- Silva-Ortega, M., Orselli, R.M., Assi, G., 2014b. Control of vortex shedding of a circular cylinder with two and four small rotating cylinders. In: *Proceedings of EPTT2014 the XI Spring School of Turbulence and Transition*. ABCM.
- Strykowski, P.J., Sreenivasan, K.R., 1990. On the formation and suppression of vortex shedding at low Reynolds numbers. *J. Fluid Mech.* 218, 71–107.
- Zdravkovich, M., 1981. Review and classification of various aerodynamic and hydrodynamic means for suppressing vortex shedding. *J. Wind Eng. Ind. Aerod.* 7, 145–189.
- Zdravkovich, M.M., 1997. *Flow Around Circular Cylinders: Fundamentals*, vol. 1. Oxford University Press, New York.
- Zdravkovich, M.M., Brand, V.P., Mathew, G., Weston, A., 1989. Flow past short circular cylinders with two free ends. *J. Fluid Mech.* 203, 557–575.



Contents lists available at ScienceDirect

## Journal of Fluids and Structures

journal homepage: [www.elsevier.com/locate/jfs](http://www.elsevier.com/locate/jfs)

## Vortex-induced vibration of a wavy elliptic cylinder

Gustavo R.S. Assi<sup>a,\*</sup>, Peter W. Bearman<sup>b</sup><sup>a</sup> Dept. of Naval Arch. & Ocean Eng., University of São Paulo, São Paulo, Brazil<sup>b</sup> Department of Aeronautics, Imperial College, London, UK

## ARTICLE INFO

## Article history:

Received 20 September 2017

Received in revised form 19 December 2017

Accepted 22 February 2018

Available online 8 March 2018

## Keywords:

Flow-induced vibration

Suppression

Drag reduction

Seal whiskers

## ABSTRACT

This paper shows that three-dimensional separation lines on a wavy cylinder may be correlated by the lateral movement of the body responding to flow-induced excitations. Vortex-induced vibration (VIV) of a wavy elliptic cylinder is investigated by mean of experiments in a water channel in the range of Reynold number between 1,500 to 15,000. Results are compared with those for a plain circular cylinder of equivalent diameter with a combined mass–damping parameter of 0.018. Curves of displacement and frequency of vibration showed that the hydroelastic mechanism that drives the wavy cylinder into VIV is not different from that of a plain cylinder. Detailed decomposition of the fluid forces supports this conclusion. The reason for such similar behaviour is the correlation of the sinuous separation lines as the wavy cylinder starts to oscillate. Flow visualization reveals that the three-dimensional surface of the wavy cylinder affects the formation of vortices in the near wake, generating streamwise and cross-flow vorticity associated with the wavelength of the surface. However, once the cylinder is free to respond to VIV, moving in the cross-flow direction, coherent vortex filaments once more dominate the near wake.

© 2018 Elsevier Ltd. All rights reserved.

## 1. Introduction

The suppression of vortex-induced vibration (VIV) of bluff bodies with low mass and damping poses a technological challenge faced by many engineering applications. The hydroelastic mechanisms behind the phenomena also generates interesting questions from a scientific point of view. Many different techniques have been proposed to mitigate VIV by controlling the formation of vortices in the near wake. Some methods interfered with the two-dimensional (2D) mechanism of vortex shedding (refer to Assi et al., 2009, 2010a, 2014; Silva and Assi, 2017, for examples), interrupting the communication of the separated shear layers as proposed by Gerrard (1966). Others promoted three-dimensional (3D) characteristics of the wake, either by breaking down the dominant vortical features in the near wake or by disrupting the coherent formation of vortices along the span (for example, Cicolin and Assi, 2017). Zdravkovich (1981) presented an interesting overview of many of these techniques, while Rashidi et al. (2016) present a brief review of a few more recent ideas.

The helical strake is the most common device employed by the offshore industry to suppress VIV of riser pipes. Normally, the geometry of the strakes presents three helical blades starting at 120° apart with a common pitch of 5 diameters and a blade height of 20% of the diameter, as seen in Fig. 1(a). As will become clearer, strakes with high blades are required for systems with low mass and damping, which is typical of light elastic structures immerse in water. Elastic structures that are heavy in relation to the displaced mass of fluid (for example, chimneys or bridge cables exposed to wind) are normally fitted

\* Correspondence to: NDF Research Group –Dept. Eng. Naval e Oceânica, Escola Politécnica da Universidade de São Paulo, Av. Prof Mello Moraes 2231, 05508-030, São Paulo - SP, Brazil.

E-mail address: [g.assi@usp.br](mailto:g.assi@usp.br) (G.R.S. Assi).

URL: <http://www.ndf.poli.usp.br> (G.R.S. Assi).

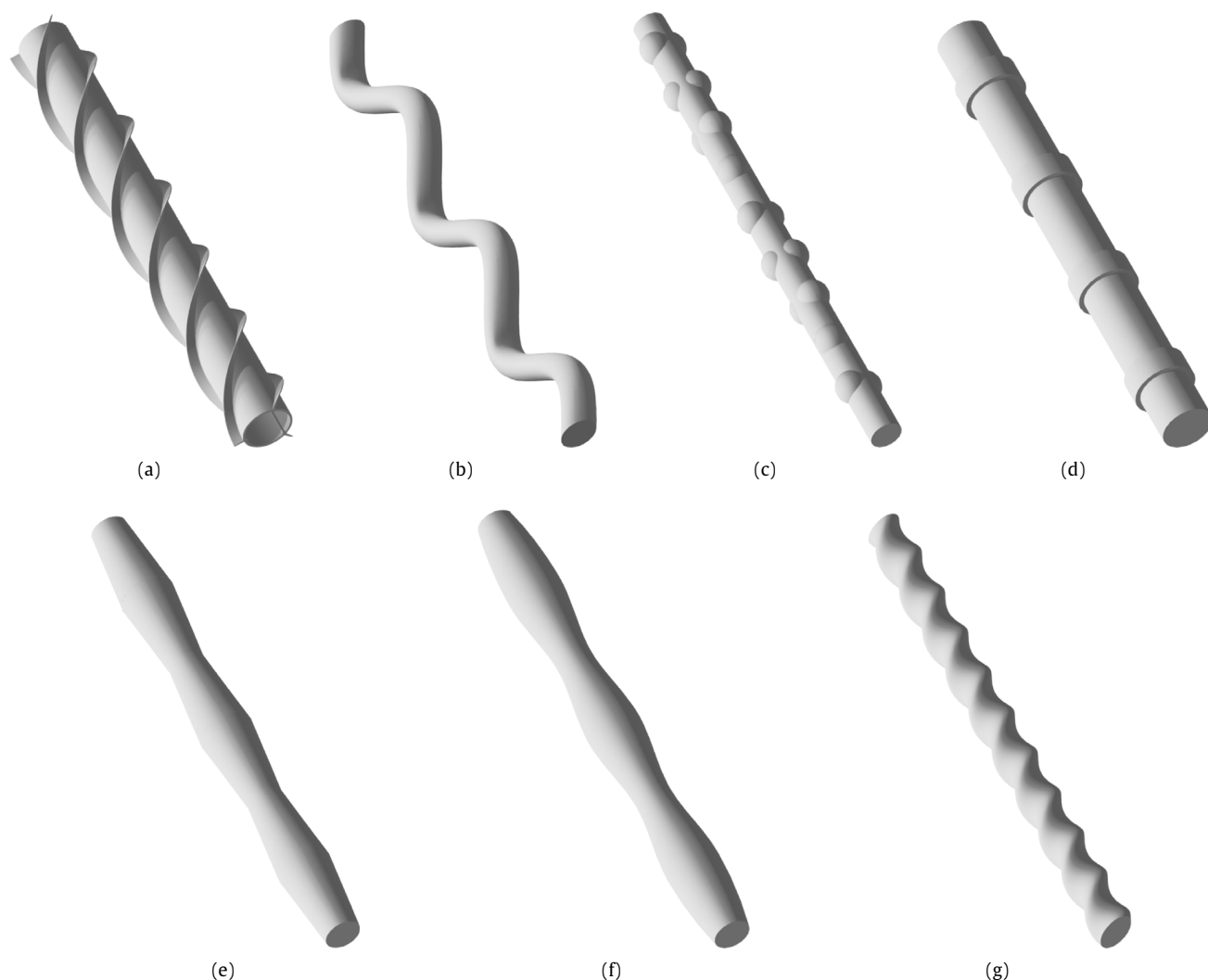


**Fig. 1.** Cylinders with three-dimensional surfaces: (a) straight cylinder with helical strakes, (b) sinuous cylinder, (c) cylinder with bumps, (d) cylinder with rings, (e) linear-wave cylinder, (f) sine-wave cylinder, (g) helical elliptic cylinder.

with smaller strakes. Helical strakes suffer from an intrinsic problem: while high blades are required to suppress VIV from light structures, they increase drag considerably.

Some researchers have investigated 3D devices other than helical strakes as a means to suppress VIV; we shall recall some of these works in the next section. However, it is worth highlighting now that even though some 3D geometries reduced drag by suppressing vortex shedding from fixed bodies, none has achieved the desired combination of VIV suppression with drag reduction, at least not for systems with low mass and damping.

In the present paper we present an experimental investigation of a 3D cylinder shaped as a *wavy elliptic cylinder* in an attempt to reduce VIV without incurring an unwanted drag penalty. This study will show that the wavy cylinder does not eliminate VIV but it reveals interesting information about the physical mechanisms occurring during the fluid–structure interaction of elastically-mounted 3D bluff bodies.

### 1.1. Suppression of vortex shedding of fixed cylinders

A relatively simple way to create a slender cylinder with a wavy geometry is by curving its axis in a sinuous path without changing the cross section, as shown in Fig. 1(b). Owen et al. (2000) and Ahmed (2010), for example, have investigated the flow past a sinuous cylinder of this type. Although this curved body does not have a straight axis, the behaviour of the flow separating from the sinuous geometry shows hints of what will happen for 3D bluff bodies with straight axes and varying cross sections.

Owen et al. (2000) performed visualization of the flow at  $Re = 100$  that revealed the intricate wake structures developing from sinusoidal separation lines. Three-dimensional vortex loops appeared correlated with the characteristic wavelength of the geometry. A large periodic variation in the wake structure along the span produced wide wakes at troughs and narrow



wakes at peaks, resulting in the disruption of a regular Kármán wake (Owen et al., 1999). A large reduction of 47% in the mean drag was observed compared to that of a 2D circular cylinder. The numerical simulations performed by Darekar and Sherwin (2001) on a square cross-section cylinder with a wavy axis, also at  $Re = 100$ , revealed that a rich 3D wake induced by the geometry of the body already exists at low Reynolds numbers. Even though their sinusoidal cylinder had a square cross section, they observed the formation of hairpin vortices similar to those found in the wake of a sphere at low  $Re$ .

The model investigated by Ahmed (2010) was slightly different and only presented a single curved section at mid length. The surface topology of the separated flow could be associated with the direction of the incoming flow in relation to a convex or concave configuration of the cylinder. Variations of node, saddle and mixed node–saddle flow attachments produced different 3D flow structures in the near wake. A symmetric shedding of vortices (that had also been observed by Owen et al., 2000) was observed with a saddle type of attachment by Ahmed (2010).

It should be noted that, unlike the geometries to be investigated in this paper, a sinuous cylinder does not present a straight axis. Consequently, the possibility of practical applications for pipes and cables is reduced because it cannot accommodate a straight circular cylinder passing along its centre. In order to allow for this, Owen et al. (2001) reproduced the external waviness on the surface by attaching hemispherical bumps along the span of a plain cylinder. In order to make it an omnidirectional device (one that does not depend on the direction of the incoming flow) they distributed the bumps in a helical pattern around the cylinder, as seen in Fig. 1(c). The model now presents a nearly elliptical cross section at the bumps, which follows a discontinuous helical pattern along the span. As a result, vortex shedding was disrupted by the 3D shape of the body and the mean drag was reduced to  $\bar{C}_x \approx 0.9$ , roughly a 25% reduction when compared to that of their plain cylinder at  $Re$  around 50,000.

While the smooth bumps emulated the waviness of the sinuous cylinder, others have fitted discrete elements to alter the diameter of the body. For example, Nakamura and Igarashi (2008) investigated modifications in the diameter by fitting “cylindrical rings along its span at an interval of several diameters”, thus creating the discrete 3D geometric disturbance seen in Fig. 1(d). Rather than observing nodal and saddle attachments associated with the curvature, they verified the formation of separation bubbles near the rings that also produced 3D perturbations in the near wake. The rings induced the formation of vortex loops, resulting in pressure recovery on the rear of the ring. Fluctuating lift acting on the body was reduced compared to a plain cylinder and a 15% reduction in the mean drag was recorded ( $Re$  varying from 3000 to 38,000).

Bumps and rings have in common a fundamental wavelength associated with their axial distribution along the span. Both Owen et al. (2001) and Nakamura and Igarashi (2008) were able to vary the pitch of their bumps and rings in order to show that there exist optimal configurations to enhance 3D wake disruption and minimize drag.

In an attempt to generate a continuous surface, the discrete rings may be replaced by a linear wave, i.e. creating increasing and decreasing conical slopes along the span with a characteristic wave length (or pitch), as seen in Fig. 1(e). A geometry of this type, with a pitch of about 2 diameters, has been investigated by Zhang et al. (2016) by means of numerical simulations of the flow at  $Re = 5000$ . They found that the “elongated vortex recirculation length led to a larger value of base pressure”, which produced a consequent drag reduction of 7% when compared to that of a plain cylinder. In the same study, Zhang et al. (2016) experimented with another 3D shape modification by smoothing out the sloped cylinder into a continuous sinusoidal surface with variable circular cross section, as seen in Fig. 1(f). A further reduction in drag was achieved, with  $\bar{C}_x$  reduced by 11% when compared to that of a plain cylinder. (Out of curiosity, Zhang et al. (2016) also investigated a variation of the cylinder with rings, but its performance regarding drag reduction was worse than the others.)

## 1.2. Wavy cylinders

The experiments of Lee and Nguyen (2007) investigated a wavy cylinder with varying circular cross sections with different wavelengths (as seen in Fig. 1(f)) in the range of  $Re = 10^4$ . They also observed that the width of the wake expanded downstream of saddle points and shrunk downstream of node points. Flow visualization revealed strong three-dimensional flow structures related to the geometry of the body. Overall, the vortex formation region was elongated and the vortex-induced fluctuations were suppressed, reducing drag acting on the cylinder by 22% compared with that of a plain cylinder. Zhang et al. (2005) performed PIV measurements of the wake of a similar body at  $Re = 3000$  and noted that such strong three-dimensional flow structures dominate the wake as far as 5 diameters downstream, with a maximum effect at around 3 diameters downstream of the body. They concluded that organized streamwise vortices with alternating positive and negative vorticity were observed along the span of the wavy cylinder. “They suppress the formation of the large-scale spanwise vortices and decrease the overall turbulent kinetic energy in the near-wake” (Zhang et al., 2005).

New et al. (2013) performed a very detailed study mapping the near wake of wavy cylinders with circular cross section with time-resolved PIV at  $Re = 2700$ . Varying the wave height and length, they concluded that the presence of streamwise vortices associated with saddles and nodes make the near wake less susceptible to other external interferences in the flow, such as aspect ratio and end conditions. They also observed three-dimensional flow structures being more prominent at 3 diameters downstream of the body.

The numerical simulations performed by Lam and Lin (2009) at  $Re = 100$  showed that there might exist optimal values of wave length and height to control the 3D wake and the related drag reduction. For their range of  $Re$  the largest drag reductions were achieved for wavelengths between 2.5 and 6 diameters. They noted that the variation of the 3D separation lines along the span resulted in the “development of a three-dimensional free shear layer with periodic repetition along the spanwise direction. The three-dimensional free shear layer of the wavy cylinder is longer and more stable than that of

the circular cylinder, and in some cases the free shear layer even does not roll up into a mature vortex street behind the cylinder". As a consequence, drag and lift are significantly reduced.

Experiments conducted by Lam et al. (2004b) at  $Re = 3000$  to  $9000$  characterized the dominant features of the near wake of a wavy cylinder. They also concluded that the average vortex formation length of a wavy cylinder is longer than that of a plain cylinder at the same  $Re$ . "For the wavy cylinder, the wake on the saddle plane has a longer vortex formation region and a more rapid reverse flow, as well as being wider than that on the nodal plane. It was deduced that the free shear layers shed from the points near the saddles extend along the spanwise direction, while the shear layers near the nodes contract". As a result, the wake of a wavy cylinder shows more incoherent structures due to enhanced turbulent mixing. Their measurements were confirmed by visualization of these flow structures at  $Re = 600$ .

Ahmed and Bays-Muchmore (1992) performed experiments in a wind tunnel and in a water channel ( $Re = 20,000$ ) to measure the pressure coefficients around wavy cylinders with various wavelengths (as seen in Fig. 1(f)). "Integration of the pressure data revealed greater sectional drag coefficients at the geometric nodes than at the geometric saddles". They also related the formation of streamwise vortices near the nodes with the sinuous three-dimensional separation lines along the wavy cylinder.

In the wind tunnel experiments performed by Lam et al. (2004a), pressure measurements of mean and fluctuating loads were made for three wavy cylinders at  $Re$  around  $10^4$ . A maximum 20% drag reduction was observed for the wavy cylinder when compared with that of a plain cylinder. Fluctuating lift was also considerably reduced, indicating that such a geometry could possibly result in VIV suppression. The most interesting result, however, came from measurements of the vortex shedding frequency at various positions along the wavy cylinder. The authors verified that the Strouhal numbers near saddles and nodes are essentially the same. In fact, Strouhal number was found to be approximately 0.2, the same value measured for a plain cylinder.

So far, all the above works dealing with the formation of the wake of a wavy cylinder agreed that the 3D wavy surface of the body significantly modifies the near-wake structure. The vortex-formation length is extended increasing base pressure (thus reducing drag) and the formation of streamwise vortices (with varying intensities) near the nodes is always observed. Similar wake structures are found not only for wavy cylinders with a circular cross section, but also for elongated bodies with wavy trailing edges, as exemplified by Cai et al. (2008) and others.

A very interesting 3D geometry was investigated by Kim et al. (2016), which they called a "helically twisted elliptic cylinder" (seen in Fig. 1(g)), by means of numerical simulations of the flow below  $Re = 3900$ . The lowest recorded drag, 23% lower than that of a plain cylinder, was obtained for a twisted cylinder with a wavelength of 3.5 diameters. The authors stated that "the lift fluctuation was zero due to a complete suppression of vortex shedding in the wake".

Jung and Yoon (2014) also investigated the flow about a helical cylinder with an elliptic cross section employing numerical simulations at  $Re = 3000$ . They also found considerable reduction in drag by 13% of that of a plain cylinder, with an almost complete elimination of fluctuating lift. This performance was 5% better than that of a similar wavy cylinder with circular cross section (Fig. 1(f)). They verified that the shear layers of the twisted cylinder are more elongated than those of the plain and wavy cylinders, "and vortex shedding from the twisted cylinder is considerably suppressed". As expected to occur for a plain cylinder, they noted that the vortex-formation length of the twisted elliptic cylinders was also reduced with increases in  $Re$ .

All previous works mentioned so far have dealt with fixed bluff bodies, i.e. cylinders that were not free to respond to the flow excitation nor forced into oscillatory motion by an external source. The effective reduction of the mean drag of a fixed cylinder with 3D surface is indeed very useful for practical applications in engineering. However, the fact that fluctuating lift was reduced in most cases (sometimes even claimed to have been completely eliminated) does not guarantee that the cylinder will not respond to vortex-induced vibrations. A few researchers attempted to apply cylinders with smooth three-dimensional surfaces to suppress VIV. We shall turn to their work next.

### 1.3. Vortex-induced vibration

A good device to mitigate fluctuating lift of a fixed cylinder is not necessarily a good device to suppress VIV of a cylinder that is free to respond to the flow. It is well known that the complex fluid–structure interaction happening with an oscillating bluff body may produce a completely different wake when compared to that of a fixed condition (Bearman, 1984). Consequently, the fluid loads exciting a free-to-respond body might also be very different. As it happens for a plain cylinder, the three-dimensional modes occurring in the wake of a fixed circular cylinder described by Williamson (1996) are drastically altered once the cylinder is oscillating, as shown in the works of Blackburn (1998), Hover et al. (2004) and Gioria et al. (2007).

Kleissl and Georgakis (2011), for example, experimented with cylinders with several 3D surfaces as a means to reduce flow-induced vibrations of cables employed in suspension bridges. They found that a wavy-cylinder cover did not increase the mean drag on a cable, but the wavy cylinder could be susceptible to fluidelastic instabilities when Reynolds number approached the critical value associated with the "drag crisis".

Owen et al. (2001) and Bearman and Brankovic (2004) performed VIV experiments fitting a circular cylinder with the bumps presented in Fig. 1(c). They measured the dynamic response of an elastically mounted cylinder with one degree of freedom in the cross-flow direction. Owen et al. (2001) experimented with bumps of various sizes and spacings on a cylinder with a variable mass–damping parameter ( $m^*\zeta$  will be properly defined later). For  $Re = 1650$  to  $7500$  and  $m^*\zeta = 0.036$ ,

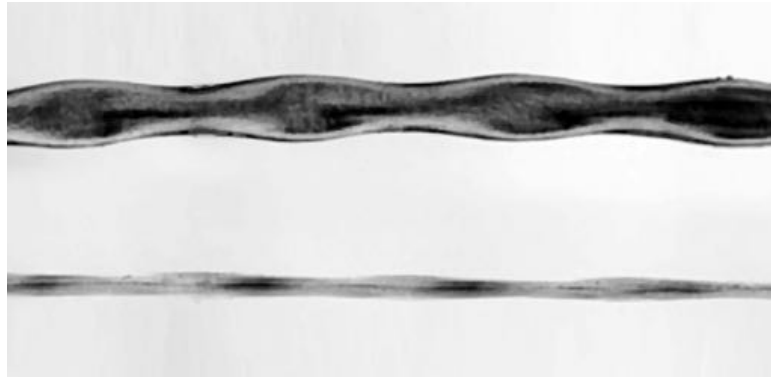


**Fig. 2.** Lateral and frontal views of a section of a harbour seal whisker showing its 3D-wavy surface.  
Source: Adapted from Hanke et al. (2010).

they observed a peak amplitude of displacement at the VIV resonance of approximately 0.62 diameters, equivalent to a 25% reduction from the peak response of a plain cylinder. Now, once the mass–damping parameter was increased the peak amplitude of response was significantly reduced. All of their bumps achieved a complete suppression of VIV for  $m^*\zeta > 1.5$ . At this level of mass and damping a plain cylinder would still be expected to vibrate with displacements of about 0.1 diameters. Their sinuous cylinder also achieved similar results, being able to suppress VIV for  $m^*\zeta > 1.0$ . Owen et al. (2001) concluded that “when the body is flexibly mounted it is able to detect a very weak force fluctuation” at the resonant frequency; the excitation increases as the response increases.

In the experiments of Bearman and Brankovic (2004) the VIV response of a cylinder fitted with bumps was compared to that of a cylinder fitted with helical strakes (height of 12% of the diameter and pitch of 5 diameters). Reynolds number was up to  $10^4$  and the combined mass–damping parameter was around  $m^*\zeta = 0.006$ . While the plain cylinder reached a peak response of 0.9 diameters, the cylinder with bumps reduced the peak vibration by 28% and the straked cylinder by 44%. The height and pitch of the bumps and strakes were comparable, suggesting that the sharp-edged surface of the strakes is indeed required to improve the degree of suppression of VIV.

Very recently, Zhang et al. (2017) performed numerical simulations at  $Re = 5000$  of the VIV of a wavy cylinder with circular cross sections (a geometry similar to that of Fig. 1(f)). They concluded that their wavy cylinder presented an “impressive flow control efficacy in the static configuration”, with Kármán vortices being “almost eliminated by the span-wise waviness” of the body. However, once the “the wavy cylinder was allowed to move in the transverse direction, the typical ‘lock-in’ phenomenon still occurred”.

#### 1.4. Wavy elliptic cylinders in nature

Recently, Beem and Triantafyllou (2015) published an interesting paper on an experimental investigation of the flow-induced vibration of harbour seal whiskers. The seal whisker has a 3D shape that resembles a flattened wavy cylinder. The greater axes of the cross-sectional ellipses are all on the same plane, thus producing a more streamlined geometry to the cross flow approaching from one direction rather than the other orthogonal direction. Hanke et al. (2010), who inspired the geometry employed by Beem and Triantafyllou (2015), presented a clear view of the three-dimensional geometry of the whisker, reproduced here in Fig. 2. Details on the morphology of seal whiskers, data on their mechanical properties and information on animal behaviour are presented by Ginter et al. (2010), Rinehart et al. (2017) and Hans et al. (2014), among others referred by them.

The natural whisker presents an interesting feature: the undulation of the leading edge (regarding the streamlined direction of the flow) is slightly out of phase with the undulation of the trailing edge. This combination of three-dimensional features produces a bluff body with many of the features discussed above: (i) a curved axis, (ii) waviness in two orthogonal directions (cross-flow), (iii) varying elliptical cross-sections and (iv) smooth surface. Hanke et al. (2010) concluded by experimental and numerical studies of the flow that the seal whiskers “possess a specialized undulated surface structure... that effectively changes the vortex street behind the whiskers and reduces the vibrations that would otherwise be induced by the shedding of vortices”. They also added that “the dynamic forces on harbour seal whiskers are, by at least an order of magnitude, lower than those on sea lion whiskers, which do not share the undulated structure”.

Beem and Triantafyllou (2015) explained how the geometry of the whisker is relevant to capture minute fluctuations in the wake present in the upcoming flow, helping the seal to navigate while tracking down its prey. They highlighted that the 3D geometry of the whisker is essential to enhance its ability to sense small pressure fluctuations in the water by allowing it to be induced into wake-induced vibrations (Assi et al., 2010b, 2013) without too much of a drag penalty. In other words, they showed how the whisker “could *slalom* among the vortices of the oncoming wake”, making it an efficient sensor. When pure VIV was considered with the flow approaching the streamlined direction of the whisker a minimal response was measured, with a maximum amplitude of displacement of only 0.15 diameters in the cross-flow direction.

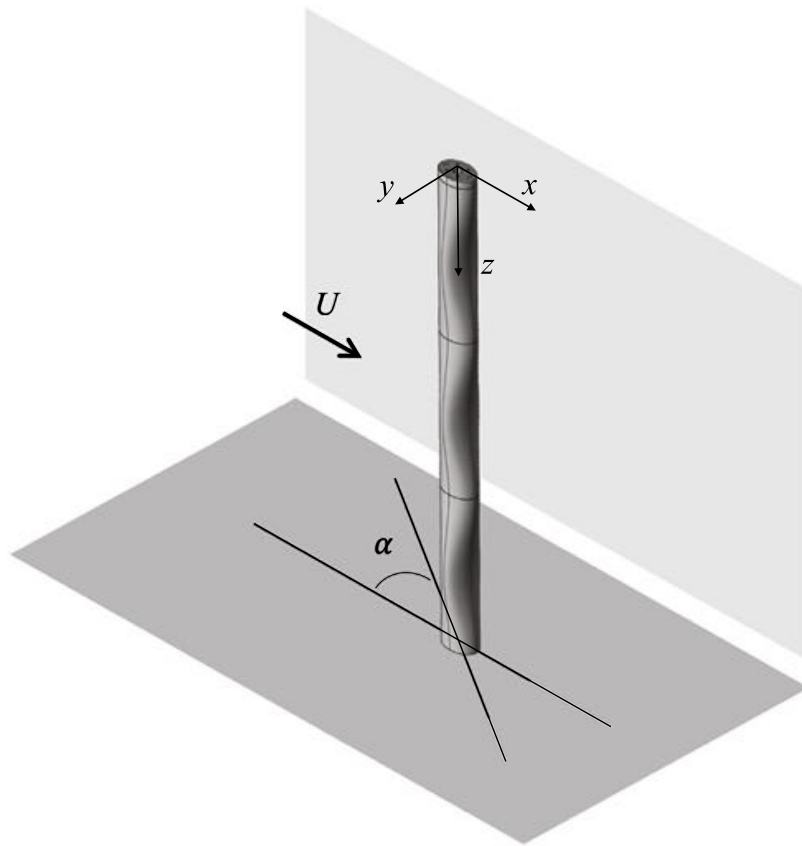


**Fig. 3.** Wavy elliptic cylinder. The angle of attack  $\alpha$  represents a positive rotation around the  $z$  axis.

### 1.5. Objective

In the present study we investigate the flow structure of the near wake and the cross-flow response to vortex-induced vibration of an elliptic wavy cylinder with low mass and damping. The present geometry, illustrated in Fig. 3, shows an elliptical cross section with sinusoidal waviness in both  $x$  and  $y$  directions. In essence, the geometry is of the same nature as the wavy cylinder with varying circular cross sections discussed above (Fig. 1(f)). Nevertheless, the elliptical cross-section produces a geometry with more intense three-dimensional effects along the span.

The current investigation has been developed in the context of finding novel suppressors for the vortex-induced vibration of slender bluff bodies with low mass and damping. Because a successful result of VIV suppression was not achieved (as will be seen in the discussion that follows), we left the data aside with no immediate interest in making it public. However, when the study by Beem and Triantafyllou (2015) on the flow-induced vibration of seal whiskers was published we were surprised by the remarkable similarity between the surface geometries of the seal whisker and that of the elliptical wavy cylinder we had tested years before. We then realized that the results that had been forgotten for a few years could have been useful as a reference for the VIV response for Beem and Triantafyllou (2015), thus we brought it to light motivated by the topic of bioinspired fluid mechanics.

## 2. Method

Experiments were performed in the Department of Aeronautics at Imperial College London, UK. Tests were carried out in a free-surface water channel with a test section 0.6 m wide, 0.7 m deep and 8.0 m long. The side walls and bottom of the section were made of glass, allowing a complete view of the models for flow visualization. Flow speed  $U$  approaching in the  $x$  direction was continuously variable up to 0.6 m/s. The maximum free-stream turbulence intensity mapped across the section was around 3% for the range of Reynolds number of the experiments. A cross-sectional diagram of the test section showing the experimental apparatus is shown in Fig. 4.

An elliptic wavy cylinder was 3D-printed in ABS plastic; the external surface was smoothed and painted black to improve contrast during flow visualizations. Fig. 5 presents the geometrical details of the model. The nominal diameter of the cylinder was  $D = 50$  mm, defined as the average of the larger (60 mm) and the smaller (40 mm) diameters of the reference ellipse, hence the sinusoidal wave height was 10 mm, or 20% of the nominal diameter. The wavelength (also called pitch) was  $P = 5D$  and the maximum elliptical ratio of 1.5 occurred at the saddle plane (elongated in the  $x$  direction) and at the node plane

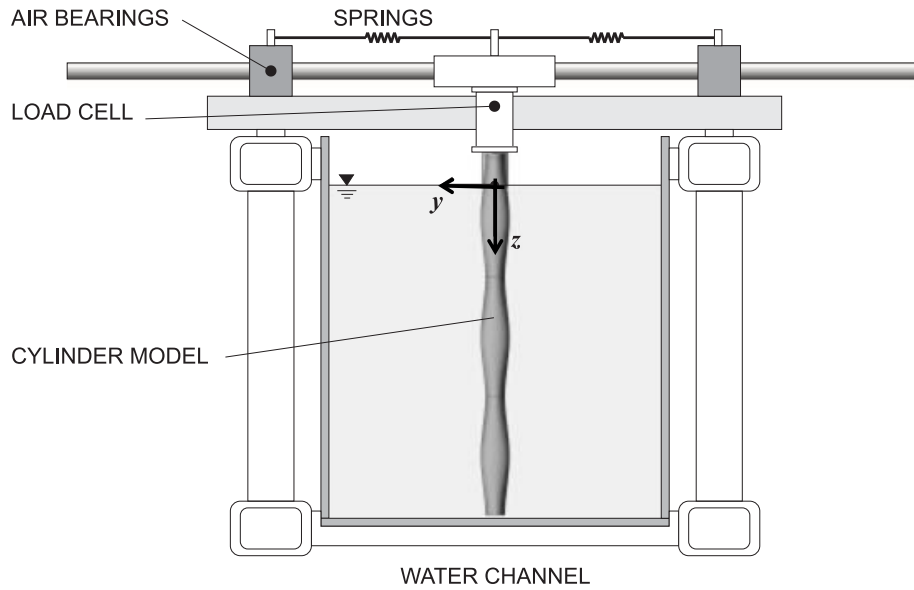
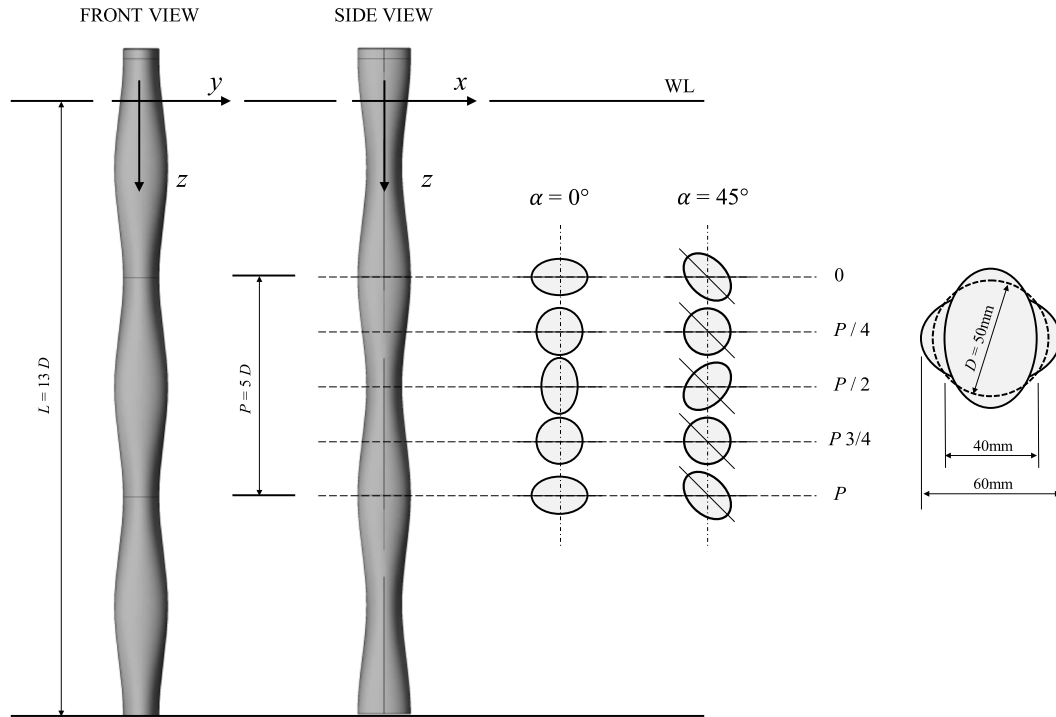


Fig. 4. Cross view of the test section.

Fig. 5. Dimensions of the wavy cylinder. Flow is in the  $x$  direction. WL means water line.

(elongated in the  $y$  direction), marked by the dashed lines at station 0 and  $P/2$  in Fig. 5. The three-dimensional sinusoidal variation between the ellipses resulted in circular cross sections in between the saddles and the nodes at  $1/4$  and  $3/4$  of one pitch. The submerged length of the cylinder was  $L = 13D$  and the geometric blockage ratio was 8.3%.

The rigid cylinder was connected to a load cell measuring the total instantaneous lift and drag acting on the body. The load cell was attached under an elastic rig supported by two long carbon-fibre tubes sliding through air bearings. The system was free to respond to the flow excitation in the cross-flow ( $y$ ) direction only; displacements were measured by an optical sensor. The mass ratio, calculated as the ratio between the total structural mass to the mass of displaced fluid, was  $m^* = 2.6$ . A pair of coil springs provided the stiffness of the system. The natural frequency of oscillation ( $f_0$ ) as well as structural damping were determined during decay tests performed in air, hence not taking into account hydrodynamic effects. The structural damping ratio was kept to a minimum value of  $\zeta = 0.7\%$ , calculated as a percentage of the critical damping during decay tests performed in air. The resultant combined mass-damping parameter was  $m^*\zeta = 0.018$ .



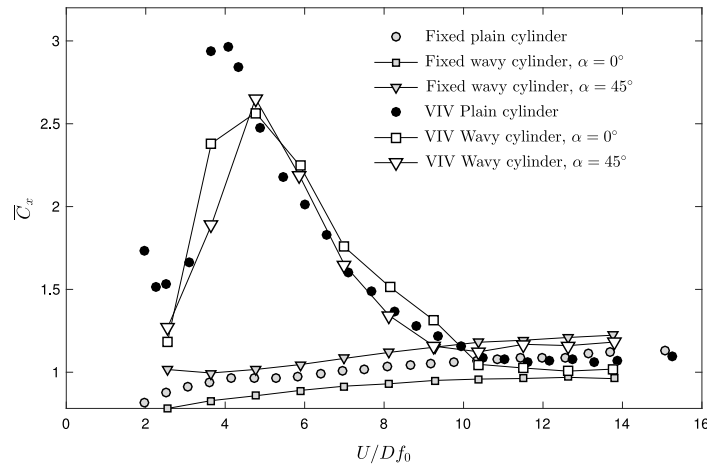


Fig. 6. Mean drag measured for fixed and oscillating cylinders.

The only flow variable changed during the course of the experiments was the flow velocity  $U$ , which altered both the Reynolds number between  $1.5 \times 10^3$  and  $1.5 \times 10^4$  ( $Re = UD/\nu$ , where  $\nu$  is the kinematic viscosity of water and  $D$  is the nominal diameter) and the reduced velocity ( $U/Df_0$ ) in the range of 2 to 16. The dynamic response to VIV was analysed across the reduced velocity range by comparing the normalized amplitude of displacement ( $\hat{y}/D$ , where  $\hat{y}$  is the RMS of  $y$  times  $\sqrt{2}$ ) and the dominant frequency of oscillation normalized by the natural frequency ( $f/f_0$ ). Fluid forces and other parameters derived from them have been calculated from the measurements obtained with the load cell. A plain circular cylinder with the same  $D$ , mass and damping parameters has also been tested to provide a reference response for VIV.

Since the elliptic wavy cylinder is not axisymmetric, experiments with two orientations regarding the incoming flow have been performed, as illustrated in Figs. 3 and 5. First the larger axis of the ellipse at the saddle plane was aligned with the direction of the flow, defining an angle of attack of  $\alpha = 0^\circ$  in relation to  $U$ . A second configuration was obtained by rotating the cylinder by  $45^\circ$  around the  $z$  axis, resulting in  $\alpha = 45^\circ$ . Results for both configurations are compared with those for a plain cylinder in the next section.

### 2.1. Flow visualization

In the present experiment, visualization of the flow by means of fluorescent dye has been performed by painting the front of the model with a solution of rhodamine, alcohol and corn syrup. Dissolved dye convected by the flow was illuminated with ultra-violet light and laser sheets. This technique allowed for a clear visualization of the separation lines along the surface of the body, but the dye tracers quickly diffused as soon as they reached the more turbulent regions of the wake.

In order to highlight the flow features in the near wake, flow visualization was also performed by means of hydrogen bubbles emitted by the electrolysis of water from two thin wires stretched parallel to the vertical axis of the cylinder. The wires were placed at about one diameter upstream of the body and slightly off the centreline of the wake. When the cylinders were oscillating, the lateral position of the wires was adjusted more to the side, so that a curtain of bubbles would reach the body during vibration. This technique allowed for visualization of the three-dimensional vortex structures present in the wake for about a distance of 7 cylinder diameters downstream.

Both techniques were performed at a Reynolds number of 3000 for  $\alpha = 0^\circ$  and  $45^\circ$ , in which the wake is already fully three-dimensional (also near the peak response of VIV). While a good understanding of the flow features was obtained by observing the flow in the water channel, recorded images and movies were not of sufficient graphical quality to be reproduced in this paper. Therefore, the dominant flow features in the near wake are illustrated by means of the sketches and diagrams originated from careful observation by the naked eye while the experiments were running.

## 3. Results and discussion

The first series of experiments was performed with fixed cylinders by restricting the movement of the elastic rig. The total drag coefficient, obtained by non-dimensionalizing the total drag force by  $\frac{1}{2}\rho U^2 DL$ , employed the nominal diameter  $D$ . The mean part of the total drag coefficient ( $\bar{C}_x$ ) is presented in Fig. 6. The mean drag for the reference plain cylinder varied around  $\bar{C}_x = 1.04$  for the  $Re$  range of the experiment, with a maximum value of  $\bar{C}_x = 1.21$  and a minimum of 0.81, which are in agreement with other works in the literature (Zdravkovich, 1997, for example). Other effects, due to free stream turbulence intensity (Bell, 1983) or cylinder aspect ratio (Zdravkovich et al., 1989), for example, may contribute to change the mean drag from the canonical value expected for a two-dimensional body. Nevertheless, since all models have been measured under the same condition, this value of  $\bar{C}_x$  for a plain cylinder will be taken as a reference for comparison.

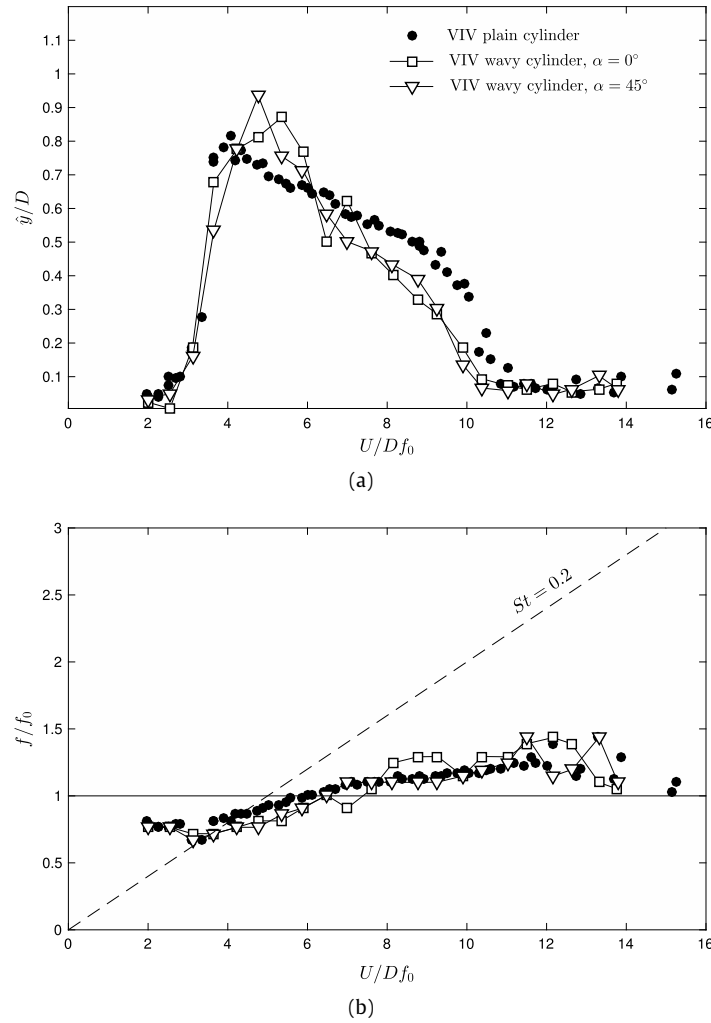


**Fig. 7.** (a) Amplitude of displacement and (b) dominant frequency of vibration versus reduced velocity.

The wavy cylinder at  $\alpha = 0^\circ$  presented a lower mean drag for the same conditions, with a consistent reduction by 12.5% throughout the  $Re$  range when compared with the  $\bar{C}_x$  of the plain cylinder. The wavy cylinder at  $\alpha = 45^\circ$ , on the other hand, presented an increase of  $\bar{C}_x$  of about 7% when compared with that of the plain cylinder. In relation to the  $\alpha = 0^\circ$  configuration,  $\bar{C}_x$  for  $\alpha = 45^\circ$  was increased by an average of 22%.

One should bear in mind that  $C_x$  was calculated using the nominal diameter  $D$  of the body. While both the plain cylinder and the wavy cylinder at  $\alpha = 0^\circ$  have the same frontal area, the wavy cylinder at  $\alpha = 45^\circ$  presents a projected frontal area increased by around 1%. If the increase in the effective diameter is taken into account in calculating  $C_x$ , the mean drag of the wavy cylinder at  $\alpha = 45^\circ$  would still be roughly at the same level. Therefore, the significant drag reduction experienced by the wavy cylinder at  $\alpha = 0^\circ$  is indeed of a hydrodynamic nature, and not simply due to an area change. As far as the flow is concerned, the three-dimensional effects of the surface affecting the near wake are not as pronounced at  $\alpha = 45^\circ$  as they were at  $\alpha = 0^\circ$ . In other words, the elliptic wavy cylinder at  $\alpha = 45^\circ$  “appears less three-dimensional” to the flow. For the sake of comparison, we shall keep all hydrodynamic coefficients in the present work non-dimensionalized by the nominal diameter  $D$ .

Bearman and Owen (1998) and others cited above attributed the drag reduction to the increase of base pressure created by the 3D shape of the separation lines. Flow visualization supporting this idea will be discussed later in this paper.

### 3.1. Response to vortex-induced vibration

The response to VIV has been determined by increasing the flow speed ( $U$ ) and keeping all other parameters constant. Fig. 7(a) presents the harmonic amplitude of displacement for the whole range of reduced velocities tested. The typical response of a plain cylinder was characterized by a build-up of vibration during the synchronization range between  $U/Df_0 \approx 3$  and 11. A maximum response of  $\hat{y}/D = 0.82$  has been observed at the peak of resonance in the upper branch. The dominant frequency of oscillation, presented in Fig. 7(b), shows the departure of the frequency curve from the  $St = 0.2$  line

towards  $f/f_0 = 1$  during the synchronization range, also called the lock-in range. These results are in good agreement with many other results presented in the literature regarding the cross-flow VIV of rigid cylinders with low mass and damping (Bearman, 1984; Williamson and Govardhan, 2004, for example). When comparing the current results with others in the literature, please bear in mind that the synchronization range might be shifted to lower reduced velocities because  $f_0$  was measured in air and not in still water.

Fig. 7 also presents the VIV response for the two configurations of the wavy cylinder. There is no significant difference between the responses of the wavy cylinder at  $\alpha = 0^\circ$  and  $45^\circ$  in Fig. 7(a). The width of the synchronization range for the wavy cylinders is just slightly reduced when compared with that of the plain cylinder and the peaks of response at resonance reach  $\hat{y}/D = 0.87$  and  $0.93$  for  $\alpha = 0^\circ$  and  $45^\circ$ , respectively. The frequency signatures seen in Fig. 7(b) are also very similar to that of the plain cylinder.

Even though the wavy cylinder at  $\alpha = 0^\circ$  presented a considerably lower mean drag than the wavy cylinder at  $\alpha = 45^\circ$ , their responses to VIV are practically identical. In fact, as far as the response is concerned, both wavy cylinders behaved very similarly to the plain cylinder, suggesting that the hydroelastic phenomena driving the oscillations (i.e. the interaction of the oscillating cylinders with an organized Kármán wake) are the same in nature and comparable in intensity.

When both wavy cylinders were held fixed, differences in the flow structures contributed to increased drag for  $\alpha = 45^\circ$  and reduced drag for  $\alpha = 0^\circ$ . Now that the cylinders are oscillating, it appears that there is no difference in the hydrodynamic effects occurring for the wavy cylinders from the plain cylinder. As seen in Fig. 6, even the mean drag during VIV followed the same behaviour for all three cases. We will argue that the different flow structures found for the three fixed bodies (especially concerning the 3D separation lines) are made the same when the bodies start to oscillate in the cross-flow direction.

### 3.2. Fluid forces

The hydroelastic system, allowing for displacements only in one degree of freedom in the  $y$ -axis, can be modelled by

$$m\ddot{y} + c\dot{y} + ky = C_y(t)\frac{1}{2}\rho U^2 DL, \quad (1)$$

$$y(t) = \hat{y} \sin(2\pi ft), \quad (2)$$

where  $y$ ,  $\dot{y}$  and  $\ddot{y}$  are respectively the displacement, velocity and acceleration of the body and  $C_y(t)$  is the time-dependent force coefficient in the cross-flow direction.

Following Bearman (1984),  $y(t)$  of a cylinder under VIV may be expressed by the harmonic response of a linear oscillator, with  $\hat{y}$  and  $f$  respectively representing the harmonic amplitude and frequency of oscillation. The fluid force and the body response oscillate at the same frequency  $f$ , which is usually close to the natural frequency of the system for large-amplitude oscillations under a steady-state regime of VIV. According to this ‘harmonic forcing and harmonic motion’ hypothesis the lift coefficient can be divided into a time-average term  $\bar{C}_y$  and a transient term modelled as a sine wave with amplitude  $\hat{C}_y$ . Hence

$$C_y(t) = \bar{C}_y + \hat{C}_y \sin(2\pi ft + \phi), \quad (3)$$

where  $\phi$  is the phase angle between the displacement and the fluid force. For body excitation to occur, the phase angle between displacement and fluid force must be between  $\phi = 0^\circ$  and  $180^\circ$ . A phase angle equal either to  $0^\circ$  or  $180^\circ$  means that no energy is transferred from the fluid to the structure to excite any vibration.

Figs. 8 and 9 show examples of the time series of instantaneous displacement ( $y/D$ ) and lift coefficient ( $C_y$ ) measured for a few cycles of oscillation of the wavy cylinders at four different reduced velocities. Again, there are no significant differences between  $\alpha = 0^\circ$  and  $45^\circ$ . In both cases, one may note a very well behaved harmonic curve of displacement in response to an also well behaved lift curve. For reduced velocities below the resonance peak at  $U/Df_0 \approx 5$ ,  $y$  and  $C_y$  appear to be almost in phase. For reduced velocities beyond the resonance peak,  $y$  and  $C_y$  appear to be almost out of phase. Nevertheless, it is evident that both  $y$  and  $C_y$  have the same dominant frequency, thus supporting the use of the harmonic models proposed above.

Fig. 10(a) presents the RMS of the lift coefficient ( $\tilde{C}_y$ ) for the wavy cylinders compared with that of the plain cylinder. The similarity between the three curves is remarkable. The range of increased  $\tilde{C}_y$  of the plain cylinder corresponding the synchronization range of VIV is matched by the wavy cylinders. The intensities of  $\tilde{C}_y$  are also of comparable values.

In the present work,  $\phi$  is estimated directly from the measurements of displacement and lift, by calculating

$$\phi = \arccos R_{(y, C_y)}, \quad (4)$$

between both signals, where  $R_{(y, C_y)}$  is the coefficient of cross-correlation between  $y$  and  $C_y$ . Bearman (1984) states that “It is clear that the phase angle  $\phi$  plays an extremely important role. The amplitude response does not depend on  $\hat{C}_y$  alone but on that part of  $\hat{C}_y$  in phase with the body velocity. Hence, measurements of the sectional fluctuating lift coefficient on a range of stationary bluff-body shapes will give little indication of the likely amplitudes of motion of similar bodies flexibly mounted”.

Fig. 10(b) presents  $\phi$  versus reduced velocity for the three cases. The phase shift corresponding to the system passing through resonance is experienced in the same way by all three models. Please bear in mind that residual vibrations beyond the synchronization range (for  $U/Df_0 > 11$ ) are due to turbulence buffeting; they present small amplitudes near the natural frequency, hence  $\phi$  is not properly defined because the harmonic assumption does not hold there anymore.

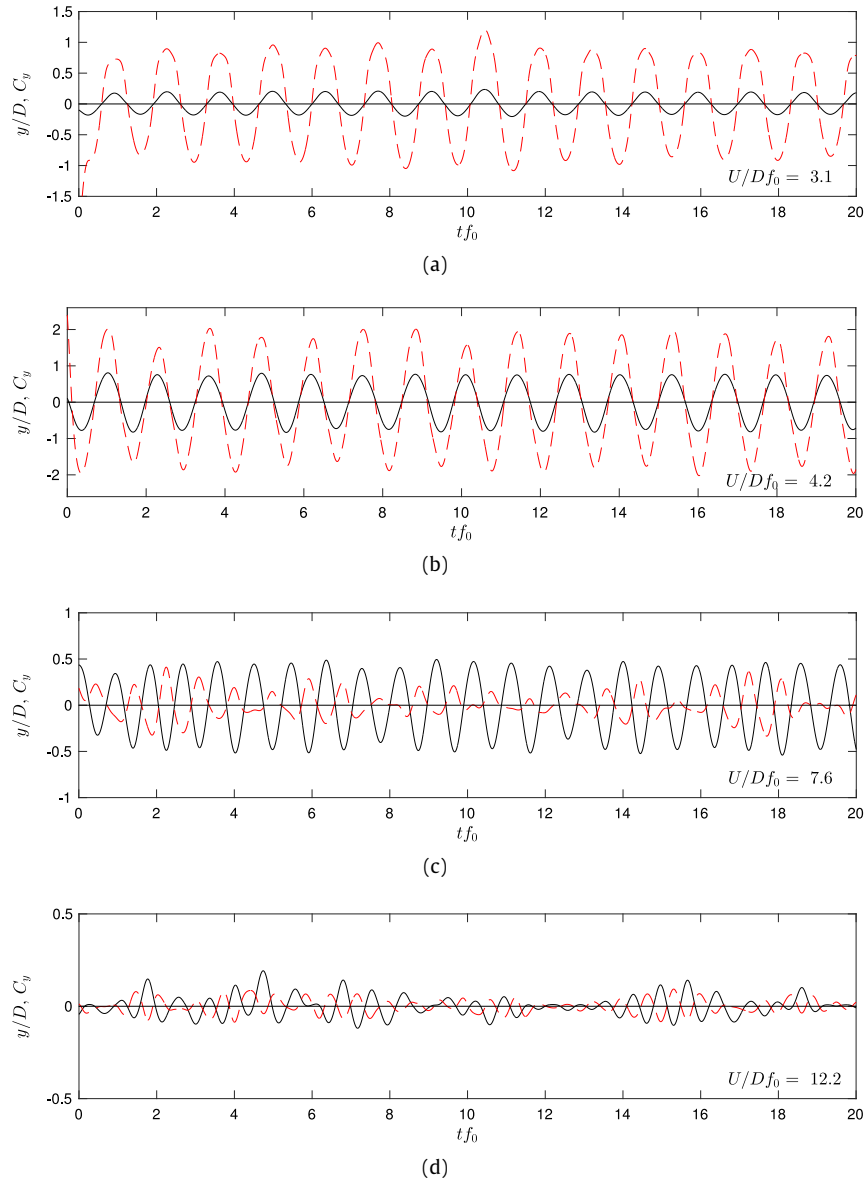


**Fig. 8.** Colour online. Time series of displacement (continuous line) and lift coefficient (dashed line) for a wavy cylinder at  $\alpha = 0^\circ$ .

As shown by Khalak and Williamson (1999) and others for plain cylinders with low  $m^*\zeta$ , the shift of almost  $180^\circ$  in  $\phi$  is associated with a change in the mode of vortex shedding. That is to say that the response of the structure is strongly dependent on the vortex shedding mechanism, and vice versa, within the synchronization range. This emphasizes the importance of the phase angle between  $y$  and  $C_y$  in transferring energy into the system to sustain different regimes of VIV.

Fig. 11 presents the power spectra of the normalized frequency of oscillation ( $f/f_0$ ) and the frequency of the lift force ( $f_{C_y}/f_0$ ) for the wavy cylinder at  $\alpha = 0^\circ$  and  $45^\circ$  versus reduced velocity. The darker shades represent peaks of the power spectra, normalize by the value of the maximum peak at each reduced velocity. The dominant frequencies for each reduced velocity are marked with symbols, hence symbols in Figs. 11(a) and 11(c) representing  $f/f_0$  are those shown in Fig. 7(b).

For both  $\alpha = 0^\circ$  and  $45^\circ$ ,  $f/f_0$  showed a pretty clear signature with a single dominant frequency for the whole of the synchronization range. The spectra of  $f_{C_y}/f_0$  also showed a clear signature, with only a broader spectrum at  $U/Df_0 \approx 6$ , near the transition from the upper to the lower branch of VIV. This might be associated with the intermittent or chaotic transitions between branches, as suggested by Khalak and Williamson (1999) to be occurring for plain cylinders, but one cannot be more conclusive only with the available data. For  $U/Df_0 > 11$ , beyond the synchronization range, the excitation presented a much broader spectrum, especially for  $\alpha = 45^\circ$ , with the dominant  $f_{C_y}/f_0$  reaching the  $St = 0.2$  line. The response, on the other hand, appears with dominant  $f/f_0$  near the natural frequency, an indication of turbulence buffeting.

These results concerning the response and the driving force (Figs. 7 and 10) already offer evidence to show that the wavy cylinder is simply responding to VIV, driven by the same mechanism as a plain cylinder. However, in order to support this

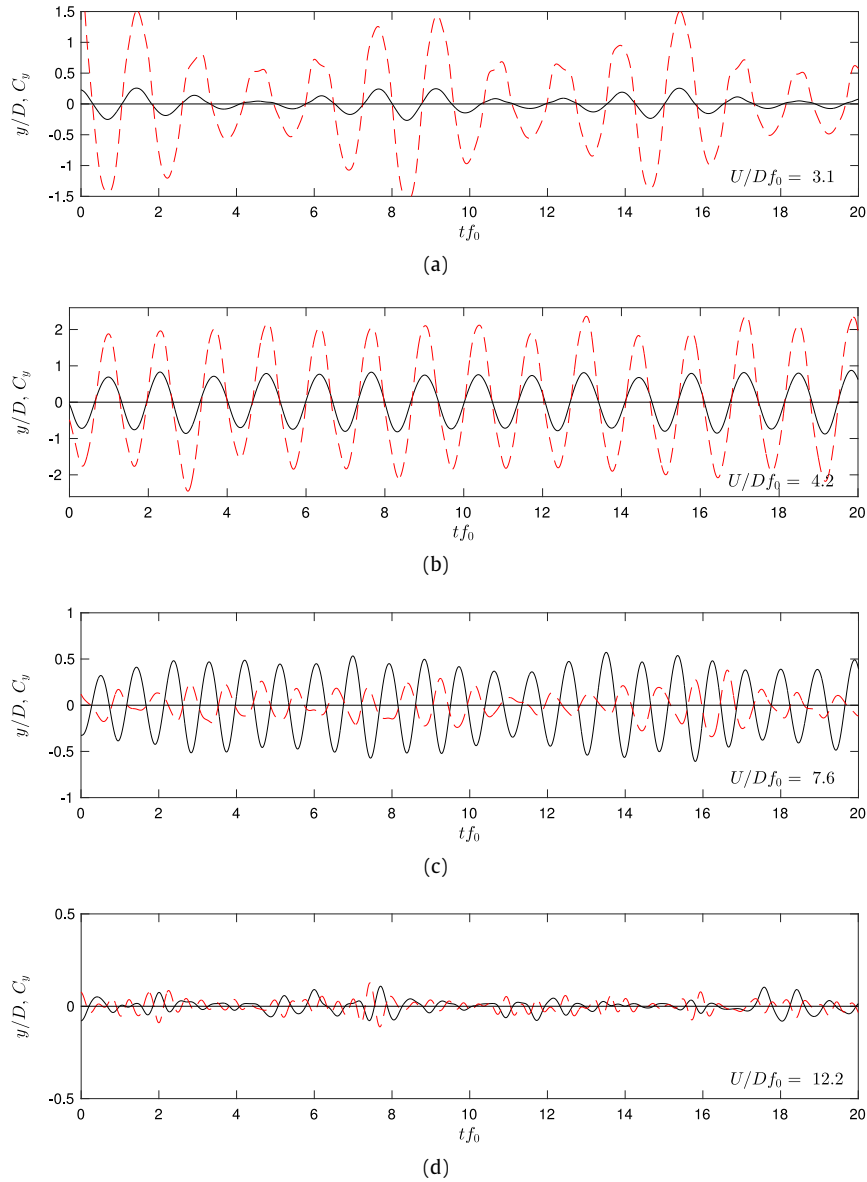


**Fig. 9.** Colour online. Time series of displacement (continuous line) and lift coefficient (dashed line) for a wavy cylinder at  $\alpha = 45^\circ$ .

hypothesis and provide data for the comparison with future investigations, we shall briefly discuss other parameters to highlight the physical principles behind the excitation.

Fig. 12(a) presents the  $C_y \cos \phi$ , the part of the lift coefficient in phase with the body acceleration that takes the form of a fluid-dynamic inertia, therefore closely related to the actual frequency of oscillation. As expected to occur for the plain cylinder,  $C_y \cos \phi$  found a peak at the VIV resonance followed by negative values corresponding to the lower branch. The behaviour observed for the two wavy cylinders was not different.

In the review presented by Williamson and Govardhan (2004), an “effective added mass” coefficient is defined by

$$C_{EA} = \frac{1}{2\pi^3} \frac{C_y \cos \phi}{\hat{y}/D} \left( \frac{U}{Df} \right)^2. \quad (5)$$

$C_{EA}$  represents the variation of the effect of the added mass of fluid with the response, taking into account not only the lift term in phase with the acceleration of the body, but also the amplitude and frequency of the response for each reduced velocity. As seen in Fig. 12(b), the effective added mass for the wavy cylinders is comparable to that observed for the plain cylinder under VIV.

Obviously, if  $C_y \cos \phi$  and  $C_{EA}$  were derived directly from  $\tilde{C}_y$  and  $\phi$ , which presented similar trends for the three models, one should not expect different behaviours between them in the results of Fig. 12. Nevertheless, Fig. 12 offers clear evidence that the effect due to the added mass of fluid is not significantly different for the wavy cylinder when compared with the



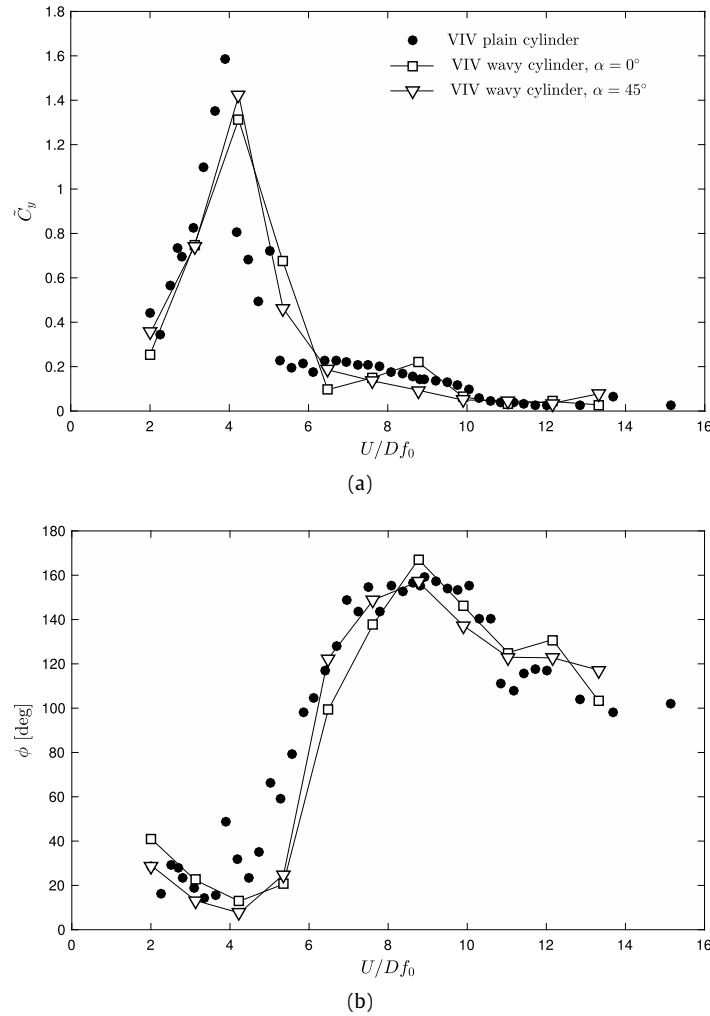


**Fig. 10.** (a) RMS of lift coefficient and (b) phase angle between lift and displacement.

plain cylinder. We conclude that, once the cylinders are oscillating, the three-dimensional surface of the wavy cylinder cannot produce any significant different fluid-dynamic effect than that produced by the movement of a plain cylinder.

Fig. 13(a), presenting the lift term in phase with the body velocity, also supports that conclusion.  $C_y \sin \phi$  takes the form of a “negative fluid-dynamic damping”, injecting energy into the system to sustain the vibrations. Results for the wavy cylinder are very similar to those of the plain cylinder. The energy transferred from the flow to the body in one cycle of oscillation is defined by

$$E = \pi \frac{\hat{y}}{D} C_y \sin \phi, \quad (6)$$

and presented in Fig. 13(b) against reduced velocity. We may conclude that the hydroelastic mechanism exciting the elliptic wavy cylinders into vibration is indeed the same as the one that excites the plain cylinder into VIV.

Now, if the excitation coming from the flow is the same in both cases (either with a plain or with our wavy cylinders), the dominant flow structures in the near wake should be similar between the two cases too. As mentioned in the literature review presented in the introduction, we know that the 3D surface of the wavy cylinder may disrupt the near wake of a fixed body (changing the separation lines, thus reducing drag). But it seems that once the body is free to oscillate, the dynamics of the wake is affected in such a way that the dominant mechanism is roughly the same for the plain cylinder and for the wavy cylinders.

We shall now turn to investigate the dominant flow structures of these cases by describing flow visualizations of the near wake.

#### 4. Three-dimensional wake structure

As mentioned before, the near wake of a wavy cylinder is affected by the 3D shape of the surface. Most of the time, the characteristic wavelength of the surface appears in the dominant flow structures developing in the near wake. The separation

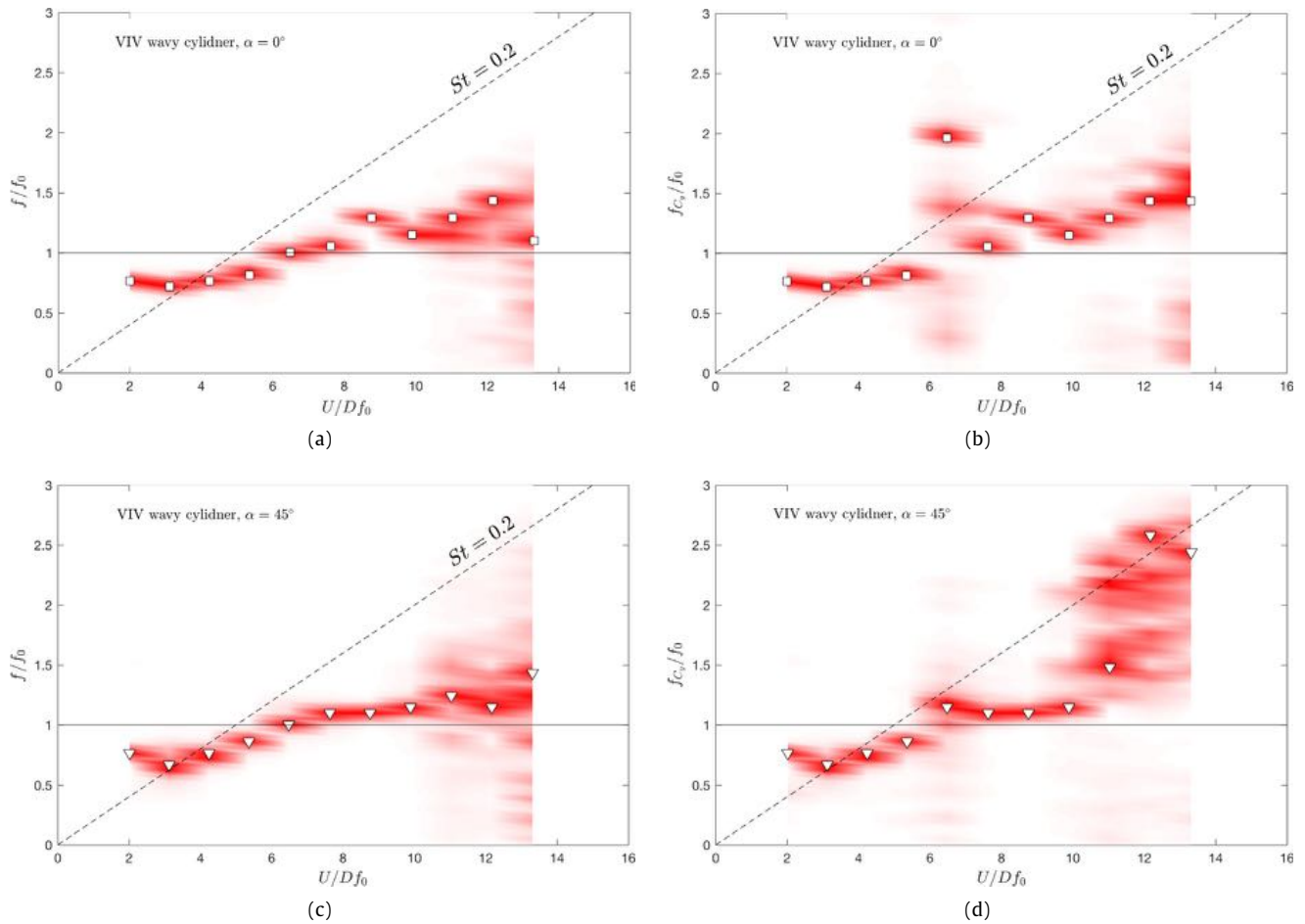


**Fig. 11.** Colour online. Power spectra of the frequency of oscillation ( $f/f_0$ ) and the frequency of the lift force ( $f_{C_y}/f_0$ ) versus reduced velocity.

lines on both sides of the bluff body are affected by the 3D shape of the surface, interfering with the behaviour of the free shear layers which alters the width and length of the near wake. The axial-type of vortex filaments that characterize the Kármán wake may still be the dominant flow feature, but longitudinal vortices appear at regular intervals related to the wavelength of the body geometry. This was observed to occur for various types of wavy cylinders and other bluff geometries with sinusoidal surfaces.

#### 4.1. Fixed cylinder at $\alpha = 0^\circ$

Fig. 14 illustrates possible 3D patterns observed in the near wake of a fixed wavy cylinder. When the body was not moving, the separation line presented a very three-dimensional shape following the saddle and node curvatures of the surface. The separation lines are represented in Fig. 14 by a solid black line along the body. The separation was delayed near the saddle regions and advanced near the nodes, extending or reducing the reach of the free shear layers before they rolled up to form coherent vortices.

Sometimes, the axial vortex filaments ( $z$ -vorticity, aligned with the axis of the body) appeared well correlated along the span for various cycles of vortex shedding, as illustrated in Fig. 14(a). An undulation of the vortex filaments at the characteristic wavelength of the surface was noticeable, with streamwise vortices appearing at regular intervals further downstream (these are represented by curled black lines), but still a coherent vortex filament was visualized. Other times, as illustrated in the example of Fig. 14(b), the axial vortex filament on one side appeared uncorrelated along the span, which also resulted in stronger three-dimensional vortices in the  $x$  and  $y$  direction in the wake (represented by the curled lines). Still at other times, as illustrated in Fig. 14(c), for a few shedding cycles, the axial vortex filaments appeared to be “broken”, alternating shorter and longer vortex-formation lengths associated with the saddle and node regions of the body. Much stronger three-dimensional vortices appeared in the wake, contributing to dissipate the bubbles rather quickly.

In summary, the coherent axial vortex filaments could take many disturbed shapes, but always followed the wavelength characteristic of the surface of the body. As a general rule, axial vortices generated near the nodes were formed closer to the base of the cylinder, while vortices generated near the saddles were developed further downstream. Vortices in the

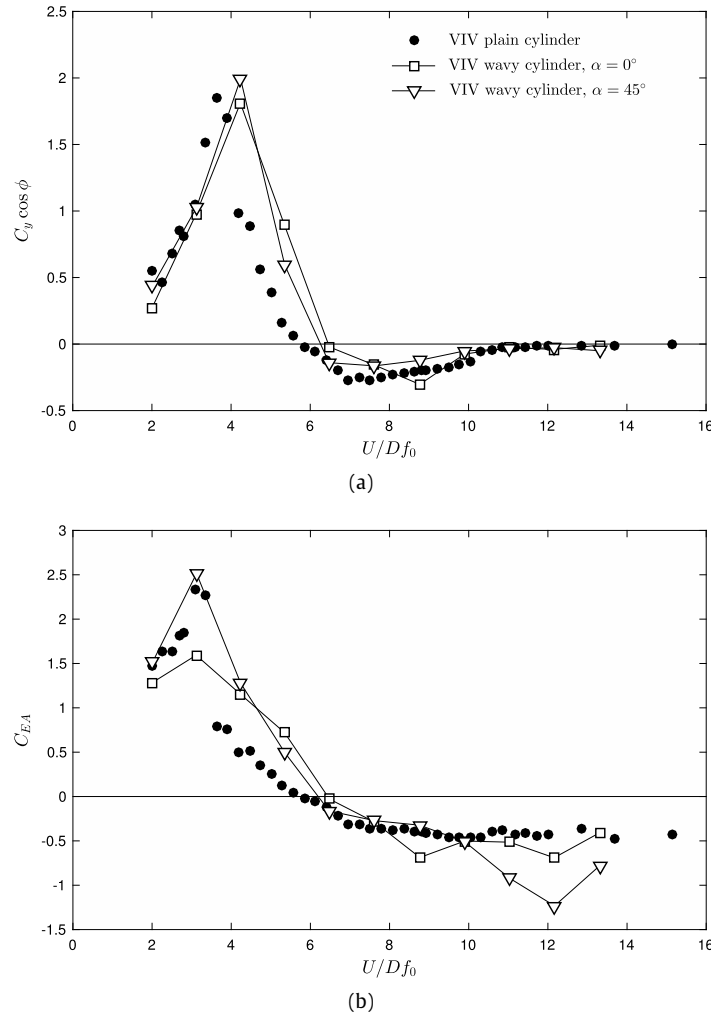


**Fig. 12.** (a) Lift coefficient in phase with body acceleration and (b) effective added mass coefficient.

$x$  direction were observed to form near the node regions. As a consequence, vortical structures in the  $y$  direction were intensified further downstream in the turbulent wake, which is rich in three-dimensionalities. This is in good agreement with the observations of Lam et al. (2004b) and Zhang et al. (2005). The wake pattern illustrated in Fig. 14(a) was the most common, sustained during most of the shedding cycles.

The reader should bear in mind that the representation of vortices in Figs. 14 and 15 are simply an illustration to emphasize the dominant features of the wake. Obviously, vortex filaments cannot end in the fluid and vortex sheets cannot be abruptly interrupted as the image may suggest. The impression of a discontinuity between the vortex filaments is not real; the intricate 3D structures of smaller scales are too complex to be detailed in these flow sketches. Our objective with these artworks is to emphasize the correlation between the separation lines and possible dominant flow structures observed in the wake.

#### 4.2. Oscillating cylinder at $\alpha = 0^\circ$

Once the wavy cylinder was allowed to oscillate under VIV, the wake pattern was considerably changed. Fig. 15(a) repeats the illustration of the dominant wake structure for a fixed wavy cylinder as a reference. The same pattern was only observed to occur for very small responses, below  $\hat{y}/D = 0.1$ , therefore only occurring at  $U/Df_0$  less than 2.5 or greater than 11 (even though visualization was difficult at higher  $Re$ ). The separation lines were closely sinusoidal (represented by a solid black line on the surface), following the saddle and node curvatures in the cross-flow and streamwise directions, as illustrated.

As the response increased slightly above  $\hat{y}/D = 0.1$  for  $U/Df_0 = 3$ , the lateral movement of the cylinder started to affect the separation lines, as seen in Fig. 15(b). As their shape became less sinusoidal (represented by a dashed black line), the axial vortex filaments in the near wake straightened up. Vortices in the  $x$  and  $y$  directions were reduced in strength.

Finally, in Fig. 15(c), as the response reached its maximum value of  $\hat{y}/D = 0.8$  for  $U/Df_0 \approx 5$ , the separation lines became fully correlated along the span, featuring an almost perfect straight line along the wavy surface (dashed black line). The axial

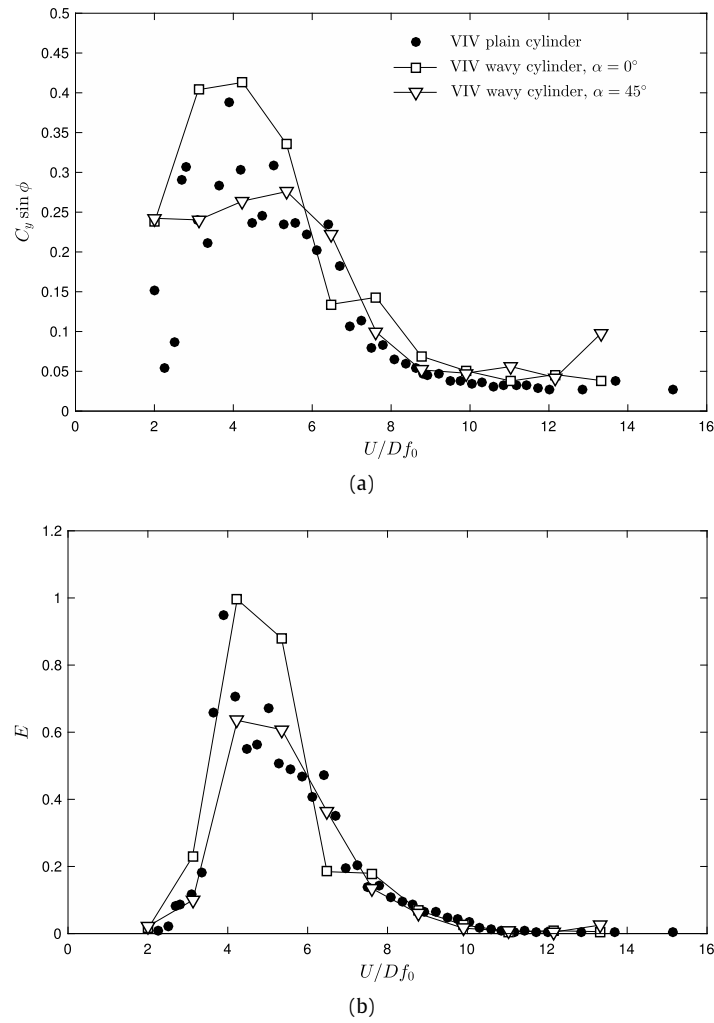


**Fig. 13.** (a) Lift coefficient in phase with body velocity and (b) energy transferred from flow to structure during one cycle of vibration.

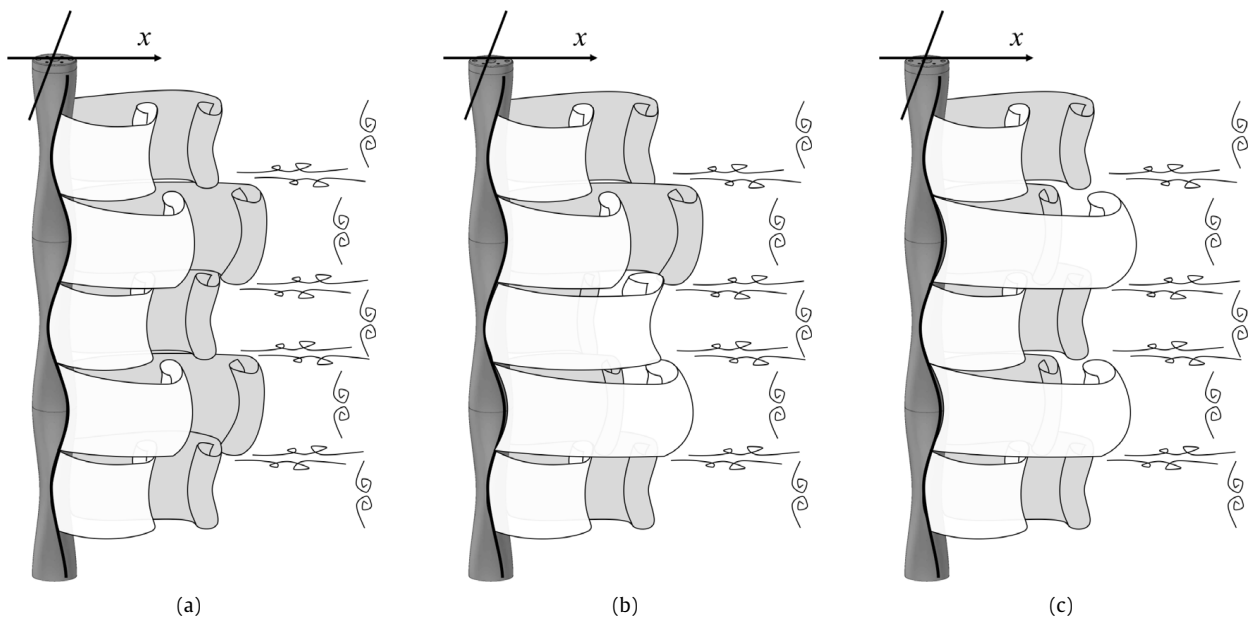


**Fig. 14.** Examples of three-dimensional wake patterns for a fixed wavy cylinder.

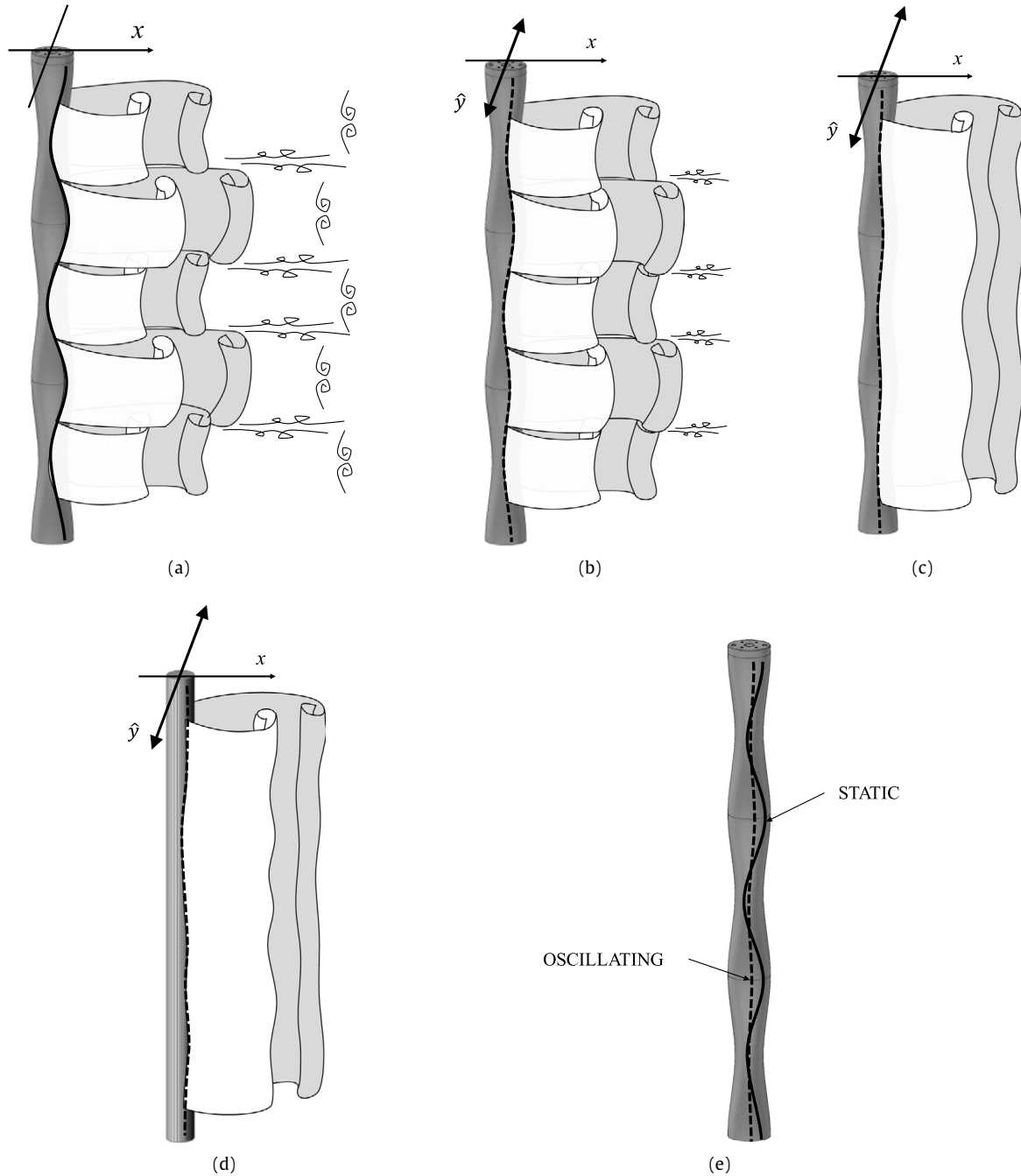


**Fig. 15.** 3D wake patterns: (a) static wavy cylinder, (b) wavy cylinder at low  $\hat{y}/D$ , (c) wavy cylinder at high  $\hat{y}/D$ , (d) oscillating plain cylinder. (e) Sketch of separation lines on a wavy cylinder.

vortex filaments recovered a degree of correlation that resembled that seen for the vortex filaments of an oscillating plain cylinder, illustrated in Fig. 15(d) for comparison. Consequently, the wake structure became closely two dimensional, with no sign of a characteristic wavelength appearing in the distribution of streamwise vortices.

As summarized in Fig. 15(e), it appeared that only a small lateral movement of the wavy cylinder was necessary for the sinusoidal separation lines found on the fixed body to correlate along the span. The 3D flow structures induced by the waviness of the surface were thus replaced by a coherent wake of almost parallel vortex filaments.

#### 4.3. Sectional wake patterns for $\alpha = 0^\circ$ and $45^\circ$

What happened for a wavy cylinder at  $\alpha = 45^\circ$  was not very different. As one can now imagine, if the lateral oscillation is able to recorelate the separation lines over the wavy surface, the variation of angle of attack should not be an obstacle.



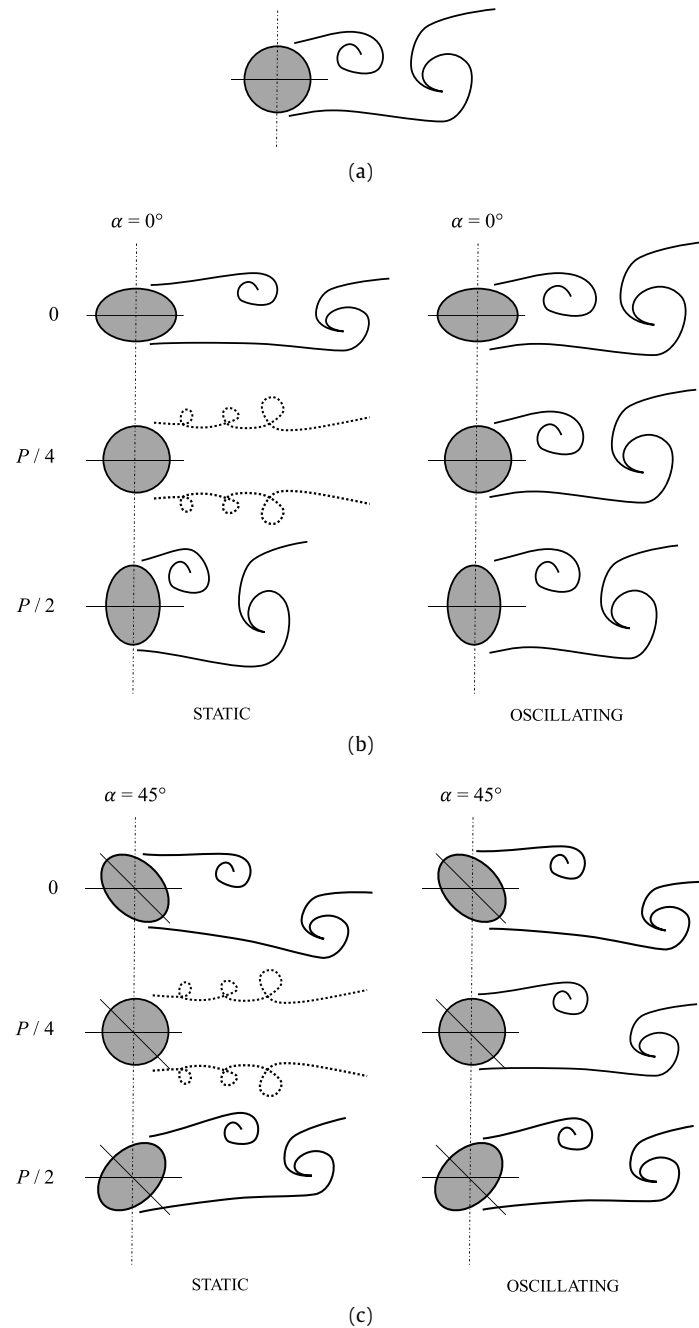


**Fig. 16.** Sectional wake patterns for fixed and oscillating cylinders: (a) plain cylinder, (b) wavy cylinder at  $\alpha = 0^\circ$ , (c) wavy cylinder at  $\alpha = 45^\circ$ .

Fig. 16(a) presents a simple diagram illustrating the vortex-shedding mechanism of a plain circular cylinder. This will serve as a reference to compare wake width and vortex-formation length.

Fig. 16(b) illustrates the vortex-shedding mechanism for a fixed and an oscillating wavy cylinder at  $\alpha = 0^\circ$  drawn at 2D planes along the span. For a fixed cylinder, the wake was narrower and longer at the saddle (station 0) and wider and shorter at the node ( $P/2$ ). The circular section at  $P/4$  represents the transition from one pattern to the other. It was near this region, although a bit closer to the node, that the streamwise vortices appeared (represented by curled dashed lines). If the cylinder was oscillating, as seen in the diagram to the right, the wake regained its correlation and very little difference was noticed between flow structures near saddle and nodes (maybe only a small variation in wake width), but a considerable variation in the vortex-formation length. The same features were observed by Wang and Liu (2016), who performed time-resolved particle-image velocimetry of the flow around a seal whisker with similar wavy morphology.

For the wavy cylinder at  $\alpha = 45^\circ$ , illustrated in Fig. 16(c), the same pattern was observed with only minor variations occurring between the saddle and the node. Now that the fixed wavy cylinder faced the flow at an incidence angle at stations 0 and  $P/2$ , the wake at these regions was slightly inclined following the more elongated shape of the elliptic cross section.

However, once the body started to oscillate (as seen on the right), the angle of incidence was barely noticed by the flow and a spanwise correlated wake appeared once more.

## 5. Final remarks

The differences in curvatures between saddles and nodes are more accentuated for elliptical cross sections and could intensify the 3D characteristics of the wake that favour drag reduction. We have verified the observations of [Bearman and Owen \(1998\)](#), who stated that reductions in drag can be achieved when the separation lines on a fixed bluff body are forced to be sinuous. However, once the body started to oscillate in the cross-flow direction, the separation lines on the sides of the wavy cylinder straightened up, recovering the shedding of vortices forming a wide Kármán wake. This observation is in agreement with the findings of [Zhang et al. \(2017\)](#), who performed numerical simulations for a free-to-oscillate wavy cylinder with circular cross sections. As shown by [Blackburn \(1998\)](#), the lateral oscillation has a tendency of straightening up the separation lines of a plain cylinder.

In general, we suggest the same occurs for a three-dimensional cylinder if the 3D features of the surface are not sufficiently pronounced to hold the sinuous separation lines in place. As a consequence, the elastic body will be able to pick up even the minute excitation from the flow acting near its resonant frequency, thus enhancing the response. If the level of mass and damping in the system is high enough, the initial excitation resulting from sinuous separation lines might not be strong enough to overcome the loss of energy due to damping, thus vibration will not develop. But for systems with a low mass–damping parameter, an initial perturbation may result in a large enough lateral movement that could in turn realign the separation lines.

This shows that the physical mechanisms driving the VIV of the wavy cylinder are not different in nature from those occurring with the plain cylinder. Response curves and a detailed analysis of fluid forces discussed above support that conclusion. When the bodies are oscillating, the separation lines for the wavy cylinder recover a less 3D shape, similar to that on a plain cylinder. We argue that sharp 3D perturbations are required to hold the separation lines in a 3D shape. Helical strakes, for example, have distinctively pronounced features in the form of sharp helical blades. It is very difficult for the flow to modify the 3D separation lines fixed by the high blades. Small vibrations would not be enough. If the height of the strake is not high enough, it might be that a small lateral movement of the body results in a roughly straight separation line on the side. Therefore, significantly higher strakes are required to suppress VIV of low mass–damping system (immersed in water, for example) than of high mass–damping systems (immersed in air, such as chimneys and cables). But if the strakes are high enough, the separation lines follow the shape of that sharp geometry, interfering with the flow. The setback, however, is the amount of drag generated. In order to hold the 3D separation lines along the span, the larger strakes will generate considerably more drag.

Therefore we argue that a combination of VIV suppression and significant drag reduction is very difficult to be achieved (if not impossible) for low mass–damping systems. Smooth three-dimensional surfaces that would generate considerably less drag (such as the present wavy cylinder) are not efficient in fixing the sinuous separation lines required to reduce the excitation. Sharp-edged surfaces might still hold the separation lines under small lateral movements, but they increase drag as a consequence.

On the other hand, this hydroelastic behaviour might be useful for the seals whose whiskers have a very similar geometry, as reported by [Beem and Triantafyllou \(2015\)](#). Out of the synchronization range of VIV the whisker would present insignificant vibration with minimal drag. However, once the whisker is triggered to vibrate – say by turbulence buffeting or by a sudden pressure fluctuation in the upstream flow coming from the wake of a swimming fish – the initial movement would be enough to cause the realignment of the separation lines, enhancing the response. This mechanism would produce a drag-efficient whisker with augmented capacity to respond with flow-induced vibrations to perturbations in the upcoming flow.

Of course the dynamic response of a seal whisker would be different from that observed for this idealized case with a rigid cylinder. The whisker would probably present higher mass and structural damping than our cylinder. Also, the flexible whisker would be deflected by the flow as a cantilever beam, responding with vibrations in both inline and cross-flow directions (not to mention the possibility of higher modes of vibration). Nevertheless, we hope that our data acquired in an idealized experiment with a rigid wavy cylinder with low mass and damping responding in one degree of freedom will help the study of marine mammals and support the development of other bioinspired applications.

## 6. Conclusion

From the present experimental investigation we can conclude that a wavy cylinder with the level of three-dimensional surface variation proposed herein developed vortex-induced vibrations with the same behaviour seen for a plain cylinder with equivalent diameter. A fixed wavy cylinder indeed presented reduced drag when compared to a plain cylinder (an average reduction of about 12.5%). The modified regions of an elongated wake with substantial 3D flow features increased the base pressure and improved the performance as far as drag is concerned.

The 3D features of the elliptical wavy cylinder are more prominent than those of a wavy cylinder with circular cross section (of equivalent mean diameter). However, once the body responded in the cross-flow direction, the separation lines of the wavy cylinder straightened up, recovering a wide Kármán wake. We conclude that the three-dimensional separation lines on a wavy cylinder were correlated by the lateral movement of the body responding to flow-induced excitations, hence the hydroelastic mechanism that drives the wavy cylinder into VIV is not different from that of a plain cylinder.

## Acknowledgements

The original research work on the development of VIV suppressors was sponsored by BP Exploration Operating Company Ltd. GRSA acknowledges the support of FAPESP (2011/00205-6, 2014/50279-4), CNPq (306917/2015-7) and the Brazilian Navy.

## References

- Ahmed, A., 2010. On the wake of a circular cylinder with nodal and saddle attachment. *J. Fluids Struct.* 26 (1), 41–49.
- Ahmed, A., Bays-Muchmore, B., 1992. Transverse flow over a wavy cylinder. *Phys. Fluids A* 4 (9), 1959–1967.
- Assi, G.R.S., Bearman, P.W., Carmo, B., Meneghini, J., Sherwin, S., Willden, R., 2013. The role of wake stiffness on the wake-induced vibration of the downstream cylinder of a tandem pair. *J. Fluid Mech.* 718, 210–245.
- Assi, G.R.S., Bearman, P.W., Kitney, N., 2009. Low drag solutions for suppressing vortex-induced vibration of circular cylinders. *J. Fluids Struct.* 25, 666–675.
- Assi, G.R.S., Bearman, P.W., Kitney, N., Tognarelli, M., 2010a. Suppression of wake-induced vibration of tandem cylinders with free-to-rotate control plates. *J. Fluids Struct.* 26, 1045–1057.
- Assi, G.R.S., Bearman, P.W., Meneghini, J., 2010b. On the wake-induced vibration of tandem circular cylinders: the vortex interaction excitation mechanism. *J. Fluid Mech.* 661, 365–401.
- Assi, G.R.S., Franco, G.S., Vestri, M.S., 2014. Investigation on the stability of parallel and oblique plates as suppressors of vortex-induced vibration of a circular cylinder. *J. Offshore Mech. Arctic Eng.* 136 (3), 031802–031802–9.
- Bearman, P.W., 1984. Vortex shedding from oscillating bluff bodies. *Annu. Rev. Fluid Mech.* 16, 195–222.
- Bearman, P.W., Brankovic, M., 2004. Experimental studies of passive control of vortex-induced vibration. *Eur. J. Mech. B Fluids* 23 (1), 9–15.
- Bearman, P.W., Owen, J.C., 1998. Reduction of bluff-body drag and suppression of vortex shedding by the introduction of wavy separation lines. *J. Fluids Struct.* 12 (1), 123–130.
- Beem, H.R., Triantafyllou, M.S., 2015. Wake-induced ‘slaloming’ response explains exquisite sensitivity of seal whisker-like sensors. *J. Fluid Mech.* 783, 306–322.
- Bell, W., 1983. Turbulence vs drag — some further considerations. *Ocean Eng.* 10 (1), 47–63.
- Blackburn, H.M., 1998. A comparison of two- and three-dimensional wakes of an oscillating circular cylinder. In: 13th Australasian Fluid Mechanics Conference, pp. 749–752.
- Cai, J., Chng, T.L., Tsai, H.M., 2008. On vortical flows shedding from a bluff body with a wavy trailing edge. *Phys. Fluids* 20 (6).
- Cicolin, M.M., Assi, G.R.S., 2017. Experiments with flexible shrouds to reduce the vortex-induced vibration of a cylinder with low mass and damping. *Appl. Ocean Res.* 65, 290–301.
- Darekar, R., Sherwin, S., 2001. Flow past a bluff body with a wavy stagnation face. *J. Fluids Struct.* 15 (3), 587–596.
- Gerrard, J., 1966. The mechanics of the formation region of vortices behind bluff bodies. *J. Fluid Mech.* 25, 401–413.
- Ginter, C.C., Fish, F.E., Marshall, C.D., 2010. Morphological analysis of the bumpy profile of phocid vibrissae. *Mar. Mammal Sci.* 26, 733.
- Gioria, R.S., Carmo, B.S., Meneghini, J.R., 2007. Three dimensional wake structures of flow around an oscillating circular cylinder. In: ASME 2007 26th International Conference on Offshore Mechanics and Arctic Engineering. American Society of Mechanical Engineers, pp. 833–839.
- Hanke, W., Witte, M., Miersch, L., Brede, M., Oeffner, J., Michael, M., Hanke, F., Leder, A., Dehnhardt, G., 2010. Harbor seal vibrissa morphology suppresses vortex-induced vibrations. *J. Exp. Biol.* 213 (15), 2665–2672.
- Hans, H., Miao, J.M., Triantafyllou, M.S., 2014. Mechanical characteristics of harbor seal (*phoca vitulina*) vibrissae under different circumstances and their implications on its sensing methodology. *Bioinspir. Biomim.* 9 (3), 036013.
- Hover, F.S., Davis, J.T., Triantafyllou, M.S., 2004. Three-dimensionality of mode transition in vortex-induced vibrations of a circular cylinder. *Eur. J. Mech. B Fluids* 23 (1), 29–40.
- Jung, J.H., Yoon, H.S., 2014. Large eddy simulation of flow over a twisted cylinder at a subcritical Reynolds number. *J. Fluid Mech.* 759, 579–611.
- Khalak, A., Williamson, C.H.K., 1999. Motions, forces and mode transitions in vortex-induced vibrations at low mass-damping. *J. Fluids Struct.* 13, 813–851.
- Kim, W., Lee, J., Choi, H., 2016. Flow around a helically twisted elliptic cylinder. *Phys. Fluids* 28 (5).
- Kleissl, K., Georgakis, C., 2011. Aerodynamic control of bridge cables through shape modification: A preliminary study. *J. Fluids Struct.* 27 (7), 1006–1020.
- Lam, K., Lin, Y.F., 2009. Effects of wavelength and amplitude of a wavy cylinder in cross-flow at low Reynolds numbers. *J. Fluid Mech.* 620, 195–220.
- Lam, K., Wang, F., Li, J., So, R., 2004a. Experimental investigation of the mean and fluctuating forces of wavy (varicose) cylinders in a cross-flow. *J. Fluids Struct.* 19 (3), 321–334.
- Lam, K., Wang, F., So, R., 2004b. Three-dimensional nature of vortices in the near wake of a wavy cylinder. *J. Fluids Struct.* 19 (6), 815–833.
- Lee, S.-J., Nguyen, A.-T., 2007. Experimental investigation on wake behind a wavy cylinder having sinusoidal cross-sectional area variation. *Fluid Dyn. Res.* 39 (4), 292.
- Nakamura, H., Igarashi, T., 2008. Omnidirectional reductions in drag and fluctuating forces for a circular cylinder by attaching rings. *J. Wind Eng. Ind. Aerodyn.* 96 (6–7), 887–899.
- New, T.H., Shi, S., Liu, Y., 2013. Cylinder-wall interference effects on finite-length wavy cylinders at subcritical Reynolds number flows. *Exp. Fluids* 54 (10), 1601.
- Owen, J.C., Bearman, P.W., Szewczyk, A.A., 2001. Passive control of VIV with drag reduction. *J. Fluids Struct.* 15, 597–605.
- Owen, J.C., Szewczyk, A.A., Bearman, P.W., 1999. Suppressing Karman vortex shedding by use of sinuous circular cylinders. In: APS Division of Fluid Dynamics Meeting Abstracts.
- Owen, J.C., Szewczyk, A.A., Bearman, P.W., 2000. Suppression of Kármán vortex shedding. *Phys. Fluids* 12 (9), S9.
- Rashidi, S., Hayatdavoodi, M., Esfahani, J.A., 2016. Vortex shedding suppression and wake control: A review. *Ocean Eng.* 126, 57–80.
- Rinehart, A., Shyam, V., Zhang, W., 2017. Characterization of seal whisker morphology: implications for whisker-inspired flow control applications. *Bioinspir. Biomim.* 12 (6), 066005.
- Silva-Ortega, M., Assi, G., 2017. Flow-induced vibration of a circular cylinder surrounded by two, four and eight wake-control cylinders. *Exp. Therm Fluid Sci.* 85, 354–362.
- Wang, S., Liu, Y., 2016. Wake dynamics behind a seal-vibrissa-shaped cylinder: a comparative study by time-resolved particle velocimetry measurements. *Exp. Fluids* 57 (3), 32.
- Williamson, C., 1996. Vortex dynamics in the cylinder wake. *Annu. Rev. Fluid Mech.* 28 (1), 477–539.
- Williamson, C.H.K., Govardhan, R., 2004. Vortex-induced vibrations. *Annu. Rev. Fluid Mech.* 36, 413–455.
- Zdravkovich, M.M., 1981. Review and classification of various aerodynamic and hydrodynamic means for suppressing vortex shedding. *J. Wind Eng. Ind. Aerodyn.* 7, 145–189.
- Zdravkovich, M.M., 1997. *Flow Around Circular Cylinders*, Vol. 1, first ed.. Oxford University Press.

- Zdravkovich, M.M., Brand, V.P., Mathew, G., Weston, A., 1989. Flow past short circular cylinders with two free ends. *J. Fluid Mech.* 203, 557–575.
- Zhang, K., Katsuchi, H., Zhou, D., Yamada, H., Han, Z., 2016. Numerical study on the effect of shape modification to the flow around circular cylinders. *J. Wind Eng. Ind. Aerodyn.* 152, 23–40.
- Zhang, K., Katsuchi, H., Zhou, D., Yamada, H., Zhang, T., Han, Z., 2017. Numerical simulation of vortex induced vibrations of a flexibly mounted wavy cylinder at subcritical Reynolds number. *Ocean Eng.* 133 (Supplement C), 170–181.
- Zhang, W., Daichin, , Lee, S.J., 2005. PIV measurements of the near-wake behind a sinusoidal cylinder. *Exp. Fluids* 38 (6), 824–832.



Contents lists available at ScienceDirect

## Journal of Fluids and Structures

journal homepage: [www.elsevier.com/locate/jfs](http://www.elsevier.com/locate/jfs)

# Control of vortex shedding from a circular cylinder surrounded by eight rotating wake-control cylinders at $Re=100$

G.R.S. Assi<sup>a,\*</sup>, R.M. Orselli<sup>b</sup>, M. Silva-Ortega<sup>c</sup><sup>a</sup> Department of Naval Architecture & Ocean Engineering, EPUSP, University of São Paulo, São Paulo SP, Brazil<sup>b</sup> Department of Aerospace Engineering, Federal University of ABC, São Bernardo do Campo SP, Brazil<sup>c</sup> Department of Naval Architecture, Universidad Veracruzana, Veracruz, Mexico

## ARTICLE INFO

## Article history:

Received 29 October 2018

Received in revised form 4 February 2019

Accepted 4 March 2019

Available online 15 March 2019

## Keywords:

Vortex shedding

Wake control

Rotating cylinders

Drag reduction

## ABSTRACT

The present work investigates the suppression of vortex shedding of a circular cylinder of diameter  $D$  surrounded by a polar array 8 rotating wake-control cylinders of a considerably smaller diameter  $d/D = 0.05$ . A numerical approach was employed to simulate the laminar flow at a Reynolds number of 100. The governing equations were discretised by the finite volume method for a two-dimensional computational domain. The main varying parameter was the rotation speed of the control cylinders, measured as a fraction of the incoming flow speed. A controlled wake (one without alternating vortices) was achieved when the tangential velocity at the surface of the control cylinders was greater than 3 times the free stream velocity. A significant reduction of the overall drag coefficient and mitigation of the unsteady hydrodynamic forces acting on the system were observed as rotation was increased. Given enough rotation, a negative mean drag (thrust) was achieved. The power spent to rotate the 8 control cylinders appeared to be higher than the power-loss associated with the mean drag of a bare cylinder. While still working with an active, open-loop control system, this investigation supports the development of a closed-loop wake-control device for offshore applications.

© 2019 Elsevier Ltd. All rights reserved.

## 1. Introduction

It is well known that bluff bodies immersed in a flow will develop a periodic wake of alternating vortices (called the *Karman street*) shed from the separated shear layers and convected further downstream (Bearman, 1984). Control over the vortex-shedding phenomenon has been investigated for decades, gaining special attention after a general physical mechanism for the formation of vortices was proposed by Gerrard (1966). Mostly aiming at reattaching the separated flow or removing the periodicity of the wake, researchers have proposed various techniques to achieve wake control. Some of these appeared as fairings (attempting to streamline the flow around the body), while others came about as interesting contraptions attached or installed around the bluff body to interact with the separated shear layers (for example, Assi et al., 2009, 2010).

It is widely accepted that if the wake is controlled and the shedding of vortices is eliminated the bluff body will not only generate considerably less drag but may also become invulnerable to vortex-induced vibrations (VIV). The present investigation is motivated by the development of novel solutions to suppress VIV from slender bluff structures without

\* Corresponding author.

E-mail address: [g.assi@usp.br](mailto:g.assi@usp.br) (G.R.S. Assi).



causing excessive drag (perhaps achieving drag reduction) and producing useful forces for dynamic positioning. In the present work, however, we shall refer only to the suppression of the vortex-shedding mechanism as a step towards the suppression of VIV. For reviews on the topic, please follow Zdravkovich (1981) or the recent compilation of Rashidi et al. (2016).

Passive wake-suppression methods rely on modifications of the bluff body geometry to affect the formation and shedding mechanism of vortices (Choi et al., 2008). They require no external energy supply to the fluid–structure system and have a much simpler implementation, which favours their use over the active methods in most engineering applications. In an effort to study a passive control device by employing interfering control rods, Strykowski and Sreenivasan (1990) have reported that the vortex shedding past a circular cylinder can be controlled over a limited range of Reynolds number ( $Re$ ) by the proper placement of a smaller control rod close to the main cylinder. Wu et al. (2012), Jimenez-Gonzalez and Huera-Huarte (2017) and Silva-Ortega and Assi (2017a, 2018) went on to investigate the passive suppression of VIV of circular cylinders by fitting multiple control rods around their circumference.

Active open- and closed-loop control techniques have received extensive attention by the scientific community (Gad-El-Hak, 2000; Cattafesta and Sheplak, 2011; Schulmeister, 2012; Silva-Ortega and Assi, 2017b), as they can be directly applied or inspire the development of more efficient passive control methods. Among the great variety of active control methods, the *moving surface boundary-layer control* (MSBC) technique relies on the injection of momentum in the boundary layers of the body by rotating small elements placed within or very near the boundary layers around the separation points (Modi, 1997). Rotating elements are usually small circular cylinders placed inside or just above the wall. It is believed that the injection of momentum postpones the effects of the adverse pressure gradient generated by the geometry of the bluff body, moving the separation points to a more advanced position. As a result, the wake becomes narrower and the recirculation region behind the body is suppressed or drastically reduced. One of the most important control parameters directly associated with the injection of momentum is the ratio between the tangential velocity of the moving surface and the flow velocity ( $U_c/U$ ).

MSBC can be applied as an active open- or closed-loop control. Patnaik and Wei (2002) numerically simulated the flow around a D-section cylinder with MSBC at  $Re = 200$  and  $400$  and verified a recirculation free zone in the wake for  $U_c/U = 1.25$ . Muddada and Patnaik (2010) made further developments to this control strategy, employing a cylinder fitted with two simple rotary type mechanical actuators located at  $120^\circ$  from the frontal stagnation point. The effectiveness of the MSBC in reducing drag was shown in all tested cases. Mittal and Raghuvanshi (2001) verified this phenomenon employing a numerical approach and observed that two control cylinders provided a local favourable pressure gradient in the wake region, thereby locally stabilising the shear layers. Following that, Mittal (2001) applied the MSBC to control the flow around a circular cylinder in two-dimensional numerical simulations at  $Re = 100$  and  $10,000$ . At  $Re = 100$  and  $U_c/U = 5$ , the wake was suppressed; at  $Re = 10,000$  the wake did not reach a steady state, but it appeared highly organised and narrower when compared to the case without any control. The effect of the gap between the control cylinders and the wall of the main cylinder at  $Re = 10,000$  was later investigated by Mittal (2003). Recently, Schulmeister et al. (2017) performed experiments at  $Re = 47,000$  that showed considerable drag reduction for two rotating control cylinders strategically located around the main body. Their numerical simulations at  $Re = 500$  revealed interesting details of the reattachment of the flow around the control cylinders.

Korkischko and Meneghini (2012) performed an experiment employing MSBC with 2 control cylinders as a means to suppress VIV of an isolated cylinder mounted on an elastic base with one degree of freedom in the cross-flow direction. VIV suppression was achieved given enough rotation of the control cylinders. Later, Zhu et al. (2015) performed numerical simulations of VIV in two degrees of freedom employing 2 rotating control cylinders for  $Re$  between  $1,000$  and  $6,500$ ; in another study (Zhu and Gao, 2017), the effect of the rotation direction was investigated. Recently, MSBC with more than 2 control cylinders has also been tested as a means to suppress vortex shedding of static cylinders as well as VIV of oscillating bodies in the experiments performed by Silva-Ortega and Assi (2018).

## 2. Objective

The present study investigated if a polar array of 8 rotating wake-control cylinders of a smaller diameter  $d$ , equally spaced about a main circular cylinder of a larger diameter  $D$  and positioned away from the main cylinders's wall (as defined in Fig. 1), was able to control the wake and suppress vortex shedding. This is part of a wider investigation that started with 2 and 4 control cylinders, not discussed here for brevity, but reported in Silva-Ortega and Assi (2017a, 2018). From those previous works, the arrangement with 8 control cylinders started to present useful characteristics of an omnidirectional device.

The gap ( $G/D$ ) separating the control cylinders from the main cylinder and the rotation speed of the control cylinders ( $U_c/U$ , defined as the ratio between the tangential velocity on the wall of the control cylinders to the speed of the incoming flow) were the main parameters of the investigation:  $U_c/U$  varied between 0 and 6, while  $G/D = 0.1$  and  $d/D = 0.05$  were kept constant. Other works have considered variations in these parameters as well (Silva-Ortega, 2015). As seen in Fig. 1, the control cylinders at the top rotate in the clockwise direction, while the control cylinders at the bottom rotate in the counter-clockwise direction. The system is considered an open-loop, active MSBC device.

The investigation was conducted by means of two-dimensional numerical simulations of the flow at  $Re = 100$  ( $Re = UD/\nu$ , based on the free stream velocity  $U$ , the diameter  $D$  of the main cylinder and the viscosity  $\nu$  of the fluid).

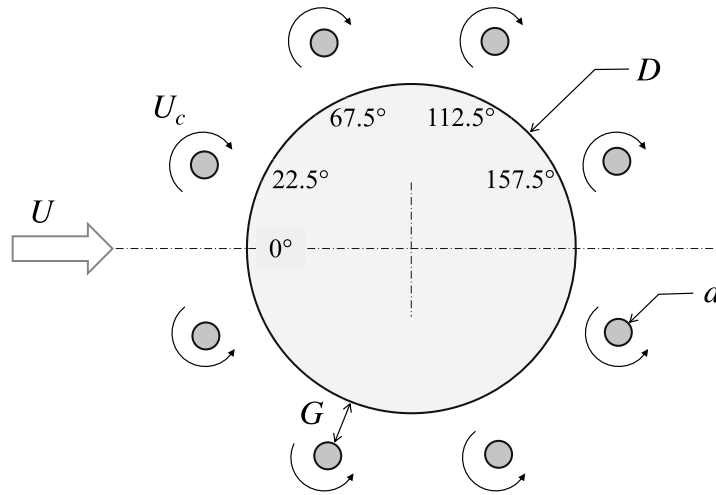


**Fig. 1.** Geometrical parameters for the main cylinder with eight wake-control cylinders. Flow approaching in the direction of the arrow; direction of rotation is marked on each cylinder.

### 3. Numerical method

Numerical simulations of the flow have been carried out employing the commercial code ANSYS Fluent (version 13.0). The flow was governed by the Navier–Stokes equations, which were considered here as incompressible and two-dimensional. The unsteady Navier–Stokes equations for the conservation of mass and momentum in the integral form were given by

$$\int_S \vec{u} \cdot \vec{n} dS = 0 \quad (1)$$

and

$$\int_{\Omega} \frac{\partial \rho \vec{u}}{\partial t} d\Omega + \int_S \rho \vec{u} (\vec{u} \cdot \vec{n}) dS = \int_S (-p \vec{n}) dS + \int_S (\vec{\tau} \cdot \vec{n}) dS, \quad (2)$$

where the viscous stress tensor for Newtonian fluid was

$$\vec{\tau} = \mu \left[ (\nabla \vec{u} + \nabla \vec{u}^T) - \frac{2}{3} (\nabla \cdot \vec{u}) I \right]. \quad (3)$$

In the equations above,  $\vec{u}$  is the flow speed,  $p$  the static pressure,  $\rho$  is the specific mass of fluid,  $\mu$  is the dynamic viscosity,  $t$  is the time,  $\Omega$  represents the control volume of the system and  $S$  denotes its external surfaces, whose outward unit normal is  $\vec{n}$ .

The equations were discretised by a cell-centred finite-volume method. The fluid domain was divided into a large number of discrete control volumes by means of a computational mesh. The resulting discretised equations were solved sequentially based on an implicit pressure-based scheme. In order to deal with the pressure–velocity coupling, the pressure-based algorithm PISO was employed due to its efficient iterative method for unsteady problems, the scheme is fully described in [Versteeg and Malalasekera \(2007\)](#).

In order to obtain the pressure on the faces of the control volume, an interpolation scheme based on a “staggered” control volume arrangement was employed (known in Fluent as PRESTO, PREssure Staggering Option). The staggered-grid scheme procedure is also described in [Versteeg and Malalasekera \(2007\)](#). An upwind second-order spatial differencing method was applied for the convective terms ([Barth and Jespersen, 1989](#)) and the diffusive terms were discretised by a central differencing scheme. The solution was time-advanced using an implicit second-order accurate scheme that employed three time levels incorporated within the PISO algorithm ([Versteeg and Malalasekera, 2007](#)). All the equations were solved iteratively, for a given time-step, until the convergence criterium was met: all residuals for each algebraic equation were less than  $10^{-4}$  and 20 internal iterations per time step.

#### 3.1. Computational domain

The cylinders were surrounded by a rectangular computation domain with upstream, lateral and downstream boundaries located respectively at  $8D$ ,  $8D$  and  $30D$  from the centre of the main cylinder, as shown in [Fig. 2](#). The size of the computational domain was verified so that the flow around the cylinder was not too much influenced by the boundaries. It is well known that the size of the domain influences Strouhal number and other hydrodynamic coefficients ([Behr et al.,](#)

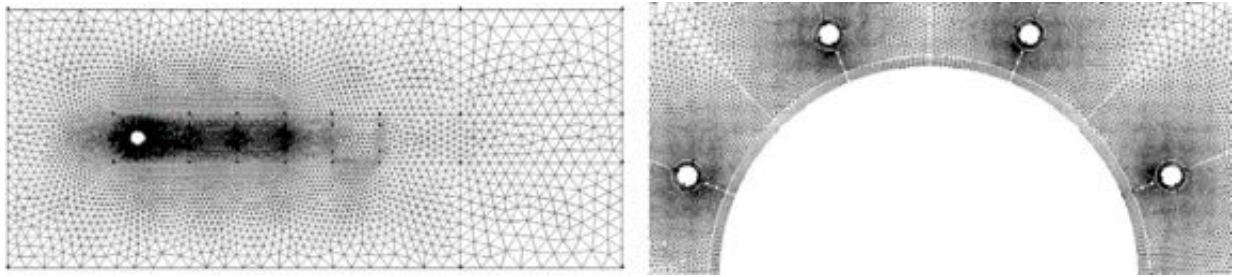


**Fig. 2.** The wider numerical domain (left) and a detail of the mesh around the control cylinders (right).

**Table 1**

Comparison of drag and lift coefficients.

|                         | $St$  | $\bar{C}_D$ | $\hat{C}_L$ |
|-------------------------|-------|-------------|-------------|
| Present work            | 0.175 | 1.401       | 0.227       |
| Blanchard et al. (2019) | 0.170 | 1.392       | 0.242       |

1995). Nevertheless, the size of the employed domain was considered a good balance between computational costs and accuracy of the physical phenomenon. Numerical domains of a similar size or smaller have been successfully employed by Mittal (2001), Young et al. (2001) and Goodarzi and Dehkordi (2017) to investigate analogous problems.

The two-dimensional, finite-volume mesh (with 89,310 cells) was fine enough to resolve the details of the flow near the walls. A structured finite-volume mesh was employed close to the main cylinder and the small cylinders. Mesh-convergence tests have been carried out until a suitable final mesh was found. (Details of this validation exercise will not be reported here for brevity.) Simulations run for enough time to gather at least six cycles of vortex shedding in a fully developed wake.

A no-slip condition was specified for the velocity on the surface of all bodies and free-stream values were assigned to the velocity at the upstream boundary. On the upper and lower boundaries, the component of velocity normal to and the component of the stress vector along these boundaries were prescribed to be zero. At the downstream boundary, an outflow boundary condition was employed, which prescribes all variables' normal gradient to zero.

The direction of the incoming flow and the direction of the rotation of the control cylinders are marked in Fig. 1. The control cylinders were distributed so that there would be no control cylinder positioned at the frontal stagnation region, thus avoiding any asymmetry of the flow around the body. (Future work should concentrate on that arrangement.) The rotation speed ( $U_c/U$ ) of the control cylinders was imposed at each case being simulated. Coefficients of lift ( $C_L$ ) and drag ( $C_D$ ) were determined by integrating the pressure field and viscous forces on the walls around the main cylinder and the control cylinders. The force coefficients per unit length were normalised by  $\frac{1}{2}\rho U^2 D$ , always in reference to the diameter  $D$  of the main cylinder (even if the body in question was a small control cylinder).

## 4. Results and discussion

### 4.1. Reference: a bare cylinder

The flow around a bare cylinder (without control cylinders) at  $Re = 100$  was simulated in order to validate the numerical model and domain as well as to serve as a reference for comparison. From the time series of lift and drag coefficients shown in Fig. 3(a), a steady state regime of vortex shedding was achieved after 70 non-dimensional time units from the beginning of the simulation. The steady-state Strouhal number (defined as  $St = f_s D/U$ , where  $f_s$  is the frequency of vortex shedding), the mean drag coefficient ( $\bar{C}_D$ ) and the fluctuation of the lift coefficient ( $\hat{C}_L$ , calculated as the root mean square of lift) are presented in Table 1 in comparison with another two-dimensional numerical simulation from the literature. These values were also in good agreement with Meneghini et al. (2001), Norberg (2003), Rajani et al. (2009) and Muddada and Patnaik (2010).

Fig. 3 also presents the vorticity field and streamlines downstream of the bare cylinder for an instant once the periodic regime of vortex shedding had been established. A typical Karman vortex street – with two single vortices shed per cycle – is clearly identified from the vorticity contours, while the region of separated flow at the base of the cylinder is highlighted by the streamlines.

### 4.2. With rotating control cylinders

The rotating control cylinders were placed close enough to the wall to interact with the boundary layer of the main cylinder, but not necessarily immersed in it. Fig. 4 illustrates the velocity profiles of the flow around the bare cylinder,

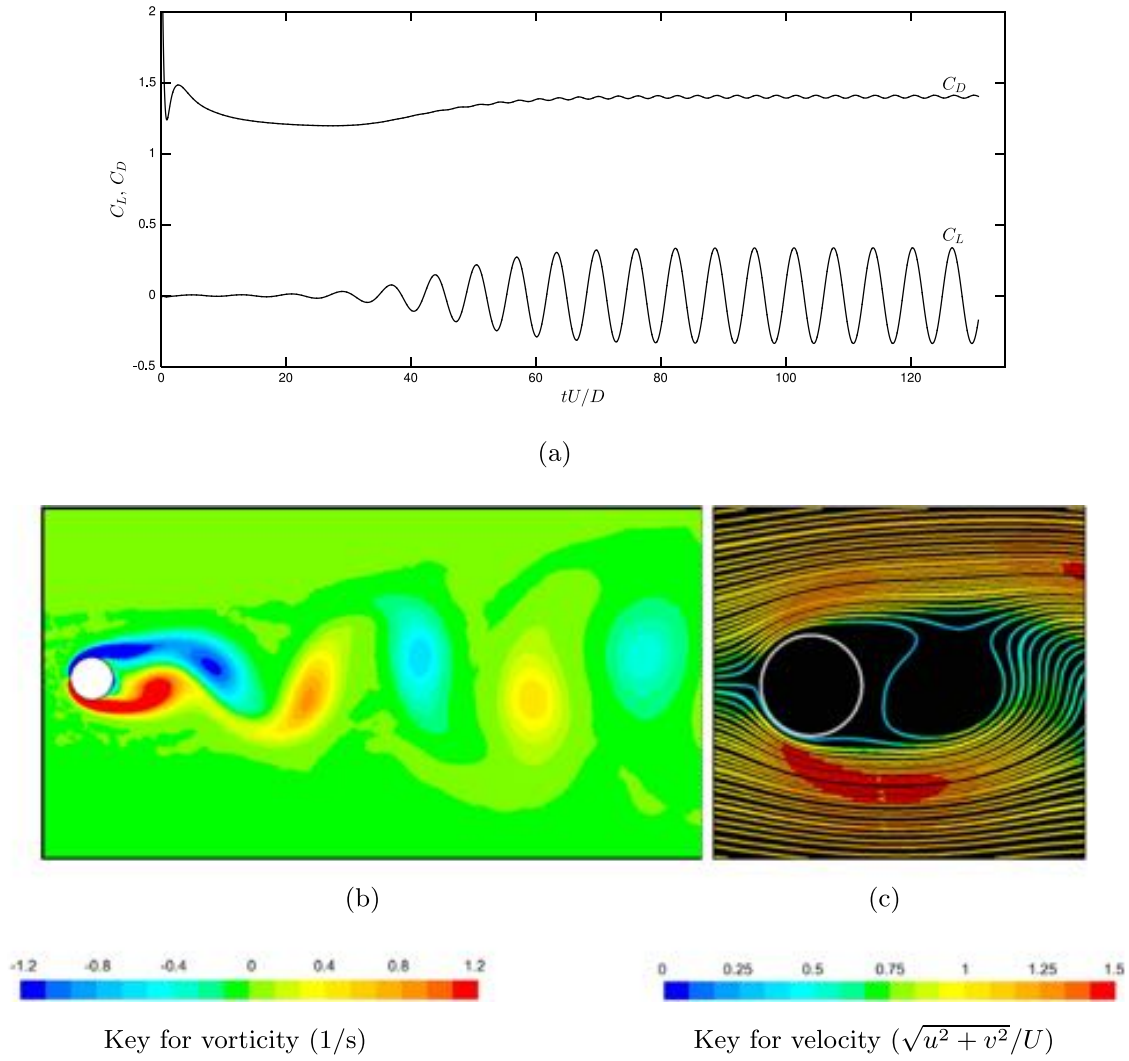


**Fig. 3.** (a) Time series of  $C_L$  and  $C_D$ , (b) instantaneous vorticity contours and (c) streamlines for the flow around a bare cylinder.

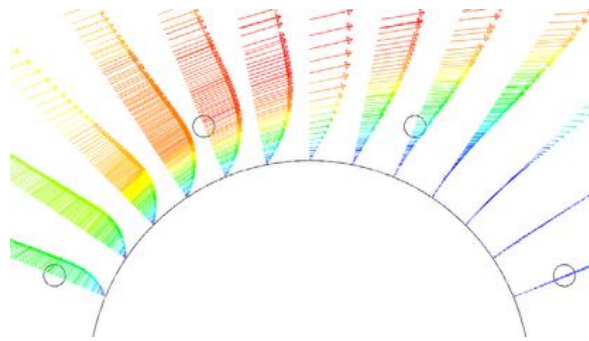


**Fig. 4.** Details of the velocity profile in the boundary layer around the bare cylinder (coloured by velocity magnitude; key in Fig. 3). Flow is from left to right.

highlighting the shear profile in the boundary layer and the eventual locations and diameter of the control cylinders (marked by the corresponding circles at  $G/D = 0.1$ ).

The rotation of the control cylinders ( $U_c/U$ ) was increased in steps. At the beginning of the simulation ( $tU/D = 0$ ),  $U_c/U$  was set to 0. Once a steady state regime of vortex shedding had been reached, the simulation would be left to run for several cycles of vortex shedding before the parameter was changed to the next step  $U_c/U = 1$ . Once more, after several cycles of established vortex shedding,  $U_c/U$  was increased to the next step, and so on, until  $U_c/U = 6$ . Following this method, a transient regime appeared after each change in  $U_c/U$ , the convergence time was reduced, but each simulation

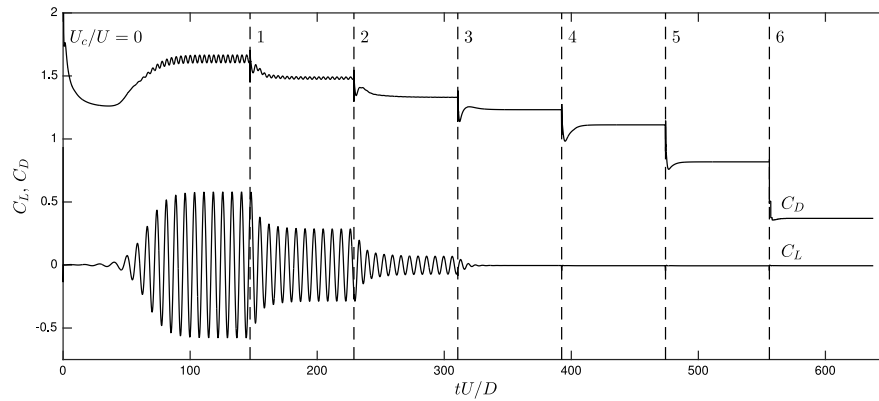


**Fig. 5.** Time series of  $C_L$  and  $C_D$  for a cylinder with 8 rotating control cylinders. Coefficients measured on the main cylinder alone.

carried information from the previous state. This procedure, also employed by Mittal (2001), produced the time series of  $C_D$  and  $C_L$  presented in Fig. 5, where the dashed lines mark the transitions in  $U_c/U$ .

Fig. 6 presents the instantaneous vorticity contours and the corresponding streamlines for the flow around a cylinder with 8 rotating control cylinders for  $U_c/U = 0$  to 6. At  $U_c/U = 0$  the wake pattern looked similar to that of a bare cylinder, as shown in Fig. 3, except that the presence of the 8 non-rotating control cylinders made the wake wider than that of the bare cylinder.

Reynolds number based on the diameter of the control cylinders was  $Re_c = 5$ , which was below the typical value of  $Re_c = 46$  from which shear layer instability should trigger the onset of vortex shedding for the individual control cylinders. Therefore, no independent vortex-shedding was observed from the control cylinders, hence the vortex wake was produced by the main and the control cylinders combined as a single body.

As shown by the streamlines, the region of separated flow (associated with the recirculation bubble) downstream of the main cylinder was reduced as  $U_c/U$  was increased. The strength of convected vortices also decreased as  $U_c/U$  increased at the same time that the vortex formation length was increased, showing that the separated shear layers were interacting further downstream to generate a weaker wake. Eventually for  $U_c/U \geq 3$ , the interaction between the separated shear layers was so much reduced that no alternating vortex shedding was noticed in the wake downstream of the main cylinder. This was also accompanied by a narrowing of the wake and a consequent increase in Strouhal number.

#### 4.3. Fluid forces

The suppression of the wake as  $U_c/U$  was increased was followed by changes in the fluid forces acting on the body, which was evident from the time series of  $C_L$  and  $C_D$  measured on the main cylinder alone (Fig. 5). The RMS of fluctuating lift coefficient decreased as the rotation of the control cylinders was increased. A periodic fluctuation of  $C_L$  was clear for  $U_c/U$  between 0 and 2, but disappeared for  $U_c/U \geq 3$  when vortex shedding was completely suppressed.

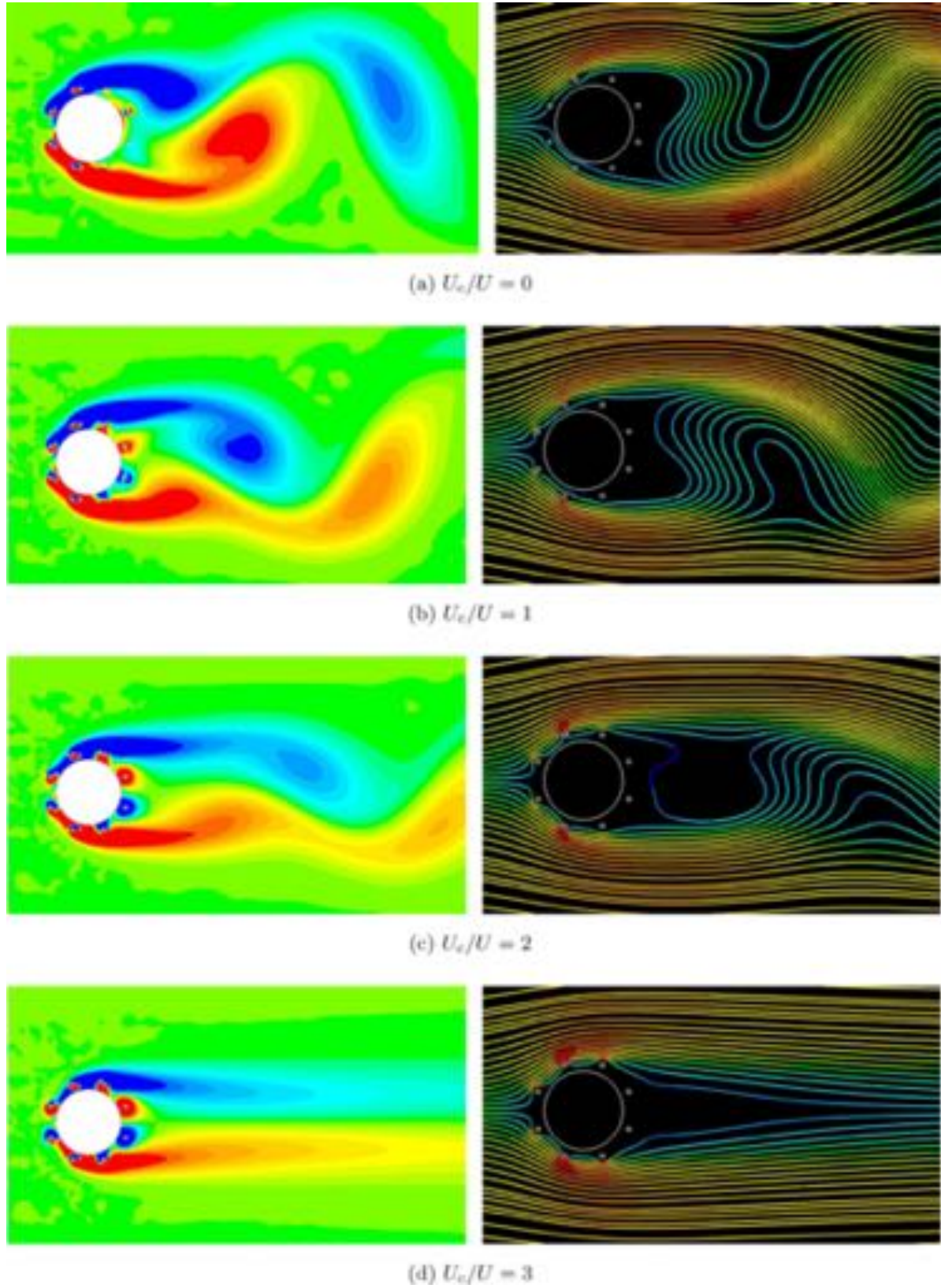
The drag coefficient followed the same behaviour. The mean drag coefficient was found to be  $\bar{C}_D = 2.1$  for  $U_c/U = 0$ , higher than that experienced by an isolated cylinder, since the presence of the static control cylinders contributed to the enhancement of the wake and increased drag on the main cylinder.  $\bar{C}_D$  was reduced as the wake got weaker for higher  $U_c/U$ . The minimum  $\bar{C}_D \approx 0.4$  (with  $\hat{C}_L \approx 0$ ) was obtained for  $U_c/U = 5$ , which was much lower than the  $\bar{C}_D = 1.4$  found for the bare cylinder (Fig. 3(a)). For the highest  $U_c/U = 6$ , the system reached the lowest drag recorded at  $\bar{C}_D \approx 0.37$  (considerably below that of the bare cylinder), but a local minimum value may still be waiting ahead.

Fig. 7(a) presents the mean drag coefficient ( $\bar{C}_D$ ) compared with the reference  $\bar{C}_D = 1.40$  for that of the bare cylinder. White symbols refer to coefficients measured on the main cylinder alone, while black symbols refer to the system as a whole (main cylinder plus wake-control cylinders). When  $\bar{C}_D$  was measured on the whole system (black symbols) a very interesting behaviour stood out: for higher  $U_c/U$  the whole system was able to achieve considerably less drag than the main cylinder alone. In fact, for the case at  $U_c/U = 6$  the mean drag was even found to be negative ( $\bar{C}_D \approx -0.1$ ). The interaction of the rotating control cylinders with the flow past the main body generated force in the opposite direction of the incoming flow. While the main cylinder was always under positive drag, the force on the control cylinders can balance or overtake that of the main body, generating a net negative drag (a small propulsion, or thrust) for the whole system.

So far, it is impossible to conclude if the total  $\bar{C}_D$  will continue to drop for higher rotation speeds. But the fact that the rotating cylinders were not only able to reduce but to overcome the overall drag of the system is quite remarkable. Nevertheless, we conclude that the negative term of the total drag was indeed coming from the rotating control cylinders.

Now turning to the absolute mean lift coefficient in Fig. 7(b). Since the cylinders on opposite sides of the body were rotating at opposite directions – and since positive  $C_L$  is defined in the cross-flow direction pointing upwards in Fig. 1 –





**Fig. 6.** Instantaneous vorticity contours (left column) and corresponding streamlines (right column) of the flow around a cylinder with 8 rotating control cylinders ( $U_c/U = 0$  to 6). Coloured by vorticity and velocity magnitude, respectively.

we shall consider the absolute value of lift. Fig. 7(b) presents lift also divided in two terms: for the main cylinder alone and for the absolute portion acting on the control cylinders (therefore  $|\bar{C}_L|$ ).

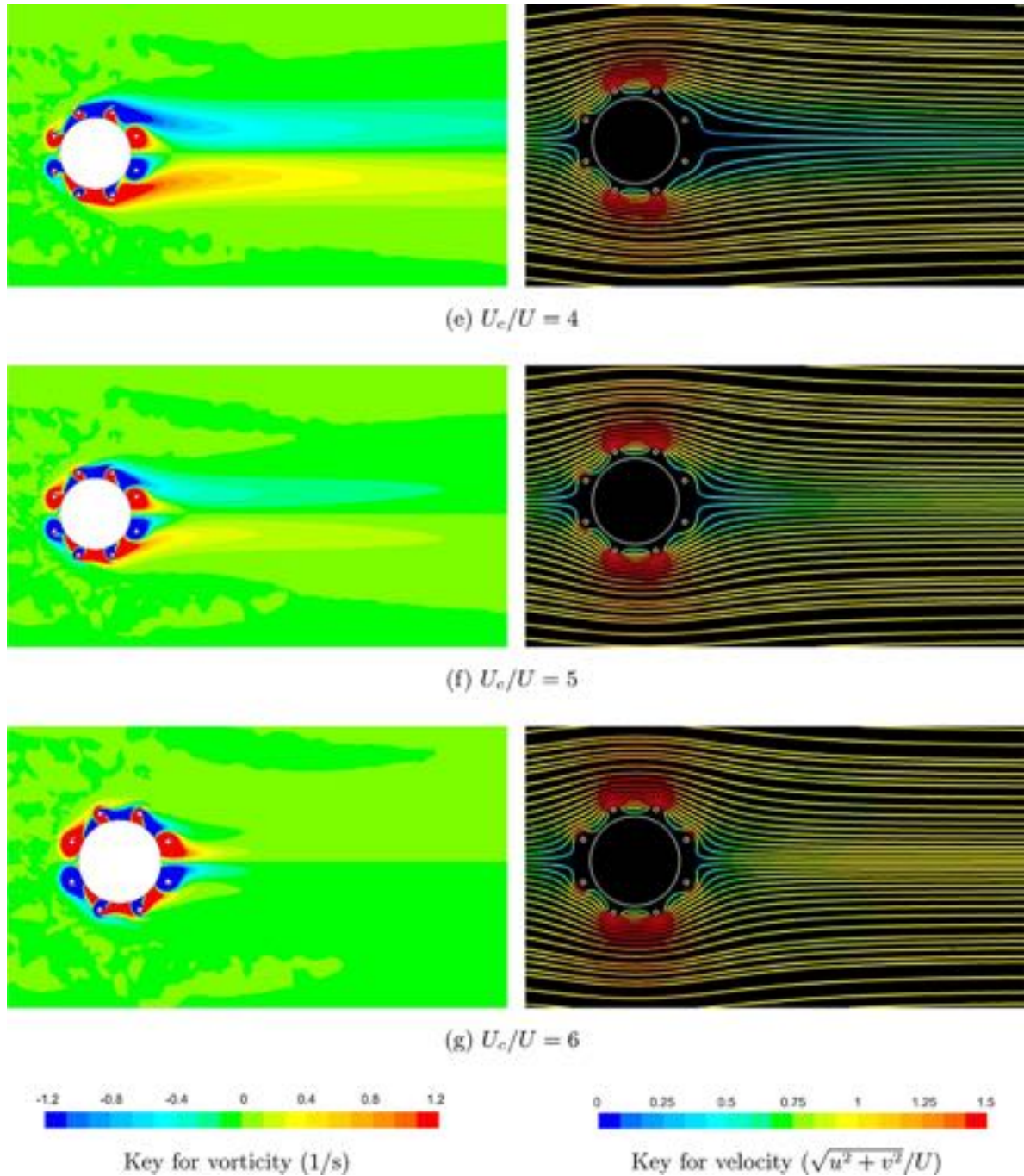


Fig. 6. (continued).

As expected, the main cylinder alone presented  $\bar{C}_L \approx 0$  due to the symmetry of the flow. (Any difference from zero was due to not having an integer number of cycles while taking the average of the time series.) The control cylinders, on the other hand, appeared to sum up a rather high value of  $|\bar{C}_L|$ , which increased continuously with  $U_c/U$ . The four control cylinders on the top side of the main cylinder produced a net lift pushing upwards; the four control cylinders on the bottom side produce a net lift of the same magnitude pushing downwards. For this reason,  $|\bar{C}_L|$  is presented in Fig. 7(b) as referring to the mean value of the cylinders on each side of the main body. If both terms were to be added, the net lift on the top side would cancel out the net lift on the bottom side, hence the total lift experienced by the whole system would also be  $\bar{C}_L \approx 0$ , as seen in Fig. 7(b).

It was shown that the 8 wake-control cylinders were indeed experiencing a considerable amount of fluid forces, either to generate negative drag or to generate lift pointing away from the centreline of the wake. A control strategy could take advantage of this net lift by rotating only the control cylinders on one side of the body, for example, to produce lift to maneuver the system. More advanced control strategies could consider the independent rotation of the control cylinders

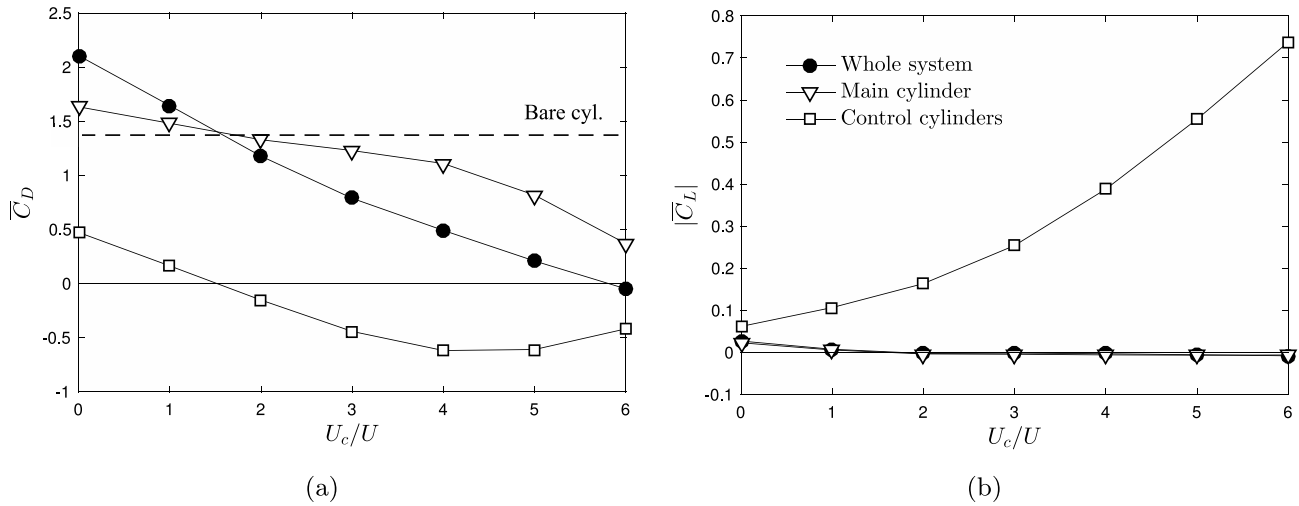


Fig. 7. (a) Mean drag and (b) absolute mean lift for the case with 8 control cylinders.

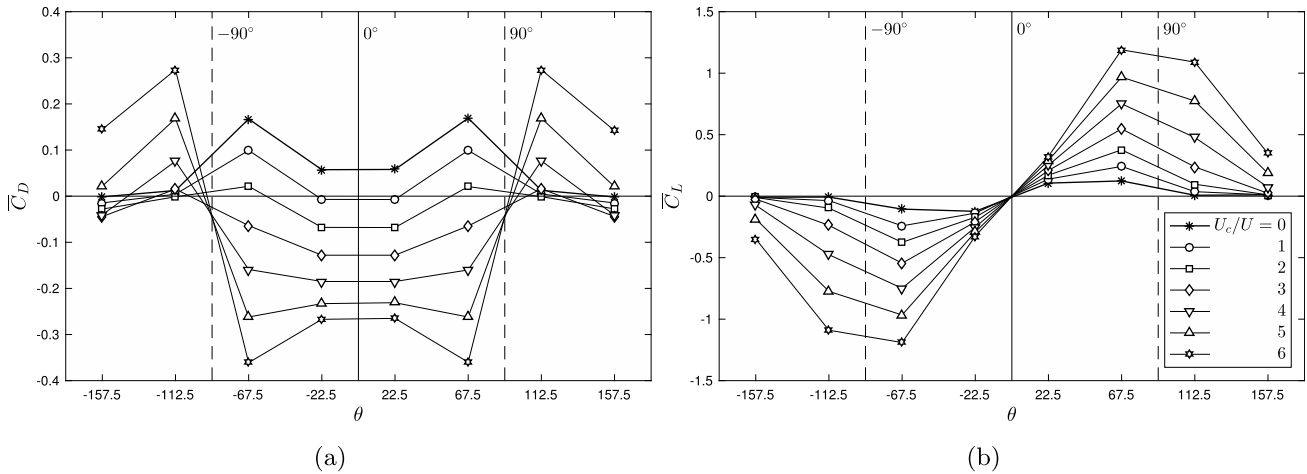


Fig. 8. Contribution of each control cylinder to the total (a) drag and (b) lift of the system.

to generate a useful force in a desired direction. To pave the way, we shall now investigate the contribution of each control cylinder independently.

#### 4.4. Force acting on each control cylinder

Fig. 8 presents the mean drag and mean lift coefficients measured for each of the 8 control cylinders around the main body for various rotation speeds. The angular position ( $\theta$ ) of the control cylinders is that shown in Fig. 1.

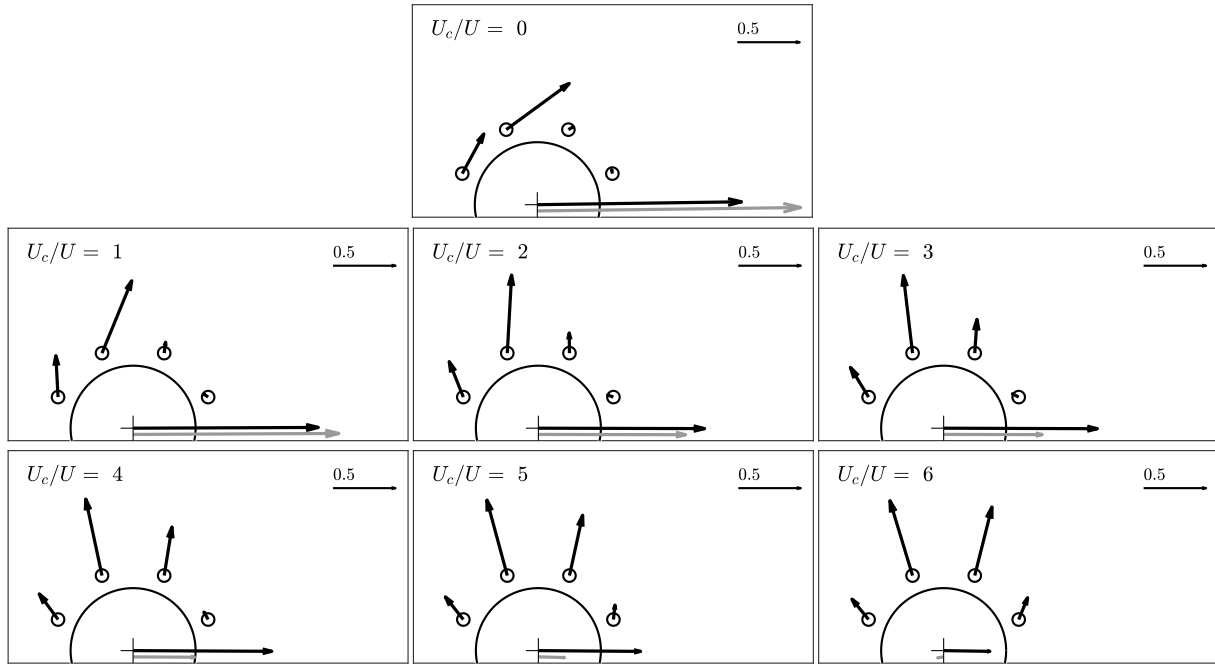
When  $U_c/U = 0$  none of the control cylinders experienced negative drag (Fig. 8(a)). But as soon as they started to rotate some of the control cylinders contributed with negative drag, especially those located at the front of the body (between the  $\pm 90^\circ$  dashed lines) where the flow had not yet separated. For the highest  $U_c/U = 6$  the control cylinders located at the front produced so much negative drag that they were able to balance off the positive drag experienced by the other control cylinders and the main cylinder. It becomes clear that the control cylinders located at  $\pm 67.5^\circ$  were the ones that contributed the most to reduce the total drag of the system. The next cylinders downstream, located at  $\pm 112.5^\circ$ , interacted with the separated shear layers and produce positive drag for most cases.

Fig. 8(b) presents the contribution of each cylinder towards lift. It is clear that all cylinders on the top side of the body produced positive lift (pointing upwards), while all cylinders on the bottom side produce negative lift. The control cylinders located at  $\pm 67.5^\circ$  were the ones with the strongest lift, reaching  $|\bar{C}_L| \approx 1.2$  for the highest rotation of  $U_c/U = 6$ .

Finally, Fig. 9 presents the resultant force in terms of a vector diagram for each of the 8 control cylinders for  $U_c/U = 0$  to 6. The resultant vector for the forces measured on the main cylinder alone are also presented as a black arrow at the centre of the main body. The grey arrow represents the resultant vector for the system as a whole.

At  $U_c/U = 0$  the control cylinders generated positive drag, except for the cylinder immersed in the recirculation region of the near wake. Adding that to the drag of the main cylinder results in the highest value of  $\bar{C}_D$  experienced by the system.





**Fig. 9.** Resultant force coefficients (shown as vector diagrams) on each control cylinder, main cylinder alone (black arrow) and the system as a whole (grey arrow). Direction of the flow is from left to right.

As  $U_c/U$  was increased the drag of the main cylinder was gradually reduced, and drag on the control cylinders (especially on those at the front) became negative, reducing  $\bar{C}_D$  of the whole system until it got negative for  $U_c/U = 6$ .

As vortex-shedding was eliminated for  $U_c/U \geq 3$  the direction of the resultant vectors of the control cylinders did not change much, but they only increased their magnitude with increasing rotation speed. Such a large lift-to-drag ratio could prove to be useful for other control applications such as dynamic positioning of offshore floating units.

#### 4.5. Driving power

One final important question regards the amount of energy spent to rotate the control cylinders compared with the energy saved due to drag reduction. Following the model for energy efficiency proposed by [Shukla and Arakeri \(2013\)](#), the power  $P_n$  needed to rotate a single control cylinder at a tangential velocity  $U_c$  is that required to overcome the total effect of shear stresses on its wall, which is integrated around the diameter  $d$ , hence

$$P_n = U_c \frac{d}{2} \int_0^{2\pi} \tau_{\theta_c} d\theta_c, \quad (4)$$

where  $\tau_{\theta_c}$  is the local shear stress on the wall of the control cylinder. Adding up the contributions of all the  $N$  control cylinders results in

$$C_N = \sum_n \frac{P_n}{\rho U^3 D/2}, \quad (5)$$

the coefficient of power spent to rotate all the control cylinders of a system at the same tangential velocity  $U_c$ .

Finally, the total power-loss coefficient

$$C_{PL} = \bar{C}_D + C_N \quad (6)$$

of the system is simply obtained by adding the total drag of the system ( $\bar{C}_D$ ) to the energy spent to rotate the  $N$  control cylinders ( $C_N$ ). In general terms, the power-loss coefficient is a means to evaluate the energy efficiency of the system regarding the amount of energy spent to drive the control cylinders and the energy lost due to the drag the system generates.

[Fig. 10](#) presents  $C_{PL}$  decomposed in  $C_N$  and  $\bar{C}_D$  as a function of  $U_c/U$ . As expected, for non-rotating control cylinders ( $U_c/U = 0$ ) all the power-loss of the system was due to drag, which was slightly higher than that experienced by a bare cylinder. As rotation speed was increased, an increasing fraction of the power was lost to the rotation of the control cylinders, but the resulting reduction of the overall  $\bar{C}_D$  dominates the behaviour of  $C_{PL}$ .

Coincidentally or not, it is interesting to note that the condition for the suppression of vortex shedding (shaded area in [Fig. 10](#)) is somewhat related to when  $C_N$  is greater than  $\bar{C}_D$ . Nevertheless, the minimum  $C_{PL}$  for when suppression is

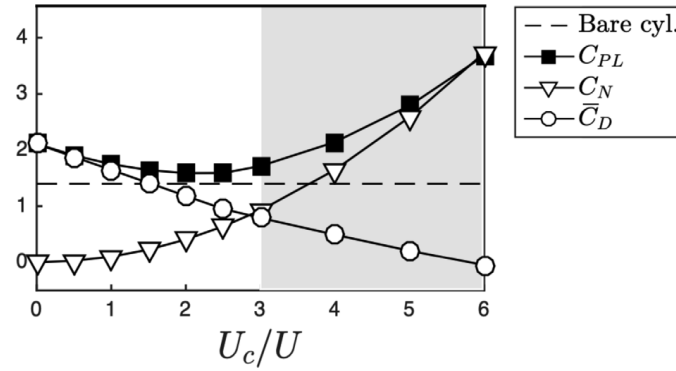


**Fig. 10.** Decomposition of the power-loss coefficient ( $C_{PL}$ ). Area shaded in grey represents when vortex shedding was suppressed. The horizontal, dashed lines represent  $\bar{C}_D = 1.4$  for a bare cylinder.

achieved (at  $U_c/U = 3$ ) is still greater than the mean drag for a bare cylinder, at least for this specific condition of  $Re$ ,  $G/D$ ,  $d/D$ , etc.

As examples, consider two applications: (1) If the objective is to suppress the fluctuating forces caused by vortex shedding with minimal energy input,  $U_c/U$  would be set around 3. (2) But if the objective is to minimise drag (or maybe generate useful thrust) at the cost of spending more energy, than the user would set higher rotation speeds.

## 5. Final remarks

Two-dimensional simulations of the flow offer a simplified view of the phenomena occurring in the wake, which is indeed much more complex and rich in three-dimensionalities, as carefully exposed by Williamson (1996). A parametric investigation, however, would be extremely expensive in terms of the computational effort required to model the three-dimensional flow at higher  $Re$  (Assi et al., 2018, for example). Therefore, simplified simulations still hold their place as a powerful and feasible tool to understand the hydrodynamic mechanisms at the beginning of the instabilities ( $Re = 100$ ). Perhaps the most useful point in the present study is that it helps us to formulate the correct questions concerning wake stability and flow control in such a simple geometry, but with too many parameters in hand.

Now, thinking in terms of practical applications (especially related to offshore and wind engineering), there are situations in which fitting 8 control cylinders is better (or actually necessary) than fitting only 2 or 4. If the direction of the incoming flow is not known or changes with time, for example, a system with 8 control cylinders would appear to be “more omnidirectional” to the flow than the previous cases. Of course a case with 16 control cylinders would be hypothetically even “more omnidirectional” (keeping this term with quotation marks as omnidirectionality is not quantifiable), but that would be just another step in one of the significant parameters.

Of course there are infinite possibilities to arrange the rotating control cylinders around the main cylinder. The present work was never intended to find an optimal solution, but simply to be a parametric study. (Refer to Patino et al. (2015) and Meliga et al. (2014) for good optimisation studies regarding the location of interfering control cylinders.) Our initial restriction, however, was to reduce the number of geometric parameters for axisymmetric arrays of control cylinders. The universe of parameters for an optimisation study is so vast that a robust optimisation method must be considered to tackle the problem. With as many significant parameters identified in this work ( $N$ ,  $d/D$ ,  $G/D$ ,  $U_c/U$ , angle of incidence in relation to the upcoming flow) as those not concerned in the investigation (control cylinders do not need to have the same diameter, or to be equally spaced, or to rotate at the same speed and direction, or to be at same distance from the centre...), one may see the possibilities are endless, making it a very exciting, non-linear problem for someone focusing on optimisation.

## 6. Conclusion

In the present work, the flow control past a circular cylinder surrounded by 8 rotating wake-control cylinders has been studied by means of numerical simulations at  $Re = 100$ . The control cylinders were able to suppress the vortex shedding mechanism of the main cylinder for rotations greater than  $U_c/U = 3$ .

Drag on the system was reduced as a consequence of the elimination of the Karman vortex street, but it appeared that a local minimum was not reached yet within the range of this investigation. Mean drag experienced by the control cylinders can be negative and, for higher rotation speeds, stronger in magnitude than the positive drag experienced by the main body. Indeed, the lowest drag of  $\bar{C}_D \approx -0.1$  was observed for  $U_c/U = 6$ . It is not clear if  $\bar{C}_D$  tends toward a minimum value or will it keep decreasing with increasing rotation speeds. On the other hand, the power spent to rotate the 8 control cylinders appear to be higher than the power loss associated with the mean drag of the bare cylinder.

The control cylinders also experience high lift, what can be useful if a control strategy requires to control the lateral force on the body. Such forces originate in the interaction of certain control cylinders with the attached boundary layers.



The two-dimensional computations set an upper bound on the control effectiveness of the rotating cylinders. It is expected that the actual behaviour of such open-loop control strategies will depend significantly on three-dimensional effects and Reynolds number (among other factors). Future numerical and experimental investigation should concentrate on that.

## Acknowledgements

MSO and RMO are grateful to CAPES Brazilian Ministry of Education. GRSA acknowledges the support of FAPESP, Brazil (2011/00205-6, 2014/50279-4), CNPq, Brazil (306917/2015-7) and the Brazilian Navy.

## References

- Assi, G.R.S., Bearman, P.W., Kitney, N., 2009. Low drag solutions for suppressing vortex-induced vibration of circular cylinders. *J. Fluids Struct.* 25, 666–675.
- Assi, G.R.S., Bearman, P.W., Kitney, N., Tognarelli, M., 2010. Suppression of wake-induced vibration of tandem cylinders with free-to-rotate control plates. *J. Fluids Struct.* 26, 1045–1057.
- Assi, G.R.S., Orselli, R.M., Silva-Ortega, M., 2018. Suppression of vortex shedding with rotating wake-control cylinders: numerical investigation at a moderate Reynolds number. In: ASME (Ed.), Proceedings of OMAE 37th International Conference on Ocean, Offshore and Arctic Engineering, No. OMAE2018-78316.
- Barth, T.J., Jespersen, D.C., 1989. The design and application of upwind schemes on unstructured meshes, AIAA PAPER 89-0366.
- Bearman, P.W., 1984. Vortex shedding from oscillating bluff bodies. *Annu. Rev. Fluid Mech.* 16, 195–222.
- Behr, M., Hastreiter, D., Mittal, S., Tezduyar, T., 1995. Incompressible flow past a circular cylinder: dependence of the computed flow field on the location of the lateral boundaries. *Comput. Methods Appl. Mech. Engrg.* 123 (1), 309–316.
- Blanchard, A., Bergman, L.A., Vakakis, A.F., 2019. Nonlinear Dyn. <http://dx.doi.org/10.1007/s11071-019-04775-3>.
- Cattafesta, L., Sheplak, M., 2011. Actuators for active flow control. *Annu. Rev. Fluid Mech.* 43, 247–272.
- Choi, H., Jeon, W.-P., Kim, J., 2008. Control of flow over a bluff body. *Annu. Rev. Fluid Mech.* 40, 113–139.
- Gad-El-Hak, M., 2000. Flow Control: Passive, Active, and Reactive Flow Management. Cambridge University Press.
- Gerrard, J., 1966. The mechanics of the formation region of vortices behind bluff bodies. *J. Fluid Mech.* 25, 401–413.
- Goodarzi, M., Dehkordi, E.K., 2017. Geometrical parameter analysis on stabilizing the flow regime over a circular cylinder using two small rotating controllers. *Comput. & Fluids* 145, 129–140.
- Jimenez-Gonzalez, J.I., Huera-Huarte, F.J., 2017. Experimental sensitivity of vortex-induced vibrations to localized wake perturbations. *J. Fluids Struct.* 74, 53–63.
- Korkischko, I., Meneghini, J., 2012. Suppression of vortex-induced vibration using moving surface boundary-layer control. *J. Fluids Struct.* 34, 259–270.
- Meliga, P., Boujo, E., Pujals, G., Gallaire, F., 2014. Sensitivity of aerodynamic forces in laminar and turbulent flow past a square cylinder. *Phys. Fluids* 26 (104101).
- Meneghini, J., Saltara, F., Siqueira, C., Ferrari, J., 2001. Numerical simulation of flow interference between two circular cylinders in tandem and side-by-side arrangements. *J. Fluids Struct.* 15 (2), 327–350.
- Mittal, S., 2001. Control of flow past bluff bodies using rotating control cylinders. *J. Fluids Struct.* 15 (2), 291–326.
- Mittal, S., 2003. Flow control using rotating cylinders: effect of gap. *J. Appl. Mech.* 70 (5), 762–770.
- Mittal, S., Raghuvanshi, A., 2001. Control of vortex shedding behind circular cylinder for flows at low Reynolds numbers. *Internat. J. Numer. Methods Fluids* 35 (4), 421–447.
- Modi, V., 1997. Moving surface boundary-layer control: a review. *J. Fluids Struct.* 11 (6), 627–663.
- Muddada, S., Patnaik, B., 2010. An active flow control strategy for the suppression of vortex structures behind a circular cylinder. *Eur. J. Mech. B/Fluids* 29 (2), 93–104.
- Norberg, C., 2003. Fluctuating lift on a circular cylinder: review and new measurements. *J. Fluids Struct.* 17, 57–96.
- Patino, G., Silva-Ortega, M., Gioria, R.S., Assi, G.S.R., Meneghini, J.R., 2015. Investigation of circular cylinder VIV passive control device using flow sensitivity analysis. In: 6th International Symposium on Bifurcations and Instabilities in Fluid Dynamics - BIFD2015.
- Patnaik, B., Wei, G., 2002. Controlling wake turbulence. *Phys. Rev. Lett.* 88, 1–4.
- Rajani, B., Kandasamy, A., Majumdar, S., 2009. Numerical simulation of laminar flow past a circular cylinder. *Appl. Math. Model.* 33, 1228–1247.
- Rashidi, S., Hayatdavoodi, M., Esfahani, J.A., 2016. Vortex shedding suppression and wake control: A review. *Ocean Eng.* 126, 57–80.
- Schulmeister, J., 2012. Flow separation control with rotating cylinders (Master's thesis, ). Massachusetts Institute of Technology.
- Schulmeister, J.C., Dahl, J.M., Weymouth, G.D., Triantafyllou, M.S., 2017. Flow control with rotating cylinders. *J. Fluid Mech.* 825, 743–763.
- Shukla, R.K., Arakeri, J.H., 2013. Minimum power consumption for drag reduction on a circular cylinder by tangential surface motion. *J. Fluid Mech.* 715, 597–641.
- Silva-Ortega, M., 2015. Suppression of vortex-induced vibration of a circular cylinder with fixed and rotating control cylinders (Master's thesis, ). Universidade de São Paulo.
- Silva-Ortega, M., Assi, G.R.S., 2017a. Flow-induced vibration of a circular cylinder surrounded by two, four and eight wake-control cylinders. *Exp. Therm Fluid Sci.* 85, 354–362.
- Silva-Ortega, M., Assi, G.R.S., 2017b. Suppression of the vortex-induced vibration of a circular cylinder surrounded by eight rotating wake-control cylinders. *J. Fluids Struct.* 74, 401–412.
- Silva-Ortega, M., Assi, G.R.S., 2018. Hydrodynamic loads on a circular cylinder surrounded by two, four and eight wake-control cylinders. *Ocean Eng.* 153, 345–352.
- Strykowski, P.J., Sreenivasan, K.R., 1990. On the formation and suppression of vortex shedding at low Reynolds numbers. *J. Fluid Mech.* 218, 71–107.
- Versteeg, H.K., Malalasekera, W., 2007. An Introduction to Computational Fluid Dynamics: The Finite Volume Method. Pearson Education.
- Williamson, C.H.K., 1996. Vortex dynamics in the cylinder wake. *Annu. Rev. Fluid Mech.* 28 (1), 477–539.
- Wu, H., Sun, D., Lu, L., Teng, B., Tang, G., Song, J., 2012. Experimental investigation on the suppression of vortex-induced vibration of long flexible riser by multiple control rods. *J. Fluids Struct.* 30, 115–132.
- Young, D., Huang, J., Eldho, T., 2001. Simulation of laminar vortex shedding flow past cylinders using a coupled BEM and FEM model. *Comput. Methods Appl. Mech. Engrg.* 190 (45), 5975–5998.
- Zdravkovich, M.M., 1981. Review and classification of various aerodynamic and hydrodynamic means for suppressing vortex shedding. *J. Wind Eng. Ind. Aerodyn.* 7, 145–189.
- Zhu, H., Gao, Y., 2017. Vortex-induced vibration suppression of a main circular cylinder with two rotating control rods in its near wake: effect of the rotation direction. *J. Fluids Struct.* 74, 469–491.
- Zhu, H., Yao, J., Ma, Y., Zhao, H., Tang, Y., 2015. Simultaneous CFD evaluation of VIV suppression using smaller control cylinders. *J. Fluids Struct.* 57, 66–80.



Contents lists available at ScienceDirect

Journal of Wind Engineering &amp; Industrial Aerodynamics

journal homepage: [www.elsevier.com/locate/jweia](http://www.elsevier.com/locate/jweia)

# Computational study on an Ahmed Body equipped with simplified underbody diffuser

Filipe F. Buscariolo<sup>a,\*</sup>, Gustavo R.S. Assi<sup>b</sup>, Spencer J. Sherwin<sup>c,\*\*</sup>

<sup>a</sup> Imperial College London, NDF-USP, McLaren Racing, United Kingdom

<sup>b</sup> NDF-USP, Brazil

<sup>c</sup> Imperial College London, United Kingdom

## ARTICLE INFO

### Keywords:

Spectral/hp element method  
ILES/uDNS simulations  
Automotive aerodynamics  
Diffusers  
Ahmed body  
High-fidelity CFD  
High-order methods

## ABSTRACT

The Ahmed body is one of the most studied 3D automotive bluff bodies and the variation of its slant angle of the rear upper surface generates different flow behaviours, similar to a standard road vehicles. In this study we extend the geometrical variation to evaluate the influence of a rear underbody diffuser which are commonly applied in high performance and race cars to improve downforce. Parametric studies are performed on the rear diffuser angle of two baseline configurations of the Ahmed body: the first with a 0° upper slant angle and the second with a 25° slant angle. We employ a high-fidelity CFD simulation based on the spectral/hp element discretisation that combines classical mesh refinement with polynomial expansions in order to achieve both geometrical refinement and better accuracy. The diffuser length was fixed to the same length of 222 mm similar to the top slant angle that have previously been studies. The diffuser angle was changed from 0° to 50° in increments of 10° with an additional case considering the angle of 5°. The proposed methodology was validated on the classical Ahmed body considering 25° slant angle, found a difference for drag and lift coefficients of 13% and 1%, respectively. For the case of an 0° slant angle on the upper surface the peak values for drag and negative lift (downforce) coefficient were achieved with a 30° diffuser angle, where the flow is fully attached with two streamwise vortical structures, analogous to results obtained from [1] but with the body flipped upside down. For diffuser angles above 30°, flow is fully separated from the diffuser. The Ahmed body with 25° slant angle and a diffuser achieves a peak value for downforce at a 20° diffuser angle, where the flow on the diffuser has two streamwise vortices combined with some flow separation. The peak drag value for this case is at 30° diffuser angle, where the flow becomes fully separated.

## 1. Introduction

Among the standard automotive bluff bodies in literature, the most studied one is the Ahmed body, firstly proposed by Ahmed (Ahmed et al., 1984). It is based on the geometry designed by Morel (1978), with the main dimensions highlighted in Fig. 1. The proposed geometry of the Ahmed body aims to reproduce the main features of road vehicles, such as the frontal stagnation, ground effect and well-defined separation points.

The most emblematic characteristic of the Ahmed Body is a angled upper back section with fixed length, here referred as slant, on the upper rear portion, allowing the simulation of different automotive body styles. According to (Huminic and Huminic, 2010), it has been shown that the

flow over the slanted surface back section is dependent on specific inclination angle. Two critical angles, at 12.5° and 30° have been observed, in which the flow structure changes significantly, and where a change of curvature of the drag coefficient is also evident. For angles below 12.5°, the airflow over the slant remains fully attached before separating from the model when it reaches the rear of the body. The flow from the angled section and the side walls produces a pair of counter rotating vortices, which then persist downstream.

For angles between 12.5° and 30°, the flow over the slant becomes highly complex. Two counter-rotating lateral vortices are shed from the sides of the angled section with increased size, which affects the flow over the whole back end, specially the previously existing three-dimensional wake. These vortices are also responsible for maintaining

\* Corresponding author.

\*\* Corresponding author.

E-mail addresses: [f.fabian-buscariolo16@imperial.ac.uk](mailto:f.fabian-buscariolo16@imperial.ac.uk) (F.F. Buscariolo), [g.assi@usp.br](mailto:g.assi@usp.br) (G.R.S. Assi), [s.sherwin@imperial.ac.uk](mailto:s.sherwin@imperial.ac.uk) (S.J. Sherwin).

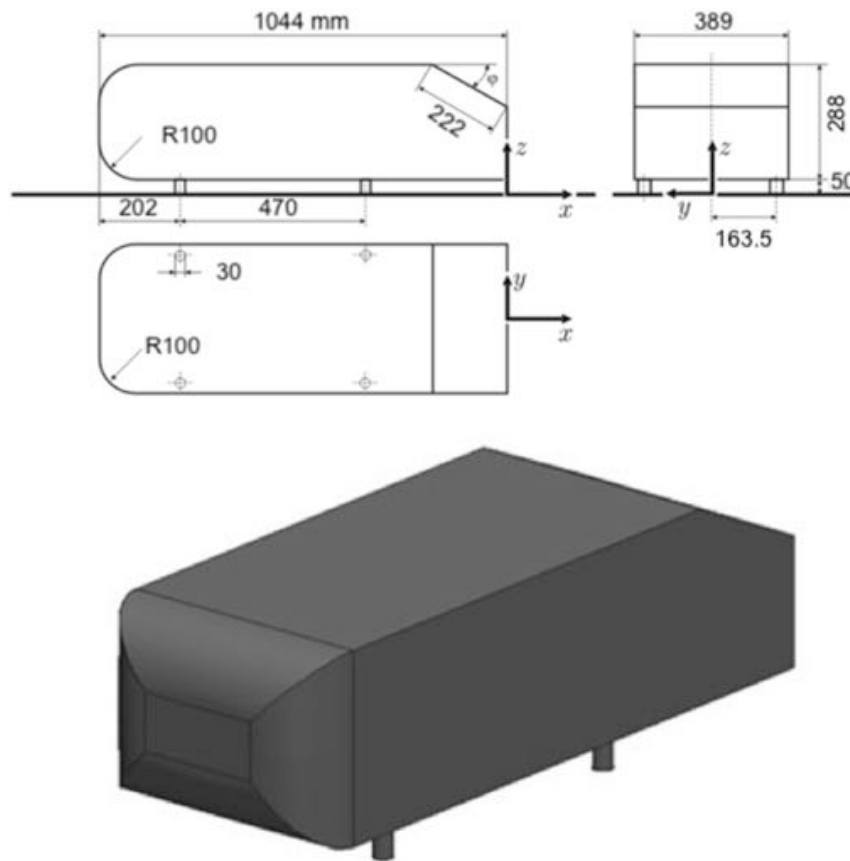


Fig. 1. Ahmed body schematic drawing. The upper slant length of 222 mm is fixed, independent of its inclination angle  $\phi$ .

attached flow over the rest of the angled surface up to a slant angle of  $30^\circ$ , and it has been shown that they are extended up to half of the length of the model beyond the trailing edge, as discussed in (Strachan et al., 2007) and (Lienhart and Becker, 2003). Close to the second critical angle, a separation bubble is also formed over the inclined slant. The flow separates from the body, but re-attaches before reaching the vertical back section.

Above a  $30^\circ$  slant angle, the flow over the or slant is fully separated. However there is a weak tendency of the flow to turn around the side of the model, as a result of the relative separation positions of the flow over model top and those over the slant side edges. When the flow is in this state, a near constant pressure is found across that region. To characterize all three flow configurations here discussed, representative slant angles are commonly used in literature with  $0^\circ$  (or squared-backed),  $25^\circ$  and  $35^\circ$ .

The first experimental study on Ahmed Body (Ahmed et al., 1984) was with static floor conditions, considering a Reynolds number  $Re = 4.29 \times 10^6$  based on its full length. In this study, results for the drag coefficient were obtained for different slant angles, ranging from  $0^\circ$  to  $40^\circ$ , in increments of  $5^\circ$  with an additional measurement at  $12.5^\circ$ . Due to limitations on the wind tunnel setup, only drag force measurements and a few flow visualization test were performed. In order to better understand the flow phenomena and turbulence structures around the model, a complementary study was performed by (Lienhart and Becker, 2003) using laser Doppler anemometry (LDA), hot-wire anemometry (HWA) and static pressure measurements.

Aiming to reproduce realistic road conditions and understand the phenomena associated to flow fields close to the ground, the authors of (Strachan et al., 2007) performed an Ahmed Body wind tunnel test using moving ground and acquired both the aerodynamic forces and the flow characteristics by employing time-averaged LDA. The flow conditions were also slightly different from the ones used on Ahmed's first test, since

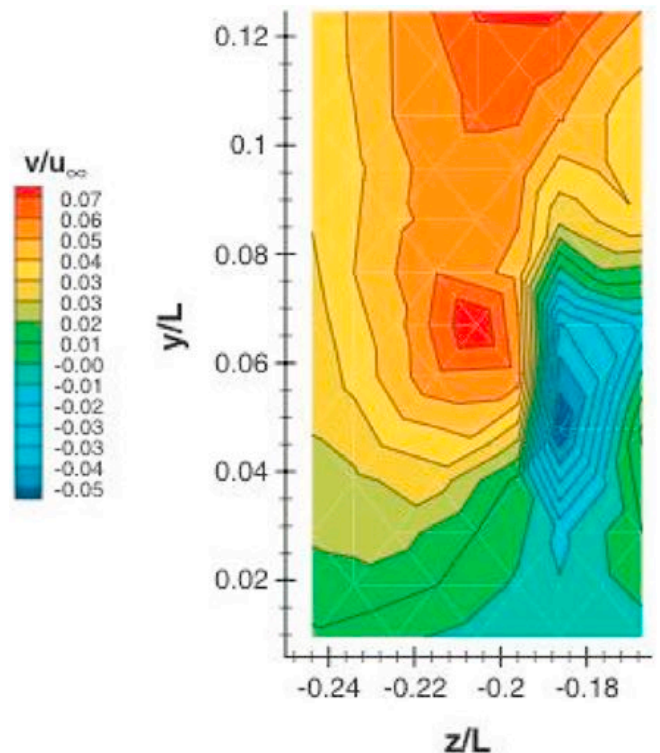


Fig. 2. Normalized V velocity on a squared-back Ahmed Body at  $x/L = 0.048$ . Reproduction from (Strachan et al., 2007).

it had a Reynolds number of  $Re = 1.7 \times 10^6$ . Nevertheless, similar flow behaviour were observed on the slant, despite the quantitative results being slightly different. One of the most interesting features found in this flow visualization results is the lower vortex system, a pair of vortices that appears close to the ground interface, which were absent in the fixed-ground studies. According to (Strachan et al., 2007), this could be attributed to the interference caused by the four studs used to support the model on the floor. Fig. 2 illustrates this phenomenon on an Ahmed Body with a squared-back.

An important development in automotive industry directly associated with the flow near the ground is the introduction of underbody diffusers, initially for high performance race vehicles with relatively low ground clearance. By providing a smoother transition from the underbody flow to the base of the car body, the strength of the rear wake can be reduced, contributing to drag reduction. In addition, it was found that at slightly inclined angles, the underbody diffuser also increases the downforce generated, assisting the acceleration and handling.

To explore detailed features of the near-ground vortices, and to examine the potential benefits of implementing underbody diffusers, we propose a series of computational studies considering same simulation conditions as the experiment from (Strachan et al., 2007), with moving ground. The Ahmed bodies used in the study are the squared-back and the slant angle of  $25^\circ$ , representing respectively estate car/station-wagons (attached flow) and performance cars (vortex generation with flow detachment). The length of the underbody diffuser is set to be the same as the classic Ahmed body slant length, with angles ranging from  $10^\circ$  to  $50^\circ$ , in increments of  $10^\circ$ . An additional case also considers a diffuser angle of  $5^\circ$ , a setting commonly found in racing vehicles. This study focus essentially on the aerodynamic quantities on the Ahmed body, as well as, on the flow structures on its geometry, such as the vortices on the slant and diffuser.

CFD has become an underpinning technology for most automotive companies to reduce development times and costs. Since the Ahmed Body is a widely studied bluff body, it has become a test case to validate new CFD codes, specially for applications in the automotive industry. Lower vortices observed by (Strachan et al., 2007) were not present in CFD simulation studies with fixing studs modelled. They were first observed by (Krajnović and Davidson, 2004), where an Ahmed Body with slant angle of  $25^\circ$  was simulated without the fixing studs. Nevertheless, the location where these vortices are generated and possible interactions with underbody components were not highlighted.

We utilise a high fidelity spectral/hp element method simulation using under-resolved direct numerical simulation (uDNS) also known as implicit large eddy simulation (iLES) ((Grinstein et al., 2007)). The spectral/hp elemental method combines the advantages of higher accuracy and rapid convergence from the spectral (p) methods, while maintaining the flexibility of the classical finite element (h) complex meshes, allowing unsteady vortical flows around geometries to be effectively captured. We present the validation of the proposed numerical methodology on the classical Ahmed body with  $25^\circ$  slant angle, as in the study of (Buscariolo et al., 2020). The Ahmed body with  $25^\circ$  slant angle, although in the pre-critical regime, still poses a challenge for most CFD codes due to the complex flow physics, however, it is a well-established test configuration, as performed by (Lienhart and Becker, 2003) and (Strachan et al., 2007).

Most computational studies on the Ahmed Body employ simplified Reynolds Averaged Navier-Stokes (RANS) solution. This approach is very reliable for simple stable flow problems, however it is not suitable to correctly predict unstable phenomena around complex geometries. In the study by (Krajnović and Davidson, 2004), for the first time for an Ahmed Body, a LES methodology was used yielding solutions of higher flow details, especially for the critical slant angle of  $25^\circ$ . A major limitation of running LES or detached eddy simulation (DES) for this kind of geometry is the requirement of high mesh resolution, with considerably higher simulation cost and time.

The latest achievements in the high-fidelity turbulence models

around an Ahmed body are found mainly for the slant angle of  $25^\circ$  and are summarized in the compilation work of (Serre et al., 2013) in which a comparative analysis of recent simulations, conducted in the framework of a French-German collaboration on LES of Complex Flows at Reynolds number of 768,000. The study offers a comparison between results obtained with different eddy-resolving modelling approaches: three classical h-type method (LES with Smagorinsky model and wall function (LES-NWM), Wall-resolving LES with dynamic Smagorinsky model (LES-NWR), and DES with shear stress tensor (DES-SST) and one spectral element method implicit LES with spectral vanishing viscosity (iLES-SVV). The iLES-SVV simulation in (Serre et al., 2013) work was conducted in various two-dimensional planes along the span-wise direction, and subsequently constructed into three-dimensional flow fields (commonly known as 2.5D simulation). Considering the drag coefficient, both LES-NWR and DES-SST overestimated the value in around 16%; the LES-NWM presented a difference around 6%, which presented the best agreement. The iLES-SVV model better modelled the flow behaviour compared to previous models, however the drag difference was around 44%

A new Improved Delayed DES (IDDES) methodology, an enhancement of the Delayed DES (DDES), is proposed by (Guilmineau et al., 2018) to solve the flow around the Ahmed body. The study presents a comparison between quantitative and qualitative results obtained with different methodologies previously presented with this newly proposed methodology. The IDDES case is the one that most closely correlates the flow behaviour and structures with experimental reference. However, results of the aerodynamic quantities are different, such as the drag coefficient with approximately 27% difference from same experimental reference.

## 2. Ahmed body equipped with rear underbody diffuser

Bluff bodies equipped with rear underbody diffusers are being studied by several researchers, especially from the automotive industry, to maximise the performance of the vehicle. The study of (Cooper et al., 1998) identified three important characteristics on a body underbody diffuser. The first is a diffuser pumping effect, which occurs once the outlet of the diffuser is set as the base pressure of the body, as identified by (Jowsey, 2013). The diffuser recovers pressure along its length, considering continuity and applying an inviscid, steady argument of constant total pressure using Bernoulli's equation implies that the diffuser inlet pressure should be reduced, causing a suction effect. The second characteristic is the interaction with the road, in which as the ground clearance between the floor and the underbody becomes smaller, flow velocity in that region increases and pressure drops, following the same continuity and Bernoulli's equation. The third characteristic is the angled upsweep, which generates vortices on the diffuser up to a certain critical angle, creating an upwash of the flow, aiding flow attachment and increasing downforce.

Complementing the work of (Cooper et al., 1998), (Senior and Zhang, 2001) investigated a new bluff body equipped with a diffuser which extended over 41% of the body length and with inclination angle of  $17^\circ$  and endplates in different ground heights. The result was the identification of four distinct regions of diffuser performance, all related to the model ground height. The first region from non-dimensional ride height  $h/H$ , where  $h$  is the distance from the body to the ground and  $H$  is the total height of the body, is defined from 0.76 to 0.38 and is defined as downforce enhancement, region where the flow on the diffuser is symmetric with some separation on the diffuser inlet. The second region, referred as maximum downforce, from  $h/H$  0.38 to 0.22, with similar flow behaviour as the first region, except for the formation of a separation bubble at the center of the diffuser. The third and fourth regions are referred both as the downforce reduction from  $h/H$  0.22 and low downforce region from  $h/H$  0.16. The third region is characterized by a sudden drop of downforce performance and the fourth region shows that further ground height reduction causes the downforce to be reduced and



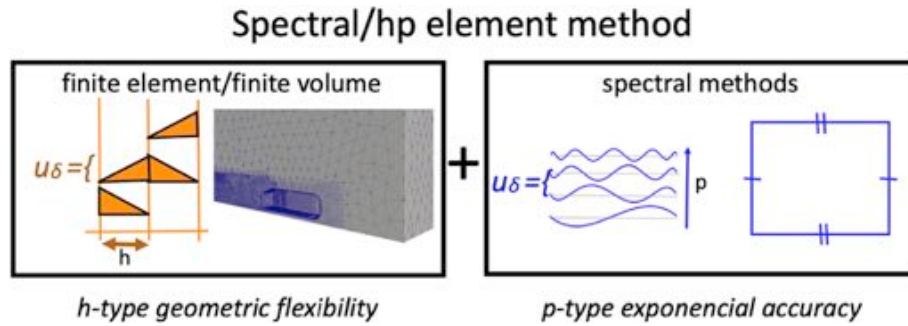


Fig. 3. Schematic explanation illustrating how finite element (h) and spectral methods (p) combine to form the spectral/hp element method.

this fact is explained by an asymmetric and separated flow behaviour at the diffuser inlet.

With substantial literature on the diffusers, such as the works from (Cooper et al., 1998) and (Senior and Zhang, 2001), we notice that each study has employed different bluff body geometries, that have not been previously studied without a diffuser. The work of (Huminic and Huminic, 2010) was the first to propose a computational study of diffusers on an Ahmed body with slant angle of  $35^\circ$  with similar conditions of (Strachan et al., 2007) study. This body style has a quasi-2D behaviour and a combination of five diffuser lengths with eight different angles were evaluated to predict drag and lift coefficients. The flow physics was not fully evaluated and no conclusions were found mainly due to the nature of the averaged flow solution employed on the study. Following the previous work (Huminic and Huminic, 2012), present a similar study, considering the Ahmed body with slant angle of  $35^\circ$  with a rear underbody diffuser, wheels and wheelhouses.

The work of (Moghimi and Rafee, 2018) performed an experimental and numerical study on an Ahmed body equipped with diffuser. Both experiments and simulations were performed at a low Reynolds number of  $Re = 9.31 \times 10^4$  considering a 10% scale half Ahmed body with slant angle of  $25^\circ$ . This study offers an experimental reference, however due to the model scale factor being extremely reduced compared to other experiments, the geometry becomes more sensitive to surface imperfections, introducing an additional source of error in the measurements. The Reynolds number is also reduced compared to other Ahmed body experimental references.

A common point on the literature presented considering the Ahmed body with diffusers is the use of CFD simulations. The CFD simulations for all references presented employ the RANS methodology combined with the  $k - \omega$  SST turbulence model and no reference using high-fidelity CFD solutions on the Ahmed body with diffuser were previously presented.

The geometry of the diffuser is proposed without the use of endplates. By evaluating the Ahmed Body equipped with a rear underbody diffuser without endplates, we also offer an interesting and simple test case, especially for the squared-back case, as it can be evaluated using a regular Ahmed body which has been flipped upside-down.

### 3. uDNS/iLES simulations using spectral/hp element method

For both Ahmed body styles with diffuser, we performed implicit LES simulations based on a spectral/hp element approach. Classical h-type method is based on dividing the domain into non-overlapping elements of the same type, similar as in the Finite Element Method (FEM), offering geometric flexibility, a key factor for many complex industrial cases. To improve the accuracy of the solution, the mesh characteristic length (h) is reduced in order to capture smaller flow features, generating a finer mesh, with larger element density of the same type. The p-type method focus on improving results by increasing the degree of the polynomial expansion used to approximate the solution on each element on a fixed mesh, with the desirable property of exponential convergence. The

spectral/hp element method used in this work combine both spatial approximations (h and p) in order to have a methodology flexible enough to handle complex geometries and providing high-fidelity solutions, such as LES and DNS with enhanced convergence properties. A summary of the methods is illustrated in Fig. 3.

The flow solution for the cases in this work is obtained by using the incompressible Navier-Stokes solver with a velocity correction scheme as proposed by (Guermont and Shen, 2003). The elliptic operators were discretised using a classical continuous Galerkin (CG) formulation and all this formulation is encapsulated in the open source package Nektar++ (Cantwell et al., 2015).

In this work we adopt an equivalent of the Taylor Hood approximation, approximating the velocity by continuous piecewise quadratic functions and the pressure by continuous piecewise linear functions. Therefore we use one higher polynomial order for velocity than the pressure. The polynomial order for velocity is also referred to as the simulation expansion order in this study.

For simulations with higher Reynolds numbers ( $10^5$  and above), such as the cases presented here, the flow is typically only marginally resolved, which means that the ratio of subgrid scale (SGS) and resolved dissipation is relatively small. Such a marginal resolution can lead to numerical instabilities related to wave interaction and wave trapping. To reach a stable solution, we employ both dealiasing and spectral vanish viscosity (SVV) stabilization techniques.

The aliasing errors related to the Navier-Stokes equations appears when handling its quadratic non-linearity term by using the Gauss integration orders  $Q$  similar to the solution polynomial order  $P$ . This is usually present in simulations considering under-resolved turbulence, such as the iLES, which leads to a significant error increment in high-frequency modes of the solution and typically cause the simulations to diverge. To avoid the aliasing errors, we employed a quadrature order consistent with the polynomial order and non-linearities of the equation. In areas of non-linear geometry deformation we also have to be mindful of geometric aliasing (aliasing arising from geometric mapping). We refer the interested reader to (Mengaldo et al., 2015) for more details.

High-order methods present low numerical diffusion, as discussed by (Karniadakis and Sherwin, 2013) and simulations with marginal spatial resolution become numerically unstable, especially in the presence of turbulence at high Reynolds numbers, condition in which most of engineering problems are. The spectral-vanishing viscosity (SVV) is a technique that adds artificial dissipation to the smallest scales of the solution and this modern strategy has been proven to effectively stabilise the simulation.

The main idea of SVV consists in expanding the Navier-Stokes Equations to include an artificial dissipation operator, leading to:

$$\frac{\partial \mathbf{u}}{\partial t} = -(\mathbf{u} \cdot \nabla) \mathbf{u} - \nabla p + \nu \nabla^2 \mathbf{u} + S_{VV}(\mathbf{u}) \quad (1a)$$

$$\nabla \cdot \mathbf{u} = 0 \quad (1b)$$

and the original operator SVV is:



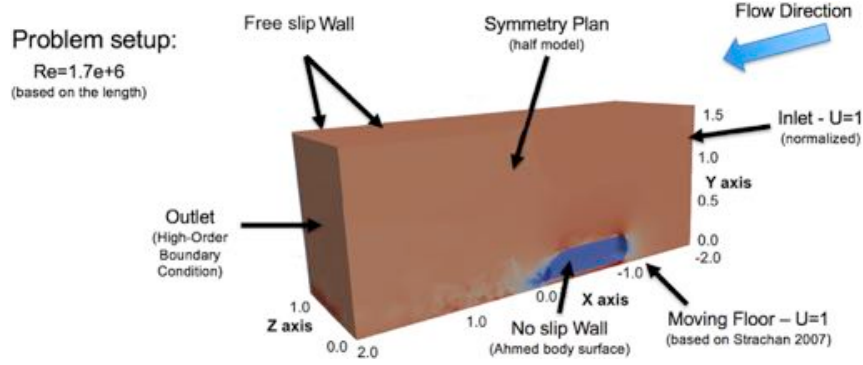


Fig. 4. Boundary condition setup.

$$S_{VV}(\mathbf{u}) = \varepsilon \sum_{i=1}^{N_{dim}} \frac{\partial}{\partial x_i} \left[ Q_i^* \frac{\partial \mathbf{u}}{\partial x_i} \right] \quad (2)$$

with  $N_{dim}$  being the spatial dimension of the problem,  $\varepsilon$  a constant coefficient, and  $*$  representing the application of the filter  $Q_i$  through a convolution operation.

For the SVV operator in this study, we run the simulation using a novel CG-SVV scheme with DGKernel as proposed by (Moura et al., 2017). The fundamental idea of this implementation is based on the fixing of the Péclet number, which can be understood as a numerical Reynolds number based on local velocity and mesh spacing. This is achieved by making the viscosity coefficient of the SVV operator proportional to both a representative velocity and a local mesh spacing. Once the Péclet number is the same for the domain, the authors in (Moura et al., 2017) proposed a SVV kernel operator for CG methods that mimics the properties of DG-based discretisation where there is natural damping of high frequency and reflected waves. In this approach the dissipation curves arising from spatial eigenanalysis of CG of order  $P_N$  are matched to those of DG with order  $P_N - 2$ . Matching both curves offers benefits such as the numerical stability of simulations at very high Reynolds number.

#### 4. Numerical methodology validation on the classical Ahmed body geometry

In this simulation study, we use a coordinate system with  $X$  as the streamwise direction,  $Y$  as the vertical direction and  $Z$  as the spanwise direction. The Ahmed body model is positioned with its back end on the coordinate  $X = 0$  and at a distance  $h$  of 50 mm from the ground ( $Y = 0$ ). The wind tunnel test section size is defined with same dimensions as the experiment from (Strachan et al., 2007) 1660 mm  $\times$  2740 mm, keeping the same blockage ratio. Air flow inlet is positioned at  $X = -2L$  and outlet at  $X = 2L$  with a total  $X$  length of  $4L$ . With such reduced wind tunnel, special outflow boundary condition is necessary to avoid interference on the flow and numerical instabilities. The outflow condition selected is the high-order outflow condition, proposed by (Dong et al., 2014), in order to avoid wave reflections back to the domain.

The Reynolds number for all simulated cases is  $Re = 1.7 \times 10^6$ , based on the Ahmed body total length  $L$  of 1044 mm. With this Reynolds number value and by imposing moving ground condition, we aim to reproduce similar conditions employed by (Strachan et al., 2007).

The high-order meshes for all cases presented in this work were generated by the mesh generator module of Nektar++: NekMesh ((Turner, 2017)). The pipeline to create a high-order mesh starts by designing the geometries for the computational simulations on a Computer Aided Design (CAD) software, exported in STEP format. Subsequently, we generate a linear mesh using a classical h-type method. Linear mesh generation on NekMesh also incorporates an optimisation step to avoid irregular and low quality elements once the surface mesh is

projected into its 3D form using the CAD surface.

Once the linear mesh was generated, the next step is to convert it into a high-order mesh which is geometry conforming. The generation of the high-order mesh requires the addition of extra points to represent the polynomial discretisation (with order  $P_M$ ), which are added along the curved edges, CAD surface geometry and in the interior of the domain. The processes then follows by the generation of a macro boundary layer on user-defined wall surfaces together with volumetric high-order mesh on rest the domain. The final operation on the mesh generation is the macro boundary layer split, by using the isoparametric approach as proposed by the authors of (Moxey et al., 2015) considering boundary layer inputted parameters.

The boundary conditions for the computational study were set as follows and shown on Fig. 4:

- Ahmed bodies with diffuser are set as wall with no-slip condition;
- A half model of the geometry is used;
- Symmetry condition imposed at  $Z = 0$ ;
- Free-slip condition imposed at tunnel walls;
- Uniform velocity profile at the inlet;
- High order outflow condition at the outlet (as proposed by (Dong et al., 2014));
- A moving ground condition on the floor with speed  $U$  in the  $X$  direction, as used by (Strachan et al., 2007);
- Convergence criteria for pressure is  $1 \times 10^{-6}$  and for the velocity components  $1 \times 10^{-8}$ ;

Simulations were performed for 7 convective time units (CTU), which can be understand as the free stream flow that has been advected over a surface or reference point for a total length of  $7L$ . The convergence criteria was set to a maximum variation of  $1 \times 10^{-6}$  for pressure and  $1 \times 10^{-8}$ , in order to minimize numerical error. Due to the use of half symmetric model, this study focus mainly on aerodynamic quantities, such as the lift and drag coefficients and flow structures on the slant and close to the body. The use of half symmetric Ahmed body was previously validated against full geometry by (Buscariolo, 2020). Under similar boundary conditions, solution and meshing configurations, the maximum difference in the aerodynamic quantities was 2%.

Considering the numerical methodology validation, as performed by (Buscariolo et al., 2020), we are focusing on the classical Ahmed body geometry, selecting the slant angle of  $25^\circ$ . Two different mesh configurations in terms of h-refinements are proposed, defined as *Original* and *Refined* meshes, based on the boundary layer setup of a total length of  $0.022L$  (macro boundary layer), which is further divided into 10 layers with a growth rate of 1.6. The possibility of evaluating two different meshes in terms of elements resolution complements the polynomial order  $P_N$ . The choice of parameters for refinements zones and boundary layer was based on automotive industry guidelines. For the mesh resolution, the study aimed to have similar number of DOFs of a Wall-Modelled LES simulation for the most refined case and further

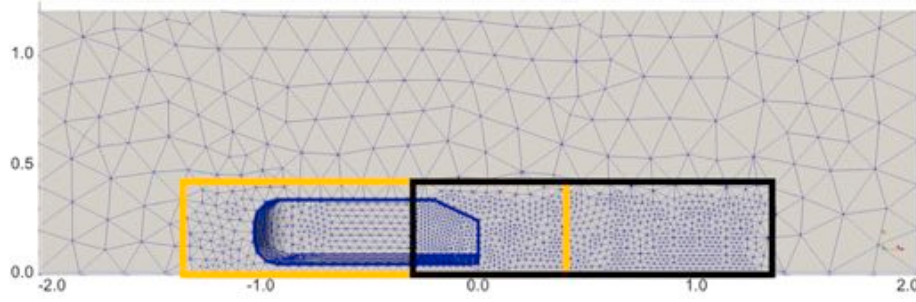


Fig. 5. Plane view  $Z = 0$  indicating the location of the refinement boxes on the Ahmed body model for the *Original* mesh case. The Ahmed body refinement region is indicated in yellow and the wake refinement region is indicated in black. (For interpretation of the references to colour in this figure legend, the reader is referred to the Web version of this article.)

Table 1

Resolution of the proposed simulations, showing total number of DOF (in Million) for each case evaluated, at different polynomial expansions accuracy  $P_N$ .

|                    |           | $P_N = 4$ | $P_N = 5$ | $P_N = 6$ |
|--------------------|-----------|-----------|-----------|-----------|
| Original Mesh (-A) | $P_M = 4$ | 2.16      | 3.85      | 6.24      |
|                    | $P_M = 5$ | 2.16      | 3.85      | 6.24      |
|                    | $P_M = 6$ | 2.16      | 3.85      | 6.24      |
| Refined Mesh (-R)  | $P_M = 4$ | 7.40      | 13.13     | 21.21     |
|                    | $P_M = 5$ | 7.40      | 13.13     | 21.21     |
|                    | $P_M = 6$ | 7.40      | 13.13     | 21.21     |

coarsening the mesh to evaluate its impact on the aerodynamic behaviour of the body.

This validation study also proposes the evaluation of three high-order meshes for both *Original* and *Refined* cases, considering the first  $P_M$  of 4th order, as previous reference studies from (Turner et al., 2017). In addition to previous reference, we propose increasing the polynomial resolution of the curved elements  $P_M$  to both 5th and 6th order. Within this, the study aims to evaluate the influence of different high-order polynomials for the boundary layer mesh element curvature, when using relatively coarse meshes. Two refinement zones are applied for all Ahmed body simulations. The first refinement zone is created over the Ahmed Body full length, referred as Ahmed body refinement, ranging from  $0.3 L$  before and  $0.3 L$  after the end of the body. The second refinement, referred as wake refinement is applied on the wake region, intercepting the first region in  $-0.3 L$  before the end of the body, to  $1.3 L$  after the end of the body. The wake refinement and overlap with smaller elements are applied in order to fully capture the flow phenomena in the separation region. Mesh refinement regions considering the *Original* mesh are illustrated in Fig. 5 on the plane  $Z = 0$ .

The *Original* mesh is generated with a total number of elements  $N_{EL}$  for half model around 94,000 h-type mesh elements, where around 14,000 are prismatic elements  $N_P$  and 80,000 are tetrahedra elements  $N_T$ . The mesh configuration parameters on NekMesh, typically found in the automotive industry, are presented below in function of  $L$ .

- Min length  $h_{\min} = 0.01 L$ ;
- Max length  $h_{\max} = 0.2 L$ ;
- Ahmed Body refinement zone length =  $0.05 L$ ;
- Wake refinement zone length =  $0.03 L$ ;

For the *Refined* mesh, the number of elements generated  $N_{EL}$  for half model is around 335,000 h-type mesh elements, where around 35,000 are prismatic elements  $N_P$  and 300,000 are tetrahedra elements  $N_T$ . Mesh parameters are presented as follow:

- Min length  $h_{\min} = 0.0075 L$ ;
- Max length  $h_{\max} = 0.2 L$ ;
- Ahmed Body refinement zone length =  $0.035 L$ ;

Table 2

Drag and lift averaged RMS and RMSE coefficients for the *Original* and *Refined* meshes considering evaluated  $P_M$  and  $P_N$  high-order, comparing with experiments from (Strachan et al., 2007).

| Simulation Case | $C_D$ | $C_L$ | Difference |        | $C_D$  | $C_L$  |
|-----------------|-------|-------|------------|--------|--------|--------|
|                 | RMS   | RMS   | Drag %     | Lift % | RMSE   | RMSE   |
| NM44-A          | 0.416 | 0.140 | 40         | -50    | 0.1202 | 0.1637 |
| NM45-A          | 0.386 | 0.090 | 29         | -68    | 0.0913 | 0.2384 |
| NM46-A          | 0.386 | 0.090 | 29         | -68    | 0.0912 | 0.2386 |
| NM54-A          | 0.322 | 0.270 | 8          | -3     | 0.0299 | 0.1043 |
| NM55-A          | 0.312 | 0.286 | 5          | 2      | 0.0157 | 0.0325 |
| NM56-A          | 0.313 | 0.285 | 5          | 2      | 0.0163 | 0.0339 |
| NM64-A          | 0.276 | 0.267 | -8         | -5     | 0.0230 | 0.0544 |
| NM65-A          | 0.251 | 0.260 | -16        | -7     | 0.0474 | 0.0225 |
| NM66-A          | 0.260 | 0.279 | -13        | -1     | 0.0393 | 0.0096 |
| NM44-R          | 0.395 | 0.249 | 33         | -11    | 0.0976 | 0.0712 |
| NM45-R          | 0.395 | 0.250 | 33         | -11    | 0.0975 | 0.0695 |
| NM46-R          | 0.395 | 0.251 | 33         | -10    | 0.0977 | 0.0693 |
| NM54-R          | 0.279 | 0.291 | -6         | 4      | 0.0200 | 0.0212 |
| NM55-R          | 0.275 | 0.287 | -8         | 2      | 0.0237 | 0.0211 |
| NM56-R          | 0.280 | 0.295 | -6         | 5      | 0.0195 | 0.0397 |
| NM64-R          | 0.258 | 0.285 | -13        | 2      | 0.0405 | 0.0371 |
| NM65-R          | 0.255 | 0.255 | -14        | -9     | 0.0436 | 0.0710 |
| NM66-R          | 0.258 | 0.282 | -13        | 1      | 0.0452 | 0.0519 |
| Experiment      | 0.298 | 0.280 |            |        |        |        |

- Wake refinement zone length =  $0.02 L$ ;

Once the six high-order meshes are generated, high fidelity numerical simulations are performed, using the implicit LES simulations based on a spectral/hp element method. The selected is the Nektar++ open source software for all simulations. The solution on each element is approximated by a high-order polynomial and three different polynomial expansions  $P_N$  are selected:  $P_N = 4$ th, 5th and 6th order. These are applied for each of the six meshes, in total eighteen cases evaluated. The total number of degrees of freedom (DOFs) of each case, in order to have a comparison with low-order solutions, is presented in Table 1, with numbers indicating in millions of DOFs and (-A) refers to *Original* mesh and (-R) to *Refined* mesh.

An important aspect to mention is that the mesh order  $P_M$  and solution order  $P_N$  are independent and values of both can be freely combined. Higher order of the  $P_M$  polynomial are used to improve the reproduction of complex surfaces by curving the elements, whereas  $P_N$  adds more DOFs to the solution.

#### 4.1. Ahmed body drag and lift coefficient validation results

We now compile quantitative results for the nine combinations of high-order meshes with polynomial expansions for the *Original* mesh (-A) and additional nine cases for the *Refined* mesh (-R) in total eighteen cases.

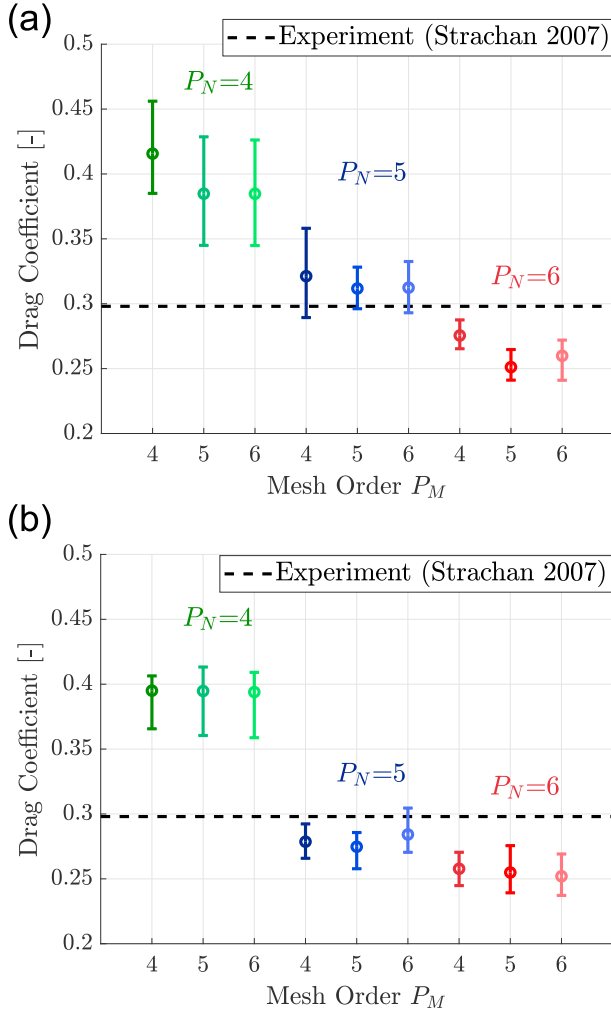


Fig. 6. Drag coefficient comparison for *Original* and *Refined* mesh cases, considering proposed high-order meshes and polynomial basis.

The first number following the term NM refers to  $P_N$  and the second number refers to the  $P_M$  employed to the case. A summary is presented on Table 2 for the Root Mean Square (RMS) and Root Mean Square Error (RMSE) drag and lift coefficients obtained in all simulations. For the coefficients of drag and lift, results were averaged from the 5th to the 7th CTU, as the results using  $P_N = 4$  start to have a more stable profile.

In order to better visualize the results of both drag and lift coefficient from the *Original* and *Refined* mesh cases, we present the averaged quantities (dotted line) with minimum and maximum deviation comparing with experimental results (dashed line) from (Strachan et al., 2007). The drag coefficient summary is presented in Fig. 6 and the lift coefficient summary in Fig. 7.

The results for the aerodynamic quantities indicate that for a simplified geometry such as the Ahmed body, once passing a threshold value, further increasing the mesh order has small influence on the results. For this type of bluff bodies, most of the relevant flow structures are generated from sharp edges of the geometry, such as the slant. The only curved surface is the frontal stagnation, where we see enhancements on capturing the curvature as the  $P_M$  increases. We select to have the highest high-order mesh resolution ( $P_M = 6$ th order) as our reference for curvature mesh for flow structure results to be presented and further application on the diffuser test cases, as also employed by (Buscariolo et al., 2019) and similar automotive studies. This study also highlights that for the *Original* mesh case, we observe similar values for drag and lift coefficients for  $P_M = 5$  and  $P_M = 6$ . It indicates that further increase on  $P_M$  will not affect results. On the *Refined* mesh case, drag coefficient values

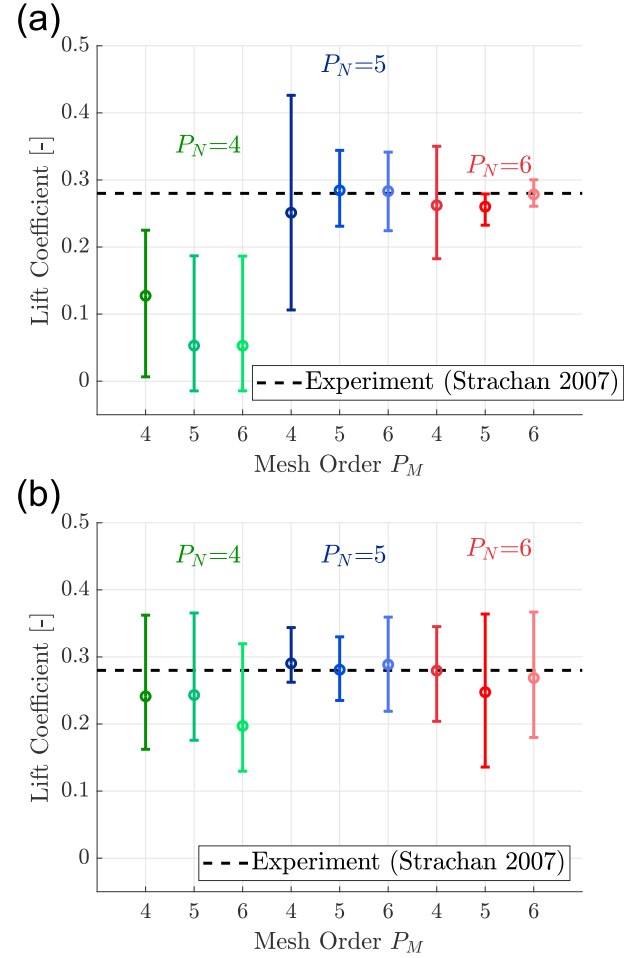


Fig. 7. Lift coefficient comparison for *Original* and *Refined* mesh cases, considering proposed high-order meshes and polynomial basis.

are similar for every  $P_M$ , however the lift coefficient improves as  $P_N$  for the solution increases.

When analysing numerical results, the outcome for the best numerical methodology are between *Original* and *Refined* meshes with  $P_N = 5$  and  $P_N = 6$  resolution, respectively for drag and lift coefficients. A point to consider is that for  $P_N = 5$ , we noticed that increasing the h-refinement from *Original* to *Refined*, the result changed from over-predicted to under-predicted. Results for drag considering  $P_N = 6$  resolution maintained similar value for both meshes, indicating consistency.

In terms of flow structure comparison, we point out that the main reference used for the aerodynamic quantities (Strachan et al., 2007) has an upper support over the body to allow the moving ground condition, which the upper support contributions for the drag forces being empirically deducted from the obtained total value. However, the influences on flow features will still remain, possibly leading to weaker vortices over the slant when comparing to results without the support. Following the findings of (Strachan et al., 2007) that the upper strut can interfere with the vortices' intensity, we are comparing aerodynamics flow visualization with results from (Lienhart and Becker, 2003) (without strut), similar as this work. We present a comparison of the normalized  $U$  on the plane ZY at  $X/L = 0.077$  in Fig. 8, aiming to compare wake structures in the flow.

Analysing the flow, *Refined* mesh with  $P_N = 5$  and  $P_N = 6$  cases qualitatively closely correlate to experimental results, with better definition of flow structures and larger contour spectrum. Especially for  $P_N = 6$  resolution, capturing similar shape of the experimental reference.

The main conclusion here presented is that the minimum resolution for this mesh setup to reproduce similar features and aerodynamic

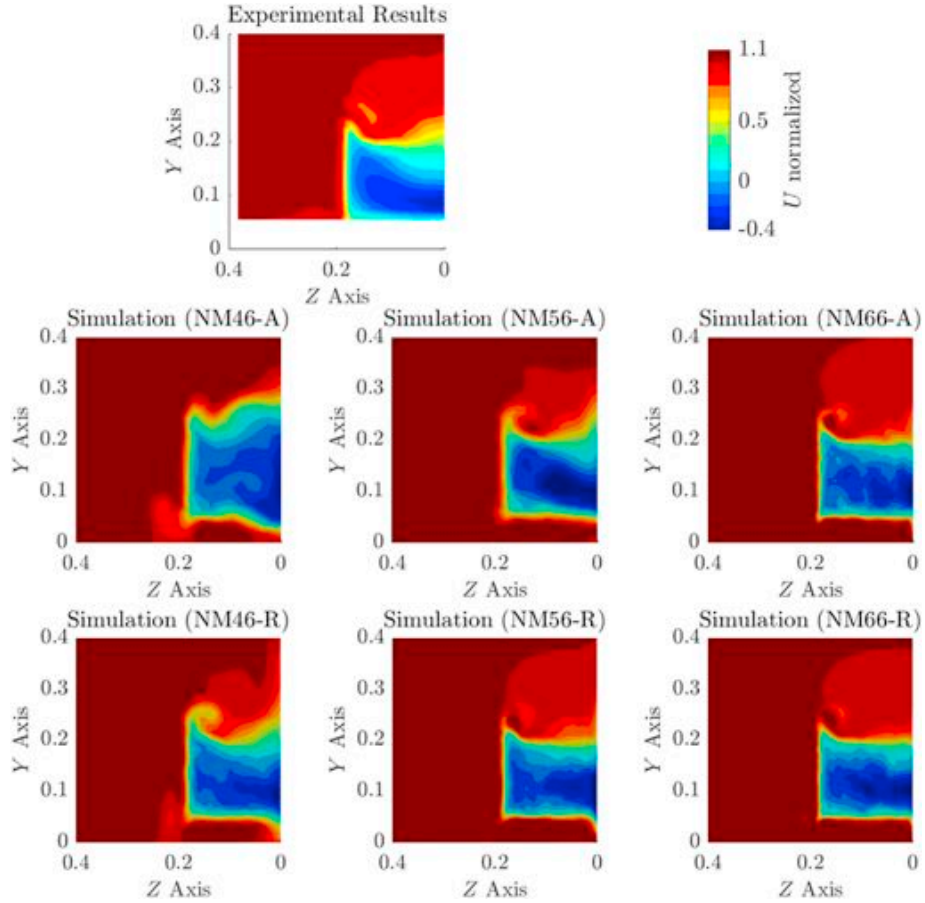


**Fig. 8.** Comparison of normalized streamwise velocity  $U$  between experiments of (Lienhart and Becker, 2003) (top) and computational simulations on plane  $ZY$  at  $X/L = 0.077$ .

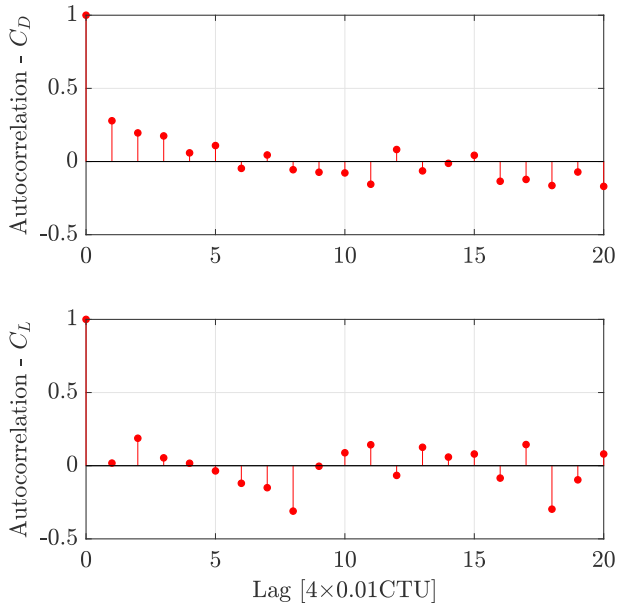


**Fig. 9.** Autocorrelation for the re-sampled unsteady drag and lift coefficient.

quantities is the *Refined* configuration combined with 6th high-order mesh ( $P_M = 6$ ) and polynomial expansion of 6th order accuracy ( $P_N = 6$ ). The *Refined* configuration combined with polynomial expansion of 6th order accuracy leads to  $y^+ \leq 1$  over the body walls, giving support to

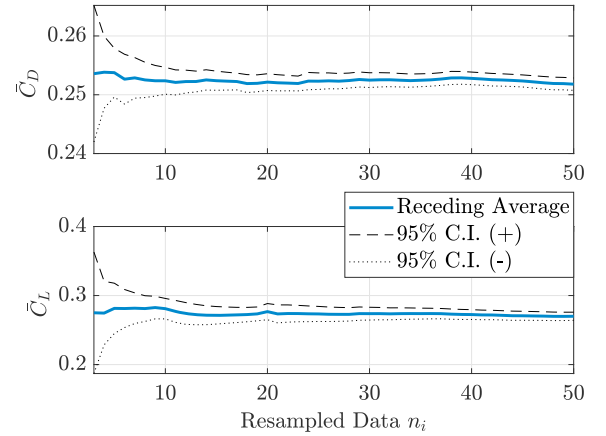


**Fig. 10.** Receding average with 95% confidence intervals.

previous statement and is applied to the all further simulations in this study.

In order to justify the reliability of the aerodynamic quantities results of the selected resolution, we applied the method proposed by (Islam et al., 2017) and further applied by (Luckhurst et al., 2019). Drag and lift coefficient data was resampled to remove the statistical dependence in the unsteady signal, between the 5 to 7 CTU, shown in Fig. 9.

Considering the resampled data for both drag and lift coefficients, the receding average of was generated with a 95% confidence interval and presented in Fig. 10. It indicates that significance of the autocorrelation is removed and the data from 5 to 7 CTUs is statically independent.

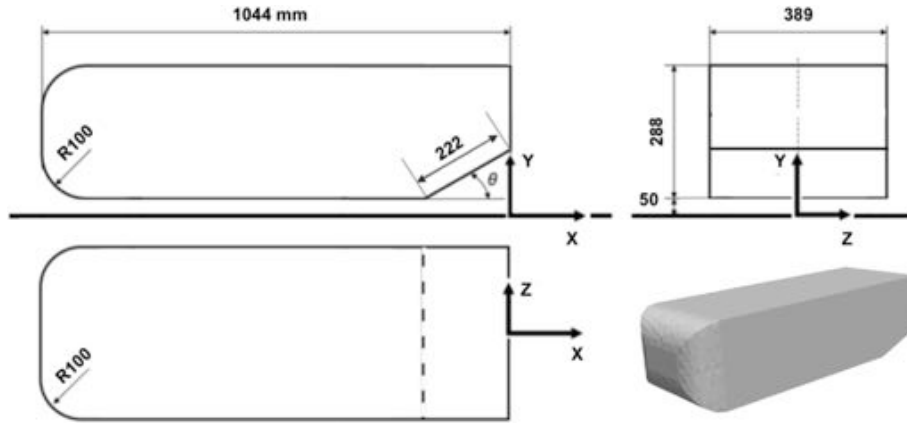


Fig. 11. Schematic drawing of the Ahmed body squared-back equipped with rear underbody diffuser.

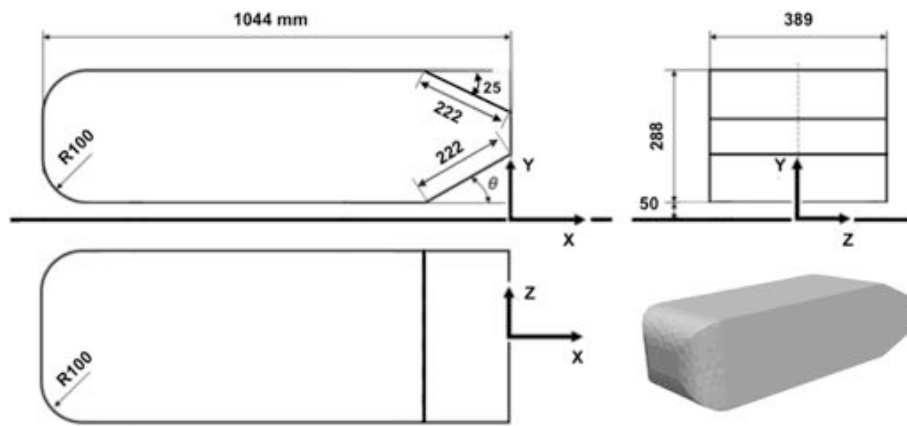


Fig. 12. Schematic drawing of the Ahmed body with slant angle of 25° equipped with rear underbody diffuser.

The results here presented are also in accordance with current literature on the use of LES solutions on the Ahmed body in terms of the drag coefficient, ranging from 6% to 16%, according to (Serre et al., 2013) studies, but showing great agreement in terms of lift coefficient. Uncertainties of the experiment might also explain the gap between computational results, such as the use of the upper strut. The strut influence on the drag coefficient results of (Strachan et al., 2007) is approximately 15% when compared to the study of (Graysmith et al., 1994). This study also highlights improvements in terms of also capturing correct flow structures and intensities. From previous reference of spectral methods applied to this bluff body, there is a reducing from 44% ((Serre et al., 2013) to 13% on the drag coefficient value.

## 5. Simulation of the Ahmed body with diffuser

With the numerical methodology validated on the classical Ahmed body, the following step is the application on a new variant of the Ahmed body equipped with underbody diffuser. Diffuser length  $D_L$  is set to be at a fixed value, which is the same as the upper slant length  $S_L$  of 222 mm, regardless of the inclination angle changes. The influence of the diffuser is evaluated in two variants of the classical Ahmed body: 0° slant (or squared-back) and 25° slant angle, as illustrated in Figs. 11 and 12. The diffuser angle evaluated for was changed from 0° to 50° in increments of 10° with an additional case considering the angle of 5°.

All simulation cases were performed based on the methodology established on previous chapter and in the study of (Buscariolo et al., 2020), considering *Refined* mesh parameters, with 6th high-order mesh ( $P_M = 6$ ) and polynomial expansion of 6th order accuracy ( $P_N = 6$ ), corresponding to the NM66-R case on the validation study. The

volumetric mesh also incorporates the two refinement zones (Ahmed body and wake refined) previously and illustrated for each body style in Fig. 13.

With this simulation setup using a polynomial expansion for the solution  $P_N = 6$ , we are able to increase the resolution of the solution by converting a relatively coarse mesh with 250,000 (h-type equivalent) elements into 19.8 million degrees of freedom (DOF) per variable. Boundary conditions and Reynolds number for the simulation cases with diffuser are the same applied for the numerical methodology validation study and following the work of (Strachan et al., 2007).

### 5.1. Results

The key findings of the study are presented as follows. We initially present a comparison of drag and lift coefficients for both Ahmed body styles when the diffuser angles changes. Both quantities are averaged from the 5th to the 7th convective length where we assure to have a fully converged physical solution. Flow structures comparison for the planes  $X/L = 0$  and  $X/L = 0.096$  and wall shear stress lines are both averaged from the same period and presented in order to complement the findings.

#### 5.1.1. Drag coefficient results

Drag coefficient results with both Ahmed body slant angles are presented in Fig. 14. Ahmed body squared back results indicate that the drag coefficient initially rises as the diffuser angle increases, reaching the maximum value at the diffuser angle of 30°. The rising drag trend suddenly breaks for diffuser angles higher than 30°, where results for further angles are similar to the diffuser with 20° inclination. Such behaviour indicates similar trends as earlier verified in studies on Ahmed body slant



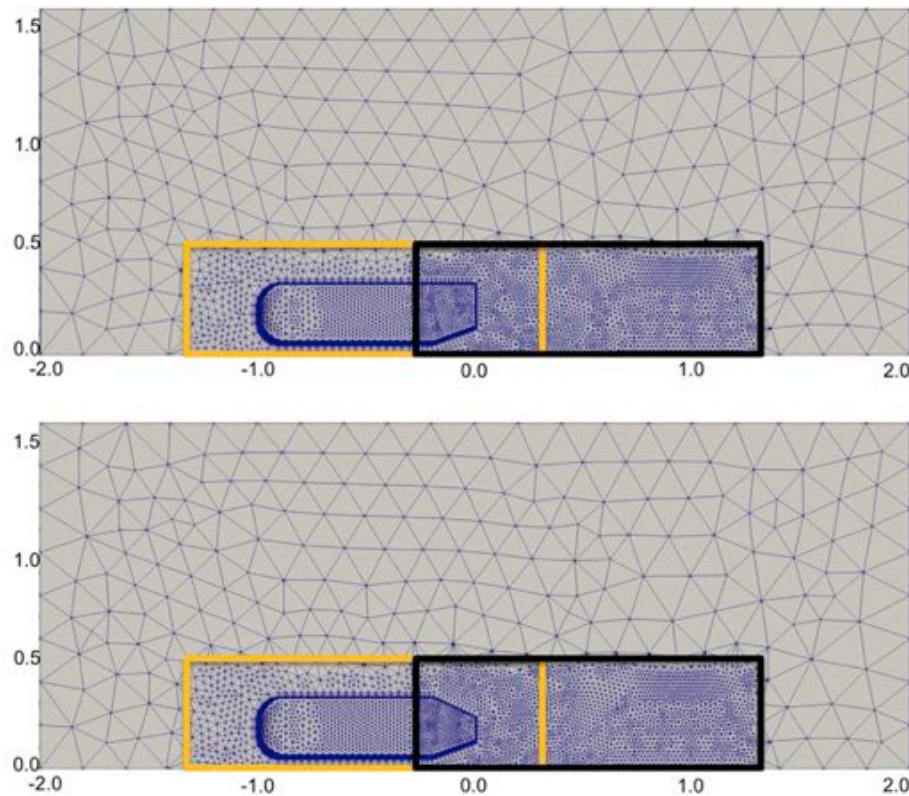


**Fig. 13.** Mesh refinement regions on both Ahmed bodies squared back (up) and with slant angle of  $25^\circ$ . Refinement region highlighted in yellow is defined as the Ahmed Body refinement and region highlighted in black is defined as Wake Refinement. (For interpretation of the references to colour in this figure legend, the reader is referred to the Web version of this article.)

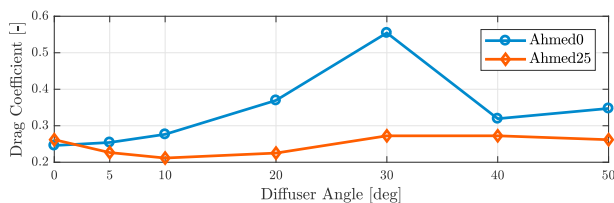


**Fig. 14.** Drag coefficient comparison for Ahmed Body squared-back (blue line) and  $25^\circ$  slant inclination (orange line) considering standard configuration and evaluated diffuser angles:  $5^\circ$ ,  $10^\circ$ ,  $20^\circ$ ,  $30^\circ$ ,  $40^\circ$  and  $50^\circ$ . (For interpretation of the references to colour in this figure legend, the reader is referred to the Web version of this article.)

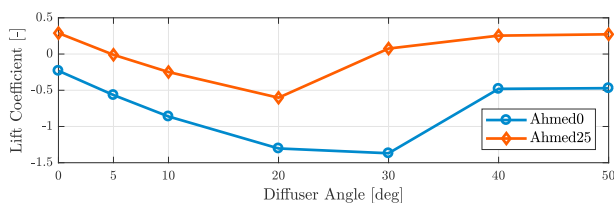


**Fig. 15.** Lift coefficient comparison for Ahmed Body squared-back (blue line) and  $25^\circ$  slant inclination (orange line) considering standard configuration and evaluated diffuser angles:  $5^\circ$ ,  $10^\circ$ ,  $20^\circ$ ,  $30^\circ$ ,  $40^\circ$  and  $50^\circ$ . (For interpretation of the references to colour in this figure legend, the reader is referred to the Web version of this article.)

angle variations of (Ahmed et al., 1984), (Lienhart and Becker, 2003) and (Strachan et al., 2007). The drag breaking point for the diffuser angle is similar to slant angle which is an indication of flow structure change on the diffuser region and is further discussed below. We conclude that any

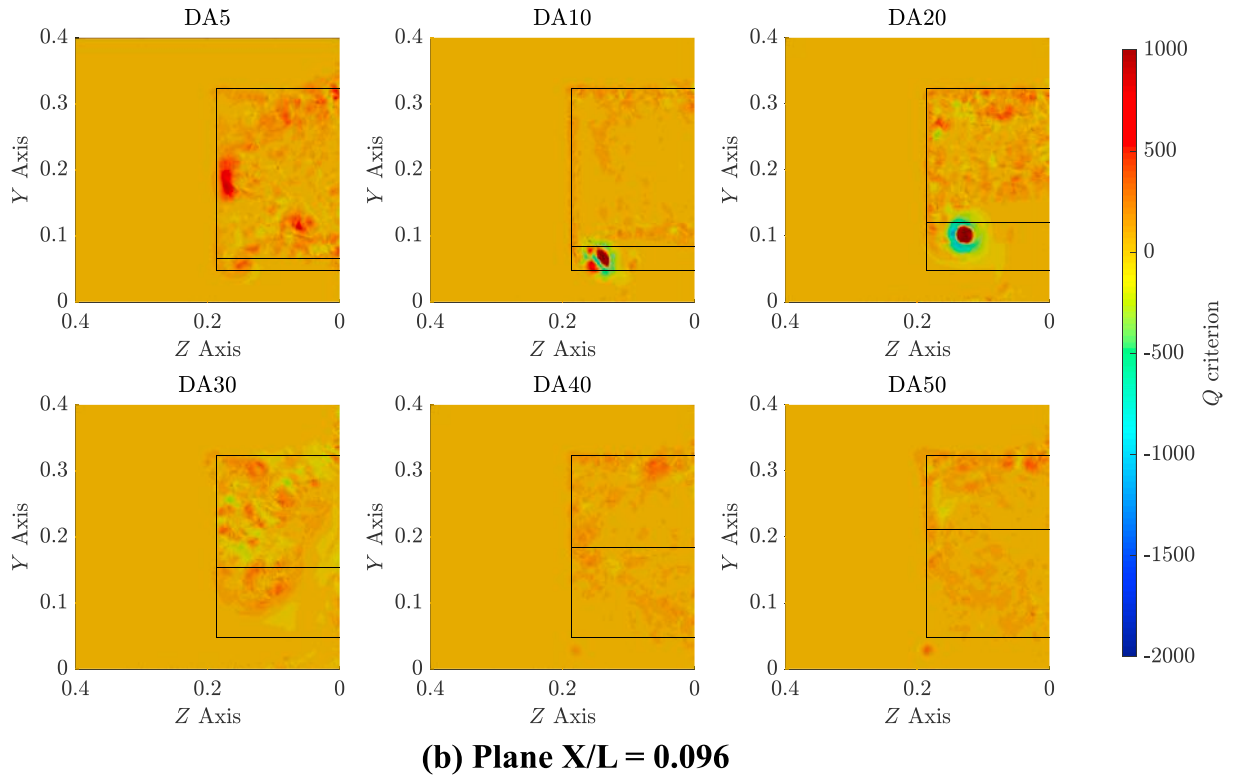
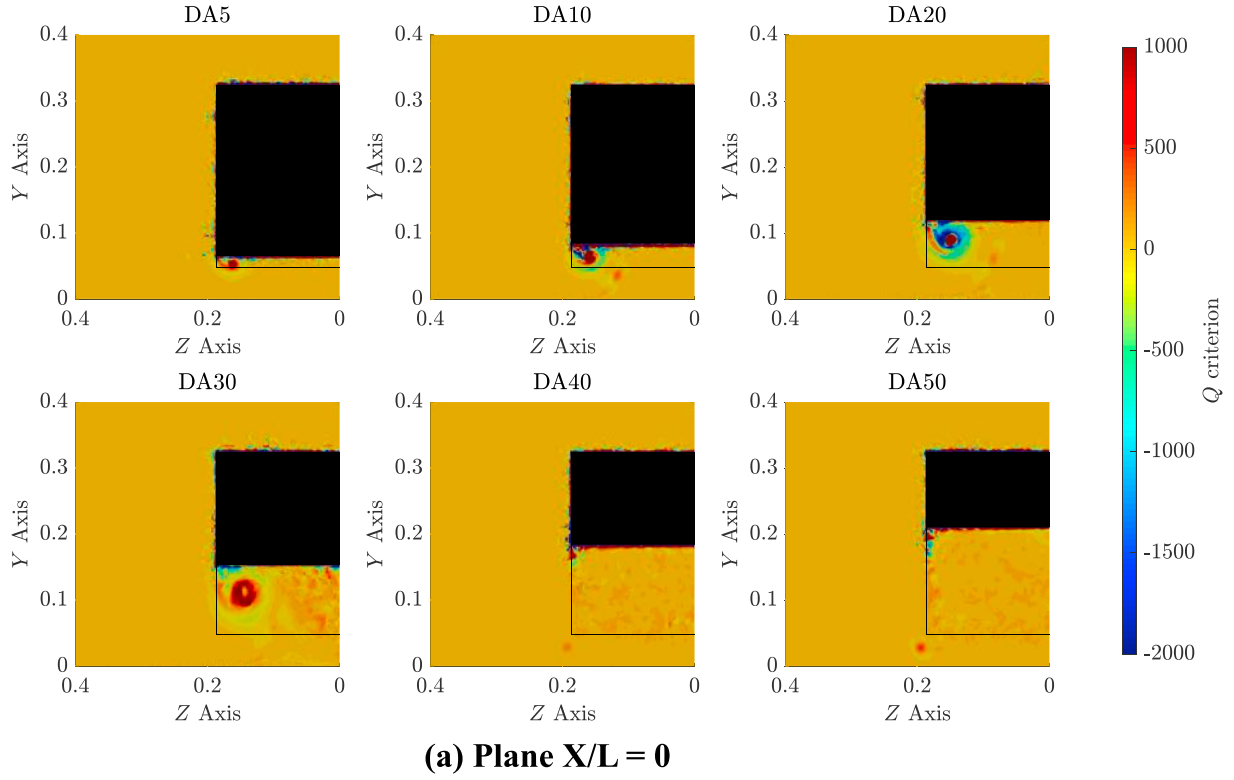
diffuser added to the Ahmed body squared back has a penalty in terms of drag performance.

The drag coefficient results for Ahmed body with  $25^\circ$  slant angle show different trend from the squared back case. Applying the diffuser with angles of  $5^\circ$ ,  $10^\circ$  and  $20^\circ$  angle leads to drag reduction with the optimum angle at  $10^\circ$ . For the other diffuser angles, the drag coefficient recovers to a similar value of the Ahmed body with  $25^\circ$  slant angle without a diffuser. We also notice that the drag performance enhancement region might be related to flow behaviour change on the diffuser region, which is further presented. Diffuser application has no negative impact on drag coefficient for this Ahmed body style.

### 5.1.2. Lift coefficient results

Lift coefficient values for both Ahmed body cases at different diffuser angles are presented in Fig. 15. When analysing the lift coefficient results for the Ahmed body squared back, downforce enhancement is obtained as the diffuser angle increases from  $0^\circ$ , reaching maximum downforce value at  $30^\circ$ . The downforce trend breaking phenomenon is observed for diffuser angles higher than  $30^\circ$ , similar as observed for the drag coefficient. For diffuser angles higher than  $30^\circ$ , downforce force values are similar to the diffuser of  $5^\circ$ , indicating saturation of downforce enhancement with this diffuser geometry.

Ahmed body with  $25^\circ$  slant inclination lift coefficient results shows similar trend of previous squared-back results. We've noticed the positive lift on the baseline case without diffuser, which might compromise gripping on performance and race cars. By implementing the diffuser, downforce performance starts to increase, where the first proposed diffuser angle of  $5^\circ$  take the lift coefficient to equilibrium. Downforce increment is noticed until the diffuser angle of  $20^\circ$ , where the maximum performance is reached. The diffuser loses its performance for diffuser angle of  $30^\circ$  and above, where the first has performance similar to the  $5^\circ$  whereas the  $40^\circ$  and  $50^\circ$  diffusers have similar performance as the baseline.

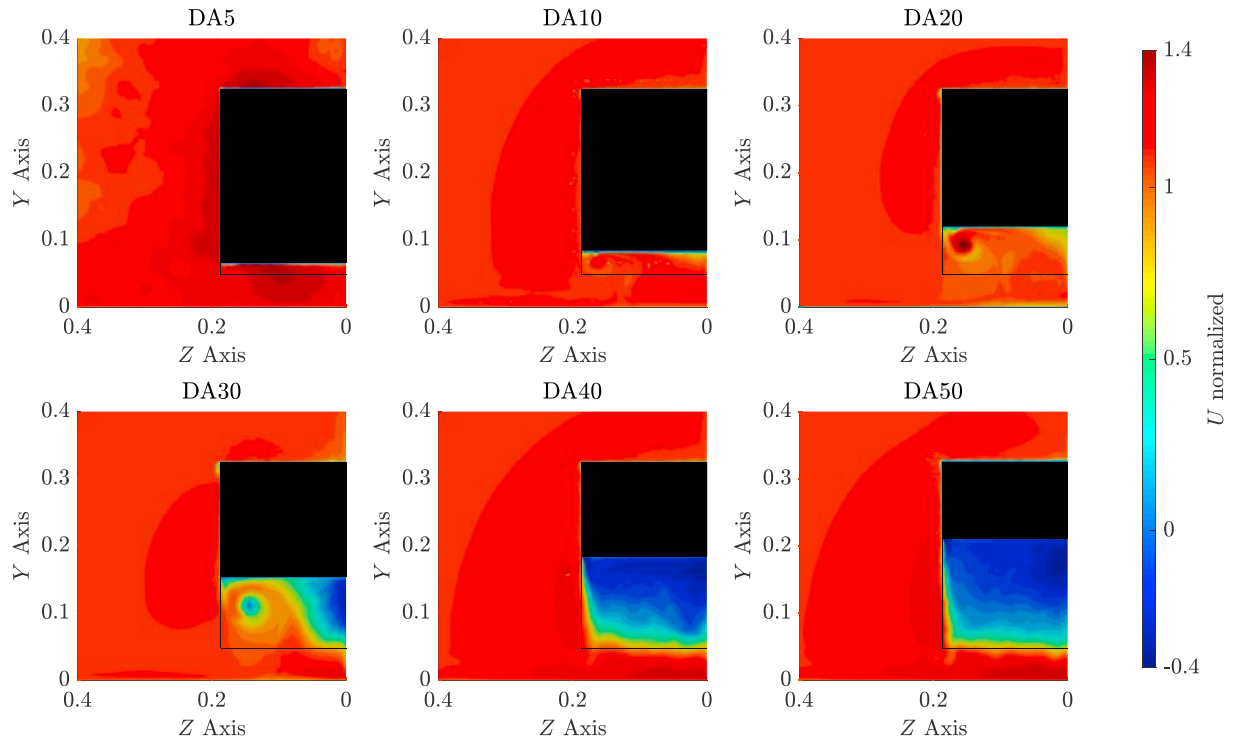
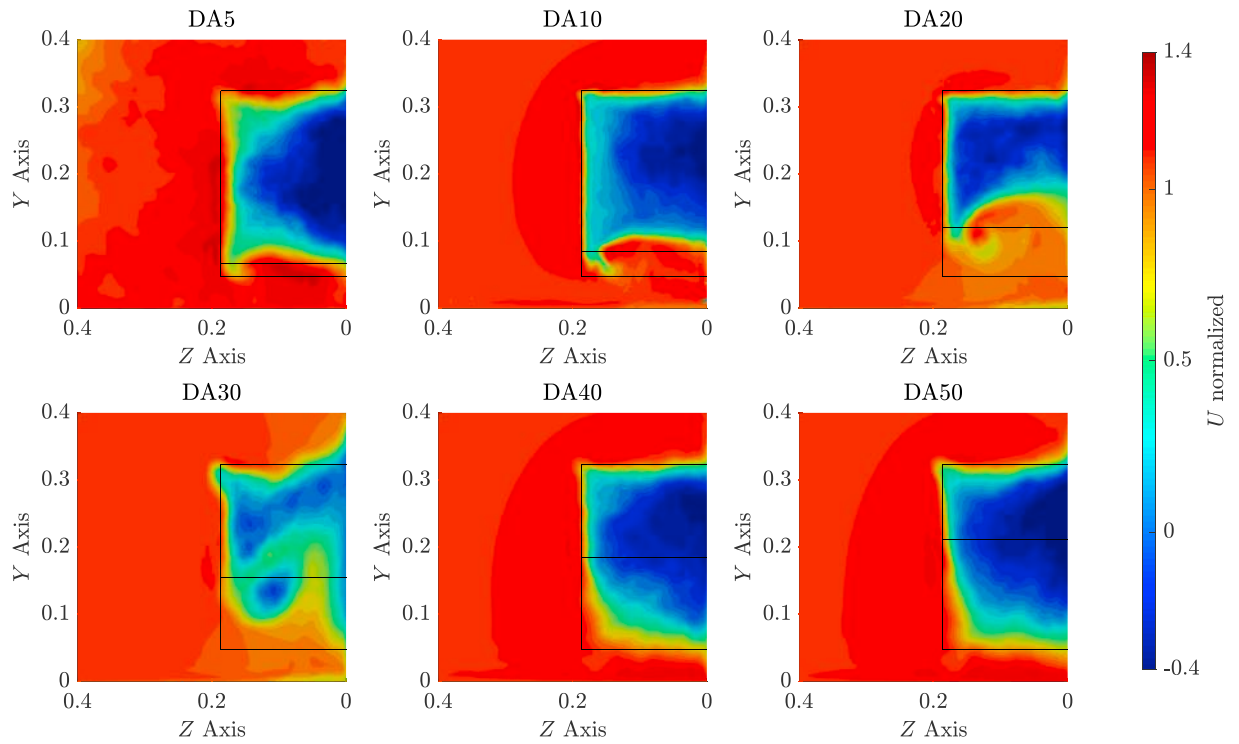


**Fig. 16.** Contours of Q-Criterion for the Ahmed body squared-back considering diffuser angle of 5° (DA5), 10° (DA10), 20° (DA20), 30° (DA30), 40° (DA40) and 50° (DA50) for planes  $X/L = 0$  and  $X/L = 0.096$ .

### 5.1.3. Flow features analysis

Comparative results for the flow structures found on the Ahmed body equipped with a diffuser are now presented and discussed. The comparisons are presented at two planes, one at  $X/L = 0$ , where the back end of the Ahmed body is placed and one downstream at  $X/L = 0.096$ , in

order to evaluate how the flow structures develop as they separate from the body. Contours of Q-criterion,  $U$  (streamwise) and  $V$  (vertical) velocities are provided for the inspection planes, aiming to identify flow structures and define its interactions with the rear wake. We also provide a flow topology comparison on the diffuser surface by plotting averaged

**(a) Plane  $X/L = 0$** **(b) Plane  $X/L = 0.096$** 

**Fig. 17.** Contours of normalized streamwise velocity  $U$  for the Ahmed body squared-back considering diffuser angle of  $5^\circ$  (DA5),  $10^\circ$  (DA10),  $20^\circ$  (DA20),  $30^\circ$  (DA30),  $40^\circ$  (DA40) and  $50^\circ$  (DA50) for planes  $X/L = 0$  and  $X/L = 0.096$ .

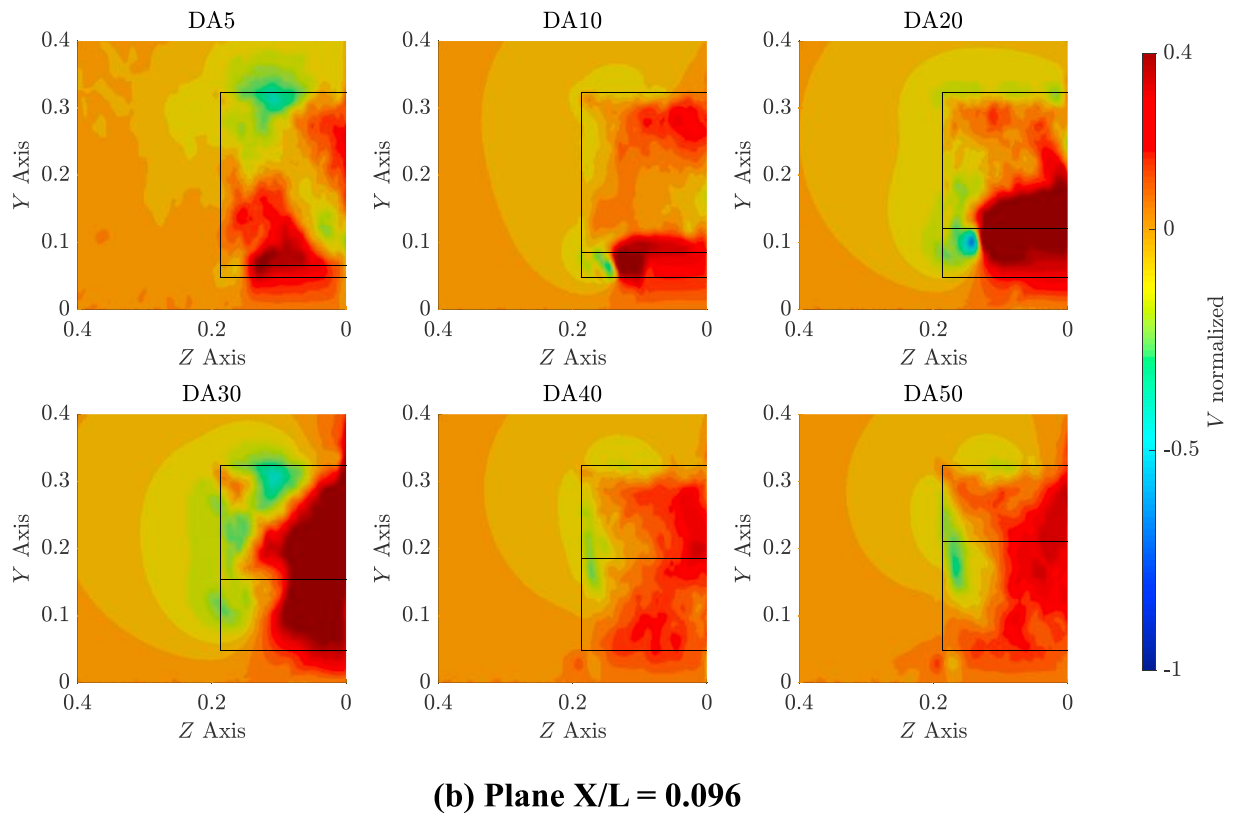
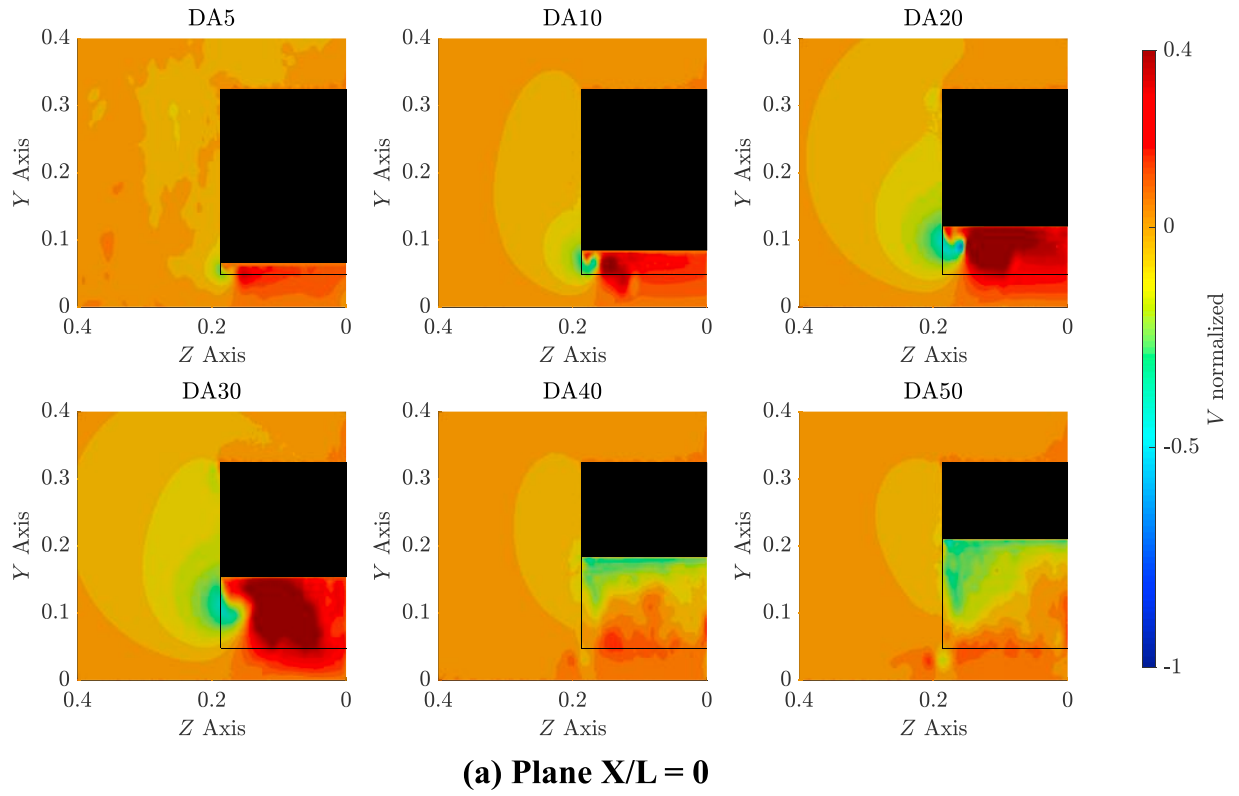


**Fig. 18.** Contours of normalized vertical velocity  $V$  for the Ahmed body squared-back considering diffuser angle of  $5^\circ$  (DA5),  $10^\circ$  (DA10),  $20^\circ$  (DA20),  $30^\circ$  (DA30),  $40^\circ$  (DA40) and  $50^\circ$  (DA50) for planes  $X/L = 0$  and  $X/L = 0.096$ .



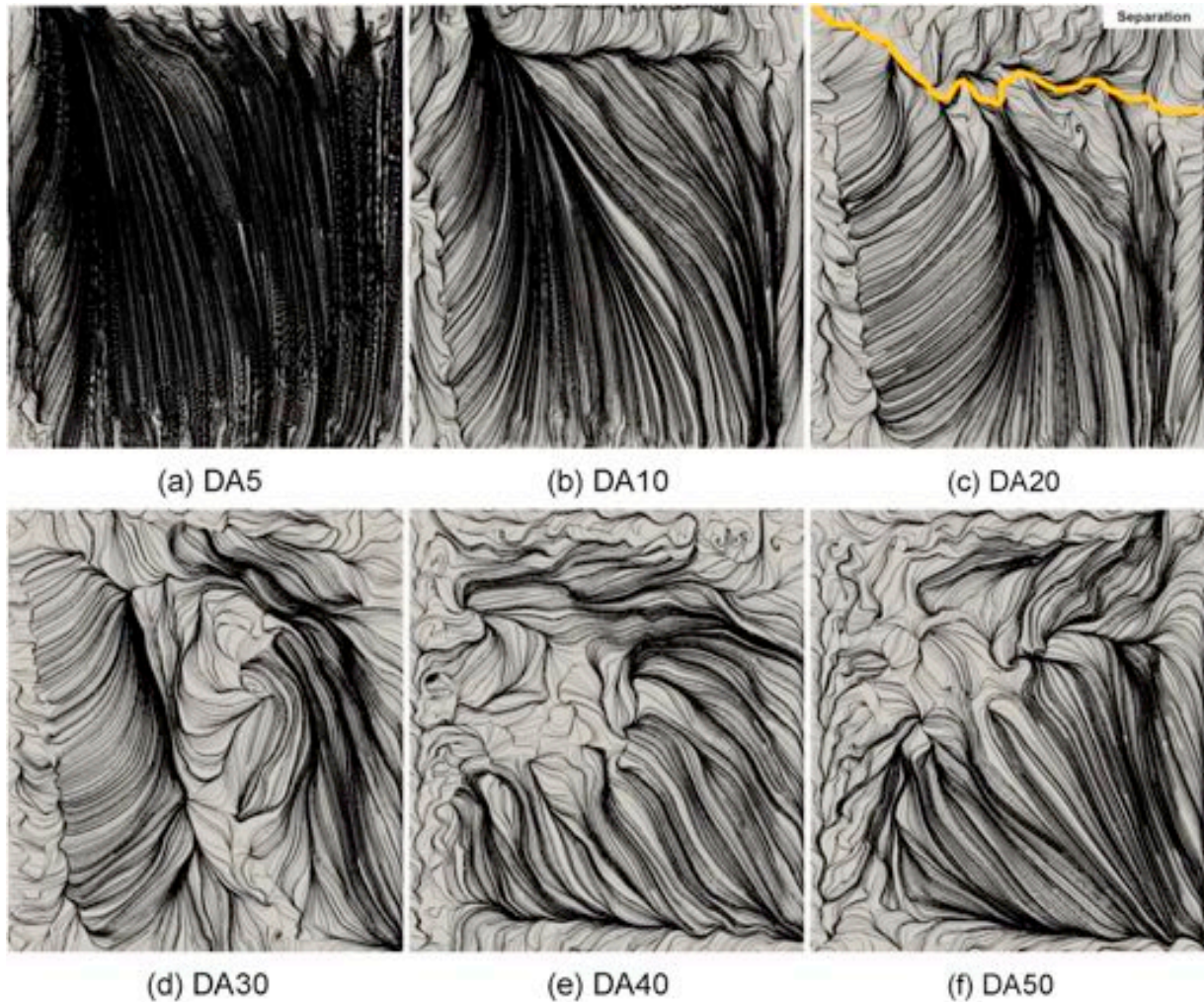


**Fig. 19.** Wall shear stress lines (black) on the diffuser surface for the Ahmed body squared-back considering the proposed diffuser angles: 5° (DA5), 10° (DA10), 20° (DA20), 30° (DA30), 40° (DA40) and 50° (DA50), bottom view, incoming flow direction from top.

wall shear stress lines from the 5th to the 7th convective length, same period as the flow quantities and aerodynamic forces. Results for the Ahmed body squared-back are firstly presented, followed by the Ahmed body with 25° slant angle with all plane views observed from downstream. We define the simulation cases by the abbreviation of diffuser angle, DA, followed by the inclination angle so diffuser angle of 30° is defined as DA30.

#### 5.1.4. Ahmed body squared back with diffuser

The first consideration of Fig. 16(a) shows a vortex arising from side of the diffuser up to the angle of 30°. The vortex intensity and core size increase as the diffuser angle becomes more inclined. A wake structure can also be noticed for the DA30 case, indicating that there is separated flow on the diffuser. Similar flow behaviour is observed on the classical Ahmed body slant variation experiment for slant angles ranging from 12.5° to 30°. For diffuser angles above 30° only a few structures are observed, such as weak vortices on the lower part of the body, near the floor. This is an indicative of fully separated flow, however the Q-Criterion image alone is not conclusive.

Moving to plane  $X/L = 0.096$ , shown Fig. 16(b), the main difference noticed is on DA30 case where the diffuser vortex has merged with the rear wake. We observed that the diffuser vortex in DA5, DA10 and DA20 cases are weaker and shifting both upwards and in the spanwise direction towards the centre plane.

Flow separation is observed for DA40 and DA50 case on plane  $X/L = 0$ . The large negative velocity area shown in Fig. 17(a) indicates that the

flow is already separated at the outlet of the diffuser. The slight higher drag for DA50 is explained by a more intense contour of negative  $U$  velocity when comparing to DA40. The negative velocity area on DA30 at mid-span, shows a combination of flow separation with vortex generation. With both flow features, the DA30 case can be characterized as a highly energetic flow.

Flow structures evolution is presented in Fig. 17(b), reaching the plane  $X/L = 0.096$ . Low velocity zones are observed on the rear vertical portion of the body, with a different contour position for DA30. The DA30 shifts the base wake upward as it moves to an inner spanwise direction. The diffuser vortex intensity is probably the main cause of this translation and  $V$  velocity results are next presented to complement the explanation of this phenomenon.

From normalized vertical velocity  $V$  contours in Fig. 18, we extract the diffuser vortex rotation direction. The diffuser vortex rotates anti-clockwise, as the most inner spanwise vortex component has positive vertical velocity and the outer negative. Vertical velocity contour for DA30 on plane  $X/L = 0.096$  explain the wake moving upwards on the spanwise direction from Fig. 17(b). A strong positive vertical velocity zone is observed at the mid-span behind both the diffuser and back of the Ahmed body.

Averaged wall shear stress lines for the diffuser cases evaluated are next presented. The bottom view of the diffuser, with flow direction coming from the top are shown in Fig. 19. We define the diffuser inlet as the top of the diffuser, and diffuser outlet as the bottom.

Analysing results in Fig. 19, we observe different flow behaviours on



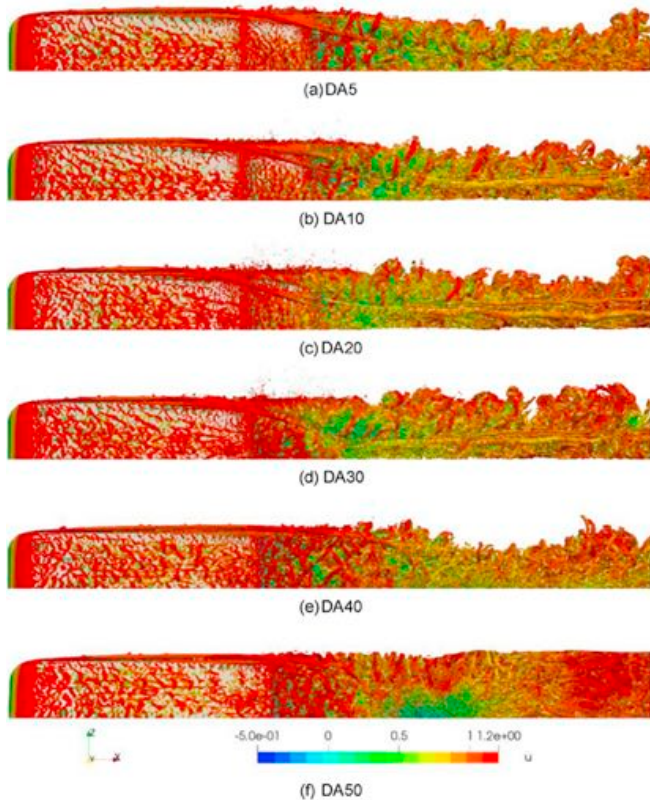


**Fig. 20.** Iso-contours of Q-Criterion ( $QCrit = 100$ ), coloured by  $U$ , of the bottom view of the Ahmed body squared-back. The following proposed diffuser angles are presented: 5° (DA5), 10° (DA10), 20° (DA20), 30° (DA30), 40° (DA40) and 50° (DA50).

the diffuser surface, detailed as follows. The DA5 and DA10 cases have the diffuser vortex influencing the diffuser surface up to the mid-span. There is a clearly defined separation area at the diffuser inlet, responsible for the pumping effect observed by (Cooper et al., 1998). The flow keeps attached on the diffuser surface until reaching the diffuser outlet. A combination of both separated flow on the diffuser surface and diffuser vortex is observed for the DA30 case. The diffuser vortex size increases, reaching almost mid-span distance at the diffuser outlet, while fully separated flow is also observed on the diffuser surface.

The pattern evident in DA20 is a combination of the DA30 and DA10 diffuser flow regimes. There is indication of the diffuser vortex, with defined separation area at the diffuser inlet followed by a small recirculation bubble due to flow separation. The flow then reattaches and follow this pattern until reaching the diffuser outlet. Considering the more extreme diffuser angles (DA40 and DA50), had no previous references, however the low performance is expected. Results show a chaotic behaviour on their surfaces due to the separated flow and a recirculation zone is observed at the diffuser outlet.

Bottom view of the Ahmed body squared-back at different diffuser angles showing iso-contours of Q-Criterion ( $QCrit = 100$ ) are presented in Fig. 20. The lower side vortex is shifting in the inner spanwise direction for DA5 up to DA30.

#### 5.1.5. Ahmed body 25° slant inclination with diffuser

We now analyse flow structures found for the Ahmed body with slant angle of 25° equipped with underbody diffuser. On the upper part of the body, the slant vortex is clearly defined in all diffuser angles evaluated. As presented for previous case, contours of Q-Criterion for planes  $X/L = 0$  and  $X/L = 0.096$  are shown in Fig. 21. The diffuser vortex appears on DA5, DA10 and DA20 together with an additional small intensity vortex on the plane  $X/L = 0$ . The diffuser vortex has similar intensity and size as

the slant vortex in the DA20 case. The other three diffuser cases, DA30, DA40 and DA50 indicate no evidence of the diffuser vortex but only the same lower side vortex, originated on the frontal part of the Ahmed body. Further downstream on plane  $X/L = 0.096$ , the vortical system have moved inward in the spanwise direction on the first three cases. The last three cases indicate that the lower side vortex gets weaker as it moved downstream.

Contours of normalized  $U$  for both  $X/L = 0$  and  $X/L = 0.096$  planes are presented in Fig. 22. On plane  $X/L = 0$ , we observe that the velocity countour on the upper slant changes as the diffuser angle becomes more inclined until the case DA20. The three other cases from DA30 to DA50 however, have similar velocity profiles. We conclude that the diffuser influences the flow over the upper slant whenever we have evidences of the diffuser vortex. From observation of the first Ahmed body case, we have indication of attached flow for diffuser angle up to 20°, whereas for higher angles, a significant wake contribution can be seen from the fully separated flow from the diffuser.

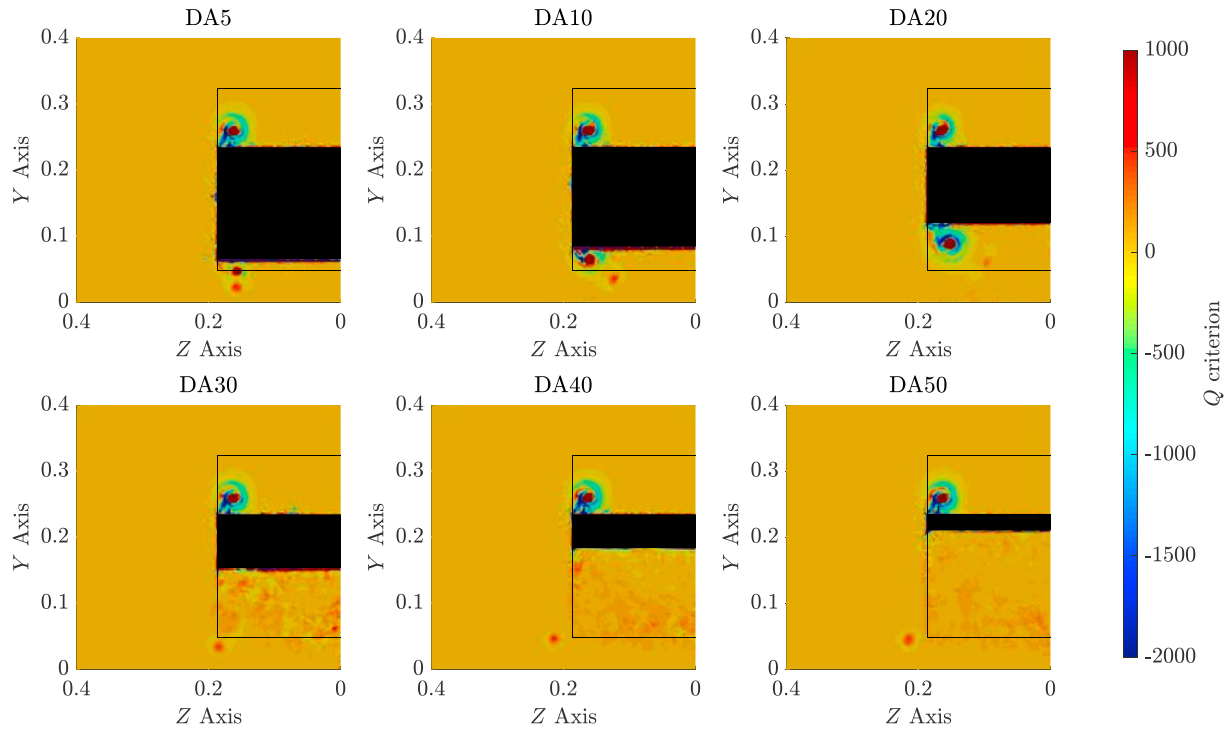
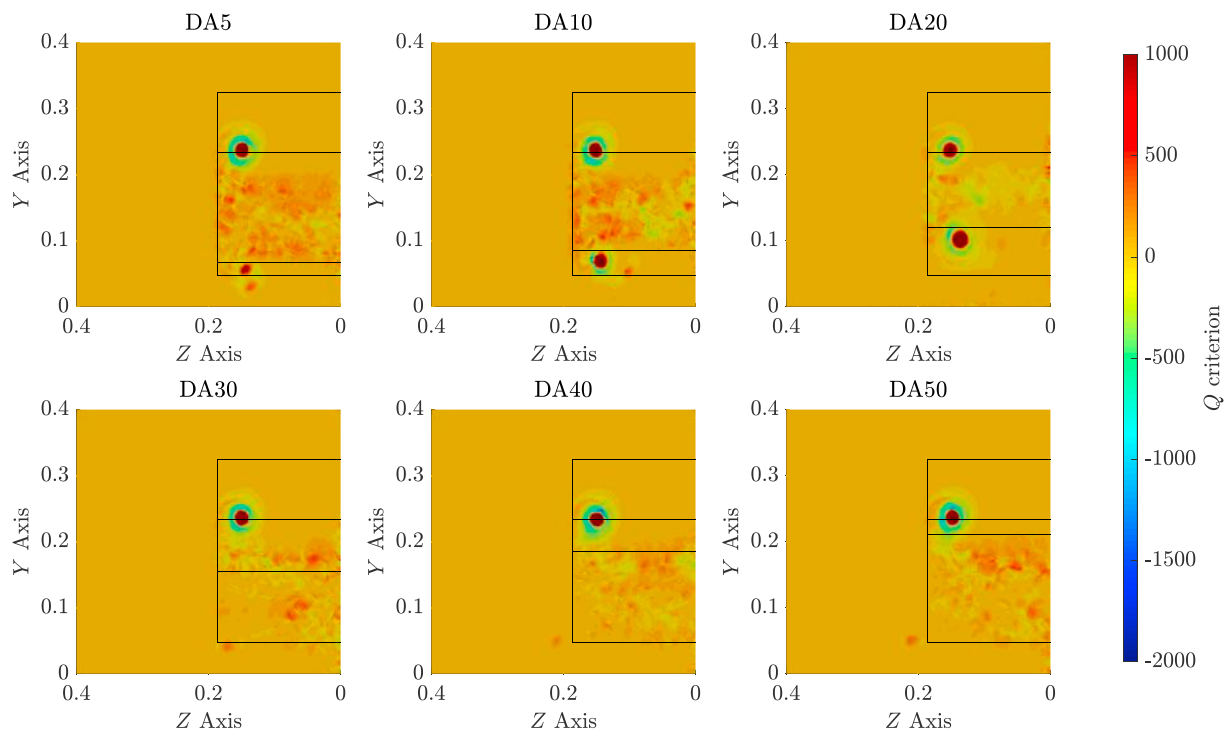
Moving downstream, normalized  $U$  velocity on plane  $X/L = 0.096$  shows the evolution of the turbulent wake and vortices. Base pressure turbulent wake with the slant and diffuser vortices are the main structures seen on cases DA5 and DA10. The  $U$  velocity contours on this plane for the DA20 case shows a very small negative velocity zone, indicating an energetic wake, together with the slant and diffuser vortices moving downstream. On DA30 case, wake profile and vortical system is similar to DA40 and DA50, except by the fact of a distortion on the lower outer area of the diffuser. At this point, the flow distortion could be caused by a vortical flow structure and further plots will provide evidences to confirm this assumption.

Normalized vertical velocity  $V$  is presented in Fig. 23 where we observe similar contour on the slant as presented by the experimental reference of (Lienhart and Becker, 2003) on plane  $X/L = 0$ . When analysing the diffuser area, two vortices are identified at similar spanwise coordinates but different heights on DA5 case. From bottom to top, the lower side vortex and the diffuser vortex are in the same region, however it is not possible to assure they are merging at this point. Only the diffuser vortex is observed for DA10 and DA20 with anti-clockwise rotation direction. The case considering diffuser angle at 30° (DA30) also has an indication of two vortices, however only the lower side vortex (bottom) can be confirmed at this point. For the DA40 and DA50 cases, the lower side vortex has similar intensity in both case and a slightly different  $V$  velocity distribution on the diffuser, with higher velocities in the most inclined diffuser.

Analysing plane  $X/L = 0.096$ , the inner spanwise component of the slant vortex is shifting downwards, once this flow structure starts to interact with the wake. On the diffuser area of DA5, the pair of vortices is merged into one single structure, with high  $V$  velocity on the positive component of the new merged vortex. DA10 and DA20 cases maintain only one single diffuser vortex structure highlighted, moving slightly up and into the spanwise direction. The DA30 case still maintain the lower side vortex in similar position as in plane  $X/L = 0$  and the additional structure does not behave as a vortex. The diffuser wake structure is still similar on DA40 compared to DA50, where the main difference relies on a low velocity zone at the mid-span of the diffuser, caused by the interference of slant vortex on the diffuser wake.

Wall shear stress lines on the surface of each diffuser case evaluated are presented in Fig. 24. This analysis follows similar terminology and setup as presented for the Ahmed body squared-back.

The flow structure on the diffuser indicates a vortex touching the diffuser surface up to angle of 20° (DA20) and separated flow from DA30 onward. We identified three flow behaviour on the diffuser surface as the previous Ahmed body squared-back, detailed as follows. The DA5 and DA10 cases have the side diffuser vortex touching the diffuser surface together with a separation area at the diffuser inlet. The flow remains attached on the surface until reaching the outlet. Separated flow on the diffuser surface and diffuser vortex is observed in the DA20 case, with a partial reattachment at the outlet. The last three diffuser angles of 30°

(a) Plane  $X/L = 0$ (b) Plane  $X/L = 0.096$ 

**Fig. 21.** Contours of Q-Criterion ( $QCrit = 100$ ) for the Ahmed body with slant angle of  $25^\circ$  considering diffuser angle of  $5^\circ$  (DA5),  $10^\circ$  (DA10),  $20^\circ$  (DA20),  $30^\circ$  (DA30),  $40^\circ$  (DA40) and  $50^\circ$  (DA50) for planes  $X/L = 0$  and  $X/L = 0.096$ .

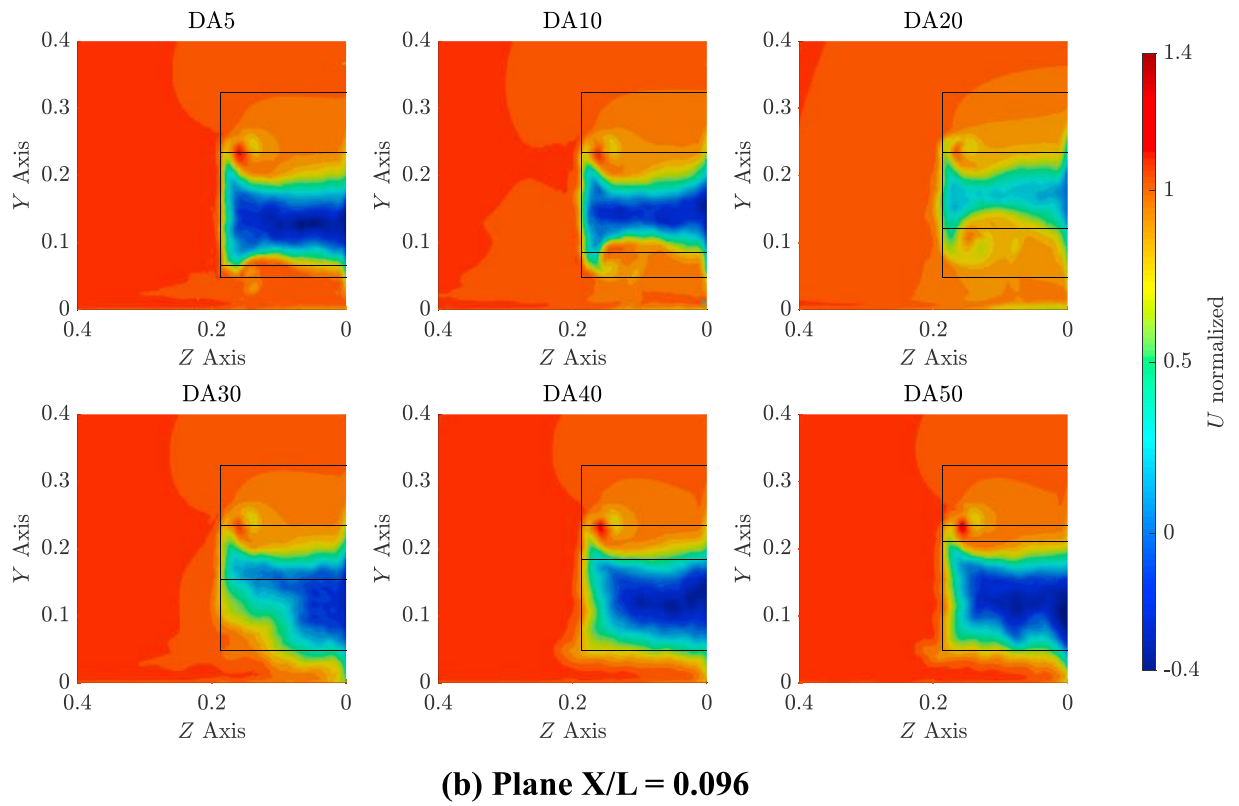
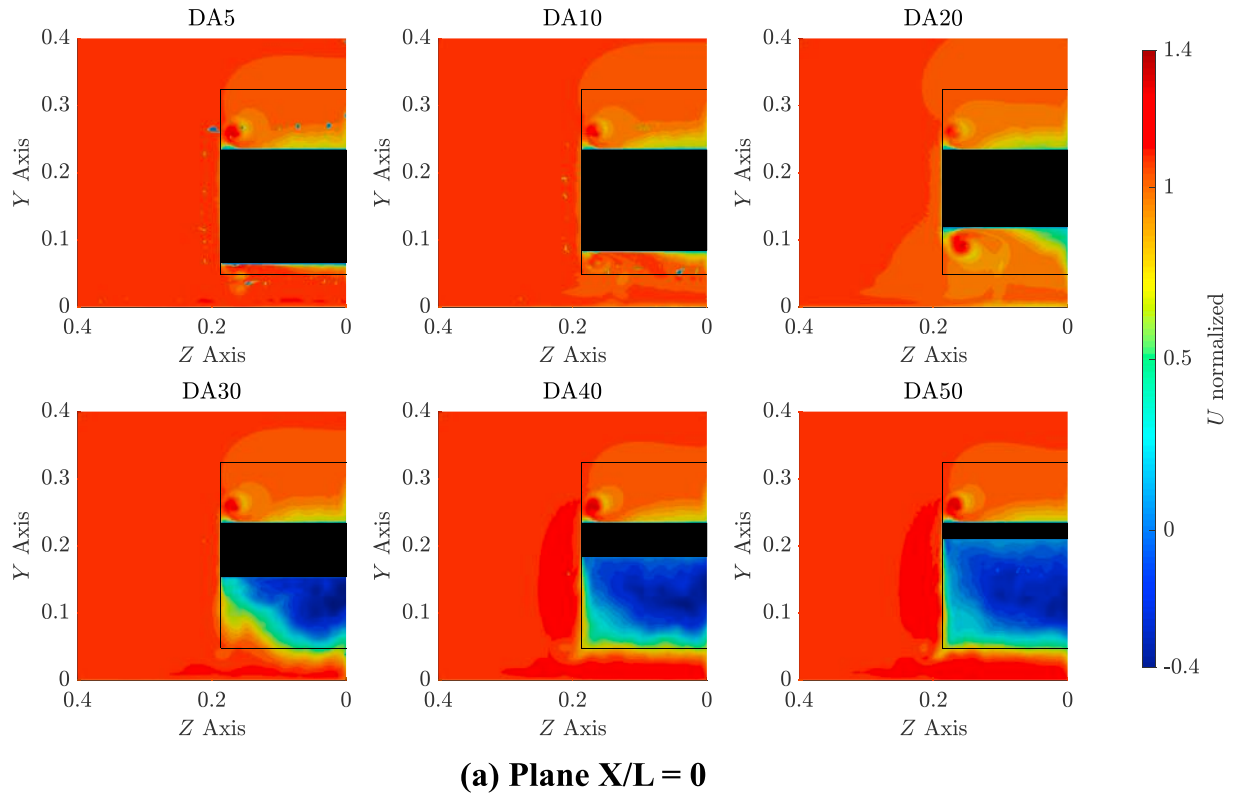


**Fig. 22.** Contours of normalized streamwise velocity  $U$  for the Ahmed body with slant angle of  $25^\circ$  considering the proposed diffuser angles:  $5^\circ$  (DA5),  $10^\circ$  (DA10),  $20^\circ$  (DA20),  $30^\circ$  (DA30),  $40^\circ$  (DA40) and  $50^\circ$  (DA50) for planes  $X/L = 0$  and  $X/L = 0.096$ .

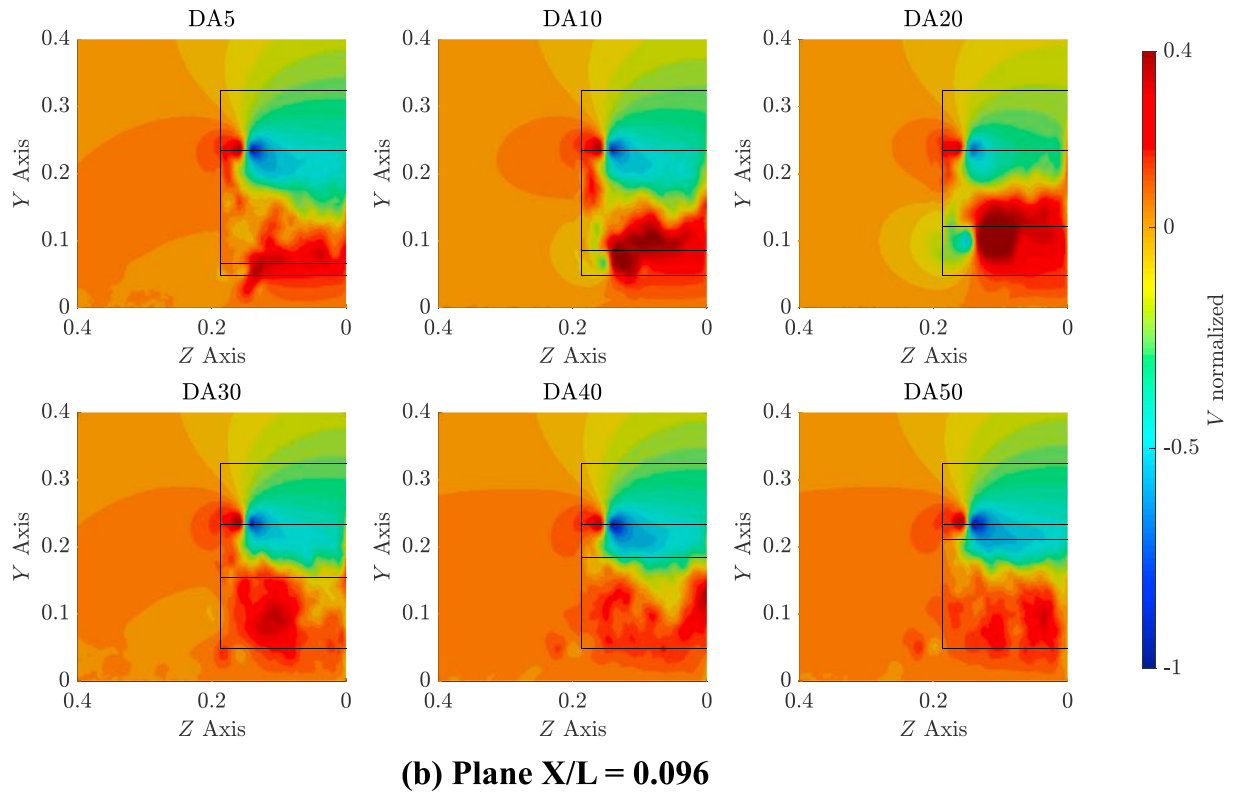
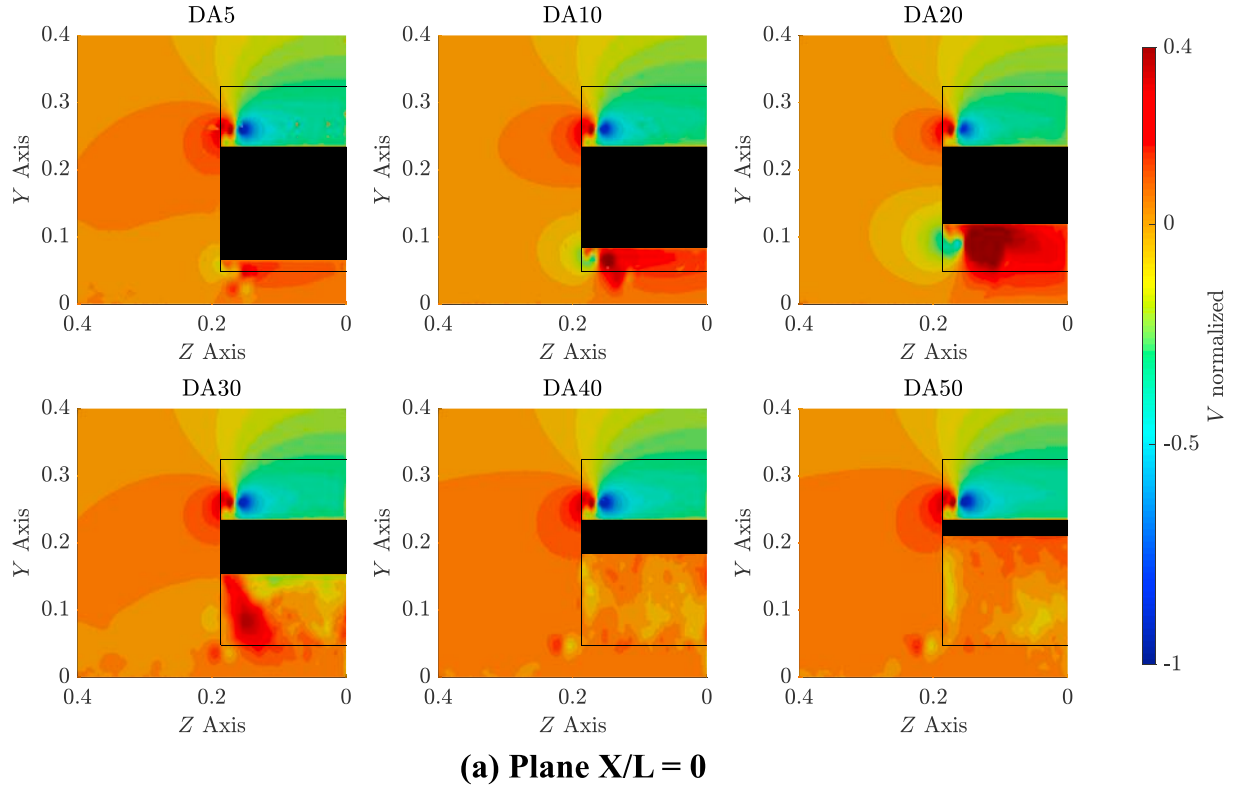


**Fig. 23.** Contours of normalized vertical velocity  $V$  for the Ahmed body with slant angle of  $25^\circ$  considering the proposed diffuser angles:  $5^\circ$  (DA5),  $10^\circ$  (DA10),  $20^\circ$  (DA20),  $30^\circ$  (DA30),  $40^\circ$  (DA40) and  $50^\circ$  (DA50) for planes  $X/L = 0$  and  $X/L = 0.096$ .



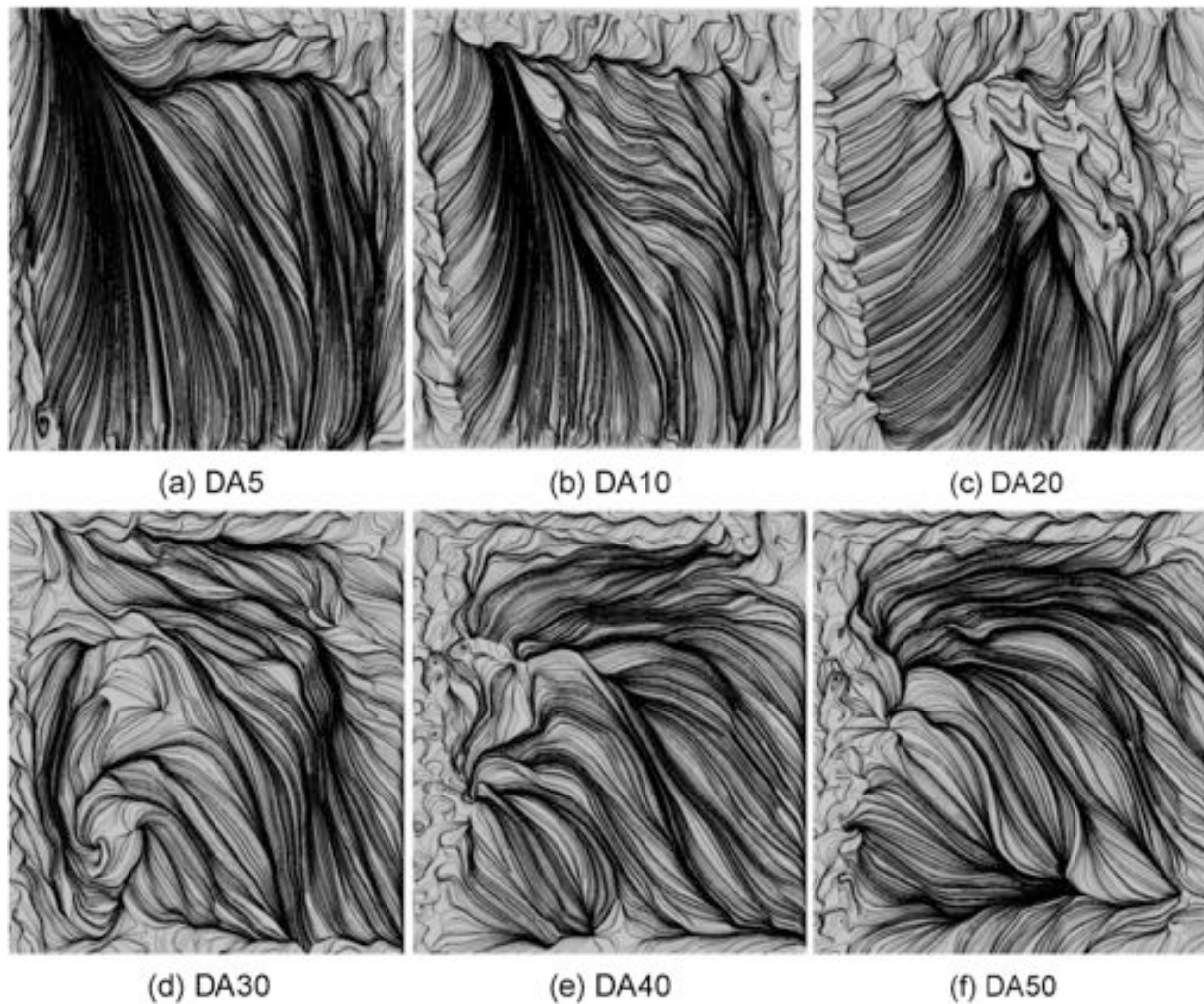


**Fig. 24.** Wall shear stress lines (black) on the diffuser surface for the Ahmed body with slant angle of  $25^\circ$  considering the proposed diffuser angles:  $5^\circ$  (DA5),  $10^\circ$  (DA10),  $20^\circ$  (DA20),  $30^\circ$  (DA30),  $40^\circ$  (DA40) and  $50^\circ$  (DA50), bottom view, incoming flow direction from top.

(DA30),  $40^\circ$  (DA40) and  $50^\circ$  (DA50) have a fully separated flow all over the diffuser surface.

Flow structures on the bottom view for the Ahmed body with slant angle of  $25^\circ$  considering different diffuser angles are presented in Fig. 25. From the iso-contours of Q-Criterion ( $QCrit = 100$ ) coloured by  $U$ , we observe the same lower side vortex behaviour shifting inwards in the spanwise direction. The lower vortex shifting only happens with the existence of the diffuser vortex, from DA5 to DA20 in this case.

## 6. Conclusions

A parametric study on the effect of diffusers is conducted on the Ahmed body at two slant cases: squared-back and  $25^\circ$  angle. The diffuser length is fixed with the same dimension of the slant and cases are evaluated at a Reynolds number of  $Re = 1.7 \times 10^6$  with moving ground condition. Diffuser angles considered range from  $10^\circ$  to  $50^\circ$  in increments of  $10^\circ$ , including one additional angle of  $5^\circ$  for both cases. The numerical methodology employed in this study was validated on the classical Ahmed body geometry, where it was found good agreement in terms of flow structures and the difference of 13% and 1% for respectively drag and lift coefficient against experiments. The application of the spectral/hp element method also allowed to have a high-fidelity solution from a relatively coarse mesh. Further increments on the resolution by increasing the solution polynomial order  $P_N$  are possible, keeping the same mesh structure, which is highly desirable for comparative purposes.

The study extended the knowledge on plane diffusers by showing the flow behaviour on a well-established bluff body when the downforce generation by the diffuser is not effective anymore. The interaction of the lower side vortices with the flow structures on the diffuser region due to the absence of endplates is an interesting phenomenon.

Ahmed body squared-back results indicate two different flow behaviours. The first is observed in diffuser angles from  $5^\circ$  up to  $30^\circ$ , indicating that downforce increment leads to higher drag coefficient. Flow structure for this regime is composed of a lateral vortex with fully attached flow on the diffuser surface for diffusers up to  $20^\circ$ . The critical angle has similar structure considering the same diffuser vortex however the flow is partially separated on the diffuser surface. The second flow regime is found for diffuser angles higher than  $30^\circ$  where downforce increment efficiency is lost, and the flow is fully separated on the diffuser surface.

On the Ahmed body with  $25^\circ$  slant angle, downforce increases while the drag coefficient is reduced for diffuser angles up to  $20^\circ$ . Maximum downforce is observed at  $10^\circ$ . The flow structure is composed of the diffuser vortex and attached flow on the diffuser surface, however only for the  $5^\circ$  and  $10^\circ$  diffuser angles. The diffuser vortex is present in the  $20^\circ$  case but the flow is mostly separated. Similar to the squared-back case, the highest drag coefficient value is observed for the  $30^\circ$  angle, and flow on the diffuser surface is fully separated from this case onward.

The downforce enhancement provided by the diffuser is connected to the presence of the diffuser vortex on the lower portion of the body. As



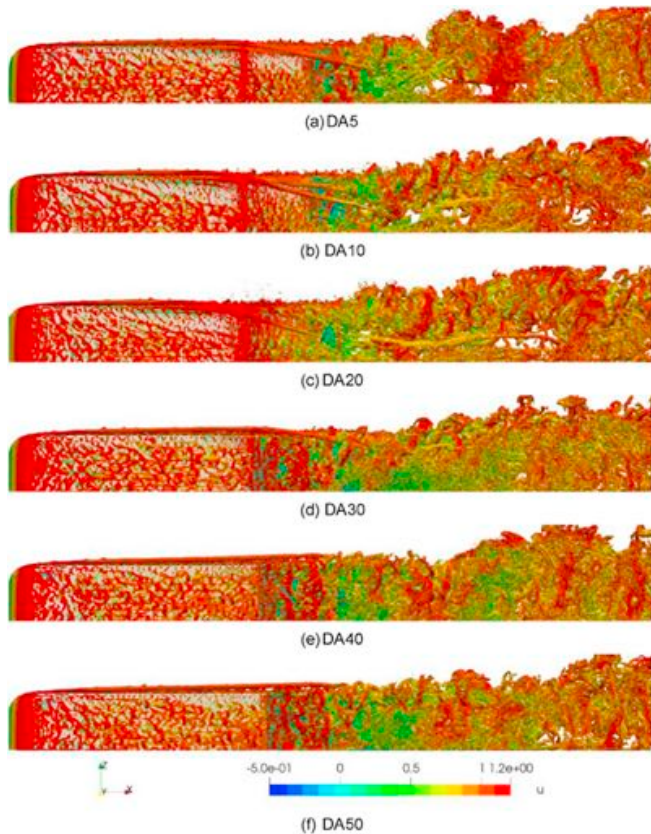


Fig. 25. Iso-contours of Q-Criterion ( $QCrit = 100$ ), coloured by  $U$ , of the bottom view of the Ahmed body with slant angle of  $25^\circ$ . The following proposed diffuser angles are presented:  $5^\circ$  (DA5),  $10^\circ$  (DA10),  $20^\circ$  (DA20),  $30^\circ$  (DA30),  $40^\circ$  (DA40) and  $50^\circ$  (DA50).

the diffuser vortex disappear and the flow becomes fully separated, only small downforce increments are observed. Before the diffuser flow separates, the effect of an increment in the diffuser angle aims to increase the intensity of the diffuser vortex, which is associated with an increase in downforce. We therefore conclude that an efficient diffuser needs to have a coherent diffuser vortex present.

The flow topology on the diffuser surface is also modified by the diffuser angle changes, from attached flow to separated flow both in the presence of the diffuser vortex. At this point, the most efficient diffuser angle in terms of downforce presents diffuser vortex and separated flow as its flow structure.

The diffuser is a passive device that is influenced by the base-pressure region. Results of the aerodynamic quantities show that although following similar trends, the downforce increment is higher for the Ahmed body squared-back, which has higher base-pressure region and also offsets by  $10^\circ$ , the most efficiency diffuser angle when compared to the Ahmed body with  $25^\circ$  slant angle.

The drag coefficient follows the opposite trends for each Ahmed body due to different flow structures on the upper slant. Considering the cases where the diffuser is most efficient, and the flow on the diffuser surface changes from attached to separated, there is a drag increment. This drag increment is very small for the Ahmed body with  $25^\circ$  slant angle but approximately 45% for the Ahmed body squared-back for a downforce increment of approximately 7%.

We conclude that the diffuser performance is connected to the body geometry and the highest downforce increment is reached once the flow structure is composed by the diffuser vortex and separated flow. For the overall aerodynamic performance, the drag coefficient should be considered in order to select the best diffuser angle.

## CRediT authorship contribution statement

**Filipe F. Buscariolo:** Methodology, development, simulation setup, Data curation, data processing, correlation study, Formal analysis, analysis, Writing – original draft, Writing – review & editing. **Gustavo R.S. Assi:** Supervision, Writing – review & editing. **Spencer J. Sherwin:** Conceptualization, Supervision, concept development, Software, implementation, Writing – original draft, Writing – review & editing, sponsor.

## Declaration of competing interest

The authors declare that they have no known competing financial interests or personal relationships that could have appeared to influence the work reported in this paper.

## Acknowledgement

We acknowledge the HPC facilities at Imperial College Research Computing Service, <https://doi.org/10.14469/hpc/2232> and also under the UK Turbulence Consortium. CNPq for the sponsorship 202578/2015-1.

## References

- Ahmed, S., Ramm, G., Faltin, G., 1984. Some Salient Features of the Time-Averaged Ground Vehicle Wake. Technical report, SAE Technical Paper.
- Buscariolo, F., 2020. Spectral/hp Large Eddy Simulation of Vortex-Dominated Automotive Flows Around Bluff Bodies with Diffuser and Complex Front Wing Geometries. Imperial College London/USP. PhD thesis.
- Buscariolo, F.F., Assi, G.R.S., Meneghini, J.R., Sherwin, S.J., 2020. Spectral/hp methodology study for iles-sv on an ahmed body. In: Spectral and High Order Methods for Partial Differential Equations ICOSAHOM 2018. Springer to be released.
- Buscariolo, F.F., Hoessler, J., Moxey, D., Jassim, A., Gouder, K., Basley, J., Murai, Y., Assi, R.S., Sherwin, S.J., 2019. Spectral/hp Element Simulation of Flow Past a Formula One Front Wing: Validation against Experiments.
- Cantwell, C., Moxey, D., Comerford, A., Bolis, A., Rocco, G., Mengaldo, G., De Grazia, D., Yakovlev, S., Lombard, J.-E., Ekelschot, D., et al., 2015. Nektar++: an open-source spectral/hp element framework. *Comput. Phys. Commun.* 192, 205–219.
- Cooper, K.R., Bertenyi, T., Dutil, G., Syms, J., Sovran, G., 1998. The Aerodynamic Performance of Automotive Underbody Diffusers. Technical report, SAE Technical Paper.
- Dong, S., Karniadakis, G.E., Chrysosostomidis, C., 2014. A robust and accurate outflow boundary condition for incompressible flow simulations on severely-truncated unbounded domains. *J. Comput. Phys.* 261, 83–105.
- Graysmith, J., Baxendale, A., Howell, J., Haynes, T., 1994. Comparisons between CFD and experimental results for the ahmed reference model. In: RAE Conference on Vehicle Aerodynamics, Loughborough, pp. 30–31.
- Grinstein, F., Margolin, L., Rider, W., 2007. 'Implicit Large Eddy Simulation: Computing Turbulent Fluid Dynamics', *Implicit Large Eddy Simulation: Computing Turbulent Fluid Dynamics*.
- Guermond, J.-L., Shen, J., 2003. Velocity-correction projection methods for incompressible flows. *SIAM J. Numer. Anal.* 41 (1), 112–134.
- Guilmineau, E., Deng, G.B., Leroyer, A., Queutey, P., Visonneau, M., Wackers, J., 2018. Assessment of hybrid rans-les formulations for flow simulation around the ahmed body. *Comput. Fluid* 176, 302–319.
- Huminic, A., Huminic, G., 2010. Computational Study of Flow in the Underbody Diffuser for a Simplified Car Model. Technical report, SAE Technical Paper.
- Huminic, A., Huminic, G., 2012. Numerical Flow Simulation for a Generic Vehicle Body on Wheels with Variable Underbody Diffuser. Technical report, No. 2012-01-0172, SAE Technical Paper.
- Islam, A., Gaylard, A., Thornber, B., 2017. A detailed statistical study of unsteady wake dynamics from automotive bluff bodies. *J. Wind Eng. Ind. Aerod.* 171, 161–177.
- Jowsey, L., 2013. An Experimental Study of Automotive Underbody Diffusers. PhD thesis. © Lydia Jowsey.
- Karniadakis, G., Sherwin, S., 2013. Spectral/hp Element Methods for Computational Fluid Dynamics. Oxford University Press.
- Krajnović, S., Davidson, L., 2004. Large-eddy Simulation of the Flow Around Simplified Car Model. Technical report, SAE Technical Paper.
- Lienhart, H., Becker, S., 2003. Flow and Turbulence Structure in the Wake of a Simplified Car Model. Technical report, SAE Technical Paper.
- Luckhurst, S., Varney, M., Xia, H., Passmore, M., Gaylard, A., 2019. Computational investigation into the sensitivity of a simplified vehicle wake to small base geometry changes. *J. Wind Eng. Ind. Aerod.* 185, 1–15.
- Mengaldo, G., Grazia, D.D., Moxey, D., Vincent, P.E., Sherwin, S.J., 2015. Dealiasing techniques for high-order spectral element methods on regular and irregular grids. *J. Comput. Phys.* 299, 56–81.
- Moghimi, P., Rafee, R., 2018. Numerical and experimental investigations on aerodynamic behavior of the ahmed body model with different diffuser angles. *J. Appl. Fluid Mech.* 11 (4).

- Morel, T., 1978. Aerodynamic Drag of Bluff Body Shapes Characteristic of Hatch-Back Cars. Technical report, SAE Technical Paper.
- Moura, R.C., Mengaldo, G., Peiró, J., Sherwin, S.J., 2017. On the eddy-resolving capability of high-order discontinuous galerkin approaches to implicit les/under-resolved dns of euler turbulence. *J. Comput. Phys.* 330, 615–623.
- Moxey, D., Green, M.D., Sherwin, S.J., Peiró, J., 2015. An isoparametric approach to high-order curvilinear boundary-layer meshing. *Comput. Methods Appl. Mech. Eng.* 283, 636–650.
- Senior, A.E., Zhang, X., 2001. The force and pressure of a diffuser-equipped bluff body in ground effect. *Transactions-American Society. Mech. Eng. J. Fluids Eng.* 123 (1), 105–111.
- Serre, E., Minguez, M., Pasquetti, R., Guilmineau, E., Deng, G., Kornhaas, M., Schäfer, M., Fröhlich, J., Hinterberger, C., Rodi, W., 2013. On simulating the turbulent flow around the ahmed body: a French–German collaborative evaluation of les and des. *Computers & Fluids* 78, 10–23.
- Strachan, R., Knowles, K., Lawson, N., 2007. The vortex structure behind an ahmed reference model in the presence of a moving ground plane. *Exp. Fluid* 42 (5), 659–669.
- Turner, M., 2017. High-order Mesh Generation for CFD Solvers. Imperial College London. PhD thesis.
- Turner, M., Moxey, D., Peiró, J., Gammon, M., Pollard, C.R., Bucklow, H., 2017. A framework for the generation of high-order curvilinear hybrid meshes for CFD simulations. *Procedia engineering* 203, 206–218.

# Experiments with novel geometries of serrated helical strakes to suppress vortex-induced vibrations

Gustavo R.S. Assi, Tommaso Crespi<sup>1</sup>,

*Dept. Naval Arch. & Ocean Engineering, EPUSP, University of São Paulo, Brazil*

Morteza Gharib

*GALCIT, California Institute of Technology, USA*

---

## Abstract

We present an experimental investigation on the effectiveness of unconventional geometries of serrated helical strakes to suppress the cross-flow vortex-induced vibrations (VIV) of a circular cylinder with low mass and structural damping. The VIV responses of five models of strakes are compared with that of a bare cylinder at moderate Reynolds numbers: one continuous helical strake, two serrated strakes and two inverted strakes. While the conventional strake suppressed 88% of the peak amplitude of response with a 48% drag reduction, the most efficient serrated strake reduced the peak amplitude of vibration by 95% producing 54% less drag than a bare cylinder. When the models were not allowed to respond to VIV they all increased drag in relation to that of bare cylinder. We verified that simply inverting the local angle of attack of the individual blades in relation to the helical pitch of the strake did not produce a favourable result in terms of VIV suppression, but reduced drag and fluctuating lift on a fixed body. Visualization of the flow around the blades helped to clarify the hydrodynamic mechanisms governing flow separation in the near wake, disrupting the formation of coherent vortices and reducing VIV.

*Keywords:* Vortex-induced vibration, suppression, drag reduction, helical strakes

---

## 1. Introduction

The vibration induced by the external flow past slender structures poses a problem to submarine and offshore cables, flexible pipes, drilling and production risers and other light and elastic

---

*Email address:* g.assi@usp.br (Gustavo R.S. Assi)

<sup>1</sup>Double-degree student between University of São Paulo and Politecnico di Milano.

structures exposed to sea currents. The excitation has its origin in the shedding mechanism of alternating vortices occurring in the wake of bluff bodies, so the hydroelastic phenomenon is called vortex-induced vibration (VIV). The vibration of risers is typical problem for the offshore industry. Flexible lines exposed to vibrations for a long time may be damaged by structural fatigue (Tognarelli et al., 2008), but the amplification of drag due to the vibration of the body is also of considerable concern, since it increases static and dynamic loads at the joints, platform and other fixtures.

One way to mitigate the effects of VIV is the installation of suppressors along the riser, or at least on the length of the line where currents are most intense. Helical strakes and fairings, for example, have been widely employed by the industry as VIV suppressors (Taggart and Tognarelli, 2008). On one hand, significant VIV suppression of light structures requires wider strakes, which increases drag. Fairings, on the other hand, tend to be more efficient in suppression as far as drag is concerned, but may suffer from hydroelastic instabilities (Assi et al., 2014) and difficulties related to their transportation, installation and maintenance. With the improvement of the moulded plastic industry, helical strakes and fairings have indeed become sturdy contraptions, but they still take considerable time to install and occupy large areas on the deck. Other devices based on the disruption of the wake by interfering control surfaces (as explored by Silva-Ortega and Assi (2017), for example) may suffer from the same problem.

During the last decades many devices have been investigated and offered as commercial products. Following the industry's demand for more efficient, robust and easy-to-install devices, the technological development for suppressing VIV has been under pursuit by both the scientific and industrial communities. Inspired by the conventional helical strakes, many have investigated other variations of this family of three-dimensional VIV suppressors (Korkischko and Meneghini, 2010). While some have invested in new geometries to reduce the drag penalty, others have focused on the robustness and ease of installation of the devices. New shapes, sizes and installation methods appeared on the market. However, as far as offshore helical strakes are concerned, it appears that a sufficient height of the blades (with the consequent drag increase) is required to promote the appropriate three-dimensional flow interaction in the near wake to disrupt the formation of coherent vortices and suppress VIV.

Among so many different geometries of strakes (many achieved by empirical variations) there

remains the scientific question on the fundamental fluid-structure interaction behind the suppression. This paper is part of a wider investigation on the physical mechanisms behind the suppression of flow-induced vibrations by means of helical strakes. By proposing small variations on the geometry of helical strakes, we hope to shed new light on the intricate hydrodynamics behind this device.

### *Objective*

Starting with the geometry of a conventional helical strake, we have divided the continuous blades into smaller, serrated blades. On a second step, the local angle of attack of each individual blade segment was altered, without changing the helical pitch of the device. Five models of strakes have been tested and their responses to VIV compared to that of a bare cylinder (BC).

## **2. Method**

### *2.1. Strake models*

Five strake models in total have been prepared for the present experimental investigation, as presented in figure 1. The conventional *continuous helical strake* (CS) was inspired by the commercial strakes available for the offshore industry. It presents three continuous blades helically wrapped around a bare cylinder — also known as a “three-start strake” — with a pitch of  $P/D = 5$  and a blade height of  $h/D = 0.2$ . The CS will serve as a reference for the others.

The unconventional devices are variations of the helical strake with serrated blades in which the local angle of the blade segments have been varied in relation to the helix of the strake. Since the pitch was set to  $P/D = 5$ , the inclination of the curved helix in relation to the axis of the cylinder is  $30^\circ$ , as seen in figure 2. The first serrated model was named *serrated 30-strake* (S30) and has been designed simply by sectioning the helical blades of the continuous strake in smaller segments hence the orientation of the segments follow the trajectory of the helix, thus keeping the same  $30^\circ$  angle with the axis of the cylinder. In the second serrated model, each individual blade segment was twisted in relation to original helix, increasing the local angle to  $45^\circ$ , thus producing the *serrated 45-strake* (S45).

As presented in figure 3a, the span of a single blade segment was  $b_1 = D/3$ , thus one full pitch of  $5D$  contained 15 blade segments. The small segment had a trapezoidal geometry, with a longer



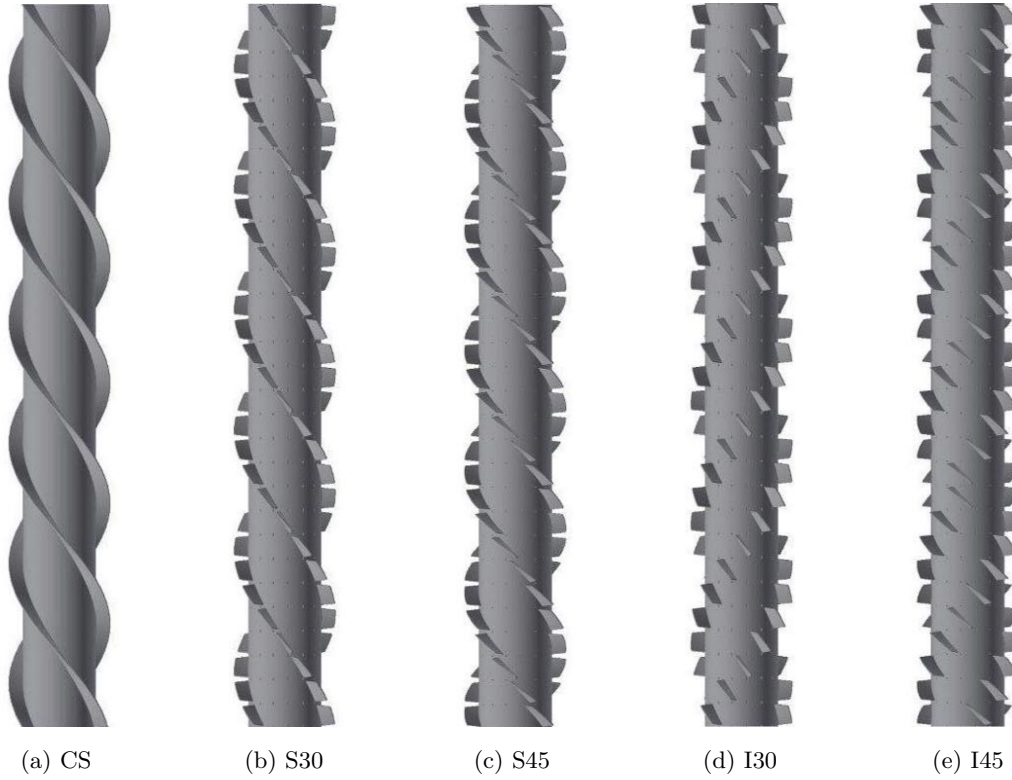


Figure 1: Models of helical strakes: (a) CS continuous strake; (b) S30 serrated 30-strake; (c) S45 serrated 45-strake; (d) I30 inverted 30-strake; (e) I45 inverted 45-strake.

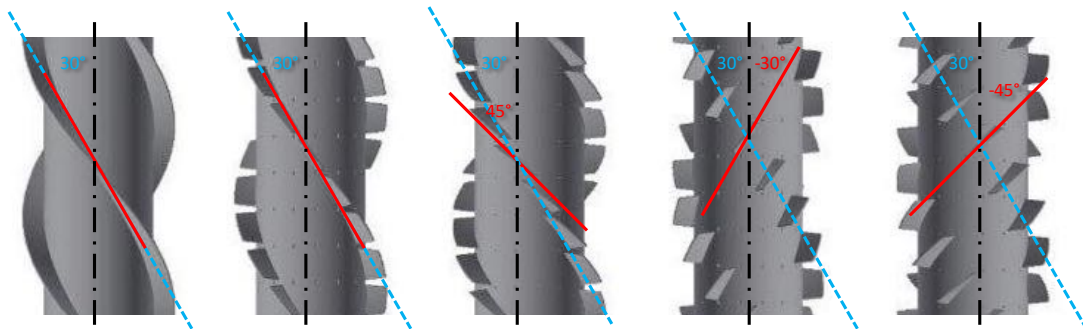


Figure 2: Orientation of blades (from left to right): CS, S30, S45, I30 and I45. The dashed line marks the pitch orientation and the continuous line marks the orientation of the blade segment.

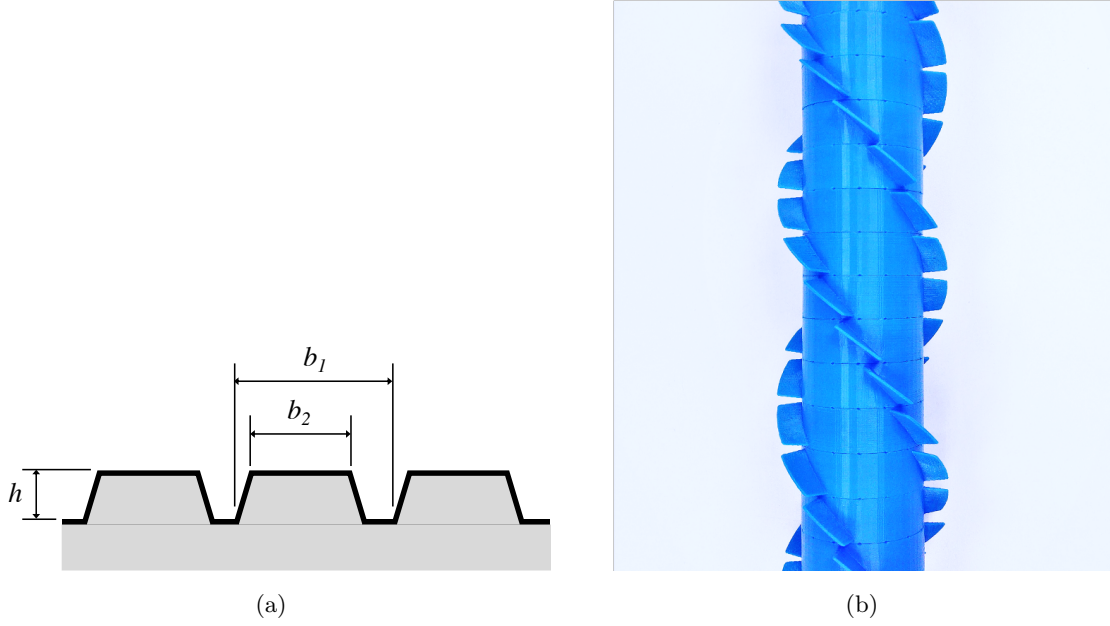


Figure 3: (a) Dimensions of the “unwrapped” blade segments for the serrated strakes. (b) Detail of the S45 model.

root and a tapered tip defined by  $b_2 = D/4$ . The blade thickness was  $t = h/6$ . Lengths  $b_1$  and  $b_2$  were inspired on some commercial devices offered to the offshore industry.

The last pair of strakes was designed by inverting the orientation of each blade segments so that the blades were orthogonal to the pitch helix. Inverting the serrated blades presented above, two models have been created: the *inverted 30-strake* (I30) and the *inverted 45-strake* (I45) with blade angles of  $-30^\circ$  and  $-45^\circ$ , respectively, in relation to the cylinder axis. A detailed view of the inverted blades is presented in figure 2. Again,  $P/D$ ,  $h/D$ ,  $b_1$  and  $b_2$  were kept the same for all models.

The idea behind the unconventional geometries of inverted strakes was to transfer momentum from the incoming flow to the spanwise direction in two different ways: (i) following the conventional pitch line and (ii) following the new angle of the individual blades. Our objective is to produce a more complex three-dimensional interaction in the near-wake region, disrupting vortex shedding.

All three models had the same core diameter of  $D = 60\text{mm}$  (also the diameter of bare cylinder used as reference) and the same underwater length of  $L/D = 11.7$ , corresponding to at least 2 fully submerged pitch lengths. The strakes were 3D-printed out of ABS plastic in the shape of rings that could be easily fitted around the core cylinder, as illustrated in figure 3b for the S45 model.

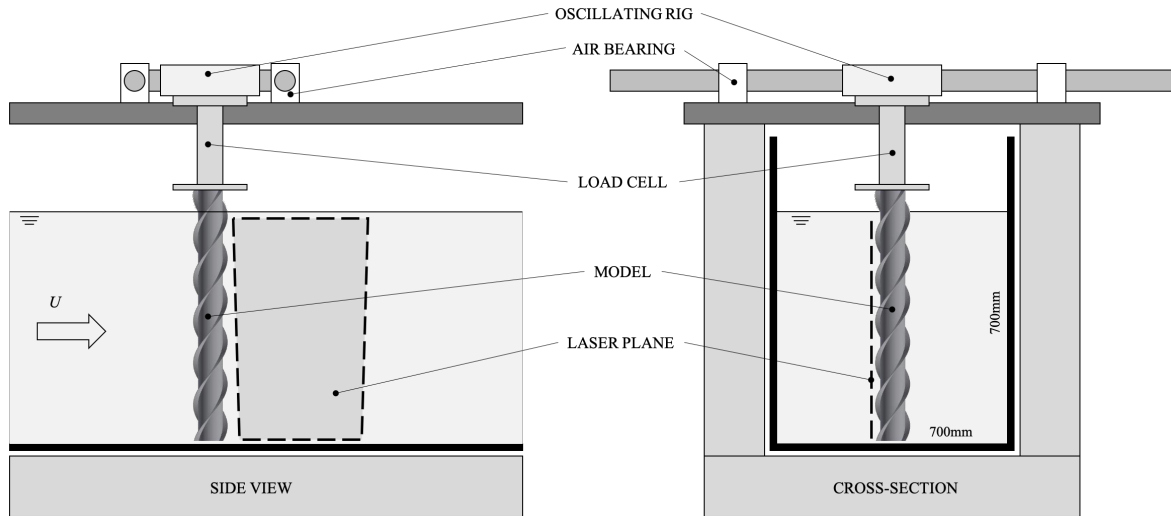


Figure 4: Lateral (left) and cross-sectional (right) view of a helical strake in the test section of the recirculating water channel.

Table 1 summarises the geometrical parameters of the strakes.

## 2.2. Experimental setup

In order to determine the dynamic response to VIV, experiments have been carried out in the recirculating water channel of NDF Fluids and Dynamics Research Group at the University of São Paulo, Brazil. The water channel has a free-surface test section which is 0.7m wide, 0.9m deep and 7.5m long. Good quality flow can be achieved up to 1.0m/s with a free-stream turbulence intensity less than 3%.

Cylinder models were mounted on a one-degree-of-freedom elastic rig built by Assi (2009) especially for experiments on flow-induced vibration. A cross-view of the experimental setup installed in the water channel is presented in figure 4. The rig consists of two long carbon-fibre pipes sliding through four air-bearings. The light structure allowed for displacements only in the cross-flow direction with very low structural damping. A pair of coil springs provided the necessary stiffness to the system and optical sensors measured the cross-flow displacement without adding extra damping. The reference bare cylinder and the other strake models were attached at the top end to a load cell designed to measure the instantaneous hydrodynamic loads on the submerged bodies.

The only flow variable changed during the course of the experiments was the flow velocity  $U$ , which altered the Reynolds number ( $Re = UD/\nu$ , based on the diameter  $D$  of the bare cylinder and

Table 1: General parameters for the present investigation.

|                        |       |  |
|------------------------|-------|--|
| Bare-cylinder diameter | $D$   | 60mm                                     |
| Underwater span        | $L$   | $11.7D$                                  |
| Helical pitch          | $P$   | $5D$                                     |
| Blade height           | $h$   | $D/5$                                    |
| Blade-segment span     | $b_1$ | $D/3$                                    |
| Blade-segment length   | $b_2$ | $D/4$                                    |
| Blade thickness        | $t$   | $h/6$                                    |
| Reynolds number        | $Re$  | $5 \times 10^3$ to $5 \times 10^4$       |
| Froude number          | $Fr$  | $5 \times 10^{-2}$ to $5 \times 10^{-1}$ |

the viscosity of water  $\nu$ ) between 5,000 and 50,000. Froude number ( $Fr = U/\sqrt{gD} < 0.5$ , where  $g$  is the acceleration of gravity) was verified to be very low and wave effects have been neglected following Chaplin and Teigen (2003).

The reduced velocity  $U/(f_N D)$  was defined by the natural frequency of the system ( $f_N$ ) determined by decay tests performed in still water. As expected, the natural frequencies of the models with strakes were slightly lower than that of the bare cylinder. As a reference, the structural damping factor of  $\zeta = 0.53\%$  (expressed as a fraction of the critical damping) was determined for the bare cylinder during similar decay tests performed in air, which also provided the natural frequency measured in air ( $f_0$ ). The ratio of the total mass of the system to the mass of the displaced water was  $m^* = 0.58$  for all models, thus producing a mass-damping factor of  $m^*\zeta = 0.0031$  for the bare cylinder. Mass and damping were intentionally kept to a minimum to promote high-amplitude vibrations.

A summary of all the geometric and flow parameters investigated in the present experiment is presented in table 1. Table 2 presents some dynamic parameters for each specific model, where  $f_0$  and  $f_N$  are the natural frequencies determined in air and in still water, respectively,  $\zeta$  is the structural damping from decay tests performed in air and  $\zeta_w$  is the cross-flow damping obtained from a decay test in still water.

Table 2: Dynamic parameters for the specific models.

| Key | Model              | $m^*$ | $f_0$ (Hz) | $f_N$ (Hz) | $\zeta$ (%) | $\zeta_w$ (%) | $m^*\zeta$ |
|-----|--------------------|-------|------------|------------|-------------|---------------|------------|
| BC  | bare cylinder      | 0.58  | 0.68       | 0.58       | 0.53        | 2.40          | 0.0031     |
| CS  | continuous strake  | 0.63  | 0.65       | 0.49       | 1.22        | 8.75          | 0.0077     |
| S30 | serrated 30-strake | 0.61  | 0.65       | 0.50       | 0.75        | 6.89          | 0.0046     |
| S45 | serrated 45-strake | 0.62  | 0.65       | 0.50       | 0.75        | 7.55          | 0.0046     |
| I30 | inverted 30-strake | 0.61  | 0.65       | 0.51       | 0.85        | 7.58          | 0.0052     |
| I45 | inverted 45-strake | 0.62  | 0.65       | 0.51       | 0.65        | 7.05          | 0.0040     |

### 3. VIV response and hydrodynamic loads

#### 3.1. Reference models: BC and CS

Preliminary VIV (vortex-induced vibration) experiments were performed with a bare cylinder (BC) to serve as a reference for comparison. Throughout this work, the “harmonic amplitude of vibration”  $\hat{y}/D$  was obtained by taking the RMS (root-mean square) of displacement and multiplying it by  $\sqrt{2}$ . The VIV response, presented in figure 5a, shows the three branches of response along the reduced velocity axis that are typical of low mass-damping structures. A peak amplitude  $\hat{y}/D = 0.80$  was observed for the resonance at  $U/(f_N D) \approx 5$ . The VIV synchronisation range occurred between  $U/(f_N D) = 3$  and 12, agreeing with Assi et al. (2010a); Williamson and Govardhan (2004) and others in the literature.

The bottom plot of figure 5a shows  $f/f_N$ , the dominant frequency of oscillation normalised by the natural frequency of the system. The dashed line represents the frequency of vortex shedding associated with a Strouhal number of 0.2. The lighter and darker shades of red behind the symbols represent the peaks of the normalised spectra of vibration for each reduced velocity. The narrow peaks are hidden behind the symbols during the lock-in range, but the broader spectra are noticeable after the end of the synchronisation for  $U/(f_N D) > 12$  (please refer to Assi et al. (2013) for further details on this technique).

Figure 5b presents the VIV response of the continuous strake (CS) model, which kept the amplitude of displacement below  $\hat{y}/D = 0.10$  for the entire range of reduced velocity. The maximum response was observed past the resonance region around  $U/(f_N D) = 11$  and is associated with



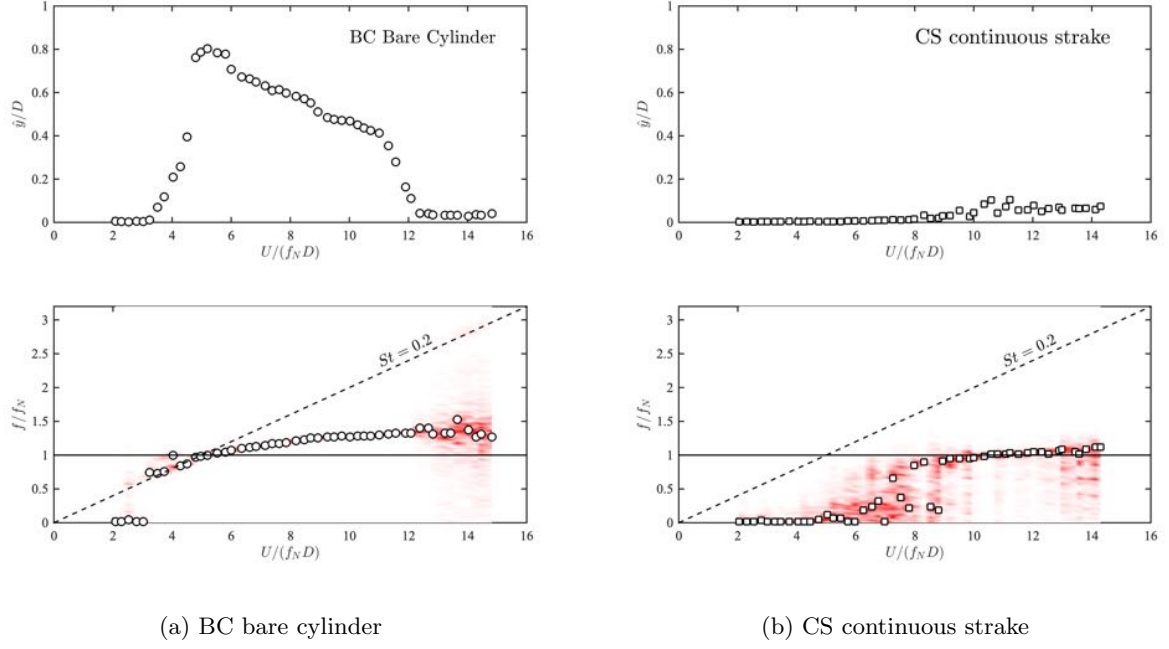


Figure 5: Amplitude of displacement (top) and dominant frequency of oscillation (bottom) for the reference models.

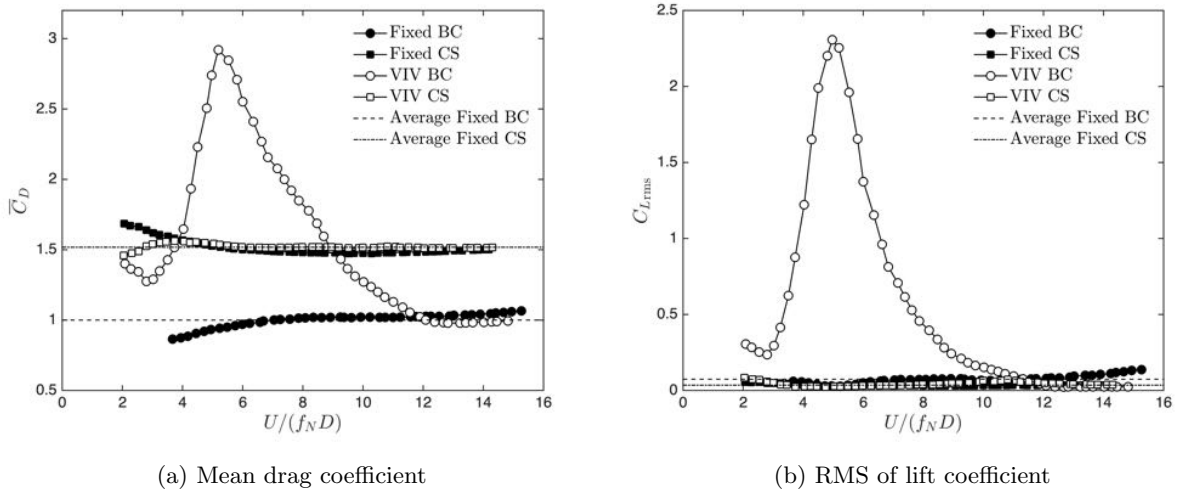


Figure 6: Hydrodynamic loads for the reference models (BC and CS).

turbulence buffeting rather than VIV. The frequency signature (bottom plot) shows vibrations occurring predominantly around the natural frequency of the system ( $f/f_N \approx 1$ ), which is typical of a broad-spectrum buffeting excitation Blevins (1990). The CS managed to suppress 88% of the peak amplitude of displacement, as summarised in table 4.

Drag and lift were measured for all models for comparison. Figure 6 presents the mean drag coefficient ( $\overline{C}_D$ ) and the RMS of lift coefficient ( $C_{L_{rms}}$ ) for the reference BC and CS models during the VIV response and for a fixed model (not allowed to respond). The amplification of drag during the VIV synchronization range was identified for the BC, reaching  $\overline{C}_D = 2.92$  at the peak of response and then dropping down to the levels of a fixed cylinder after the synchronization for  $U/(f_N D) > 12$ . Taking an average of mean drag for all reduced velocities resulted in an average  $\langle \overline{C}_D \rangle = 1.00$  represented by the dashed lines repeated in all figures. While a small average  $\langle C_{L_{rms}} \rangle = 0.074$  was observed for the fixed BC, the amplified fluctuation of lift occurred during synchronization and reached a maximum of  $C_{L_{rms}} \approx 2.3$  at resonance. The reference hydrodynamic loads measured for the BC are in good agreement with other measurements presented in the literature (Norberg, 2003).

The suppression of the VIV response produced by the CS was accompanied by the mitigation of mean drag and fluctuating lift during the synchronization range. In fact, both  $\overline{C}_D$  and  $C_{L_{rms}}$  approximate during the VIV response followed closely the curves for the fixed models. While the  $\langle C_{L_{rms}} \rangle$  for the CS was below that of the BC, the average  $\langle \overline{C}_D \rangle$  represented a 52% increase (marked by the dot-dashed lines in figure 6). VIV suppression with consequent drag increase is a typical behaviour of continuous strakes, as shown by Korkischko and Meneghini (2011a), Assi et al. (2010b) and others.

### 3.2. Serrated strakes: S30 and S45

The serrated S30 model appeared as the most efficient device concerning VIV suppression and drag reduction. The maximum amplitude of displacement, presented in figure 7a, was below  $\hat{y}/D = 0.04$  for the entire range of reduced velocities. A resonant peak of response was not observed and any residual vibration recorded for  $U/(f_N D) > 10$  is likely to be due to weak turbulence buffeting. The frequency signature produced a much broader spectrum without a clear trend for the dominant frequency, suggesting that the serrated blades at that specific angle make the device less susceptible to buffeting.

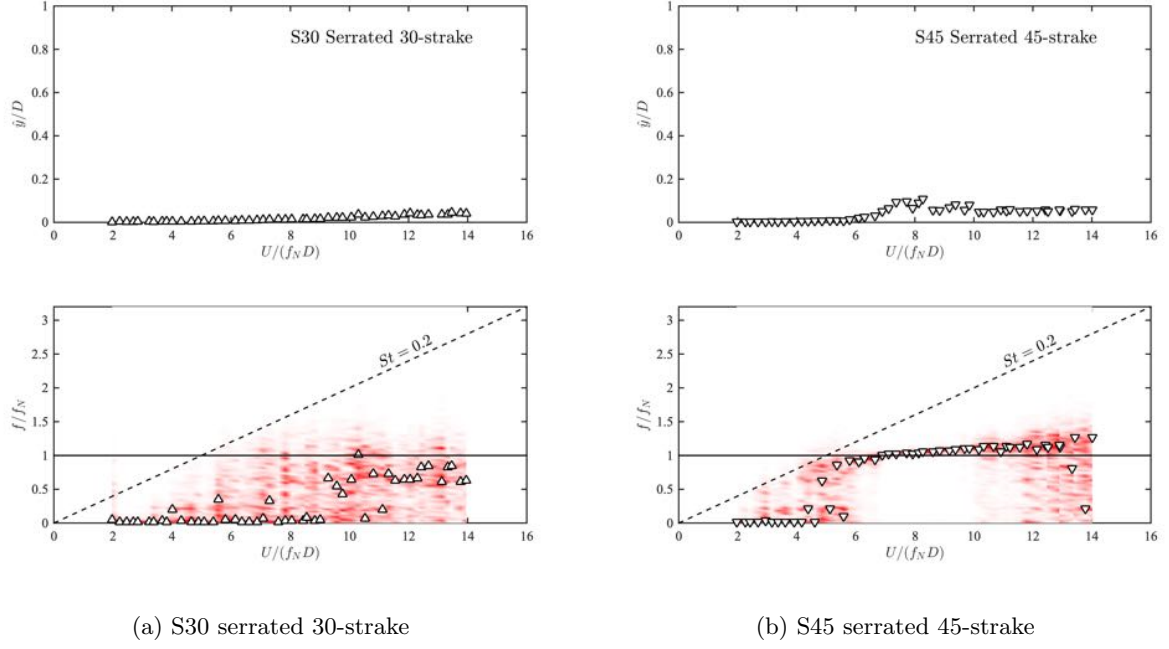


Figure 7: Amplitude of displacement (top) and dominant frequency of oscillation (bottom) for the serrated strakes.

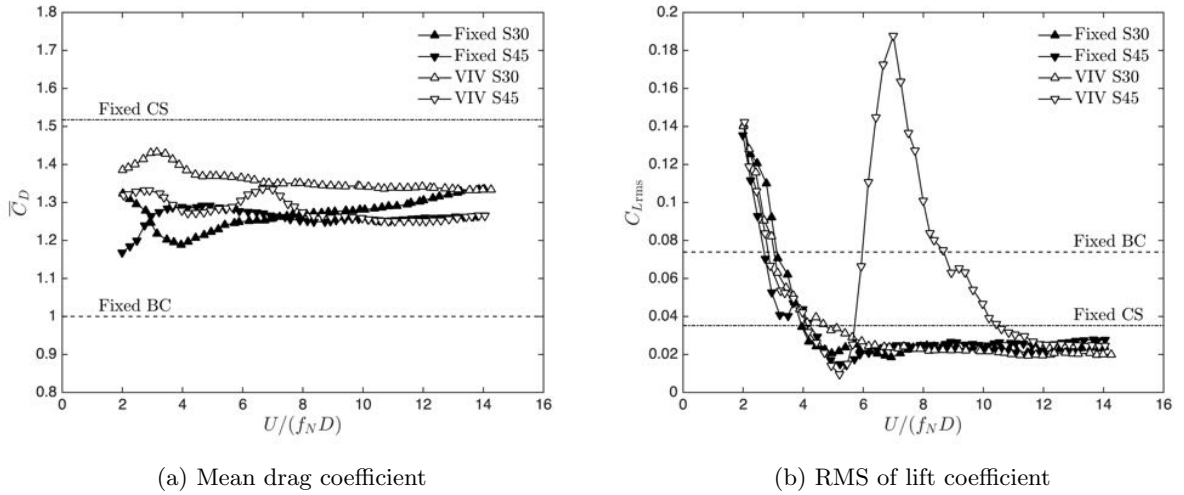


Figure 8: Hydrodynamic loads for the serrated strakes (S30 and S45).

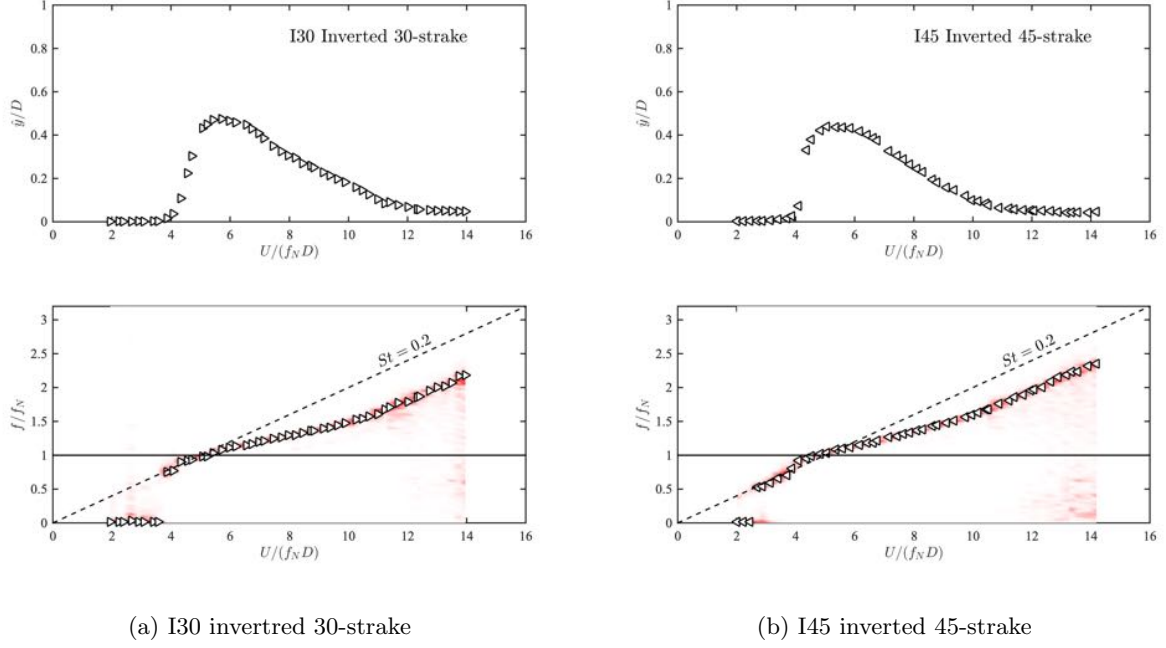


Figure 9: Amplitude of displacement (top) and dominant frequency of oscillation (bottom) for the inverted strakes.

Even though the S45 model was also quite effective in suppressing VIV, a small peak of  $\hat{y}/D = 0.11$  was observed at  $U/(f_N D) \approx 8$ . The frequency signature of the response suggests that this model was either more susceptible to turbulence buffeting or a local resonance occurred around that reduced velocity. A clear trend of dominant frequency close to  $f/f_N = 1$  corresponding to the local increase in displacement.

As far as hydrodynamic loads are concerned, shown in figure 8a, both serrated strakes managed to suppress VIV generating less drag than a fixed bare cylinder. In fact, the S45 device produced an average drag for the entire range of reduced velocities of  $\langle \overline{C_D} \rangle = 1.26$ , which corresponds to only a 26% drag increase in reference to a fixed BC.

When fluctuating lift is analysed (figure 8b) the S45 produced an expected amplification of  $C_{L_{rms}} = 0.19$  related to that local peak of response between  $U/(f_N D) = 6$  and 10. But the S30 presented insignificant fluctuations of lift, with both fixed models producing  $C_{L_{rms}}$  curves below the level obtained for the CS and well below that of the BC.

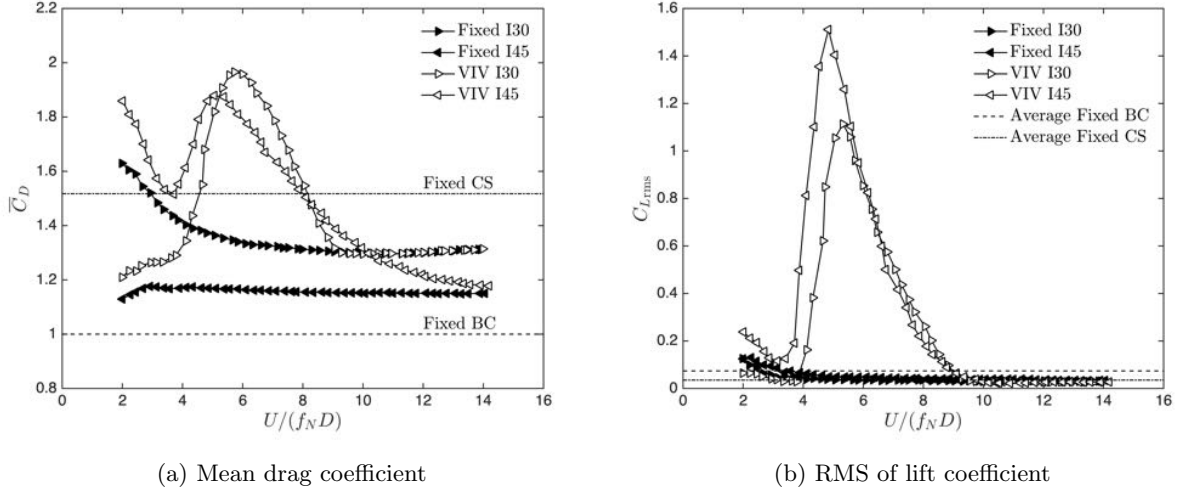


Figure 10: Hydrodynamic loads for the inverted strakes (I30 and I45).

### 3.3. Inverted strakes: I30 and I45

The inverted strakes make up the novel devices proposed in this investigation. The original hypothesis was that the inverted angle of the blades would disrupt the formation of vortices and suppress VIV without a considerable drag penalty. That was not verified, as seen in figure 9. Both I30 and I45 models presented a considerable peak of response within a clear synchronization range, reaching a maximum  $\hat{y}/D = 0.47$  and  $0.44$ , respectively. The peak VIV suppression was only 45% at best when compared with that of a BC. The frequency signature for both devices also showed that a typical VIV excitation was governing the response; turbulence buffeting was not observed.

Since I30 and I45 did not suppress VIV, an amplification of drag was expected, as verified in figure 10a. But when both models were held fixed,  $\overline{C_D}$  was below that of a fixed CS for most of the reduced velocity range, with the I45 model producing the smallest average drag of  $\langle \overline{C_D} \rangle = 1.16$  for the entire range of  $U/(f_N D)$ , only a 16% increase in referent to the fixed BC.

The lift coefficients presented in figure 10b confirmed the expected amplification of  $C_{L_{rms}}$  during the synchronization range of VIV. But an average  $\langle C_{L_{rms}} \rangle$  of only 0.04 measured for the I30 device showed a 45% reduction regarding the fluctuation of lift for the bare cylinder. One could suggest that the inverted strakes, while not the most effective VIV suppressor for this low mass-damping structure, might be a good option to mitigate fluctuating loads on static bodies without producing too much drag. Reduction of wake-generated noise might also make an interesting application,



Table 3: Average drag and lift coefficients for fixed models.

| Model                        | $\langle \overline{C}_D \rangle$ | drag increase | $\langle C_{L_{rms}} \rangle$ | lift reduction |
|------------------------------|----------------------------------|---------------|-------------------------------|----------------|
| Fixed BC bare cylinder       | 1.00                             | ref.          | 0.074                         | ref.           |
| Fixed CS continuous strake   | 1.52                             | 52%           | 0.035                         | 53%            |
| Fixed S30 serrated 30-strake | 1.27                             | 27%           | 0.035                         | 53%            |
| Fixed S45 serrated 45-strake | 1.26                             | 26%           | 0.033                         | 55%            |
| Fixed I30 inverted 30-strake | 1.36                             | 36%           | 0.041                         | 45%            |
| Fixed I45 inverted 45-strake | 1.16                             | 16%           | 0.052                         | 30%            |

Table 4: Summary of VIV results.

| Model                  | $(\hat{y}/D)_{\max}$ | suppression | $\overline{C}_D$ at $(\hat{y}/D)_{\max}$ | drag reduction |
|------------------------|----------------------|-------------|--|----------------|
| BC bare cylinder       | 0.80                 | ref.        | 2,92                                     | ref.           |
| CS continuous strake   | 0.10                 | 88%         | 1.52                                     | 48%            |
| S30 serrated 30-strake | 0.04                 | 95%         | 1.33                                     | 54%            |
| S45 serrated 45-strake | 0.11                 | 86%         | 1.26                                     | 57%            |
| I30 inverted 30-strake | 0.47                 | 41%         | 1.96                                     | 33%            |
| I45 inverted 45-strake | 0.44                 | 45%         | 1.88                                     | 36%            |

especially if the tonal noise generated by vortex shedding is to be avoided. As seen in table 3, which presents a summary of averaged drag and lift coefficients for the fixed models, the CS continuous strake produces the highest drag for a static body, increasing the average drag in 52% and reducing the RMS of fluctuating lift in 53% when compared with that of a bare cylinder. Serrated devices also reached the same level of  $\langle C_{L_{rms}} \rangle$  reduction, with much less drag penalty; the S45 serrated strakes, for example, reduced  $\langle C_{L_{rms}} \rangle$  in 55% with only a 26% increase in  $\langle \overline{C}_D \rangle$  for a fixed body.

Finally, table 4 presents the summary of results for all testes models, showing the recorded  $\overline{C}_D$  at the peak amplitude of response  $(\hat{y}/D)_{\max}$ . The serrate strake S30 was highlighted as the most efficient in suppressing VIV (95% reduction of peak amplitude) and reducing drag (54% peak-drag reduction) when compared to the peak-response of the bare cylinder. The serrated

strake S45 produced an even greater drag reduction (57% less peak-drag than the BC), but the peak-amplitude of displacement was slightly higher than the S30.

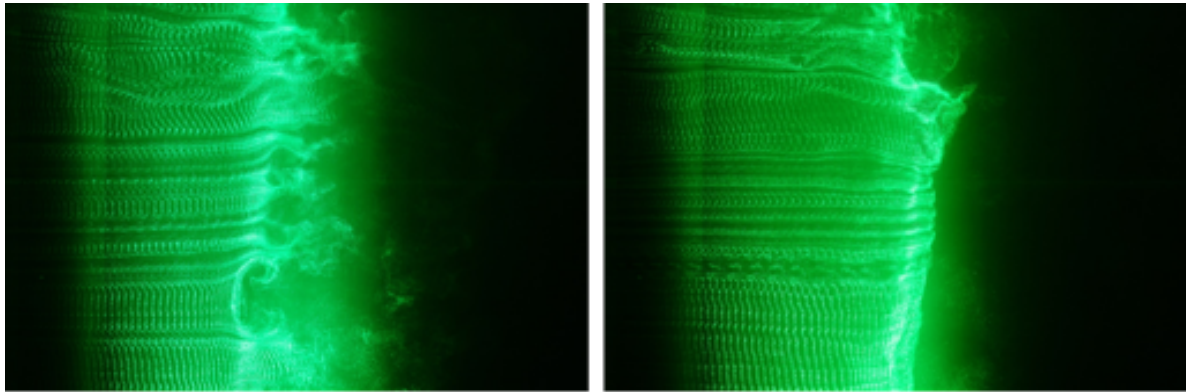
It is reasonable to speculate that the same hydrodynamic effect that made the serrated strakes generate less drag than the continuous strake (as seen for the static models, for example) may have caused the serrated systems to produce less hydrodynamic damping in the cross-flow direction, thus increasing the amplitude of VIV response (see table 2). However, this was not observed. In fact the serrated geometry of the blades promotes enhanced mixing in various length-scales in the wake (this will be discussed in the next section on flow visualization), keeping the hydrodynamic damping at the same level as the CS. Because the serrated strakes are as effective as the CS in suppressing the VIV response, the average drag is not amplified by the formation of a wider wake due to the cross-flow vibration.

#### 4. Flow visualization

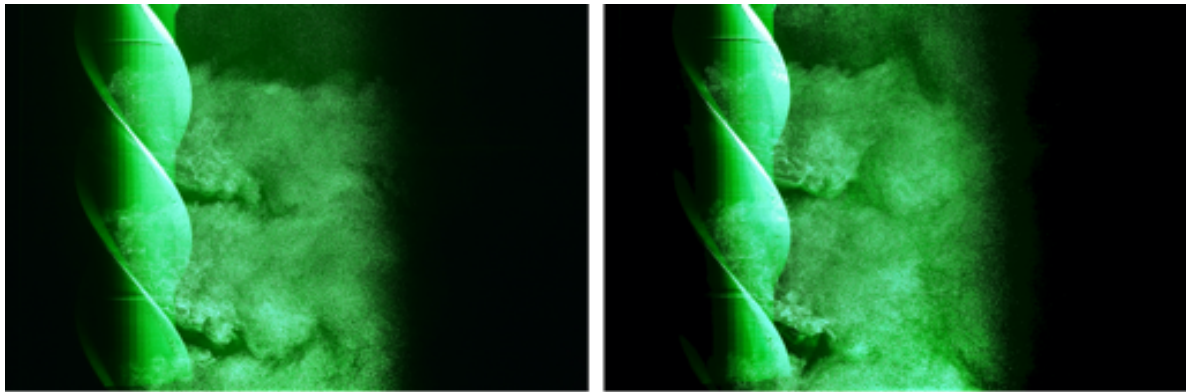
Visualization of the flow structures in the near wake of the cylinders have been performed in recirculating water in the Noah Flume at the California Institute of Technology (GALCIT). The model was not allowed to respond to VIV, but held fixed at the centre of the test section. A thin stainless steel wire was stretched upstream of the model, across the test section and parallel to the axis of the cylinder. A constant electric current flowing through this cathode wire released a stream of tiny hydrogen bubbles, convected downstream by the water flow. The position of the electrolysis wire was set so that the curtain of bubbles reached the helical strakes near the blades.

A sheet of green laser light was employed to illuminate the bubbles on a plane parallel to the axis of the cylinder and offset almost  $1D$  from the centreline of the wake. Photography taken perpendicular to the illuminated plane revealed the coherent flow structures along the span of the cylinder (shown in figures 11, 13 and 15, to be discussed later). Changing the orientation of the camera and flooding the test section with white light made it possible to investigate in more detail the three-dimensional flow structures around the blades and near the recirculation region downstream of the models (shown in figures 12, 14 and 16, to be discussed later).

This may sound nostalgic, but when so many sophisticated techniques to quantify flow fields are available to the researcher, one should not disregard simple, qualitative techniques that can offer so much insight on the dynamics of the flow around complex structures. The elementary



(a) Bare cylinder.



(b) CS continuous helical strake.

Figure 11: Flow visualization with hydrogen bubbles for the bare cylinder (reference) and the continuous helical strake.  $Re = 9.4 \times 10^3$ .

flow visualizations with dye, bubbles and other tracers are often neglected over other expensive techniques, such as volumetric PIV (particle-image velocimetry) for example. But sometimes simple flow visualization is precisely what is needed to clarify our understanding on the behaviour of three-dimensional vortical structures.

Figure 11a presents a longitudinal view of the wake of a bare cylinder illuminated with laser; this will serve as a reference to evaluate the wake patterns in the wake of the various helical strakes. The cylinder model can be seen behind the curtain of bubbles near the left edge of the images. Reynolds number is  $9.4 \times 10^3$  and the flow direction is from left to right. It is possible to see the formation of vortices on one side of the model at two different moments in time, with a coherent vortex tube parallel to the axis of the cylinder. The flow in the near wake is fairly organised and

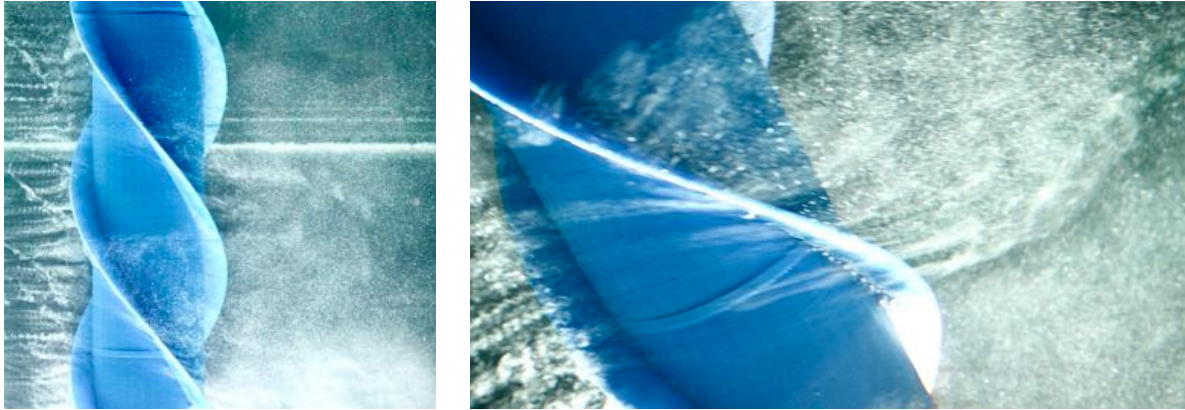
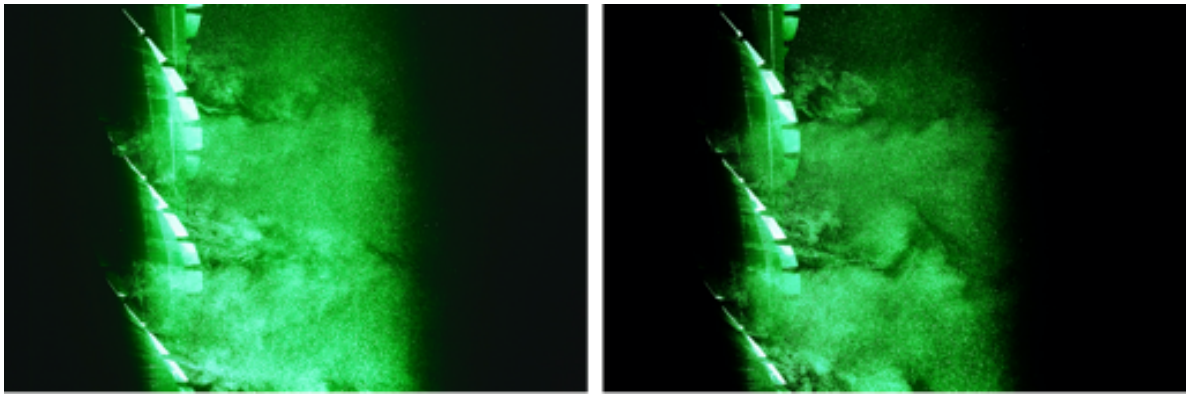


Figure 12: Detail of flow visualization with hydrogen bubbles for the continuous helical strake.  $Re = 9.4 \times 10^3$ .

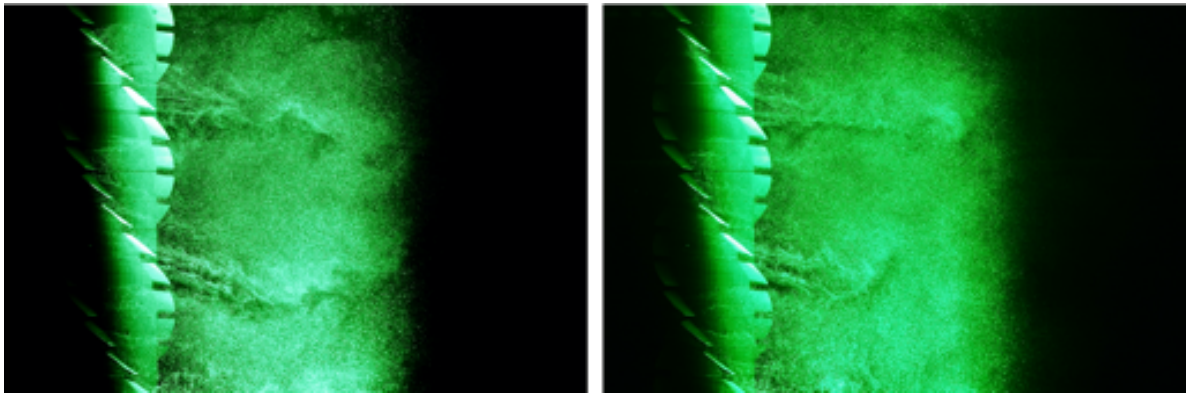
strong three-dimensionalities only appear after the vortex tube is shed and convected by the flow. The vortex formation length for the bare cylinder was qualitatively estimated at approximately  $1.6D$ , which is in good agreement with Norberg (1987); Unal and Rockwell (1988); Cicolin and Assi (2017) for this  $Re$  range.

A similar visualization is presented in figure 11b for the near wake of the continuous helical strake (CS). The most striking difference compared to the wake of the bare cylinder is the absence of a coherent vortex tube being formed close to the body (the vortex-formation length is considerably increased). The near wake is more turbulent, dominated by small-scale three-dimensional vortices that promote mixing of the separated shear layers near the body. A periodic flow structure is observed along the span at a wavelength of  $P/3$  (i.e. the pitch length divided by the number of helices that make the strake). The continuous helical blades promote the separation of the flow at fixed points around the body, also inducing momentum downward along the axis of the cylinder (momentum is induced upwards on the other side of the body), disrupting the interaction between the shear layers and consequent formation of vortices. The detailed visualization presented in figure 12 clearly shows the separation line along the continuous blade. These observations are supported by the measurements of Korkischko and Meneghini (2011b), who presented a volumetric reconstruction of the near wake of a straked cylinder employing stereo PIV.

Now, figure 13 presents the near-wake visualization for the cylinder with serrated strakes. The spanwise wavelength of  $P/3$  is clearly identifiable for both both S30 and S45 models. But distinct flow structures with a smaller scale related to the  $b_1$  dimension of the blade segment are clearly seen. The vortex-formation length is increased beyond the reach of the laser plane, so no coherent



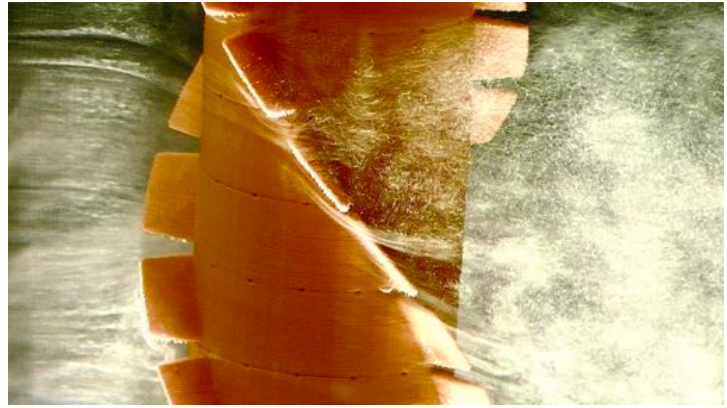
(a) S30 serrated 30-strake.



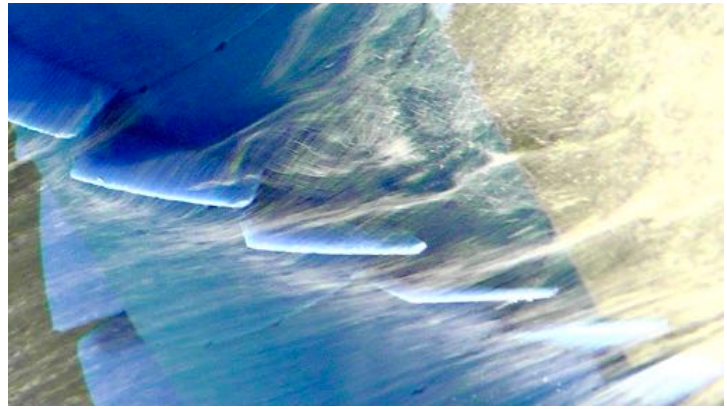
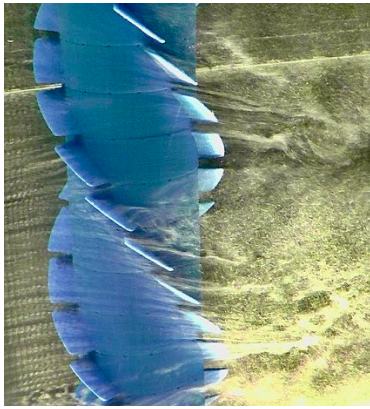
(b) S45 serrated 45-strake.

Figure 13: Flow visualization with hydrogen bubbles for the serrated helical strakes.  $Re = 9.4 \times 10^3$ .





(a) S30 serrated 30-strake.



(b) S45 serrated 45-strake.

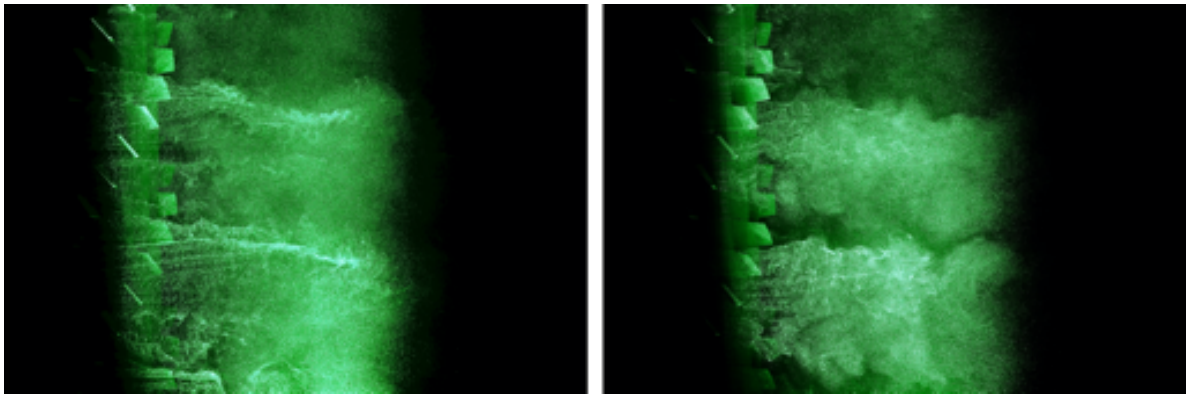
Figure 14: Detail of flow visualization with hydrogen bubbles for continuous and serrated strakes.  $Re = 9.4 \times 10^3$ .

vortex tube is found in the near wake. The main difference between the two serrated models is in the level of mixing near the separation lines. While figure 13a for the S30 model reveals stronger coherent vortices, the wake shown in figure 13b is smoother. Based on the detailed visualizations presented in figures 14a and 14b one might infer that the S30 serrated blades that encounter the incoming flow at a higher angle of attack ( $60^\circ = 90^\circ - 30^\circ$ ) produce more local separation than the serrated blades of the S45 model (twisted at  $45^\circ$ ).

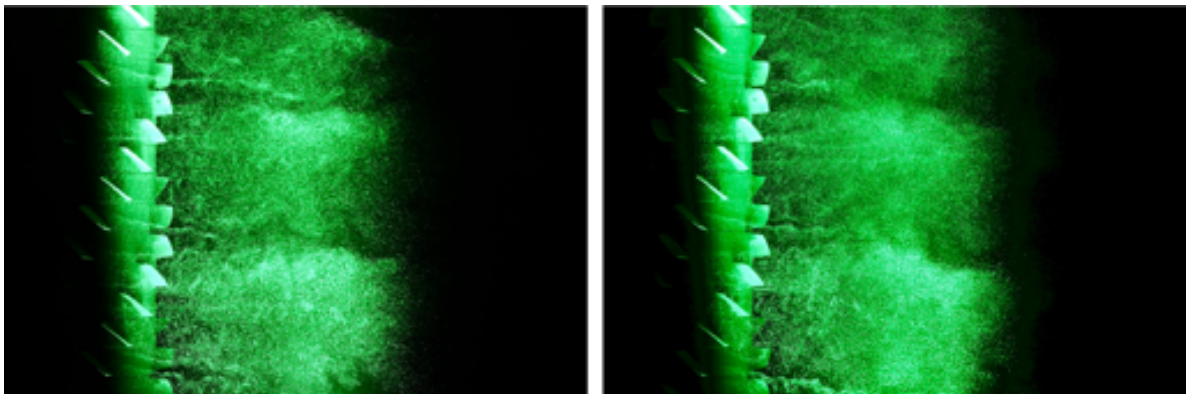
In general, the CS, S30 and S45 models (those in which the orientation of the blades followed the helix line) presented the same behaviour of fixing the separation line along the intended helices around the cylinder, inducing momentum along the span and disrupting the formation of vortices in the near wake. The main difference between them was related to the scales of the three-dimensional vortex structures they induced after the flow had separated, which is associated with the energy dissipated in the process.

The inverted strakes I30 and I45, on the other hand, produced a different result over the separated flow, as presented in figure 15. The inverted blades increased the level of mixing in the near wake, generating strong turbulent flow downstream of the body. The  $P/3$  wavelength was still visible in the flow structures along the cylinder span, but the near wake seemed more dominated by stronger vortices associated with the dimensions of the individual blade segments rather than by the periodic flow typical of helical strakes. Figures 15a and 15b show that no coherent vortex tubes were found in the near wakes of the bodies. But perhaps the most interesting flow visualization was observed in detail on the flow around the inverted blades, presented in figure 16. The blades of model I30, with greater angle of attack in relation to the incoming flow, produced strong separation with clear regions of recirculation behind the blade segments (figure 16a). The I45 inverted blades, by contrast, appeared more streamlined to the incoming flow, allowing for more streamwise momentum to be injected into the near wake (figure 16b).

With carefully performed flow visualization it was possible to identify the dominant flow structures in the near wake of the five models of strakes. Compared to the wake of the bare cylinder, none produced coherent vortex tubes near the bodies. While the wake of the serrated strakes (S30 and S45) were dominated by flow structures associated with the  $P/3$  wavelength, the flow downstream of the inverted strakes (I30 and I45) was dominated by smaller scales associated with the dimensions of the blade segments ( $b_1$  and  $b_2$ ).

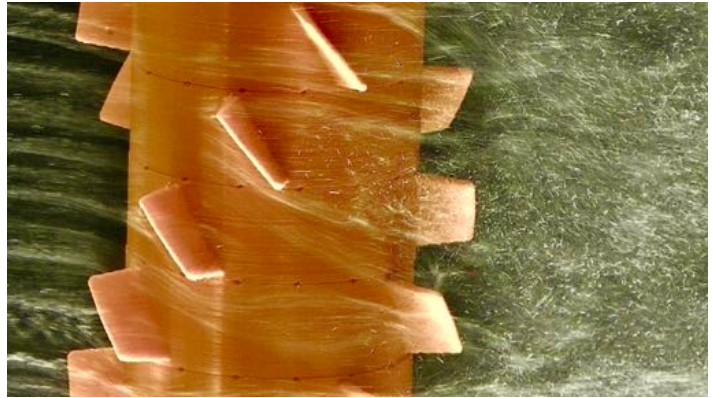
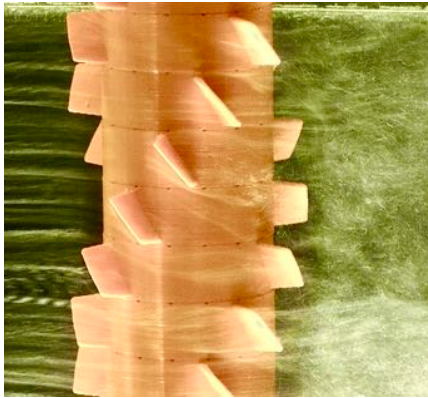


(a) I30 inverted 30-strake.

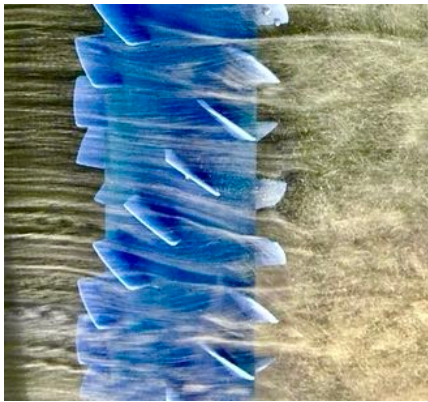


(b) I45 inverted 45-strake.

Figure 15: Flow visualization with hydrogen bubbles for the inverted helical strakes.  $Re = 9.4 \times 10^3$ .



(a) I30 inverted 30-strake.



(b) I45 inverted 45-strake.

Figure 16: Detail of flow visualization with hydrogen bubbles for the inverted strakes.  $Re = 9.4 \times 10^3$ .

## 5. Conclusion

We have evaluated the effectiveness of five unconventional serrated helical strakes to suppress the cross-flow VIV of a circular cylinder with low mass and structural damping. While the conventional continuous strake suppressed 88% of the peak amplitude of response with a 48% drag reduction, the most efficient serrated strake (S30) reduced the peak amplitude of vibration by 95% producing 54% less drag than a bare cylinder. When the models were held fixed in the flume (not allowed to respond to VIV) they all increased drag in relation to the average drag of a fixed bare cylinder. The serrated strake (S45) achieved a 55% reduction in fluctuating lift with only a 26% drag penalty.

We verified that simply inverting the local angle of attack of the individual blades in relation to the helical pitch of the strake (producing the two inverted models) did not produce a favourable result in terms of VIV suppression. Perhaps the inverted blades annihilate the effect that the continuous blades produce in the near wake, allowing for the formation of more coherent vortices in the near wake to drive VIV (even though the inverted blades did produce more mixing and turbulence in the near wake when compared to the effect of the continuous strake).

This paper is part of an ongoing research work to investigate the physical mechanisms behind helical strakes and clarify their effect in suppressing VIV. The controlled experiments at moderate Reynolds numbers and with only a single degree of freedom (cross-flow direction) provided a good database to compare the behaviour of the different systems depending on the geometric parameters of blade continuity, segment angle and direction. Good insight was obtained for future optimisation of this promising family of helical strakes. Even though only a couple of models of each type have been tested, it became clear that varying the geometry of the blades can produce an optimised device as far as suppression and drag reduction are concerned.

Visualization of the flow around the blades helped to clarify the intricate hydrodynamic mechanisms governing flow separation and the injection of flow structures at various length-scales in the near wake, disrupting the formation of coherent vortices and reducing the excitation that drives VIV. We observed that the continuous strake is important to hold the helical separation line around the body while the cylinder is oscillating. The serrated strakes may also provide this kind of control of the separation line while allowing for more momentum to flow into the near wake. However, when this helical characteristics is lost—say by too much spacing between the serrated blades—



that separation line recorrelates along the span and the VIV excitation restarts. We verified that the inverted strakes were not able to sustain this kind of control as did the serrated and continuous devices. Interestingly, the same level of fluctuating lift was observed for a fixed cylinder equipped with serrated and with inverted strakes, confirming that the loss of helical continuity (characteristic of the inverted strakes) allowed for a correlated excitation once the cylinder started to oscillate transversally.

Finally, from another perspective, the novel concept of the inverted strakes was not completely ineffective. Considering static bluff bodies, the inverted strakes were able to reduce fluctuating loads with a minimal drag penalty. This might be rather interesting for static structures or even for the field of aeroacoustics and flow-induced noise.

## Acknowledgments

We gratefully acknowledge support of the RCGI Research Centre for Gas Innovation, hosted by the University of São Paulo (USP) and sponsored by FAPESP (2014/50279-4) and Shell Brasil. GRSA acknowledges the support of FAPESP (2011/00205-6), CNPq (306146/2019-3) and the Brazilian Navy. We are grateful to Prof Beverly McKeon for providing the use of the Noah Flume at Caltech to perform the flow visualizations.

## References

- Assi, G. R. S., 2009. Mechanisms for flow-induced vibration of interfering bluff bodies. Phd thesis, Imperial College London.
- Assi, G. R. S., Bearman, P. W., Carmo, B. S., Meneghini, J. R., Sherwin, S. J., Willden, R. H. J., 3 2013. The role of wake stiffness on the wake-induced vibration of the downstream cylinder of a tandem pair. *Journal of Fluid Mechanics* 718, 210–245.
- Assi, G. R. S., Bearman, P. W., Kitney, N., Tognarelli, M., 2010a. Suppression of wake-induced vibration of tandem cylinders with free-to-rotate control plates. *Journal of Fluids and Structures* 26, 1045–1057.
- Assi, G. R. S., Bearman, P. W., Kitney, N., Tognarelli, M., 2010b. Suppression of wake-induced vibration of tandem cylinders with free-to-rotate control plates. *J. Fluids Structures* 26, 1045–1057.
- Assi, G. R. S., Bearman, P. W., Tognarelli, M. A., 2014. On the stability of a free-to-rotate short-tail fairing and a splitter plate as suppressors of vortex-induced vibration. *Ocean Engineering* 92, 234 – 244.
- Blevins, R. D., 1990. *Flow-Induced Vibration*, 2nd Edition. Van Nostrand Reinhold, New York.
- Chaplin, J. R., Teigen, P., 2003. Steady flow past a vertical surface-piercing circular cylinder. *Journal of Fluids and Structures* 18 (3), 271 – 285.

- Cicolin, M. M., Assi, G. R. S., 2017. Experiments with flexible shrouds to reduce the vortex-induced vibration of a cylinder with low mass and damping. *Applied Ocean Research* 65, 290 – 301.
- Korkischko, I., Meneghini, J. R., 2010. Experimental investigation of flow-induced vibration on isolated and tandem circular cylinders fitted with strakes. *Journal of Fluids and Structures* 26 (4), 611–625.
- Korkischko, I., Meneghini, J. R., 2011a. Volumetric reconstruction of the mean flow around circular cylinders fitted with strakes. *Experiments in Fluids* 51, 1109–1122.
- Korkischko, I., Meneghini, J. R., 2011b. Volumetric reconstruction of the mean flow around circular cylinders fitted with strakes. *Experiments in Fluids* 51 (4), 1109.
- Norberg, C., 1987. Effects of reynolds number and a low-intensity freestream turbulence on the flow around a circular cylinder. Chalmers University, Goteborg, Sweden, Technological Publications 87 (2), 1–55.
- Norberg, C., 2003. Fluctuating lift on a circular cylinder: review and new measurements. *Journal of Fluids and Structures* 17, 57–96.
- Silva-Ortega, M., Assi, G. R. S., 2017. Flow-induced vibration of a circular cylinder surrounded by two, four and eight wake-control cylinders. *Experimental Thermal and Fluid Science* 85, 354 – 362.
- Taggart, S., Tognarelli, M., 2008. Offshore drilling riser VIV suppression devices - what's available to operators? In: *Proceedings of the 27th International Conference on Ocean, Offshore and Arctic Engineering (ASME-OMAE 2008)*. p. 57047.
- Tognarelli, M., Taggart, S., Campbell, M., 2008. Actual VIV fatigue response of full scale drilling risers: With and without suppression devices. In: *Proceedings of the 27th International Conference on Ocean, Offshore and Arctic Engineering (ASME-OMAE 2008)*. p. 57046.
- Unal, M. F., Rockwell, D., 1988. On vortex formation from a cylinder. part 1. the initial instability. *Journal of Fluid Mechanics* 190, 491–512.
- Williamson, C. H. K., Govardhan, R., 2004. Vortex-induced vibrations. *Ann. Rev. Fluid Mech.* 36, 413–455.

# The Role of Separation on the Forces acting on a Circular Cylinder with a Control Rod

M.M. Cicolin<sup>1,2†</sup>, O.R.H. Buxton<sup>1</sup>, G.R.S. Assi<sup>2</sup> and P.W. Bearman<sup>1</sup>

<sup>1</sup>Department of Aeronautics, Imperial College London, SW7 2AZ, UK

<sup>2</sup>Polytechnic School, University of São Paulo, Brazil

(Received xx; revised xx; accepted xx)

The development of the flow around a circular cylinder with a smaller diameter control rod in close proximity is the subject of this paper. It has long been known that this is an effective way to attenuate regular vortex shedding leading to reductions in its adverse effects on bluff body flow. The aim of this study is to improve understanding of the ways the control rod affects the near wake flow including how it influences the positions of boundary layer separation. Experiments were carried out in a water channel to measure lift and drag forces and PIV was employed to obtain detailed information on flow structure. The values of important properties were fixed as follows: Reynolds number 20,000; ratio of cylinder and control rod diameters 10:1; centre to centre distance between main cylinder and control rod  $0.7D$ , where  $D$  is main cylinder diameter. The adjustable parameter was the angular position of the rod,  $\theta$ , which was varied between  $90^\circ$  and  $180^\circ$  from the front stagnation line. Lift and drag forces were measured separately for the main cylinder and the control rod. A new method for identifying flow states is introduced using PIV to interrogate the instantaneous flow velocity in the gap between the main cylinder and the control rod. Similarly to previous studies, three stable flow states were observed together with a bi-stable state. The bi-stable state is very sensitive to the control rod angle with a small change of  $\pm 1^\circ$  being sufficient to change the flow state.

## 1. Introduction

Understanding the flow around bluff bodies has been a long-standing challenge in fluid mechanics. Due to the variety of flow phenomena and the wide range of applications such as pipelines, offshore risers, masts etc., the circular cylinder has been the object of extensive study for many decades. The fundamentals of vortex formation and shedding, wake characteristics and fluid loading are detailed in the works of Roshko (1954), Gerrard (1966) and many others and in reviews by Bearman (1984), Williamson (1996) and Zdravkovich (1997). The majority of applications occur in a range of Reynolds number ( $Re$ ) where, resulting from an interaction between the cylinder's free shear layers, regular vortex shedding develops. Vortex shedding is responsible for increased time-mean drag and the generation of oscillatory drag and lift forces. In practical situations the unsteady forces can excite a circular cylinder into vortex-induced vibrations, possibly leading to structural failure. In order to mitigate such effects, a range of passive and active devices have been developed which in one way or another interfere with the instability mechanism leading to vortex shedding. Choi *et al.* (2008) published a comprehensive review of methods to control bluff body flow, classifying them according to how control is achieved. This paper addresses a control method that can be found in their category, "Control based on local/global instability". The method was pioneered by Strykowski

† Email address for correspondence: m.marangon-cicolin18@imperial.ac.uk/mmcicolin@usp.br

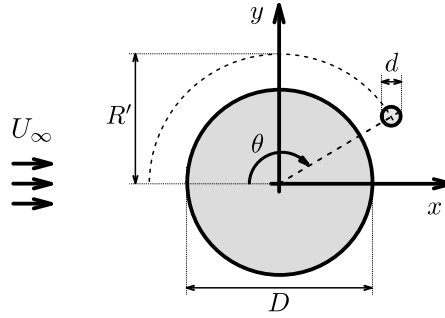
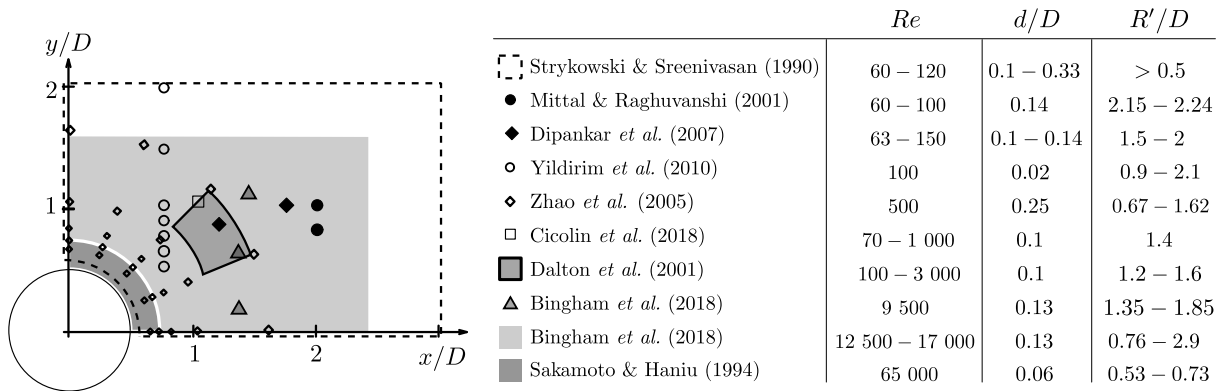


FIGURE 1. Coordinate system

FIGURE 2. Positions of the control rod in the range  $90^\circ \leq \theta \leq 180^\circ$  for different cases found in the literature.

& Sreenivasan (1990) and involves placing a small diameter control cylinder in or close to a free shear layer separating from a significantly larger main cylinder. They found that the presence of the control cylinder in an appropriate position has the effect of suppressing the absolute instability in the near wake that initiates vortex shedding. This finding generated much interest but complete suppression of vortex shedding was only obtained up to a Reynolds number of 100. Subsequent research showed that at higher Reynolds numbers the careful placing of a control cylinder has the effect of reducing drag coefficients and lowering the levels of unsteady forces due to vortex shedding. This finding encouraged further research into seeking the optimum size and position for a control cylinder where it has the most beneficial effect.

Key variables affecting the flow around a fixed circular cylinder with a control cylinder, here called a control rod, are illustrated in Figure 1. Besides the main cylinder  $Re$ , the flow depends on the position of the rod,  $R'/D$  and  $\theta$ , and the ratio between the diameters of the control rod,  $d$ , and the main cylinder,  $D$ . Figure 2 is a compilation of past studies with one control rod for  $90^\circ \leq \theta \leq 180^\circ$ ,  $d/D < 0.33$  and for a range of  $Re$  between 60 and 65,000. It shows the positions of control rods in the various studies illustrating the wide range of  $R'/D$  that has been investigated. The results of Dipankar *et al.* (2007) and Mittal & Raghuvanshi (2001) agree with the findings of Strykowski & Sreenivasan (1990), and they found vortex shedding suppression for low  $Re$  and for similar values of  $d/D$ . Still in the range  $Re < 100$  and for a smaller diameter of  $d/D = 0.02$ , Yildirim *et al.* (2010) did not observe complete vortex suppression, but found a significant attenuation of vortex strength. Dalton *et al.* (2001) performed numerical simulations in the range  $100 \leq Re \leq 3\,000$  and with  $d/D = 0.1$ , only observing complete suppression of vortex shedding at  $Re = 100$ . For  $Re = 3\,000$ , they reported a drag reduction of approximately

25% when  $R'/D = 1.2$  and  $\theta = 160^\circ$ . The fluctuating lift was also decreased, in their case by almost 85%. These results confirmed that there is a significant  $Re$  dependency on the optimal position where the rod should be located. This was reinforced by the results of Cicolin *et al.* (2018), where the control rod was kept at a fixed position ( $R'/D = 1.4, \theta = 135^\circ$ ) and  $Re$  was varied. It completely suppressed vortex shedding at  $Re = 70$ , attenuated the fluctuating forces at  $Re = 200$  and had little effect at  $Re = 1\,000$ . At moderate values of  $Re = 12\,500$  in the sub critical range, Bingham *et al.* (2018b) adopted a different approach and used an evolutionary algorithm to home in on the position of the control rod that minimised fluctuating lift on the main cylinder. The extensive area they covered for placing a control rod is shown shaded in Figure 2. They concluded that fluctuating lift could be reduced by 90% using a control rod with  $d/D = 0.125$ , placed at  $R'/D = 1.31$  and  $\theta = 116^\circ$ .

However, not all research on this topic has been limited to a circular cylinder as the bluff body. Parezanovic & Cadot (2012) performed a comprehensive study of the sensitivity of the wake past a D-shaped cylinder with one control rod. Their study included control rod diameters in the range  $d/H = 0.04 - 0.12$ , where in this case  $H$  is the height of the base of the body. A significant difference between this study and many previous ones is that the separation points on the main body are not free to move. Nevertheless, they identified a number of flow states that have characteristics with some similarities to those found with a circular cylinder as the main body. According to the position of the control rod, they separated their results into different states. Sakamoto & Haniu (1994) visualised the flow in the wake of a circular cylinder with a single control rod using smoke and identified 5 different flow patterns. Their sketches of the flow indicate the importance of the proximity of the control rod to a free shear layer separating from the main cylinder. Returning to Parezanovic & Cadot (2012), they sketched four flow patterns in the wake of their D-shaped body with a single control rod. Their near wake configurations are entitled: external flow, outer shear, mid-shear and inner shear. The descriptions relate to the positions of the control rod relative to a free shear layer. Common to both of these studies, they found states that were bi-stable. Parezanovic *et al.* (2015) extended research on the D-shaped body to obtain more information on the bi-stability they had observed.

The present experiment-based investigation complements previous studies by providing further insight into the quintessential case of a circular cylinder with a single control rod. The main emphasis is on the fluid mechanisms involved rather than optimising the effectiveness of this form of flow control. The Reynolds number,  $Re = 20\,000$  was in the sub-critical range, well away from both the low  $Re$  regime and the onset of the drag crisis. In order to reduce the number of possible variables the diameters of the main cylinder and the control rod were fixed, as was the distance between their centres. Previous works showed that when the rod and the cylinder have different orders of magnitude, the size of the rod is less relevant to the system's physics than its position, so we kept the ratio between the rod and the cylinder fixed,  $d/D = 1/10$ . Past studies also revealed that there is a relationship between  $Re$  and the sensitive regions for actuation. As  $Re$  increases, the positions where the rod most affects the system gets closer to the cylinder. Besides, If the control rod is close to the cylinder surface the more likely there will be interactions with the cylinder boundary layer, hence  $R'/D$  was fixed at 0.7 giving a gap between the surfaces of the cylinder and control rod equal to  $0.15D$ . The important parameter that was varied was the angular position of the control rod,  $\theta$ , measured from the front stagnation line and moved from  $90^\circ$  to  $180^\circ$ . This range of control rod angle was chosen as it is common to a number of previous studies as shown in figure 2.

As found by previous authors, the influence a control rod has on the flow field around



a bluff body depends on how the development of the shear layers separating from the body are affected by the presence of the control rod. With a single control rod it is the shear layer separating from the same side of the body as the rod that plays the most important role. By changing the angular position of the rod, the approaching shear layer has several possible paths. It may pass above the control rod or take a route between the cylinder wall and the control rod. Possibly the most challenging case is when the control rod is directly in the path of the shear layer and descriptions such as cutting and splitting the shear layer can be found in the literature. When the control rod is outside the path of the shear layer it is exposed to an approaching flow with a velocity of a similar magnitude to that of the main cylinder. In our experiments the ratio of the diameters of the control rod and main cylinder,  $d/D$ , was fixed at 0.1 indicating a  $Re_d$  for the control rod of approximately 2000, which is well above the threshold for vortex shedding.

Following the Introduction there is a detailed section on the Experimental Arrangement and Methodology. Mean lift and drag forces were measured separately on the main cylinder and the control rod as well as on the combined system of main cylinder and control rod. The fluctuating forces were also measured but not separately for the control rod. Extensive PIV measurements were made and post processed using an optimal mode decomposition (OMD) based 'smart filter' in order to have a clearer picture of the flow states and to be able to locate separation. In the Results and Discussion section a diagnostic tool is presented that is used to identify the various flow states including a bi-stable state. Each state is described in detail calling on both the force and PIV data as well as animations derived from PIV. This is followed by the Conclusions section that lists new findings on the influence imposed on the flow around a circular cylinder by a control rod.

## 2. Experimental Arrangement and Methodology

Experiments were carried out in the recirculating water channel of the Department of Aeronautics at Imperial College London. The facility has a 0.6 m square test section and the length is 8.2 m. For all experiments the flow velocity was set at 0.4 m/s and at this speed the turbulence intensity is approximately 1.5% at the position of the test cylinder. A thorough characterisation of the freestream turbulence in this facility, including its two-point correlation can be found in Baj & Buxton (2017). The Froude number in these experiments was  $Fr = U_\infty/\sqrt{gH} \approx 0.16$ . Based on the studies of Reichl *et al.* (2005) and Bingham *et al.* (2018a), for  $Fr < 0.3$ , we did not expect an influence of surface deformations on the flow dynamics. Two main sets of experiments were carried out: one was to measure hydrodynamic forces and the other was to investigate flow fields using PIV. The key properties relating to the experiments are provided in Table 1 and the symbols used are depicted in figure 1.

### 2.1. Force Measurements

For measuring forces the cylinder was attached to a load cell that was fixed above the water level. The load cell was an ATI Gamma IP68-SI-65-5 Force Transducer, capable of acquiring forces up to 65 N in the  $x$ - and  $y$ -directions with a resolution of  $\pm 0.012$  N. The main cylinder was an acrylic tube with a diameter of 50 mm and a wetted length of 485 mm, giving an aspect ratio of 9.7. Its upper end was connected directly to the load cell. In order to minimise end effects at the lower end of the cylinder an end plate was fixed to the floor of the flume. The distance between the floor and the end plate was 75 mm and this is larger than the thickness of the boundary layer, which at this position was found to be approximately 35 mm. The gap between the cylinder and the end plate was

|                                |                        |        |
|--------------------------------|------------------------|--------|
| $D$                            | 50 mm                  |        |
| $d$                            | 5 mm                   | $0.1D$ |
| $R'$                           | 35 mm                  | $0.7D$ |
| $\theta$                       | $90^\circ - 180^\circ$ |        |
| $U_\infty$                     | 0.4 m/s                |        |
| $Re = \frac{DU_\infty}{\nu}$   | 20 000                 |        |
| $Re_d = \frac{dU_\infty}{\nu}$ | 2 000                  |        |

TABLE 1. Properties of models and experiments common to all campaigns

kept less than 1 mm. The control rod was a carbon fibre tube with an outer diameter of 5 mm. Forces were acquired for two different arrangements for mounting the control rod, as shown in figure 3. In configuration 1, the rod's upper end was fixed in the outer shield of the load cell, whereas the lower end was fixed to the end plate. In this way, the load cell acquired the forces acting on the main cylinder only. In configuration 2, the rod was attached to the cylinder through two rings, allowing the load cell to acquire the forces acting on the combined system, i.e. the two bodies together. In both configurations, the end supports for the control rod kept the distance between it and the main cylinder constant along its length. The supports could be rotated around the cylinder, enabling different angular positions of the control rod to be set. The supports and the control rod were designed such that the deflection of the rod under hydrodynamic loading was negligible. The main quantities relating to the force measurements are given in Table 2, where  $f_{acq}$  is the data acquisition rate,  $T_{acq}$  is the acquisition time and  $\Delta\theta$  is the increment for changing  $\theta$ .

The forces on the main cylinder were found from measurements made in configuration 1 and their dimensionless forms are given by:

$$C_{D,L}^{\text{Cylinder}} = \frac{F_{D,L}^{\text{Conf.1}}}{\frac{1}{2}\rho U_\infty^2 D L_c} \quad (2.1)$$

where suffixes  $D, L$  refer to the drag and lift forces, respectively. We term the component of the hydrodynamic force acting in the  $x$ -direction to be the drag and the component acting in the  $y$ -direction to be the lift. The force coefficients for just the control rod were obtained by the difference between the time-mean forces in configurations 2 and 1:

$$C_{D,L}^{\text{Rod}} = \frac{(F_{D,L}^{\text{Conf.2}} - F_{D,L}^{\text{Conf.1}})}{\frac{1}{2}\rho U_\infty^2 D L_c} \quad (2.2)$$

In addition to time-mean force coefficients, coefficients of the fluctuating forces acting on the cylinder and cylinder plus control rod were also found. However, it was not possible to deduce the fluctuating forces on the control rod and only its time-mean coefficients could be found.

## 2.2. PIV Measurements

For PIV measurements the main cylinder was attached at its lower end to an acrylic disc with a diameter of 350 mm which acted as an effective end plate. The gap between the floor of the flume and the disc was fixed at 50mm so that it was above the flume's boundary layer. The top end of the main cylinder was attached to a square plate partially immersed in the water, as illustrated in Figure 4. The control rod was fixed to the

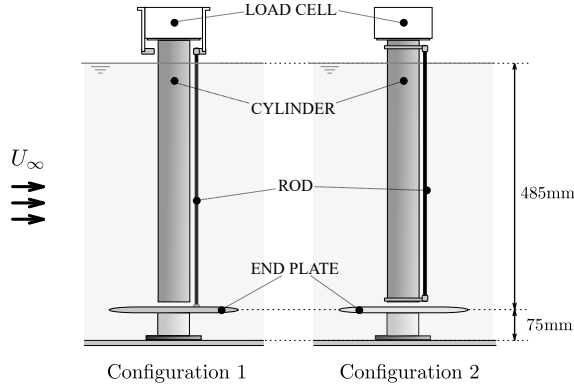


FIGURE 3. Arrangement of the system for force measurements. Configuration acquiring the forces on the combined system (right) and only on the main cylinder (left).

|                |                        |
|----------------|------------------------|
| $L_c$ [mm]     | 485 (9.7D)             |
| $f_{acq}$ [Hz] | 200                    |
| $T_{acq}$ [s]  | 200                    |
| $\theta$       | $90^\circ - 180^\circ$ |
| $\Delta\theta$ | $5^\circ$              |

TABLE 2. Properties of the force measurements experiments

cylinder with supports similar to those used for the force measurements so as to keep the gap constant and to allow different angles to be set. The top and bottom plates were transparent to allow image recording, as shown in figure 4. As also illustrated in figure 4, PIV data were acquired at a plane located near the middle of the cylinder. The illumination source was a high-speed Litron LDY304 Nd:YLF laser, which operated at a constant frequency of 1400 Hz. An optical system formed by mirrors and lenses directed the laser beam through the channel's glass walls. The flow was seeded with polyamide particles with an average diameter of  $7 \mu\text{m}$ . The acquisition of images was obtained using two cameras, one looking from the top of the model and the other from the bottom. Each camera was a Phantom v641 model with maximum resolution of  $2460 \times 1600$  px and internal storage memory for 5700 images at the highest resolution. In order to capture simultaneously different scales of the flow, each camera focused on a different field of view (FoV), set by two lenses (Nikon 70 mm  $f=2:8$  and 105 mm  $f=2:8$ ). The cameras operated at different acquisition rates, and their synchronization with the laser pulses was controlled through an external pulse generator Stanford DG645.

The PIV measurements were also carried out at a flow velocity of 0.4 m/s, yielding  $Re = 20\,000$ . The angular position of the control rod ( $\theta$ ) was varied from  $90^\circ$  to  $140^\circ$  with a  $5^\circ$  step between consecutive cases and an average error of  $\pm 1^\circ$ . For each run, the flow was established by accelerating the flume from still water up to the desired velocity, and the acquisition started after the stabilization of the flow. Table 3 summarises the main properties of the PIV set-up. The cameras acquired images in different regions of the flow for the same time period  $T_{acq}$ , which covered approximately 70 cycles of vortex shedding from the main cylinder. For certain cases, an additional run was recorded over a longer time period and with a 5 times lower acquisition frequency. Camera 1 focused on a field of view that captured a large part of the near wake, while Camera 2 focused on two narrow strips (acquired in different runs), capturing smaller scales at an acquisition frequency higher than Camera 1. The main purpose of recording with Camera 2 was to provide longer time series. Figure 5 illustrates the Field of View of each camera.

The images were pre-processed and the flow fields calculated using the commercial software *DaVis* 8.4. The frequency of acquisition  $f_{acq}$  was set to be high enough to capture at least twice the frequencies of vortex shedding of the main cylinder and the control rod. Initially a Gaussian filter was applied to the PIV data followed by the subtraction of the mean local intensity with side 3 px. Every pixel then had its intensity confined

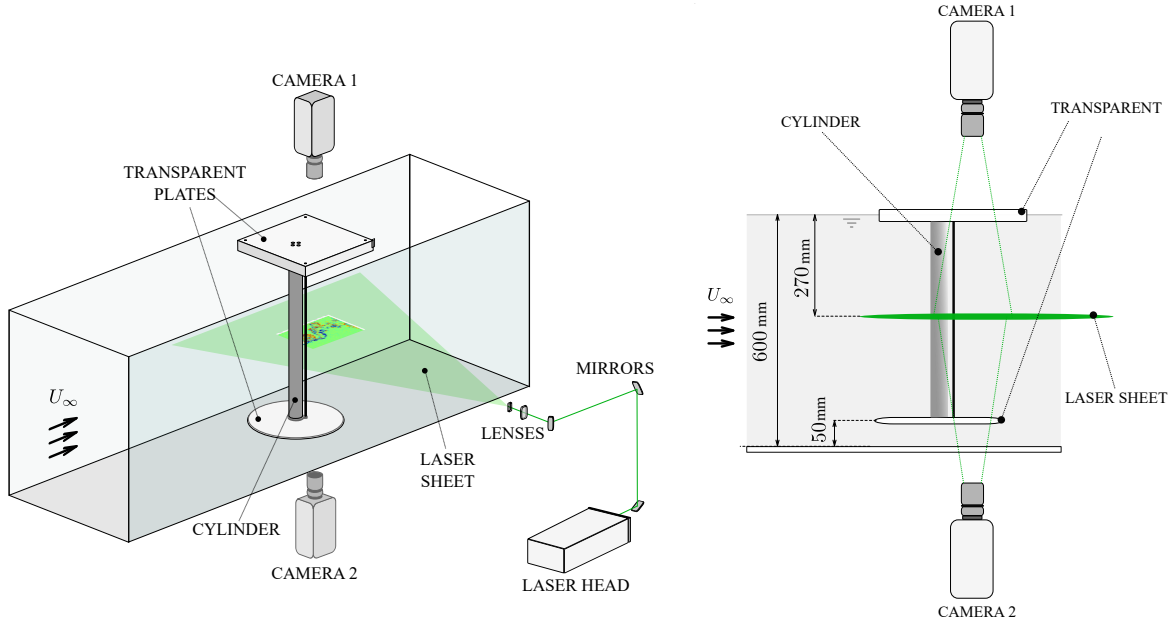


FIGURE 4. Arrangement of model, cameras and laser sheet in the flume.

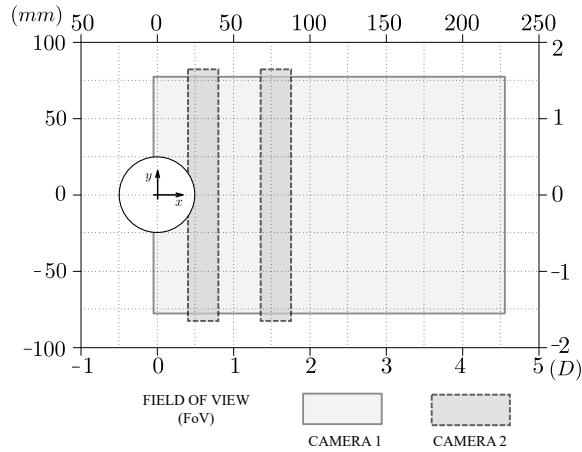


FIGURE 5. Field-of-view (FoV) for each camera

|                       | Camera 1           |       | Camera 2          |       |
|-----------------------|--------------------|-------|-------------------|-------|
| $f_{acq}$ [Hz]        | 70                 | 14    | 200               | 40    |
| $T_{acq}$ [s]         | 42.83              | 214.1 | 42.83             | 214.3 |
| $N_{acq}$             | 3000               |       | 8575              |       |
| $\Delta t$ [ $\mu$ s] | 1428               |       | 714               |       |
| IW [px]               | 16                 |       | 12                |       |
| WO [%]                | 75                 |       | 75                |       |
| $\Delta x$ [mm]       | 1.88               |       | 0.75              |       |
| FoV [px]              | $2400 \times 1400$ |       | $400 \times 2000$ |       |

TABLE 3. Properties of the PIV experiments

between a minimum of 0 and a maximum of 2000 counts. These processes were carried out in order to smooth the image, mitigate the interference of the image background and prevent vector contamination by high intensity peaks. Flow fields were calculated using a standard multi-pass cross correlation method. The first step had a one pass, 50% window overlap (WO) and a 48 px interrogation window (IW) for all cases. The second and final pass had a different configuration for each camera. The main properties are presented in Table 3, including the number of images ( $N_{acq}$ ), the time interval between adjacent images ( $\Delta t$ ) and the spatial resolution ( $\Delta x$ ). As for post processing, a Universal Outlier Detector filter (Westerweel & Scarano 2005) with size  $5 \times 5$  px was applied to remove spurious vectors. For each case, the total number of replaced vectors was lower than 1% of the total.

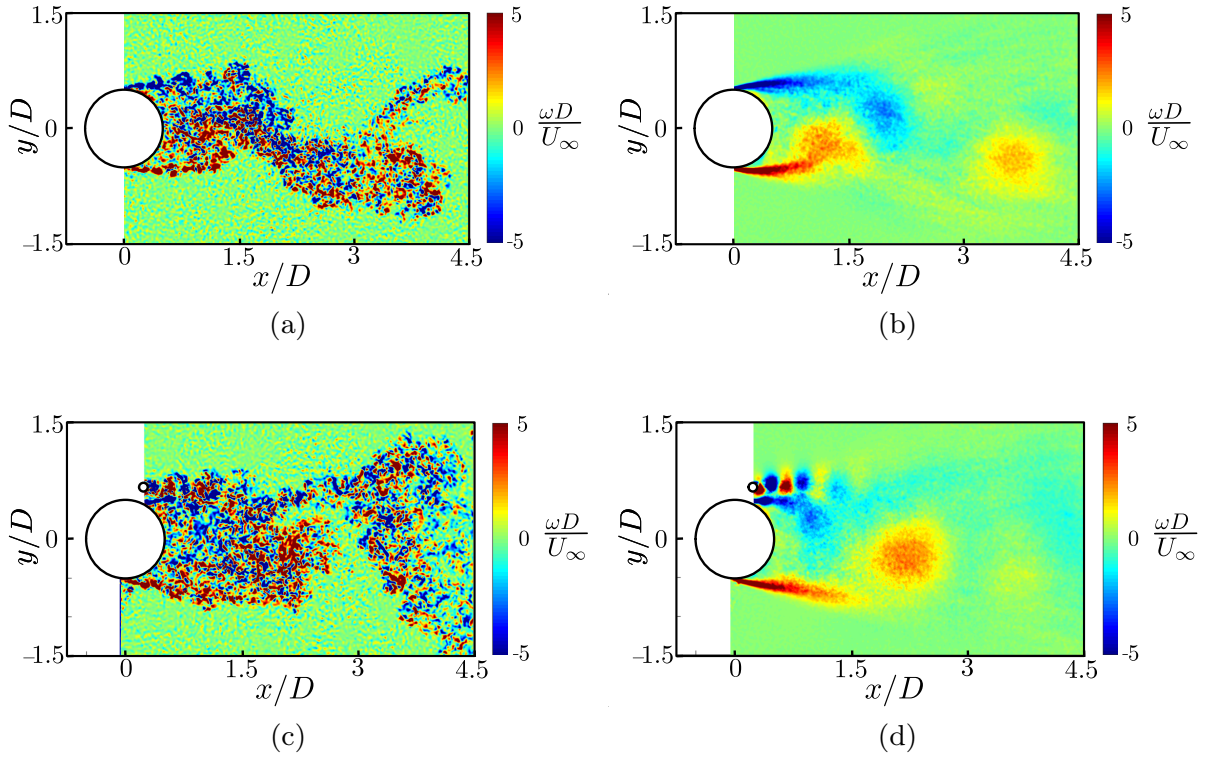
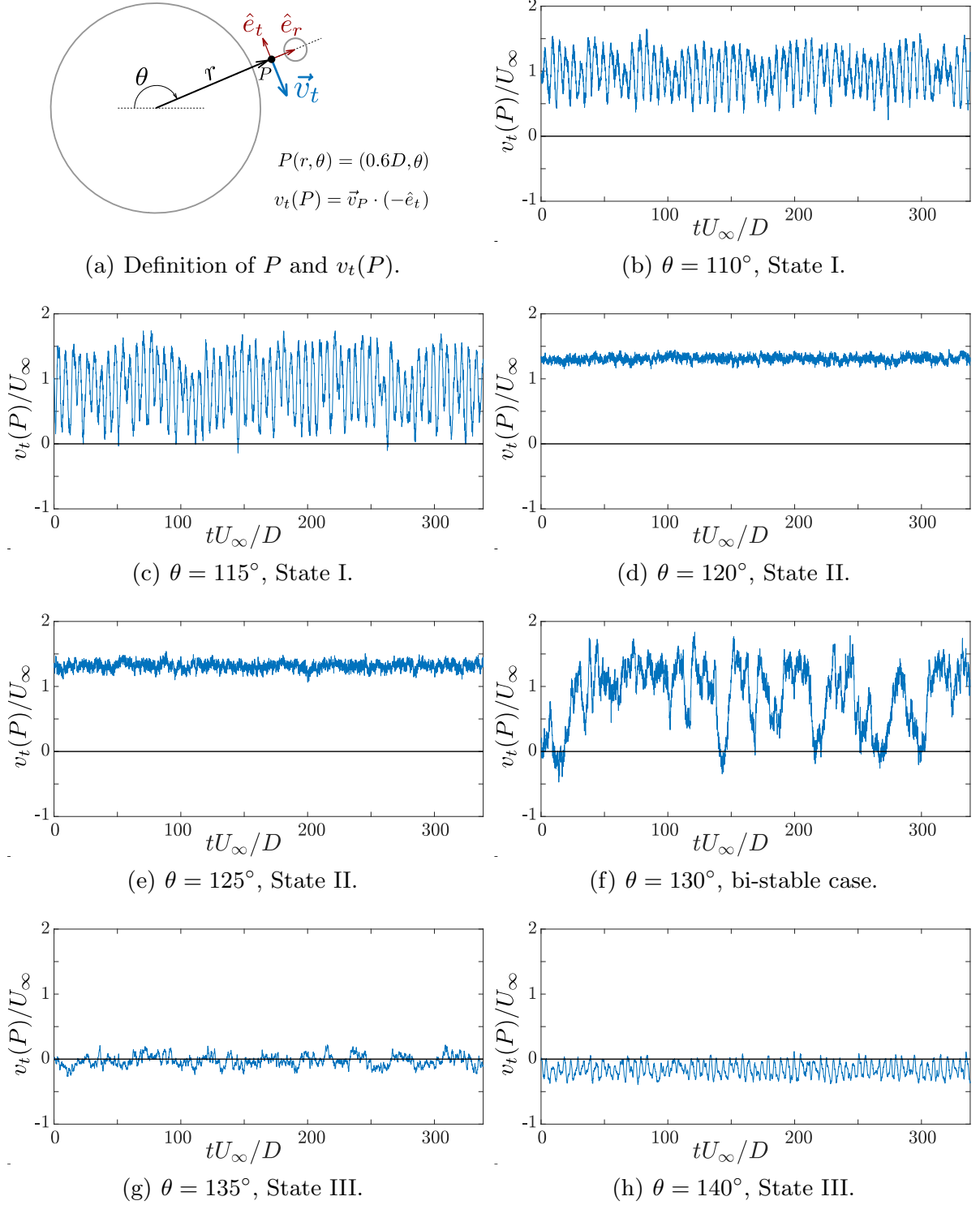


FIGURE 6. Instantaneous vorticity fields (a) bare cylinder and (c) case  $\theta = 110^\circ$ ; and fields to which the smart OMD-based filtering has been applied: (b) bare cylinder and (d) case  $\theta = 110^\circ$ .

### 2.2.1. Post processing

The processed velocity fields exported from *DaVis* had high spatial resolution, even those with the largest FoV. Each instantaneous field contained information on both coherent structures and fine-scale turbulent fluctuations. Since our main interest is focused on the former, we needed to process the velocity fields again in order to remove fluctuations less relevant to the large-scale dynamics of the system. The process adopted was a “smart filter”, understood as a filter capable of removing highly damped fluctuations regardless of their frequency or energy content. This is a key factor since the vortex shedding induced by the control rod is expected to be one order of magnitude higher in frequency than that of the main cylinder. Whilst these fluctuations are not especially energetic, they are dynamically important. We employed Optimal Mode Decomposition (OMD), which is a method proposed by Wynn *et al.* (2013) as a generalization of the Dynamical Mode Decomposition, first proposed by Schmid (2010). The algorithm used was based on that provided by Wynn *et al.* (2013) and is further described in Appendix A. An example of the previous application of such an OMD-based “smart filter” to turbulent velocity data is given in Rodríguez-López *et al.* (2016). Figure 6 shows two examples of vorticity fields reconstructed using OMD: one is for the bare cylinder (the main cylinder without a control rod) and the other for a case with the cylinder and control rod. All instantaneous velocity and vorticity fields presented hereafter were processed using the same procedure. Time series and power spectra of velocity, however, were calculated from the original un-filtered fields.



FIGURE 7. Time series of  $v_t(P)$  for different values of  $\theta$ .

### 3. Results and Discussion

The placement of a rod in the range  $90^\circ \leq \theta \leq 180^\circ$  causes significant changes in the development of the wake. Based on the flow characteristics, and in common with previous researchers, angular positions are divided into groups associated with particular flow states, including one which is a bi-stable case. In order to identify the states, PIV was used to measure the tangential velocity component of the flow nearest to the mid point,  $P$ , of the gap between the cylinder and the control rod,  $v_t(P)$ . This velocity proved to be

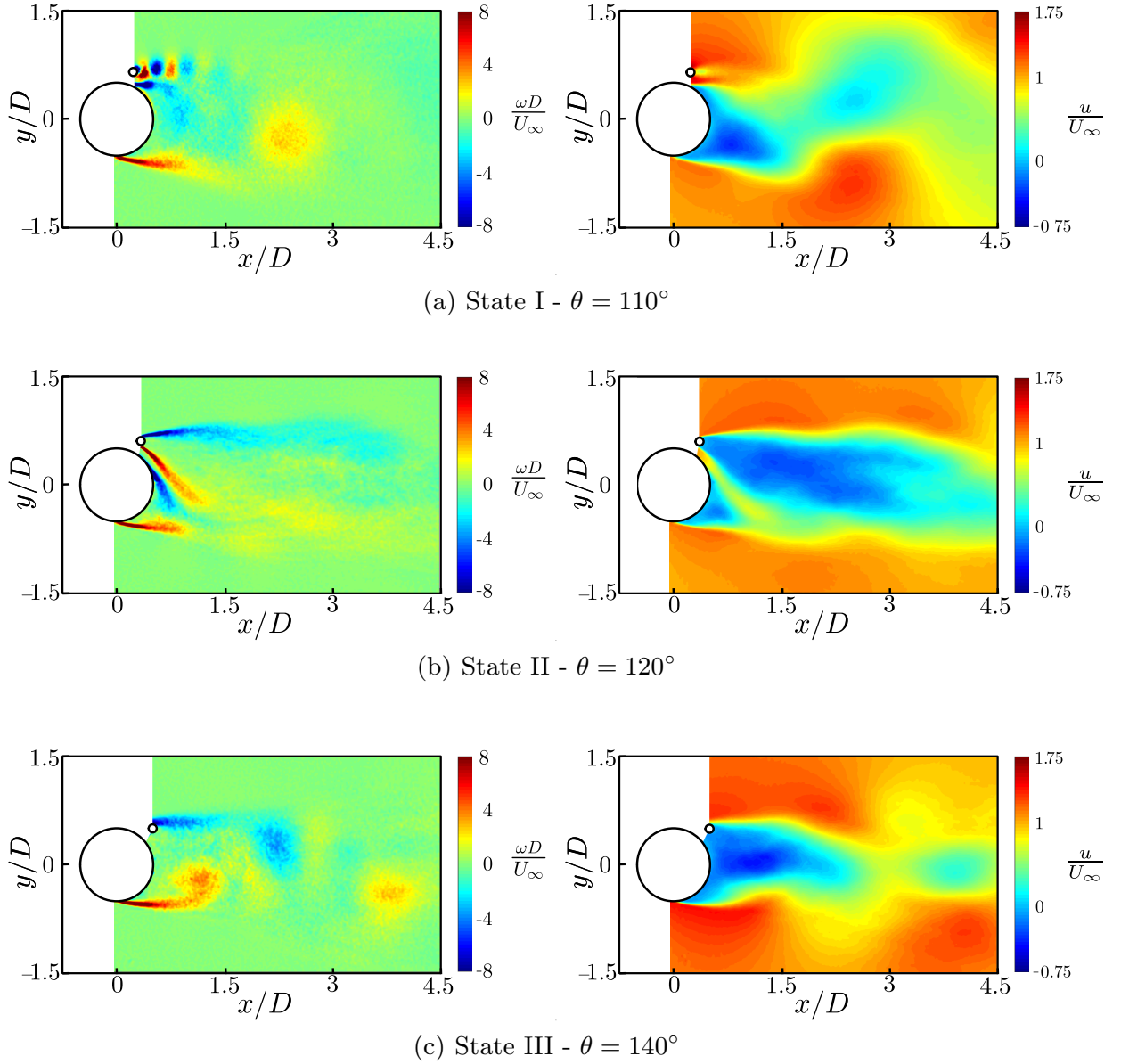


FIGURE 8. Instantaneous vorticity (left) and velocity (right) fields for each of the three stable dynamical states characterised in this work. Their development can also be seen in the supplementary videos.

very useful as a diagnostic tool. Figure 7(a) illustrates how the velocity is defined, and time series of  $v_t(P)$  are shown in the other plots in Figure 7. In order to link flow states to the velocity traces, reference will be made to Figure 8(a) which shows instantaneous vorticity and velocity fields for the 3 stable states observed in our investigation.

For  $90^\circ \leq \theta \leq 115^\circ$  the time-mean value of  $v_t(P)$  is close to the free stream velocity and the fluctuating component has a dominant frequency equal to the shedding frequency of the main cylinder. Examples of the flow in this state, State I, are shown in Figure 8(a), and it is characterised by the formation of distinct wakes, developed by the main cylinder and the control rod. Both wakes shed vortices but with very different frequencies and length scales. Moving to  $\theta = 120^\circ$  and  $\theta = 125^\circ$ , an intense jet appears in the gap between the cylinder and the control rod, with  $v_t(P)/U_\infty \approx 1.3$  and it is relatively steady, as seen in Figures 7(d) and 7(e). This jet is a dominant feature of State II, as observed in Figure

8(b). The third stable state, State III, was identified for  $\theta = 135^\circ$  and  $\theta = 140^\circ$ . In this state the average value of  $v_t(P)$  is close to zero, as shown in Figures 7(g) and 7(h). The cylinder boundary layer separates sufficiently far upstream of the control rod for the free shear layer to pass above it, leaving point  $P$  within the cylinder's recirculation zone. This state is illustrated in Figure 8(c) and is characterized by the development of a vortex street wake, similar to the bare cylinder case. The velocity trace plotted in Figure 7(f) for  $\theta = 130^\circ$  shows  $v_t(P)$  varying over the range  $0 - 1.5$ , and it is very different to those for the 3 stable states. This is an example from the state showing bi-stability.

Measurements of the variation of hydrodynamic force coefficients with  $\theta$ , are shown in Figure 9 together with an indication of the ranges of  $\theta$  occupied by the flow states introduced above. The forces acting on the cylinder without a control rod, the bare cylinder, were measured first to serve as reference data. The results are a mean drag coefficient,  $\overline{C}_D = 1.10$ , a coefficient of fluctuating lift,  $C'_L = 0.27$  and a Strouhal number,  $St = 0.194$ . These values are in close agreement with data to be found in works by Zdravkovich (1997) and Norberg (2003). It should be noted that as well as Reynolds number the free stream turbulence level has an effect on circular cylinder flow. For the parameters used in our investigation,  $Re = 20\,000$  and a free stream turbulence level of 1.5%, Fage & Warsap (1929) reported a similar value of mean drag coefficient. Note that fluctuating forces are computed as the root-mean-square values acting on the full span. In Figure 9, the bare cylinder values are denoted by a solid dark line.

With the control rod in place the mean lift and drag coefficients acting on it are also presented in Figure 9(b), but note that all coefficients are calculated using the diameter of the main cylinder ( $D$ ) and the free stream velocity. This makes it easier to compare the relative contributions of the main cylinder and control rod to the overall forces. With the addition of a control rod it can experience lift and drag forces on itself as well as influencing the forces acting on the main cylinder. Hence the total mean force coefficient has been calculated separately for the main cylinder and control rod. Mean drag, lift and total force coefficients for the combined system of cylinder and control rod are shown in Figure 9(c).

In State I, comparing with the bare cylinder, the cylinder has a lower drag coefficient, a small but positive mean lift coefficient, a similar level of fluctuating lift and a Strouhal number increasing with increasing  $\theta$ , but consistently lower than the bare cylinder case. The control rod in State I is exposed to a velocity greater than the free stream velocity and, depending on  $\theta$ , its drag ranges between 9% and 14% of the main cylinder's drag. Its lift force is negative and acts to offset a small amount of the lift on the main cylinder. Moving to State II, the mean drag on the cylinder falls by about 10% with respect to the reference case, however the mean lift increased so dramatically that the magnitude of the mean of the total hydrodynamic force acting on the cylinder was higher than for the reference case. The coefficient of fluctuating lift dropped to a minimum of  $C'_L \approx 0.05$  at  $\theta = 120^\circ$ , indicating an attenuation of vortex shedding and/or a reduction in its spanwise correlation. The corresponding power spectrum of the lift force did not have a prominent peak in the frequency range normally associated with vortex shedding, but scattered values in the range  $0 < fd/U_\infty < 0.2$ . The control rod exhibited positive values of both lift and drag in State II. For State III the control rod is in the range  $135^\circ \leq \theta \leq 180^\circ$  which places it in the recirculation region of the near wake of the main cylinder. The mean drag coefficient acting on the main cylinder and the Strouhal number, have similar values to those of the bare cylinder. The mean lift coefficient was small and positive with values less than 0.1. As a result, the magnitude of the mean total force coefficient acting on the main cylinder was little different to the drag coefficient of the bare cylinder. With the control rod in the recirculation zone it experienced small negative drag and lift forces.

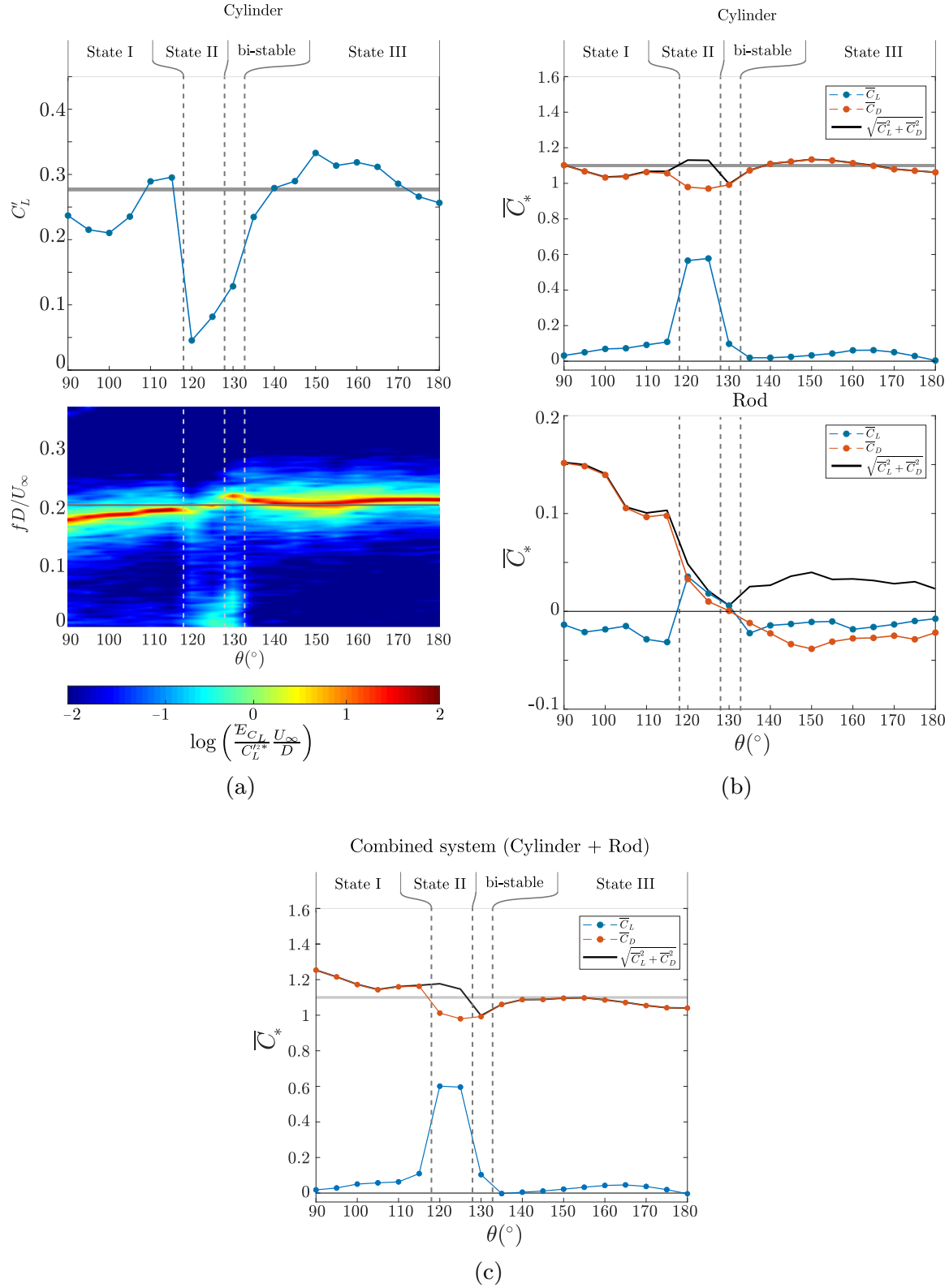


FIGURE 9. (a) RMS of the fluctuating Lift force on the cylinder (top) and their relative Power-Spectral Density (bottom) for the cases  $90^\circ \leq \theta \leq 180^\circ$ . The solid lines represent the RMS and the peak  $St$  of  $C'_L$  for the bare cylinder case, respectively. (b) Average hydrodynamic force coefficients over the cylinder (top) and the control rod (bottom). (c) Average hydrodynamic force coefficients over the combined system. The solid grey line represents the mean drag coefficient of the bare cylinder case.

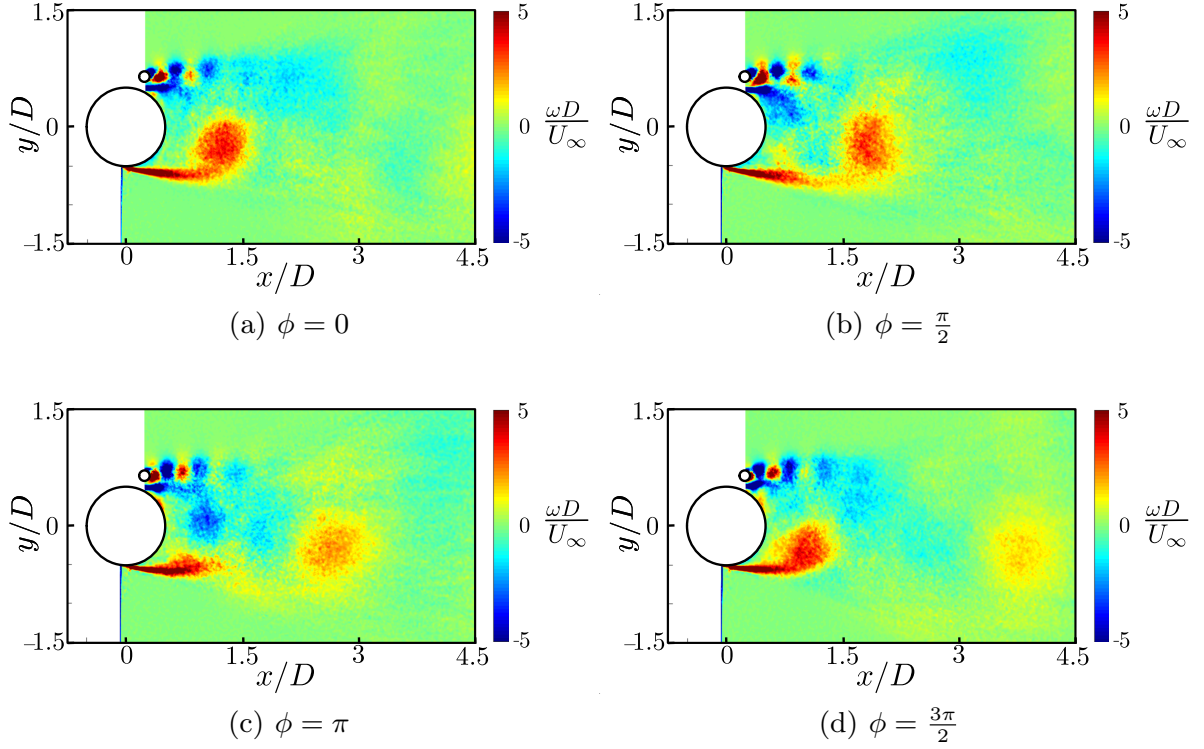


FIGURE 10. Vortex shedding cycle for the case  $\theta = 110^\circ$ , which is representative of State I. Vorticity fields are calculated from the smart-filtered velocity fields.  $Re = 20\,000$ .

It was in this state that the highest value of fluctuating lift on the main cylinder was recorded with  $C'_L \approx 0.34$ . These 3 flow states and the bi-stable case are analysed in more detail in §3.1 to §3.4 and compared with findings of previous investigators.

### 3.1. State I

State I was observed for the cases with the control rod in the range  $90^\circ \leq \theta \leq 115^\circ$ . Its main feature is the formation and interaction of the distinct wakes of the main cylinder and the control rod. Downstream this interaction results in a vortex street similar to that formed by a bare cylinder. The two shear layers from the main cylinder developed differently with the upper shear layer passing between the control rod and the main cylinder, as shown in Figure 10. The sequence of instantaneous fields (and the supplementary video) show that the upper boundary layer remains attached beyond the point where the gap between the two bodies is a minimum, up to a separation angle  $\theta_{sep} > \theta$ . The positions of the mean separation points, for various values of  $\theta$ , are shown in Figure 11. Close agreement was found between separation points obtained from time mean streamline patterns and from the mean tangential velocity component  $\bar{v}_t$  measured at about 0.9 mm from the cylinder surface, separation being identified as the angular position at which  $\bar{v}_t = 0$ .

The upper and lower boundary layer separation angles are shown plotted in figure 12 together with the cylinder drag coefficients for the range of  $\theta$  from  $90^\circ$  to  $135^\circ$ . It is interesting to note that there is very little variation in the lower separation angle across the range of control rod placements. In contrast, separation of the upper boundary layer changes over a wide range of angles. In State I, Figure 10 indicates that during a vortex shedding cycle the negatively signed vorticity of the cylinder's upper separated shear layer interacts with vortices shed from the control rod. Comparing with the bare



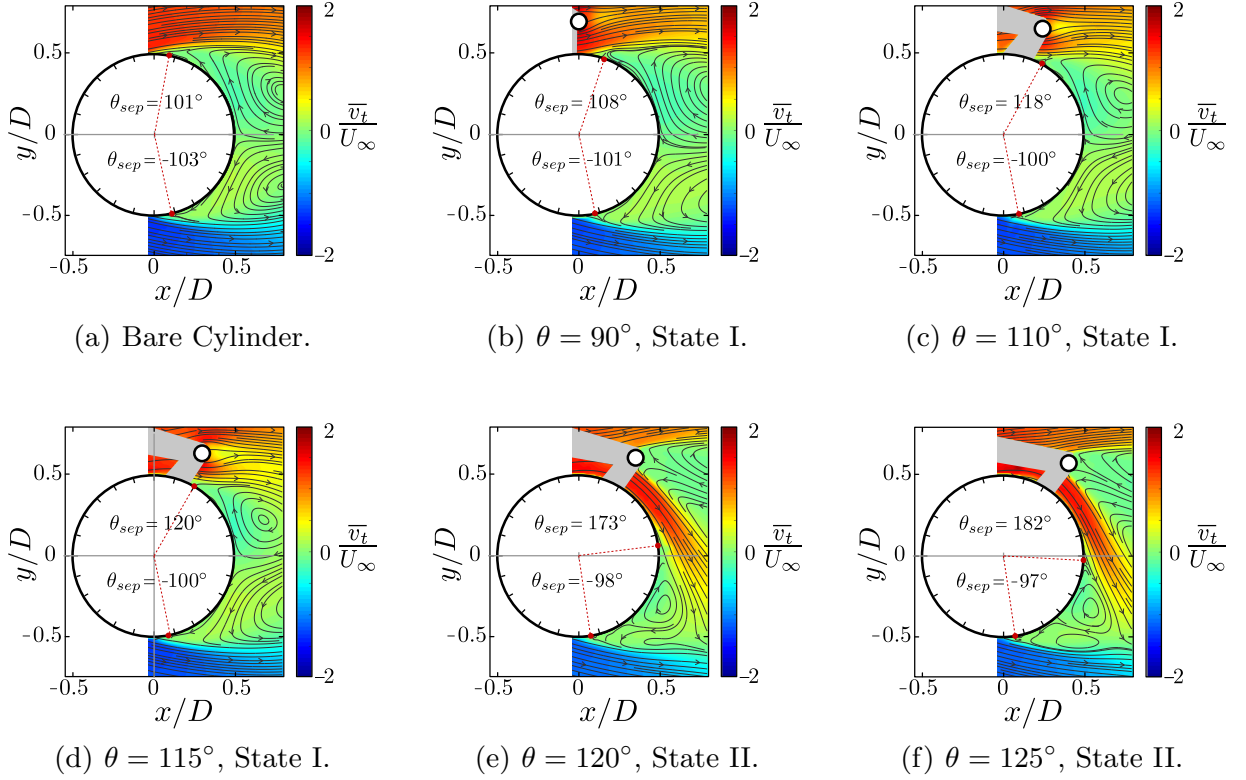


FIGURE 11.  $\bar{v}_t$  fields for the cases bare cylinder and  $90^\circ \leq \theta \leq 125^\circ$ . The separation point ( $\theta_{sep}$ ) was estimated using both the mean streamlines patterns and the tangential velocity  $\bar{v}_t$ . It is estimated that  $\theta_{sep}$  is accurate to within  $\pm 2^\circ$ .

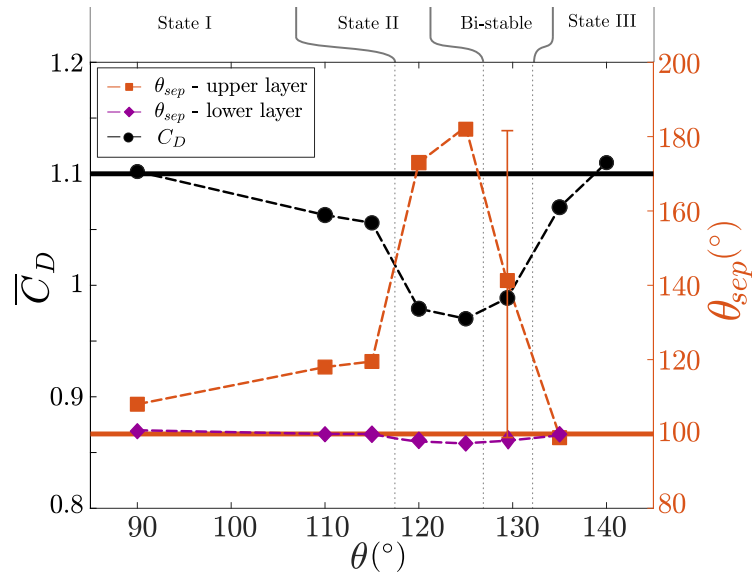


FIGURE 12. Variation of mean drag coefficients and separation points with  $\theta$  (for which PIV data was available). The solid lines represent the mean drag coefficient and separation point of the bare cylinder case

cylinder case, this results in increased diffusion of the shear layer with negative vorticity. The interaction of the cylinder's top shear layer with the wake of the control rod can be readily observed in the supplementary video.

It is known for a bare cylinder that if  $\theta_{sep}$  moves further round its surface this results in

a drag reduction, due to increased pressure recovery ahead of the separation points and hence an increase in the base pressure. This is illustrated in Figure 12 where an increase in the upper surface separation angle is accompanied by a reduction in the drag coefficient, and vice versa. In state I we found that if the characteristic length used in the definition of drag coefficient was changed from  $D$  to  $D'$ , where  $D'$  is the vertical distance between the upper and lower separation points, a drag coefficient of 1.14 resulted, regardless of the control rod angle. It suggests that separation of the upper boundary layer is directly influenced by the adverse pressure gradient caused by the presence of the control rod. It should be noted that the upper boundary layer separates at an angle beyond the position of the control rod. This is compatible with the flow locally speeding up in the gap between the cylinder surface and the control rod and then decelerating. Studies have been carried out by Parezanovic & Cadot (2012) and Sakamoto *et al.* (1991) into the effect of control rods on the flow around bluff bodies with fixed separation points. In these cases there will be some variations in the flow mechanisms compared with our experiments where substantial changes in separation position are observed.

Figure 9(b) shows that for all values of  $\theta$  comprising State I there is a positive lift force on the cylinder and a negative lift force on the control rod. The signs of these forces are consistent with the upper cylinder boundary layer remaining attached until just beyond the control rod. In State I figure 7 shows that the gap flow has a marked unsteady component due to vortex shedding from the main cylinder, see Figure 8(a) and the supplementary video.

It is observed that the frequency of vortex shedding in State I is lower than that found for the bare cylinder (Figures 9(a) and 14). Figure 13 shows comparisons of mean velocity and vorticity fields between the bare cylinder and the case  $\theta = 110^\circ$ . A number of factors influence the shedding frequency including the distance between the separated shear layers and the flow velocity at their outer edges. Gerrard (1966) established that in addition the Strouhal frequency is influenced by both the vortex formation length and the lateral diffusion of vorticity within the shear layers. He quantified diffusion by defining a diffusion length related to shear layer thickness and argued that the greater the diffusion length the longer it takes for a vortex to form and hence the lower the Strouhal number. Also he reasoned that the longer the vortex formation length the greater the diffusion length as the shear layer has further to diffuse ahead of vortex formation. Considering a bare circular cylinder over a large  $Re$  range, it is found that where the drag coefficient falls it is accompanied by a rising Strouhal number, and vice versa. With a circular cylinder a reduction in drag coefficient is associated with the separation points moving further round the surface and the near wake becoming narrower. Roshko (1954) developed the concept of a universal Strouhal number by using the velocity at the edge of the shear layers at separation as the characteristic velocity and the distance between the shear layers as the characteristic length. For a circular cylinder his analysis supports the finding that as the distance between the shear layers reduces the Strouhal number increases.

Within State I, the Strouhal number and drag coefficient behave in a similar way to the bare cylinder with the increase in the separation angle with increasing control rod angle leading to a reduction in drag and an increase in vortex shedding frequency. With the control rod at  $\theta = 90^\circ$  the value of the drag coefficient for the main cylinder is very close to that for the bare cylinder but in Figure 14a the Strouhal number is significantly lower. Searching for a reason for this we followed previous researchers and made measurements of the vortex formation length. Earlier measurements have been based on a hot-wire traverse along the centre-line of the wake to find the position of the maximum value of the RMS of the longitudinal component of fluctuating velocity. We processed our PIV data to reproduce what a hot-wire probe would have measured. For the bare cylinder the

vortex formation length was  $1.29 D$  and this is in good agreement with published data (Szepessy & Bearman 1992) and with the control rod at  $\theta = 110^\circ$  it increases to  $1.68 D$ . Also the PIV data showed a thickening of the upper separated shear layer from the main cylinder caused by interaction with the control rod's wake. According to Gerrard (1966), together these changes will increase the diffusion length, leading to a reduction in the shedding frequency. However, for  $\theta = 90^\circ$  the vortex formation length rather than increasing reduced slightly from the bare cylinder value. In the literature vortex formation lengths have mainly been presented for bluff bodies that do not generate a mean lift force. Since in the presence of lift the cylinder wake is deflected at an angle to the free stream velocity this brings into question how vortex formation lengths should be defined. Since lift coefficients as large as 0.6 were generated in some cases it was decided not to present further measurements of vortex formation length. Parezanovic & Cadot (2009) point out the difficulty of predicting the vortex shedding frequency of a bluff body using stability theory when separation points are free to move, such as on a circular cylinder. Using the wake of a bare circular cylinder as the base flow, the introduction of a control rod cannot be considered as a small perturbation if there are changes in boundary layer separation positions.

Sakamoto & Haniu (1994) carried out experiments with a control rod at  $Re = 65\,000$  and varied  $\theta$  between  $0^\circ$  and  $180^\circ$  to find angular positions where the control rod was most effective at reducing fluid forces. In the range of control rod angles we classify as State I they also found that the Strouhal number at  $\theta = 90^\circ$  was below the value for the bare cylinder. Also throughout the range of  $\theta$  in State I the shedding frequency increased with increasing  $\theta$  but remained below the value for the bare cylinder. They do not include reasons for this behaviour. States similar to State I can be found in the literature, for example the 'Free Stream' case reported by Bingham *et al.* (2018a) at  $Re = 9,500$  with the control rod at  $R'/D = 1.85$  and with  $\theta = 142^\circ$ . Compared with their bare cylinder the mean drag coefficient dropped by 8%. As expected the Strouhal number increased and in their case it rose by almost 5% indicating an interaction between the shear layer and the control rod and a change in where separation occurs.

Parezanovic & Cadot (2012) performed a study with a bluff body with fixed separation points, a D-shaped cylinder. They present sketches of 4 flow fields they observed depending on the position of the control rod. Their 'Outer Shear' (OS) configuration is the closest to our State 1 with a reduction in drag due to an increase in base pressure.

It is interesting to note that in the low  $Re$  study by Strykowski & Sreenivasan (1990), the rod's wake did not develop vortex shedding, which would have made the interaction with the main cylinder shear layer different from the present study. Figure 15 shows in State I the spectrum of  $v'$  along the line  $x/D = 1.0$ . The peaks in  $fD/U_\infty \approx 0.2$  and  $fD/U_\infty \approx 2.4$  are due to the periodic vortex shedding of the main cylinder ( $f_D$ ) and the control rod ( $f_d$ ), respectively. Besides these, two other clear frequency signatures appeared, at  $f_d \pm f_D$  with a well defined spatial arrangement, as the highest frequency ( $f_d + f_D$ ) resides between the wakes of the main cylinder and the control rod and the other ( $f_d - f_D$ ) resides closer to the control rod's wake. Baj & Buxton (2017) investigated the interactions between wakes produced by a multi-scale array of bluff bodies and identified the same spectral signature with the same spatial arrangement at the intersection of different-sized wakes. Although the geometries and  $Re$  were different, the similarity between the spectra and their spatial configuration is remarkable, which suggests that the physical phenomena behind the interaction is also similar. They reported that these frequencies  $f_d \pm f_D$  are associated to secondary modes, which are the result of nonlinear interactions between the primary shedding modes in close proximity to one another. These modes play an important role in feeding kinetic energy to the residual turbulent

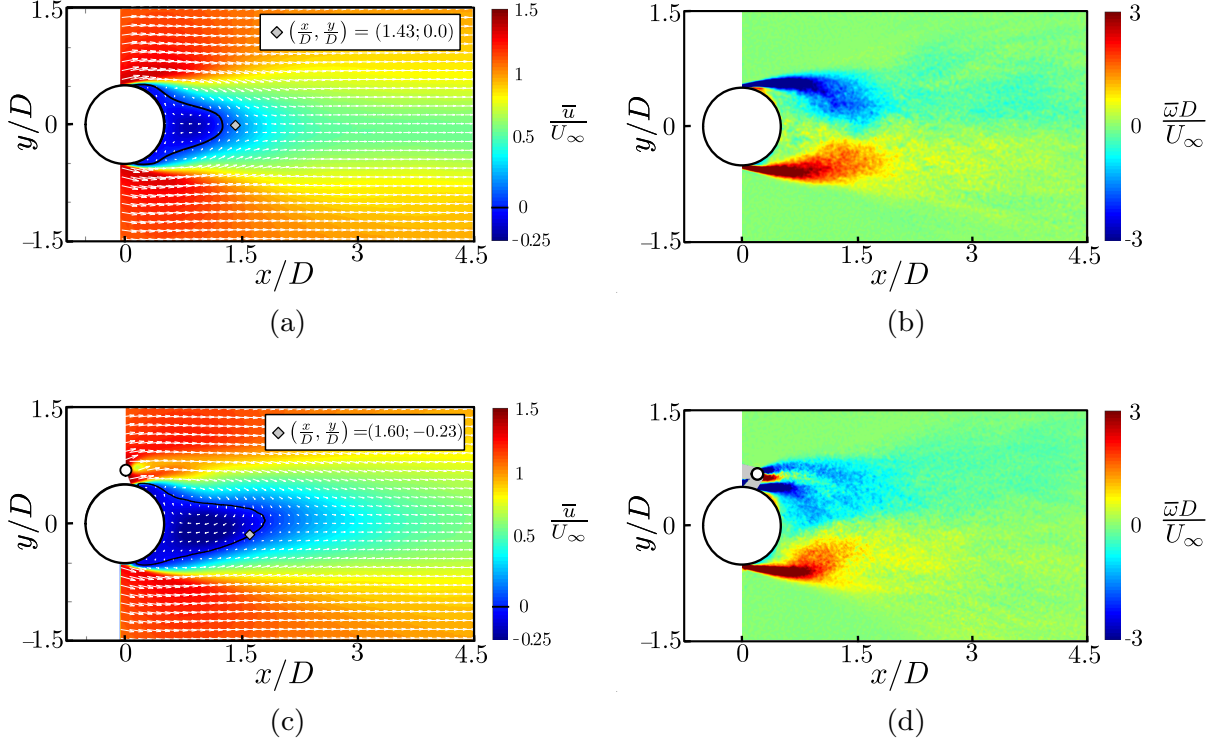


FIGURE 13. Mean velocity fields, where the gray points mark  $\max(\bar{v}^2/U_\infty^2)$ , for the cases (a) bare cylinder and (c)  $\theta = 110^\circ$  which is typical for State I. Mean vorticity fields for the cases (b) bare cylinder and (d)  $\theta = 110^\circ$ .

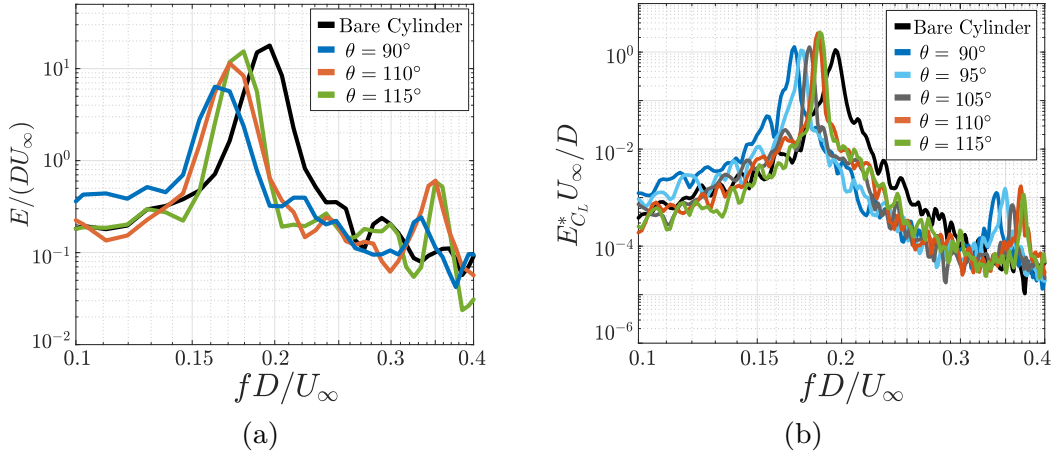


FIGURE 14. Comparison of the spectra between State I and the bare cylinder: (a)  $v$  at the point of  $\max(\bar{v}^2/U_\infty^2)$  and (b) Lift coefficient.

fluctuations (understood as  $u''$  in the triple decomposition of a turbulent velocity field  $u = \bar{u} + \tilde{u} + u''$  in which  $\tilde{u}$  corresponds to the periodic component of the fluctuating velocity). These residual fluctuations in turn are responsible for the majority of the dissipation of turbulent kinetic energy during such multi-scale wake interactions.

### 3.2. State II

State II was observed for control rod angles  $\theta = 120^\circ$  and  $125^\circ$ . Its major feature is that separation of the upper boundary layer moves substantially further round the

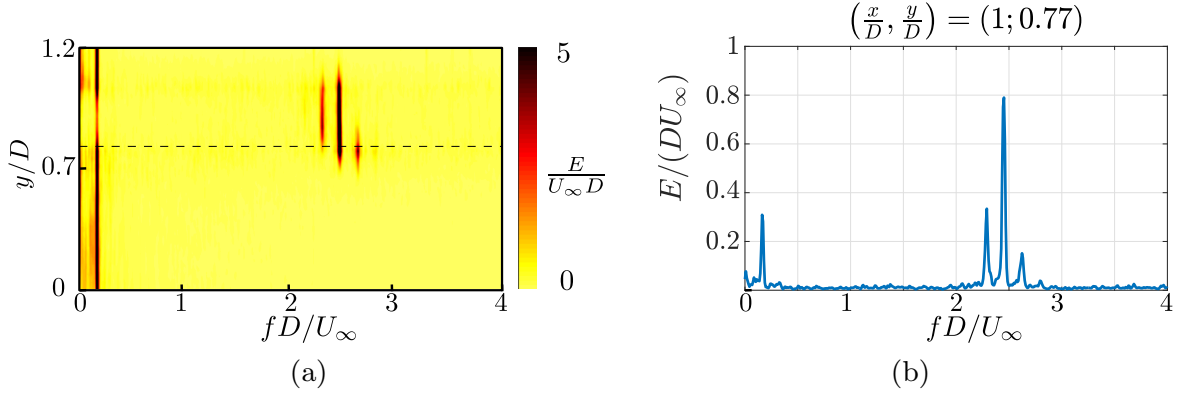


FIGURE 15. Spectra along  $x/D = 1.0$  for the case  $\theta = 90^\circ$  (a). The dark lines represent the signatures of the vortex shedding of the main cylinder ( $f_D$ ) and the control rod ( $f_d$ ), as well as the secondary modes ( $f_d \pm f_D$ ), showing their spatial distribution. (b) Spectrum at the point  $(x/D; y/D) = (1.0; 0.77)$  where the four modes coexist.

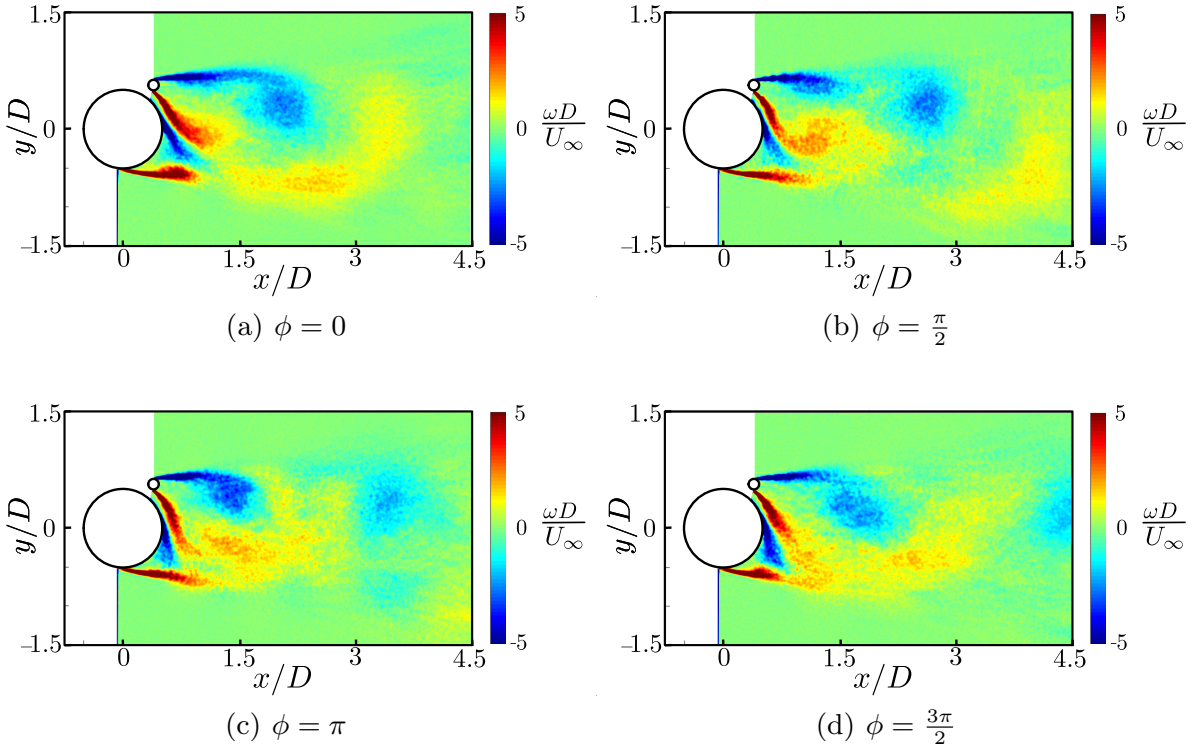


FIGURE 16. Vortex shedding cycle for the case  $\theta = 125^\circ$  which is representative of State II. Vorticity fields calculated from the smart-filtered velocity fields.  $Re = 20\,000$

cylinder, as show in Figures 11(e) and 11(f). With the rod placed at  $\theta = 120^\circ$  and  $125^\circ$ ,  $\theta_{sep} = 173^\circ$  and  $182^\circ$ , respectively. The relatively high speed flow that develops between the control rod and the cylinder surface acts to energise the cylinder boundary layer which remains attached for a considerable distance. It is possible that transition to turbulent flow occurs in the main cylinder upper boundary layer leading to the delayed separation, but this could not be verified. The behaviour of the flow is an example of the Coandă effect and such a fully attached jet would not form on a bluff body with fixed separation points. However, the study by Parezanovic & Cadot (2012) on a D-shaped body revealed a related phenomenon whereby a straight jet penetrated into the near wake, replenishing



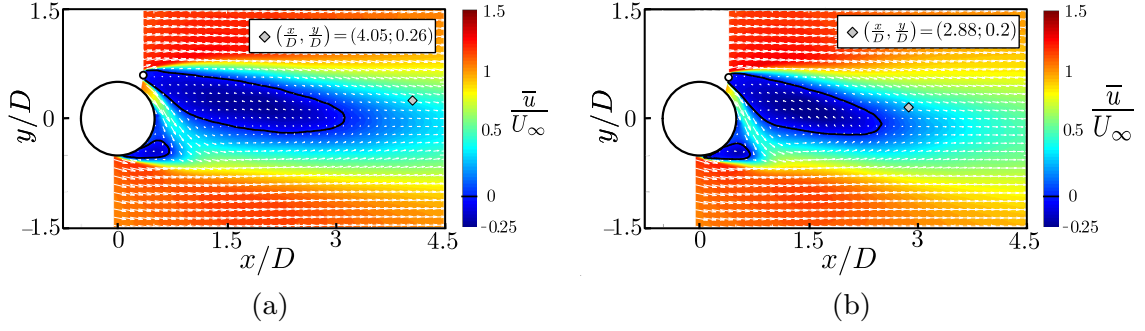


FIGURE 17. Mean velocity fields, where the solid line is the contour  $\bar{u}/U_\infty = 0$  and the grey diamonds represent the points where  $v'/U_\infty$  is maximum. (a)  $\theta = 120^\circ$ , and (b)  $\theta = 125^\circ$  which are both representative of State II.

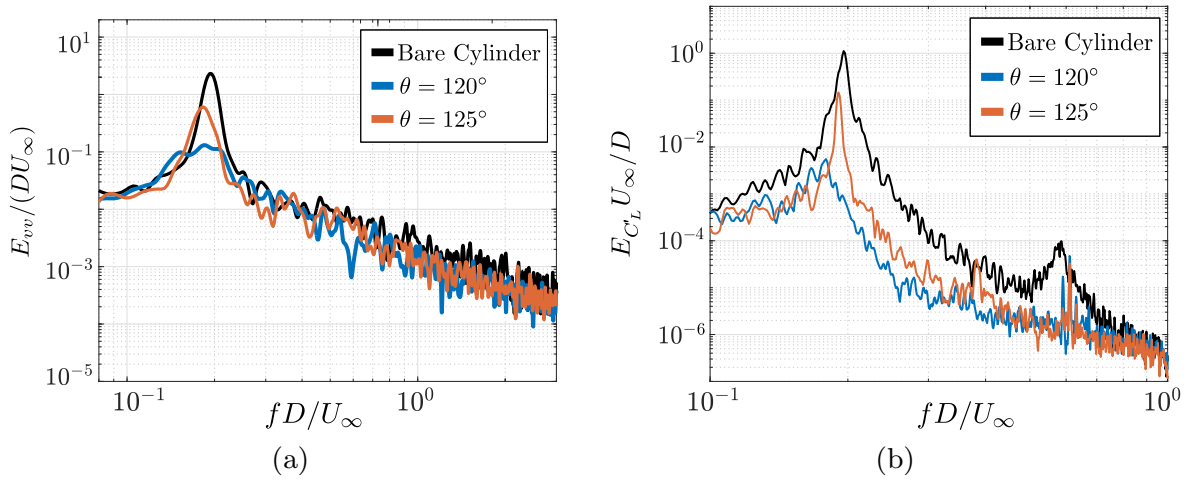


FIGURE 18. Comparison of the spectra between State II and the bare cylinder. (a) Spectra evaluated at the  $\max(\overline{v'^2}/U_\infty^2)$  point for each case; (b) Spectra of lift force.

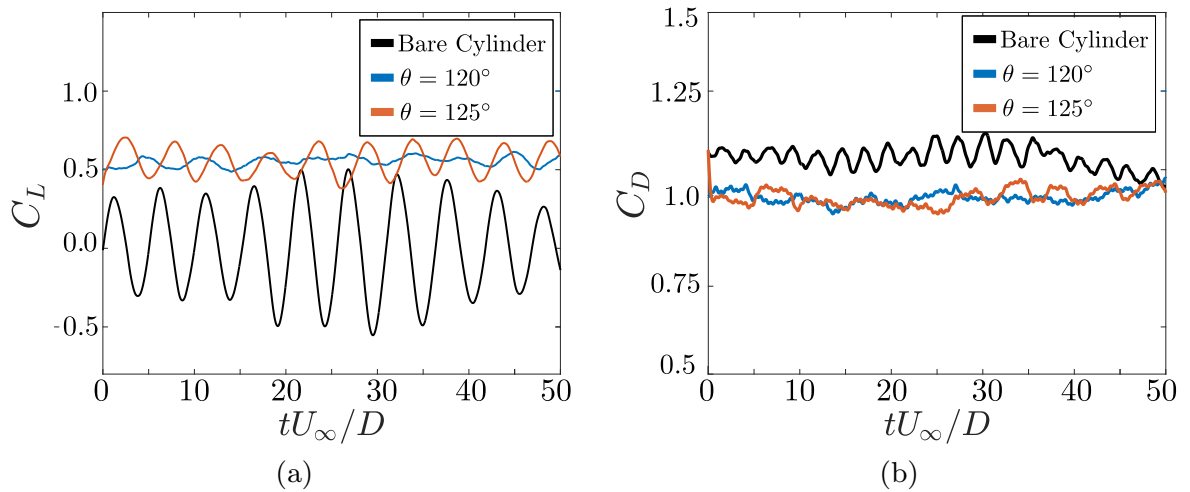


FIGURE 19. Time series of the forces of bare cylinder and cases in State II. (a) Lift and (b) Drag.

fluid removed by entrainment by the free shear layers. In a diagram they show the jet entering the near wake just ahead of their control cylinder. As in our experiments this results in a reduction in drag. Following the large movement in the position of the upper separation point on the circular cylinder, the drag coefficient,  $\overline{C}_D$  decreased to  $\approx 0.98$ , which is a reduction of 11% below that of the bare cylinder, whereas  $\overline{C}_L$  increased to  $\approx 0.55$ . These changes result in the magnitude of the mean overall hydrodynamic force acting on the main cylinder being greater than the drag force acting on the bare cylinder. This highlights the danger of considering only the change in the mean drag when using a control rod as a passive flow control device. However, in State II the control rod is effective in reducing fluctuating forces due to vortex shedding. The RMS of the lift force on the main cylinder decreased significantly, especially for  $\theta = 120^\circ$  where  $C'_L \approx 0.05$ , which is more than 80% lower than for the bare cylinder.

In this State, as well as a large change in the flow around the main cylinder, there is also a substantial change in the control rod's wake when compared with State I. As a result, the time mean forces acting on the rod change. For  $\theta = 125^\circ$ ,  $\overline{C}_D \approx 0.02$ , which is more than 80% lower than the expected value of 0.1 if the rod was exposed to just a free-stream. When considering these values note that all coefficients for the control rod have the main cylinder diameter,  $D$ , as the representative length scale. The lift force on the rod changes from being negative in State I to positive in State II with a lift to drag ratio close to 1.0.

Figure 16 shows a cycle of vortex shedding and illustrates how four shear layers interact to form the combined system's wake. Following separation of the upper boundary layer on the main cylinder it reaches the separated shear layer from the bottom of the cylinder in the vicinity of  $(x/D, y/D) \approx (0.75, -0.5)$ . The jet flow draws down the lower shear layer from the control rod such that it also follows the contour of the main cylinder. The mixing of these three shear layers results in one diffused shear layer with positively signed vorticity. The drawing down of the lower shear layer from the control rod causes a very broad near wake to form with a large region of low speed flow. It is assumed that the resulting pressure recovery in the wake of the control rod is responsible for its large drag reduction. The upper shear layer originating from the control rod with negatively signed vorticity interacts with the diffused lower main cylinder shear layer with positive vorticity to initiate vortex shedding. Visually the vortices forming in the combined system's wake appear weaker than those in State I which is compatible with the reduction in fluctuating lift.

Figure 17 presents the mean velocity fields for two cases in State II. As discussed above, the most striking features are the strong jet formed between the bodies and the long region of near stagnant fluid in the wake of the control rod. Figures 11(e), 11(f), 16 and 17 clearly show that the upper boundary layer on the main cylinder remains attached up to  $\theta_{sep} \approx 180^\circ$ . In contrast, the lower boundary layer separates at  $\theta_{sep} \approx 100^\circ$ . This marked asymmetry in the separation locations is responsible for the large mean lift coefficient which, as shown Figure 9, is unique to State II. It is interesting to observe that in Figure 17 there is a very large difference between the sizes of the two recirculation zones. Whereas in State I we discussed the flow in terms of the wakes of two bluff bodies, in State II the configuration appears closer to a single body with a passage through it that supplies fluid to the near wake resulting in a drag reduction.

Figure 18(a) shows spectra of  $v'^2/U_\infty^2$  at the point in the wake where it is maximum and also shows spectra of  $C'_L$ . The spectral peaks for State II cases are lower with respect to the bare cylinder case, particularly for  $\theta = 120^\circ$ . The flow patterns close to the rear of the main cylinder for  $\theta = 120^\circ$  and  $\theta = 125^\circ$ , shown in Figures 8(b) and 16 respectively, are similar but show differences a short distance further downstream. For  $\theta = 125^\circ$

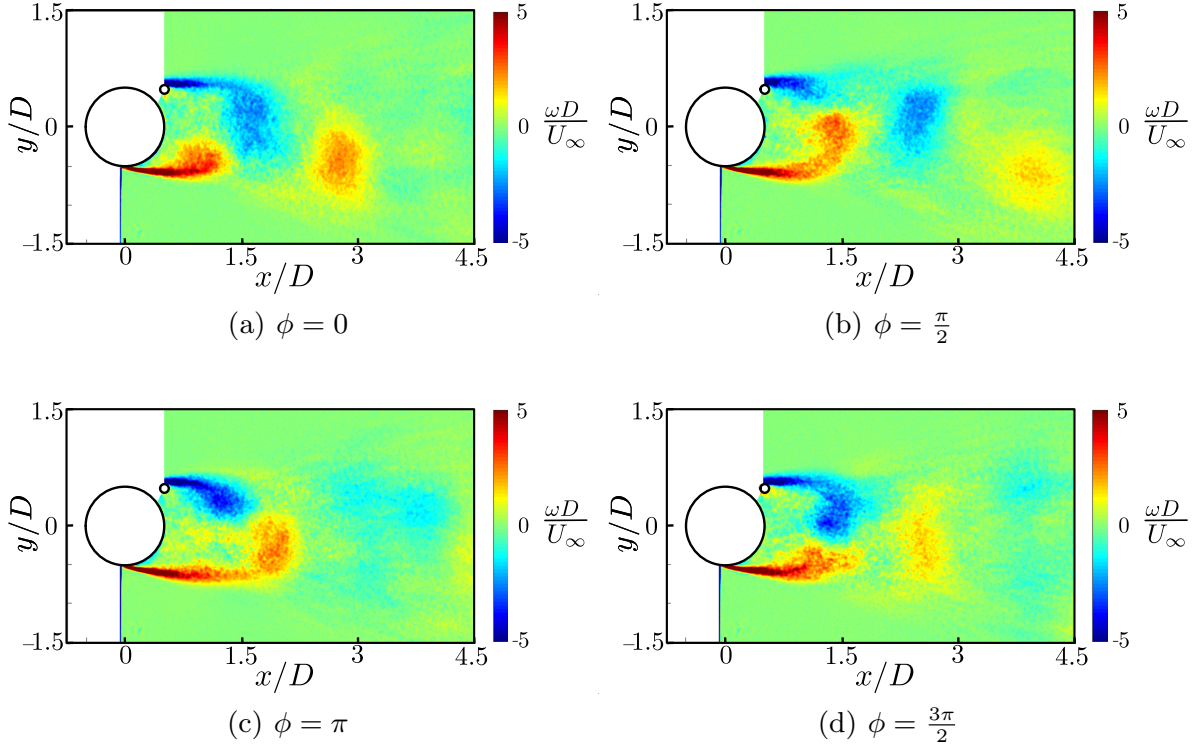


FIGURE 20. Vortex shedding cycle for the case  $\theta = 135^\circ$  which is representative of State III. The vorticity fields are calculated after the application of the OMD-based smart-filter to the velocity fields.  $Re = 20\,000$ .

there is evidence of regular vortex shedding while for  $\theta = 120^\circ$  the wake structure is less well organised and there is mixing of opposite sign vorticities. Figure 8(b) shows this mixing leads to lateral diffusion of the shear layers and an apparent lack of regular vortex shedding. This is also displayed in the supplementary video for this case. The spectra plotted in Figure 18(a) and 18(b) confirm the weakening of regular vortex shedding in State II as the angle of the control rod is reduced. They are also compatible with the observation that the lowest value of  $C'_L$  was found in State II for  $\theta = 120^\circ$ . It is interesting to note in Figure 19(a) that the time series of lift for  $\theta = 120^\circ$  has a weak fluctuation at a frequency close to the vortex shedding frequency for the bare cylinder. Hence, it cannot be concluded that vortex shedding has been totally suppressed but rather it has been substantially weakened.

In State II the main cylinder's upper boundary layer appears to pass between the cylinder and the control rod and if there was a free shear layer there is no evidence of it impacting on the control rod. A related State found in the literature is the Type D case reported by Sakamoto & Haniu (1994) at  $Re = 65\,000$ . By measuring the time-averaged pressure distribution around the main cylinder they were able to identify a short separation bubble at the position on the cylinder closest to their control cylinder. Due to the presence of the shadow of the control rod it was not possible in our study to confirm for State II from PIV that a short separation bubble formed but the possibility cannot be dismissed.

### 3.3. State III

State III is characterised by the control rod being positioned within the recirculation zone of the main cylinder and is found to occur for  $\theta \geq 135^\circ$  up to  $\theta = 180^\circ$ . The

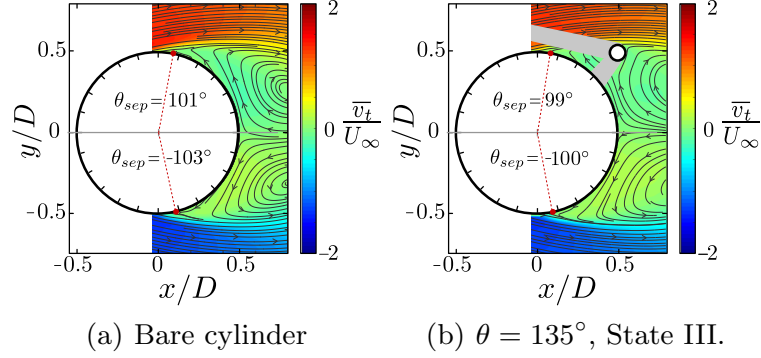


FIGURE 21.  $\bar{v}_t$  fields for the cases of (a) bare cylinder and (b)  $\theta = 135^\circ$  which is representative of State III. The separation point ( $\theta_{sep}$ ) for each case was defined as described in the text.

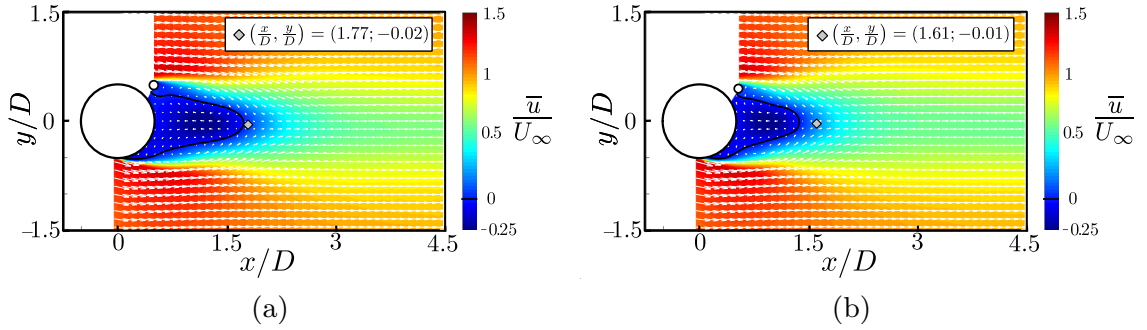


FIGURE 22. Mean velocity fields, where the gray points square define  $\max(\bar{v}'^2/U_\infty^2)$ , for the cases (a)  $\theta = 135^\circ$  and (b)  $\theta = 140^\circ$ .

prominent feature of State III is the von Kármán vortex street formed by the interaction between shear layers shed from the main cylinder in a form very similar to the bare cylinder case. Figure 20 shows a cycle of vortex shedding for the combined system with the control rod at  $\theta = 135^\circ$ . The upper shear layer from the main cylinder passes above the control rod. After which it is drawn into the near wake and forms a vortex as it interacts with the separated shear layer originating from the boundary layer on the lower half of the main cylinder thereby forming a vortex street. In the figure, due to the shadow formed above the main cylinder, it is not possible to follow the path of the upper shear layer to the control rod. Evidence that the majority of the negative sign vorticity in the upper shear layer has originated from the main cylinder is provided by the absence of vorticity of significant strength and opposing sign being shed from the lower half of the control rod. The reason for this is that the control rod is situated in a recirculation region where the fluid velocity is very low, as indicated in figure 7(g).

In State III the upper separation point on the main cylinder does not vary as significantly as in the previous two states. Figure 21 shows that with  $\theta = 135^\circ$  the separation points remain close to those for the bare cylinder,  $\theta_{sep} \approx 100^\circ$ . The position of the upper separation point could not be measured for the other angles in State III due to the presence of the shadow of the rod in the PIV fields. However, we assume that the separation positions will not vary significantly for  $\theta > 135^\circ$  since as the angle increases the control rod moves further from the upper shear layer. This would explain why the force coefficients in State III remain relatively close to the values for the bare cylinder case .

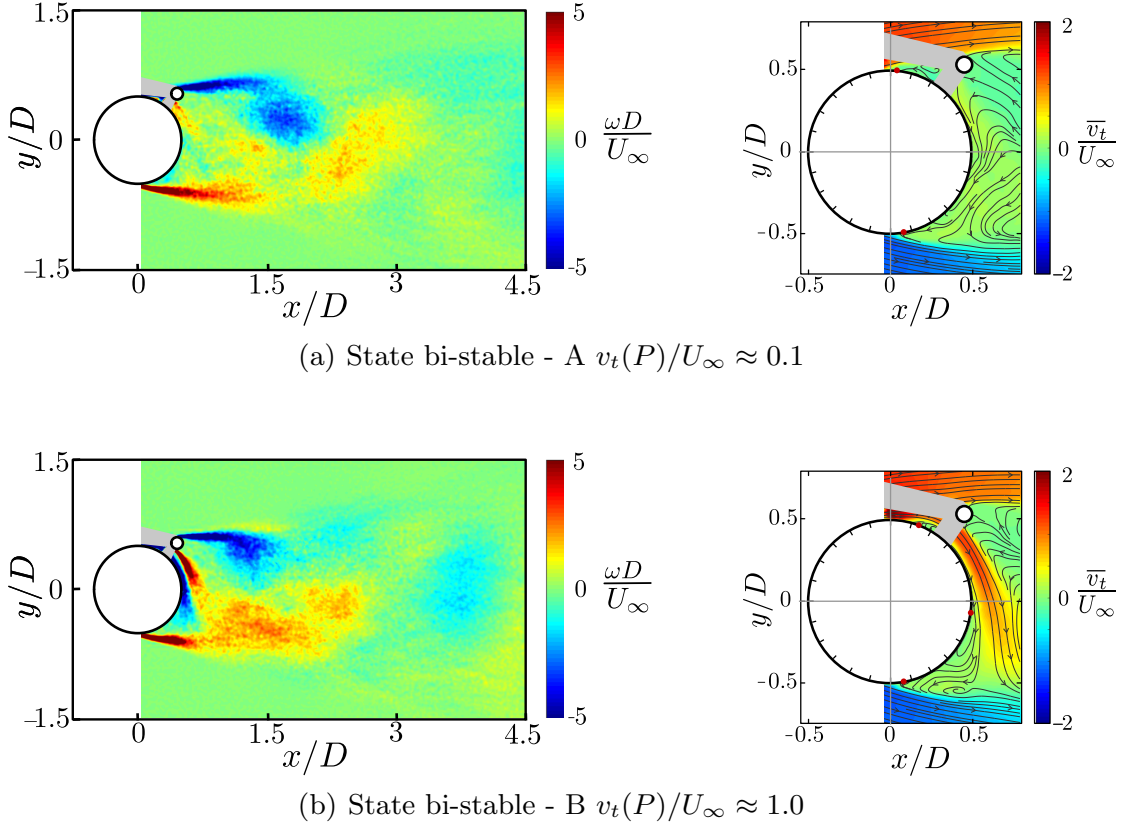


FIGURE 23. Instantaneous vorticity fields and streamline patterns for  $\theta = 130^\circ$ : (a) bi-stable - A and (b) bi-stable-B. Switching between the states can be viewed in the supplementary video.

The main effects due to the presence of the control rod in State III are related to changes in the near wake. Figures 22 show the time-averaged velocity fields for the cases associated with State III. The recirculation length was extended in both cases when compared to the flow around the bare cylinder; it increased from  $1.25 D$  to  $1.75 D$  and  $1.39 D$  for the cases  $\theta = 135^\circ$  and  $140^\circ$ , respectively.

For  $\theta \geq 140^\circ$ , the control rod had a limited effect on the development of the shear layer and hence on the wake as a whole. These results suggest that the primary effect of the control rod in this State III is to divert the top separated shear layer, thereby forcing the interaction further downstream relative to the bare cylinder. As for the control rod it is notable that it has a negative drag for all  $\theta$  values tested, indicating that it is in a reversed flow within the near wake. As an interesting consequence, the total drag of the combined system, i.e. cylinder and control rod, is lower than for the bare cylinder for all cases investigated in State III.

### 3.4. Bi-stable case

Figure 7 reveals that states I, II and III yield distinctive time series for  $v_t(P)$ , with a well-defined mean value and frequency of oscillation. Figure 7(f) shows  $v_t(P)$  with the control rod at  $\theta = 130^\circ$  and it is clear that its characteristics are quite different to those for the other states. The trace switches between high ( $v_t(P)/U_\infty \approx 1$ ) and low ( $v_t(P)/U_\infty \approx 0$ ) velocity at time intervals that are significantly longer than those associated with the vortex shedding. Figure 23(a) presents an instantaneous vorticity field for  $\theta = 130^\circ$  at a time instant for which  $v_t(P)/U_\infty \approx 1$  whilst figure 23(b) presents an instantaneous vorticity field in which  $v_t(P)/U_\infty \approx 0.1$ . It is clear that there is a fundamentally different



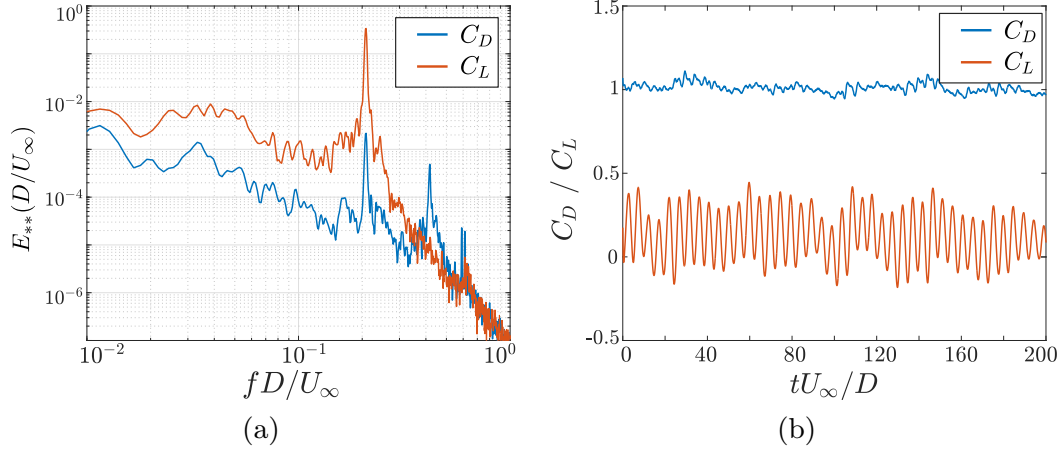


FIGURE 24. Force measurements at  $\theta = 130^\circ$ . (a) time series and (b) Power spectral densities.

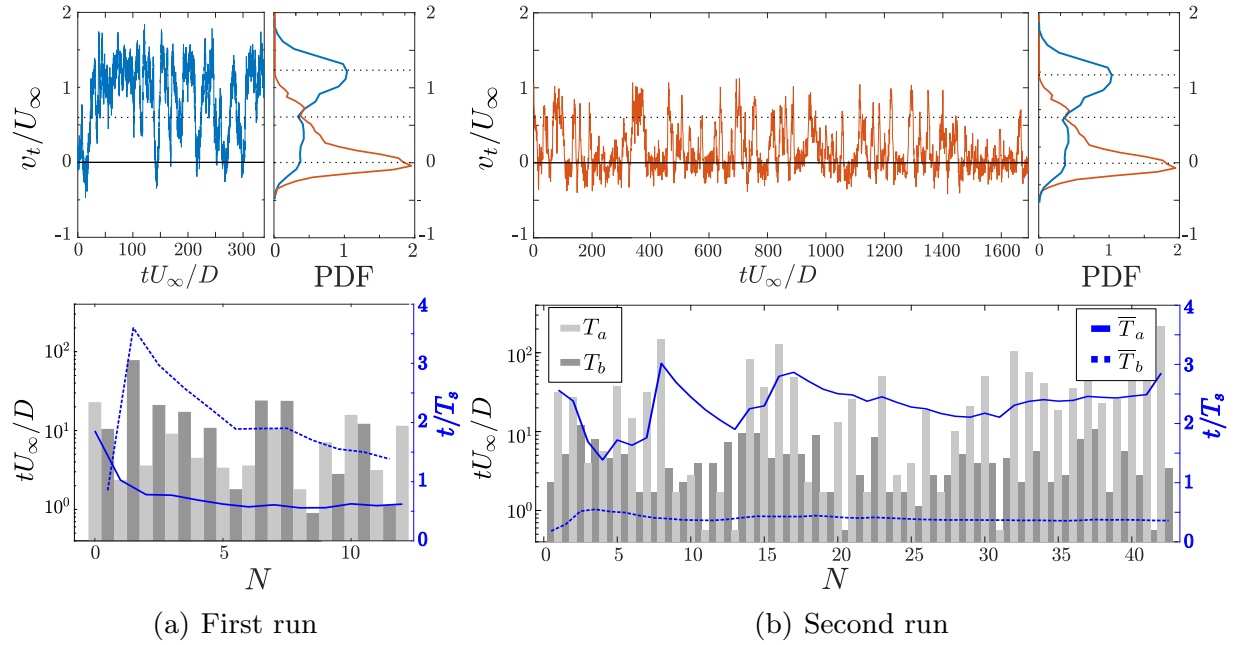


FIGURE 25. Time series and Probability Density Function of  $v_t$  (top) and time duration of the two states in the bi-stable case (bottom). (a) first run and (b) second run, which is five times longer.

flow structure at the two time instants and the case  $\theta = 130^\circ$  is a bi-stable case. Non-stable flow configurations have also been found in previous literature on controlling bluff body wakes with control rods. Sakamoto & Haniu (1994) ( $Re = 65\,000$ ) observed a tri-stable case (in which their type D flow pattern resembles the current State II) and Parezanovic *et al.* (2015) identified a bi-stable phenomenon in the flow over a D-shaped cylinder with a leeward control rod.

We will refer to the bi-stable states as Bi-stable A ( $v_t/U_\infty \approx 0$ ) and Bi-stable B ( $v_t/U_\infty \gtrsim 1.0$ ). For Bi-stable A the combined wake of cylinder and control rod develops a von Kármán vortex street. The vorticity field has features in common with those in State III. When Bi-stable A switches to Bi-stable B the velocity at point  $P$  between the main cylinder and control rod increases significantly and a jet forms between the two bodies. When this happens the upper boundary layer on the main cylinder finally separates close to  $\theta_{sep} \approx 180^\circ$ , after which it interacts strongly with the separated shear

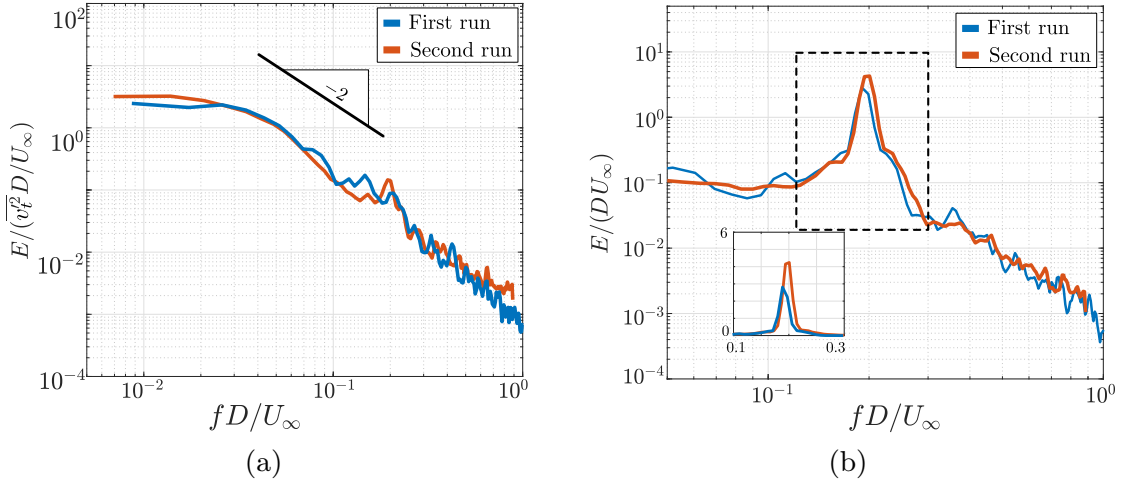


FIGURE 26. Comparison of spectra between the two runs. (a) Power Spectral Density of  $v_t$  and (b) Spectra of  $v'$  at the point  $(x/D; y/D) = (1.5; 0)$ .

layer originating from the bottom of the cylinder. This means that Bi-stable-B is visually similar to State II. Close inspection of the streamline pattern in Figure 23(b) indicates the possible presence of a short separation bubble forming on the main cylinder at an angular position close to that of the control rod. As previously stated, Sakamoto & Haniu (1994) observed a short separation bubble in their type D flow pattern at  $Re = 65\,000$  whereas we are working at  $Re = 20\,000$ . However, the geometric parameters in the two studies are quite similar and it is plausible that the closeness of the control rod to the main cylinder surface plays an important role in the formation of a separation bubble. It is proposed that the reason for the switching back and forth between Bi-stable states A and B is due to the formation and breakdown of a short separation bubble.

Previous studies have noted that placing the control rod in close proximity to the separating shear layer is very favourable for reduction of both drag and fluctuating lift. As highlighted by figure 9 the overall hydrodynamic force (on both the main cylinder and the combined system) is a minimum for the case  $\theta = 130^\circ$ . For the cylinder only, the drag is slightly higher than in State II but the mean lift drops significantly from  $\overline{C}_L \approx 0.5$  in State II to  $\overline{C}_L \lesssim 0.1$  in the bi-stable case, yielding a total force coefficient of  $\approx 0.99$ , more than 10% lower than for the bare cylinder. Dalton *et al.* (2001) found the greatest reduction of mean drag and fluctuating lift when the rod was placed in the middle of the shear layer ( $R'/D = 1.2$ ;  $\theta = 160^\circ$ ;  $Re = 3\,000$ ) and Bingham *et al.* (2018a) reported a drag reduction of 15% and attenuation of the RMS of lift of 66% for a rod placed in the middle of the shear layer, although further away from the cylinder ( $R'/D = 1.5$ ;  $\theta = 155^\circ$ ;  $Re = 9\,500$ ). The wake patterns in those cases were stable and visually similar to State Bi-stable-B, however in the present case Bi-stable B was never observed in stable isolation, only as one of two bi-stable states for  $\theta = 130^\circ$ . The time series and spectra of the forces over the main cylinder are presented in figure 24. The main peaks in the spectra at  $fD/U_\infty \approx 0.2$  are related to vortex shedding, that occurs for both states. No characteristic frequency of switching could be observed in the signal as there is no distinct peak at a frequency lower than the vortex shedding. As for the rod, the average net force is very close to zero in the bi-stable case ( $|\overline{C}_D| < |\overline{C}_L| < 0.01$ ), as seen in figure 9(b). Since we did not measure the forces directly on the rod, there is no information about instantaneous values. Based on the average values, however, we consider that the level of the forces on the rod at Bi-stable A is similar to State III, producing negative drag and lift while State Bi-stable-B produces positive drag and lift,

similarly to State II. We conclude that the switching between states is hence responsible for the minimal mean force magnitude on the rod.

In order to acquire data on the switching process between bi-stable states, a second run was carried out with an acquisition period 5 times longer than the first. Whilst these two runs were acquired in nominally the same configuration ( $\theta = 130^\circ$ ) the apparatus was assembled from scratch for both runs, yielding a small uncertainty in the precise angular position of the control rod. Figures 25(a) and 25(b) show the Probability-Density-Functions (PDFs - top right hand plots) of the time series of  $v_t(P)$  (top left hand plots) for the two runs. Both runs exhibit bi-stable behaviour with  $v_t(P)$  varying from lower velocities, which characterise Bi-stable-A, to high velocities typical of Bi-stable-B. However, the distribution of velocities for the two runs is different. The first run has a modal peak at  $v_t(P) \approx 1.2$  whereas the distribution of the second is concentrated around  $v_t(P) \approx 0$ . A threshold of  $v_t(P)/U_\infty = 0.6$ , which is equidistant from the modes of the PDFs for the first and second runs, was thus defined to delimit Bi-stable state A and Bi-stable state B. The time series were divided into periods during which the flow resided in a particular state before switching. In total  $N$  switches of state were recorded and these are displayed in the bottom plots of figures 25(a) and 25(b). In particular, the flow's residence time in a particular bi-stable state before switching is denoted by the grey bars. The blue lines show the cumulative mean residence times of the flow in each state, plotted on the right-hand axes. In the first run, the flow started in Bi-stable B for a period of  $\approx 20U_\infty/D$  and then switched to Bi-stable state A, where it remained for a period approximately  $\approx 10U_\infty/D$  and so on. In total, the flow switched 12 times in the first run and 43 times in the second run. Considering  $T_s = 1/f_s$  as the period of one cycle of vortex shedding for the bare cylinder, the mean residence time in Bi-stable A was approximately  $0.6T_s$  in the first run and approximately  $3T_s$  in the second run. The mean residence time in Bi-stable B was approximately  $1.5T_s$  in the first run and  $0.4T_s$  in the second run.

From the PDFs and switching statistics we conclude that despite a nominally identical configuration of  $\theta = 130^\circ$  the two runs are biased towards different bi-stable states and the dynamics of the residence times/switching between the states behave differently for each run. Further, we note that the mean residence time in the bi-stable states converges for both runs. Thus, we infer that the flows of the first and second runs are fundamentally different and not simply the result of unconverged statistics or unrepresentative sampling during the shorter of the two experimental runs. Considering that the system has a setting angle error of about  $\pm 1^\circ$ , the position of the rod was likely subtly different between the two runs. This reveals the high level of sensitivity of the flow in the Bi-stable case  $\theta = 130^\circ$ . This high level of sensitivity to the precise angular position of the control rod makes this configuration an ideal test case for high-fidelity computational fluid dynamics.

Figure 26(a) shows the spectra of  $v_t(P)$  for the two runs. In spite of their different time series, the spectra are quite similar, as no distinct frequency associated to state switching was found for any run. Instead, we observe that the spectra have close to a  $-2$  slope at low frequencies. This is consistent with the rapid transitions between bi-stable states, resembling a step, having a random nature to their occurrence which gives rise to a low-frequency cut-off in the spectrum with a  $-2$  power law (Grandemange 2013). The spectra obtained from the time series of  $v$  at  $(x/D; y/D) = (1.5; 0)$  revealed that the intensity of vortex shedding was higher in the second run, and its associated frequency was lower for the first run. These spectra can be explained by the observation that during the short run the flow spent more time in State Bi-stable-B, in which the vortex shedding process is weaker and its frequency lower than in State Bi-stable-A, which is similar to State III.

#### 4. Conclusions

Experiments were performed in a water channel on a circular cylinder with a control rod attached. The angular position of the rod was varied from  $\theta = 90^\circ$  to  $180^\circ$  while the Reynolds number of the circular cylinder was kept constant at  $Re = 20\,000$ . The other parameters held constant were the centre to centre spacing between the cylinder and the control rod,  $R'/D = 0.7$ , and the ratio of diameters of the control rod and the cylinder,  $d/D = 0.1$ . Flow field measurements were made using PIV and fluid forces were obtained for the cylinder and the control rod. By measuring forces separately on the control rod valuable information was obtained about the local flow field to supplement the PIV data. In common with previous investigations, several distinct flow regimes were observed depending on the angular position of the control rod. Three stable flow states were identified in addition to a bi-stable case and it was observed that compared to the bare cylinder, changes in the positions of boundary layer separation took place. Some particularly large changes in separation angle were noted for the boundary layer on the same side of the cylinder as the control rod giving rise to substantial lift forces. A new method was devised to identify the various flow states. Using PIV, the component of the flow velocity normal to a line between the centres of the cylinder and control rod was recorded at the mid-point of the gap between the bodies. Each flow state was found to have a characteristic value of the ratio of the local mean velocity to the free stream velocity and a distinctive variation of velocity with time.

State I,  $\theta = 90^\circ$  to  $115^\circ$ , is characterised by the formation of individual vortex street wakes from the cylinder and control rod. In common with other states there was very little movement of the separation position of the boundary layer on the side of the cylinder opposite to the control rod. In this state separation of the upper boundary layer moved to just beyond the angular position of the control rod. There was no significant change in the drag of the main cylinder but it developed a small lift force. In State II,  $\theta = 120^\circ$  to  $125^\circ$ , there is a large delay in the separation of the cylinder boundary layer and an energetic jet forms that follows the contour of the main cylinder. While there is a reduction of about 10% in the drag coefficient, a mean lift coefficient of about  $\overline{C}_L \approx 0.55$  develops. As a result of the high lift the total mean force acting on the combined body of cylinder and control rod is greater than the mean drag on the bare cylinder. However, fluctuating lift was substantially reduced for  $\theta = 120^\circ$ , with the RMS of lift force fluctuations decreasing by more than 80% due to the weakening of vortex shedding. Over the range  $135^\circ \leq \theta \leq 180^\circ$ , the control rod remains within the recirculation zone of the main cylinder and this is the main characteristic of State III. The separation points and the drag coefficient are close to those of the bare cylinder and with the control rod in the recirculation zone it experiences a small negative drag force.

A finding regarding the flow structure is that the free shear layer arising from separation of the upper boundary layer on the cylinder is deflected by the control rod and not split as observed by other investigators, where the control rod was placed relatively further from the main cylinder. In State I the free shear layer passes between the cylinder and the control rod whereas in State III the free shear layer passes over the control rod. In State II the boundary layer appears to remain attached until well after passing below the control rod, in a manifestation of the Coandă effect.

A bi-stable case exists for  $\theta = 130^\circ$  where the flow switches between Bi-Stable A, with characteristics very close to State III and Bi-Stable B, where there is delayed final separation, similar to State II. It was found that a small change in the control rod's angular position, of about  $\pm 1^\circ$ , would influence the time the flow was in one or other of

Bi-Stable states A and B. Further research is required to confirm that the instability is due to the formation and bursting of a separation bubble.

## 5. Acknowledgements

We gratefully acknowledge support of the RCGI Research Centre for Gas Innovation, hosted by the University of Sao Paulo and sponsored by FAPESP São Paulo Research Foundation (2014/50279-4) and Shell Brasil, and the support of ANP Brazil's National Oil, Natural Gas and Biofuels Agency through the R&D levy regulation. M.M.Cicolin is thankful for the support of CNPq (201176/2018-1).

## 6. Declaration of Interests

The authors report no conflict of interest.

## Appendix A. OMD Decomposition

Dynamic mode decomposition (DMD) relies on the basic idea that there is a linear dependency, approximately constant throughout the sampling period, between successive velocity-field snapshots, that can be written as:

$$\begin{aligned}\mathbf{v}_{\mathbf{n}+1} &= \mathbf{A}\mathbf{v}_{\mathbf{n}}, \\ \mathbf{A} &\in \mathbb{R}^{p \times p}\end{aligned}\tag{A 1}$$

where  $\mathbf{v}_{\mathbf{n}}$  is an arbitrary snapshot having length denoted by  $p$ , which corresponds to the total number of vectors in the PIV vector field, and  $\mathbf{A}$  represents the underlying linear system. The DMD algorithm estimates the dynamic properties of  $\mathbf{A}$  and its successful adaptation relies on having a sufficiently large ensemble of snapshots. Optimal mode decomposition (OMD) estimates the properties of  $\mathbf{A}$  by replacing it with its low rank form  $\mathbf{LML}^T$  and solving an optimisation problem for both  $L$  and  $M$ . For a series of  $N$  snapshots, the problem becomes:

$$\begin{aligned}\min \quad & \left\| [\mathbf{v}_2, \dots, \mathbf{v}_N] - \mathbf{LML}^T [\mathbf{v}_1, \dots, \mathbf{v}_{N-1}] \right\|^2 \\ \text{subject to } & \mathbf{LL}^T = \mathbf{I}, \quad \mathbf{L} \in \mathbb{R}^{p \times r}, \quad \mathbf{M} \in \mathbb{R}^{r \times r}\end{aligned}\tag{A 2}$$

The OMD eigenvalues ( $\lambda^*$ ) are then defined as:

$$\lambda_n^* = \frac{\log \lambda_n(M)}{\Delta t_{acq}}\tag{A 3}$$

where  $\lambda_n(M)$  are the eigenvalues of the matrix  $\mathbf{M}$  and  $\Delta t_{acq} = 1/f_{acq}$  is the period between two consecutive velocity fields. There is one OMD mode associated with each  $\lambda_n^*$ :

$$\Phi_{\mathbf{n}}^* = \mathbf{Lz}_{\mathbf{n}}\tag{A 4}$$

where  $\mathbf{Lz}_{\mathbf{n}}$  is an eigenvector corresponding to the eigenvalue  $\lambda_n(M)$ . A low-order model (LOM) representation of the velocity fields is then given by:



$$\mathbf{v}_{\text{LOM}} = \sum_{n=1}^r c_n \Phi_{\mathbf{n}}^* e^{\lambda_n^*} \quad (\text{A } 5)$$

where  $c_n$  are the coefficients associated with the OMD modes. Further details about OMD/DMD methods can be found in Wynn *et al.* (2013) and its use to extract coherent modes in flows forced simultaneously by multiple bluff bodies at multiple different length scales in Baj *et al.* (2015). The low order representation of the velocity fields using OMD fields can be seen as a “smart” dynamical filter, as it keeps the structures more relevant to the dynamics of the flow regardless of their energy content, i.e the velocities are not filtered in relation to their size or time scale but considering their dynamic relevance to the flow.

## REFERENCES

- BAJ, P., BRUCE, P.J.K. & BUXTON, O.R.H. 2015 The triple decomposition of a fluctuating velocity field in a multiscale flow. *Physics of Fluids* **27**, 075104.
- BAJ, P. & BUXTON, O.R.H. 2017 Interscale energy transfer in the merger of wakes of a multiscale array of rectangular cylinders. *Physical Review Fluids* **2** **114607**.
- BEARMAN, P.W. 1984 Vortex shedding from oscillating bluff bodies. *Annual Review of Fluid Mechanics* **16**, 195–222.
- BINGHAM, C., MORTON, C. & MARTINUZZI, R.J. 2018a Influence of control cylinder placement on vortex shedding from a circular cylinder. *Experiments in Fluids* **59**, 158.
- BINGHAM, C., RAIBAUDO, C., MORTON, C. & MARTINUZZI, R.J. 2018b Suppression of fluctuating lift on a cylinder via evolutionary algorithms: Control with interfering small cylinder. *Physics of Fluids* **30**, 127104.
- CHOI, H., JEON, W.P. & KIM, J. 2008 Control of flow over a bluff body. *Annual Review of Fluid Mechanics* **40**, 113–139.
- CICOLIN, M.M., SERSON, D., ASSI, G.R.S. & MENEGHINI, J.R. 2018 Experimental and numeric study of the control of flow over a circular cylinder using control rods. *7th Conference on Bluff Body Wakes and Vortex-Induced Vibrations*.
- DALTON, C., XU, Y. & OWEN, J.C. 2001 The suppression of lift on a circular cylinder due to vortex shedding at moderate reynolds numbers. *Journal of Fluids and Structures* **15**, 617–628.
- DIPANKAR, A., SENGUPTA, T.K. & TALLA, S.B. 2007 Suppression of vortex shedding behind a circular cylinder by another control cylinder at low reynolds numbers. *journal of Fluid Mechanics* **573**, 171–190.
- FAGE, A. & WARSAP, J.H. 1929 The effects of turbulence and surface roughness on the drag of a circular cylinder. *Technical Report Ae 429 - Aeronautical Research Committee, London*.
- GERRARD, J.H. 1966 The mechanics of the formation region of vortices behind bluff bodies. *J. Fluid Mech.* **25**, 401–413.
- GRANDEMANGE, M. 2013 Analysis and control of three-dimensional turbulent wakes : from axisymmetric bodies to road vehicles. PhD thesis, ENSTA ParisTech.
- MITTAL, S. & RAGHUVANSHI, A. 2001 Control of vortex shedding behind circular cylinder for flows at low reynolds numbers. *International Journal for Numerical Methods in Fluids* **35**, 421–447.
- NORBERG, C. 2003 Fluctuating lift on a circular cylinder: review and new measurements. *Journal of Fluids and Structures* **17** (1), 57 – 96.
- PAREZANOVIC, V. & CADOT, O. 2009 The impact of a local perturbation on global properties of a turbulent wake. *Physics of Fluids* **21**, 071071.
- PAREZANOVIC, V. & CADOT, O. 2012 Experimental sensitivity analysis of the global properties of a two-dimensional turbulent wake. *J. Fluid Mech.* **693**, 115–149.
- PAREZANOVIC, V., MONCHAUX, ROMAIN & CADOT, O. 2015 Characterization of the turbulent

- bistable flow regime of a 2d bluff body wake disturbed by a small control cylinder. *Experiments in Fluids* **56-12**, 1–8.
- REICHL, P., HOURIGAN, K. & THOMPSON, M.C. 2005 Flow past a cylinder close to a free surface. *Journal of Fluid Mechanics* **533**, 269–296.
- RODRÍGUEZ-LÓPEZ, EDUARDO, BRUCE, PAUL J. K. & BUXTON, OLIVER R. H. 2016 Near field development of artificially generated high reynolds number turbulent boundary layers. *Phys. Rev. Fluids* **1**, 074401.
- ROSHKO, A. 1954 On the development of turbulent wakes from vortex streets. *Report 1191 - National advisory Committee for Aeronautics* **1191**.
- SAKAMOTO, H. & HANIU, H. 1994 Optimum suppression of fluid forces acting on a circular cylinder. *Journal of Fluids Engineering* **116**, 221–227.
- SAKAMOTO, H., TAN, K. & HANIU, H. 1991 An optimum suppression of fluid forces by controlling a shear layer separated from a square prism. *Journal of Fluids Engineering* **113**, 183–189.
- SCHMID, P.J. 2010 Dynamic mode decomposition of numerical and experimental data. *J. Fluid Mech.* **656**, 5–28.
- STRYKOWSKI, P.J. & SREENIVASAN, R. 1990 On the formation and suppression of vortex ‘shedding’ at low reynolds numbers. *J. Fluid Mech.* **218**, 71–107.
- SZEPESSY, S. & BEARMAN, P.W. 1992 Aspect ratio and end plate effects on vortex shedding from a circular cylinder. *Journal of Fluid Mechanics* **234**, 191–217.
- WESTERWEEL, J. & SCARANO, F. 2005 Universal outlier detection for piv data. *Experiments in Fluids* **39**, 1096–1100.
- WILLIAMSON, C.H.K. 1996 Vortex dynamics in the cylinder wake. *Annual Review of Fluid Mechanics* **28**, 477–539.
- WYNN, A., PEARSON, D.S., GANAPATHISUBRAMANI, B. & GOULART, P.J. 2013 Optimal mode decomposition for unsteady flows. *J. Fluid Mech.* **733**, 473–503.
- YILDIRIM, I., RINDT, C. C. M. & STEENHOVEN, A. A. 2010 Vortex dynamics in a wire-disturbed cylinder wake. *Physics of Fluids* **22**, 094101.
- ZDRAVKOVICH, M. 1997 *Flow around circular cylinders, Vol. I: Fundamentals..* Oxford Science Publications.